



ATLAS NOTE

August 6, 2014

**1 ATL-COM-2014-051: Search for the Production of a Standard Model
2 Higgs Boson produced in association with a Vector Boson and decaying to
3 a pair of b-quarks**

4 F. Ahmadov¹, Da Palma, A. M.⁷, L. Alio², B.M.M. Allbrooke³, T. Bristow⁴, D. Buescher⁵, A.
5 Buzatu⁶, Y. Coadou², P. Conde Muio⁷, C. Debenedetti⁸, Y. Enari⁹, G. Facini¹⁰, W. Fisher¹¹, P.
6 Francavilla¹², G. Gaycken¹³, R. Goncalo⁷, G. Gonzalez Parra¹⁴, H.M. Gray¹⁵, J.F. Grivaz¹⁶, C.
7 Gwilliam¹⁷, S. Hageböck¹³, G. Halladjian¹¹, M. Jackson¹⁷, D. Jamin¹⁸, R. Jansky¹⁹, K.
8 Kiuchi²⁰, V. Kostyukhin¹³, K. Lohwasser²¹, D. Lopez Mateos²², U. Mallik²³, J. Maneira⁷, G.
9 Marchiori¹², M. Martinez Perez¹⁴, A. Mehta¹⁷, K. Mercurio²², K. Mochizuki², N. Morange²³,
10 Y. Ming²⁴, P. Mullen⁶, Y. Nagai², J. Nielsen⁸, I. Ochoa²⁵, A. Palma⁷, C. Pandini¹², R. Pedro⁷,
11 G. Piacquadio²⁶, M. Proissl⁴, T. Ravenscroft⁶, P. Rose⁸, T. Scanlon²⁵, E. Schopf¹³, S. Shaw¹¹,
12 B. Smart⁴, V. Sorin¹⁴, M. Sousa⁷, F. Sforza²⁷, J. Therhaag¹³, P.D. Thompson³, L. Vacavant², J.
13 Wang²¹, C. Wang^{18,28}, S. Wang¹⁸, C. Weiser⁵, R. Zaidan²³, L. Zhang¹⁸

14 ¹JINR

15 ²CPPM Marseille

16 ³Birmingham

17 ⁴Edinburgh

18 ⁵University of Freiburg

19 ⁶University of Glasgow

20 ⁷LIP

21 ⁸Santa Cruz

22 ⁹University of Tokyo

23 ¹⁰University of Chicago

24 ¹¹Michigan State University

25 ¹²LPNHE

26 ¹³Bonn

27 ¹⁴Barcelona

28 ¹⁵*CERN*
29 ¹⁶*LAL*
30 ¹⁷*Liverpool*
31 ¹⁸*Academica Sinica*
32 ¹⁹*Innsbruck*
33 ²⁰*Tsukuba*
34 ²¹*DESY*
35 ²²*Harvard*
36 ²³*University of Iowa*
37 ²⁴*Wisconsin*
38 ²⁵*UCL*
39 ²⁶*SLAC*
40 ²⁷*MPI, Munich*
41 ²⁸*Nanjing University*

42 Abstract

43 This note describes the dijet mass and multivariate VH(bb) analyses for the ATLAS Run
44 I Publication. It includes discussion of the Monte Carlo simulation samples used, object
45 and event selection, the accuracy to which the backgrounds are modeled, the systematic
46 uncertainties and the statistical treatment used to extract the signal strength.

47 **Contents**

48	1 Introduction	29
49	2 Updates since summer 2013	30
50	3 Data selection and event reconstruction	31
51	3.1 Introduction on the data and Monte Carlo simulation.	31
52	3.2 Object Definition	32
53	3.2.1 Lepton	32
54	3.2.2 Jet	35
55	3.2.3 b -Jet	37
56	3.2.4 E_T^{miss} and track-based missing transverse momentum	37
57	3.2.5 Overlap Removal	39
58	3.3 Event Selection	40
59	3.3.1 Event Cleaning	40
60	3.3.2 Trigger Selection	41
61	3.3.3 Lepton Selection	41
62	3.3.4 Jet Selection	41
63	3.4 Event Kinematics Selection	44
64	3.5 Dijet Mass Resolution and the Kinematic Fit	45
65	3.5.1 Energy corrections to the selected b -jets	45
66	3.5.2 Kinematic Fit	48
67	4 VH\rightarrowbb: Signal Characterization	50
68	4.1 Simulation	50
69	4.1.1 qq and gg Initiated Production	50
70	4.1.2 NLO Electroweak Differential Correction	51
71	4.2 Theoretical Uncertainties	51
72	4.2.1 Inclusive Cross Section	51
73	4.2.2 Acceptance and p_T^V	53
74	5 Backgrounds	56
75	5.1 Vector boson+jets	58
76	5.1.1 Z+jets Modeling, Corrections and Systematic Uncertainties	60
77	5.1.2 W+jets modeling, correction and systematics	65
78	5.2 $t\bar{t}$ and single-top	74
79	5.2.1 $t\bar{t}$ modeling, corrections and systematics	74
80	5.2.2 Single-top modeling and systematics	82
81	5.3 Diboson	86
82	5.3.1 Uncertainties in the Modeling of the Diboson Processes	86
83	5.4 Multijet and non-collision background	91
84	5.4.1 0-lepton	91
85	5.4.2 2-lepton	91
86	5.4.3 1-lepton	91

Not reviewed, for internal circulation only

Not reviewed, for internal circulation only

87	6 Multivariate analysis	95
88	6.1 Input variables	95
89	6.2 Boosted Decision Tree: Setup and Training	100
90	6.2.1 Algorithm Description	100
91	6.2.2 Boosting	100
92	6.2.3 Overtraining	101
93	6.2.4 Parameter Optimization	103
94	6.3 The correlations between input variables and output variables	105
95	6.4 MVA for the diboson and for the other mass points	107
96	7 Experimental Systematic uncertainties	109
97	7.1 Experimental Systematics	109
98	7.1.1 Luminosity and pile up	109
99	7.1.2 Electrons	109
100	7.1.3 Muons	109
101	7.1.4 E_T^{miss} Trigger	110
102	7.1.5 Jets	110
103	7.1.6 Missing Transverse Energy	111
104	7.1.7 Flavor Tagging	111
105	7.2 Smoothing	112
106	8 Statistical model and Systematic Uncertainties	113
107	8.1 Likelihood Definition: Variables and Regions	113
108	8.2 Likelihood Philosophy	115
109	8.3 Systematics Uncertainties and Nuisance Parameters	116
110	8.3.1 Naming Conventions	116
111	8.3.2 Signal Specific Nuisance Parameters	117
112	8.3.3 V+jets Specific Nuisance Parameters	118
113	8.3.4 $t\bar{t}$ Specific Nuisance Parameters	118
114	8.3.5 Single Top Specific Nuisance Parameters	120
115	8.3.6 Diboson Specific Nuisance Parameters	120
116	8.3.7 Multijet Specific Nuisance Parameters	120
117	8.3.8 Experimental Nuisance Parameters	120
118	8.4 Output Transform	123
119	8.4.1 General description	123
120	8.5 Pruning of the Systematic Uncertainties	126
121	8.6 Understanding the Likelihood	128
122	8.6.1 Dijet Mass Analysis Fit Studies	128
123	8.6.2 MVA Analysis Fit Studies	136
124	8.6.3 Comparison of Dijet Mass and MVA Analysis Fits	144
125	8.6.4 Nuisance Parameter Ranking Plots	149
126	8.7 Dijet Mass Analysis Post Fit Plots	154
127	8.7.1 Normal binning	164
128	8.7.2 Post fit b-tagging for the m_{jj} shape analysis	174
129	8.8 MVA background-only post fit plots	176
130	8.8.1 Post fit b-tagging for the MVA analysis	180
131	8.9 Compatibility between the m_{bb} shape analysis and the MVA analysis	182

Not reviewed, for internal circulation only

132	9 Results	184
133	9.1 Nominal results	184
134	9.2 Cross-checks	186
135	A E_T^{miss} trigger	195
136	A.1 Emulation of the BGRP7 in the Monte Carlo for the EF_xe80T_tlcw_loose trigger	196
137	A.2 Trigger efficiency and interdependence with offline variables	198
138	A.2.1 Dependence of the E_T^{miss} trigger efficiency on kinematic variables entering in the multivariate analysis	199
139	A.2.2 Trigger efficiency parametrization	202
140	A.3 E_T^{miss} trigger data driven scale factors	205
142	B Delayed stream	206
143	B.1 Introduction to delayed stream	206
144	B.2 Delayed stream E_T^{miss} trigger efficiency and scale factor	206
145	B.3 E_T^{miss} trigger bias	206
146	B.4 Apply delayed stream in 0-lepton study	207
147	B.5 Mis-modelling issue in 0-lepton analysis	208
148	C Low E_T^{miss} analysis for Zero Lepton Channel	215
149	C.1 Event selection	215
150	C.2 QCD rejection and estimation	215
151	C.3 Mis-modelings	218
152	C.4 Sensitivity gain and prospect with delayed trigger	218
153	D E_T^{miss} trigger for 1 lepton events	220
154	D.1 E_T^{miss} triggered muon events	220
155	D.2 E_T^{miss} trigger efficiency and scale factor	220
156	D.3 QCD multi-jet background estimation	220
157	D.4 Sensitivity gain	220
158	E Electron Isolation	228
159	E.1 Tag and Probe Algorithm	228
160	E.2 Results	229
161	F Muon isolation	230
162	F.1 Results	230
163	G Global sequential calibration	232
164	G.1 GSC validation analysis	232
165	G.1.1 Monte Carlo samples	232
166	G.1.2 Event and jet selection	232
167	G.1.3 Calculation of energy scale and resolution	233
168	G.2 GSC performance	233
169	G.2.1 Energy scale of b -jets	233
170	G.2.2 Energy resolution for b -jets	234
171	G.2.3 Closure tests for b -jets	234

Not reviewed, for internal circulation only

172	H Muon-Jet Overlap Removal	237
173	H.1 Characterization of the muons overlapping jets	237
174	H.2 Studies on the strategies to solve the muon-jet overlap	238
175	I Signal modeling	241
176	J Z+jet Modeling	245
177	J.1 Effect of Strict Jets Cuts	245
178	J.2 Determination of the data-driven corrections and systematics	245
179	J.3 Comparison with other Monte Carlo samples	246
180	K W+jet Modeling	250
181	K.1 $\Delta\phi$ Correction Derivation	250
182	K.2 $\Delta\phi$ Correction Usage	256
183	L W+Heavy-Flavor Modeling	257
184	L.1 Monte-Carlo samples	257
185	L.1.1 aMC@NLO sample	258
186	L.2 Uncertainties considered in the fit	258
187	L.3 W+Heavy-Flavor Modeling for MVA variables	262
188	M Single-top modeling	272
189	M.1 t-channel	272
190	M.2 s-channel	282
191	M.3 Wt	287
192	N $t\bar{t}$ modeling	292
193	N.1 m_{bb} systematic	292
194	N.2 E_T^{miss} systematic	294
195	N.3 top p_T reweighting of ALPGEN+PYTHIA	295
196	N.4 The 2-to-3-jet and high-to-low- p_T^W uncertainties	296
197	N.5 Flavor compositions of the $t\bar{t}$ generators	297
198	N.6 Generator variations of the BDT input variables	299
199	O Top Modeling from EPS	308
200	O.1 Top Composition	308
201	P Diboson modeling	309
202	P.1 Cross section	309
203	P.2 Modelling systematic uncertainties	309
204	P.2.1 Stewart-Tackmann estimate of perturbative uncertainties on the diboson cross-section	310
205	P.2.2 PDF and α_S uncertainties	312
206	P.2.3 Parton shower and hadronization model	313
208	Q Multi-jet background for 0-lepton analysis	330
209	Q.1 Introduction: ABCD	330
210	Q.2 Cross Checks	332
211	Q.3 Final Product	333

Not reviewed, for internal circulation only

212	R Multijet background for 1-lepton analysis	336
213	R.1 Template Overview	336
214	R.2 Multijet Rejection	336
215	R.3 Multijet Template Region	337
216	R.4 Multijet Normalization	338
217	R.5 Template Statistics: Using 1 b-tag events for the 2 b-tag regions	339
218	S Multi-jet background for 2-lepton analysis	358
219	T <i>b</i>-tagging Related Studies	360
220	T.1 Custom <i>b</i> -tagging Efficiency Maps	360
221	T.2 <i>b</i> -tagging generator dependence scale factor	366
222	T.3 truth <i>b</i> -tagging efficiency maps closure test	369
223	U Event-level Kinematic Likelihood Fit	374
224	U.1 Likelihood Model	374
225	U.2 Resolutions	375
226	U.3 Results	375
227	V Dijet Mass (m_{jj}) Distributions: Zero Lepton	378
228	W Dijet Mass (m_{jj}) Distributions: One Lepton	384
229	X Dijet Mass (m_{jj}) Distributions: Two Lepton	389
230	Y MVA Input Variable Distributions: Zero Lepton	394
231	Z MVA Input Variable Distributions: One Lepton	407
232	AAMVA Input Variable Distributions: Two Lepton	440
233	ABMVA Training Diagnostics	465
234	ACMVA optimization and the transformation D	476
235	ADMVA Distributions	479
236	AE Correlations between MVA Variables: Zero Lepton	490
237	AF Correlations between MVA Variables: One Lepton	501
238	AGCorrelations between MVA Variables: Two Lepton	522
239	AHPulls for the Individual Channels	531
240	AH.1 Dijet Mass Analysis	531
241	AH.1.1 0-lepton	531
242	AH.1.2 Pre-fit and Post-Fit for the m_{jj} shape analysis in the 0-lepton fit	536
243	AH.1.3 1-lepton	543
244	AH.1.4 Pre-fit and Post-Fit for the m_{jj} shape analysis in the 1-lepton fit	548
245	AH.1.5 2-lepton	555
246	AH.1.6 Pre-fit and Post-Fit for the m_{jj} shape analysis in the 2-lepton fit	560

Not reviewed, for internal circulation only

247	AH.2 mva	567
248	AH.2.1 0-lepton pull plots	567
249	AH.2.2 Pre-fit and Post-Fit for the mva analysis in the 0-lepton fit	572
250	AH.2.3 1-lepton pull plots	575
251	AH.2.4 Pre-fit and Post-Fit for the mva analysis in the 1-lepton fit	580
252	AH.2.5 2-lepton pull plots	583
253	AH.2.6 Pre-fit and Post-Fit for the mva analysis in the 2-lepton fit	588
254	AH.3 Dijet Mass versus mva	591
255	AH.3.1 0-lepton pull plots	591
256	AH.3.2 1-lepton pull plots	596
257	AH.3.3 2-lepton pull plots	601
258	AI Postfit p_T^V Spectrums	606
259	AI.1 Dijet Mass p_T^V	606
260	AI.2 mva p_T^V	606
261	AJ Yield Tables	619
262	AJ.1 Dijet Mass Analysis: Prefit	619
263	AJ.2 Dijet Mass Analysis: Postfit	632
264	AJ.3 Dijet Mass Analysis: Postfit over Prefit	645
265	AJ.4 mva Analysis: Prefit	658
266	AJ.5 mva Analysis: Postfit	662
267	AJ.6 mva Analysis: Postfit over Prefit	666
268	AKCombining 7 TeV and 8 TeV results	670
269	AK.1 Consistency of the results	670
270	AK.2 Pulls on the combination	673
271	AK.3 Post-fit 2011 distributions	673
272	ALStudies for the diboson VZ fit	684
273	AL.1 Ranking plots for mva diboson analysis	684
274	AL.2 Pulls for mva diboson analysis	687
275	AL.3 Correlation Plots for the mva diboson fit	687
276	AL.4 Ranking plots for m_{jj} shape diboson analysis	687
277	AL.5 Pulls for m_{jj} shape diboson analysis	697
278	AL.6 Correlation Plots for the m_{jj} diboson fit	697
279	AL.7 Correlation between diboson and Higgs signal strength	705
280	AL.8 Diboson MVA post fit plots	708
281	AL.9 Diboson dijet Mass Analysis Post Fit Plots	712
282	AMImpact of the BCH cleaning on the VH analysis	722
283	AM.1BCH cleaning for dummies	722
284	AM.2Samples used	722
285	AM.3Impact on selection yield	722
286	AM.4Impact on distribution shapes	723
287	AM.5Impact on b -tagging	724
288	AM.6Conclusion	724

289	ANChanges in different versions of this note	727
290	AN.1 v0.1	727
291	AN.2 v0.2	727
292	AN.3 v0.3	727
293	AN.4 v0.4	728
294	AN.5 v0.5	728
295	AN.6 v0.6	729
296	AN.7 v0.7	729
297	AN.8 What we had foreseen from version v0.6 to version v0.7	729
298	AN.9 v0.8.1	730
299	AN.10 v0.9.1	730
300	AN.11 v1.0.1	730
301	AN.12 v1.1.1	731
302	AN.13 v1.2.1	731
303	AN.14 Outstanding Specific Ed Board Requests	731
304	AOMissing	731
305	AP Package List	732

Not reviewed, for internal circulation only

306 List of Tables

307 1	Trigger table used in the 2012 data analysis.	31
308 2	Electron efficiencies for the cut-based and likelihood definitions.	32
309 3	Inclusive VH Loose, Medium and Tight lepton definitions.	34
310 4	Ordered list of jet properties used in the GSC calibration.	36
311 5	Selection criteria for tracks associated with jets.	36
312 6	Jet selection definitions.	37
313 7	MV1c versus MV1 operating points.	38
314 8	Track selection for p_T^{miss}	39
315 9	Overlap hierarchy.	40
316 10	Signal lepton analysis selection.	41
317 11	Analysis jet multiplicity requirements.	42
318 12	Event kinematic selection.	47
319 13	Muon selection for muon-in-jet correction.	47
320 14	Inclusive cross sections and related uncertainties for WH production.	52
321 15	Inclusive cross sections and related uncertainties for ZH production.	52
322 16	Inclusive cross sections and related uncertainties for qq and gg initiated ZH production.	53
323 17	Parameters for linear p_T^V signal shape uncertainty.	53
324 18	Inclusive acceptance uncertainties derived from scale and PDF variations.	55
325 19	Monte Carlo programs used.	56
326 20	Monte Carlo samples and channel numbers and statistics used for the W samples	58
327 21	Monte Carlo samples and channel numbers and statistics used for the Z samples.	59
328 22	Simple sample composition for Z +jets modeling studies.	60
329 23	Summary of Z +jet specific samples used to checks the background modelling	61
330 24	Normalization change from W +jets $\Delta\phi$ corrections.	66
331 25	V +jets samples considered for systematic variations.	71
332 26	Summary of W +jet specific samples used to checks the background modelling	73
333 27	Monte Carlo samples and channel numbers and statistics used for top samples.	74
334 28	$t\bar{t}$ jet composition in the 1-lepton analysis.	75
335 29	$t\bar{t}$ jet composition in the 1-lepton multivariate analysis.	75
336 30	Summary of $t\bar{t}$ specific samples used to checks the background modelling	81
337 31	Top samples considered for systematics.	81
338 32	Top samples considered for systematics.	82
339 33	Top samples considered for systematics.	83
340 34	Systematics for the single top	84
341 35	Monte Carlo generator used for the modelling of the diboson processes and correspondent MC channel number, cross sections and number of generated events.	86
343 36	Main settings for the MCFM software used to compute the cross-sections for the diboson processes.	88
345 37	PDF+ α_S systematic uncertainties for ZZ, WZ and WW processes, in the 2-jet and 3-jet categories.	88
347 38	Probative systematics on σ_2 from the C_1 term of the covariance matrix across the different p_T^V bins.	89
349 39	Perturbative systematics on σ_2 from the C_2 term of the covariance matrix across the different p_T^V bins.	89
351 40	Perturbative systematics on $\sigma_{\geq 3}$ from the C_2 term of the covariance matrix across the different p_T^V bins.	90

Not reviewed, for internal circulation only

353	41	Summary of the diboson modelling systematic uncertainties, with the name of the corre-		
354		spondent nuisance parameter.		90
355	42	Normalization nuisance parameters for multijet entering the fit. The 0-lepton uncertain-		
356		ties are correlated between regions.		91
357	43	Summary of multijet specific samples used to checks the background modelling		93
358	44	Normalization nuisance parameters for multijet entering the fit. The 0-lepton uncertain-		
359		ties are correlated between regions. All 2-lepton uncertainties are correlated except for		
360		when the top $e - \mu$ control region is included in the standalone fit.		94
361	45	Variable used to train the multivariate discriminant.		96
362	46	BDT parameters.		103
363	47	Regions used in profile likelihood		114
364	48	Summary of signal specific nuisance parameters.		117
365	49	Summary of $Z + \text{jet}$ specific nuisance parameters.		118
366	50	Summary of $W + \text{jet}$ specific nuisance parameters.		119
367	51	Summary of $t\bar{t}$ specific nuisance parameters.		119
368	52	Summary of single top specific nuisance parameters.		120
369	53	The nuisance parameters used in the fit to parametrize the systematics on the diboson		
370		backgrounds. For VVJ ℓ PDFAlphaPt, the two values represent the normalization change		
371		in 2/3Jet region respectively. S=“Shape”, and SO=“Shape Only” meaning explicitly the		
372		normalization of each N-jet/M-b-tag/ p_T^V region is preserved while the shape is varied.		121
373	54	Normalization nuisance parameters for multijet entering the fit. The 0-lepton uncertain-		
374		ties are correlated between regions. [†] All 2-lepton uncertainties are correlated except for		
375		when the top $e - \mu$ control region is included in the 2-lepton standalone fit.		121
376	55	Summary of Combined Performance and experimental systematics.		122
377	56	Variable used to train the multivariate discriminant.		125
378	57	Correlation between the dijet mass and MVA analyses		182
379	58	The fitted numbers of signal and background events and the observed numbers of events		
380		after MVA selection for the most sensitive four bins in figure 94a. These numbers are for		
381		the 8 TeV dataset, corresponding to an integrated luminosity of 20.3 fb^{-1}		187
382	59	E_T^{miss} trigger table used in the 2012 data analysis.		195
383	60	Summary of E_T^{miss} triggers used in the analysis. The threshold values are in GeV.		195
384	61	Data period, integrated luminosity and threshold at each level (in GeV)		206
385	62	Fitting parameters at each level of trigger for $Z \rightarrow \mu\mu$ and $W \rightarrow \mu\nu$ samples (MC)		209
386	63	signal acceptance gain after applying trigger EF_xe60_tclcw_loose_delayed instead of		
387		nominal triggers		210
388	64	Signal significance gain after applying trigger EF_xe60_tclcw_loose_delayed over the		
389		trigger EF_xe80_tclcw_loose		211
390	65	Low E_T^{miss} 0-lepton selection cuts.		215
391	66	1 lepton significance with E_T^{miss} triggered events.		227
392	67	MC samples used for GSC studies.		232
393	68	Signal acceptance increase from the improved <i>muon</i> overlap removal.		240
394	69	2-lepton 3-jet yield changes from relaxed jet cuts.		245
395	70	0-tag yield comparison for 2-lepton events.		246
396	71	Functions and parameters used for $Z + \text{jets}$ data-driven corrections and systematics.		246
397	72	ALPGEN samples considered for cross-check.		247
398	73	ALPGEN/SHERPA jet heavy-flavor fraction comparison in 2-lepton 2-tag events.		247
399	74	ALPGEN/SHERPA heavy-flavor jet multiplicity comparison in 2-lepton 2-tag events.		247
400	75	Functions and parameters used for $W + \text{jets}$ $\Delta\phi$ correction.		250

Not reviewed, for internal circulation only

401	76	Normalization change for $W+jets$ $\Delta\phi$ corrections.	255
402	77	MC samples used in the estimation of the modeling uncertainties. All samples were centrally-produced with the exception of aMC@NLO and Sherpa $W+b\bar{b}$	257
403	78	MC samples used in the estimation of the flavor composition, at reconstruction-level.	258
404	79	List of electroweak physical parameters used in the generation of aMC@NLO events with the CT10 PDF set. Dimension quantities given in GeV.	258
405	80	Top samples considered for systematics.	272
406	81	$t\bar{t}$ 3-to-2-jet and high-to-low p_T^W uncertainties.	299
407	82	$t\bar{t}$ jet composition of all generators in the 1-lepton analysis.	300
408	83	$t\bar{t}$ jet composition in EPS.	308
409	84	Comparison between diboson cross-sections provided by POWHEG and computed with MCFM.	315
410	85	Relative contribution of $gg \rightarrow VV$ processes to WW and ZZ backgrounds.	315
411	86	Monte Carlo generator used for the modelling of the diboson processes and correspondent cross-sections.	315
412	87	Main settings for the MCFM software used to compute the cross-sections for the diboson processes.	316
413	88	Parton-level jet-bins definition applied on the output of the MCFM simulation. The j_1 and j_2 objects are the two jets originated by the hadronically decaying V boson, while j_3 is the extra parton produced by the NLO calculation.	316
414	89	Perturbative systematics on σ_2 from the C_1 term of the covariance matrix across the different p_T^V bins.	316
415	90	Perturbative systematics on σ_2 from the C_2 term of the covariance matrix across the different p_T^V bins.	316
416	91	Perturbative systematics on $\sigma_{\geq 3}$ from the C_2 term of the covariance matrix across the different p_T^V bins.	319
417	92	PDF+ α_S systematic uncertainties for ZZ, WZ and WW processes, in the 2-jet and 3-jet categories.	319
418	93	0-lepton multijet closure test.	332
419	94	Event b -tagging rate cross check for 0-lepton multijet.	333
420	95	0-lepton multijet estimate results for the dijet mass analysis.	335
421	96	0-lepton multijet estimate results for the mva analysis.	335
422	97	Scale factors used for the normalization of the prefit plots	378
423	98	Variable used to train the multivariate discriminant.	476
424	99	Table of prefit yields for 0-lepton 2 and 3-jet 1-tag events in the dijet mass selection.	620
425	100	Table of prefit yields for 0-lepton 2 and 3-jet 2L-tag events in the dijet mass selection.	621
426	101	Table of prefit yields for 0-lepton 2 and 3-jet 2M-tag events in the dijet mass selection.	622
427	102	Table of prefit yields for 0-lepton 2 and 3-jet 2T-tag events in the dijet mass selection.	623
428	103	Table of prefit yields for 1-lepton 2 and 3-jet 1-tag events in the dijet mass selection.	624
429	104	Table of prefit yields for 1-lepton 2 and 3-jet 2L-tag events in the dijet mass selection.	625
430	105	Table of prefit yields for 1-lepton 2 and 3-jet 2M-tag events in the dijet mass selection.	626
431	106	Table of prefit yields for 1-lepton 2 and 3-jet 2T-tag events in the dijet mass selection.	627
432	107	Table of prefit yields for 2-lepton 2 and 3-jet 1-tag events in the dijet mass selection.	628
433	108	Table of prefit yields for 2-lepton 2 and 3-jet 2L-tag events in the dijet mass selection.	629
434	109	Table of prefit yields for 2-lepton 2 and 3-jet 2M-tag events in the dijet mass selection.	630
435	110	Table of prefit yields for 2-lepton 2 and 3-jet 2T-tag events in the dijet mass selection.	631
436	111	Table of post unconditional fit yields for 0-lepton 2 and 3-jet 1-tag events in the dijet mass selection.	633

Not reviewed, for internal circulation only

449	112	Table of post unconditional fit yields for 0-lepton 2 and 3-jet 2L-tag events in the dijet mass selection.	634
450	113	Table of post unconditional fit yields for 0-lepton 2 and 3-jet 2M-tag events in the dijet mass selection.	635
451	114	Table of post unconditional fit yields for 0-lepton 2 and 3-jet 2T-tag events in the dijet mass selection.	636
452	115	Table of post unconditional fit yields for 1-lepton 2 and 3-jet 1-tag events in the dijet mass selection.	637
453	116	Table of post unconditional fit yields for 1-lepton 2 and 3-jet 2L-tag events in the dijet mass selection.	638
454	117	Table of post unconditional fit yields for 1-lepton 2 and 3-jet 2M-tag events in the dijet mass selection.	639
455	118	Table of post unconditional fit yields for 1-lepton 2 and 3-jet 2T-tag events in the dijet mass selection.	640
456	119	Table of post unconditional fit yields for 2-lepton 2 and 3-jet 1-tag events in the dijet mass selection.	641
457	120	Table of post unconditional fit yields for 2-lepton 2 and 3-jet 2L-tag events in the dijet mass selection.	642
458	121	Table of post unconditional fit yields for 2-lepton 2 and 3-jet 2M-tag events in the dijet mass selection.	643
459	122	Table of post unconditional fit yields for 2-lepton 2 and 3-jet 2T-tag events in the dijet mass selection.	644
460	123	Table of post unconditional fit over prefit yields for 0-lepton 2 and 3-jet 1-tag events in the dijet mass selection.	646
461	124	Table of post unconditional fit over prefit yields for 0-lepton 2 and 3-jet 2L-tag events in the dijet mass selection.	647
462	125	Table of post unconditional fit over prefit yields for 0-lepton 2 and 3-jet 2M-tag events in the dijet mass selection.	648
463	126	Table of post unconditional fit over prefit yields for 0-lepton 2 and 3-jet 2T-tag events in the dijet mass selection.	649
464	127	Table of post unconditional fit over prefit yields for 1-lepton 2 and 3-jet 1-tag events in the dijet mass selection.	650
465	128	Table of post unconditional fit over prefit yields for 1-lepton 2 and 3-jet 2L-tag events in the dijet mass selection.	651
466	129	Table of post unconditional fit over prefit yields for 1-lepton 2 and 3-jet 2M-tag events in the dijet mass selection.	652
467	130	Table of post unconditional fit over prefit yields for 1-lepton 2 and 3-jet 2T-tag events in the dijet mass selection.	653
468	131	Table of post unconditional fit over prefit yields for 2-lepton 2 and 3-jet 1-tag events in the dijet mass selection.	654
469	132	Table of post unconditional fit over prefit yields for 2-lepton 2 and 3-jet 2L-tag events in the dijet mass selection.	655
470	133	Table of post unconditional fit over prefit yields for 2-lepton 2 and 3-jet 2M-tag events in the dijet mass selection.	656
471	134	Table of post unconditional fit over prefit yields for 2-lepton 2 and 3-jet 2T-tag events in the dijet mass selection.	657
472	135	Table of prefit yields for 0-lepton 2 and 3-jet events in the mva selection.	659
473	136	Table of prefit yields for 1-lepton 2 and 3-jet events in the mva selection.	660

497	137	Table of prefit yields for 2-lepton 2 and 3-jet events in the MVA selection.	661
498	138	Table of post unconditional fit yields for 0-lepton 2 and 3-jet events in the MVA selection.	663
499	139	Table of post unconditional fit yields for 1-lepton 2 and 3-jet events in the MVA selection.	664
500	140	Table of post unconditional fit yields for 2-lepton 2 and 3-jet events in the MVA selection.	665
501	141	Table of post unconditional fit over prefit yields for 0-lepton 2 and 3-jet events in the MVA selection.	667
502	142	Table of post unconditional fit over prefit yields for 1-lepton 2 and 3-jet events in the MVA selection.	668
503	143	Table of post unconditional fit over prefit yields for 2-lepton 2 and 3-jet events in the MVA selection.	669
504	144	Impact of BCH cleaning on yield after the full 0-lepton selection in data (last column) and for the signal sample for all triggers. For MC both the medium and tight BCH cleaning are given.	723
505	145	Impact of BCH cleaning on signal yield after the full 1-lepton selection.	723
506	146	Impact of BCH cleaning systematic uncertainty on yield after the full 0-lepton selection for the signal sample. The percentages shown correspond to the difference between applying the nominal BCH cleaning and the all-quark or all-gluon BCH mode.	723
507	147	List of packages	732
508			
509			
510			
511			
512			
513			
514			

Not reviewed, for internal circulation only

515 List of Figures

516 1	EM likelihood background rejection comparison.	33
517 2	Schematic of 1-lepton lepton selection.	35
518 3	Representative b -tagging scale factors.	38
519 4	b -tagging categories.	42
520 5	Truth tagging ΔR correction.	43
521 6	Generator dependence of flavor tagging for exclusive MV1c 70% OP.	44
522 7	Motivation for M_{eff} cut over E_T^{miss} and m_T^W from the MVA analysis.	46
523 8	m_T^W without a cut in the 1-lepton dijet mass analysis for $120 < p_T^W < 160$	46
524 9	Current p_T -reco correction and a comparison to the EM+JES based correction.	48
525 10	Dijet invariant mass before and after applying a kinematic likelihood fit in $ZH(125)$ simulation.	49
526 11	Leading order Feynman diagrams for quark-initiated VH production.	50
527 12	Leading order Feynman diagrams for gluon-initiated ZH production.	51
528 13	Differential NLO EW VH production correction.	52
529 14	Normalized p_T^V distribution for signal QCD scale uncertainty studies.	54
530 15	Data-driven $\Delta\phi$ correction for Z +jets events	62
531 16	p_T^Z for Z +jets events before any corrections have been applied.	63
532 17	m_{bb} systematics for Z +jets events	64
533 18	Uncorrected $\Delta\phi$ and p_T^W distributions in 1-lepton 0-tag and 1-tag events.	67
534 19	Inclusively corrected $\Delta\phi$ distributions in 1-lepton 0-tag events.	68
535 20	1-lepton 2-jet 0-tag χ^2 improvements from the $\Delta\phi$ corrections.	69
536 21	1-lepton 2-jet p_T^W distribution in 0-tag after $\Delta\phi$ correction.	70
537 22	1-lepton 2-jet $\Delta\phi$ corrections for low and high p_T^W	70
538 23	W -boson p_T distribution of 2-jet bb events at truth-level.	72
539 24	Invariant mass distribution of 2-jet bb events at truth-level. The plot on the left compares the generator predictions for the $W + b\bar{b}$ process, and the plot on the right compares the same Sherpa prediction to the nominal B-filtered sample	73
540 25	ATLAS $t\bar{t} p_T^{top}$ unfolded result.	76
541 26	$t\bar{t} m_{bb}$ systematic.	78
542 27	$t\bar{t} E_T^{\text{miss}}$ systematic.	79
543 28	$t\bar{t}$ coverage of systematic effects in the BDT output.	80
544 29	Shape systematics for the Wt-ch single top	85
545 30	Stewart-Tackmann method shape perturbative systematics on σ_2 for the $W \rightarrow l\nu$ and $Z \rightarrow q\bar{q}$ process.	89
546 31	POWHEG+Pythia8 versus Herwig comparison for the WZ diboson processes.	90
547 32	MVA Training input plot example.	98
548 33	Optimization of the input variables for the one Lepton MVA.	99
549 34	MVA overtraining plot example.	102
550 35	Optimization of the BDT parameters for the one Lepton MVA.	104
551 36	Frequency of the input variables	104
552 37	MVA correlation plot for 2 leptons	105
553 38	MVA correlation plot for 1 leptons	106
554 39	MVA optimization for different Higgs mass for Zero lepton	108
555 40	2D Expected limit as a function of the z_s and z_b parameters.	125
556 41	MVA binning transform	125
557 42	m_{bb} binning transform	125

Not reviewed, for internal circulation only

562	43	0+1+2 lepton MVA fit pulls for b and c -jet tagging.	129
563	44	0+1+2 lepton MVA fit pulls for light-jet tagging and lepton systematics.	130
564	45	0+1+2 lepton MVA fit pulls for JES.	131
565	46	0+1+2 lepton MVA fit pulls for diboson/top and W/Z.	132
566	47	0+1+2 lepton MVA fit pulls for normalization NPs.	133
567	48	0+1+2 lepton MVA fit pulls for the remaining NPs.	134
568	49	Correlation plot for the full dijet masss analysis fit.	135
569	50	0+1+2 lepton MVA fit pulls for b and c -jet tagging.	137
570	51	0+1+2 lepton MVA fit pulls for light-jet tagging and lepton systematics.	138
571	52	0+1+2 lepton MVA fit pulls for JES.	139
572	53	0+1+2 lepton MVA fit pulls for diboson/top and W/Z.	140
573	54	0+1+2 lepton MVA fit pulls for normalization NPs.	141
574	55	0+1+2 lepton MVA fit pulls for the remaining NPs.	142
575	56	Correlation plot for the full MVA analysis fit.	143
576	57	m_{jj} vs MVA pull plots for 0+1+2 fit: b - and c -jet tagging.	144
577	58	m_{jj} vs MVA pull plots for 0+1+2 fit: light-jet tagging and leptons.	145
578	59	m_{jj} vs MVA pull plots for 0+1+2 fit: Jet NPs.	146
579	60	m_{jj} vs MVA pull plots for 0+1+2 fit: Diboson and Top related uncertainties.	147
580	61	m_{jj} vs MVA pull plots for 0+1+2 fit: Normalization and residual uncertainties.	148
581	62	Ranking plots for combined dijet masss analysis.	150
582	63	Ranking plots for 0-lepton , 1-lepton and 2-leptons dijet masss analysis.	151
583	64	Ranking plots for combined MVA analysis.	152
584	65	Ranking plots for 0-lepton , 1-lepton and 2-leptons MVA analysis.	153
585	66	Post-fit dijet mass analysis plots for the 0-lepton 2-jets regions with $p_T^V < 200$ GeV.	155
586	67	Post-fit dijet mass analysis plots for the 0-lepton 3-jets regions with $p_T^V < 200$ GeV.	156
587	68	Post-fit dijet mass analysis plots for the 0-lepton regions with $p_T^V > 200$ GeV.	157
588	69	Post-fit dijet mass analysis plots for the 1-lepton 2-jets regions with $p_T^V < 200$ GeV.	158
589	70	Post-fit dijet mass analysis plots for the 1-lepton 3-jets regions with $p_T^V < 200$ GeV.	159
590	71	Post-fit dijet mass analysis plots for the 1-lepton regions with $p_T^V > 200$ GeV.	160
591	72	Post-fit dijet mass analysis plots for the 2-lepton 2-jets regions with $p_T^V < 200$ GeV.	161
592	73	Post-fit dijet mass analysis plots for the 2-lepton 3-jets regions with $p_T^V < 200$ GeV.	162
593	74	Post-fit dijet mass analysis plots for the 2-lepton regions with $p_T^V > 200$ GeV.	163
594	75	Post-fit dijet mass analysis plots for the 0-lepton 2-jets regions with $p_T^V < 200$ GeV.	165
595	76	Post-fit dijet mass analysis plots for the 0-lepton 3-jets regions with $p_T^V < 200$ GeV.	166
596	77	Post-fit dijet mass analysis plots for the 0-lepton regions with $p_T^V > 200$ GeV.	167
597	78	Post-fit dijet mass analysis plots for the 1-lepton 2-jets regions with $p_T^V < 200$ GeV.	168
598	79	Post-fit dijet mass analysis plots for the 1-lepton 3-jets regions with $p_T^V < 200$ GeV.	169
599	80	Post-fit dijet mass analysis plots for the 1-lepton regions with $p_T^V > 200$ GeV.	170
600	81	Post-fit dijet mass analysis plots for the 2-lepton 2-jets regions with $p_T^V < 200$ GeV.	171
601	82	Post-fit dijet mass analysis plots for the 2-lepton 3-jets regions with $p_T^V < 200$ GeV.	172
602	83	Post-fit dijet mass analysis plots for the 2-lepton regions with $p_T^V > 200$ GeV.	173
603	84	Post-fit unfolded b -tagging scale factors.	175
604	85	Post-fit MVA plots for high p_T^V 0-lepton events.	177
605	86	Post-fit MVA plots for 1-lepton events.	178
606	87	Post-fit MVA plots for 2-lepton events.	179
607	88	Post-fit unfolded b -tagging scale factors.	181

Not reviewed, for internal circulation only

608	89	The distribution of the difference of the signal strength for the m_{bb} shape and MVA analyses from the pseudo-data from the bootstrap technique for the combination of the 0, 1, 2 and 0+1+2 lepton channels.	183
609	90	The relation between the signal strength obtained from the m_{bb} shape and MVA analyses for the combination of the 0- and 2-lepton channels.	183
610	91	Observed (solid) and expected 95% CL cross section upper limits, normalised to the SM Higgs-boson production cross section, as a function of m_h for all channels and data taking periods combined, as obtained using the dijet mass analysis for the 7 TeV dataset and BDTs trained at each individual mass for the 8 TeV dataset. The expected upper limit is given for the background-only hypothesis (dashed) and with the injection of a SM Higgs-boson signal at a mass of 125 GeV (dotted). The green and yellow bands represent the 1σ and 2σ ranges of the expectation in the absence of a signal.	185
611	92	Observed (solid) and expected p_0 values as a function of m_h for all channels and data taking periods combined, as obtained using the dijet mass analysis for the 7 TeV dataset and BDTs trained at each individual mass for the 8 TeV dataset. The expected p_0 values are given for the background-only hypothesis (dashed) and with the injection of a SM Higgs-boson signal at a mass of 125 GeV (dotted).	185
612	93	The fitted values of the Higgs-boson signal-strength parameter μ for $m_h = 125$ GeV: (a) for the 7 TeV and 8 TeV datasets; (b) for the 0-, 1- and 2-lepton channels, with the 7 and 8 TeV datasets combined; and (c) for the WH and ZH processes, with the 7 and 8 TeV datasets combined. The result of the combination of all channels and all datasets is shown in all. The individual μ -values for the lepton channels (for the $(W/Z)H$ processes) are obtained from a simultaneous fit with the signal strength for each of the lepton channels (for each of the WH and ZH processes) floating independently.	186
613	94	Event yields as a function of $\log(S/B)$ for data, background and Higgs-boson signal with $m_h = 125$ GeV for the (a) 8 TeV data and (b) 7 TeV data. Final-discriminant bins in all signal regions are combined into bins of $\log(S/B)$. The signal S and background B yields are expected and fitted, respectively. The Higgs-boson signal contribution is shown as expected for the SM cross section (indicated as $\mu = 1.0$). The ratio of the data to the background-only prediction is also shown. The red line indicates the ratio of the prediction for signal ($\mu = 1$) and background to the background-only prediction.	187
614	95	The distribution of m_{bb} in data after subtraction of all backgrounds except for the diboson processes, as obtained with the dijet-mass analysis for the (a) 8 TeV and (b) 7 TeV data. The contributions from all lepton channels, p_T^V intervals, number-of-jets and 2-tag b -tagging categories are summed weighted by their respective values of expected Higgs-boson-signal over fitted background ratio. The contribution of the associated WH and ZH production of a SM Higgs boson with $m_h = 125$ GeV is shown as expected for the SM cross section (indicated as $\mu = 1.0$). The size of the combined statistical and systematic uncertainty on the fitted background is indicated by the hashed band.	188
615	96	The fitted values of the diboson signal strength μ_{VZ} for (a) the 7 TeV, 8 TeV and combined datasets, and (b) for the three lepton channels separately and combined, for the combined dataset. The MVA is used for the 8 TeV data. The individual μ_{VZ} -values for the lepton channels are obtained from a simultaneous fit with the signal strength for each floating independently.	189
616	97	Comparison between the events belonging to the BGRP7 (red) and the rest of the events (blue) in the Monte Carlo simulation for some of the variables (number of jets, inclusive jet p_T , inclusive jet ϕ , inclusive jet η).	197
617	98	selected $W \rightarrow \mu\nu$ offline E_T^{miss} distribution, data(cross points) and MC(colored histogram)	198
618			
619			
620			
621			
622			
623			
624			
625			
626			
627			
628			
629			
630			
631			
632			
633			
634			
635			
636			
637			
638			
639			
640			
641			
642			
643			
644			
645			
646			
647			
648			
649			
650			
651			
652			
653			
654			
655			

Not reviewed, for internal circulation only

656 657 658 659 660 661 662 663 664 665 666 667 668 669 670 671 672 673 674 675 676 677 678 679 680 681 682 683 684 685 686 687 688 689 690 691 692 693 694 695 696 697 698 699 700 701 702	<p>99 selected $Z \rightarrow \mu\mu$ offline E_T^{miss} distribution, data(cross points) and MC(colored histogram) 198</p> <p>100 calculated xe80_tclcw_loose efficiency correlation between E_T^{miss} (abscissa) and sum of leading two jet p_T using Sherpa $Z \rightarrow \mu\mu$ Monte Carlo. The four plots, are the L1 (top, left), the L2 (top, right), the EF (bottom left) efficiencies, and the combination of the three (bottom right). 199</p> <p>101 calculated EF_xe80_tclcw_loose efficiency correlation between E_T^{miss} (abscissa) and leading jet p_T using Sherpa $Z \rightarrow \mu\mu$ Monte Carlo. The four plots, are the L1 (top, left), the L2 (top, right), the EF (bottom left) efficiencies, and the combination of the three (bottom right). 200</p> <p>102 calculated EF_xe80_tclcw_loose efficiency correlation between E_T^{miss} (abscissa) and 2nd leading jet p_T using Sherpa $Z \rightarrow \mu\mu$ Monte Carlo. The four plots, are the L1 (top, left), the L2 (top, right), the EF (bottom left) efficiencies, and the combination of the three (bottom right). 200</p> <p>103 calculated EF_xe80_tclcw_loose efficiency correlation between E_T^{miss} (abscissa) and important variables (first row: left m_{jj}, right $\min(\Delta\phi(E_T^{\text{miss}}, \text{jet}))$; second row: $\Delta\phi(\text{jet}, \text{jet})$) for the analysis using Sherpa $Z \rightarrow \mu\mu$ Monte Carlo. The plots, showing the combination of the L1, L2, EF efficiencies, are obtained after the selection cut described in this appendix has been applied. 201</p> <p>104 Comparison of 2012 data and MC E_T^{miss} distributions. Offline E_T^{miss} distribution of selected $Z \rightarrow \mu\mu$ events (top left). L1 E_T^{miss} distribution of selected $Z \rightarrow \mu\mu$ events (top right). L2 E_T^{miss} distribution after L1 trigger with 40 GeV threshold (bottom left). EF E_T^{miss} distribution after L2 trigger with 45 GeV threshold (bottom right). 202</p> <p>105 EF_xe80_tclcw_loose efficiency calculated using Sherpa $W \rightarrow \mu\nu$ MC events. The efficiency is shown for each trigger level: L1 (top left), L2 (top right), EF (bottom left) and for the overall(bottom right). 203</p> <p>106 Trigger Efficiency turn on estimate using $W(\rightarrow \mu\nu) + \text{jets}$ and $Z(\rightarrow \mu\mu) + \text{jets}$ events for data (top left), Alpgen (top right) and Sherpa (bottom). 204</p> <p>107 Calculated scale factor for EF_xe80_tclcw_loose from the $W \rightarrow \mu\nu$, and the $Z \rightarrow \mu\mu$ samples. 205</p> <p>108 Trigger efficiencies for each level and for over all (bottom right) of trigger EF_xe60_tclcw_loose_delayed using $W \rightarrow \mu\nu + 2$ jets Sherpa events. 207</p> <p>109 Trigger efficiencies for each level and for over all (bottom right) of trigger EF_xe60_tclcw_loose_delayed using $Z \rightarrow \mu\mu + 2$ jets Sherpa events. 208</p> <p>110 Correlation of trigger efficiencies between E_T^{miss} and sum of p_T of jets for each level and for over all (bottom right) of trigger EF_xe60_tclcw_loose_delayed using $W \rightarrow \mu\nu + 2$ jets Sherpa samples. 209</p> <p>111 Correlation of trigger efficiencies between E_T^{miss} and sum of p_T of jets for each level and for over all (bottom right) of trigger EF_xe60_tclcw_loose_delayed using $W \rightarrow \mu\nu + 3$ jets Sherpa samples. 210</p> <p>112 Scale factor of trigger EF_xe60_tclcw_loose_delayed after applying sum of p_T of jets cleaning cut using $Z \rightarrow \mu\mu + 2$ jets, $W \rightarrow \mu\nu$ and $t\bar{t}$ events. 210</p> <p>113 Distribution of mass invariant (top) and E_T^{miss} (bottom) of two b jets using MV1c tagger with 80 % of working point in E_T^{miss} bin from 90 to 120 GeV in bin of 2 jet for data and MC samples using delayed stream trigger (left) and nominal triggers (right). 211</p> <p>114 Distribution of transverse momentum of 4–vector sum of 2 jets (pre b–tagging procedure) in E_T^{miss} bin 90–120 GeV (left) and E_T^{miss} bin 120–160 GeV (right) using nominal E_T^{miss} triggers. 212</p>
---	--

Not reviewed, for internal circulation only

703	115 Distributions of E_T^{miss} (top), $E_T^{\text{miss}}/\sqrt{J12pT}$ (middle) and $\Delta\phi(jet, jet)$ (bottom) in E_T^{miss} bin 90–120 GeV for jets (before b -tagging) before (left) and after (right) applying the additional QCD rejection cuts using delayed stream E_T^{miss} trigger exclusively.	213
704		
705		
706	116 Distributions of transverse momentum of 4–vector sum of 2 jets (pre b -tagging procedure) in E_T^{miss} bin 90–120 GeV using delayed stream trigger exclusively (left) and nominal E_T^{miss} triggers.	214
707		
708		
709	117 $\Delta\phi(jet_1, jet_2)$ and E_T^{miss} significance in the 0-lepton low E_T^{miss} region.	216
710		
711	118 Input variables for low E_T^{miss} 0-lepton multijet likelihood ratio discriminant.	217
712		
713	119 0-lepton low E_T^{miss} <i>LR</i> output distribution.	217
714		
715	120 0-lepton low E_T^{miss} kinematics before and after the <i>LR</i> cut.	218
716		
717	121 mis H_T distributions for the low E_T^{miss} 0-lepton channel.	219
718		
719	122 Validation of $\Delta\phi(jet_1, jet_2)$ as not source of low E_T^{miss} mis-modeling in 0-lepton.	219
720		
721	123 E_T^{miss} without muon contribution in $120 < p_T^W < 160$ GeV1 lepton 2 jet events.	221
722		
723	124 E_T^{miss} without muon contribution in $160 < p_T^W < 200$ GeV1 lepton 2 jet events.	221
724		
725	125 E_T^{miss} without muon contribution in $p_T^W > 200$ GeV1 lepton 2 jet events.	222
726		
727	126 E_T^{miss} without muon contribution in $120 < p_T^W < 160$ GeV1 lepton 3 jet events.	222
728		
729	127 E_T^{miss} without muon contribution in $160 < p_T^W < 200$ GeV1 lepton 3 jet events.	223
730		
731	128 E_T^{miss} without muon contribution in $p_T^W > 200$ GeV1 lepton 3 jet events.	223
732		
733	129 m_{jj} in E_T^{miss} triggered events with $120 < p_T^W < 160$ GeV1 lepton 2 jet events.	224
734		
735	130 m_{jj} in E_T^{miss} triggered events with $160 < p_T^W < 200$ GeV1 lepton 2 jet events.	224
736		
737	131 m_{jj} in E_T^{miss} triggered events with $p_T^W > 200$ GeV1 lepton 2 jet events.	225
738		
739	132 m_{jj} in E_T^{miss} triggered events with $120 < p_T^W < 160$ GeV1 lepton 3 jet events.	225
740		
741	133 m_{jj} in E_T^{miss} triggered events with $160 < p_T^W < 200$ GeV1 lepton 3 jet events.	226
742		
743	134 m_{jj} in E_T^{miss} triggered events with $p_T^W > 200$ GeV1 lepton 3 jet events.	226
744		
745	135 Electron isolation efficiencies and derived scale factors.	229
746		
747	136 Muon isolation efficiencies and derived scale factors.	230
748		
749	137 Muon isolation efficiencies as a function of the number of reconstructed vertices (a) and with track isolation probing only (b) as well as a function of close-by jets (c-d).	231
750		
751	138 b -jet GSC versus EM+JES scale.	233
752		
753	139 b -jet GSC versus EM+JES resolution.	234
754		
755	140 b -jet scale as a function of $f_{\text{tile}0}$ for the GSC versus EM+JES calibrations.	235
756		
757	141 b -jet scale as a function of $f_{\text{em}3}$ for the GSC versus EM+JES calibrations.	235
758		
759	142 b -jet scale as a function of n_{trk} for the GSC versus EM+JES calibrations	235
760		
761	143 b -jet scale as a function of W_{track} for the GSC versus EM+JES calibrations	235
762		
763	144 Acceptance gain when changing ΔR cuts between μ and jets for overlap removal.	237
764		
765	145 The scalar p_T sum of charged particle tracks around a μ for various μ types.	238
766		
767	146 Fraction of jet EM energy as a function of $\Delta R(\mu, \text{jet})$	238
768		
769	147 N_{track} of jets overlapping prompt μs and μs from semi-leptonic decays.	239
770		
771	148 Jet vertex fraction when not using <i>muons</i>	240
772		
773	149 Normalized p_T^V distribution for signal PDF uncertainty studies.	242
774		
775	150 PDF re-weighted p_T^V distribution for ZH events that pass a truth-level event selection.	243
776		
777	151 PDF re-weighted p_T^V distribution for WH events that pass a truth-level event selection.	243
778		
779	152 Normalized p_T^V distribution for signal NLO vs. LO comparisons.	244
780		
781	153 p_T^Z correction for Z+jets events derived for ALPGEN.	248
782		
783	154 m_{bb} systematics for Z+jets events from ALPGEN.	249
784		
785	155 Uncorrected $\Delta\phi$ and p_T^W distributions in 1-lepton 0 tag events.	251
786		
787	156 Uncorrected $\Delta\phi$ distributions in 1-lepton 1-tag events.	252
788		
789	157 Inclusively corrected $\Delta\phi$ distributions in 1-lepton 0 and 1-tag events.	253
790		

Not reviewed, for internal circulation only

751	158	1-lepton 2-jet χ^2 improvements from $\Delta\phi$ corrections.	254
752	159	1-lepton 2 and 3-jet $\Delta\phi$ corrections.	255
753	160	Improvement from applying the W +jet $\Delta\phi$ correction to W +jets or W +ll/cl.	256
754	161	Distribution of number of signal jets in the baseline aMC@NLO sample and in the samples where the μ_R and μ_F parameters have been varied (independently). Normalized to same area.	259
756	162	W -boson p_T distribution of 2-jet bb events at truth-level. The ratio is taken of each sample where the μ_R and μ_F parameters have been varied (independently) with respect to the baseline aMC@NLO sample. Normalized to same area.	259
758	163	Invariant mass distribution of 2-jet bb events at truth-level as predicted by the available W +bb generators (left) and the Sherpa samples (right). Normalized to same area.	260
760	164	Fit functions to the ratio plots shown in Figure 163.	260
762	165	, for $p_T(W) < 120$ GeV (left) and $p_T(W) > 120$ GeV (right). Normalized to same area.	261
764	166	Distribution of the number of jets in bb events at truth-level. Comparison between generators (left) and between the different Sherpa samples (right). Normalized to same area.	261
766	167	Fit function to the observed aMC@NLOto SHERPARATIO in the p_T^W distribution, for 2-jet bb events at truth levee.	262
768	168	Fraction of events with each flavor label in the 2-jet (left) and 3-jet (right) pre-tag regions, for Alpgen and Sherpa W +jets. Reconstruction-level distribution. Normalized to same area.	262
770	169	$\min \Delta\phi(\ell, j) $ variable in the low and high $p_T(W)$ regions, for the 2- and 3-jet cases. Events with leading jets matched to b-hadrons.	263
772	170	$ \Delta\phi(V, H) $ variable in the low and high $p_T(W)$ regions, for the 2- and 3-jet cases. Events with leading jets matched to b-hadrons.	264
774	171	$\Delta R(b, b)$ variable in the low and high $p_T(W)$ regions, for the 2- and 3-jet cases. Events with leading jets matched to b-hadrons.	265
776	172	MET variable in the low and high $p_T(W)$ regions, for the 2- and 3-jet cases. Events with leading jets matched to b-hadrons.	266
778	173	Dijet mass in the low and high $p_T(W)$ regions, for the 2- and 3-jet cases. Events with leading jets matched to b-hadrons.	267
780	174	$M_T(W)$ in the low and high $p_T(W)$ regions, for the 2- and 3-jet cases. Events with leading jets matched to b-hadrons.	268
782	175	$p_T(j_1)$ in the low and high $p_T(W)$ regions, for the 2- and 3-jet cases. Events with leading jets matched to b-hadrons.	269
784	176	$p_T(j_2)$ in the low and high $p_T(W)$ regions, for the 2- and 3-jet cases. Events with leading jets matched to b-hadrons.	270
786	177	$p_T(j_3)$ in the low and high $p_T(W)$ 3-jet regions. Events with leading jets matched to b-hadrons.	271
788	178	m_{bbj} in the low and high $p_T(W)$ 3-jet regions. Events with leading jets matched to b-hadrons.	271
790	179	One Lepton t-channel single top variables in 2 b-tag 2 jet $p_T^W < 120$ GeV events.	274
792	180	One Lepton t-channel single top variables in 2 b-tag 2 jet $p_T^W < 120$ GeV events.	275
793	181	One Lepton t-channel single top variables in 2 b-tag 2 jet $p_T^W > 120$ GeV events.	276
794	182	One Lepton t-channel single top variables in 2 b-tag 2 jet $p_T^W > 120$ GeV events.	277
795	183	One Lepton t-channel single top variables in 2 b-tag 3 jet $p_T^W < 120$ GeV events.	278
796	184	One Lepton t-channel single top variables in 2 b-tag 3 jet $p_T^W < 120$ GeV events.	279
797	185	One Lepton t-channel single top variables in 2 b-tag 2 jet $p_T^W > 120$ GeV events.	280
798	186	One Lepton t-channel single top variables in 2 b-tag 3 jet $p_T^W > 120$ GeV events.	281

Not reviewed, for internal circulation only

799	187 One Lepton s-channel single top variables in 2 <i>b</i> -tag 2 jet $p_T^W < 120$ GeV events.	283
800	188 One Lepton s-channel single top variables in 2 <i>b</i> -tag 2 jet $p_T^W > 120$ GeV events.	284
801	189 One Lepton s-channel single top variables in 2 <i>b</i> -tag 3 jet $p_T^W < 120$ GeV events.	285
802	190 One Lepton s-channel single top variables in 2 <i>b</i> -tag 3 jet $p_T^W > 120$ GeV events.	286
803	191 One Lepton Wt-channel single top variables in 2 <i>b</i> -tag 2 jet $p_T^W < 120$ GeV events.	288
804	192 One Lepton Wt-channel single top variables in 2 <i>b</i> -tag 2 jet $p_T^W > 120$ GeV events.	289
805	193 One Lepton Wt-channel single top variables in 2 <i>b</i> -tag 3 jet $p_T^W < 120$ GeV events.	290
806	194 One Lepton Wt-channel single top variables in 2 <i>b</i> -tag 3 jet $p_T^W > 120$ GeV events.	291
807	195 All generator comparisons for $t\bar{t} m_{bb}$ systematics.	293
808	196 PowHEG+PYTHIA and ALPGEN+PYTHIA comparisons for $t\bar{t} m_{bb}$ systematics.	294
809	197 $t\bar{t} m_{bb}$ systematic function.	295
810	198 All generator comparisons for $t\bar{t} E_T^{\text{miss}}$ systematics.	296
811	199 PowHEG+PYTHIA and ALPGEN+PYTHIA comparisons for $t\bar{t} E_T^{\text{miss}}$ systematics.	297
812	200 $t\bar{t} E_T^{\text{miss}}$ systematic function.	298
813	201 $t\bar{t}$ ALPGEN+PYTHIA to PowHEG+PYTHIA top p_T reweighting distribution.	299
814	202 $t\bar{t}$ difference between ALPGEN and PYTHIA for m_{bb} flavor splitted	301
815	203 $t\bar{t}$ difference between ALPGEN and PYTHIA for m_{bb} for <i>bl</i> events	302
816	204 $t\bar{t}$ generator variations for BDT input variables, 2tag2jet, lpt.	303
817	205 $t\bar{t}$ generator variations for BDT input variables, 2tag2jet, hpt.	304
818	206 $t\bar{t}$ generator variations for BDT input variables, 2tag3jet, lpt.	305
819	207 $t\bar{t}$ generator variations for BDT input variables, 2tag3jet, hpt.	306
820	208 $t\bar{t}$ generator variations for additional 2tag3jet BDT input variables	307
821	209 Perturbative systematics on σ_2 for the six diboson processes obtained applying scale variations according to the Stewart-Tackmann method. The solid line corresponds to the errors derived from the C_1 term and the dotted line from the C_2 term of the covariance matrix C	317
825	210 Perturbative systematics on $\sigma_{\geq 3}$ for the six diboson processes obtained applying scale variations according to the Stewart-Tackmann method. The solid line corresponds to the errors derived from the C_2 term of the covariance matrix C , while the C_1 term of the matrix does not provide any contribution to the 3-jet errors.	318
829	211 Systematic uncertainties due to PDF errors on the 2-jet exclusive cross section for the six diboson processes, computed from the CT10 PDF set, across the five $p_T(V)$ bins.	319
831	212 Systematic uncertainties due to PDF errors on the 3-jet inclusive cross section for the six diboson processes, computed from the CT10 PDF set, across the five $p_T(V)$ bins.	320
833	213 Systematic uncertainties due to PDF errors on the 2-jet exclusive cross section for the six diboson processes, computed from the MSTW PDF set, across the five $p_T(V)$ bins.	320
835	214 Systematic uncertainties due to PDF errors on the 3-jet inclusive cross section for the six diboson processes, computed from the MSTW PDF set, across the five $p_T(V)$ bins.	321
837	215 Systematic uncertainties from α_S on the 2-jet exclusive cross section for the six diboson processes, computed from the CT10 PDF set, across the five $p_T(V)$ bins. The solid line corresponds to the variation of the central value $\alpha_S = 0.117$, while the dotted line corresponds to the variation of $\alpha_S = 0.119$	321
841	216 Systematic uncertainties from α_S on the 3-jet inclusive cross section for the six diboson processes, computed from the CT10 PDF set, across the five $p_T(V)$ bins. The solid line corresponds to the variation of the central value $\alpha_S = 0.117$, while the dotted line corresponds to the variation of $\alpha_S = 0.119$	322

Not reviewed, for internal circulation only

845	217 Systematic uncertainties from α_S on the 2-jet exclusive cross section for the six diboson processes, computed from the MSTW PDF set, across the five $p_T(V)$ bins. The solid line corresponds to the variation of the central value $\alpha_S = 0.117$, while the dotted line corresponds to the variation of $\alpha_S = 0.119$	323
846		
847		
848		
849	218 Systematic uncertainties from α_S on the 3-jet inclusive cross section for the six diboson processes, computed from the MSTW PDF set, across the five $p_T(V)$ bins. The solid line corresponds to the variation of the central value $\alpha_S = 0.117$, while the dotted line corresponds to the variation of $\alpha_S = 0.119$	324
850		
851		
852		
853	219 Envelope of the systematic uncertainties from $\text{PDF} + \alpha_S$ on the 2-jet exclusive cross section for the six diboson processes. The solid line corresponds to the variations from the CT10 PDF set, while the dotted line from the MSTW PDF set.	325
854		
855		
856	220 Envelope of the systematic uncertainties from $\text{PDF} + \alpha_S$ on the 3-jet inclusive cross section for the six diboson processes. The solid line corresponds to the variations from the CT10 PDF set, while the dotted line from the MSTW PDF set.	326
857		
858		
859	221 POWHEG+Pythia8 versus Herwig comparison for the WZ diboson processes applying the 0-lepton selection in the 2-tag inclusive (LL+MM+TT) category: the systematic uncertainties from the PS/hadronization model is estimated taking the fit of the ratio of the different MC predictions.	327
860		
861		
862		
863	222 POWHEG+Pythia8 versus Herwig comparison for the ZZ diboson processes applying the 0-lepton selection in the pre-tag category: the systematic uncertainties from the PS/hadronization model is estimated taking the fit of the ratio of the different MC predictions.	328
864		
865		
866		
867	223 POWHEG+Pythia8 versus Herwig comparison for the WW diboson processes applying the 0-lepton selection in the pre-tag category: the systematic uncertainties from the PS/hadronization model is estimated taking the fit of the ratio of the different MC predictions.	329
868		
869		
870		
871	224 $\Delta\phi(E_T^{\text{miss}}, p_T^{\text{miss}})$ and $\min \Delta\phi(E_T^{\text{miss}}, \text{jet}) $ distribution	330
872		
873	225 Two-dimensional kinematic plane for estimating QCD multi-jet background in the 0-lepton signal region (region A). $dphi(E_T^{\text{miss}}, p_T^{\text{miss}}) > \pi/2$ defines region A/C.	331
874		
875	226 Correlation test for two variables in 0-lepton multijet ABCD estimate.	331
876		
877	227 De-correlation check for variables used in 0-lepton MJ estimate.	333
878		
879	228 Sketch of jets, E_T^{miss} , and p_T^{miss} in the regions used for the 0-lepton multijet estimate.	334
880		
881	229 Truth label of the jet with $\min \Delta\phi(E_T^{\text{miss}}, \text{jet}) $	334
882		
883	230 Shape used for MJ in 0-lepton analysis.	335
884		
885	231 Motivation for M_{eff} cut over E_T^{miss} and m_T^W from the MVA analysis.	337
886		
887	232 m_T^W without a cut in the 1-lepton dijet mass analysis for $120 < p_T^W < 160$	338
888		
889	233 $\Delta R(bb)$ and p_T^W corrections for 1-electron multijet estimate	339
890		
891	234 Comparison of multijet template in muon 1-tag and 2-tag 2-jet events with $p_T^W < 120 \text{ GeV}$	340
	235 Comparison of multijet template in muon 1-tag and 2-tag 2-jet events with $p_T^W > 120 \text{ GeV}$	341
	236 Comparison of multijet template in muon 1-tag and 2-tag 3-jet events with $p_T^W < 120 \text{ GeV}$	342
	237 Comparison of multijet template in muon 1-tag and 2-tag 3-jet events with $p_T^W > 120 \text{ GeV}$	343
	238 Variables used for 1-lepton electron multijet reweight and final variables for 2L tag $p_T^W < 120 \text{ GeV}$ events.	344
	239 Variables used for 1-lepton electron multijet reweight and final variables for 2L tag $p_T^W > 120 \text{ GeV}$ events.	345
	240 Variables used for 1-lepton electron multijet reweight and final variables for 2M tag $p_T^W < 120 \text{ GeV}$ events.	346

Not reviewed, for internal circulation only

892	241	Variables used for 1-lepton electron multijet reweight and final variables for 2M tag $p_T^W > 120$ GeV events.	347
893	242	Variables used for 1-lepton electron multijet reweight and final variables for 2T tag $p_T^W < 120$ GeV events.	348
894	243	Variables used for 1-lepton electron multijet reweight and final variables for 2T tag $p_T^W > 120$ GeV events.	349
895	244	Reweighted variables for the 1-lepton electron multijet template in 2L tag $p_T^W < 120$ GeV events.	350
896	245	Reweighted variables for the 1-lepton electron multijet template in 2L tag $p_T^W > 120$ GeV events.	351
897	246	Reweighted variables for the 1-lepton electron multijet template in 2M tag $p_T^W < 120$ GeV events.	352
898	247	Reweighted variables for the 1-lepton electron multijet template in 2M tag $p_T^W > 120$ GeV events.	353
899	248	Reweighted variables for the 1-lepton electron multijet template in 2T tag $p_T^W < 120$ GeV events.	354
900	249	Reweighted variables for the 1-lepton electron multijet template in 2T tag $p_T^W > 120$ GeV events.	355
901	250	Comparison of multijet template in electron 1-tag and 2-tag 3-jet events with $ptW > 120$ GeV.	356
902	251	Comparison of multijet template in electron 1-tag and 2-tag 3-jet events with $ptW > 120$ GeV.	357
903	252	The di-electron invariant mass distribution for (a) 0-tag, (b) 1-tag and (c) 2-tag. The background expectations have been scaled by the results of the fits. The purple distribution is $Z+jets$, the green is the other non-multijet backgrounds, and the blue histogram is the multijet background.	358
904	253	Distribution of the sum of the MV1c values of the two tagged jets in the 2 tag multijet template (black points). Also shown is the distribution of the multijet template using the truth tagging method (red points).	359
905	254	Comparison of multijet in 2-lepton electron and muon channels	359
906	255	b -jet efficiency maps.	361
907	256	c -jet efficiency maps.	362
908	257	$light$ -jet efficiency maps.	363
909	258	τ -jet efficiency maps.	364
910	259	Example of a varied efficiency map.	365
911	260	Impact of varied efficiency map on Zcc in 0-lepton analysis.	365
912	261	Generator dependence of flavor tagging for exclusive MV1c 100% OP.	366
913	262	Generator dependence of flavor tagging for exclusive MV1c 80% OP.	367
914	263	Generator dependence of flavor tagging for exclusive MV1c 70% OP.	367
915	264	Generator dependence of flavor tagging for exclusive MV1c 60% OP.	368
916	265	Generator dependence of flavor tagging for MV1c 50% OP.	368
917	266	Comparison between truth tagging and direct tagging for $V+ll$ events.	369
918	267	Comparison between truth tagging and direct tagging for $V+cl$ events.	370
919	268	Comparison between truth tagging and direct tagging for $V+cc$ events.	371
920	269	Comparison between truth tagging and direct tagging for WW events.	371
921	270	Ratio of truth to direct tagged $V+cc$ events.	372
922	271	Truth tagging ΔR correction.	372
923	272	Closure test of truth tagging ΔR correction.	373

Not reviewed, for internal circulation only

940	273	Balance of event from truth using $ZH(125)$ simulation.	376
941	274	Dijet invariant mass before and after applying a kinematic likelihood fit in $ZH(125)$ simulation.	377
942	275	Improvement in m_{jj} resolution in $ZH(125)$ simulation according to system balance.	377
943	276	Zero Lepton m_{jj} distributions in 1 b -tag 2 jet events.	380
944	277	Zero Lepton m_{jj} distributions in 1 b -tag 3 jet events.	380
945	278	Zero Lepton m_{jj} distributions in 2L b -tag 2 jet events.	381
946	279	Zero Lepton m_{jj} distributions in 2L b -tag 3 jet events.	381
947	280	Zero Lepton m_{jj} distributions in 2M b -tag 2 jet events.	382
948	281	Zero Lepton m_{jj} distributions in 2M b -tag 3 jet events.	382
949	282	Zero Lepton m_{jj} distributions in 2T b -tag 2 jet events.	383
950	283	Zero Lepton m_{jj} distributions in 2T b -tag 3 jet events.	383
951	284	One Lepton m_{jj} distributions in 1 b -tag 2 jet events.	385
952	285	One Lepton m_{jj} distributions in 1 b -tag 3 jet events.	385
953	286	One Lepton m_{jj} distributions in 2L b -tag 2 jet events.	386
954	287	One Lepton m_{jj} distributions in 2L b -tag 3 jet events.	386
955	288	One Lepton m_{jj} distributions in 2M b -tag 2 jet events.	387
956	289	One Lepton m_{jj} distributions in 2M b -tag 3 jet events.	387
957	290	One Lepton m_{jj} distributions in 2T b -tag 2 jet events.	388
958	291	One Lepton m_{jj} distributions in 2T b -tag 3 jet events.	388
959	292	Two Lepton m_{jj} distributions in 1 b -tag 2 jet events.	390
960	293	Two Lepton m_{jj} distributions in 1 b -tag 3 jet events.	390
961	294	Two Lepton m_{jj} distributions in 2L b -tag 2 jet events.	391
962	295	Two Lepton m_{jj} distributions in 2L b -tag 3 jet events.	391
963	296	Two Lepton m_{jj} distributions in 2M b -tag 2 jet events.	392
964	297	Two Lepton m_{jj} distributions in 2M b -tag 3 jet events.	392
965	298	Two Lepton m_{jj} distributions in 2T b -tag 2 jet events.	393
966	299	Two Lepton m_{jj} distributions in 2T b -tag 3 jet events.	393
967	300	Zero Lepton MVA input variables in 1 b -tag 2-jet events.	395
968	301	Zero Lepton MVA input variables in 1 b -tag 2-jet events postfit.	396
969	302	Zero Lepton MVA input variables in 2 loose b -tags 2-jet events.	397
970	303	Zero Lepton MVA input variables in 2 loose b -tags 2-jet events postfit.	398
971	304	Zero Lepton MVA input variables in 2 MM+TT b -tags 2-jet events.	399
972	305	Zero Lepton MVA input variables in 2 MM+TT b -tags 2-jet events postfit.	400
973	306	Zero Lepton MVA input variables in 1 b -tag 3-jet events.	401
974	307	Zero Lepton MVA input variables in 1 b -tag 3-jet events postfit.	402
975	308	Zero Lepton MVA input variables in 2 loose b -tags 3-jet events.	403
976	309	Zero Lepton MVA input variables in 2 loose b -tags 3-jet events postfit.	404
977	310	Zero Lepton MVA input variables in 2 MM+TT b -tags 3-jet events.	405
978	311	Zero Lepton MVA input variables in 2 MM+TT b -tags 3-jet events postfit.	406
979	312	One Lepton MVA input variables in 1 b -tag 2-jet $p_T^W < 120$ GeV events.	408
980	313	One Lepton MVA input variables in 1 b -tag 2-jet $p_T^W < 120$ GeV events postfit.	409
981	314	One Lepton MVA input variables in 1 b -tag 2-jet $p_T^W > 120$ GeV events.	410
982	315	One Lepton MVA input variables in 1 b -tag 2-jet $p_T^W > 120$ GeV events postfit.	411
983	316	One Lepton MVA input variables in 2 LL b -tag 2-jet $p_T^W < 120$ GeV events.	412
984	317	One Lepton MVA input variables in 2 LL b -tag 2-jet $p_T^W < 120$ GeV events postfit.	413
985	318	One Lepton MVA input variables in 2 LL b -tag 2-jet $p_T^W > 120$ GeV events.	414
986	319	One Lepton MVA input variables in 2 LL b -tag 2-jet $p_T^W > 120$ GeV events postfit.	415

Not reviewed, for internal circulation only

988	320 One Lepton MVA input variables in 2 MM b -tag 2-jet $p_T^W < 120$ GeV events.	416
989	321 One Lepton MVA input variables in 2 MM b -tag 2-jet $p_T^W < 120$ GeV events postfit.	417
990	322 One Lepton MVA input variables in 2 MM b -tag 2-jet $p_T^W > 120$ GeV events.	418
991	323 One Lepton MVA input variables in 2 MM b -tag 2-jet $p_T^W > 120$ GeV events postfit.	419
992	324 One Lepton MVA input variables in 2 TT b -tag 2-jet $p_T^W < 120$ GeV events.	420
993	325 One Lepton MVA input variables in 2 TT b -tag 2-jet $p_T^W < 120$ GeV events postfit.	421
994	326 One Lepton MVA input variables in 2 TT b -tag 2-jet $p_T^W > 120$ GeV events.	422
995	327 One Lepton MVA input variables in 2 TT b -tag 2-jet $p_T^W > 120$ GeV events postfit.	423
996	328 One Lepton MVA input variables in 1 b -tag 3-jet $p_T^W < 120$ GeV events.	424
997	329 One Lepton MVA input variables in 1 b -tag 3-jet $p_T^W < 120$ GeV events postfit.	425
998	330 One Lepton MVA input variables in 1 b -tag 3-jet $p_T^W > 120$ GeV events.	426
999	331 One Lepton MVA input variables in 1 b -tag 3-jet $p_T^W > 120$ GeV events postfit.	427
1000	332 One Lepton MVA input variables in 2 LL b -tag 3-jet $p_T^W < 120$ GeV events.	428
1001	333 One Lepton MVA input variables in 2 LL b -tag 3-jet $p_T^W < 120$ GeV events postfit.	429
1002	334 One Lepton MVA input variables in 2 LL b -tag 3-jet $p_T^W > 120$ GeV events.	430
1003	335 One Lepton MVA input variables in 2 LL b -tag 3-jet $p_T^W > 120$ GeV events postfit.	431
1004	336 One Lepton MVA input variables in 2 MM b -tag 3-jet $p_T^W < 120$ GeV events.	432
1005	337 One Lepton MVA input variables in 2 MM b -tag 3-jet $p_T^W < 120$ GeV events postfit.	433
1006	338 One Lepton MVA input variables in 2 MM b -tag 3-jet $p_T^W > 120$ GeV events.	434
1007	339 One Lepton MVA input variables in 2 MM b -tag 3-jet $p_T^W > 120$ GeV events postfit.	435
1008	340 One Lepton MVA input variables in 2 TT b -tag 3-jet $p_T^W < 120$ GeV events.	436
1009	341 One Lepton MVA input variables in 2 TT b -tag 3-jet $p_T^W < 120$ GeV events postfit.	437
1010	342 One Lepton MVA input variables in 2 TT b -tag 3-jet $p_T^W > 120$ GeV events.	438
1011	343 One Lepton MVA input variables in 2 TT b -tag 3-jet $p_T^W > 120$ GeV events postfit.	439
1012	344 Two Lepton MVA input variables in 1 b -tag 2-jet $p_T^Z < 120$ GeV events.	441
1013	345 Two Lepton MVA input variables in 1 b -tag 2-jet $p_T^Z < 120$ GeV events postfit.	442
1014	346 Two Lepton MVA input variables in 1 b -tag 2-jet $p_T^Z > 120$ GeV events.	443
1015	347 Two Lepton MVA input variables in 1 b -tag 2-jet $p_T^Z > 120$ GeV events postfit.	444
1016	348 Two Lepton MVA input variables in 2 LL b -tags 2-jet $p_T^Z < 120$ GeV events.	445
1017	349 Two Lepton MVA input variables in 2 LL b -tag 2-jet $p_T^Z < 120$ GeV events postfit.	446
1018	350 Two Lepton MVA input variables in 2 LL b -tags 2-jet $p_T^Z > 120$ GeV events.	447
1019	351 Two Lepton MVA input variables in 2 LL b -tag 2-jet $p_T^Z > 120$ GeV events postfit.	448
1020	352 Two Lepton MVA input variables in 2 MM+TT b -tags 2-jet $p_T^Z < 120$ GeV events.	449
1021	353 Two Lepton MVA input variables in 2 MM+TT b -tag 2-jet $p_T^Z < 120$ GeV events postfit.	450
1022	354 Two Lepton MVA input variables in 2 MM+TT b -tags 2-jet $p_T^Z > 120$ GeV events.	451
1023	355 Two Lepton MVA input variables in 2 MM+TT b -tag 2-jet $p_T^Z > 120$ GeV events postfit.	452
1024	356 Two Lepton MVA input variables in 1 b -tag 3-jet $p_T^Z < 120$ GeV events.	453
1025	357 Two Lepton MVA input variables in 1 b -tag 3-jet $p_T^Z < 120$ GeV events postfit.	454
1026	358 Two Lepton MVA input variables in 1 b -tag 3-jet $p_T^Z > 120$ GeV events.	455
1027	359 Two Lepton MVA input variables in 1 b -tag 3-jet $p_T^Z > 120$ GeV events postfit.	456
1028	360 Two Lepton MVA input variables in 2 LL b -tags 3-jet $p_T^Z < 120$ GeV events.	457
1029	361 Two Lepton MVA input variables in 2 LL b -tag 3-jet $p_T^Z < 120$ GeV events postfit.	458
1030	362 Two Lepton MVA input variables in 2 LL b -tags 3-jet $p_T^Z > 120$ GeV events.	459
1031	363 Two Lepton MVA input variables in 2 LL b -tag 3-jet $p_T^Z > 120$ GeV events postfit.	460
1032	364 Two Lepton MVA input variables in 2 MM+TT b -tags 3-jet $p_T^Z < 120$ GeV events.	461
1033	365 Two Lepton MVA input variables in 2 MM+TT b -tag 3-jet $p_T^Z < 120$ GeV events postfit.	462
1034	366 Two Lepton MVA input variables in 2 MM+TT b -tags 3-jet $p_T^Z > 120$ GeV events.	463
1035	367 Two Lepton MVA input variables in 2 MM+TT b -tag 3-jet $p_T^Z > 120$ GeV events postfit.	464

Not reviewed, for internal circulation only

1036	368 MVA Training for 0 lepton, 2 jets, $p_T^V > 120 \text{ GeV}$	466
1037	369 MVA Training for 0 lepton, 3 jets, $p_T^V > 120 \text{ GeV}$	467
1038	370 MVA Training for 1 lepton, 2 jets, $p_T^V < 120 \text{ GeV}$	468
1039	371 MVA Training for 1 lepton, 2 jets, $p_T^V > 120 \text{ GeV}$	469
1040	372 MVA Training for 1 lepton, 3 jets, $p_T^V < 120 \text{ GeV}$	470
1041	373 MVA Training for 1 lepton, 3 jets, $p_T^V > 120 \text{ GeV}$	471
1042	374 MVA Training for 2 leptons, 2 jets, $p_T^V < 120 \text{ GeV}$	472
1043	375 MVA Training for 2 leptons, 2 jets, $p_T^V > 120 \text{ GeV}$	473
1044	376 MVA Training for 2 leptons, 3 jets, $p_T^V < 120 \text{ GeV}$	474
1045	377 MVA Training for 2 leptons, 3 jets, $p_T^V > 120 \text{ GeV}$	475
1046	378 MVA binning optimization	477
1047	379 MVA binning transform	478
1048	380 Zero Lepton MVA distributions	480
1049	381 Zero Lepton MVA distributions	481
1050	382 One Lepton MVA distributions $p_T^W < 120 \text{ GeV}$	482
1051	383 One Lepton MVA distributions $p_T^W < 120 \text{ GeV}$	483
1052	384 One Lepton MVA distributions $p_T^W > 120 \text{ GeV}$	484
1053	385 One Lepton MVA distributions $p_T^W > 120 \text{ GeV}$	485
1054	386 Two Lepton MVA distributions $p_T^W < 120 \text{ GeV}$	486
1055	387 Two Lepton MVA distributions $p_T^W < 120 \text{ GeV}$	487
1056	388 Two Lepton MVA distributions $p_T^W > 120 \text{ GeV}$	488
1057	389 Two Lepton MVA distributions $p_T^W > 120 \text{ GeV}$	489
1058	390 Zero Lepton Correlation between mva and mBB	491
1059	391 Zero Lepton Correlation between mva and dRBB	492
1060	392 Zero Lepton Correlation between mva and MET	493
1061	393 Zero Lepton Correlation between mva and dPhiVBB	494
1062	394 Zero Lepton Correlation between mBB and dRBB	495
1063	395 Zero Lepton Correlation between mBB and MET	496
1064	396 Zero Lepton Correlation between mBB and dPhiVBB	497
1065	397 Zero Lepton Correlation between dRBB and MET	498
1066	398 Zero Lepton Correlation between dRBB and dPhiVBB	499
1067	399 Zero Lepton Correlation between MET and dPhiVBB	500
1068	400 One Lepton Correlation between mvaWlvH125 and mBB ($p_T^W > 120 \text{ GeV}$)	502
1069	401 One Lepton Correlation between mvaWlvH125 and dRBB ($p_T^W > 120 \text{ GeV}$)	503
1070	402 One Lepton Correlation between mvaWlvH125 and MET ($p_T^W > 120 \text{ GeV}$)	504
1071	403 One Lepton Correlation between mvaWlvH125 and dPhiVBB ($p_T^W > 120 \text{ GeV}$)	505
1072	404 One Lepton Correlation between mBB and dRBB ($p_T^W > 120 \text{ GeV}$)	506
1073	405 One Lepton Correlation between mBB and MET ($p_T^W > 120 \text{ GeV}$)	507
1074	406 One Lepton Correlation between mBB and dPhiVBB ($p_T^W > 120 \text{ GeV}$)	508
1075	407 One Lepton Correlation between dRBB and MET ($p_T^W > 120 \text{ GeV}$)	509
1076	408 One Lepton Correlation between dRBB and dPhiVBB ($p_T^W > 120 \text{ GeV}$)	510
1077	409 One Lepton Correlation between MET and dPhiVBB ($p_T^W > 120 \text{ GeV}$)	511
1078	410 One Lepton Correlation between mvaWlvH125 and mBB ($p_T^W < 120 \text{ GeV}$)	512
1079	411 One Lepton Correlation between mvaWlvH125 and dRBB ($p_T^W < 120 \text{ GeV}$)	513
1080	412 One Lepton Correlation between mvaWlvH125 and MET ($p_T^W < 120 \text{ GeV}$)	514
1081	413 One Lepton Correlation between mvaWlvH125 and dPhiVBB ($p_T^W < 120 \text{ GeV}$)	515
1082	414 One Lepton Correlation between mBB and dRBB ($p_T^W < 120 \text{ GeV}$)	516
1083	415 One Lepton Correlation between mBB and MET ($p_T^W < 120 \text{ GeV}$)	517

Not reviewed, for internal circulation only

1084	416 One Lepton Correlation between mBB and dPhiVBB ($p_T^W < 120$ GeV)	518
1085	417 One Lepton Correlation between dRBB and MET ($p_T^W < 120$ GeV)	519
1086	418 One Lepton Correlation between dRBB and dPhiVBB ($p_T^W < 120$ GeV)	520
1087	419 One Lepton Correlation between MET and dPhiVBB ($p_T^W < 120$ GeV)	521
1088	420 One Lepton Correlation between mva and mBB ($p_T^Z > 120$ GeV)	523
1089	421 One Lepton Correlation between mva and dRBB ($p_T^Z > 120$ GeV)	524
1090	422 One Lepton Correlation between mva and pTV ($p_T^Z > 120$ GeV)	525
1091	423 One Lepton Correlation between mva and dPhiVBB ($p_T^Z > 120$ GeV)	526
1092	424 Two Lepton Correlation between mva and mBB ($p_T^W < 120$ GeV)	527
1093	425 Two Lepton Correlation between mva and dRBB ($p_T^W < 120$ GeV)	528
1094	426 Two Lepton Correlation between mva and pTV ($p_T^W < 120$ GeV)	529
1095	427 Two Lepton Correlation between mva and dPhiVBB ($p_T^W < 120$ GeV)	530
1096	428 Pull plots for 0-lepton channel: b - and c -jet tagging.	531
1097	429 Pull plots for 0-lepton channel: light-jet tagging and leptons.	532
1098	430 Pull plots for 0-lepton channel: Jet NPs.	533
1099	431 Pull plots for 0-lepton channel: Diboson and Top related uncertainties.	534
1100	432 Pull plots for 0-lepton channel: Normalization and residual uncertainties.	535
1101	433 Pre-fit dijet mass analysis plots for the 0-lepton 2-jets regions with $p_T^V < 200$ GeV in the 0-lepton fit	537
1103	434 Pre-fit dijet mass analysis plots for the 0-lepton 3-jets regions with $p_T^V < 200$ GeV in the 0-lepton fit.	538
1105	435 Pre-fit dijet mass analysis plots for the 0-lepton regions with $p_T^V > 200$ GeV in the 0-lepton fit.	539
1107	436 Post-fit dijet mass analysis plots for the 0-lepton 2-jets regions with $p_T^V < 200$ GeV in the 0-lepton fit	540
1109	437 Post-fit dijet mass analysis plots for the 0-lepton 3-jets regions with $p_T^V < 200$ GeV in the 0-lepton fit.	541
1111	438 Post-fit dijet mass analysis plots for the 0-lepton regions with $p_T^V > 200$ GeV in the 0-lepton fit.	542
1113	439 Pull plots for 1-lepton channel: b - and c -jet tagging.	543
1114	440 Pull plots for 1-lepton channel: light-jet tagging and leptons.	544
1115	441 Pull plots for 1-lepton channel: Jet NPs.	545
1116	442 Pull plots for 1-lepton channel: Diboson and Top related uncertainties.	546
1117	443 Pull plots for 1-lepton channel: Normalization and residual uncertainties.	547
1118	444 Pre-fit dijet mass analysis plots for the 1-lepton 2-jets regions with $p_T^V < 200$ GeV in the 1-lepton fit.	549
1120	445 Pre-fit dijet mass analysis plots for the 1-lepton 3-jets regions with $p_T^V < 200$ GeV in the 1-lepton fit.	550
1122	446 Pre-fit dijet mass analysis plots for the 1-lepton regions with $p_T^V > 200$ GeV in the 1-lepton fit.	551
1124	447 Post-fit dijet mass analysis plots for the 1-lepton 2-jets regions with $p_T^V < 200$ GeV in the 1-lepton fit.	552
1126	448 Post-fit dijet mass analysis plots for the 1-lepton 3-jets regions with $p_T^V < 200$ GeV in the 1-lepton fit.	553
1128	449 Post-fit dijet mass analysis plots for the 1-lepton regions with $p_T^V > 200$ GeV in the 1-lepton fit.	554
1130	450 Pull plots for 2-lepton channel: b - and c -jet tagging.	555
1131	451 Pull plots for 2-lepton channel: light-jet tagging and leptons.	556

Not reviewed, for internal circulation only

1132	452	Pull plots for 2-lepton channel: Jet NPs.	557
1133	453	Pull plots for 2-lepton channel: Diboson and Top related uncertainties.	558
1134	454	Pull plots for 2-lepton channel: Normalization and residual uncertainties.	559
1135	455	Pre-fit dijet mass analysis plots for the 2-lepton 2-jets regions with $p_T^V < 200$ GeV in the 2-lepton fit.	561
1137	456	Pre-fit dijet mass analysis plots for the 2-lepton 3-jets regions with $p_T^V < 200$ GeV in the 2-lepton fit.	562
1139	457	Pre-fit dijet mass analysis plots for the 2-lepton regions with $p_T^V > 200$ GeV in the 2-lepton fit.	563
1141	458	Post-fit dijet mass analysis plots for the 2-lepton 2-jets regions with $p_T^V < 200$ GeV in the 2-lepton fit.	564
1143	459	Post-fit dijet mass analysis plots for the 2-lepton 3-jets regions with $p_T^V < 200$ GeV in the 2-lepton fit.	565
1145	460	Post-fit dijet mass analysis plots for the 2-lepton regions with $p_T^V > 200$ GeV in the 2-lepton fit.	566
1147	461	Pull plots for 0-lepton channel: b - and c -jet tagging.	567
1148	462	Pull plots for 0-lepton channel: light-jet tagging and leptons.	568
1149	463	Pull plots for 0-lepton channel: Jet NPs.	569
1150	464	Pull plots for 0-lepton channel: Diboson/Top and W/Z related uncertainties.	570
1151	465	Pull plots for 0-lepton channel: Other model and normalization uncertainties.	571
1152	466	Pre-fit MVA plots for high p_T^V 0-lepton events in the 0 lepton fit.	573
1153	467	Post-fit MVA plots for high p_T^V 0-lepton events in the 0 lepton fit.	574
1154	468	Pull plots for 1-lepton channel: b - and c -jet tagging.	575
1155	469	Pull plots for 1-lepton channel: light-jet tagging and leptons.	576
1156	470	Pull plots for 1-lepton channel: Jet NPs.	577
1157	471	Pull plots for 1-lepton channel: Diboson/Top and W/Z related uncertainties.	578
1158	472	Pull plots for 1-lepton channel: Other model and normalization uncertainties.	579
1159	473	Pre-fit MVA plots for 1-lepton events in the 1 lepton fit.	581
1160	474	Post-fit MVA plots for 1-lepton events in the 1 lepton fit.	582
1161	475	Pull plots for 2-lepton channel: b - and c -jet tagging.	583
1162	476	Pull plots for 2-lepton channel: light-jet tagging and leptons.	584
1163	477	Pull plots for 2-lepton channel: Jet NPs.	585
1164	478	Pull plots for 2-lepton channel: Diboson/Top and W/Z related uncertainties.	586
1165	479	Pull plots for 2-lepton channel: Other model and normalization uncertainties.	587
1166	480	Pre-fit MVA plots for 2-lepton events in the 2 lepton fit.	589
1167	481	Post-fit MVA plots for 2-lepton events in the 2 lepton fit.	590
1168	482	Pull plots for 0-lepton channel: b - and c -jet tagging.	591
1169	483	Pull plots for 0-lepton channel: light-jet tagging and leptons.	592
1170	484	Pull plots for 0-lepton channel: Jet NPs.	593
1171	485	Pull plots for 0-lepton channel: Diboson/Top and W/Z related uncertainties.	594
1172	486	Pull plots for 0-lepton channel: Other model and normalization uncertainties.	595
1173	487	Pull plots for 1-lepton channel: b - and c -jet tagging.	596
1174	488	Pull plots for 1-lepton channel: light-jet tagging and leptons.	597
1175	489	Pull plots for 1-lepton channel: Jet NPs.	598
1176	490	Pull plots for 1-lepton channel: Diboson/Top and W/Z related uncertainties.	599
1177	491	Pull plots for 1-lepton channel: Other model and normalization uncertainties.	600
1178	492	Pull plots for 2-lepton channel: b - and c -jet tagging.	601
1179	493	Pull plots for 2-lepton channel: light-jet tagging and leptons.	602

Not reviewed, for internal circulation only

1180	494	Pull plots for 2-lepton channel: Jet NPs.	603
1181	495	Pull plots for 2-lepton channel: Diboson/Top and W/Z related uncertainties.	604
1182	496	Pull plots for 2-lepton channel: Other model and normalization uncertainties.	605
1183	497	0-Leptons: 1 and inclusive 2-tag postfit p_T^V plots from m_{jj} analysis.	607
1184	498	0-Leptons: 2-tag postfit p_T^V plots from m_{jj} analysis.	608
1185	499	1-Leptons: 1 and inclusive 2-tag postfit p_T^V plots from m_{jj} analysis.	609
1186	500	1-Leptons: 2-tag postfit p_T^V plots from m_{jj} analysis.	610
1187	501	2-Leptons: 1 and inclusive 2-tag postfit p_T^V plots from m_{jj} analysis.	611
1188	502	2-Leptons: 2-tag postfit p_T^V plots from m_{jj} analysis.	612
1189	503	0-Leptons: 1 and inclusive 2-tag postfit p_T^V plots from MVA analysis.	613
1190	504	0-Leptons: 2-tag postfit p_T^V plots from MVA analysis.	614
1191	505	1-Leptons: 1 and inclusive 2-tag postfit p_T^V plots from MVA analysis.	615
1192	506	1-Leptons: 2-tag postfit p_T^V plots from MVA analysis.	616
1193	507	2-Leptons: 1 and inclusive 2-tag postfit p_T^V plots from MVA analysis.	617
1194	508	2-Leptons: 2-tag postfit p_T^V plots from MVA analysis.	618
1195	509	Fitted Higgs signal strength for dijet mass 7 TeV analysis.	671
1196	510	Fitted Higgs signal strength for MVA 8 TeV analysis.	671
1197	511	Fitted Higgs signal strength for combined 7 TeV dijet mass and MVA 8 TeV analysis.	672
1198	512	Expectation for 7 TeV and 8 TeV combination.	672
1199	513	0+1+2 lepton MVA fit pulls for b , c and light-jet tagging and lepton systematics.	674
1200	514	0+1+2 lepton MVA fit pulls for JES, diboson/top and W/Z.	675
1201	515	0+1+2 lepton MVA fit pulls for normalization NPs and remaining NPs.	676
1202	516	Correlation plot for the full MVA analysis fit in the combined fit.	677
1203	517	Post-fit dijet mass analysis plots for 2-jets 0-lepton regions.	678
1204	518	Post-fit dijet mass analysis plots for 3-jets 0-lepton regions.	679
1205	519	Post-fit dijet mass analysis plots for 2-jets 1-lepton regions.	680
1206	520	Post-fit dijet mass analysis plots for 3-jets 1-lepton regions.	681
1207	521	Post-fit dijet mass analysis plots for 2-jets 2-lepton regions.	682
1208	522	Post-fit dijet mass analysis plots for 3-jets 2-lepton regions.	683
1209	523	Ranking plots for combined MVA analysis.	685
1210	524	Ranking plots for 0-lepton, 1-lepton and 2-leptons MVA analysis.	686
1211	525	0+1+2 lepton MVA diboson fit pulls for b and c -jet tagging.	688
1212	526	0+1+2 lepton MVA diboson fit pulls for light-jet tagging and lepton systematics.	689
1213	527	0+1+2 lepton MVA diboson fit pulls for JES.	690
1214	528	0+1+2 lepton MVA diboson fit pulls for diboson/top and W/Z.	691
1215	529	0+1+2 lepton MVA diboson fit pulls for normalization NPs.	692
1216	530	0+1+2 lepton MVA diboson fit pulls for the remaining NPs.	693
1217	531	Correlation plot for the full MVA diboson analysis fit.	694
1218	532	Ranking plots for combined m_{jj} analysis.	695
1219	533	Ranking plots for 0-lepton, 1-lepton and 2-leptons m_{jj} analysis.	696
1220	534	0+1+2 lepton m_{jj} diboson fit pulls for b and c -jet tagging.	698
1221	535	0+1+2 lepton m_{jj} diboson fit pulls for light-jet tagging and lepton systematics.	699
1222	536	0+1+2 lepton m_{jj} diboson fit pulls for JES.	700
1223	537	0+1+2 lepton m_{jj} diboson fit pulls for diboson/top and W/Z.	701
1224	538	0+1+2 lepton m_{jj} diboson fit pulls for normalization NPs.	702
1225	539	0+1+2 lepton m_{jj} diboson fit pulls for the remaining NPs.	703
1226	540	Correlation plot for the full m_{jj} diboson analysis fit.	704
1227	541	Correlation plot between the Higgs and the diboson VZ signal strength in the MVA Higgs fit.	706

Not reviewed, for internal circulation only

1228	542 Correlation plot between the Higgs and the diboson VZ signal strength in the m_{jj} shape	707
1229	Higgs fit.	
1230	543 Post-fit MVA plots for high p_T^V 0-lepton events.	709
1231	544 Post-fit MVA plots for 1-lepton events.	710
1232	545 Post-fit MVA plots for 2-lepton events.	711
1233	546 Post-fit diboson dijet mass analysis plots for the 0-lepton 2-jets regions with $p_T^V < 200$ GeV.	713
1234	547 Post-fit diboson dijet mass analysis plots for the 0-lepton 3-jets regions with $p_T^V < 200$ GeV.	714
1235	548 Post-fit diboson dijet mass analysis plots for the 0-lepton regions with $p_T^V > 200$ GeV.	715
1236	549 Post-fit diboson dijet mass analysis plots for the 1-lepton 2-jets regions with $p_T^V < 200$ GeV.	716
1237	550 Post-fit diboson dijet mass analysis plots for the 1-lepton 3-jets regions with $p_T^V < 200$ GeV.	717
1238	551 Post-fit diboson dijet mass analysis plots for the 1-lepton regions with $p_T^V > 200$ GeV.	718
1239	552 Post-fit diboson dijet mass analysis plots for the 2-lepton 2-jets regions with $p_T^V < 200$ GeV.	719
1240	553 Post-fit diboson dijet mass analysis plots for the 2-lepton 3-jets regions with $p_T^V < 200$ GeV.	720
1241	554 Post-fit diboson dijet mass analysis plots for the 2-lepton regions with $p_T^V > 200$ GeV.	721
1242	555 Leading jet p_T , m_{bb} , E_T^{miss} , $\phi(E_T^{\text{miss}})$, $\Delta\phi_{\min}(E_T^{\text{miss}}, \text{jet})$ and $\Delta R(jj)$ in the 0-lepton signal sample for events passing (black) and failing (red) BCH cleaning.	725
1243		
1244	556 Leading jet p_T , m_{bb} , E_T^{miss} , $\phi(E_T^{\text{miss}})$, $\Delta\phi_{\min}(E_T^{\text{miss}}, \text{jet})$ and $\Delta R(jj)$ in the 0-lepton JetTauEtMiss sample for events passing (black) and failing (red) BCH cleaning.	726
1245		

Not reviewed, for internal circulation only

1246 1 Introduction

1247 The search for the Standard Model (SM) [1–3] Higgs boson [4–7], is a central component of the physics
 1248 program at the Large Hadron Collider (LHC). The observation of a narrow resonance decaying to a pair
 1249 of photons, a pair of Z bosons, or a pair of W bosons has been reported by the ATLAS [8] and CMS [9]
 1250 collaborations. A Higgs boson with a mass of ≈ 125 GeV would be accessible in a number of channels
 1251 at the LHC. Measurements by ATLAS have thus far demonstrated that this narrow resonance can decay
 1252 to bosons. Observing the decay to a pair of b quarks would be the first direct observation of the coupling
 1253 to quarks by ATLAS and CMS. The decay to b quarks plays a particularly important role, as most of the
 1254 Higgs bosons with a mass of ≈ 125 GeV are predicted by the SM to decay to b quarks ($BR \approx 58\%$ [10])
 1255 and therefore an observation in this channel is crucial in providing a constraint to the overall Higgs
 1256 decay width, which is not directly measurable at the LHC. The cross section for associated production is
 1257 lower than the inclusive Higgs cross section by more than an order of magnitude, however the signature
 1258 provided by the leptonic decay modes of the associated vector boson is essential to reduce overwhelming
 1259 multi-jet backgrounds.

1260 We present an update with respect to [11] in the search for the Higgs boson decaying to a pair of b
 1261 quarks with the Higgs produced in association with a vector boson. This update uses 20.3 fb^{-1} of data
 1262 at $\sqrt{s} = 8 \text{ TeV}$ delivered by the LHC in 2012. As of now the 4.7 fb^{-1} of data at $\sqrt{s} = 7 \text{ TeV}$ delivered
 1263 by the LHC in 2011 will not be reanalyzed but will be included for the signal strength extraction. The
 1264 analysis is performed in three categories for events containing zero, one or two leptons. This targets
 1265 three channels of Higgs production: $ZH \rightarrow v\bar{v}b\bar{b}$, $WH \rightarrow \ell v\bar{b}\bar{b}$ and $ZH \rightarrow \ell^+\ell^-b\bar{b}$, where ℓ , or the term
 1266 lepton, is understood to be either an electron or a muon. The 2-lepton category is only sensitive to the ZH
 1267 production mode and the 1-lepton category is most sensitive to WH production. The 0-lepton category
 1268 is most sensitive to ZH production, but with a small although not insignificant contribution from WH
 1269 production.

1270 Two version of the analysis are documented; one using the dijet mass as the final variable used to
 1271 separate signal from background and another using a multivariate discriminant. The version using the
 1272 dijet mass is usually referred to as the dijet masss analysis by the analysis team. Referring to this version
 1273 as the dijet mass analysis helps the reader keep in mind that even though modeling all the variables which
 1274 are cut on is important, the understanding of the dijet mass shape and the quantities used to calculate it
 1275 is paramount since the signal extraction is done with a shape comparison. This thought process is not
 1276 different for a multivariate analysis, only more intricate.

1277 This note presents in parallel both versions of the analysis noting the common elements and the dif-
 1278 ferences. Section 3 discusses the data, triggers, and object definitions which are common to both analysis
 1279 as well as a side-by-side comparison of the event selection used. The signal samples and are discussed
 1280 in Section 4 and Section 5 includes a description of the backgrounds. Both sections include information
 1281 concerning systematic uncertainties specific to the processes discussed within. Section 6 introduces the
 1282 multivariate techniques used in the analysis. Section 7 briefly notes the systematic uncertainties already
 1283 discussed in the previous sections and detail those which are common to all (or most) processes. The
 1284 statistical model is introduced and motivated in Section 8 with the results given in Section 9.

1285 This analysis does not suffer from simplicity and so the documentation follows suit. Related sections
 1286 are referenced in a hope that if one chooses to not read the note from front to back, the necessary
 1287 information to understand the piece of the analysis chosen for investigation can be found easily. Enjoy!

1288 Appendix AN contains a list of the changes between each version of this note.

1289 2 Updates since summer 2013

1290 Several optimizations and changes in modeling were implemented in the analysis with respect to the
 1291 previous result reported in [11], in order to improve the search sensitivity. Some of these improvements
 1292 are briefly summarized in the following list:

- 1293 • Object selection changes

1294 The electron quality cuts for the signal have been changed to the likelihood definition;

1295 Removal of d_0 cut for electron identification;

1296 The lepton p_T used in the lepton veto have been lowered to 7 GeV;

1297 The Global Sequential Calibration (GSC) calibration is used for jets;

1298 The p_T -reco correction has been updated;

1299 The calorimeter isolation cut for leptons was tightened;

1300 The muon-jet overlap was revamped to take into account muons from V decays overlapping
 1301 jet objects;

1302 A new heavy flavor tagger, which has a better b-c jet discrimination, has been used (MV1c),
 1303 and a dedicated pseudo-continuous calibration has been derived;

1304 A $\sum p_T^{jet}$ cut was introduced in the 0-lepton analysis;

- 1305 • The Monte-Carlo (MC) samples were updated with more statistics when available.

- 1306 • A new multi-variate analysis have been produced.

- 1307 • The cut-based m_{jj} analysis have been updated including new tagging categories.

- 1308 • A more mature multijet suppression for the 1-lepton analysis have been derived and the multijet
 1309 model was updated.

- 1310 • In the 2-leptons analysis, a kinematic likelihood fit have been studied and used to improve the m_{jj}
 1311 resolution.

- 1312 • The missing transverse energy (MET) trigger modeling was studied and the efficiency scale factors
 1313 parametrized as function of the missing transverse energy and a specific cut on $\sum p_T^{jet_i}$ has been
 1314 used to avoid regions with trigger bias.

- 1315 • A MET based trigger was implemented to recover sensitivity on the 1-lepton analysis, by triggering
 1316 on events containing muons which have escaped due to limited acceptance of the L1 trigger muon
 1317 chambers (30% increase in statistics). MET triggered 1-lepton event have been studied and in-
 1318 cluded in the analysis for the 1-muon channel with $p_T^V > 120$ GeV (previously only $p_T^V > 160$ GeV
 1319 was included).

- 1320 • Detailed studies on the 0-lepton final state with $90 \text{ GeV} < E_T^{\text{miss}} < 120 \text{ GeV}$ have been done, with
 1321 the goal of including this region in the final fit. A dedicated effort have been made to validate the
 1322 use of the delayed stream in this E_T^{miss} region.

- 1323 • Revisit and change of the $\Delta\phi$ corrections to $V+jets$ simulations.

- 1324 • Every modeling systematic was reevaluated.

3 Data selection and event reconstruction

This section describes the event reconstruction and selection. The signal is characterized by a leptonically decaying vector boson and a Higgs decaying to a pair of heavy-flavor jets. The selection criteria was designed to maximize the acceptance of the expected signal topology while reducing the multijet and electroweak backgrounds contributions to a minimum. Section 3.1 details the data sets and triggers used. Section 3.2 describes the criteria used to reconstruct objects followed by how the objects are used to optimally select events compatible with the signal topology in Section 3.3.

3.1 Introduction on the data and Monte Carlo simulation.

The data used in this analysis were recorded by the ATLAS experiment during the 2012 LHC runs at a center-of-mass energy of $\sqrt{s} = 8$ TeV with an integrated luminosity of 20.3 fb^{-1} [12].

The Monte Carlo (MC) samples used in the analysis are generated at the same center-of-mass energy as the corresponding data sample and passed through the ATLAS detector simulation [13] which is based on the GEANT 4 [14] program. In order to have significant amount of MC statistics, the “ATLFast II” simulation [15] is used for almost all the samples (the exceptions are noted in Section 5). Due to the differences in the distribution of pile-up events in the MC simulation with respect to the one measured in data, the standard pile-up re-weighting strategy has been adopted [16].

Event with leptons are primarily selected using the lowest un-prescaled single lepton triggers in addition to dilepton triggers where appropriate from EGamma and Muon streams in data. The lowest un-prescaled single lepton triggers used include a requirement on track isolation (iso_{track}) to combat the high pile-up conditions in the 2012 LHC data at the cost of a slight trigger inefficiency. To recover the lost events higher threshold triggers without a iso_{track} requirement are considered. To ensure that the trigger efficiency is well-defined, trigger matching is used to ensure that the offline lepton is the same lepton which fired the trigger. Missing transverse energy (E_T^{miss}) triggers in the JetTauEtmiss data stream are used to select events where the vector boson decays to neutrinos or charged leptons which are not identified or reconstructed. The full list of triggers considered is given in Table 1.

Trigger Object	Data Period	Trigger Names	iso_{track}	Luminosity (fb $^{-1}$)
$E_T^{\text{miss}} < 160 \text{ GeV}$	A-B5	EF_xe80T_tclcw_loose	NA	1.91928
	B6-L	EF_xe80_tclcw_loose		18.132
$E_T^{\text{miss}} > 160 \text{ GeV}$	A-B5	EF_xe80_tclcw	NA	2.1257
	B6-L	EF_xe80_tclcw_loose		18.132
single electron	A-L	EF_e24vhi_medium1	✓	20.2769
		EF_e60_medium1		
single muon		EF_mu24i_tight	✓	20.2769
		EF_mu36_tight		
di-electron di-muon	A-L	EF_2e12Tvh_loose1		20.2769
		EF_2mu13		

Table 1: Trigger table used in the 2012 data analysis. The digits exceed the precision on the measurement of the luminosity, but they are reported here for future reference, since these are the numbers used to normalize the Monte Carlo predictions.

Not reviewed, for internal circulation only

1350 3.2 Object Definition

1351 The following sections outlines the requirements used to select leptons (Section 3.2.1), jets (Section 3.2.2),
 1352 b -jets (Section 3.2.3), and E_T^{miss} (Section 3.2.4), as well as the overlap removal criteria (Section 3.2.5)
 1353 used to ensure no object is double counted. More technical information concerning the common perfor-
 1354 mance group packages and tags used is given in Appendix AP.

1355 3.2.1 Lepton

1356 Three inclusive lepton definitions are listed below in increasing order of purity: loose (Section 3.2.1.1),
 1357 medium (Section 3.2.1.2), and tight (Section 3.2.1.3). As discussed in the next pages, tight leptons are
 1358 used for the selection of the W events, medium and loose for Z , and loose leptons are also used to veto
 1359 events with extra leptons (like $t\bar{t}$). A lepton must also pass the overlap removal rules specified in Sec-
 1360 tion 3.2.5 to be considered in any analysis. Scale factors to correct for differences in the modeling of the
 1361 efficiency of the isolation cuts discussed in the following sections have been calculated using tag and
 1362 probe analysis with the Z boson and are discussed in Appendix E and F for electrons and muons respec-
 1363 tively. With respect to the previous analysis [11], using the same calibration ?? the lepton minimum p_T
 1364 requirement for Loose muons was decreased to 7 GeV (from 10 GeV) in order to maximize the 2-lepton
 1365 signal acceptance and the rejection of $t\bar{t}$ events in the 0 and 1-lepton analyses. The electron quality was
 1366 also changed to the likelihood definition which provides almost two times larger jet rejection for same
 1367 electron efficiency compared to the cut-based one [17] [18]. Table 2 is a excerpt from Table 2 in [17]
 1368 which compares the efficiency of real and fake electrons for the three cut-based definitions used for
 1369 EPS and the corresponding likelihood definitions used for the current version. Figure 1 shows a similar
 1370 comparison of the cut-based and likelihood definitions as a function of the electron E_T .

Menu	$20 < E_T < 50 \text{ GeV}$	
	Data efficiency (%) $Z \rightarrow ee$	Data efficiency (%) Background
Loose Cuts	95.68 ± 0.17	5.414 ± 0.025
Very Loose LH	97.77 ± 0.14	3.028 ± 0.019
Tight Cuts	77.48 ± 0.24	0.463 ± 0.008
Very Tight LH	76.97 ± 0.29	0.278 ± 0.006

Table 2: Taken from [17], signal and background efficiencies for likelihood and cut-based menus, averaged over η and E_T between 20 and 50 GeV. Both signal and background efficiencies are determined with respect to basic track quality cuts in the denominator and errors on the signal include statistical and systematic uncertainties, while uncertainties in background are statistical only.

1371 3.2.1.1 VH Loose Lepton

1372 The VH loose lepton criteria are defined in Table 3. Calorimeter ?? and stand-alone ?? muons are used
 1373 to increase the muon acceptance in η . Track isolation is defined as:

$$iso_{track}(\ell) = \frac{1}{p_T^\ell} \sum_{trk} p_T^{trk} \text{ for } \Delta R(\ell, trk) < 0.2. \quad (1)$$

1374 The calo-muon candidates within $\Delta R < 0.1$ of a selected combined, segmented tagged or stand-alone
 1375 muon are rejected to avoid double counting.

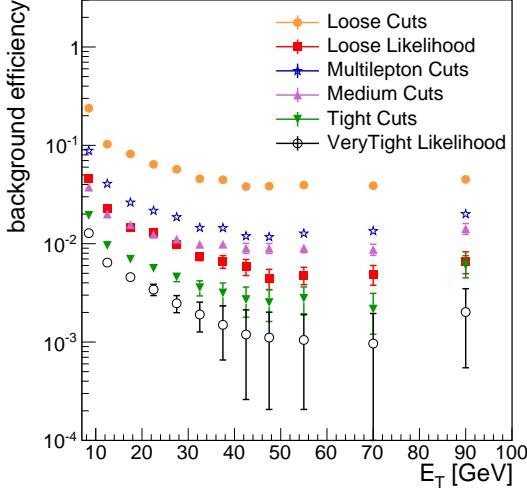


Figure 1: A comparison of the cut and likelihood qualities is shown as a function of the transverse energy of the electron object. This shows the increase in background rejection for the same signal efficiency for the various quality definitions.

Not reviewed, for internal circulation only

1376 3.2.1.2 VH Medium Lepton

1377 VH Medium leptons have additional requirements in addition to those used to define loose leptons. For
 1378 muons, only combined/segment-tagged muons are considered. Stand-alone and Calo muons are not
 1379 considered to identify the decay products of the vector boson as this would lead to an increase in the
 1380 multijet background. The medium lepton cuts are outlined in Table 3.

1381 3.2.1.3 VH Tight Lepton

1382 VH Tight leptons are medium candidates satisfying tight isolation requirements. In addition, tight elec-
 1383 trons should pass the very tight LH selection. The VH Tight lepton cuts are defined in Table 3. Calorime-
 1384 ter isolation (iso_{calo}) is defined as:

$$1385 iso_{calo}(\ell) = \frac{1}{p_T^\ell} \sum_{TC} E_T^{TC} \text{ for } \Delta R(\ell, TC) < 0.3. \quad (2)$$

1386 where TC stands for topoclusters. The electron isolation is corrected in order to subtract out-of-cluster
 1387 leakage in the isolation cone, and energy density from underlying event and pileup (using the jet area
 1388 technique).

1389 The tight lepton selection has been re-optimized in concert with the 1-lepton multijet model lepton
 1390 selection. In comparison to the EPS result [11] the calorimeter isolation criterion has been tightened from
 1391 0.07 to 0.04 in both the electron and muon channel. A loose d_0 significance requirement, $\left(\frac{d_0}{\sigma_{d_0}}\right)$, had been
 1392 entertained in the muon channel to help reduce the multijet contribution but this cut was shown to be
 ineffective after applying the event level cuts.

1393 3.2.1.4 Notable Change from EPS

1394 For over two years now the impact parameter (d_0) has been required to be less than 0.1 mm for both the
 1395 electron and muon channel. For electrons, a d_0 cut should be used with associated scale factors which do
 1396 not exist and therefore would have to be derived by this analysis group. With the interest of time, this cut

1397 as been dropped from the electron channel only resulting in an over 10% increase of the 2-electron signal
 1398 acceptance with the cost of a non-negligible multijet contribution described in detail in Appendix S and
 1399 summarized in Section 5.4.2. In the 1-electron channel the signal acceptance increased less than 2% as
 1400 the EM likelihood has a decreased efficiency at larger d_0 values.

1401 **3.2.1.5 1-lepton Multijet Model Leptons**

1402 Data events are used to estimate the contribution of multijet (MJ) events which satisfy the 1-lepton
 1403 selection since generating sufficient MC statistics to model this process would be extremely difficult.
 1404 A MJ model region is defined from which data events are extracted and the electroweak contribution
 1405 subtracted to obtain the MJ template. The MJ model region is defined as Medium VH leptons with the
 1406 modification of $0.05(0.07) < iso_{track} < 0.12(0.5)$ in the $e(\mu)$ channel and $iso_{calo} < 0.07$ in both and the
 1407 quality of MediumPP [19] in the e channel on top of the *VeryLoose* LH criteria. The choice of cuts is
 1408 motivated in Appendix R but stated briefly the cuts were determined in order to have decent agreement
 1409 with template sufficient statistics to populate the high p_T^V regions. All event level cuts are then required.
 1410 Full details on the MJ estimation including normalization, b -tagging, and systematic uncertainties are
 1411 given in Section 5.4.3. The template region has changed since EPS [11]. Then the iso_{track} range was
 1412 changed from $0.04 \leq iso_{track} \leq 0.1$ to reduce the fraction of EW contamination (increase lower cut)
 1413 and increase the available statistics (increase the upper cut). The *VeryTight* LH criteria was checked
 1414 in the electron channel but was shown to produce a template similar to the MediumPP choice but with
 1415 less statistics. The iso_{calo} cut was not tightened to 0.04 as it was for the signal lepton to maintain more
 1416 statistics in the template. The details of the studies performed to make these decisions are given in
 1417 Appendix R but these changes resulted in an increase in the MJ statistics by a factor of 2. Figure 2 shows
 1418 a schematic of all the lepton selections used for the 1-lepton analysis.

Flavor Type	Electrons Author 1 or 3	Muons		
		Comb/Seg-Tag	Calo	Stand Alone
VH Loose				
Quality	VeryLoose LH [17] [18]	Tight MuID & MCP hit requirements		
$ \eta $	< 2.47	< 2.7	< 0.1	in [2.5, 2.7]
E_T (GeV)	> 7	> 7	> 20	> 7
$ d_0 $ (mm)	–	< 0.1	< 0.1	NA
$ z_0 $ (mm)	–	< 10	< 10	NA
iso_{track}	< 0.1	< 0.1	< 0.1	NA
VH Medium				
E_T (GeV)	> 25	> 25	NU	NU
$ \eta $	–	< 2.5		
VH Tight				
Quality	VeryTight LH	–		
iso_{track}	< 0.04	< 0.04	NU	NU
iso_{calo}	< 0.04	< 0.04		

Table 3: Inclusive VH Loose, Medium and Tight lepton definitions. NU stands for ‘Not Used’. Additional information is given in Sections 3.2.1.1-3.2.1.3.

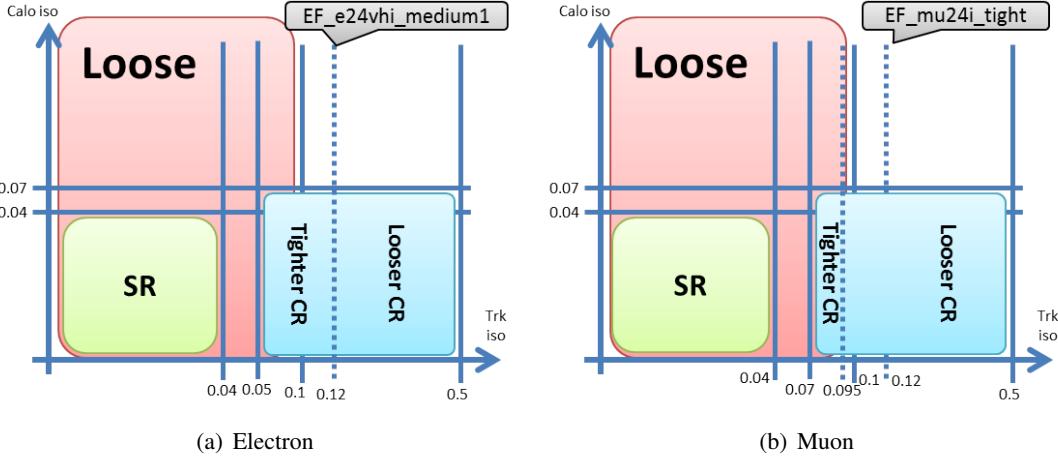


Figure 2: The 1-lepton selection is shown for electrons (a) and muons (b) in the $\text{iso}_{\text{track}}$ versus iso_{calo} plane. The red box fills the region used for Loose leptons and the green box fills the Tight lepton region. The blue box represents the region used for the 1-lepton multijet selection. One can clearly see that only some multijet leptons satisfy the loose lepton criteria. For electrons, the Tight CR is used for the nominal template and the loose for the systematic variation. For muons, the inclusive CR is used for the nominal while Tight and Loose are used individually for the Up and Down systematic variation of the $\text{iso}_{\text{track}}$ cut.

3.2.2 Jet

Jets are reconstructed using the anti- k_T algorithm [20] with a radius parameter $R = 0.4$. The jet energy dependence on in-time pile-up is mitigated by applying two data-derived corrections: one based on the product of the event p_{T} density and the jet area [21], and one that depends on the number of reconstructed primary vertices and the mean number of expected interactions which primarily affects jets in the forward region. The second correction addresses effects due to out-of-time pile-up. After the two corrections, an energy and η -dependent MC-based calibration is applied to all jets. Finally, a residual correction from in situ measurements is applied to data.

Since the previous version of this analysis was released [11] a new calibration known as Global Sequential Calibration (GSC) has been introduced and is applied on top of the EM+JES calibration. GSC was proposed as a way of incrementally improving the jet energy resolution and making the jet response,

$$R = \langle p_{\text{T}}^{\text{reco}} / p_{\text{T}}^{\text{truth}} \rangle, \quad (3)$$

less dependent whether the jet is more quark-like or gluon-like. In ATLAS, this is referred to as flavor dependence which should not be confused with the quark flavor (b, c, light) assigned to jets. In this note, jet flavor usually refers to the quark flavor and in cases where the terminology is used to denote quark-gluon differences, the meaning of flavor is clarified. Sequential corrections are applied as

$$C(x, p_{\text{T}}) = R^{-1}(x, p_{\text{T}}) \quad (4)$$

where x is the jet property under consideration. This list of jet properties considered can be found in Table 4. Ghost-matched tracks ?? selected by the criteria listed in Table 5 with $p_{\text{T}} > 1$ GeV and associated to the 0th primary vertex are used for the track related properties including the track width, W_{track} , which is defined as

$$W_{\text{track}} = \frac{\sum_{\text{trk}} p_{\text{T}} \Delta R(\text{jet}, \text{trk})}{\sum_{\text{trk}} p_{\text{T}}} \quad (5)$$

1439 The W_{track} correction has been shown to be the modification which reduces the difference in response
 1440 between light-quark and gluon jets. Coincidentally this correction is applied last and can be removed
 1441 to understand the effect on b -jets. More details about the correction technique can be found in Refer-
 1442 ences [22], [23] as well as in Appendix G. The main motivation for using this calibration in a quark-
 1443 dominated final state analysis such as this one is for the improvement in the dijet mass resolution.

Jet Property	Order	Definition
f_{tile0}	1	fraction of energy deposited in the first layer of the Tile calorimeter
f_{em3}	2	fraction of energy deposited in the third layer of the EM calorimeter
n_{trk}	3	track multiplicity
W_{track}	4	p_T weighted average ΔR of tracks in the jet

Table 4: Ordered list of jet properties used in the GSC calibration. More details are given in Section 3.2.2 including the track selection shown in Table 5.

Observable	Cut
Track Selection Criteria	
p_T (GeV)	> 0.5 OR > 1.0
$ \eta $	< 2.5
pixel hits	> 0
SCT hits	> 5
$ z $ (mm)	< 200
d_0 (mm)	< 5.0
d_0/σ_{d_0}	< 100
χ^2/DOF	< 5
Track-Vertex $_i$ Association	
d_i (mm)	< 1.0
$z_i \sin(\theta)$ (mm)	< 1.0

Table 5: Selection used for tracks to be associated to jets and vertices. Additional information, including the various p_T cuts, is given in Section 3.2.2.

1444 Two orthogonal categories of jets, *signal* and *forward*, are defined by the criteria outlined in Table 6.
 1445 Only signal jets are considered to potentially have originated from a Higgs decay which motivates the
 1446 usage of these jets for event kinematics calculations. A jet must also pass the overlap removal rules
 1447 specified in Section 3.2.5 to be considered in any analysis. To suppress the contribution from jet produced
 1448 by pile-up interactions, a cut on the Jet Vertex Fraction (JVF) is used. Tracks with $p_T > 0.5$ GeV and
 1449 satisfying the requirements given in Table 5 are used in the JVF definition,

$$\text{JVF}(jet_j, vtx_k) = \frac{\sum_i p_T^{trk_{ijk}}}{\sum_k \sum_i p_T^{trk_{ijk}}}, \quad (6)$$

1450 where trk_{ijk} is the i^{th} track ghost-matched to the j^{th} jet associated to the k^{th} vertex. The JVF used in
 1451 the analysis is evaluated for the highest $\sum p_T^2$ vertex, or the 0^{th} vertex in the event and is only applied to
 1452 jets with $p_T < 50$ GeV and $|\eta| < 2.4$. This limited application is because the cut discriminates against

1453 jets which are not produced in the primary interaction, so called pile-up jets, which tend to have a softer
 1454 spectrum and the cut is not applied unless the jet falls completely within the inner tracker acceptance.

Type	Signal Jet	Forward Jet
$p_T(\text{GeV})$	$\text{jet}_{i=1} > 45$ $\text{jet}_{i>1} > 20$	> 30
$ \eta $	< 2.5	$2.5 < 4.5$
$ \text{JVF} $	$> 0.5^{\dagger}$	–

Table 6: Selection used to define orthogonal sets of central and forward jets. [†]The JVF cut if only required for jets with $p_T < 50 \text{ GeV}$ and $|\eta| < 2.4$. More information can be found in Section 3.2.2.

1455 The flavor of reconstructed Monte Carlo jets is determined by the hadrons with $p_T > 5 \text{ GeV}$ within a
 1456 cone of $R = 0.4$ defined by the jet axis. The flavor hierarchy is b, c , then τ such that the jet is labeled by
 1457 the highest hadron-lepton within the list found in the jet. The *light-jet* category is used if neither a heavy
 1458 flavored hadron nor a τ are found.

1459 3.2.3 *b*-Jet

1460 Jets which originate from *b* quarks are identified using algorithms which exploit the long lifetime of *b*
 1461 hadrons. The *b*-tagging algorithm MV1c [24–26] is used, which combines information from an impact
 1462 parameter based algorithm, an inclusive secondary vertex finder, and a $b \rightarrow c$ hadron decay chain fit
 1463 into a single neural network based discriminant, w , such that jets with higher w are more likely to be
 1464 *b*-jets. The MV1 algorithm which was used in the EPS result [11] has been abandoned in favor of the
 1465 MV1c tagger. MV1c has superior *c*-jet rejection, at the price of a smaller *light*-jet rejection factor in
 1466 the tighter operating points, achieved by training the discriminant against a mixture of *light* and *c*-jets¹.
 1467 Section 5.2.1.1 motivates the need for enhanced *c*-jet rejection. A comparison of MV1 and MV1c tagger
 1468 performance in Table 7. Another change compared to EPS is the fact that the MV1c tagger has been
 1469 calibrated such that one can apply upper and lower cuts on w which is referred to as *continuous* or
 1470 *pseudo-continuous tagging*. In other words, the operating points described in Table 7 are inclusive, such
 1471 that a ‘Tight’ *b*-tagged jet will always satisfy the ‘Loose’ requirement, however the information can
 1472 be used in an exclusive way, by requesting jets which satisfy ‘Medium not Tight’ for example. This
 1473 feature allows for the division of the sample into regions of higher sensitivity through the use of multiple
 1474 operating points as discussed in Section 3.3.4. For EPS only the 70% operating point was used. These
 1475 changes improve the 0, 1, and 2-lepton dijet mass analysis *approximately* 7, 15, and 9% respectively
 1476 without considering systematics.

1477 The w distribution needs to be calibrated such that the efficiency in MC matches that in data. A
 1478 combinatorial likelihood method [27] has been used in dilepton $t\bar{t}$ events [28] [29] to calibrate the *b*-jet
 1479 efficiency. The *c* and *light* jet efficiencies were calibrated from D^* [30] and dijet [31] samples respec-
 1480 tively. The pseudo-continuous calibration is described in [32] from where the Figure 3 showing scale
 1481 factors for representative jet p_T bins was extracted.

1482 3.2.4 E_T^{miss} and track-based missing transverse momentum

1483 E_T^{miss} and the track-based missing transverse momentum (p_T^{miss}) are reconstructed using the standard
 1484 techniques developed in the JetEtMiss performance group. For the E_T^{miss} , the METRefFinal_Eflow has

¹MV1 was trained only against *light* jets

Not reviewed, for internal circulation only

Name	w value	b -jet eff. (%)	c -jet RF		τ -jet RF		l -jet RF	
			MV1c	$\frac{\text{MV1c}}{\text{MV1}}$	MV1c	$\frac{\text{MV1c}}{\text{MV1}}$	MV1c	$\frac{\text{MV1c}}{\text{MV1}}$
80 ‘Loose’ or ‘L’	0.4050	79.85	3.04	0.98	6.40	1.13	29.12	1.07
70 ‘Medium’ or ‘M’	0.7028	70.00	5.34	1.07	14.90	1.01	135.76	0.91
60	0.8353	59.99	10.45	1.31	33.92	1.35	453.53	0.70
50 ‘Tight’ or ‘T’	0.9237	49.99	26.22	1.9	120.33	2.6	1388.28	0.55

Table 7: The efficiencies for the available calibrated operating points for the MV1c algorithm and a comparison to the MV1 algorithm performance. These values have been determined in di-leptonic $t\bar{t}$ events with a jet p_T threshold of 20 GeV. RF stands for Rejection Factor which is the reciprocal of the efficiency. These numbers were taken from Reference ??.

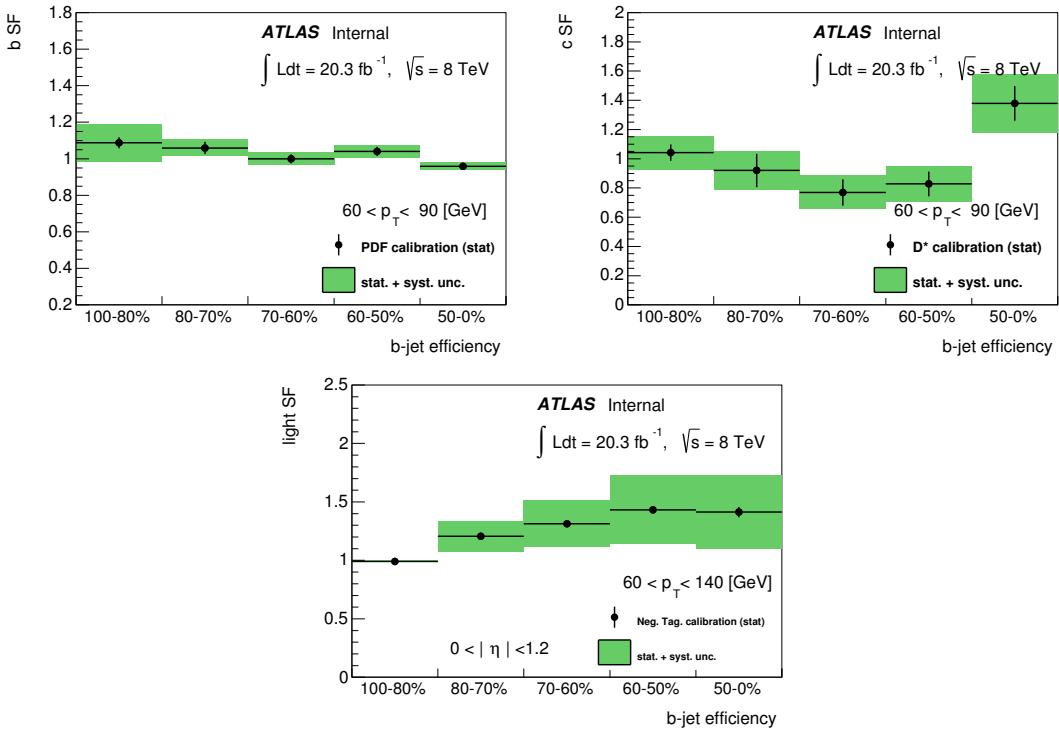


Figure 3: Taken from Ref. [32], the final MC-to-data calibration scale factors for the MV1c b , c -jet and $|\eta| < 1.2$ light-jet calibration is shown for a representative jet p_T bin. The data results are compared to the MC expectations. Error bars refer to statistical uncertainties, while the total error bands include systematics as well.

1485 been used, while the p_T^{miss} with no object (cluster or jet) corrections have been used. For consistency
 1486 with the object definition, in both the METRefFinal_Eflow and p_T^{miss} muID muons have been used.

1487 The METRefFinal_Eflow includes all the standard terms: RefEle, RefGamma, RefTau, RefJet,
 1488 MuonTotal, and SoftTerm. Each of these terms, with the exception of RefGamma and RefTau, is
 1489 recalculated from each object, synchronizing all the correction and systematic variations for the objects
 1490 described above. For RefGamma and RefTau the pre-calculated terms in the D3PD are used. Specific
 1491 corrections for the jet-egamma overlap have been used. Due to the E_T^{miss} setup used in the analysis, the
 1492 jet-egamma overlap correction has an effect between jet and electrons which results in a potential double
 1493 counting of energy. The impact of the jet-gamma overlap correction has been evaluated to be negligible
 1494 for the specific selection of the analysis, nevertheless the fix is used. Reference [33] shows the effect of
 1495 the problem and the solution in a different analysis.

1496 The E_T^{miss} enters in different part of the analysis: as input variable for the multi-variate analysis, and,
 1497 just to mention some uses, to estimate the p_T^W in the 1-lepton channel, to estimate the $Z p_T$ in the 0-lepton
 1498 channel, and to suppress the top background in the 2-lepton channel.

1499 On the contrary, the use of the p_T^{miss} is limited to suppress the non-collision and to extract the estimate
 1500 of the multi-jet background in the 0-lepton channel. A cut of $p_T^{\text{miss}} > 30 \text{ GeV}$ cleans the non-collision
 1501 background while avoiding any cuts on the jets (like the cuts on the EM fractions and on the maximum
 1502 layer fraction, used in other 0-lepton analysis in ATLAS). Since a direct cut on jet variables can cause
 1503 a bias in both the jet calibration, and the b -tagging calibration with respect to the other channels in this
 1504 search, the p_T^{miss} cut has been selected. The other p_T^{miss} quantity used is the direction. A coarse cut on
 1505 the $\Delta\phi(E_T^{\text{miss}}, p_T^{\text{miss}})$ is used in the ABCD method to extract the multijet template and normalization from
 1506 data for the 0-lepton analysis. The track selection ?? is described in Table 8. No mis-reconstructed tracks
 1507 removal have been used.

Observable	Cut
p_T (GeV)	> 0.5
$ \eta $	< 2.4
pixel hits	> 0
SCT hits	> 5
d_0 (mm)	< 1.5
$z_0 \sin(\theta)$ (mm)	< 1.5

Table 8: Tracks for p_T^{miss} definition ?? Additional information is given in Section 3.2.4.

1508 3.2.5 Overlap Removal

1509 To ensure objects are not double counted a hierarchy shown in Table 9 has been established in order to
 1510 decide which interpretation of the energy deposit in the detector is most likely correct for objects which
 1511 satisfy the loosest of the above mentioned criteria. The order in which the ambiguities are resolved is
 1512 given in the table. Already stated previously (Section 3.2.1.1), calo-muons are required to have $\Delta R > 0.1$
 1513 from any other muon in the event. N_{trk} is the track multiplicity of ghost-matched tracks with $p_T >$
 1514 0.5 GeV , satisfy the track selection in Table 5, and are compatible with the 0^{th} primary vertex as defined
 1515 in said table. A complicated muon-jet overlap such as this is motivated by the fact that the muon from
 1516 the vector boson decay can randomly fall on top of a jet. Removing these muons, as was done for EPS,
 1517 reduces the 2-lepton signal acceptance 12%. In order to increase the signal acceptance as much as
 1518 possible as well as avoid counting muons from semi-leptonic b and c decays as signal muons, the N_{trk}
 1519 cut was adopted. Appendix H details the studies arriving at this conclusion.

Case	Order	Keep μ	Keep e	Keep jet
$\Delta R(jet, e) < 0.4$	1	–	Yes	No
$\Delta R(jet, \mu) < 0.4$	2	$N_{trk} \leq 3$	–	$N_{trk} \geq 4$
$\Delta R(\mu, e) < 0.2$	3	if not Calo μ	if Calo μ	–

Table 9: Overlap hierarchy and the order in which the ambiguity is checked. N_{trk} is the track multiplicity of ghost-matched tracks with $p_T > 0.5$ GeV, satisfy the track selection in Table 5, and are compatible with the 0th primary vertex as defined in said table.

Not reviewed, for internal circulation only

1520 3.3 Event Selection

1521 The following sections outlines how the objects described in Section 3.2 are used to define analysis categories and the event kinematic cuts applied. First event level cleaning cuts are described in Section 3.3.1
 1522 then trigger selection is discussed in Section 3.3.2. The use of leptons (Section 3.3.3), and jets (Section
 1523 3.3.4) to define analysis categories if followed by the event level kinematic cuts (Section 3.4) to
 1524 conclude the description of the selection and categorization of events. The final section (Section 3.5)
 1525 details the improvements to the dijet mass resolution pursued by the analysis group itself.
 1526

1527 3.3.1 Event Cleaning

1528 The data are required to satisfy conditions ensuring essential elements of the ATLAS detector were
 1529 operational with good efficiency while the data were collected. The data quality requirements are imple-
 1530 mented using a Good Run List (GRL) based on the ATLAS Data Quality (DQ) flags. The GRL used in
 1531 this analysis is

1532 `data12_8TeV.periodAllYear_DetStatus-v61-`
 1533 `pro14-02_DQDefects-00-01-00_PHYS_StandardGRL_All_Good.xml`

1534 On top of the GRL request, a series of standard cleaning cuts are applied to avoid sporadic event
 1535 problems in the detector, during reconstruction, or due to activity in the detector from non-collision
 1536 background. The cuts are as follows:

1537 On data:

- 1538 **Incomplete Events:** remove events that have Core EventInfo error flag (`coreFlags&0x40000! = 0` in D3PD);
- 1539 **LAr Error Flag:** remove events that have LAr EventInfo error flag;
- 1540 **TileCal Error Flag:** remove events that have Tile EventInfo error flag;
- 1541 **Corrupted Tile Events:** remove corrupted tile events using TileTripReader;
- 1542 **Hot Tile Cells:** Reject events with jets (after overlap removal and before JVFCut) pointing to
 the Hot Tile Cell in the runs : 202660, 202668, 202712, 202740, 202965, 202987, 202991,
 203027, 203169.

1546 On simulations:

- 1547 **Incomplete Events:** reject MC events that have no truth particles (`mc_n == 0` in D3PDs).

1548 On both data and simulations:

- 1549 **Vertex Selection:** Require that the first primary vertex contains at least 3 tracks;

Not reviewed, for internal circulation only

1550 **MET Cleaning:** Reject any data or MC event containing a looser bad jet ?? with $p_T > 20 \text{ GeV}$,
 1551 $|\eta| < 4.5$ (after overlap removal and before JVF cut).

1552 Recently the BCH cleaning prescription has been modified to remove jets in regions of the detector where
 1553 entire modules in the tile calorimeter were non-operational during data taking. Most of these modules
 1554 were not simulated in the MC and a correction derived by the Jet/ETMiss group to correct for these dead
 1555 modules has been shown to be inaccurate. The result of the detailed studies is discussed in Appendix .
 1556 No jet or event removal have been adopted in this analysis.

1557 3.3.2 Trigger Selection

1558 This section describes how the triggers noted in Section 3.1 are used in each analysis. The 0-lepton
 1559 analysis uses all the E_T^{miss} triggers and the parametrization of these triggers is detailed in Appendix A.
 1560 0-lepton events with $p_T^Z < 120 \text{ GeV}$ were not included in the EPS analysis due to the difficulty of the
 1561 parametrization of the E_T^{miss} trigger turn-on. Appendix C details the work done to include as much of the
 1562 phase space below 120 GeV into the analysis. The 1-lepton analysis uses all the single-lepton triggers
 1563 and in events with $p_T^W > 120 \text{ GeV}$ E_T^{miss} triggers are used to supplement holes the muon trigger coverage
 1564 (was 160 GeV for EPS). The 2-lepton analysis uses the single and dilepton triggers.

1565 3.3.3 Lepton Selection

1566 This section describes how the lepton classifications described in Section 3.2.1 are used in define the
 1567 three orthogonal analyses. The leptons used to reconstruct the vector boson are given in Table 10. Tighter
 1568 requirements are used in the 1-lepton analysis to reconstruct the W compared to those used to reconstruct
 1569 the Z because of the potential of a larger multijet background faking leptonic W-decays. Note events
 1570 with exactly one VH Loose lepton that fail the VH Tight selection are not used. Preliminary studies not
 1571 documented here showed that including these events would bring minimal improvement to the sensitivity
 1572 and are therefore not considered in this analysis.

Analysis	VH Loose	VH Medium	VH Tight
0-lepton	0	–	–
1-lepton	0	0	1
2-lepton	1	1	–

Table 10: Signal lepton selection from the 3 inclusive VH lepton definitions.

1573 3.3.4 Jet Selection

1574 This section describes how the jet classifications described in Section 3.2.2 are used to select events
 1575 compatible with a Higgs decay and define analysis categories in order to isolate regions with a large
 1576 signal to background ratio. The analysis jet multiplicity requirements are given in Table 11. Events with
 1577 forward jets are vetoed in order to reduce contributions from single and pair production of top-quarks
 1578 which is a major background in the 0 and 1-lepton analysis.

1579 Events are categorized by the number of signal jets present in the event and are further divided by
 1580 the number of b-jets present as shown in Figure 4. Three exclusive double b-tag categories are used in
 1581 both the dijet and MVA analyses ² given criteria but fails the next highe

²As explained in Section 3.2.3, an exclusive b-tag means that the jet passes the operating point in question but does not satisfy the adjacent tighter one. Concretely, exclusive Loose, referred to as Loose, is used for jets which pass the Loose cut but

Jet Type	Signal	Forward
0-lepton		
1-lepton	2-3	0
2-lepton		

Table 11: Jet multiplicity requirements for each analysis.

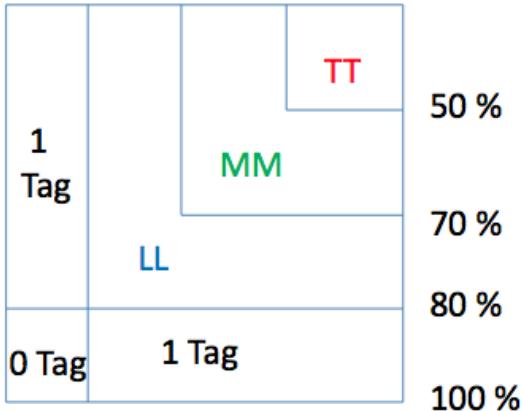
- 1582 • Two exclusive Loose b -tags: ‘LL’ or ‘2L’

- 1583 • Two exclusive Medium b -tags: ‘MM’ or ‘2M’

- 1584 • Two tight b -tags: ‘TT’ or ‘2T’

1585 The single b -tag regions are inclusive in the operating points given. In the fit model, discussed in Section 8, some of the double b -tag regions have been combined for the sake of simplicity. 3-signal jet (or
 1586 3-jet) events are vetoed if the the lowest p_T jet passes the loose b -tag cut given in Table 7. N.B. in this
 1587 document, when an event is characterized by a jet multiplicity, it refers only to signal jets furthermore
 1588 only signal jets are considered for event-level kinematic variables such as M_{eff} , ΔR , m_{jj} , etc. Recall,
 1589 section 3.2.3 motivated the use of a pseudo-continuous flavor-tagging algorithm (including a pointer to
 1590 Section 5.2.1.1).

1591 In the 2-lepton channel the strict jet requirements are not completely needed since the main back-
 1592 ground is not top events and the sensitivity evolves differently in jet multiplicity bins. Since the reader
 1593 has not been introduced to all the backgrounds, signals, selection etc, a more quantitative discussion is
 1594 located in Appendix J.1.

Figure 4: A graphical representation of the exclusive b -tagging categories used.

1596 3.3.4.1 Truth Tagging Versus Direct Tagging

1597 Due to the powerful discrimination of the MV1c algorithm against non- b -jets, it is difficult to produce
 1598 enough Monte Carlo to have reasonable statistics after requiring 2 b -tags for events without b -jets. A
 1599 method known as ‘truth tagging’ is therefore used in 2 b -tag events in which neither of the two leading
 1600 p_T jets is a truth-matched b -jet. Truth tagging is a method by which a random MV1c value above the

fail the Medium requirement. Medium is for jets which pass the Medium cut but fail the Tight cut.

1601 loose operating point is generated for a given jet. This is done by creating a ‘random efficiency’ obtained
 1602 from sampling a cumulative distribution built from the tagging efficiency above the loose operating point
 1603 and assigning the MV1c value corresponding to the random efficiency generated to the jet in question.
 1604 The sample dependent ($t\bar{t}$, $W+\text{jets}$, $Z+\text{jets}$) efficiencies used to build the cumulative distribution are
 1605 parametrized as a function of the flavor, transverse momentum and pseudo-rapidity of the given jet as
 1606 well as the process type (see Appendix T.1). After the generation of a random MV1c value every jet will
 1607 by construction satisfy the loose b -jet cut, so to correct for this bias, the event must be weighed down by
 1608 the efficiency of the jet to pass the loose operating point. In events where one of the leading two jets is
 1609 truth-matched to a b -hadron, this procedure is note used, and the original w of each jet is directly cut on;
 1610 the event is said to have been ‘direct tagged’. Full details of the efficiency maps and closure tests can be
 1611 found in Appendix T.1.

1612 3.3.4.2 Biases from Truth Tagging

1613 Truth-tagging is wonderful in that it dramatically increases the available statistics but this method ignores
 1614 correlations in the tagging efficiencies of jets in the same event. For events with two c -jets a bias in the
 1615 tagging efficiency as a function of $\Delta R(cc)$ has been seen and a correction was derived; both are shown in
 1616 Figure 5. Half the correction is used as a systematic uncertainty (BTagTruthTagDR). More details are
 1617 given in Appendix T.3.

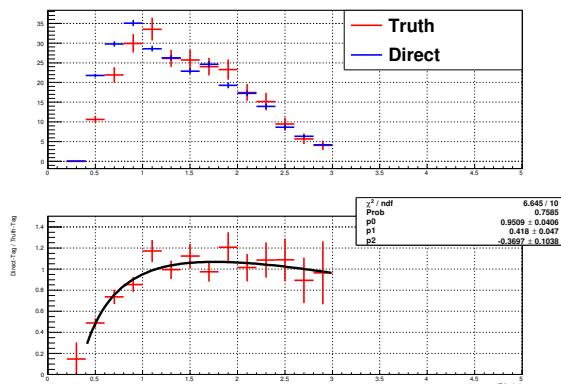


Figure 5: Truth tagging ΔR correction derived from the ratio truth to directed tagged events using $W+cc$ and $Z+cc$ in 2 and 3-jet events (top) in the 0-lepton mvaselection. The correction itself is obtained from a fit to the ratio (bottom): $0.9509 + 0.418 \times \ln(\Delta R) - 0.3697 \times \ln^2(\Delta R)$.

1618 3.3.4.3 Biases from Generators

1619 The data-MC scale factors were derived with respect to PYTHIA6 for b -jets and c -jets alike. As shown
 1620 in Figure 6 for the exclusive 70% MV1c operating point, the efficiency for jets truth-matched to a b -
 1621 jet and c -jets different for the three generators used in this analysis (PYTHIA6, PYTHIA8, and SHERPA). A
 1622 correction is not applied to *light* jets since the effect and the light jet contribution are both small. Half
 1623 the correction is used as a systematic which is decorrelated for b and c jets as well as for the PYTHIA8,
 1624 and SHERPA(BTagBSherpa, BTagBPythia8, BTagCSherpa, BTagCPythia8). More details are given in
 1625 Appendix T.2.

Not reviewed, for internal circulation only

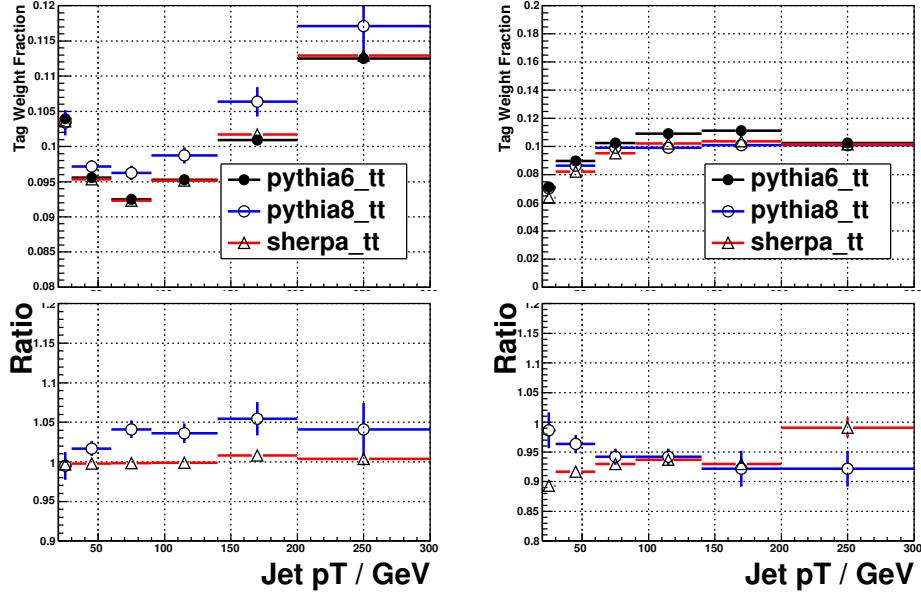


Figure 6: b -jet (left) and c -jet (right) tagging efficiency for the jets between the 70% OP and 60% OP ($0.7028 < \text{MV1c} < 0.8353$) in $t\bar{t}$ events produced by PYTHIA6 (Black), PYTHIA8 (Blue) and SHERPA (Red). The ratio is the MC-to-MC scale factor. Similar plots for all operating points are shown in Appendix T.2.

1626 3.4 Event Kinematics Selection

1627 After the above mentioned selection, events are classified by the lepton, jet, and b -jet multiplicity. Events
 1628 are further categorized by the vector boson transverse momentum (p_T^V) with the higher boost categories
 1629 having a larger signal to background ratio. The dijet mass analysis has tighter cuts while the multivariate
 1630 analysis uses a looser selection in order to maximize the information available in the training. Unless
 1631 a cut is perfectly efficient for the signal it is usually better to loosen or completely release the cut in
 1632 question and allow the multivariate discriminant training to optimize its usage. This reasoning motivates
 1633 the absence of the ΔR cuts in the MVA selection as well as other differences. The choice of two p_T^V bins
 1634 for the MVA, as apposed to five for the dijet mass, was further motivated by the fact that the performance
 1635 of any multivariate technique increases with the available training statistics. A fine binning in p_T^V would
 1636 not have left sufficient statistics for training. On the other hand, training on the inclusive p_T^V spectrum has
 1637 been shown to be sub-optimal since the low p_T^V statistics dominant preventing the learning algorithm from
 1638 focusing sufficiently on the higher boost region where the bulk of the sensitivity comes from. This could
 1639 be avoided if infinite statistics were available. The multivariate discriminant configuration is detailed in
 1640 Section 6. The full list of event selection criteria is given in Table 12. The cut optimization for both
 1641 interpretations was done with at least the approximate expected sensitivity³. Most of the variables used
 1642 are self-explanatory but a few definition are clarified here:

- 1643 • V : vector boson constructed from the E_T^{miss} , vectoral sum of E_T^{miss} and p_T^ℓ , and vectoral sum of $p_T^{\ell_{1,2}}$
 1644 in the 0, 1, and 2 lepton analysis respectively.
- 1645 • H : Higgs constructed from the vectoral sum of the two leading p_T jets.

³From a binned sum of s/\sqrt{b} to p-value calculations without systematics.

- 1646 • M_{eff} : scalar sum p_T of all the objects in the event, specifically the signal jets, leptons, and E_T^{miss} .
 1647 In the 1-lepton channel only the two jets used to build the Higgs mass are considered while in
 1648 the 0-lepton channel the third jet is considered in three jet events. This is clarified by the use
 1649 of M_{eff} ³ for the later. This difference in definition exists since the variables were optimized in
 1650 parallel in the different lepton selections and frozen before the subtle difference was noticed.

1651 As stated above, 0-lepton events with $p_T^Z < 120$ GeV are difficult to include due to the challenge of
 1652 modeling the E_T^{miss} trigger turn-on (Appendix A). Appendix C details the work done to include as many
 1653 of the events below 120 GeV into the 0-lepton analysis. In the 2-lepton channel, the so called ‘ e - μ ’ control
 1654 region which is dominated by top-pair events is selected with the MVA selection with the additional
 1655 requirements that the two lepton are of different flavor and opposite sign; the same-sign events are used
 1656 for the multijet template.

1657 In the previous version of this analysis [11], cuts on the minimum transverse mass of the W (m_T^W)⁴
 1658 and E_T^{miss} were used for $p_T^W < 160$ GeV in events with one lepton. From an optimization study performed
 1659 in the MVA selection, these cuts were dropped in favor of an M_{eff} cut in the low p_T^W region, $p_T^W <$
 1660 120 GeV, which increased the statistical sensitivity in that region(s) by 17 (22)% for the MVA (dijet
 1661 mass) analysis⁵. Figure 7 shows an MVA output for the multijet and signal, left and right respectively,
 1662 for the EPS (optimized) cuts in blue (red). Two different trainings were used but one can clearly see
 1663 that the change in cuts resulted in a large increase in the signal and no considerable increase of the
 1664 multijet component in the sensitive region of the MVA output. This optimization study called for a
 1665 E_T^{miss} cut of 20 GeV for the high p_T^W region ($p_T^W > 120$ GeV). Therefore in the dijet analysis with
 1666 $120 < p_T^W < 200$ GeV the E_T^{miss} cut was reduced to 20 GeV (from 25 GeV [11]). Above p_T^W of 200 GeV a
 1667 reduction of the E_T^{miss} cut from 50 GeV decreases the expected dijet mass sensitivity so the EPS value was
 1668 maintained. The success of dropping the m_T^W cut for $p_T^W < 120$ GeV prompted a test to abandon it in the
 1669 region $120 < p_T^W < 160$ GeV in the dijet mass analysis which subsequently showed an increase in both
 1670 the signal and background yield by more than 50% and no large increase in the multijet component was
 1671 observed as shown in Figure 8. In total these changes increased the expected statistical sensitivity of the
 1672 2-jet region in the 1-lepton analysis 5 (8)% in the MVA (dijet) analysis. Note the upper bound of m_T^W
 1673 which was present for EPS has been maintained in the dijet mass analysis.

1674 Electron events with $p_T^W < 120$ GeV in the 1-lepton channel are not considered in the extraction of
 1675 the signal as explained in Section 5.4.3.

1676 3.5 Dijet Mass Resolution and the Kinematic Fit

1677 Reconstructing the mass of a resonant decay is always a very powerful discriminant against the back-
 1678 grounds which are either not resonant decays or have a different mass. This analysis is no exception but
 1679 jets are not the most precise objects available and therefore care has been taken to maximize the dijet
 1680 mass resolution.

1681 3.5.1 Energy corrections to the selected b -jets

1682 Two corrections are applied to selected signal b -jets: the ‘muon-in-jets’ and ‘ p_T -reco’ corrections. With
 1683 the first, known as the ‘muon-in-jets’ correction, the jet resolution is improved by adding the 4-vector of
 1684 muons passing the criteria in Table 13 to the jet 4-vector after subtracting the muon’s energy deposit in
 1685 the calorimeter. If two such muons are found, the closer of the two to the jet is taken.

$${}^4m_T^W = \sqrt{2p_T^\ell E_T^{\text{miss}}(1 - \cos \Delta\phi(\ell, E_T^{\text{miss}}))}$$

⁵This difference in the MVA analysis includes the addition of a $|d_0 \text{ significance}| < 3$ cut in the muon channel and tightening the iso_{calo} which decrease the significance 1%.

Not reviewed, for internal circulation only

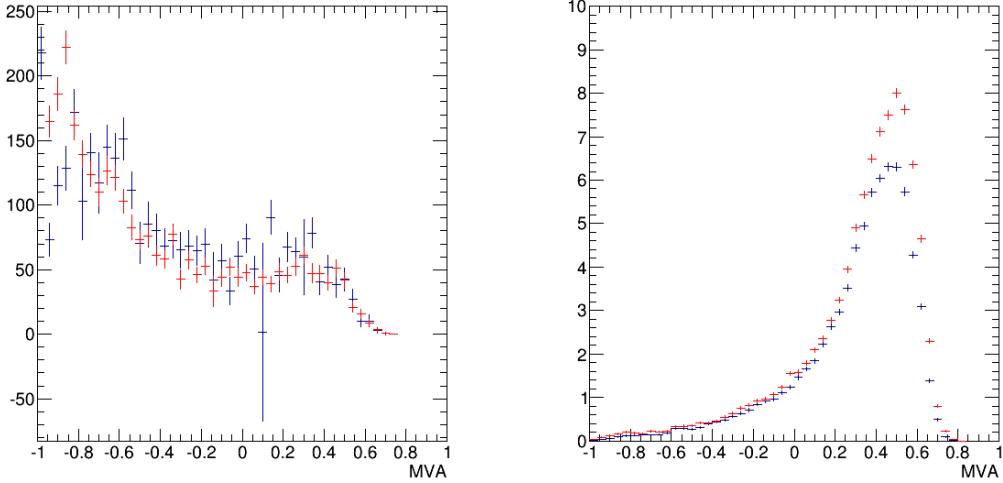


Figure 7: This figure shows an MVA output for the multijet and signal on the left and right respectively for the EPS (optimized) cuts in blue (red) discussed in Section 3.4. The optimized cuts also include the changes to the MJ template selection described in Section 3.2.1.5. Two different trainings were used but one can clearly see that the change in cuts resulted in a large increase in the signal and no considerable increase of the multijet component in the sensitive region of the MVA output. The difference yields a 17% increase in the MVA analysis sensitivity.

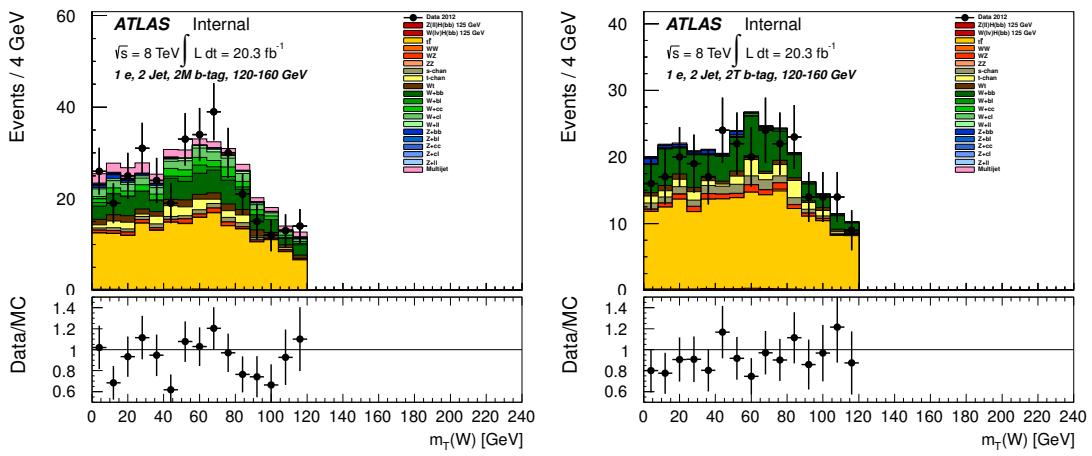


Figure 8: This figure shows the m_T^W distribution in the for $120 < p_T^W < 160$ in the electron channel of the dijet mass analysis after requiring two exclusive medium and tight tags on the left and right respectively. For $m_T^W < 40$ GeV, which was excluded previously [11], the agreement is acceptable and the multijet contribution is not significantly more then above 40 GeV. Removing this cut increases the signal and background in this p_T^W range by 50%.

Not reviewed, for internal circulation only

Variable	Dijet Mass Analysis						Multivariate Analysis					
	Common Selection											
p_T^V (GeV)	0-90	90-120	120-160	160-200	> 200	0-120	> 120					
$\Delta R(jet_1, jet_2)$	0.7-3.4	0.7-3.0	0.7-2.3	0.7-1.8	< 1.4	$> 0.7 \ (p_T^V < 200 \text{ GeV})$						
0-Lepton Selection												
p_T^{miss} (GeV)	NU	App. C	> 30		> 30		> 30					
$\Delta\phi(E_T^{\text{miss}}, p_T^{\text{miss}})$			< $\pi/2$		< $\pi/2$		< $\pi/2$					
$\Delta\phi(E_T^{\text{miss}}, jets)$			> 1.5		NU		> 1.5					
$\Delta\phi(V, H)$			> 2.8		-		-					
$\sum p_T^{jeti} N_{jet} = 2$			> 120		> 120		> 120					
$\sum p_T^{jeti} N_{jet} = 3$			> 150		> 150		> 150					
1-Lepton Selection												
M_{eff} (GeV)	> 180		-		> 180	-						
E_T^{miss} (GeV)	-		> 20		-	> 20						
m_T^W (GeV)	< 120				-							
2-Lepton Selection												
$m_{\ell\ell}$ (GeV)	83-99				71-121							
E_T^{miss} (GeV)	< 60				-							

Table 12: Event kinematic selection. NU stands for ‘Not Used’. Electron events with $p_T^W < 120$ GeV in the 1-lepton channel are not considered in the extraction of the signal as explained in Section 5.4.3.

Criteria	Value
Quality	Tight MuID MCP hit requirements
p_T (GeV)	> 4
$\Delta R(\mu, jet)$	< 0.4

Table 13: Muon selection for muons reconstructed within a jet cone $\Delta R(\mu, jet) < 0.4$ and then included in the jet. If two such muons are found in a jet, the closer is used.

Not reviewed, for internal circulation only

Furthermore, another correction referred to as ‘ p_T -reco’ compensates for the bias in the average migrations of jets due to the underlying jet spectrum has been derived [34]. The current correction is shown in Figure 9. Jets tend to more often migrate down (up) in p_T on the rising (falling) part of the truth jet p_T spectrum during reconstruction. This correction improves the invariant mass resolution by 8% and even though it also changes the background shape. After this correction is applied, the signal dijet mass resolution improvement from the GSC calibration compared to only using the EM+JES calibration is 3.5% **G**.

Dedicated systematics have been evaluated to be used with these corrections. They consist of an uncertainty on the b-jet energy scale of 0.4% (SysJetBE) and an uncertainty on the b-jet energy resolution, estimated by applying an extra smearing to the jets (SysBJetReso). Both are applied before the ‘ p_T -reco’ correction have been applied.

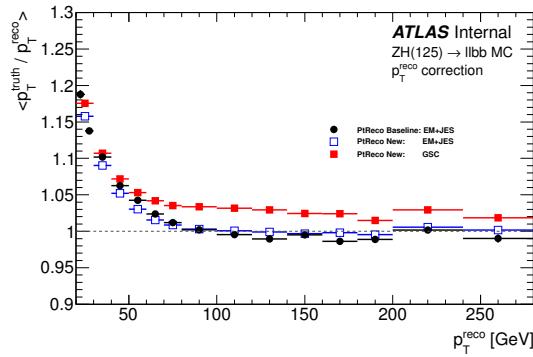


Figure 9: Three versions of the p_T -reco correction are shown with the black points showing what was used for EPS [11], the blue uses the updated object selection (except for the GSC calibration) and signal sample with increased statistics, and the red is analogous to the blue but using GSC calibrated jets.

3.5.2 Kinematic Fit

One expects to have fully reconstructed $ZH \rightarrow \ell^+ \ell^- b\bar{b}$ events in the 2-lepton channel. Since the resolution of the leptons is much better than the resolution of the jets and the entire ZH system has limited if any total transverse momentum, one can adjust the jet energies such that the event is balanced in the transverse momentum. This greatly improves the jet resolution resulting in a $\sim 22\%$ improvement in the dijet mass resolution as shown in Figure 10. Further details are given in Appendix U.

Not reviewed, for internal circulation only

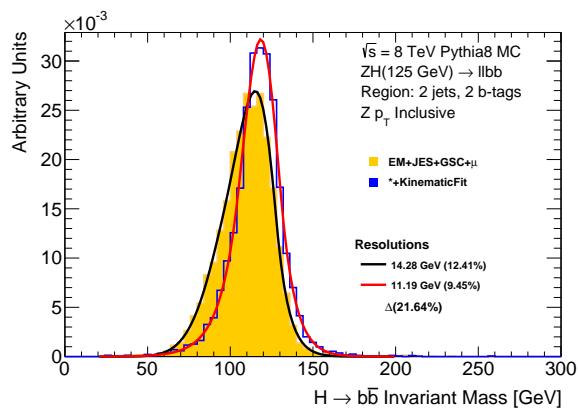


Figure 10: Dijet invariant mass before and after applying a kinematic likelihood fit in ZH $m_H = 125$ GeV signal Monte Carlo events showing a $\sim 22\%$ resolution improvement.

1703 4 VH \rightarrow bb: Signal Characterization

1704 This section details the signal samples themselves. Sample simulation (Section 4.1) as well as the-
 1705 oretical uncertainties (Section 4.2) are discussed. In the description of the systematic uncertainties,
 1706 this font is used to note the name of the nuisance parameter used in the profile likeli-
 1707 hood described in Section 8. The reader is encouraged to read Sections 8.1 and 8.2 to better understand
 1708 how the information here will be used in the profile likelihood.

1709 **4.1 Simulation**

1710 The VH signals, $ZH \rightarrow v\bar{v}b\bar{b}$, $WH \rightarrow \ell v b\bar{b}$, and $ZH \rightarrow \ell^+ \ell^- b\bar{b}$, where $\ell = e, \mu, \tau$ are modeled using
 1711 Monte Carlo (MC) events produced by the PYTHIA 8.165 [35] event generator configured with the AU2
 1712 tune [36], using the CTEQ6L1 PDF [37], interfaced to PHOTOS [38] for QED final-state radiation, and
 1713 TAUOLA [39] for the simulation of τ decays. The decay of $V \rightarrow \tau\nu$ leptons is simulated to account
 1714 for the small fraction of additional signal events selected due to the decay $\tau \rightarrow \nu_\tau l v_l$ where l is either
 1715 an electron or muon. Samples are generated in the Higgs boson mass range between 100 GeV and
 1716 150 GeV at 5 GeV intervals. The same samples which were used for the previous result [11], however
 1717 since then, the available statistics has increased by a factor of 10 to 3×10^6 events for each of the
 1718 three channels at the 125 GeV mass point. The additional statistics indeed helps with the training of
 1719 multivariate discriminants discussed in Section 6. The total cross sections and uncertainties for the Higgs
 1720 mass productions considered are taken from Reference [10] and the $H \rightarrow b\bar{b}$ decay branching ratios come
 1721 from Reference [10,40] (TheoryBRbb). The central values of the cross sections are calculated at next-to-
 1722 next-to-leading-order (NNLO) in QCD corrections [41] and next-to-leading-order (NLO) in electroweak
 1723 (EW) corrections [42] assuming factorization between the production of a virtual V^* boson and its decay
 1724 to VH. The decay branching ratios of W^\pm and Z bosons are taken from the Particle Data Group [43]
 1725 assuming lepton universality.

1726 **4.1.1 qq and gg Initiated Production**

1727 In the Standard Model, VH production is dominated by the quark-initiated process. For this process,
 1728 for $m_H = 125$ GeV, additional VH samples have been generating at NLO using PowHEG showered with
 1729 PYTHIA8, and they have been used to check the effect of the NLO in the shape of the important variables
 1730 for the analysis (as reported in Appendix I). In the case of ZH, a significant contribution from the gluon-
 1731 initiated process contributes. Figures 11 and 12 show the leading order Feynman diagrams for both of
 1732 these production mechanisms.

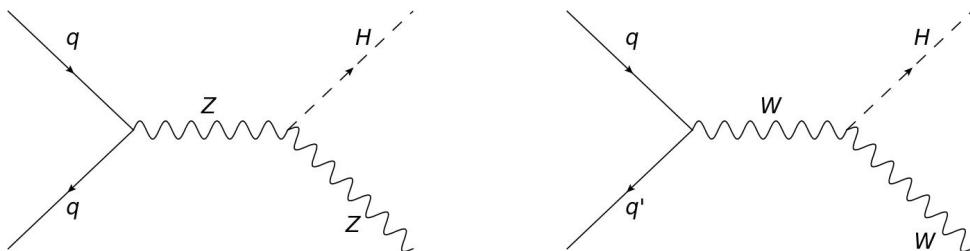


Figure 11: Leading order Feynman diagrams for quark-initiated VH production.

1733 For EPS, and therefore what is used for the 7 TeV analysis, the gluon-initiated process was considered
 1734 as an overall correction to the inclusive ZH cross section with a contribution of approximately 5%. Since
 1735 then, it was realized that the $gg \rightarrow ZH$ contribution is not flat as function of the vector boson p_T due to
 1736 the top quark loop threshold [44]. Therefore, $gg \rightarrow ZH$ events were generated using PowHEG showered

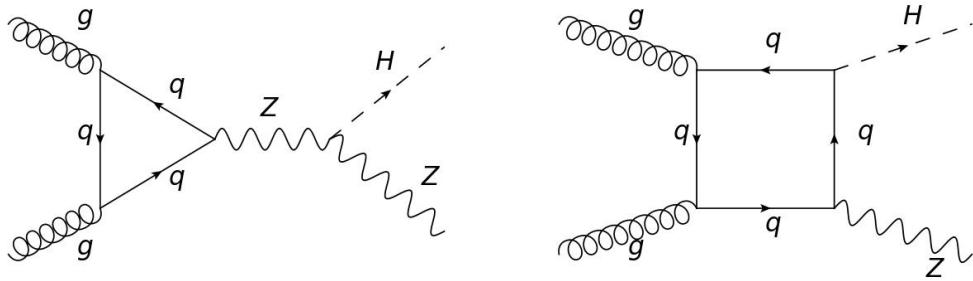


Figure 12: Leading order Feynman diagrams for gluon-initiated ZH production.

1737 with PYTHIA8 for each of the Higgs boson mass points stated above. The $gg \rightarrow ZH$ samples and the
 1738 $qq \rightarrow ZH$ samples are combined using weights derived from their relative cross sections.

1739 4.1.2 NLO Electroweak Differential Correction

1740 The following was considered and documented for the EPS analysis. In the interest of completeness and
 1741 brevity, this section includes only the main points. For the details of the correction i.e. the difference
 1742 between bare and dressed leptons, the reader is encouraged to consult Section 5.3 of Ref. [11].

1743 As stated above the total cross section is calculated to NLO in EW corrections but since these correc-
 1744 tions have a strong dependence in p_T^V , more care must be taken. The HAWK MC program was used to
 1745 calculate a differential NLO EW cross section correction as a function of p_T^V [45, 46] shown, along with
 1746 the associated uncertainty, in Figure 13. Fluctuations due to limited MC statistics are smoothed by fitting
 1747 the correction above 200 GeV with a first-order polynomial. The correction is applied to qq initiated VH
 1748 production and is being calculated for the gg initiated processes. The next-order (NNLO) electroweak
 1749 corrections considering additional α_s vertices are expected to be on the order of the NLO correction
 1750 squared (Δ_{NLO}^2). To ensure the uncertainty does not vanish, $\max(2\%, \Delta_{NLO}^2)$ is used (TheoryVHPt).

1751 4.2 Theoretical Uncertainties

1752 Theoretical uncertainties on the VH signal can be divided into renormalization/factorization scale un-
 1753 certainties and PDF uncertainties. For both of these, the uncertainty on the inclusive cross section,
 1754 acceptance, and differential p_T^V distribution has been considered.

1755 4.2.1 Inclusive Cross Section

1756 The scale and PDF uncertainties on the inclusive cross sections at $\sqrt{s} = 7$ and 8 TeV are quoted in
 1757 the CERN Yellow Report [47]. The reported ZH production uncertainties are larger than those for WH
 1758 production due to the one-loop-induced sub-process $gg \rightarrow ZH$. For the 8 TeV analysis, the $qq \rightarrow ZH$
 1759 uncertainty is assumed to be the same as $qq \rightarrow WH$ and the uncertainty on $gg \rightarrow ZH$ are chosen such
 1760 that the total uncertainty of the Yellow Report is preserved. An additional factor is included which
 1761 accounts for the uncertainty on the ratio of the number of 2 and 3 jet events when scaling the $gg \rightarrow$
 1762 ZH cross section from LO to NLO. This method produces results that are consistent with an overall
 1763 50% uncertainty suggested by theorists in the LHC Higgs Cross Section VH Working Group. These
 1764 uncertainties are summarized in Tables 14, 15, and 16 (TheoryQCDscale).

Not reviewed, for internal circulation only

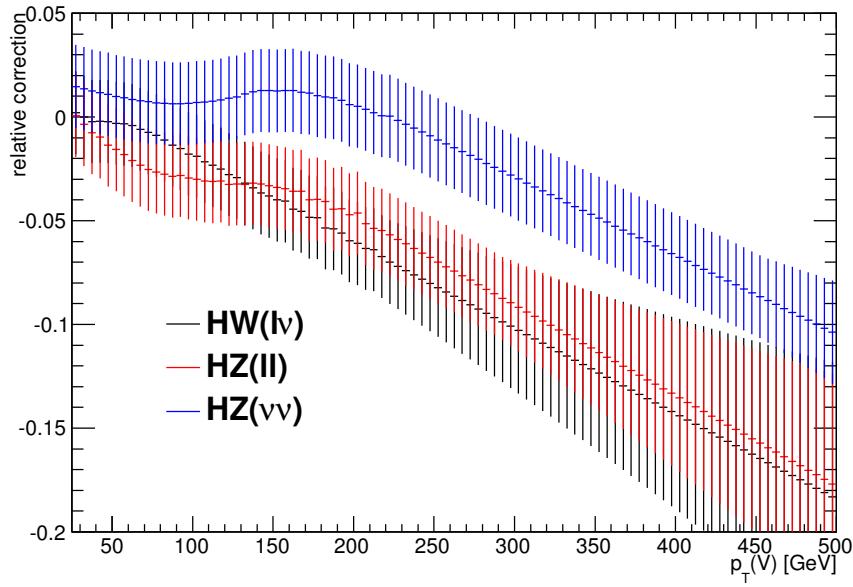


Figure 13: Relative NLO electroweak corrections to signal cross sections and the size of the associated uncertainties is shown as a function of p_T^V calculated from the HAWK MC generator.

m_H (GeV)	7 TeV			8 TeV		
	$\sigma(WH)$ (pb)	Scale (%)	PDF+ α_s (%)	$\sigma(WH)$ (pb)	Scale (%)	PDF+ α_s (%)
115	0.7517	± 0.9	± 2.4	0.9266	± 1.0	± 2.3
120	0.6617	± 0.9	± 2.6	0.8052	± 1.0	± 2.5
125	0.5785	± 0.9	± 2.6	0.7046	± 1.0	± 2.3
130	0.5059	± 0.9	± 2.6	0.6169	± 0.9	± 2.4
135	0.4431	± 1.0	± 2.6	0.5416	± 1.0	± 2.5

Table 14: NNLO QCD + NLO EW inclusive cross sections and related uncertainties for WH production quoted from the CERN Yellow Report [47].

m_H (GeV)	7 TeV			8 TeV		
	$\sigma(ZH)$ (pb)	Scale (%)	PDF+ α_s (%)	$\sigma(ZH)$ (pb)	Scale (%)	PDF+ α_s (%)
115	0.4345	± 2.6	± 2.7	0.5358	± 2.8	± 2.5
120	0.3808	± 2.8	± 2.8	0.4710	± 3.0	± 2.5
125	0.3351	± 2.9	± 2.7	0.4153	± 3.1	± 2.5
130	0.2957	± 3.0	± 2.8	0.3671	± 3.3	± 2.5
135	0.2616	± 3.2	± 2.8	0.3259	± 3.5	± 2.7

Table 15: NNLO QCD + NLO EW inclusive cross sections and related uncertainties for ZH production quoted from the CERN Yellow Report [47].

m_H (GeV)	qqZH			ggZH		
	$\sigma(qqZH)$ (pb)	Scale (%)	PDF+ α_s (%)	$\sigma(ggZH)$ (fb)	Scale (%)	PDF+ α_s (%)
115	0.4995	± 1.0	± 2.3	36.34	± 50.0	± 19.0
120	0.4366	± 1.0	± 2.5	34.39	± 50.0	± 12.8
125	0.3828	± 1.0	± 2.3	32.46	± 50.0	± 16.9
130	0.3365	± 1.0	± 2.4	30.60	± 50.0	± 14.2
135	0.2971	± 1.0	± 2.5	28.79	± 50.0	± 16.4

Table 16: NNLO QCD + NLO EW inclusive cross sections and related uncertainties for $qq \rightarrow ZH$ and $gg \rightarrow ZH$ production at 8 TeV derived from the CERN Yellow Report [47].

1765 4.2.2 Acceptance and p_T^V

1766 QCD scale uncertainties on the acceptance and p_T^V distribution shape are evaluated at truth level using
 1767 privately-made samples generated with PowHEG [48] and showered with PYTHIA8. The renormalization
 1768 (μ_R)¹ and factorization (μ_F)² scales were varied independently by factors of 2 and 0.5 in all possible
 1769 combinations whilst maintaining $0.5 \leq \mu_R/\mu_F \leq 2.0$. Each sample was normalized to the nominal
 1770 cross section reported above to avoid double counting the inclusive cross section uncertainties. After a
 1771 full truth-level event selection was performed, the difference in inclusive yields compared to the nomi-
 1772 nal $\mu_R = \mu_F = 1$ sample is used to determine the acceptance uncertainty. The “Stewart-Tackmann
 1773 method” [49] [50] is deployed to treat correlations in the acceptance scale uncertainty between the 2 and
 1774 3-jet analysis bins. Under this procedure, the uncertainty in the 2-jet bin consists of two components. The
 1775 first component is the inclusive 2+3 jet acceptance uncertainty (TheoryAcc_J2); the second component
 1776 is the absolute 3-jet exclusive uncertainty relative to the nominal 2-jet acceptance (TheoryAcc_J3). This
 1777 second component acts on the 2 and 3-jet events with an opposite sign creating an anti-correlation in the
 1778 change in 2-jets versus 3-jets from this single uncertainty. The p_T^V uncertainty was taken by comparing
 1779 the p_T^V distribution of the varied and nominal samples plotted with unit normalization. A linear fit was
 1780 performed to envelope the most discrepant samples as shown in Figure 14 for each $qq \rightarrow WH$ (a-b),
 1781 $qq \rightarrow ZH$ (c-d), and $gg \rightarrow ZH$ (e-f) for 2 and 3-jet events. The functional form for the linear fit is

$$f(p_T^V) = 1 \pm \left(a + b \frac{p_T^V}{400 \text{ GeV}} \right) \quad (7)$$

1782 with a and b given in Table 17 for each of the processes.

Process	Region	a	b
$qq \rightarrow VH$	2 jet	-0.02	0.10
$qq \rightarrow VH$	3 jet	-0.03	0.13
$gg \rightarrow ZH$	2+3 jet	-0.05	0.25

Table 17: Parameters for the linear fit of Equation 7 for p_T^V shape uncertainty for renormalization and factorization scales.

1783 PDF uncertainties on the acceptance and p_T^V shape are obtained in a manner similar to that used to
 1784 evaluate the scale uncertainties. Additional samples are generated with PowHEG and showered with
 1785 PYTHIA8 using the MSTW2008NLO68CL [51] and NNPDF23_NLO_AS_0120 [52] PDF set central value

¹‘renscfact’ parameter.

²‘facscfact’ parameter.

Not reviewed, for internal circulation only

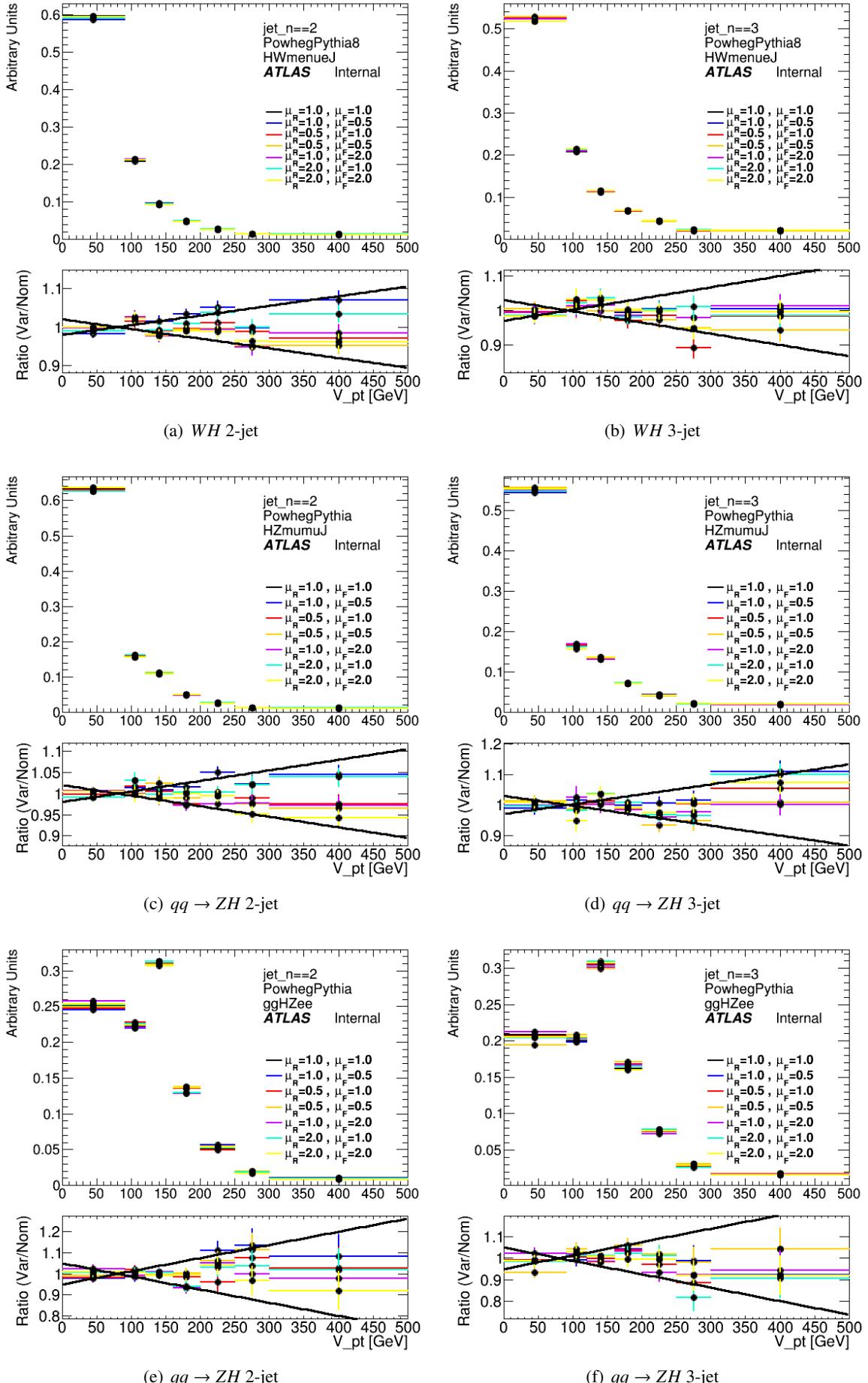


Figure 14: Normalized p_T^V distributions after truth-level selection for WH , $qq \rightarrow ZH$, and $gg \rightarrow ZH$ scale uncertainty studies on the 1st, 2nd, and 3rd row respectively.

members, as recommended by the PDF4LHC [53] Working Group. Again, after performing a full truth-level analysis, the varied sample yields are compared to the nominal sample made with the CT10NLO [54] central value PDF set member to derive uncertainties on the acceptance yields stated in Table 18 (TheoryAccPDF). PDF uncertainties are considered to be correlated between the 2- and 3-jet bins. Additionally, no evidence for a p_T^V shape uncertainty was found. As a cross check to this method, the PDF4LHC re-weighting guidelines were used to re-weight the existing PYTHIA samples on an event-by-event basis from the CTEQ6LL central value PDF set member to each of the full PDF sets stated above (central value and error members). The weight applied to each event is calculated as,

$$w = \frac{PDF(x_1, f_1, Q) * PDF(x_2, f_2, Q)}{PDF_0(x_1, f_1, Q) * PDF_0(x_2, f_2, Q)} \quad (8)$$

where $PDF(x, f, Q)$ is the new PDF and $PDF_0(x, f, Q)$ is the original PDF. The results from this weighting method are found to be consistent with those obtained by generating distinct samples with different PDFs (Figure 149) in Appendix I).

Process	PDF		Scale		
	2-jet [%]	3-jet [%]	2+3-jet [%]	3-jet rel. 2-jet [%]	3-jet rel. 3-jet [%]
WH	± 3.5	± 2.8	± 3.0	∓ 1.1	± 4.2
$qq \rightarrow ZH$	± 3.0	± 5.0	± 3.4	∓ 0.9	± 3.6
$gg \rightarrow ZH$	± 2.1	± 3.4	± 1.5	∓ 1.8	± 3.3

Table 18: Inclusive acceptance uncertainties derived from scale and PDF variations.

The NLO QCD+EWK corrections affect the production of the Higgs boson. This directly changes the boost of the vector boson which then defines the kinematics of the event. Changing the p_T^V at the truth level will propagate this change to all important observables. The rate of 2 and 3 jet production is covered separately. For the signal it is important to properly parametrize the rate in VpT and jet multiplicities. Changes in the m_{bb} shape due to differences in parton shower are believed to be below the threshold of the sensitivity of this analysis at this time. However, further checks are being done.

The uncertainty induced by the parton shower, hadronization and multiple parton interactions have been evaluated by comparing the event yields for the nominal pythia 8 samples, and Powheg+Herwig. The following systematic have been evaluated:

- 2 jets $p_T^V() < 120$ GeV: 8%
- 2 jets $p_T^V() > 120$ GeV: 6.5%
- 3 jets $p_T^V() < 120$ GeV: 13%
- 3 jets $p_T^V() > 120$ GeV: 6.5%

Special samples with the Multiple Parton Interactions (MPI) turned off (PartonLevel:MPI = off) have been used to evaluate the impact of the MPI to the signal acceptance. The effect have been evaluated to be negligible for the 2 jet case, while in the case of the 3 jets the changes are smaller than the uncertainty estimated comparing the nominal samples with Powheg+Herwig, so no special additional systematics have been associated to the modelling of the MPI, to avoid a double counting.

1815 5 Backgrounds

1816 The background processes are modeled with several different event generators. This analysis inherits the
 1817 dedicated campaign of Monte Carlo (MC) production carried out to attempt to reduce the uncertainty
 1818 due to MC statistics to <5% in the most sensitive bins for the EPS analysis. The increase in statistics was
 1819 achieved by collaboration with other working groups in producing common samples, making extensive
 1820 use of the “ATLFastII” [15] simulation and implementing a number of filters on the final state hadrons
 1821 and leptons to reduce the number of events that required detector simulation. A subset of the $V+jets$
 1822 samples (noted in Table 20 and 21) were not produced with the fast simulation; highly boosted samples
 1823 without b ’s and those in which the vector boson decays to τ s are usually full simulation. Table 19
 1824 gives a summary of the different MC samples used for each background process. A detailed discussion
 1825 of the modeling and systematics for each of the backgrounds considering both the dijet mass and the
 1826 multivariate analysis follows. $V+jets$ is described in Section 5.1, single and pair production of top quarks
 1827 in Section 5.2, dibosons in Section 5.3, and finally multijet and non-collision backgrounds in Section 5.4.

1828 In the description of the systematic uncertainties which follow, this font is used to note
 1829 the name of the nuisance parameter used in the profile likelihood described in Section 8. The
 1830 reader is encouraged to read Sections 8.1 and 8.2 to better understand how the information here will
 1831 be used in the profile likelihood. The adopted philosophy was to apply a correction if and only if one is
 1832 obviously needed: it is foolish to apply a correction which has the potential to over-correct a background.

Process	Generator	$\sigma \times BR$	N_{events}
Vector boson + jets			
$W \rightarrow \ell\nu$	SHERPA 1.4.1	12.07 nb	390M
$Z/\gamma^* \rightarrow \ell\ell$	SHERPA 1.4.1		66M
$m_{\ell\ell} > 40$ GeV		1.24 nb	
$Z\gamma^* \rightarrow \nu\nu$	SHERPA 1.4.1		98M
$m_{\nu\nu} > 5$ GeV		6.71 nb	
Top-quark			
$t\bar{t}$	PowHEG+PYTHIA	252.89 pb	100M
t -channel	ACERMC+PYTHIA	87.76 pb	9M
s -channel	PowHEG+PYTHIA	5.61 pb	6M
Wt -channel	ACERMC+PYTHIA	22.37 pb	20M
Di-boson			
WW	PowHEG+PYTHIA8	52.44 pb	10M
WZ	PowHEG+PYTHIA8		15M
$m_{\ell\ell} > 20$ GeV and one of the boson hadronically decaying		9.241 pb	
ZZ	PowHEG+PYTHIA8		15M
$m_{\ell\ell} > 20$ GeV and one of the boson hadronically decaying		3.171 pb	

Table 19: Monte Carlo programs used for modeling signal and background processes and the cross sections times branching ratio (BR) used to normalize the different processes at $\sqrt{s} = 8$ TeV. Branching ratios correspond to the decays shown.

1833 The estimate of the modeling systematic uncertainties are done for each background. When possible,
 1834 specific control regions have been designed to extract information directly from data. This is the case for
 1835 the $Z+jets$, $W+light$ jets, and $t\bar{t}$ backgrounds. In view of the sensitivity of the analysis to $t\bar{t}$ modeling, a
 1836 detailed study of this background has been completed by using a series of MC generators with different
 1837 underlying assumption of the $t\bar{t}$ physics in compliance with the Top Group’s recommendations. Given
 1838 the difficulty to design proper control regions with enough statistical power to study processes like single

1839 top, $W + b\bar{b}$ and diboson production, modeling studies are done by comparing different MC predictions.
 1840 If available, the comparison between different MC was done with fully reconstructed detector objects
 1841 and the full analysis selection. This is the case of the single top background. For $W + b\bar{b}$ and diboson,
 1842 the comparisons have been done mostly at the particle or parton level. When different MC predictions
 1843 are compared to the baseline, the most discrepant is chosen to derive an uncertainty first, then the next on
 1844 the list is considered. This continues until any discrepancy left between predictions viewed on the final
 1845 variable is covered by the already considered differences. In order to not put statistical fluctuations from
 1846 these comparisons into the analysis, a function is fit to the ratio and used to produce the variation.

1847 All Modeling studies have focused on the most relevant variables which are the input variables for
 1848 the multivariate discriminant described in Section 6, variables strongly related to them, or the variables
 1849 used to select events (Table 12). The variables of interest can be divided into two categories (with a few
 1850 exceptions):

- 1851 • kinematics of b -jet system: This is our Higgs candidate; the description of variables like the jet p_T
 1852 and multiplicity, angles between jets, and the dijet mass (m_{jj}) is critical.
- 1853 • kinematics of the system recoiling from the Higgs: In this analysis, the recoiling system, formed
 1854 by the E_T^{miss} , the lepton and the E_T^{miss} , or the dilepton system in the 0, 1 and 2 lepton categories
 1855 respectively, gives the kinematics of the associated vector boson and is paramount. This is the
 1856 handle used to reject the potentially overwhelming multijet background and find the region of
 1857 phase space, the high p_T^V regime, where the signal-to-background ratio is expected to be maximal.

1858 In the following subsections, each background will be introduced and the corrections and systematics
 1859 adopted in the analysis will be discussed. The information presented is meant to be enough for the reader
 1860 to learn what decisions were made. However, not all the details as to why these decisions were made can
 1861 be put into the main body of the text if there is any hope of presenting a readable document. A complete
 1862 description is therefore contained in several dedicated appendices which are referred to throughout the
 1863 following text.

1864 For a clear description on how the systematics described are employed in the profile likelihood i.e.
 1865 correlations across channels, b -tag categories, etc. the reader should refer to Section 8.

Not reviewed, for internal circulation only

1866 5.1 Vector boson+jets

1867 The $W/Z+\geq 1b$, $W/Z+\geq 1c$ and $W/Z+\geq 1$ light jet events are produced with the `SHERPA` generator [55]
 1868 with massive b/c quarks and interfaced with CT10 PDFs. Filters were developed to select events con-
 1869 taining b , c and *light* flavored hadrons. This allowed the statistics of the critical $V+$ heavy-flavor samples
 1870 to be increased with less resources. In addition, filters were developed to select events with high vector
 1871 boson transverse momentum with division of $p_t^V < 40$, $40 < p_t^V < 70$, $70 < p_t^V < 140$, $140 < p_t^V < 280$,
 1872 $280 < p_t^V < 500$ and $p_t^V > 500$ GeV allowing for the increase in statistics of the most sensitive high
 1873 p_T^V regions. The detailed list of MC samples for the Vector boson+jets production is listed in Tables 20
 1874 and 21. A complexity which is particular to $V+$ jet simulation is the prediction of the relative rates of
 1875 b , c , and *light* jets, referred to as flavor fractions in the text. Obtaining as much information from the
 1876 concerning the proportions of the various flavors adds a great deal of complexity to the analysis. The
 1877 following sections describe the modeling studies used to validate the simulation agreement with data
 1878 and also derive systematics. More details are given in Appendix J for $Z+$ jets and K-L for $W+$ jets. The
 1879 reader is encouraged to read the introduction to Section 5 to better understand how the information here
 1880 will be utilized.

Process	Channel num.	tag	N_{events}
$W \rightarrow ev$, Massive C and B, Sherpa, CT10			
Pt0	167740-2	e1585_a159_a171_r3549_p1328	14997980 / 9998989 / 49885967
Pt40_70	180534-6	e1867_a188_a171_r3549_p1328	2999998 / 4499994 / 16997491
Pt70_140	167761-3	e1620_a159_a171_r3549_p1328	2000000 / 2996497 / 4998998
Pt140_280	167770-2	e1620_a159_a171_r3549_p1328	4998995 / 1999997 / 2000000
Pt280_500	167779	a159_a171_r3549_p1328	899999
Pt280_500 [†]	167780-81	e1714_s1581_s1586_r3658_r3549_p1328	199898 / 499891
Pt500	167788	e1620_a159_a171_r3549_p1328	100000
Pt500 [†]	167789-90	e1620_s1499_s1504_r3658_r3549_p1328	10000 / 10000
$W \rightarrow \mu\nu$, Massive C and B, Sherpa, CT10			
Pt0	167743-5	e1585_a159_a171_r3549_p1328	14989485 / 9992484 / 49846965
Pt40_70	180537-9	e1867_a188_a171_r3549_p1328	2996996 / 4498998 / 16988984
Pt70_140	167764-6	e1714_a159_a171_r3549_p1328	1998999 / 2995999 / 4998992
Pt140_280	167773-5	e1741_a159_a171_r3549_p1328	4983993 / 1995998 / 1723999
Pt280_500	167782	e1714_a159_a171_r3549_p1328	898000
Pt280_500 [†]	167783-4	e1714_s1581_s1586_r3658_r3549_p1328	30000 / 499698
Pt500	167791	e1714_a159_a171_r3549_p1328	90000
Pt500 [†]	167792-93	e1714_s1581_s1586_r3658_r3549_p1328	10000 / 49700
$W \rightarrow \tau\nu$, Massive C and B, Sherpa, CT10			
Pt0	167746-8	e1585_a159_a171_r3549_p1328	14925982 / 9993984 / 49920968
Pt40_70	180540-2	e1867_a188_a171_r3549_p1328	2998997 / 4498999 / 16996492
Pt70_140 [†]	167767-9	e1714_s1581_s1586_r3658_r3549_p1328	1099995 / 2999890 / 4999786
Pt140_280	167776	e1741_a159_a171_r3549_p1328	3998996
Pt140_280 [†]	167777-8	e1714_s1581_s1586_r3658_r3549_p1328	1998688 / 1999994
Pt280_500	167785	e1714_a159_a171_r3549_p1328	898999
Pt280_500 [†]	167786-7	e1714_s1581_s1586_r3658_r3549_p1328	199998 / 499998
Pt500	167794	e1714_a159_a171_r3549_p1328	90000
Pt500 [†]	167795-6	e1714_s1581_s1586_r3658_r3549_p1328	10000 / 49998

Table 20: Monte Carlo samples and channel numbers and statistics used for the W samples. Samples marked with [†] were made with the full simulation while the rest were made with ATLFastII [15] simulation. More information is given in Section 5.1.

Not reviewed, for internal circulation only

Process	Channel num.	tag	N_{events}
$Z \rightarrow ee$, Massive C and B, Sherpa, CT10			
Pt0	167749-51	e1585_a159_a171_r3549_p1328	3999000 / 2999995 / 4978999
Pt40_70	180543-5	e1867_a188_a171_r3549_p1328/	1199999 / 600000 / 1399998
Pt70_140	167797-9	e1714_a159_a171_r3549_p1328	1366999 / 999999 / 1999998
Pt140_280	167809-11	e1714_a159_a171_r3549_p1328	999999 / 399999 / 600000
Pt280_500	167821	e1714_a159_a171_r3549_p1328	180000
Pt280_500 [†]	167822-3	e1714_s1581_s1586_r3658_r3549_p1328	49899 / 49999
Pt500	167833	e1714_a159_a171_r3549_p1328	90000
Pt500 [†]	167834-5	e1714_s1581_s1586_r3658_r3549_p1328	10000 / 50000
$Z \rightarrow \mu\mu$, Massive C and B, Sherpa, CT10			
Pt0	167752-4	e1585_a159_a171_r3549_p1328	3997997 / 2937995 / 4993999
Pt40_70	180546-8	e1867_a188_a171_r3549_p1328	1199000 / 599000 / 1398999
Pt70_140	167800-2	e1620_a159_a171_r3549_p1328	1394999 / 1000000 / 1996998
Pt140_280	167812-4	e1620_a159_a171_r3549_p1328	987999 / 399000 / 599500
Pt280_500	167824	e1714_a159_a171_r3549_p1328	175000
Pt280_500 [†]	167825-6	e1714_s1581_s1586_r3658_r3549_p1328	50000 / 50000
Pt500	167836	e1620_a159_a171_r3549_p1328	100000
Pt500 [†]	167837-8	e1620_s1499_s1504_r3658_r3549_p1328	10000 / 139999
$Z \rightarrow \tau\tau$, Massive C and B, Sherpa, CT10			
Pt0	167755-7	e1585_a159_a171_r3549_p1328	3997994 / 2998998 / 4989999
Pt40_70	180549-51	e1867_a188_a171_r3549_p1328	1198999 / 600000 / 1399996
Pt70_140 [†]	167803-5	e1714_s1581_s1586_r3658_r3549_p1328	1399396 / 999998 / 1969693
Pt140_280	167815	e1714_a159_a171_r3549_p1328	798998
Pt140_280 [†]	167816-7	e1714_s1581_s1586_r3658_r3549_p1328	399999 / 598897
Pt280_500	167827	e1714_a159_a171_r3549_p1328	180000
Pt280_500 [†]	167828-9	e1714_s1581_s1586_r3658_r3549_p1328	50000 / 49899
Pt500	167839	e1714_a159_a171_r3549_p1328	90000
Pt500 [†]	167840-41	e1714_s1581_s1586_r3658_r3549_p1328	10000 / 20000
$Z \rightarrow vv$, Massive C and B, Sherpa, CT10			
Pt0	167758-60	e1585_a159_a171_r3549_p1328	24932972 / 19757479 / 24919979
Pt70_140	167806-8	e1620_a159_a171_r3549_p1328	5998993 / 2998998 / 4999996
Pt140_280	167818-20	e1620_s1499_s1504_r3658_r3549_p1328	10000 / 10000 / 10000
Pt140_280	167818-20	e1620_a159_a171_r3549_p1328	499995 / 1999998 / 2999999
Pt280_500	167830	e1741_a159_a171_r3549_p1328	1799997
Pt280_500 [†]	167831-2	e1741_s1581_s1586_r3658_r3549_p1328	199999 / 249999 / 999892
Pt500	167842	e1741_a159_a171_r3549_p1328	450000
Pt500 [†]	167843-4	e1741_s1581_s1586_r3658_r3549_p1328	49999 / 50000 / 199699

Table 21: Monte Carlo samples and channel numbers and statistics used for Z samples. Samples marked with [†] were made with the full simulation while the rest were made with ATLFastII [15] simulation. More details are given in Section 5.1.

Not reviewed, for internal circulation only

1881 5.1.1 Z+jets Modeling, Corrections and Systematic Uncertainties

1882 The following describes the main features of the Z +jets modeling studies and the sources of systematic
 1883 error. Appendix J contains further details. A summary of the this section is given in Table 23 and
 1884 a summary of the systematics used in the profile likelihood is given in the statistical model overview
 1885 (Section 8) in Table 49.

1886 In dilepton events the top background is fairly controllable and a relatively pure Z +jets sample can
 1887 be obtained. Using the event selection for the mva analysis given in table given in Table 12, with tighter
 1888 dijet mass analysis E_T^{miss} (< 60 GeV) and $m_{\ell\ell}$ (83-99 GeV) cuts, as well as only using the events with
 1889 $m_{bb} < 100$ GeV or $m_{bb} > 150$ GeV in 2-tag events, a signal-depleted pure Z +jets sample is selected; a
 1890 breakdown of yields given in Table 22.

process	0-tag (%)	1-tag (%)	2-tag (%)
Z +light	85	46	12
Z +heavy	12	50	69
$t\bar{t}$	0.07	1.5	12

Table 22: Simple sample composition for Z +jets modeling studies using the selection described in Section 5.1.1.

1891 5.1.1.1 Jet multiplicity and flavor fractions

1892 As stated previously, the simulation's predictions of jet multiplicity and flavor fractions in V +jet events
 1893 cannot be trusted completely. It is not possible to determine everything from data and this ignorance must
 1894 be properly encapsulated for the profile likelihood described in Section 8. Using the above mentioned
 1895 selection, data/MC yields were compared in the 0-tag and summarized in Table 70 in Appendix J. From
 1896 these numbers, a 5% uncertainty has been estimated for both the $Z+1$ normalization ($Z1Norm$) and ratio
 1897 of 3 to 2 jet production ($Z1Norm_3J$). Both the $Z+c1$ and $Z+hf$ ($hf=bb+bl+cc$) normalizations are deter-
 1898 mined from data in the profile likelihood. SHERPA-ALPGEN comparisons after 2-tags shown in Tables 74-73
 1899 in Appendix J are used to estimate the uncertainties on the:

- 1900 • 3/2-jet ratio for the heavy flavor components

1901 $Z+c1$: 26% ($ZclNorm_3J$)

1902 $Z+hf$: 13% ($ZbbNorm_3J$)

- 1903 • relative heavy flavor composition in $Z+2$ -jet and $Z+3$ -jet events

1904 $Z+bl$ to $Z+b(b/c)$: 10% ($ZblZbbRatio$)

1905 $Z+cc$ to $Z+b(b/c)$: 20% ($ZccZbbRatio$)

1906 5.1.1.2 $\Delta\phi(jj)$ and p_T^Z

1907 For the EPS analysis [11], a systematic disagreement in $\Delta\phi(jj)$ was observed and a correction was derived
 1908 resulting in markedly better agreement of many kinematic variables including p_T^Z and m_{jj} . For this
 1909 version of the analysis the correction has been refined. In Figure 15 the $\Delta\phi(jj)$ distribution is shown
 1910 after the above cuts have been applied. The 0 and 1-tag distributions show a slope in the data/MC ratio
 1911 which tends to be larger at low p_T^Z and the slope vanishes after asking for 2-b-tags. This suggests a
 1912 correction is appropriate for the Z +light background but not the Z +heavy-flavor. Therefore a correction

is derived from 0-tag events applied to only the Z+light background separately for $p_T^Z < 120$ GeV and $p_T^Z > 120$ GeV by fitting $a(1 + bx)$ to the data minus non-Z background over Z+jets ratio. With this correction applied, the Z+light normalization changes by less than 2% and good data-MC agreement is restored in the 1-tag region, where the contribution from Z+light jets is non-negligible. A systematic of half the correction is applied to Z+light simulation and the full size of the correction to Z+b/c simulation with a de-correlation between Z+l and Z+b/c as well as 2 and 3-jet events (ZDPhi). After applying this correction to the Z+light background the agreement in p_T^Z (Figure 16) was checked for the same selection. Again, there is an obvious slope which *increases* as more *b*-tags are required. A correction is derived in the 2-tag region by fitting $a + b \log(p_T^V)$ to the ratio of again, the non-Z background subtracted from the data over the Z+jets background and is applied to Z+b/c events only. Below $p_T^Z = 100$ GeV a constant correction is used. A systematic of half the correction is applied to the entire Z+jet simulation but de-correlated between Z+l and Z+b/c (ZPtV).

5.1.1.3 m_{jj}

The most important variable in a search such as this is m_{jj} . Using the same selection noted above, the systematic used for EPS [11] was reduced with further study and more statistics. Figure 17 shows the data/MC agreement in the 0, 1 and 2-tag regions. A systematic uncertainty was derived following the functional form of $a(m_{bb} \times 10^{-3} - b)$ and is applied to all Z+jets events with Z+l and Z+b/c de-correlated. A comparison was done between the default generator, SHERPA, and ALPGEN and the difference is covered by this uncertainty (Appendix J).

Description	Samples	Nuissance parameters
Zl Normalization	Data VS. Sherpa	Z1Norm
Z 3/2 ratio	Data VS. Sherpa	Z1Norm_J3,ZclNorm_J3,ZbbNorm_J3
Z jet flavour composition	Sherpa VS. Alpgen+Herwig+Jimmy	ZblZbbRatio, ZbcZbbRatio, ZccZbbRatio
$\Delta\phi$ correction and systematics	Data VS. Sherpa	ZDPhi
$\Delta\phi$ checks	Data VS. Alpgen+Herwig+Jimmy	
p_T^V correction and systematics	Data VS. Sherpa	ZPtV
p_T^V checks	Data VS. Alpgen+Herwig+Jimmy	
m_{bb} systematics	Data VS. Sherpa	ZMbb
m_{bb} checks	Data VS. Alpgen+Herwig+Jimmy	

Table 23: Summary of the Z+jet specific samples used to checks the background modelling. The list of the nuissance parameters is given for reference, and it will be discussed in Section 8

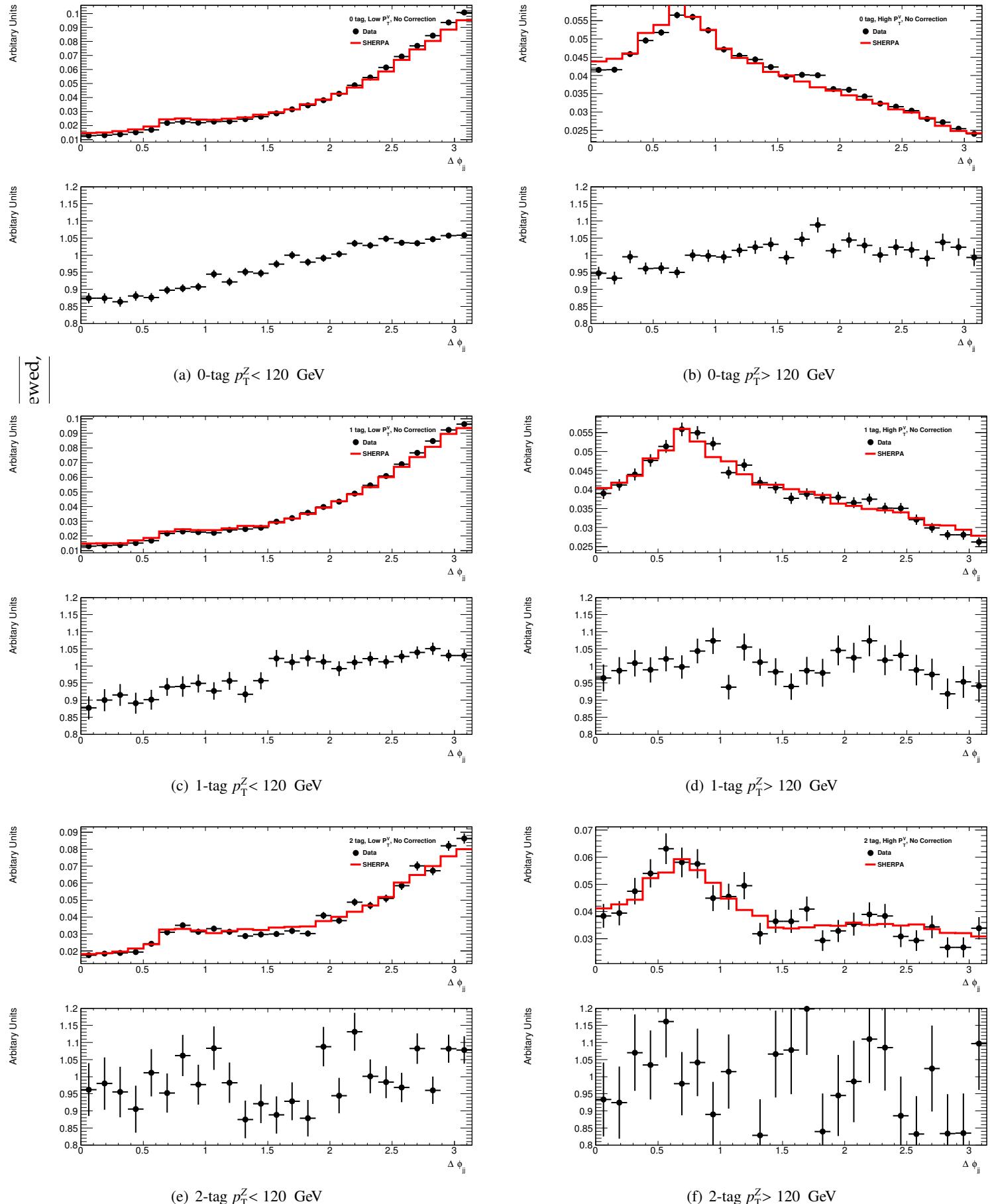


Figure 15: A data-driven $\Delta\phi_{jj}$ correction derived from data-MC ratios for $Z + \text{light}$ events motivated by the decrease in discrepancy with increased number of b -tags for both $p_T^V > 120$ GeV and $p_T^V < 120$ GeV.

Not reviewed, for internal circulation only

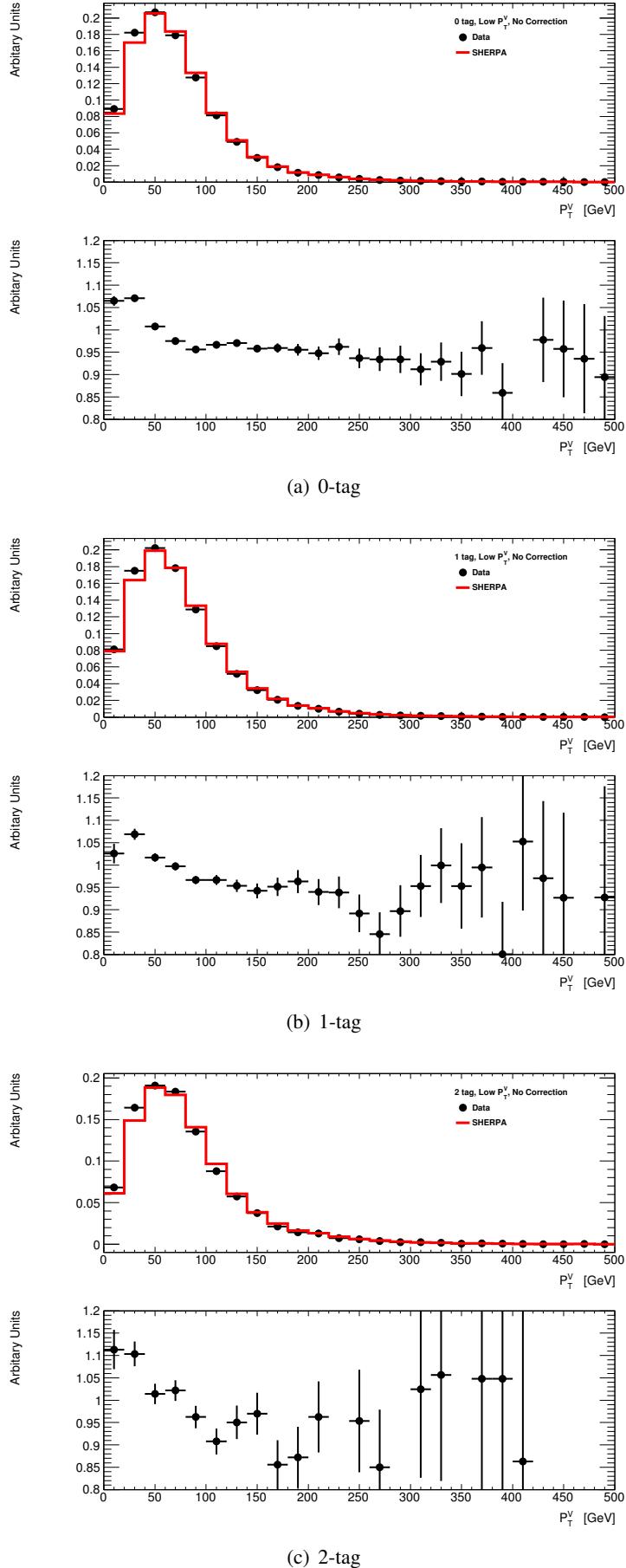


Figure 16: A data-driven p_T^Z correction derived from data-MC ratios for $Z + \text{heavy}$ events motivated by the increase in discrepancy with increased number of b -tags.

Not reviewed, for internal circulation only

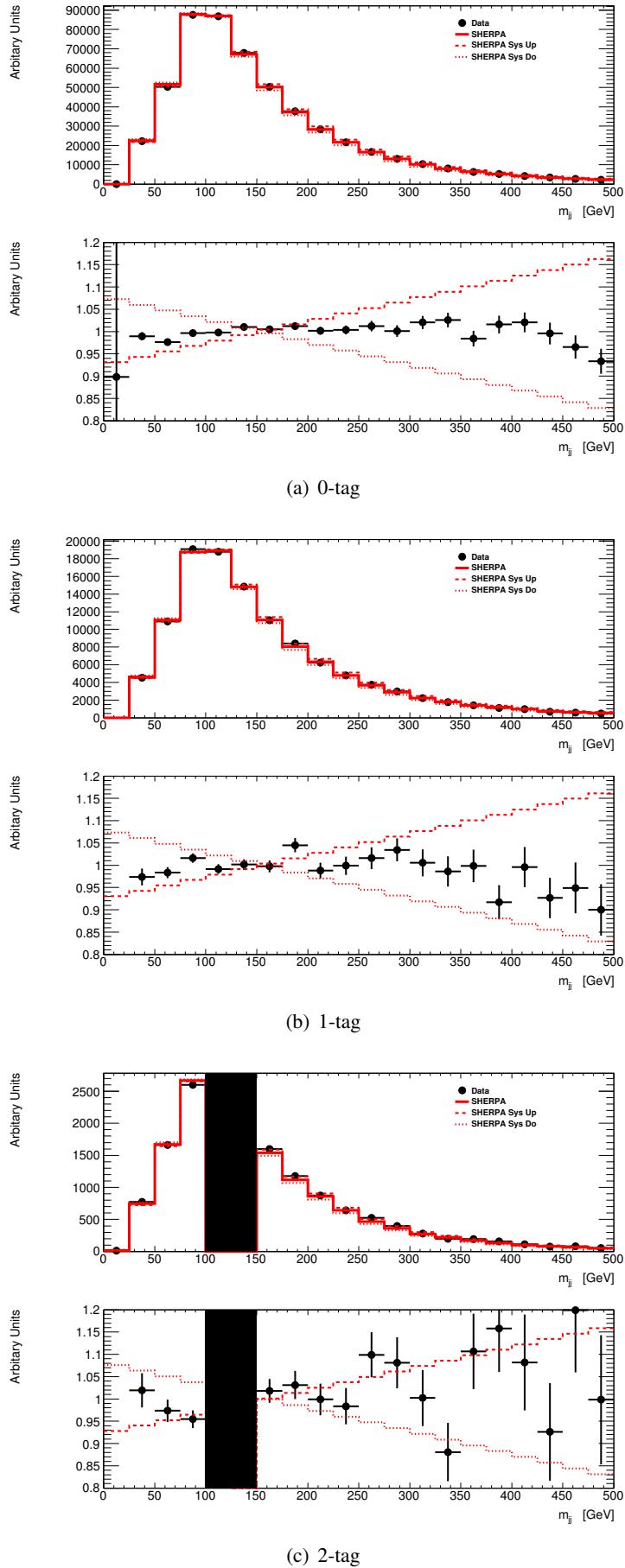


Figure 17: m_{jj} distribution in 2-lepton events from which a systematics uncertainty on the Monte Carlo modeling m_{bb} shape has been derived.

5.1.2 W+jets modeling, correction and systematics

1-lepton events with 0 or 1-tag are inundated with $W+l/c$ events but after 2-tags, the $t\bar{t}$ background swamps the $W+heavy-flavor$ ($hf=bb+bc+bl+cc$) events. Access to the $W+jets$ background in the 0 and 1-tag channels is not problem free since the very difficult multijet background is sizable, especially in the electron channel. In the following, the $W+l/c$ studies from control regions are described in Sections 5.1.2.1-5.1.2.2 (Appendix K) while Sections 5.1.2.3-5.1.2.6 detail the Monte Carlo (MC) studies used to probe the $W+hf$ background (Appendix L). Unless stated otherwise the MVA selection is used for the $W+light$ studies and the dijet mass analysis cuts for the $W+hf$ studies (Table 12). A summary of the this section is given in Table 26 and a summary of the systematics used in the profile likelihood is given in the statistical model overview (Section 8) in Table 50.

5.1.2.1 $W+light$ Jet Normalization and Jet Multiplicity

Inherited from EPS, from studies of profile-likelihood fits including the 0-tag region as well from the general agreement the following uncertainties are used:

- normalization of $W+ll$ background: 10% (WlNorm)

- 3/2-jet ratio for the light jet production

$W+ll$: 10% (WlNorm_3J)

$W+cl$: 10% (WclNorm_3J)

The $W+cl$ and $W+hf$ overall rates are determined from data.

5.1.2.2 $W+light$ $\Delta\phi(jj)$ and p_T^W

Systematic disagreements were observed in 0-tag and 1-tag regions of both the electron and muon selection of the 1-lepton analysis, in particular in the p_T^V and $\Delta\phi$ of the two leading jets. A pervasive mis-modeling such as this can not be explained by a poor multijet estimate and is similar to features seen in the 2-lepton $Z+jets$ dominated selection (Section 5.1.1). Figure 18 shows the level of agreement of $\Delta\phi(jet_1, jet_2)$ (simply $\Delta\phi$ from now on) and p_T^W before applying any non-standard corrections in 0 and 1-tag events. As was done in EPS (Ref [11] Sections 4.2 and 4.3), a data driven correction is employed. Full details are given in Appendix K. The modeling was studied using bin-to-bin corrections but when the final prescription was chosen, a continuous function was fit to the appropriate ratio. Figure 19 shows when a correction is derived inclusively in p_T^W , the high p_T^W region is over-corrected. This motivated a separate correction at low and high p_T^W which is a change compared to EPS.

It is clear from the shape of the mis-modeling that events should migrate from high to low p_T^W . Therefore, a normalization change is included in the corrections derived exclusively at high and low p_T^W to bring the simulation yield to that of the data in each region. Table 24 shows explicitly the change in the simulation yield.

Figure 20 shows the χ^2 value for many kinematic variables without applying a re-weighting, with an inclusive re-weight, and with separate functions at low and high p_T^W for 2-jet 0-tag events. A dramatic improvement in the modeling is seen.

The flavor composition of the $W+jets$ background is predominantly $W+l$ in 0-tag and $W+l$ and $W+cl$ in 1-tag. The contribution from the heavy flavor components in both categories is too small to draw a clear conclusion about whether the same mis-modeling exists. Therefore it was decided to apply the $\Delta\phi$ correction only to the $W+l$ and $W+cl$ backgrounds and to include 50% of the size of the correction as a systematic uncertainty. For the remaining heavy-flavor components, no correction is applied, but the full

Region		Scale Factor (%)
2-jet	$p_T^W < 120 \text{ GeV}$	+0.7
	$p_T^W > 120 \text{ GeV}$	-5.6
3-jet	$p_T^W < 120 \text{ GeV}$	+5.8
	$p_T^W > 120 \text{ GeV}$	-2

Table 24: The normalization changes from the $\Delta\phi$ correction in each of the four regions is show. This is necessary in order to maintain overall agreement while events are migrated between high p_T^W and low p_T^W .

¹⁹⁷³ size of the correction is taken as a systematic uncertainty (WDPhi). Figure 21 shows the improved p_T^W
¹⁹⁷⁴ distribution in the 0-tag after the bin-to-bin correction is applied to the $W+1$ and $W+cl$ backgrounds.

¹⁹⁷⁵ As mentioned above a bin-to-bin correction was used for these studies however the statistical fluc-
¹⁹⁷⁶ tuations of the ratio should not be considered for the correction. Figure 22 shows the function fit used
¹⁹⁷⁷ to parametrized the correction derived with respect to $W+1$ and $W+cl$ in 2-jet 0-tag events separately for
¹⁹⁷⁸ high and low p_T^W (3-jet correction is shown in Appendix K Figure 159).

¹⁹⁷⁹ Electron events with $p_T^W < 120 \text{ GeV}$ were considered for the derivation of the correction but are not
¹⁹⁸⁰ considered in the extraction of the signal as explained in Section 5.4.3.

Not reviewed, for internal circulation only

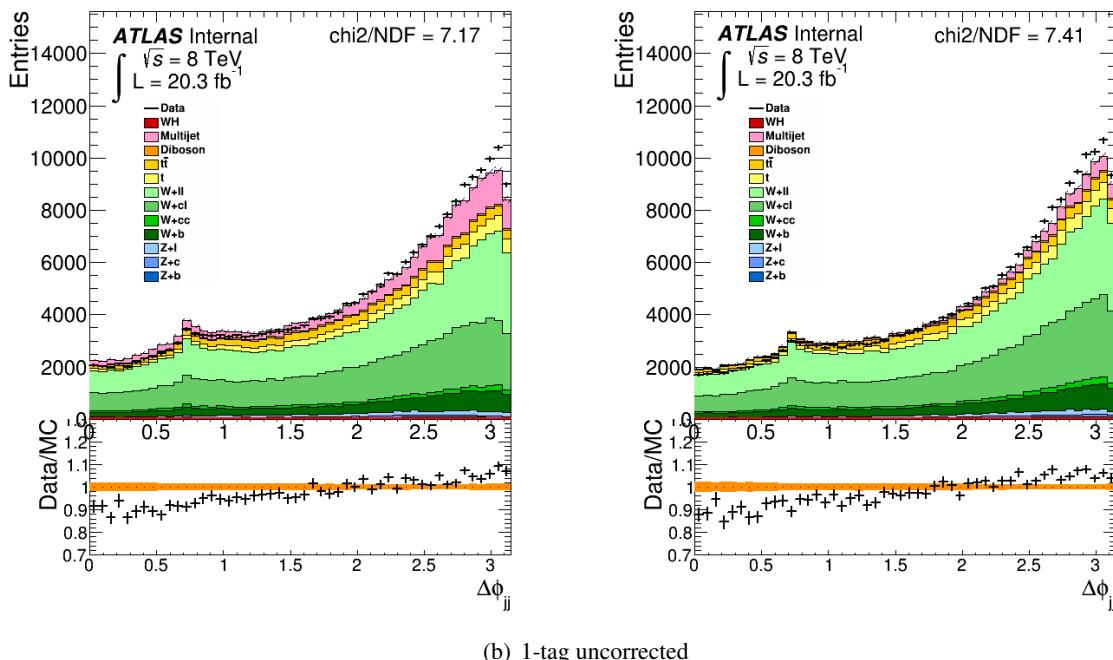
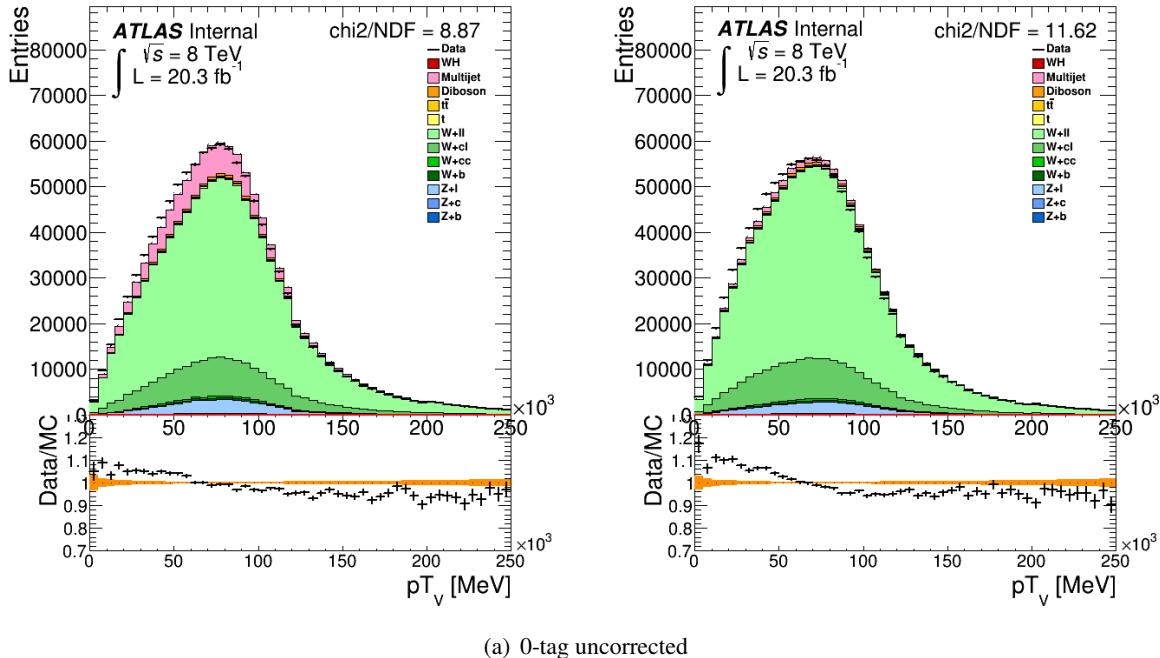


Figure 18: 1-lepton 2-jet 0-tag p_T^W and the 1-tag $\Delta\phi$ distributions before any corrections are applied to the $W+jets$ background. The electron (muon) channel is shown on the left (right).

Not reviewed, for internal circulation only

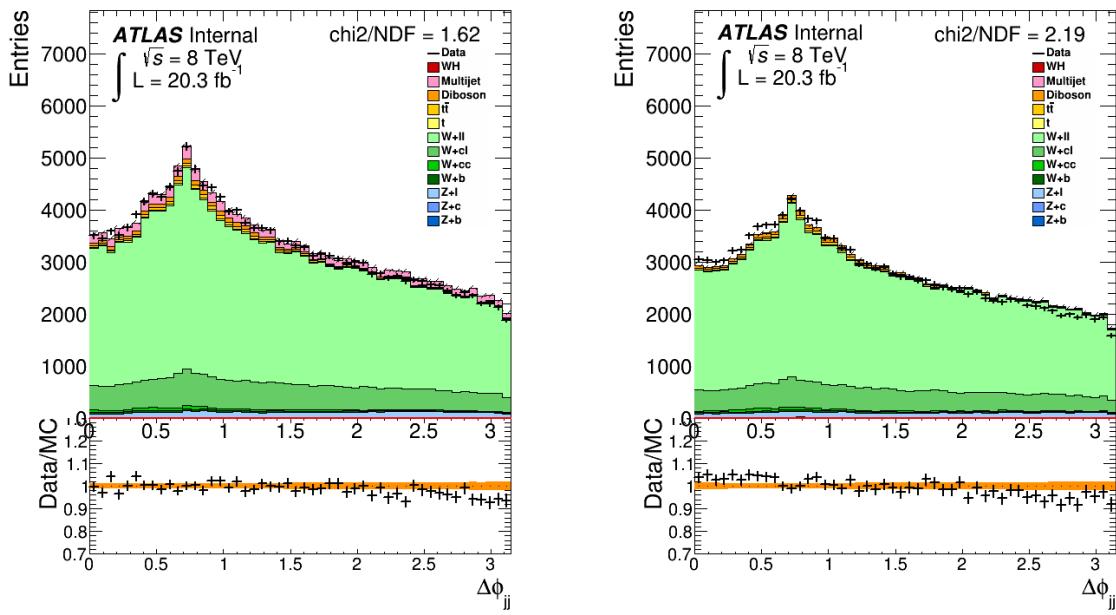


Figure 19: 1-lepton 2-jet 0-tag $\Delta\phi$ distributions using an inclusive $\Delta\phi$ correction similar to the one used for EPS shown in the low ($p_T^W < 120 \text{ GeV}$) and high ($p_T^W > 120 \text{ GeV}$) region on the left and right respectively. Notice the high p_T^W region is over-corrected. The electron (muon) channel is shown on the left (right).

ulation only]

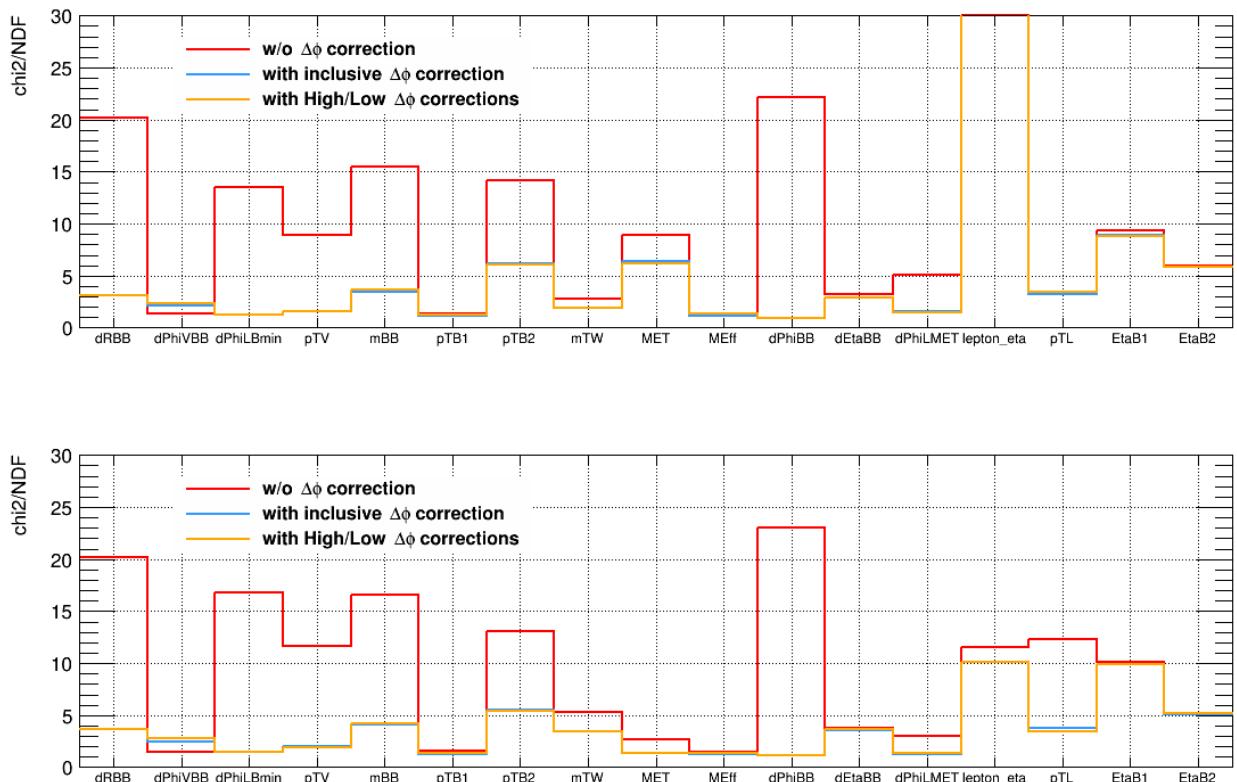


Figure 20: Improvements in the data/MC agreement (χ^2) of many kinematic variables in the 1-lepton 2-jet 0-tag events after various bin-to-bin $\Delta\phi$ corrections derived from the 0-tag region. The electron channel is shown in top half of each plot and the muon channel in the bottom.

Not reviewed, for internal circulation only

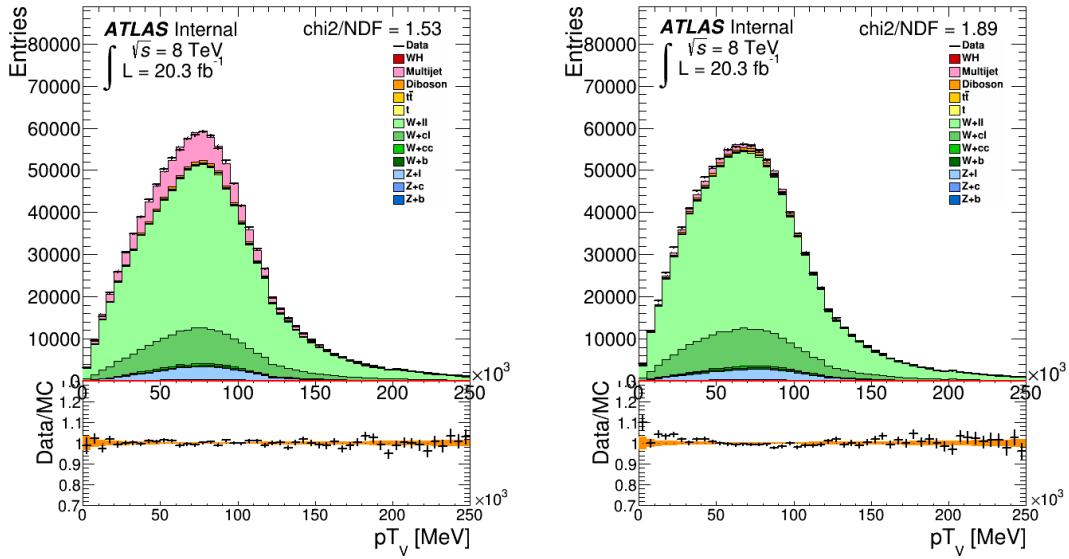


Figure 21: 1-lepton 2-jet 0-tag p_T^W distribution after a bin-to-bin $\Delta\phi$ correction for $p_T^W < 120$ GeV and $p_T^W > 120$ GeV separately. The agreement is improved significantly. The electron (muon) channel is shown on the left (right).

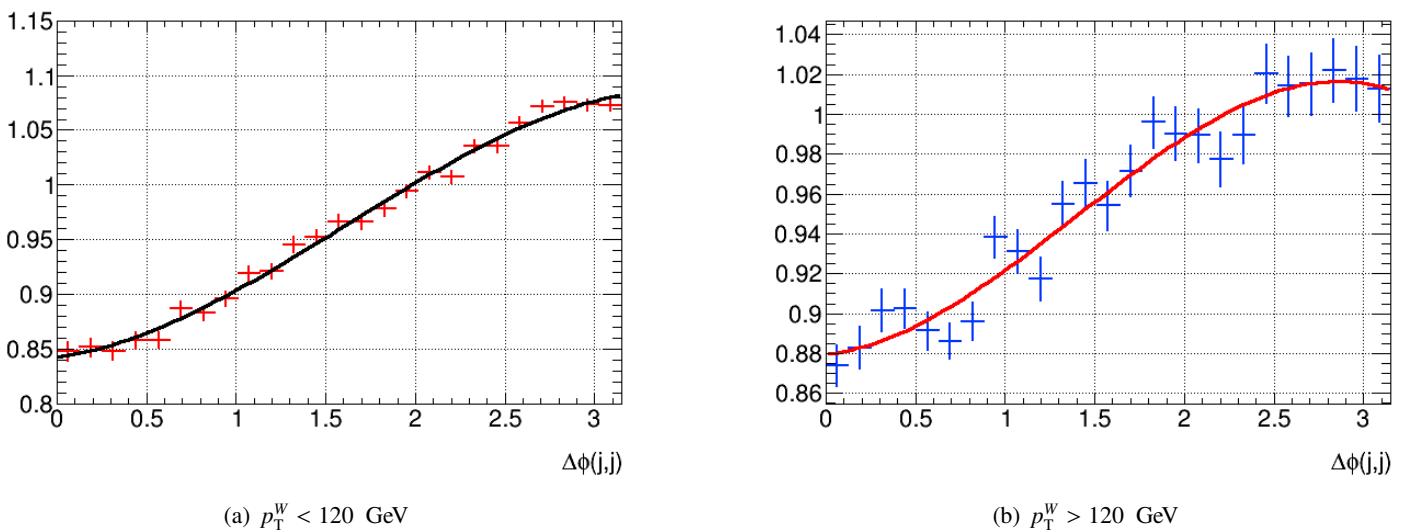


Figure 22: 1-lepton 2-jet 0-tag $\Delta\phi$ correction for $p_T^W < 120$ GeV and $p_T^W > 120$ GeV separately.

5.1.2.3 Specific W +Heavy-Flavor Studies

W +heavy-flavor is a tricky background since it can potentially mimic the signal but lacks a good control region. Generator comparisons are therefore utilized to probe the possible variations of the kinematic distributions (at truth-level) and the production rates of the various flavor combinations $bb/bc/bl/cc$ (at reconstruction-level). The following comparisons describe the different aspects studied for the W +hf background:

- *Compare SHERPA to SHERPA.* The baseline sample uses a b-filter to create $W+b$ events which include b 's from the parton shower. A $W+b\bar{b}$ sample was privately produced where no b 's from the parton shower are included.
- *Compare SHERPA to aMC@NLO+HERWIG++ and PowHEG.* This tests for sensitivity to differences in the matrix element (MX), higher order effects and parton showering. The aMC@NLOsample has been privately produced.

Process	Channel num.	tag	N_{events}
$W^+ \rightarrow ev + bb$	167000	evgen.EVNT.e1386	2495000
$W^+ \rightarrow \mu\nu + bb$	167001	evgen.EVNT.e1386	2490000
$W^+ \rightarrow \tau\nu + bb$	167002	evgen.EVNT.e1386	2500000
$W^- \rightarrow ev + bb$	167003	evgen.EVNT.e1386	1500000
$W^- \rightarrow \mu\nu + bb$	167004	evgen.EVNT.e1386	1500000
$W^- \rightarrow \tau\nu + bb$	167005	evgen.EVNT.e1386	1490000

Table 25: Monte Carlo samples and channel numbers and statistics used for centrally produced W samples considered for systematics variations. More information is given in Section 5.1.

Separately, the baseline aMC@NLO sample will be compared to other aMC@NLO samples with varied

- renormalization scale (0.5x,2x).
- factorization scale (0.5x,2x).
- different PDF sets used for the matrix element(NNPDF and MSTW).

More details are contained in Appendix L.

5.1.2.4 Jet multiplicity and flavor fractions

The following normalization systematics have been derived:

- 3/2-jet ratio for the heavy flavor components from SHERPA-aMC@NLO $W + b\bar{b}$ comparisons

10% (`WbbNorm_J3`)

- relative heavy flavor composition in W + jet events from SHERPA-ALPGEN comparisons

$W+bl$ to $W+bb$: 35% (`WblWbbRatio`)

$W+bc$ to $W+bb$: 12% (`WbcWbbRatio`)

$W+cc$ to $W+bb$: 12% (`WccWbbRatio`)

An uncertainty on the fraction of gluon splitting to this final state and how it affects the 3/2-jet ratio is estimated by comparing the Sherpa $W + b\bar{b}$ prediction with the baseline Sherpa sample where the heavy flavor also comes from the parton shower (see Appendix L). Half of this uncertainty is considered (2%), which has a negligible impact on the total 3/2-jet ratio uncertainty.

2011 **5.1.2.5 $\Delta\phi(jj)$ and p_T^W**

2012 An uncertainty on the p_T^W shape is estimated from a truth-level study, where the aMC@NLO generator
 2013 prediction is compared to that of SHERPA $W + b\bar{b}$ (Figure 23).

2014 **5.1.2.6 m_{jj}**

2015 Two m_{bb} -specific uncertainties were derived from generator differences after a truth-level selection; ALP-
 2016 GEN-SHERPA comparisons and $W + b\bar{b}$ versus b -filter SHERPA for the fraction of gluon splitting contribution.
 2017 Figure 24 shows the first (and larger) uncertainty can shift the distribution by $\pm 20\%$ for $m_{bb} = 50$ GeV
 2018 and $\pm 30\%$ for $m_{bb} = 200$ GeV. The latter has a smaller effect of approximately $\pm 5\%$ across the spectrum
 2019 since only half of the effect is considered. The choice of half for only the second comparison is moti-
 2020 vated, by the nature of the comparison itself. The full difference is to say that gluon splitting does not
 2021 exist which we know is not true so a fraction (50%) of the difference is applied. Since this last difference
 2022 can be already be covered by the systematic uncertainty assigned on m_{bb} by comparing different MC
 2023 generators, the fit will not use it, but detailed studies on its impact have been done while building the
 2024 final fit model.

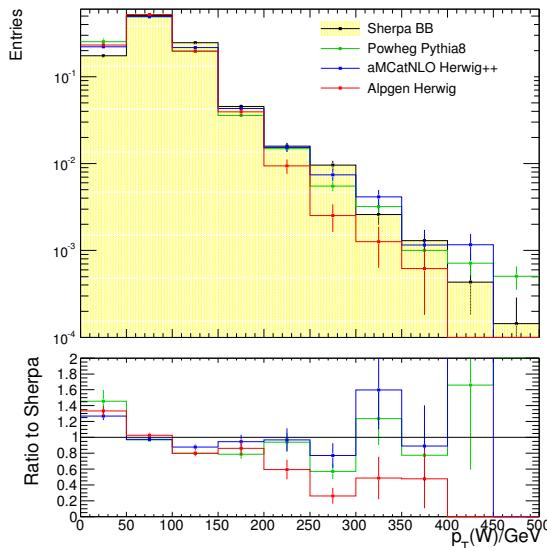


Figure 23: W-boson p_T distribution of 2-jet bb events at truth-level.

Not reviewed, for internal circulation only

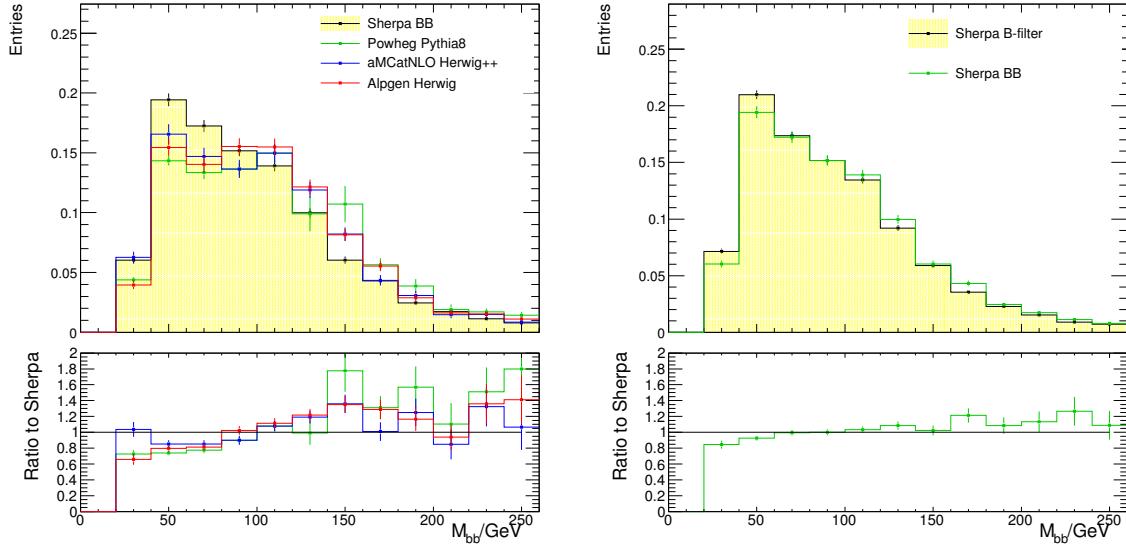


Figure 24: Invariant mass distribution of 2-jet bb events at truth-level. The plot on the left compares the generator predictions for the $W + b\bar{b}$ process, and the plot on the right compares the same Sherpa prediction to the nominal B-filtered sample .

Not reviewed, for internal circulation only

Description	Samples	Nuissance parameters
W1 Normalization	Data VS. Sherpa	W1Norm
W 3/2 ratio	Sherpa VS. aMC@NLO	W1Norm_J3,WclNorm_J3,WbbNorm_J3
W jet flavour composition	Sherpa VS. Alpgen+Herwig+Jimmy	WblWbbRatio, WbcWbbRatio, WccWbbRatio
$\Delta\phi$ correction and systematics	Data VS. Sherpa	WDPPhi
$\Delta\phi$ checks	Data VS. Alpgen+Herwig+Jimmy	
p_T^V systematics	Sherpa VS. aMC@NLO	WPtV
p_T^V checks	Sherpa VS. Powheg VS. Alpgen+Herwig+Jimmy	
m_{bb} systematics	Sherpa VS. Alpgen+Herwig+Jimmy	WMbb
m_{bb} checks	Sherpa VS. Powheg VS. aMC@NLO	
m_{bb} gluon splitting systematics	Sherpa with and without bb from gluon splitting	WbbMbbGS

Table 26: Summary of the $W+jet$ specific samples used to checks the background modelling. The list of the nuissance parameters is given for reference, and it will be discussed in Section 8

2025 5.2 $t\bar{t}$ and single-top

2026 The top-pair samples are generated with PowHEG [56–58] interfaced to PYTHIA with a filter which specifies
 2027 that at least one of W from top decays into charged lepton (e, μ, τ). The parton showering and hadro-
 2028 nisation is generated according to the *Perugia2011C* tune which uses CTEQL1 PDF. For the single-top
 2029 processes, s -channel and Wt -channel are generated with PowHEG+PYTHIA, and the t -channel simulated
 2030 with AcerMC+PYTHIA. All single top channels use the CTEQL1 PDF and the *Perugia2011C* tune. The
 2031 detailed list of MC samples for the top production is listed in Table 27. The reader is encouraged to read
 2032 the introduction to Section 5 to better understand how the information here will be utilized.

Process	Channel num.	tag	N_{events}
Single top, s -ch., PowhegPythia, P2011C			
s -ch.	110119	e1720_a188_a171_r3549_p1328	5995993
Single top, t -ch. and Wt -ch., AcerMCPythia, P2011CCTEQ6L1			
t -ch.	110101	e2096_a188_a171_r3549_p1328	59962956
Wt -ch.	110140	e1743_a188_a171_r3549_p1328	19937980
$t\bar{t}$, PowhegPythia, P2011C			
$t\bar{t}$	117050	e1727_a188_a171_r3549_p1328	99930891

Table 27: Monte Carlo samples and channel numbers and statistics used for the single top and the $t\bar{t}$ samples. More details are given in Section 5.2.

2033 5.2.1 $t\bar{t}$ modeling, corrections and systematics

2034 The $t\bar{t}$ modeling has been explored in depth by other groups within ATLAS. Given the specific final state
 2035 selected, of particular interest for this analysis is the $t\bar{t}$ composition and the capability of the MC, to
 2036 reproduce the top p_T observed in data. This section discusses the derivation of systematic uncertainties
 2037 for the $t\bar{t}$ modeling considering the recommendation and feed-back from the top group. A summary of
 2038 the this section is given in Table 30 and a summary of the systematics used in the profile likelihood is
 2039 given in the statistical model overview (Section 8) in Table 51.

2040 5.2.1.1 $t\bar{t}$ Composition

2041 Due to the ΔR cuts placed in the dijet mass analysis the composition of $t\bar{t}$ events evolve as a function
 2042 of p_T^W with the leading two jets both being b 's at lower p_T^W values and a b - c pair at high p_T^W . A similar
 2043 statement holds for the MVA. The reader should keep this evolution in mind when considering the top-
 2044 pair modeling and systematic studies in the following sections. The flavor compositions are shown in
 2045 Appendix O in Table 83 for the EPS analysis and in Table 28 for the current 1-lepton analysis³. Given that
 2046 there are exactly two b-tagged jets, the flavor composition for the 1-Lepton MVA input selection is shown
 2047 in Table 29. For the following comparisons in Section 5.2.1.3 with other generators for $t\bar{t}$ it is important
 2048 to investigate if these model a similar flavor composition. It was found that the flavor compositions of
 2049 all of them are as expected. The corresponding studies and their numbers are given in the Appendix
 2050 Section N.5 in Table 82.

³The new object selection was utilized but the EPS event selection cuts were used. The table should be updated.

Not reviewed, for internal circulation only

Jet Flavors	p_T^W GeV				
	0-90	90-120	120-160	160-200	>200
2T b -tags					
bb	96.0	96.5	94.7	78.8	40.5
bc	3.0	3.1	4.6	18.8	46.8
$b\tau$	<1	<1	<1	1	9.1
2M b -tags					
bb	79.9	80.2	71.6	46.9	15.0
bc	14.8	14.8	22.2	42.1	63.8
$b\tau$	3.0	5.3	3.3	4.7	7.9
2L b -tags					
bb	62.3	61.0	51.4	26.4	10.6
bc	19.8	20.5	27.0	38.9	50.1
$b\tau$	5.5	4.9	5.1	6.6	5.3

Table 28: The fraction of jet flavor pairs in the 1-lepton EPS [11] analysis from events with two jets as a function of p_T^W . The new object selection was utilized but the EPS event selection cuts were used. The table should be updated.

Jet Flavors	p_T^W GeV	
	0-120	>120
bb	79.8	67.3
bc	11.5	20.4
bl	8.5	11.6

Table 29: The fraction of jet flavor pairs in the 1-lepton multivariate analysis from events with two b-tagged jets separated into low and high p_T^W events. The MVA input selection was applied.

2051 The presence of a high fraction of events with bc final state jets at high p_T^V , and the need to suppress
 2052 as much as possible the background in this region, are the reasons which guided the decision to move to
 2053 the mv1c tagging.

2054 **5.2.1.2 The p_T^{top} correction**

2055 A systematic disagreement in $\Delta\phi$ is not observed in the $t\bar{t}$ sample. However it has been noted in the
 2056 time leading up to EPS that the reconstructed p_T^W in the 1-lepton top-enriched regions and p_T^Z in the 2-
 2057 lepton $e - \mu$ control sample show a disagreement which is consistent with the top p_T being too hard in
 2058 simulation. The ATLAS 7 TeV [59] result shows the same trend so the unfolded measurement shown in
 2059 Figure 25 was used to reweight the average top p_T in MC. Half the reweighting function was used as
 2060 a systematic (TopPt) Further details can be found in Sections 4.4 and 4.5.3 and Appendix J of the EPS
 2061 note [11].

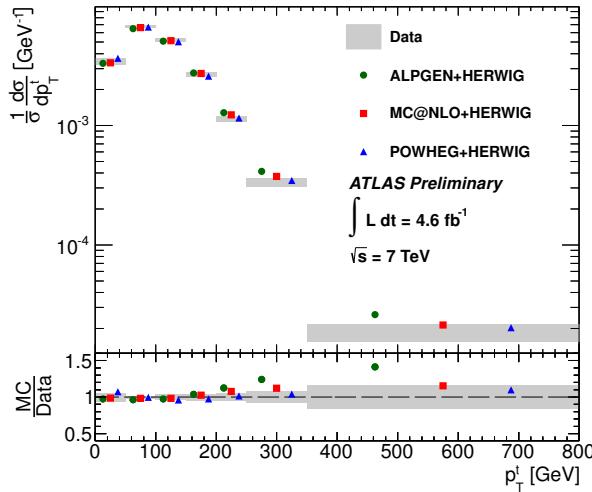


Figure 25: The ATLAS 7 TeV $t\bar{t}$ p_T^{top} unfolded result taken from [60] used to reweight the top p_T spectrum.

2062 **5.2.1.3 Specific $t\bar{t}$ systematics**

2063 The $t\bar{t}$ systematic generator variations have been explored in depth by other groups within ATLAS. The
 2064 baseline approach is to consider all the ‘normal’ variations which are applicable to this analysis. The list
 2065 of checks are as follows:

- 2066 • *Compare to AcerMC with more or less PS.* This will test the effect of the parton showering. The
 2067 recommendation is to obtain the systematic as (morePS-lessPS)/2. For comparisons with other
 2068 generators this variation is added to our nominal sample.
- 2069 • *Compare to PowHeg+Herwig.* This will test different PS and hadronization models. There is some
 2070 difficulty in that since it is not completely orthogonal to the previous comparison.
- 2071 • *Compare to Alpgen.* This will show the sensitivity to higher order effects such as gluon radiation
 2072 since ALPGEN is a LO generator in contrary to PowHEG(NLO).
- 2073 • *Compare to PowHeg+Pythia with HeraPDFs.* This will test the effect of the PDF set. The Hera-
 2074 PDF set is supposed to describe ATLAS data better especially quantities like top p_T . This test will
 2075 suffer from low statistics since the HeraPDF sample has only 5 million events.

- 2076 • *Compare to aMC@NLO.* This probes the potential effects from different matrix element calculations.
- 2077

2078 The top group does recommend several other tests which currently are not planned since they are
 2079 not considered as having large effects on the analysis. A list of those tests and the reasons for excluding
 2080 them are given in Appendix N.

2081 Unless directly stated, all systematic samples will be compared to the nominal sample which is
 2082 PowHEG+PYTHIA with a dedicated top p_T correction applied. Table 31 gives technical details of the sam-
 2083 ples considered. From the above mentioned comparisons the largest discrepancies between generators
 2084 were taken as systematic uncertainties.

2085 The effect of different modeling of the BDT input variables between the generators was taken into
 2086 account as a set of shape uncertainties. These shape uncertainties were derived for the distributions
 2087 of the input variables from the largest discrepancies between generators . If no significant difference
 2088 between the generators is observable no dedicated uncertainty will be assigned. For a further reduction
 2089 of shape systematics advantage was taken of the correlation between the input variables. Therefore a
 2090 minimal set of shape systematics were chosen which are able to cover the observed differences. For this
 2091 set it was observed that the largest discrepancy to the nominal is given by ALPGEN+PYTHIA. As there was
 2092 already a systematic uncertainty assigned to the top p_T correction double counting of systematic effects
 2093 was avoided by reweighting ALPGEN+PYTHIA to the same top p_T in the 7 TeV analysis mentioned above.
 2094 Details of this study are described in Appendix Section N.3. After this study shape uncertainties were
 2095 derived from a fit through the difference between ALPGEN+PYTHIA without the top p_T reweighting and the
 2096 nominal sample in the distributions for m_{bb} and E_T^{miss} . Since the shapes for the 2 jet and 3 jet region are
 2097 similar for the E_T^{miss} distributions those two regions were merged and a single uncertainty was derived.
 2098 For m_{bb} a similar merging was not possible. A combination of the high and low p_T^W region was not
 2099 possible in both cases due to different shapes originating e.g. from different E_T^{miss} cuts.

2100 Figure 26 details the m_{bb} systematic for $t\bar{t}$ 2-jet events (TtbarMBBCont). Similar plots are shown for
 2101 3-jet events along with more details in Appendix Section N.1. The first row shows the comparison of all
 2102 generators with the most discrepant from the baseline being ALPGEN+PYTHIA without the p_T^{top} reweight. A
 2103 fit to the ratio was performed up to 200 GeV as shown in the bottom row. Details of the fit function are
 2104 described in Appendix Section N.1. Unfortunately, the comparisons with and without the p_T^{top} correction
 2105 shown in the middle row came soon after this systematic was propagated into the analyses. Since no
 2106 large difference in the ratio is seen in the region used for the systematic derivation, it was decided to not
 2107 change the prescription.⁴ The ratio was different enough in the four regions such that a separate function
 2108 was fit to each.

2109 The E_T^{miss} distribution also showed considerable differences, the largest being between ALPGEN+PYTHIA
 2110 and PowHEG+PYTHIA yet again. Full details are shown in Appendix Section N.2. Figure 27 shows
 2111 for $p_T^W > 120$ GeV the comparison of all the generators in the top row, a specific ALPGEN+PYTHIA-
 2112 PowHEG+PYTHIA comparison with and without the top p_T systematics in the middle row, followed by
 2113 the systematic used in 2 and 3 jet events alike (TtbarMetCont). Again the differences in the systematic
 2114 after the top p_T correction is applied were deemed small enough to avoid. Since the ratios for the 2-jet
 2115 and 3-jet region were similar for the E_T^{miss} distributions, these two regions were merged and a single
 2116 uncertainty was derived.

2117 The functional form used for the systematic is constant above 300 GeV as to maintain a reasonable
 2118 size in the tail of the E_T^{miss} distribution. Since the definition and source of E_T^{miss} is analysis specific, this
 2119 is only used in the 1-lepton analysis.

2120 The effect of these two systematics were each propagated to the BDT itself and compared to the
 2121 differences from the full list of generator comparisons. Since the two systematics along with the top

⁴Time dependence is an unfortunate consequence of the complexity of ATLAS software and this analysis in general.

Not reviewed, for internal circulation only

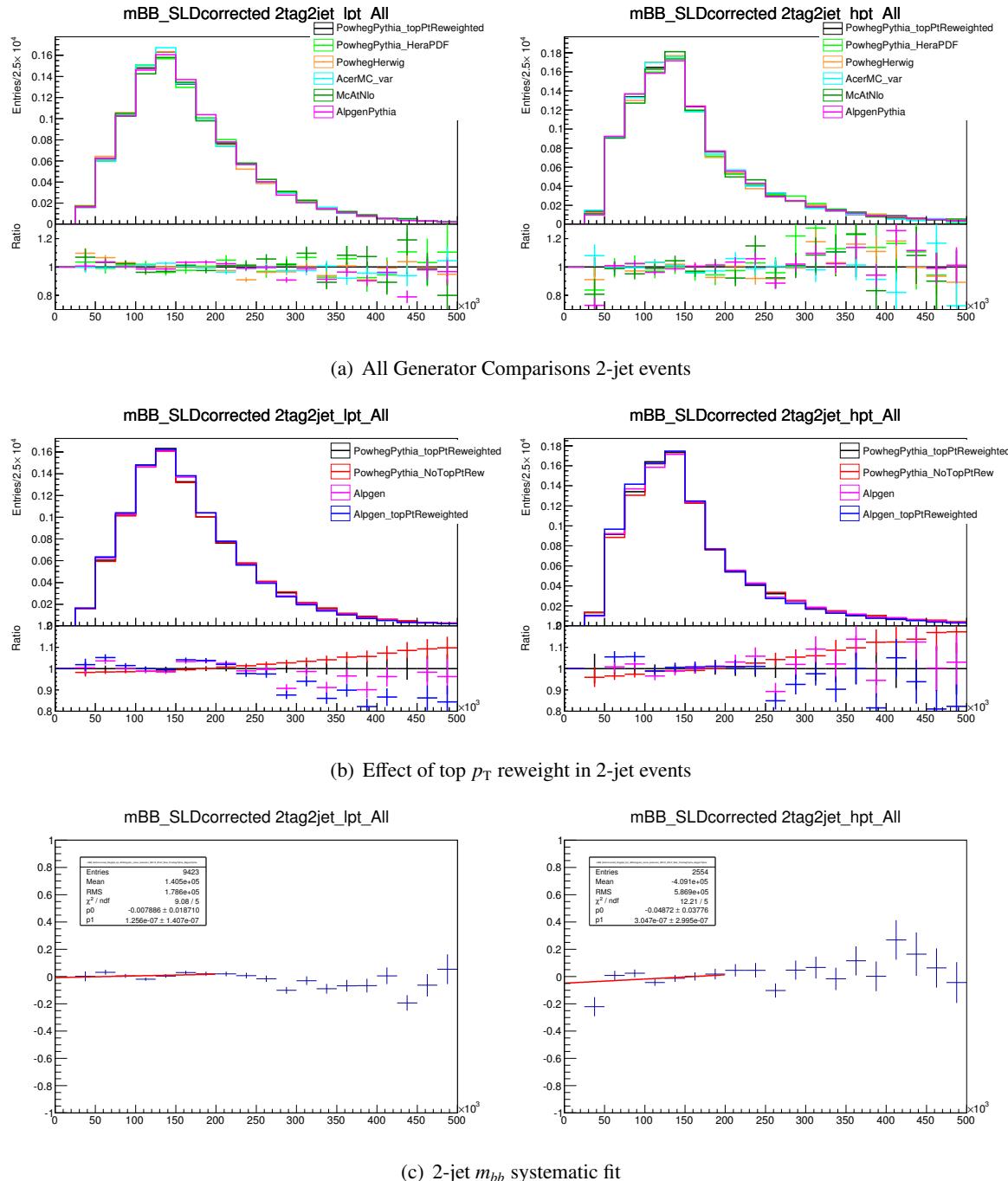


Figure 26: m_{bb} systematic for $t\bar{t}$ in 2-jet events (3-jet in Appendix N) $p_T^W < 120$ GeV is shown on the left and $p_T^W > 120$ GeV is shown on the right. The top row shows the all generator comparison, the middle is a closer look at the most discrepant compared to the nominal, ALPGEN+PYTHIA, with and without the top p_T correction, and finally, the systematic itself derived from the ALPGEN+PYTHIA to PowHEG+PYTHIA ratio in the top row of plots.

Not reviewed, for internal circulation only

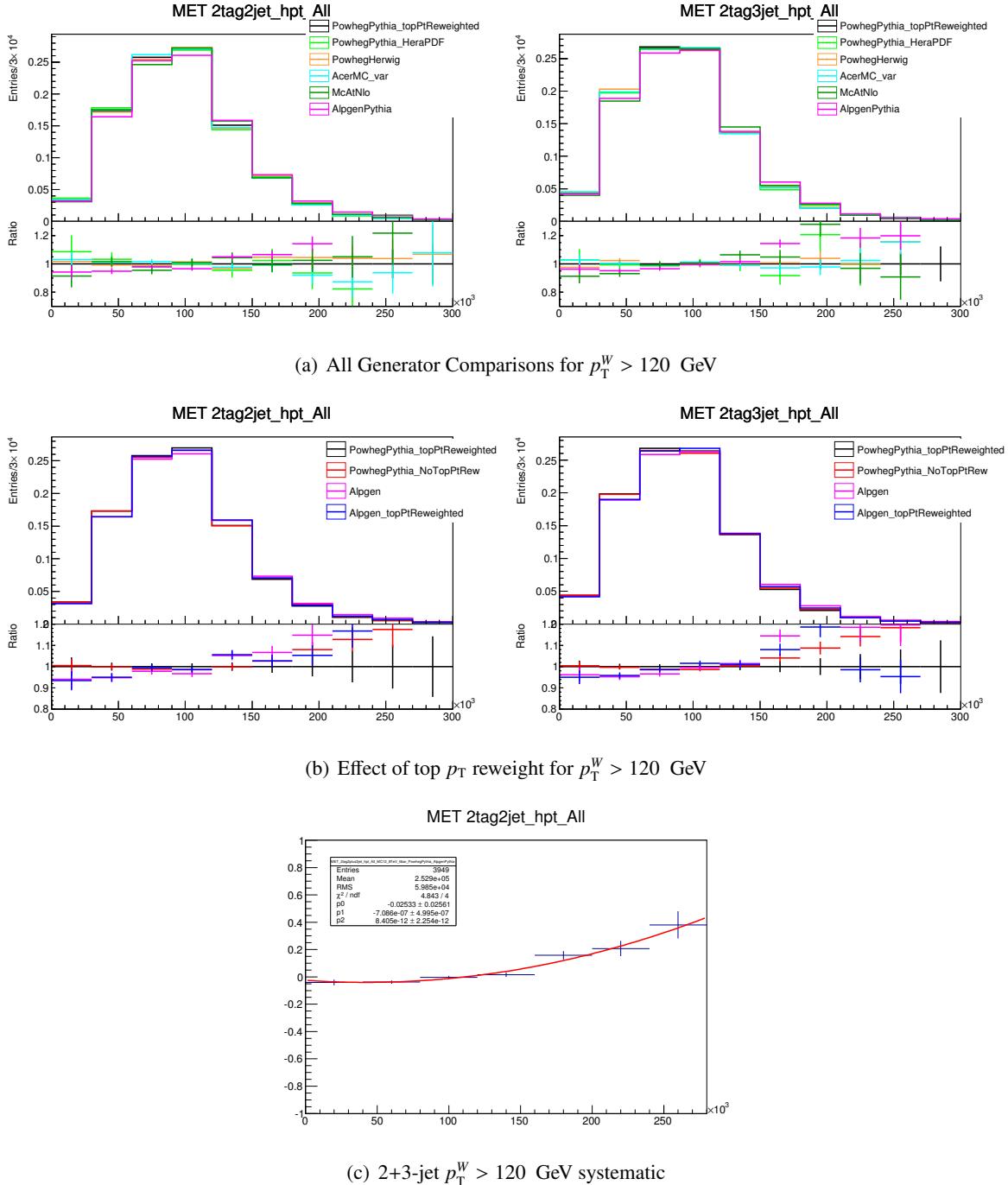


Figure 27: E_T^{miss} systematic for $t\bar{t}$ events in 2+3-jet events for $p_T^W > 120$ GeV the 2 and 3-jet regions on the left and right respectively. These were obtained from a comparison of ALPGEN+PYTHIA to PowHEG+PYTHIA. More details including the $p_T^W < 120$ GeV are given in Appendix N

2122 p_T systematic covered all other differences in the BDT input variables, no further modeling systematics
 2123 were included. The effect of the overall shape systematics (top p_T , E_T^{miss} , m_{bb}) on the BDT output for
 2124 the 2-jet and 3-jet region is shown in Figure 28. Considering the statistical fluctuations the set of shape
 2125 systematics show a good coverage of systematic effects in the BDT output for the high p_T^W region. In the
 2126 low p_T^W region the coverage in the high BDT output bins is a bit worse but it was decided to not introduce
 2127 additional systematics.

Not reviewed, for internal circulation only

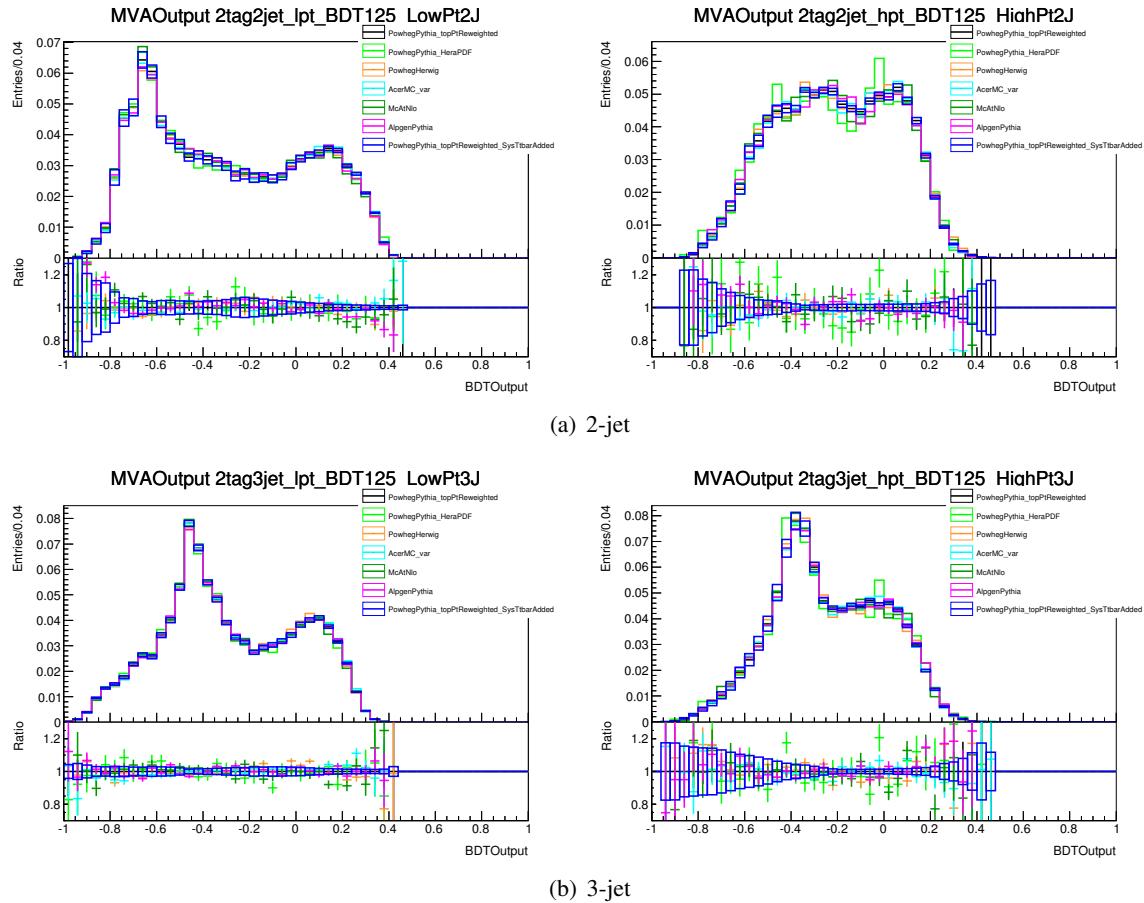


Figure 28: Coverage of systematic effects in the BDT output for $t\bar{t}$, the top p_T , m_{bb} and E_T^{miss} shape systematics were applied.

2128 Since the multivariate analysis is separated into regions with two jets and three jets, always given
 2129 that there are exactly two b-tagged jets, as well as into regions with a high p_T^W and a low p_T^W additional
 2130 uncertainties have to be assigned which take the differences between the generators regarding this categorization
 2131 into account. From a comparison of the ratio of high to low p_T^W events a 7.5% uncertainty was as-
 2132 signed from ALPGEN+PYTHIA which was the most different from the baseline PowHEG+PYTHIA($t\bar{t}\text{barHighPtV}$).
 2133 Similarly a 20% uncertainty was derived for the ratio of 2-to-3 jet production from the comparison to ALP-
 2134 GEN+PYTHIA ($t\bar{t}\text{barNorm_J3}$). The details of these comparisons are included in Table 81 in Appendix N.

Not reviewed, for internal circulation only

Description	Samples	Nuissance parameters
Systematics on High/low p_T^V ratio	Powheg VS. Alpgen+Herwig+Jimmy	<code>ttbarHighPtV</code>
Systematics on 3/2 jet ratio	Powheg VS. Alpgen+Herwig+Jimmy	<code>ttbarNorm_J3</code>
Top p_T correction and systematics	Data VS. Powheg	<code>TopPt</code>
p_T^V shape systematics	Powheg VS. Alpgen+Herwig+Jimmy	<code>TtbarPtWCont</code>
m_{bb} shape systematics	Powheg VS. Alpgen+Herwig+Jimmy	<code>TtbarMBBCont</code>
Leading jet p_T shape systematics	Powheg VS. Alpgen+Herwig+Jimmy	<code>TtbarPtB1Cont</code>
E_T^{miss} shape systematics	Powheg VS. Alpgen+Herwig+Jimmy	<code>TtbarMETCont</code>
Checks done with :	ALPGEN, PowHEG, AcerMC with more or less PS PowHEG+HERWIG, aMC@NLO.	

Table 30: Summary of the $t\bar{t}$ specific samples used to checks the background modelling. The list of the nuisance parameters is given for reference, and it will be discussed in Section 8.

Process	Channel num.	tag	N_{events}
$t\bar{t}$	105200	$t\bar{t}$, aMC@NLO, CT10 e1513_s1499_s1504_r3945_r3549	14990603
$t\bar{t}$	105860	$t\bar{t}$, PowhegHerwig, AUET2CT10 e1576_a159_a171_r3549	25886964
$t\bar{t}$	117001	$t\bar{t}$, PowhegPythia, P2011CHERAPDF15NLO e2397_a188_a171_r3549	4997997
$t\bar{t}$	117209	$t\bar{t}$, AcerMCPythia, AUET2BMorePSCTEQ6L1 e1378_a159_a171_r3549	14040986
$t\bar{t}$	117210	$t\bar{t}$, AcerMCPythia, AUET2BLessPSCTEQ6L1 e1378_a159_a171_r3549	14988492
$t\bar{t}, lnlnNp0$	201020	$t\bar{t}$, AlpgenPythia, P2012 e2356_s1581_s1586_r3925_r4540	3199485
$t\bar{t}, lnlnNp1$	201021	e2356_s1581_s1586_r3925_r4540	3187981
$t\bar{t}, lnlnNp2$	201022	e2356_s1581_s1586_r3925_r4540	2091691
$t\bar{t}, lnlnNp3$	201023	e2356_s1581_s1586_r3925_r4540	971691
$t\bar{t}, lnlnNp4inc$	201024	e2356_s1581_s1586_r3925_r4540	589998
$t\bar{t}, lnqqNp0$	201220	e2356_s1581_s1586_r3925_r4540	6293873
$t\bar{t}, lnqqNp1$	201221	e2356_s1581_s1586_r3925_r4540	6389459
$t\bar{t}, lnqqNp2$	201222	e2356_s1581_s1586_r3925_r4540	1814984
$t\bar{t}, lnqqNp3$	201223	e2356_s1581_s1586_r3925_r4540	1949886
$t\bar{t}, lnqqNp4inc$	201224	e2356_s1581_s1586_r3925_r4540	1179291

Table 31: Monte Carlo samples and channel numbers and statistics used for the single top and the $t\bar{t}$ systematics. More information is given in Section 5.2.1.

2135 **5.2.2 Single-top modeling and systematics**

2136 As for the $t\bar{t}$ background, the single top systematic generator variations have been explored in depth by
 2137 other groups within ATLAS. The baseline approach is to consider all the ‘normal’ variations which are
 2138 applicable to this analysis. The single top group has recommended a list of generator comparisons which
 2139 are summarized in Table 5.2.2. If only one sample is mentioned then a comparison to the baseline sample
 2140 is implied. Table 80 gives technical details of the samples considered.

2141 A summary of the this section is given in Table 34 and a summary of the systematics used in the
 2142 profile likelihood is given in the statistical model overview (Section 8) in Table 52.

Process	Samples	Description	Nuisance Parameters
t -ch.	aMCAtNlo AcerMC more vs less PS	higher order, hadronization and showering parton shower effects	SysTChanPtB2
Wt -ch.	Herwig AcerMC PowhegPythia DS MCAtNlo AcerMC more vs less PS	hadronization and showering models higher order Diagram Removal vs Subtraction hadronization and showering models parton shower effects	SyWtChanPythiaHerwig SyWtChanAcerMC
s -ch.	AcerMC MCAtNlo AcerMC more vs less PS	higher order effects hadronization and showering models parton shower effects	SysSChanAcerMC SysSChanAcerMCPC

Table 32: Monte Carlo samples considered for systematics and what each comparison brings. More information is given in Section 5.2.2.

2143 To perform the study, the events passing the MVA selection for the 1-lepton channel have been used
 2144 and the shapes of all the relevant variables entering in the multivariate analysis were analyzed. For each
 2145 of the single top channel (s – channel, t – channel and Wt – channel) the systematics have been divided
 2146 into two categories: normalization and shape systematics.

2147 The normalization systematics takes into account the renormalization and factorization scale variation,
 2148 the α_s uncertainty and the errors on the parton density functions. They are of the order of 3.9%,
 2149 6.8% and 3.9% for the t – channel, Wt – channel and s – channel respectively.

2150 The second set of errors is coming from the comparisons of the different available Monte Carlo
 2151 samples. It is estimated for the two analysis signal regions - 2 jets or 3 jets and 2 tags - and in two p_T^V bins
 2152 - above and below 120 GeV. Since the different Monte Carlo estimate can differ in the event acceptance
 2153 and in the shape of the different kinematic variables, a detailed campaign of checks have been carried
 2154 out for each channel. The strategy adopted in this case was for each of the p_T^V region, jet multiplicity,
 2155 and each production channel, to check which Monte Carlo sample shows the worst agreement in terms
 2156 of acceptance and/or shape of the variables of interest. In this way, a normalization error and a shape
 2157 variation for specific variables (if needed), have been derived . As a coverage test, the impact of the
 2158 shape variations have been propagated to the BDT output and compared with the agreement obtained
 2159 when using the Monte Carlo sample used to derive the systematics.

2160 The major differences are mostly from comparisons of the nominal sample with a next-to-leading
 2161 order Monte Carlo, or, in the case of the s – channel, from the samples with more or less parton shower.
 2162 This result in the systematics summarized in Table 34. The selected variables and the functions used
 2163 for the systematics are summarized in the Table 34. Figure 29 show for each production channel, p_T^V

Not reviewed, for internal circulation only

Process	Channel num.	tag	N_{events}
Single top, AcerMCPythia, P2011CCTEQ6L1			
$s\text{-ch.}$	110102	e2092_a188_a205_r4540_p1328	1199999
$Wt\text{-ch.}$	110103	e2092_a188_a205_r4540_p1328	998997
Single top, PowhegHerwig, AUET2CT10			
$Wt\text{-ch}$	110144	e1743_s1581_s1586_r3658_r3549_p1328	998896
Single top, PowhegPythia, P2011C, DS			
$Wt\text{-ch.}$	110142	e1743_s1581_s1586_r3658_r3549_p1328	994894
Single top, aMcAtNloJimmy, AUET2CT10			
$t\text{-ch.}$	110095	e2240_a188_a205_r4540_p1328	996999
Single top, McAtNloJimmy, AUET2CT10			
$s\text{-ch.}$	108343	e1525_a159_a171_r3549_p1328	999998
	108344	e1525_a159_a171_r3549_p1328	998000
	108345	e1525_a159_a171_r3549_p1328	999998
$Wt\text{-ch.}$	108346	e1525_a159_a171_r3549_p1328	4996492
Single top AcerMCPythia, P2011CMorePSCTEQ6L1			
$t\text{-ch.}$	110105	e2092_a188_a205_r4540_p1328	2978000
$s\text{-ch.}$	110107	e2092_a188_a205_r4540_p1328	1199999
$Wt\text{-ch}$	110109	e2092_a188_a205_r4540_p1328	998999
Single top AcerMCPythia, P2011CLessPSCTEQ6L1			
$t\text{-ch.}$	110106	e2092_a188_a205_r4540_p1328	2997999
$s\text{-ch.}$	110108	e2092_a188_a205_r4540_p1328	1198998
$Wt\text{-ch}$	110110	e2092_a188_a205_r4540_p1328	1000000

Table 33: Monte Carlo samples and channel numbers and statistics used for the single top and the $t\bar{t}$ systematics. More information is given in Section 5.2.2.

2164 region, and number of jets, the selected input variable used to parametrize the systematic uncertainty,
 2165 and its impact on the BDT output. It must be noted that since the final contribution from the s – *channel*
 2166 is negligible, no specific shape systematic uncertainty have been derived. In the case of the t – *channel*,
 2167 the BDT input variables were found to exhibit no significant shape differences between different Monte
 2168 Carlo. A detailed description of all the Monte Carlo studies are presented in Appendix M.

Not reviewed, for internal circulation only

Process	Systematic Name	Normalization systematic (%)	Shape systematics
		2 jets, 2 tag $p_T^V < (>) 120 \text{ GeV}$	3 jets, 2 tag $p_T^V < (>) 120 \text{ GeV}$
t -ch.	SysTChanPtB2	52 (25)	12 (-18) no shape systematic
Wt -ch.	SyWtChanPythiaHerwig	5 (3)	2 jets, $p_T^V < 120 \text{ GeV}$: $\pm(1.3 - 0.004 \times p_{T,b1})$
	SyWtChanAcerMC	1 (-2)	2 jets, $p_T^V > 120 \text{ GeV}$: $\pm(0.6 + 0.004 \times m_{bb})$ 3 jets, $p_T^V < 120 \text{ GeV}$: $\pm(1.2 - 0.003 \times p_{T,b1})$ 3 jets, $p_T^V > 120 \text{ GeV}$: $\pm(1.4 - 0.003 \times m_{bb})$
s -ch.	SysSChanAcerMC	13 (22)	no shape systematic
	SysSChanAcerMCPC	6 (8)	no shape systematic

Table 34: Single-top systematics obtained comparing different Monte Carlo samples. $p_{T,b1}$ and m_{bb} are the p_T of the leading b-jet and the di-bjet invariant mass.

Not reviewed, for internal circulation only

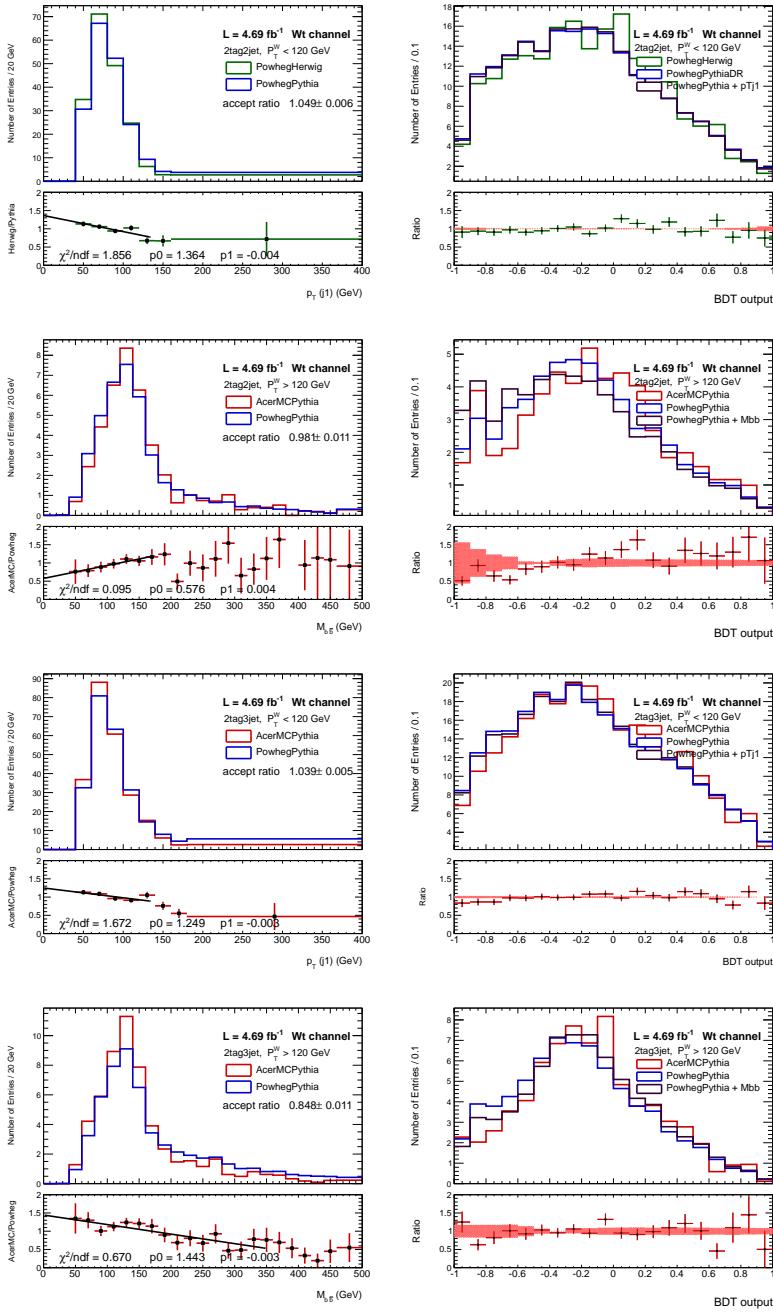


Figure 29: Wt -ch. shape systematics, obtained by comparing Herwig with Pythia and AcerMC with Powheg, and its impact on the BDT output.

Not reviewed, for internal circulation only

2169 5.3 Diboson

2170 5.3.1 Uncertainties in the Modeling of the Diboson Processes

2171 The diboson background includes the diboson production processes which originate from a final state
 2172 with two vector bosons (WW , WZ , ZZ). Several diboson processes give significant contribution in the
 2173 analysis signal regions: $Z \rightarrow vv$ and $Z \rightarrow b\bar{b}$ for the 0-lepton channel, $Z \rightarrow ll$ and $Z \rightarrow b\bar{b}$ for the
 2174 2-lepton channel; $W \rightarrow lv$ and $Z \rightarrow b\bar{b}$ for the 1-lepton channel. Additional processes can give smaller
 2175 contributions, thanks to the miss-tag of a jet from a W decay or to the failed reconstruction of one of the
 2176 leptons; $Z \rightarrow vv$ and $W \rightarrow q\bar{q}$, $Z \rightarrow ll$ and $W \rightarrow q\bar{q}$, WW (inclusive) production. The rate of $V(Z \rightarrow bb)$
 2177 is roughly 5 times that of the signal and so this background provides a great opportunity to validate the
 2178 analysis against a known process. This is discussed in Section REF. The reader is encouraged to read the
 2179 introduction to Section 5 to better understand how the information here will be utilized.

2180 The PowHEG generator provides a next-to-leading-order (NLO) estimate, relying on the CT10nlo
 2181 PDF set and interfacing the Pythia8 parton shower and hadronization model. The MC samples for the
 2182 diboson processes are listed on Table 35 along with their cross-sections at $\sqrt{s} = 8$ TeV.

Process	Powheg+Pythia8 channel	Cross-Section ($\sqrt{s} = 8$ TeV) [pb]	Nevents
$Z \rightarrow vv Z \rightarrow q\bar{q}$	181967	1.964	11520000
$Z \rightarrow ll Z \rightarrow q\bar{q}$	181966	1.207	4000000
$W \rightarrow lv Z \rightarrow q\bar{q}$	181970	4.870	10000000
$Z \rightarrow vv W \rightarrow q\bar{q}$	181969	2.777	3000000
$Z \rightarrow ll W \rightarrow q\bar{q}$	181968	1.594	1500000
WW	181971	52.44	10000000

Table 35: Monte Carlo generator used for the modelling of the diboson processes and correspondent MC channel number, cross sections and number of generated events.

2183 Previous studies conducted using the HERWIG generator show that the contribution of the diboson
 2184 processes not listed on Table 35 is less than 1%, and it is thus neglected in the analysis.

2185 The estimated NLO cross-sections quoted in Table 35 are provided directly by the PowHEG samples,
 2186 and are used to normalize the different processes. For the WW and ZZ processes the PowHEG cross-
 2187 section does not include the contributions of gluon-gluon initiated processes, which is thus computed
 2188 and added back to the cross-section value using the MCFM software, set to the configuration outlined in
 2189 Table 36. In detail the factorization and renormalization scales of the processes are set to half the invariant
 2190 mass of the bosons decay products, $m(3456)$, and the CT10nlo PDF set is used. For the processes with
 2191 one leptonically decaying Z boson a cut on $m_{ll} > 20$ GeV is applied for consistency with the PowHEG
 2192 samples.

2193 The following sources are considered as a source of systematic uncertainty

- 2194 • Perturbative uncertainties on the fixed-order NLO cross-section computation
- 2195 • knowledge of PDF and α_S coupling

2196 and are obtained using the MCFM software.

2197 5.3.1.1 Perturbative uncertainties

2198 Since the analysis requires exactly 2 or 3 jets, the uncertainties are derived separately in the 2-jet and
 2199 3-jet bins, which are defined cutting on the transverse momentum and the pseudorapidity of the final state

2200 partons produced by MCFM. Since MCFM does not provide the cross-section computation at higher
 2201 order than NLO, the 3-jet bin corresponds to the inclusive cross-section $\sigma_{\geq 3}$ for VV+1 jet, while the
 2202 2-jet bin corresponds to the exclusive cross-section σ_2 for VV+0 jets.

2203 The uncertainties due to higher-order perturbative corrections to the cross-section are usually esti-
 2204 mated through scales variations. To consider a simple scales variation however leads to an underestima-
 2205 tion of the uncertainty on exclusive fixed-order cross-sections, due to cancellations occurring between the
 2206 large corrections to the total cross section and the perturbative corrections from logarithmic dependence
 2207 on the jet veto. To obtain a robust estimate of these uncertainties, treating properly these cancellations,
 2208 the “Stewart-Tackmann method” [49] [50] method is applied to derive systematic errors in the 2-jet and
 2209 3-jet categories.

2210 According to [49] the covariance matrix for the perturbative uncertainties on the 2-jet and 3-jet cate-
 2211 gories is built as:

$$2212 C(\sigma_2, \sigma_{\geq 3}) = \begin{pmatrix} \Delta_{\geq 2}^2 + \Delta_{\geq 3}^2 & -\Delta_{\geq 3}^2 \\ -\Delta_{\geq 3}^2 & \Delta_{\geq 3}^2 \end{pmatrix},$$

2213 where $\Delta_{\geq 2}$ and $\Delta_{\geq 3}$ are the absolute uncertainties on the inclusive 2-jet cross-section ($\sigma_{\geq 2}$) and the in-
 2214 clusive 3-jet cross-section, derived varying the factorization and renormalization scales down to half and
 2215 up to double the initial value of $m(3456)$. The covariance matrix C is decomposed in the sum of two
 2216 matrices,

$$2217 C(\sigma_2, \sigma_{\geq 3}) = \begin{pmatrix} \Delta_{\geq 2}^2 & 0 \\ 0 & 0 \end{pmatrix} + \begin{pmatrix} \Delta_{\geq 3}^2 & -\Delta_{\geq 3}^2 \\ -\Delta_{\geq 3}^2 & \Delta_{\geq 3}^2 \end{pmatrix} = C_1 + C_2.$$

2218 The first term C_1 results in an absolute systematic error $\Delta_{\geq 2}$ on the 2jet-exclusive cross section σ_2
 2219 (VVJetScalePtST2), while the second term C_2 has one singular eigenvector (hence no systematic vari-
 2220 ation) and one non-singular eigenvector which provides an anti-correlated $\Delta_{\geq 3}$ absolute systematic on σ_2
 2221 and $\sigma_{\geq 3}$ (VVJetScalePtST1). This procedure is applied for each of the diboson processes, obtaining
 2222 two orthogonal relative uncertainties on σ_2 and one relative systematic uncertainty on $\sigma_{\geq 3}$.

2223 These systematic uncertainties are derived separately in the different p_T^V regions used in the analysis:
 2224 the errors show a non negligible dependence with respect to p_T^V , therefore they are treated as normaliza-
 2225 tion and shape systematics, correlated in p_T^V , on the cross-sections. Figure 30 shows the two orthogonal
 2226 shape systematics for the $W \rightarrow l\nu$ and $Z \rightarrow q\bar{q}$ process obtained with this procedure on the 2-jet bin
 2227 cross-section σ_2 . Table 38, Table 39 and Table 40 summarize the values of these uncertainties across the
 2228 5 p_T^V bins for the 6 different diboson processes considered.

2229 5.3.1.2 PDF and α_S uncertainties

2230 The uncertainties on PDF and α_S are evaluated according to the latest prescription from PDF4LHC: the
 2231 global PDF+ α_S uncertainty is derived taking the envelope of the error bands provided by the CT10 and
 2232 MSTW2008 PDF sets, evaluated for two different α_S central values of 0.117 and 0.119. This set of
 2233 uncertainties does not show a significant dependence with respect to p_T^V , therefore the errors are con-
 2234 sidered as normalization systematics on the cross-sections of the diboson backgrounds. The systematic
 2235 errors are derived separately for the 2-jet and 3-jet categories but used in a correlated fashion, and do not
 2236 depend on the decay of the vector boson but only on the V boson pair produced. The full list of PDF+ α_S
 2237 uncertainties for the diboson processes is quoted on Table 37.

2238 5.3.1.3 Parton shower and hadronization model

2239 To quote a systematic uncertainty on the parton shower and hadronization scheme interfaced with the
 2240 Powheg generator we studied the differences between two different shower models: Powheg+Pythia8

MCFM parameter	Value
hmass	126d0
scale:QCD scale choice	+0.5
facscale:QCD fac_scale choice	+0.5
dynamicscale	m(3456)
itmx1, itmx2	10
ncall1, ncall2	500000
LHAPDF group	CT10nlo.LHgrid

Table 36: Main settings for the MCFM software used to compute the cross-sections for the diboson processes.

Process	PDF+ α_S (2-jet)	PDF+ α_S (3-jet)
ZZ	0.03	0.03
WZ	0.04	0.02
WW	0.03	0.02

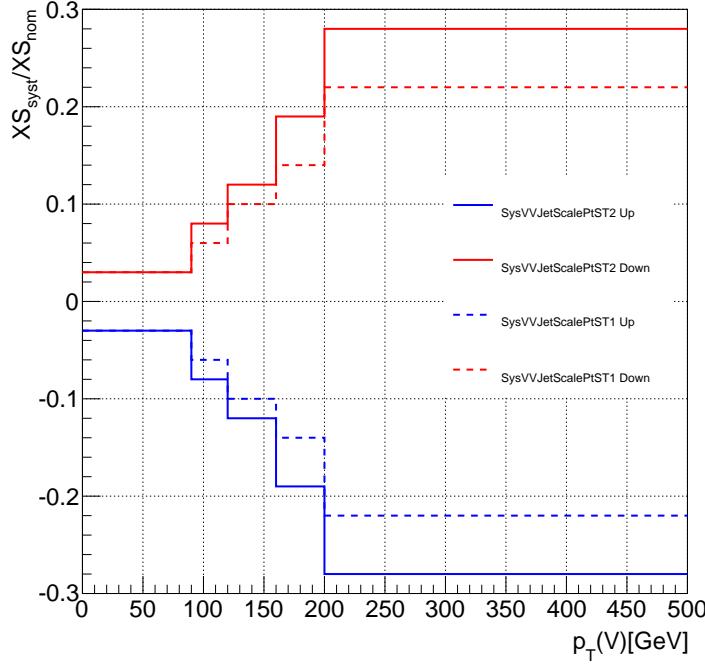
Table 37: PDF+ α_S systematic uncertainties for ZZ, WZ and WW processes, in the 2-jet and 3-jet categories.

and **Herwig**. Powheg+Pythia8 is the nominal MC used in the analysis, while Herwig provides a LO prediction interfaced with a LL parton shower.
 To estimate the systematic errors we considered the distribution of the invariant mass of the jets pair m_{jj} , which is particularly sensitive to hadronization effects, for the two MC generators: since Herwig doesn't provide a separate estimate of the different decay modes of the bosons pair, the errors are derived in the inclusive cases WW, WZ and ZZ.
 The systematic effect is extracted from the ratio between the shapes of the m_{jj} distribution, therefore the predictions from the two generators are normalized to unit area, applying the full 0-lepton event selection except the b-tagging requirement. The m_{jj} ratio is fitted with a parametric function to reduce the effect of statistical fluctuation; the resulting systematic errors are applied consistently in all the three decay channels.
 Figure 31 shows the Powheg+Pythia8 versus Herwig comparison for the WZ processes: the resulting systematic errors range from 10% to about 20% for ZZ, from 10% to 40-50% for WZ and up to about 20% for WW processes. These systematics are included as shape-only nuisance parameters in the fit model.

5.3.1.4 Summary of the systematics

A summary of the systematics used in the fit for the diboson is shown in Table 41.

WInuZhad - Stewart-Tackmann systematics - 2-jet exclusive XS



Not reviewed, for internal circulation only

Figure 30: Shape perturbative systematics on σ_2 for the $W \rightarrow l\nu$ and $Z \rightarrow q\bar{q}$ process obtained applying scale variations according to the Stewart-Tackmann method. The solid line corresponds to the errors derived from the C_1 term and the dotted line from the C_2 term of the covariance matrix C .

p_T^V bins [GeV]	0-90	90-120	120-160	160-200	> 200
$Z \rightarrow vv Z \rightarrow q\bar{q}$	0.03	0.05	0.07	0.10	0.14
$Z \rightarrow ll Z \rightarrow q\bar{q}$	0.03	0.05	0.07	0.10	0.13
$W \rightarrow lv Z \rightarrow q\bar{q}$	0.03	0.08	0.12	0.19	0.28
$Z \rightarrow vv W \rightarrow q\bar{q}$	0.03	0.07	0.12	0.18	0.28
$Z \rightarrow ll W \rightarrow q\bar{q}$	0.03	0.08	0.13	0.19	0.29
WW	0.03	0.06	0.09	0.13	0.19

Table 38: Probative systematics on σ_2 from the C_1 term of the covariance matrix across the different p_T^V bins.

p_T^V bins [GeV]	0-90	90-120	120-160	160-200	> 200
$Z \rightarrow vv Z \rightarrow q\bar{q}$	0.02	0.04	0.05	0.07	0.11
$Z \rightarrow ll Z \rightarrow q\bar{q}$	0.02	0.04	0.06	0.08	0.11
$W \rightarrow lv Z \rightarrow q\bar{q}$	0.03	0.06	0.10	0.14	0.22
$Z \rightarrow vv W \rightarrow q\bar{q}$	0.02	0.05	0.08	0.12	0.20
$Z \rightarrow ll W \rightarrow q\bar{q}$	0.02	0.06	0.09	0.13	0.21
WW	0.02	0.04	0.06	0.09	0.13

Table 39: Perturbative systematics on σ_2 from the C_2 term of the covariance matrix across the different p_T^V bins.

p_T^V bins [GeV]	0-90	90-120	120-160	160-200	> 200
$Z \rightarrow vv Z \rightarrow q\bar{q}$	-0.11	-0.12	-0.13	-0.15	-0.16
$Z \rightarrow ll Z \rightarrow q\bar{q}$	-0.10	-0.12	-0.14	-0.15	-0.16
$W \rightarrow lv Z \rightarrow q\bar{q}$	-0.12	-0.13	-0.15	-0.16	-0.17
$Z \rightarrow vv W \rightarrow q\bar{q}$	-0.11	-0.12	-0.14	-0.15	-0.17
$Z \rightarrow ll W \rightarrow q\bar{q}$	-0.12	-0.13	-0.14	-0.16	-0.18
WW	-0.11	-0.12	-0.14	-0.15	-0.17

Not reviewed, for internal circulation only

Table 40: Perturbative systematics on $\sigma_{\geq 3}$ from the C_2 term of the covariance matrix across the different p_T^V bins.

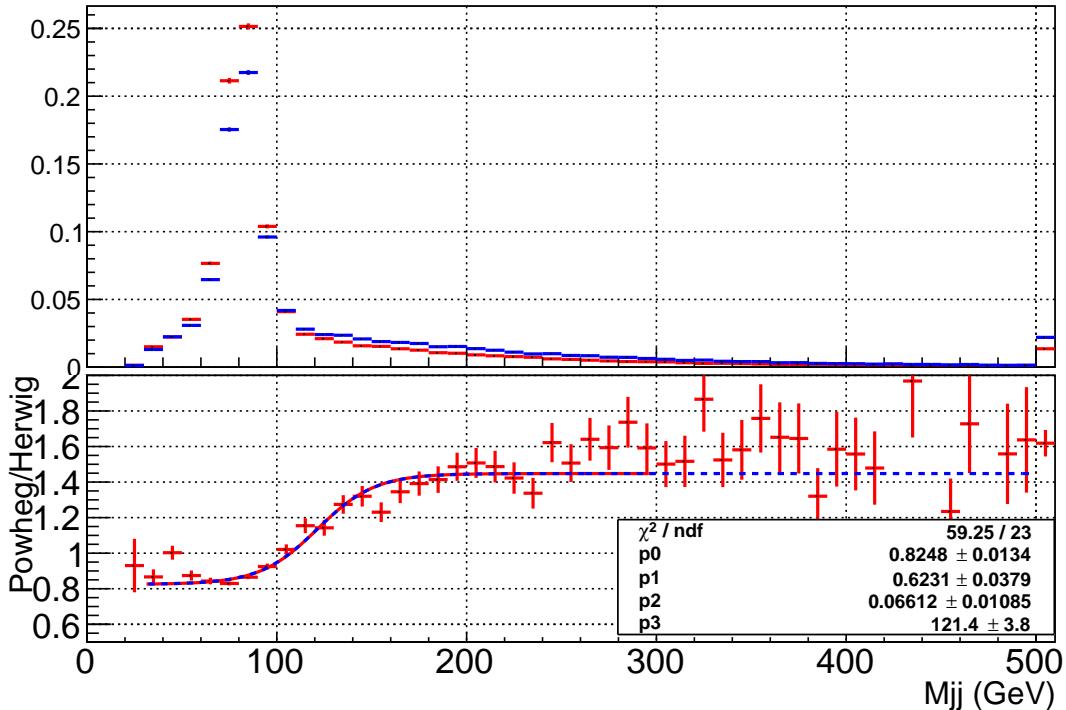


Figure 31: POWHEG+Pythia8 versus Herwig comparison for the WZ diboson processes: the systematic uncertainties from the PS/hadronization model is estimated taking the fit of the ratio of the different MC predictions between.

Description	Samples	Nuisance Parameters
S-T scale $p_T(V)$ -systematic on σ_{2jet} and σ_{3jet}	MCFM	VVJetScalePtST1
S-T scale $p_T(V)$ -systematic on σ_{2jet}	MCFM	VVJetScalePtST2
PDF+ α_S normalization-systematic	MCFM	VVJetPDFAlphaPt
m_{bb} shape-only systematic	Powheg+Pythia8 vs Herwig	VVMbb

Table 41: Summary of the diboson modelling systematic uncertainties, with the name of the corresponding nuisance parameter.

Not reviewed, for internal circulation only

2258 5.4 Multijet and non-collision background

2259 The reader is encouraged to read the introduction to Section 5 to better understand how the information here will be utilized. The multijet backgrounds arise from jets faking charged leptons or real E_T^{miss} .
 2260 The rate of these instrumental effects is never well modeled and they occur so rarely (but during pro-
 2261 cesses with very large cross sections) that a large amount of computing resources would be consumed.
 2262 Therefore, data driven methods are used. In the following the multijet background of each analysis is
 2263 described. Only in the 1-lepton channel is this background sizable and is therefore described last.

2265 5.4.1 0-lepton

2266 The method used to estimate the multijet background for the 0-lepton channel is described in Ap-
 2267 pendix Q. A data driven template from a dedicated control region is normalized via the ABCD method.
 2268 The contribution from the multijet background range from 0.5-2% in each region. A systematic uncer-
 2269 tainty is assessed due to statistical uncertainties and systematic effects. In the fits, a gaussian priors on the
 2270 multijet normalization is used, with an error of -95% +100% on its normalization. These priors correlate
 2271 LL, MM, TT categories for the different p_T^V regions (with the exception of the region with $100 < p_T^V < 120$
 2272 GeV), while it takes non correlated regions with different number of jets and different number of tagged
 2273 jets (i.e. 1-tag VS. 2-tag). The names used in the fit are summarised in Table 42.

Nuisance Parameter	Description	Region	Value	NP Count
0-lepton				
MJ_L0	normalization	[2,3]-jet [1/2]-tag	100%	4

Table 42: Normalization nuisance parameters for multijet entering the fit. The 0-lepton uncertainties are correlated between regions.

2274 5.4.2 2-lepton

2275 2-lepton channel multijet is described in Appendix S. Events in which the $\text{iso}_{\text{track}}$ cut for Loose leptons
 2276 (0.1) is inverted, and therefore dominated by jets faking leptons, are used to extract a template, and the
 2277 normalization is determined by extrapolating information in the m_{ll} sidebands to the phase space used by
 2278 the analysis. In the $e - \mu$ control region, the template is obtained from same-sign events. The contribution
 2279 from the multijet background is small and a systematic uncertainty of 100% is assessed. In EPS the
 2280 multijet background for the 2-lepton channel was deemed negligible. As stated in Section 3.2.1.4, the
 2281 $d_0 < 0.1 \text{ mm}$ requirement was removed from the definition of a loose electron and therefore the multijet
 2282 contribution is not longer negligible.

2283 5.4.3 1-lepton

2284 This difficult background is described in more detail in Appendix R. The template definition was refined
 2285 since EPS in concert with the Tight lepton defintion as described in Section 3.2.1.3. The method to extract
 2286 the multijet background can be divided into 3 different steps:

- 2287 • event selection for the template;
- 2288 • the usage of 1 b-tag events as the 2 b-tag template (so-called *spoofing*)
- 2289 • normalization

2290 5.4.3.1 Template Selection

2291 The multijet template is described in Section 3.2.1.5. In summary, with all event level cuts applied, data
 2292 events from an orthogonal region are selected by modifying the signal lepton criteria and the electroweak
 2293 contribution is subtracted off to create the multijet template. This region is contructed to be orthogonal
 2294 to the signal region by selecting leptons with inverted track isolation criteria and vetoing any event with
 2295 multiple leptons (counting both the normal leptons and the leptons used to obtain the multijet template
 2296 described here). The modified signal lepton selection is given here for convience:

- 2297 • Medium leptons and in the e channel, passing MediumPP
- 2298 • inverted iso_{track} cut (compared to Tight leptons): $0.05(0.07) < iso_{track} < 0.12(0.5)$ in the $e(\mu)$
 2299 channel (instead of $iso_{track} < 0.04$)
- 2300 • looser iso_{calo} cut (compared to Tight leptons): $iso_{calo} < 0.07$ (instead of 0.04).

2301 Note, for overlap removal, $0.05(0.07) < iso_{track} < 0.5$ is used in the $e(\mu)$ channel to select multijet
 2302 leptons. For counting the number of multijet leptons, the iso_{track} range is then modified to the above for
 2303 the nominal selection and again changed (noted below) for systematic variations.

2304 5.4.3.2 Generation of MV1c Weight

2305 The templates have decent statistics but after 2-tags and in the high p_T^W region, the events dry up. It
 2306 has been shown that the kinematics of 1-tag match quite well the kinematic of 2 b-tag events in the
 2307 muon channel and in 2L tag electron events. The 2T tag events are considerably different from the 1-tag
 2308 kinematics in the electron channel. A procedure was developed which, given the rank (leading or sub-
 2309 leading) of the un-tagged jet and the MV1c value of the tagged jet, a MV1c value is generated for the un-
 2310 tagged jet promoting this event into the 2-tag region. After this redistribution, in 2-jet events in the electron
 2311 channel, the 1-tag events used in the 2L, 2M, and 2T tagged template are each kinematically reweighting to
 2312 match the distribution of the 'real' 2-tag template. The reweighting is performed sequentially on $\Delta R(bb)$
 2313 and p_T^W using using a the ratio of 1-tag to 2-tag events after passing through the TH1:Smooth algorithm
 2314 five times such that the statistical fluctuations of the limited 2-tag events are not encapsulated in the
 2315 reweighting. 'Real' 2-tag events are not discarded and represent roughly 10% of the events used for the
 2316 final 2-tag multijet templates. More details of this procedure are given in Appendix R.

2317 5.4.3.3 Normalization

2318 The above template method does not determine the normalization. A fit to data is performed using the
 2319 E_T^{miss} distribution. This fit is performed separately for muon and electron events, 2 and 3 jet events, and 1
 2320 and 2 b-tag events. The 2 b-tag region is fit inclusively, that is 2L, 2M, and 2T events are all fit with one
 2321 multijet scale factor. Due to the small contribution of multijet events to the 2T region, this helps stabilize
 2322 the normalization estimate. Since the multijet normalization is coupled to the electroweak background
 2323 normalization, a scale factor for the electroweak background is also used. Also, a set of scale factors
 2324 from the profile likelihood, determined from the ratio of the post-fit yield to the pre-fit yield, are also
 2325 used to have the electroweak background as close to our best guess as possible. The E_T^{miss} variable was
 2326 found to be the most stable interms of template variations. Other variables such as m_T^W and lepton p_T
 2327 were considered. More details are given in Appendix R.

2328 5.4.3.4 Systematics

2329 To estimate the systematic uncertainty from the template choice, the iso_{track} cut is modified. In the elec-
 2330 tron channel the range $0.12 < iso_{track} < 0.50$ is used and the difference to the nominal is symmetrized

2331 to obtain a symmetric systematic variation (`SysMJE1TrkIso`). For the muon channel, the full range
 2332 used for the nominal template is divided into two ~equal statistics region $0.07 < iso_{track} < 0.095$ and
 2333 $0.095 < iso_{track} < 0.50$ which represent the down and up variations respectively (`SysMJMuTrkIso`). In
 2334 the electron channel only, it was found that restricting the iso_{calo} to 0.04 thus matching the signal region
 2335 modifies the template in a different way than the iso_{track} variations due. Therefore, this restricted region
 2336 is used and the effect is symmetrized for an additional systematic (`SysMJE1CaloIso`). One half of the
 2337 kinematic reweighting applied in the electron 2-jet 2-tag events is used as shape systematic (`SysMJDR`
 2338 and `SysMJPtV`). The normalization fit is repeated with each variation resulting in a normalization change
 2339 accompanying the shape change. It should be noted that the template variations change the heavy fla-
 2340 vor contribution, therefore altering the ratio of 2L, 2M, and 2T events. The normalization uncertainty
 2341 (`SysMJMuNorm` and `SysMJE1Norm`) is derived from two sources added in quadrature. One is the statisti-
 2342 cal error of the multijet scale factor. The normalization fit is performed inclusively in 2-tag events, but
 2343 the statistical error is take from the exclusive fits. That is the normalization in each 2L, 2M, and 2T
 2344 events separately. Even though the inclusive fit is used to determine the normalization, the statistical error
 2345 of exclusive fits are used for the systematic to reflect our imperfect knowledge of the heavy-flavor con-
 2346 tribution to the multijet template. The second, is the difference in the multijet yield when the EW scale
 2347 factors are used compared to when they are not used. More details are given in Appendix R. Table 43
 2348 summarizes the source of multijet shape and normalization errors while Table ?? explicitly states the
 2349 values of the normalization errors.

2350 Electron events with $p_T^W < 120$ GeV in the 1-lepton channel are not considered in the extraction of
 2351 the signal. Even with errors obtained for the MJ, the contribution in this region remains significant. The
 2352 change in the expected sensitivity is less than 1% and the potential for a bias is much larger. Therefore
 2353 there is little motivation to keep this problematic region.

Description	Origin	Nuissance parameters
Normalization	Norm. fit error for 1 and 2 b-tag events	<code>SysMJE1Norm</code> <code>SysMJMuNorm</code>
Template iso_{track}	Alteration of iso_{track} range	<code>SysMJE1TrkIso</code>
Template iso_{calo}	Alteration of iso_{calo} range	<code>SysMJE1CaloIso</code>
$\Delta R(bb)$ reweight for spoofed events	$\frac{1}{2}$ of reweight	<code>SysMJDR</code>
p_T^W reweight for spoofed events	$\frac{1}{2}$ of reweight	<code>SysMJPtV</code>

Table 43: Summary of the multijet specific samples used to checks the background modelling. The list of the nuissance parameters is given for reference, and it will be discussed in Section 8. Electron events with $p_T^W < 120$ GeV, even though errors were derived, are not considered in the extraction of the signal.

Not reviewed, for internal circulation only

Nuisance Parameter	Region	Value	
SysMJMuNorm	normalization	2-jet 1/2L/2M/2T-tag	12/28/42/60%
		3-jet 1/2-tag	11/14%
SysMJE1Norm	normalization	2-jet 1/2L/2M/2T-tag	3/11/14/22%
		3-jet 1/2-tag	3/6%

Table 44: Normalization nuisance parameters for multijet entering the fit. The 0-lepton uncertainties are correlated between regions. All 2-lepton uncertainties are correlated except for when the top $e-\mu$ control region is included in the standalone fit.

2354 6 Multivariate analysis

2355 Multivariate techniques become ubiquitous in HEP in recent years. There is rarely one single variable
 2356 which has the possible maximum separation between signal and background. A multivariate algorithm
 2357 can learn how to construct such a discriminant from a set of well chosen variables and well optimized
 2358 algorithm parameters. All multivariate classification methods must be trained and evaluated on separate,
 2359 independent samples to ensure an unbiased result. The training should be such that the general trends
 2360 and correlations of a sample and not the random fluctuations dictate the final algorithm. A supervised
 2361 learning method is one in which the desired output for any input in the training set is known. In general,
 2362 there is no universal recipe concerning the usage, tuning, and training of multivariate tools. Each case
 2363 must be considered in the context in which it is needed. However, techniques such as Decision Trees and
 2364 Neural Networks based techniques generally outperform likelihood-based classifiers in the presence of
 2365 strong non-linear correlations among the input variables.

2366 6.1 Input variables

2367 The object and event selection criteria are outlined in Section 3.4. The input variables chosen are de-
 2368 scribed in Table 45 and below is a list of those variables which might need further clarification:

- 2369 • V : vector boson constructed from the E_T^{miss} , vectoral sum of E_T^{miss} and p_T^ℓ , and vectoral sum of $p_T^{\ell_{1,2}}$
 2370 in the 0, 1, and 2 lepton analysis respectively.
- 2371 • H : Higgs candidate constructed from the vectoral sum of the two leading p_T jets.
- 2372 • M_{eff} : scalar sum p_T of all the objects in the event, specifically the signal jets, leptons, and E_T^{miss} .
 2373 In the 1-lepton channel only the two jets used to build the Higgs mass are considered while in
 2374 the 0-lepton channel the third jet is considered in three jet events. This is clarified by the use of
 2375 $M_{eff\ 3}$ for the later.
- 2376 • m_{jj} : dijet mass constructed from the leading two p_T signal jets.
- 2377 • m_T^W : transverse mass of the W and defined as $m_T^W = \sqrt{2p_T^\ell E_T^{\text{miss}}(1 - \cos \Delta\phi(\ell, E_T^{\text{miss}}))}$.
- 2378 • jet : signal jets are only considered.

2379 Distributions of these variables are shown in Appendix Y, Z, and AA for the 0, 1, and 2-lepton selections
 2380 respectively. Figure 32 shows the input variables for the high p_T^Z region of the 0-lepton channel. The
 2381 signal is shown in red and the background in blue. Both are normalized to the same integral as is done
 2382 in the training. Similar figures can be found in Appendix AB for all analyses.

2383 Several studies have been done to determine a good set of variables in each of the channel. As
 2384 a starting point for these studies, a simplified version of the multivariate analysis, with just m_{bb} and
 2385 ΔR_{bb} as input has been used. These two variables have been selected for the starting point thanks to
 2386 their discriminator power between signal and background. One-by-one, all the other variables have
 2387 been tested as a candidate to be the third variable in the multivariate analysis. The variable giving
 2388 the best significance was selected to join the m_{bb} and ΔR_{bb} in the bdt definition. By using the same
 2389 algorithm, the fourth, and recursively all the other variables have been studied and selected. As an
 2390 example, for the Boosted Decision Tree training parameters described in the next section, Figure 33
 2391 shows the significance for the 1-lepton 2jets, $p_T^V < 120$ GeV, 1-lepton 2jets, $p_T^V > 120$ GeV, and 0-lepton
 2392 2jets, $p_T^V > 120$ GeV for the different studied set of input variables. In 3-jet events, two more variables,
 2393 m_{jjj} and p_T^{jet3} were added to improve the 3-jet binned sensitivity by roughly 30% and the total 1-lepton
 2394 binned sensitivity by slightly less than 3%. Electron events with $p_T^W < 120$ GeV in the 1-lepton channel

Not reviewed, for internal circulation only

Variable	Name	0-Lepton	1-Lepton	2-Lepton
p_T^V	pTV		✓	✓
E_T^{miss}	MET	✓	✓	✓
$p_T^{jet_1}$	pTB1	✓	✓	✓
$p_T^{jet_2}$	pTB2	✓	✓	✓
$MV1c(jet_1)$	MV1cB1	✓	✓	✓
$MV1c(jet_2)$	MV1cB2	✓	✓	✓
m_{jj}	mBB	✓	✓	✓
$\Delta R(jet_1, jet_2)$	dRBB	✓	✓	✓
$ \Delta\eta(jet_1, jet_2) $	dEtaBB	✓		✓
$ \Delta\phi(V, H) $	dPhiVBB	✓	✓	✓
$ \Delta\eta(V, H) $	dEtaVBB			✓
$M_{eff}(M_{eff \ 3})$	HT	✓		
$\min \Delta\phi(\ell, jet) $	dPhiLBmin		✓	
m_T^W	mTW		✓	
$m_{\ell\ell}$	mLL			✓
Only in 3 Jet Events				
$p_T^{jet_3}$	pTJ3	✓	✓	✓
m_{jjj}	mBBJ	✓	✓	✓

Table 45: Variables used to train the multivariate discriminant. Additional information can be found in Section 6.1. Distributions are shown in Appendix Y, Z, and AA for the 0, 1, and 2 lepton selections respectively.

2395 are not considered in the extraction of the signal as explained in Section 5.4.3 but were considered in the
2396 optimization here.

Not reviewed, for internal circulation only

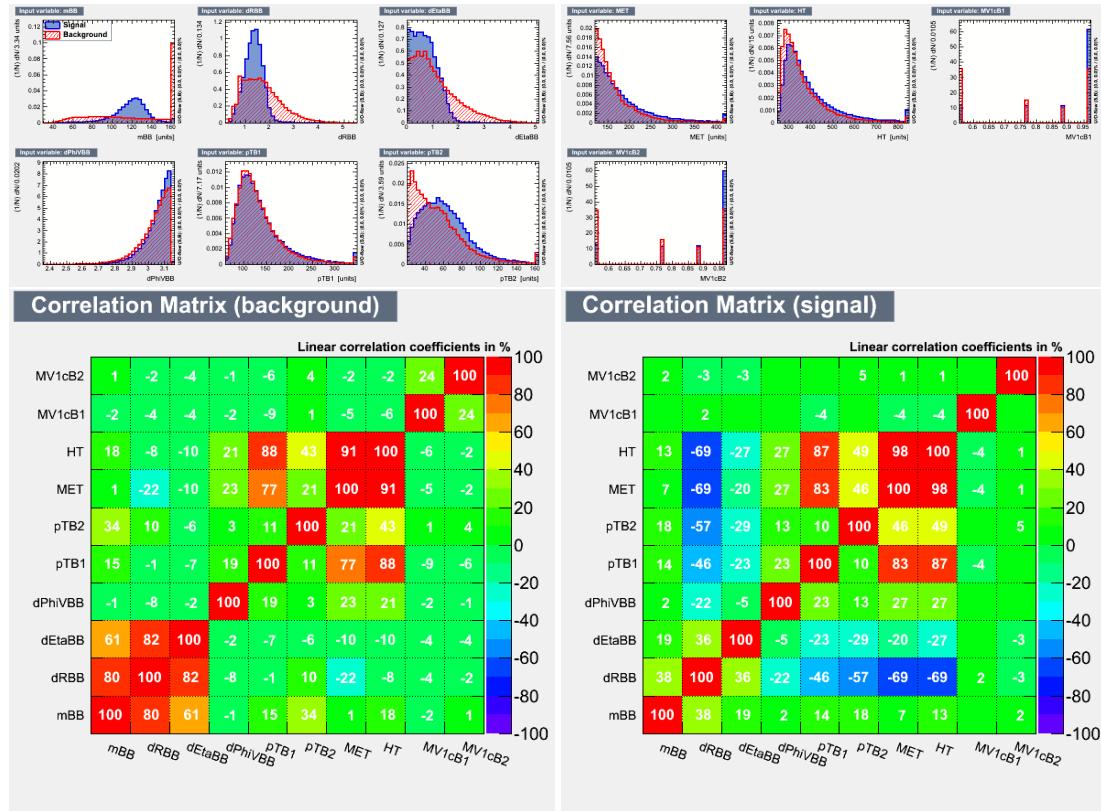


Figure 32: Input variables for the zero lepton analysis, 2 jets final state $p_T^V > 120 \text{ GeV}$ shown on the top with red representing the signal and blue the background. The bottom row shows the correlation matrix for the background and signal (left and right respectively). A complete set of such plots is contained in Appendix AB.

Not reviewed, for internal circulation only

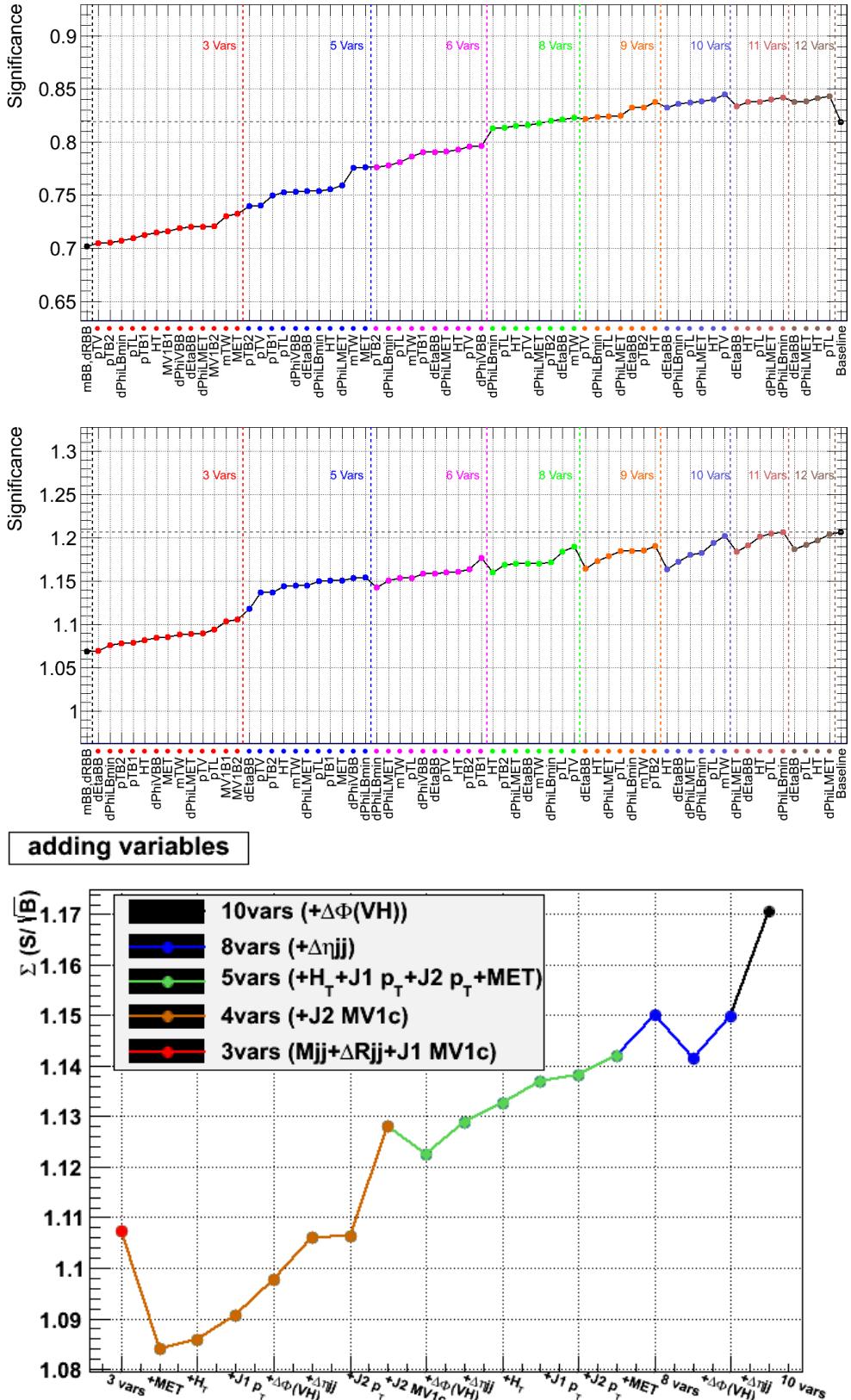


Figure 33: Significance for the 1-lepton 2 jet $p_T^V < 120$ GeV (top), 1-lepton 2 jet $p_T^V > 120$ GeV (middle), and 0-lepton 2 jet $p_T^V > 120$ GeV (bottom) as a function of the input variables using the boosted decision tree discriminant. ‘Baseline’ in the top two plots refers to the sensitivity before this optimization was done.

2397 6.2 Boosted Decision Tree: Setup and Training

2398 Among the available multivariate techniques available in the Toolkit for Multivariate Data Analysis
 2399 (TMVA) package [61], a Boosted Decision Tree (BDT) was chosen as similar performance was seen from
 2400 different techniques and BDTs are in general easy to visualize and train. To maximize the statistics in the
 2401 training, truth tagging (Section 3.3.4.1) is always applied.

2402 6.2.1 Algorithm Description

2403 A decision tree is a logical extension to a simple dijet masss analysis. It is a rooted binary tree where the
 2404 root node is the entire training sample consisting of signal (s) and background (b) events. Each variable
 2405 is scanned with a user defined number of cuts to find the cut which gives the best separation gain. Since
 2406 the range of the variable by default is determined by the minimum and maximum of the training set and
 2407 the speed of training is related to the number of cuts chosen, the range of the input variables is restricted
 2408 to 99% of the signal integrating from the mean outward. This make very little difference in the resultant
 2409 sensitivity but stabilized the final set of cuts determined by the training. The best separation gain can be
 2410 measured with various quantities but the most commonly used, and the one used in this analysis, is the
 2411 Gini-index, $p(1-p)$, where the purity, $p = s/(s+b)$. Since a cut which selects predominantly background
 2412 is as valuable as a cut which selects signal, the criterion is symmetric with respect to the event class. The
 2413 maximum, 0.5, is when the samples are fully mixed. If sum of the Gini-index of the two daughter nodes,
 2414 weighted by their relative fraction of events, is less than that of the parent then the separation of the two
 2415 populations has increased. This splitting is continued at each node, dividing the training phase space into
 2416 hypercubes, until a stop criteria is met. Examples of stop criteria are the minimum number of events per
 2417 node, maximum number of nodes, maximum depth, or when splitting the nodes further does not gain
 2418 anymore separation. The final nodes are called leaves and are labeled signal (s) or background (b) by the
 2419 purity. This method is independent of monotonous variable transformations, relatively immune against
 2420 outliers, and weakly discriminating variables do not deteriorate the performance very much.

2421 6.2.2 Boosting

2422 A single decision tree can be sensitive to statistical fluctuations in the training data. The idea of com-
 2423 bining many, or a forest of decision trees was proposed to overcome this stability problem. There are
 2424 several ways to increase the performance of a forest of DTs. A very powerful technique to improve the
 2425 performance of any weak classifier by sequentially applying an MVA algorithm to re-weighted versions of
 2426 the training data and taking a weighted average to produce the final discriminant is known as *boosting*.
 2427 The most popular boosting algorithm, and the one used in this analysis, is adaptive boosting, known in
 2428 the literature as ‘AdaBoost’. In this method, the original event weights are used for the training of the
 2429 first tree while subsequent trees are multiplied by a common boost weight give by $\alpha = 1 - \chi$ where χ
 2430 is the sum of weights of the misclassified events divided by the total sum of weights. The weights of the
 2431 entire tree are then re-normalized such that the total remains constant.

2432 Let us look at function estimation through boosting in another light, that is by considering a simple
 2433 additive expansion approach. The function under consideration is assumed to be the weighted sum of
 2434 parametrized base functions, $f(x; a_m)$, or ‘weak learners’, such as an individual decision tree or any
 2435 machine learning technique, where x represents the set of variables for the events in the tree and a_m is
 2436 the rule used to separate the signal and background populations, which would be the cut at each node for
 2437 a decision tree. The function is therefore written as the following summation:

$$F(x; P) = \sum_{m=0}^M \beta_m f(x; a_m); P \in \beta_m; a_m \in \mathcal{A}_m \quad (9)$$

2438 where β_m is some multiplicative factor. Boosting adjusts the parameters, P , such that the difference
 2439 between the response, $F(x; P)$, and the true value y is minimized. The figure of merit for this difference
 2440 is the loss-function $L(F, y)$. This function fully determines the boosting procedure. AdaBoost is based
 2441 on exponential loss, $L(F, y) = e^{F(x; P)y}$, which lacks robustness in the presence of outliers or mislabeled
 2442 data points and thus performance degrades in noisy settings. By choosing a different loss function, such
 2443 as a binomial log-likelihood,

$$L(F, y) = \ln(1 + e^{2F(x; P)y}), \quad (10)$$

2444 one can improve on this performance. Since an analytical minimization of some functions is nontrivial
 2445 the method of steepest-descent is employed. Thus the name, gradient boosting. Robustness is further
 2446 enhanced by reducing the learning rate of the algorithm, or the step size of the minimization of the loss
 2447 function. The smaller this number the slower the learning process and hence the more trees that must be
 2448 grown. Alternative lose functions were tested resulting in similar performance compared to AdaBoost.

2449 6.2.3 Overtraining

2450 Sensitivity to fluctuations in the training data is more commonly know as over-training in the forest ap-
 2451 plication. Over-training occurs when there are too few data points to properly set the model parameters;
 2452 in other words, there are too many degrees of freedom with respect to the available statistics. The severity
 2453 of this problem depends on the machine technique used. BDTs usually suffer from at least partial over-
 2454 training, owing to the large number of nodes in the constituent trees. If over-trained, the DT performance
 2455 measured in the training sample and an independent test sample will differ considerably. The training
 2456 (test) sample performance will be better (worse) than the objectively achievable performance. Therefore,
 2457 a simple way to test for and measure the amount of over-training is to compare the performance results
 2458 between the independent training and test samples. In the cases where the tree is allowed to grow beyond
 2459 a handful of nodes, pruning techniques such as removing sub-trees which in total add less improvement
 2460 than some cut-off can be employed to curb over-training. Another way to avoid over-training is to use
 2461 a large number of relatively short trees instead of using any of the pruning techniques. Figure 34 shows
 2462 an example of an overtrainig check for the 1-lepton BDT. Appendix AB contains the same check for all
 2463 BDTs trained for this analysis. In order to maximize the MC statistics available for the signal extraction
 2464 all events are used to training and evaluation in an unbiased way. The entire set of event is split into two
 2465 samples, A and B, with the BDT trained on sample A (B) evaluated by sample B (A). To be clear, an event
 2466 used to train a BDT is never used to evaluated that same BDT.

Not reviewed, for internal circulation only

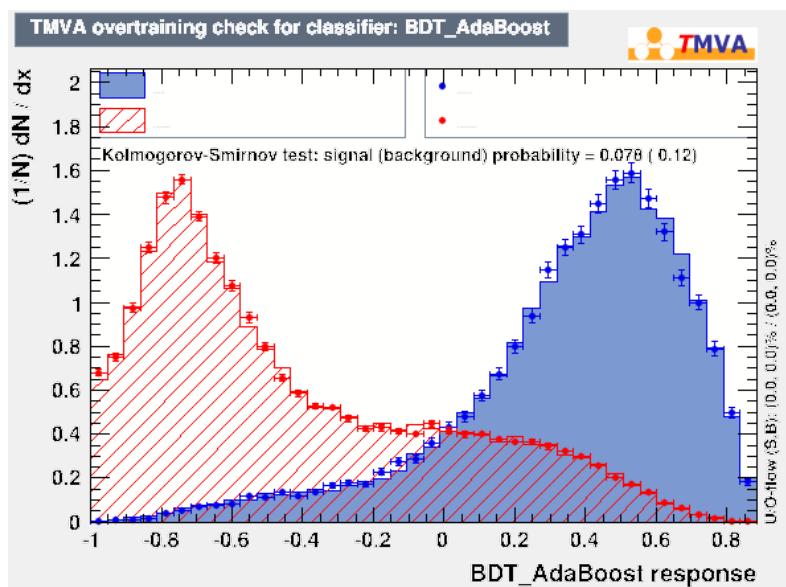


Figure 34: An example of an overtrainig check for the one-lepton analysis, 2 jets final state $p_T^V > 120$ GeV. Red represents the signal and blue the background. A complete set of such plots is contained in Appendix AB.

2467 6.2.4 Parameter Optimization

2468 BDTS in general perform well on the first iteration as this simple method only requires a one-dimensional
 2469 cut optimization. Also the performance is not degraded by the inclusion of poorly discriminating vari-
 2470 ables as they are largely ignored in favor of the most discriminating variable available at each node. In
 2471 theory, the given performance should be inferior to other techniques like neural networks but in prac-
 2472 tice, either because of a lack of training statistics or difficulty in finding the optimal configuration for
 2473 other classifiers, BDTS often outperform other techniques. A one-dimensional scan of each of the training
 2474 parameters was performed to arrive at the an optimal set of parameters given in Table 46. As an exam-
 2475 ple, the scans for the 1-lepton channel, in the 2 jet category for $p_T^V > 120$ GeV is shown in Figure 35.
 2476 These plots are obtained with a 2-step procedure. In the first one, a 350 randomly selected configura-
 2477 tions have been used to find a first optimal set of parameters. From this first optimal point, a granular
 2478 one-dimensional scan has been used to optimize the choice for each parameter.

2479 Two-dimensional scans have been produced for some of the training parameters to get a deeper
 2480 understanding of the combined effect of the two. An example is shown in Figure 35 for the 1-lepton
 2481 channel, in the 2 jet category for $p_T^V > 120$ GeV.

TMVA Setting	Value	Meaning
BoostType	AdaBoost	boost procedure
AdaBoostBeta	0.15	learning rate
SeparationType	GiniIndex	node separation gain
PruneMethod	NoPruning	pruning method
NTrees	200	number of trees
MaxDepth	4	maximum tree depth
nCuts	100	number of equally spaced cuts tested per variable per node
nEventsMin	100	minimum number of events in a node

Table 46: BDT parameters. Additional information is given in Section 6.2.

2482 Dedicated studies have been done on the capability of the BDT to explore all the features of the phase-
 2483 space with a certain MaxDepth (defined in Table 46). Figure 36, shows for two different MaxDepth
 2484 settings, the fraction of nodes using a certain variable (weighted by the boost weight of the parent tree)
 2485 as a function of the depth of the node in its parent tree. One can notice that m_{bb} is the most frequently
 2486 used variable by the BDT in the first node for both the configurations. In both cases, a good fractions of
 2487 the input variables have a non negligible frequency from the 3rd node. All variables being used equally
 2488 below a certain depth is indicative of there being limited discrimination power left in any one variable
 2489 and fluctuations start to dictate the training. With additional statistics a larger MaxDepth might explore
 2490 the phase space in a better way. It can be seen that a tree with MaxDepth of four can still use in an
 2491 efficient way the available information, while maintaining short trees in order to avoid overtraining.

Not reviewed, for internal circulation only

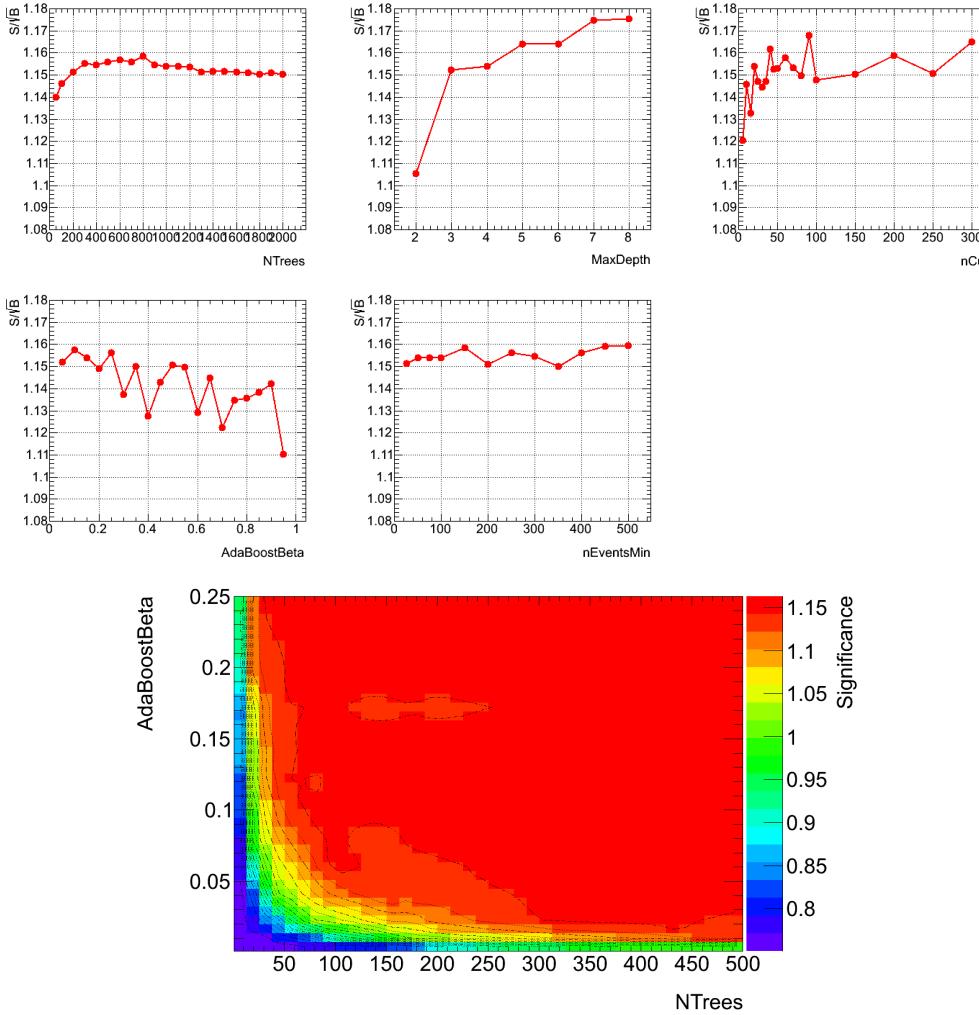


Figure 35: Top: one-dimensional scans of each of the training parameters for the 1-lepton channel, in the 2 jet category for $p_T^V > 120$ GeV. Bottom: two-dimensional plot showing the combined effect of changing the number of trees and the AdaBoostBeta on the significance.

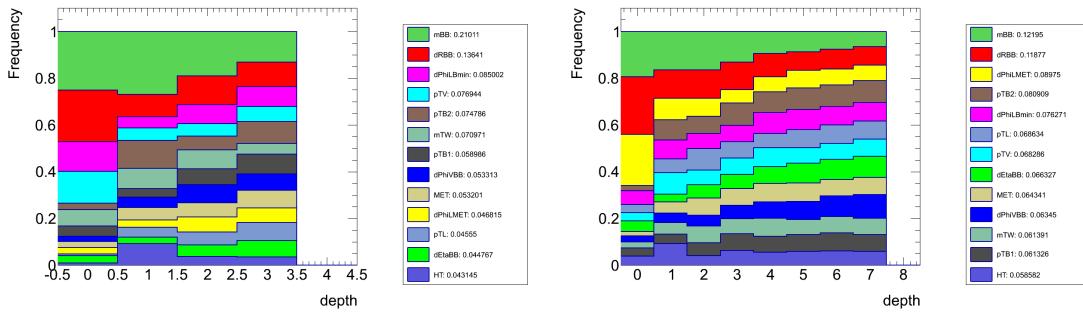


Figure 36: Fraction of nodes using a certain variable (weighted by the boost weight of the parent tree) as a function of the depth of the node in its parent tree. MaxDepth=4 (left); MaxDepth=8 (right).

2492 6.3 The correlations between input variables and output variables

2493 The construction of BDT discriminant relies on the goodness in modeling the properties of the input
 2494 variables and of their correlations. In this section, we introduce the studies done to ensure the capability
 2495 of the Monte Carlo simulation to reproduce the correlations present in data. A first way described here
 2496 is to study the 2 dimensional distribution for all the couple of input variables. For each of these 2-
 2497 dimensional distributions, 2 projections, one on the horizontal axis, and the other on the vertical axis are
 2498 done. By comparing these projections on data, and on the sum of all the background, one can check if
 2499 the Monte Carlo is able to describe some of the underlying relationship between the variables used in
 2500 the BDT. Figures 37 and 38 show one example. In this case, the 2-dimensional histograms show the
 2501 distribution of the multivariate output versus the m_{bb} distribution for the sum of all the background. The
 2502 two projections, along the two axes, are shown, and when allowed by the blinding policy, the data is
 2503 shown. In this case and in general for the other correlation plots, the data Monte Carlo agreement is
 2504 good. A complete set of plot for each lepton category has already been prepared in the past and it will be
 2505 given in a dedicated appendix.

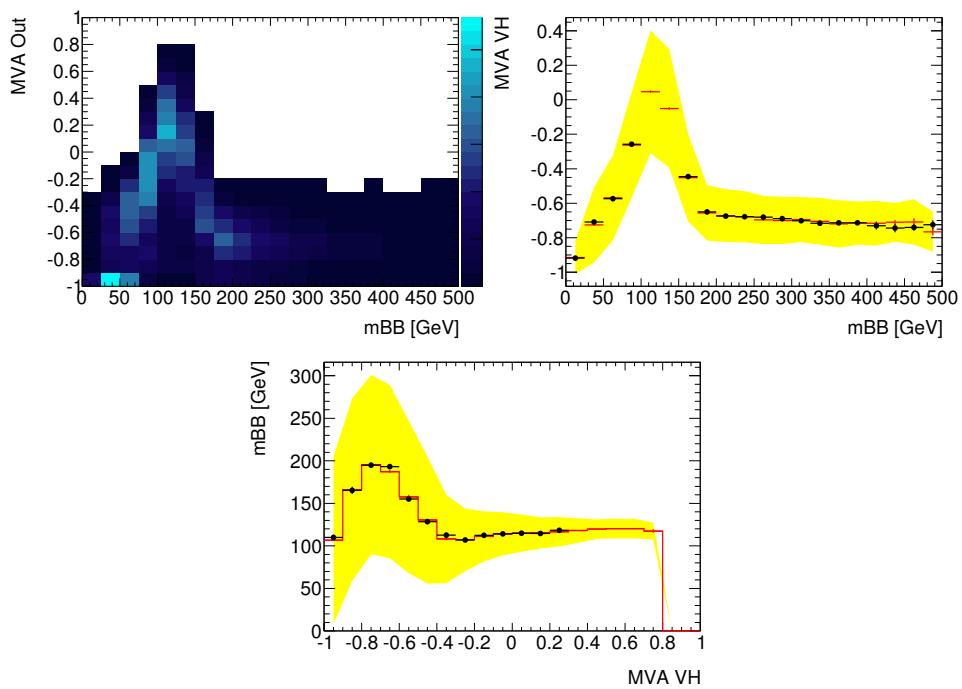


Figure 37: Two dimensional plot showing the BDT output versus the m_{bb} . The projections along the two axis shows the data - Monte Carlo comparison. Distribution for the 2-lepton analysis, for the 2 tagged 2 jet region, $p_T^V > 120$ GeV.

Not reviewed, for internal circulation only

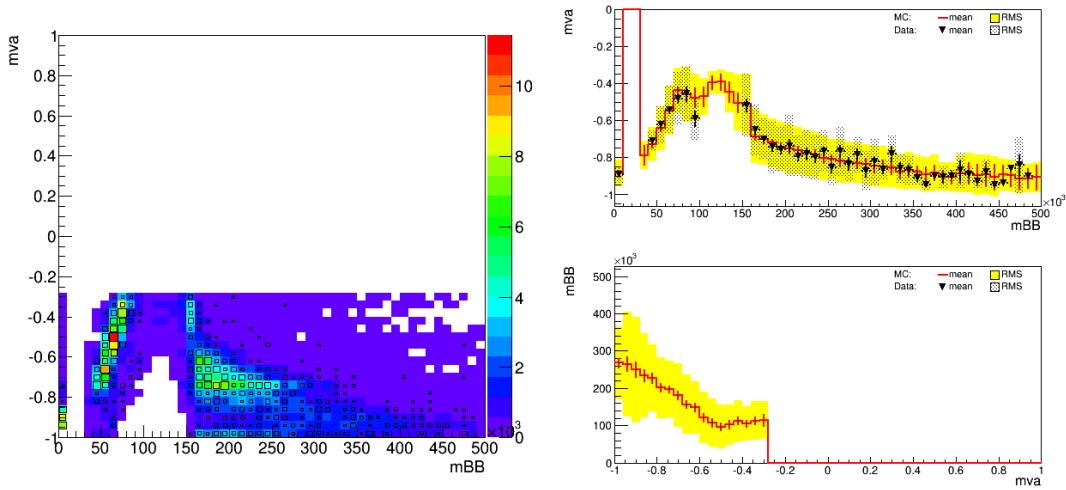


Figure 38: Two dimensional plot showing the BDT output versus the m_{bb} . The projections along the two axis shows the data - Monte Carlo comparison. Distribution for the 1-lepton analysis, for the 2 tagged 2 jet region, $p_T^V > 120$ GeV.

2506 6.4 MVA for the diboson and for the other mass points

2507 The MVA studies discussed so far has been performed for the search of a Standard Model Higgs boson
2508 with a mass of 125 GeV. This value is of particular interest, given the recent discovery at the LHC,
2509 but it is important to explore even other values for the masses. While in the m_{bb} shape analysis, this
2510 is obtained in a natural way, the MVA analysis, trained for a specific mass has less discriminating power
2511 for other masses if compared with an ad-hoc training. A first preliminary study has been done for the
2512 0-lepton channel. The result of the training for each mass hypothesis in 2 TT b-tagged jets events, with
2513 $p_T^V > 120$ GeV is shown in Figure 39. In addition, we use the diboson processes $Z \rightarrow vv + Z \rightarrow bb$,
2514 $W \rightarrow lv + Z \rightarrow bb$ and $Z \rightarrow ll + Z \rightarrow bb$ as test-bench of the analysis, so an ad-hoc training have been
2515 done for these processes (again shown in Figure 39).

2516 The use of these training, improves the expected limit for $m_h \bar{1}20$ GeV and $m_h \bar{1}30$ GeV by almost
2517 20% . So these different trainings will be used to test the search for other Higgs masses.

2518 To check if any simplification is possible, a test which uses the BDT to split the phase space in different
2519 categories, containing more and more signal events, and fitting in each category the shape of the m_{bb} have
2520 been done. It showd a degradation in the performances, not only for the other mass points, but even for
2521 the point at 125 GeV.

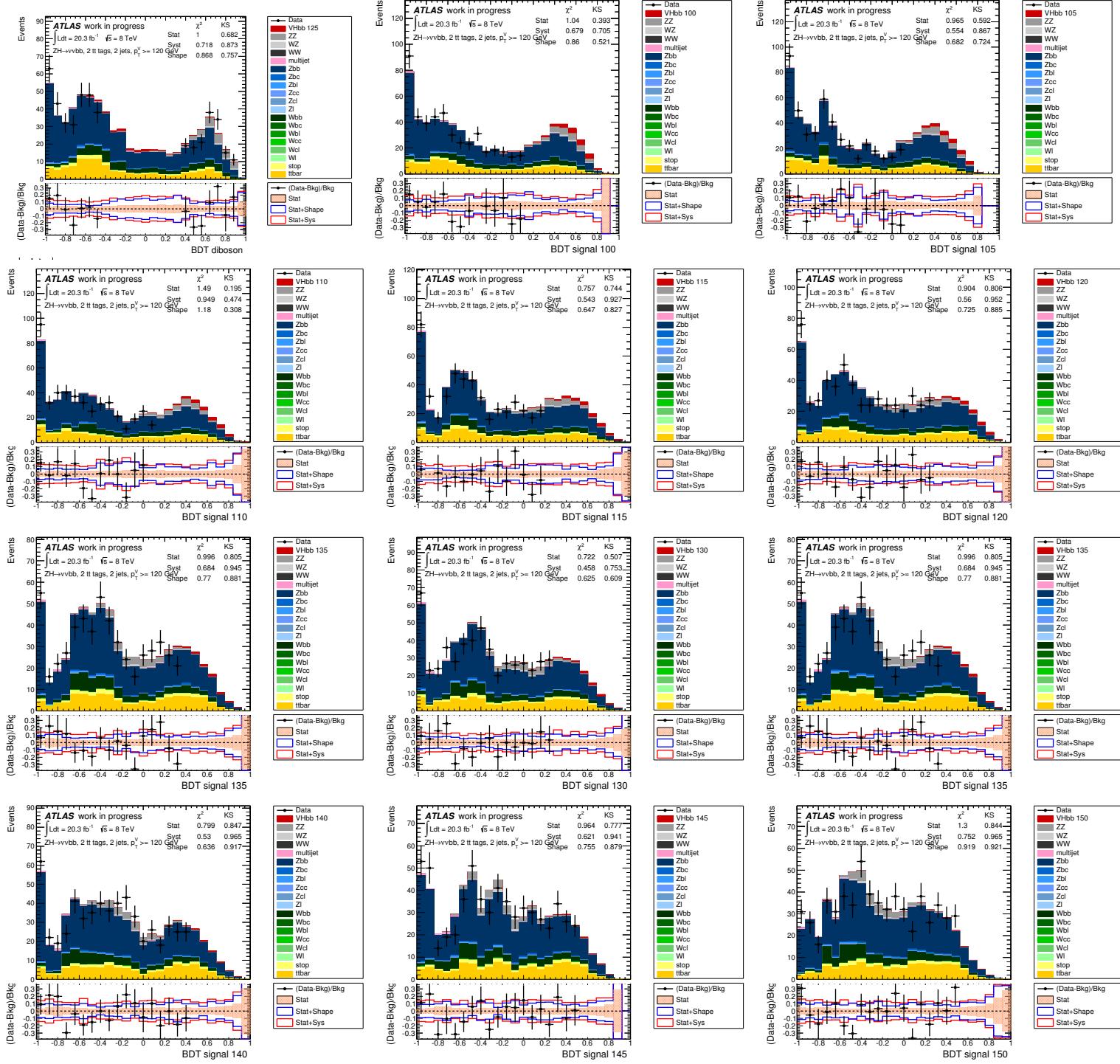


Figure 39: Distribution for the 0-lepton analysis, for the 2 tagged 2 jet region, $p_T^V > 120$ GeV.

2522 7 Experimental Systematic uncertainties

2523 In the following section the uncertainty on corrections to the efficiency and/or calibration of simulated
 2524 objects is described. The majority of these corrections have been provided by the Combined Performance
 2525 (CP) groups along with several possible configurations for how the error can be treated. The rest have
 2526 been developed as part of this analysis. An important point to keep in mind is that between low and
 2527 high p_T^V regions, light and heavy-flavor jets, and various amounts/types of E_T^{miss} , the phase space of this
 2528 analysis is tremendous. In a given corner of this phase space a certain *component* of an uncertainty
 2529 can be dominant while almost negligible in another where a different component is large. If these two
 2530 components arise from truly different sources then one must be sure to properly decorrelate before ever
 2531 attempting a profile likelihood maximization such as the one described in Section 8. Maintaining a
 2532 correlation is an overstatement of knowledge and can lead to unwanted effects such as a bias or an incorrect
 2533 assessment of precision. When such a decorrelation is done, the components of the uncertainty are briefly
 2534 described. A summary is contained in Table 55. In Section 7.2 a smoothing procedure is described which
 2535 is used to minimize the effects of limited MC statistics in the evaluation of systematic uncertainties.

2536 7.1 Experimental Systematics

2537 The leading CP uncertainties are those on the b-tagging efficiency and the jet energy scale (JES). A more
 2538 precise assessment of the impact of uncertainties can be found in Sections 8.6.4.2 and 8.6.4.1.

2539 7.1.1 Luminosity and pile up

2540 The uncertainty on the integrated luminosity is applied to the signal and backgrounds estimated from
 2541 MC simulation (all except for the multijet background). The uncertainty on the integrated luminosity is
 2542 $\pm 2.8\%$. It is derived, following the same methodology as that detailed in Ref. [12], from a preliminary
 2543 calibration of the luminosity scale derived from beam-separation scans performed in November 2012.
 2544 An uncertainty due to the modeling of the additional interactions is applied following [16].

2545 7.1.2 Electrons

2546 The electron trigger [62], reconstruction, and identification [18] efficiencies are corrected and have a
 2547 relatively small associated error $O(1\%)$. Each efficiency correction weight is shifted coherently to eval-
 2548 uate one systematic variation for the lot (`ElecEff1c`). The isolation efficiency correction is described
 2549 in Appendix E and was done in collaboration with the EGamma group (`LepIso`). Uncertainties on the
 2550 electron energy and resolution corrections [63] are evaluated separately by shifting the electron energies
 2551 up and down and re-selecting events and named `ElecE` and `ElecEResol` respectively. In the 0-lepton
 2552 channel, a systematic uncertainty needs to be evaluated for the lepton veto efficiency - this was done
 2553 using the 2-lepton selection (`LepVeto`).

2554 7.1.3 Muons

2555 The muon trigger, reconstruction, and identification [64] efficiencies are corrected and have a relatively
 2556 small associated error $O(1\%)$. Each efficiency correction weight is shifted coherently to evaluate one sys-
 2557 tematic variation for the lot (`MuonEff1c`). The isolation efficiency correction is described in Appendix F
 2558 and was done in collaboration with the Muon CP group (`LepIso`). Uncertainties on the resolution smear-
 2559 ing from the inner detector and muon system component of the muon reconstruction [64] are evaluated
 2560 separately by shifting the smearing up and down and reselecting events and named `MuonEResol1D` and
 2561 `MuonEResol1MS` respectively. In the 0-lepton channel, a systematic uncertainty needs to be evaluated for
 2562 the lepton veto efficiency - this was done using the 2-lepton selection (`LepVeto`).

2563 7.1.4 E_T^{miss} Trigger

2564 The full discussion of the E_T^{miss} trigger parametrization is in Appendix A. The uncertainties have been
 2565 reduced since [11] as further study showed a significant dependence on the scalar sum of the signal jets
 2566 $p_T(\text{JpT_Sum})$. A cut was introduced on JpT_Sum directly to remove this, which resulted in a significantly
 2567 reduced uncertainty. One nuisance parameter is used to cover differences seen in the efficiency curve fits:
 2568 METTrigZ for differences between W and Z events. The statistical uncertainty of the efficiency curve fit
 2569 is represented by METTrigStat.

2570 7.1.5 Jets

2571 The experimental uncertainties relating to jets are uncertainties on the energy scale, resolution, and the
 2572 JVF cut efficiency.

2573 7.1.5.1 The Jet Energy Scale Uncertainty

2574 A detailed discussion of the JES and associated uncertainty is found in [65] and a discussion of the
 2575 uncertainties can be found in [66]. As discussed in Section 3.2.2, the so-called GSC calibration is used.
 2576 The jet energy scale has been broken down into 56 nuisance parameters:

- 2577 • 47 for the various in-situ JES calibration analyses and are combined in an eigenvector decomposi-
 2578 tion into 6 parameters (`JetNP1-JetNP6_rest`). This does not allow for correlations between
 2579 7 TeV and 8 TeV analyses,
- 2580 • 2 for η inter-calibration, specifically comparisons of Pythia and Herwig and the statistical compo-
 2581 nent of this comparison. It arises from potential mis-modeling of the additional radiation that may
 2582 affect the p_T and η of the dijet system (`JetEtaModel` and `JetEtaStat`),
- 2583 • 1 for jets with $p_T > 1$ TeV and is ignored for obvious reasons,
- 2584 • 1 for MC non-closure relative to full simulation MC12a/Pythia8 since other MC do not satisfy
 2585 closure. The calibration was derived on MC12a and any given MC sample can be classified as
 2586 MC12a, Pythia8 or AFII (`JetNonClos`),
- 2587 • 4 for pile-up, 3 of which are μ/N_{PV} dependent and the last is dependent on the event energy
 2588 density, ρ , (`JetMu`, `JetNPV`, `JetPilePt`, `JetPileRho`),

2589 Additionally, 4 more systematics are included for flavor and topology uncertainties:

- 2590 • 1 for differences in b -jet response studying the detector response using a variety of different MC
 2591 simulations, truth b -jets only (`JetFlavB`),
- 2592 • 1 for μ and ν energies from b -hadron decay [34], truth b -jets only (`JetBE`),
- 2593 • 1 for the unknown mixture of light-quarks and gluons, non-truth b -jets only (`JetFlavComp_X`),
- 2594 • 1 for the difference in response between light-quarks and gluons assessed from MC comparisons,
 2595 non-truth b -jets only (`JetFlavResp_X`).

2596 The b -jet energy scale uncertainty is $\sim 1 - 2\%$. The flavor composition and response above are sep-
 2597 arated for different processes as the quark/gluon mixture can be different in each. X is replaced with
 2598 Wjets, Zjets, Top, or VHVV. The quark/gluon mixture (of non- b -jets) is assumed to be 50% with 100%
 2599 uncertainty thus the effect of this error is maximal. After including all sources of uncertainty, the total
 2600 fractional systematic uncertainty on the JES ranges from 3% at 20 GeV to 1% for a 1 TeV jet.

Not reviewed, for internal circulation only

2601 7.1.5.2 Jet Energy Resolution Uncertainty

2602 Two systematics are used - one for all jets and one specifically for b -jets.

- 2603 • 1 for jet resolution (`JetEResol`),
- 2604 • 1 for b -jet resolution [34], truth b -jets only (`BJetReso`).

2605 Good jet energy resolution (JER) is crucial for an analysis where the dijet mass is one of the most
 2606 discriminating variables. The range for the relative JER is from $\sim 25\%$ at 20GeV to $\sim 5\%$ near 1TeV.
 2607 The resolution is found to be well described by MC simulation when validated by in-situ analyses using
 2608 the dijet balance and bisector methods. The relative uncertainty was determined from the *observed*
 2609 *differences between data and MC* in the resolution as determined by those in-situ studies *as well as* from
 2610 uncertainties on the methods themselves. This is known to be an overestimate of the error, therefore
 2611 constraints in a profile likelihood can be expected. The impact of both JER uncertainties is obtained
 2612 in this analysis by smearing the jet p_T according to a Gaussian distribution centered at 1, with a width
 2613 equal to the true resolution plus the value of the relative uncertainty given by the jet's p_T and for the
 2614 general JER uncertainty, the η as well. The effect on the final variable is then symmetrized to obtain the
 2615 a symmetric error.

2616 7.1.5.3 Jet Fraction Uncertainty

2617 The JVF efficiency uncertainty is obtained from the differences between data and simulation in the JVF
 2618 cut efficiency in $Z+jets$ events. The cut value is nominally 0.5 and varied to 0.47 and 0.53 for the
 2619 systematic evaluation (`JetJVFSyst`).

2620 7.1.6 Missing Transverse Energy

2621 All systematic variations of object energies is propagated to the E_T^{miss} calculation which is the reasonable
 2622 thing to do. Uncertainties on E_T^{miss} itself is variations of the scale (`METScaleSoftTerms`) and resolution
 2623 (`METResoSoftTerms`) of energy in calorimeter clusters which have not been associated with a recon-
 2624 structed object - the *Soft Term*. This systematic has a large impact on the expected signal strength as
 2625 shown in Section 8.6.4.2.

2626 7.1.7 Flavor Tagging

2627 As discussed in Section 3.2.3, the MV1c discriminant is used to separate light and heavy-flavor jets.
 2628 In MC, jets are truth labeled as a b , c or *light* and scale factors have been derived for each flavor as a
 2629 function of jet p_T and MV1c output [32] to correct the MC efficiency to that of data. Representative
 2630 scale factors with the associated uncertainty are shown in Figure 3. The scale factors of course come
 2631 with an associated error. This error is a mix of experimental errors (i.e. JES), theoretical errors (i.e.
 2632 the top quark p_T spectrum in $t\bar{t}$ events), and statistical errors from the data in each $p_T \times$ MV1c ($\times \eta$ for
 2633 light jets) bin. To make this suite of errors more manageable, just as with the JES errors an eigenvector
 2634 decomposition is done only the leading 10 for b -jets, 15 for c -jets and 10 for light jets are applied in
 2635 the analysis⁵. All other nuisance parameters have been neglected and it was checked that the remaining
 2636 nuisance parameters have an impact of at most 1% on the analysis. The details of this check can be found
 2637 in Appendix T. As this analysis is very sensitive to possible p_T dependence is it crucial to take care when
 2638 correlating low and high jet p_T effects. The eigenvector decomposition. A generator dependence was

⁵ After the eigenvector method is applied, they are ordered from the one corresponding to the bigger error to the smaller one. In the analysis, the top 10/15/10 systematics for b/c /light jets are used out of 24/16/48. The remaining systematic uncertainties correspond to small components or statistical errors from $p_T(\eta)$ -MV1c binned scale factor fits.

2639 observed for the b and c jet tagging efficiencies. Scale factors (Section 3.3.4.3 and Appendix T.2) were
 2640 derived to correct each generator to the PYTHIA6 efficiency which is what the efficiency scale factors are
 2641 derived with respect to (BTagBSherpa, BTagBPythia8, BTagCShерпа, BTagCPythia8).

2642 As discussed in Section 3.3.4.1, truth-tagging is used for samples without a truth-matched b -jet and
 2643 a bias has been measured as a function of $\Delta R(\text{jet}, \text{jet})$ for events with two c -jets only. The effect was
 2644 not seen in *light-light*, nor *c-light* events and truth-tagging is not used in events with a truth-matched
 2645 b -jet. A correction has been derived and (Section 3.3.4.2 with full details given in Appendix T.3) half the
 2646 correction is taken as the uncertainty (BTagTruthTagDR).

2647 7.2 Smoothing

2648 The uncertainties on CP objects are evaluated in two different ways: shifting weights or re-selecting
 2649 events. For flavor tagging, where a scale factor is used to correct the simulation efficiency to data, this
 2650 weight is shifted up (down) and the change in the final distribution is noted as the $+1$ (-1) σ shift. For jet
 2651 energy scale (JES) uncertainties, the jet energies are shifted and therefore events can migrate in and out
 2652 of the acceptance. Again the difference in the final variable is noted as the 1σ error but if the variations
 2653 are small and/or the sample statistics are small, the 1σ band can be contaminated with the MC statistical
 2654 uncertainty. If one has multiple JES errors, which we do, then this MC error should not be included in
 2655 each one. To mitigate these effects, two algorithms are used to merge consecutive bins in these templates.
 2656 First, bins from one extremum to the next are merged until no (at most one) local extremum remains in
 2657 the multivariate (dijet-mass) analysis. If there are more than two extrema, merging is performed at each
 2658 step of this iterative process where the difference between merged and unmerged templates is smallest.
 2659 Second, the bins resulting from this first algorithm are sequentially merged, starting from the upper end
 2660 of the distribution, until the statistical uncertainty in each of the merged bins, calculated in the nominal
 2661 template, is smaller than 5%.

2662 In the 1-tag regions, it does not make sense to merge neighboring bins as described in Section 7.2
 2663 since the MV1c distribution is discrete. Therefore in this region, only a pruning is performed which
 2664 drops one-sided systematics in a given MV1c bin.

Not reviewed, for internal circulation only

2665 8 Statistical model and Systematic Uncertainties

2666 The culmination of this analysis is a complex profile likelihood in which our knowledge is parametrized
 2667 and tested against the data. This is not simple business since the likelihood is defined in over 100
 2668 constrained dimensions and up to 9 free dimensions. The following gives a basic introduction to the
 2669 procedure followed by a detailed description of the likelihood itself.

2670 8.1 Likelihood Definition: Variables and Regions

2671 The statistical analysis of the data employs a binned likelihood function constructed as the product of
 2672 Poisson probability terms,

$$\text{Pois}(n|\mu S + B) \left[\prod_{b \in \text{bins}}^N \frac{\mu v_b^{sig} + v_b^{bkg}}{\mu S + B} \right], \quad (11)$$

2673 where μ , a signal strength parameter, multiplies the expected signal yield v^{sig} in each histogram bin,
 2674 b , and v^{bkg} represents the background content per bin. In this analysis the signal is normalized to the
 2675 Standard Model Higgs boson production cross section so any deviation in the measured μ value is a
 2676 deviation from the SM. The dependence of the signal and background predictions on the systematic
 2677 uncertainties is described by a set of nuisance parameters (NP), θ , which are parametrized by Gaussian
 2678 or log-normal priors. Log-normal priors are used for normalization uncertainties to maintain a positive
 2679 PDF. The parametrization is chosen such that the rates in each category are log-normally distributed for
 2680 a normally distributed θ . The expected number of signal and background events in each bin are functions
 2681 of θ such that the total number of events for a given process is

$$v_{tot}^p = \sum_{b \in \text{bins}}^N f_b^p(\theta) \quad (12)$$

2682 where p is either the signal or background processes and f_b^p is the number of events in the b^{th} bin as a
 2683 function of θ . Most NP have been determined from some other dataset and so it not completely unknown.
 2684 To enforce this knowledge, a so called penalty term or auxiliary measurement is added to the likelihood
 2685 which will always increase when any nuisance parameter is shifted from the nominal value of zero.
 2686 Formally the auxiliary measurement is added to the likelihood in a way that emphasises the fact that this
 2687 NP comes from a measurement in a different dataset:

$$\text{Pois}(m|B_{CR}) \quad (13)$$

2688 where m and B_{CR} are the measured and expected number of events used to determine the nominal value.
 2689 Some NPs, such as floating normalizations do not have priors and are completely determined from the
 2690 analysis dataset. The likelihood function is therefore a function of μ and θ and given by

$$\mathcal{L}(\mu, \theta) = \text{Pois}(n|\mu S(\theta) + B(\theta)) \left[\prod_{b \in \text{bins}}^N \frac{\mu v(\theta)_b^{sig} + v(\theta)_b^{bkg}}{\mu S(\theta) + B(\theta)} \right] \text{Pois}(m|B_{CR}) \quad (14)$$

2691 The nominal fit result in terms of μ and σ_μ is obtained by maximizing the likelihood function with respect
 2692 to all parameters. This is referred to as the maximized log-likelihood value MLL. The test statistic q_μ is
 2693 then constructed according to the profile likelihood:

$$q_\mu = 2\ln(\mathcal{L}(\mu, \hat{\theta}_\mu)/\mathcal{L}(\hat{\mu}, \hat{\theta})), \quad (15)$$

2694 where $\hat{\mu}$ and $\hat{\theta}$ are the parameters that maximize the likelihood (with the constraint $0 \leq \hat{\mu} \leq \mu$), and $\hat{\theta}_\mu$
 2695 are the nuisance parameter values that maximize the likelihood for a given μ . This test statistic is used

2696 to measure the compatibility of the background only model with the observed data and for exclusion
 2697 intervals derived with the CL_s method [67, 68].

2698 The likelihood function is build based on the expected distributions of either the di- b -jet invariant
 2699 mass of the two signal jets (in the dijet mass analysis) or of the multi-variate discriminant (BDT) (in
 2700 the MVA analysis). These variables are used in events with at least 2 b -tagged jets. In both dijet mass
 2701 and MVA analyses, the 2-tag regions are further subdivided into three flavor categories, LL, MM and
 2702 TT, as defined in Sec. 3.3.4. In addition, in order to further control the flavor fractions of the $W/Z+\text{jet}$
 2703 backgrounds, the MV1c distribution of the tagged jet is used in the 1-tag region. The regions entering
 2704 the fit are summarized in Table 47.

		dijet mass			MVA		
Channel		0 lepton	1 lepton	2 lepton	0 lepton	1 lepton	2 lepton
1-tag	2-jet	MV1c			MV1c		
	3-jet	MV1c			MV1c		
2L-tag	2-jet	m_{bb}			BDT		
		m_{bb}			BDT	BDT	BDT
		m_{bb}					
2L-tag	3-jet	m_{bb}			BDT		
		m_{bb}			BDT	BDT	BDT
		m_{bb}					

Table 47: The regions entering the likelihood fit for the cut based and MVA analysis and the distributions used. Vertically merged rows should be interpreted as regions treated with one distribution. For example, 2M and 2L are combined for 0-lepton MVA analysis. In the 1-lepton analysis, electron events with $p_T^W < 120$ GeV are not included.

2705 The regions described are further subdivided in p_T^V bins. The dijet mass 2-tag regions are subdivided
 2706 into five p_T^V bins

$$2707 p_T^V: [0-90), [90-120), [120-160), [160-200), \text{ and } [200,\infty) \text{ GeV}$$

2708 while the MVA analysis uses the two p_T^V bins

$$2709 p_T^V: [0-120) \text{ and } [120,\infty) \text{ GeV}$$

2710 also detailed in Table 12. For the 1-tag region, in both versions, the two MVA p_T^V bins are used. NOTE: for
 2711 the 1-lepton $p_T^W < 120$ GeV, only the muon channel have been used. Studies have shown that using two
 2712 p_T^V bins in the 1-tag improves the expected sensitivity by 2% compared to not using the 1-tag region at
 2713 all. The choice of two p_T^V bins differs from the 2-tag region of the dijet mass analysis. It would be quite
 2714 aggressive to have the MV1c distribution so finely binned in p_T^V and would require very careful modeling
 2715 systematics. This would give access to the jet p_T spectrums which the flavor tagging scale factors are
 2716 parameterized as a function of. A minimal choice of two bins was used in order to have some access to
 2717 the p_T^V spectrum but not to re-fit the scale factors themselves.

2718 In the 0-lepton analysis the low p_T^V region of the phase space is not accessible due to the high thresh-
 2719 old of the E_T^{miss} trigger. However, in the dijet mass analysis, a 100 – 120 GeV region has been taken
 2720 into account, adding a region in which the trigger turn-on curve is well-modeled, as described in Ap-
 2721 pendix C. In the 1-lepton channel no distinction is made between events triggered by the lepton triggers
 2722 and by the E_T^{miss} trigger, which is used to recover muon events outside the muon trigger acceptance, as
 2723 described in Appendix C.4. The multijet (MJ) background in the 1-lepton channel is concentrated at low

2724 p_T^W , and ranges in the 2-jet 2-tag sample with $p_T^W < 120$ GeV from 11% of the total background in the
 2725 LL category to 6% in the TT category. The main purpose of including the $p_T^W < 120$ GeV intervals is to
 2726 provide constraints on the largest backgrounds ($V+jets$ and $t\bar{t}$) in the global fit. Since the MJ background
 2727 is twice larger for $p_T^W < 120$ GeV in the 1-electron sub-channel than in the 1-muon sub-channel, only
 2728 the 1-muon sub-channel is kept for $p_T^W < 120$ GeV so as to provide the most reliable constraints on the
 2729 non-MJ backgrounds. The resulting loss in sensitivity is 0.6%. For $p_T^W > 120$ GeV, the MJ background
 2730 is much smaller: for 2-jet events, 4% and 2% in the LL and TT categories, respectively.

2731 In the fit the dijet mass low-MET 0-lepton region (with p_T^V from 100-120 GeV) is also added to the
 2732 MVA analysis. Therefore the total number of regions for the MVA analysis is 30, while for the dijet
 2733 mass analysis the total number of regions is 80. When the 2-lepton channel is considered standalone
 2734 for validation purposes, the $e - \mu$ region obtained selecting opposite sign and different flavour leptons is
 2735 added as an additional control region in the fit to constrain the $t\bar{t}$ background normalization. This control
 2736 region is not included in the combined fit, since the $t\bar{t}$ contribution is already well constrained in the
 2737 1-lepton regions for the dijet mass analysis and in the 2-lepton low BDT region in the MVA analysis.

2738 8.2 Likelihood Philosophy

2739 This likelihood is the manifestation of the knowledge accrued by the analysis team. Correlations of
 2740 NPs across regions is a statement of knowledge - the effect which that particular NP represents has the
 2741 same source in both regions and therefore a change in one regions dictates the *same* change (in terms
 2742 of number of sigma) in the other. Priors represent a degree of belief as to where the true value lies for
 2743 parameters which the model is dependent on. Care must be taken as this analysis covers a tremendous
 2744 phase space with several different SM processes having yields larger than the expected signal.

2745 One might ask why so many regions are included in the likelihood. Part of the reason is that the
 2746 flavor fractions ($bb-bc-bl-cc-cl-l\bar{l}$ relative rates) of the $V+jet$ events cannot be trusted from simulation.
 2747 Therefore the 1-tag is considered. Removing the 1-tag events in the MVA analysis decreases the sensitivity
 2748 4% as allows for degeneracies in the shapes of the various flavor productions. The 3-jet region in the 1
 2749 and 0-lepton analyses is top-enriched (more so for the 1-lepton) and therefore is needed to constrain the
 2750 top normalization in a region of phase space that is the odd 1-lepton, 2-tagged jet signal enriched region
 2751 (Table 28). The signal in the 3-jet region is not negligible. The 3-jet 2-lepton region is very pure in $Z+hf$
 2752 and provides a better constraint on the $Z+hf$ production. Using only 2-jet events (discarding 3-jet events)
 2753 decreases the MVA sensitivity 8% with up to a 14% loss seen in the 2-lepton channel. The low p_T^V regions
 2754 are used to get a handle on the modeling. As discussed in the previous sections (Section 5.1 and 5.2),
 2755 the boost of top-pairs and vector bosons is not well modeled by the MC. One can either remove the low
 2756 p_T^V and let the data in the high p_T^V fix the overall normalizations or fix the normalization at low p_T^V and
 2757 propagate that to high p_T^V very carefully. The later approach is the one chosen here. It is not the easier
 2758 of the two, but the potentially more informative and fruitful one. On top of that, it is the more sensitive
 2759 since removing events with $p_T^V < 120$ GeV decreases the sensitivity 10%. Once the fit has moved to a
 2760 point of stability, the exact impact of each of the above claims can be quantified.

2761 In the construction of such a large and powerful likelihood model, choices have to be made consist-
 2762 ently and carefully. For $V+jets$ and $t\bar{t}$ the data holds a significant amount of information. In this case we
 2763 try to minimize the prior knowledge assumed as to not cause an unwanted bias if the knowledge assumed
 2764 is incorrect. This can come at the price of a larger uncertainty. To be more concrete, a hypothetical
 2765 situation: Consider a comparison of two generators for $W+jets$ systematics. In this comparison it is
 2766 noted that both p_T^W and the ratio of $W+bb$ to $W+cc$ to $W+bl$ (flavor fractions) are different. Both effects
 2767 can be correlated in one NP. In the dijet mass analysis, with 5 p_T^W bins, the data contains a lot of clear
 2768 information of the shape of the p_T^W spectrum and can fix this NP. Through the correlation *assumed* of the
 2769 change in p_T^W and the flavor fractions, this now means that the flavor fractions are known to the same
 2770 degree as the p_T^W spectrum – a very aggressive statement. Building on the hypothetical, now consider the

addition of MV1c distributions in 1-tag events giving direct access to the flavor fractions. The same NP above which correlated p_T^W and flavor fraction changes can now be pulled/constrained from the flavor fraction point of view. The correlation derived from the difference between the two generators needs to match exactly the difference between the nominal MC and nature in order to have a ‘corret’ pull. If the correlation is not correct, unrelated NPs can be pulled to recover any data-MC differences and potentially cause knock-on effects such as biases.

By having separate NPs for p_T^W and flavor fractions, we allow the data to determine each independently. This is a conservative statement of knowledge. For processes such as single-top and dibosons, where less information is available in data, we chose to correlate more of the differences between generators. Conflicting information from the data is less likely to occur and the total number of NPs should be maintained at a reasonable level. The expected impact on μ is checked for each NP (Section 8.6). If one of these smaller sample NPs ranks high on the list, then the assumptions are reconsidered before proceeding.

8.3 Systematics Uncertainties and Nuisance Parameters

As stated above, nuisance parameters are used to build a model as a function of information which is not completely known. This is interpreted as systematic and statistical uncertainties in high-energy physics. There are two different types of nuisance parameters used: floating parameters and parameters with priors. A floating normalization is generally associated with the cross section and acceptance where absolute ignorance of the rate is assumed and completely determined from data. When a prior is used, the statement is that the parameter is not known completely nor it is completely unknown but there is a reasonable range within which the true value is believed to lie. The following contains a summary of the 105 constrained modeling nuisance parameters, 8 floating normalization (including μ), as well as the 80 nuisance parameters representing the imperfect knowledge of experimental effects (192 parameters in total).

8.3.1 Naming Conventions

In the following, several formulae illustrate how the nuisance parameters are used to calculate the total number of events which should help the reader build a more clear picture of the complex PDF used in the profile likelihood maximization. Nuisance parameters and changes from them are represented in three ways:

- 2800 1. ϕ are unconstrained normalization factors
- 2801 2. $\eta(\alpha)$ represents relative changes in the overall normalization as function of the nuisance parameters, α
- 2803 3. $\sigma(\alpha)$ parametrizes uncertainties in the shape of the distribution of the discriminating variable as 2804 function of the nuisance parameters, α

2805 θ , defined above, represents the set of nuisance parameters and α represents the configuration of these 2806 parameters. For example, the nominal expectation is given by all $\alpha = 0$ and a $+1\sigma$ pull for nuisance 2807 parameter i is represented by $\alpha_i = 1$.

2808 Nuisance parameters with the same name are correlated. Therefore, to decorrelate NPs across regions 2809 or channels a short string is added to the name which represents where that NP acts. These short strings 2810 are as follows:

- 2811 • Lepton Multiplicity: LX with X=0, 1, 2
- 2812 • Jet Multiplicity: JX with X=2, 3

- 2813 • p_T^V region (bin): BX with X=0, 1, 2, 3, 4 or X=0, 2 for the MVA p_T^V binning
 2814 • b -tagging bin: TTypeX with X=' ', 1L, 2L, 2M, 2T, and 2M+2T
 2815 b -tag regions

2816 In the following section, other NP specific naming conventions are described where appropriate. In the
 2817 tables below, the regions listed are the regions where the NP is applied and decorrelated. For example
 2818 ‘all regions’ means the NP is applied and correlated everywhere while ‘2/3 jet, 1/2 tag’ means the NP
 2819 is decorrelated between 2 and 3 jets as well as between 1 and 2-tags. In pull and correlation plots, one
 2820 should see the basename listed in the table and the appropriate string listed above when applicable.

2821 8.3.2 Signal Specific Nuisance Parameters

2822 Table 48 lists the complete set of nuisance parameters specific to the signal which are described in
 2823 Section 4.1. The uncertainties have been separately parametrized for the $qq \rightarrow WH$, $qq \rightarrow ZH$ and
 2824 $gg \rightarrow ZH$ processes. The theory uncertainties on the recently calculated $gg \rightarrow ZH$ are significantly
 2825 larger because it is only calculated at leading order. The nuisance parameters are fully correlated in all
 2826 regions of phase-space. $qq \rightarrow VH$ (denoted with qqVH) and $gg \rightarrow ZH$ (denoted with ggZH) specific
 2827 errors are never correlated. TheoryBRbb is only applied when this analysis is combined with analyses
 2828 which include Higgs decays besides $H \rightarrow bb$.

Nuisance Parameter	Description	qqWH	qqZH	ggZH	NP Count	Section
μ	ratio to SM cross section		float		1	–
TheoryQCDscale	Scale Uncertainty	1%	1%	50%	2	4.2.1
TheoryBRbb	Branching Ratio	3.3%	3.3%	3.3%	1	
TheoryVHPt	NLO EW Correction	S	S	–	1	4.1.2
TheoryAcc_J2	Inclusive Acceptance	3.0%	3.4%	1.5%	2	
TheoryAcc_J3	Scale Acc. 3-jet rel. 2-jet	-1.1%	-0.9%	-1.9%	2	4.2.2
	Scale Acc. 3-jet rel. 3-jet	4.1%	3.5%	3.3%		
TheoryAccPDF	PDF Acc. 2-jet	3.5%	3.0%	2.1%	2	4.2.2
	PDF Acc. 3-jet	2.8%	5.0%	3.4%		
TheoryAcc_PS	PS, had and UE Acceptance	7% - 13% in different p_T^V and N_{jets}			1	4.2.2
	QCD Scale	S	S	S	2	
TheoryPDF	PDF Sets	2.4%	2.4%	17%	2	
Total		15 with priors, 1 floating				

Table 48: The nuisance parameters used to parametrize the signal-specific systematics. All signal systematics are correlated throughout all phase space regions. All are de-correlated between the $qq \rightarrow VH$ (qqVH) and $gg \rightarrow ZH$ (ggZH) processes except for the TheoryBRbb, which is fully correlated. S=“Shape” and SO=“Shape Only” meaning explicitly the normalization of each N-jet/M-b-tag/ p_T^V region is preserved while the shape is varied.

2829 The nuisance parameters used to parametrize our ignorance of each background are listed in Table 50
 2830 for the $W+jets$ background, Table 49 for the $Z+jets$ background, Table 51 for the $t\bar{t}$ background, Table 52
 2831 for the single-top background, Table 53 for the diboson background, and Table 54 for the multijet back-
 2832 grounds.

Not reviewed, for internal circulation only

2833 8.3.3 $V+jets$ Specific Nuisance Parameters

2834 Table 49 contains the summary of $Z+jets$ specific nuisance parameters. Due to the different diagrams con-
 2835 tributing to $Z+jets$ production compared to that of the W and because of the controllable $t\bar{t}$ background,
 2836 both $Z+light$ and $Z+heavy-flavor$ modeling checks can be done from data-MC studies. Section 5.1.1
 2837 discusses the main results of these studies.

2838 Table 50 contains the summary of $W+jets$ specific nuisance parameters. Section 5.1.2 contains a
 2839 discussion of $W+jets$ focusing on data-MC comparisons which is the main probe into the $W+l1$ and
 2840 $W+c1$ modeling. The $W+heavy-flavor$ systematics, which are from generator comparisons, are discussed
 2841 in Section 5.1.2.3.

2842 It is illustrative to show how the total number of Z and W events are parametrized in terms of nuisance
 2843 parameters. In the following the convention outlined in Section 8.3.1 is maintained. With V representing
 2844 either Z or W , the total number of events is given by

$$N_V = N_{Vl} + N_{Vcl} + N_{Vhf} \quad (16)$$

$$N_{Vl} = \eta(\alpha_{VlNorm})(N_{Vl}^{2Jet} + \eta(\alpha_{VlNorm_J3})N_{Vl}^{3Jet}) \quad (17)$$

$$N_{Vcl} = \phi_{Vcl}(N_{Vcl}^{2Jet} + \eta(\alpha_{VclNorm_J3})N_{Vcl}^{3Jet}) \quad (18)$$

$$N_{Vhf} = \phi_{Vbb}(N_{Vhf}^{2Jet} + \eta(\alpha_{VbbNorm_J3})N_{Vhf}^{3Jet}) \quad (19)$$

2845 where

$$N_{Vhf}^{iJet} = N_{Vbb}^{iJet} + \eta(\alpha_{VblVbbRatio})N_{Vbl}^{iJet} + \eta(\alpha_{VbbVbcRatio})N_{Vbc}^{iJet} \quad (20)$$

2846 with $iJet$ equal to $2Jet$ or $3Jet$.

Nuisance Parameter	Description	Correlation/Samples	Value	NP Count	Section
Z1Norm	Z1 normalization	all regions	5%	1	
Z1Norm_J3	Z1 3/2-jet ratio	3Jet regions	5%	1	
norm_Zcl	Zcl norm	all regions	Float	1	
ZclNorm_J3	Zcl 3/2-jet ratio	3Jet regions	26%	1	
norm_Zbb	Zhf normalization	all regions	Float	1	
ZbbNorm_J3	Zhf 3/2-jet ratio	3Jet regions	20%	1	
ZblZbbRatio	ZblZ/bb ratio	2, 3Jets	12%	2	
ZblZbcRatio	ZbcZ/bb ratio	all regions	12%	1	
ZccZbbRatio	Zcc/Zbb ratio	all regions	12%	1	
ZDPsi	$\Delta\phi$ shape	Z+b/c, Z1 \times 2, 3Jets	S	4	5.1.1.2
ZPtV	p_T^V shape	Z+b/c, Z1 each in all regions	S	2	5.1.1.2
ZMbb	m_{bb} shape	Z+b/c, Z1 each in all regions	SO	2	5.1.1.3
Total		16 with priors, 2 floating			

Table 49: The nuisance parameters used in the fit to parametrize the normalization of the $Z+jets$ back-
 grounds and the correlation of these parameters between regions. $Zhf = Zbb + Zcc + Zbl$, $Z+b/c = all Z+jets$
 besides $Z+l1$, S=“Shape”, and SO=“Shape Only” meaning explicitly the normalization of each N -jet/ M -
 b -tag/ p_T^V region is preserved while the shape is varied. Further details are given in Section 5.1.1.

2847 8.3.4 $t\bar{t}$ Specific Nuisance Parameters

2848 Table 51 contains the summary of the $t\bar{t}$ specific nuisance parameters. Section 5.2.1 contains a dis-
 2849 cussion of the $t\bar{t}$ modeling followed by the method used to determine most of modeling systematics in

Nuisance Parameter	Description	Correlation/Samples	Value	Count	Section
WlNorm	Wl normalization	all regions	10%	1	
WlNorm_J3	Wl 3/2-jet ratio	3Jet regions	10%	1	
norm_Wcl	Wcl normalization	all regions	Float	1	5.1.2
WclNorm_J3	Wcl 3/2-jet ratio	3Jet regions	10%	1	
norm_Wbb	Whf normalization	all regions	Float	1	
WbbNorm_J3	Whf 3/2-jet ratio	3Jet regions	10%	1	
WblWbbRatio	Wbl/Wbb ratio	$p_T^V = [0-90], [90-120], 120 + \text{GeV}^d$ agger	35%	3	5.1.2.3
WbcWbbRatio	Wbc/Wbb ratio	all regions	12%	1	
WccWbbRatio	Wcc/Wbb ratio	all regions	12%	1	
WDPhi	$\Delta\phi$ shape	Whf, Wcl, Wl \times 2, 3Jets	S	6	5.1.2
WMbb	m_{bb} shape	$Wbb/cc (p_T^V = [0-90], [90-120], 120 + \text{GeV})^\dagger$ Wbc/bl, Wcl, Wl each in all regions	SO	6	
WPtV	p_T^V shape	Whf in 2-jet, 3jets regions	S	2	
Total		23 with priors, 2 floating			

Not reviewed, for internal circulation only

Table 50: The nuisance parameters used in the fit to parametrize the normalization of the W+jets backgrounds and the correlation of these parameters between regions. Whf = Wbb+Wcc+Wbl, S=“Shape”, and SO=“Shape Only” meaning explicitly the normalization of each N-jet/M-b-tag/ p_T^V region is preserved while the shape is varied. Further details are given in Section [5.1.2](#). [†]In the mva analysis the $90 < p_T^V < 120$ GeV NP only pertains to the 0-lepton channel $100 < p_T^Z < 120$ GeV events.

2850 [Section 5.2.1.3](#).

2851 It is illustrative to show how the total number of $t\bar{t}$ events is parametrized in terms of nuisance
 2852 parameters. In the following the convention outlined in Section [8.3.1](#) is maintained. The total number of
 2853 $t\bar{t}$ events is given by

$$N_{t\bar{t}} = \phi_{t\bar{t}} \left(N_{t\bar{t}}^{2Jet} + \eta(\alpha_{ttbarNorm_J3}) N_{t\bar{t}}^{3Jet} \right) \quad (21)$$

2854 where

$$N_{t\bar{t}}^{iJet} = \left(N_{t\bar{t}}^{lowp_T^V} + \eta(\alpha_{ttbarHighPtV}) N_{t\bar{t}}^{highp_T^V} \right)^{iJet} \quad (22)$$

2855 with $iJet$ equal to 2Jet or 3Jet.

Nuisance Parameter	Description	Correlation	Value	NP Count	Section
norm_ttbar	$t\bar{t}$ normalization	3 lepton selections	Float	3	
ttbarHighPtV	high/low p_T^V	$p_T^V > 120$ GeV	7.5%	1	5.2.1.3
ttbarNorm_J3	3/2-jet ratio	3-jet in 2,0+1 lepton	20%	2	
TopPt	top p_T corr. variation	all regions	S	1	5.2.1.2
TtbarMBBCont	m_{bb} shape	all regions	SO	1	
TtbarMetCont	E_T^{miss} shape	all 1-leptons regions	1	S	
Total		6 with priors, 3 floating			

Table 51: The nuisance parameters used in the fit to parametrize the systematics on the $t\bar{t}$ background. S=“Shape” and SO=“Shape Only” meaning explicitly the normalization of each N-jet/M-b-tag/ p_T^V region is preserved while the shape is varied.

Not reviewed, for internal circulation only

2856 8.3.5 Single Top Specific Nuisance Parameters

2857 Table 52 contains the summary of the single top specific nuisance parameters. Section 5.2.2 contains
 2858 a discussion of the single top modeling systematics. Since it is fairly difficult to get a solid control
 2859 region for any of the three single top production channels, this analysis relies, for better or worse, on
 2860 MC comparisons. The suite of comparisons contains the list of samples recommended by the single top
 2861 working group.

Nuisance Parameter	Description	2-jet		3-jet		Section
		low p_T^V	high p_T^V	low p_T^V	high p_T^V	
s-channel						
stopsNorm	cross section			4%		
SChanAcerMC	AcerMC vs Powheg+Pythia	13%	22%	18%	30%	5.2.2
SChanAcerMCPS	shower uncertainty	6%	8%	4%	4%	
t-channel						
stoptNorm	cross section			4%		
TChanPtB2	aMCatNLO vs. AcerMC	52%	25%	12%	-18%	5.2.2
Wt channel						
stopWtNorm	cross section			7%		
WtChanAcerMC	AcerMC vs Powheg+Pythia	1%	S/-2%	S/4%	S/-15%	5.2.2
WtChanPythiaHerwig	Shower uncertainty	S/5%	3%	5%	-3%	
Total	8 with priors, 0 floating					

Table 52: The nuisance parameters used in the fit to parametrize the systematics on the single top background. All NP are correlated across the full phase-space. The value represents the normalization change in the given region for the given NP while S=“Shape” is used to note regions where a shape variation exists. Low p_T^V is below 120 GeV and high is above this value.

2862 8.3.6 Diboson Specific Nuisance Parameters

2863 Table 53 contains the summary of the diboson specific nuisance parameters. Section 5.3.1 contains a
 2864 discussion of the diboson modeling systematics. Since it is fairly difficult to get a solid control region
 2865 for any of the three diboson production channels with hadronic decays and far enough from the analysis
 2866 selection to get a control region from the fully leptonic decays, this analysis relies, for better or worse,
 2867 on MC comparisons and theoretical calculations. Section 5.3.1 contains the most important information.

2868 8.3.7 Multijet Specific Nuisance Parameters

2869 The following is a summary of the multijet nuisance parameters. A brief description of the multijet
 2870 backgrounds is given in Section 5.4 and more in-depth information is available in Appendix Q, R, and S
 2871 for 0, 1, and 2-lepton respectively.

2872 8.3.8 Experimental Nuisance Parameters

2873 The nuisance parameters used to describe the experimental uncertainties are summarized in Table 55 and
 2874 described in more detail in Section 7.

Not reviewed, for internal circulation only

Nuisance Parameter	Description	Correlation	WW	WZ	ZZ	Section
VVJetScalePtST1	Scale		S	S	S	
VVJetScalePtST2	Scale		S	S	S	
VVJetPDFAlphaPt	PDF, α_S 2-jet PDF, α_S 3-jet	all regions	2% 3%	2% 4%	3% 3%	5.3.1
VVMbb_WW	m_{bb} shape		SO	–	–	
VVMbb_WZ	m_{bb} shape		–	SO	–	
VVMbb_ZZ	m_{bb} shape		–	–	SO	
Total	6 with priors, 0 floating					

Table 53: The nuisance parameters used in the fit to parametrize the systematics on the diboson backgrounds. For **VVJetPDFAlphaPt**, the two values represent the normalization change in 2/3Jet region respectively. S=“Shape”, and SO=“Shape Only” meaning explicitly the normalization of each N-jet/M- b -tag/ p_T^V region is preserved while the shape is varied.

Nuisance Parameter	Description	Region	Value	NP Count	Section
0-lepton					
MJ_L0	normalization	2,3-jet 1/2-tag >,< 120 GeV	100%	6	5.4
1-lepton					
SysMJMuNorm	normalization	2-jet 1/2L/2M/2T-tag 3-jet 1/2-tag	12/28/42/60% 11/14%	4 2	5.4
SysMJE1Norm	normalization	2-jet 1/2L/2M/2T-tag 3-jet 1/2-tag	3/11/14/22% 4/6%	4 2	5.4
SysMJMuTrkIso	template iso_{track} cut	2/3-jet 1/2-tag	S	4	5.4
SysMJE1TrkIso	template iso_{track} cut	2/3-jet 1/2-tag	S	4	5.4
SysMJE1CaloIso	template iso_{calo} cut	2-jet 1/2-tag	S	2	5.4
SysMJDR	reweight for spoofed events	(ele) 2-jet 2-tag	S	1	5.4
SysMJPtV	reweight for spoofed events	(ele) 2-jet 2-tag	S	1	5.4
2-lepton					
MJ_L2	normalization	top e- μ decorrelated [†]	100%	1	5.4
Total	31 with priors, 0 floating				

Table 54: Normalization nuisance parameters for multijet entering the fit. The 0-lepton uncertainties are correlated between regions. [†]All 2-lepton uncertainties are correlated except for when the top $e - \mu$ control region is included in the 2-lepton standalone fit.

Nuisance Parameter	Description	NP Count	Section
Luminosity (2)			
Lumi	error on total integrated error	1	
MuScale	error of profile	1	7.1.1
Leptons (8)			
ElecEffic	trigger, reco., and id. efficiencies	1	
ElecE	energy scale	1	7.1.2
ElecEResol	energy resolution	1	
MuonEffic	trigger, reco., and id. efficiencies	1	
MuonEResolID	energy resolution from inner detector	1	7.1.3
MuonEResolMS	energy resolution from muon system	1	
LepIso	isolation scale factors	1	App. E,F
LepVeto	lepton veto efficiency in 0-lepton selection	1	7.1.2, 7.1.3
E_T^{miss} Trigger (2)			
METTrigZ	W efficiency curve versus Z curve	1	
METTrigStat	statistical uncertainty of efficiency curve fit	1	7.1.4
Jet Energy Scale (23)			
JetNPX	eigenvector decomposition of in-situ calibration ($X = 1\text{-}6\text{rest}$)	6	
JetEtaModel	η inter-calibration model	1	
JetEtaStat	statistical error of η inter-calibration	1	
JetNonClos	calibration non-closure	1	
JetMu	μ correction based on average number of pile-up interactions	1	
JetNPV	uncertainty due to N_{PV} correction	1	
JetPilePt	pile-up in jet area correction	1	
JetPileRho	pile-up in jet area correction	1	
JetFlavB [†]	b -jet energy scale	1	
JetBE [†]	b -jet scale for μ and ν energy	1	
JetFlavComp_X [‡]	knowledge of light quark vs gluon fraction	4	
JetFlavResp_X [‡]	different response of light quarks vs gluon jets	4	
Jet Energy Resolution (2)			
JetEResol	resolution applied to all jets	1	
BJetReso [†]	b -jet specific resolution	1	7.1.5.2
Jet Quality (1)			
JetJVF	jet vertex fraction efficiency	1	7.1.5.3
$E_T^{\text{miss}}(2)$			
METResoSoftTerms	resolution of soft component	1	
METScaleSoftTerms	scale of soft component	1	7.1.6
Flavor Tagging (40)			
BTagBNEffic	b -jet uncertainty in 10 eigenvector ($N = 0 - 9$)	10	
BTagCNEffic	c -jet uncertainty in 15 eigenvector ($N = 0 - 14$)	15	7.1.7
BTagLNEffic	light-jet uncertainty in 10 eigenvector ($N = 0 - 9$)	10	
BTagTruthTagDR	correction to $\Delta R(cc)$ bias from truth-tagging	1	3.3.4.2
BTagBSherpa		1	
BTagCSherpa		1	
BTagBPythia8	generator dependent heavy flavor tagging efficiecy	1	3.3.4.3
BTagCPythia8		1	
Total	80 with priors, 0 floating		

Not reviewed, for internal circulation only

Table 55: A summary of the names and meaning of systematics from the combined performance tools and other experimental systematics as well as the associated nuisance parameter names. For flavor composition and response systematics, $X=W\text{jets}, Z\text{jets}, \text{Top}, \text{VHVV}$.

[†] Applied only to truth-matched b -jets.

[‡] Applied only to non-truth-matched b -jets.

2875 8.4 Output Transform

2876 The original BDT distribution is put into a 1000 bin histogram, while the m_{bb} distribution in the dijet masss
 2877 analysis has 500 bins in the range 0-500 GeV. In both the cases, an algorithm to reduce the number of
 2878 bins is needed.

2879 Since the BDT is a classification algorithm which maximizes the separation of two populations, for
 2880 measuring the signal strength, the optimal performance is not necessarily achieved by the default output
 2881 distribution from TMVA. Furthermore the value of the output distribution itself is essentially meaningless
 2882 so a remapping of the default MVA output is a reasonable approach to maximizing the analysis potential.

2883 A simple rebin of the m_{bb} distribution of the m_{bb} shape analysis was used in all previous versions. In
 2884 order to reduce statistical uncertainties in the tails of the dijet mass, wider bins were needed. However
 2885 this reduces the sensitivity in the signal rich region. A natural conclusion is a variable size binning. To
 2886 optimize the signal strength while giving stability to the fit, an improved variable size binning has been
 2887 developed for the distributions entering in the statistical model (for both the m_{bb} shape and the multivariate
 2888 analysis). A technical note: RooStats cannot handle variable size bins so the output distribution in
 2889 both cases is mapped to a constant-bin-width histogram. In the case of the m_{bb} this needs to be mapped
 2890 back to a physically meaningful representation while for the BDT, this is not necessary.

2891 The two figures-of-merit used to optimize the binning are the final expected sensitivity, and the
 2892 reduction of number of bins. As an example, the total number of bins in the dijet masss analysis, if
 2893 the m_{bb} distribution has a fixed bins width of 20 GeV (in the range 10 GeV < m_{bb} < 250 GeV), is
 2894 almost 1000, and the fits would need to handle all of them, all the errors (including statistical) and the
 2895 correlations across them.

2896 8.4.1 General description

2897 To remap the histograms entering in the final fit, we define a function:

$$Z(I[k, l]) = Z(z_s, n_s(I[k, l]), N_s, z_b, n_b(I[k, l]), N_b) \quad (23)$$

2898 where

- 2899 • $I[k, l]$ is an interval of the histograms containing the bins between the bin k and the bin l ;
- 2900 • N_s is the total number of signal events in the histogram;
- 2901 • N_b is the total number of background events in the histogram;
- 2902 • $n_s(I[k, l])$ is the total number of signal events in the interval $I[k, l]$;
- 2903 • $n_b(I[k, l])$ is the total number of background events in the interval $I[k, l]$;
- 2904 • z_s and z_b are parameters used to tune the algorithm.

2905 Different possible Z functions have been tested. In the following sections, 2 different algorithms will
 2906 be described: the transformation D and the transformation F⁶.

- 2907 • **Transformation D** This transformation uses a Z equal to:

$$Z = z_s n_s / N_s + z_b n_b / N_b \quad (24)$$

2908 where z_s and z_b are parameters, which can be used to optimize the strategy.

⁶NOTE: we keep here the names used in when the studies were performed to keep track of the name convention.

- 2909 • **Transformation F** This transformation uses a Z equal to:

$$llr_s = \sum_{i \text{ in interval}} s_i \times \log(1 + s_i/b_i) \quad (25)$$

$$Z = \sqrt{z_b n_b / N_b} + \sqrt{z_s llr_s} \quad (26)$$

(27)

2910 where s_i and b_i are the number of signal and background events in the bin i , and z_s, z_b are parameters
 2911 which can be used to optimize the strategy.. In addition to the condition on Z , the interval in
 2912 the general algorithms are requested to satisfy the condition:

$$\sigma_b < 0.10 \quad (28)$$

2913 where σ_b is the relative statistical uncertainty on the background.

2914 While the transformation D was historically used for both the multivariate analysis (see App. AC)
 2915 and the m_{bb} shape analysis, the transformation F resulted recently in performing better than the D in the
 2916 multivariate analysis, becoming the default transformation for this analysis.

2917 Both the transformation B and the transformation F share the following steps:

- 2918 • Starting from the last bin on the right of the original histogram, increase the range of the interval
 2919 $I(k, last)$ by adding one after the other, the bins from the right to the left;
- 2920 • Calculate the value of Z at each step;
- 2921 • Once $Z(I[k_0, last]) > 1$ (let's say for the interval from the bin k_0 to the bin $last$), remap all the bins
 2922 in the interval $I(k_0, last)$ into a single bin;
- 2923 • Repeat these last 3 points, starting this time from the last bin on the right, not included in the
 2924 previous remap (the new $last$ is $k_0 - 1$).

2925 8.4.1.1 MVA Optimization and Transformation F

2926 The optimization for the mva analysis has been evaluated by looking at the dependence of the expected
 2927 limit and the number of bins as a function of z_s and z_b (see Figure 40). The selected working point is z_s
 2928 = z_b = 4.5. This reduce the number of bins by 53

2929 The optimization for the MVA analysis has been evaluated by looking at the dependence of the ex-
 2930 pected limit and the number of bins as a function of z_s and z_b (see Figure 40). The selected working point
 2931 is $z_s = z_b = 4.5$. This reduce the number of bins by 53% and therefore increase the stability of the fit
 2932 significantly compared to a binning which maps the original 1000 bins to 20 bins of equal size. These
 2933 choice of parameters reduces the number of bins by 17% with no change in the expected significance
 2934 compared to transformation D described in Appendix AC.

2935 As an example, one of the MVA distributions, before and after the transform can be seen in Figure 41.

2936 8.4.1.2 m_{bb} shape optimization and the transformation D

2937 For the dijet masss analysis, the optimization has the advantage of increasing the number of bins where
 2938 signal is expected while avoiding the proliferation of bins in background only regions. The optimized
 2939 binning for the cut based has been evaluated individually for each lepton channel, resulting in the param-
 2940 eters in Table 56.

2941 The new setup, if compared with the 20 GeV bins in m_{bb} used for EPS reduces the numbers of bins by
 2942 almost 45% and improves the final results by 2% in the total expected sensitivity. As an example, one of
 2943 the m_{bb} distribution, before and after the transform can be seen in Figure 42.

Cut based :lepton region	2-jets	3 -jets
0 leptons	$z_s = 6, z_b = 2$	$z_s = 4, z_b = 2$
1 leptons	$z_s = 6, z_b = 2$	$z_s = 4, z_b = 2$
2 leptons	$z_s = 4, z_b = 4$	$z_s = 2, z_b = 2$

Table 56: Binning optimization for the cut based analysis

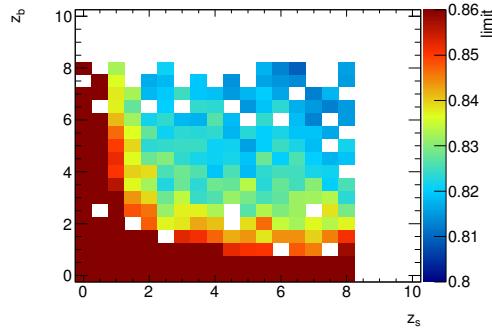
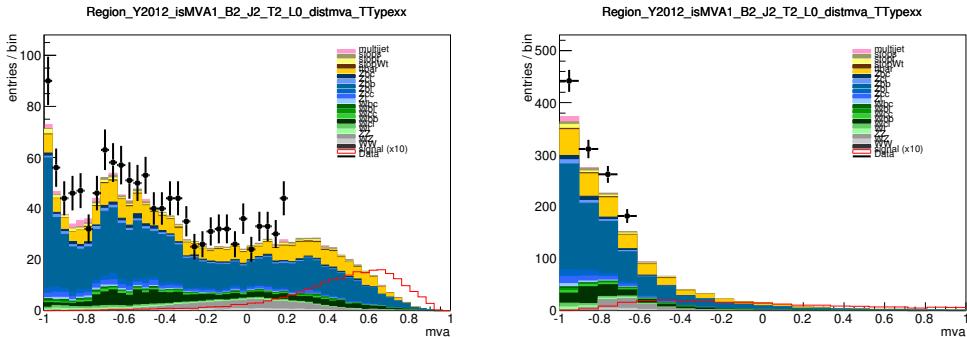
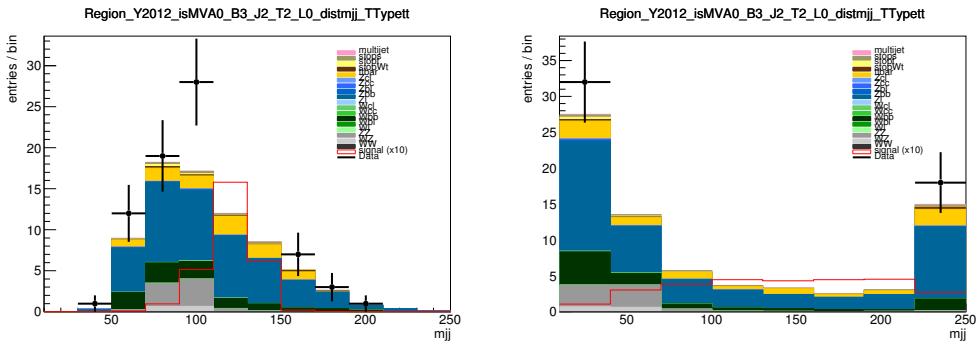
Figure 40: 2D Expected limit as a function of the z_s and z_b parameters.

Figure 41: Example of the effect of the binning transform F on the mvaoutput for one of the signal regions. Left: before the binning transform; Right: After the binning Transform.

Figure 42: Example of the effect of the binning transform on the m_{bb} output for one of the signal regions. Left: before the binning transform; Right: After the binning Transform. NOTE: The labels on the horizontal axis shown in the plot after the transformation are not anymore meaningful but will be in future versions.

2944 8.5 Pruning of the Systematic Uncertainties

2945 Limited statistics in the MC nominal distributions can produce systematic templates with large fluctuations,
 2946 introducing noise in the fit. Therefore, the uncertainties are treated according to the following
 2947 procedure which has an additional step compared to EPS [11] and is carried out for each process in each
 2948 region after the final distribution is manipulated according to the procedures discussed in Section 8.4:

- 2949 • reduce statistical fluctuations by the smoothing procedure described in Section 7.2 only to those
 2950 systematic which require a re-sampling of the events (i.e. JES and not b -tagging)
- 2951 • neglect the normalization uncertainty if for a given sample in a region either is true:
 - 2952 – the variation is less than 0.5%
 - 2953 – both up and down variations have the same sign
- 2954 • neglect the shape uncertainty if for a given sample in a given region either is true:
 - 2955 – not one single bin has a deviation over 0.5% after the overall normalization is removed
 - 2956 – if only up or the down variation is non-zero and passed the previous pruning steps
- 2957 • neglect the shape and normalization uncertainty for a given sample in a given region if the sample
 2958 is less than 2% of the total background (new since EPS):
 - 2959 – if the signal < 2% of the total background in all bins
 if shape and normalization error are each < 0.5% of the total background
 - 2960 – if at least one bin has a signal contribution > 2% of the total background
 in those bins if the shape and normalization error are each < 2% of the signal yield

2963 The additional step developed after EPS was tuned to ensure the expected p_0 and $\hat{\mu}$ along with its associ-
 2964 ated error do not change more than 2% using the EPS workspaces.

2965 The above procedure removed the following systematics completely from the MVA Higgs fit:

- 2966 • METTrigZ
- 2967 • METTrigStat
- 2968 • LepIso

2969 In checking the sizes of the remaining NPs, the following were found to be on very few background and
 2970 showed evidence of statistical fluctuations so were subsequently removed ‘by hand’ for all analyses:

- 2971 • JetNP5
- 2972 • MuonEResolMS
- 2973 • MuonEResolID
- 2974 • ElecEResol
- 2975 • MuScale

2976 Therefore the total number of parameters in the likelihood is 184 (183 for conditional fits).

2977 For those nuisance parameters remaining after applying this procedure, the normalization uncertainty
2978 is taken into account with a log-normal prior and the shape uncertainty with Gaussian prior. Usually the
2979 $\pm 1\sigma$ ($\alpha_i = \pm 1$) and the nominal ($\alpha_i = 0$) are known. When the likelihood is constructed, a PDF is cre-
2980 ated defined from $\alpha_i = \pm 5$ is needed. To do this an extrapolation is needed from the known points out to
2981 $\alpha_i = \pm 5$ and an interpolation between the know points as well which should guarantee the PDF is contin-
2982 uous and smooth everywhere (especially if the error is asymmetric). For shape uncertainties a piecewise
2983 exponential extrapolation and a 6th order polynomial interpolation are used while a quadratic interpola-
2984 tion and linear extrapolation are used for normalization uncertainties. This is the default configuration in
2985 RooStats.

2986 8.6 Understanding the Likelihood

2987 The likelihood can be maximized with respect to the observed data or pseudo data derived from the
2988 nominal MC expectation or any variation by created an Asimov data set. When fitting to the nominal
2989 MC expectation, the pulls constrained NPs should all remain at 0 and floating normalizations at 1. The
2990 post-fit error represents the expected post-fit uncertainty on a given parameter. The post-fit error can be
2991 compared to fits to data to check if the constraints from data match the expectation given the size of the
2992 error, the samples, and the region(s) on which it acts. Unless otherwise stated, when Asimov data is
2993 mentioned it is built from the nominal expectation.

2994 An important tool to understand the important NPs is the so called NP ranking which evaluates the
2995 impact of each NP on the expected or measured signal strength. This is discussed in Section 8.6.4 and
2996 shown in Section 8.6.4.1 and 8.6.4.2 for the dijet and MVA analysis respectively.

2997 8.6.1 Dijet Mass Analysis Fit Studies

2998 The pull plots for combined fit for the dijet masss analysis are shown in Figures 43-48. Each plot
2999 compares the result from a fit to either the Asimov data set (red) or to the observed data (black) on the
3000 left, and the result of the fit for each individual lepton channel on the right. The individual channel results
3001 are shown in Appendix AH.1.

Not reviewed, for internal circulation only

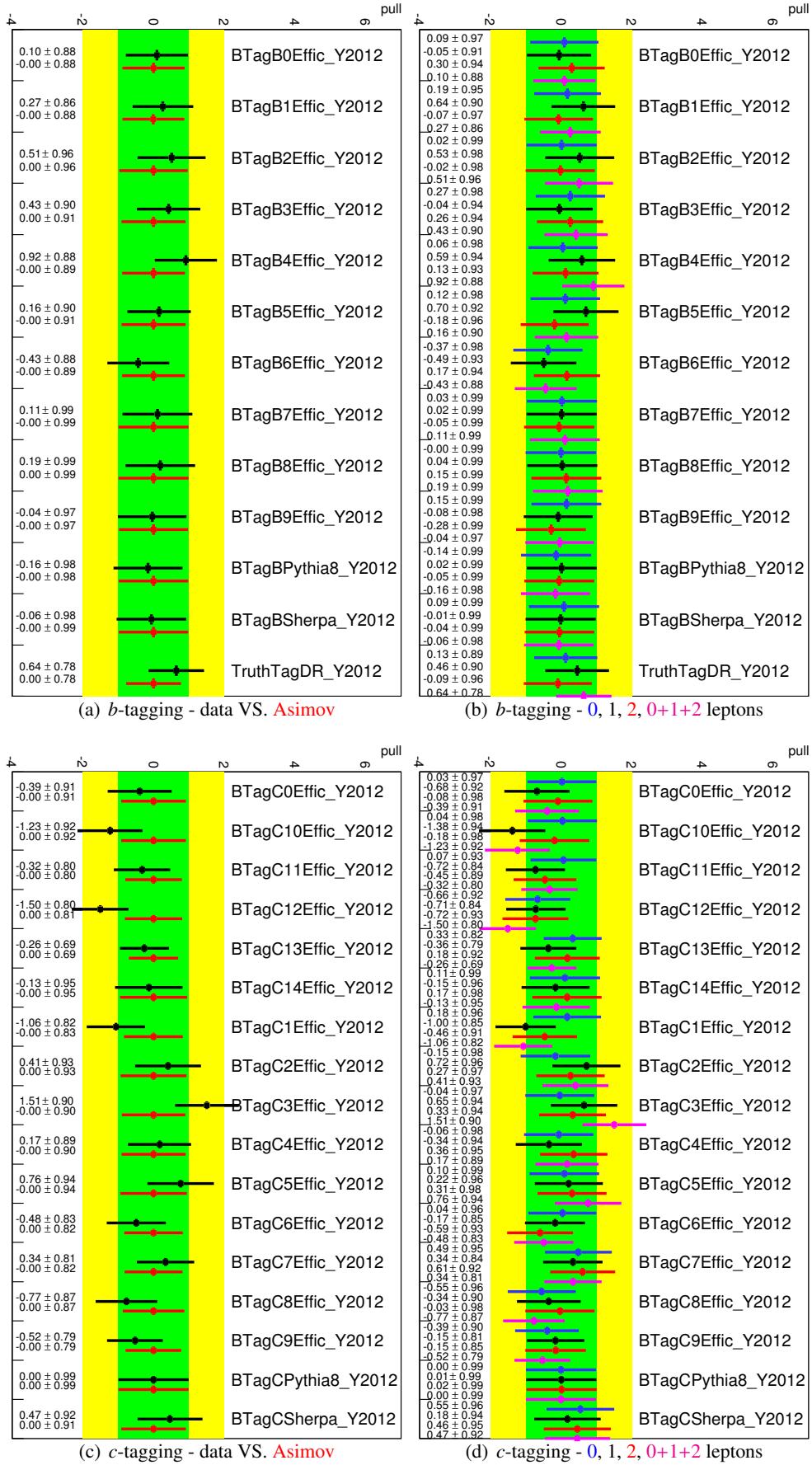


Figure 43: Pull plots for *b* and *c* tagging in the 0+1+2 lepton m_{bb} shape fit. The fit to the Asimov data set is shown in red and the fit to the data in black on the left. The fits to 0 lepton (blue), 1 lepton (black) and 2 leptons (red) data and the combined fit to data (magenta) is shown on the right.

Not reviewed, for internal circulation only

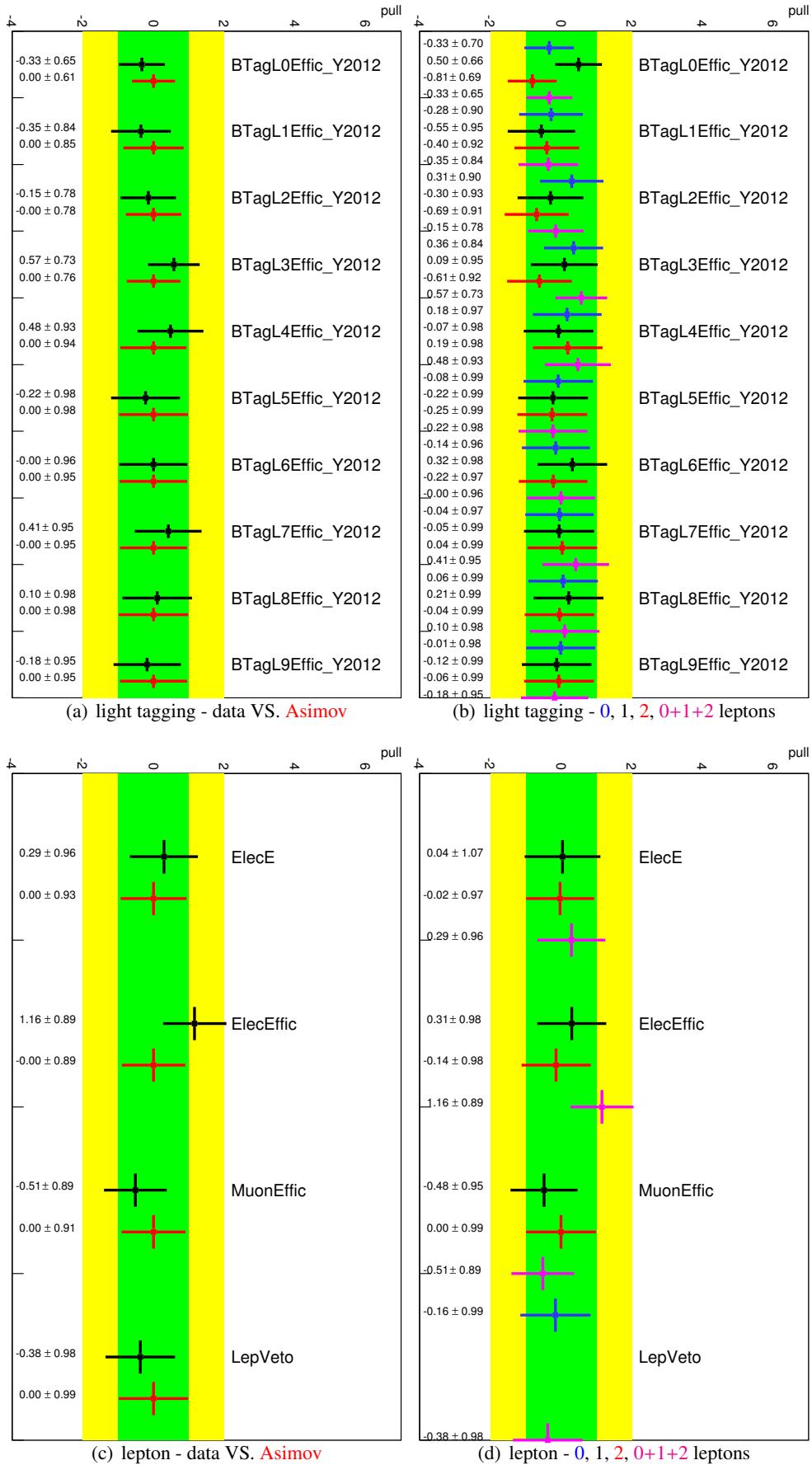


Figure 44: Pull plots for light-jet tagging and lepton related systematics in the 0+1+2 lepton m_{bb} shape fit. The fit to the Asimov data set is shown in red and the fit to the data in black on the left. The fits to 0 lepton (blue), 1 lepton (black) and 2 leptons (red) data and the combined fit to data (magenta) is shown on the right.

Not reviewed, for internal circulation only

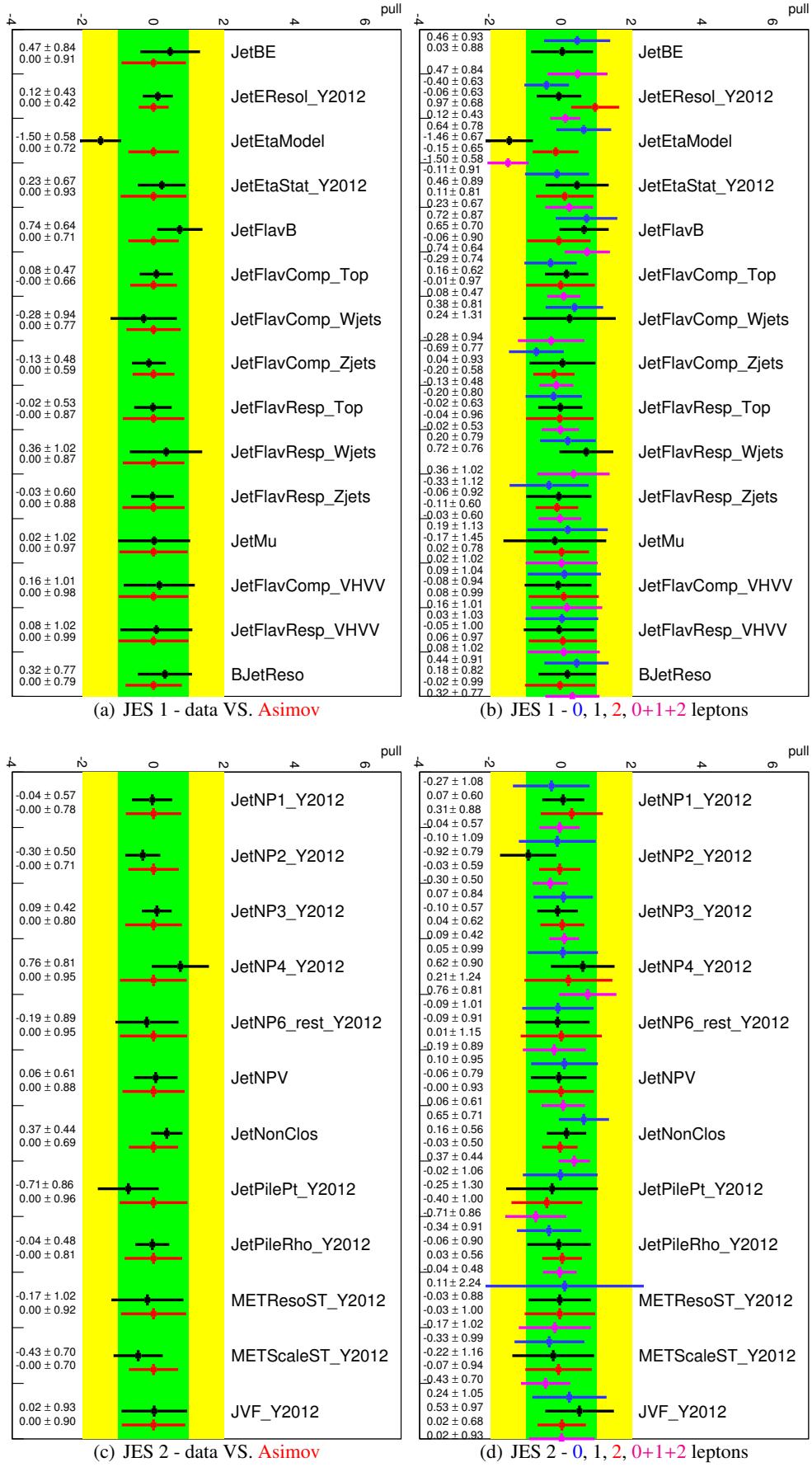


Figure 45: Pull plots for JES systematics in the 0+1+2 lepton m_{bb} shape fit. The fit to the Asimov data set is shown in red and the fit to the data in black on the left. The fits to 0 lepton (blue), 1 lepton (black) and 2 leptons (red) data and the combined fit to data (magenta) is shown on the right.

Not reviewed, for internal circulation only

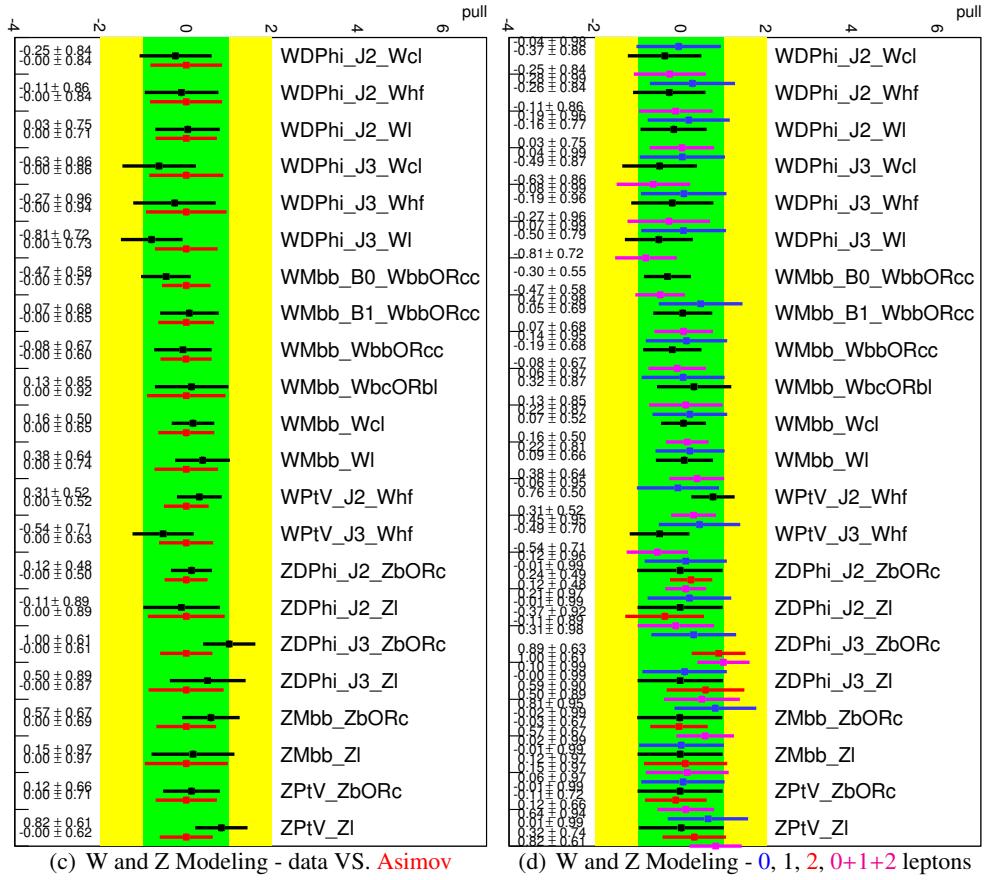
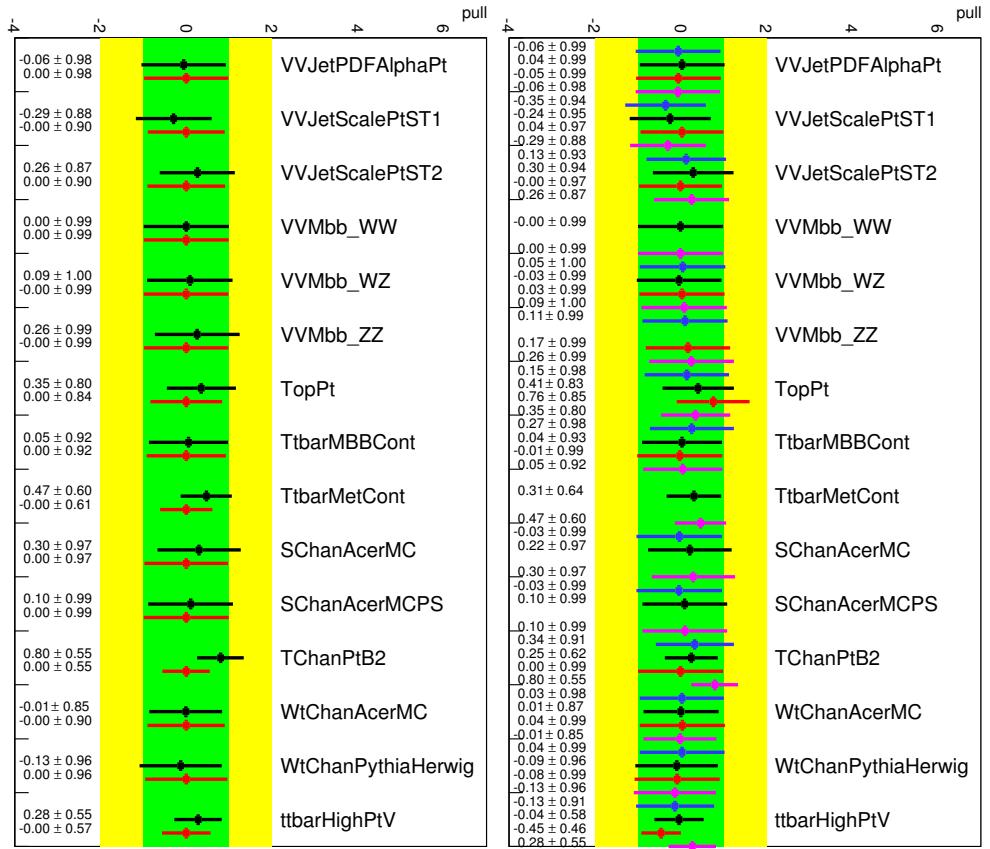


Figure 46: Pull plots for diboson/top and W/Z systematics in the 0+1+2 lepton m_{bb} shape fit. The fit to the Asimov data set is shown in red and the fit to the data in black on the left. The fits to 0 lepton (blue), 1 lepton (black) and 2 leptons (red) data and the combined fit to data (magenta) is shown on the right.

Not reviewed, for internal circulation only

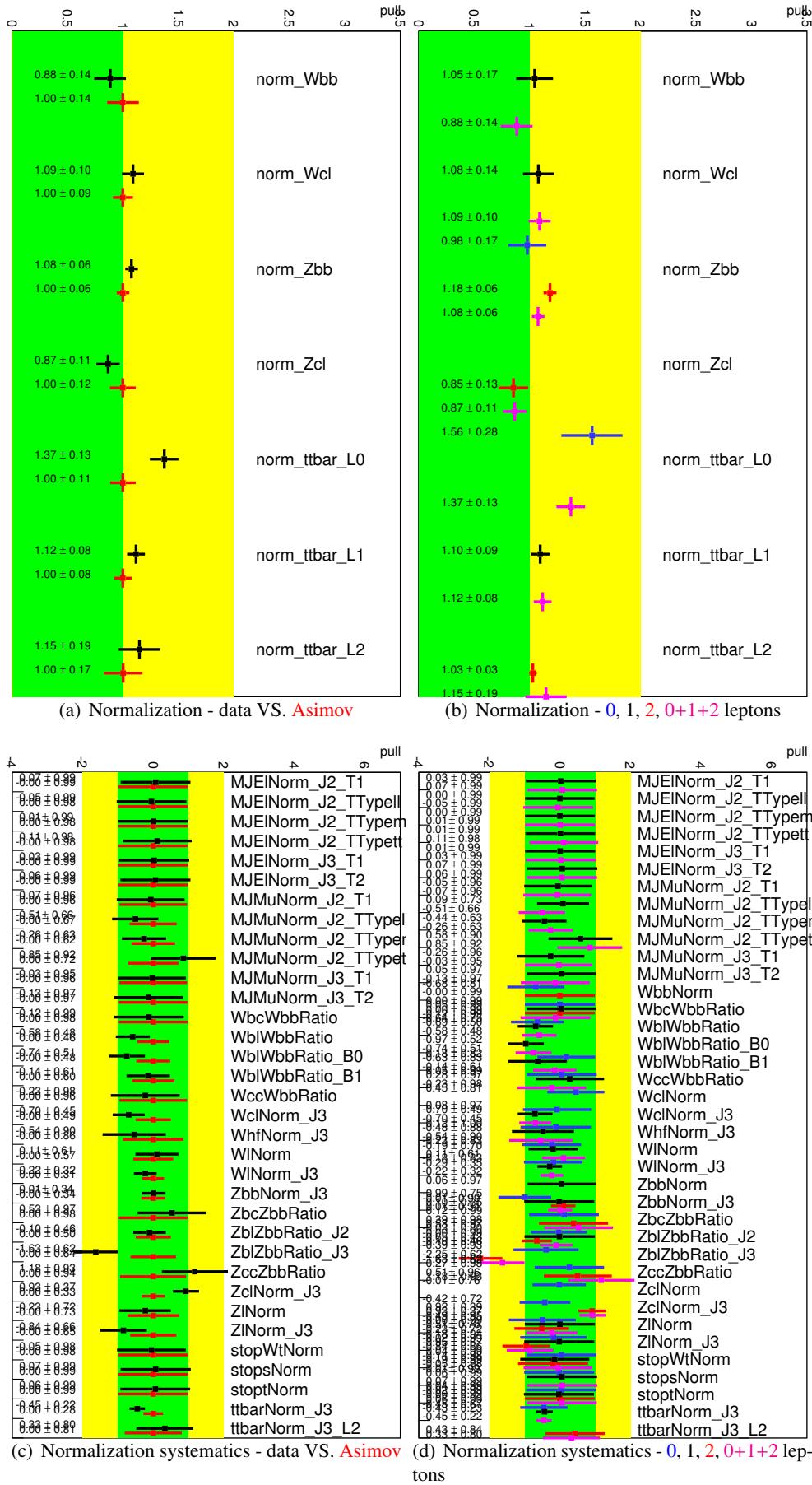


Figure 47: Pull plots for normalization in the 0+1+2 lepton m_{bb} shape fit. The fit to the Asimov data set is shown in red and the fit to the data in black on the left. The fits to 0 lepton (blue), 1 lepton (black) and 2 leptons (red) data and the combined fit to data (magenta) is shown on the right.

Not reviewed, for internal circulation only

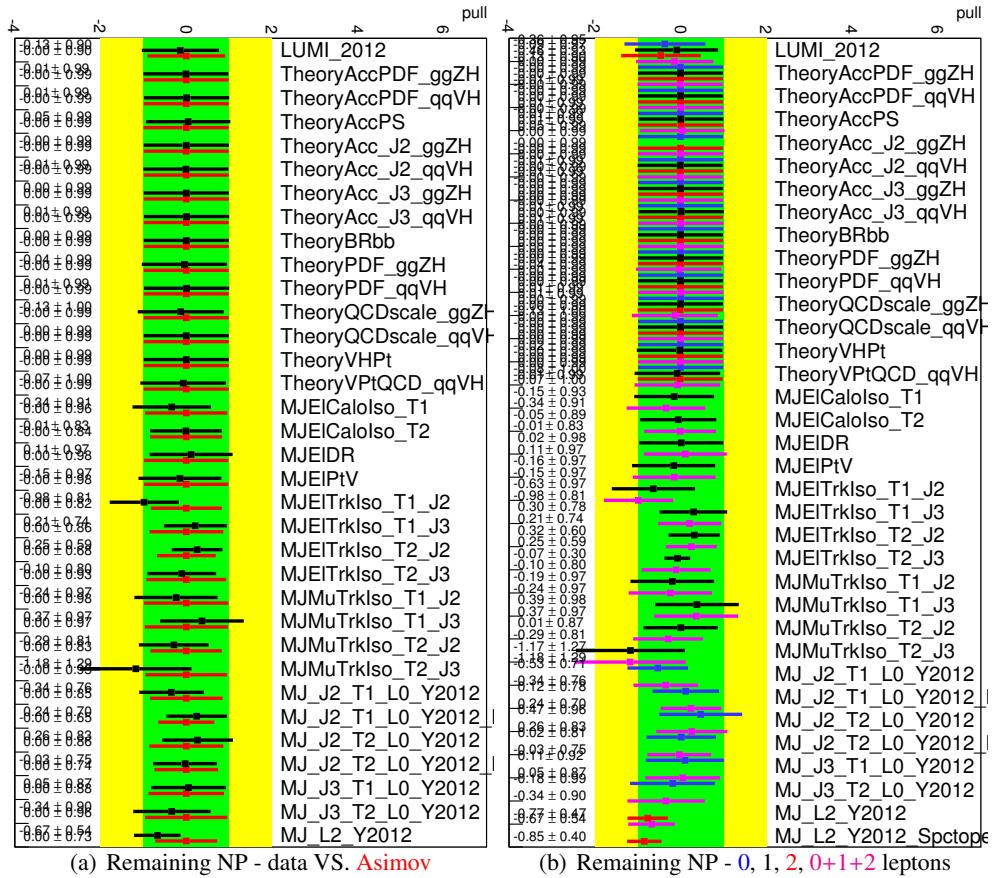


Figure 48: Pull plots for remaining systematics in the 0+1+2 lepton m_{bb} shape fit. The fit to the Asimov data set is shown in red and the fit to the data in black on the left. The fits to 0 lepton (blue), 1 lepton (black) and 2 leptons (red) data and the combined fit to data (magenta) is shown on the right.

3002 8.6.1.1 Correlation Plots

3003 Figure 49 shows the largest correlations in the full dijet massss analysis. This plot is produced by selecting
 3004 all NP, which have a correlation larger than 20% with any another NP. Note that the parameter of interest,
 3005 μ has been included by default not because it has particularly large correlations.

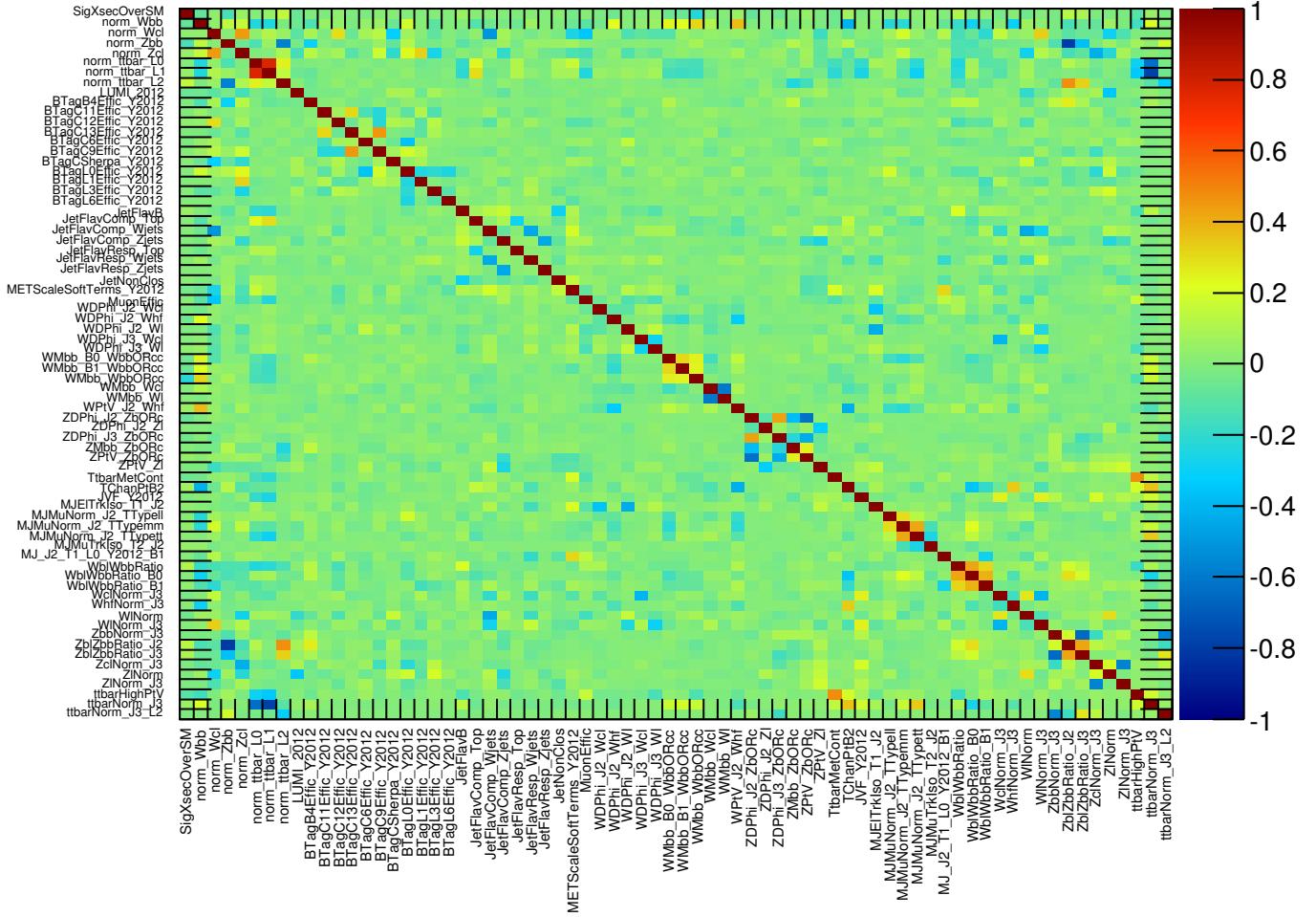


Figure 49: The correlation of all NP with a correlation larger than 20% in the 0+1+2 lepton m_{bb} shape fit. Note that the parameter of interest, μ has been included by default not because it has particularly large correlations.

3006 8.6.2 MVA Analysis Fit Studies

3007 The pull plots for combined fit for the MVA analysis are shown in Figures 50-55. Each plot compares the
3008 result from a fit to either the Asimov data set (red) or to the observed data (black) on the left, and the
3009 result of the fit for each individual lepton channel on the right. The individual channel results are shown
3010 in Appendix AH.2.

Not reviewed, for internal circulation only

Not reviewed, for internal circulation only

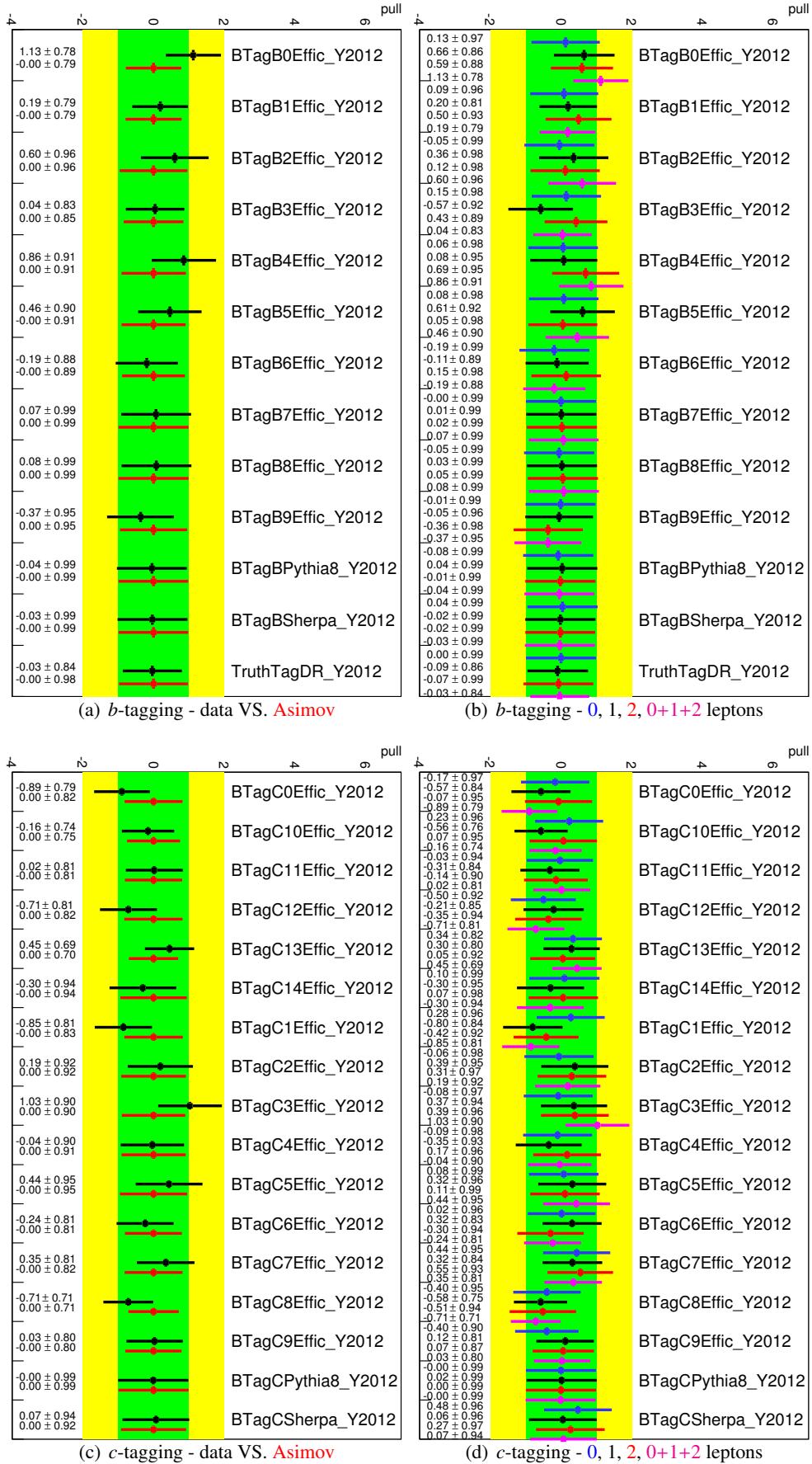


Figure 50: Pull plots for *b* and *c* tagging in the 0+1+2 lepton MVA fit. The fit to the Asimov data set is shown in red and the fit to the data in black on the left. The fits to 0 lepton (blue), 1 lepton (black) and 2 leptons (red) data and the combined fit to data (magenta) is shown on the right.

Not reviewed, for internal circulation only

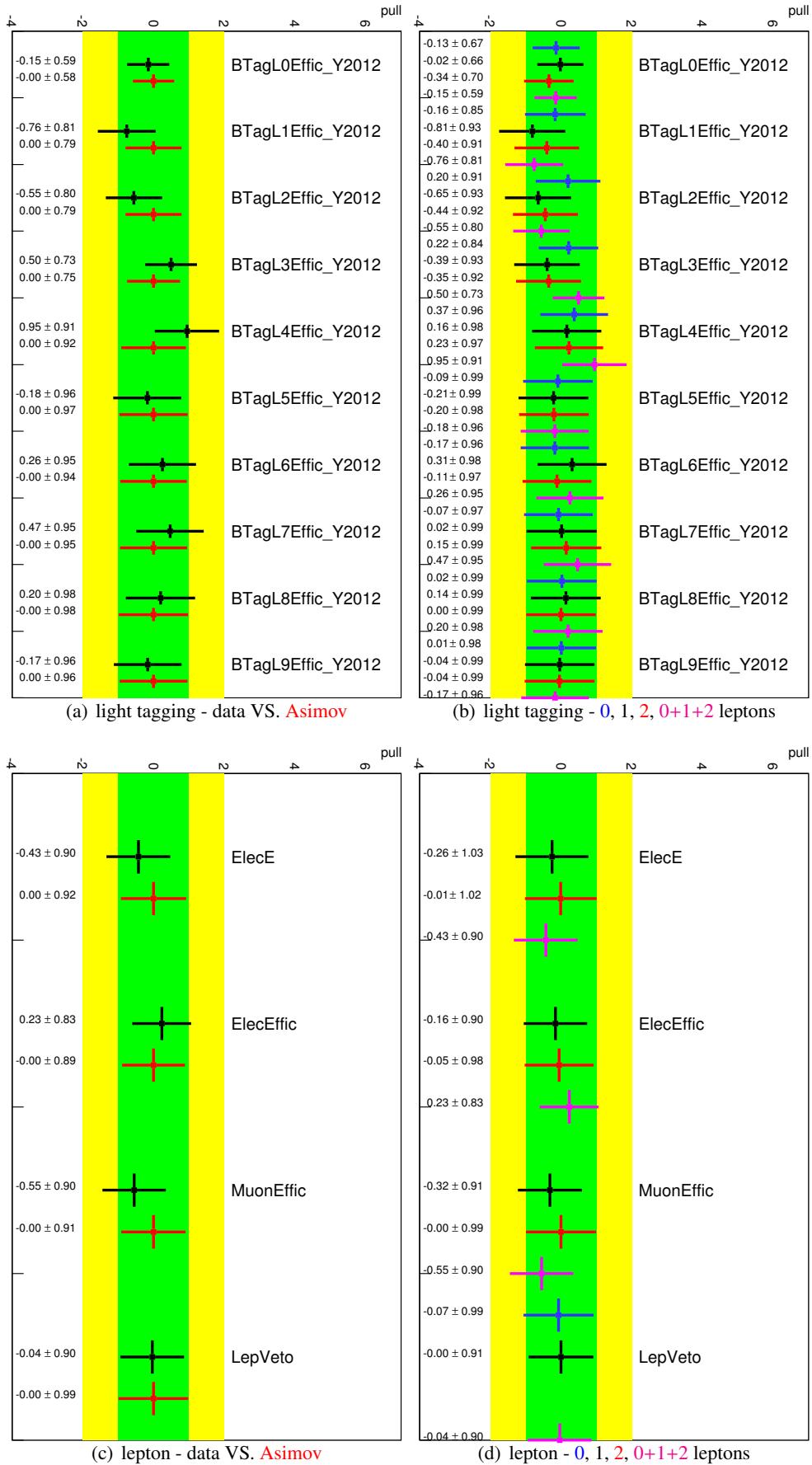


Figure 51: Pull plots for light-jet tagging and lepton related systematics in the 0+1+2 lepton MVA fit. The fit to the Asimov data set is shown in red and the fit to the data in black on the left. The fits to 0 lepton (blue), 1 lepton (black) and 2 leptons (red) data and the combined fit to data (magenta) is shown on the right.

Not reviewed, for internal circulation only

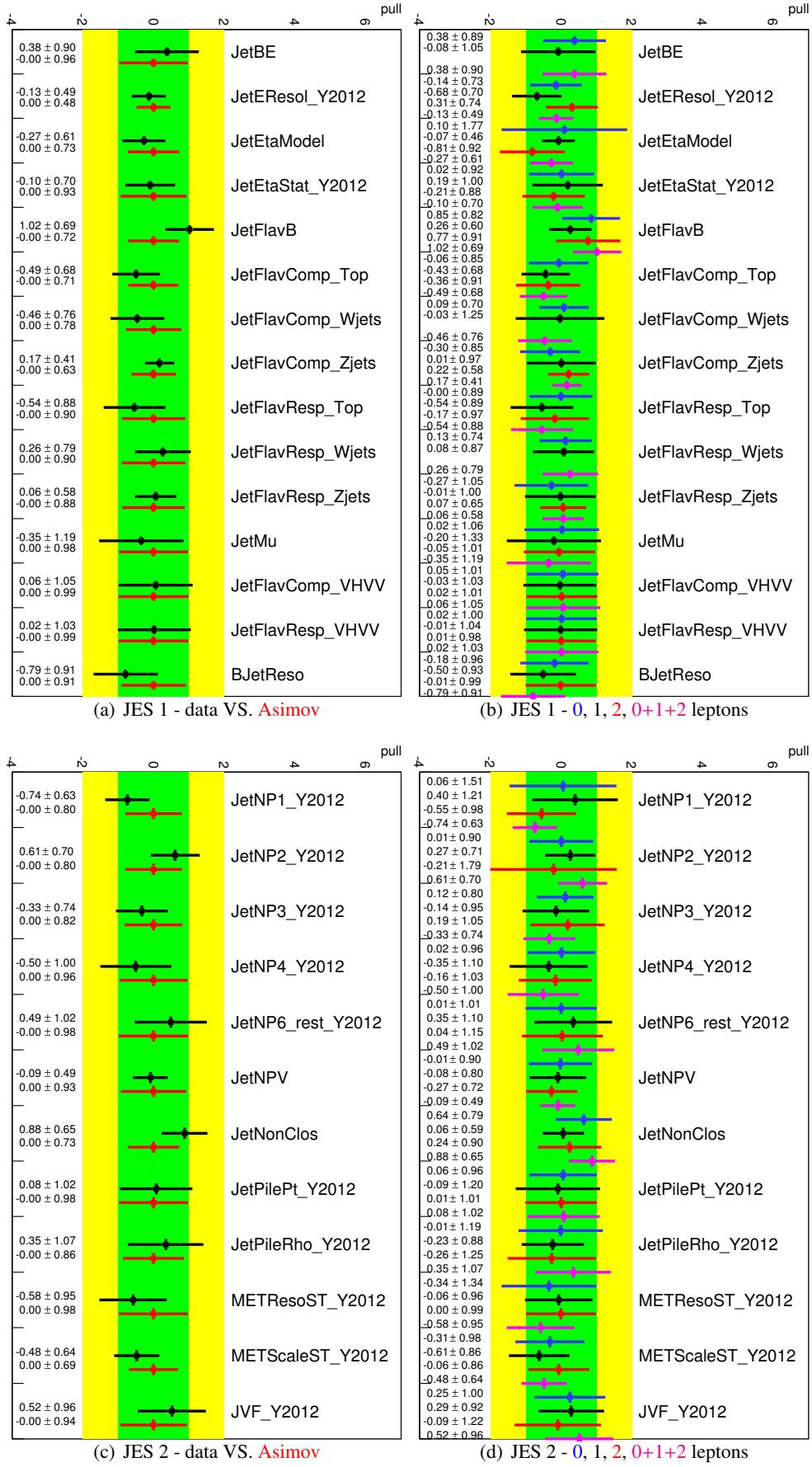


Figure 52: Pull plots for JES systematics in the 0+1+2 lepton MVA fit. The fit to the Asimov data set is shown in red and the fit to the data in black on the left. The fits to 0 lepton (blue), 1 lepton (black) and 2 leptons (red) data and the combined fit to data (magenta) is shown on the right.

Not reviewed, for internal circulation only

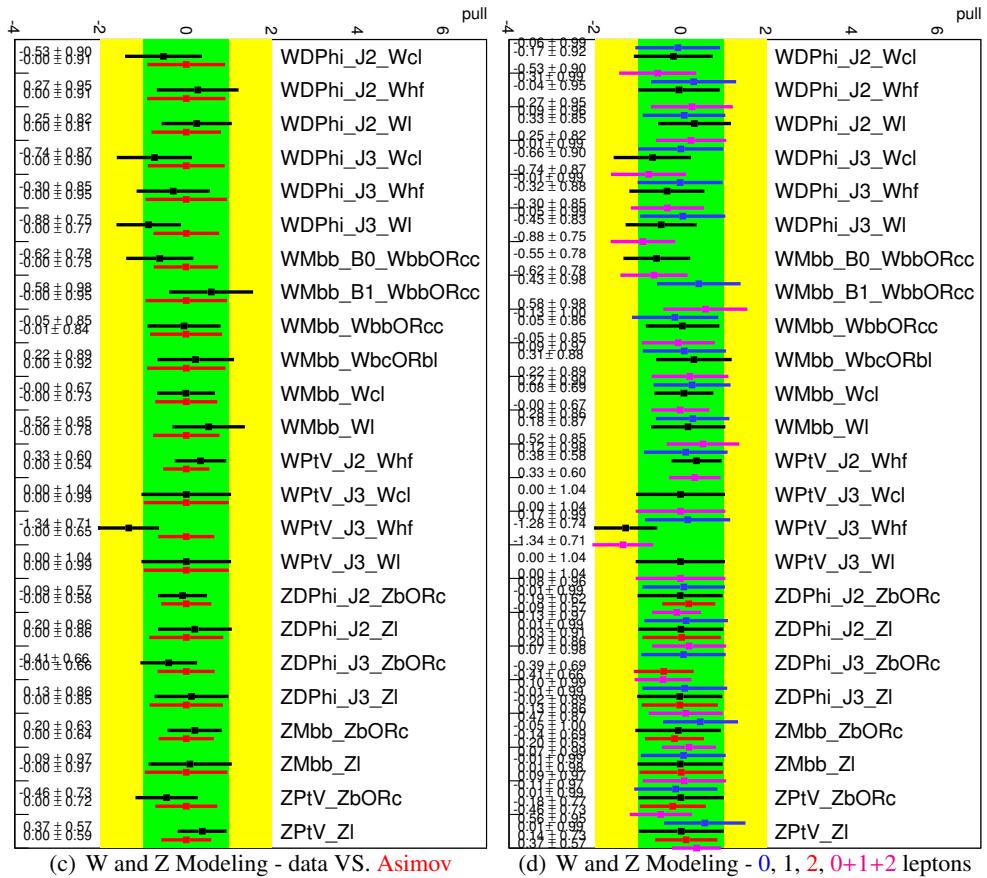
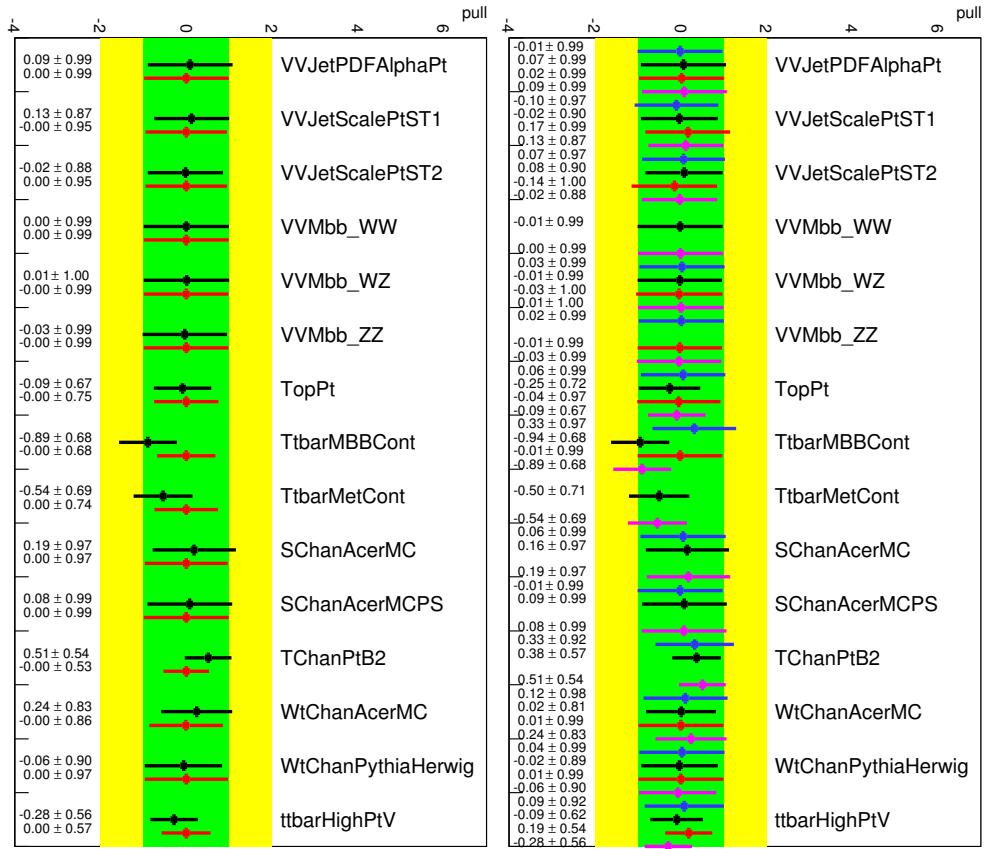


Figure 53: Pull plots for diboson/top and W/Z systematics in the 0+1+2 lepton MVA fit. The fit to the Asimov data set is shown in red and the fit to the data in black on the left. The fits to 0 lepton (blue), 1 lepton (black) and 2 leptons (red) data and the combined fit to data (magenta) is shown on the right.

Not reviewed, for internal circulation only

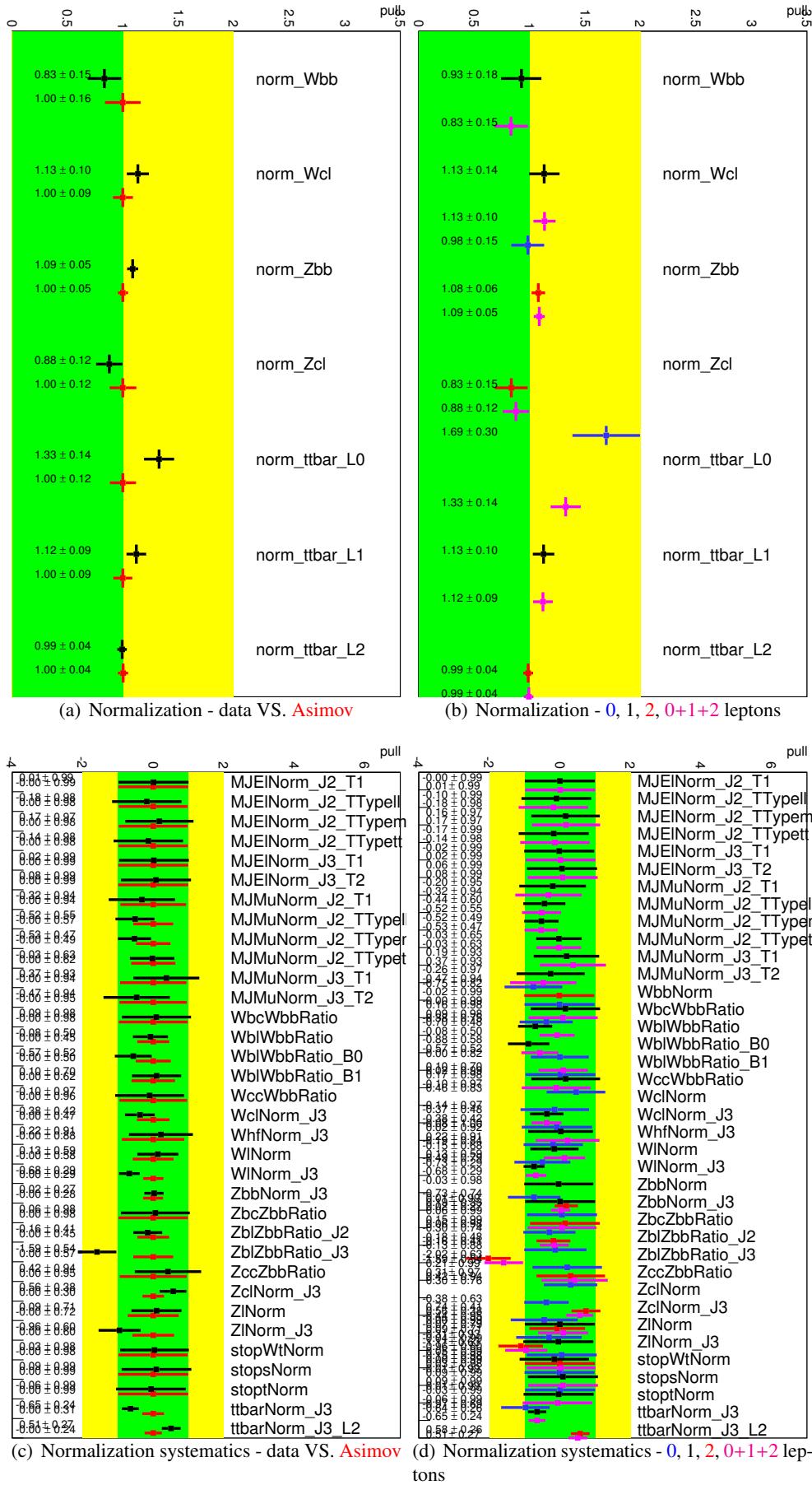


Figure 54: Pull plots for normalization in the 0+1+2 lepton MVA fit. The fit to the Asimov data set is shown in red and the fit to the data in black on the left. The fits to 0 lepton (blue), 1 lepton (black) and 2 leptons (red) data and the combined fit to data (magenta) is shown on the right.

Not reviewed, for internal circulation only

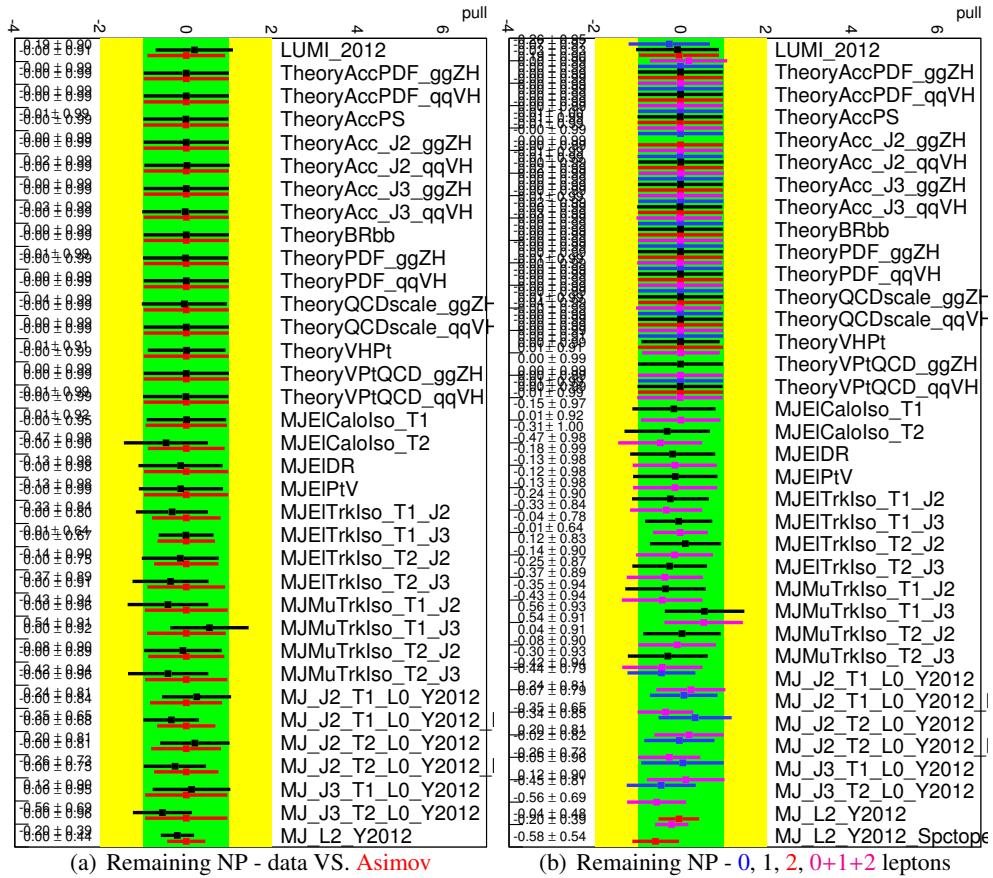


Figure 55: Pull plots for remaining systematics in the 0+1+2 lepton MVA fit. The fit to the Asimov data set is shown in red and the fit to the data in black on the left. The fits to 0 lepton (blue), 1 lepton (black) and 2 leptons (red) data and the combined fit to data (magenta) is shown on the right.

3011 8.6.2.1 Correlation Plots

Figure 56 shows the largest correlations in the full MVA analysis. This plot is produced by selecting all NP, which have a correlation larger than 20% with any other NP. Note that the parameter of interest, μ has been included by default not because it has particularly large correlations.

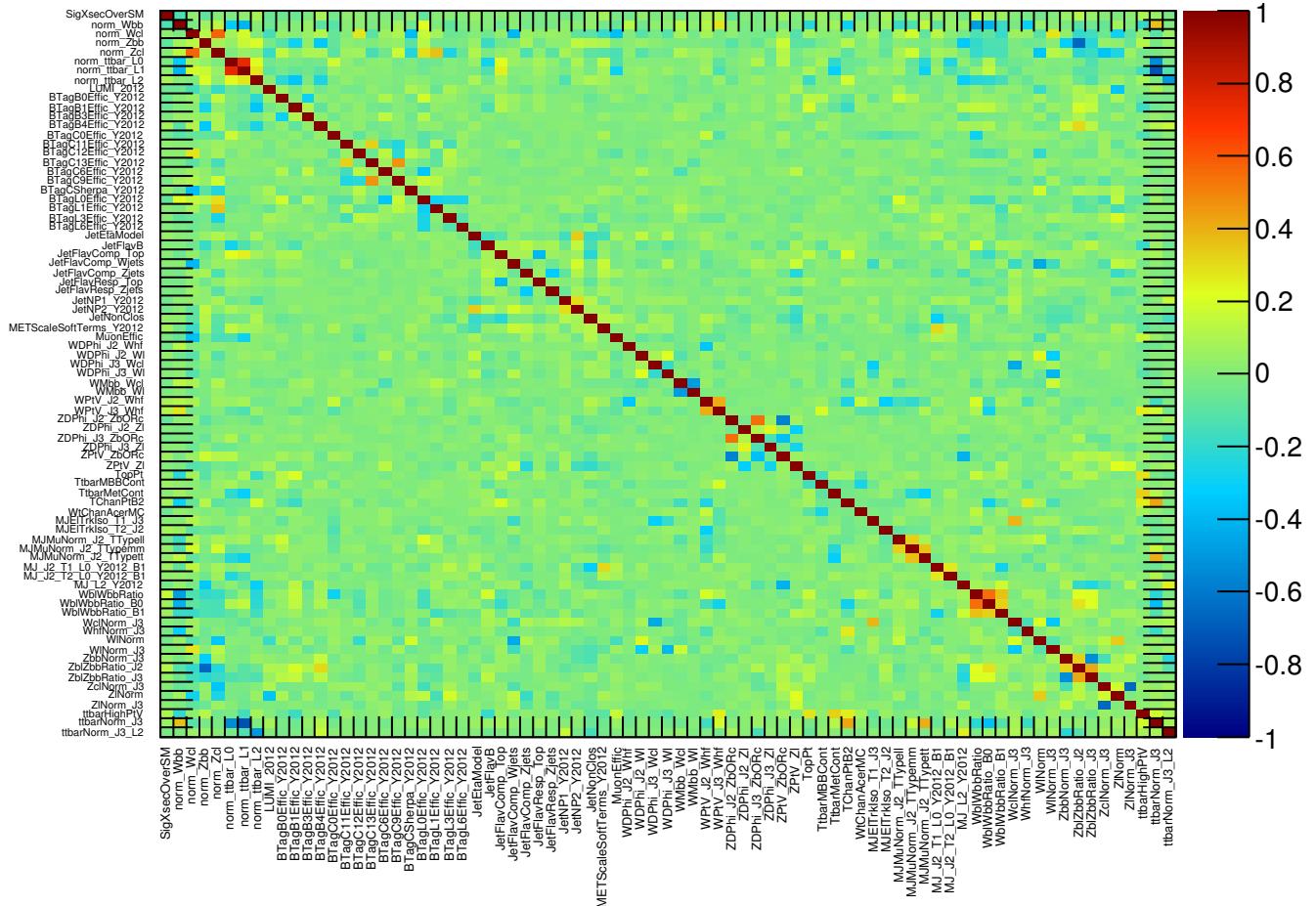


Figure 56: The correlation of all NP with a correlation larger than 20% in the 0+1+2 lepton MVA fit. Note that the parameter of interest, μ has been included by default not because it has particularly large correlations.

3015 **8.6.3 Comparison of Dijet Mass and MVA Analysis Fits**

3016 The MVA combined fit results are shown in black while the dijet mass analysis pulls are shown in red. A
 3017 comparison of the individual channels in given in Appendix ??.

Not reviewed, for internal circulation only

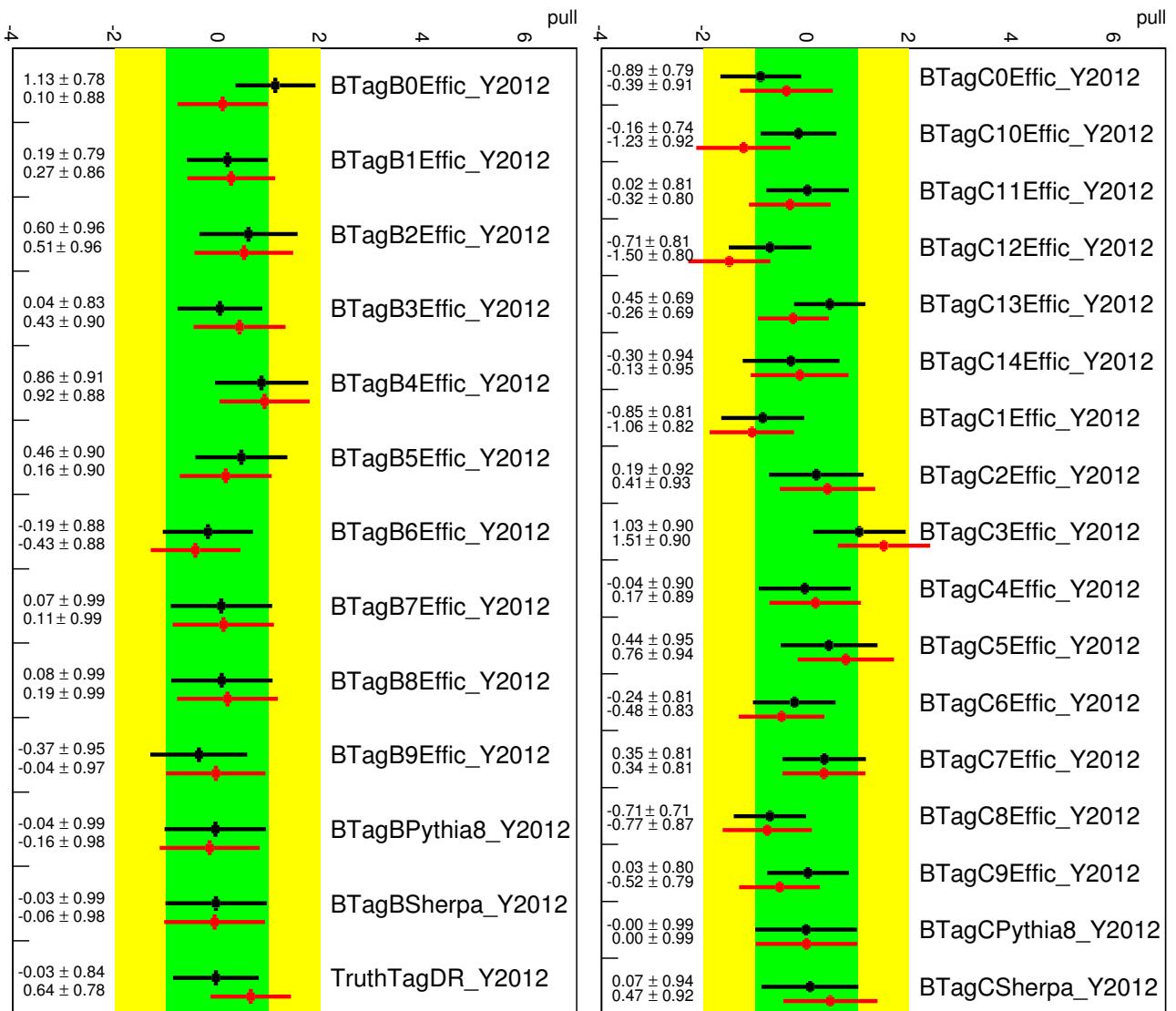


Figure 57: m_{jj} vs MVA pull plots for 0+1+2 fit: b- and c-jet tagging.

Not reviewed, for internal circulation only

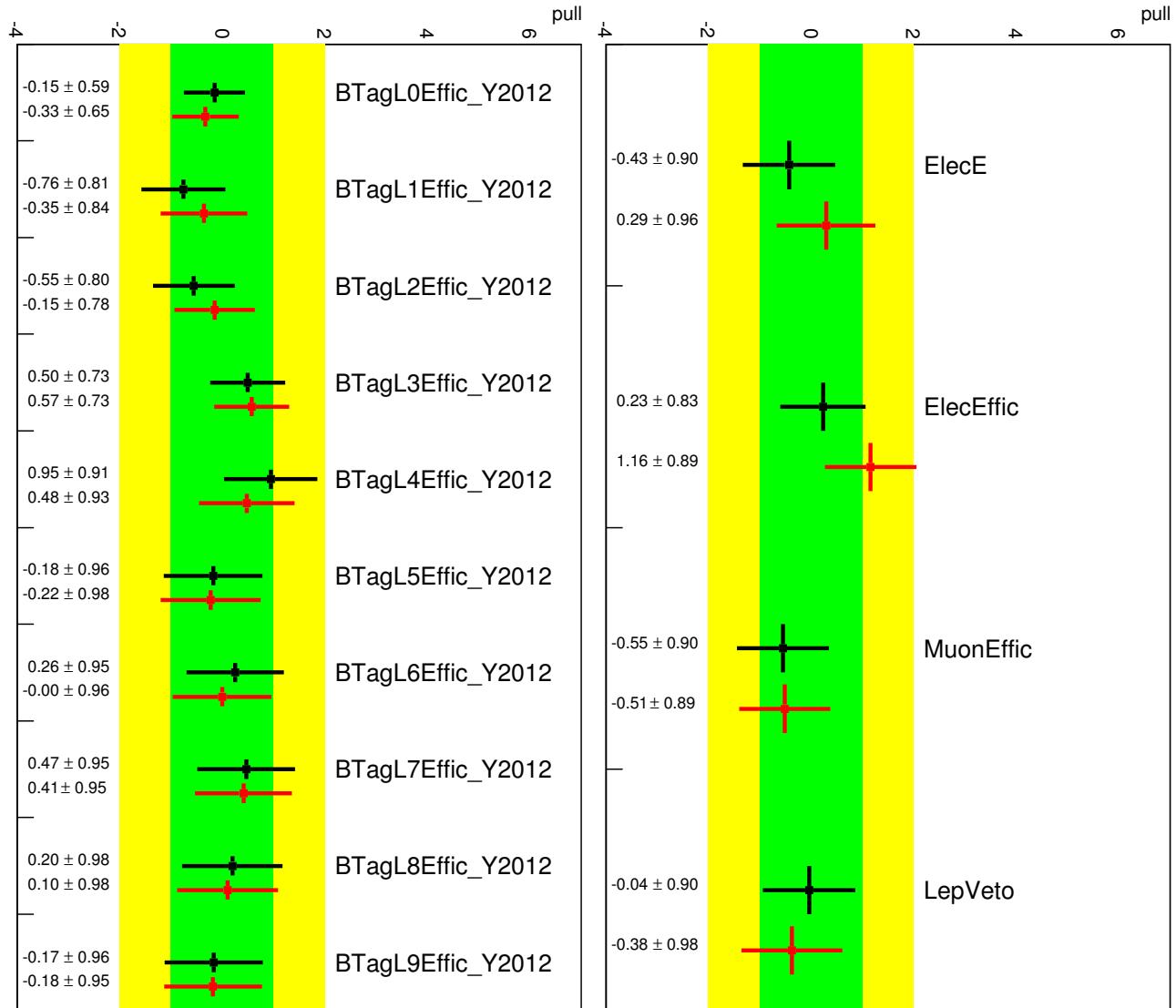


Figure 58: m_{jj} vs MVA pull plots for 0+1+2 fit: light-jet tagging and leptons.

Not reviewed, for internal circulation only

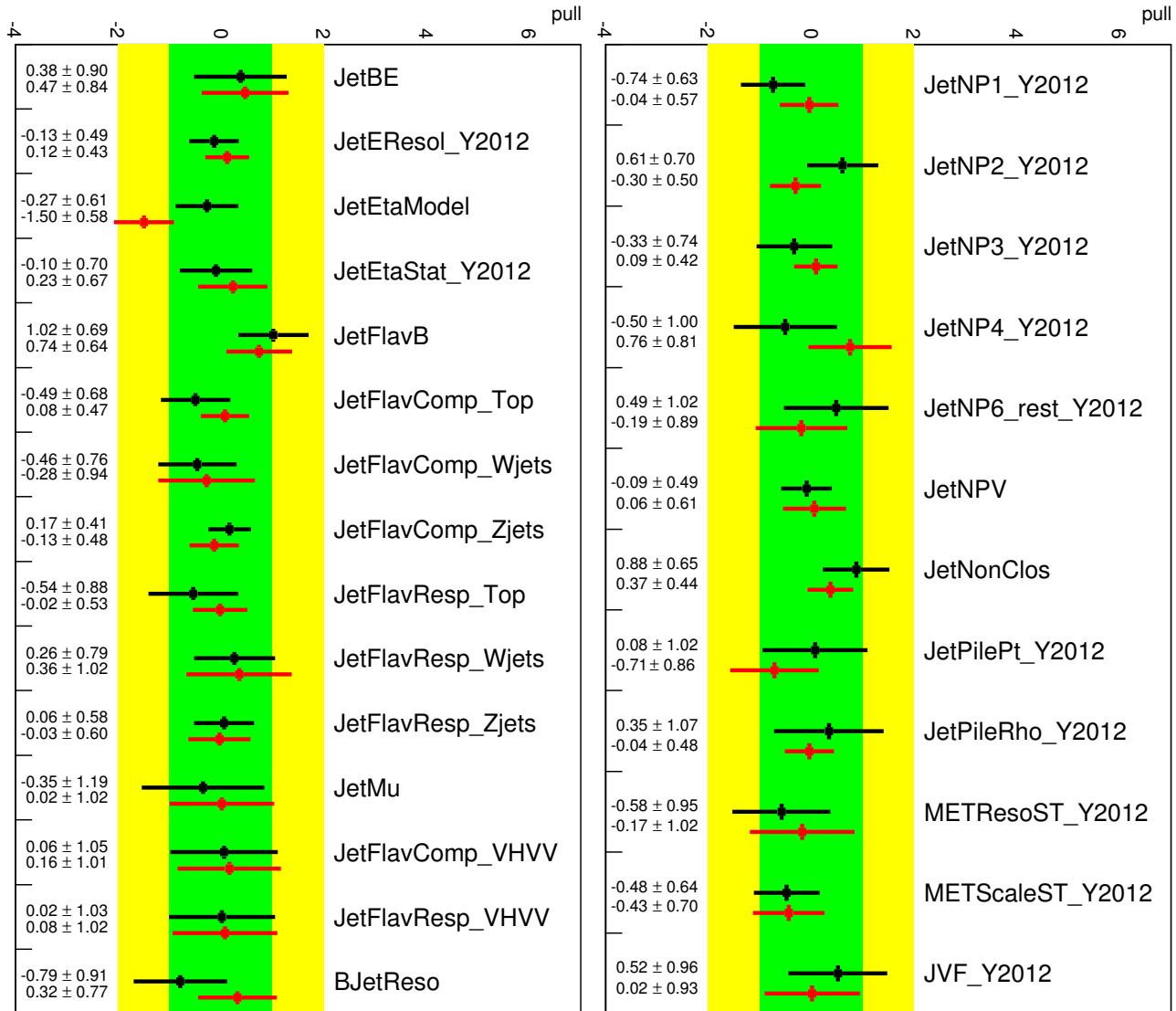
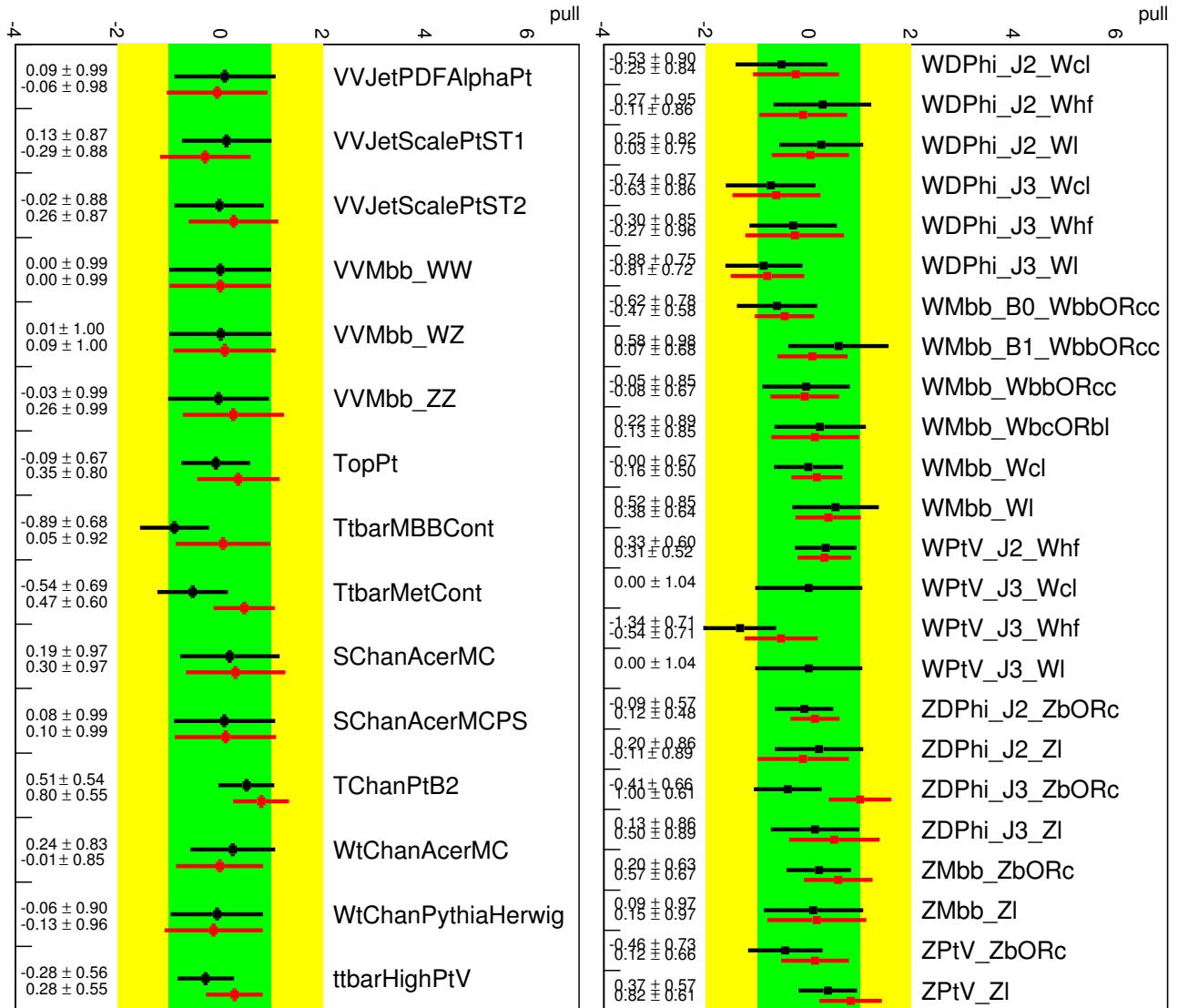
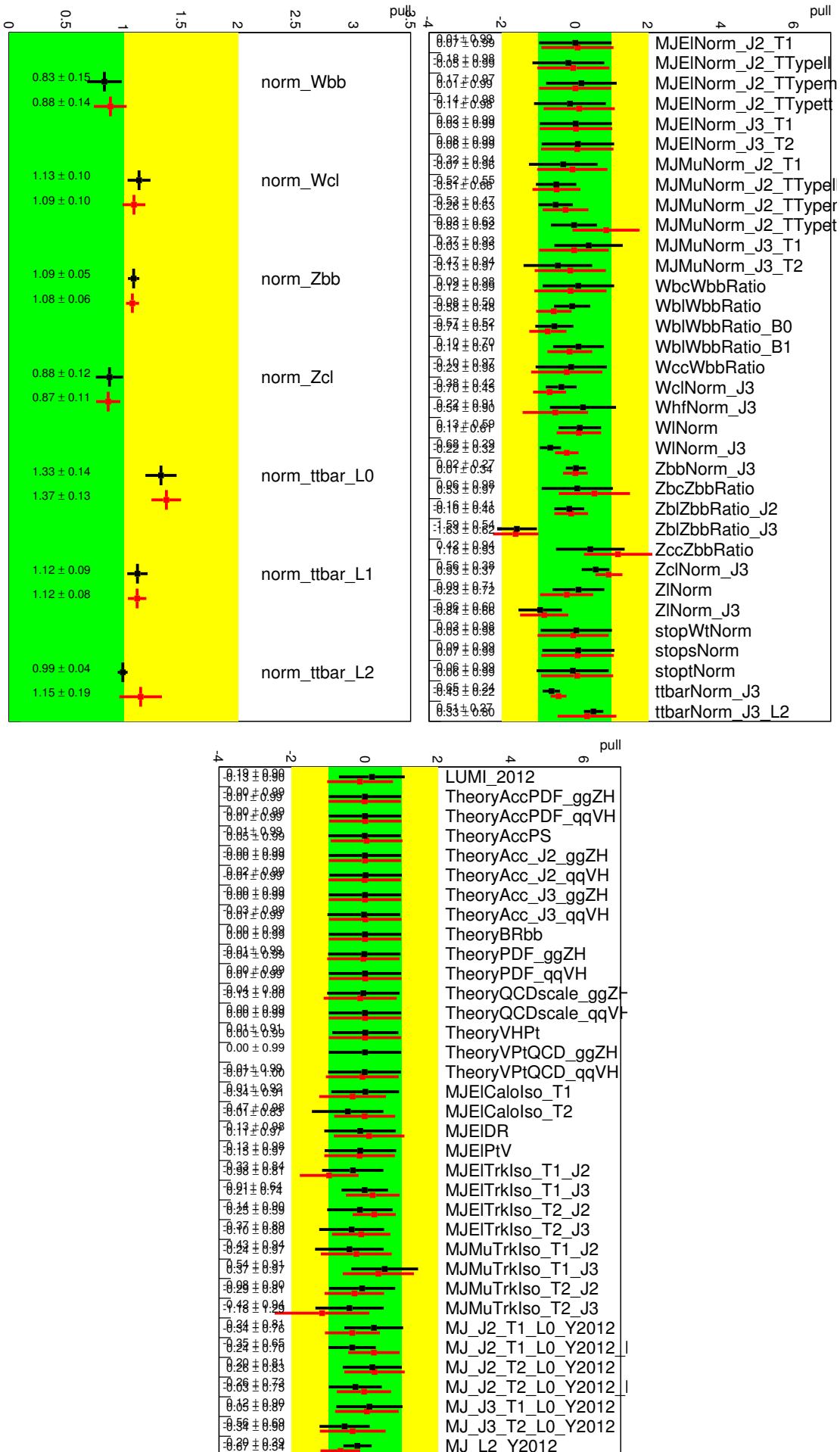


Figure 59: m_{jj} vs MVA pull plots for 0+1+2 fit: Jet NPs.

Not reviewed, for internal circulation only

Figure 60: m_{jj} vs MVA pull plots for 0+1+2 fit: Diboson and Top related uncertainties.

Not reviewed, for internal circulation only

Figure 61: m_{jj} vs MVA pull plots for 0+1+2 fit: Normalization and residual uncertainties.

3018 8.6.4 Nuisance Parameter Ranking Plots

3019 After the MLL value is found, each NP is pulled $\pm 1\sigma$ and the likelihood is maximized again. The change
3020 in the best fit μ value gives the inclusive sensitivity of the measured value to the give NP. The impact
3021 is judged using fits to data. Figures 62 and 63 show the ranking plots for the full dijet massss analysis,
3022 then the 0 through 2-lepton analysis individually. Figures 64 and 65 show the ranking plots for the full
3023 MVA analysis, then the 0 through 2-lepton analysis individually. The plots show both pre-fit and post-fit
3024 impacts, together with displaying the pulls on the data. All plots are obtained through a fit on the data

3025 8.6.4.1 Dijet Mass Analysis**3026 8.6.4.2 Ranking plots for MVA**

Not reviewed, for internal circulation only

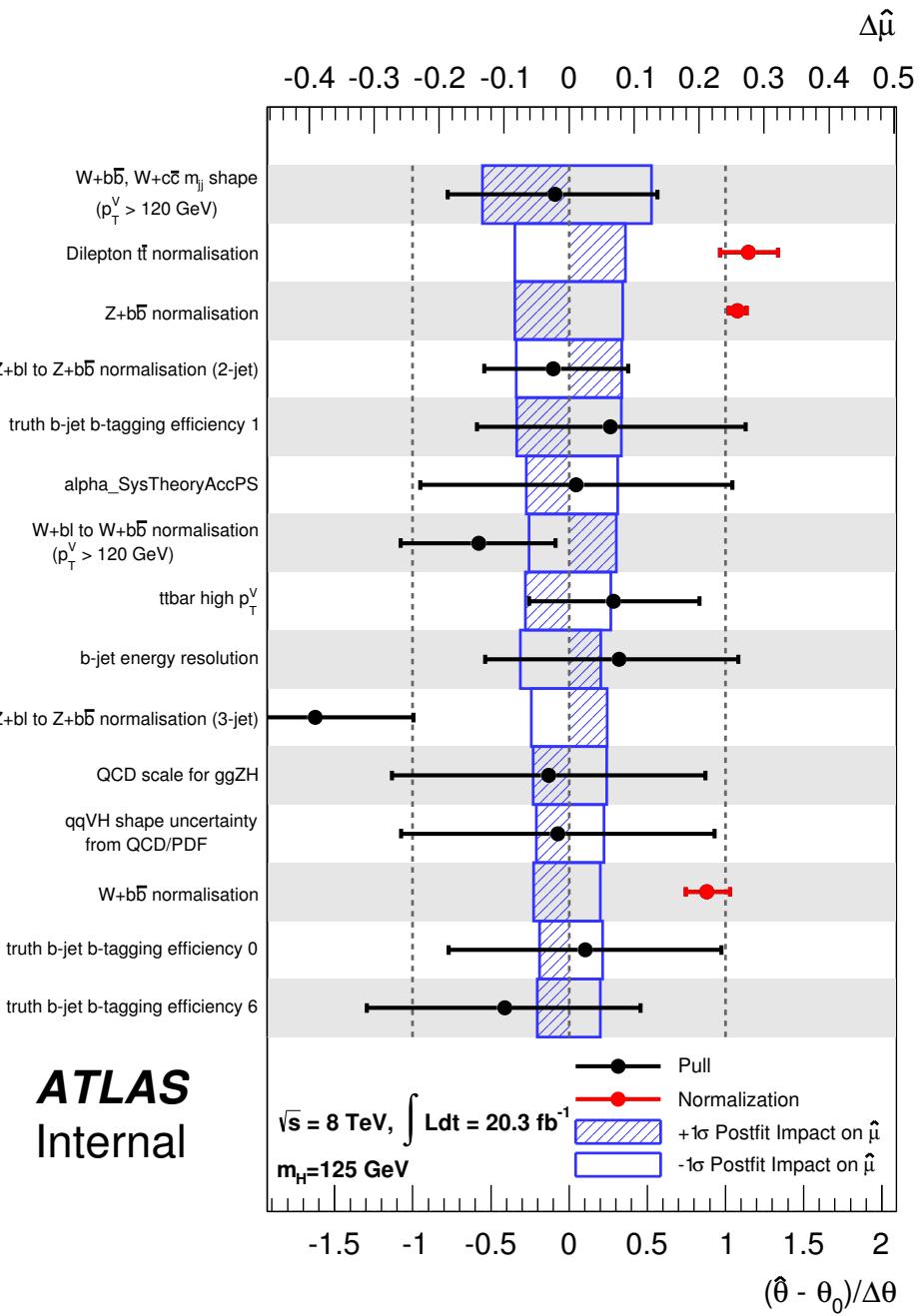


Figure 62: Ranking of systematic uncertainties in the dijet mass analysis for the combined fit.

Not reviewed, for internal circulation only

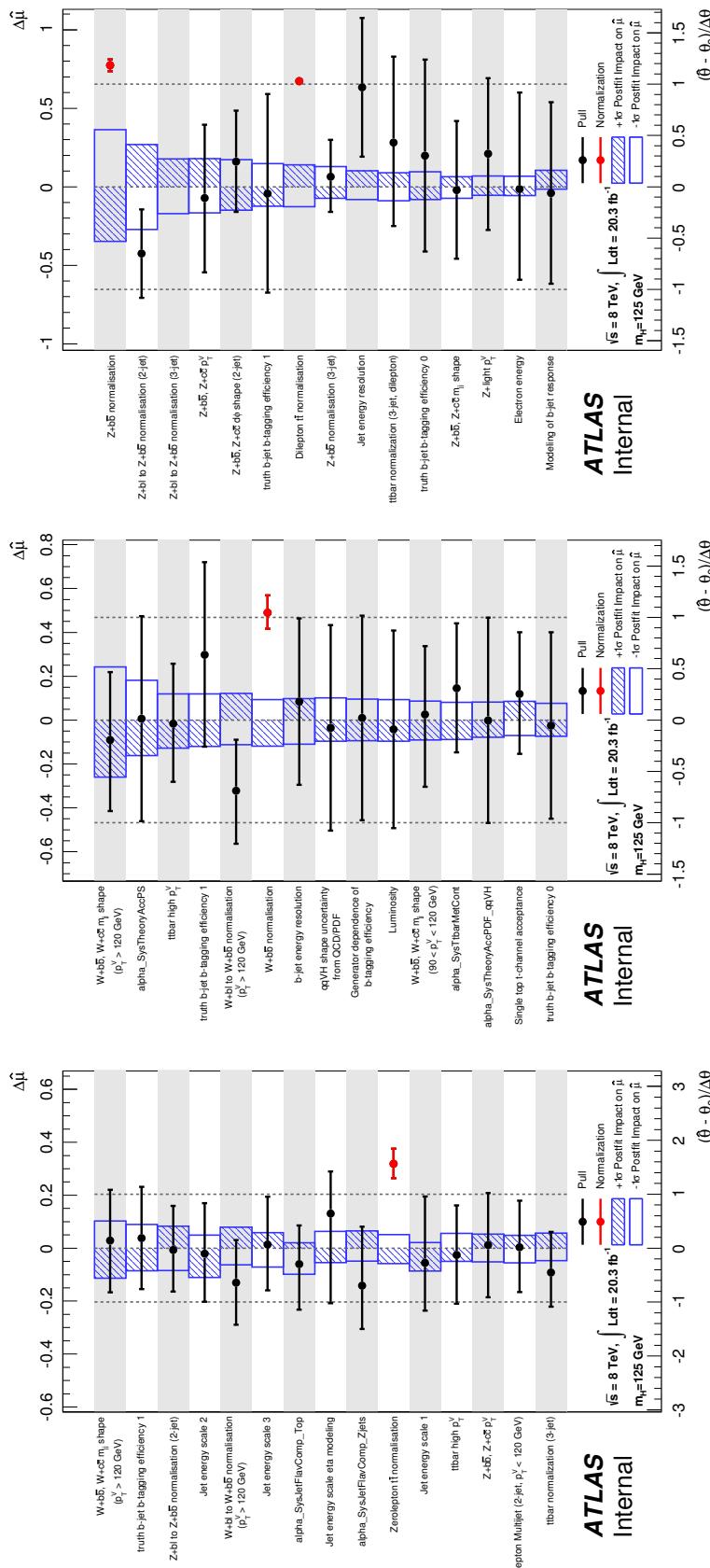


Figure 63: Ranking of systematic uncertainties in the dijet mass analysis for the , 1 lepton and 2-leptons channels.

Not reviewed, for internal circulation only

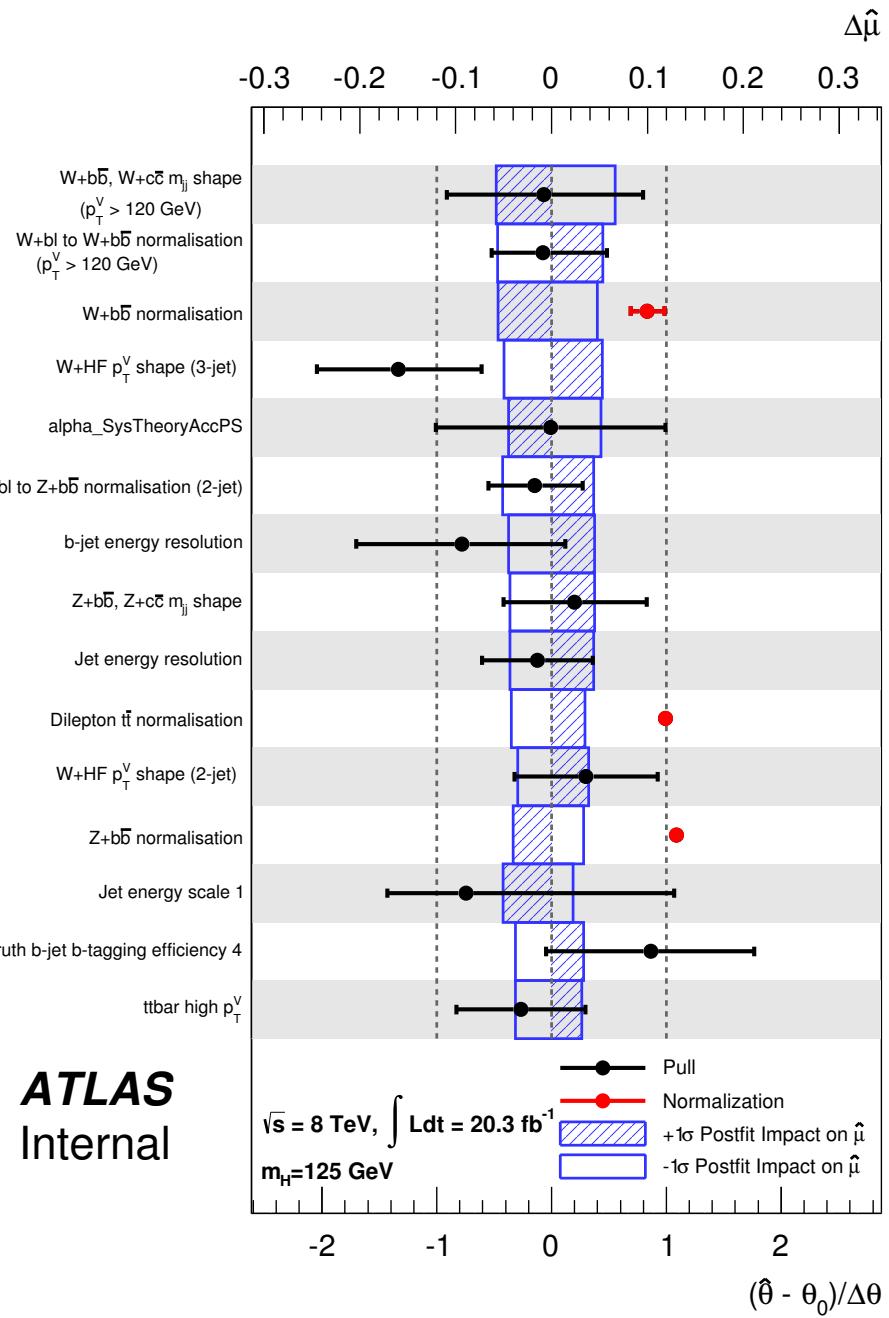


Figure 64: Ranking of systematic uncertainties in the MVA analysis for the combined fit.

Not reviewed, for internal circulation only

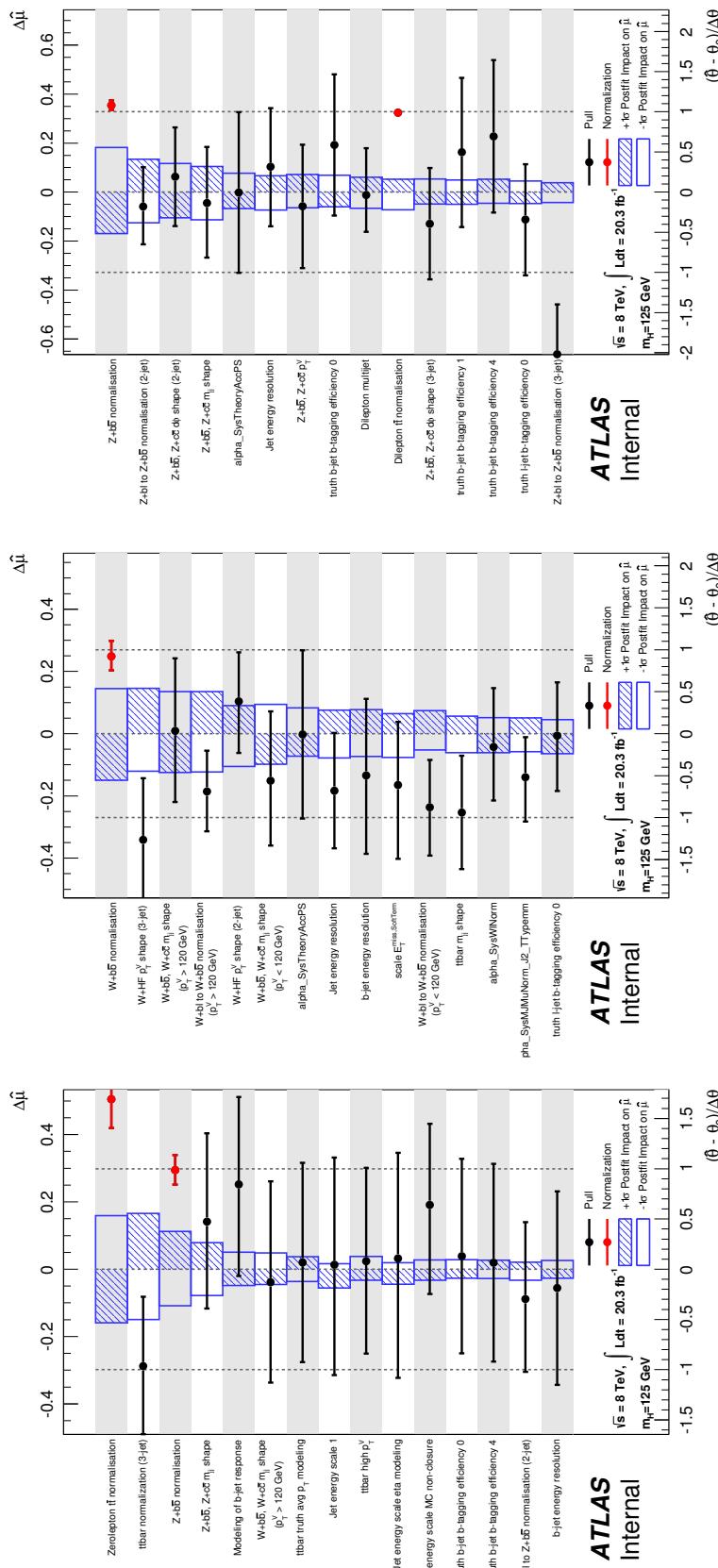


Figure 65: Ranking of systematic uncertainties in the MVA analysis for the 0-lepton, 1 lepton and 2-leptons channels.

3027 8.7 Dijet Mass Analysis Post Fit Plots

3028 In the following sections post-fit plots corresponding to unconditionnal μ fits to the data for the dijet
3029 massss analysis are presented. In all cases the MC expectations have been adapted to the pulls from the
3030 data in the combined 0+1+2 lepton fit. As a comparison, the total nominal background prediction is
3031 indicated by the dashed blue curve.

3032 In Figures 66 - 68, 69 - 71, 72 - 74 post-fit plots for the m_{bb} shape analysis are shown for the 0, 1 and
3033 2-lepton channel respectively in the various 1-tag and 2-tag categories in different p_T^V bins.

Not reviewed, for internal circulation only

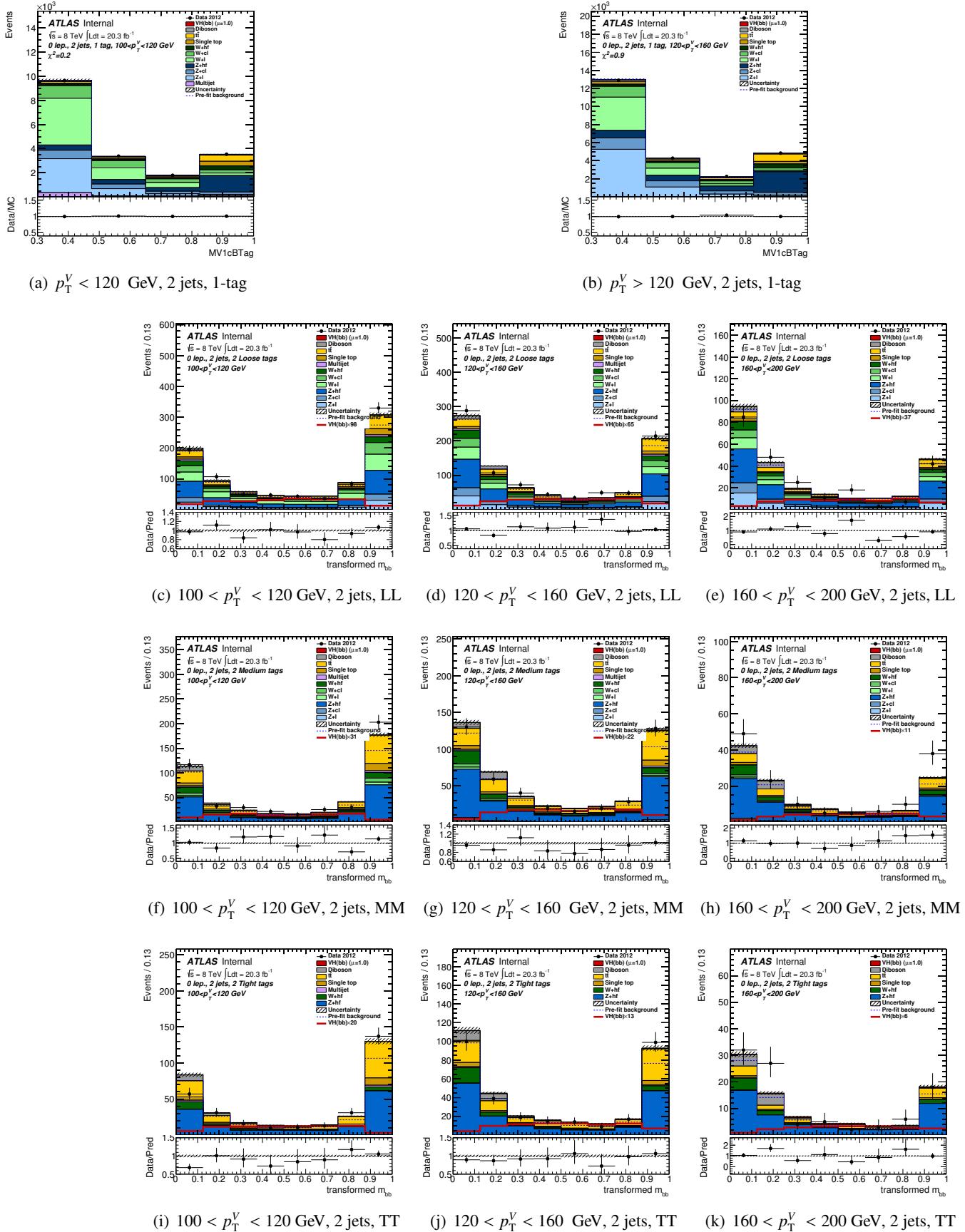


Figure 66: Post-fit plots for m_{jj} distribution in 0-lepton events in the 1-tag (where mv1c is used in the fit) LL , MM and TT tag categories for the 2-jets events. Plots are shown for $100 < p_T^V < 120$ GeV, $120 < p_T^V < 160$ GeV and $160 < p_T^V < 200$ GeV. The pre-fit background expectation is indicated by the dashed blue line.

Not reviewed, for internal circulation only

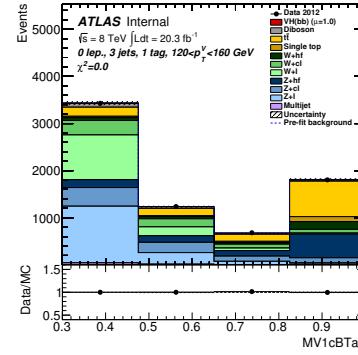
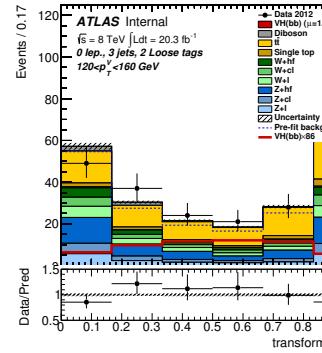
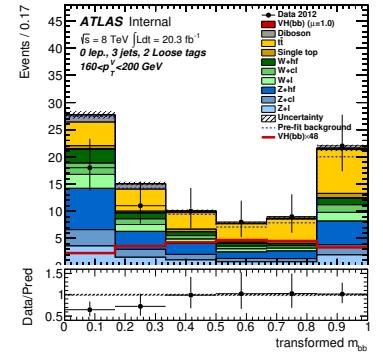
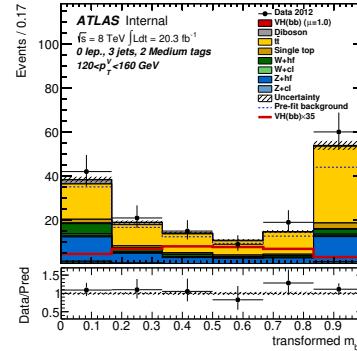
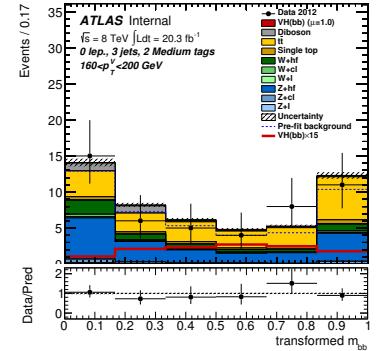
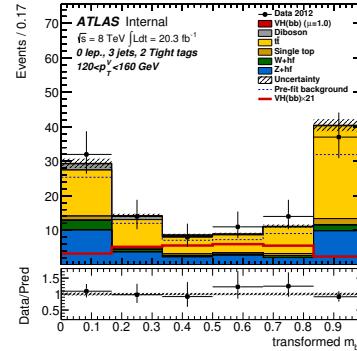
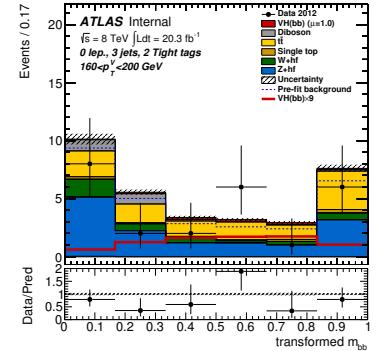
(a) $p_T^V > 120 \text{ GeV}, 3 \text{ jets}, 1\text{-tag}$ (b) $120 < p_T^V < 160 \text{ GeV}, 3 \text{ jets}, \text{LL}$ (c) $160 < p_T^V < 200 \text{ GeV}, 3 \text{ jets}, \text{LL}$ (d) $120 < p_T^V < 160 \text{ GeV}, 3 \text{ jets}, \text{MM}$ (e) $160 < p_T^V < 200 \text{ GeV}, 3 \text{ jets}, \text{MM}$ (f) $120 < p_T^V < 160 \text{ GeV}, 3 \text{ jets}, \text{TT}$ (g) $160 < p_T^V < 200 \text{ GeV}, 3 \text{ jets}, \text{TT}$

Figure 67: Post-fit plots for m_{jj} distribution in 0-lepton events in the 1-tag (where mv1c is used in the fit) LL, MM and TT tag categories for the 3-jets events. Plots are shown for $120 < p_T^V < 160 \text{ GeV}$ and $160 < p_T^V < 200 \text{ GeV}$. The pre-fit background expectation is indicated by the dashed blue line.

Not reviewed, for internal circulation only

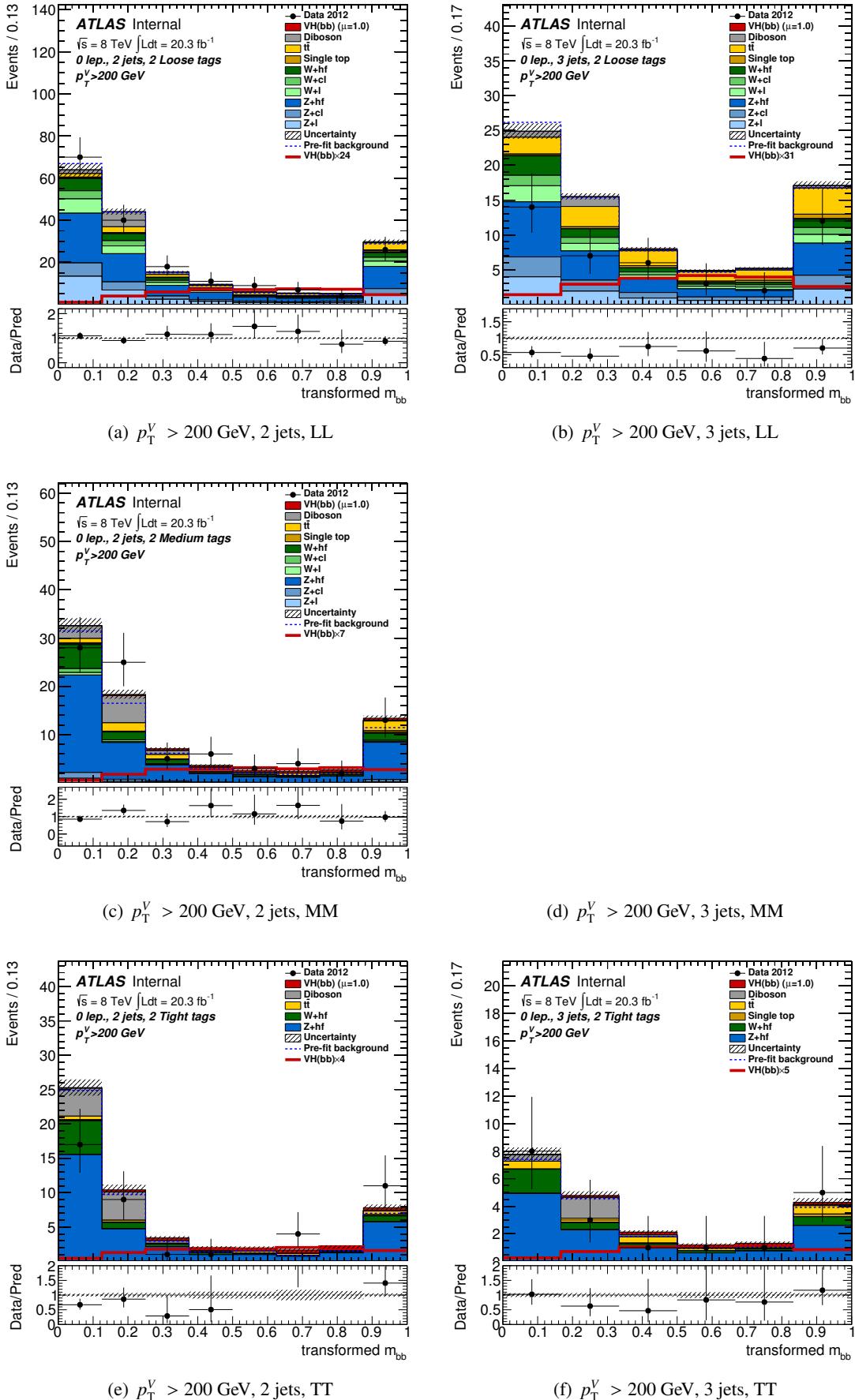


Figure 68: Post-fit plots for m_{jj} distribution in 0-lepton events in the *LL*, *MM* and *TT* tag categories for the 2-jets and the 3-jets events. Plots are shown for $p_T^V > 200 \text{ GeV}$. The pre-fit background expectation is indicated by the dashed blue line.

internal circulation only

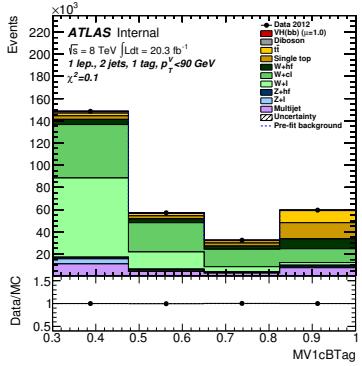
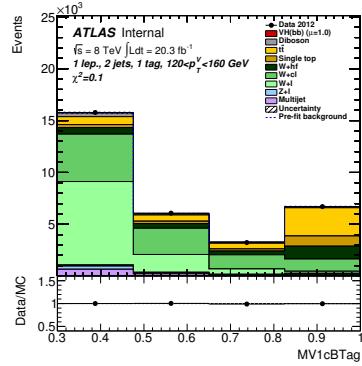
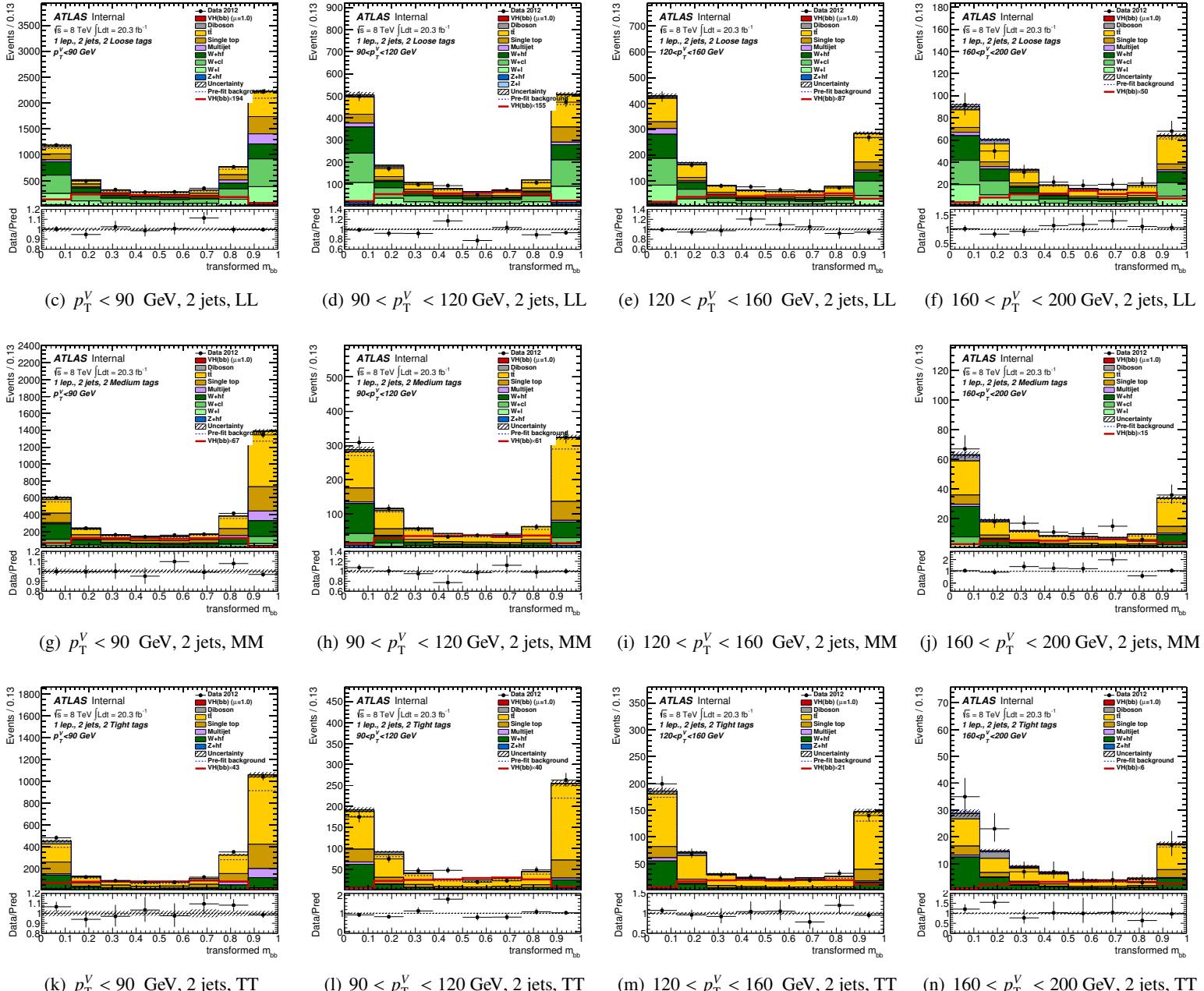
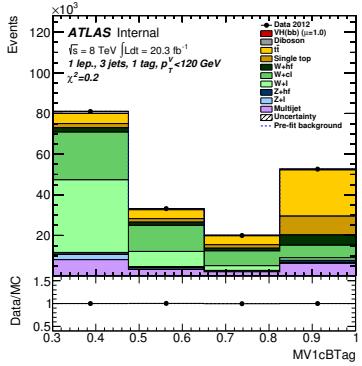
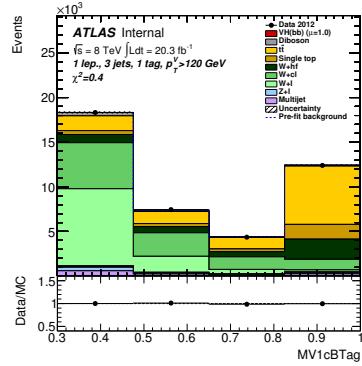
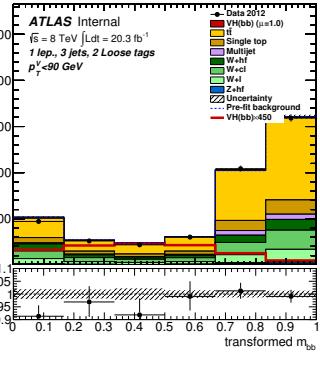
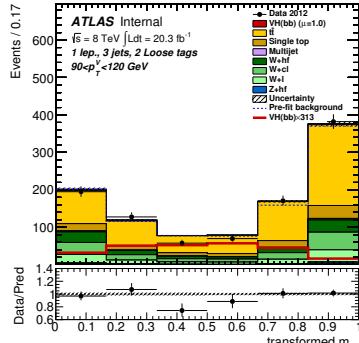
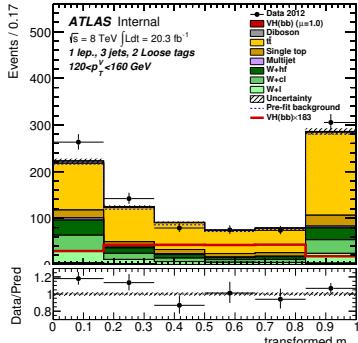
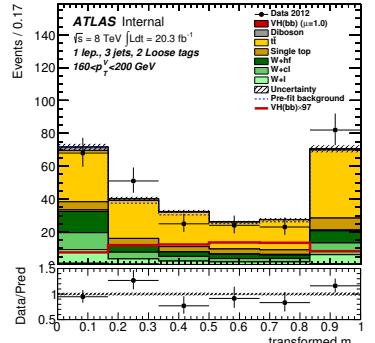
(a) $p_T^V < 120$ GeV, 2 jets, 1-tag(b) $p_T^V > 120$ GeV, 2 jets, 1-tag

Figure 69: Post-fit plots for m_{jj} distribution in 1-lepton events in the 1-tag (where mv1c is used in the fit) LL , MM and TT tag categories for the 2-jets events. Plots are shown for $p_T^V < 90$ GeV, $90 < p_T^V < 120$ GeV, $120 < p_T^V < 160$ GeV and $160 < p_T^V < 200$ GeV. The pre-fit background expectation is indicated by the dashed blue line.

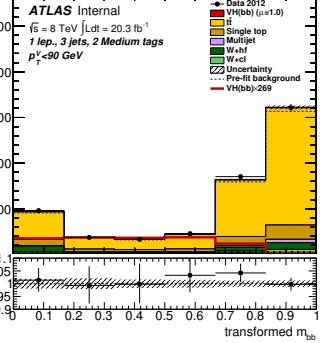
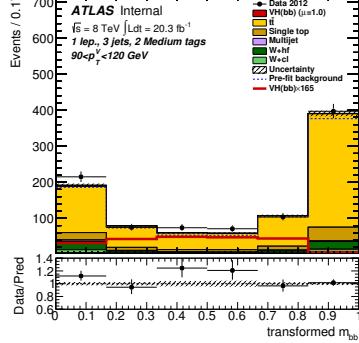
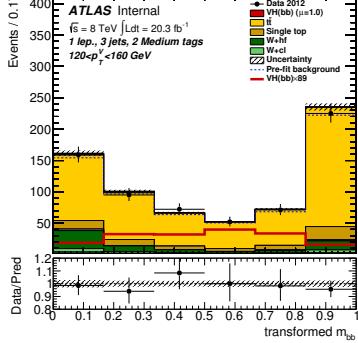
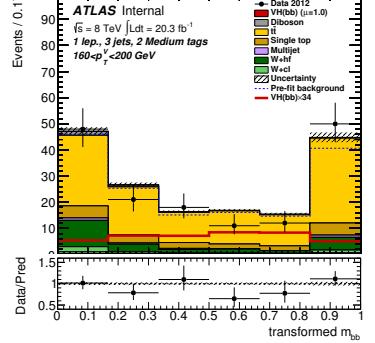
internal circulation only

(a) $p_T^V < 120$ GeV, 3 jets, 1-tag(b) $p_T^V > 120$ GeV, 3 jets, 1-tag

Events / 0.17

(c) $p_T^V < 90$ GeV, 3 jets, LL(d) $90 < p_T^V < 120$ GeV, 3 jets, LL(e) $120 < p_T^V < 160$ GeV, 3 jets, LL(f) $160 < p_T^V < 200$ GeV, 3 jets, LL

Events / 0.17

(g) $p_T^V < 90$ GeV, 3 jets, MM(h) $90 < p_T^V < 120$ GeV, 3 jets, MM(i) $120 < p_T^V < 160$ GeV, 3 jets, MM(j) $160 < p_T^V < 200$ GeV, 3 jets, MM

Events / 0.17

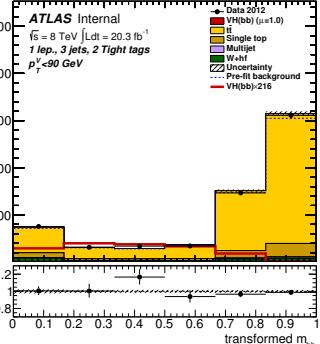
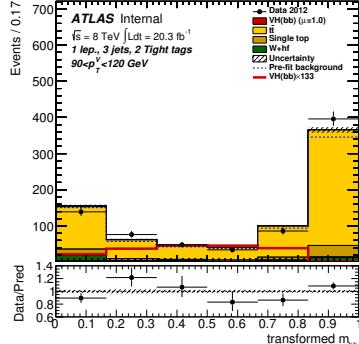
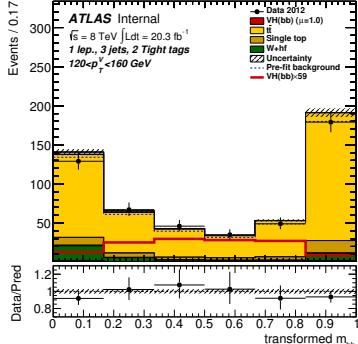
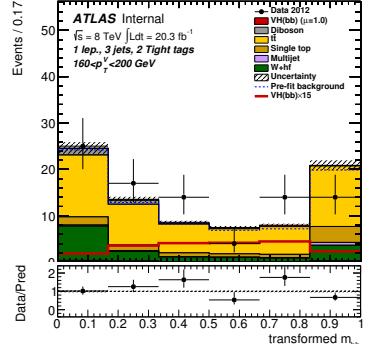
(k) $p_T^V < 90$ GeV, 3 jets, TT(l) $90 < p_T^V < 120$ GeV, 3 jets, TT(m) $120 < p_T^V < 160$ GeV, 3 jets, TT(n) $160 < p_T^V < 200$ GeV, 3 jets, TT

Figure 70: Post-fit plots for m_{jj} distribution in 1-lepton events in the 1-tag (where mv1c is used in the fit) LL, MM and TT tag categories for the 3-jets events. Plots are shown for $p_T^V < 90$ GeV, $90 < p_T^V < 120$ GeV, $120 < p_T^V < 160$ GeV and $160 < p_T^V < 200$ GeV. The pre-fit background expectation is indicated by the dashed blue line.

Not reviewed, for internal circulation only

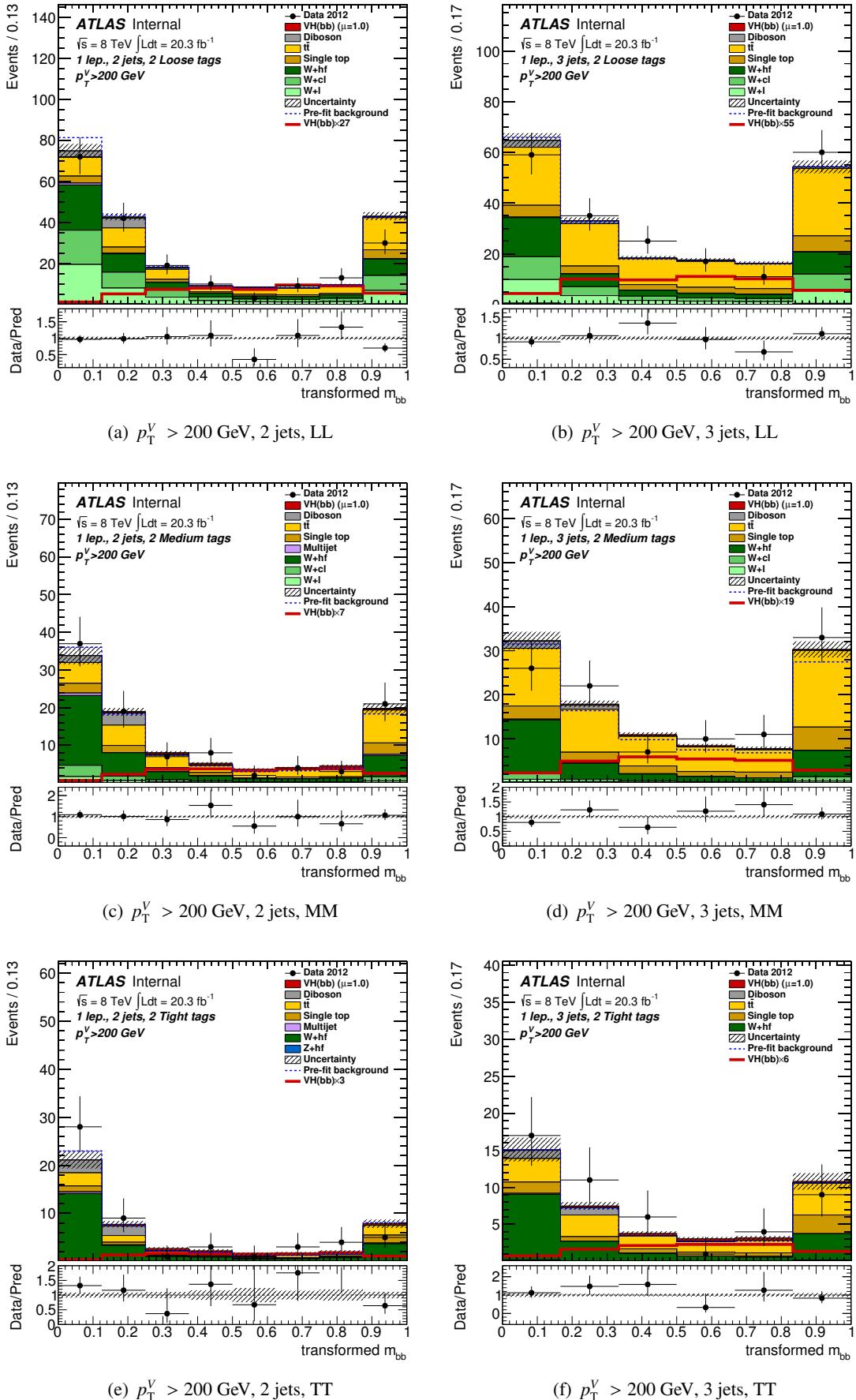


Figure 71: Post-fit plots for m_{jj} distribution in 1-lepton events in the LL , MM and TT tag categories for the 2-jets and the 3-jets events. Plots are shown for $p_T^V > 200 \text{ GeV}$. The pre-fit background expectation is indicated by the dashed blue line.

final circulation only

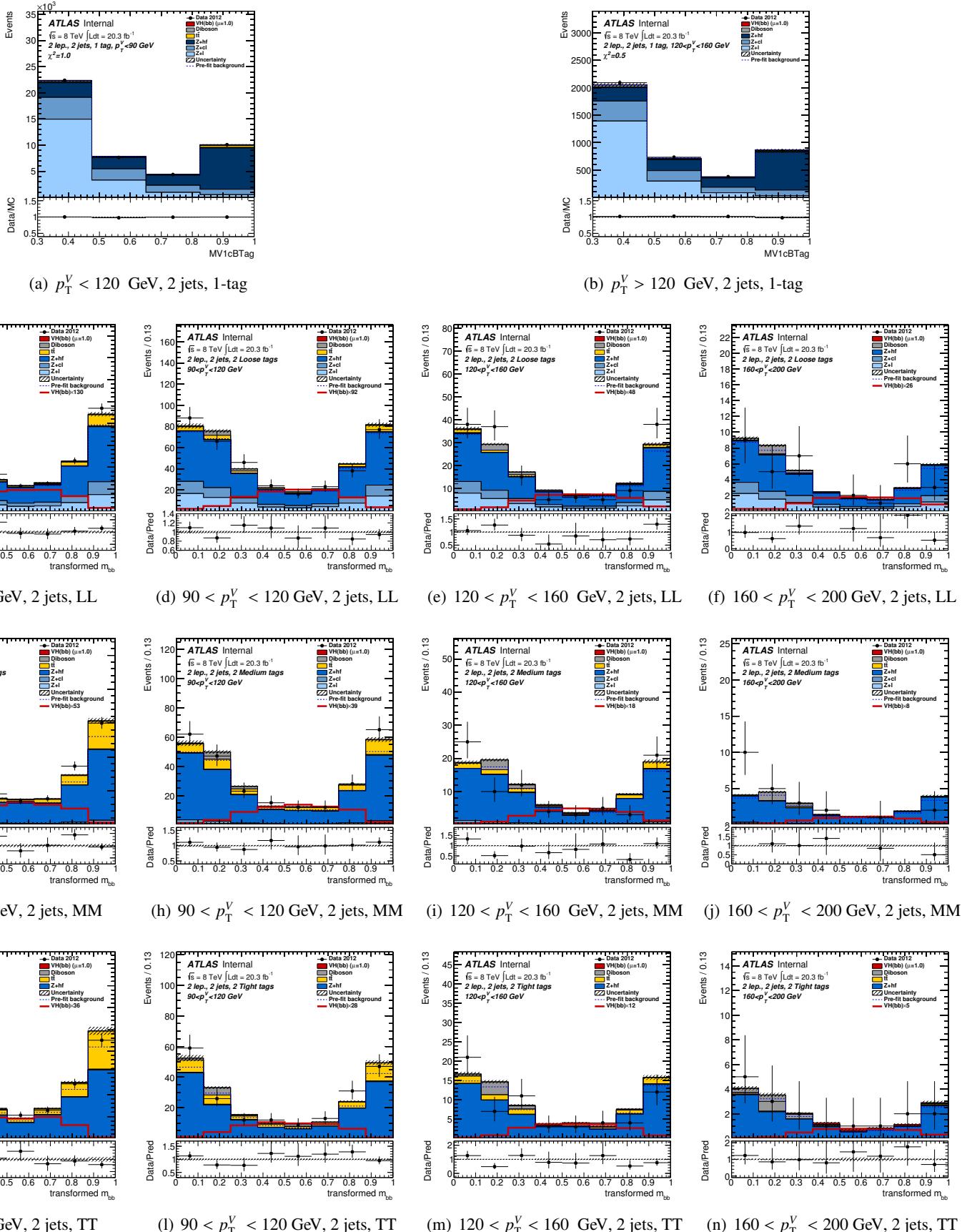


Figure 72: Post-fit plots for m_{jj} distribution in 2-lepton events in the 1-tag (where mv1c is used in the fit) LL , MM and TT tag categories for the 2-jets events. Plots are shown for $p_T^V < 90$ GeV, $90 < p_T^V < 120$ GeV, $120 < p_T^V < 160$ GeV and $160 < p_T^V < 200$ GeV. The pre-fit background expectation is indicated by the dashed blue line.

n al circulation only

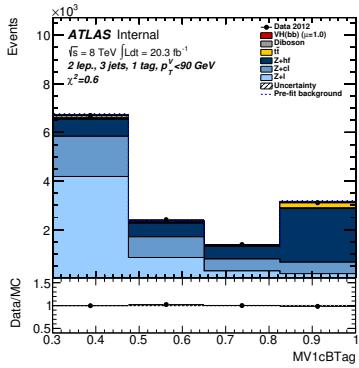
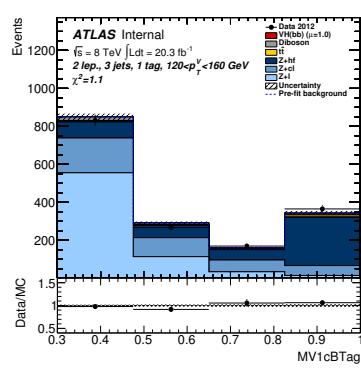
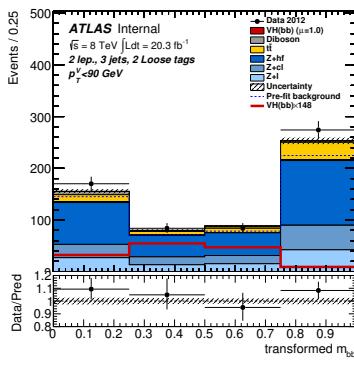
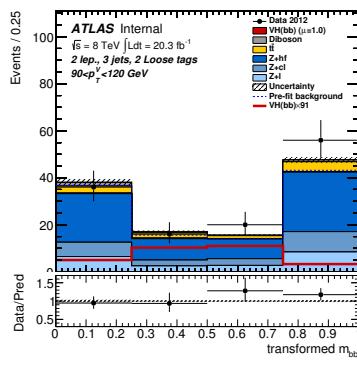
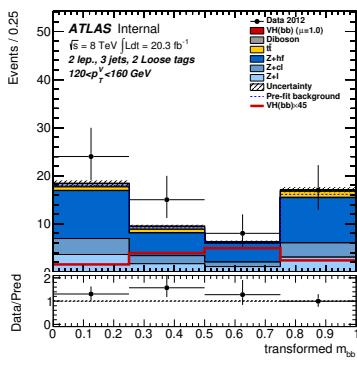
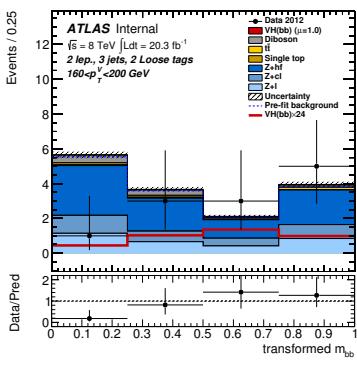
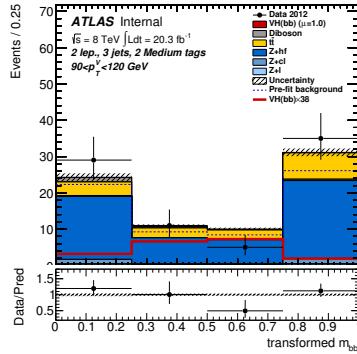
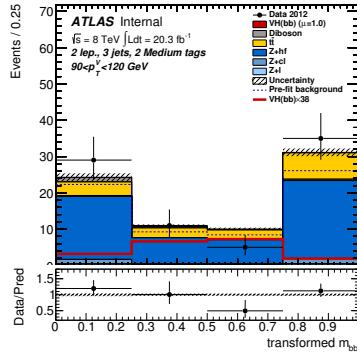
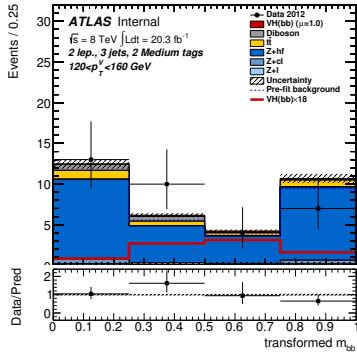
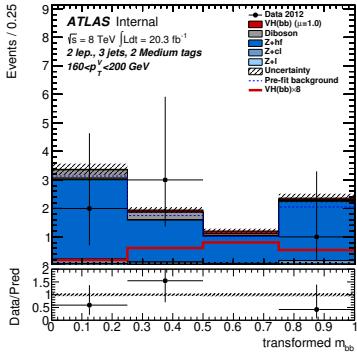
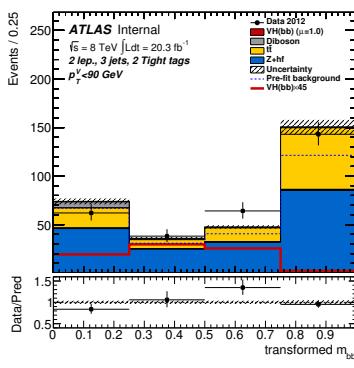
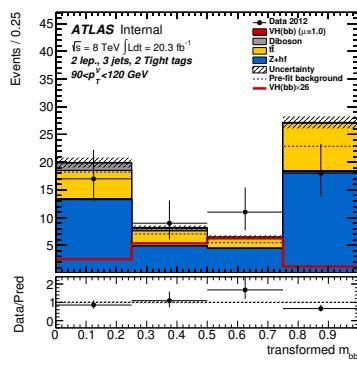
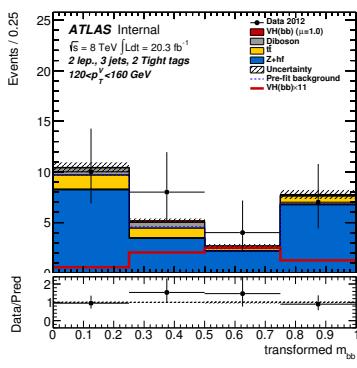
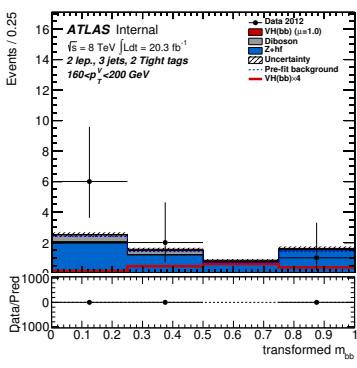
(a) $p_T^V < 120$ GeV, 3 jets, 1-tag(b) $p_T^V > 120$ GeV, 3 jets, 1-tag(c) $p_T^V < 90$ GeV, 3 jets, LL(d) $90 < p_T^V < 120$ GeV, 3 jets, LL(e) $120 < p_T^V < 160$ GeV, 3 jets, LL(f) $160 < p_T^V < 200$ GeV, 3 jets, LL(g) $p_T^V < 90$ GeV, 3 jets, MM(h) $90 < p_T^V < 120$ GeV, 3 jets, MM(i) $120 < p_T^V < 160$ GeV, 3 jets, MM(j) $160 < p_T^V < 200$ GeV, 3 jets, MM(k) $p_T^V < 90$ GeV, 3 jets, TT(l) $90 < p_T^V < 120$ GeV, 3 jets, TT(m) $120 < p_T^V < 160$ GeV, 3 jets, TT(n) $160 < p_T^V < 200$ GeV, 3 jets, TT

Figure 73: Post-fit plots for m_{jj} distribution in 2-lepton events in the 1-tag (where mv1c is used in the fit) LL, MM and TT tag categories for the 3-jets events. Plots are shown for $p_T^V < 90$ GeV, $90 < p_T^V < 120$ GeV, $120 < p_T^V < 160$ GeV and $160 < p_T^V < 200$ GeV. The pre-fit background expectation is indicated by the dashed blue line.

Not reviewed, for internal circulation only

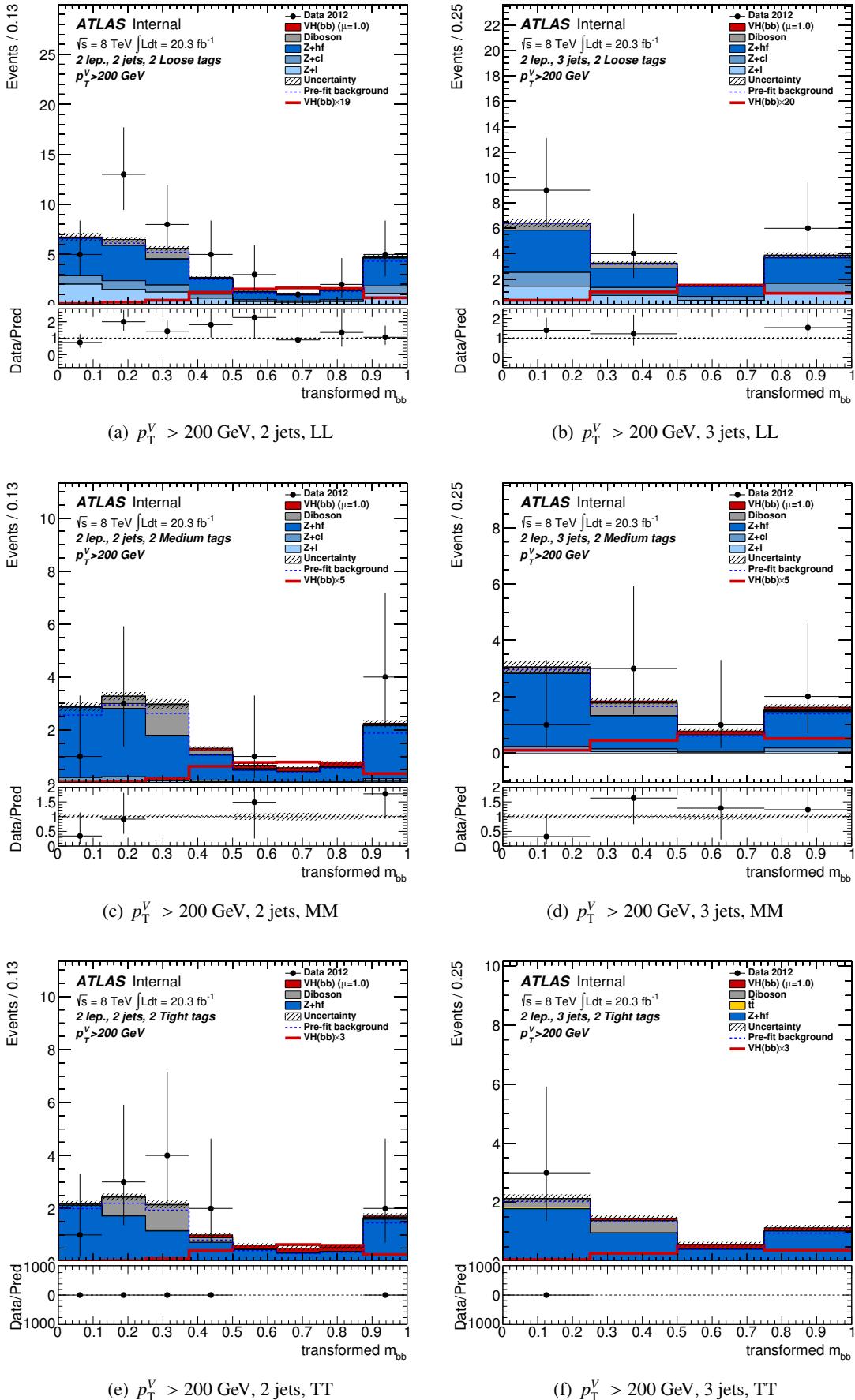


Figure 74: Post-fit plots for m_{jj} distribution in 2-lepton events in the LL , MM and TT tag categories for the 2-jets and the 3-jets events. Plots are shown for $p_T^V > 200 \text{ GeV}$. The pre-fit background expectation is indicated by the dashed blue line.

8.7.1 Normal binning

The binning adopted for the fit, coming from the Transformation D, does not allow an easy interpretation of the m_{jj} distribution. The following plots show, the m_{jj} distribution in a fixed bin size.

In Figures 75 - 77, 78 - 80, 81 - 83 post-fit plots for the m_{bb} shape analysis are shown for the 0, 1 and 2-lepton channel respectively in the various 1-tag and 2-tag categories in different p_T^V bins. They correspond to the plots in Figures 66 - 74.

Not reviewed, for internal circulation only

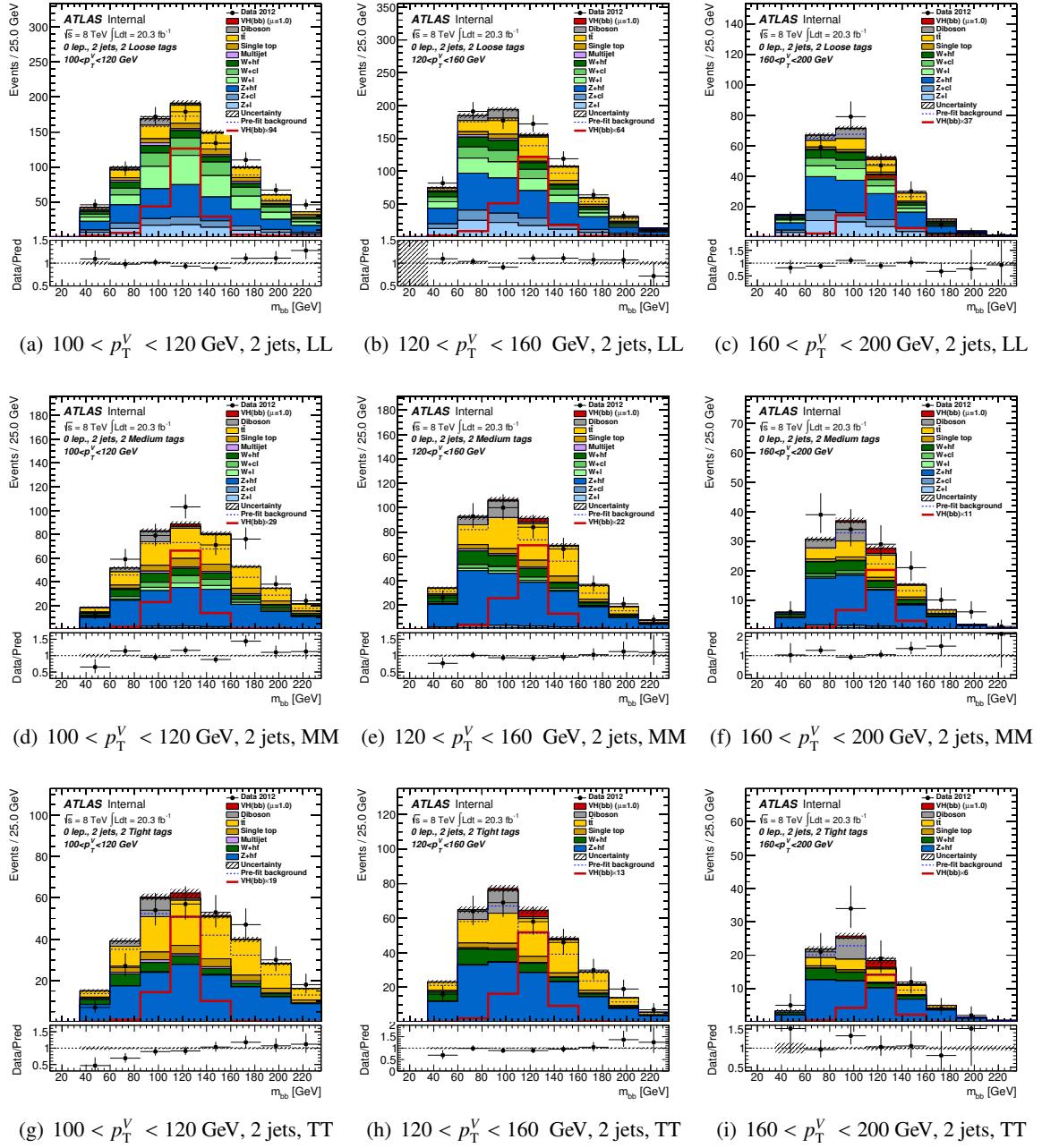


Figure 75: Post-fit plots for m_{jj} distribution in 0-lepton events in the 1-tag (where mv1c is used in the fit) LL , MM and TT tag categories for the 2-jets events. Plots are shown for $100 < p_T^V < 120 \text{ GeV}$, $120 < p_T^V < 160 \text{ GeV}$ and $160 < p_T^V < 200 \text{ GeV}$. The pre-fit background expectation is indicated by the dashed blue line.

Not reviewed, for internal circulation only

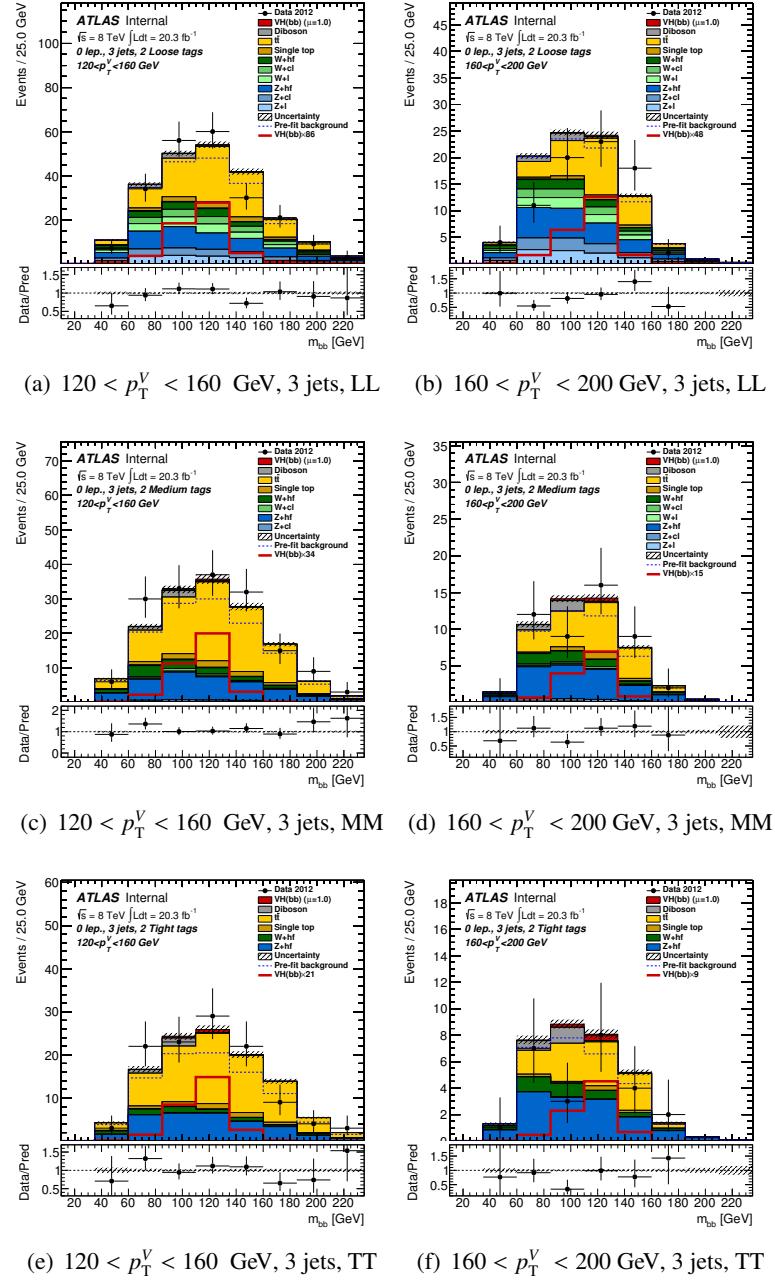


Figure 76: Post-fit plots for m_{jj} distribution in 0-lepton events in the 1-tag (where mv1c is used in the fit) *LL*, *MM* and *TT* tag categories for the 3-jets events. Plots are shown for $120 < p_T^V < 160$ GeV and $160 < p_T^V < 200$ GeV. The pre-fit background expectation is indicated by the dashed blue line.

Not reviewed, for internal circulation only

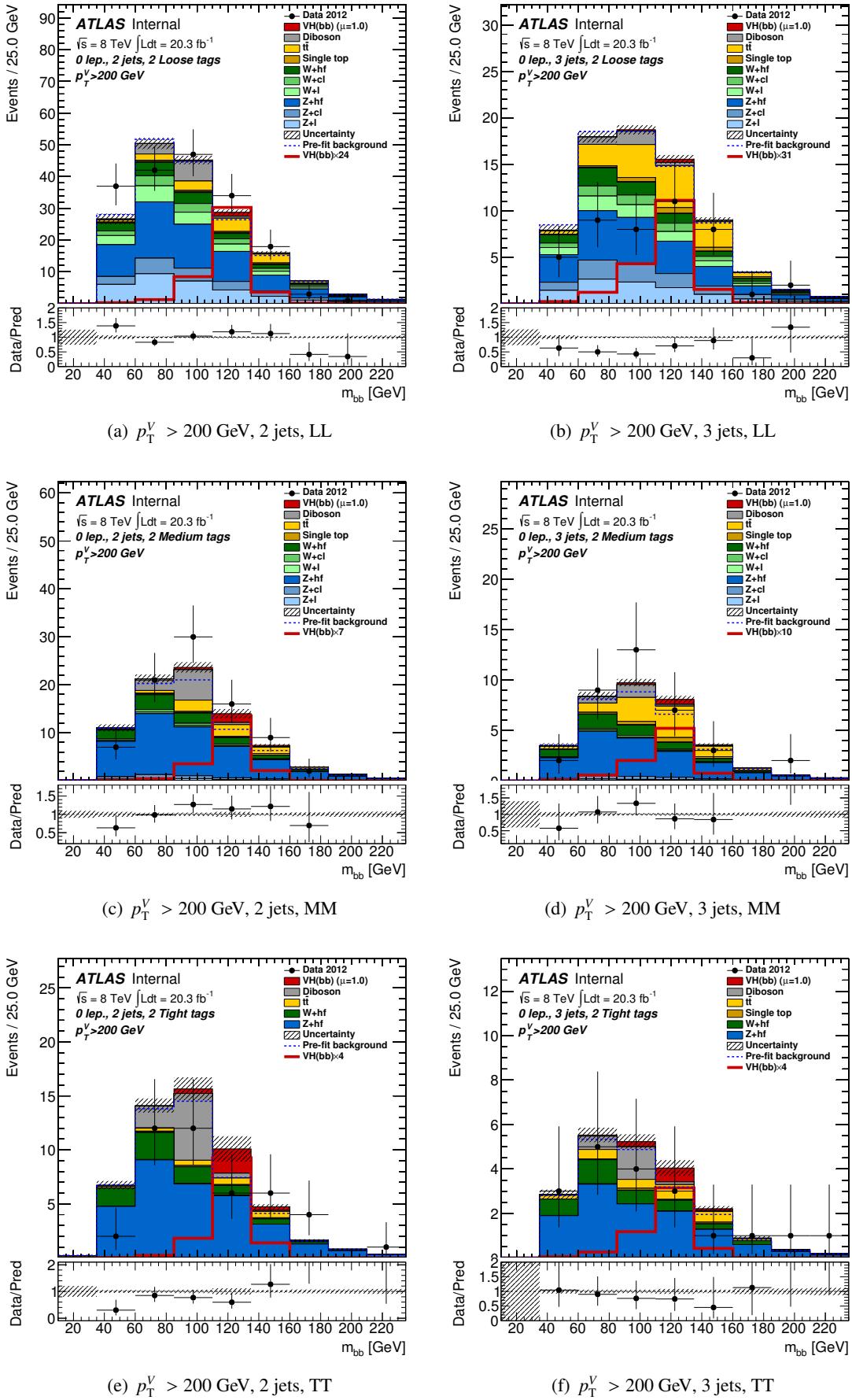


Figure 77: Post-fit plots for m_{jj} distribution in 0-lepton events in the *LL*, *MM* and *TT* tag categories for the 2-jets and the 3-jets events. Plots are shown for $p_T^V > 200$ GeV. The pre-fit background expectation is indicated by the dashed blue line.

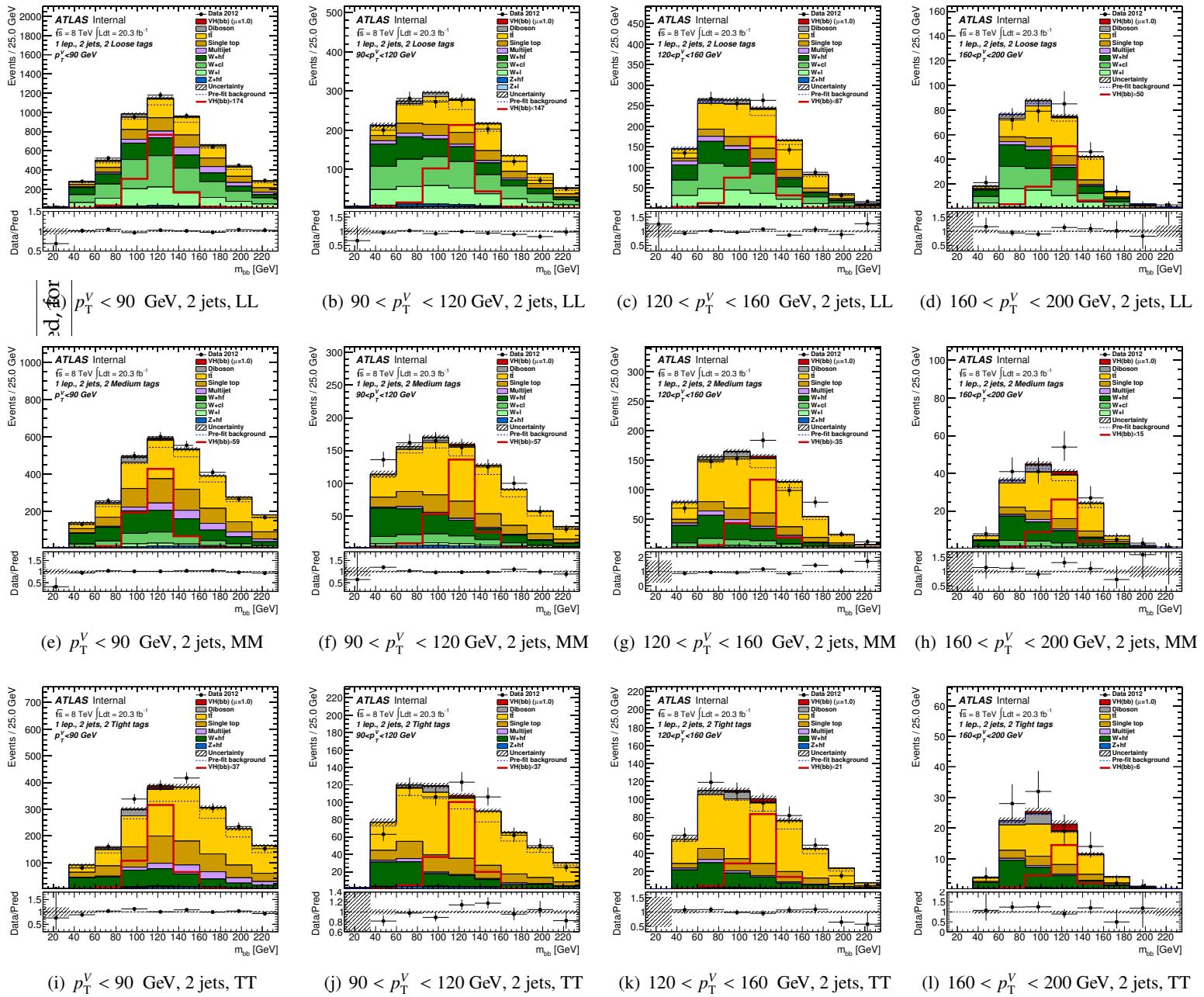


Figure 78: Post-fit plots for m_{jj} distribution in 1-lepton events in the 1-tag (where mv1c is used in the fit) LL , MM and TT tag categories for the 2-jets events. Plots are shown for $p_T^V < 90$ GeV, $90 < p_T^V < 120$ GeV, $120 < p_T^V < 160$ GeV and $160 < p_T^V < 200$ GeV. The pre-fit background expectation is indicated by the dashed blue line.

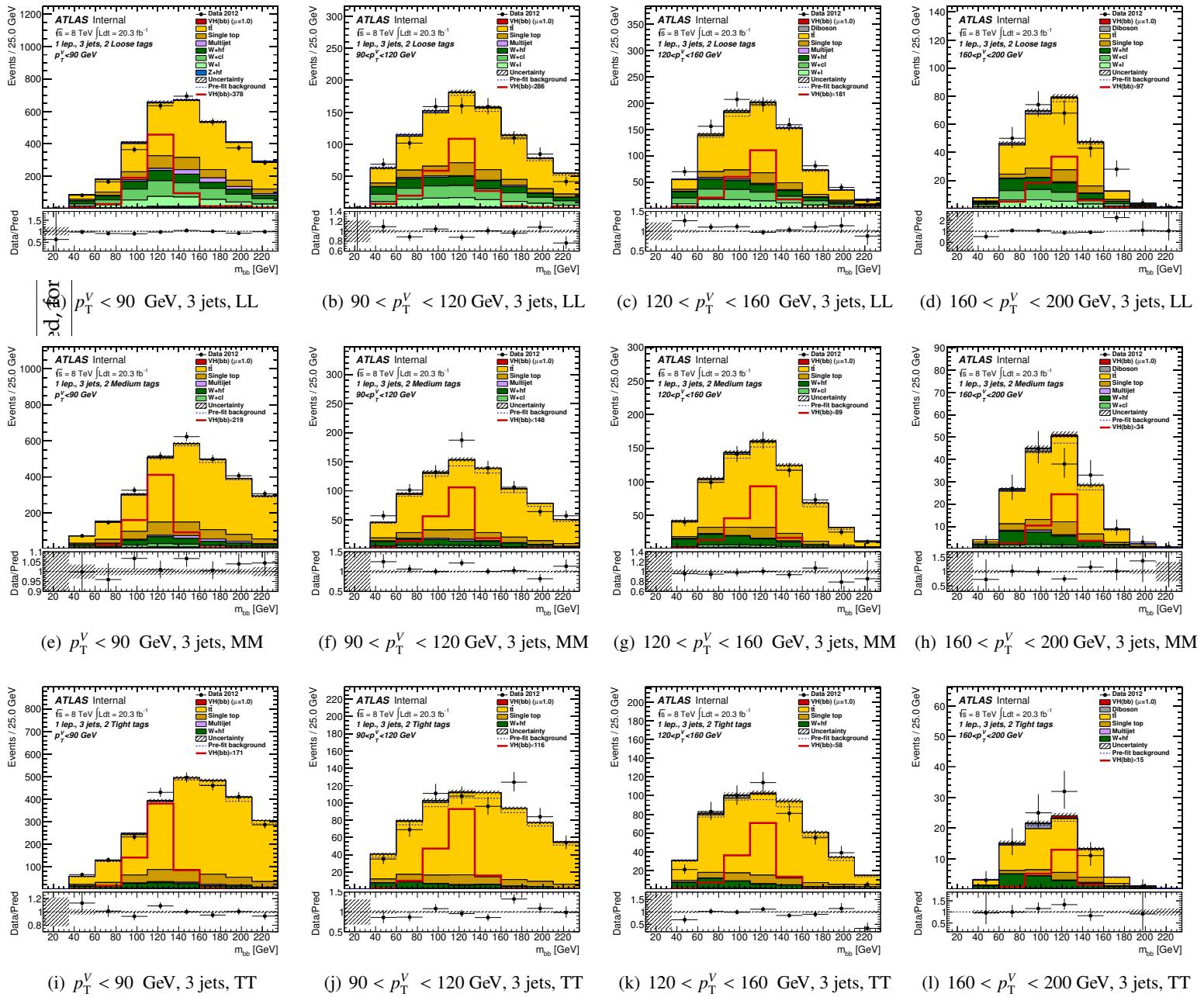


Figure 79: Post-fit plots for m_{jj} distribution in 1-lepton events in the 1-tag (where mv1c is used in the fit) LL , MM and TT tag categories for the 3-jets events. Plots are shown for $p_T^V < 90$ GeV, $90 < p_T^V < 120$ GeV, $120 < p_T^V < 160$ GeV and $160 < p_T^V < 200$ GeV. The pre-fit background expectation is indicated by the dashed blue line.

Not reviewed, for internal circulation only

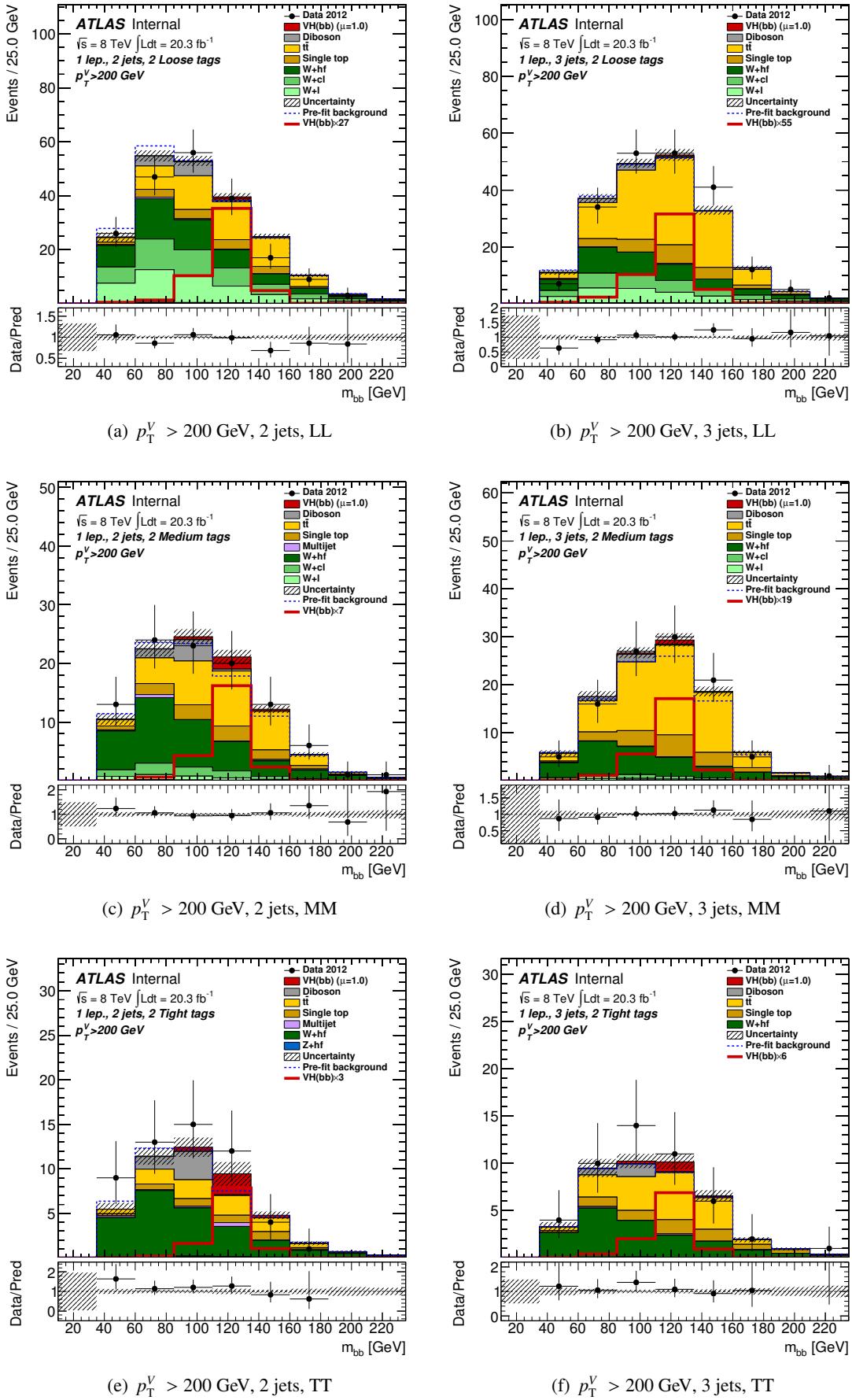


Figure 80: Post-fit plots for m_{jj} distribution in 1-lepton events in the LL , MM and TT tag categories for the 2-jets and the 3-jets events. Plots are shown for $p_T^V > 200 \text{ GeV}$. The pre-fit background expectation is indicated by the dashed blue line.

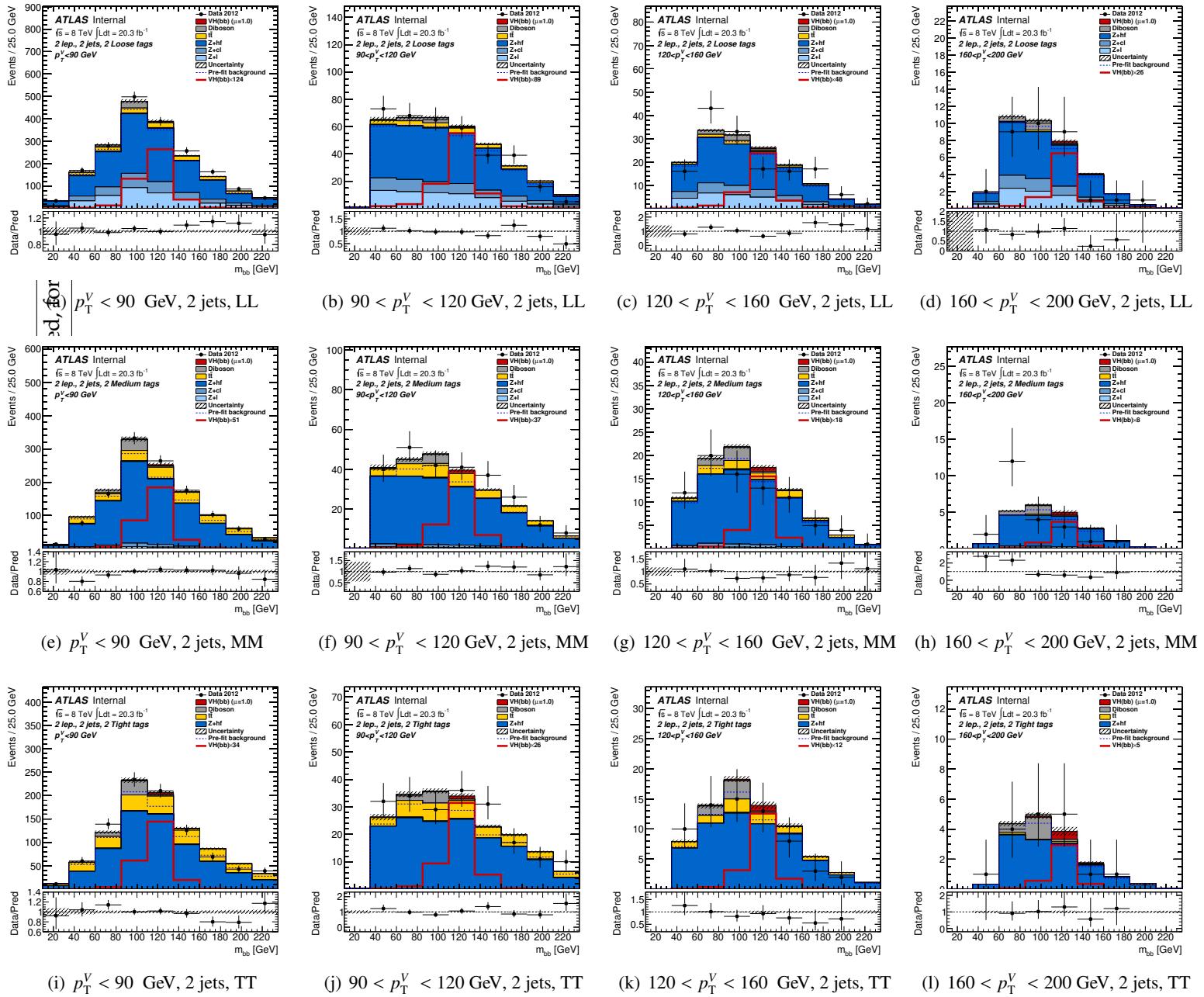


Figure 81: Post-fit plots for m_{jj} distribution in 2-lepton events in the 1-tag (where mv1c is used in the fit) LL , MM and TT tag categories for the 2-jets events. Plots are shown for $p_T^V < 90$ GeV, $90 < p_T^V < 120$ GeV, $120 < p_T^V < 160$ GeV and $160 < p_T^V < 200$ GeV. The pre-fit background expectation is indicated by the dashed blue line.

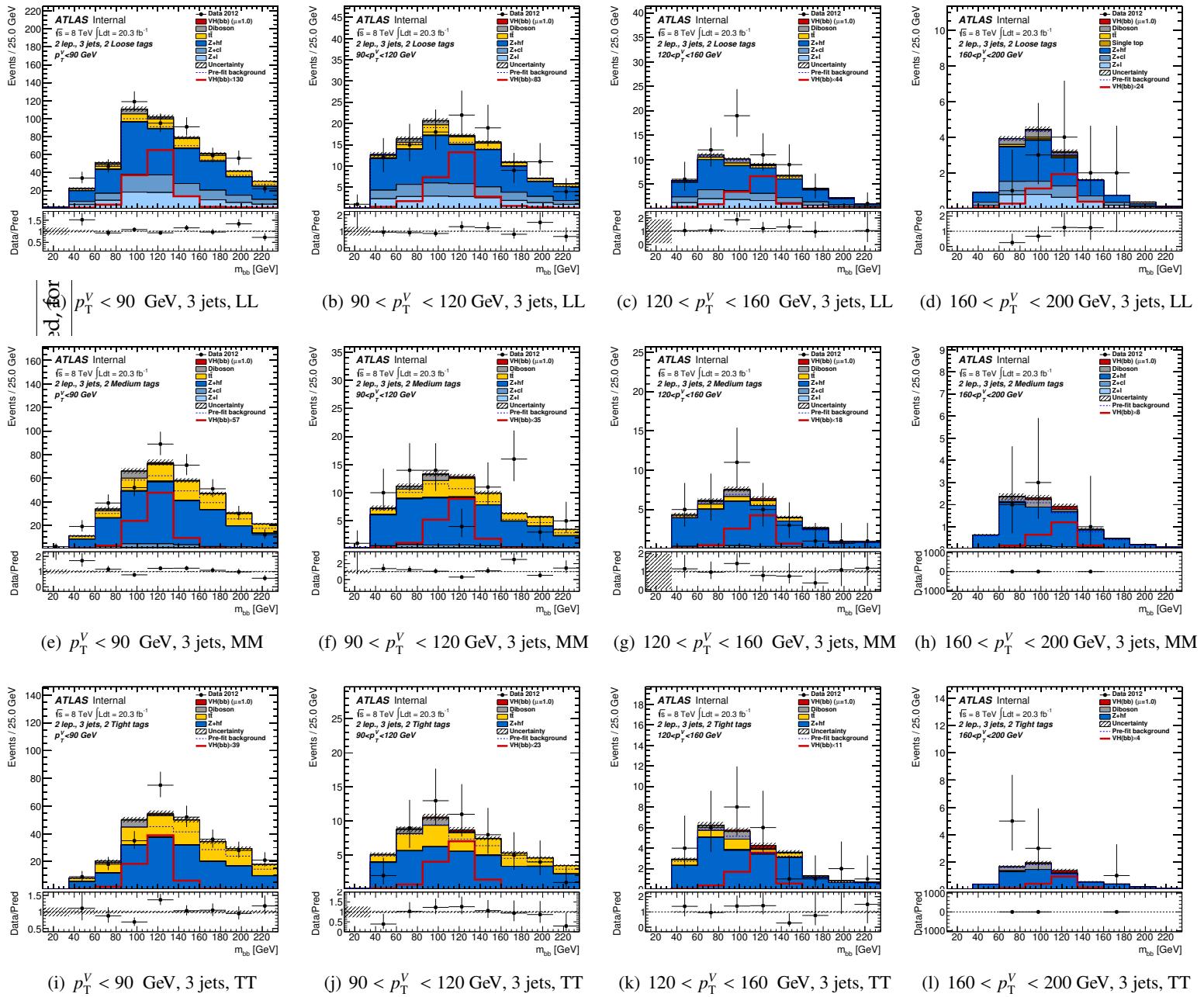


Figure 82: Post-fit plots for m_{jj} distribution in 2-lepton events in the 1-tag (where mv1c is used in the fit) LL, MM and TT tag categories for the 3-jets events. Plots are shown for $p_T^V < 90$ GeV, $90 < p_T^V < 120$ GeV, $120 < p_T^V < 160$ GeV and $160 < p_T^V < 200$ GeV. The pre-fit background expectation is indicated by the dashed blue line.

Not reviewed, for internal circulation only

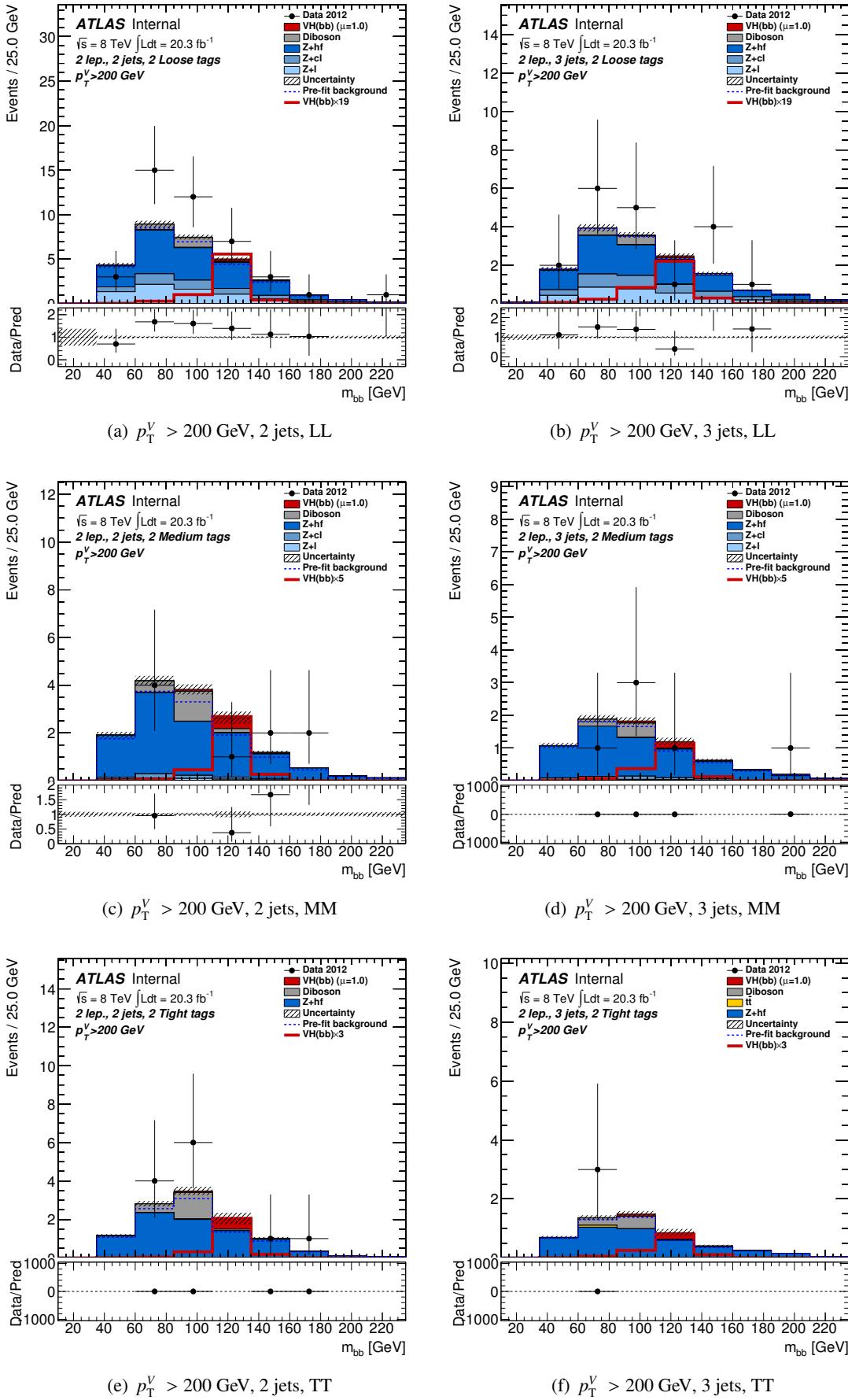


Figure 83: Post-fit plots for m_{jj} distribution in 2-lepton events in the *LL*, *MM* and *TT* tag categories for the 2-jets and the 3-jets events. Plots are shown for $p_T^V > 200$ GeV. The pre-fit background expectation is indicated by the dashed blue line.

3040 8.7.2 Post fit b-tagging for the m_{jj} shape analysis

3041 In order to understand the effect of the pulls on the b-tagging related parameters the scale factor and
3042 related uncertainties are unfold from the fit and shown as a function of jet p_T .

3043 As an examples, in Figure 84 we show the plots for the scale factors obtained in the m_{jj} 0+1+2
3044 leptons combined fit .

Not reviewed, for internal circulation only

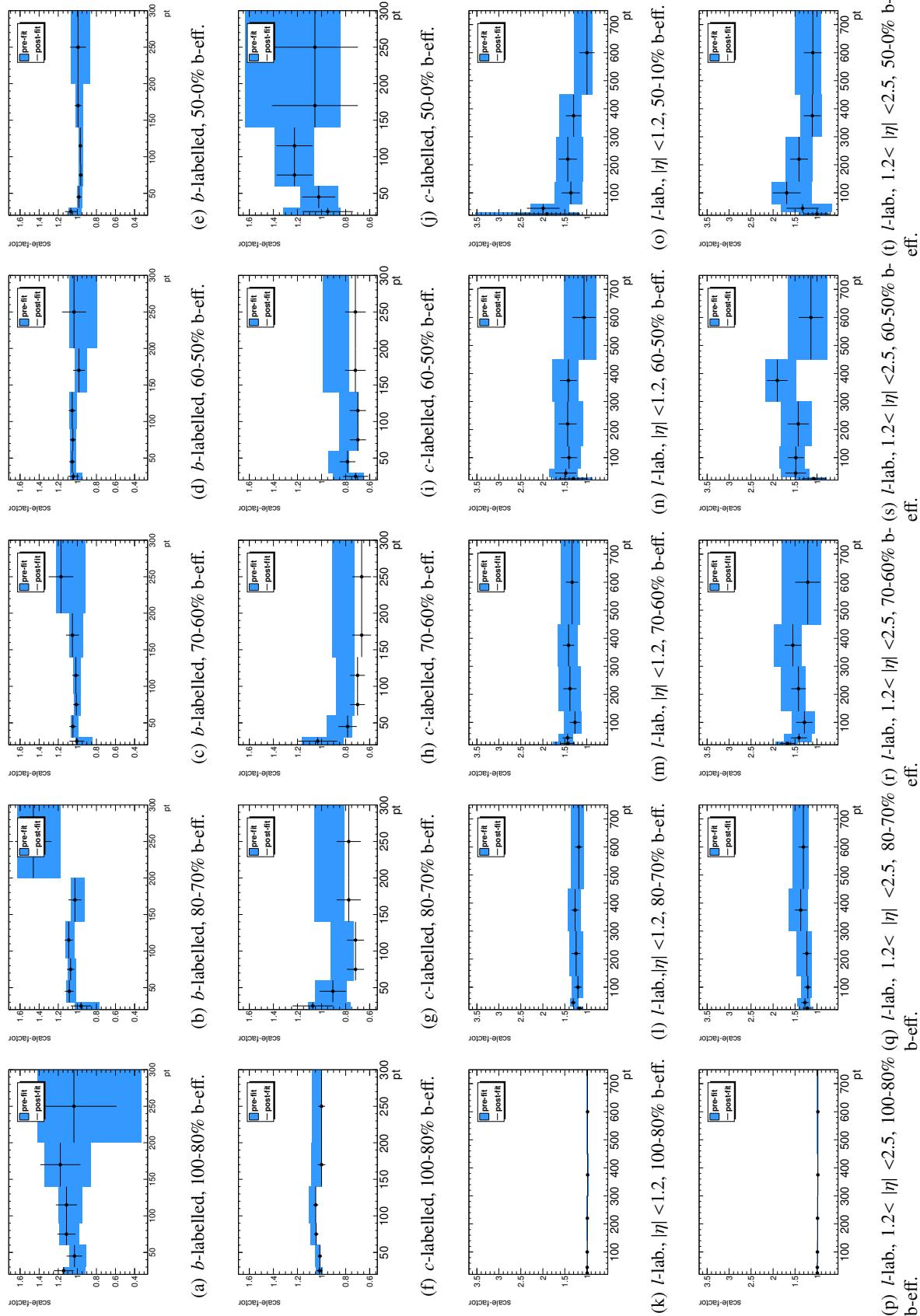


Figure 84: The MC-to-data post-fit unfolded calibration scale factors for the MV1c b , c -jet as a function of the jet p_T .

3045 8.8 MVA background-only post fit plots

3046 In the following sections post-fit plots corresponding to background-only fits to the data for the MVA
3047 analysis are presented. In all cases the MC expectations have been adapted to the pulls from the data in
3048 the combined 0+1+2 lepton fit. As a comparison, the total nominal background prediction is indicated
3049 by the dashed blue curve. Only statistical uncertainties are indicated. All the plots do not show the data
3050 points in the regions where the signal is expected to be at least 2% of the total background.

3051 In Figures 543, 544 and 545 shown the post-fit distribution for the variables used in the MVA shape
3052 analysis for the 0, 1 and 2-lepton channel respectively in the various 2-tag categories in different p_T^V bins.

Not reviewed, for internal circulation only

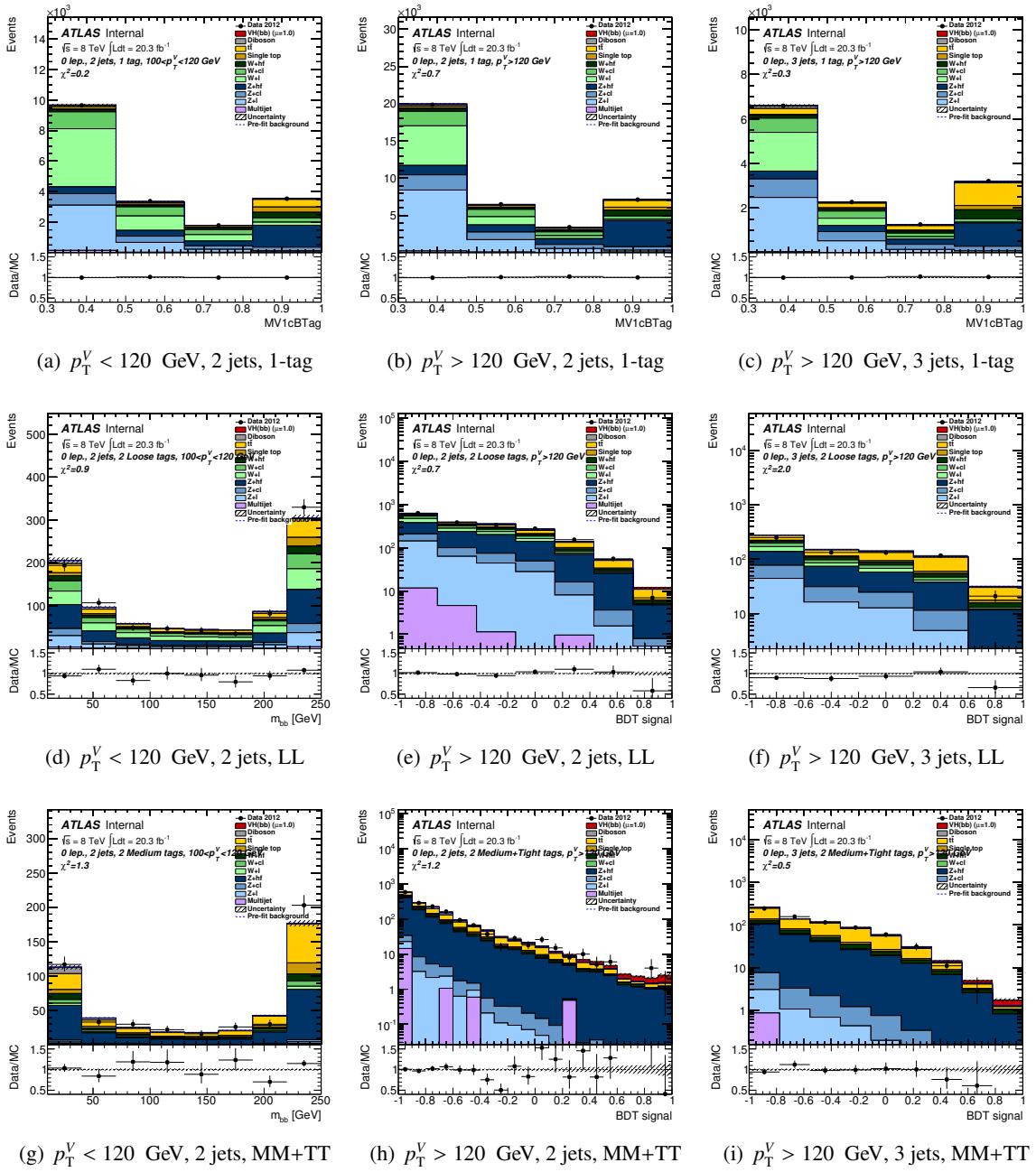


Figure 85: Post-fit plots for mva distribution in 0-lepton events with 1 b-tag (MV1c is fit here), LL and $MM + TT$ b-tags in the 0+1+2 lepton fit. The pre-fit background expectation is indicated by the dashed blue line. Only statistical uncertainties are indicated.

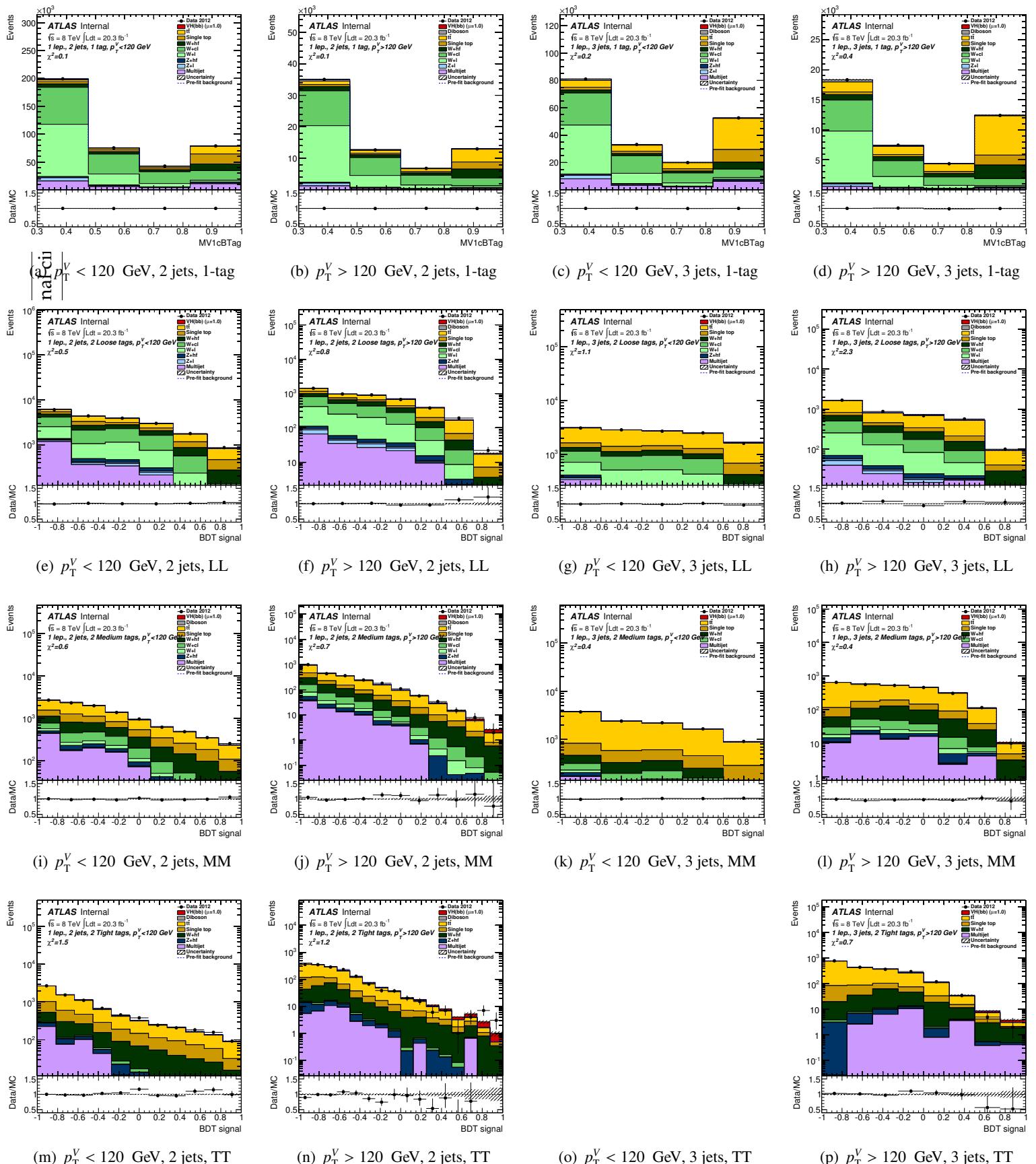


Figure 86: Post-fit plots for MVA distribution in 1-lepton 2-jet and 3-jets, $p_T^V < 120$ GeV and $p_T^V > 120$ GeV events with 1 b-tag (MV1c is fit here), LL, MM and TT b-tags in the 0+1+2 lepton fit. The pre-fit background expectation is indicated by the dashed blue line. Only statistical uncertainties are indicated.

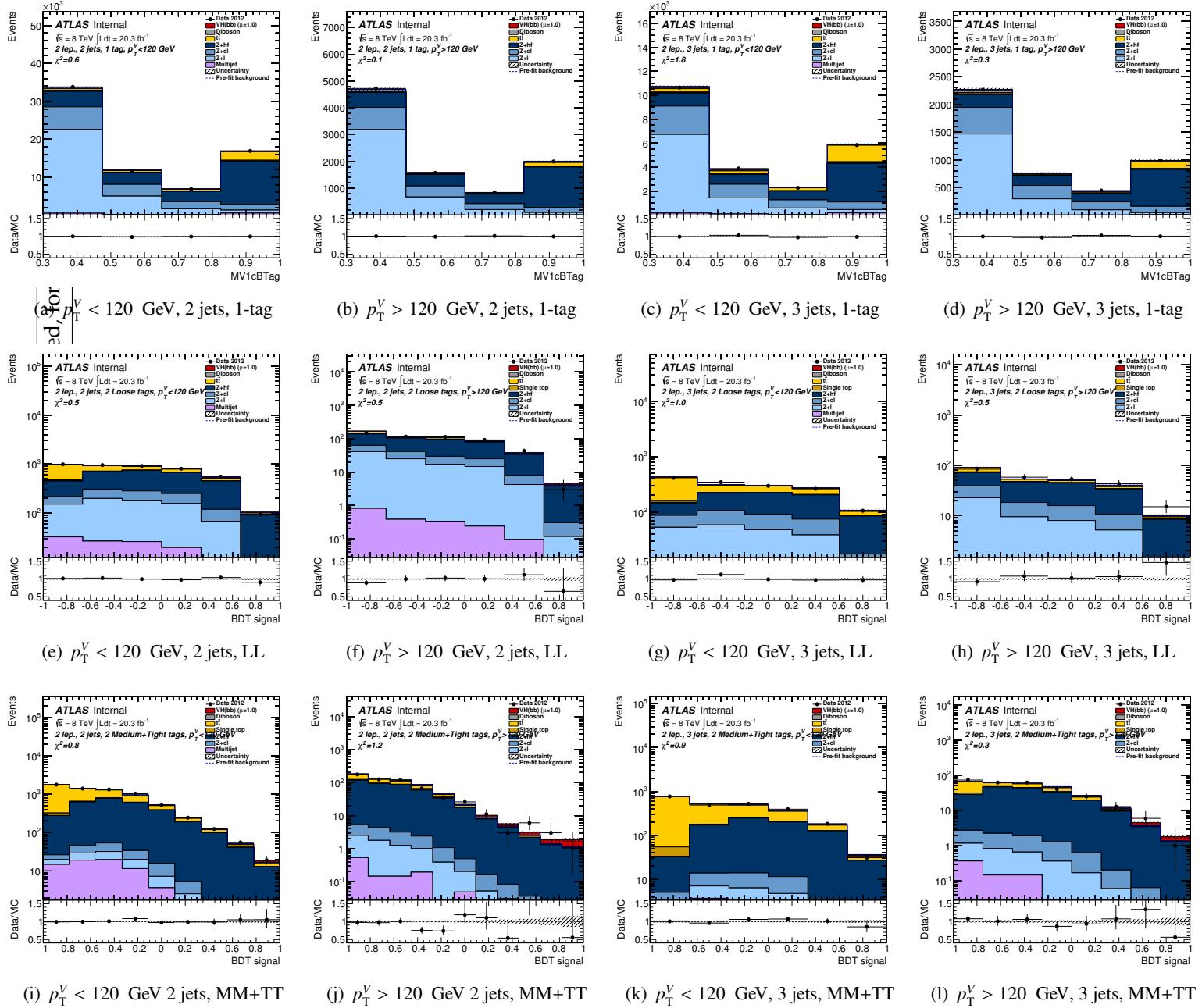


Figure 87: Post-fit plots for MVA distribution in 2-lepton 2-jet and 3-jets , $p_T^V < 120 \text{ GeV}$ (left) and $p_T^V > 120 \text{ GeV}$ (right) events with 1 b-tag (MV1c is fit here), *LL* and *MM + TT* b-tags in the 0+1+2 lepton fit. The pre-fit background expectation is indicated by the dashed blue line. Only statistical uncertainties are indicated.

3053 8.8.1 Post fit b-tagging for the MVA analysis

3054 In order to understand the effect of the pulls on the b-tagging related parameters the scale factor and
3055 related uncertainties are unfold from the fit and shown as a function of jet p_T .

3056 As an examples, in Figure 88 we show the plots for the scale factors obtained in the MVA0+1+2
3057 leptons combined fit .

Not reviewed, for internal circulation only

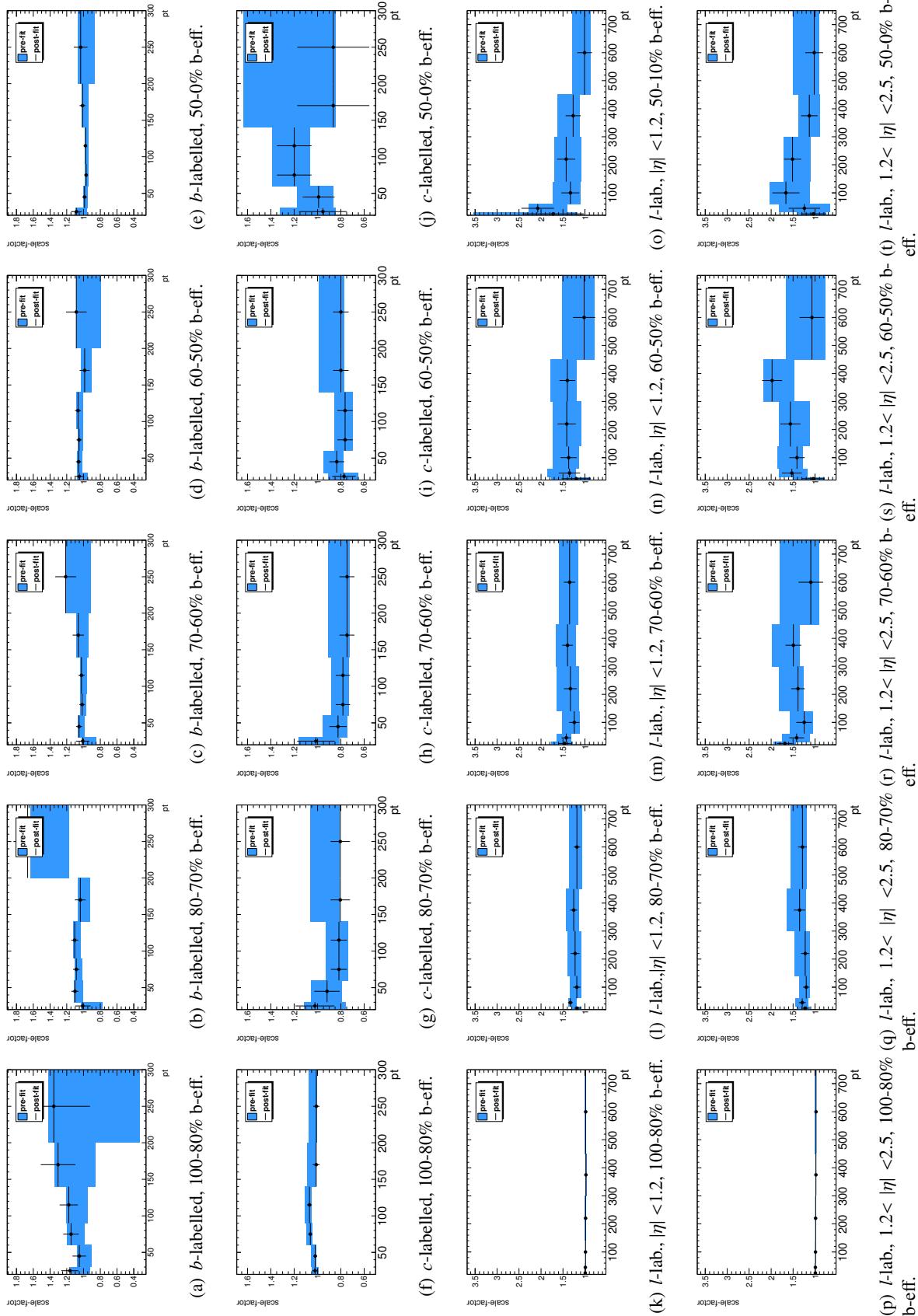


Figure 88: The MC-to-data post-fit unfolded calibration scale factors for the MV1c b , c -jet as a function of the jet p_T .

3058 8.9 Compatibility between the m_{bb} shape analysis and the MVA analysis

3059 Given the significant but incomplete statistical overlap between the datasets used for the m_{bb} shape and
 3060 MVA analyses, the correlation between the results needs to be estimated. A modified bootstrap technique
 3061 was used to assess the correlation due to the statistical overlap. No attempt was made to estimate the
 3062 correlation due to the systematics.

3063 Synchronised pseudo-datasets for the m_{bb} shape and MVA analyses are produced. These pseudo-
 3064 datasets are then fit and the correlation between the $\hat{\mu}$ value obtained in each analysis is estimated.

3065 The modified bootstrap technique is implemented technically considering each event from each MC
 3066 sample used in the analysis. For each event, a number, n is drawn from a Poisson distribution of mean
 3067 $|w|$, where w is the weight corresponding to the specific MC event. The event is then added n times to
 3068 the pseudo-dataset with the weight as ± 1 . This effectively selects a subsets of the full statistics of the
 3069 MC sample by weighting each event appropriately. The final events in the pseudo-data are unweighted
 3070 as a result of the technique. The seeds for the random numbers are determined by the event number such
 3071 that the selected events are correlated between the pseudo-data for the m_{bb} shape analysis and the MVA
 3072 analysis.

3073 Figure 89 shows the distribution of the difference of $\hat{\mu}$ obtained for the m_{bb} shape analysis and the
 3074 MVA analysis respectively using 800 - 900 (285 events for the combined 0+1+2 leptons analysis) events
 3075 from the pseudo-data for the combination for 0, 1, 2 and 0+1+2 lepton analyses. The relation between
 3076 $\hat{\mu}_{\text{MVA}}$ obtained in each analysis is shown in Figure 90. There is a clear relation between the two and the
 3077 correlation factor was extracted and found to be 0.68. The same study was repeated for fits to each of the
 3078 individual channels and the results are summarised in Table 57. The correlation is largest for the 0-lepton
 3079 channel (0.74) and slightly lower for the 2-lepton channel (0.58), as expected because the phase space
 3080 accessed by the MVA analysis differs more significantly in the 2-lepton channel than the 0-lepton channel.

Channel	Correlation
0-lepton	0.74
1-lepton	0.65
2-lepton	0.58
Combination	0.66

Table 57: The correlation between the measured signal strength in the dijet mass and MVA analyses.

Not reviewed, for internal circulation only

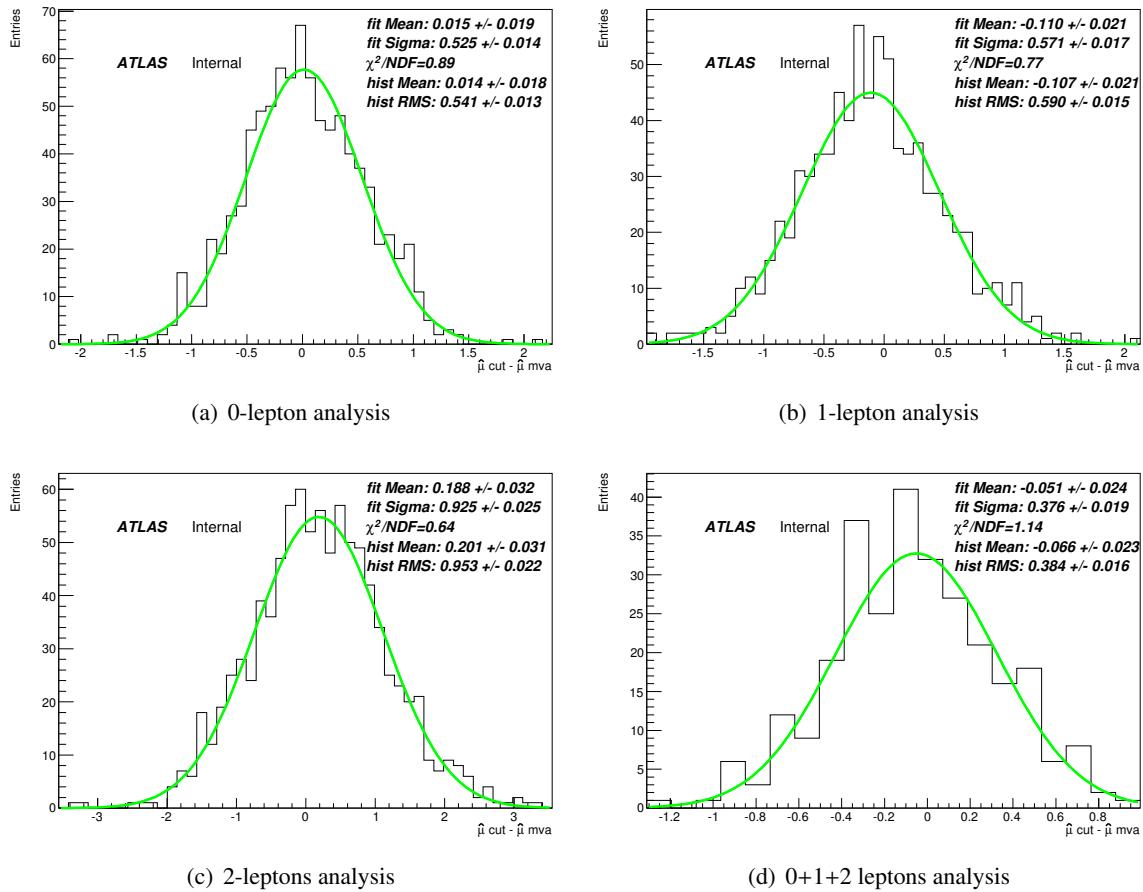


Figure 89: The distribution of the difference of the signal strength for the m_{bb} shape and MVA analyses from the pseudo-data from the bootstrap technique for the combination of the 0, 1, 2 and 0+1+2 lepton channels.

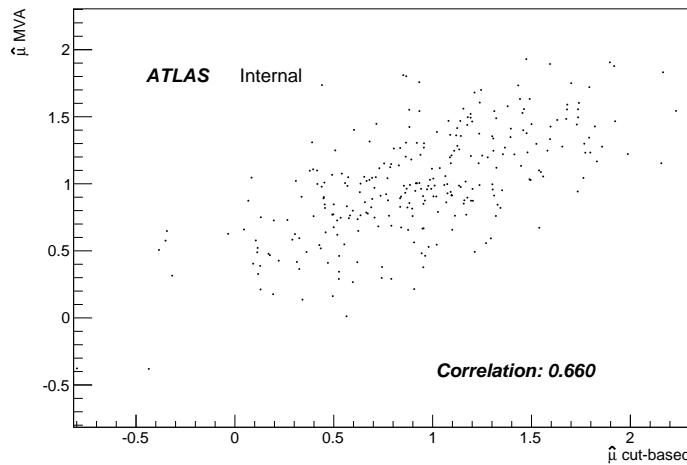


Figure 90: The relation between the signal strength obtained from the m_{bb} shape and MVA analyses for the combination of the 0- and 2-lepton channels.

3081 9 Results

3082 As explained in Section 8, the results are obtained from maximum-likelihood fits to the data, where the
 3083 inputs are the distributions of final discriminants in the 2-tag signal regions and the $MV1c$ distributions
 3084 of the b -tagged jet in the 1-tag control regions, with nuisance parameters either floating or constrained by
 3085 priors. The final discriminants are the transformed m_{bb} for the dijet-mass analysis and the BDT discrim-
 3086 inants for the MVA. Results are extracted independently for the dijet-mass and multivariate analyses.
 3087 Since the MVA has better expected sensitivity to a Higgs-boson signal, it is used for the nominal results,
 3088 while the dijet-mass analysis provides a cross-check (cf. Section 9.2). For the 7 TeV data, however, only
 3089 a dijet-mass analysis is performed. Unless otherwise specified, all results refer to a Higgs-boson mass of
 3090 125 GeV.

3091 **9.1 Nominal results**

3092 The nominal results are obtained from global fits using the MVA for the 8 TeV data and the dijet-mass
 3093 analysis of the 7 TeV data.

3094 Distributions of the BDT discriminant and of $MV1c$, with background normalisations and nuisance
 3095 parameters adjusted by the global fit to the 8 TeV data were already presented in Section 8. Dijet-mass
 3096 distributions in the 7 TeV data analysis were shown in Section AK which need to be updated in this note.
 3097 Agreement between data and estimated background is observed within the uncertainties shown by the
 3098 hashed bands.

3099 Figure 91 shows the 95% CL upper limits on the cross section times branching ratio for $pp \rightarrow$
 3100 $(W/Z)(H \rightarrow b\bar{b})$ in the mass range 110–140 GeV. The observed limit for $m_h = 125$ GeV is 1.2 times the
 3101 SM value, to be compared to an expected limit, in the absence of signal, of 0.8. For the 8 TeV (7 TeV)
 3102 data only, the observed and expected limits are 1.4 (2.3) and 0.8 (3.2), respectively.

3103 The probability p_0 of obtaining a result at least as signal-like as observed if no signal is present is 8%
 3104 for a tested Higgs-boson mass of 125 GeV, to be compared to an expectation of 0.5% in the presence of
 3105 a SM Higgs boson with that mass. This corresponds to an excess observed with a significance of 1.4σ ,
 3106 to be compared to an expectation of 2.6σ . For the 8 TeV data only, the observed and expected levels of
 3107 significance are 1.7σ and 2.5σ , respectively. For the 7 TeV data only, the expected significance is 0.7σ
 3108 and there is a deficit rather than an excess in the data, as can be seen in figure 95.b. Figure 92 shows the
 3109 p_0 values in the mass range 110–140 GeV, as obtained for the 7 TeV and 8 TeV combined dataset.

3110 The fitted μ values for $m_h = 125$ GeV are shown in figure 93 for the 7 TeV, 8 TeV and combined
 3111 datasets. With all lepton channels and data-taking periods combined, the fitted value of the signal-
 3112 strength parameter is⁷ $\mu = 0.51 \pm 0.31(\text{stat.}) \pm 0.24(\text{syst.})$. For the 8 TeV (7 TeV) data, the fitted value of
 3113 the signal-strength parameter is $\mu = 0.65 \pm 0.32(\text{stat.}) \pm 0.26(\text{syst.})$ ($\mu = -1.6 \pm 1.2(\text{stat.}) \pm 0.9(\text{syst.})$).

3114 For a Higgs boson with a mass of 125.36 GeV, as measured by ATLAS [69], the signal-strength
 3115 parameter is $\mu = 0.52 \pm 0.32(\text{stat.}) \pm 0.24(\text{syst.})$.

3116 Fits are also performed where the signal strengths are floated independently for (i) the WH and
 3117 ZH production processes, or (ii) the three lepton channels. The results of these fits are also shown in
 3118 figure 93. The consistency of the fitted signal strengths in the WH and ZH processes is at the level of
 3119 20%. For the lepton channels, the consistency between the three fitted signal strengths is at the level
 3120 of 72% for the 7 TeV data, and of 8% for the 8 TeV data. The low values of the fitted signal strengths
 3121 for the ZH process and in the 0-lepton channel are associated with the data deficit observed in the most
 3122 sensitive bins of the BDT discriminant in the 0-lepton channel.

3123 Figure 94 shows the data, background and signal yields, where final-discriminant bins in all signal
 3124 regions are combined into bins of $\log(S/B)$, separately for the 7 and 8 TeV datasets. Here, S is the

⁷The uncertainties of the normalisations of the floating backgrounds are included in the systematic uncertainties; however, the contribution is only 0.07.

Not reviewed, for internal circulation only

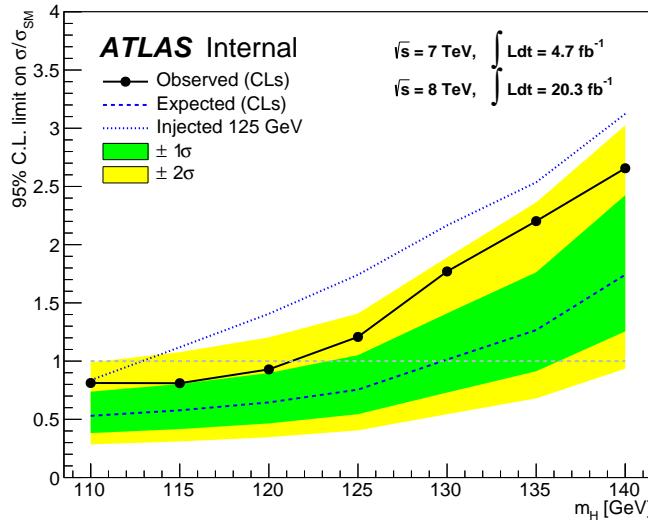


Figure 91: Observed (solid) and expected 95% CL cross section upper limits, normalised to the SM Higgs-boson production cross section, as a function of m_h for all channels and data taking periods combined, as obtained using the dijet mass analysis for the 7 TeV dataset and BDTs trained at each individual mass for the 8 TeV dataset. The expected upper limit is given for the background-only hypothesis (dashed) and with the injection of a SM Higgs-boson signal at a mass of 125 GeV (dotted). The green and yellow bands represent the 1σ and 2σ ranges of the expectation in the absence of a signal.

₃₁₂₅ expected signal yield and B is the fitted background yield. Details of the fitted values of the signal and

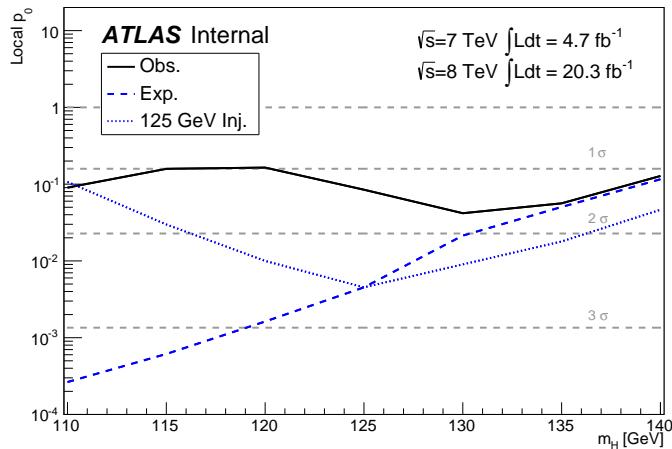


Figure 92: Observed (solid) and expected p_0 values as a function of m_h for all channels and data taking periods combined, as obtained using the dijet mass analysis for the 7 TeV dataset and BDTs trained at each individual mass for the 8 TeV dataset. The expected p_0 values are given for the background-only hypothesis (dashed) and with the injection of a SM Higgs-boson signal at a mass of 125 GeV (dotted).

Not reviewed, for internal circulation only

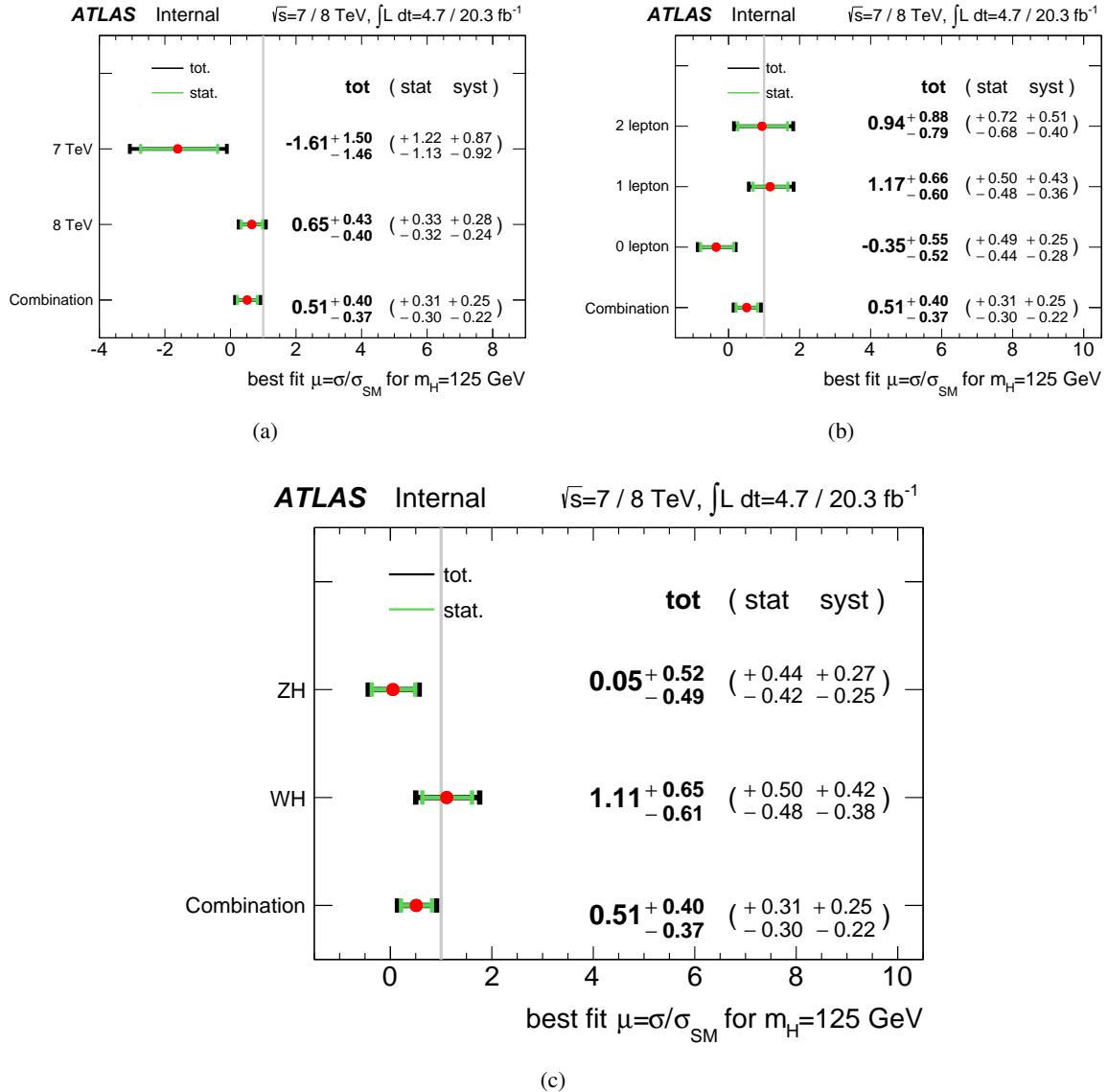


Figure 93: The fitted values of the Higgs-boson signal-strength parameter μ for $m_h = 125 \text{ GeV}$: (a) for the 7 TeV and 8 TeV datasets; (b) for the 0-, 1- and 2-lepton channels, with the 7 and 8 TeV datasets combined; and (c) for the WH and ZH processes, with the 7 and 8 TeV datasets combined. The result of the combination of all channels and all datasets is shown in all. The individual μ -values for the lepton channels (for the $(W/Z)H$ processes) are obtained from a simultaneous fit with the signal strength for each of the lepton channels (for each of the WH and ZH processes) floating independently.

3126 of the various background components are provided in table 58 for the four most significant bins of the
 3127 8 TeV MVA analysis.

3128 9.2 Cross-checks

3129 **Dijet-mass analysis:** In the dijet-mass analysis, agreement between data and estimated background is
 3130 observed within the uncertainties shown by the hashed bands.

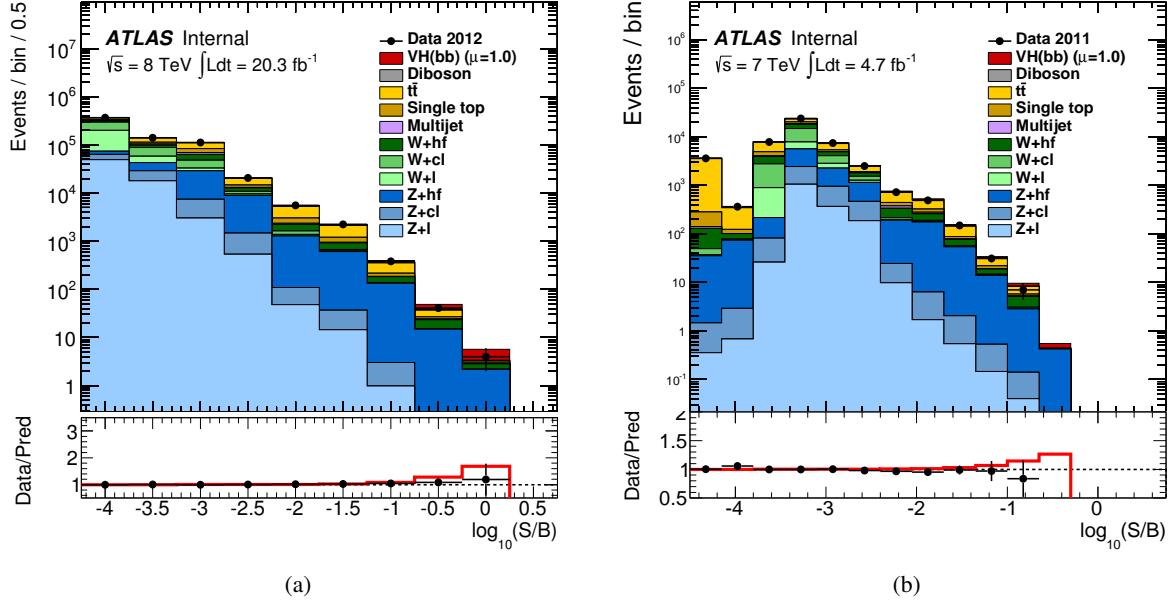


Figure 94: Event yields as a function of $\log(S/B)$ for data, background and Higgs-boson signal with $m_h = 125$ GeV for the (a) 8 TeV data and (b) 7 TeV data. Final-discriminant bins in all signal regions are combined into bins of $\log(S/B)$. The signal S and background B yields are expected and fitted, respectively. The Higgs-boson signal contribution is shown as expected for the SM cross section (indicated as $\mu = 1.0$). The ratio of the data to the background-only prediction is also shown. The red line indicates the ratio of the prediction for signal ($\mu = 1$) and background to the background-only prediction.

Process	Bin 6	Bin 7	Bin 8	Bin 9
Data	2245	382	41	4
Signal	62	32	10.7	2.3
Background	2189	364	37.9	3.4
S/B	0.03	0.09	0.3	0.7
W+hf	250	45	8.2	0.7
W+cl	50	4	0.2	0.005
W+l	16	1	0.03	0.001
Z+hf	577	130	14.8	2.2
Z+cl	22	2	0.1	0.008
Z+l	15	1	0.05	0.004
$t\bar{t}$	922	137	10	0.3
single top	252	31	2.7	0.1
diboson	62	10	1	0.2
multijet	26	3	0.9	0

Table 58: The fitted numbers of signal and background events and the observed numbers of events after MVA selection for the most sensitive four bins in figure 94a. These numbers are for the 8 TeV dataset, corresponding to an integrated luminosity of 20.3 fb^{-1} .

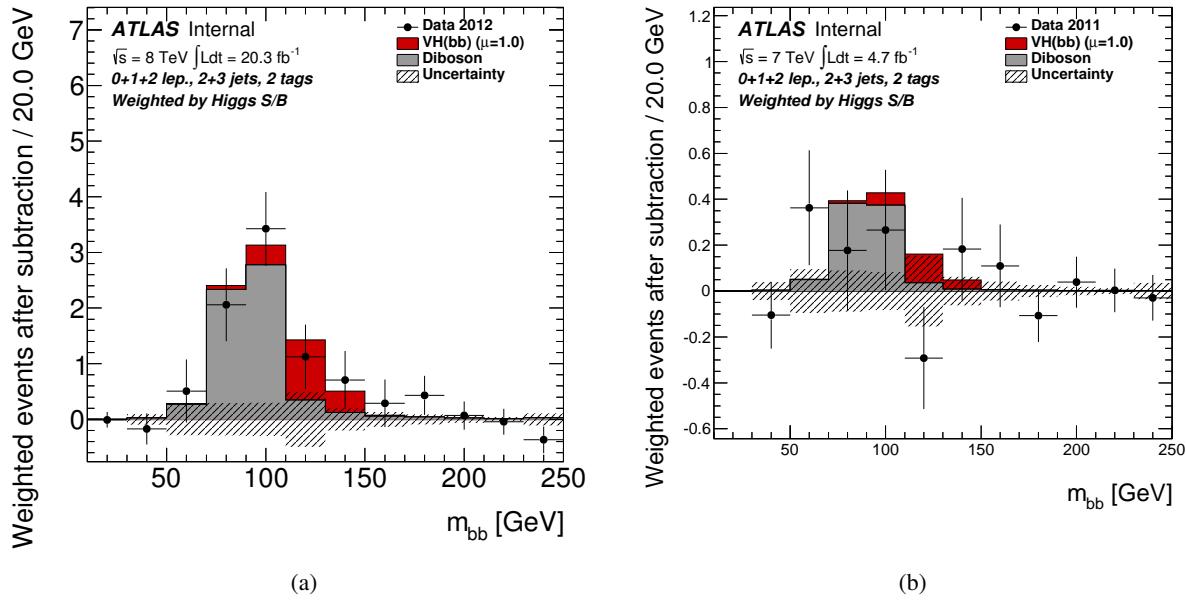


Figure 95: The distribution of m_{bb} in data after subtraction of all backgrounds except for the diboson processes, as obtained with the dijet-mass analysis for the (a) 8 TeV and (b) 7 TeV data. The contributions from all lepton channels, p_T^V intervals, number-of-jets and 2-tag b -tagging categories are summed weighted by their respective values of expected Higgs-boson-signal over fitted background ratio. The contribution of the associated WH and ZH production of a SM Higgs boson with $m_h = 125 \text{ GeV}$ is shown as expected for the SM cross section (indicated as $\mu = 1.0$). The size of the combined statistical and systematic uncertainty on the fitted background is indicated by the hashed band.

3131 In the dijet-mass analysis, a μ value of $1.23 \pm 0.44(\text{stat.}) \pm 0.41(\text{syst.})$ is obtained for the 8 TeV dataset.
 3132 The consistency of the results of the three lepton channels is at the level of 8%. Using the “bootstrap”
 3133 method mentioned in Section 8.9, the results for the 8 TeV data with the dijet-mass analysis and with the
 3134 MVA are expected to be 67% correlated, and the observed results are found to be statistically consistent
 3135 at the level of 8%. The expected significance in the dijet-mass analysis is 1.9σ , to be compared to 2.5σ
 3136 for the MVA, which is the reason for choosing the MVA for the nominal results.

3137 Figure 95 shows the m_{bb} distribution in data after subtraction of all backgrounds except for diboson
 3138 production for the 7 and 8 TeV data, as obtained with the dijet-mass analysis. In this figure, the con-
 3139 tributions of all 2-tag signal regions in all channels are summed weighted by their respective ratios of
 3140 expected Higgs-boson signal to fitted background. The VZ contribution is clearly seen, located at the
 3141 expected Z mass. The Higgs-boson signal contribution is shown as expected for the SM cross section.

3142 **Diboson analysis:** To validate the analysis procedures, VZ fits are performed, the technical details of
 3143 which are discussed in Appendix AL.

3144 The measured signal strength for the 8 TeV dataset with the MVA is $\mu_{VZ} = 0.77 \pm 0.10(\text{stat.}) \pm$
 3145 $0.15(\text{syst.})$. This result is consistent with the observations already made on figure 95. The signal strengths
 3146 obtained for the three lepton channels are consistent at the 85% level. In the dijet-mass analysis at 8 TeV,
 3147 a μ_{VZ} value of $0.79 \pm 0.11(\text{stat.}) \pm 0.16(\text{syst.})$ is obtained.

3148 Fits are performed with the same final discriminants as used to obtain the results for the Higgs boson
 3149 based on the 8 TeV dataset, but with both the VZ and Higgs-boson signal-strength parameters μ_{VZ} and
 3150 μ left freely floating. The results are unchanged with respect to those from the separate fits reported

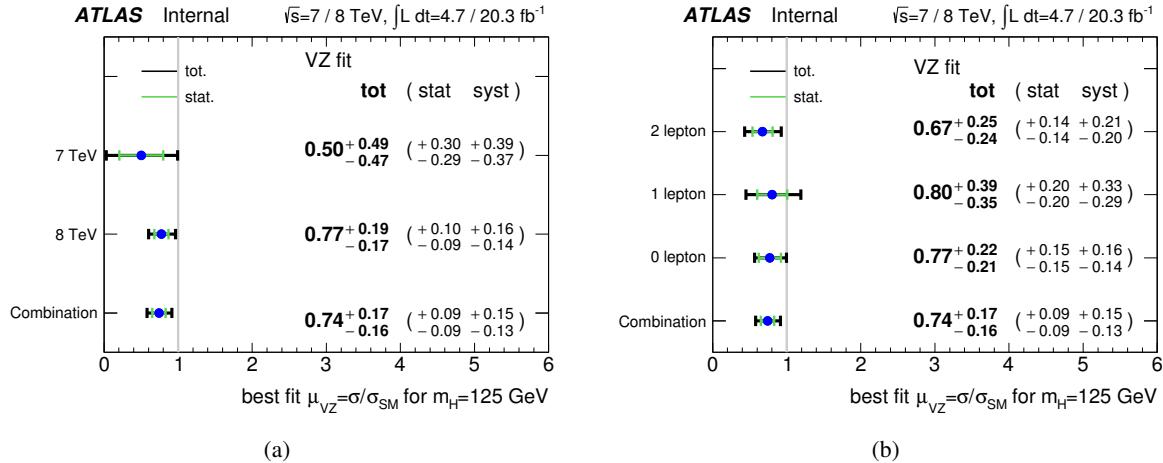


Figure 96: The fitted values of the diboson signal strength μ_{VZ} for (a) the 7 TeV, 8 TeV and combined datasets, and (b) for the three lepton channels separately and combined, for the combined dataset. The MVA is used for the 8 TeV data. The individual μ_{VZ} -values for the lepton channels are obtained from a simultaneous fit with the signal strength for each floating independently.

above, and the correlation between the two signal-strength parameters is found to be -3% in the MVA and 9% in the dijet-mass analysis. The main reason for these low correlations is the different shape of the p_T^V distributions for VZ and for the Higgs-boson signal, the p_T^V variable being used by both the MVA and the dijet-mass analysis. The yield tables in the appendix show that the ratio of the diboson contribution to that of the Higgs boson is indeed smaller in the higher than in the lower p_T^V interval. The additional variables input to the BDT provide further separation in the MVA, leading to a very small diboson contribution in the most significant bins of the BDT discriminant, as can be read off table 58.

A value of $\mu_{VZ} = 0.50 \pm 0.30(\text{stat.}) \pm 0.38(\text{syst.})$ is obtained for the 7 TeV dataset. The signal strength obtained for the combined 7 and 8 TeV dataset is $0.74 \pm 0.09(\text{stat.}) \pm 0.14(\text{syst.})$. The VZ signal is observed with a significance of 4.9σ , to be compared to an expected significance of 6.3σ .

The fitted μ_{VZ} values are shown in figure 96 for the 7 TeV, 8 TeV and combined datasets, and for the three lepton channels separately for the combined dataset, all with the MVA used for the 8 TeV data.

3163 References

- 3164 [1] S. L. Glashow, *Partial Symmetries of Weak Interactions*, *Nucl. Phys.* **22** (1961) 579–588.
- 3165 [2] S. Weinberg, *A Model of Leptons*, *Phys. Rev. Lett.* **19** (1967) 1264–1266.
- 3166 [3] A. Salam, *Weak and electromagnetic interactions*, Proc. of the 8th Nobel Symposium (1969) 367.
- 3167 [4] F. Englert and R. Brout, *Broken Symmetry and the Mass of Gauge Vector Mesons*, *Phys. Rev. Lett.* **13** (1964) 321.
- 3169 [5] P. W. Higgs, *Broken Symmetries and the Masses of Gauge Bosons*, *Phys. Rev. Lett.* **13** (1964) 508.
- 3170 [6] P. W. Higgs, *Broken Symmetries, Massless Particles and Gauge Fields*, *Phys. Lett.* **12** (1964) 132.
- 3171 [7] G. Guralnik, C. Hagen, and T. Kibble, *Global Conservation Laws and Massless Particles*, *Phys.*
3172 *Rev. Lett.* **13** (1964) 585.
- 3173 [8] ATLAS Collaboration, *Observation of a new particle in the search for the Standard Model Higgs*
3174 *boson with the ATLAS detector at the LHC*, *Phys.Lett.* **B716** (2012) 1–29, [arXiv:1207.7214](https://arxiv.org/abs/1207.7214)
3175 [[hep-ex](#)].
- 3176 [9] CMS Collaboration, *Observation of a new boson at a mass of 125 GeV with the CMS experiment*
3177 *at the LHC*, *Phys.Lett.* **B716** (2012) 30–61, [arXiv:1207.7235](https://arxiv.org/abs/1207.7235) [[hep-ex](#)].
- 3178 [10] LHC Higgs Cross Section Working Group, S. Dittmaier, C. Mariotti, G. Passarino, and
3179 R. Tanaka (Eds.), *Handbook of LHC Higgs Cross Sections: 1. Inclusive Observables*,
3180 CERN-2011-002 (CERN, Geneva, 2011), [arXiv:1101.0593](https://arxiv.org/abs/1101.0593) [[hep-ph](#)].
- 3181 [11] ATLAS Collaboration, *Search for the Standard Model Higgs boson in associated production with*
3182 *a vector boson and decaying to bottom quarks with the ATLAS detector*, Tech. Rep.
3183 ATL-COM-PHYS-2013-465, CERN, Geneva, Aug, 2013.
- 3184 [12] ATLAS Collaboration, *Luminosity Determination in pp Collisions at $\sqrt{s} = 7$ TeV Using the*
3185 *ATLAS Detector at the LHC*, *Eur. Phys. J. C* **71** (2011) 1630, [arXiv:1101.2185](https://arxiv.org/abs/1101.2185) [[hep-ph](#)].
- 3186 [13] ATLAS Collaboration, *The ATLAS Simulation Infrastructure*, *Eur. Phys. J. C* **70** (2010) 823,
3187 [arXiv:1005.4568](https://arxiv.org/abs/1005.4568) [[physics.ins-det](#)].
- 3188 [14] GEANT4 Collaboration, S. Agostinelli et al., *GEANT4: A Simulation toolkit*, *Nucl.Instrum.Meth.*
3189 **A506** (2003) 250–303.
- 3190 [15] “Atlfast ii.” [Https://twiki.cern.ch/twiki/bin/viewauth/atlas/atlfastii](https://twiki.cern.ch/twiki/bin/viewauth/atlas/atlfastii).
- 3191 [16] “Pile up rescaling.” [https://twiki.cern.ch/twiki/bin/view/AtlasProtected/
3192 InDetTrackingPerformanceGuidelines#Pile_up_rescaling](https://twiki.cern.ch/twiki/bin/view/AtlasProtected/InDetTrackingPerformanceGuidelines#Pile_up_rescaling).
- 3193 [17] J. Alison, K. Brendlinger, S. Heim, J. Kroll, and C. M. Lester, *Description and Performance of the*
3194 *Electron Likelihood Tool at ATLAS using 2012 LHC Data*, Tech. Rep.
3195 ATL-COM-PHYS-2013-378, CERN, Geneva, Apr, 2013.
- 3196 [18] C. Anastopoulos, E. Benhar-Noccioli, A. Bocci, K. Brendlinger, F. Bhrer, L. Iconomidou-Fayard,
3197 M. Delmastro, O. Ducu, R. Fletcher, D. Froidevaux, T. Guillemin, S. Heim, F. Hubaut,
3198 M. Karnevskiy, J. Kretzschmar, J. Kroll, C. Lester, K. Lohwasser, J. B. Maurer, A. Morley,

- 3199 G. Psztor, E. Richter-Was, A. Schaffer, T. Serre, P. Sommer, E. Tiouchichine, and H. Williams,
 3200 *Supporting document on electron efficiency measurements using the 2012 LHC proton-proton*
 3201 *collision data*, Tech. Rep. ATL-COM-PHYS-2013-1295, CERN, Geneva, Sep, 2013.
- 3202 [19] ATLAS Collaboration, *Electron performance measurements with the ATLAS detector using the*
 3203 *2010 LHC proton-proton collision data*, Eur. Phys. J **C72** (2012) 1909, [arXiv:1110.3174v2](https://arxiv.org/abs/1110.3174v2)
 3204 [[hep-ex](#)].
- 3205 [20] M. Cacciari, G. P. Salam, and G. Soyez, *The anti- k_t jet clustering algorithm*, JHEP **04** (2008) 063,
 3206 [arXiv:0802.1189](https://arxiv.org/abs/0802.1189) [[hep-ph](#)].
- 3207 [21] “Jet-area-based pile-up subtraction.”
 3208 [Https://twiki.cern.ch/twiki/bin/viewauth/atlasprotected/jetareas](https://twiki.cern.ch/twiki/bin/viewauth/atlasprotected/jetareas).
- 3209 [22] ATLAS Collaboration, *Jet energy measurement with the ATLAS detector in proton-proton*
 3210 *collisions at $\sqrt{s} = 7$ TeV*, [arXiv:1112.6426](https://arxiv.org/abs/1112.6426) [[hep-ex](#)]. Submitted to Eur. Phys. J. C.
- 3211 [23] ATLAS Collaboration, HSG5, *Invariant Mass Studies for the $H \rightarrow b\bar{b}$ Measurements for LHCP*,
 3212 Tech. Rep. ATL-COM-PHYS-2013-449, CERN, Geneva, Apr, 2013.
- 3213 [24] ATLAS Collaboration, *b-jet tagging calibration on c-jets containing D^{*+} mesons*,
 3214 ATLAS-CONF-2012-039 (2012), <https://cdsweb.cern.ch/record/1435193>.
- 3215 [25] ATLAS Collaboration, *Measurement of the Mistag Rate with 5 fb^{-1} of Data Collected by the*
 3216 *ATLAS Detector*, ATLAS-CONF-2012-040 (2012),
 3217 <https://cdsweb.cern.ch/record/1435194>.
- 3218 [26] ATLAS Collaboration, *Measurement of the b-tag Efficiency in a Sample of Jets Containing Muons*
 3219 *with 5 fb^{-1} of Data from the ATLAS Detector*, ATLAS-CONF-2012-043 (2012),
 3220 <https://cdsweb.cern.ch/record/1435197>.
- 3221 [27] G. Piacquadio, *Calibration of b-tagging using di-leptonic top pair events and a combinatorial*
 3222 *likelihood approach*, Tech. Rep. ATL-COM-PHYS-2013-395, CERN, Geneva, Apr, 2013.
 3223 b-tagging calibration aiming at being approved in time for analyses to be presented at LHCP.
- 3224 [28] G. Piacquadio, *Calibration of b-tagging using di-leptonic top pair events applying the*
 3225 *combinatorial likelihood approach to 2011 data*, Tech. Rep. ATL-COM-PHYS-2013-1083,
 3226 CERN, Geneva, Aug, 2013.
- 3227 [29] M. zur Nedden, G. Piacquadio, J. Jovicevic, F. Filthaut, T. Scanlon, and F. Parodi, *Calibration of*
 3228 *b-tagging using dileptonic top pair events in a combinatorial likelihood approach with the ATLAS*
 3229 *experiment*, Tech. Rep. ATLAS-COM-CONF-2014-003, CERN, Geneva, Jan, 2014.
- 3230 [30] G. Aad, H. Arnold, and C. Weiser, *b-jet tagging calibration on c-jets produced in association with*
 3231 *W^\pm bosons*, Tech. Rep. ATL-COM-PHYS-2013-1365, CERN, Geneva, Sep, 2013.
- 3232 [31] I. Burmeister, I. Connelly, A. Ferretto, F. Filthaut, R. Goncalo, R. Hawkings, H. Esch, F. Parodi,
 3233 D. Sidorov, C. Schiavi, J. Thomas-Wilsker, J. Yu, and M. Zur Nedden, *Measurement of the*
 3234 *b-tagging performance in the 2012 ATLAS data*, Tech. Rep. ATL-COM-PHYS-2013-456, CERN,
 3235 Geneva, Apr, 2013.
- 3236 [32] P. Berta, F. Filthaut, V. Dao, E. Le Menedeu, F. Parodi, G. Piacquadio, T. Scanlon, M. Ughetto,
 3237 and L. Zhang, *Continuous b-tagging for the ATLAS experiment*, Tech. Rep.
 3238 ATL-COM-PHYS-2014-035, CERN, Geneva, Jan, 2014.

Not reviewed, for internal circulation only

- 3239 [33] “Elejet overlap removal problem in susy 1/2-lepton analysis.”
 3240 <Https://indico.cern.ch/event/242559/material/slides/0?contribid=2>.
- 3241 [34] A. e. a. Buzatu, *Invariant Mass Studies for the $H \rightarrow b\bar{b}$ Measurements for HCP*, Tech. Rep.
 3242 ATL-COM-PHYS-2012-1451, CERN, Geneva, Oct, 2012.
- 3243 [35] T. Sjostrand, S. Mrenna, and P. Z. Skands, *A Brief Introduction to PYTHIA 8.1*,
 3244 [Comput.Phys.Commun. 178 \(2008\) 852–867](Comput.Phys.Commun. 178 (2008) 852–867), <arXiv:0710.3820> [hep-ph].
- 3245 [36] *Summary of ATLAS Pythia 8 tunes*, Tech. Rep. ATL-PHYS-PUB-2012-003, CERN, Geneva, Aug,
 3246 2012.
- 3247 [37] J. Pumplin, D. Stump, J. Huston, H. Lai, P. M. Nadolsky, et al., *New generation of parton
 3248 distributions with uncertainties from global QCD analysis*, [JHEP 0207 \(2002\) 012](JHEP 0207 (2002) 012),
 3249 <arXiv:hep-ph/0201195> [hep-ph].
- 3250 [38] P. Golonka and Z. Was, *PHOTOS Monte Carlo: A Precision tool for QED corrections in Z and W
 3251 decays*, [Eur.Phys.J. C45 \(2006\) 97–107](Eur.Phys.J. C45 (2006) 97–107), <arXiv:hep-ph/0506026> [hep-ph].
- 3252 [39] Z. Was, *TAUOLA the library for tau lepton decay, and KKMC / KORALB / KORALZ/... status
 3253 report*, [Nucl.Phys.Proc.Suppl. 98 \(2001\) 96–102](Nucl.Phys.Proc.Suppl. 98 (2001) 96–102), <arXiv:hep-ph/0011305> [hep-ph].
- 3254 [40] A. Djouadi, J. Kalinowski, and M. Spira, *HDECAY: A program for Higgs boson decays in the
 3255 Standard Model and its supersymmetric extension*, [Comput. Phys. Commun. 108 \(1998\) 56–74](Comput. Phys. Commun. 108 (1998) 56–74).
- 3256 [41] O. Brein, A. Djouadi, and R. Harlander, *NNLO QCD corrections to the Higgs-strahlung processes
 3257 at hadron colliders*, [Phys.Lett. B579 \(2004\) 149–156](Phys.Lett. B579 (2004) 149–156), <arXiv:hep-ph/0307206> [hep-ph].
- 3258 [42] M. Ciccolini, S. Dittmaier, and M. Kramer, *Electroweak radiative corrections to associated WH
 3259 and ZH production at hadron colliders*, [Phys.Rev. D68 \(2003\) 073003](Phys.Rev. D68 (2003) 073003), <arXiv:hep-ph/0306234>
 3260 [hep-ph].
- 3261 [43] K. e. a. Nakamura, *Review of particle physics*, <J. Phys. G>.
- 3262 [44] C. Englert, M. McCullough, and M. Spannowsky, *Gluon-initiated associated production boosts
 3263 Higgs physics*, [Phys. Rev. D 89 \(2014\) 013013](Phys. Rev. D 89 (2014) 013013).
 3264 <http://link.aps.org/doi/10.1103/PhysRevD.89.013013>.
- 3265 [45] A. Denner, S. Dittmaier, S. Kallweit, and A. Muck, *EW corrections to Higgs strahlung at the
 3266 Tevatron and the LHC with HAWK*, PoS [EPS-HEP2011](#) (2011) 235, <arXiv:1112.5258>
 3267 [hep-ph].
- 3268 [46] M. Ciccolini, A. Denner, and S. Dittmaier, *Strong and electroweak corrections to the production of
 3269 Higgs + 2 jets via weak interactions at the LHC*, [Phys. Rev. Lett. 99 \(2007\) 161803](Phys. Rev. Lett. 99 (2007) 161803).
- 3270 [47] LHC Higgs Cross Section Working Group, S. Dittmaier, C. Mariotti, G. Passarino, and
 3271 R. Tanaka (Eds.), *Handbook of LHC Higgs Cross Sections: 2. Differential Distributions*,
 3272 CERN-2012-002 (CERN, Geneva, 2012), <arXiv:1201.3084> [hep-ph].
- 3273 [48] G. Luisoni, P. Nason, C. Oleari, and F. Tramontano, *$HW^\pm/HZ + 0$ and 1 jet at NLO with the
 3274 POWHEG BOX interfaced to GoSam and their merging within MiNLO*, [JHEP 1310 \(2013\) 083](JHEP 1310 (2013) 083),
 3275 <arXiv:1306.2542> [hep-ph].

Not reviewed, for internal circulation only

- 3276 [49] I. W. Stewart and F. J. Tackmann, *Theory uncertainties for Higgs mass and other searches using*
 3277 *jet bins*, Phys. Rev. D **85** (2012) 034011.
 3278 <http://link.aps.org/doi/10.1103/PhysRevD.85.034011>.
- 3279 [50] S. Gangal and F. J. Tackmann, *Next-to-leading-order uncertainties in Higgs + jets from gluon*
 3280 *fusion*, Phys. Rev. D **87** (2013) 093008.
 3281 <http://link.aps.org/doi/10.1103/PhysRevD.87.093008>.
- 3282 [51] A. Martin, W. Stirling, R. Thorne, and G. Watt, *Parton distributions for the LHC*, Eur.Phys.J. **C63**
 3283 (2009) 189–285, [arXiv:0901.0002](https://arxiv.org/abs/0901.0002) [hep-ph].
- 3284 [52] R. D. Ball, V. Bertone, S. Carrazza, C. S. Deans, L. Del Debbio, et al., *Parton distributions with*
 3285 *LHC data*, Nucl.Phys. **B867** (2013) 244–289, [arXiv:1207.1303](https://arxiv.org/abs/1207.1303) [hep-ph].
- 3286 [53] M. Botje, J. Butterworth, A. Cooper-Sarkar, A. de Roeck, J. Feltesse, et al., *The PDF4LHC*
 3287 *Working Group Interim Recommendations*, [arXiv:1101.0538](https://arxiv.org/abs/1101.0538) [hep-ph].
- 3288 [54] H.-L. Lai, M. Guzzi, J. Huston, Z. Li, P. M. Nadolsky, et al., *New parton distributions for collider*
 3289 *physics*, Phys.Rev. **D82** (2010) 074024, [arXiv:1007.2241](https://arxiv.org/abs/1007.2241) [hep-ph].
- 3290 [55] T. Gleisberg et al., *Event generation with SHERPA 1.1*, JHEP **02** (2009) 007, [arXiv:0811.4622](https://arxiv.org/abs/0811.4622)
 3291 [hep-ph].
- 3292 [56] S. Alioli et al., *NLO Higgs boson production via gluon fusion matched with shower in POWHEG*,
 3293 JHEP **0904** (2009) 002, [arXiv:0812.0578](https://arxiv.org/abs/0812.0578) [hep-ph].
- 3294 [57] P. Nason and C. Oleari, *NLO Higgs boson production via vector-boson fusion matched with*
 3295 *shower in POWHEG*, JHEP **1002** (2010) 037, [arXiv:0911.5299](https://arxiv.org/abs/0911.5299) [hep-ph].
- 3296 [58] C. Oleari and L. Reina, *$W^\pm b\bar{b}$ production in POWHEG*, JHEP **1108** (2011) 061,
 3297 [arXiv:1105.4488](https://arxiv.org/abs/1105.4488) [hep-ph].
- 3298 [59] W. e. a. Bell, *Measurement of top quark pair differential cross section with ATLAS in pp collisions*
 3299 *at $\sqrt{s}=7$ TeV: Measurement of top quark pair differential cross section with ATLAS using 5/fb*
 3300 *of data collected in 2011 and the rel.17 version of the Atlas software*, Tech. Rep.
 3301 ATL-COM-PHYS-2012-1137, CERN, Geneva, Jul, 2012.
- 3302 [60] *Measurement of top-quark pair differential cross-sections in the l+jets channel in pp collisions at*
 3303 *$\sqrt{s} = 7$ TeV using the ATLAS detector*, Tech. Rep. ATLAS-CONF-2013-099, CERN, Geneva, Sep,
 3304 2013.
- 3305 [61] A. e. a. Hoecker, *TMVA - Toolkit for Multivariate Data Analysis*, ArXiv Physics e-prints (2007),
 3306 [physics/0703039](https://arxiv.org/abs/physics/0703039).
- 3307 [62] D. Damazio, T. Kono, F. Monticelli, and G. Pasztor, *Performance of the ATLAS Electron and*
 3308 *Photon Triggers in p-p Collisions at $\sqrt{s} = 8$ TeV in 2012*, Tech. Rep. ATL-COM-DAQ-2013-121,
 3309 CERN, Geneva, Oct, 2013.
- 3310 [63] J.-B. Blanchard, J.-B. de Vivie, and P. Mastrandrea, *In situ scales and smearings from Z and J/Ψ*
 3311 *events*, Tech. Rep. ATL-COM-PHYS-2013-1653, CERN, Geneva, Dec, 2013.
- 3312 [64] *Preliminary results on the muon reconstruction efficiency, momentum resolution, and momentum*
 3313 *scale in ATLAS 2012 pp collision data*, Tech. Rep. ATLAS-CONF-2013-088, CERN, Geneva,
 3314 Aug, 2013.

Not reviewed, for internal circulation only

- 3315 [65] ATLAS Collaboration, *Jet energy scale and its systematic uncertainty in proton-proton collisions*
 3316 at $\sqrt{s} = 7 \text{ TeV}$ with ATLAS 2011 data, ATLAS-CONF-2014-004 (2013),
 3317 <http://cds.cern.ch/record/1509552>.
- 3318 [66] “Jes uncertainty twiki.”
 3319 <Https://twiki.cern.ch/twiki/bin/viewauth/atlasprotected/jetuncertainties2012>.
- 3320 [67] A. L. Read, *Presentation of search results: The CL(s) technique*, J.Phys. **G28** (2002) 2693–2704.
- 3321 [68] G. Cowan et al., *Asymptotic formulae for likelihood-based tests of new physics*, Eur. Phys. J. **C71**
 3322 (2011) 1554, <arXiv:1007.1727> [physics.data-an].
- 3323 [69] ATLAS Collaboration, *Measurement of the Higgs boson mass from the $H \rightarrow \gamma\gamma$ and*
 3324 *$H \rightarrow ZZ^* \rightarrow 4\ell$ channels with the ATLAS detector using 25 fb^{-1} of pp collision data*, submitted to
 3325 Phys. Rev. D (2014), <arXiv:1406.3827> [hep-ex].
- 3326 [70] K. Arnold, L. d’Errico, S. Gieseke, D. Grellscheid, K. Hamilton, et al., *Herwig++ 2.6 Release*
 3327 *Note*, <arXiv:1205.4902> [hep-ph].
- 3328 [71] S. Frixione and B. R. Webber, *Matching NLO QCD computations and parton shower simulations*,
 3329 JHEP **0206** (2002) 029, <arXiv:hep-ph/0204244> [hep-ph].
- 3330 [72] V. H. et al., *Automation of one-loop QCD corrections*, JHEP **05** (2011) 044, <arXiv:1103.0621>
 3331 [hep-ph].
- 3332 [73] R. Frederix, S. Frixione, F. Maltoni, and T. Stelzer, *Automation of next-to-leading order*
 3333 *computations in QCD: The FKS subtraction*, JHEP **0910** (2009) 003, <arXiv:0908.4272>
 3334 [hep-ph].
- 3335 [74] F. e. a. Ahmadov, *Search for the Standard Model Higgs Boson in the $ZH \rightarrow \nu\nu b\bar{b}$ Channel with*
 3336 *the ATLAS Detector at the LHC*, Tech. Rep. ATL-COM-PHYS-2012-062, CERN, Geneva, Jan,
 3337 2012. Intended as support material for the expected $H \rightarrow b\bar{b}$ publication of the Higgs search results
 3338 using 2011 LHC data.
- 3339 [75] ATLAS Collaboration, HSG5, *B-tagging for VH, with $H \rightarrow b\bar{b}$* , Tech. Rep.
 3340 ATL-COM-PHYS-2013-697, CERN, Geneva, May, 2013.
- 3341 [76] G. Unal, *Electron and Photon energy resolutions and their uncertainties for run-1 calibration*,
 3342 Tech. Rep. ATL-COM-PHYS-2013-1651, CERN, Geneva, Dec, 2013.
- 3343 [77] a. many, *Electron and photon energy calibration with the ATLAS detector using LHC Run 1 data*,
 3344 Tech. Rep. ATL-COM-PHYS-2013-1652, CERN, Geneva, Dec, 2013.
- 3345 [78] K. Ecker, M. Goblirsch-Kolb, and O. Kortner, *Muon Response Modelling for the Measurement of*
 3346 *the Mass of the Higgs Boson Candidate in 4l Final State*, Tech. Rep.
 3347 ATL-COM-PHYS-2012-1736, CERN, Geneva, Nov, 2012.

3348 A E_T^{miss} trigger

3349 As introduction to the use of the E_T^{miss} trigger in the analysis, we report here in Table 59 part of the table
 3350 shown in section 3.1. The analysis used the E_T^{miss} triggers (the EF_xe80 family) for both the 0-lepton
 channel and the 1-lepton channel.

Trigger Object	Data Period	Trigger Names	Luminosity (fb $^{-1}$)
$E_T^{\text{miss}} < 160 \text{ GeV}$	A-B5	EF_xe80T_tclcw_loose	1.91928
	B6-L	EF_xe80_tclcw_loose	18.132
$E_T^{\text{miss}} > 160 \text{ GeV}$	A-B5	EF_xe80_tclcw	2.1257
	B6-L	EF_xe80_tclcw_loose	18.132

Table 59: E_T^{miss} trigger Trigger table used in the 2012 data analysis.

3351
 3352 This complex use of the trigger is the result of the attempt to maximize the event acceptance for
 3353 2012 data. Thanks to the successful L1Calo noise suppression in the forward region of the calorimeter,
 3354 EF_xe80_tclcw_loose was installed from period B6 on. Before period B6, two E_T^{miss} triggers with different
 3355 threshold were available:

- The trigger EF_xe80T_tclcw_loose has a lower threshold, but it vetoed the first 3 bunches (BGRP7) in a bunch train. This BGRP7 mask is intended to suppress spurious high trigger rate bunches in E_T^{miss} trigger due to the relatively long calorimeter response affecting the L1Calo. The details for the three triggers are shown in Table 60.

- The trigger, xe80_tclcw, has a higher threshold without this bunch mask.

Trigger Name	Start Date	VBRP7	L1	L2	EF
EF_xe80_tclcw	period A	No	50	55	80
EF_xe80T_tclcw_loose	period A	Yes	40	45	80
EF_xe80_tclcw_loose	period B6	No	40	45	80

Table 60: Summary of E_T^{miss} triggers used in the analysis. The threshold values are in GeV.

3361 The EF_xe80T_tclcw_loose and EF_xe80_tclcw triggers have been used in this analysis up to period B6,
 3362 to cover different E_T^{miss} regions (as summarised in Table 59).

3363 To maximize the performance of the analysis, part of the phase space is in a region where the triggers
 3364 are not completely efficient (in the turn-on). It is important to study in detail the trigger efficiency and to
 3365 check the interdependencies with the offline reconstructed variables entering in the multivariate analysis.
 3366 The final goals are:

- to avoid phase spaces with non trivial interdependencies between efficiency, E_T^{miss} and other reconstructed variables,
- to derive data driven corrections and systematic uncertainties to be applied to the Monte Carlo simulation.

3371 Since we use three different triggers, the studies have been done for each trigger individually.

3372 An extra study has been done to check the level of detail simulated for the EF_xe80T_tclcw_loose
 3373 trigger in the Monte Carlo sample. This appendix has been divided in three different parts:

- 3374 • Emulation of the BGRP7 in the Monte Carlo for the EF_xe80T_tclcw_loose trigger;
- 3375 • Trigger efficiency and interdependence with offline variables;
- 3376 • Data driven scale factors and systematics.

3377 **A.1 Emulation of the BGRP7 in the Monte Carlo for the EF_xe80T_tclcw_loose trigger**

3378 Despite the fact that the EF_xe80T_tclcw_loose trigger is present in the Monte Carlo samples, it is not
3379 actively removing events in the 3 first bunches of the trains in the simulations. A detailed study of the
3380 offline kinematic properties of these events, compared with the events in the other bunches, have been
3381 done on the $ZH \rightarrow v\bar{v}b\bar{b}$ signal Monte Carlo sample. Given the fact that no significant differences have
3382 been found (i.e. Fig. 97), the BGRP7 events have not been removed when analyzing the Monte Carlo
3383 samples, but the proper luminosity calculation and PU profile have been adopted.

Not reviewed, for internal circulation only

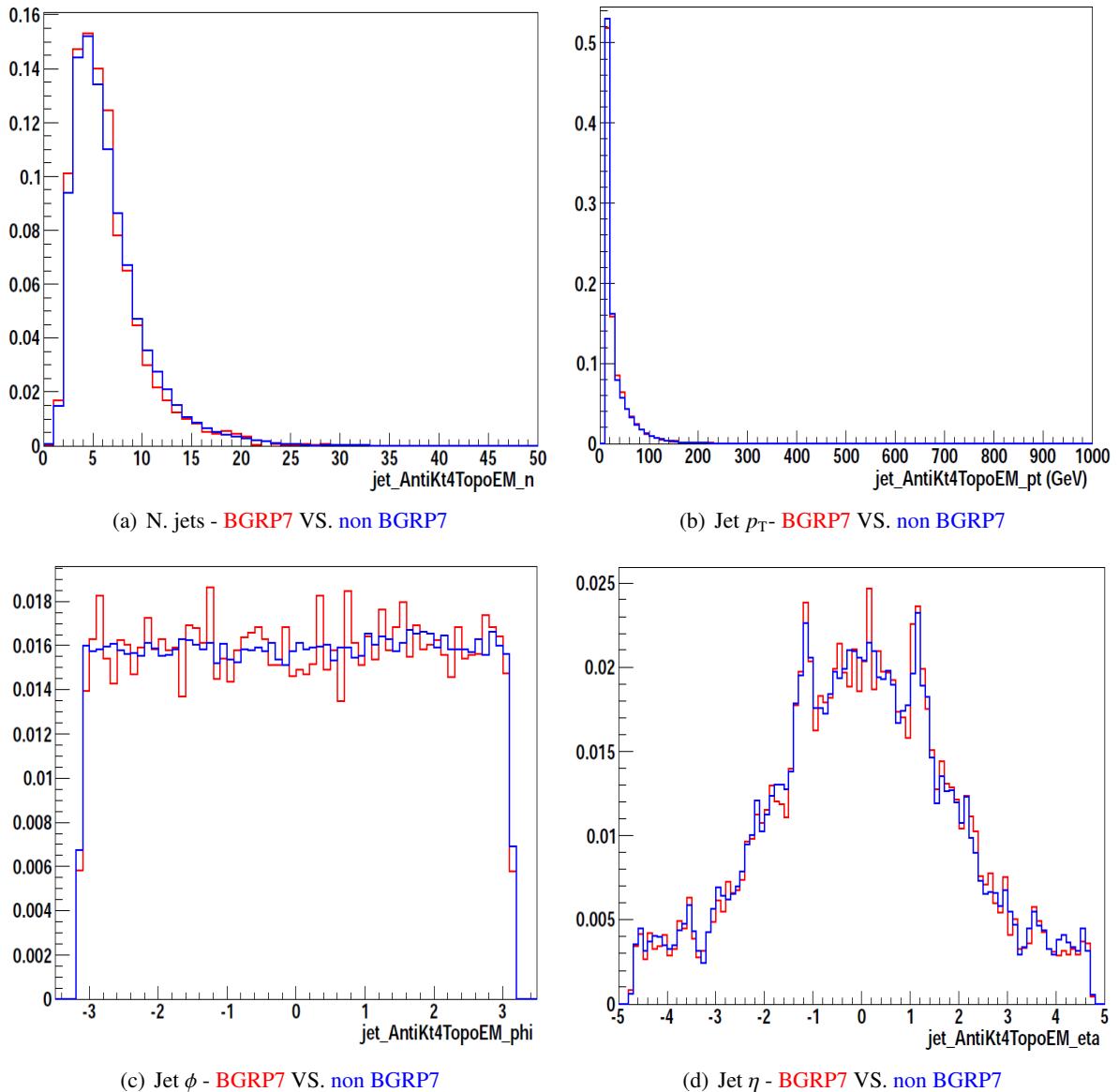


Figure 97: Comparison between the events belonging to the BGRP7 (red) and the rest of the events (blue) in the Monte Carlo simulation for some of the variables (number of jets, inclusive jet p_T , inclusive jet ϕ , inclusive jet η).

Not reviewed, for internal circulation only

3384 A.2 Trigger efficiency and interdependence with offline variables

3385 The final trigger efficiency is the product of the trigger efficiency in the three different trigger levels
 3386 (L1, L2, Event-Filter). It is defined at each level as follow:

$$Efficiency_{L1} = L1 \text{ passed} / Total \quad (29)$$

$$Efficiency_{L2} = L2 \text{ passed} / L1 \text{ passed} \quad (30)$$

$$Efficiency_{EF} = EF \text{ passed} / L2 \text{ passed} \quad (31)$$

$$Efficiency_{Total} = Efficiency_{L1} \times Efficiency_{L2} \times Efficiency_{EF} \quad (32)$$

3387 To measure it on data, orthogonal samples acquired by the muon trigger (in the muon triggered
 3388 data stream) have been used. Since the on-line trigger E_T^{miss} does not contain inner detector and muon
 3389 spectrometer information, the muon momentum is not counted in the on-line trigger E_T^{miss} calculation
 3390 (apart the energy loss in the calorimeter). This makes from the point of view of the E_T^{miss} trigger, $W \rightarrow \mu\nu$
 3391 and $Z \rightarrow \mu\mu$ very similar to $Z \rightarrow \nu\nu$. To study the trigger efficiency, we selected $W(\rightarrow \mu\nu) + jets$ or
 3392 $Z(\rightarrow \mu\mu) + jets$ events in the lowest non pre-scaled muon triggers, and check how many of them pass the
 3393 L1, the L2 and the EF for the E_T^{miss} triggers. In this way we can calculate the efficiencies in the formulas
 3394 above.

3395 The event selection (for $W(\rightarrow \mu\nu) + jets$ and $Z(\rightarrow \mu\mu) + jets$ processes) are quite similar to the
 3396 common VH analysis selections. The presence of exactly one muon or two muons defines if one event
 3397 belongs to the $W \rightarrow \mu\nu$ or $Z \rightarrow \mu\mu$ sample. In order to be as close to the analysis phase space as possible,
 3398 two signal jets with leading jet p_T greater than 45 GeV are required. Tight multi-jet rejection cuts($\text{trkIso} < 0.03$ and $m_T^W > 60$ GeV) and b -jet veto are applied for $W \rightarrow \mu\nu$ events, to remove residual multi-jet
 3399 and $t\bar{t}$ backgrounds. With the above selections applied, $W \rightarrow \mu\nu$ and $Z \rightarrow \mu\mu$ events are selected
 3400 at almost 100% purity, see Figs. 98 and 99. These plots show the offline E_T^{miss} distribution, calculated

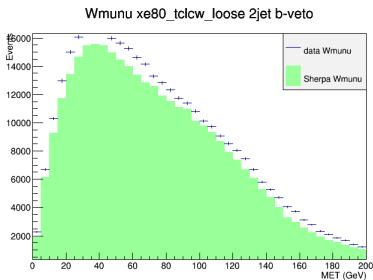


Figure 98: selected $W \rightarrow \mu\nu$ offline E_T^{miss} distribution, data(cross points) and MC(colored histogram)

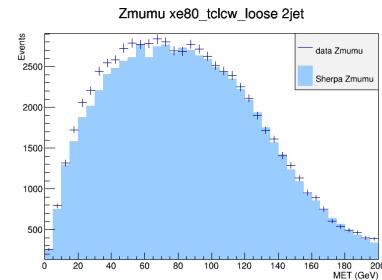


Figure 99: selected $Z \rightarrow \mu\mu$ offline E_T^{miss} distribution, data(cross points) and MC(colored histogram)

3401 by subtracting the muon contributions for the $W \rightarrow \mu\nu$ and $Z \rightarrow \mu\mu$ cases. These subtracted versions
 3402 of the E_T^{miss} , used only in this context, have similar kinematic properties (with some approximation) to
 3403 the E_T^{miss} in $Z \rightarrow \nu\nu$ events. Note: no normalization factors have been used, so the data-Monte Carlo
 3404 difference is partially coming from them.

3406 **A.2.1 Dependence of the E_T^{miss} trigger efficiency on kinematic variables entering in the multivariate analysis**

3408 We expect a clear dependence between the efficiency and the offline E_T^{miss} (in this case, for the $Z \rightarrow \mu\mu$ and $W \rightarrow \mu\nu$ events, the muon contributions have been subtracted from the offline E_T^{miss}). To model these, we extract data driven scale factors and systematic uncertainties. It can be more difficult to study all the needed details of the Monte Carlo modeling if we have additional dependencies between the trigger efficiency and other variables O entering in the multivariate analysis. For this reason, we studied several 2-dimensional efficiency scans (efficiency in the 2-D plan E_T^{miss} vs O).

3414 The scalar sum of jet $p_T(\text{JpT_Sum})$ and leading jet p_T have a strong correlation with the E_T^{miss} trigger efficiency (Fig. 100), while the others variables O have almost no bias in the signal region (Fig. 101, 102).

3417 These studies highlight a non-trivial dependence of the trigger efficiency on jet activity. We adopted an extra cut on JpT_Sum to avoid any trigger bias induced by this dependence. This was decided because the jet activity in the Monte Carlo simulation can depend on several different aspects (i.e. pile-up, perturbation order of the calculation, parton shower algorithm,...), making harder, in case of data-Monte carlo differences, their traceability to the real source. Here JpT_Sum is defined as follow:

$$\text{JpT_Sum} = p_T^{j1} + p_T^{j2} \text{ for 2-jets events} \quad (33)$$

$$\text{JpT_Sum} = p_T^{j1} + p_T^{j2} + p_T^{j3} \text{ for 3-jets events} \quad (34)$$

(35)

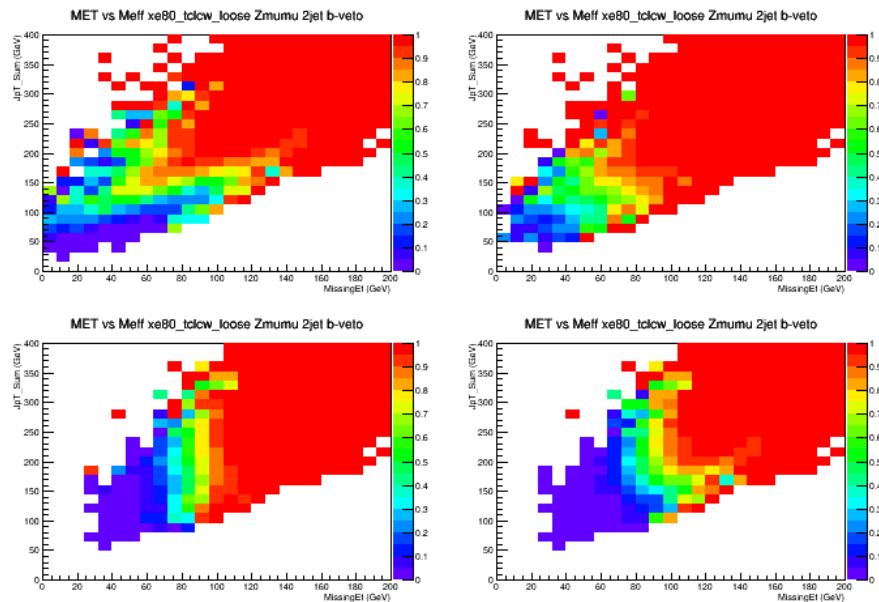


Figure 100: calculated xe80_tclcw_loose efficiency correlation between E_T^{miss} (abscissa) and sum of leading two jet p_T using Sherpa $Z \rightarrow \mu\mu$ Monte Carlo. The four plots, are the L1 (top, left), the L2 (top, right), the EF (bottom left) efficiencies, and the combination of the three (bottom right).

Not reviewed, for internal circulation only

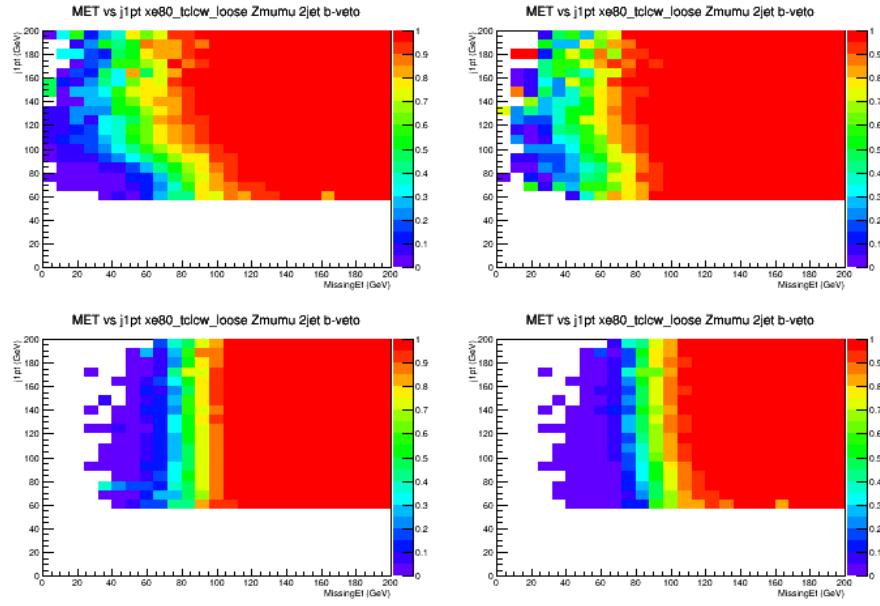


Figure 101: calculated E_T^{miss} (abscissa) and leading jet p_T using Sherpa $Z \rightarrow \mu\mu$ Monte Carlo. The four plots, are the L1 (top, left), the L2 (top, right), the EF (bottom left) efficiencies, and the combination of the three (bottom right).

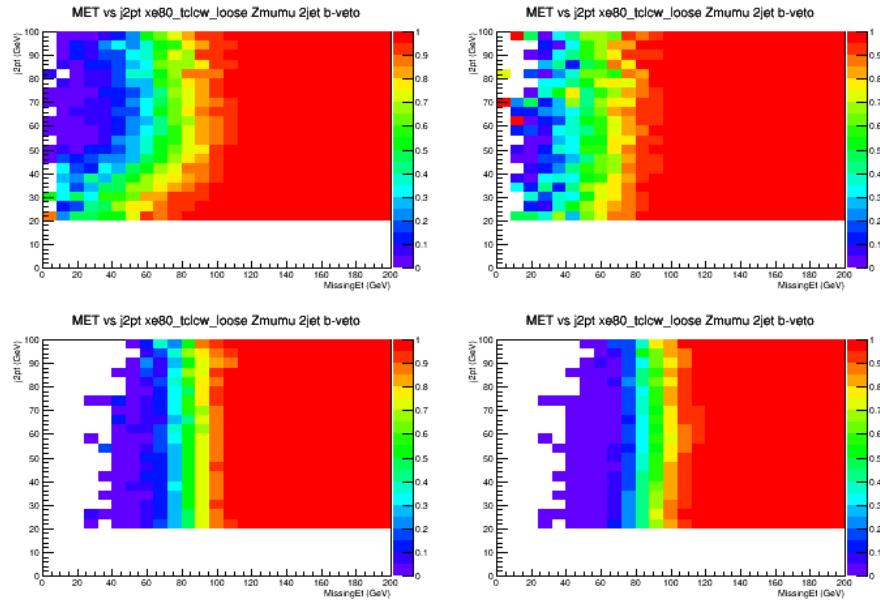


Figure 102: calculated E_T^{miss} (abscissa) and 2nd leading jet p_T using Sherpa $Z \rightarrow \mu\mu$ Monte Carlo. The four plots, are the L1 (top, left), the L2 (top, right), the EF (bottom left) efficiencies, and the combination of the three (bottom right).

Not reviewed, for internal circulation only

For the 2-jets case, the lowest threshold on JpT_Sum to remove the biased region is 120 GeV. This cleaning cut slightly improves the sensitivity for $E_T^{\text{miss}} < 120$ GeV and has almost no effect for $E_T^{\text{miss}} > 120$ GeV.

For the 3-jets events, the optimization of the cut on JpT_Sum is 150 GeV for $E_T^{\text{miss}} > 120$ GeV and 170 GeV for $E_T^{\text{miss}} < 120$ GeV. The cleaning cut for the 3jet region kills half the sensitivity in the 3 jet events with 100 GeV $< E_T^{\text{miss}} < 120$ GeV, but this region does not enter in the final fit due to very low sensitivity. The effect of the cleaning cut for 3 jet events is negligible in the other p_T^V regions. Once these cuts are applied, the non trivial dependence of the trigger efficiency by the jets activity is drastically reduced, and the MET trigger efficiency has a dependence only on the reconstructed E_T^{miss} . To complete the study, some other important variables have been shown in Figure 103.

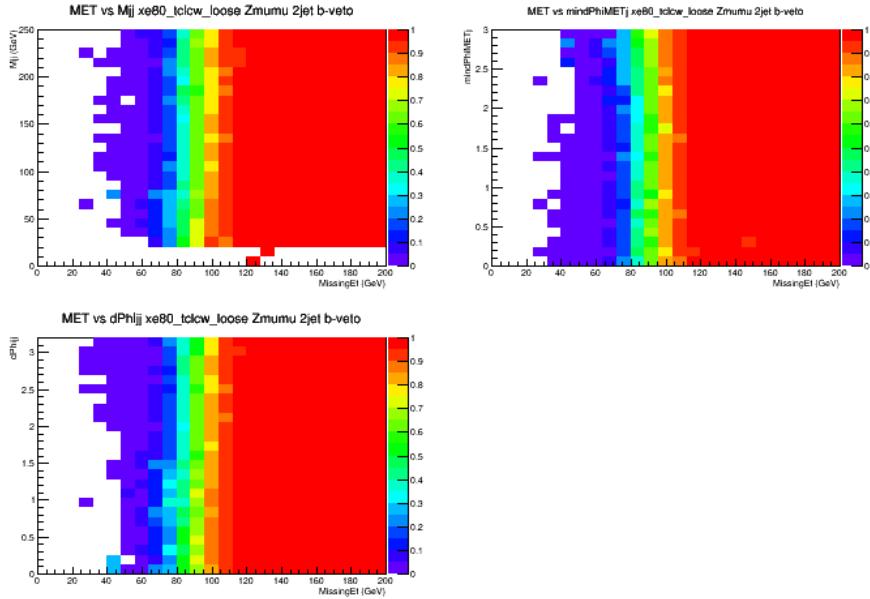


Figure 103: calculated EF_xe80_tclcw_loose efficiency correlation between E_T^{miss} (abscissa) and important variables (first row: left m_{jj} , right $\min(\Delta\phi(E_T^{\text{miss}}, \text{jet}))$; second row: $\Delta\phi(\text{jet}, \text{jet})$) for the analysis using Sherpa $Z \rightarrow \mu\mu$ Monte Carlo. The plots, showing the combination of the L1, L2, EF efficiencies, are obtained after the selection cut described in this appendix has been applied.

3422 A.2.2 Trigger efficiency parametrization

3423 The selection of $Z \rightarrow \mu\mu$ and $W \rightarrow \nu\nu$ events allow us to study the dependence of the trigger efficiency
 3424 as a function of the offline E_T^{miss} at each level of the trigger. As shown in Figure 104, while the E_T^{miss}
 3425 distribution before any trigger selection shows a good data-Monte Carlo agreement, each trigger level
 3426 induces a change in the shape of the distribution. It is than crucial to study in detail the shape of the
 trigger turn on, and to derive data driven corrections.

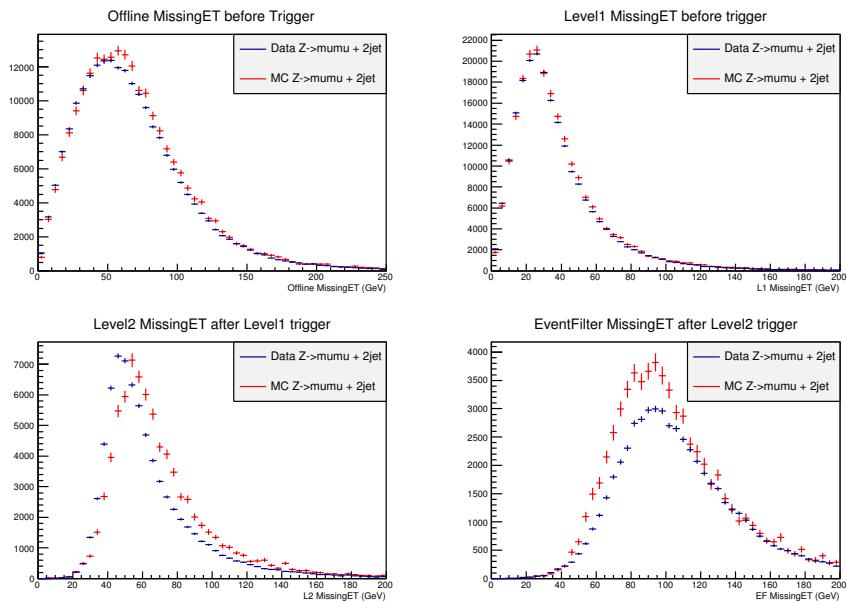


Figure 104: Comparison of 2012 data and MC E_T^{miss} distributions. Offline E_T^{miss} distribution of selected $Z \rightarrow \mu\mu$ events (top left). L1 E_T^{miss} distribution of selected $Z \rightarrow \mu\mu$ events (top right). L2 E_T^{miss} distribution after L1 trigger with 40 GeV threshold (bottom left). EF E_T^{miss} distribution after L2 trigger with 45 GeV threshold (bottom right).

3427
 3428 The efficiencies in Formula 32 has been plotted as a function of the offline E_T^{miss} , and each efficiency
 3429 has been fitted using the error function:

$$\text{Efficiency} = 0.5 \times \left(1 + \text{Erf} \left(\frac{E_T^{\text{miss}} - \text{threshold}}{\sqrt{2} \times \text{width}} \right) \right) \quad (36)$$

3430 The fit range for each level is 80-250 GeV. The threshold (50% efficiency point) and the width of the turn
 3431 on curve are estimated by the fit. Fig. 105 is a result using Sherpa $W \rightarrow \nu\nu$ events.

3432 The Figure 106 shows the comparison of trigger turn-on curves between two different physics pro-
 3433 cesses: $W(\rightarrow \nu\nu) + \text{jets}$ and $Z(\rightarrow \mu\mu) + \text{jets}$. We can clearly see in both data and MC, the good agreement
 3434 between the $W(\rightarrow \nu\nu) + \text{jets}$ process and the $Z(\rightarrow \mu\mu) + \text{jets}$ process.

Not reviewed, for internal circulation only

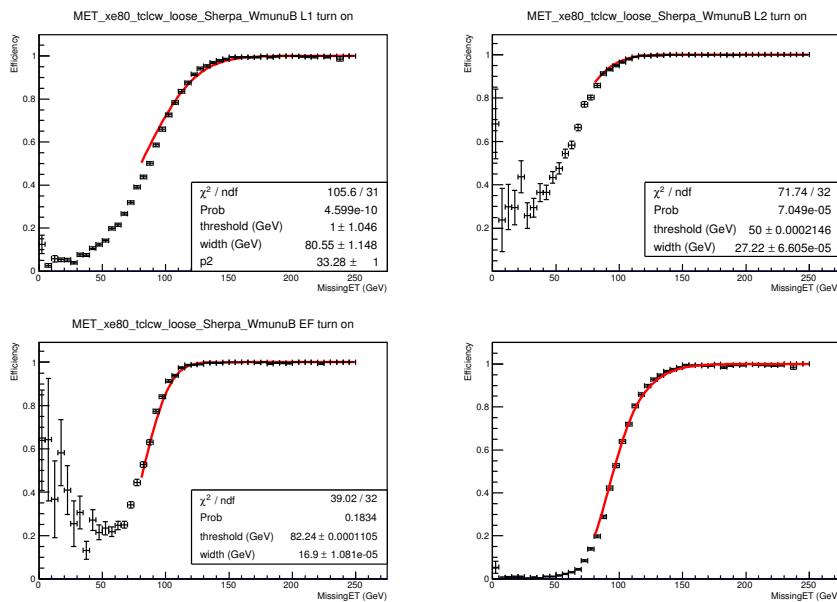


Figure 105: EF_xe80_tclcw_loose efficiency calculated using Sherpa $W \rightarrow \mu\nu$ MC events. The efficiency is shown for each trigger level: L1 (top left), L2 (top right), EF (bottom left) and for the overall(bottom right).

Not reviewed, for internal circulation only

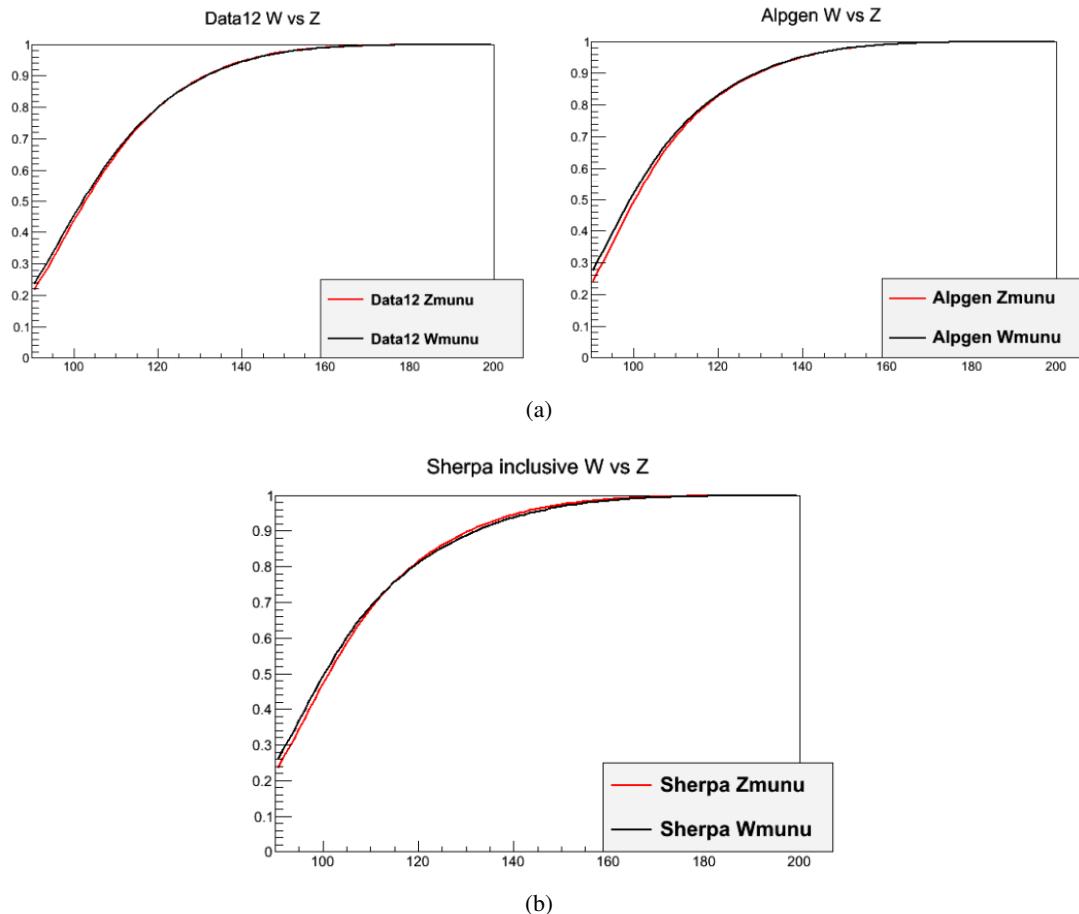


Figure 106: Trigger Efficiency turn on estimate using $W(\rightarrow \mu\nu) + jets$ and $Z(\rightarrow \mu\mu) + jets$ events for data (top left), Alpgen (top right) and Sherpa (bottom).

3435 **A.3 E_T^{miss} trigger data driven scale factors**

3436 The E_T^{miss} trigger scale factor is calculated using the fitted efficiency curve obtained by the method de-
 3437 scribed above:

$$SF = \frac{Turn - On_{W(\rightarrow\mu\nu)+\text{jets}/Z(\rightarrow\mu\mu)+\text{jets}}^{\text{Data}}}{Turn - On_{W(\rightarrow\mu\nu)+\text{jets}/Z(\rightarrow\mu\mu)+\text{jets}}^{\text{MC}}} \quad (37)$$

3438 Even if the shape of turn on curves depends on the number of jets, the calculated scale factors do not
 3439 significantly depends to the number of jets, meaning that Monte Carlo is able to properly simulate part
 3440 of the relevant correlations entering in the trigger decision. The comparison of the scale factors for
 3441 the $W(\rightarrow\mu\nu)$ and for the $Z(\rightarrow\mu\mu)$ (SF_W and SF_Z) shows a good agreement within 3% (Fig. 107):
 3442 METTrigZ. This small difference is considered as a systematic uncertainty in the analysis . Statistical
 3443 errors are calculated from the fit error (Fig. ??) and are taken into account as a separate systematics
 3444 (METTrigStat). Additional studies and comparisons with the top samples, show statistically coherent
 3445 scale factors.

xe80_tclcw_loose SF comaprison

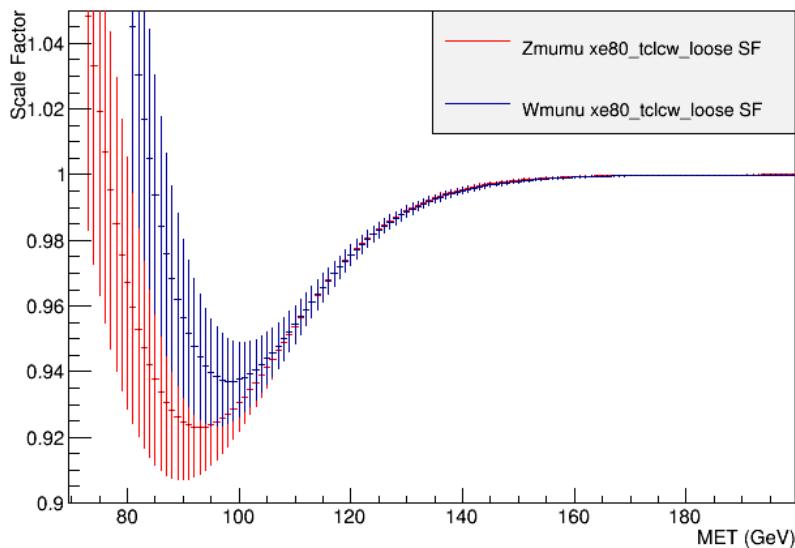


Figure 107: Calculated scale factor for EF_xe80_tclcw_loose from the $W \rightarrow \mu\nu$, and the $Z \rightarrow \mu\mu$ samples.

3446 B Delayed stream

3447 B.1 Introduction to delayed stream

3448 The delayed stream of 2012 data (HadDelayed) is taken from period E1 to the end of the year. It corre-
 3449 sponds to data collected on top of regular data taking and processed later, depending on available com-
 3450 puting resources. This stream is inclusive in the total data of 2012 with an integrated luminosity of 7.29
 3451 fb^{-1} . Apart from the nominal triggers (EF_xe80_tclcw, EF_xe80T_tclcw_loose, EF_xe80_tclcw_loose),
 3452 there is another E_T^{miss} trigger which is only available in delayed stream that can be used in the analysis
 3453 named EF_xe60_tclcw_loose_delayed (see Table 61). This trigger has lower threshold than the nominal
 3454 triggers, which is useful if we want to analyze the low E_T^{miss} region (less than 120 GeV) in 0-lepton study.
 3455 However this trigger is off if the instantaneous luminosity is greater than 5.77×10^{33} .

Table 61: Data period, integrated luminosity and threshold at each level (in GeV)

Trigger Name	Data period	$\int \mathcal{L} dt [\text{fb}^{-1}]$	L1	L2	EF
EF_xe80_tclcw_loose	B6-L3	18.1	40	45	80
EF_xe60_tclcw_loose_delayed	E1-L3	7.29	35	40	60

3456 B.2 Delayed stream E_T^{miss} trigger efficiency and scale factor

3457 Like the method we use to measure the trigger turn-on of the nominal triggers, we can parameterize
 3458 the trigger of delayed stream EF_xe60_tclcw_loose_delayed by the following method: first measure the
 3459 trigger turn-on curves and then, calculate the trigger scale factor using $Z \rightarrow \mu\mu$ and $W \rightarrow \mu\nu$ events (with
 3460 the same selection as in App. A). Due to the trigger availability on data, in order to measure the trigger
 3461 turn-on using data, events where the delayed stream trigger is off should be removed, this can be done
 3462 using lumiblock information. The trigger turn-on fitting is done by using error function, the fit range (for
 3463 each level) is from 40 to 200 GeV. Fit results using Sherpa $W \rightarrow \mu\nu$ and $Z \rightarrow \mu\mu$ events are shown in
 3464 Fig. 108, 109, respectively. The result for $W \rightarrow \mu\nu$ is used as central value while the result for $Z \rightarrow \mu\mu$
 3465 is used as systematic variation.

3466 We also check the dependence of trigger turn-on and scale factor on the following categories of
 3467 selection:

- 3468 • QCD rejection cuts: $E_T^{\text{miss}} > 90 \text{ GeV}$, $p_T^{\text{miss}} > 30 \text{ GeV}$, $\Delta\phi(E_T^{\text{miss}}, p_T^{\text{miss}}) < \frac{\pi}{2}$, $\Delta\phi(V, H) > 2.8$,
 3469 $0.7 < \Delta R(\text{jet}, \text{jet}) < 3$
- 3470 • 3-jet events versus 2-jet events
- 3471 • Studied samples: $Z \rightarrow \mu\mu$, $W \rightarrow \mu\nu$ or $t\bar{t}$ (for cross-check purpose).

3472 The results obtained from these categories of selection yield a little difference from the original
 3473 selection ($W \rightarrow \mu\nu$ with 2 jets and no QCD cuts). (Table 62)

3474 B.3 E_T^{miss} trigger bias

3475 Trigger efficiency bias is observed from variables sum of 2 leading jets J12pT (or sum of 3 jets J123pT
 3476 in 3-jet bin) (Fig. 110, 111) and p_T of leading jet as in nominal triggers, but as already mentioned in
 3477 the App. A, a cut on J12pT/J123pT is applied in order to avoid this bias while maintaining high signal
 3478 significance without losing much signal acceptance.

3479 The same cleaning cuts for sum of p_T of jets as in E_T^{miss} trigger section are used:

Not reviewed, for internal circulation only

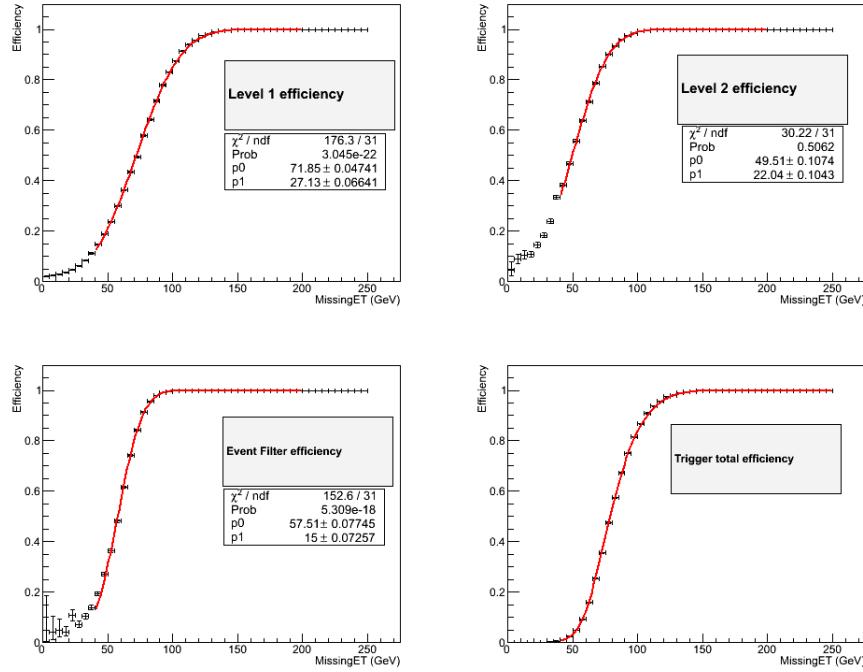


Figure 108: Trigger efficiencies for each level and for over all (bottom right) of trigger EF_xe60_tclcw_loose_delayed using $W \rightarrow \mu\nu + 2$ jets Sherpa events.

- 3480 • for 2 jets: $\text{J12pT} > 120 \text{ GeV}$
- 3481 • for 3 jets and $E_T^{\text{miss}} < 120 \text{ GeV}$: $\text{J123pT} > 170 \text{ GeV}$
- 3482 • for 3 jets and $E_T^{\text{miss}} > 120 \text{ GeV}$: $\text{J123pT} > 150 \text{ GeV}$.

3483 For $E_T^{\text{miss}} > 200 \text{ GeV}$, the trigger scale factor is consistent with 1. The scale factor for $E_T^{\text{miss}} <$
 3484 200 GeV is calculated from the trigger turn-on parameters of data and MC, obtained from the fits. The
 3485 trigger uncertainties are composed of two parts: one is error of the fit from statistical fluctuations, the
 3486 other uncertainty is obtained from the difference between the scale factor of $W \rightarrow \mu\nu$ events and $Z \rightarrow \mu\mu$
 3487 events. The scale factor of $t\bar{t}$ events is for cross-checking the consistency with the others only, as the $t\bar{t}$
 3488 sample is statistically limited.

3489 The scale factors obtained from $Z \rightarrow \mu\mu$, $W \rightarrow \mu\nu$ samples are consistent within statistical uncer-
 3490 tainty (Fig. 112), the scale factor for $t\bar{t}$ is also compatible with the two former scale factors. The total
 3491 uncertainty of trigger is small, about 1% at $E_T^{\text{miss}}=90 \text{ GeV}$, which is small compared to other uncertain-
 3492 ties.

3493 B.4 Apply delayed stream in 0-lepton study

3494 In 0-lepton study, the delayed stream and its trigger can be used in order to gain more events in the low
 3495 E_T^{miss} region. For this study we apply the 0-lepton selection with lepton veto plus 2 or 3 jets selection with
 3496 exactly 2 b -tagged jets. The nominal E_T^{miss} triggers and EF_xe60_tclcw_loose_delayed are used, cleaning
 3497 cuts on sum of jet p_T for 2 and 3 jets bin are also applied to avoid trigger biases. The QCD rejection cuts
 3498 are also applied to reduce the QCD contribution (more at App. C).

Not reviewed, for internal circulation only

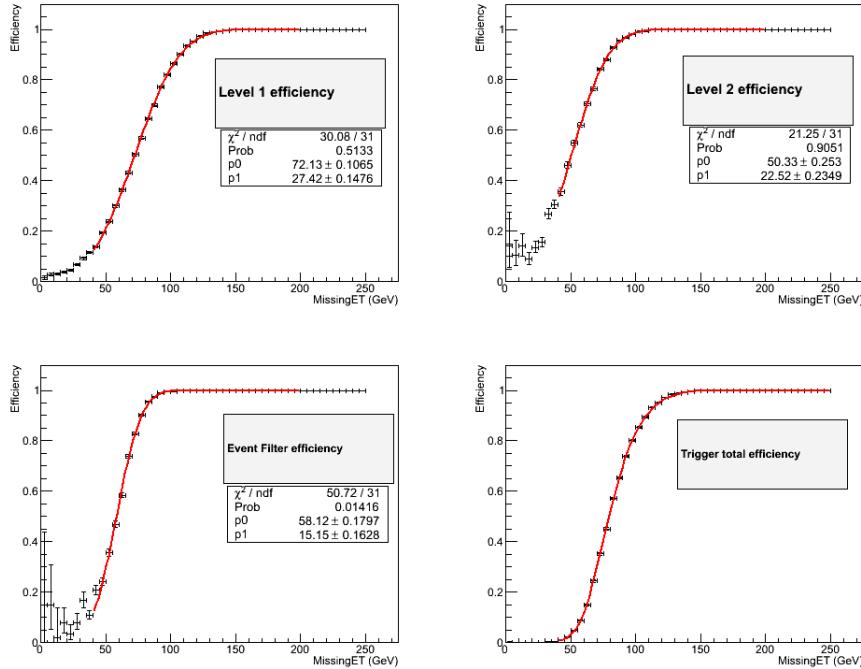


Figure 109: Trigger efficiencies for each level and for over all (bottom right) of trigger EF_xe60_tclcw_loose_delayed using $Z \rightarrow \mu\mu + 2$ jets Sherpa events.

3499 Due to the delayed stream trigger availability, the delayed stream can be used as following: for data
 3500 periods A to D, nominal triggers and nominal data stream are used (As in App. A), from period E1
 3501 onward, if the delayed stream trigger is available, the delayed trigger and data stream will be used in the
 3502 analysis, else, use the nominal triggers and nominal stream instead. Figure 113 shows the data points and
 3503 MC distribution for invariant mass of two b -tagged jets and E_T^{miss} of two b -jets after applying 0-lepton
 3504 selection using delayed stream trigger and nominal triggers.

3505 Using delayed stream trigger in the analysis can help us gaining a total 4% of signal acceptance and
 3506 2% of signal significance in the lowest E_T^{miss} bin (Tables 63, 64), the higher E_T^{miss} bins do not benefit
 3507 from the delayed stream.

3508 The delayed stream implementation and its trigger usage is included in the TrigMETEfficiency pack-
 3509 age (version 00-00-13).

3510 B.5 Mis-modelling issue in 0-lepton analysis

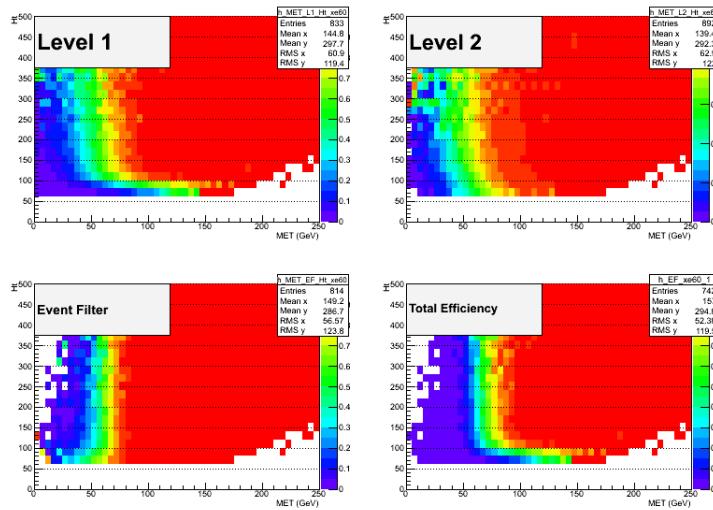
3511 (This part make the section C-4 of App. C obsolete...) In 0-lepton channel of Higgs analysis, at the
 3512 lowest E_T^{miss} bin (90–120 GeV), a mis-modelling issue is observed in the distribution of p_T of vector
 3513 sum of two leading jets while no significant mis-modelling observed at higher E_T^{miss} bin (Figure 114,
 3514 more details are in App. C-3). This issue may be from the bias of trigger modelling, so we can check if
 3515 this bias still exist with the delayed stream trigger since the thresholds of this trigger are lower than the
 3516 ones of nominal triggers.

3517 To check this mis-modelling, we will only interest in the exclusive part of data that delayed stream
 3518 trigger is available. The event selection for this check is as for 0-lepton one, except the trigger require-
 3519 ment, that we require only the delayed stream trigger. We also apply other cuts: $\Delta\phi(jet, jet) < 2.0$ and

Table 62: Fitting parameters at each level of trigger for $Z \rightarrow \mu\mu$ and $W \rightarrow \mu\nu$ samples (MC)

$Z \rightarrow \mu\mu$	without QCD cuts		with QCD cuts	
	Mean value (GeV)	Width	Mean value (GeV)	Width
Level 1	72.13 ± 0.11	27.42 ± 0.15	73.66 ± 0.18	27.7 ± 0.24
Level 2	50.33 ± 0.25	22.52 ± 0.23	51.1 ± 0.48	22.24 ± 0.39
Event Filter	58.12 ± 0.18	15.15 ± 0.16	56.24 ± 0.41	15.81 ± 0.32
$W \rightarrow \mu\nu$	without QCD cuts		with QCD cuts	
	Mean value (GeV)	Width	Mean value (GeV)	Width
Level 1	71.85 ± 0.11	27.13 ± 0.07	73.4 ± 0.08	27.23 ± 0.11
Level 2	49.51 ± 0.11	22.04 ± 0.1	51.57 ± 0.2	20.8 ± 0.17
Event Filter	57.51 ± 0.08	15 ± 0.07	55.72 ± 0.18	15.59 ± 0.14

Not reviewed, for internal circulation only

Figure 110: Correlation of trigger efficiencies between E_T^{miss} and sum of p_T of jets for each level and for over all (bottom right) of trigger EF_xe60_tclcw_loose_delayed using $W \rightarrow \mu\nu + 2$ jets Sherpa samples.

3520 $E_T^{\text{miss}} / \sqrt{J12pT} > 9.0$ to reject more QCD contributions (Figure 115).

3521 Figure 116 show the distributions of transverse momentum of vector sum of 2 jets using delayed
 3522 stream trigger and nominal trigger under the new selection. The results shows that the mis-modelling
 3523 issue still exist if the nominal triggers are used while applying delayed stream trigger shows almost no
 3524 mis-modelling. This may come from the reason that the mis-modelling issue comes from the higher
 3525 thresholds of nominal triggers while delayed stream trigger has smaller ones. This resolve the mis-
 3526 modelling issue and the nominal E_T^{miss} triggers still can be used normally in the Higgs analysis.

Not reviewed, for internal circulation only

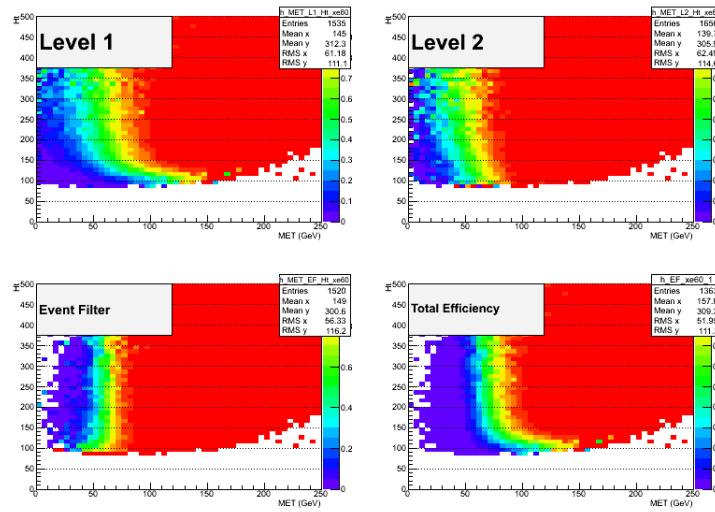


Figure 111: Correlation of trigger efficiencies between E_T^{miss} and sum of p_T of jets for each level and for over all (bottom right) of trigger EF_xe60_tclcw_loose_delayed using $W \rightarrow \mu\nu + 3$ jets Sherpa samples.

Table 63: signal acceptance gain after applying trigger EF_xe60_tclcw_loose_delayed instead of nominal triggers

Number of jets	E_T^{miss} bin 0	E_T^{miss} bin 1
2 jets	1.04 (4 %)	1.02 (2 %)
3 jets	1.03 (4 %)	1.02 (2 %)
2 or 3 jets	1.04 (4 %)	1.02 (2 %)

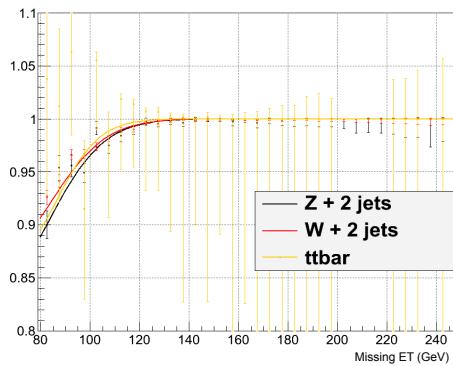


Figure 112: Scale factor of trigger EF_xe60_tclcw_loose_delayed after applying sum of p_T of jets cleaning cut using $Z \rightarrow \mu\mu + 2$ jets, $W \rightarrow \mu\nu$ and $t\bar{t}$ events.

Not reviewed, for internal circulation only

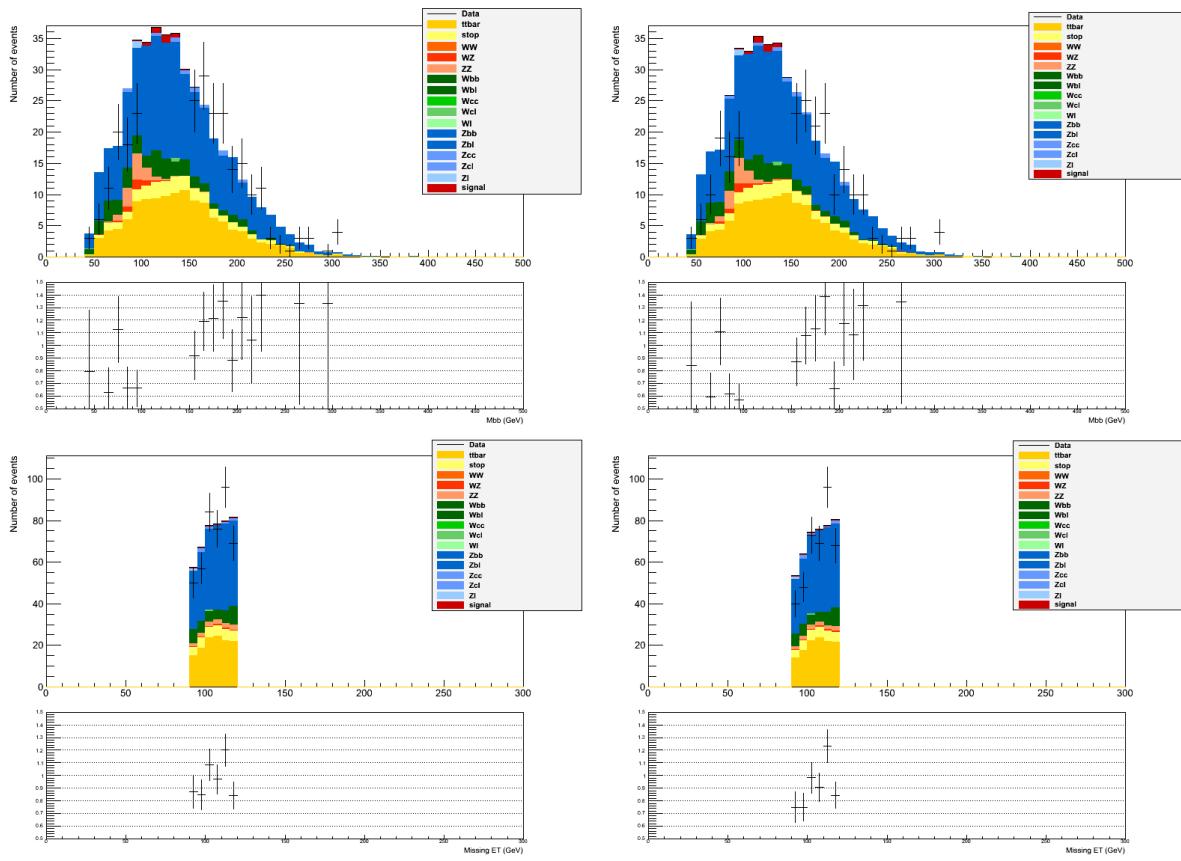


Figure 113: Distribution of mass invariant (top) and E_T^{miss} (bottom) of two b jets using MV1c tagger with 80 % of working point in E_T^{miss} bin from 90 to 120 GeV in bin of 2 jet for data and MC samples using delayed stream trigger (left) and nominal triggers (right).

Table 64: Signal significance gain after applying trigger EF_xe60_tclcw_loose_delayed over the trigger EF_xe80_tclcw_loose

E_T^{miss} bin + N_{jets} bin	Use delayed stream	Use nominal triggers	% gain
bin 0 + 2 jets	0.308	0.302	2 %
bin 0–3 + 2 jets	0.861	0.857	< 1 %
bin 1–3 + 2/3 jets	0.874	0.872	< 1 %
bin 1–3 + 2/3 jets and bin 0 + 2 jets	0.927	0.923	< 1 %

Not reviewed, for internal circulation only

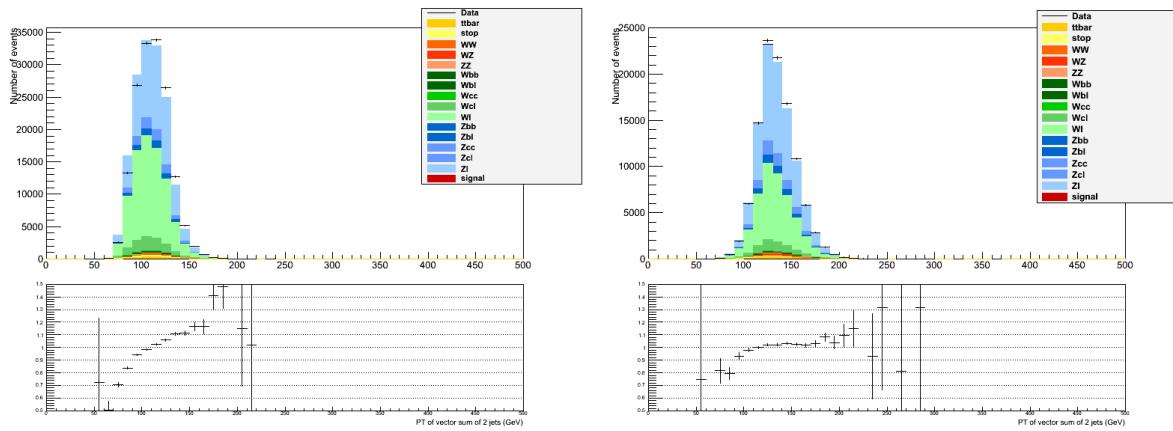


Figure 114: Distribution of transverse momentum of 4–vector sum of 2 jets (pre b –tagging procedure) in E_T^{miss} bin 90–120 GeV (left) and E_T^{miss} bin 120–160 GeV (right) using nominal E_T^{miss} triggers.

Not reviewed, for internal circulation only

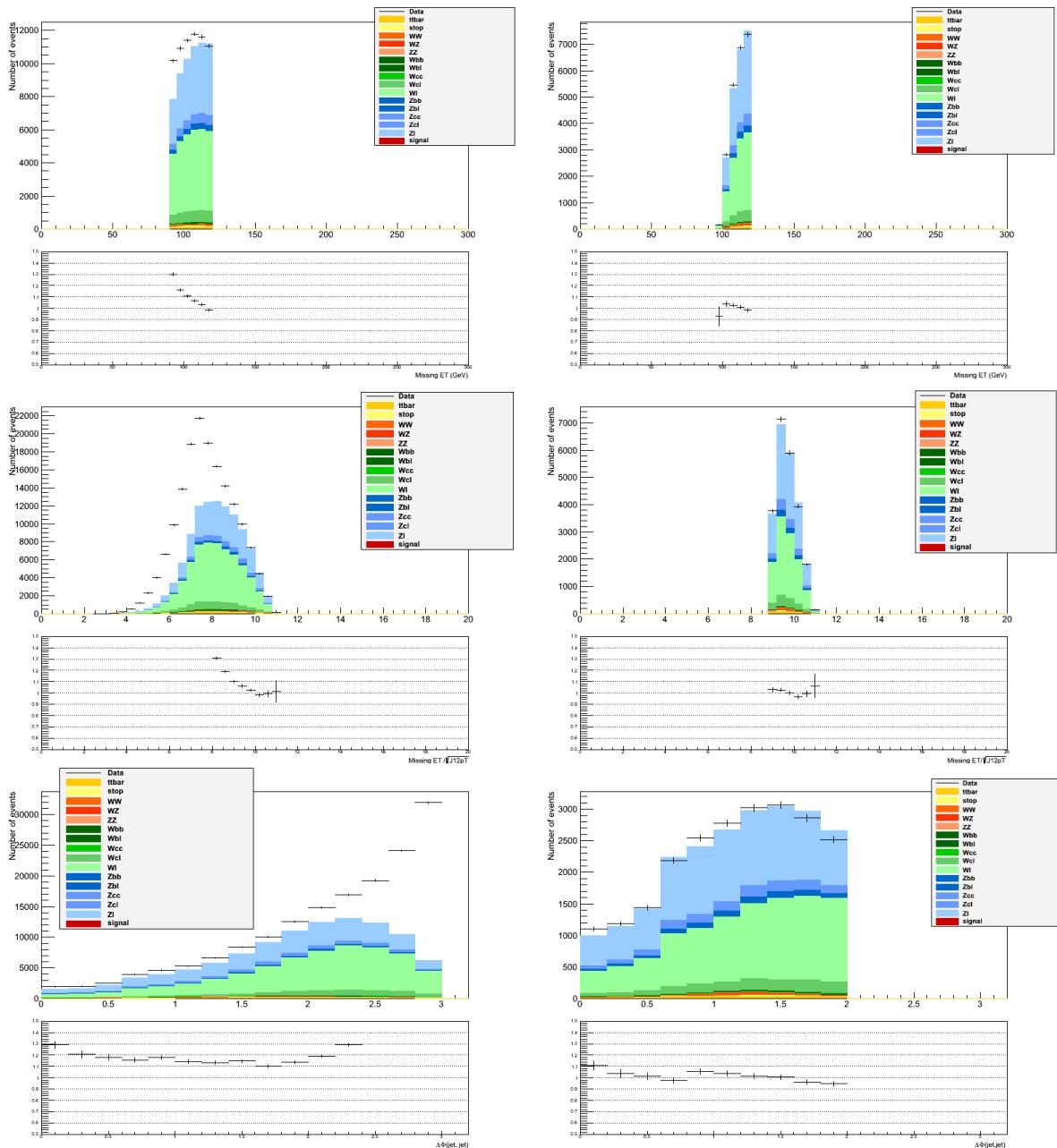


Figure 115: Distributions of E_T^{miss} (top), $E_T^{\text{miss}}/\sqrt{J12pT}$ (middle) and $\Delta\phi(\text{jet}, \text{jet})$ (bottom) in E_T^{miss} bin 90–120 GeV for jets (before b -tagging) before (left) and after (right) applying the additional QCD rejection cuts using delayed stream E_T^{miss} trigger exclusively.

Not reviewed, for internal circulation only

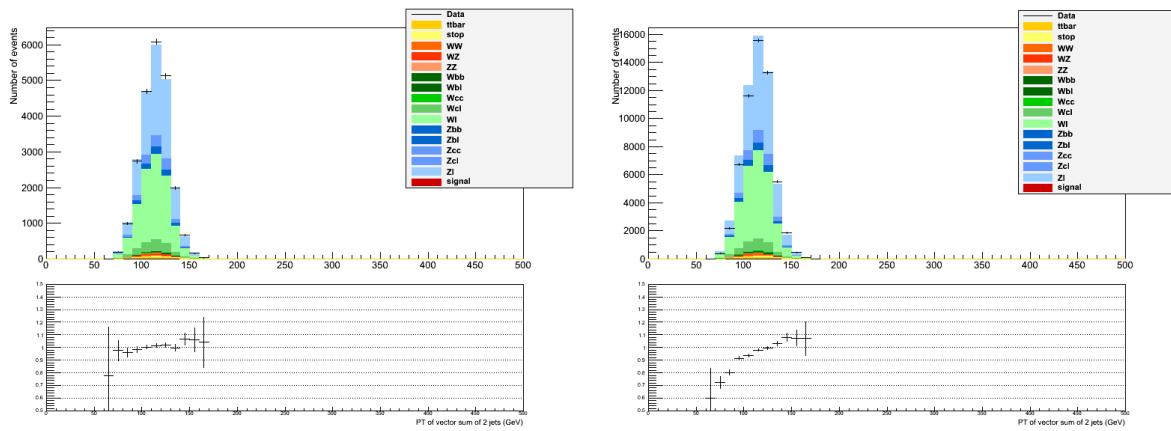


Figure 116: Distributions of transverse momentum of 4–vector sum of 2 jets (pre b –tagging procedure) in E_T^{miss} bin 90–120 GeV using delayed stream trigger exclusively (left) and nominal E_T^{miss} triggers.

Not reviewed, for internal circulation only

3527 C Low E_T^{miss} analysis for Zero Lepton Channel

3528 The former $ZH \rightarrow v\bar{v}b\bar{b}$ analysis [11] only considered $E_T^{\text{miss}} > 120$ GeV mainly because it is difficult
 3529 to parametrize the complete turn on of a E_T^{miss} trigger. For this round of analysis, thanks to the new
 3530 trigger parametrization detailed in Appendix A, it is possible to lower the E_T^{miss} threshold down to 90 or
 3531 100GeV and to gain $ZH \rightarrow v\bar{v}b\bar{b}$ signal acceptance.

3532 Section C.1 describes event selection for low E_T^{miss} regions and shows kinematic distributions which
 3533 have been introduced for low E_T^{miss} region specifically. Section C.2 presents the rejection of QCD multijet
 3534 background and its estimation using a likelihood ratio technique. Section C.3 discusses observed mis-
 3535 modelings and further studies. Finally, Section C.4 discusses the expected sensitivity gain from the low
 3536 E_T^{miss} regions and what is expected once the delayed stream trigger (see Appendix B.5) is implemented
 3537 into low E_T^{miss} region analysis as well.

3538 C.1 Event selection

3539 The kinematic cuts outlined in Section 3.4 are not fully efficient for this region so the selection cuts were
 3540 re-optimized. The $\min\Delta\phi(E_T^{\text{miss}}, \text{jets})$ cut is very efficient at rejecting the multijet background but in this
 3541 lower boost region this cuts removes a large fraction of the $ZH \rightarrow v\bar{v}b\bar{b}$ signal. Instead, $\Delta\phi(\text{jet}_1, \text{jet}_2)$
 3542 and E_T^{miss} significance defined as

$$E_T^{\text{miss}} \text{ Sig} = E_T^{\text{miss}} / \sqrt{p_{T,j1} + p_{T,j2}} \quad (38)$$

3543 are used to reject the QCD multijet background. The remaining multijet background after these cuts is
 3544 further reduced using a multivariate Likelihood-based technique as described in following. Although
 3545 the second $p_T(V)$ bin for the one lepton and two lepton channels is defined between 90-120GeV, in the
 3546 0-lepton low E_T^{miss} region it was decided to tighten the lower E_T^{miss} threshold to 100GeV to avoid possible
 3547 modeling problem due to the trigger bias. This is further discussed in Section C.3. A summary of the
 3548 event selection cuts is given in Table 65. The main differences compared to other signal regions are
 3549 summarized in the Table 65.

3550 3-jet low E_T^{miss} region does not dramatically increase the sensitivity but it does provide a region to test
 3551 the background modeling with higher statistics, especially for $t\bar{t}$ background.

E_T^{miss} (GeV)	100-120	100-120
N_{jet}	2	3
$\Delta\phi(V, H)$	>2.2	>2.8
$\min\Delta\phi(E_T^{\text{miss}}, \text{jets})$	–	>1.5
$\Delta\phi(\text{jet}_1, \text{jet}_2)$	<2.7	–
E_T^{miss} Sig	>7.0	–
Likelihood	>0.5	–

Table 65: Event selection for the 0-lepton analysis between low E_T^{miss} region (100-120GeV) Only cuts optimized or newly implemented are shown.

3552 Figure 117 shows E_T^{miss} Sig and $\Delta\phi(\text{jet}_1, \text{jet}_2)$ distributions and demonstrate the fact that the multijet
 3553 background is controlled with this set of cuts.

3554 C.2 QCD rejection and estimation

3555 After applying cuts discussed in the previous section, the multijet background is not the predominant
 3556 background but is still sizable contribution (5-10% depending on the b-tag category within the 100-

Not reviewed, for internal circulation only

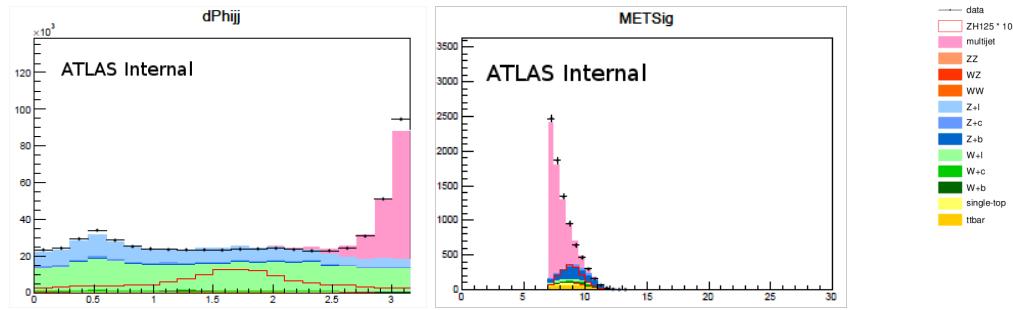


Figure 117: Pre b -tag low E_T^{miss} region kinematics before applying cuts. (left) $\Delta\phi(jet_1, jet_2)$ (right) E_T^{miss} significance.

150GeV $b\bar{b}$ mass window). Since the multijet background is hard to precisely estimate a new multi-variate Likelihood-based multijet rejection technique was developed to further to specifically reject the multijet background.

A likelihood ratio (LR) is defined as: $LR = LH^{\text{signal}} / (LH^{\text{signal}} + LH^{\text{QCD}})$, $LH^{\text{signal}} = \prod_{i=1}^{n_{\text{kin}}} P_i^{\text{signal}}$ and $LH^{\text{QCD}} = \prod_{i=1}^{n_{\text{kin}}} P_i^{\text{QCD}}$, where $P_i^{\text{signal}} (P_i^{\text{QCD}})$ is probability obtained from PDF distribution constructed from Z +jets (multijet) data using the side-band of $\Delta\phi(E_T^{\text{miss}}, p_T^{\text{miss}}) > \pi/2$ pretag events. To produce the PDF templates, the $\Delta\phi(jet_1, jet_2)$ cut is not applied. The kinematic variables used to build the discriminant are:

- $\Delta\phi(jet_1, jet_2)$
- $\Delta\phi(V, H)$
- $\text{mis}H_T$
- $\text{mis}H_T/H_T$

Access to the tool used to apply this likelihood in the analysis is documented in Appendix AP.

Figure 118 shows the PDF distributions used to construct Likelihood function and Figure 119 shows output distributions of the LR . We found that using Z +jets template as the signal PDF does not degrade QCD rejection performance compared to the PDF from $ZH \rightarrow v\bar{v}b\bar{b}$ itself. Furthermore, Z +jets PDF templates make it is possible to be Higgs mass independent and to avoid introducing bias due to $ZH \rightarrow v\bar{v}b\bar{b}$ MC usage. Therefore Z +jet events are used instead of the actual signal to construct the Likelihood.

Figure 120 to Figure 120 shows kinematic distributions before and after applying LR cut.

To estimate the multijet background after applying every cuts, the so-called ABCD method similarly to that discussed in Section 5.4 However, $\min\Delta\phi(E_T^{\text{miss}}, jets)$ cannot be used for the ABCD method since it is not used in the this low E_T^{miss} region. Instead, LR is used to construct ABCD 2-D plane together with $\Delta\phi(E_T^{\text{miss}}, p_T^{\text{miss}})$.

Multijet shapes are obtained from data after subtracting the small electroweak background contributions using the ‘C’-region defined as $\Delta\phi(E_T^{\text{miss}}, p_T^{\text{miss}}) > \pi/2$. For 2 b -tagged events, statistics of data side-band ‘C’ is very limited, therefore shapes are obtained from 1 b -tagged events.

Not reviewed, for internal circulation only

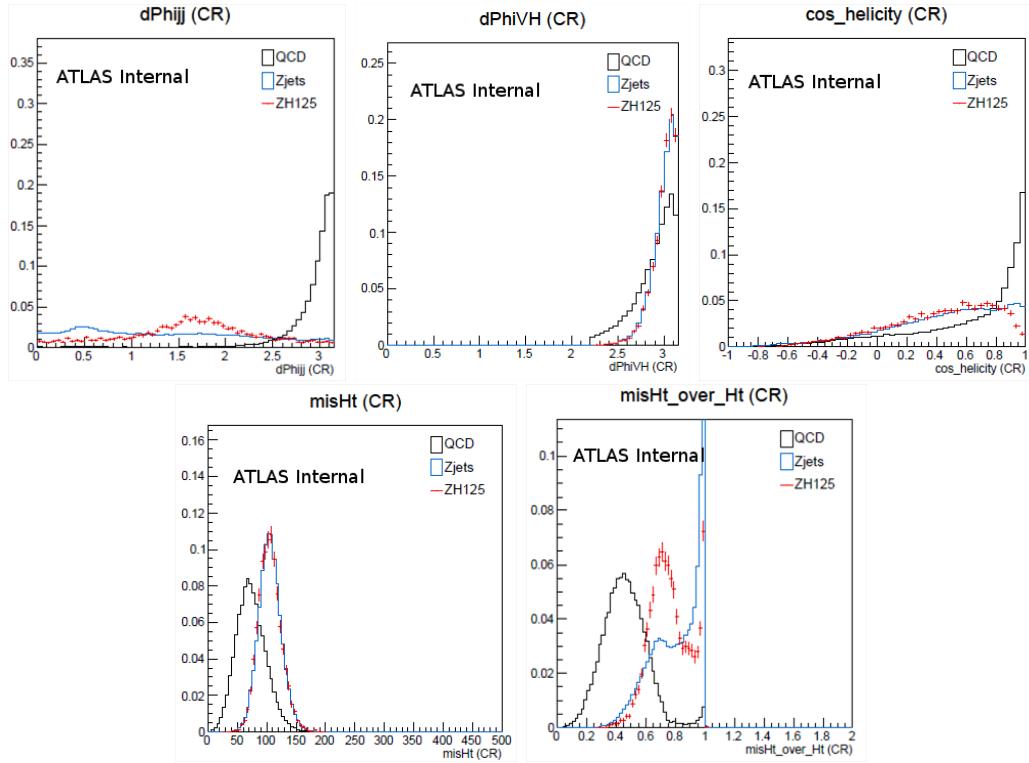


Figure 118: Likelihood PDF kinematics. From top left to bottom right, $\Delta\phi(jet_1, jet_2)$, $\Delta\phi(V, H)$, $\cos(\text{helicity})$, $\text{mis}H_T$ and $\text{mis}H_T/H_T$, respectively. Black line shows QCD template and light blue line shows $Z+jets$ template. As a reference, ZH (125 GeV) signal is shown in red line.

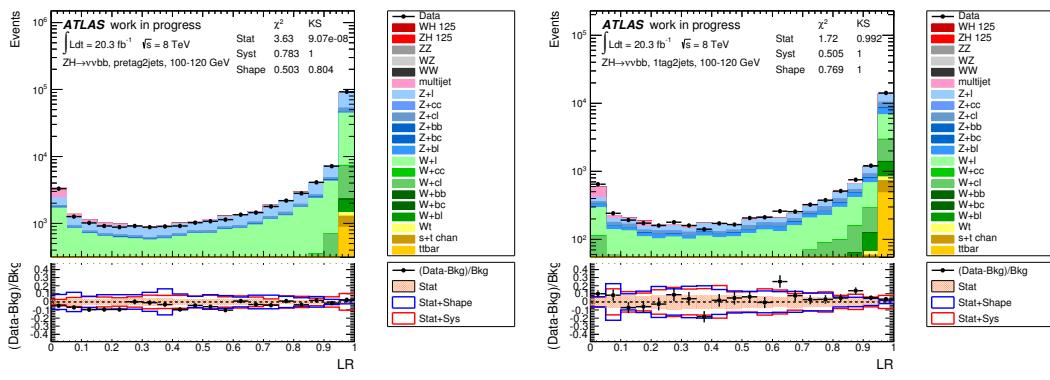


Figure 119: LR distributions. (Left) pretag. (Right) 1-tag.

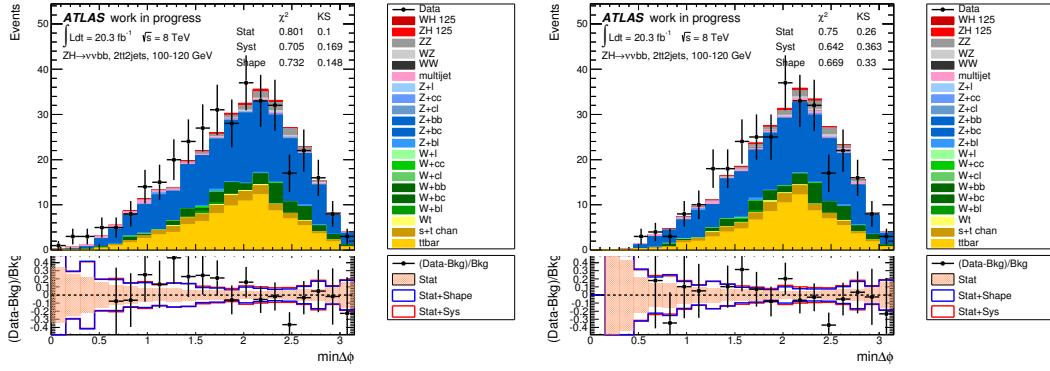


Figure 120: Kinematics before and after applying *LR* QCD rejection cut. (Left) 2-tt tag plot for $\min\Delta\phi(E_T^{\text{miss}}, \text{jets})$ before applying *LR* cut. (Right) 2-tt tag plot for $\min\Delta\phi(E_T^{\text{miss}}, \text{jets})$ after applying *LR* cut.

3583 C.3 Mis-modelings

3584 It was found that the possible mis-modeling of the vector sum of two leading jet p_T ($\text{mis}H_T$) in the low
 3585 E_T^{miss} region, could possibly originated from the bias in the E_T^{miss} trigger modeling. Figure 121 shows
 3586 data-MC agreement for $\text{mis}H_T$ for the E_T^{miss} region: $90 < E_T^{\text{miss}} < 100$ GeV, $100 < E_T^{\text{miss}} < 120$ GeV, and
 3587 $120 < E_T^{\text{miss}} < 160$ GeV. While the $90 < E_T^{\text{miss}} < 100$ GeV region shows possible modeling problems,
 3588 modeling is improved once the E_T^{miss} lower cut threshold is raised to 100 GeV. The agreement is then on
 3589 a similar level as the $120 < E_T^{\text{miss}} < 160$ GeV region.

3590 To further check and understand the source of this mis-modeling the following checks have been
 3591 done.

- 3592 1. Effect from $\Delta\phi(\text{jet}_1, \text{jet}_2)$ correction for $W/Z+\text{jets}$.
- 3593 2. Validation using $W \rightarrow \mu\nu+\text{jets}$ and $Z \rightarrow \mu\mu+\text{jets}$ events.
- 3594 3. JES systematic covers the disagreement.

3595 Figure 122 shows comparisons among lepton categories on $\text{mis}H_T$ distribution with and without the
 3596 $\Delta\phi(\text{jet}_1, \text{jet}_2)$ correction applied. There is no reason to believe this is the source of the mis-modeling.
 3597 For the second test, events which fires E_T^{miss} trigger and request $W \rightarrow \mu\nu$ or $Z \rightarrow \mu\mu$ candidates,
 3598 similarly to the E_T^{miss} trigger parametrization measurement described in Appendix A. No evidence of a
 3599 source of the mis-modeling was seen from this study.

3600 C.4 Sensitivity gain and prospect with delayed trigger

3601 Studies ongoing, an estimate will be added soon.

Not reviewed, for internal circulation only

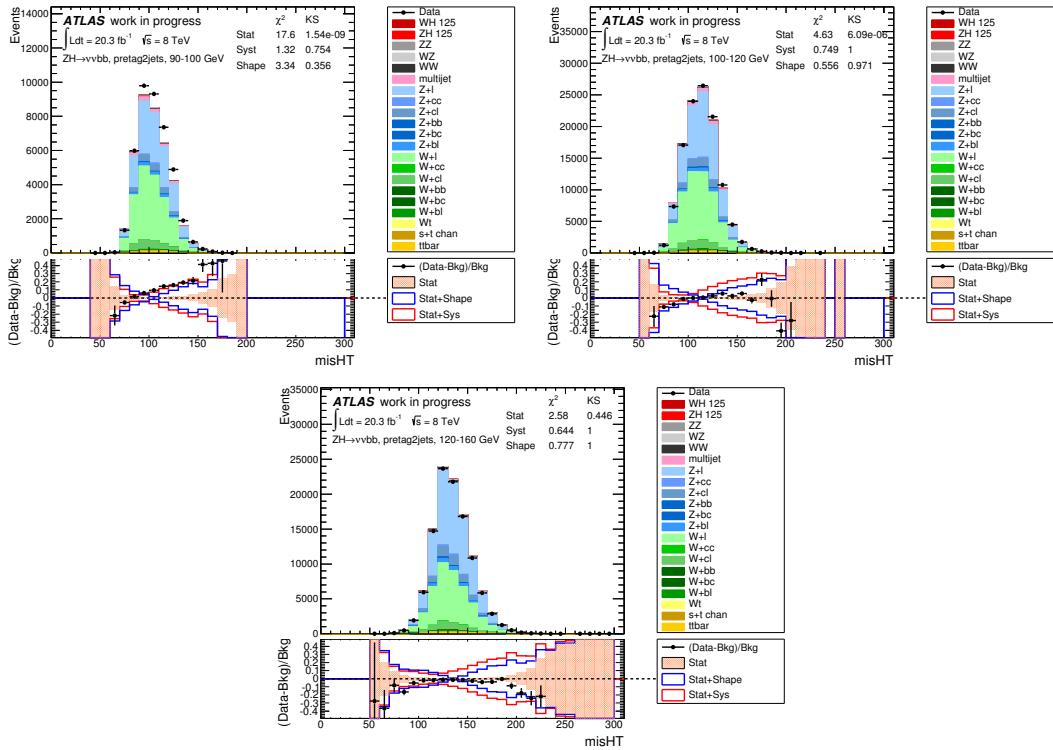


Figure 121: Ptag $\text{mis}H_T$ distributions for low E_T^{miss} region. From left to right, $90 < E_T^{\text{miss}} < 100$ GeV, $100 < E_T^{\text{miss}} < 120$ GeV, $120 < E_T^{\text{miss}} < 160$ GeV, respectively.

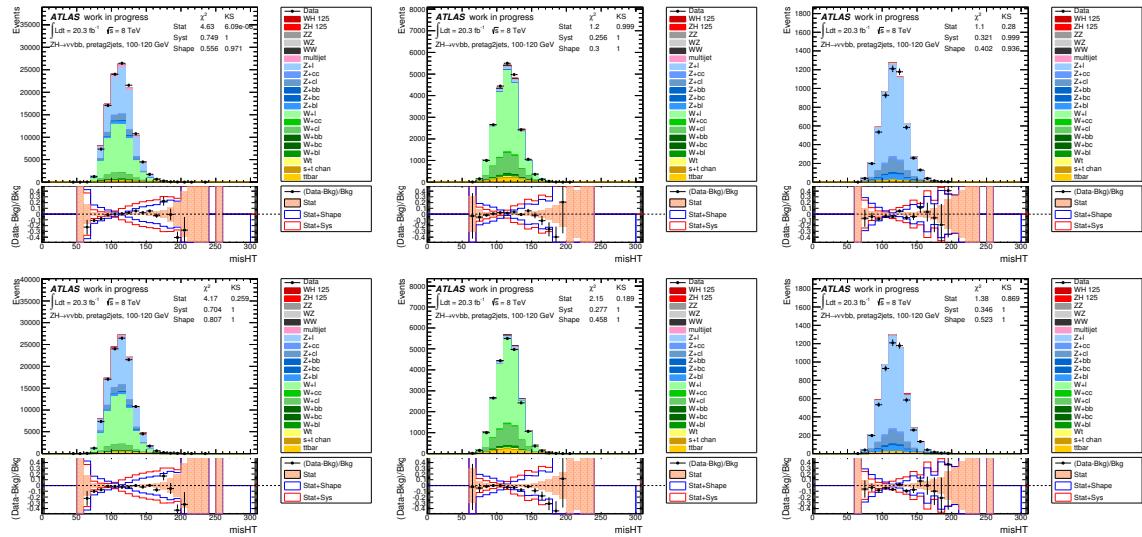


Figure 122: Ptag $\text{mis}H_T$ distributions for $100 < E_T^{\text{miss}} < 120$ GeV (Top) From left to right, 0-lepton, 1-lepton, 2-lepton with applying $\Delta\phi(j_1, j_2)$ correction for $W+\text{jets}/Z+\text{jets}$ modeling. (Bottom) From left to right, 0-lepton, 1-lepton, 2-lepton without applying $\Delta\phi(j_1, j_2)$ correction for $W+\text{jets}/Z+\text{jets}$ modeling.

3602 D E_T^{miss} trigger for 1 lepton events

3603 For 1-lepton ($WH \rightarrow \ell v b\bar{b}$) analysis in muon channel, events triggered by E_T^{miss} are used in addition to
 3604 single lepton triggered events in order to recover the inefficiency of the muon trigger. In the EPS analysis
 3605 E_T^{miss} triggered events were also used when $p_T^W > 160$ GeV. In this analysis, the application threshold is
 3606 lowered to 120 GeV, thanks to well described E_T^{miss} trigger properties derived in 0-lepton analysis.

3607 D.1 E_T^{miss} triggered muon events

3608 At the level of on-line physics objects, E_T^{miss} is calculated by using only calorimeter components, thus
 3609 the muon momentum is not propagated to the E_T^{miss} calculation. This is the reason why E_T^{miss} triggers are
 3610 helpful for this analysis.

3611 In muon channel of 1-lepton analysis, the primary triggers are single muon triggers which are
 3612 EF_mu24vhi_medium1 and EF_mu36_medium1. However, the plateaus of these trigger efficiencies are
 3613 around 80%. This is because of the limited acceptance of L1 muon chambers in some region of the
 3614 detector and also the inefficiency for the high p_T muons. In order to recover this inefficiency coming
 3615 from muon trigger requirement, E_T^{miss} triggers are introduced. They are a combination of EF_xe80_tclcw,
 3616 EF_xe80T_tclcw_loose and EF_xe80_tclcw_loose. Details of the combination of E_T^{miss} triggers are de-
 3617 scribed in Appendix A.

3618 In case of $p_T^W > 120$ GeV, E_T^{miss} triggers are used only when the single muon triggers mentioned
 3619 above are not fired.

3620 D.2 E_T^{miss} trigger efficiency and scale factor

3621 Trigger scale factor is provided by the 0 lepton analysis which is parametrized by E_T^{miss} . However to
 3622 emulate this scale factor, E_T^{miss} should be calculated without muon momentum in 1-lepton muon channel.
 3623 This is because muons are not taken into account in the calculation of E_T^{miss} at trigger level. Therefore,
 3624 the data/MC agreement of E_T^{miss} without muon contribution ($E_T^{\text{miss}}(\mu)$) should be checked. Figures 123–
 3625 125(126–128) show the distribution of $E_T^{\text{miss}}(\mu)$ for 2 (3) jet bin.

3626 D.3 QCD multi-jet background estimation

3627 QCD multijet background is estimated from data with fitting of the muon p_T . The estimation method
 3628 is the same as the nominal 1-lepton analysis except changing the trigger requirement for the templates
 3629 from data. Details are described in Appendix R.

3630 D.4 Sensitivity gain

3631 Figures 129–131 (132–134) show the m_{jj} distribution for each p_T^W bin and b -tagging category in 2 (3)
 3632 jet bin. Based on this distribution in each category, Poisson significance is calculated within the range
 3633 of $100 < m_{jj} < 150$ GeV. The combined significance of the three 2 tag categories (loose, medium and
 3634 tight) are shown in Table 66 for 2 and 3 jet bins with the final combined sensitivity of 2 and 3 jet bins.
 3635 The sensitivity gain by E_T^{miss} triggered events compared to single muon triggered events is 10.8%. The
 3636 sensitivity gain compared to nominal 1-lepton analysis including electron channel is XX%(to be updated
 3637 with the final fit).

Not reviewed, for internal circulation only

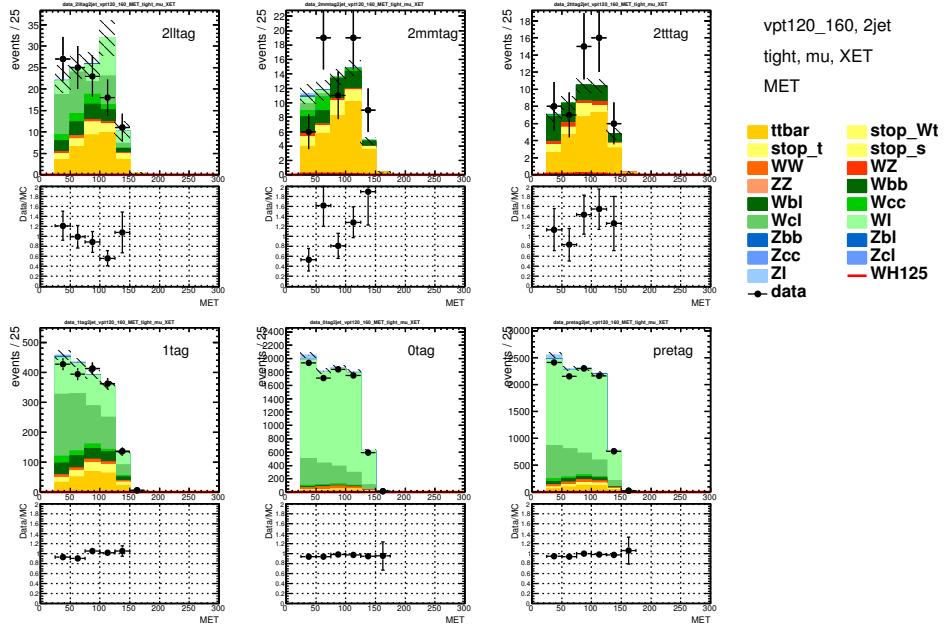


Figure 123: The distribution of E_T^{miss} without muon contribution ($E_T^{\text{miss}}(\mu)$) of E_T^{miss} triggered events in 2 jet bin, $120 < p_T^W < 160$ GeV. Each b -tagging category is shown in 2 loose tag (top left), 2 medium tag (top middle), 2 tight tag (top right), 1 tag (bottom left), 0 tag (bottom middle) and pre-tag (bottom right). Now plots are just E_T^{miss} (including muon), PLOTS TO BE UPDATED.

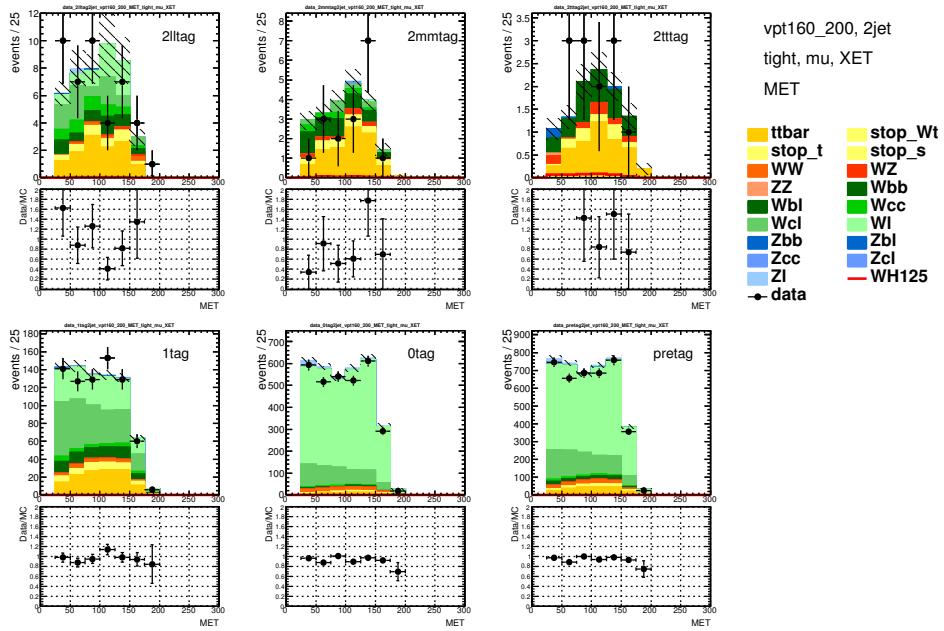


Figure 124: The distribution of E_T^{miss} without muon contribution ($E_T^{\text{miss}}(\mu)$) of E_T^{miss} triggered events in 2 jet bin, $160 < p_T^W < 200$ GeV. Each b -tagging category is shown in 2 loose tag (top left), 2 medium tag (top middle), 2 tight tag (top right), 1 tag (bottom left), 0 tag (bottom middle) and pre-tag (bottom right). Now plots are just E_T^{miss} (including muon), PLOTS TO BE UPDATED.

Not reviewed, for internal circulation only

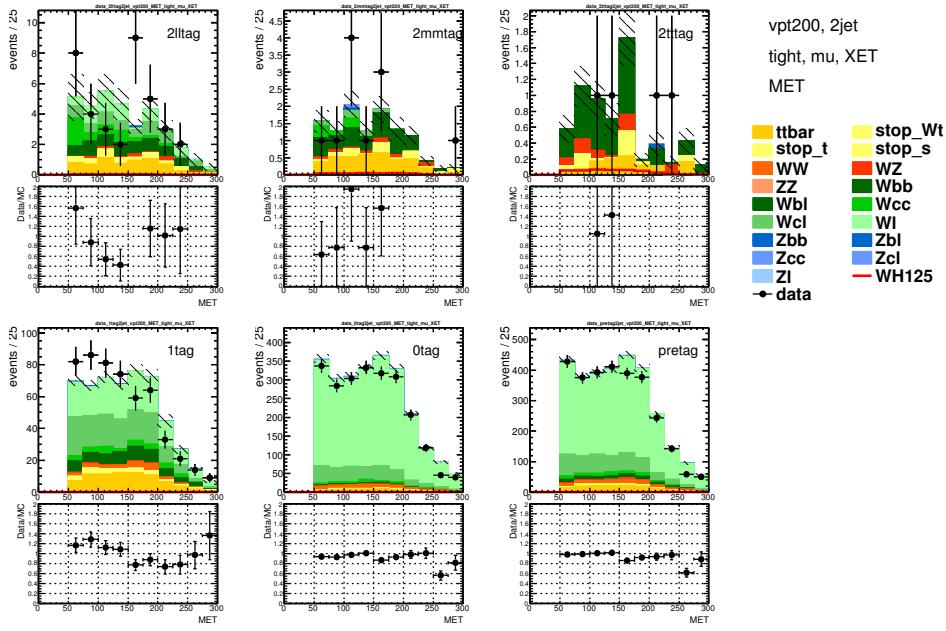


Figure 125: The distribution of E_T^{miss} without muon contribution ($E_T^{\text{miss}}(\mu)$) of E_T^{miss} triggered events in 2 jet bin, $p_T^W > 200$ GeV. Each b -tagging category is shown in 2 loose tag (top left), 2 medium tag (top middle), 2 tight tag (top right), 1 tag (bottom left), 0 tag (bottom middle) and pre-tag (bottom right). Now plots are just E_T^{miss} (including muon), PLOTS TO BE UPDATED.

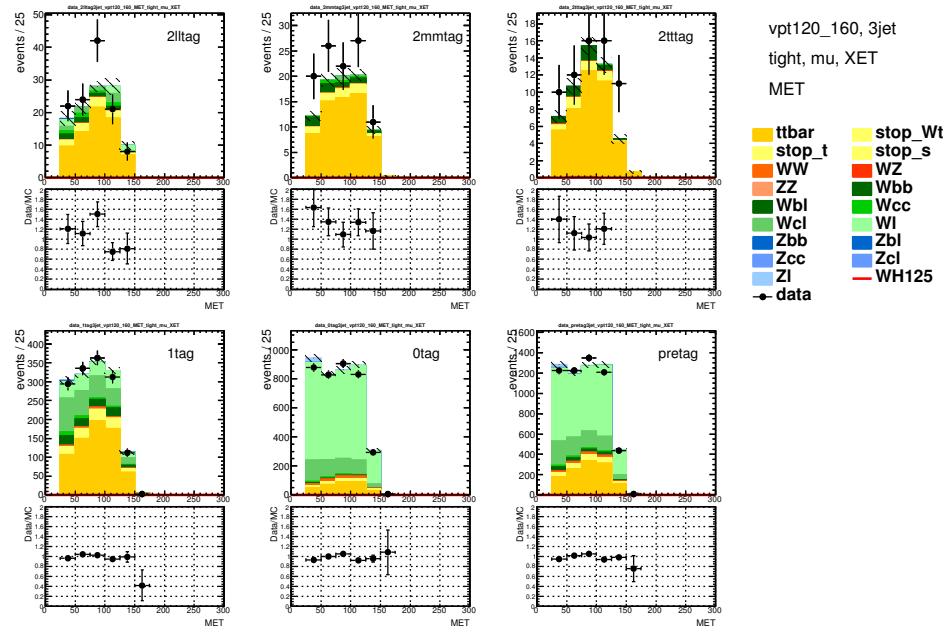


Figure 126: The distribution of E_T^{miss} without muon contribution ($E_T^{\text{miss}}(\mu)$) of E_T^{miss} triggered events in 3 jet bin, $120 < p_T^W < 160$ GeV. Each b -tagging category is shown in 2 loose tag (top left), 2 medium tag (top middle), 2 tight tag (top right), 1 tag (bottom left), 0 tag (bottom middle) and pre-tag (bottom right). Now plots are just E_T^{miss} (including muon), PLOTS TO BE UPDATED.

Not reviewed, for internal circulation only

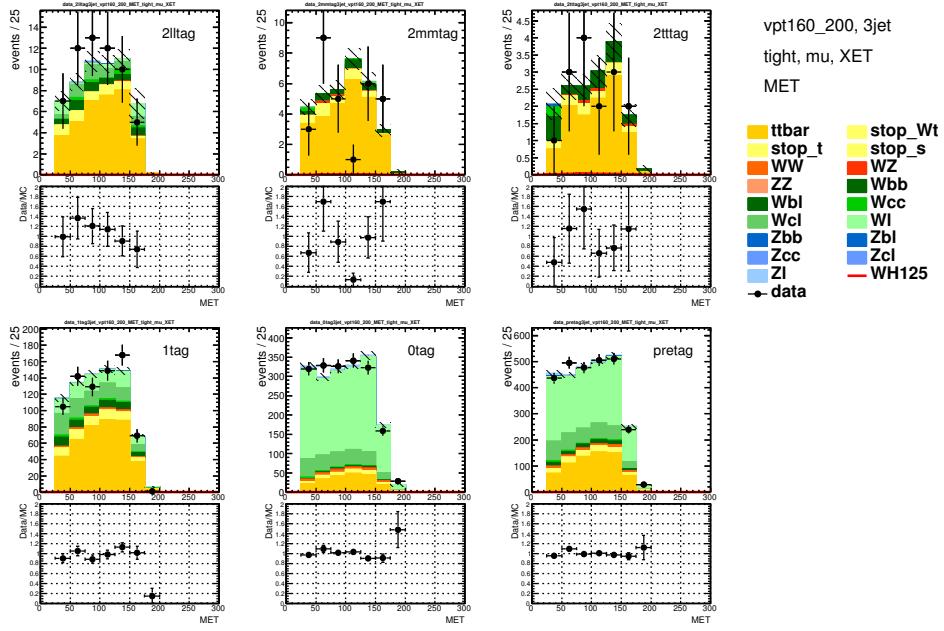


Figure 127: The distribution of E_T^{miss} without muon contribution ($E_T^{\text{miss}}(\mu)$) of E_T^{miss} triggered events in 3 jet bin, $160 < p_T^W < 200$ GeV. Each b -tagging category is shown in 2 loose tag (top left), 2 medium tag (top middle), 2 tight tag (top right), 1 tag (bottom left), 0 tag (bottom middle) and pre-tag (bottom right). Now plots are just E_T^{miss} (including muon), PLOTS TO BE UPDATED.

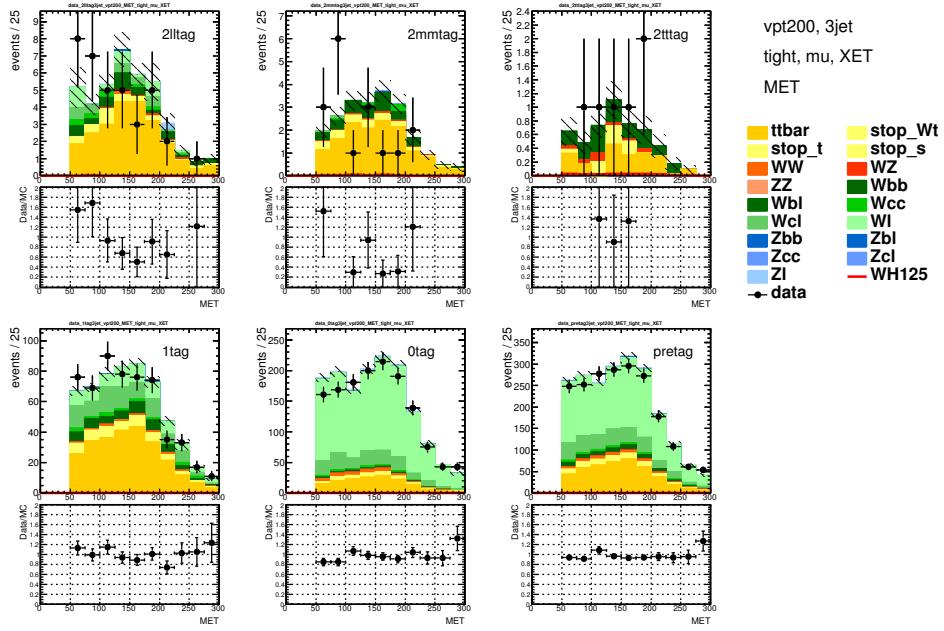


Figure 128: The distribution of E_T^{miss} without muon contribution ($E_T^{\text{miss}}(\mu)$) of E_T^{miss} triggered events in 3 jet bin, $p_T^W > 200$ GeV. Each b -tagging category is shown in 2 loose tag (top left), 2 medium tag (top middle), 2 tight tag (top right), 1 tag (bottom left), 0 tag (bottom middle) and pre-tag (bottom right). Now plots are just E_T^{miss} (including muon), PLOTS TO BE UPDATED.

Not reviewed, for internal circulation only

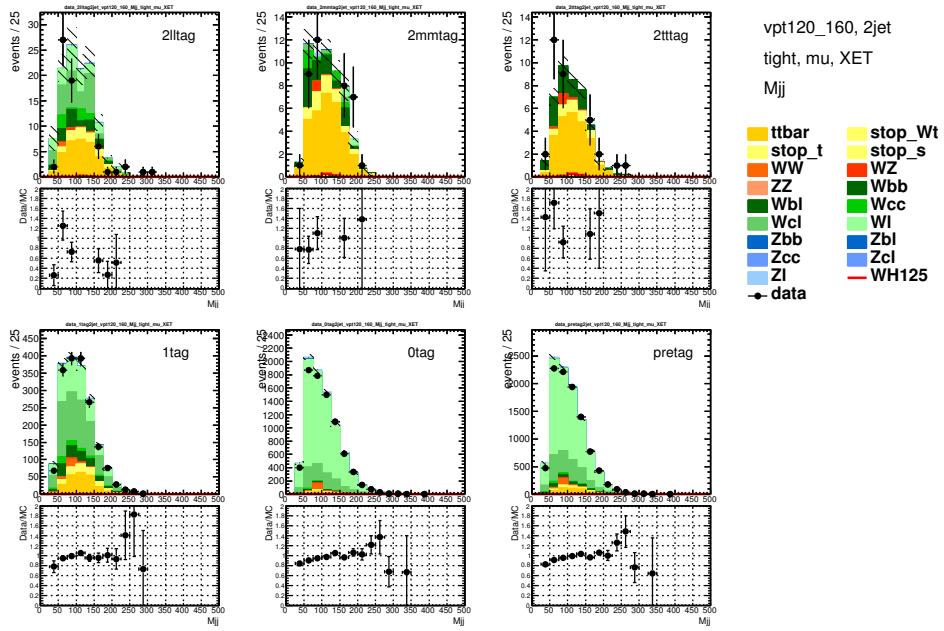


Figure 129: m_{jj} distributions of E_T^{miss} triggered events in 2 jet bin, $120 < p_T^W < 160$ GeV. Each b -tagging category is shown in 2 loose tag (top left), 2 medium tag (top middle), 2 tight tag (top right), 1 tag (bottom left), 0 tag (bottom middle) and pre-tag (bottom right). Data points are blinded in $100 < m_{jj} < 150$ GeV in 2 tag categories. PLOTS TO BE UPDATED.

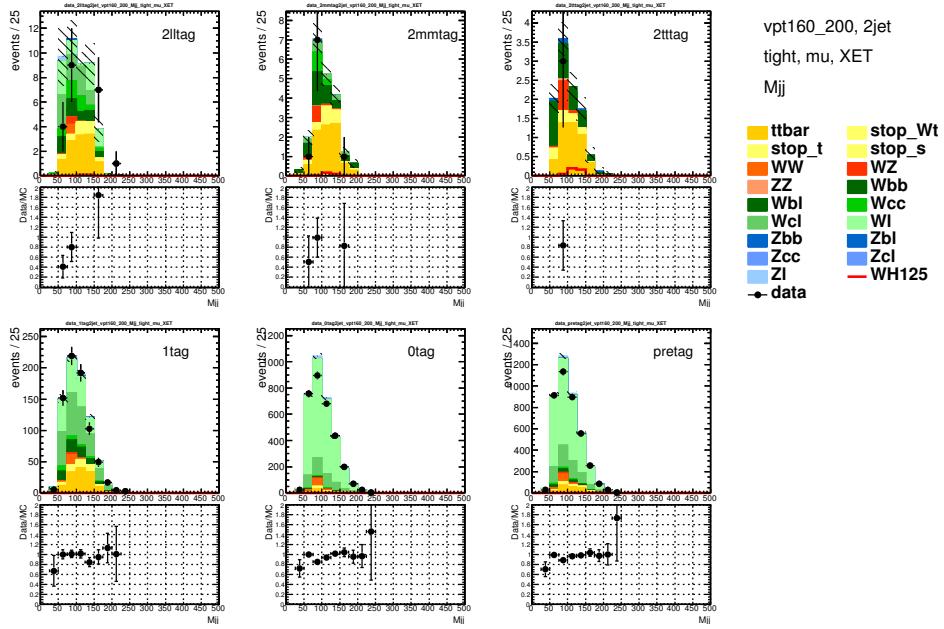


Figure 130: m_{jj} distributions of E_T^{miss} triggered events in 2 jet bin, $160 < p_T^W < 200$ GeV. Each b -tagging category is shown in 2 loose tag (top left), 2 medium tag (top middle), 2 tight tag (top right), 1 tag (bottom left), 0 tag (bottom middle) and pre-tag (bottom right). Data points are blinded in $100 < m_{jj} < 150$ GeV in 2 tag categories. PLOTS TO BE UPDATED.

Not reviewed, for internal circulation only

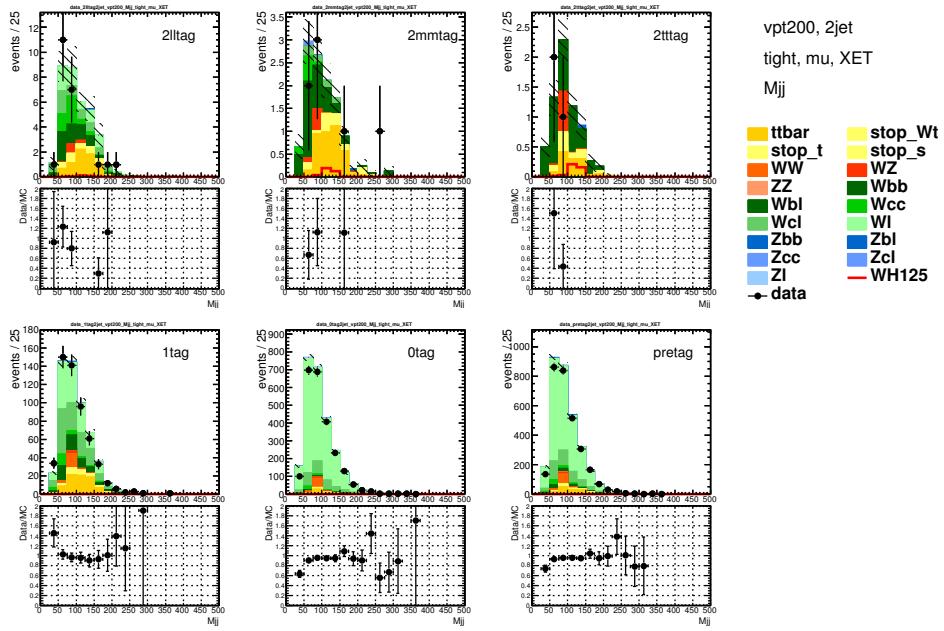


Figure 131: m_{jj} distributions of E_T^{miss} triggered events in 2 jet bin, $p_T^W > 200$ GeV. Each b -tagging category is shown in 2 loose tag (top left), 2 medium tag (top middle), 2 tight tag (top right), 1 tag (bottom left), 0 tag (bottom middle) and pre-tag (bottom right). Data points are blinded in $100 < m_{jj} < 150$ GeV in 2 tag categories. PLOTS TO BE UPDATED.

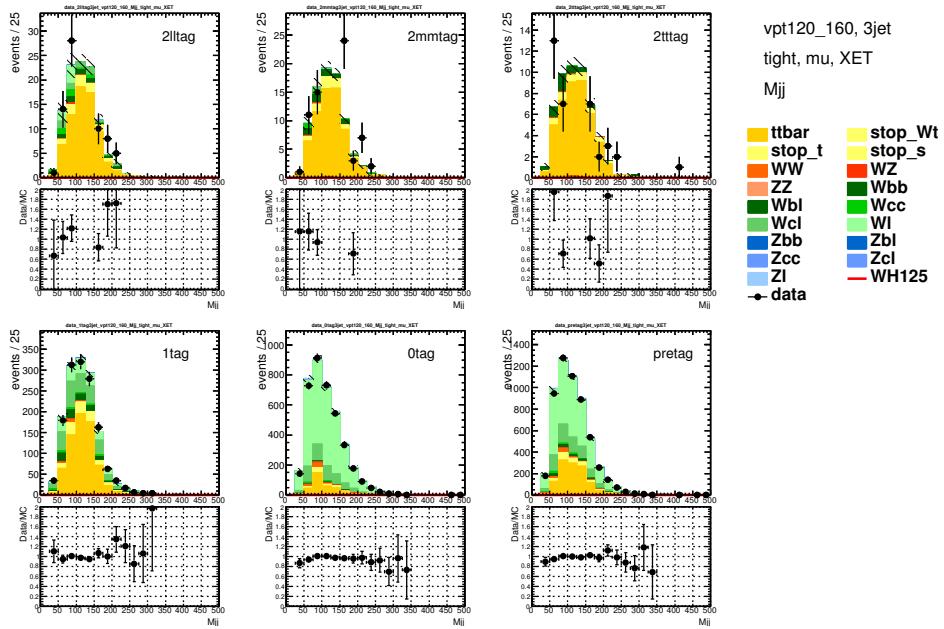


Figure 132: m_{jj} distributions of E_T^{miss} triggered events in 3 jet bin, $120 < p_T^W < 160$ GeV. Each b -tagging category is shown in 2 loose tag (top left), 2 medium tag (top middle), 2 tight tag (top right), 1 tag (bottom left), 0 tag (bottom middle) and pre-tag (bottom right). Data points are blinded in $100 < m_{jj} < 150$ GeV in 2 tag categories. PLOTS TO BE UPDATED.

Not reviewed, for internal circulation only

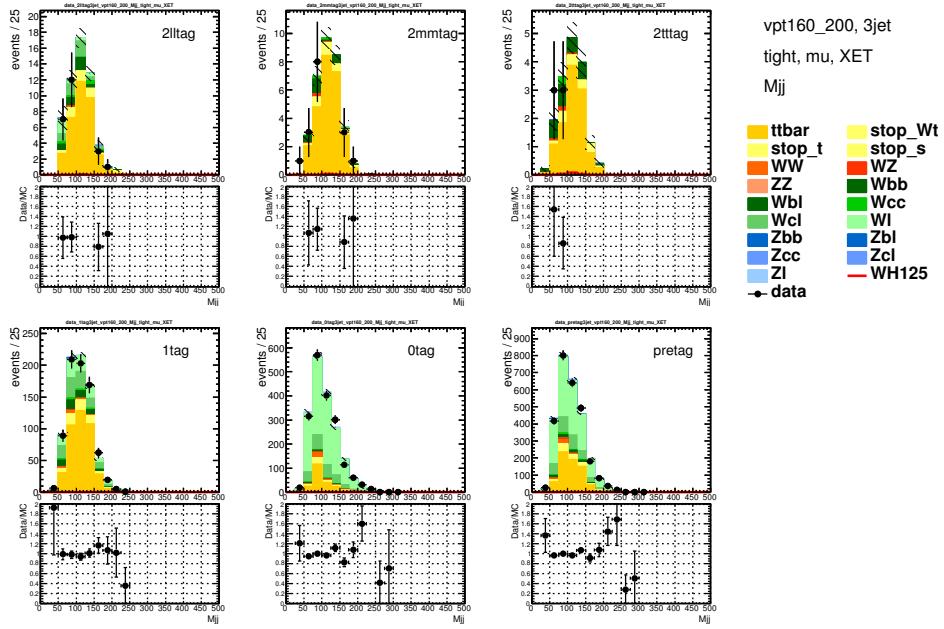


Figure 133: m_{jj} distributions of E_T^{miss} triggered events in 3 jet bin, $160 < p_T^W < 200$ GeV. Each b -tagging category is shown in 2 loose tag (top left), 2 medium tag (top middle), 2 tight tag (top right), 1 tag (bottom left), 0 tag (bottom middle) and pre-tag (bottom right). Data points are blinded in $100 < m_{jj} < 150$ GeV in 2 tag categories. PLOTS TO BE UPDATED.

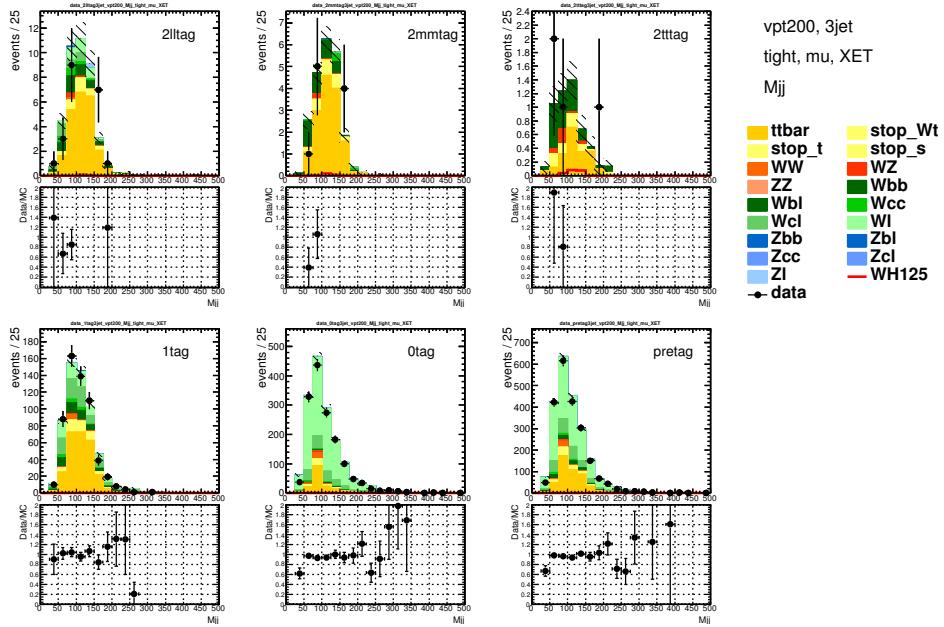


Figure 134: m_{jj} distributions of E_T^{miss} triggered events in 3 jet bin, $p_T^W > 200$ GeV. Each b -tagging category is shown in 2 loose tag (top left), 2 medium tag (top middle), 2 tight tag (top right), 1 tag (bottom left), 0 tag (bottom middle) and pre-tag (bottom right). Data points are blinded in $100 < m_{jj} < 150$ GeV in 2 tag categories. PLOTS TO BE UPDATED.

Not reviewed, for internal circulation only

Table 66: Significance in 2 and 3 jet bins, and in the combination. NUMBERS TO BE UPDATED.

p_T^W GeV	all categories - muon channel
2 jet bin	
Single muon trigger	0.8256
E_T^{miss} trigger	0.3943
3 jet bin	
Single muon trigger	0.2660
E_T^{miss} trigger	0.1378
combination of 2 and 3 jet bins	
Single muon trigger	0.8674
E_T^{miss} trigger	0.4157
Total	0.9619

3638 E Electron Isolation

3639 A Tag&Probe measurement of electron isolation efficiencies and derived scale factors is presented using
 3640 $Z \rightarrow e^+e^-$ resonances in 2012 LHC data and AF-II *Sherpa Z+jets* Monte Carlo events. The measure-
 3641 ment considers **VeryTightLH** electrons [17, 18] probing track and calorimeter isolation parameters as
 3642 defined in Sections 3.2.1.3 (Equation 1) and 3.2.1.1 (Equation 2) respectively. Both parameter thresh-
 3643 olds are set to 0.04 as previously defined for VH tight leptons. Furthermore, a variation of tag and probe
 3644 quality requirements is applied to estimate systematic uncertainties of the method.

3645 E.1 Tag and Probe Algorithm

3646 Electrons may qualify to become a tag or probe candidate if the following criteria are fulfilled:

- 3647 • a transverse energy $E_T > 20$ GeV,
- 3648 • within a pseudorapidity range of $|\eta| < 2.47$ (Si tracking region),
- 3649 • matched to a single lepton trigger (EF_e24vhi_medium1 or EF_e60_medium1),
- 3650 • truth matched to a Z boson incl. Bremsstrahlung and final state radiation in Monte Carlo events.

3651 In addition, the tag selection excludes any electrons in the crack region ($1.37 < |\eta| < 1.52$), requires
 3652 $E_T > 25$ GeV and uses 4 quality variations based on isolation:

- 3653 1. no isolation requirement,
- 3654 2. pass track isolation only,
- 3655 3. pass calorimeter isolation only,
- 3656 4. pass both track and calorimeter isolation.

3657 The probe electron must be of opposite charge to the selected tag electron and form together an invariant
 3658 di-electron mass close to the Z boson mass using 3 quality variations:

- 3659 1. loose mass window of $|m_Z - m_{e^+e^-}| < 30$ GeV,
- 3660 2. medium mass window of $|m_Z - m_{e^+e^-}| < 20$ GeV,
- 3661 3. tight mass window of $|m_Z - m_{e^+e^-}| < 10$ GeV.

3662 All possible permutations of tag&probe pairs in any given event are used for each of the 4×3 quality
 3663 variations and finally contribute to the efficiency measurement, which is defined as

$$\varepsilon = \frac{N_{\text{probe} + \text{iso}}}{N_{\text{probe}}} \quad \text{per variation and event,} \quad (39)$$

3664 where N_{probe} is the number of probes passing the basic selection criteria described above and $N_{\text{probe} + \text{iso}}$
 3665 is the number of probes that pass additionally the track and calorimeter isolation criteria. This is done
 3666 for both data and Monte Carlo events in order to derive scale factors for each variation v . These are then
 3667 combined using standard error propagation:

$$SF_{\text{comb}} = N_v^{-1} \sum SF_v, \quad \sigma_{\text{comb}}^{\text{stat}} = N_v^{-1} \sum \sigma_{SF_v}^{\text{stat}}, \quad \sigma_{\text{comb}}^{\text{syst}} = \sqrt{N_v^{-1} \sum (SF_v - \mu)^2}. \quad (40)$$

3668 The measurement is done as a function of E_T and η , while other dependencies have also been studied,
 3669 such as the dependence on jets and their multiplicity in the vicinity of the probing electron.

3670 E.2 Results

3671 The electron isolation efficiency measured in both 8TeV data and Monte Carlo events using the above
 3672 Tag&Probe method is shown in Fig. 135(a)–135(b) as a function of E_T and η . Generally the efficiency
 3673 drops down to $\sim 73\%$ at low E_T and central η and rises above 90% for all η for $E_T > 60$ GeV. The
 3674 derived scale factors using these efficiencies are shown both as a function of E_T and η in Fig. 135(c)
 3675 as well as inclusive in E_T in Fig. 135(d). This former nominal 2D scale factor map is used only in the
 3676 1-lepton analysis.

3677 A similar measurement has been made for VeryLooseLH electrons probing track isolation only for
 3678 the 2-lepton analysis. Since the resulting scale factors were ~ 1 , no isolation scale factors are applied in
 3679 this analysis.

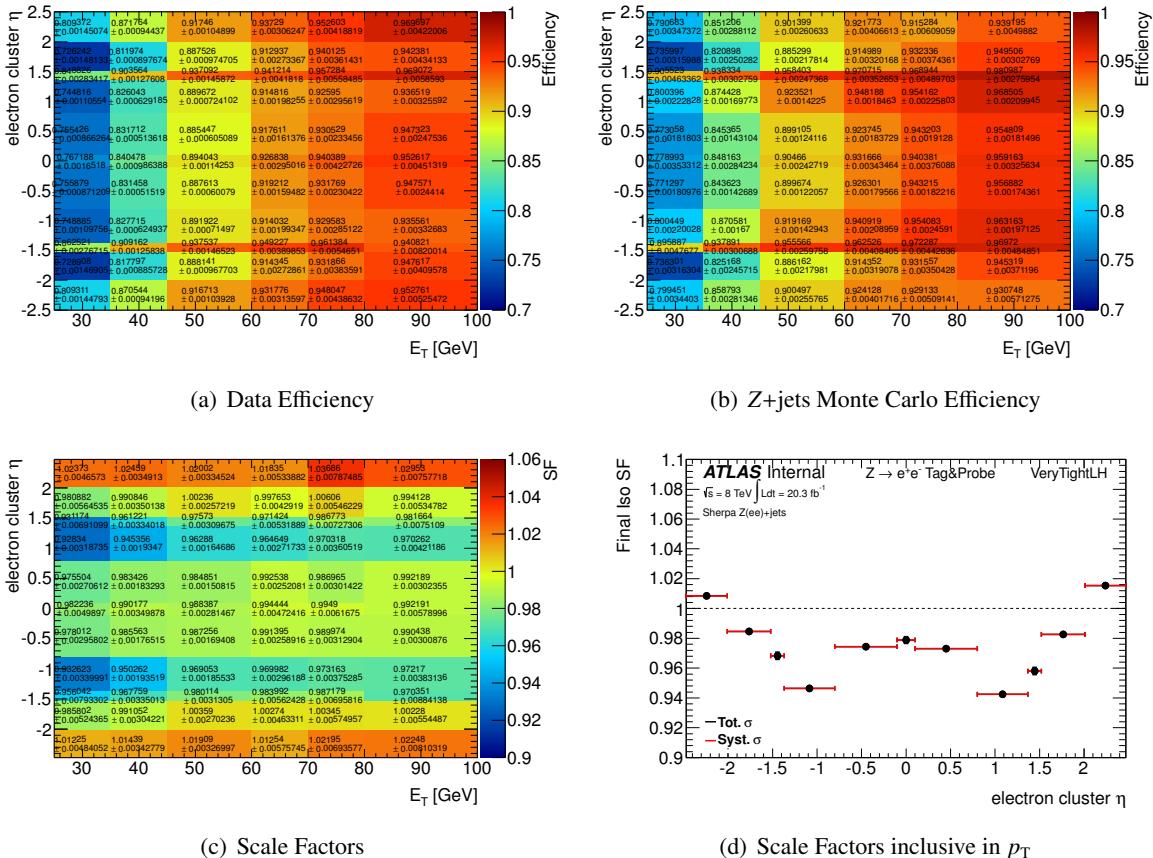


Figure 135: Electron isolation efficiencies and derived scale factors.

Not reviewed, for internal circulation only

3680 F Muon isolation

3681 A Tag&Probe measurement of muon isolation efficiencies and derived scale factors is presented using
 3682 $Z \rightarrow \mu^+ \mu^-$ resonances in 2012 LHC data and AF-II *Sherpa Z+jets* Monte Carlo events. The mea-
 3683 surement considers **Tight** muons probing track and calorimeter isolation thresholds and uses the same
 3684 method as described in the previous section with only minor changes:

- 3685 • the probe (tag) muon has a transverse momentum $p_T > 15(20)$ GeV,
- 3686 • within a pseudorapidity range of $|\eta| < 2.5$,
- 3687 • matched to a single lepton trigger (EF_mu24i_tight or EF_mu36_tight),
- 3688 • no Z boson truth matching.

3689 F.1 Results

3690 The muon isolation efficiency measured in both 8TeV data and Monte Carlo events using the above
 3691 Tag&Probe method is shown in Fig. 136(a)–136(b) as a function of p_T and η . Generally the efficiency
 3692 decreases down to $\sim 73\%$ at low p_T and central η and rises above 90% for all η for $E_T > 50$ GeV. The
 3693 derived scale factors using these efficiencies are shown both as a function of p_T and η in Fig. 136(c) as
 3694 well as inclusive in p_T in Fig. 136(d). This former nominal 2D scale factor map is used in the 1-lepton
 3695 analysis.

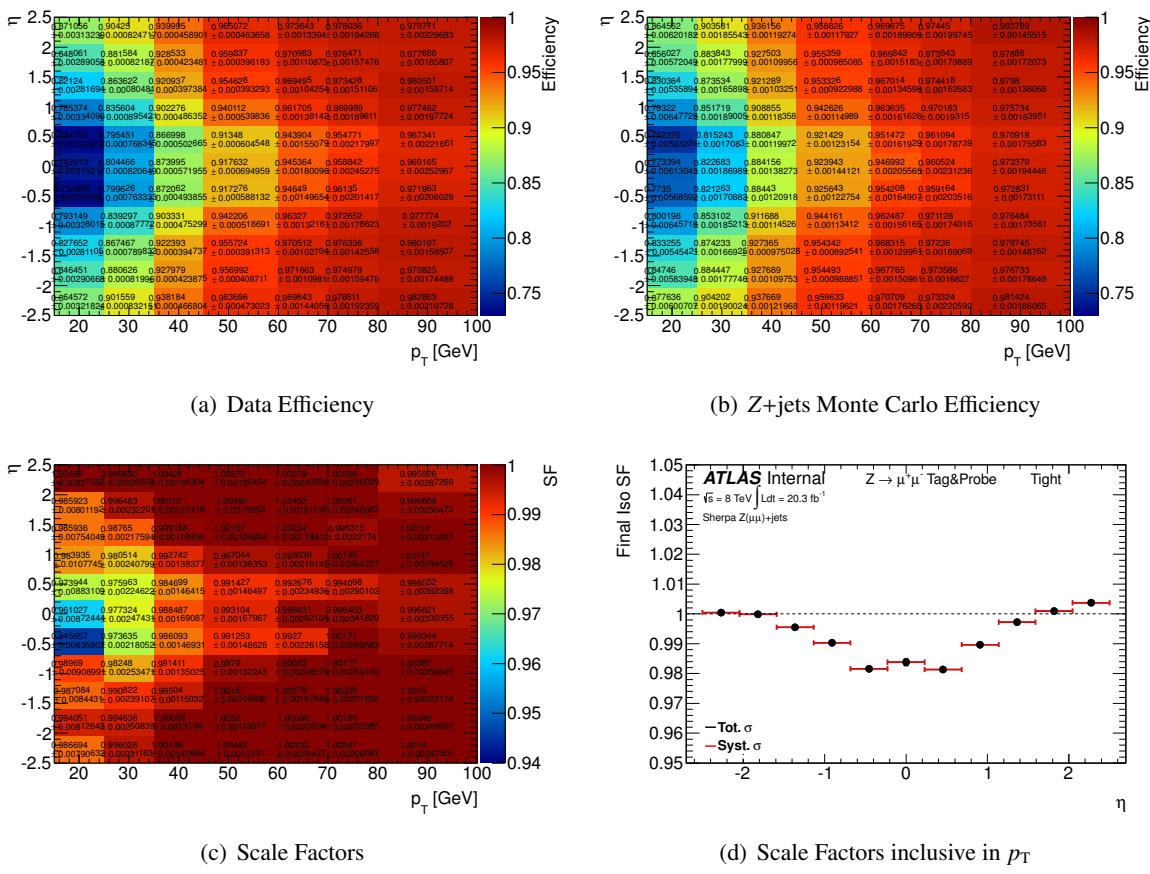


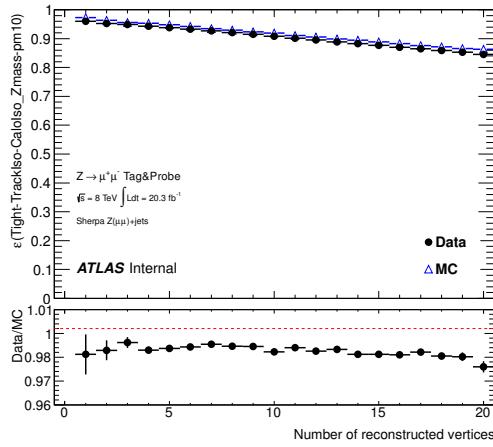
Figure 136: Muon isolation efficiencies and derived scale factors.

Not reviewed, for internal circulation only

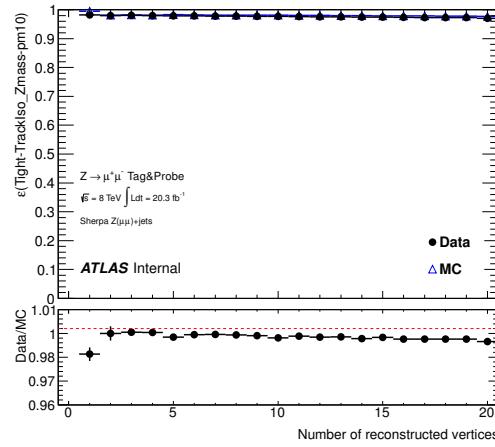
3696 Further efficiency dependencies have been studied. The muon isolation efficiency as a function of
 3697 the number of reconstructed vertices shown in Fig. 137(a) reveals a pile-up dependence; the efficiency
 3698 drops down to $\sim 85\%$ as the number of vertices increases. However, as Fig. 137(b) shows, if one does
 3699 the probing for the track isolation parameter only, the efficiency of this cut remains stable. Thus the
 3700 calorimeter isolation requirement causes this dependence.

3701 The efficiency also depends on close-by jets and their multiplicity. The raw $\Delta R(\mu, \text{nearest jet})$ dis-
 3702 tribution in Fig. 137(c) is as expected similar to the electron results discussed in the previous section.
 3703 Fig. 137(d) shows a significant decrease of the muon isolation efficiency to $\sim 60\%$ as jets get closer to
 3704 the probing muon.

Not reviewed, for internal circulation only



(a) Number of vertices



(b) Number of vertices (track iso. probing only)

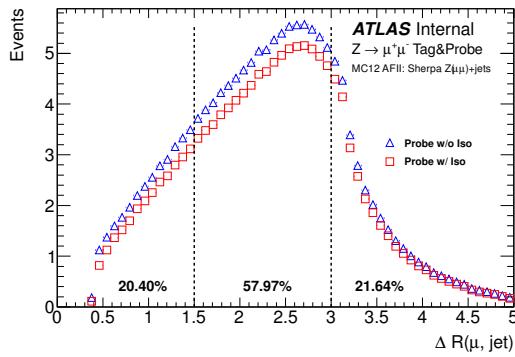
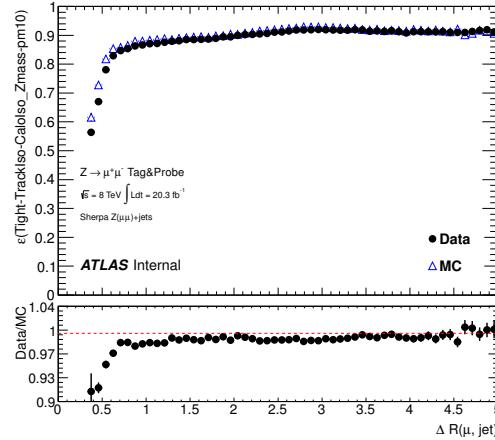
(c) Raw ΔR distribution(d) $\Delta R(\mu, \text{nearest jet})$

Figure 137: Muon isolation efficiencies as a function of the number of reconstructed vertices (a) and with track isolation probing only (b) as well as a function of close-by jets (c-d).

3705 G Global sequential calibration

3706 The Global Sequential Calibration (GSC) is a method dedicated to improve the resolution of the energy
 3707 response of jets, and to reduce its flavor dependence. It has been introduced in Section 3.2.2 and is also
 3708 discussed in Reference [23]. A note is in preparation by the JetETMiss group.

3709 This Appendix describes the validation of the GSC method, in the specific case of its application
 3710 to b-jets, in the context of VH(bb) analyses. Section G.1 describes the main common aspects of the
 3711 validation analysis. The response results are described in Section G.2, and the comparisons between
 3712 different Monte Carlo sets, from which one can derive systematic uncertainties, are shown in Section ??.

3713 G.1 GSC validation analysis

3714 G.1.1 Monte Carlo samples

3715 The impact of GSC on the jet response was evaluated with Monte Carlo simulations of inclusive QCD
 3716 di-jet production, of $t\bar{t}$ production and with a sample of associated production of a leptonic W boson
 3717 and a 125 GeV Higgs boson decaying to b -quark pairs. The references and version tags for the used
 3718 MC samples are listed in Table 67. The WH and the inclusive QCD di-jet samples were generated
 3719 with PYTHIA8, using two different PDF sets (CTEQ6L1 and CT10, respectively). Both use the same
 3720 underlying event tuning, UA2. For details on the underlying event tunings see [36] and references therein.

Generator & Tune	Channel num.	tag
	di-jet JW[0-8]Z	
Pythia8 AU2CT10	14791[0-8]	e1126_s1469_s1470_r3542_r3549_p1328 e1126_a159_a171_r3549_p1328
$t\bar{t}$		
PowhegPythia P2011C	117050	e1728_s1581_s1586_r3658_r3549_p1328 e1727_a188_a171_r3549_p1328
MadGraphPythia AUET2BCTEQ6L1	17483*	e1672_s1499_s1504_r3658_r3549_p1328
AlpGenAutoPythia_P2012	20102*	e2356_s1581_s1586_r3928_r4540_p1328
Sherpa_CT10	11780*	e1434_s1499_s1504_r3658_r3549_p1328
$WH \rightarrow \ell\nu b\bar{b}$		
Pythia8 AU2CTEQ6L1	161805	e1812_a188_a171_r3549_p1328

Table 67: References and version tags for the different Monte Carlo samples used the GSC analysis.

3721 G.1.2 Event and jet selection

3722 The study was carried out with TopoEM, Anti- k_T [20] jets with $R = 0.4$, with the EM+JES calibra-
 3723 tion scheme. In the case of samples including leptons, these were ignored in the analysis. No pile-up
 3724 reweighting corrections were applied, but the pile-up conditions in the Monte-Carlo were realistic, and
 3725 were used in the calculation of the EM+JES Jet Area correction.

3726 The following selection cuts were applied:

- 3727 • Primary vertex selection, requiring that the first primary vertex contains at least three vertices;
- 3728 • Truth jet isolation, requiring no additional truth jets in a cone of $R \times 2.5$;
- 3729 • Isolation from sub-leading jet, requiring no additional reconstructed jets in a cone of $R \times 2.5$.

3730 Truth p_T is defined for Monte Carlo jets by applying the same jet reconstruction algorithm, using the
 3731 Monte Carlo particles as the jet constituents. Truth jets do not include muons or neutrinos.

3732 In the case of the di-jet sample, a further cut was applied, by calculating the average truth p_T of the
 3733 leading and sub-leading jets and defining a ratio of that average over to the leading jet p_T . The value of
 3734 that ratio is required to be in the range $0.6 < \frac{p_T^{avg}(\text{truth})}{p_T^{\text{lead}}(\text{reco})} < 1.4$.

3735 The jet flavor selection was carried out by using the standard hadron matching for the identification
 3736 of b-jets as discussed in Section 3.2.2, and using a dedicated parton matching (based on the highest p_T
 3737 truth parton within the jet cone) for the distinction between gluon and light-quark jets.

3738 G.1.3 Calculation of energy scale and resolution

3739 The jet response was calculated by matching each reconstructed jet to the closest truth jet that passed the
 3740 isolation criteria within a radius of 0.3, and taking the ratio of reconstructed to truth p_T . The response
 3741 distributions in several bins of eta and p_T were fit to a Gaussian function. In order to eliminate the
 3742 sensitivity to tails, the fit was initially truncated to the $\pm 1.5 \times RMS$ region, and a second iteration done
 3743 in the $\pm 1.5\sigma$ region, where σ is the width of the first Gaussian fit. For the highest p_T bins, where the
 3744 response distribution is a very narrow Gaussian, a fixed window of 1 ± 0.4 is used for the fit.

3745 The mean value (μ) of the second iteration Gaussian fit was taken as the jet energy scale, and the
 3746 ratio σ/μ as the resolution.

3747 Several alternative fitting schemes were tried, in order to obtain the best description of the central
 3748 part of the response distribution, and the selected scheme proved to be robust, especially for the low p_T
 3749 bins.

3750 G.2 GSC performance

3751 The following section details the GSC performance in comparison to the EM+JES calibration.

3752 G.2.1 Energy scale of b-jets

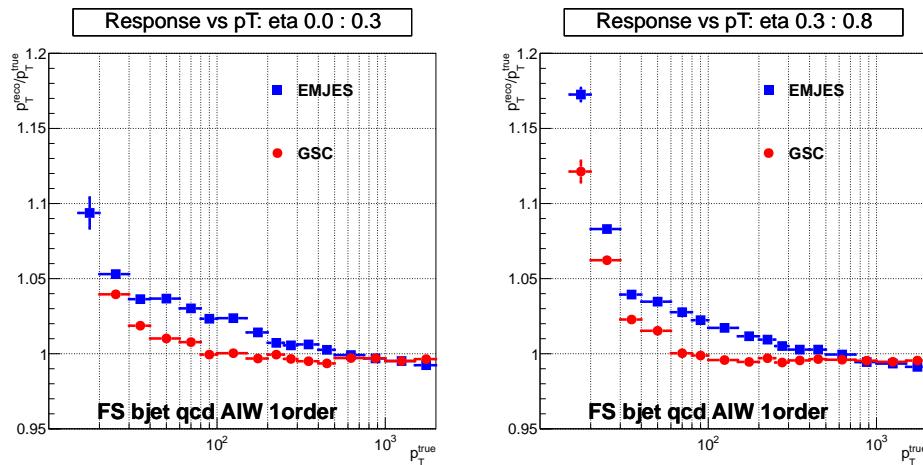


Figure 138: b -jet scale for the GSC versus EM+JES calibrations for jet in $0 < \eta < 0.3$ and $0.8 < \eta < 1.2$. More details are given in Section G.2.1.

3753 Figure 138 shows the energy response as a function of the jet p_T , for b-jets from the QCD di-jet
 3754 samples. GSC is compared with EM+JES. The response for b-jets is, in general, above 1, meaning that

3755 the reconstructed p_T is overestimated with respect to the truth p_T . The reason for this is that both GSC
 3756 and EM+JES calibrations were obtained for an inclusive QCD sample, dominated by gluon and light-
 3757 quark jets, that have different response from b-jets. For p_T above 30 GeV, the EM+JES response scale
 3758 is always better than 4%, while for lower p_T the differences with respect to the truth p_T may be up to
 3759 15-20%. One can see that GSC improves the response by few %, particularly for p_T below 200 GeV or
 3760 so, that is the dominant range in this analysis. After GSC, the response is always better than 2% for p_T
 3761 above 30 GeV, becoming better than 1% for p_T greater than 40-50 GeV.

3762 G.2.2 Energy resolution for b -jets

3763 Figure 139 shows the resolution for b-jets selected from the QCD di-jet MC samples as a function of the
 3764 truth jet p_T . Two pseudorapidity bins are shown: $0 < \eta < 0.3$ and $0.8 < \eta < 1.2$ although the conclusions
 3765 apply to all the p_T bins studied. GSC improves the jet resolution almost for all the p_T range, except for
 3766 very low p_T jets (between 15 and 20-30 GeV), where it does not change it. For a 100 GeV jet, the typical
 3767 improvement is of the order of 20%.

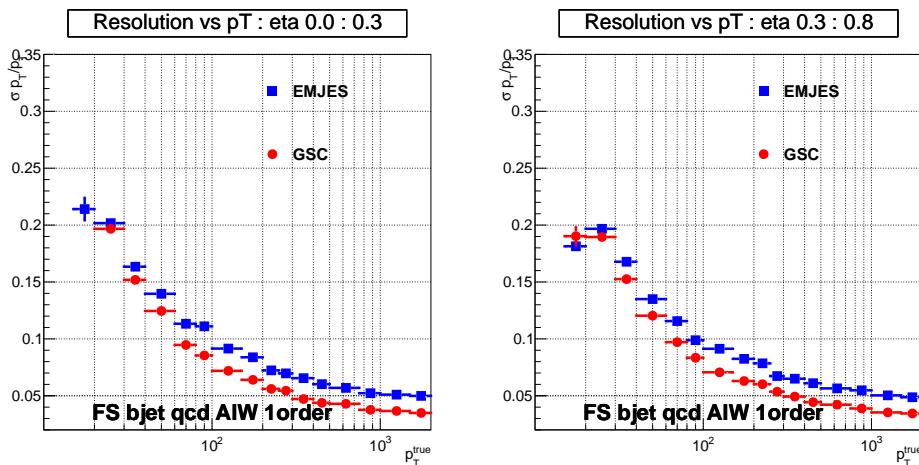


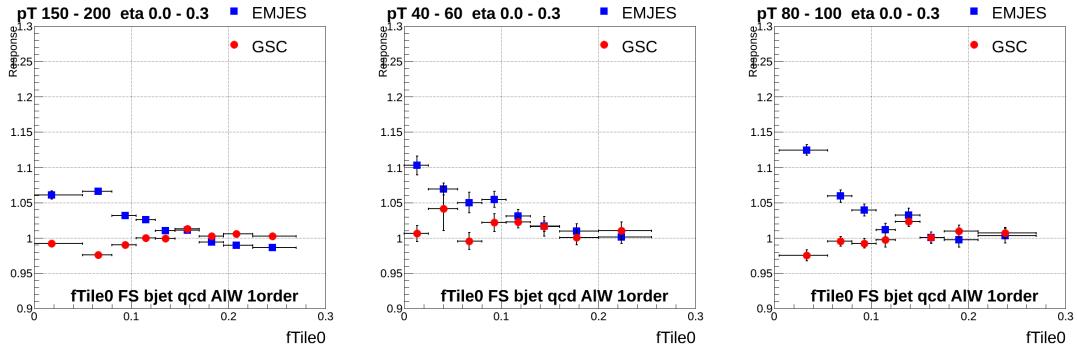
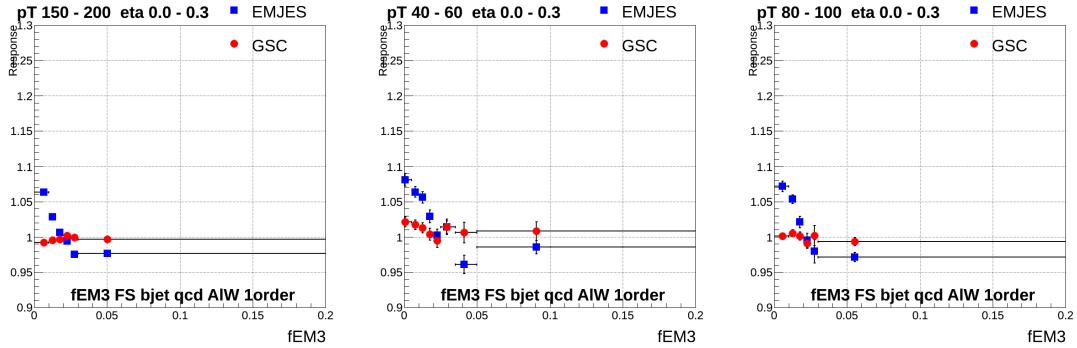
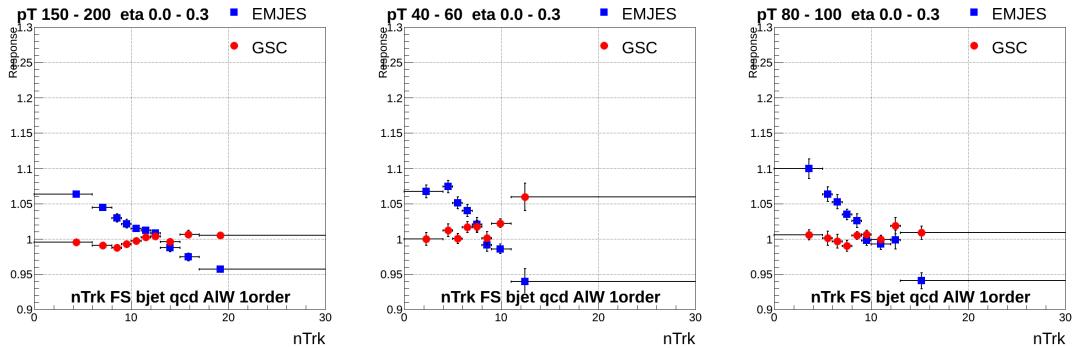
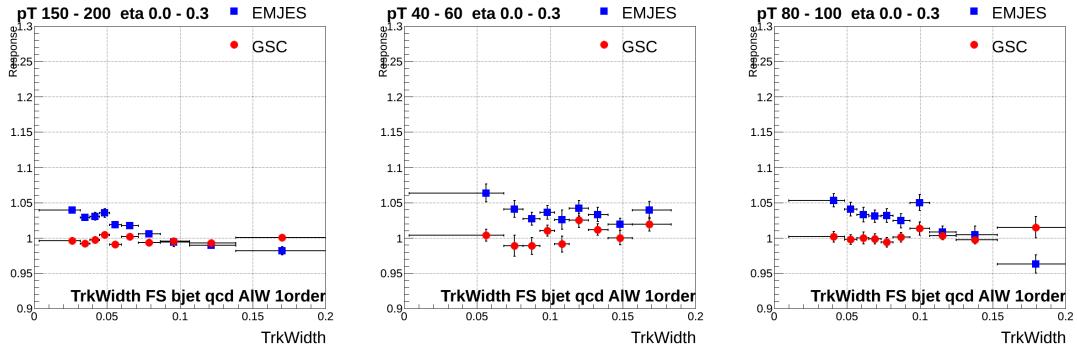
Figure 139: b -jet resolution for the GSC versus EM+JES calibrations for jet in $0 < \eta < 0.3$ and $0.8 < \eta < 1.2$. More details are given in Section G.2.2.

3768 G.2.3 Closure tests for b -jets

3769 The following shows the energy scale as a function of the four variables used in the GSC calibration.
 3770 These variables are listed and defined in Table 4 with further details given in Section 3.2.2 including the
 3771 track selection shown in Table 5.

- 3772 • $f_{\text{tile}0}$ - fraction of energy deposited in the first layer of the Tile calorimeter
- 3773 • $f_{\text{em}3}$ - fraction of energy deposited in the third layer of the EM calorimeter
- 3774 • n_{trk} - track multiplicity
- 3775 • W_{track} - p_T weighted average ΔR of tracks in the jet

Not reviewed, for internal circulation only

Figure 140: b -jet scale as a function of $f_{\text{Tile}0}$ for the GSC versus EM+JES calibrationsFigure 141: b -jet scale as a function of $f_{\text{EM}3}$ for the GSC versus EM+JES calibrationsFigure 142: b -jet scale as a function of n_{trk} for the GSC versus EM+JES calibrationsFigure 143: b -jet scale as a function of W_{track} for the GSC versus EM+JES calibrations

3776 Since GSC does not correct the average response, the jet energy scale after the calibration is not
3777 necessarily at $p_T^{\text{reco}}/p_T^{\text{truth}} \sim 1$. For a given p_T bin, GSC corrects the scale as a function of the previous
3778 variables, flattening the response and therefore reducing the resolution.

3779 The small non-closure observed in certain bins (normally smaller than 2% but that can reach up to
3780 5%) is due to the fact that the calibrations were not derived for b-jets but for inclusive QCD jets.

3781 H Muon-Jet Overlap Removal

3782 The strategy adopted in [11] to solve the muon-jet overlap have been updated to increase the 2-lepton
 3783 channel acceptance, while keeping under control any source of mis-identification in the other channels.

3784 **H.1 Characterization of the muons overlapping jets**

3785 In [11], all muons overlapping with a jet within $\Delta R < 0.4$ were removed. In the optimization of the
 3786 2-leptons channels, it was found that when accepting all muons with $p_T > 20$ GeV, overlapping with a jet,
 3787 the signal acceptance in that channel can increase by 12% (Fig. 144). Even if muon overlapping jet can
 3788 be generated in the semi-leptonic decays of heavy hadrons, the requirement $p_T > 20$ GeV and the cut on
 3789 $m_{\mu\mu}$ adopted by the 2-lepton analysis drastically reduce the muons produced in the semi-leptonic decays.

3790 The same overlap removal have been tested in the 1-lepton channels. Here a strong selection like
 3791 the dilepton invariant mass does not exist, and this overlap removal strategy will lead to a significant
 3792 increase in muons from semi-leptonic bottom or charm decays, in particular when inverting the track
 3793 isolation for the construction of the multijet template (see Figure 145). In the case of the prompt muons,
 3794 a more detailed analysis of the muon-jet overlap showed that in the majority of the cases in which a
 3795 prompt muon overlap a jet in signal events, the jets are electromagnetic showers probably caused by
 3796 the electroweak final state radiation emitted by the muon or the jet is a caused by the muons showers
 3797 when traversing the calorimeters (see Figure 146). So in summary, in the inclusive di-lepton channel, the
 3798 muon-jet overlap is due to:

- 3799 • prompt muons overlapping with showers from muon radiation in 66% of the cases,
 - 3800 • prompt muons overlapping with bottom flavored jets in 25% of the cases, and
 - 3801 • muons from semi-leptonic decays overlapping with bottom (or charm) flavored jets in 8% of the
 3802 cases
- 3803 not counting muons which are not prompt or due to semi-leptonic decays (e.g. τ , Kaon decays), and
 3804 overlaps with pileup jets. Given the nature of the prompt muons in the first 2 items, the overlapping jets
 feature low multiplicities of the associated charged particle tracks.

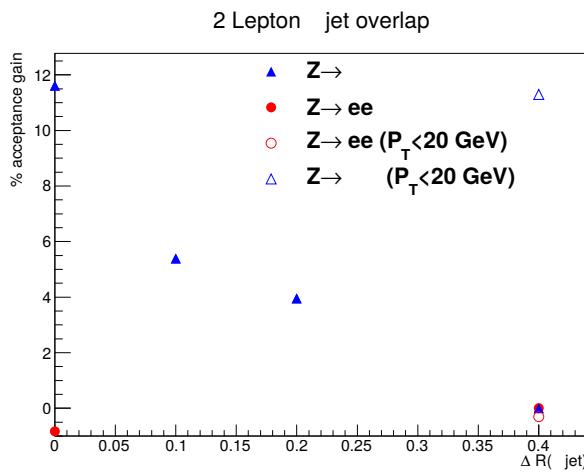


Figure 144: Acceptance gain when reducing the ΔR between muons and jets for which muons are removed.

Not reviewed, for internal circulation only

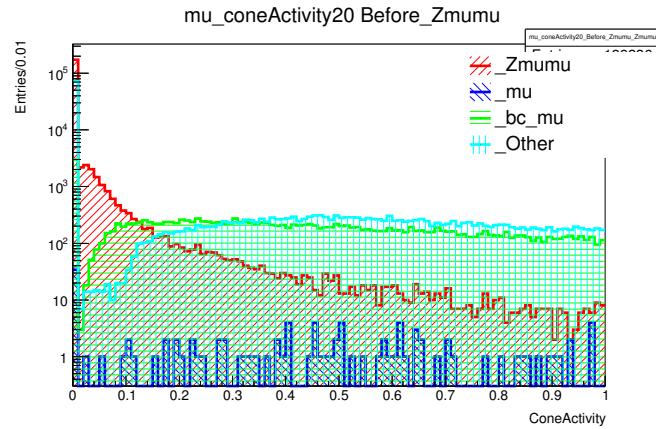


Figure 145: The scalar p_T sum of charged particle tracks around the muon inside a cone of $\Delta R < 0.2$ for prompt muons (`_Zmumu`) and muons from semi-leptonic decays (`_bc_mu`), and other non-truth matched (`a`)muons.

(b)

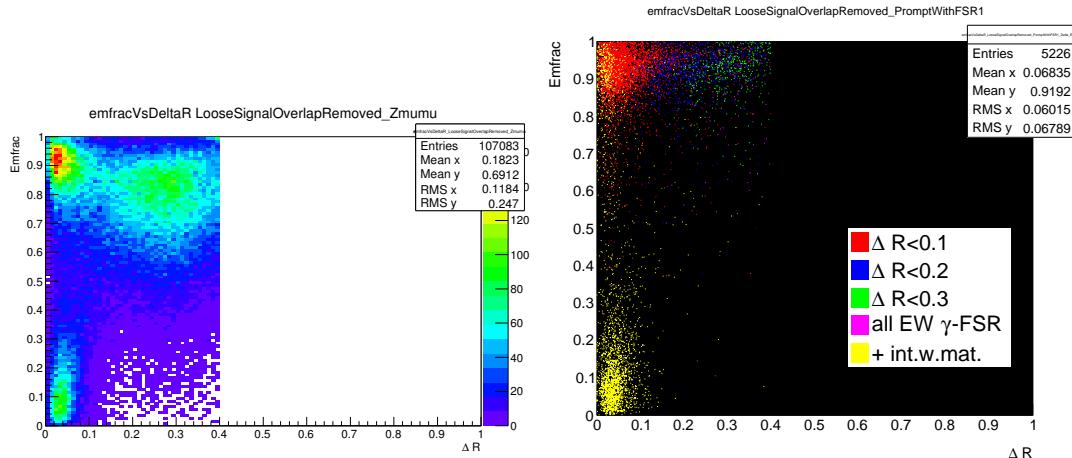


Figure 146: The fraction of the electromagnetic energy in a jet vs. the ΔR between the muon and the closest jet for all muons overlapping with jets (a) for prompt muons with FSR of total $p_T > 15$ GeV with the given cone (b).

3806 H.2 Studies on the strategies to solve the muon-jet overlap

3807 To get a better signal acceptance for the 2-lepton region, while keeping a proper identification of the
 3808 objects for the 1-lepton analysis, the strategy for the muon-jet overlap removal for the 0-, 1- and 2-lepton
 3809 channels are identical and

- 3810 1. first perform the jet-electron overlap removal;
- 3811 2. then jets which overlap with a muon with $\Delta R < 0.4$ and which feature a charged particle track
 3812 multiplicity below or equal to 3 are removed where charged particle tracks must fulfill $p_T^{\text{track}} >$
 3813 500 MeV and are associated to the primary vertex of the hard interaction (the majority of the jets
 3814 from muon radiation has a multiplicity of 1 but a sizable fraction has a multiplicity of 2 or larger -
 3815 Figure 147. Jets with semi-leptonic b- or c- decays tend to have a multiplicity above 3, but there is
 3816 already a significant fraction with a multiplicity of 2 or three);

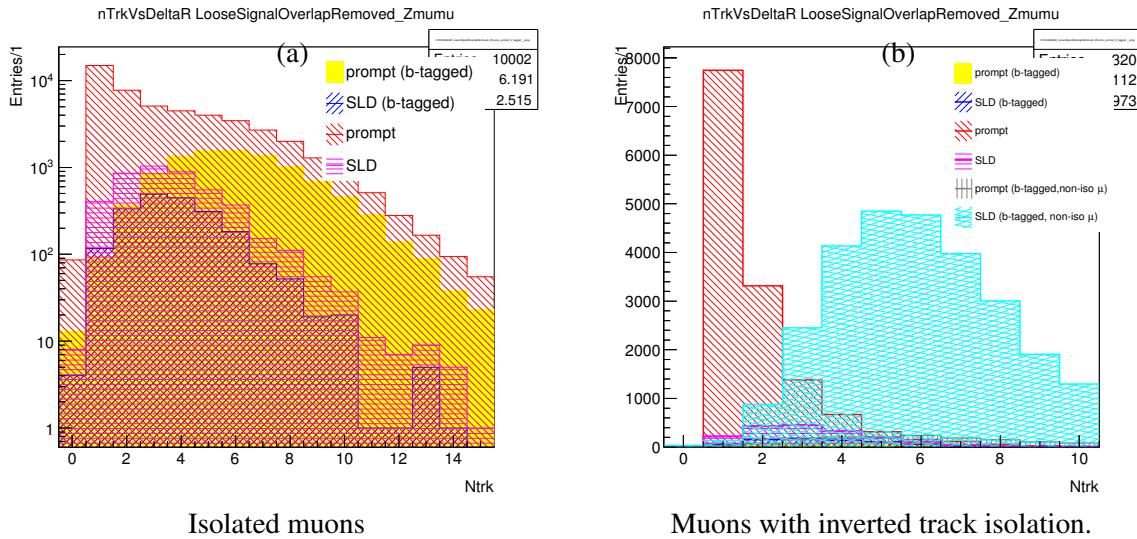


Figure 147: Charged track multiplicity of jets overlapping with prompt muons or muons from semi-leptonic b or c -decays with $\Delta R < 0.4$ for all signal jets and b-tagged signal jets only.

3817 3. finally all muons overlapping with the remaining jets are removed.

3818 With this procedure, the final acceptance gain the 2-lepton channel amounts to $\sim 6\%$ and in the 1-lepton
3819 channel to 2% .

3820 Different strategies have been proposed and studied:

- 3821 • same as above but only remove jets with a charged track multiplicity below or equal to two
- 3822 • remove jets with a charged particle track multiplicity below or equal to one, where charged particle
3823 tracks are considered only if $p_T^{\text{track}} > 1 \text{ GeV}$ and if they are associated to the primary vertex of the
3824 hard interaction. Moreover to remove jets from pileup, all jets for which the jet-vertex-fraction
3825 drops below 0.5, when the contribution of the muon is subtracted (see Figure 148), where the cut
3826 of 0.5 on the muon subtracted jet-vertex fraction is chosen to be identical to the criterion for for
3827 signal jets.

3828 Of these strategies, the highest acceptance gain wrt. to removing all muons overlapping with jets is
3829 achieved when removing all jets with a track multiplicity below or equal to three (the used selection).
3830 Since the track multiplicity only considers track associated to the primary vertex, this also rejects pileup
3831 jets. An explicitly removal of pileup jets using the muon-subtracted-jet-vertex-fraction does not lead to
3832 an advantage. For reference also a multivariate technique was tried which exploited multiple variables
3833 to distinguish overlaps with jets from radiation, jets with semi-leptonic decays etc. . This multivariate
3834 technique could not improve substantially over the simple track multiplicity based criterion.

3835 The acceptance can be further improved by trying to recover some the overlaps of prompt muons with
3836 b-jets, by accepting both, the muon and the jet, in case the muon p_T is larger than 30 GeV and the ΔR is
3837 larger than 0.25. While these requirements suppress muons from semi-leptonic decays, the constructed
3838 multi-jet templates show significant distortion wrt. to the templates determined after the original muon-
3839 jet overlap removal. Since, the b-tagging performance is not known in case of muons overlapping with
3840 b-jets and moreover it is difficult to estimate the contamination of multijet background for such events,
3841 the recovery of prompt muons overlapping with b-jets is not performed.

Not reviewed, for internal circulation only

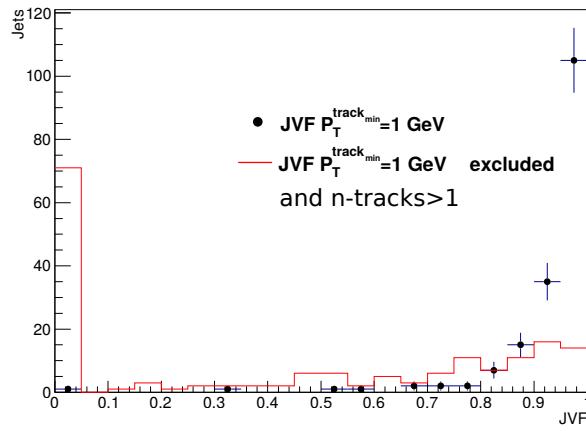


Figure 148: Jet vertex fraction after subtracting the contribution of the muon.

Sample Region	Signal Acceptance Increase (%)							
	ZH				WH			
	$p_T^V \leq 120$ GeV 2-jet	$p_T^V > 120$ GeV 2-jet	$p_T^V \leq 120$ GeV 3-jet	$p_T^V > 120$ GeV 3-jet	$p_T^V \leq 120$ GeV 2-jet	$p_T^V > 120$ GeV 2-jet	$p_T^V \leq 120$ GeV 3-jet	$p_T^V > 120$ GeV 3-jet
remove ≤ 2 track jets	3.7	3.3	5.7	5.8				
Remove ≤ 3 track jets	4.1	3.7	6.2	6.5	1.2	2.2	2.5	3.1
+ accept $p_T^\mu > 30$ GeV, $\Delta R > 0.25$	5.7	5.7	6.3	7.1				
remove ≤ 1 track jets, or no- μ -JVF < 0.5	3.4	3.9	3.7	6.0	1.3	1.6	1.2	2.4
accept all muons $p_T > 20$ GeV	2.7	15	0.2	13	0.4	5.1	0.0	4.8

Table 68: The signal acceptance increase of the 2 (ZH) and 1-lepton channel (WH) for different muon jet overlap removal strategies. The selected strategy is “Remove ≤ 3 track jets”.

3842 I Signal modeling

3843 Section 4 covers the systematics specific to the signal. Some investigations of the signal modeling con-
 3844 cluded with null results - that is a systematic uncertainty was not needed. The studies yielding such a
 3845 result were all introduced in Section 4.2.2 with the less interesting plots deferred to this appendix for
 3846 interested parties.

3847 Figure 149 shows the normalized p_T^V distribution of VH signal events for different PDF choices.
 3848 No strong evidence for an additional shape uncertainty beyond what is already covered by the scale
 3849 uncertainty (Section 4.2.2) is seen.

3850 Figures 150 and 151 show results from the PDF uncertainty study cross-check outlined in Sec-
 3851 tion 4.2.2. Here, the nominal PYTHIA 8.165 sample generated with CTEQ6L1 PDF was reweighted to
 3852 each the full (central value and error) MSTW2008NLO68CL, CT10NLO, and NNPDF23_NLO_AS_0120 PDF
 3853 sets. For each event and each choice of PDF, a unique weight is applied according to equation 8. Because
 3854 this procedure does not preserve normalization, the results are presented as a relative uncertainty. For
 3855 this, the smallest envelope that spans the full range of PDF variations is used. The upper and lower un-
 3856 certainty bounds in Figures 150 are calculated by dividing the maximum and minimum of this envelope
 3857 by its central value. The results here are consistent with those obtained using the samples that had been
 3858 regenerated with different central value PDFs.

3859 Finally, figure 152 shows the comparison of the $p_T^V()$ distributions for PYTHIA 8.165 and PowHEG
 3860 showered with Pythia8, to check the differences in the $p_T^V()$ induced by the use of a PowHEG method to
 3861 get the NLO cross section. Given the small differences in the plots, covered by the systematics described
 3862 in Section 4, no additional corrections or systematics have been derived from these comparisons.

Not reviewed, for internal circulation only

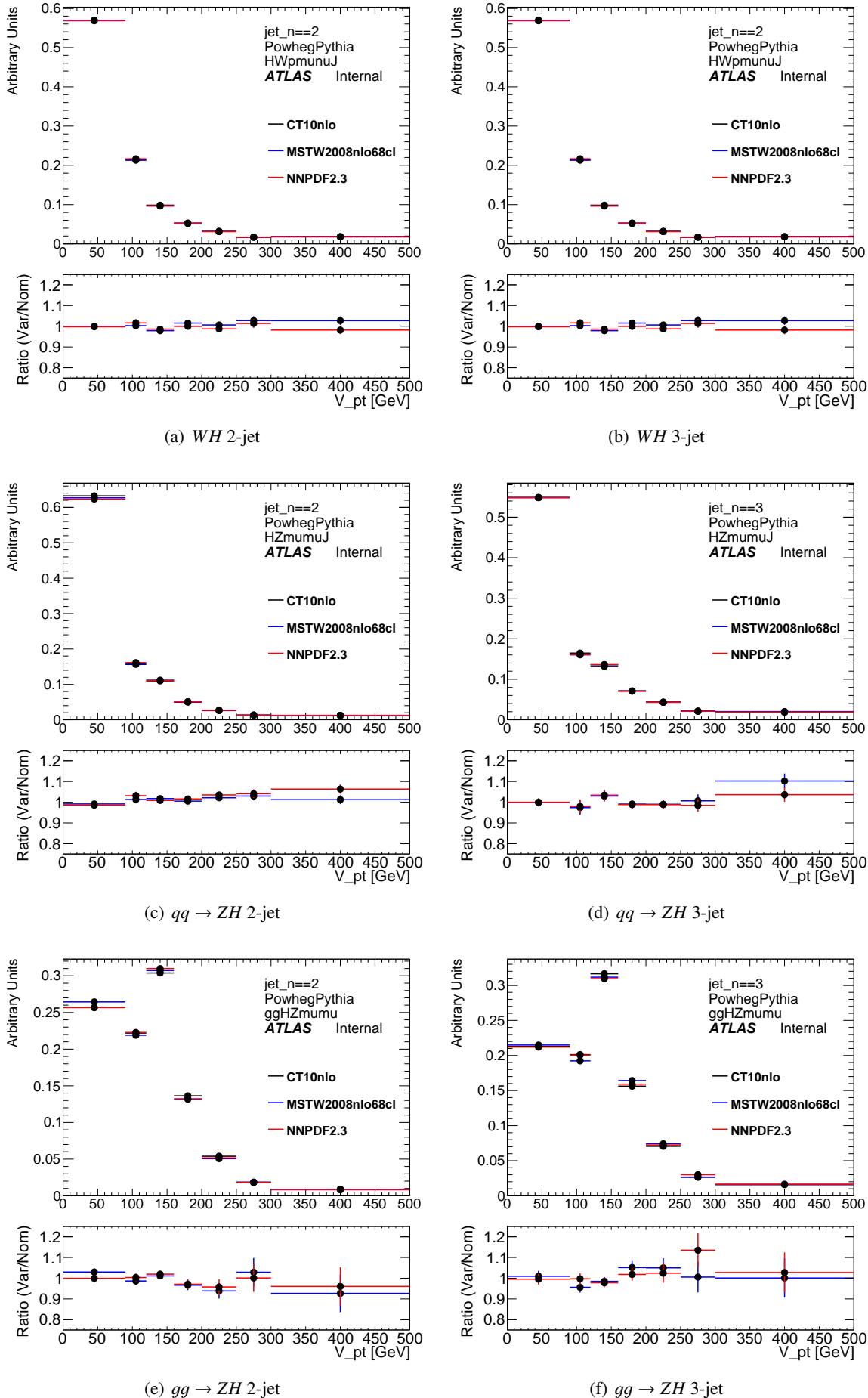


Figure 149: Normalized p_T^V distributions after truth-level selection for WH , $qq \rightarrow ZH$, and $gg \rightarrow ZH$ PDF uncertainty studies on the 1st, 2nd, and 3rd row respectively.

Not reviewed, for internal circulation only

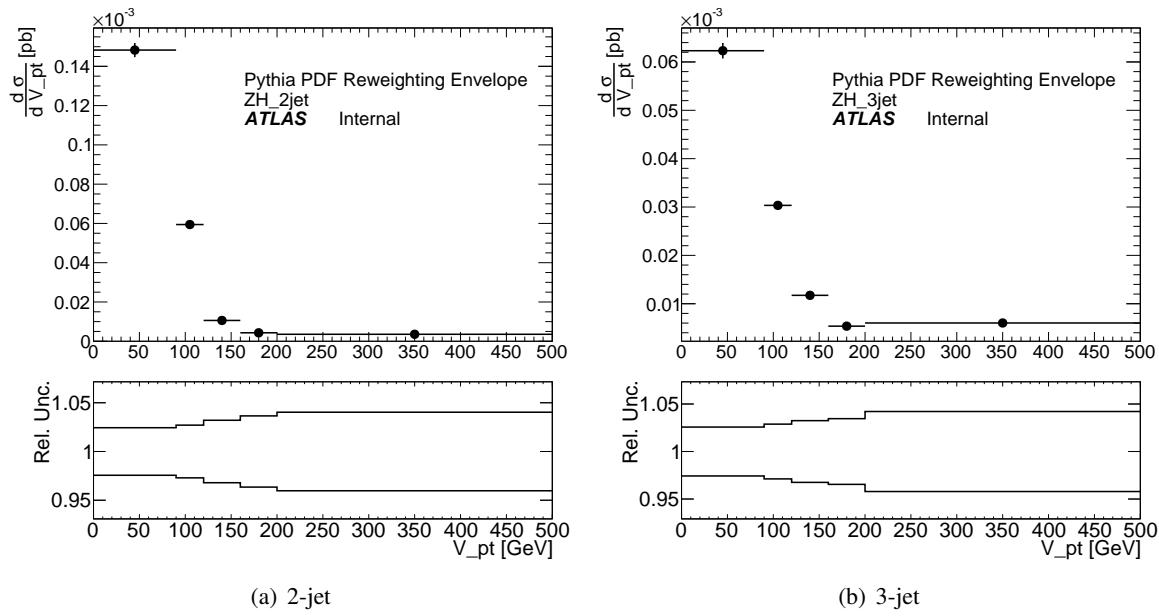


Figure 150: PDF re-weighted p_T^V distribution for ZH events that pass a truth-level event selection.

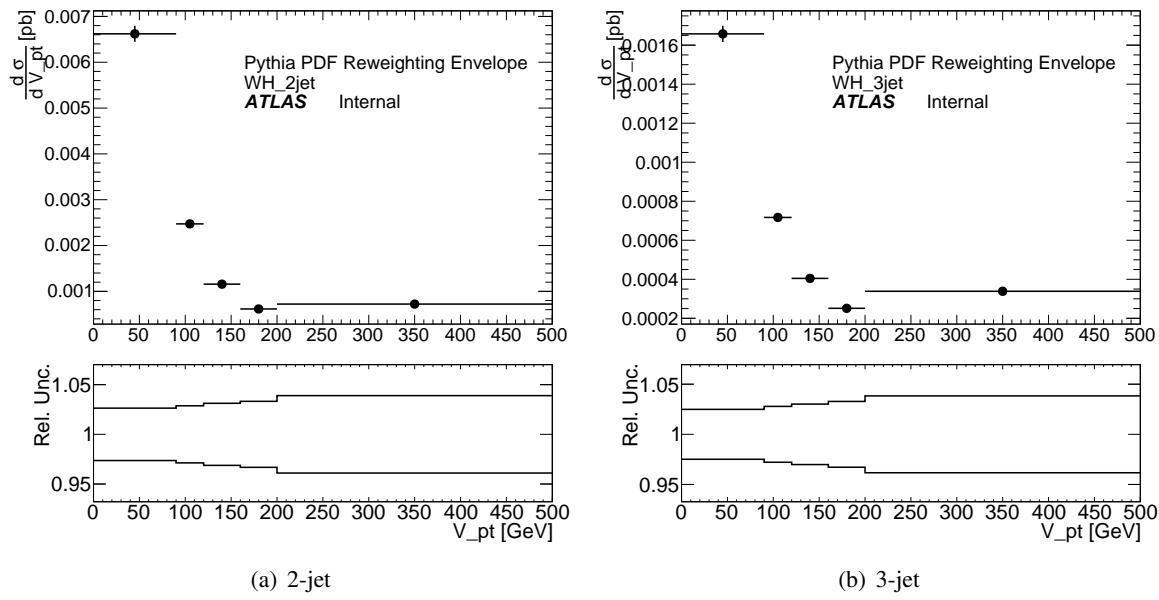


Figure 151: PDF re-weighted p_T^V distribution for WH events that pass a truth-level event selection.

Not reviewed, for internal circulation only

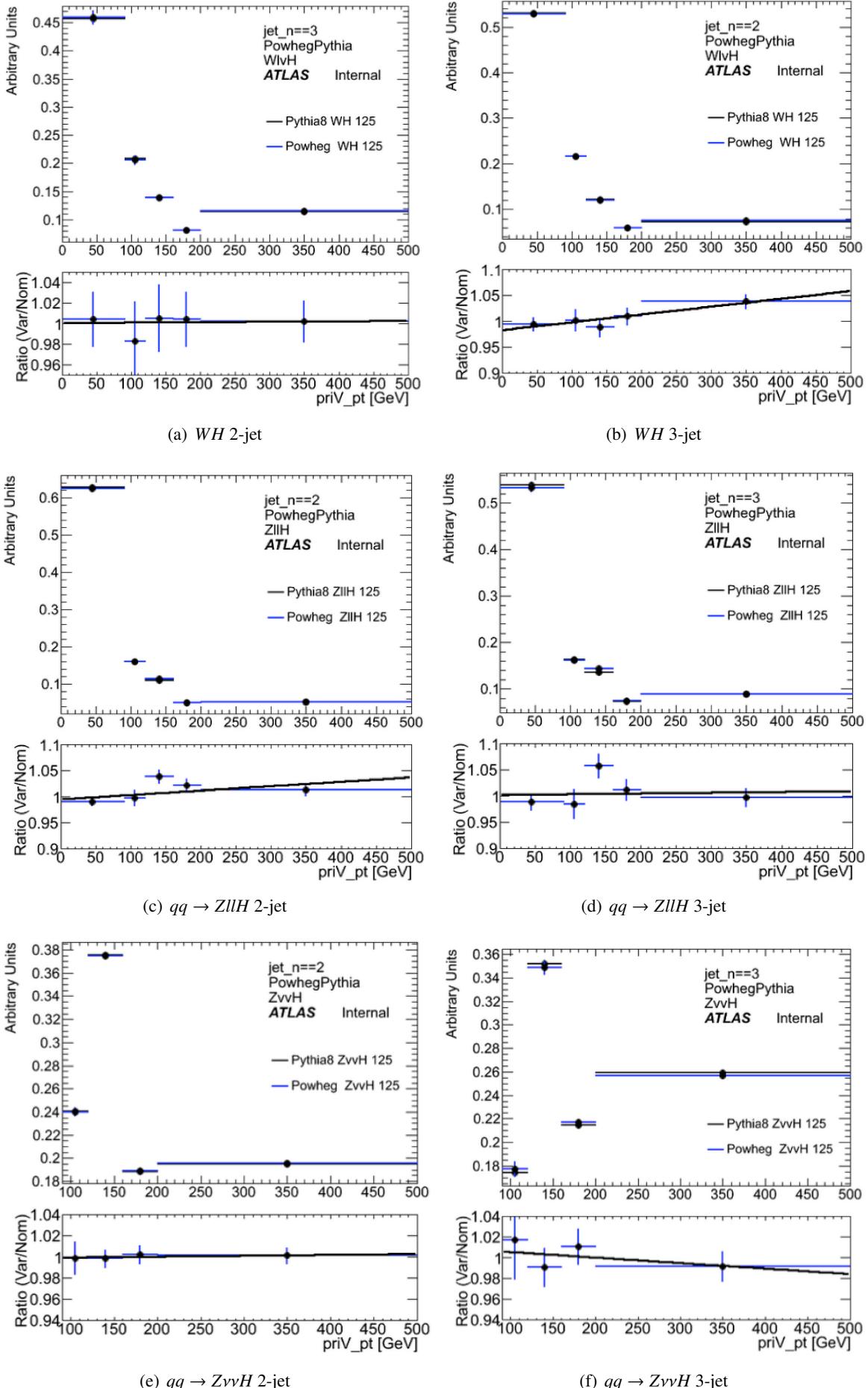


Figure 152: Normalized p_T^V distributions after truth-level selection for WH , $qq \rightarrow ZllH$, and $qq \rightarrow ZvvH$ NLO vs LO studies on the 1st, 2nd, and 3rd row respectively.

3863 J Z+jet Modeling

3864 This appendix summarize the studies done for the modeling of the Z+jets background.

3865 J.1 Effect of Strict Jets Cuts

3866 In Section 3.3.4, a mention of the fact that the jet cuts could be loosened for 2-lepton events was made.
 3867 The main background in 2-lepton events is still Z+jets which is not characterized by forward jets like the
 3868 top background in the 0 and 1-lepton analysis. Table 69 shows the total effect to the signal and the total
 3869 background in 2 and 3-jet events above and below $p_T^Z = 120$ GeV after removing

- 3870 • forward jet veto
- 3871 • veto of events with more than 3 signal jets
- 3872 • veto of events with more than 2 b-tags

3873 The changes in 2-jet events are solely from the removal of the forward jet veto. The change in the 3-
 3874 jet event is minimally impacted by the 3rd b-tag veto. This change in acceptance would increase the
 3875 2-lepton sensitivity 4% and the overall MVA sensitivity 1-2%. At the cost of added complexity and having
 3876 the regions of phase space in each of the lepton selections further apart, these cuts were not released in
 3877 the 2-lepton analysis. Clearly if the sensitivity was driven by the 2-lepton events or if this analysis was
 3878 solely run on 2-lepton events the more relaxed set of cuts would have been used.

Sample	2-jet		3-jet	
	$p_T^Z < 120$ GeV	$p_T^Z > 120$ GeV	$p_T^Z < 120$ GeV	$p_T^Z > 120$ GeV
$qq \rightarrow Z(\rightarrow ll)H$	1.03	1.04	2.61	2.77
$gg \rightarrow Z(\rightarrow ll)H$	1.18	1.21	5.02	5.12
Background	1.12	1.13	3.82	3.82

Table 69: The default jet selection is to veto events with forward jets, use exactly 2 or 3 jet events (instead of 2 or 3+ jet events), and veto events with more than 2 b-tagged jets. This table shows the increase in 2 and 3-jet events above and below $p_T^Z = 120$ GeV for the 2-lepton selection after releasing the above mentioned cuts. The smallest impact is from the veto on 3 or more b-tag events. The change in 2-jet events shows the impact from the release of the forward jet veto.

3879 J.2 Determination of the data-driven corrections and systematics

3880 In the in dilepton events, a relatively pure sample of Z+ jets can be obtained fairly well. Using the
 3881 event selection for the MVA analysis given in table given in Table 12, with tighter dijet mass analysis
 3882 $E_T^{\text{miss}} < 60$ GeV and m_{ll} (83-99 GeV) cuts, as well as only using the events with $m_{bb} < 100$ GeV or
 3883 $m_{bb} > 150$ GeV in 2-tag events, a signal-depleted pure Z+jets sample is selected; These control regions
 3884 have been used to derive data-driven corrections and systematics uncertainties. Tables 70 and 71 give a
 3885 summary of the data-driven corrections and systematics for the Z+jets modelling.

3886 The first table shows the fraction of events in the 2 and 3 jet categories, and the data/MC comparisons
 3887 have been used to estimate the uncertainty on the 2/3 jets ratio for the Z+jets.

3888 The second includes the correction and systematics on $\Delta\phi(jj)$ the correction and systematics on
 3889 p_T^V and the systematics on m_{bb} . The plots showing the distributions used to derived these corrections
 3890 and systematics have been shown in Section 5.1.1.

p_T^Z	N Jet	data/MC
$p_T^Z < 120 \text{ GeV}$	2	1.018 ± 0.002
	3	0.994 ± 0.004
$p_T^Z > 120 \text{ GeV}$	2	1.016 ± 0.005
	3	1.014 ± 0.007

Table 70: Yield ratios for 2-lepton 0-tag events used to derive the 3/2 jet ratio systematic.

Variable	Function	Region	Parameter Value
$\Delta\phi(jj)$	$a(1 + b\Delta\phi)$	$p_T^V < 120 \text{ GeV}$	$a=8.63343 \times 10^{-1}$ $b=8.62769 \times 10^{-2}$
		$p_T^V > 120 \text{ GeV}$	$a=9.33017 \times 10^{-1}$ $b=3.16033 \times 10^{-2}$
p_T^V	$a + b \log(p_T^V)$	all regions	$a=1.39975$
		constant for $p_T^V < 100 \text{ GeV}$	$b=-9.38026 \times 10^{-2}$
m_{bb}	$a(m_{bb} \times 10^{-3} - b)$	all regions	$a=5 \times 10^{-4}$
		constant for $m_{bb} > 300 \text{ GeV}$	$b=100$

Table 71: Functions and parameters used for $Z+jets$ data-driven corrections and systematics. p_T^V and m_{bb} have units of MeV.

3891 J.3 Comparison with other Monte Carlo samples

3892 In addition to the SHERPA samples, other Monte Carlo samples have been studies, both to have a check of
 3893 the corrections and systematics derived from the data, partially to complete the derivation of systematics
 3894 uncertainties which cannot be derived from data. In particular, the systematics on the flavour fractions in
 3895 $Z+jets$ has been estimated by comparing different generators.

3896 The natural generator to performace these comparisons is ALPGEN Both ALPGEN and SHERPA are leading
 3897 order multi leg generators, but they diffears in different aspects:

- 3898 • The mass of the heavy quarks in the calculation: While SHERPA have been forced to have a massive
 3899 heavy quarks, for the ALPGEN samples, a massless approach have been used.
- 3900 • The parton density functions (CTEQ6L1 VS. CT10)
- 3901 • The treatement of the matrix element and Parton shower matching.
- 3902 • The parton shower model, where SHERPA used its internal implementation, while ALPGEN relies on
 3903 Herwig.
- 3904 • The hadronization model, where SHERPA used its internal implementation, while ALPGEN relies on
 3905 Herwig.
- 3906 • The underlying event model, where SHERPA used its internal implementation, while ALPGEN relies on
 3907 Jimmy.

3908 The list of samples used for these studies are listed the Table 72.

3909 These samples have been used to estimate the relative havy flavor composition in $Z+2$ jets and $Z+3$
 3910 jets events. Tables 73 and 74 show the flavor composition uncertainty and the 3/2 jet ratio systematic for
 3911 the heavy flavor events, determined from the comparison of the event yield in SHERPA and ALPGEN .

Process	Channel num.	tag	N_{events}
Z samples, ALPGEN Jimmy, AUET2CTEQ6L1			
$Z \rightarrow ee$, Np0-5+	107650-5	e1571_s1499_s1504_r3658_r3549_p1328	6608782, 1335000, 404499, 110000, 30000, 10000
$Z \rightarrow \mu\mu$, Np0-5+	107660-5	e1571_s1499_s1504_r3658_r3549_p1328	6619489, 1334706, 404997, 110000, 30000, 10000
$Z \rightarrow \tau\tau$, Np0-5+	107670-5	e1571_s1499_s1504_r3658_r3549_p1328	6619683, 1334996, 404997, 110000, 30000, 10000
$Z \rightarrow ee + cc$, Np0-3+	126414-7	e1601_s1499_s1504_r3658_r3549_p1328	604899, 259999, 109999, 40000
$Z \rightarrow \mu\mu + cc$, Np0-3+	126418-21	e1601_s1499_s1504_r3658_r3549_p1328	599397, 265000, 115000, 39999
$Z \rightarrow \tau\tau + cc$, Np0-3+	117706-9	e1601_s1499_s1504_r3658_r3549_p1328	599999, 264999, 115000, 39999
$Z \rightarrow ee + bb$, Np0-3+	109300-3	e1601_s1499_s1504_r3658_r3549_p1328	150000, 80000, 45000, 4999
$Z \rightarrow \mu\mu + bb$, Np0-3+	109305-8	e1601_s1499_s1504_r3658_r3549_p1328	149900, 80000, 45000, 5000
$Z \rightarrow \tau\tau + bb$, Np0-3+	109310-3	e1601_s1499_s1504_r3658_r3549_p1328	149900, 79999, 45000, 5000

Table 72: Monte Carlo samples and channel numbers and statistics used for Z+ jets systematics.

Not reviewed, for info

Jet Flavors	ALPGEN	SHERPA	difference (%)
bb	0.318	0.280	13.3
bl	0.394	0.357	10.3
cl	0.480	0.382	25.7

Table 73: Yield ratios for 2-lepton 2-tag events in ALPGEN and SHERPA used to derive the heavy-flavor fraction systematic.

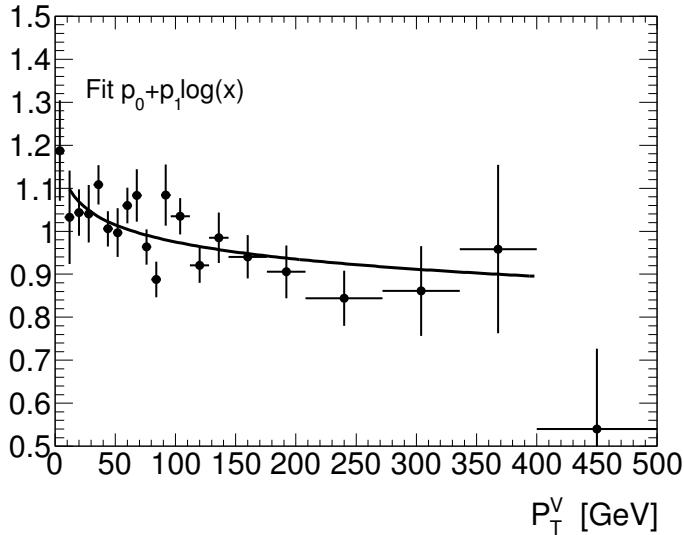
p_T^Z	N Jet	ALPGEN	SHERPA	% difference
bl/bb				
$p_T^Z > 0$ GeV	2+3	0.207	0.225	-7.6
$p_T^Z > 120$ GeV	2+3	0.241	0.238	1.4
$p_T^Z > 0$ GeV	2	0.196	0.212	-7.4
$p_T^Z > 0$ GeV	3	0.243	0.270	-9.9
cc/bb				
$p_T^Z > 0$ GeV	2+3	0.161	0.146	9.9
$p_T^Z > 120$ GeV	2+3	0.110	0.133	-17.5
$p_T^Z > 0$ GeV	2	0.155	0.144	-7.2
$p_T^Z > 0$ GeV	3	0.178	0.151	17.7

Table 74: ALPGEN/SHERPA heavy-flavor jet multiplicity comparison in 2-lepton 2-tag events used to derive the 3/2 jet ratio systematic.

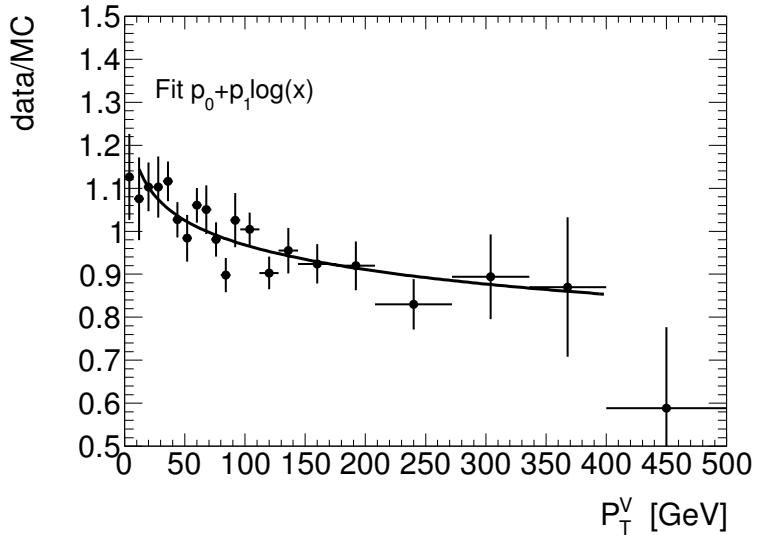
3912 In addition to the determination of the systematics listed above, a consistency check for the important
 3913 kinematic distribution entering in the analysis have been done.

3914 Since the goal of this comparison, is a qualitative comparison of SHERPA and ALPGEN in this last one
 3915 no corrections have been derived and applied. This means that some deviation are expected, especially
 3916 in the m_{bb} distributions. Figure 153 show the p_T^V correction derived for SHERPA and compared with the
 3917 equivalent correction one could derive from ALPGEN. Despite the fact the Z p_T can depends on different
 3918 aspects of the generator modeling, the p_T^V corrections are not that different.

on only



(a) 2-tag ALPGEN

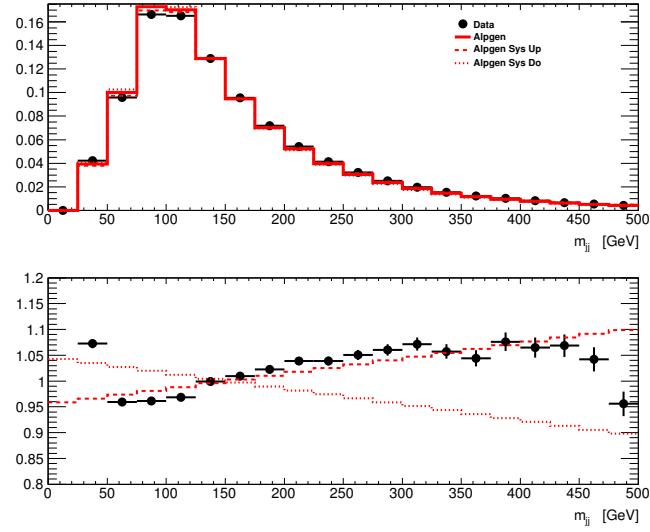


(b) 2-tag SHERPA

Figure 153: A data-driven p_T^Z correction derived from data-MC ratios for Z +heavy events for ALPGEN motivated by the increase in discrepancy with increased number of b -tags.

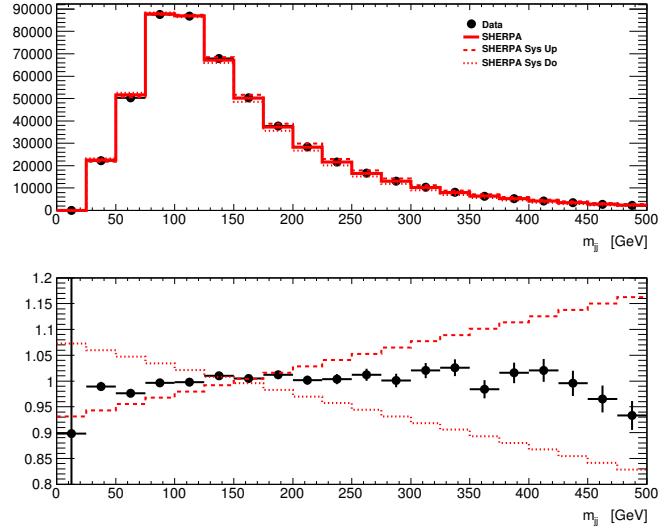
3919 Another important check done to validate the Z +jets modelling in SHERPA is to compare the data/MC
 3920 agreement for the m_{bb} distribution. Figure 154 shows the data/MC comparisons for ALPGEN and SHERPA in
 3921 each the 0, 1, and inclusive 2-btag regions. It shows that the systematics uncertainties derived for SHERPA,
 3922 and here used on ALPGEN, are consistent with the data/MC discrepancies.

Arbitrary Units



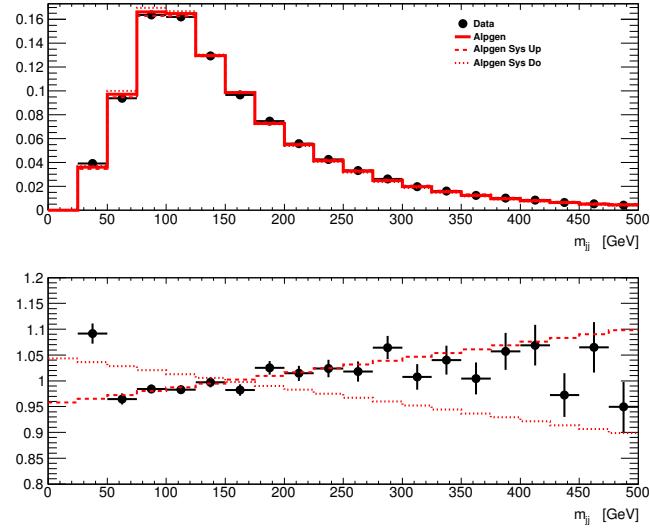
(a) 0-tag ALPGEN

Arbitrary Units



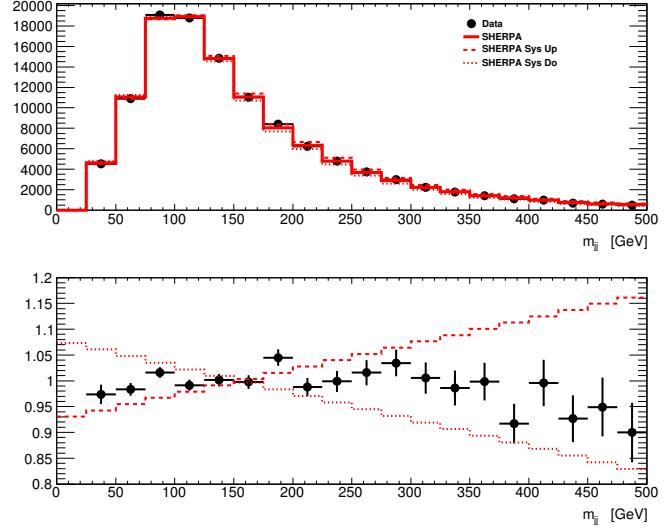
(b) 0-tag SHERPA

Arbitrary Units



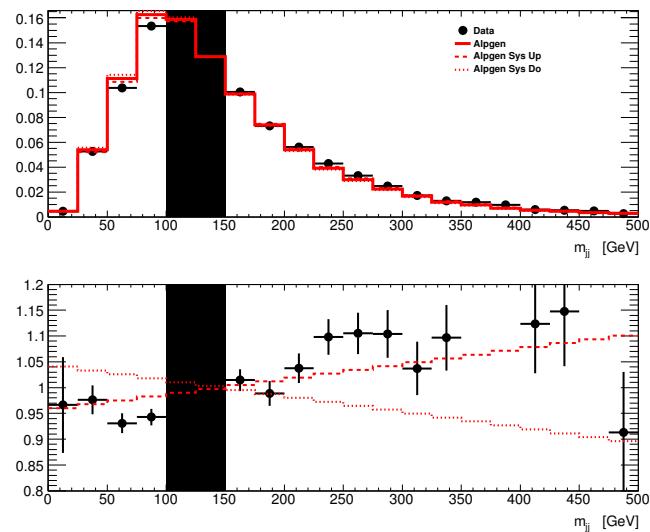
(c) 1-tag ALPGEN

Arbitrary Units



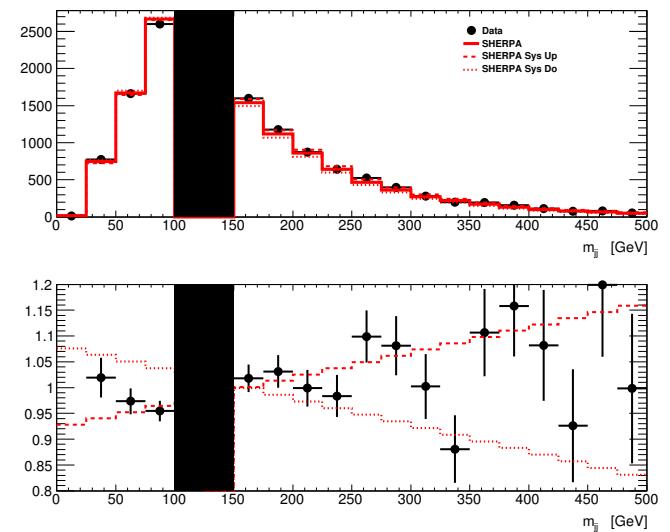
(d) 1-tag SHERPA

Arbitrary Units



(e) 2-tag ALPGEN

Arbitrary Units



(f) 2-tag SHERPA

Figure 154: m_{jj} distribution in 2-lepton events from which a systematics uncertainty on the Monte Carlo modeling m_{bb} shape has been derived.

3923 K W+jet Modeling

3924 K.1 Δϕ Correction Derivation

3925 Pervasive mismodeling is observed in regions dominated by W +light jets such as the 0-lepton 0 and
 3926 1-tag regions. Section 5.1.2.2 describes the data-driven reweighting used to correct the simulation. This
 3927 appendix supplements the information given in said section with more details and more plots. Figure
 3928 155 and 156 show the level of disagreement $\Delta\phi(jet_1, jet_2)$ (simply $\Delta\phi$ from now on) and p_T^W out of
 3929 the box. Ref [11] (Sections 4.2 and 4.3) motivate the stance that the issue is not driven by the multijet
 3930 background. In short, when harsh multijet-killing cuts are applied, the problem persists. Also the dis-
 3931 agreement is seen in both the 1-lepton muon and electron channel which have different levels of multijet
 3932 contamination. For EPS [11], an inclusive correction in p_T^W was derived. However, as shown in Figure 157
 3933 this over-corrects the high p_T^W $\Delta\phi$ distribution. Therefore, a correction below and above $p_T^W = 120$ GeV
 3934 is derived separately for 2 and 3-jets from the 0-tag region. A bin-by-bin correction was applied to yield
 3935 the improvement in modeling summarized in Figure 158. A polynomial is fit to the correction as to not
 3936 propagate the statistical fluctuations from the correction into the analysis as shown in Figure 159. The
 3937 parameters of these polynomials are give in Table 75. From the information provided, it should be clear
 3938 to the reader that the $\Delta\phi$ correction in effect migrates events from high p_T^W to low p_T^W . When doing an
 3939 inclusive correction, this migration was done ‘automatically’. However, now with a separate correction
 3940 at low and high p_T^W (the boarder is $p_T^W = 120$ GeV), some of the migration has to be done ‘by hand’.
 3941 Scale factors were derived to this end by requiring the normalization of the simulation to agree with data.
 3942 Table 76 holds the values of these scale factors.

Function	N-Jet	p_T^W	Parameter Value
$a + b\Delta\phi + c\Delta\phi^2 + d\Delta\phi^3$	2	$p_T^V < 120$ GeV	$a=0.842588$ $b=2.24706 \times 10^{-2}$ $c=4.87832 \times 10^{-2}$ $d=-1.00914 \times 10^{-2}$
		$p_T^V > 120$ GeV	$a=0.87972$ $b=8.59855 \times 10^{-3}$ $c=4.40779 \times 10^{-2}$ $d=-1.06175 \times 10^{-2}$
	3	$p_T^V < 120$ GeV	$a=0.872138$ $b=9.37018 \times 10^{-3}$ $c=-1.44165 \times 10^{-2}$ $d=1.06$
		$p_T^V > 120$ GeV	$a=0.978826$ $b=-0.169663$ $c=0.284077$ $d=0.0187571$ $e=0.98$

Table 75: Functions and parameters used for W +jets data-driven $\Delta\phi$ corrections and systematics.

3943 Electron events with $p_T^W < 120$ GeV in the 1-lepton channel are not considered in the extraction of
 3944 the signal as explained in Section 5.4.3 however those events were used in the derivation of the correction.

Not reviewed, for internal circulation only

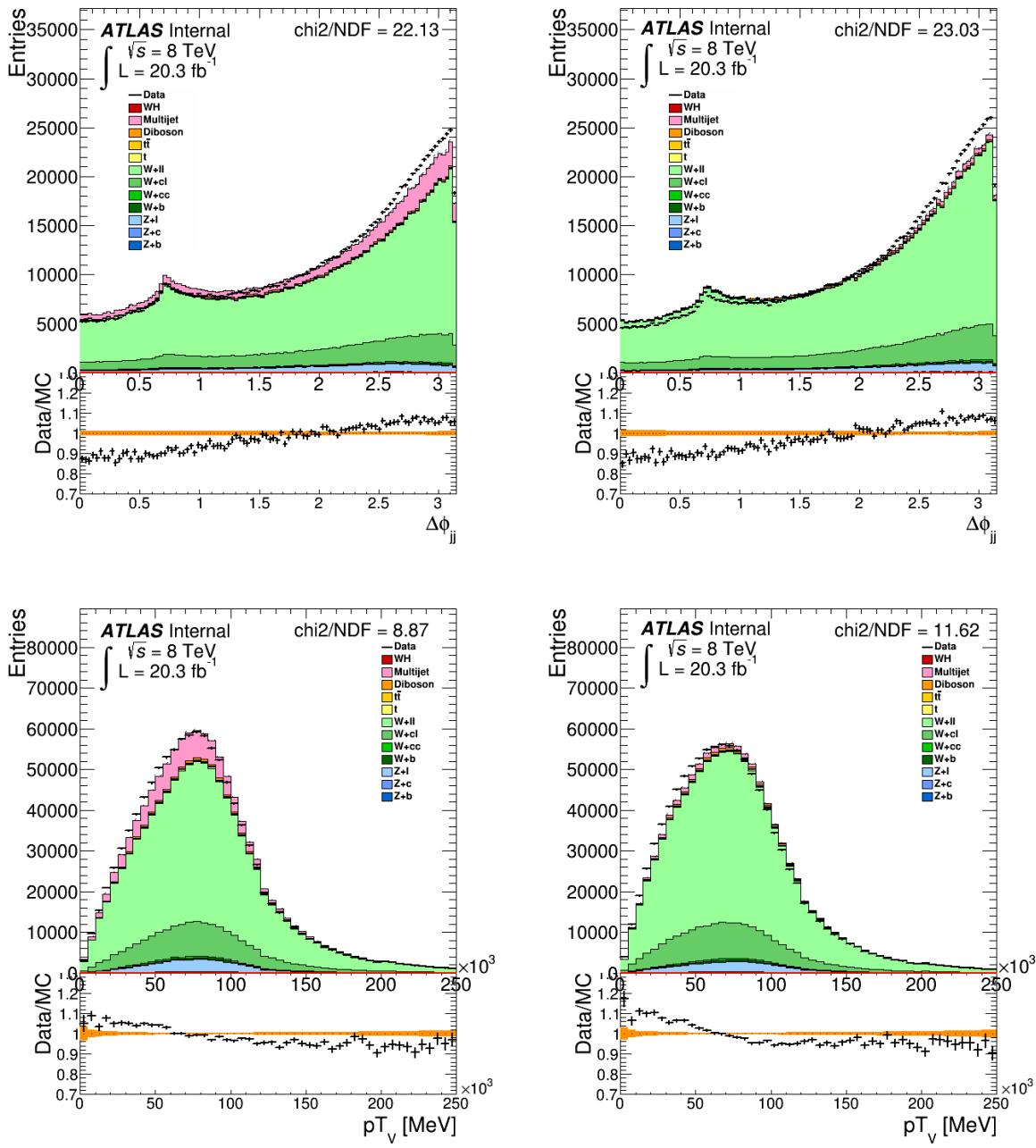


Figure 155: 1-lepton 2-jet 0-tag $\Delta\phi$ and p_T^W distributions before any corrections with electron (muon) events on the left (right).

Not reviewed, for internal circulation only

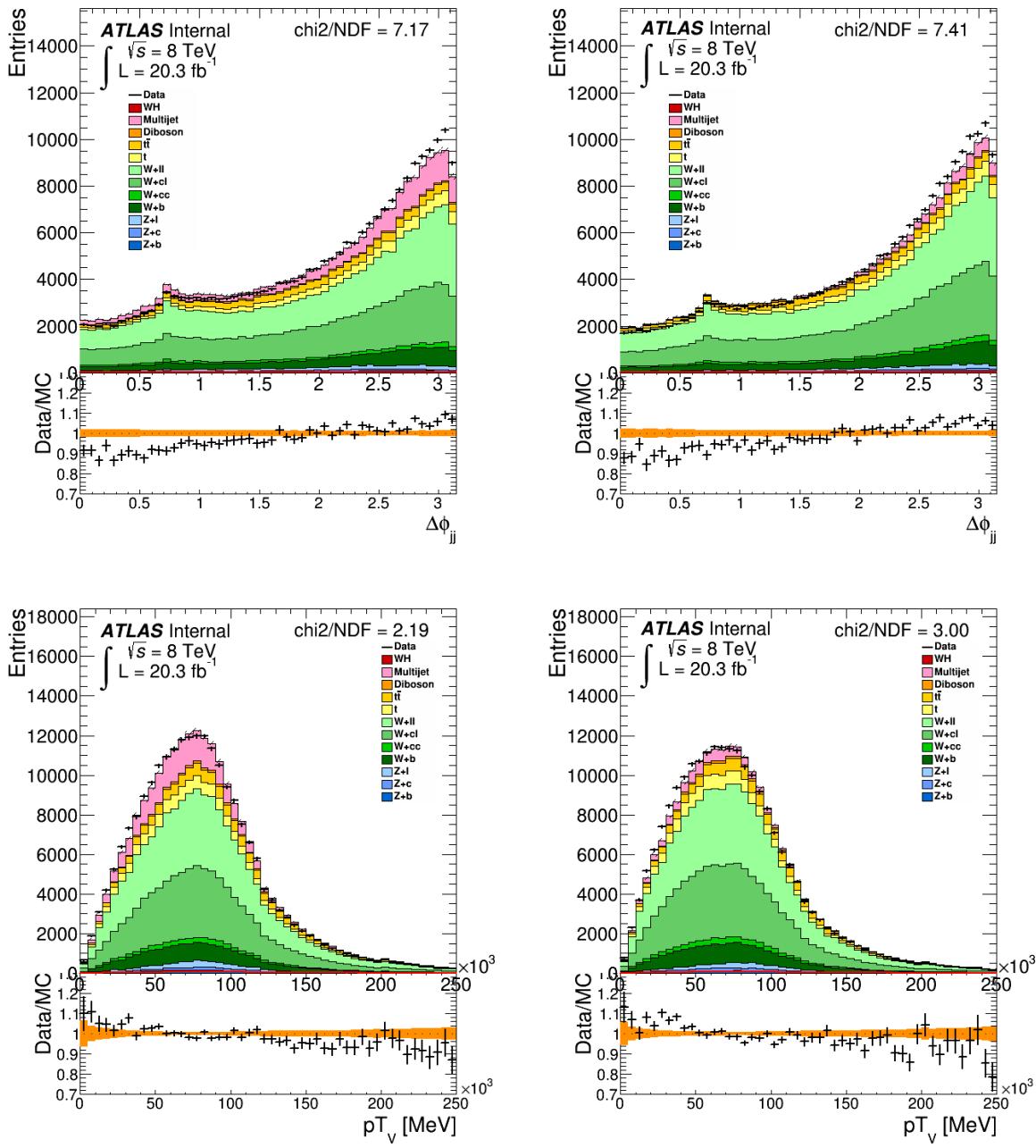


Figure 156: 1-lepton 2-jet 1-tag $\Delta\phi$ and p_T^W distributions before any corrections with electron (muon) events on the left (right).

Not reviewed, for internal circulation only

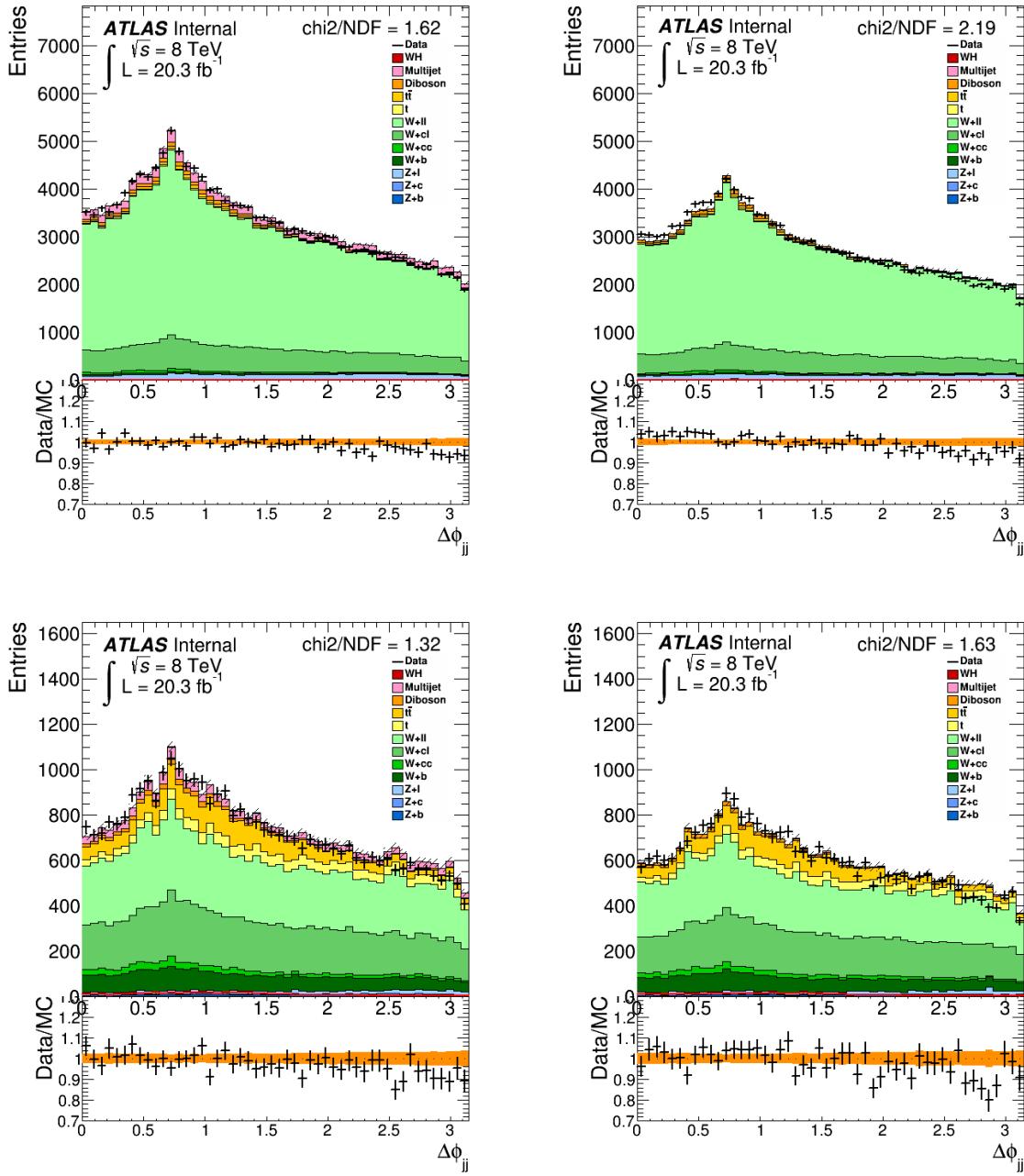
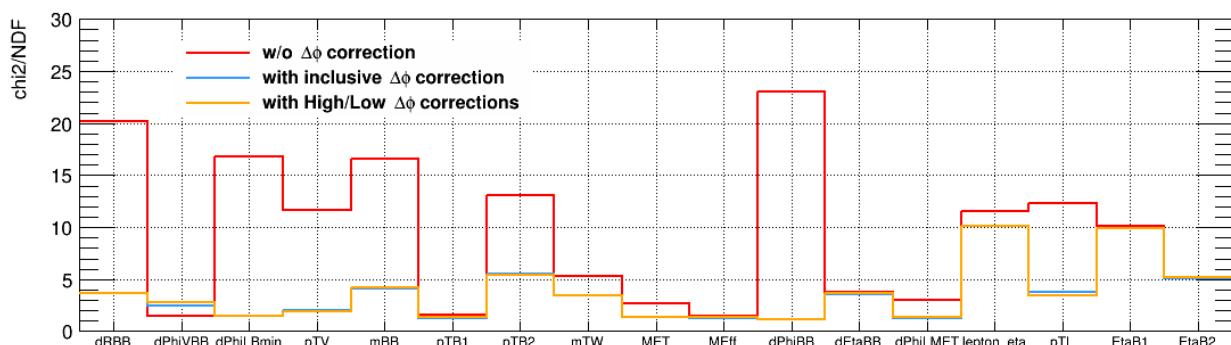
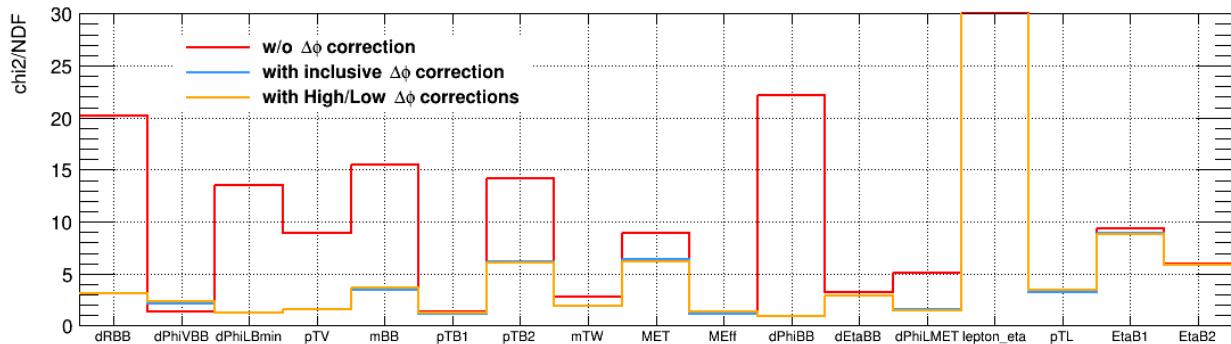
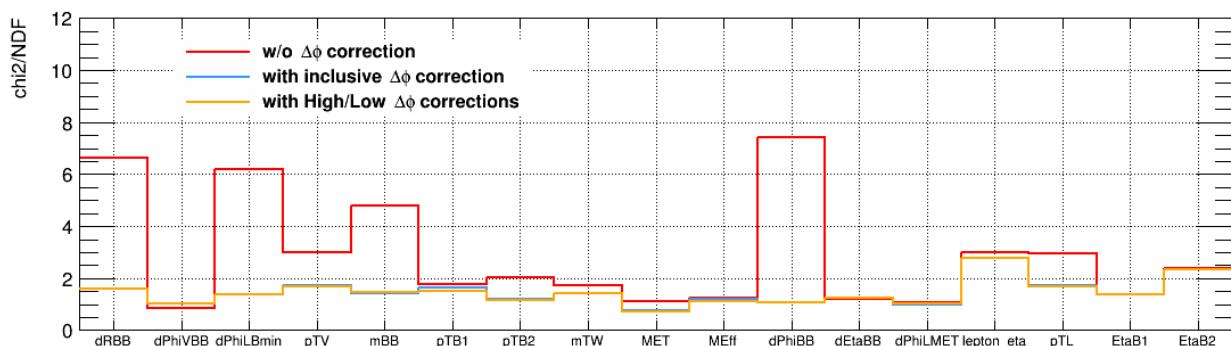
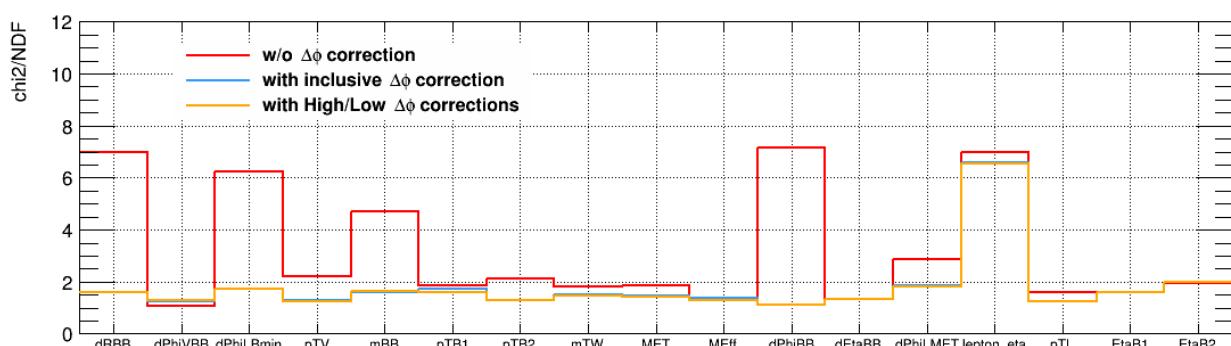


Figure 157: 1-lepton 2-jet 0 and 1-tag $\Delta\phi$ distributions using inclusive $\Delta\phi$ correction similar to the one used for EPS. Notice the high p_T^W region is over corrected. Electron (Muon) events are shown on the left (right) with 0-tag on the top and 1-tag on the bottom.



(a) 0-tag 2-jet



(b) 1-tag 2-jet

Figure 158: Improvements in the data/MC agreement (χ^2) of many kinematic variables in the 1-lepton 2-jet 0-tag and 1-tag events after various $\Delta\phi$ corrections derived from the 0-tag region. The electron channel is shown in top half of each plot and the muon channel in the bottom.

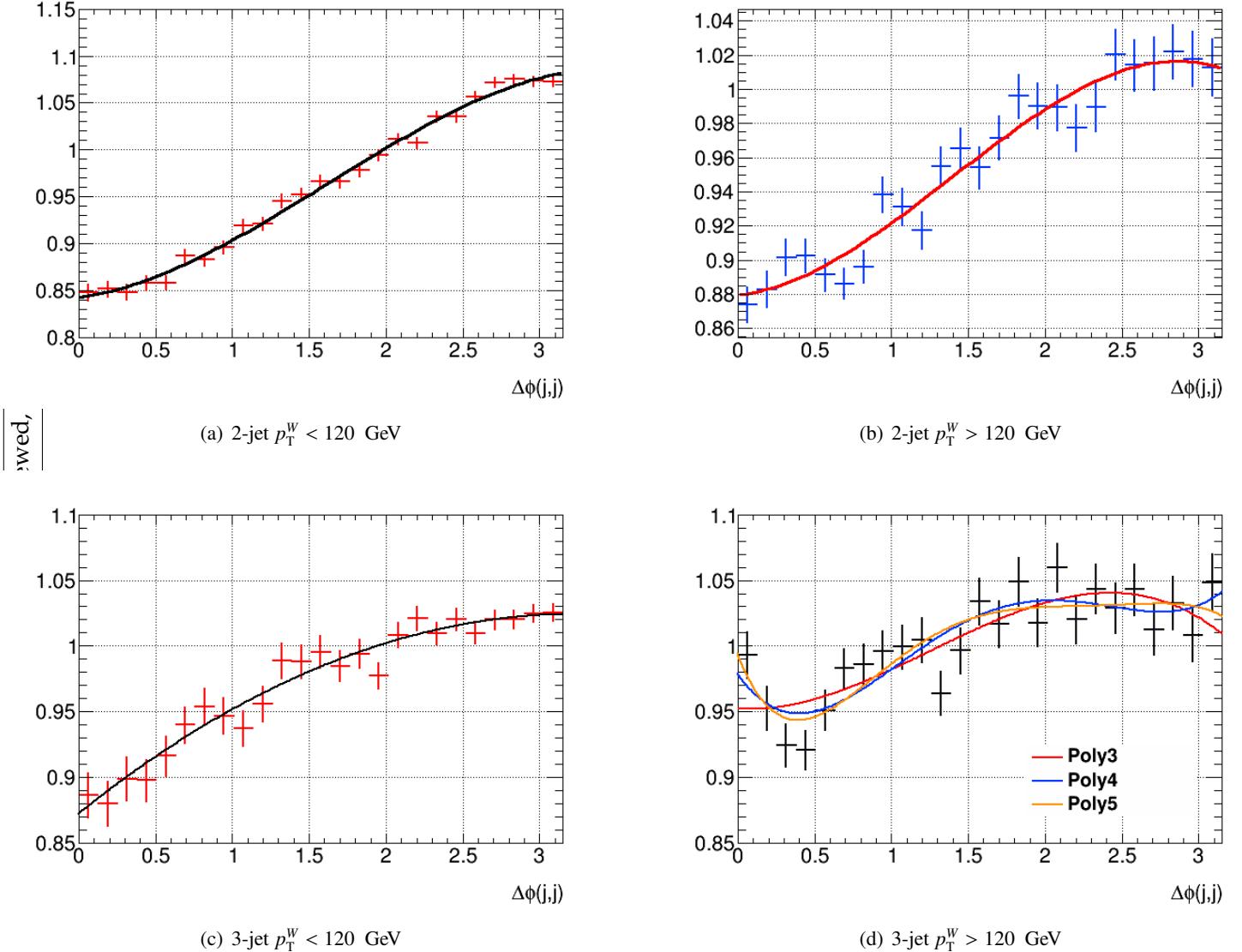


Figure 159: 1-lepton 2 and 3-jet $\Delta\phi$ corrections derived from the 0-tag region for $p_T^W < 120$ GeV and $p_T^W > 120$ GeV separately.

	Region	Scale Factor (%)
2-jet	$p_T^W > 120$ GeV	+7
	$p_T^W < 120$ GeV	-5.6
3-jet	$p_T^W > 120$ GeV	+5.8
	$p_T^W < 120$ GeV	-2

Table 76: The normalization changes for the $\Delta\phi$ correction in each of the four regions is shown. This is necessary in order to maintain overall agreement while events are migrated between high p_T^W and low p_T^W .

3945 K.2 $\Delta\phi$ Correction Usage

3946 From the 1-lepton 0-tag plots shown above, it is clear a correction is needed for $W+l$ and $W+cl$ events.
 3947 However it is not clear that the correction should be applied to $W+hf$. The agreement in the 1-tag was
 3948 tested applying the corrections to all $W+jet$ events and only to $W+ll/cl$ as shown in Figure 160. Since no
 3949 strong evidence is seen for applying the correction to $W+hf$, one is not applied. For a systematic, half the
 3950 correction is applied to $W+ll/cl$ events and the full correction is used as a systematic for $W+hf$ events.
 3951 These are then decorrelated and so is the effect in 2 and 3-jet events.

ion only

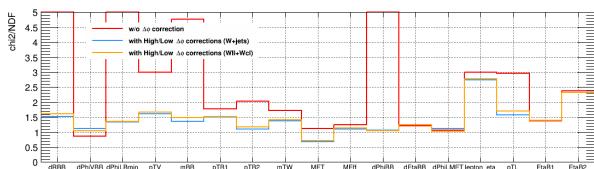
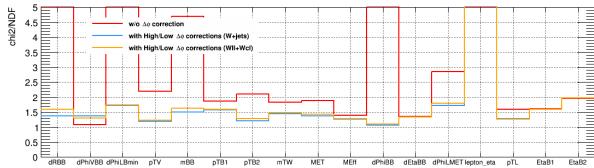
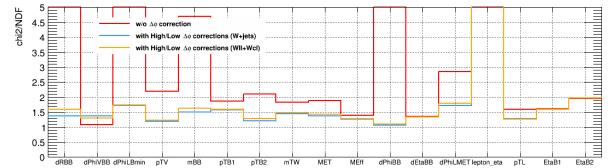
(a) 2-jet $p_T^W < 120$ GeV(b) 2-jet $p_T^W > 120$ GeV

Figure 160: The improvement in modeling is shown after applying the bin-by-bin $\Delta\phi$ correction to either all $W+jet$ events or just to $W+ll/cl$. The agreement is slightly better when only correcting the light jet contribution.

3952 L W+Heavy-Flavor Modeling

3953 The modeling of the process where a W -boson is produced in association with heavy flavor quarks is
 3954 described in detail in this appendix. There is no pure region in the $VH(bb)$ analysis where this process
 3955 can be studied with data-driven techniques. Therefore, a Monte-Carlo study is performed to estimate
 3956 uncertainties on the most relevant quantities.

3957 The 1-lepton object and event dijet mass analysis selection is applied. The flavor labeling of the
 3958 events is performed according to the flavor of hadrons with $p_T > 5$ GeV and their decay products in the
 3959 contents of the signal jets.

3960 This study is done in two approaches: a generator comparison of the main kinematic variables per-
 3961 formed at truth-level, focusing on the $W + b(b)$ final state; and a generator comparison of the flavor
 3962 composition at reconstruction-level, considering all $W+jets$ final states (light, charm, bottom).

3963 L.1 Monte-Carlo samples

3964 The $W+jets$ background is simulated with the Sherpa generator, where the matrix element is inclusive
 3965 in the flavor of jets. Event filters are then applied to select the light, C and B-filtered samples, based on
 3966 the flavor of hadrons with $p_T > 5$ GeV. This means that light matrix elements where the heavy flavor is
 3967 coming from the parton shower can be present in the B-filtered sample.

3968 The alternative Monte-Carlo samples available, however, produce heavy flavor quarks in the matrix
 3969 element by definition. These samples are listed in Table 77, as well as the corresponding parton shower
 3970 programs. For the purpose of this study, a dedicated $W + b\bar{b}$ Sherpa sample was privately produced
 3971 (which will be referred to as Sherpa $W + b\bar{b}$ as opposed to the baseline Sherpa B -filter).

3972 Given the available samples, the estimation of uncertainties related to the $W + b\bar{b}$ background can be
 3973 parametrized into two different effects.

3974 Firstly, the different predictions between Sherpa $W + b\bar{b}$ and the other generators are evaluated, and
 3975 the full variations are considered to define the uncertainty. The specific choice of alternative generator
 3976 will depend on the variable in question.

3977 Secondly, the effect of having bottom quarks produced in the parton shower is studied by comparing
 3978 the baseline Sherpa B -filter with the Sherpa $W + b\bar{b}$ sample. This comparison allows for the estimation
 3979 of uncertainties related to the gluon splitting contribution in the parton shower, for which the rate is not
 3980 well constrained from data at present. 50% of the observed variations are taken as the uncertainty in this
 3981 case.

3982 For the case of the flavor composition uncertainty estimation, the study is performed at reconstruction
 3983 level. The Sherpa and Alpgen MC samples used are listed in Table 78. Given that the relative rates of
 3984 bb , bc , bl , cc , cl and ll events need to be quantified, it is essential to use the full $W+jets$ predictions in
 3985 both Sherpa and Alpgen, i.e., heavy flavor produced both in the matrix element and in the parton shower.
 3986 In the Alpgen case, this requires the use of the HFor tool to remove events in the heavy flavor samples
 3987 where the bb/cc pair have $\Delta R < 0.4$, and avoid double counting of events. This tool is not available at the
 3988 EVNT level at which the truth-level was performed, which motivated the reconstruction-level approach.

MC generator	Parton Shower	Comments
Sherpa	built-in	$W+jets$ with B-filter
Sherpa	built-in	$W + b\bar{b}$
Alpgen	Herwig	$W + bb$
Powheg	Pythia8	$W + b\bar{b}$
aMC@NLO	Herwig++	$W + b\bar{b}$

Table 77: MC samples used in the estimation of the modeling uncertainties. All samples were centrally-produced with the exception of aMC@NLO and Sherpa $W + bb$.

MC generator	Parton Shower	Comments
Sherpa	built-in	$W+jets$ with B-filter
Sherpa	built-in	$W+jets$ with C-filter and B-veto
Sherpa	built-in	$W+jets$ with C- and B-vetoes
Alpgen	Herwig	$W + b\bar{b} + Np0-3$ with HFor
Alpgen	Herwig	$W + c\bar{c} + Np0-3$ with HFor
Alpgen	Herwig	$W + c + Np0-4$ with HFor
Alpgen	Herwig	$W + Np0-5$

Table 78: MC samples used in the estimation of the flavor composition, at reconstruction-level.

Not reviewed, for internal circulation only

3989 **L.1.1 aMC@NLO sample**

3990 The aMC@NLO sample was produced specifically for this study, and its details are described in this
 3991 section. In the aMC@NLO implementation, the NLO QCD corrections to the $W + b\bar{b}$ process are com-
 3992 puted and consistently matched to the HERWIG++ parton shower [70] according to the MC@NLO
 3993 formalism [71]. One-loop corrections are obtained with MADLOOP [72] and all other contributions to the
 3994 parton-level NLO cross section are dealt with by MADFKS [73].

3995 The aMC@NLO prediction is generated using the electroweak parameters listed in Table 79. The
 3996 CT10 PDF [54] was used for the computation, which also sets the value of $\alpha_S(M_Z)$. The renormalization
 3997 and factorization scales are based on the sum of the transverse masses of all final state particles and
 3998 partons ($H_T/2$). The HERWIG++ parton shower uses CTEQ6L1 UE-EE-3 tune with CT10 ME pdf.

3999 The jets are defined with the anti- k_T algorithm with $R = 0.4$ and required to have a $p_T > 7$ GeV.
 4000 There is no minimum p_T cut on the leptons (electrons or muons) applied at generation level.

Table 79: List of electroweak physical parameters used in the generation of aMC@NLO events with the CT10 PDF set. Dimension quantities given in GeV.

Parameter	value
m_W	80.419
G_F	1.166390×10^{-5}
m_t	173
$\alpha_S^{(NLO)}(m_Z)$	0.11798
Γ_W	2.0476
m_Z	91.118

4001 The effect of varying the factorization and renormalization scales on the jet multiplicity and $p_T(W)$
 4002 distributions can be seen on Figures 161 and 162.

4003 **L.2 Uncertainties considered in the fit**4004 **L.2.0.1 m_{jj}**

4005 The uncertainty on the dijet mass distribution is derived at truth-level, by considering only events where
 4006 both leading and sub-leading jets are matched to a b-hadron. The dominant contribution to this uncer-
 4007 tainty comes from the comparison of Alpgen to Sherpa $W+b\bar{b}$, and to this ratio a second order polynomial
 4008 is fitted (see Figure 163, left). The full variation of this function is considered, symmetrized around 1.
 4009 Due to the fact that $W+bb/cc$, $W+bl/bc$, $W+cl$, and $W+l$ are all different physics processes, the m_{bb} sys-
 4010 tematic is decorrelated between the them. Since from the studies comparing different MC generators, no
 4011 clear indication was found for correlation the dominant $W+hf$ modeling in different p_T^V regions, to avoid
 4012 introducing spurious propagations from low to high p_T^V , the $W+bb/W+cc$ systematic is decorrelated in

Not reviewed, for internal circulation only

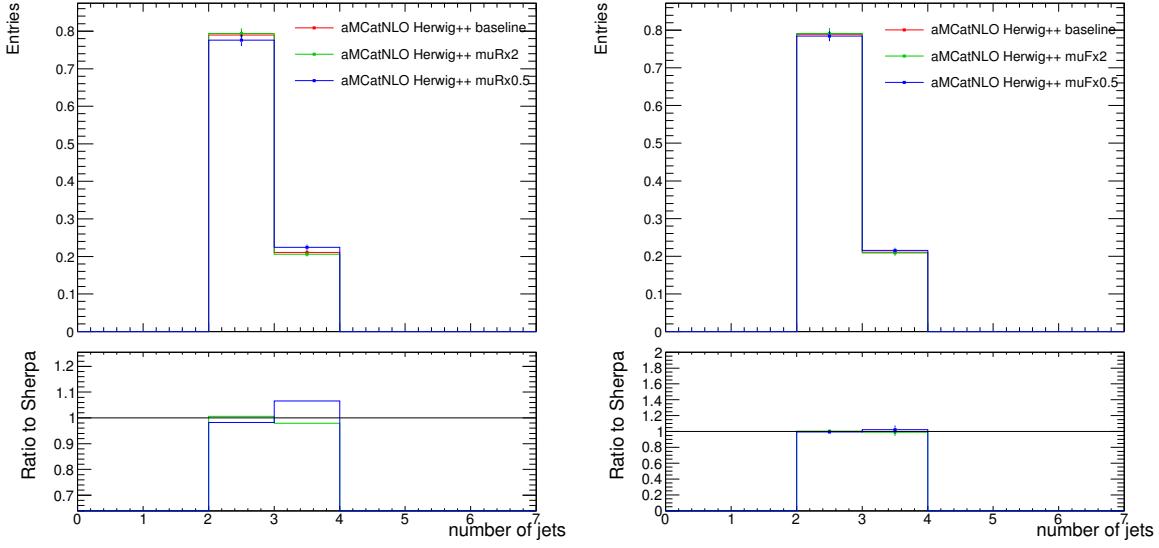


Figure 161: Distribution of number of signal jets in the baseline aMC@NLO sample and in the samples where the μ_R and μ_F parameters have been varied (independently). Normalized to same area.

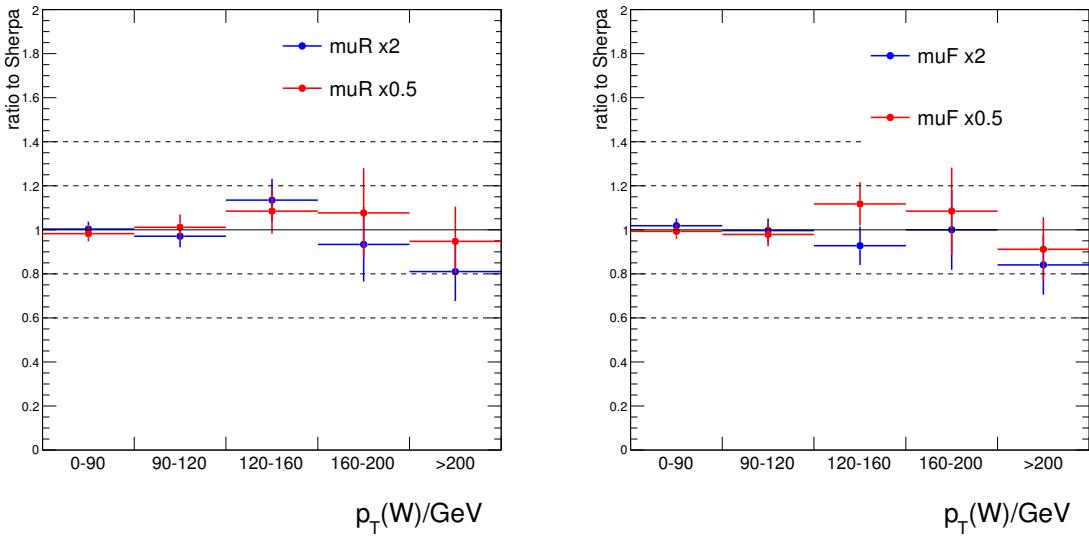


Figure 162: W-boson p_T distribution of 2-jet bb events at truth-level. The ratio is taken of each sample where the μ_R and μ_F parameters have been varied (independently) with respect to the baseline aMC@NLO sample. Normalized to same area.

4013 the lower p_T^V bins ([0-90], [90-120], 120+ GeV). The other (smaller) contribution originates from the
 4014 ratio of Sherpa $W + b\bar{b}$ to Sherpa B-filter, also fitted with a second-order polynomial and considering
 4015 50% of the up and down variation (see Figure 163, right). Both fit functions are shown in Figure 164.
 4016 This latter systematic is degenerate with the larger m_{bb} systematic described above. And since the above
 4017 has been de-correlated and acts on exactly the same samples, this NP has been dropped.

4018 The dependence of the $M_{b\bar{b}}$ shape with $p_T(W)$ was investigated and the ratios with respect to the
 4019 baseline found to have the same trend (see Figure 165).

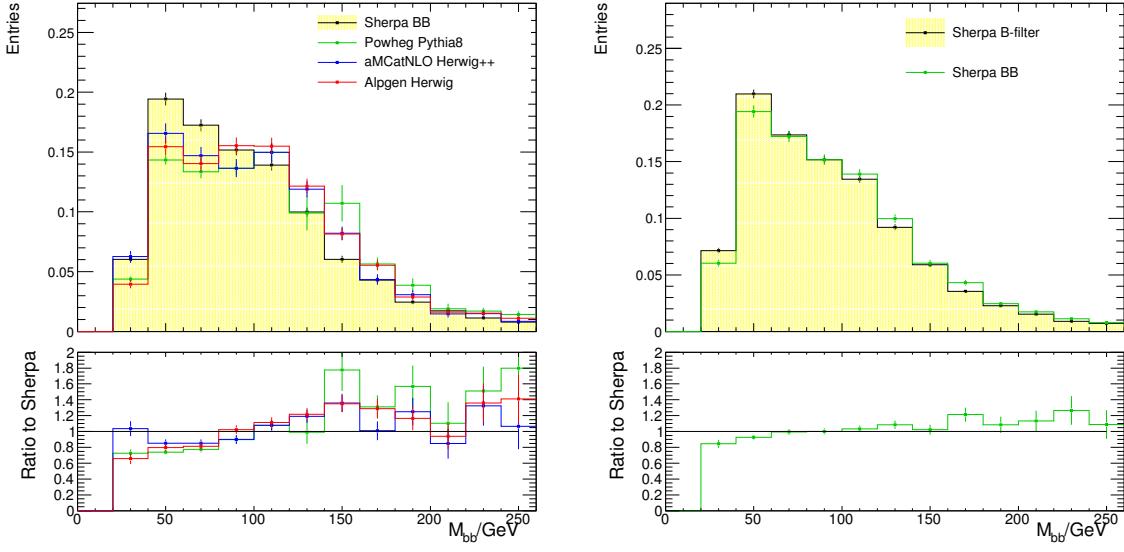


Figure 163: Invariant mass distribution of 2-jet $b\bar{b}$ events at truth-level as predicted by the available $W+b\bar{b}$ generators (left) and the Sherpa samples (right). Normalized to same area.

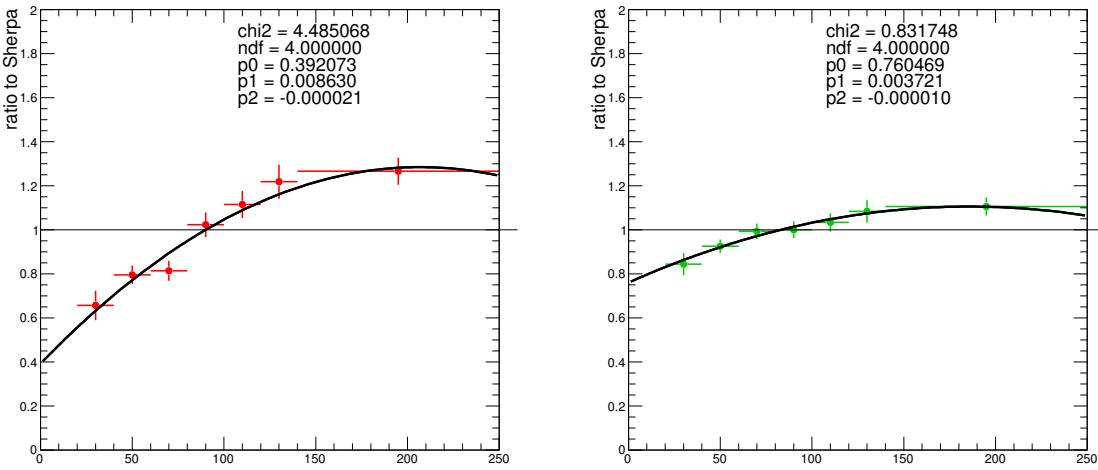


Figure 164: Fit functions to the ratio plots shown in Figure 163.

4020 L.2.0.2 3- to 2-jet ratio

4021 Figure 166 shows the number of events with 2 and 3 jets, for each sample, passing the full event selection
 4022 at truth-level. The uncertainty on the normalization between the 3-jet and 2-jet region is derived from the
 4023 relative difference in the ratios observed, with respect to the Sherpa prediction. It's clear from the plot
 4024 that Powheg predicts a very discrepant 3-jet rate, when compared to the other generators and also to the
 4025 effect of the scale variations seen on Figure 161. Powheg's prediction is therefore left out at the moment,
 4026 while its behavior in the 3-jet bin is better understood.

4027 A 10% uncertainty is derived for the 3- to 2-jet ratio from the aMC@NLOto SHERPA $W + b\bar{b}$ compari-
 4028 son. The effect from the Sherpa $W + b\bar{b}$ to Sherpa B-filter comparison is negligible.

Not reviewed, for internal circulation only

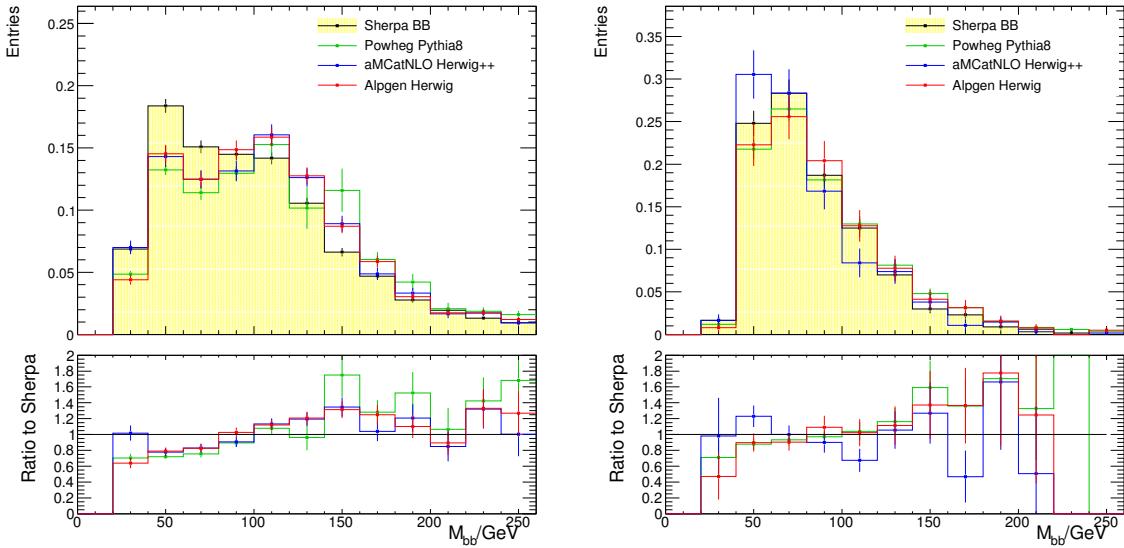
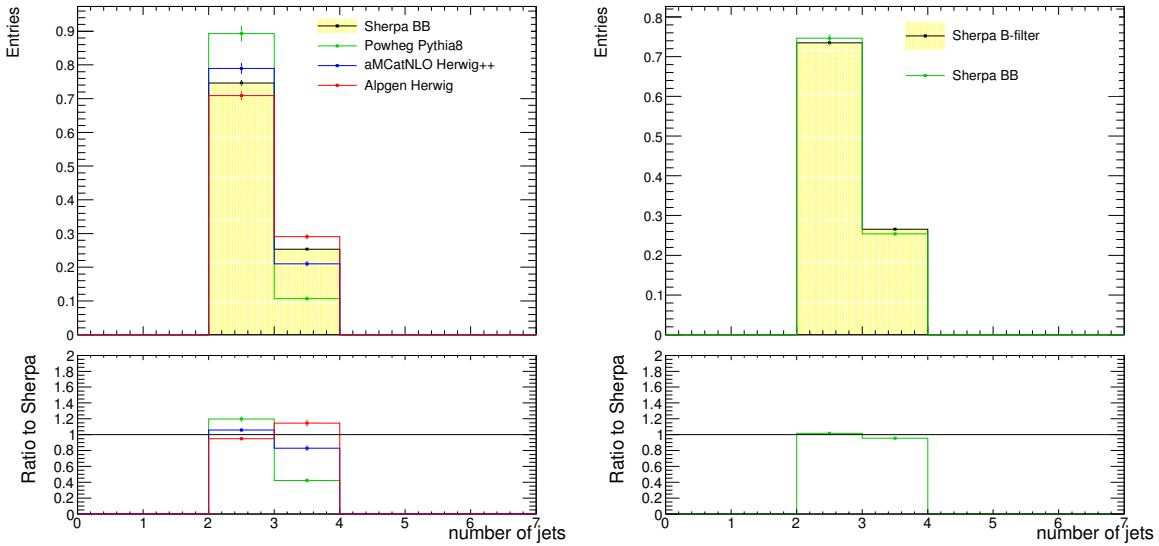
Figure 165: , for $p_T(W) < 120 \text{ GeV}$ (left) and $p_T(W) > 120 \text{ GeV}$ (right). Normalized to same area.

Figure 166: Distribution of the number of jets in bb events at truth-level. Comparison between generators (left) and between the different Sherpa samples (right). Normalized to same area.

4029 L.2.0.3 p_T^W

4030 The transverse momentum of the W is also compared at truth-level among the $W + b\bar{b}$ predictions.
 4031 To define a shape uncertainty on this distribution, the aMC@NLO to SHERPA ratio is considered, and a
 4032 function of the form $a + b \log(p_T)$ is fitted (see Figure 167). The p_T^W spectrum and ratios between the
 4033 generator predictions are shown in Figure 23, on Section 5.1.2.3.

4034 L.2.0.4 Flavor Composition

4035 The uncertainty on the flavor composition is defined by comparing the fractions of bl, cc and bc events
 4036 with respect to bb, using Sherpa and Alpgen generators, as described above. The comparison is done at

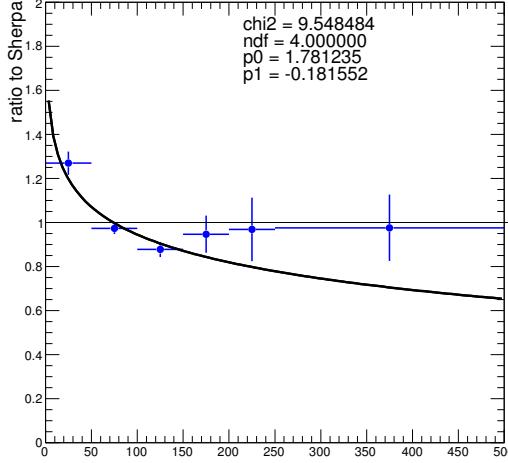


Figure 167: Fit function to the observed aMC@NLOto SHERPARATIO in the p_T^W distribution, for 2-jet bb events at truth levee.

4037 reconstruction level, without requiring the leading jets to be b-tagged, see Figure 168. The conservative
 4038 estimate of 12% is taken for the bc/bb and cc/bb uncertainties, in accordance to what was derived also for
 4039 Z+jets. For the specific bl/bb fraction in the W+jets case, a larger uncertainty of 35% was considered,
 4040 given the discrepancy observed.

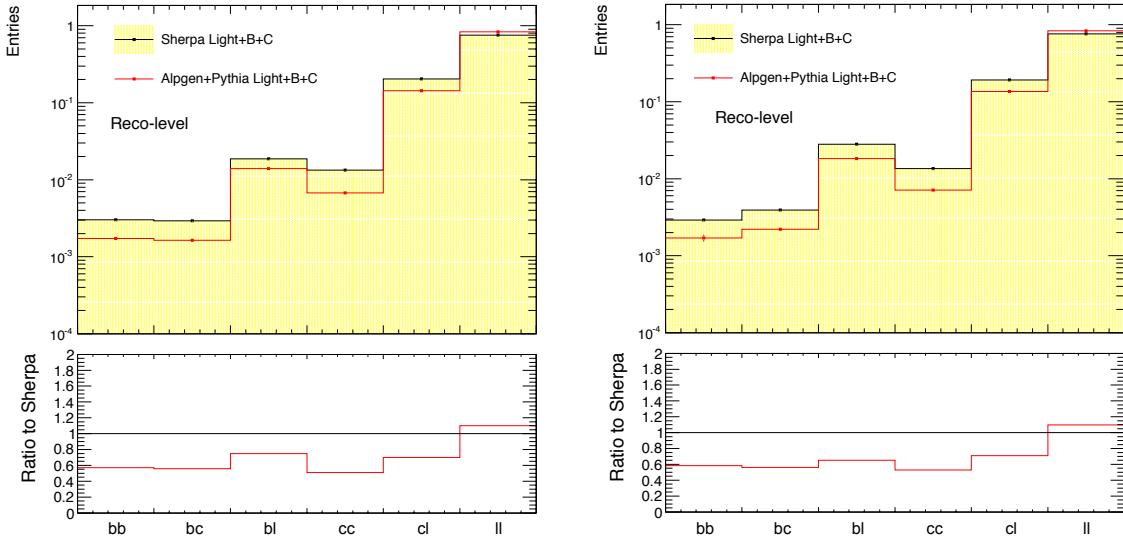


Figure 168: Fraction of events with each flavor label in the 2-jet (left) and 3-jet (right) pre-tag regions, for Alpgen and Sherpa W+jets. Reconstruction-level distribution. Normalized to same area.

4041 L.3 W+Heavy-Flavor Modeling for MVA variables

4042 The comparison between generators for the $W + b\bar{b}$ process was also performed with the MVA event
 4043 selection, for the input variables that can be defined at truth-level. The following Figures 169-178 show

4044 each distribution in the low and high $p_T(W)$, 2-jet and 3-jet regions, in events where the leading jets
 4045 are matched to b-hadrons. The MV1c variables are not defined at truth level, however the difference
 4046 between this variable in different MCs is already encapsulated in the MC-to-MC scale factors introduced
 4047 in Section 3.3.4.3 and described in full detail in Appendix T.2.

4048 The shape uncertainties derived with the dijet mass analysis selection, and applied to the $m_{b\bar{b}}$ and
 4049 $p_T(W)$ distributions should in principle be designed to cover also the variations in the MVA output from
 4050 any discrepancies in the input variables.

4051 The 3- to 2-jet ratio in the low and high $p_T(W)$ MVA regions was cross-checked to be compatible
 4052 with the one derived inclusively with the dijet mass analysis selection.

Not reviewed, for internal circulation only

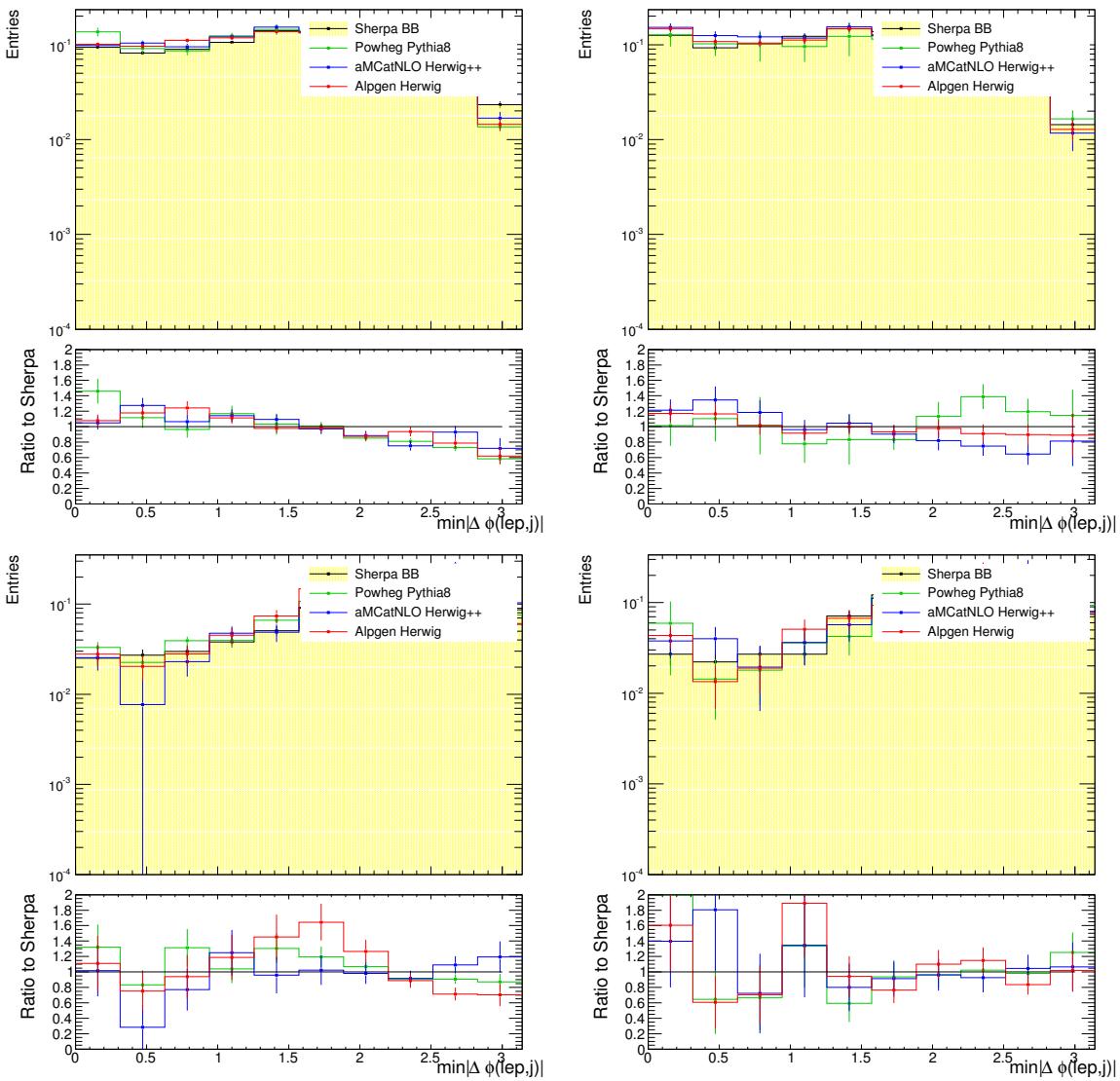


Figure 169: $\min|\Delta\phi(\ell, j)|$ variable in the low and high $p_T(W)$ regions, for the 2- and 3-jet cases. Events with leading jets matched to b-hadrons.

Not reviewed, for internal circulation only

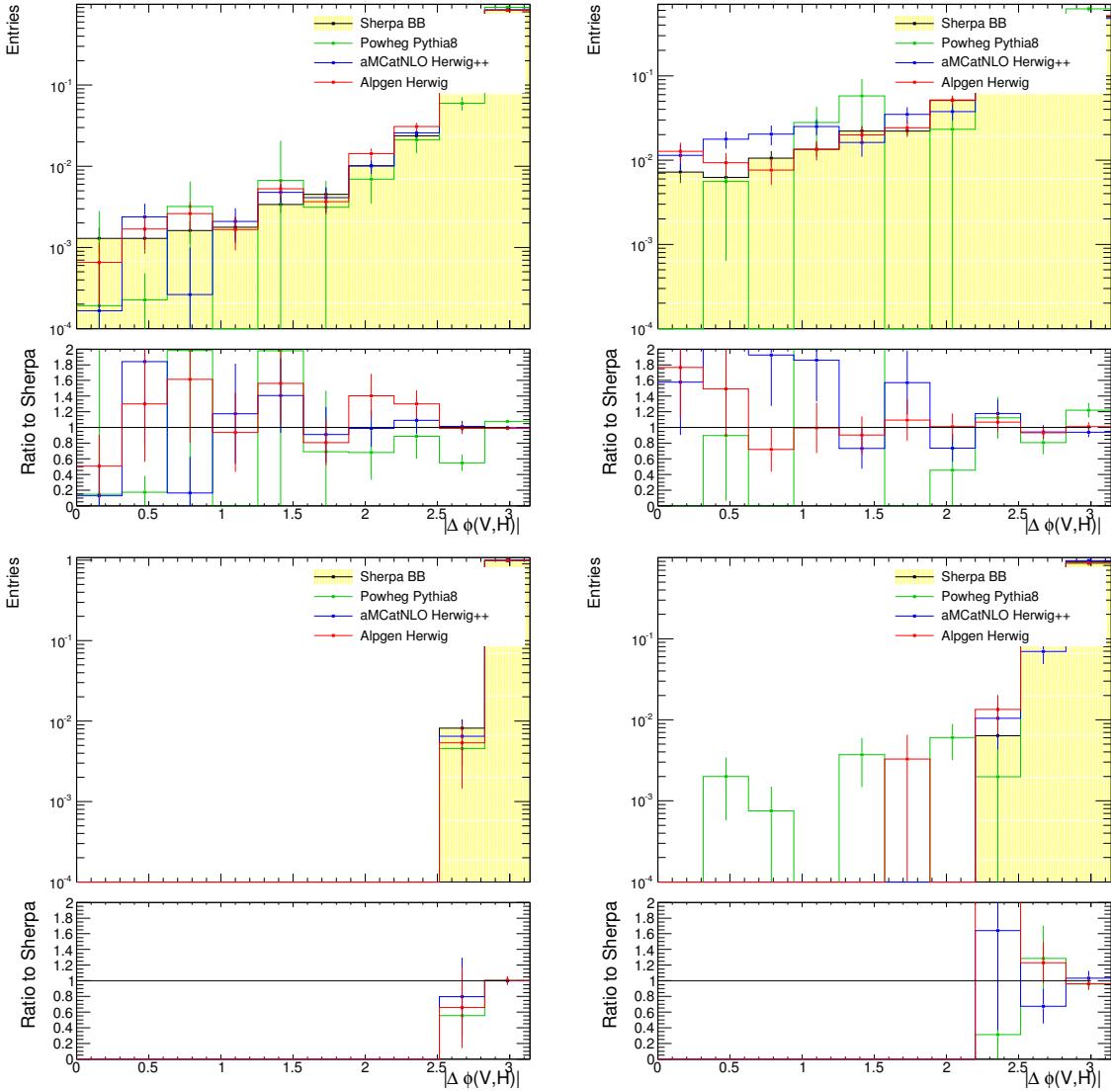


Figure 170: $|\Delta\phi(V, H)|$ variable in the low and high $p_T(W)$ regions, for the 2- and 3-jet cases. Events with leading jets matched to b-hadrons.

Not reviewed, for internal circulation only

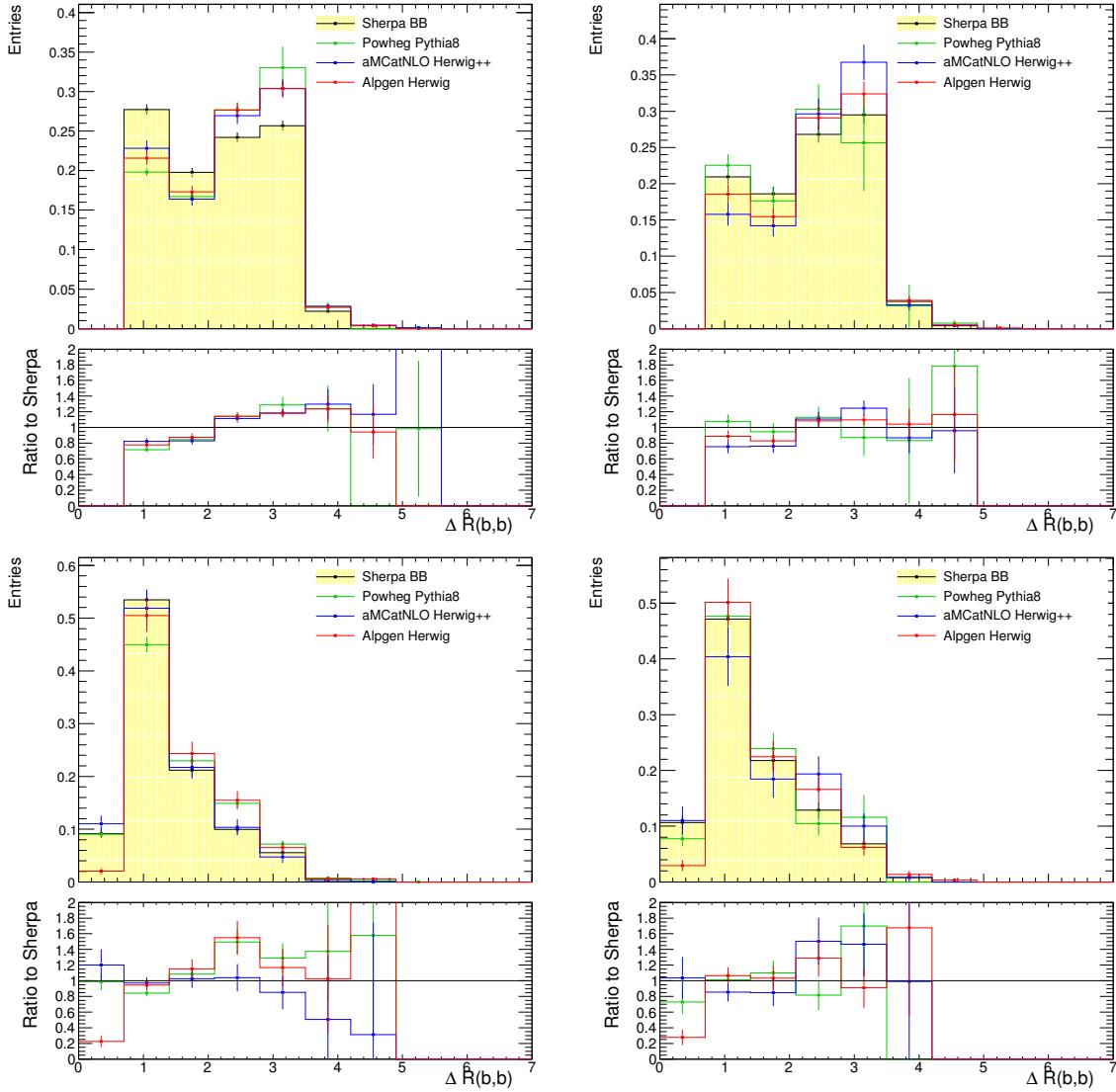


Figure 171: $\Delta R(b, b)$ variable in the low and high $p_T(W)$ regions, for the 2- and 3-jet cases. Events with leading jets matched to b-hadrons.

Not reviewed, for internal circulation only

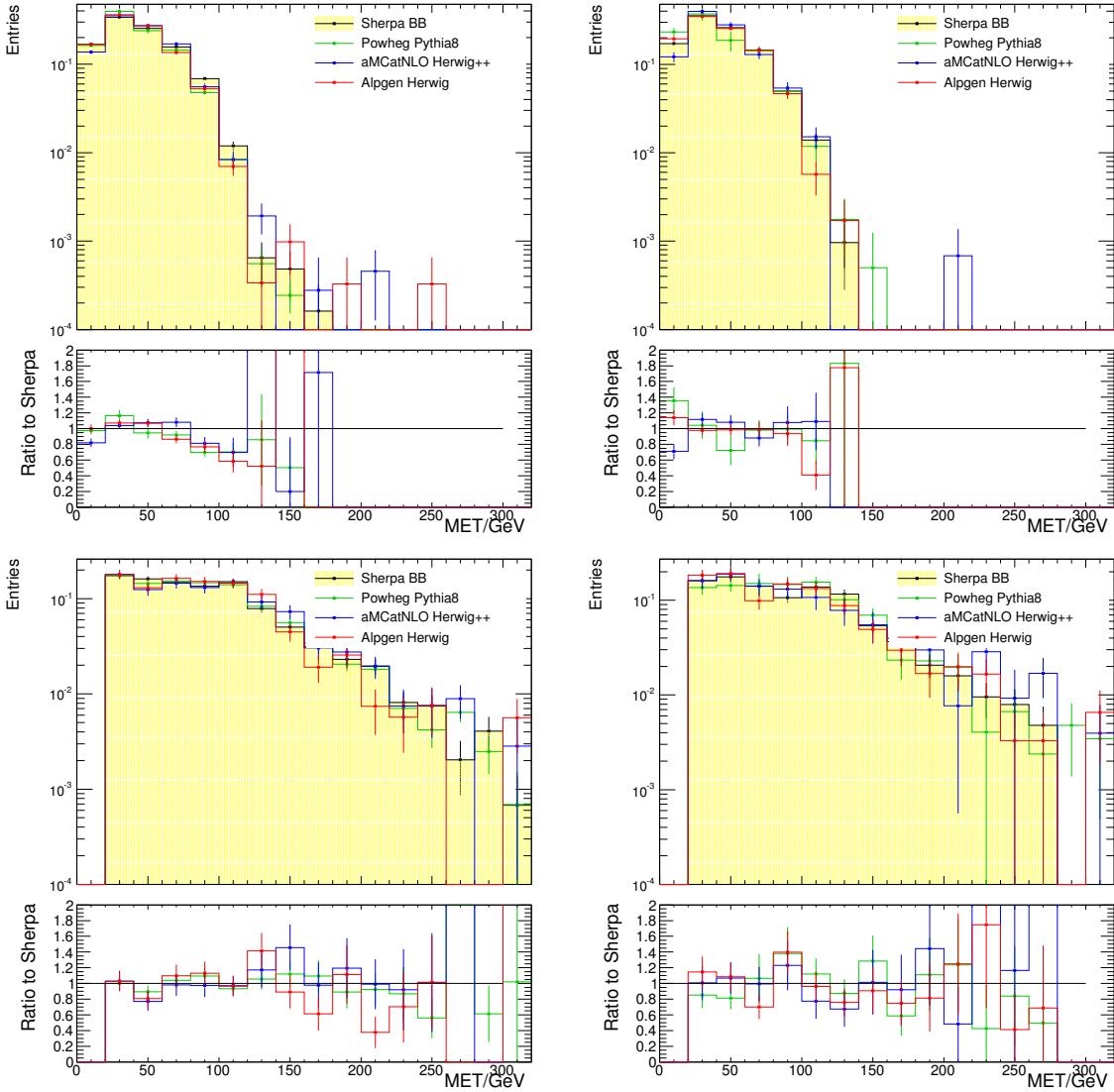


Figure 172: MET variable in the low and high $p_T(W)$ regions, for the 2- and 3-jet cases. Events with leading jets matched to b-hadrons.

Not reviewed, for internal circulation only

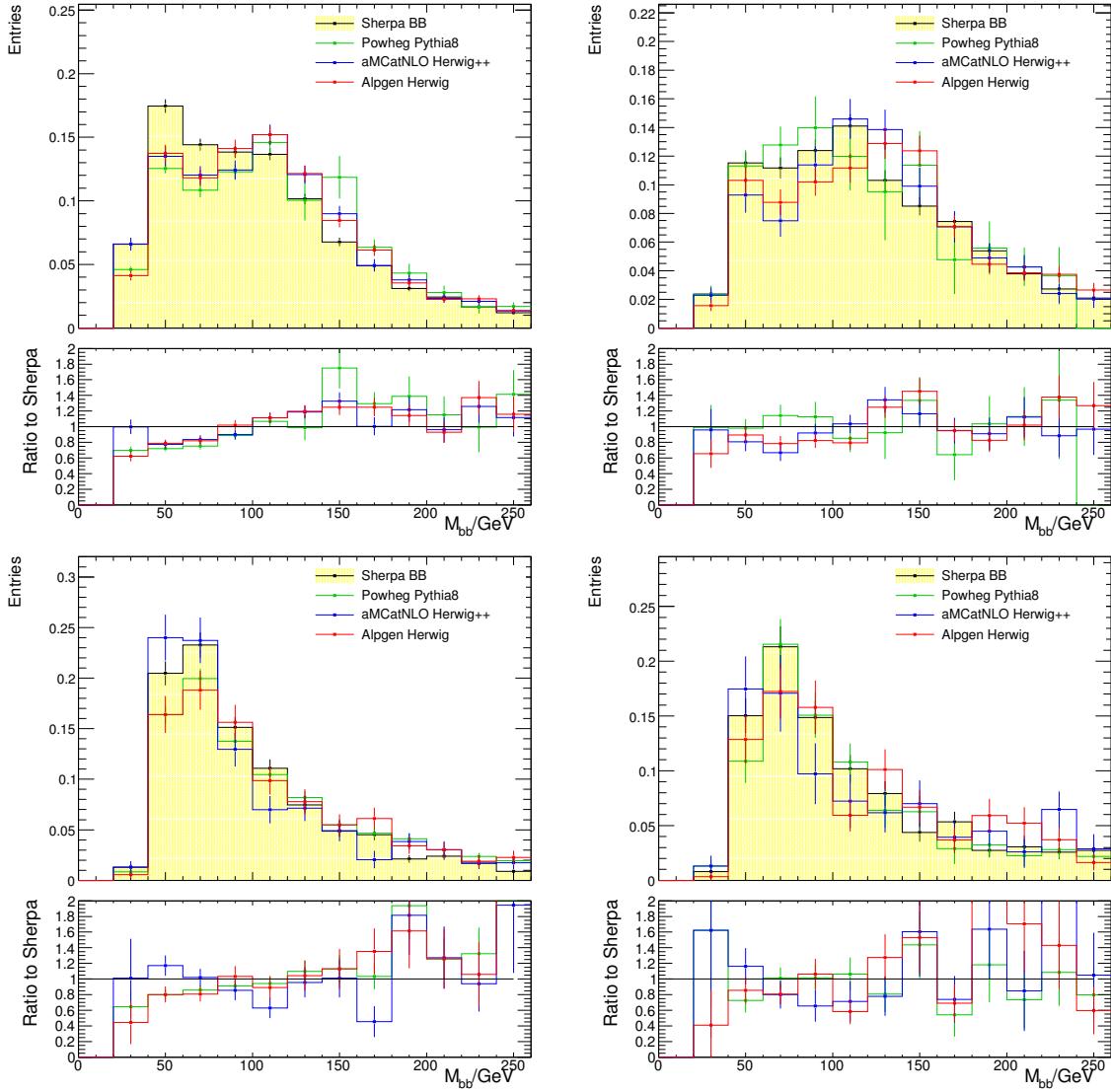


Figure 173: Dijet mass in the low and high $p_T(W)$ regions, for the 2- and 3-jet cases. Events with leading jets matched to b-hadrons.

Not reviewed, for internal circulation only

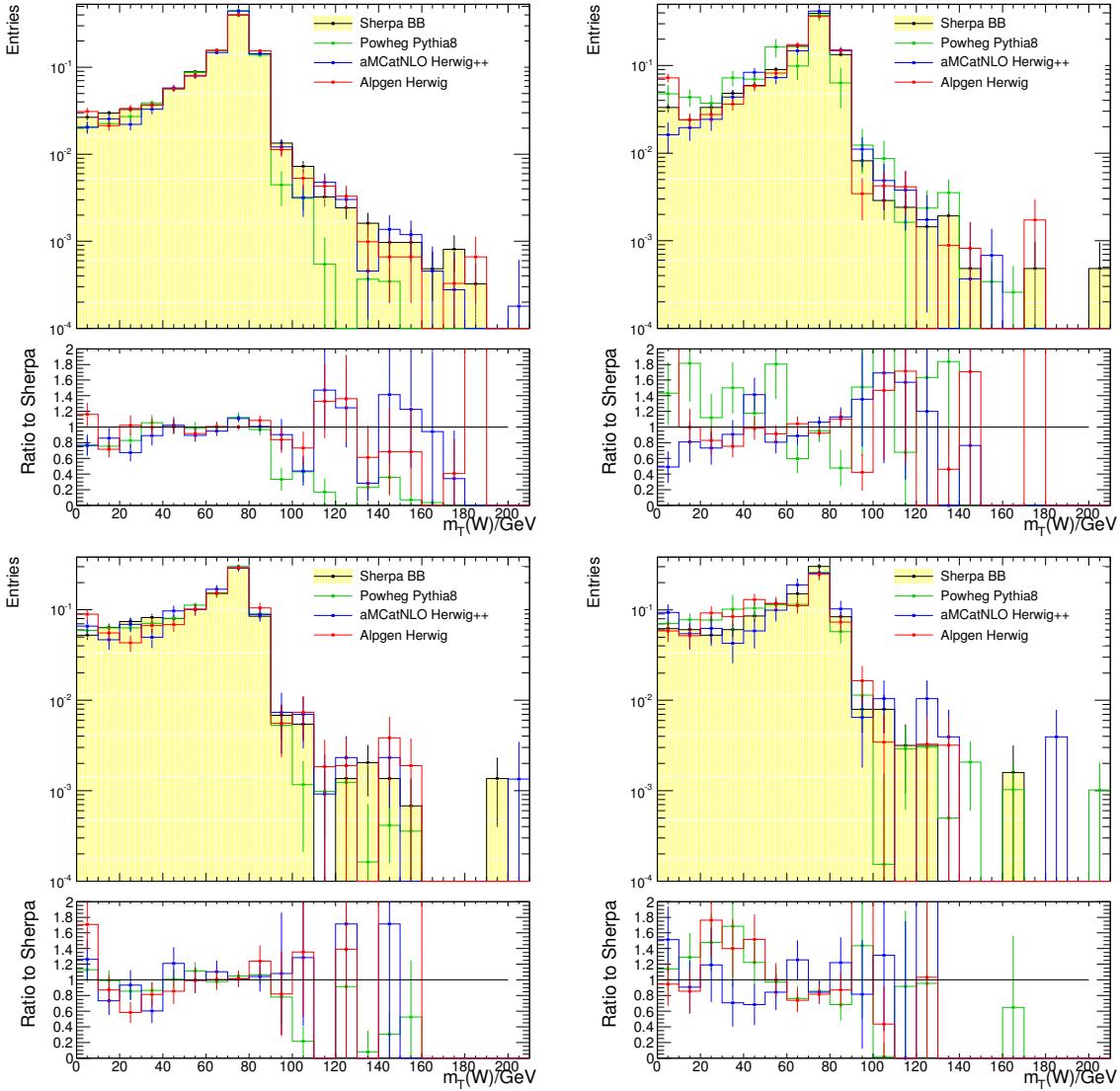


Figure 174: $M_T(W)$ in the low and high $p_T(W)$ regions, for the 2- and 3-jet cases. Events with leading jets matched to b-hadrons.

Not reviewed, for internal circulation only

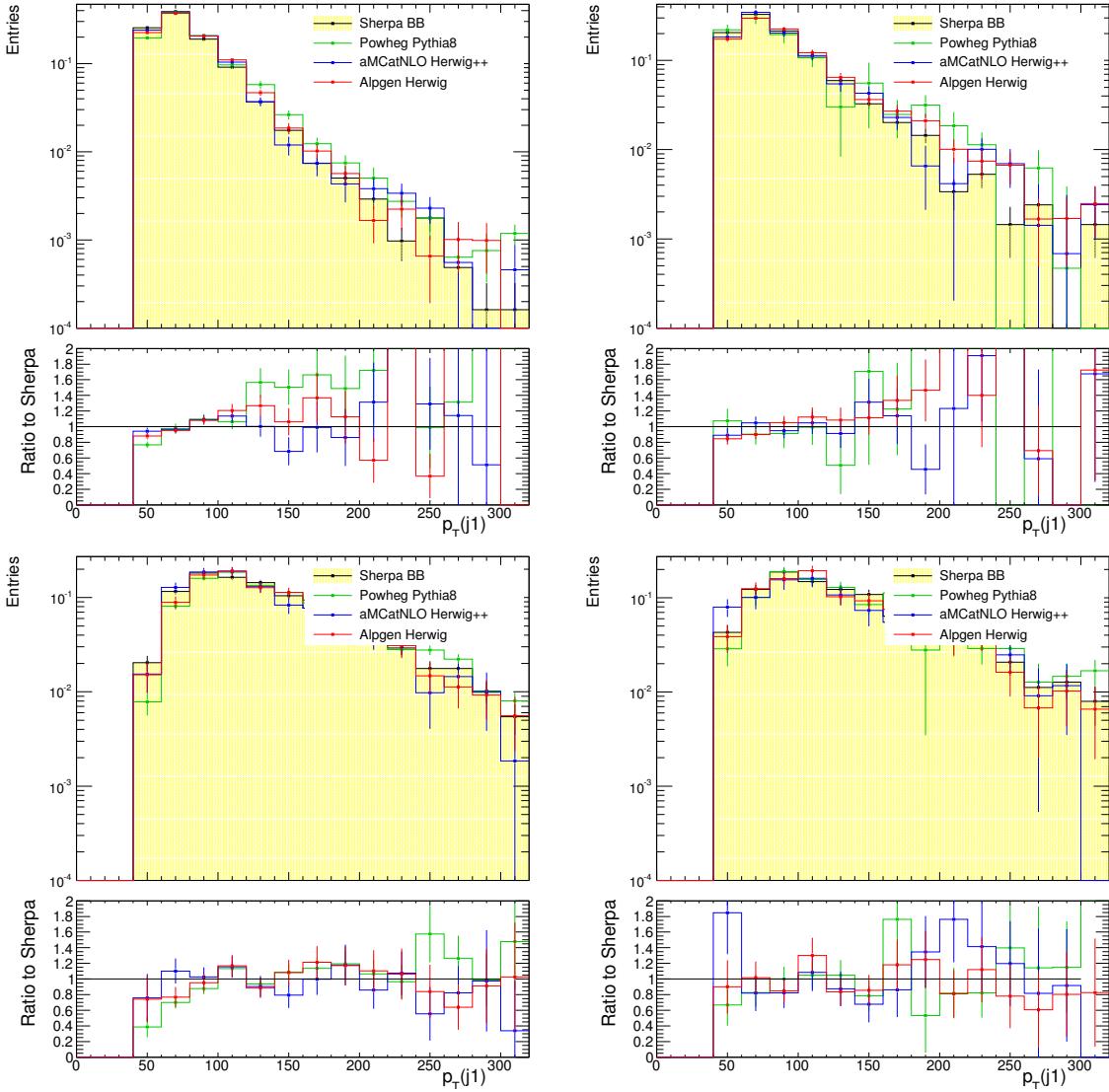


Figure 175: $p_T(j_1)$ in the low and high $p_T(W)$ regions, for the 2- and 3-jet cases. Events with leading jets matched to b-hadrons.

Not reviewed, for internal circulation only

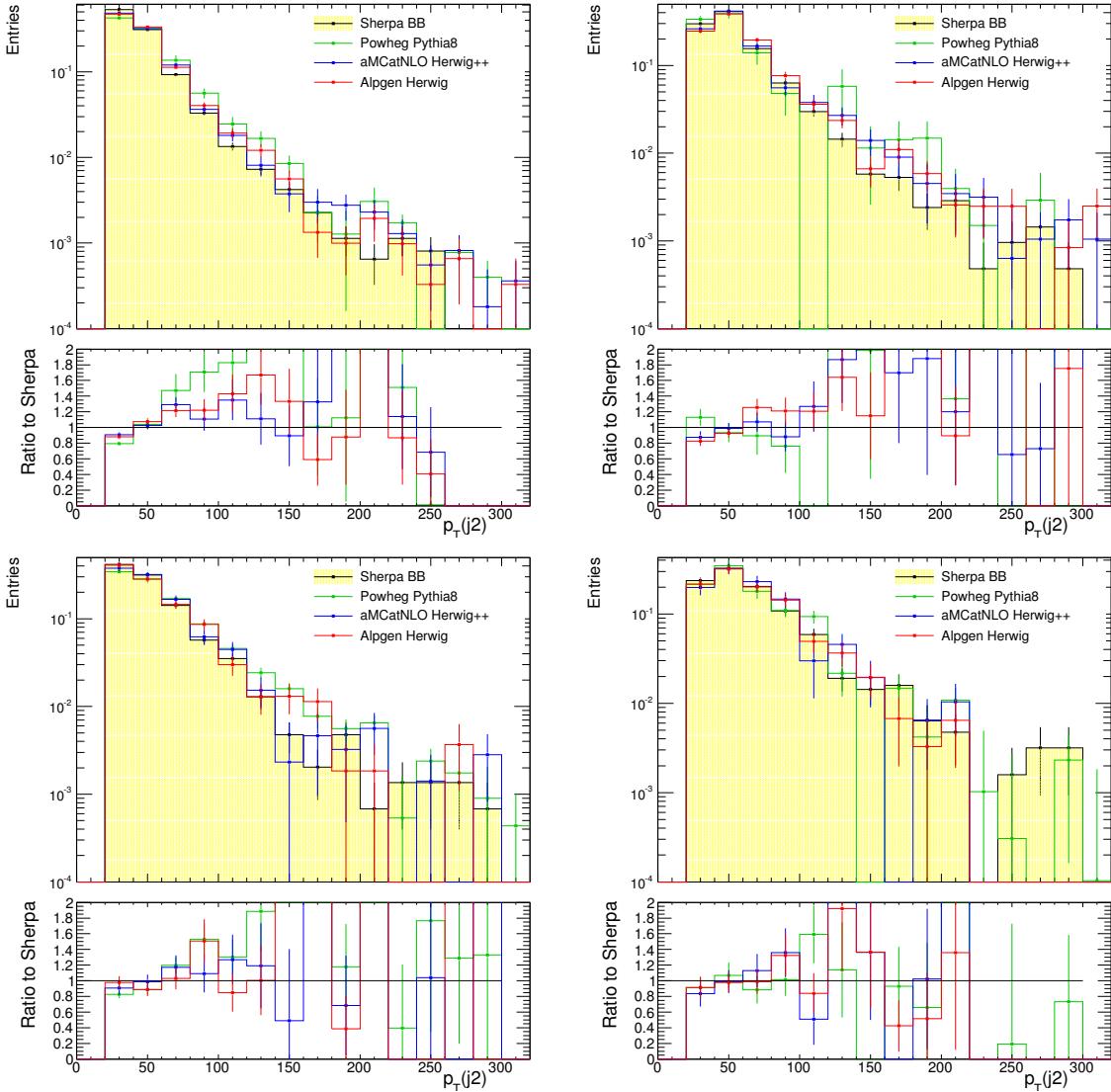


Figure 176: $p_T(j_2)$ in the low and high $p_T(W)$ regions, for the 2- and 3-jet cases. Events with leading jets matched to b-hadrons.

Not reviewed, for internal circulation only

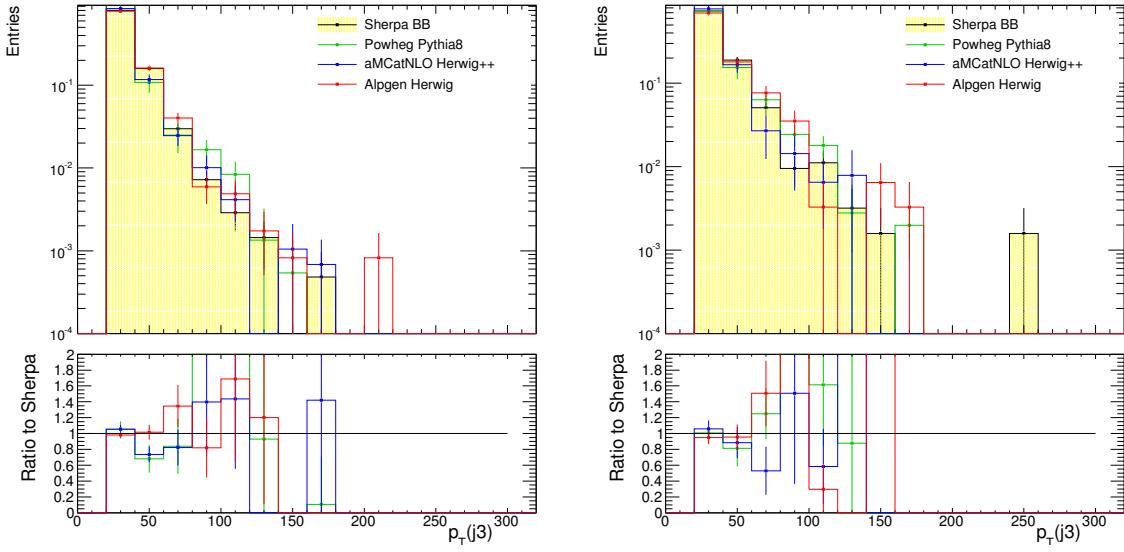


Figure 177: $p_T(j_3)$ in the low and high $p_T(W)$ 3-jet regions. Events with leading jets matched to b-hadrons.

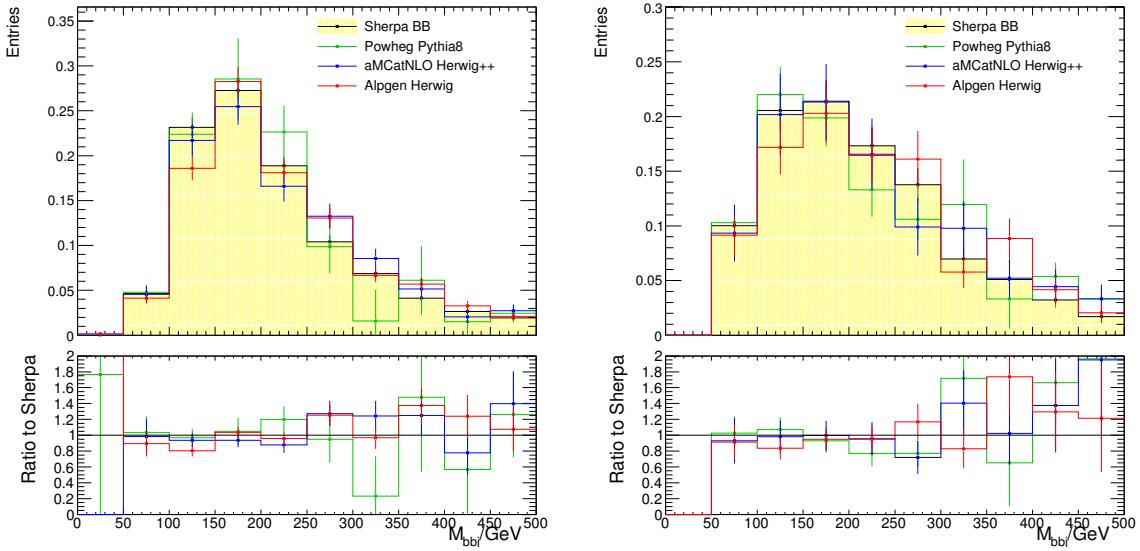


Figure 178: m_{bbj} in the low and high $p_T(W)$ 3-jet regions. Events with leading jets matched to b-hadrons.

Not reviewed, for internal circulation only

4053 M Single-top modeling

4054 The study of the single-top modelling have been been done by comparing the agreement of different
 4055 monte carlo generators in producing important distributions for the analysis while using the 1-lepton
 4056 MVA-based selection. The Monte Carlo samples used for these studies are summarised in Table 80 and
 4057 reproduced here. In this appendix, we show the comparisons for m_{bb} , p_T^V and the leading and second
 4058 leading jet p_T for the s-channel production and the Wt production mechanisms, while for the t-channel,
 4059 the appendix is completed with different additional variables.

Process	Channel num.	tag	N_{events}
Single top, AcerMCPythia, P2011CCTEQ6L1			
s-ch.	110102	e2092_a188_a205_r4540_p1328	1199999
Wt-ch.	110103	e2092_a188_a205_r4540_p1328	998997
Single top, PowhegHerwig, AUET2CT10			
Wt-ch	110144	e1743_s1581_s1586_r3658_r3549_p1328	998896
Single top, PowhegPythia, P2011C, DS			
Wt-ch.	110142	e1743_s1581_s1586_r3658_r3549_p1328	994894
Single top, aMcAtNloJimmy, AUET2CT10			
t-ch.	110095	e2240_a188_a205_r4540_p1328	996999
Single top, McAtNloJimmy, AUET2CT10			
s-ch.	108343	e1525_a159_a171_r3549_p1328	999998
	108344	e1525_a159_a171_r3549_p1328	998000
	108345	e1525_a159_a171_r3549_p1328	999998
Wt-ch.	108346	e1525_a159_a171_r3549_p1328	4996492
Single top AcerMCPythia, P2011CMorePSCTEQ6L1			
t-ch.	110105	e2092_a188_a205_r4540_p1328	2978000
s-ch.	110107	e2092_a188_a205_r4540_p1328	1199999
Wt-ch	110109	e2092_a188_a205_r4540_p1328	998999
Single top AcerMCPythia, P2011CLessPSCTEQ6L1			
t-ch.	110106	e2092_a188_a205_r4540_p1328	2997999
s-ch.	110108	e2092_a188_a205_r4540_p1328	1198998
Wt-ch	110110	e2092_a188_a205_r4540_p1328	1000000

Table 80: Monte Carlo samples and channel numbers and statistics used for the single top and the $t\bar{t}$ systematics. More information is given in Section 5.2.2.

4060 M.1 t-channel

4061 For the single top t-channel, the baseline sample AcerMCPythia was compared to the aMcNLOJimmy
 4062 sample. From this comparison, systematic uncertainties in normalization were extracted and found to be
 4063 52 and 25% for 2 b-tag 2 jet events at low and high p_T^V , respectively and 12 and -18% for 2 b-tag 3 jet
 4064 events. The yield difference between the two samples comes primarily from the b-tagging procedure and
 4065 jets p_T .

4066 Figures 179 and 180 show the distributions for the t-channel single top variables in 1-lepton events
4067 for $p_T^W < 120$ GeV with 2 *b*-tag and 2 jets.

4068 Figures 181 and 182 show the distributions for the t-channel single top variables in 1-lepton events for
4069 $p_T^W > 120$ GeV with 2 *b*-tag and 2 jets.

4070 Figures 183 and 184 show the distributions for the t-channel single top variables in 1-lepton events for
4071 $p_T^W < 120$ GeV with 2 *b*-tag and 3 jets.

4072 Figures 185 and 186 show the distributions for the t-channel single top variables in 1-lepton events for
4073 $p_T^W > 120$ GeV with 2 *b*-tag and 3 jets.

4074

4075 Several variables have different distribution shapes for the two Monte-Carlo generators. This mis-
4076 modelling is most of the time covered by the statistical uncertainties and no shape uncertainty was con-
4077 sidered for the t-channel originating from this comparison.

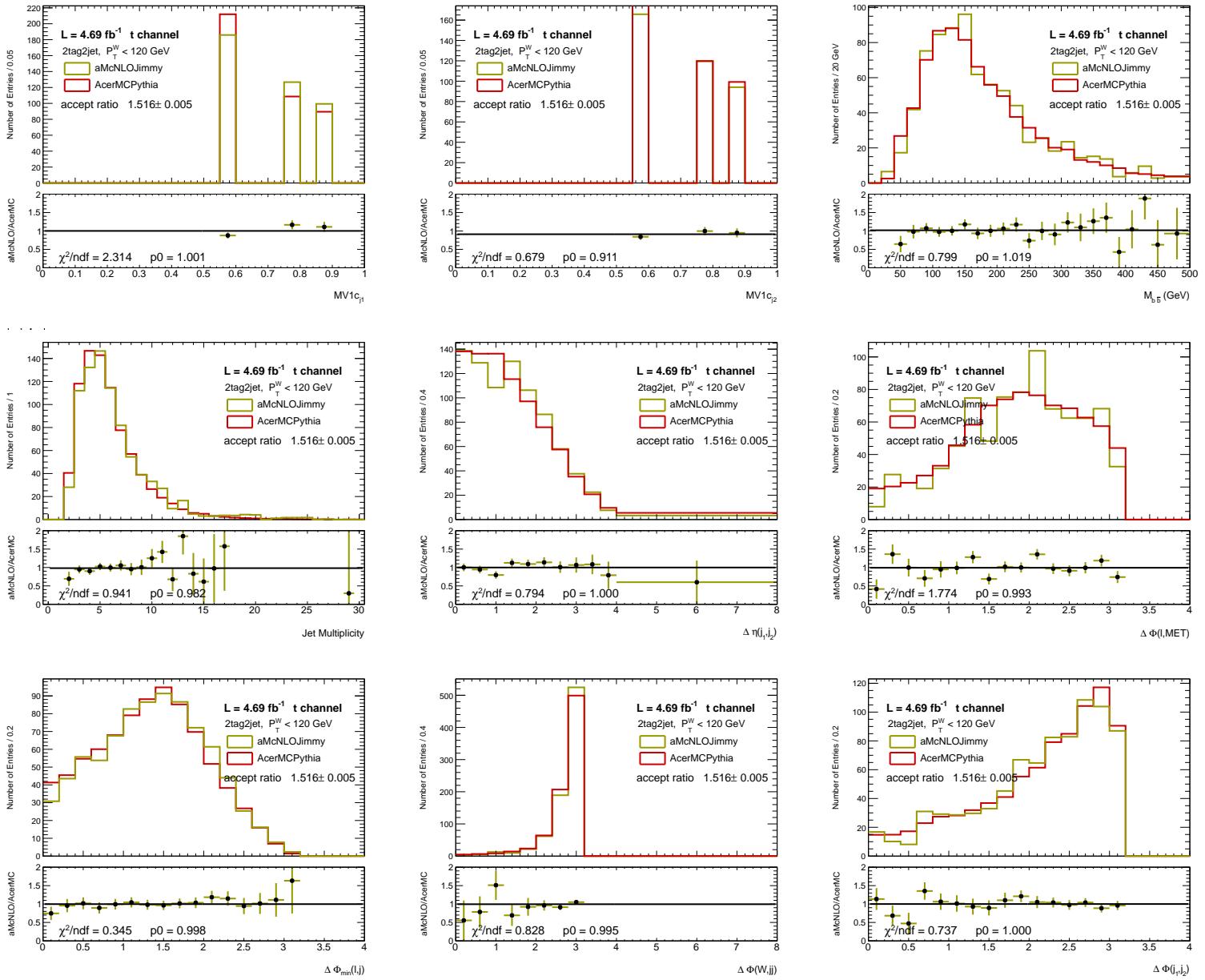


Figure 179: Distributions of t-channel single top variables used in 1-lepton events for $p_T^W < 120 \text{ GeV}$ with 2 b-tag and 2 jets. From left to right: Row 1 - Pseudo-continuous MV1c distributions for leading then sub-leading jet and the m_{bb} of the same two jets. Row 2 - Number of jets, $\Delta\eta_{jj}$, $|\Delta\phi(\ell, E_T^{\text{miss}})|$; Row 3 - $\min|\Delta\phi(\ell, \text{jet})|$, $\Delta\phi(V, H)$, $\Delta\phi_{jj}$.

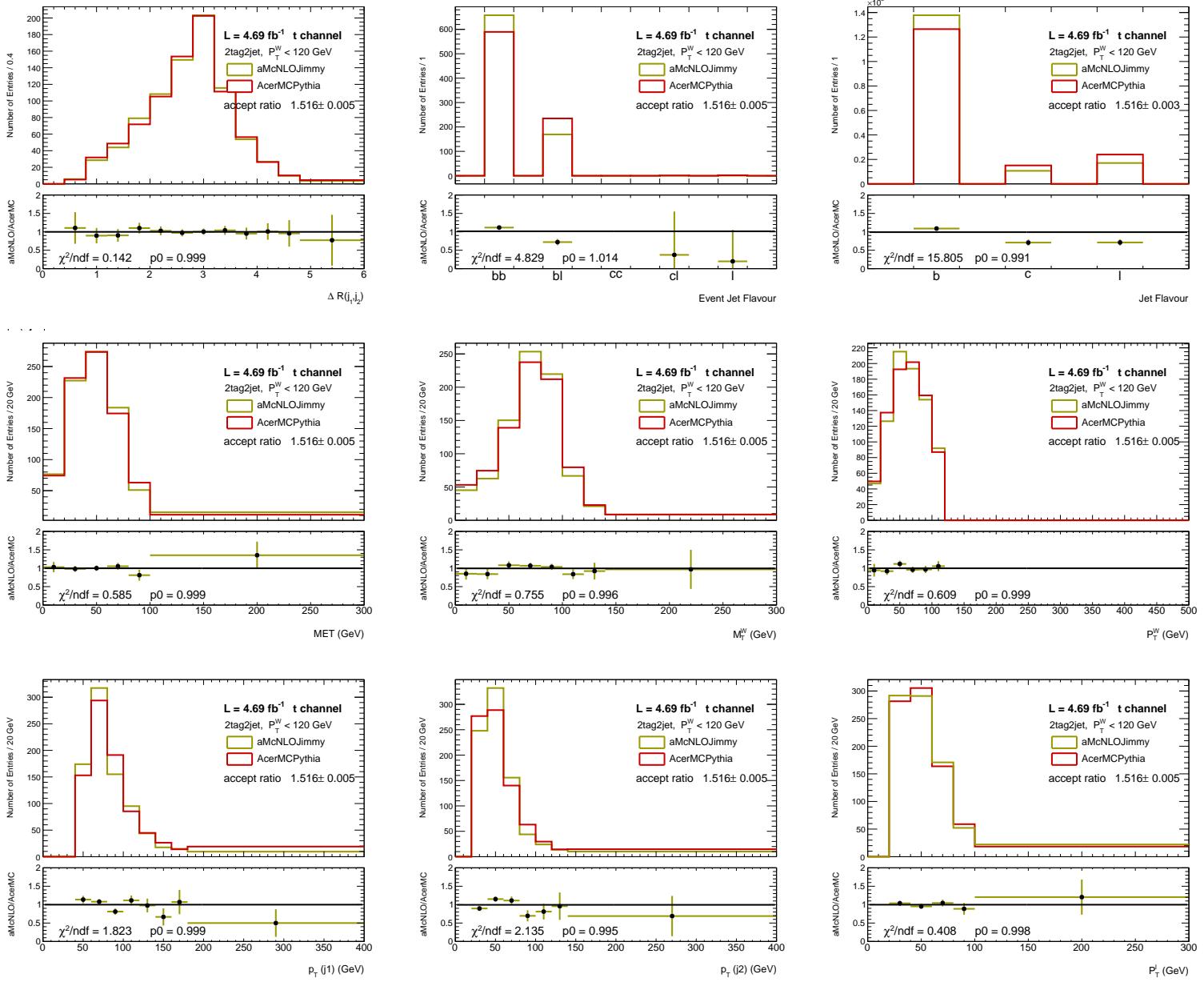


Figure 180: Distributions of t-channel single top variables used in 1-lepton events for $p_T^W < 120 \text{ GeV}$ with 2 b-tag and 2 jets. From left to right: Row 1 - ΔR , Event flavour and jet flavour (using the truth information of the two leading jets in p_T). Row 2 - $E_{\text{T}}^{\text{miss}}$, m_T^W and P_T^W . Row 3 - Leading then sub-leading jet p_T and lepton p_T .

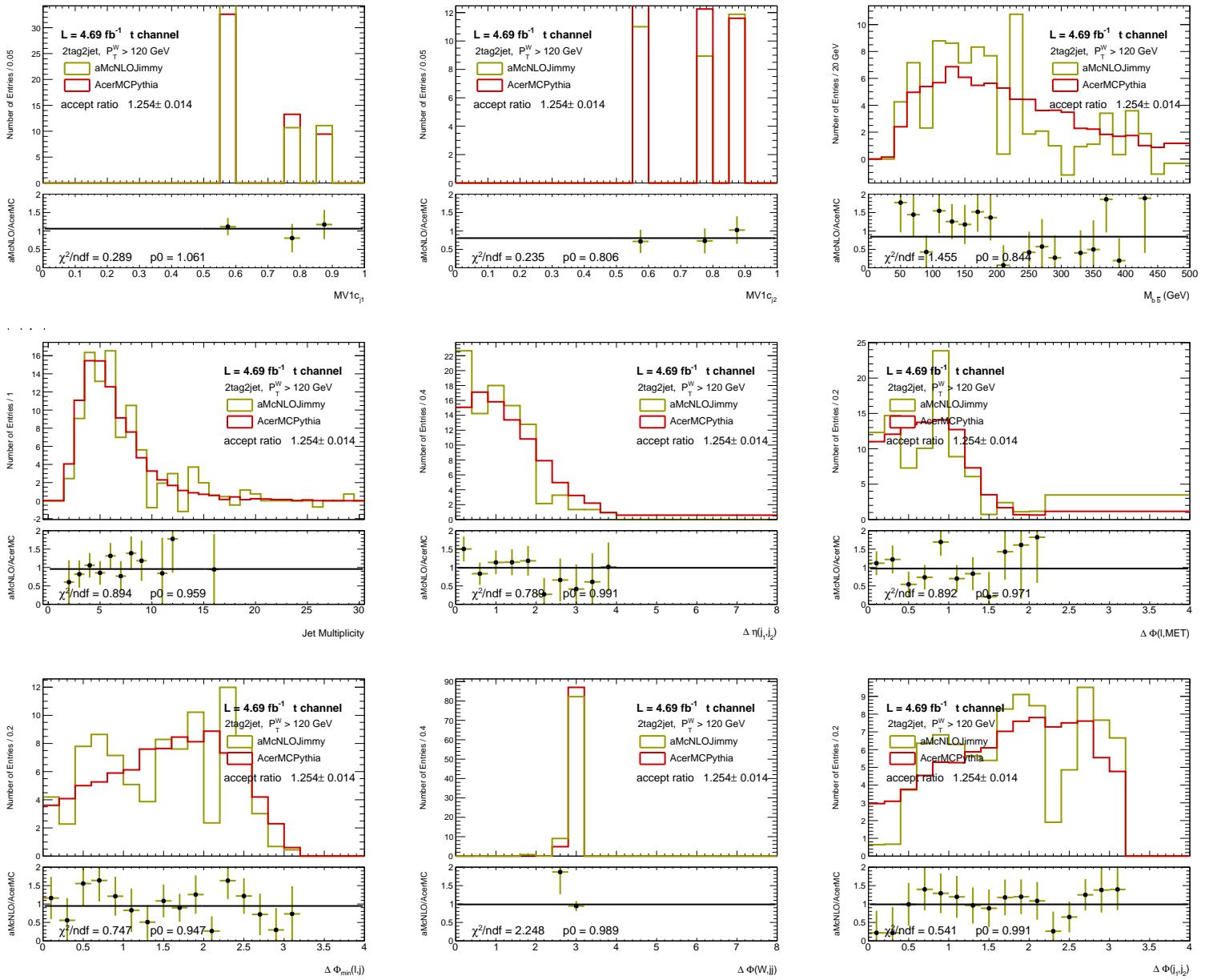


Figure 181: Distributions of t-channel single top variables used in 1-lepton events for $P_T^W > 120$ GeV with 2 b-tag and 2 jets. From left to right: Row 1 - Pseudo-continuous MV1c distributions for leading then sub-leading jet and the m_{bb} of the same two jets. Row 2 - Number of jets, $\Delta\eta_{jj}$, $|\Delta\phi(\ell, E_T^{\text{miss}})|$; Row 3 - $\min|\Delta\phi(\ell, \text{jet})|$, $\Delta\phi(V, H)$, $\Delta\phi_{jj}$.

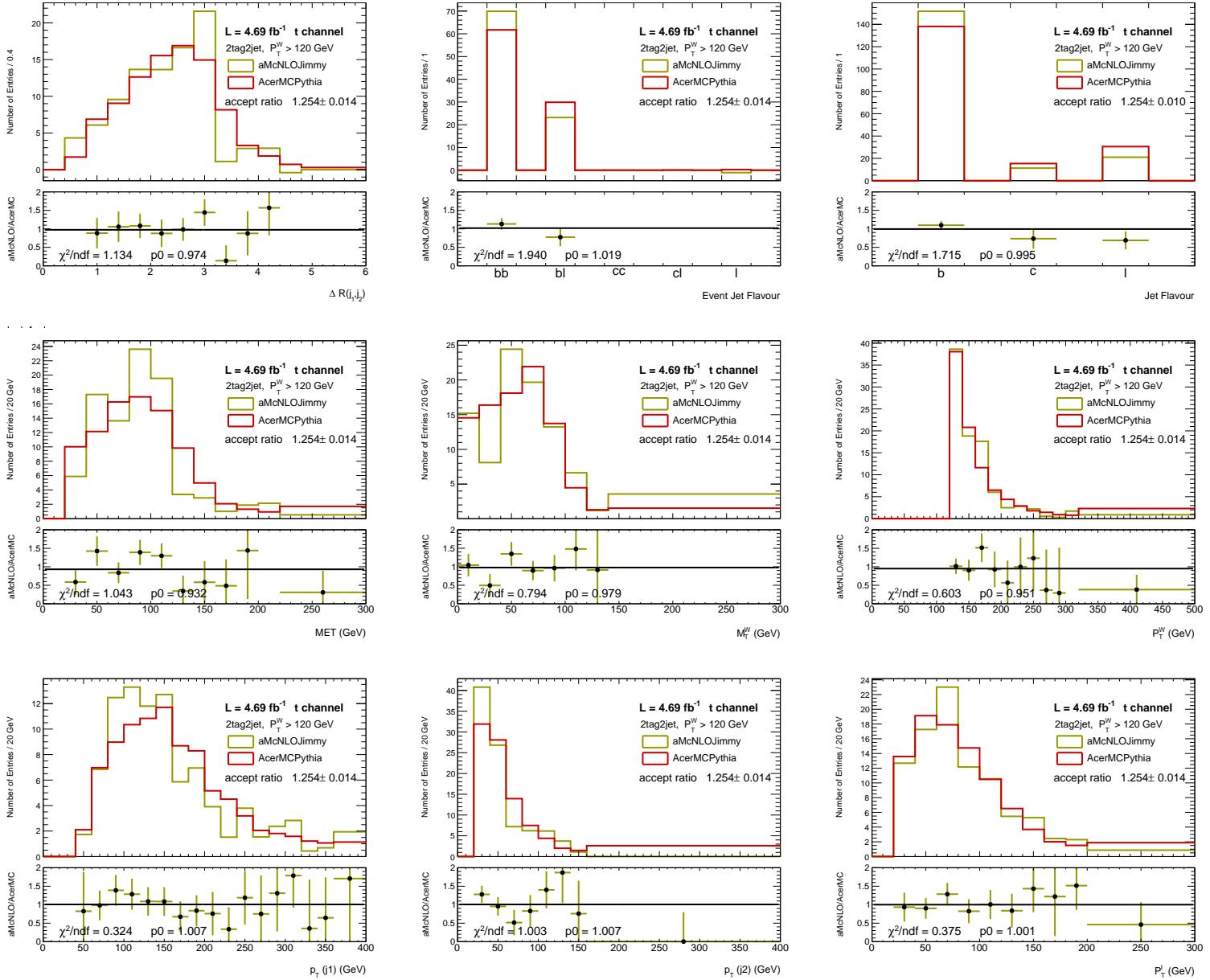


Figure 182: Distributions of t-channel single top variables used in 1-lepton events for $p_T^W > 120$ GeV with 2 b-tag and 2 jets. From left to right: Row 1 - ΔR , Event flavour and jet flavour (using the truth information of the two leading jets in p_T). Row 2 - E_T^{miss} , m_T^W and p_T^W . Row 3 - Leading then sub-leading jet p_T and lepton p_T .

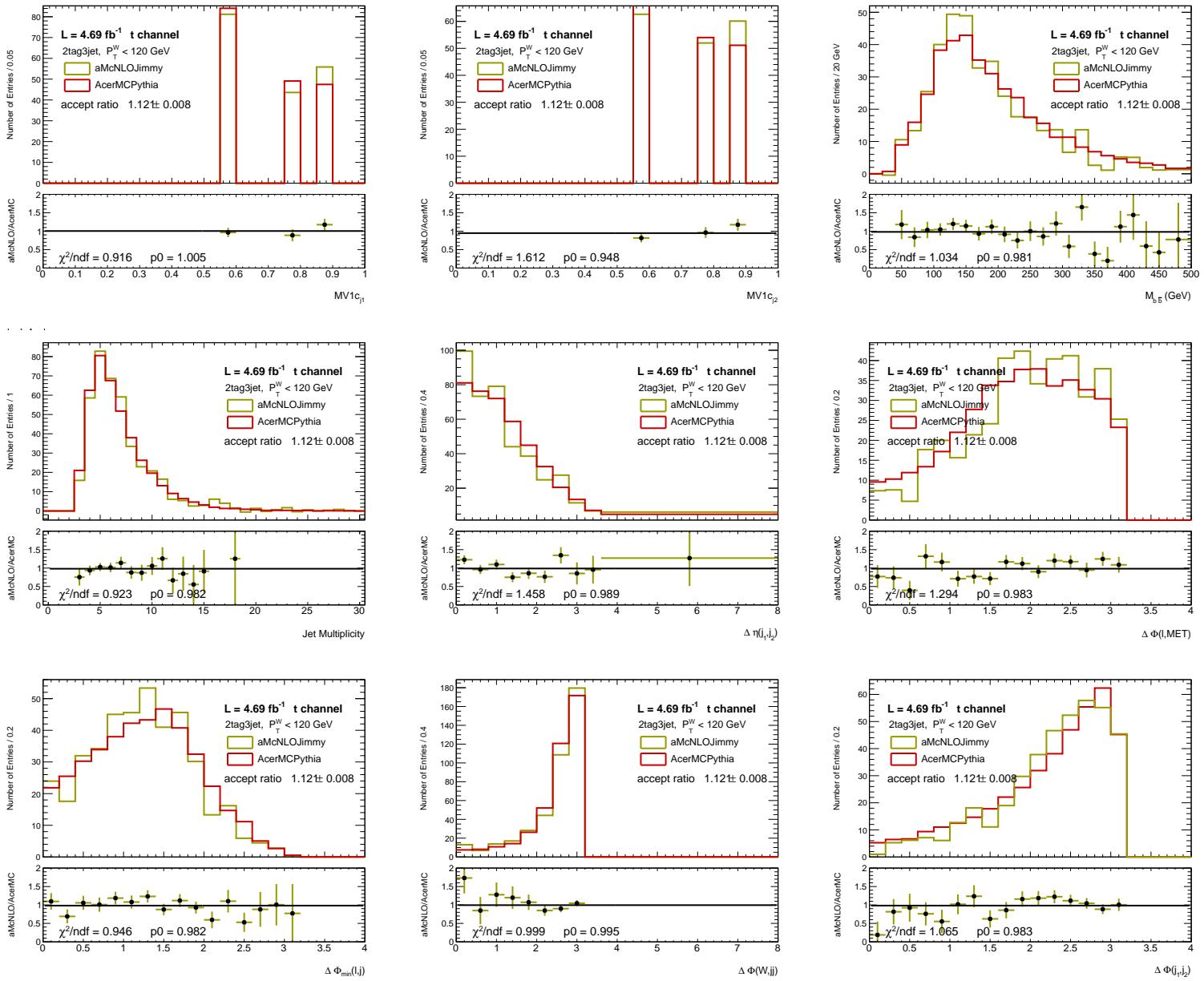


Figure 183: Distributions of t-channel single top variables used in 1-lepton events for $p_T^W < 120$ GeV with 2 b-tag and 3 jets. From left to right: Row 1 - Pseudo-continuous MV1c distributions for leading then sub-leading jet and the m_{bb} of the same two jets. Row 2 - Number of jets, $\Delta\eta_{jj}$, $|\Delta\phi(\ell, E_T^{\text{miss}})|$; Row 3 - $\min|\Delta\phi(\ell, \text{jet})|$, $\Delta\phi(V, H)$, $\Delta\phi_{jj}$.

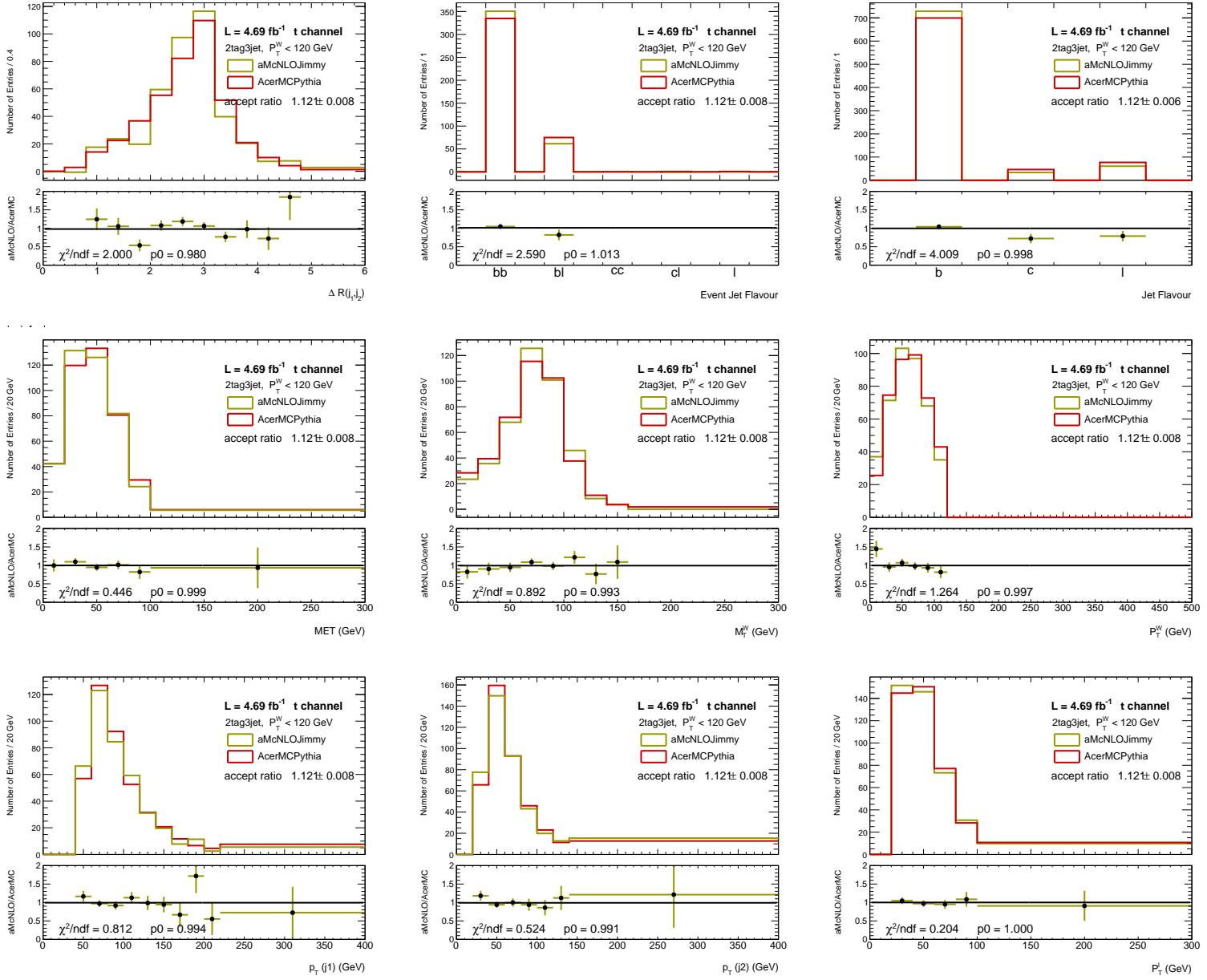


Figure 184: Distributions of t-channel single top variables used in 1-lepton events for $p_T^W < 120 \text{ GeV}$ with 2 b-tag and 3 jets. From left to right: Row 1 - ΔR , Event flavour and jet flavour (using the truth information of the two leading jets in p_T). Row 2 - E_T^{miss} , m_T^W and p_T^W . Row 3 - Leading then sub-leading jet p_T and lepton p_T .

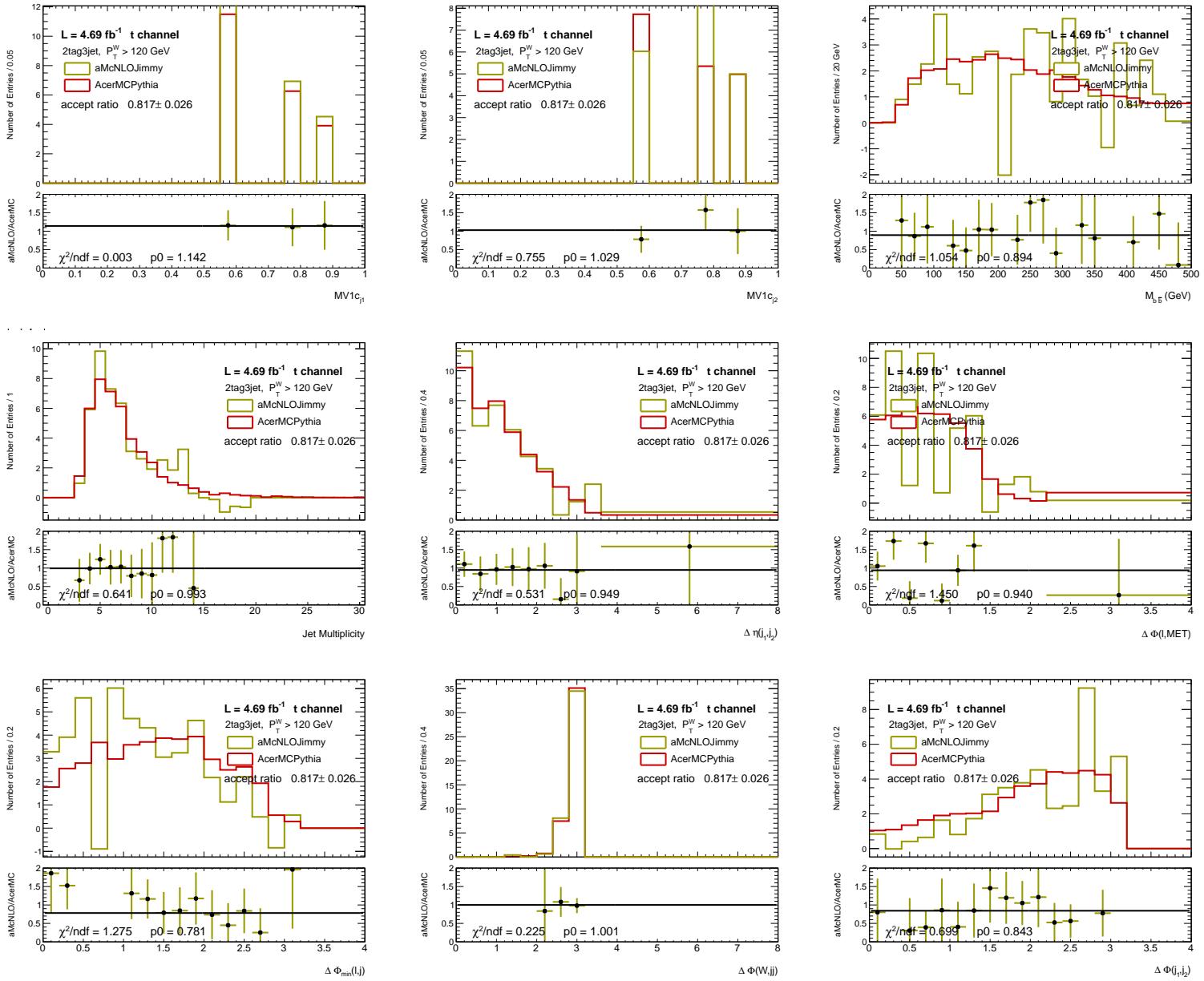


Figure 185: Distributions of t-channel single top variables used in 1-lepton events for $p_T^W > 120$ GeV with 2 b-tag and 3 jets. From left to right: Row 1 - Pseudo-continuous MV1c distributions for leading then sub-leading jet and the m_{bb} of the same two jets. Row 2 - Number of jets, $\Delta\eta_{jj}$, $|\Delta\phi(\ell, E_T^{\text{miss}})|$; Row 3 - $\min|\Delta\phi(\ell, \text{jet})|$, $\Delta\phi(V, H)$, $\Delta\phi_{jj}$.

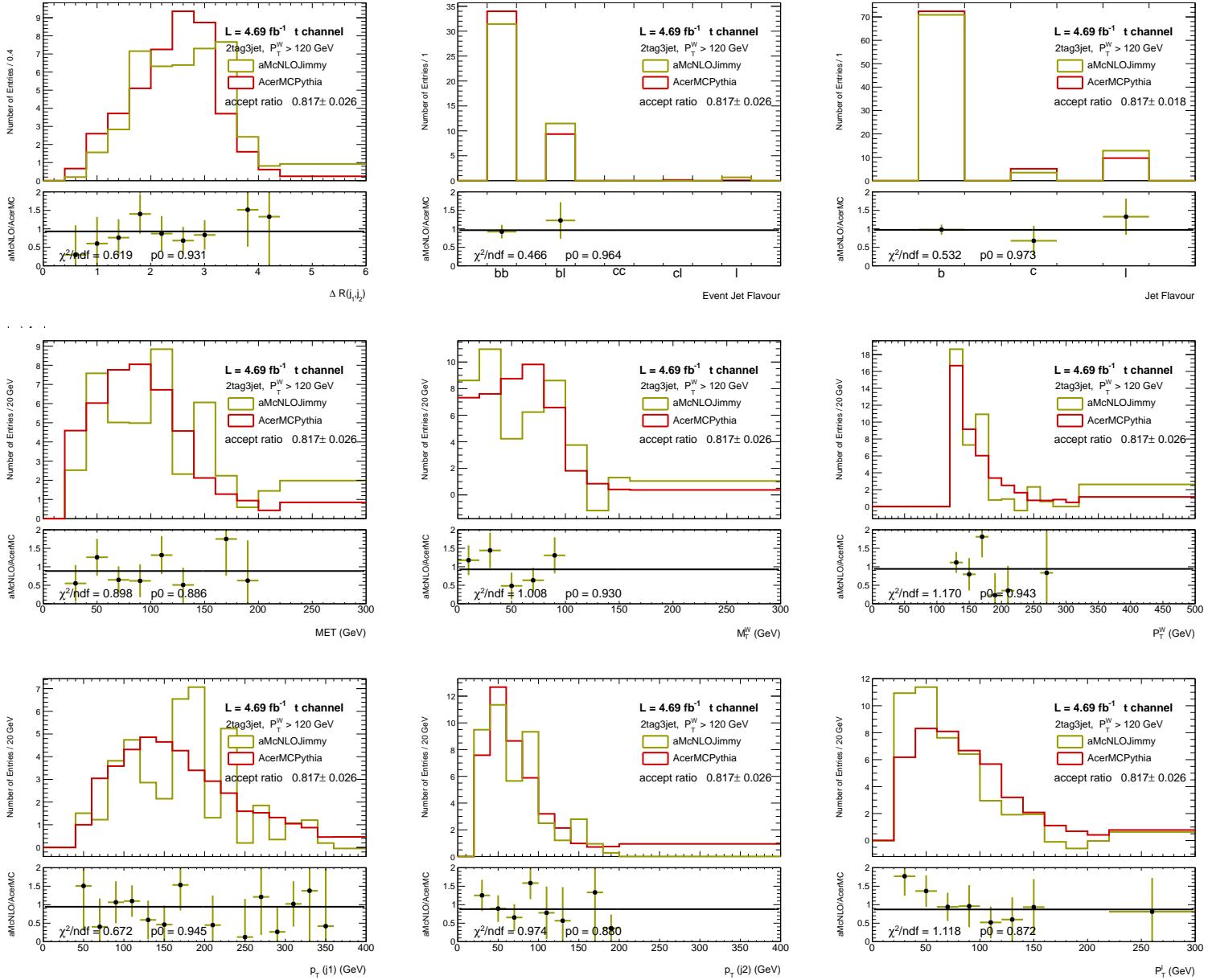


Figure 186: Distributions of t-channel single top variables used in 1-lepton events for $p_T^W > 120 \text{ GeV}$ with 2 b-tag and 3 jets. From left to right: Row 1 - ΔR , Event flavour and jet flavour (using the truth information of the two leading jets in p_T). Row 2 - E_T^{miss} , m_T^W and p_T^W . Row 3 - Leading then sub-leading jet p_T and lepton p_T .

4078 **M.2 s-channel**

4079 For the single top s-channel, the baseline sample AcerMCPythia was compared to the McNLOJimmy
 4080 and PowhegPythia samples. Systematic uncertainties in normalization were extracted from the yield
 4081 difference observed between the baseline sample and the PowhegPythia sample. These systematics were
 4082 found to be 13 and 22% for 2 b-tag 2 jet events at low and high p_T^V , respectively and 28 and 30% for 2 b-
 4083 tag 3 jet events. The baseline yield differences to the McNLOJimmy sample was negligible with respect
 4084 to the later ones. Furthermore, the parton shower effect, obtained by comparing the AcerMCPythia more
 4085 PS and less PS dedicated samples, contributes with a normalization systematic uncertainty of 6 and 8%
 4086 for 2 b-tag 2 jet events at low and high p_T^V , respectively and 4 and 4% for 2 b-tag 3 jet events.

4087 Figure 187 shows the distributions for the s-channel single top variables in 1-lepton events for
 4088 $p_T^W < 120$ GeV with 2 b-tag and 2 jets.

4089 Figure 188 shows the distributions for the s-channel single top variables in 1-lepton events for $p_T^W >$
 4090 120 GeV with 2 b-tag and 2 jets.

4091 Figure 189 shows the distributions for the s-channel single top variables in 1-lepton events for $p_T^W <$
 4092 120 GeV with 2 b-tag and 3 jets.

4093 Figure 190 shows the distributions for the s-channel single top variables in 1-lepton events for $p_T^W >$
 4094 120 GeV with 2 b-tag and 3 jets.

4095

4096 The McNLOJimmy and PowhegPythia samples modelling for m_{bb} , p_T^V and leading and second-leading
 4097 jets p_T is similar to the baseline sample for the selected events. The rare exceptions where mismodelling
 4098 is observed have statistical uncertainty coverage. For the single top s-channel, no shape systematic un-
 4099 certainty was considered.

Not reviewed, for internal circulation only

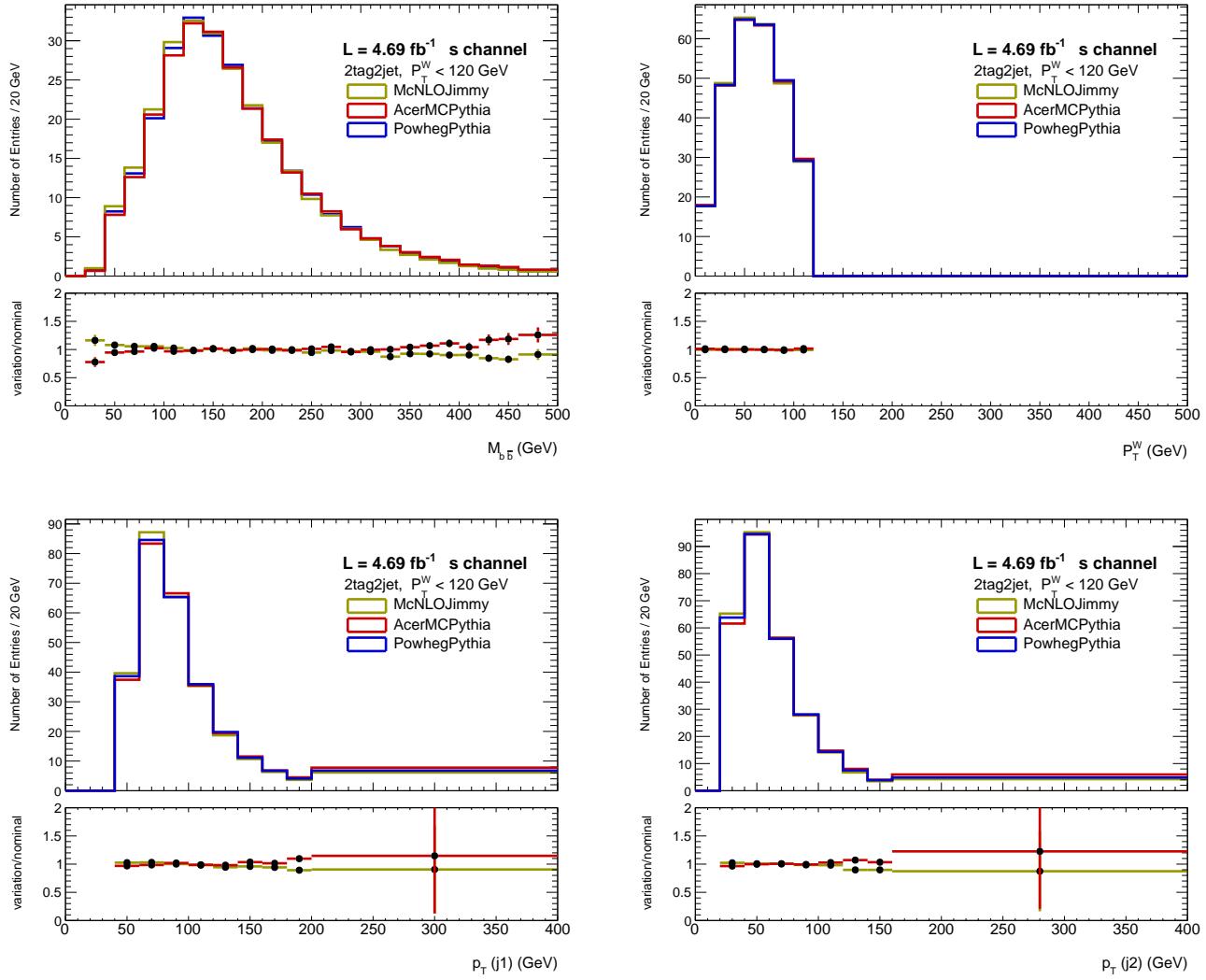


Figure 187: Distributions of s-channel single top variables used in 1-lepton events for $p_T^W < 120$ GeV with 2 b -tag and 2 jets. From left to right: Row 1 - m_{bb} and p_T^W . Row 2 - leading then sub-leading jet p_T .

Not reviewed, for internal circulation only

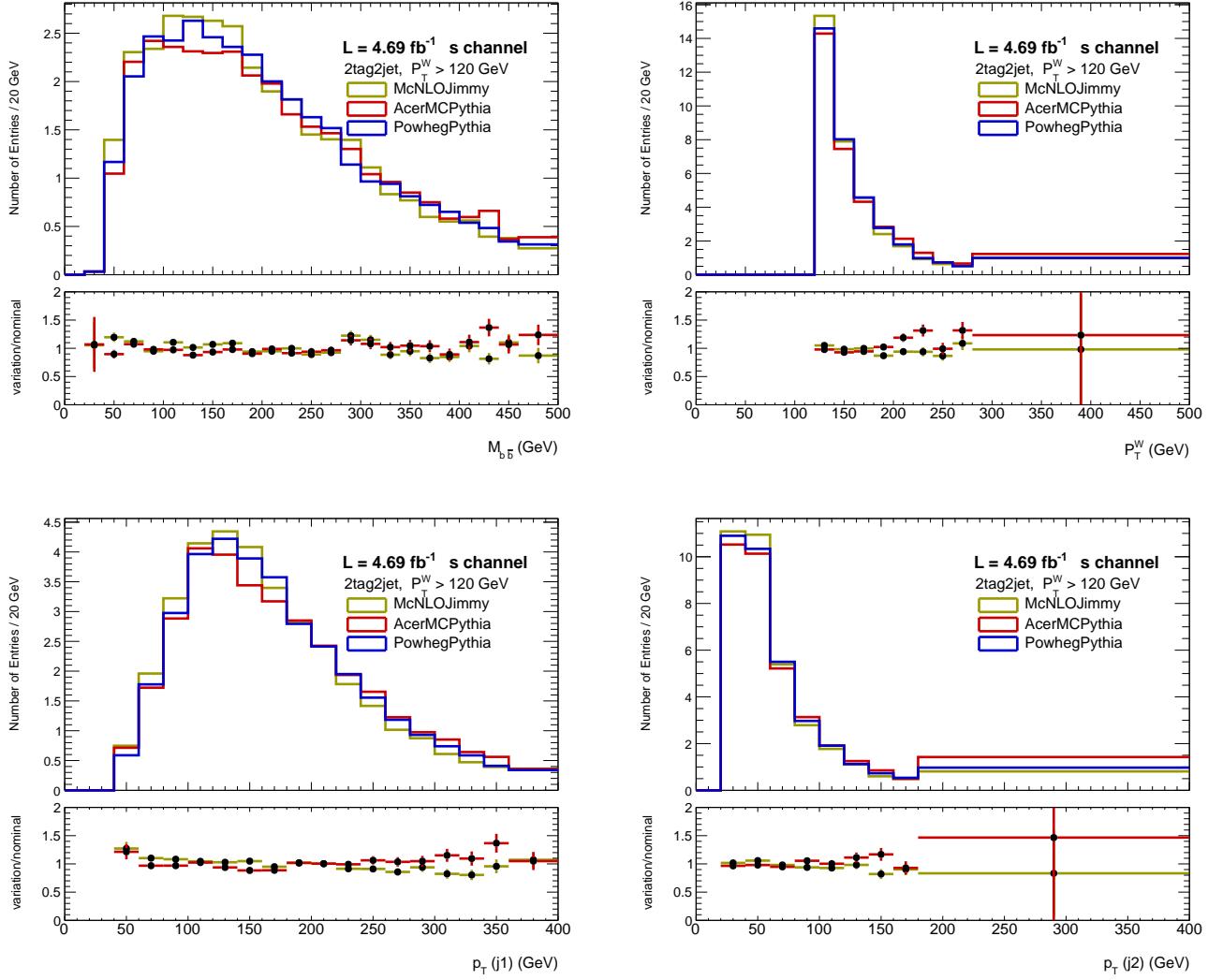


Figure 188: Distributions of s-channel single top variables used in 1-lepton events for $p_T^W > 120 \text{ GeV}$ with 2 b -tag and 2 jets. From left to right: Row 1 - m_{bb} and p_T^W . Row 2 - leading then sub-leading jet p_T .

Not reviewed, for internal circulation only

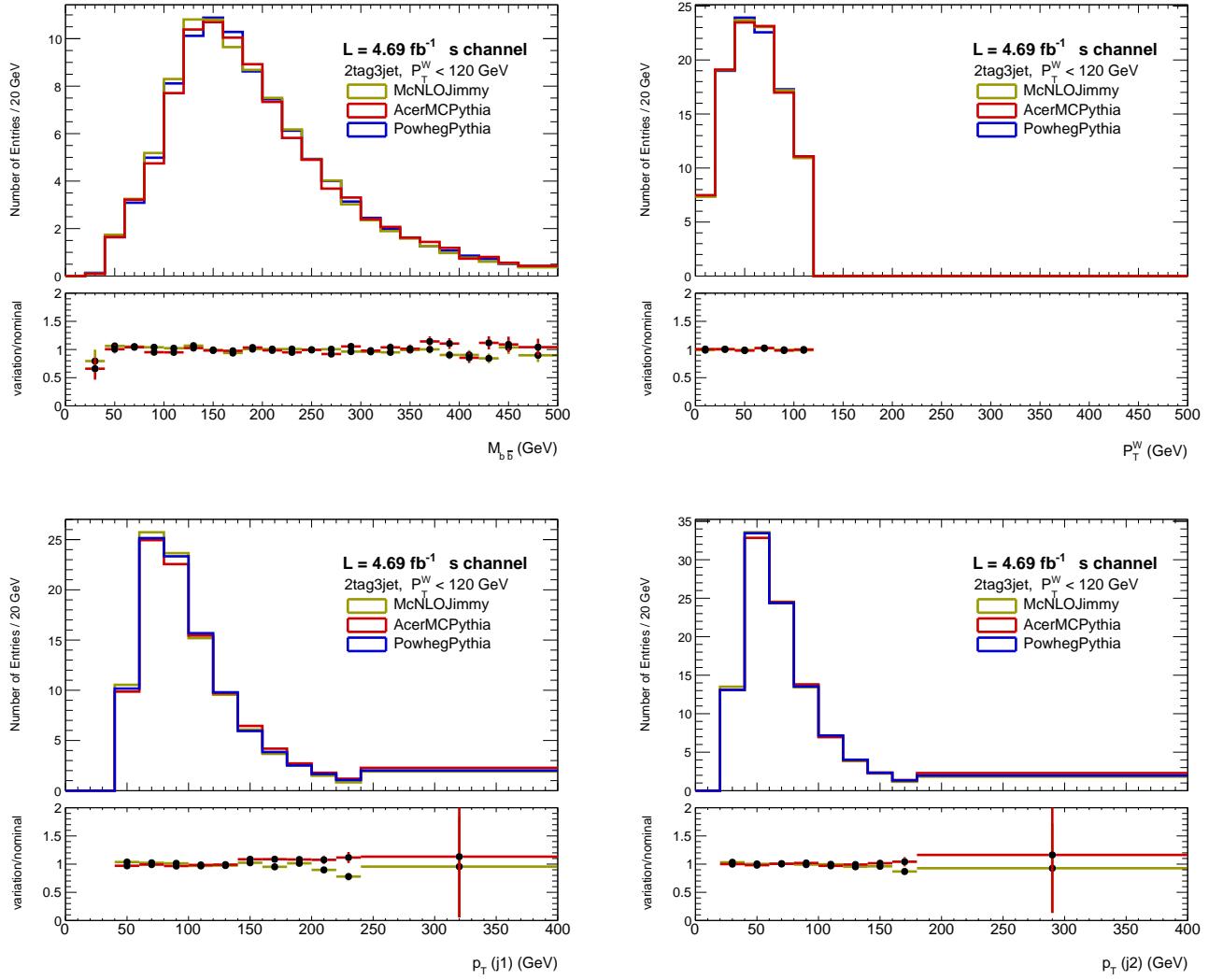


Figure 189: Distributions of s-channel single top variables used in 1-lepton events for $p_T^W < 120$ GeV with 2 b -tag and 3 jets. From left to right: Row 1 - m_{bb} and p_T^W . Row 2 - leading then sub-leading jet p_T .

Not reviewed, for internal circulation only

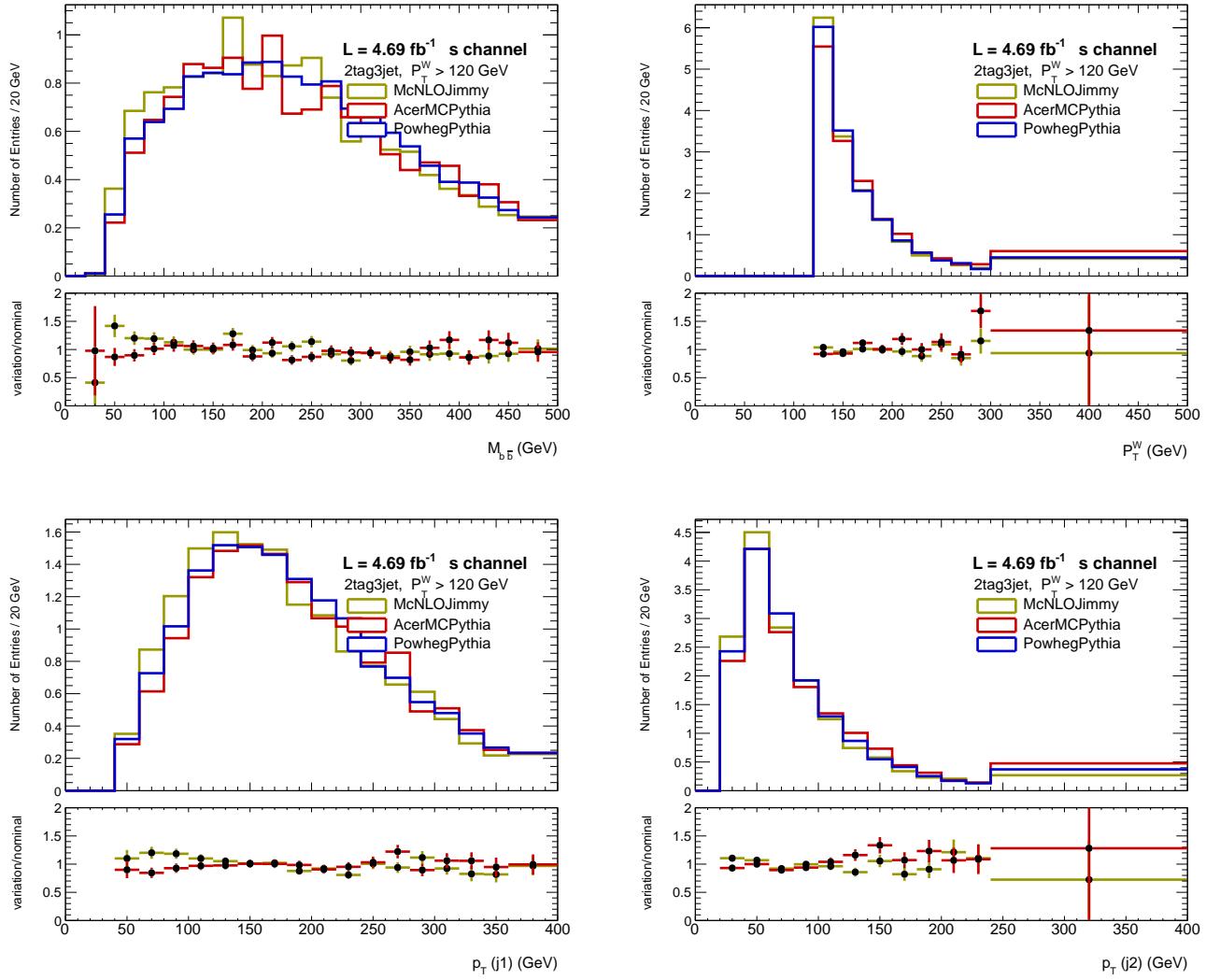


Figure 190: Distributions of s-channel single top variables used in 1-lepton events for $p_T^W > 120 \text{ GeV}$ with 2 b -tag and 3 jets. From left to right: Row 1 - m_{bb} and p_T^W . Row 2 - leading then sub-leading jet p_T .

Not reviewed, for internal circulation only

4100 M.3 Wt

4101 For the single top Wt-channel, the baseline sample AcerMCPythia was compared to several alternative
 4102 samples -AcerMCPythia, McNLOJimmy and PowhegHerwig. The overlap between some of the single
 4103 top Wt-channel production diagrams with $t\bar{t}$ events can be extracted in simulation either by diagram
 4104 removal (DR) or diagram subtraction (DS). This ambiguity was exploited by comparing the DR base-
 4105 line sample with the PowhegPythiaDS sample. Systematic uncertainties in normalization were extracted
 4106 from the yield difference observed between the baseline sample and the AcerMCPythia sample. These
 4107 systematics were found to be 1 and -2% for 2 b-tag 2 jet events at low and high p_T^V , respectively and 4
 4108 and -15% for 2 b-tag 3 jet events. Furthermore, the comparison to PowhegHerwig, contributes with a
 4109 normalization systematic uncertainty of 5 and 3% for 2 b-tag 2 jet events at low and high p_T^V , respec-
 4110 tively and 5 and -3% for 2 b-tag 3 jet events. The baseline yield differences to the McNLOJimmy and
 4111 PowhegPythiaDS samples were negligible with respect to the later ones.

4112 Figure 191 shows the distributions for the Wt-channel single top variables in 1-lepton events for
 4113 $p_T^W < 120$ GeV with 2 b-tag and 2 jets.

4114 Figure 192 shows the distributions for the Wt-channel single top variables in 1-lepton events for $p_T^W >$
 4115 120 GeV with 2 b-tag and 2 jets.

4116 Figure 193 shows the distributions for the Wt-channel single top variables in 1-lepton events for $p_T^W <$
 4117 120 GeV with 2 b-tag and 3 jets.

4118 Figure 194 shows the distributions for the Wt-channel single top variables in 1-lepton events for $p_T^W >$
 4119 120 GeV with 2 b-tag and 3 jets.

4120

4121 At 2 b-tags 2 jets low p_T^V a mismodelling is observed for the leading and second-leading jets p_T distributions.
 4122 A shape uncertainty on the leading jet p_T was extracted from the comparison between the baseline and
 4123 PowhegHerwig samples where the mismodelling is more prominent, covering the difference observed to
 4124 the other alternative samples.

4125 The same applies for m_{bb} at the 2 b-tags 2 jets high p_T^V , where a shape uncertainty was obtained
 4126 from the comparison between the baseline sample and the AcerMCPythia sample. For the 2 b-tags 3
 4127 jets low p_T^V events, a shape uncertainty on the leading jet p_T was extracted from the comparison between
 4128 the baseline sample and the AcerMCPythia sample while for the high p_T^V events the shape uncertainty
 4129 comes from the m_{bb} distribution. It was observed that this systematics could also cover the mismodelling
 4130 observed in the remaining alternative samples. For the high p_T^V region, the shape uncertainty on m_{bb} is
 4131 expected to vanish the mismodelling observed at the jets p_T , since these variables are highly correlated.
 4132 All the systematic shape uncertainties mentioned were obtained through a linear fit of the alternative to
 4133 baseline sample ratio.

Not reviewed, for internal circulation only

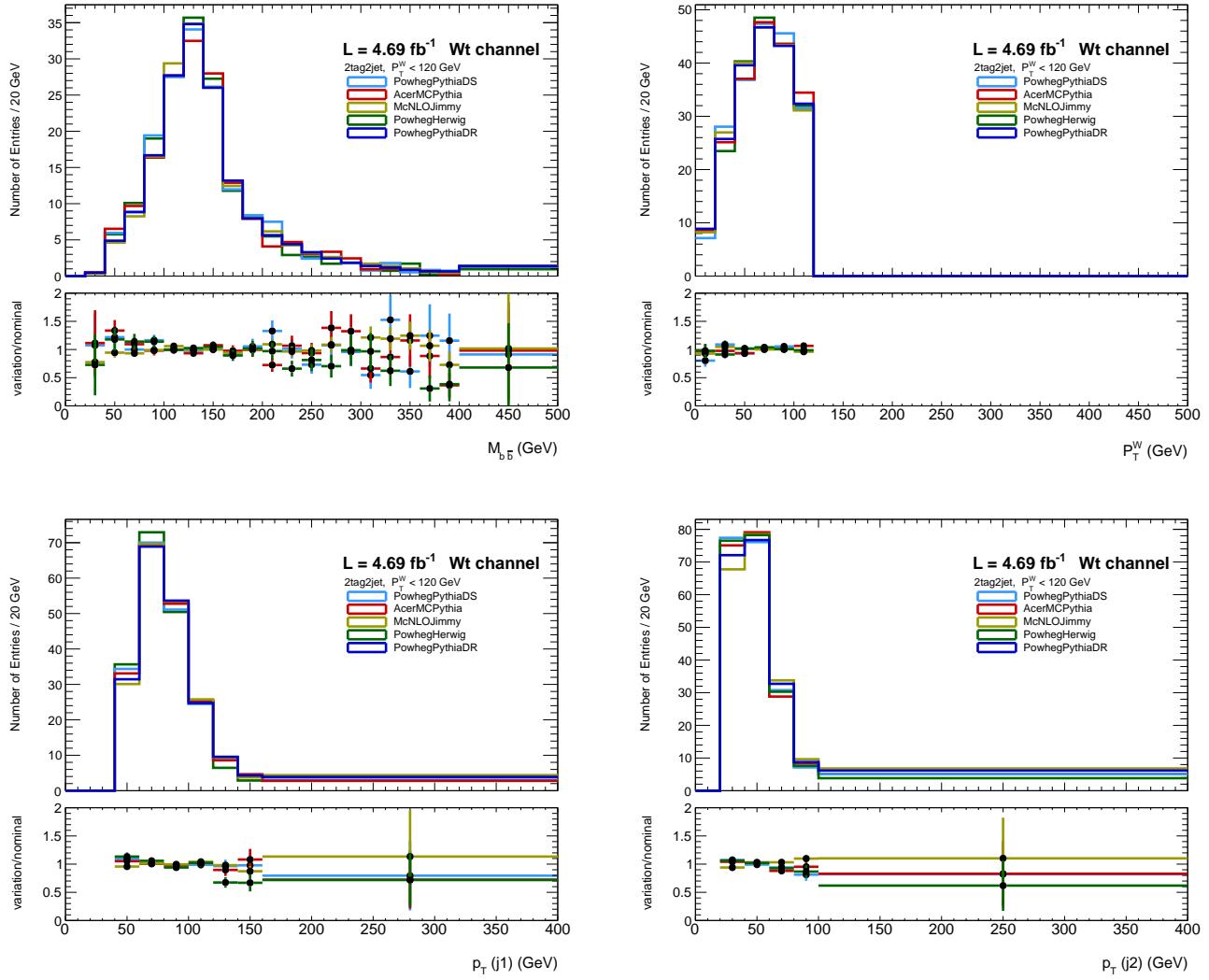


Figure 191: Distributions of Wt-channel single top variables used in 1-lepton events for $p_T^W < 120$ GeV with 2 b-tag and 2 jets. From left to right: Row 1 - m_{bb} and p_T^W . Row 2 - leading then sub-leading jet p_T .

Not reviewed, for internal circulation only

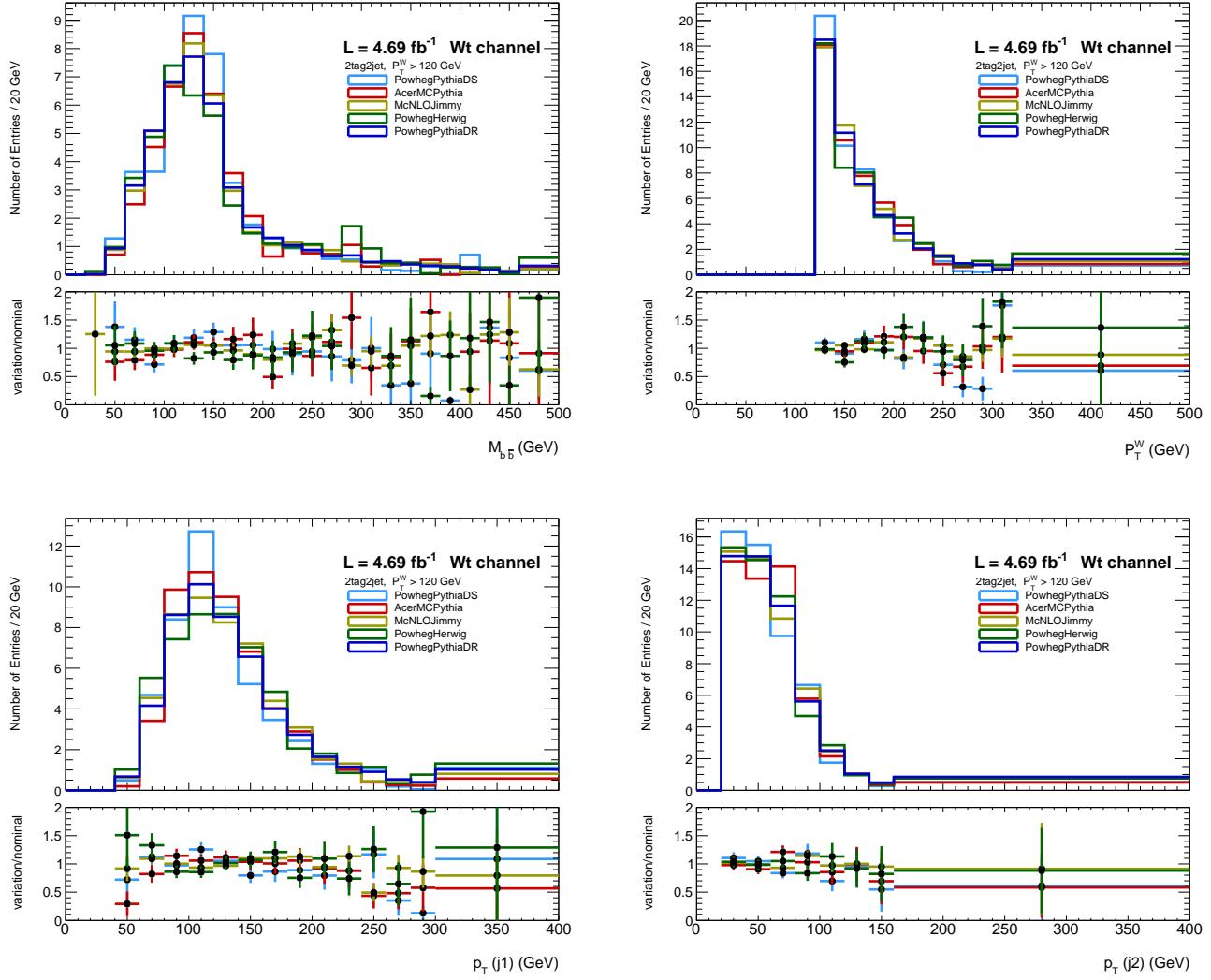


Figure 192: Distributions of Wt-channel single top variables used in 1-lepton events for $p_T^W > 120$ GeV with 2 b-tag and 2 jets. From left to right: Row 1 - m_{bb} and p_T^W . Row 2 - leading then sub-leading jet p_T .

Not reviewed, for internal circulation only

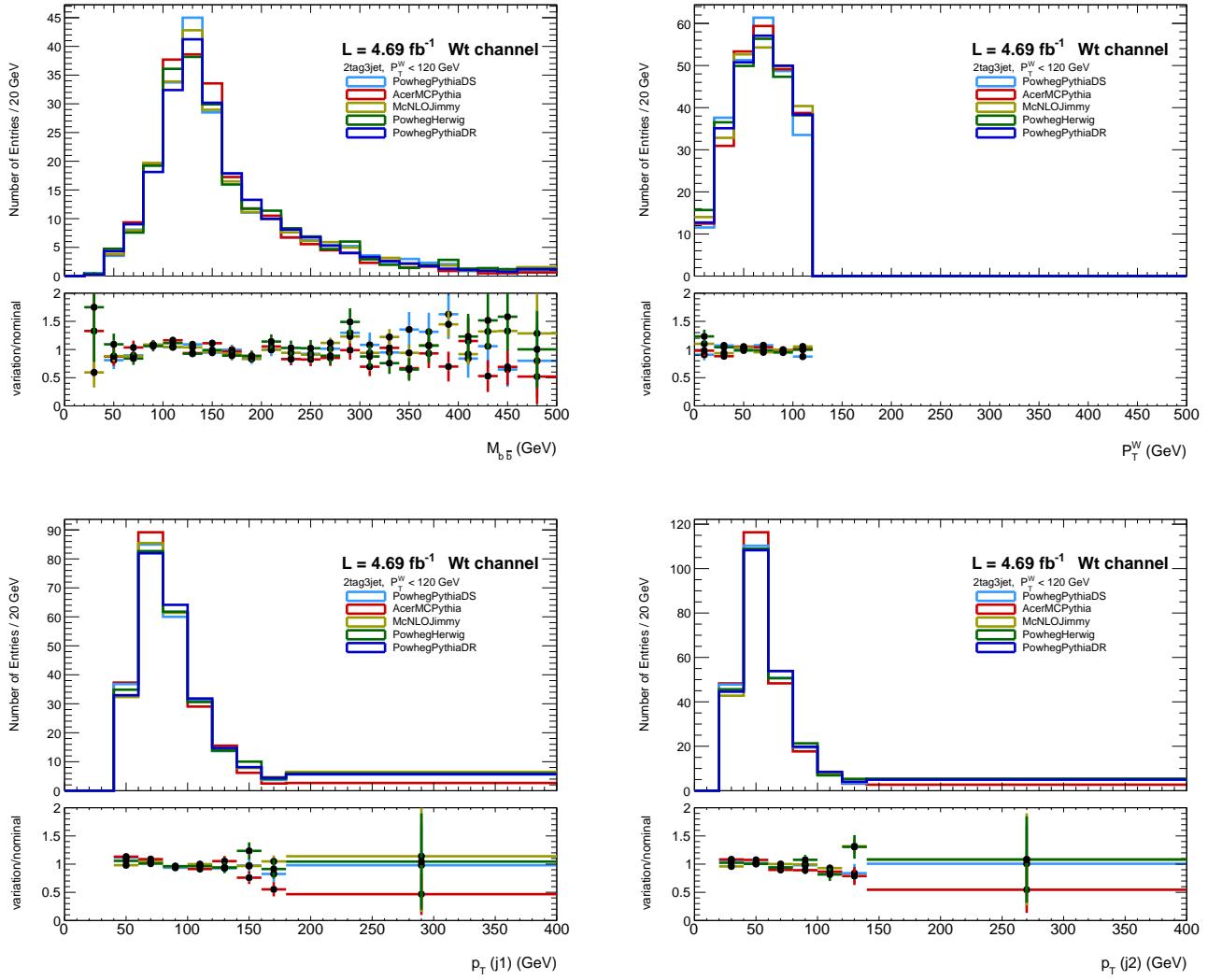


Figure 193: Distributions of Wt-channel single top variables used in 1-lepton events for $p_T^W < 120$ GeV with 2 b -tag and 3 jets. From left to right: Row 1 - m_{bb} and p_T^W . Row 2 - leading then sub-leading jet p_T .

Not reviewed, for internal circulation only

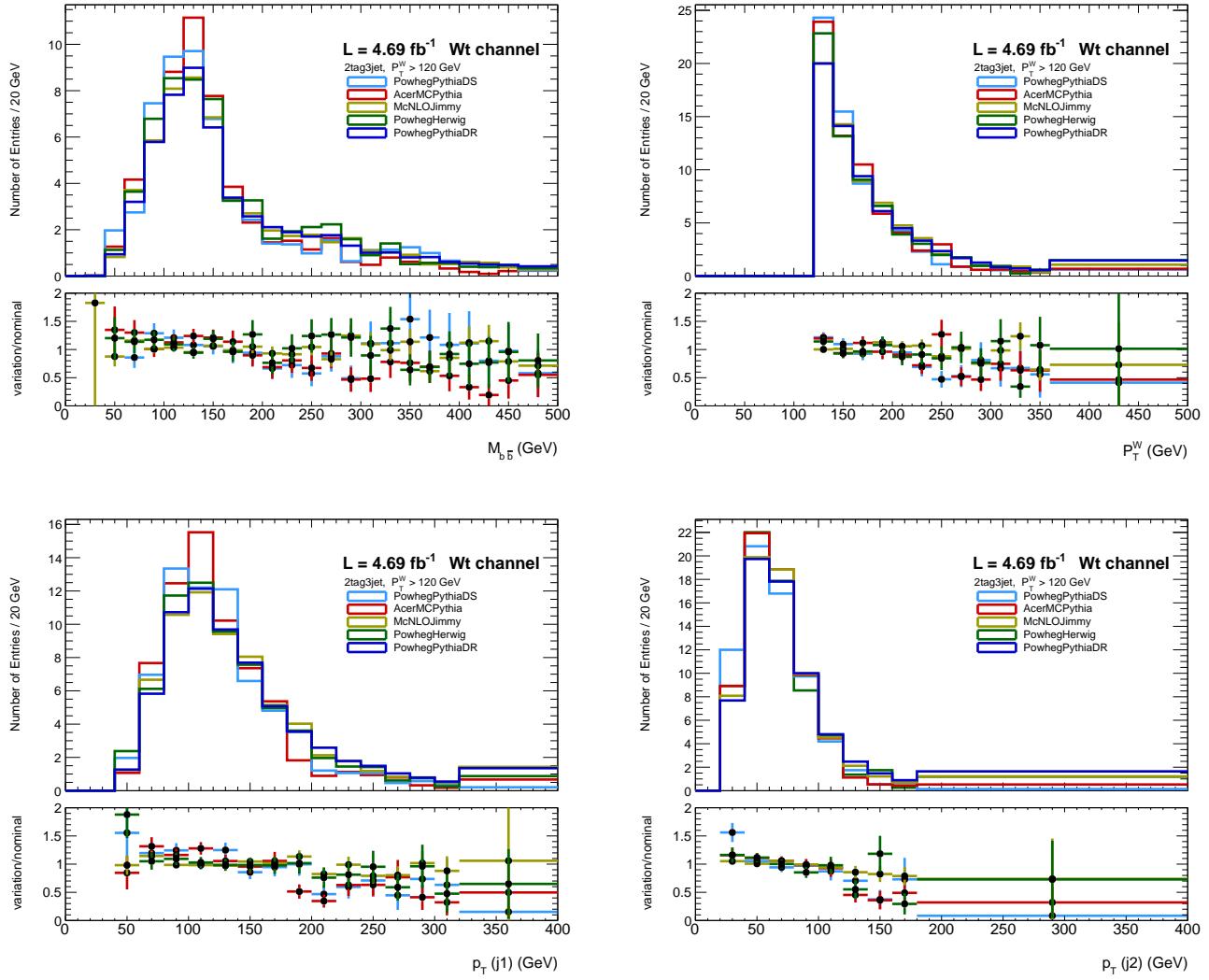


Figure 194: Distributions of Wt-channel single top variables used in 1-lepton events for $p_T^W > 120$ GeV with 2 b -tag and 3 jets. From left to right: Row 1 - m_{bb} and p_T^W . Row 2 - leading then sub-leading jet p_T .

4134 N $t\bar{t}$ modeling

4135 Many generator comparison studies were performed to understand the $t\bar{t}bar$ modeling. The most impor-
 4136 tant differences were used to derive a set of systematics which are given in more detail here. A large
 4137 variety of generators and modifications of those generators are available. The list of generators con-
 4138 sidered is shown in Table 31 and the list of systematics used is described in Section 5.2.1.3 as well as
 4139 summarized in Section 8.3. Comparisons and checks from where systematics were not derived are also
 4140 described in the following along with explanations as to why these were not considered for the analysis.
 4141 In practice, the Top group recommendations for comparisons was followed except in the following cases
 4142 where the comparison was not considered at all:

- 4143 • *Compare samples with varied renormalization and factorization scales.* In this case only EvtGen
 4144 files are available which adds some additional complication and reduces the comparability with the
 4145 other tests which all use files with information on the reconstruction level. For a future analysis it
 4146 would be useful to investigate the influence of the renormalization and factorization scale.
- 4147 • *Compare to Sherpa with massive c/b quarks.* These samples have been shown to not model basic
 4148 kinematic distributions such as lepton p_T and jet multiplicity. In addition these samples do not
 4149 include tau final states and limited statistics are available.
- 4150 • *Compare to $t\bar{t}$ without spin corrections.* This study should lead to no gain from since spin correla-
 4151 tions are included in the Standard Model.
- 4152 • *Compare to $t\bar{t}$ without modified branching ratios.* This study should lead to no gain since the
 4153 assumptions for the modified BRs are unrealistic, e.g. $BR(t \rightarrow b) = 0.5$.
- 4154 • *Compare to $t\bar{t}$ with top mass variations.* This study should lead to no gain since the top mass is
 4155 sufficiently well known.
- 4156 • *Compare FullSim to AFII for baseline PowHeg+Pythia.* FullSim has very limited statistics and
 4157 this difference is already at the object level.

4158 The 1-lepton MVA selection with 2 b-tags was used in the following and the derived systematics are
 4159 applied to all channels in both the dijet mass and MVA analysis unless otherwise noted. The input variables
 4160 to the BDT are compared between the generators. A ratio of the most discrepant variable is taken and used
 4161 to reweight the events. After the reweighting, a ratio of the next most discrepant variables is used for
 4162 another reweighting. This continues until all shape differences on the BDT are covered. Each ratio used
 4163 as a reweighting is then taken as a separate systematics.

4164 N.1 m_{bb} systematic

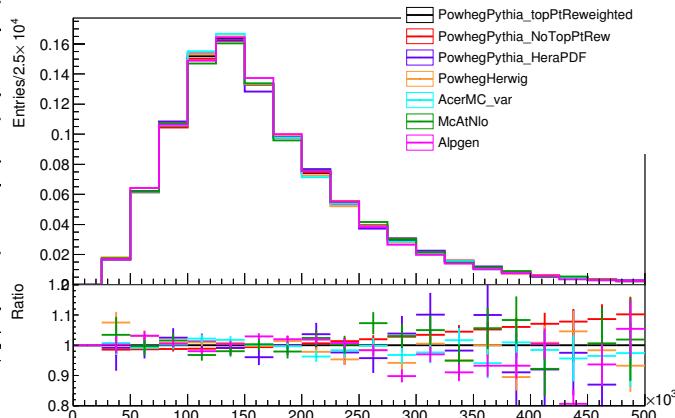
4165 As m_{bb} is the most important variable in both versions of the analysis therefore a careful check is in
 4166 order. For this a comparison was made between all considered generators for the regions which are rele-
 4167 vant to the analysis — those are the region with 2 jets and 3 jets and in both cases exactly two b-tagged
 4168 jets are required. These regions are again separated into a high and low p_T^W region ($p_T^W > 120$ GeV and
 4169 $p_T^W < 120$ GeV respectively). Plots of the comparisons for all regions are shown in Figure 195. From the
 4170 ratios shown at the bottom of each plot, it was concluded that ALPGEN+PYTHIA (magenta) has the largest
 4171 difference to the nominal. Also PowHEG+PYTHIA with the HERAPDF set (violet) shows significant devi-
 4172 ation but those are dominated by statistical fluctuations due to the limited statistics available. Therefore
 4173 ALPGEN+PYTHIA was used to derive a systematics uncertainty. The influence of the top p_T correction,
 4174 which was applied to the nominal sample, was tested on ALPGEN+PYTHIA and shown in Figure 196. De-
 4175 tails on the ALPGEN+PYTHIA top p_T reweighting are given in Appendix Section N.3. Since the top p_T

4176 reweighting has a negligible effect on the m_{bb} shape in the range of $0 < m_{bb} < 200$ GeV for the 2-jet
 4177 events and $0 < m_{bb} < 300$ GeV for the 3-jet events, the systematic uncertainty was derived in this range
 4178 the full difference between ALPGEN+PYTHIA without the top p_T correction to PowHEG+PYTHIA with the
 4179 top p_T correction. This difference for all regions is shown in Figure 197. Linear fits (Table ??) were
 4180 performed in the above mentioned m_{bb} ranges and used as systematic uncertainties.

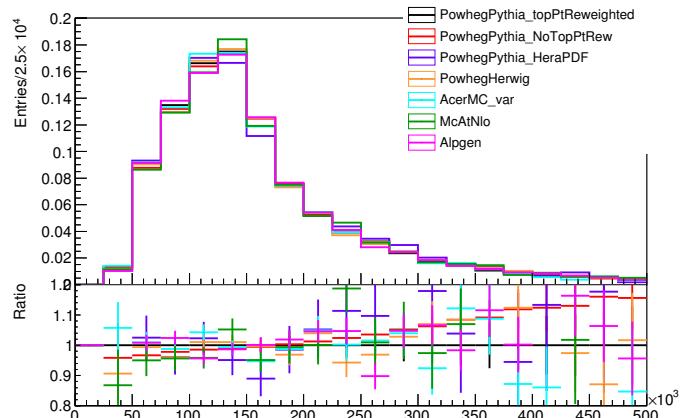
4181 The plots in Figure 197 as well as the fitted functions show that the slopes are opposite for the 2 and
 4182 3-jet region. Therefore a combined systematic uncertainty for the 2 and 3-jet region cannot be derived.
 4183 Furthermore the systematic effect is significantly larger for $p_T^W > 120$ GeV so four different fits are
 4184 needed but the effect is correlated in all four regions in all channels.

ulation only

mBB_SLDcorrected 2tag2jet_lpt_All

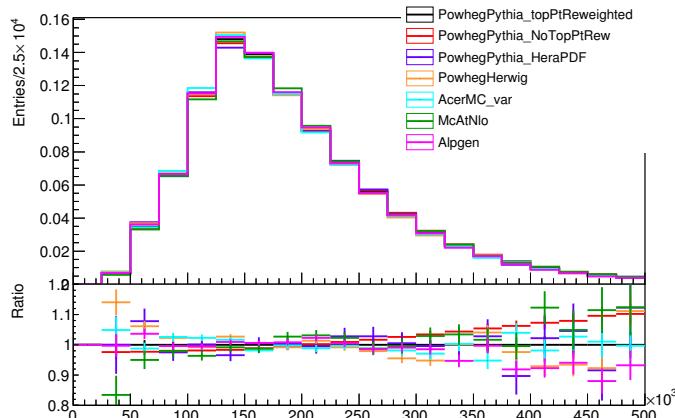


mBB_SLDcorrected 2tag2jet_hpt_All

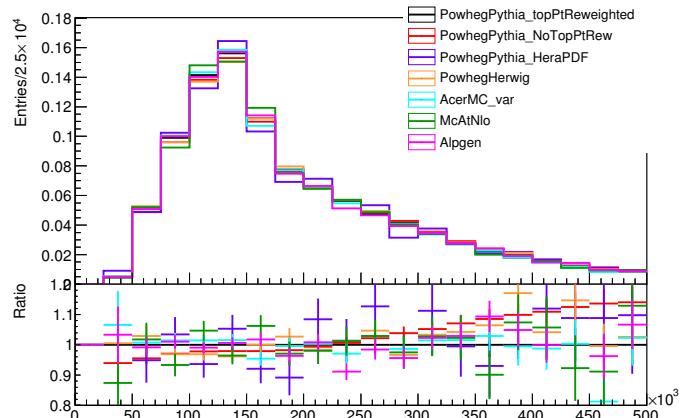


(a) 2-jet

mBB_SLDcorrected 2tag3jet_lpt_All



mBB_SLDcorrected 2tag3jet_hpt_All



(b) 3-jet

Figure 195: 1-lepton 2 and 3-jet 2-tag MC comparisons for the $t\bar{t}$ m_{bb} systematic. The largest difference is between PowHEG+PYTHIA and ALPGEN+PYTHIA and is taken as the systematic uncertainty. $p_T^W < 120$ GeV is shown on the left and $p_T^W > 120$ GeV is shown on the right.

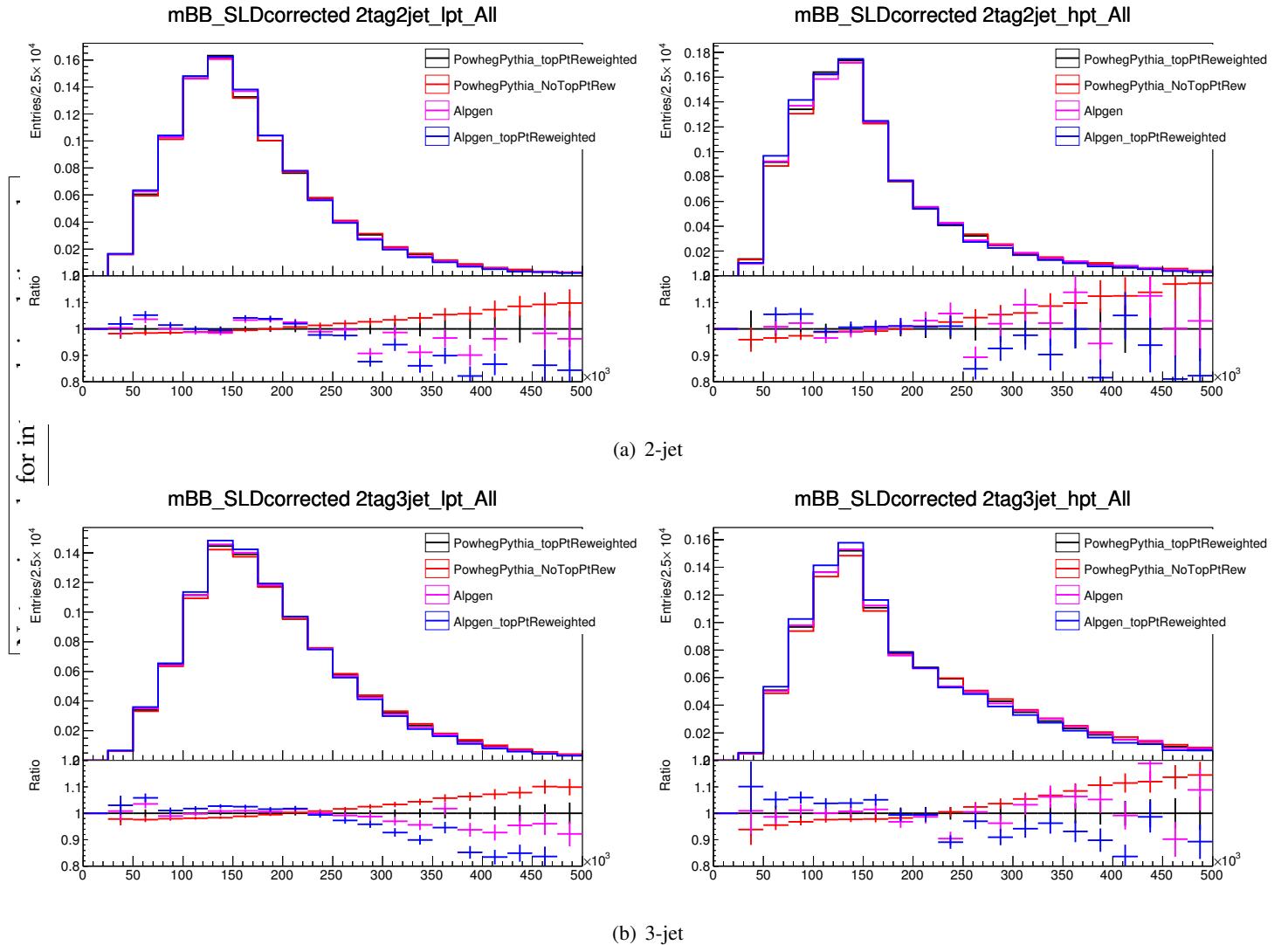


Figure 196: 1-lepton 2 and 3-jet 2-tag MC comparisons for the $t\bar{t} m_{bb}$ systematic. ALPGEN+PYTHIA with and without the p_T^{top} correction is compared to PowHEG+PYTHIA with and without the same correction. $p_T^W < 120$ GeV is shown on the left and $p_T^W > 120$ GeV is shown on the right.

4185 N.2 E_T^{miss} systematic

4186 After taking into account the coverage of the m_{bb} systematic described above, a systematic on the E_T^{miss}
 4187 shape was found to be necessary. Similar to m_{bb} , a comparison was made between all considered gener-
 4188 ators for the relevant analysis regions shown in Figure 198. From the ratio plots shown on the bottom of
 4189 each plot it was concluded that ALPGEN+PYTHIA (magenta) again has the largest difference to the nominal
 4190 and therefore was used to derive a systematics uncertainty. The influence of the top p_T correction, which
 4191 was applied nominally in the analysis to PowHEG+PYTHIA, was tested on ALPGEN+PYTHIA and are shown
 4192 in Figure 199. Since the top p_T reweighting has a small effect on ALPGEN+PYTHIA in the E_T^{miss} distribution
 4193 the full difference between ALPGEN+PYTHIA without the top p_T correction to PowHEG+PYTHIA with the
 4194 correction was used. This difference for all regions is shown in Figure 197 (b) and (c). The (linear) fits
 4195 for the 2 and 3-jet region agree amongst each other within the fitting errors so the regions were com-
 4196 bined. After the combination (Figure 197a) the difference between ALPGEN+PYTHIA and PowHEG+PYTHIA

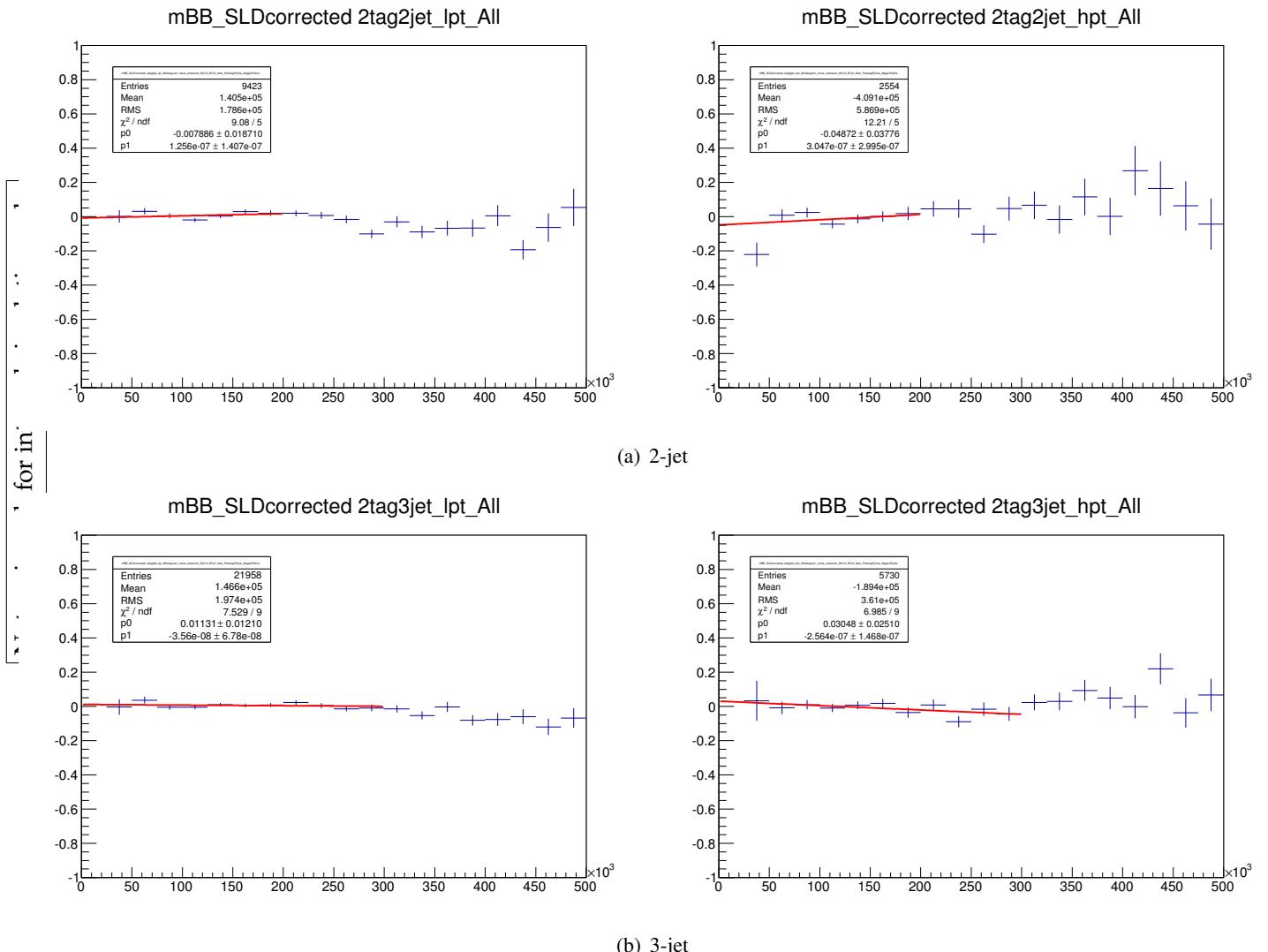


Figure 197: 1-lepton 2 and 3-jet 2-tag m_{bb} systematic for $t\bar{t}$. The fit is made to the ratio of ALPGEN+PYTHIA without the p_T^{top} correction and PowHEG+PYTHIA with the p_T^{top} correction. $p_T^W < 120$ GeV is shown on the left and $p_T^W > 120$ GeV is shown on the right.

4197 follows a second order polynomial which is different for the low and high p_T^W . Therefore the combination
 4198 of the different p_T^W regions was not done. Table ?? contains the exact values of the polynomial fit to
 4199 these points. This systematic is only applied to 1-lepton events since E_T^{miss} itself is very different in each
 4200 analysis. It is correlated in all 1-lepton regions. The functions are only valid up to 300 GeV. Above this
 4201 value they are constant to maintain a reasonable size in the tail of the E_T^{miss} distribution.

4202 N.3 top p_T reweighting of ALPGEN+PYTHIA

4203 As described in Section 5.2.1.2 it was found that the p_T of the top is modeled incorrectly in PowHEG+PYTHIA
 4204 which lead to a correction based on comparisons with the ATLAS 7 TeV data [59]. It can be assumed
 4205 that similar mismodelings are also present in other generators. While deriving $t\bar{t}$ systematics a top p_T
 4206 reweighting was applied to the generator which shows the largest difference to the nominal and from
 4207 which the systematic uncertainties for m_{bb} and E_T^{miss} were derived. This allows to see the effect of the

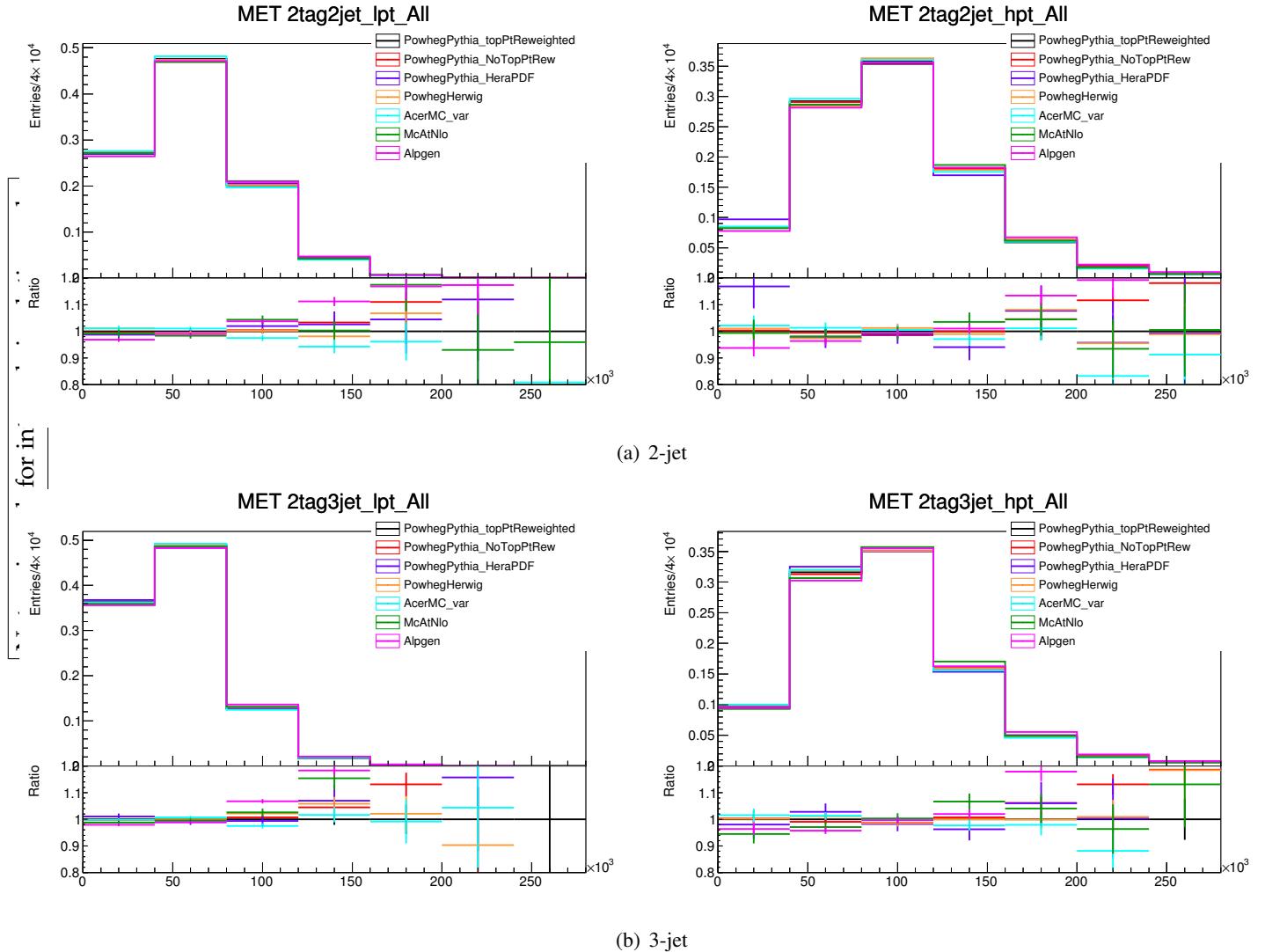


Figure 198: 1-lepton 2 and 3-jet 2-tag MC comparisons for the $t\bar{t} E_T^{\text{miss}}$ systematic. The largest difference is between PowHEG+PYTHIA and ALPGEN+PYTHIA and is taken as the systematic uncertainty. $p_T^W < 120$ GeV is shown on the left and $p_T^W > 120$ GeV is shown on the right.

4208 top p_T reweighting on ALPGEN+PYTHIA. Since no official top p_T reweighting function is provided for
 4209 ALPGEN+PYTHIA the function for PowHEG+PYTHIA was used. Before this was done, ALPGEN+PYTHIA was
 4210 reweighted to PowHEG+PYTHIA according to the distributions of the average p_T of the two truth tops.
 4211 This leads to a binned reweighting for the combination of the 2 and 3-jet region also combined in high
 4212 and low p_T^W . The reweighting distribution is shown in Figure 201.

4213 For future analyses it may be useful to redo this study with dedicated top p_T reweighting strategies
 4214 for all $t\bar{t}$ generators.

4215 N.4 The 2-to-3-jet and high-to-low- p_T^W uncertainties

4216 The categorization of the analysis in terms of the number of jets and the p_T^W is dependent on the modeling
 4217 of these properties in the different $t\bar{t}$ generators. The ratio of 3-to-2 jet production as well as low-to-high
 4218 p_T^W production was checked for the generator dependence. Table 81 shows the ratio of these quantities for

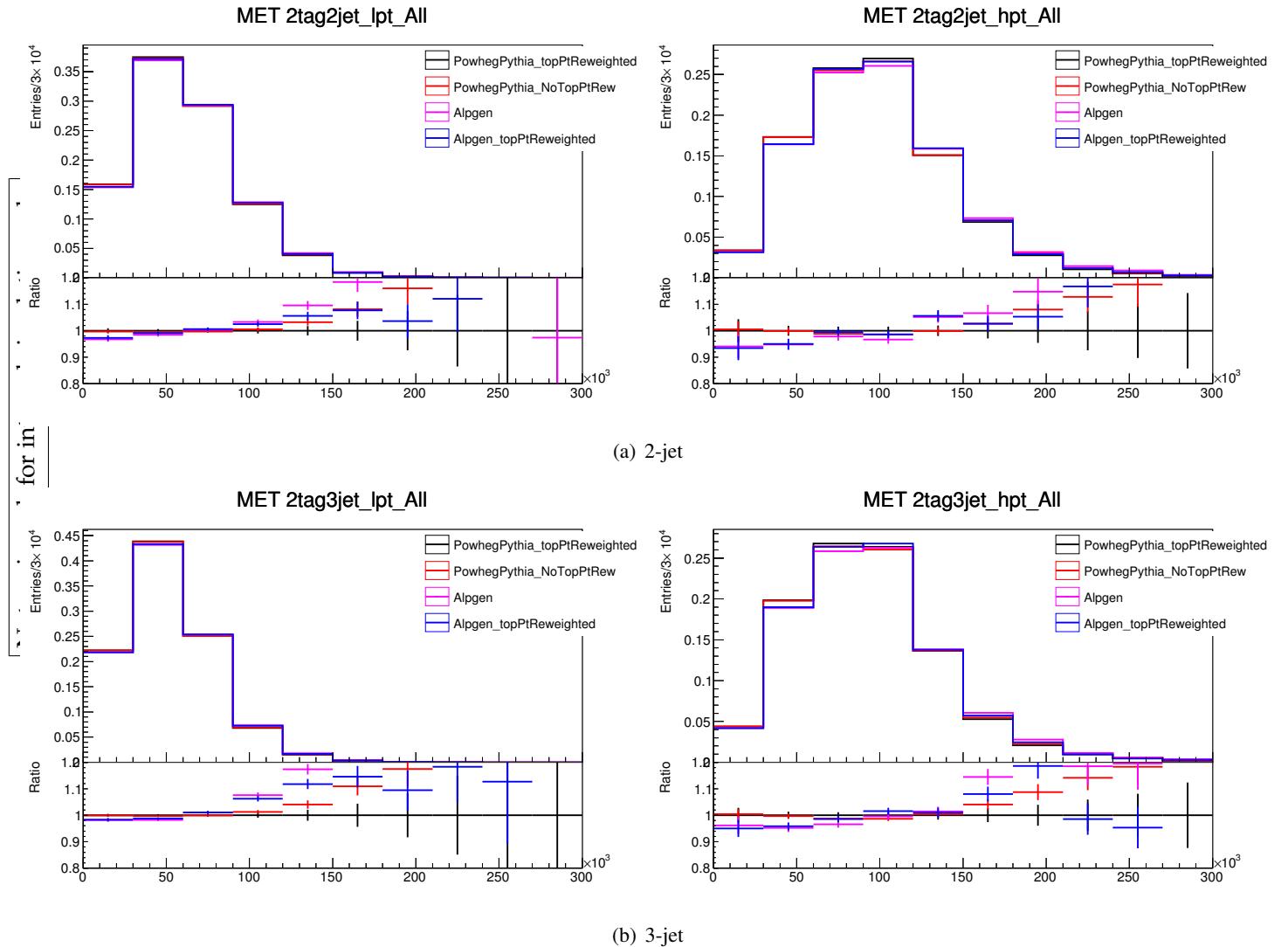


Figure 199: 1-lepton 2 and 3-jet 2-tag MC comparisons for the $t\bar{t} E_T^{\text{miss}}$ systematic. ALPGEN+PYTHIA with and without the p_T^{top} correction is compared to PowHEG+PYTHIA with and without the same correction. $p_T^W < 120$ GeV is shown on the left and $p_T^W > 120$ GeV is shown on the right.

4219 the given generators. The uncertainty was derived from the largest difference which is ALPGEN+PYTHIA in
 4220 both cases.

4221 N.5 Flavor compositions of the $t\bar{t}$ generators

4222 The flavor composition of the $t\bar{t}$ sample is not only important for the nominal sample which was used in
 4223 the analysis but also for the generators which were used to derive the systematics uncertainties. Table 82
 4224 shows the flavor fractions of all considered generators and the general agreement amongst the set. The
 4225 fraction of bc events increases while the fraction of bb decreases from the low to high p_T^W region. The
 4226 difference between the 2 and 3 jet region is non-significant for the bb and bc fraction and the bl fraction
 4227 in the 3 jet region shows only a small decrease. The largest difference to the nominal in bb and bc comes
 4228 from ALPGEN+PYTHIA. ALPGEN+PYTHIA predicts a larger fraction of bb and smaller fraction bc events than
 4229 the other generators. The fraction of bl events agree quite well between the generators. Since there are

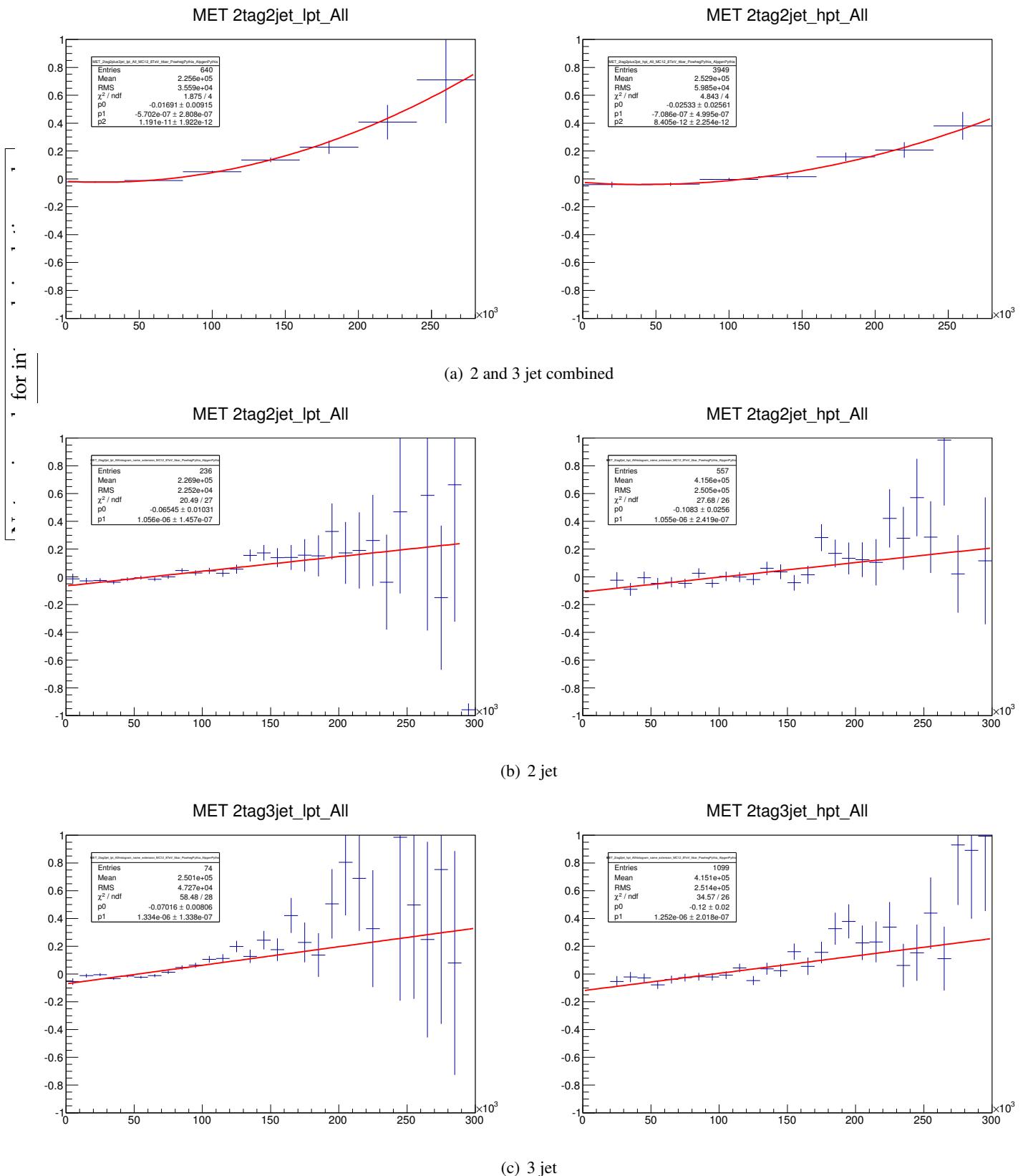


Figure 200: 1-lepton E_T^{miss} systematic for $t\bar{t}$ (a) 2+3-jet 2-tag which is used in the analysis, (b) only 2 jet 2-tag, (c) only 3 jet 2-tag . The fit is made to the ratio of ALPGEN+PYTHIA without the p_T^{top} correction and PowHEG+PYTHIA with the p_T^{top} correction. $p_T^W < 120$ GeV is shown on the left and $p_T^W > 120$ GeV is shown on the right.

Not reviewed, for internal circulation only

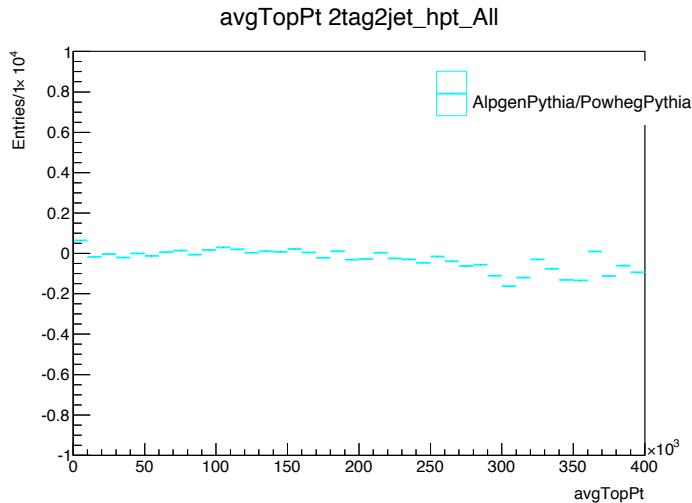


Figure 201: 1-lepton, 2+3 jet and low+high p_T^W distribution of the average top p_T of the two truth tops for the ratio between ALPGEN+PYTHIA and PowHEG+PYTHIA subtracted by 1. It was used to reweight ALPGEN+PYTHIA to apply the PowHEG+PYTHIA top p_T reweighting afterward.

Generator	3 jet/2 jet	ratio to PowHEG+PYTHIA	high p_T^W /low p_T^W	ratio to PowHEG+
PowhegPythia with top p_T reweighting	1.854	1.00	0.193	1.00
MC@NLO	1.872	1.01	0.207	1.07
PowhegHerwig	1.890	1.019	0.191	0.99
PowhegPythia with HERAPDF	1.841	0.99	0.197	1.02
AlpgenPythia	1.481	0.80	0.208	1.08

Table 81: $t\bar{t}$ 3-to-2-jet and high-to-low p_T^W uncertainties. In both cases the uncertainty was derived from the largest difference to the nominal. This is ALPGEN+PYTHIA for the 3-to-2-jet uncertainty as well as for the high-to-low p_T^W uncertainty.

4230 significant differences in the fractions of bb and bc events between ALPGEN+PYTHIA and PowHEG+PYTHIA it
 4231 was investigated if this leads to a difference in the shapes of kinematic variables. Figure 202 and 203
 4232 show the these shape comparisons for m_{bb} for bb , bc and bl events. Within the statistical fluctuations
 4233 no significant difference between the shapes is observable. When the top p_T reweighting is applied to
 4234 ALPGEN+PYTHIA these differences are even smaller.

4235 N.6 Generator variations of the BDT input variables

4236 For the determination of the shape systematics the spread between all considered $t\bar{t}$ generators for the dif-
 4237 ferent BDT input variables was investigated. As described in Sec 5.2.1.3 systematics have been assigned
 4238 according to the generator differences in m_{bb} and E_T^{miss} . All other variables did not show significant
 4239 differences between the generators or the differences were already covered by the systematics for top p_T
 4240 m_{bb} and E_T^{miss} . Fig 204-208 show the generator differences for the remaining BDT input variables for the
 4241 1-lepton channel for the 2 and 3 jet region.

Not reviewed, for internal circulation only

Generator	Jet Flavors	p_T^W GeV	
		0-120	>120
2 jets, 2-tag			
PowhegPythia with top p_T reweighting	<i>bb</i>	79.8	67.3
	<i>bc</i>	11.5	20.4
	<i>bl</i>	8.5	11.6
MC@NLO	<i>bb</i>	81.9	68.5
	<i>bc</i>	9.8	19.5
	<i>bl</i>	8.1	11.5
PowhegHerwig	<i>bb</i>	80.6	67.6
	<i>bc</i>	11.1	19.9
	<i>bl</i>	8.1	11.9
PowhegPythia with HERAPDF	<i>bb</i>	79.7	70.0
	<i>bc</i>	11.6	18.9
	<i>bl</i>	8.6	10.7
AlpgenPythia	<i>bb</i>	84.4	74.8
	<i>bc</i>	6.7	12.7
	<i>bl</i>	8.8	11.9

	Jet Flavors	p_T^W GeV	
		0-120	>120
3 jets, 2-tag			
PowhegPythia with top p_T reweighting	<i>bb</i>	81.1	66.0
	<i>bc</i>	12.5	23.0
	<i>bl</i>	6.3	10.4
MC@NLO	<i>bb</i>	82.1	67.3
	<i>bc</i>	11.5	21.8
	<i>bl</i>	6.3	10.2
PowhegHerwig	<i>bb</i>	81.8	66.3
	<i>bc</i>	11.8	21.9
	<i>bl</i>	6.3	11.1
PowhegPythia with HERAPDF	<i>bb</i>	81.5	65.7
	<i>bc</i>	12.3	22.9
	<i>bl</i>	6.1	10.8
AlpgenPythia	<i>bb</i>	83.6	70.5
	<i>bc</i>	9.6	17.8
	<i>bl</i>	6.7	11.0

Table 82: The fraction of jet flavor pairs in the 1-lepton analysis from events with two and three jets as a function of p_T^W for all $t\bar{t}$ generators which were considered for deriving the systematics.

Not reviewed, for internal circulation only

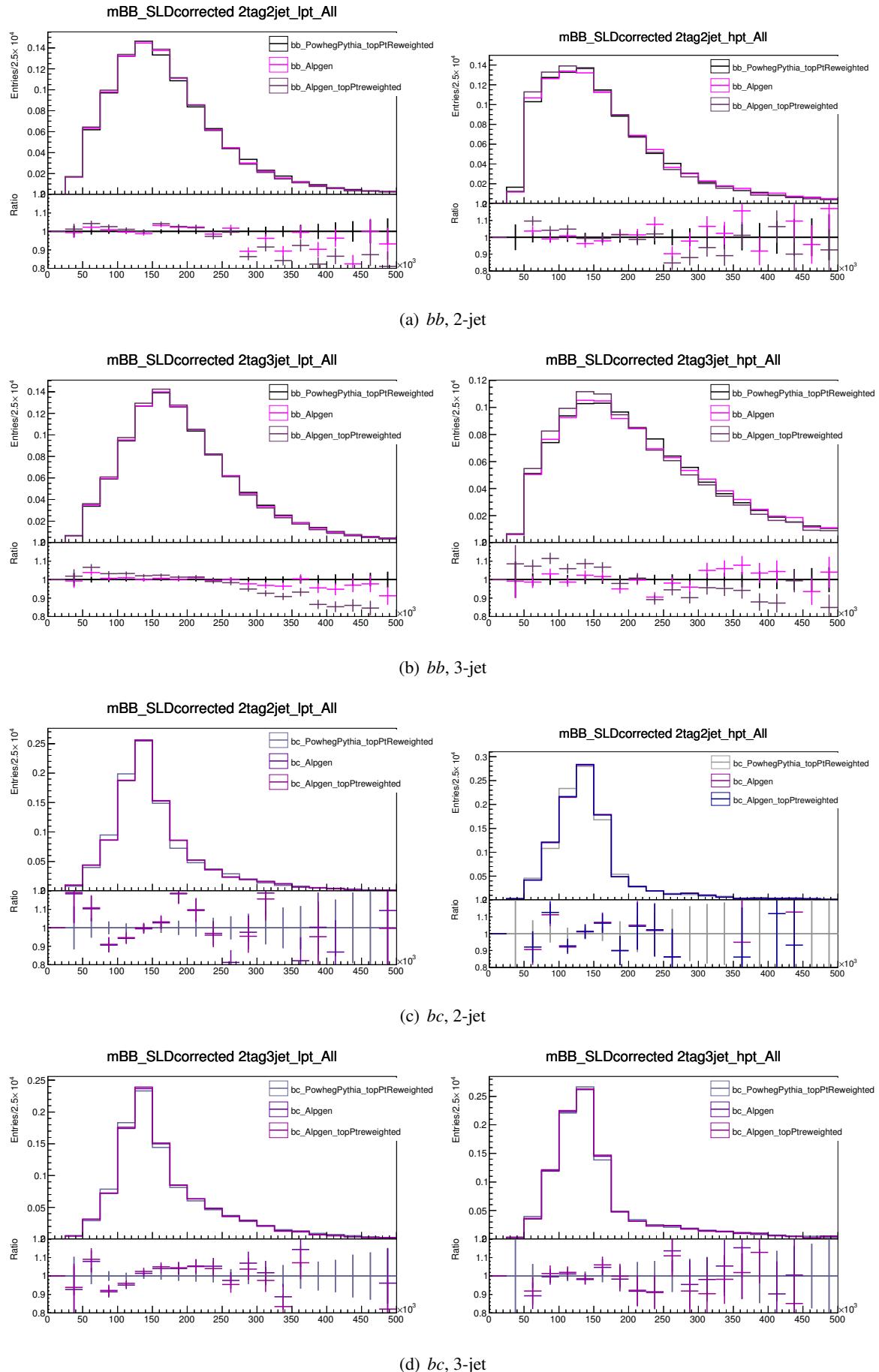


Figure 202: $t\bar{t}$ comparison of m_{bb} shapes between ALPGEN+PYTHIA with and without the top p_T reweighting and PowHEG+PYTHIA with the top p_T reweighting splitted into bb and bc events. No significant difference is observable.

Not reviewed, for internal circulation only

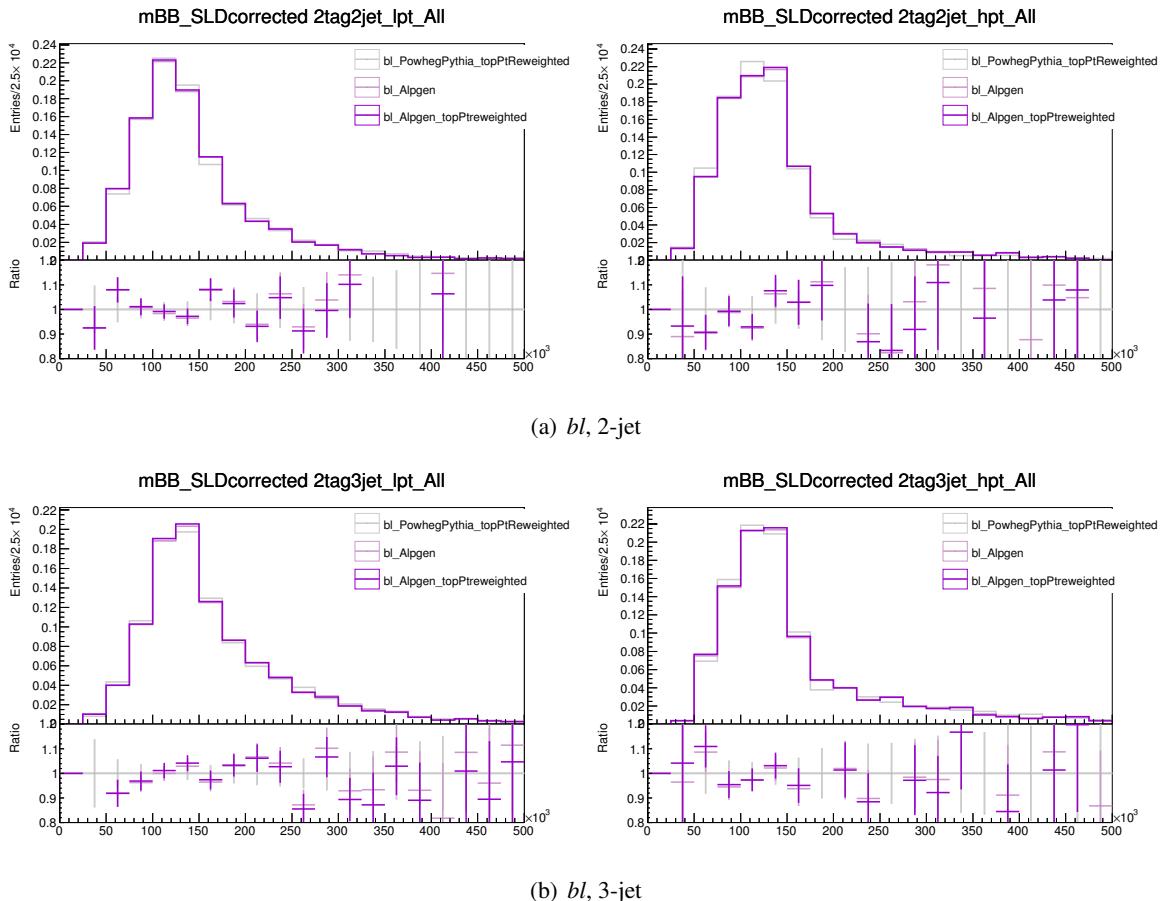


Figure 203: $t\bar{t}$ comparison of m_{bb} shapes between ALPGEN+PYTHIA with and without the top p_T reweighting and PowHeg+PYTHIA with the top p_T reweighting splitted for bl events. No significant difference is observable.

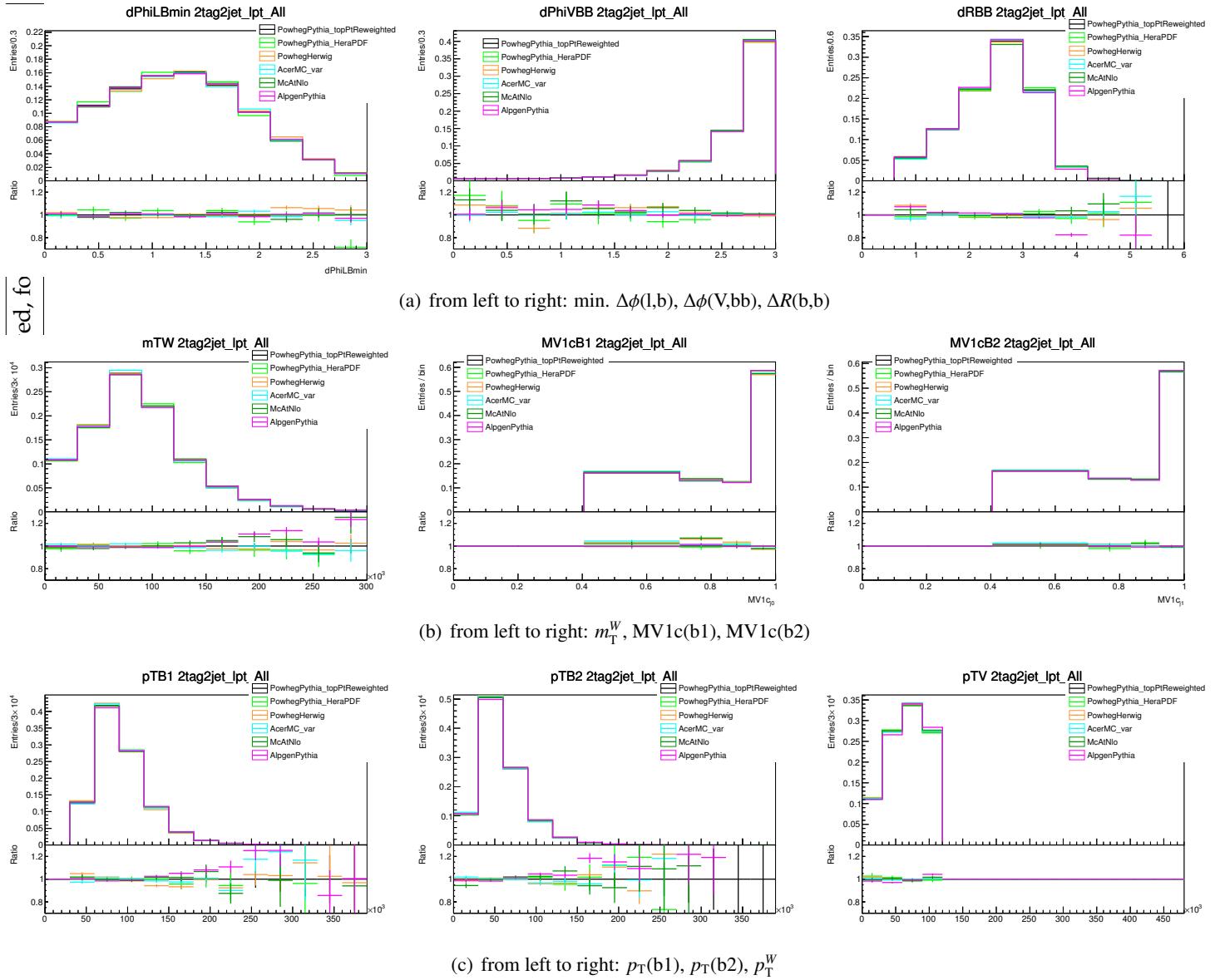


Figure 204: $t\bar{t}$ generator comparisons in the 2 jet region for low p_T^W for the BDT input variables (from left to right): min. $\Delta\phi(l,b)$, $\Delta\phi(V,bb)$, $\Delta R(b,b)$ (first row), m_T^W , MV1c(b1), MV1c(b2) (second row), $p_T(b1)$, $p_T(b2)$, p_T^W (third row); the effects were either already covered by the systematics or considered as negligible.

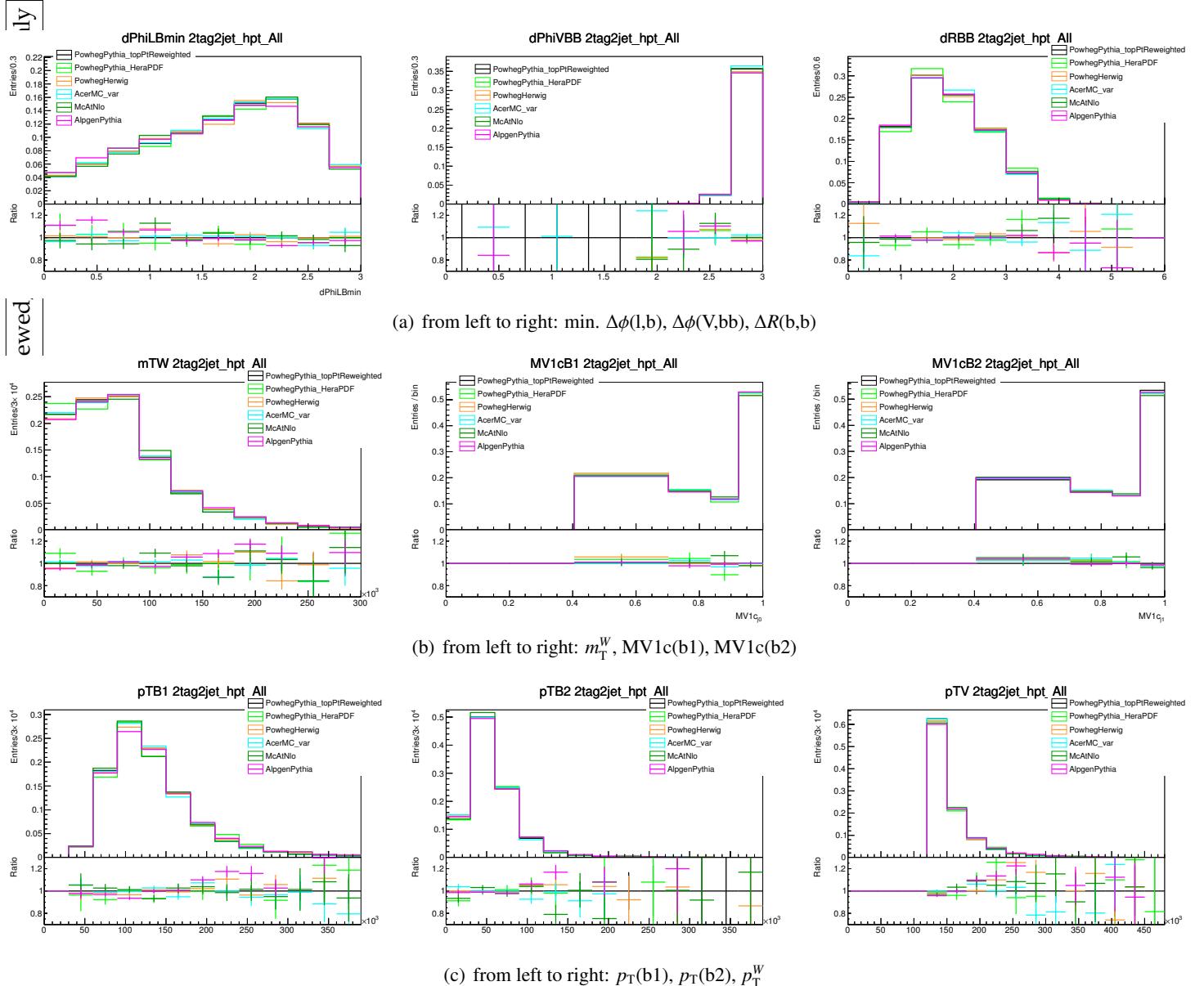


Figure 205: $t\bar{t}$ generator comparisons in the 2 jet region for high p_T^W for the BDT input variables; the effects were either already covered by the systematics or considered as negligible.

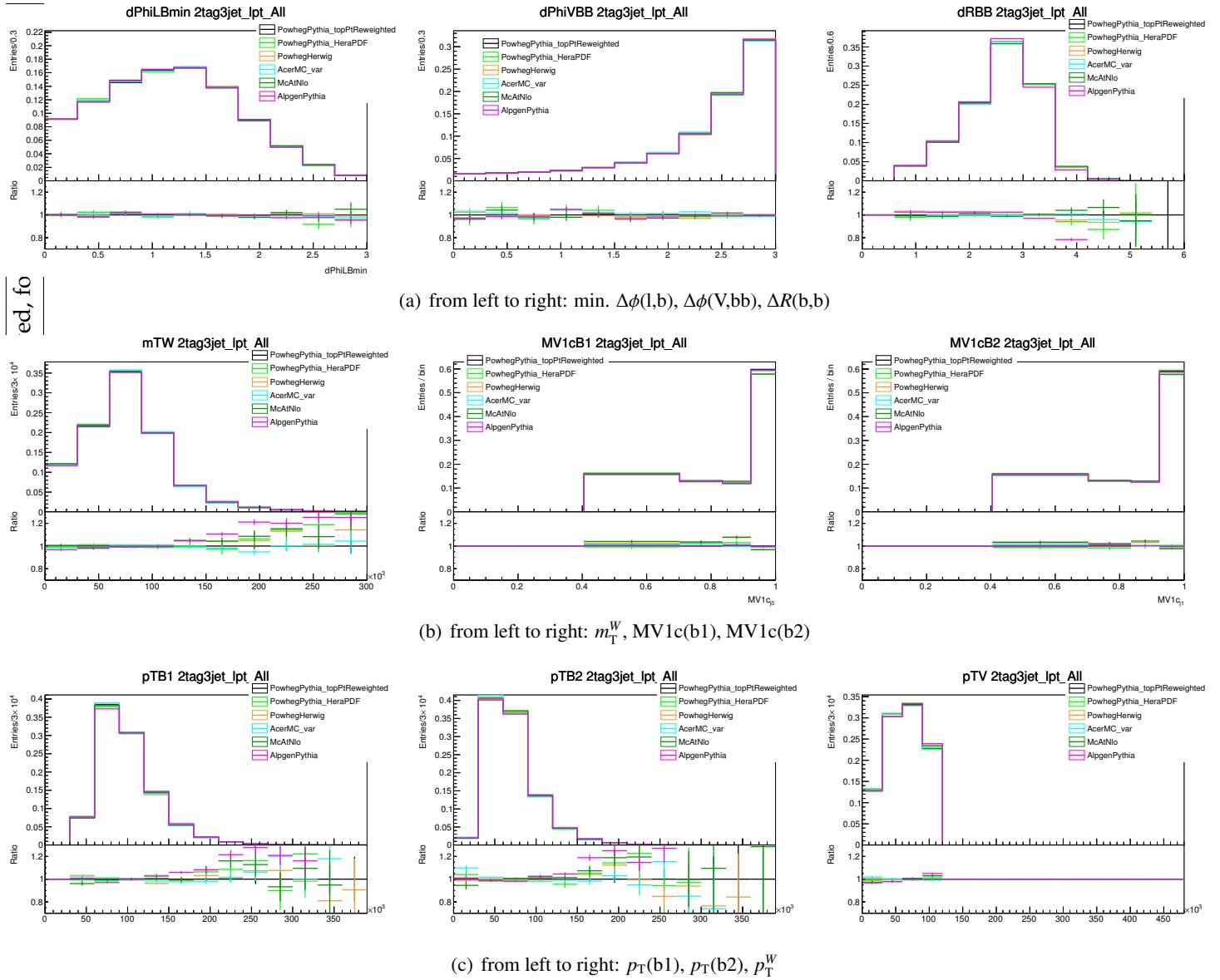


Figure 206: $t\bar{t}$ generator comparisons in the 3 jet region for low p_T^W for the BDT input variables (from left to right): min. $\Delta\phi(l,b)$, $\Delta\phi(V,bb)$, $\Delta R(b,b)$ (first row), m_T^W , MV1c(b1), MV1c(b2) (second row), $p_T(b1)$, $p_T(b2)$, p_T^W (third row); the effects were either already covered by the systematics or considered as negligible.

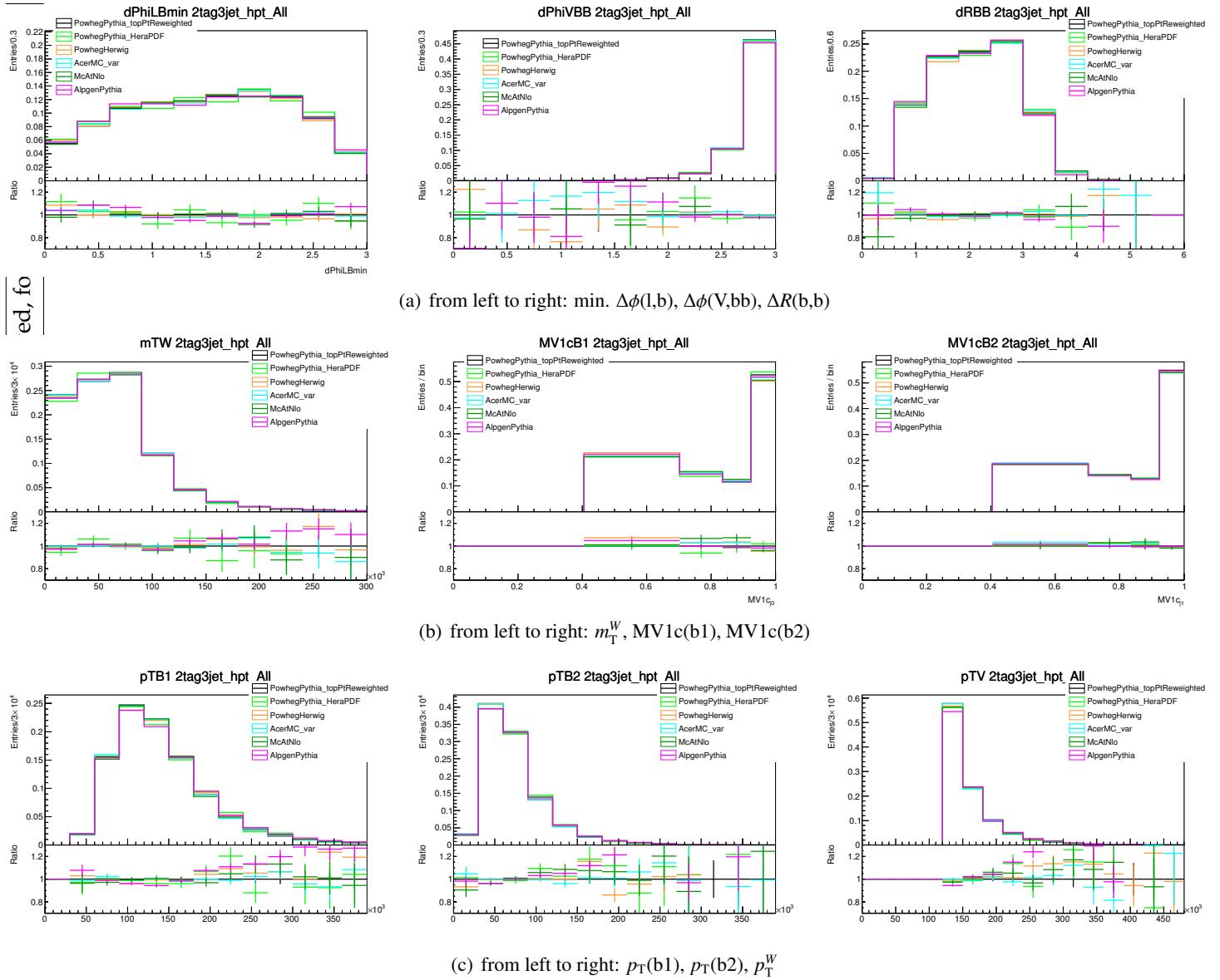


Figure 207: $t\bar{t}$ generator comparisons in the 3 jet region for high p_T^W for the BDT input variables (from left to right): $\min. \Delta\phi(l,b)$, $\Delta\phi(V,bb)$, $\Delta R(b,b)$ (first row), m_T^W , MV1c(b1), MV1c(b2) (second row), $p_T(b1)$, $p_T(b2)$, p_T^W (third row); the effects were either already covered by the systematics or considered as negligible.

Not reviewed, for internal circulation only

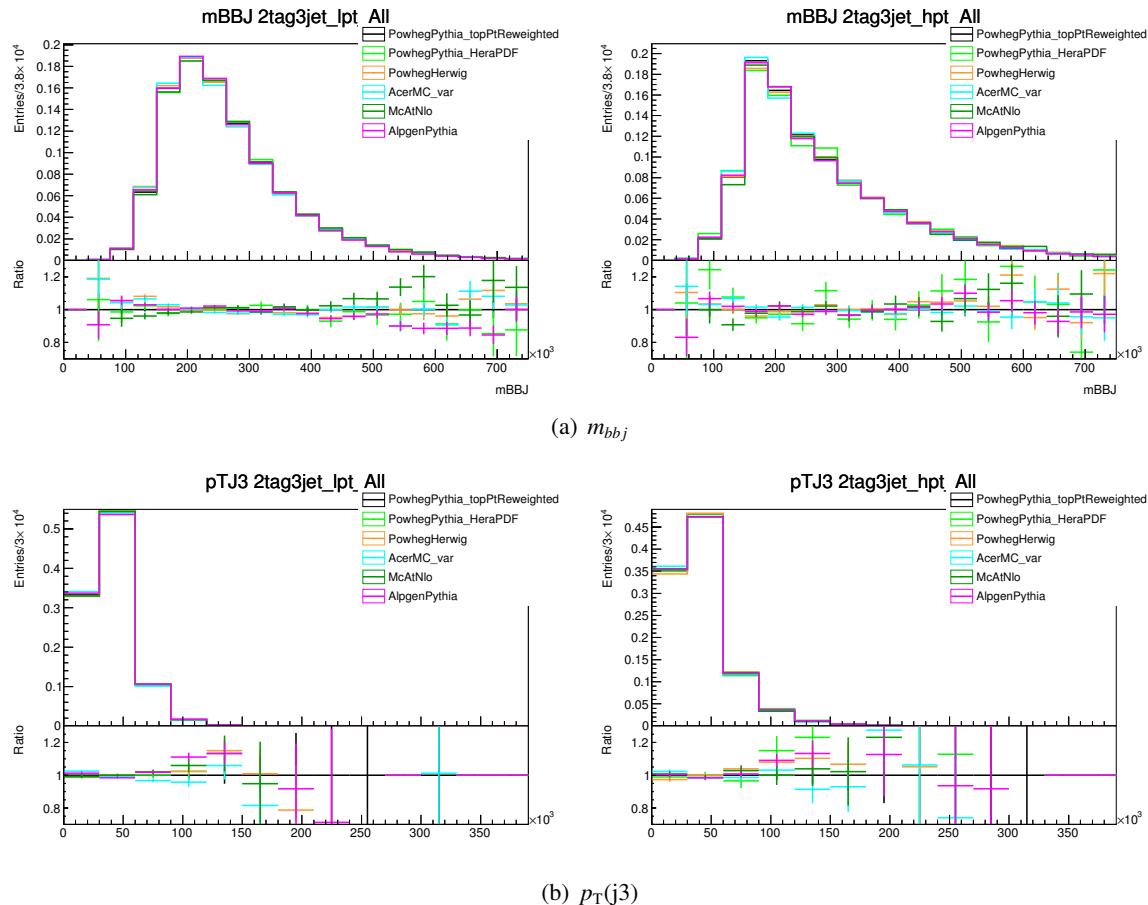


Figure 208: $t\bar{t}$ generator comparisons for the additional BDT input variables for the 3 jet region in low and high p_T^W (bottom row); the effects were either already covered by the systematics or considered as negligible.

Not reviewed, for internal circulation only

4242 O Top Modeling from EPS

4243 O.1 Top Composition

4244 Table 83 shows the fraction of events which are from top-pair events with one and two leptonically de-
 4245 caying W 's and the flavor of the leading two jets in two and three jet events. This table was made using
 4246 the EPS [11] selection with the MV1 tagger at the 70% operating point. One can see the increase in bc
 4247 events at high p_T^W because of the ΔR cuts which motivates the change from the MV1 to the MV1c tagger
 4248 discussed in Section 3.2.3. A more current top composition table is given in Section 5.2.1.1.

$N W \rightarrow \ell\nu$	Jet Flavors	p_T^W GeV					
		Inclusive	0-90	90-120	120-160	160-200	>200
2 Jets							
1	bb	24.5	25.9	22.1	21.6	19.2	11.4
	bc	10.8	9.1	10.3	13.5	36.7	63.1
	bl	1.1	0.9	1.0	1.2	2.5	5.5
	!b	0.1	0.0	0.1	0.1	0.4	1.2
2	bb	61.2	61.7	64.5	61.0	37.0	10.7
	b!b	2.2	2.3	2.0	2.5	4.0	8.1
3 Jets							
1	bb	51.4	55.7	46.6	35.8	20.2	9.2
	bc	16.6	13.6	16.8	27.6	53.0	74.1
	bl	1.6	1.3	1.6	2.4	6.7	6.8
	!b	0.1	0.1	0.1	0.3	0.8	1.6
2	bb	28.2	27.5	32.8	31.7	13.8	3.1
	b!b	2.0	1.9	2.0	2.2	5.5	5.0

Table 83: The fraction of jet flavor pairs in the 1-lepton EPS [11] analysis from events with one or two leptonically decaying tops and two or three jets as a function of p_T^W . l includes τ jets.

Not reviewed, for internal circulation only

4249 P Diboson modeling

4250 The modelling of the processes where a final state with two vector boson is produced is described in detail
 4251 in this appendix. The diboson processes considered as background in this analysis are the following:

- 4252 • $Z \rightarrow vv$ and $Z \rightarrow q\bar{q}$
- 4253 • $Z \rightarrow ll$ and $Z \rightarrow q\bar{q}$
- 4254 • $W \rightarrow lv$ and $Z \rightarrow q\bar{q}$
- 4255 • $Z \rightarrow vv$ and $W \rightarrow q\bar{q}$
- 4256 • $Z \rightarrow ll$ and $W \rightarrow q\bar{q}$
- 4257 • WW (inclusive)

4258 There is no pure region in the VH(bb) analysis where this process can be studied with data-driven tech-
 4259 niques. Therefore, a Monte-Carlo study is performed to estimate uncertainties on the most relevant
 4260 variables.

4261 The diboson processes are modelled using the POWHEG MC generator, which provides a NLO pre-
 4262 diction of this background, interfaced with the Pythia8 parton shower model. The Monte Carlo (MC)
 4263 samples for the diboson processes are listed on Table 86 along with their cross-sections at $\sqrt{s} = 8$ TeV.

4264 P.1 Cross section

4265 The diboson MC samples are normalized to the cross-sections provided directly by the POWHEG gen-
 4266 erator. These cross-section have been validated by computing the NLO cross-sections for all the diboson
 4267 processes considered using MCFM [*insert reference - here or in the previous diboson section*] with the
 4268 setup outlined in Table 87. Note that some of the MCFM parameters may differ from the ones used in
 4269 the POWHEG computation (e.g. energy scales), but the comparison still provides a fair cross-check.
 4270 The cross-section comparison between POWHEG and MCFM is shown in Table 84. The MCFM soft-
 4271 ware does not provide an NLO calculation for the $Z \rightarrow vv$ and $Z \rightarrow q\bar{q}$, and the $Z \rightarrow ll$ and $Z \rightarrow q\bar{q}$
 4272 processes with quarks other than b-quarks, hence their contribution is computed separately by hand and
 4273 added to the cross-section. The comparison shows larger discrepancies for these processes, but the agree-
 4274 ment is overall good.
 4275 After the validation the cross-sections provided directly from the POWHEG generator are used to nor-
 4276 malize the diboson samples.

4277 **$gg \rightarrow VV$ contribution** The contribution of gluon-gluon initiated VV processes is not included
 4278 in the POWHEG prediction of the diboson background. We use the MCFM software (setup outlined in
 4279 Table 87) to compute the relative contribution of these processes, which is used to correct the normaliza-
 4280 tion of the POWHEG samples. Table 85 shows the relative contribution of $gg \rightarrow VV$ processes to the ZZ
 4281 and WW backgrounds, which is added to the correspondent cross-sections from Table 84 to get the final
 4282 normalization.

4283 P.2 Modelling systematic uncertainties

4284 The following sources of systematic uncertainties are considered to assess the modelling errors on the
 4285 diboson background:

- 4286 • Scale variations (higher order perturbative corrections)

- 4287 • Parton density function (PDF) uncertainties
 4288 • α_S strong coupling constant uncertainties
 4289 • Parton shower (PS) and hadronization model uncertainties
- 4290 For each of these errors we determined the effect on the shape and the normalization of the background.
 4291 In the following paragraphs the details of the estimate of these systematic uncertainties is explained.

4292 **P.2.1 Stewart-Tackmann estimate of perturbative uncertainties on the diboson cross-section**

4293 The systematic uncertainties due to the perturbative nature of the cross-section are estimated through
 4294 renormalization and factorization scale variation using the MCFM software. The dependence of the
 4295 systematic errors with respect to $p_T(V)$ is tested to assess their shape effect on the $p_T(V)$ distributions.
 4296 The analysis regions are defined requiring exactly 2 or 3 jets, so the uncertainties are estimated separately
 4297 in the 2-jet and 3-jet categories defined using the parton-level variables provided by the MCFM software
 4298 as outlined in Table 88, and applying the Stewart-Tackmann method [add reference] to account for the
 4299 effect of the jet veto in the definition of regions.

4300 **P.2.1.1 Scale variations**

4301 The variation of the diboson cross sections due to changing the factorization (μ_F) and renormalization
 4302 (μ_R) scales of the process (Δ) is computed using the MCFM software. The nominal value of both the
 4303 μ_R and μ_F is initially set to half the invariant mass of the four decay products from the VV bosons pair
 4304 (dynamic mass $m(3456)$), and then varied down to $\frac{1}{4} \times m(3456)$ and up to $m(3456)$, in a fully correlated
 4305 way between μ_R and μ_F .

4306 **P.2.1.2 Shape dependence on $p_T(V)$**

4307 The effect of scale variations on the diboson cross sections shows a clear dependence with respect to
 4308 the transverse momentum of the leptonically decaying V boson $p_T(V)$, resulting in a larger error for
 4309 higher values of $p_T(V)$. To account for this dependence the perturbative uncertainties on σ_2 and $\sigma_{\geq 3}$ are
 4310 derived separately in 5 $p_T(V)$ bins, correspondent to the $p_T(V)$ regions defined for the dijet mass analysis
 4311 described in this note:

4312 $p_T(V)$ bins = [0, 90, 120, 160, 200, 500] (GeV)

4313 **P.2.1.3 Symmetrization and smoothening**

4314 The upwards and downwards relative systematic variations obtained across the $p_T(V)$ regions are sym-
 4315 metrized and smoothed in order to reduce the impact of statistical fluctuations due to the limited statistics
 4316 of the MCFM generated samples, and avoid instabilities in the fit model.
 4317 The symmetrization is performed according to the following schema:

- 4318 • symmetric up variation = $2 \times (\text{up variation}) / (\text{up variation} + \text{down variation})$
- 4319 • symmetric down variation = $2 \times (\text{down variation}) / (\text{up variation} + \text{down variation})$

4320 While the smoothening is done in order to obtain a final shape uncertainty which is a monotonically
 4321 increasing function of $p_T(V)$ across the chosen bins:

- 4322 • if $\text{bin}[i] > \text{bin}[i+1] \Rightarrow \text{bin}[i] = \text{average}(\text{bin}[i-1], \text{bin}[i+1])$

4323 These procedures are applied, in this order, on top of the systematic estimate for all the diboson processes,
 4324 across the full $p_T(V)$ range.

Not reviewed, for internal circulation only

4325 P.2.1.4 Uncertainties on the 2-jet and 3-jet cross-sections

4326 MCFM does not provide the cross-section computation at orders higher than NLO, therefore the 3-jet
 4327 bin corresponds necessarily to the inclusive 3-jet cross-section $\sigma_{\geq 3}$ for VV+1 jet, while the 2-jet bin
 4328 corresponds to the exclusive 2-jet cross-section σ_2 for VV+0 jets.

4329 The definition of the jet-bins used in the estimate of the systematics, shown in detail in Table 88, differs
 4330 from the one used in the analysis: the categories are defined cutting on the kinematic of the parton-
 4331 level objects provided by MCFM instead that on the reconstructed jets, always selecting the extra parton
 4332 produced by the NLO calculation to discriminate between the 2-jet and the 3-jet bins. Note that the
 4333 MCFM software is not interfaced with a parton shower algorithm, therefore the jet-bins are defined with
 4334 truly parton-level quantities.

4335 The calculation of the uncertainties in different jet bins relies on the assumption that the exclusive 2-
 4336 jet cross section (σ_2) can be written as the difference between the 2-jet inclusive ($\sigma_{\geq 2}$) and the 3-jet
 4337 inclusive ($\sigma_{\geq 3}$) cross sections: $\sigma_2 = \sigma_{\geq 2} - \sigma_{\geq 3}$, where the 2-jet inclusive term is defined as the 2-jet
 4338 exclusive dropping the requirements on the extra NLO parton in MCFM. We can therefore write down
 4339 the covariance matrix for the 2-jet exclusive and the 3-jet inclusive cross sections, assuming that $\sigma_{\geq 2}$ and
 4340 $\sigma_{\geq 3}$ are uncorrelated, as:

$$4341 C(\sigma_2, \sigma_{\geq 3}) = \begin{pmatrix} \Delta_{\geq 2}^2 + \Delta_{\geq 3}^2 & -\Delta_{\geq 3}^2 \\ -\Delta_{\geq 3}^2 & \Delta_{\geq 3}^2 \end{pmatrix},$$

4342 where $\Delta_{\geq 2}$ and $\Delta_{\geq 3}$ are the absolute uncertainties on the inclusive 2-jet cross-section ($\sigma_{\geq 2}$) and the inclu-
 4343 sive 3-jet cross-section, obtained through scale variations and smoothed and symmetrized as explained
 4344 in the previous paragraphs.

4345 The covariance matrix C is decomposed in the sum of two matrices, which are then separately diagonal-
 4346 ized to obtain a set of uncorrelated systematic variations on σ_2 and $\sigma_{\geq 3}$:

$$4347 C(\sigma_2, \sigma_{\geq 3}) = \begin{pmatrix} \Delta_{\geq 2}^2 & 0 \\ 0 & 0 \end{pmatrix} + \begin{pmatrix} \Delta_{\geq 3}^2 & -\Delta_{\geq 3}^2 \\ -\Delta_{\geq 3}^2 & \Delta_{\geq 3}^2 \end{pmatrix} = C_1 + C_2.$$

4348 The first term C_1 results in an absolute systematic error $\Delta_{\geq 2}$ on the 2jet-exclusive cross section σ_2 only
 4349 (**SysVVJetScalePtST2**), while the second term C_2 has one singular eigenvector (hence no systematic
 4350 variation) and one non-singular eigenvector which provides an anticorrelated $\Delta_{\geq 3}$ absolute systematic on
 4351 σ_2 and $\sigma_{\geq 3}$ (**SysVVJetScalePtST1**).

4352 This procedure is applied for each of the diboson processes, obtaining two orthogonal relative uncertain-
 4353 ties on σ_2 and one relative systematic uncertainty on $\sigma_{\geq 3}$:

4354

4355 SysVVJetScalePtST1:

- 4356 • relative uncertainty on $\sigma_2 = \frac{\Delta_{\geq 3}}{\sigma_2}$

- 4357 • relative uncertainty on $\sigma_{\geq 3} = -\frac{\Delta_{\geq 3}}{\sigma_3}$

4358 SysVVJetScalePtST2:

- 4359 • relative uncertainty on $\sigma_2 = \frac{\Delta_{\geq 2}}{\sigma_2}$

4360 Figure 209 and Figure 210 summarize the result of the full uncertainties computation for the 2-jet exclu-
 4361 sive and 3-jet inclusive cross sections of the six diboson processes, showing the effect of the variation of
 4362 σ_2 along the two eigenvectors and the change in $\sigma_{\geq 3}$ along the only non-singular eigenvector. The un-
 4363 certainties are estimated in the different $p_T(V)$ bins, after applying the symmetrization and smoothening

4364 procedures on $\Delta_{\geq 2}$ and $\Delta_{\geq 3}$. The shape dependence with respect to $p_T(V)$ is clear for both the orthogonal
 4365 variation **SysVVJetScalePtST1** and **SysVVJetScalePtST2**.

4366
 4367 The resulting relative perturbative uncertainties on σ_2 and $\sigma_{\geq 3}$ for the six diboson processes, across
 4368 the five $p_T(V)$ regions are summarized in Table 89, Table 90 and Table 91. The tables show that the
 4369 errors on the 2-jet exclusive cross sections go from 2-3% in the lowest $p_T(V)$ bin, up to 15-30% in the
 4370 latest $p_T(V)$ bin; while for the 3-jet inclusive cross sections they range from 10% to 15%.

4371 **P.2.2 PDF and α_S uncertainties**

4372 In order to estimate the uncertainties on the diboson cross sections due to PDF and α_S we followed the
 4373 latest prescription from PDF4LHC, using the MCFM software with the setup outlined in Table 87. As for
 4374 the perturbative uncertainties these errors are computed separately in the five $p_T(V)$ bins to test the shape
 4375 dependence of the resulting systematics.

4376 **P.2.2.1 PDF uncertainties**

4377 The systematic variations of the cross section due to PDF errors is computed as follow (Hessian method):

- 4378 • compute the up and down variations of the cross section for each of the eigenvector of the PDF
 4379 set: X_i^{pm} are the plus and minus variation for the i-th eigenvector.
- 4380 • compute the total upwards variation of the cross section as the quadrature sum of all the variations
 4381 which result in an increase of the cross section:

$$4383 \quad \Delta X_{max}^+ = \sqrt{\sum_{i=1}^N [max(X_i^+ - X_0, X_i^- - X_0, 0)]^2},$$

4384 where X_0 is the nominal cross section.

- 4385 • compute the total downwards variation of the cross section as the quadrature sum of all the variations
 4386 which result in a decrease of the cross section:

$$4388 \quad \Delta X_{max}^- = \sqrt{\sum_{i=1}^N [max(X_0 - X_i^+, X_0 - X_i^-, 0)]^2}.$$

- 4389 • repeat this procedure for two different PDF sets (CT10 and MSTW) and take the envelope of the
 4390 two resulting uncertainties.

4391 Since the CT10 and MSTW PDF sets are derived using different CL threshold for the eigenvector com-
 4392 putation (CL=90% for CT10, CL=68% for MSTW), the CT10 variations are corrected with a simple
 4393 rescaling to be consistent with the MSTW ones.

4394 These uncertainties are computed for all six diboson processes, across the five $p_T(V)$ bins, for the 2-jet
 4395 exclusive and the 3-jet inclusive cross sections (defined as in Table 88). The resulting errors are shown in
 4396 Figure 211 and 213 for the 2-jet exclusive cross section, respectively from the CT10 and MSTW PDF
 4397 sets, for all the diboson processes, and in Figure 212 and Figure 214 for the 3-jet inclusive cross section.
 4398 The relative variations do not show a significant dependence on the $p_T(V)$, and are overall smaller than
 4399 the perturbative uncertainties. The errors from the CT10 set are larger than the MSTW ones across the
 4400 whole $p_T(V)$ range.

Not reviewed, for internal circulation only

4401 P.2.2.2 α_S uncertainties

4402 The cross section errors due to our knowledge of the strong coupling constant are derived as follow:

- 4403 • consider two different central values for α_S : 0.117 and 0.119
- 4404 • for each of the α_S central values calculate the cross section errors correspondent to a 90% CL
4405 variation of α_S : this is obtained by considering the cross section computation for $\alpha_S \pm 0.002$ for
4406 both the central values
- 4407 • rescale the resulting error to 68% CL, for consistency with respect to the PDF uncertainties
- 4408 • repeat for both the PDF sets considered (CT10 and MSTW)

4409 Following this schema we obtain four variations of the cross section, for two α_S central values and two
4410 PDF sets. The uncertainties are computed in the different $p_T(V)$ bins, and are shown in Figure 215
4411 and Figure 217 for the 2-jet exclusive cross section of the six diboson processes, for CT10 and MSTW
4412 respectively, and in Figure 216 and Figure 218 for the 3-jet inclusive cross section. While it is possible
4413 to observe a dependence with respect to $p_T(V)$, the size of this systematic variation is rather smaller than
4414 the PDF and the perturbative errors. It can be noted that the two α_S central values produce a very similar
4415 variation of the cross sections.

4416 P.2.2.3 PDF and α_S combination

4417 The uncertainties from our knowledge of PDF and α_S are combined taking the quadrature sum of the
4418 two separately for the two PDF sets considered, for both the α_S central values, resulting in four relative
4419 variation of the cross section: $\Delta_{CT10}^{0.117}$, $\Delta_{CT10}^{0.119}$, $\Delta_{MSTW}^{0.117}$ and $\Delta_{MSTW}^{0.119}$, according to the formula:

$$4420 \quad \Delta_{PDF_i}^{\alpha_S^j} = \sqrt{\Delta_{PDF_i}^2 + \Delta_{\alpha_S^j - PDF_i}^2}$$

4422 where $i = CT10, MSTW$ and $j = 0.117, 0.119$.

4423 The final systematic uncertainty on the cross section is derived taking the envelop of these four uncer-
4424 tainties. Figure 219 and Figure 219 show these envelops for the 2-jet exclusive and the 3-jet inclusive
4425 cross section respectively, for the six diboson processes. It is worth noting that since the α_S uncertainties
4426 are much smaller than the PDF ones, when taking the quadrature sum of the two the shape dependence
4427 coming from the α_S variations does not appear anymore, therefore these systematic uncertainties are
4428 taken as a variation of the normalization only, neglecting the shape dependence with respect to $p_T(V)$.
4429 For the same reason the difference between the uncertainties for the two different α_S central values is
4430 completely negligible (and thus it is not shown in the plots).

4431 These systematics are estimated for all the six diboson processes, in the 2-jet exclusive and the 3-jet
4432 inclusive cases. Both the PDF and the α_S uncertainties do not depend on the decay of the vector bosons,
4433 but only on the V bosons pair considered, therefore the uncertainties are grouped for the three different
4434 VV pairs. The final normalization systematic variations obtained are shown in Table 92.

4436 P.2.3 Parton shower and hadronization model

4437 The last set of systematics uncertainties is derived comparing different models of parton shower and
4438 hadronization: in detail we considered a comparison between POWHEG+Pythia8, the nominal MC gen-
4439 erator used to model the diboson background in this analysis, and the Herwig LO+LL MC prediction.

4440 The estimate the systematic uncertainties we compared the distribution of the invariant mass of the jets
 4441 pair (m_{jj}), which is considered most sensitive to PS and hadronization effects, between the two genera-
 4442 tors. Since the Herwig generator does not provide a separate computation of the diboson cross sections
 4443 for different decay modes, the uncertainties are derived separately for the three VV pairs (ZZ, WW, WZ),
 4444 combining together the different final states.

4445 The comparison is done applying the full event selection for the 0-lepton channel except the b-tagging re-
 4446 quirement, outlined in Section [add reference] as pre-tag selection, for the WZ and WW processes, while
 4447 for the ZZ processes the b-tagging requirement is applied for the two leading jets (corresponding to the
 4448 inclusive MV1c operating point of 80%). Since we are mainly interested to differences in the shapes of
 4449 the m_{jj} distribution, the comparison is done normalizing the prediction from the two MC generator to
 4450 unit area, neglecting discrepancies in the normalization which may be due to the different matrix element
 4451 computation. The uncertainties obtained from this estimate are then applied consistently in all the three
 4452 decay channels: 0-lepton, 1-lepton, 2-lepton.

4453 Figure 221, 222, and 223 shows the POWHEG+Pythia8 versus Herwig comparison for the WZ, ZZ and
 4454 WW diboson process: to reduce the impact of statistical fluctuations the ratio between the two predic-
 4455 tions is fitted with a function that best describe the variations. This fitting function is the same for the ZZ
 4456 and WZ processes:

$$4457 \quad f(x) = p_0 + p_1 \frac{1}{1 + e^{-p_2(x-p_3)}},$$

4458 while a simple linear function is found better describe the variations for WW processes. The fits are
 4459 performed between 30 GeV and 300 GeV for the WZ processes, between 30 GeV and 500 GeV for the
 4460 WW and ZZ processes.

4461 The resulting systematic uncertainties range from about 10% to 20% in the ZZ case, from 10% to 40-
 4462 50% in the WZ, and up to about 20% for the WW processes. These systematic uncertainties affect only
 4463 the shape of the m_{jj} distribution and they don't have any effects on the normalization of the diboson
 4464 processes.

	$\sigma_{MCFM}[\text{pb}]$	$\sigma_{POWHEG}[\text{pb}]$
$Z \rightarrow vv Z \rightarrow q\bar{q}$	2.202	1.964
$Z \rightarrow ll Z \rightarrow q\bar{q}$	1.259	1.145
$W \rightarrow lv Z \rightarrow q\bar{q}$	4.658	4.870
$Z \rightarrow vv W \rightarrow q\bar{q}$	2.663	2.777
$Z \rightarrow ll W \rightarrow q\bar{q}$	1.611	1.594
WW (inclusive)	52.173	51.022

Table 84: Comparison between diboson cross-sections provided by POWHEG and computed with MCFM.

$gg \rightarrow WW$	2.65%
$gg \rightarrow Z_{ee}Z_{b\bar{b}}$	5.43%
$gg \rightarrow Z_{vv}Z_{b\bar{b}}$	5.97%

Table 85: Relative contribution of $gg \rightarrow VV$ processes to WW and ZZ backgrounds.

Process	Generator	Cross-Section ($\sqrt{s} = 8 \text{ TeV}$) [pb]
$Z \rightarrow vv Z \rightarrow q\bar{q}$	POWHEG+PYTHIA8	2.081
$Z \rightarrow ll Z \rightarrow q\bar{q}$		1.207
$W \rightarrow lv Z \rightarrow q\bar{q}$		4.870
$Z \rightarrow vv W \rightarrow q\bar{q}$		2.777
$Z \rightarrow ll W \rightarrow q\bar{q}$		1.594
WW		52.4

Table 86: Monte Carlo generator used for the modelling of the diboson processes and correspondent cross-sections.

MCFM parameter	Value
hmass	126d0
scale:QCD scale choice	+0.5
facscale:QCD fac_scale choice	+0.5
dynamicscale	m(3456)
itmx1, itmx2	10
ncall1, ncall2	500000
LHAPDF group	CT10nlo.LHgrid

Table 87: Main settings for the MCFM software used to compute the cross-sections for the diboson processes.

2-jet inclusive bin	$p_T(j1) > 20 \text{ GeV} \wedge \eta(j1) < 2.5$ $p_T(j2) > 20 \text{ GeV} \wedge \eta(j2) < 2.5$
2-jet exclusive bin	$p_T(j1) > 20 \text{ GeV} \wedge \eta(j1) < 2.5$ $p_T(j2) > 20 \text{ GeV} \wedge \eta(j2) < 2.5$ $p_T(j3) < 20 \text{ GeV}$
3-jet inclusive bin	$p_T(j1) > 20 \text{ GeV} \wedge \eta(j1) < 2.5$ $p_T(j2) > 20 \text{ GeV} \wedge \eta(j2) < 2.5$ $p_T(j3) > 20 \text{ GeV} \wedge \eta(j3) > 2.5$

Table 88: Parton-level jet-bins definition applied on the output of the MCFM simulation. The j_1 and j_2 objects are the two jets originated by the hadronically decaying V boson, while j_3 is the extra parton produced by the NLO calculation.

p_T^V bins [GeV]	0-90	90-120	120-160	160-200	> 200
$Z \rightarrow vv Z \rightarrow q\bar{q}$	0.03	0.05	0.07	0.10	0.14
$Z \rightarrow ll Z \rightarrow q\bar{q}$	0.03	0.05	0.07	0.10	0.13
$W \rightarrow lv Z \rightarrow q\bar{q}$	0.03	0.08	0.12	0.19	0.28
$Z \rightarrow vv W \rightarrow q\bar{q}$	0.03	0.07	0.12	0.18	0.28
$Z \rightarrow ll W \rightarrow q\bar{q}$	0.03	0.08	0.13	0.19	0.29
WW	0.03	0.06	0.09	0.13	0.19

Table 89: Perturbative systematics on σ_2 from the C_1 term of the covariance matrix across the different p_T^V bins.

p_T^V bins [GeV]	0-90	90-120	120-160	160-200	> 200
$Z \rightarrow vv Z \rightarrow q\bar{q}$	0.02	0.04	0.05	0.07	0.11
$Z \rightarrow ll Z \rightarrow q\bar{q}$	0.02	0.04	0.06	0.08	0.11
$W \rightarrow lv Z \rightarrow q\bar{q}$	0.03	0.06	0.10	0.14	0.22
$Z \rightarrow vv W \rightarrow q\bar{q}$	0.02	0.05	0.08	0.12	0.20
$Z \rightarrow ll W \rightarrow q\bar{q}$	0.02	0.06	0.09	0.13	0.21
WW	0.02	0.04	0.06	0.09	0.13

Table 90: Perturbative systematics on σ_2 from the C_2 term of the covariance matrix across the different p_T^V bins.

Not reviewed, for internal circulation only

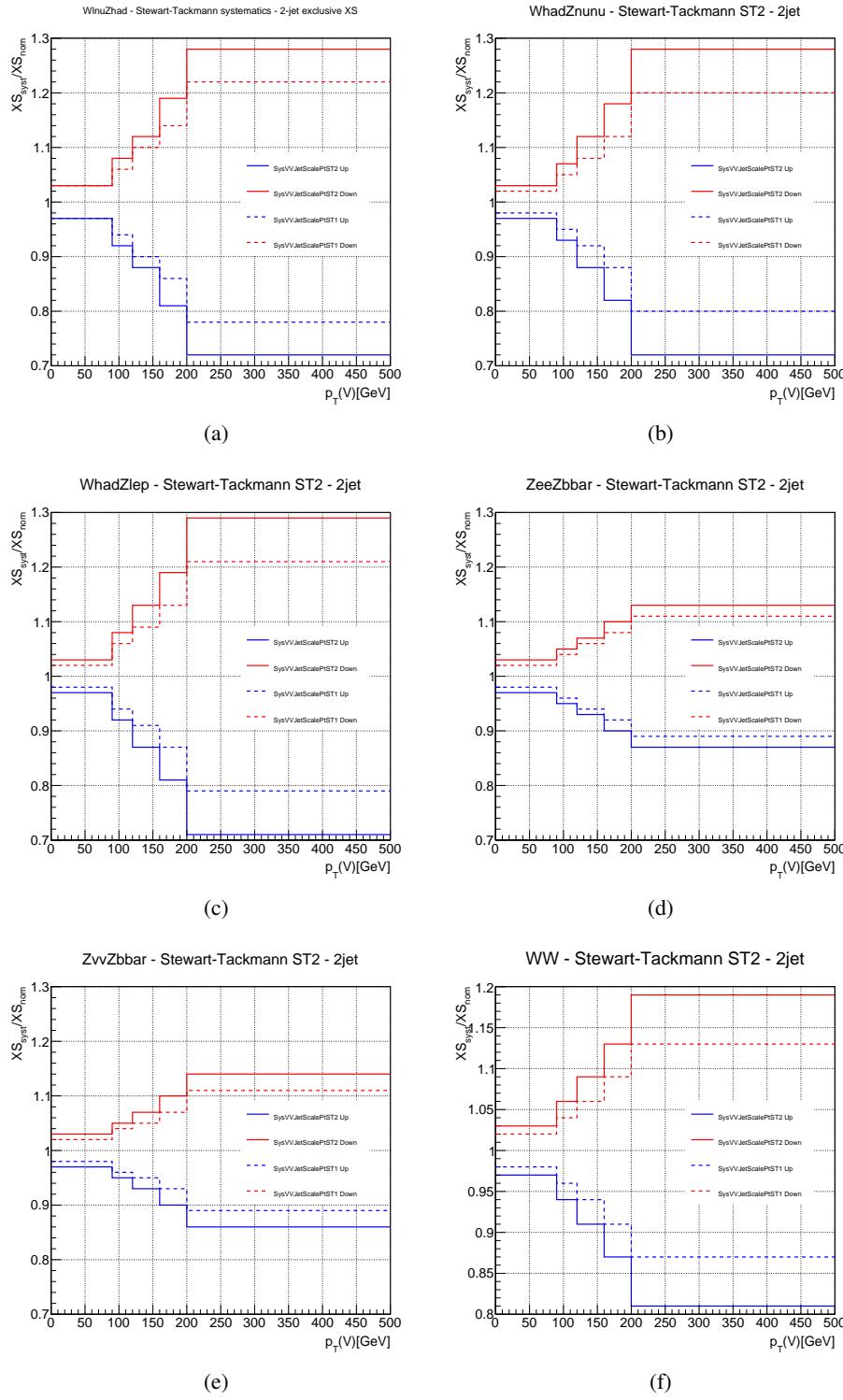


Figure 209: Perturbative systematics on σ_2 for the six diboson processes obtained applying scale variations according to the Stewart-Tackmann method. The solid line corresponds to the errors derived from the C_1 term and the dotted line from the C_2 term of the covariance matrix C .

Not reviewed, for internal circulation only

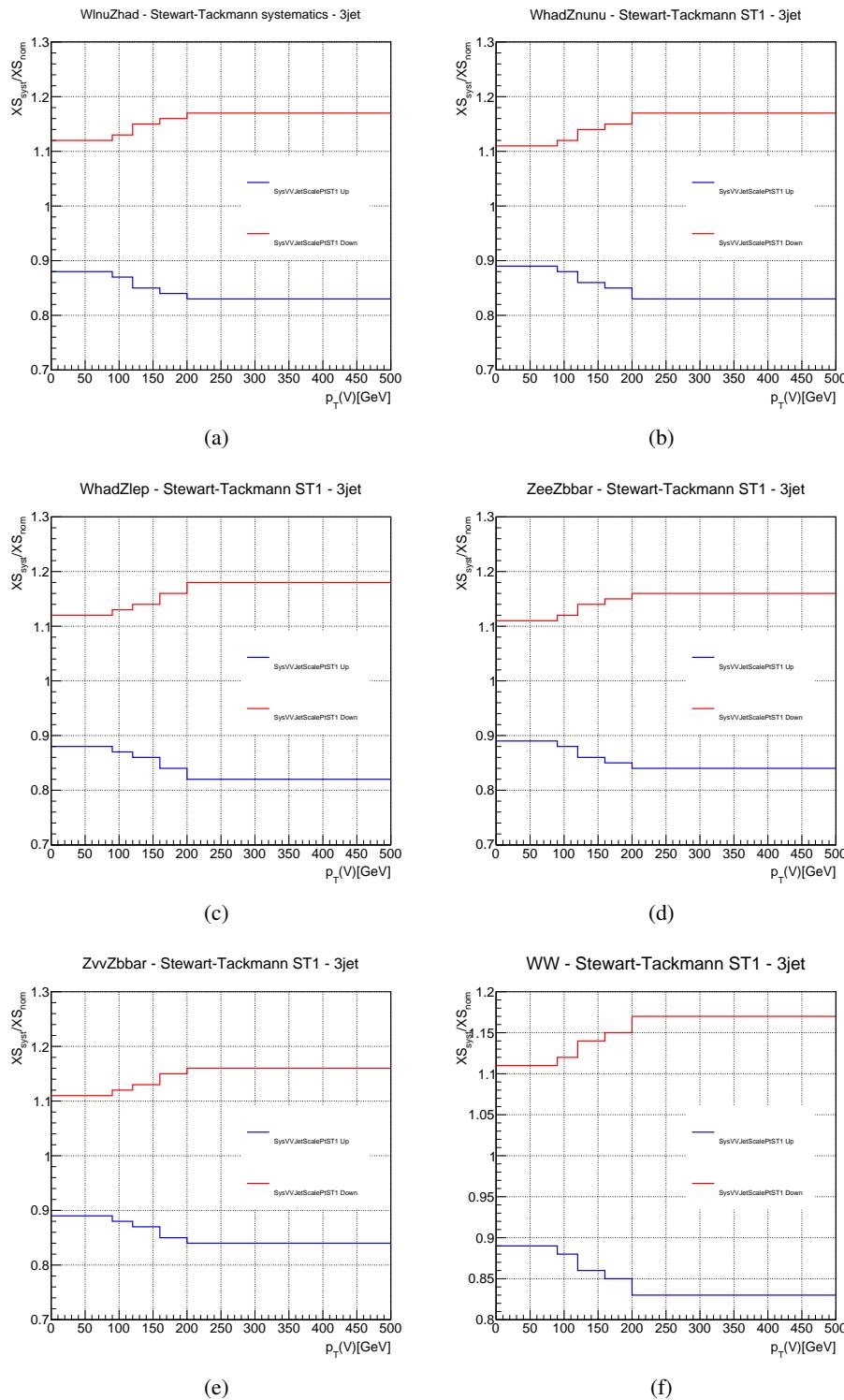


Figure 210: Perturbative systematics on $\sigma_{\geq 3}$ for the six diboson processes obtained applying scale variations according to the Stewart-Tackmann method. The solid line corresponds to the errors derived from the C_2 term of the covariance matrix C , while the C_1 term of the matrix does not provide any contribution to the 3-jet errors.

Not reviewed, for internal circulation only

p_T^V bins [GeV]	0-90	90-120	120-160	160-200	> 200
$Z \rightarrow vv Z \rightarrow q\bar{q}$	-0.11	-0.12	-0.13	-0.15	-0.16
$Z \rightarrow ll Z \rightarrow q\bar{q}$	-0.10	-0.12	-0.14	-0.15	-0.16
$W \rightarrow lv Z \rightarrow q\bar{q}$	-0.12	-0.13	-0.15	-0.16	-0.17
$Z \rightarrow vv W \rightarrow q\bar{q}$	-0.11	-0.12	-0.14	-0.15	-0.17
$Z \rightarrow ll W \rightarrow q\bar{q}$	-0.12	-0.13	-0.14	-0.16	-0.18
WW	-0.11	-0.12	-0.14	-0.15	-0.17

Table 91: Perturbative systematics on $\sigma_{\geq 3}$ from the C_2 term of the covariance matrix across the different p_T^V bins.

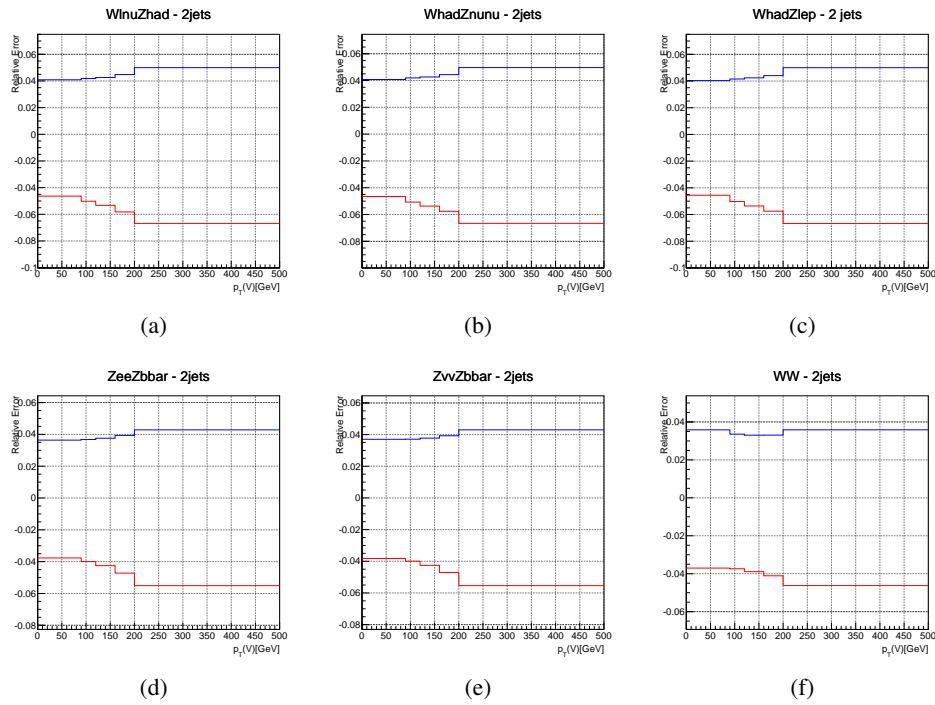


Figure 211: Systematic uncertainties due to PDF errors on the 2-jet exclusive cross section for the six diboson processes, computed from the CT10 PDF set, across the five $p_T(V)$ bins.

Process	PDF+ α_S (2-jet)	PDF+ α_S (3-jet)
ZZ	0.03	0.03
WZ	0.04	0.02
WW	0.03	0.02

Table 92: PDF+ α_S systematic uncertainties for ZZ, WZ and WW processes, in the 2-jet and 3-jet categories.

Not reviewed, for internal circulation only

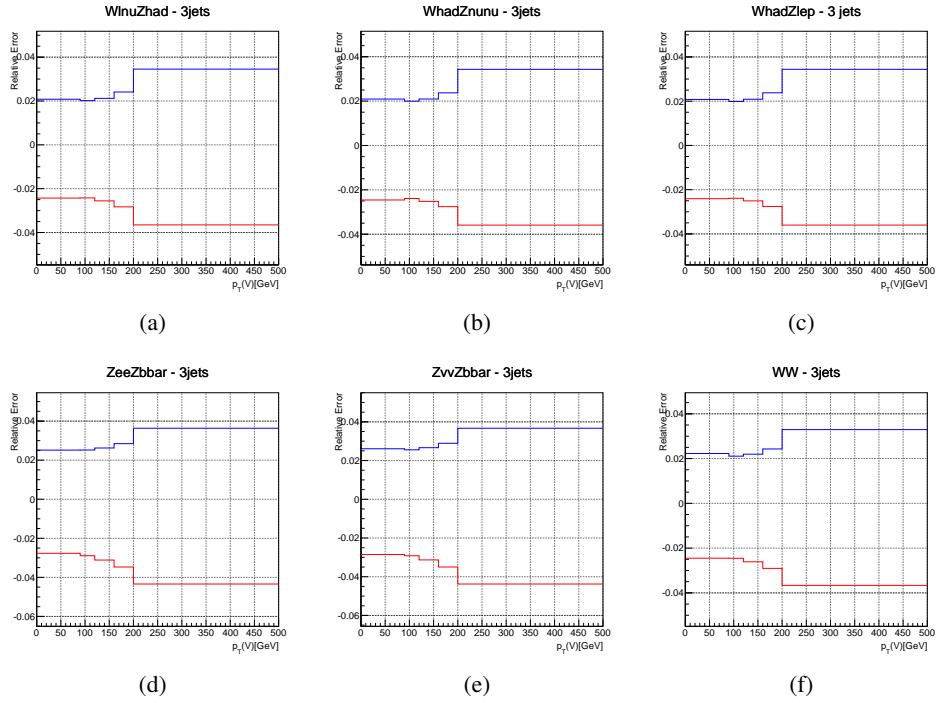


Figure 212: Systematic uncertainties due to PDF errors on the 3-jet inclusive cross section for the six diboson processes, computed from the CT10 PDF set, across the five $p_T(V)$ bins.

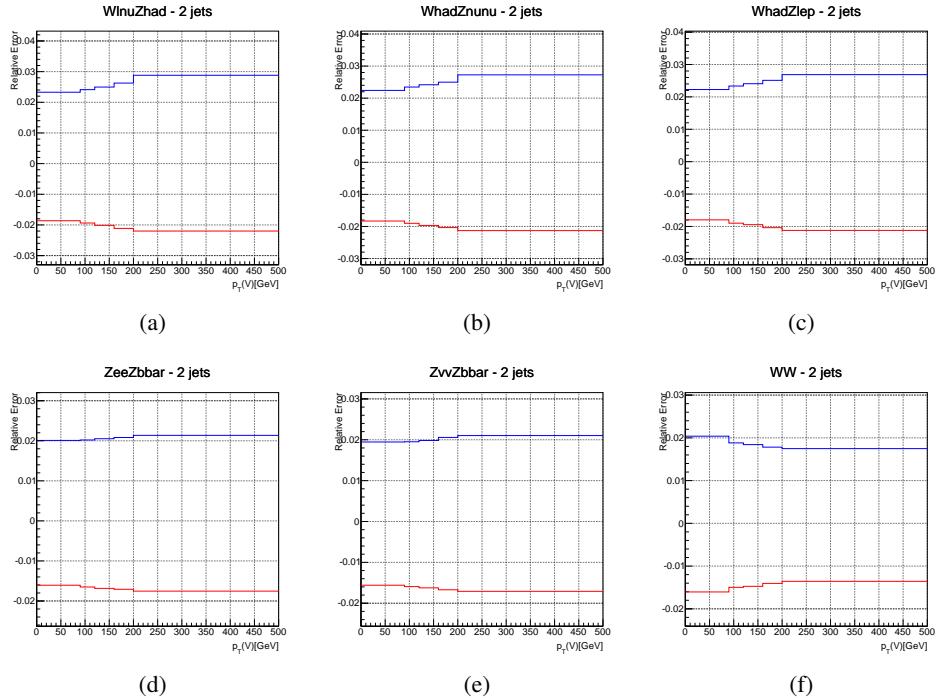


Figure 213: Systematic uncertainties due to PDF errors on the 2-jet exclusive cross section for the six diboson processes, computed from the MSTW PDF set, across the five $p_T(V)$ bins.

Not reviewed, for internal circulation only

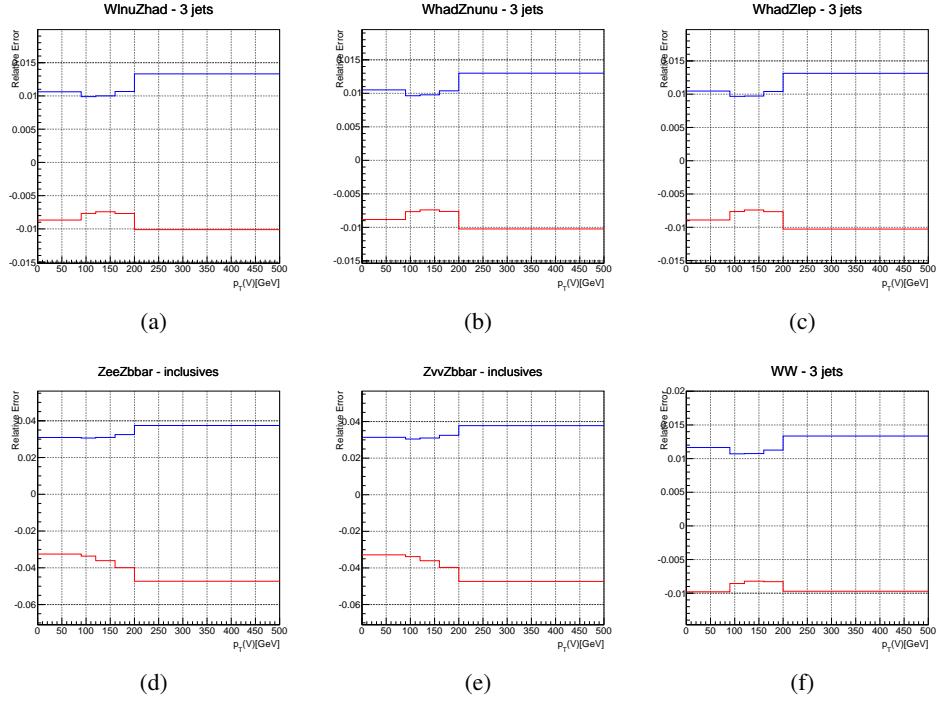


Figure 214: Systematic uncertainties due to PDF errors on the 3-jet inclusive cross section for the six diboson processes, computed from the MSTW PDF set, across the five $p_T(V)$ bins.

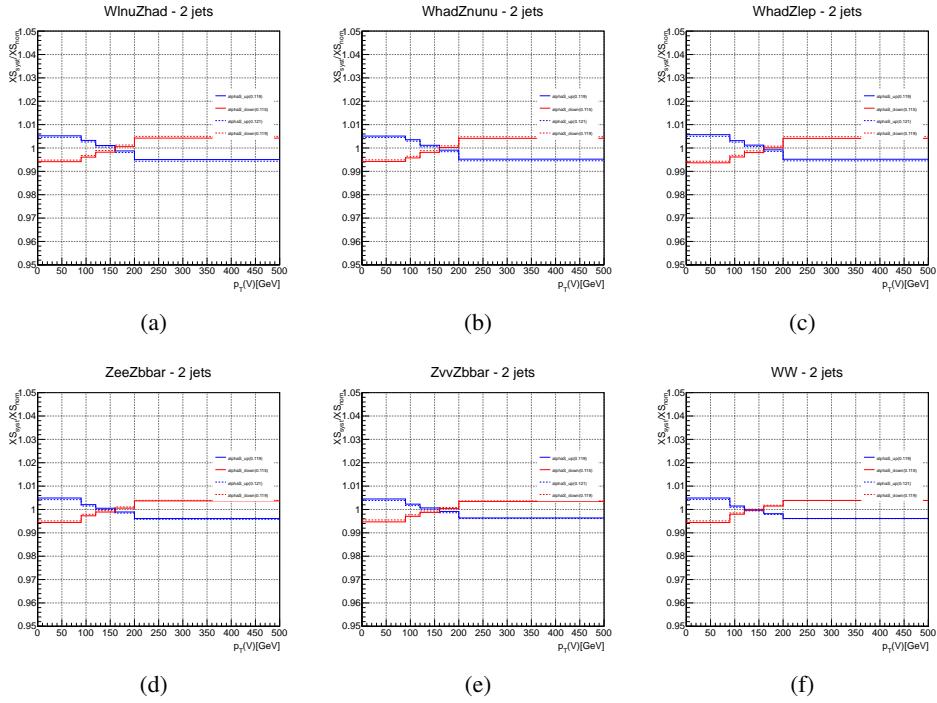


Figure 215: Systematic uncertainties from α_S on the 2-jet exclusive cross section for the six diboson processes, computed from the CT10 PDF set, across the five $p_T(V)$ bins. The solid line corresponds to the variation of the central value $\alpha_S = 0.117$, while the dotted line corresponds to the variation of $\alpha_S = 0.119$.

Not reviewed, for internal circulation only

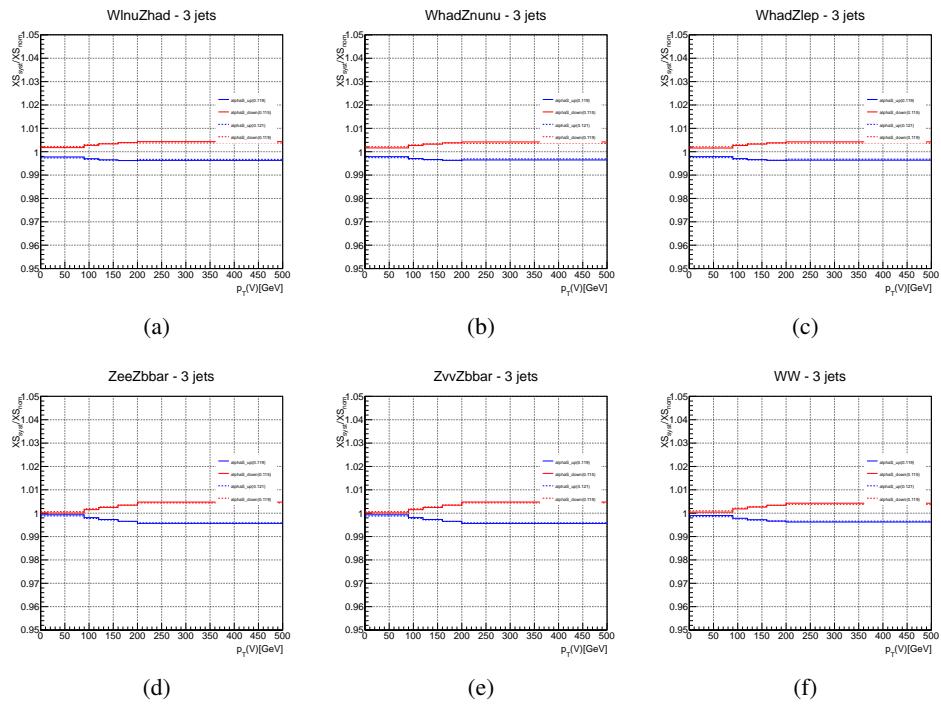


Figure 216: Systematic uncertainties from α_S on the 3-jet inclusive cross section for the six diboson processes, computed from the CT10 PDF set, across the five $p_T(V)$ bins. The solid line corresponds to the variation of the central value $\alpha_S = 0.117$, while the dotted line corresponds to the variation of $\alpha_S = 0.119$.

Not reviewed, for internal circulation only

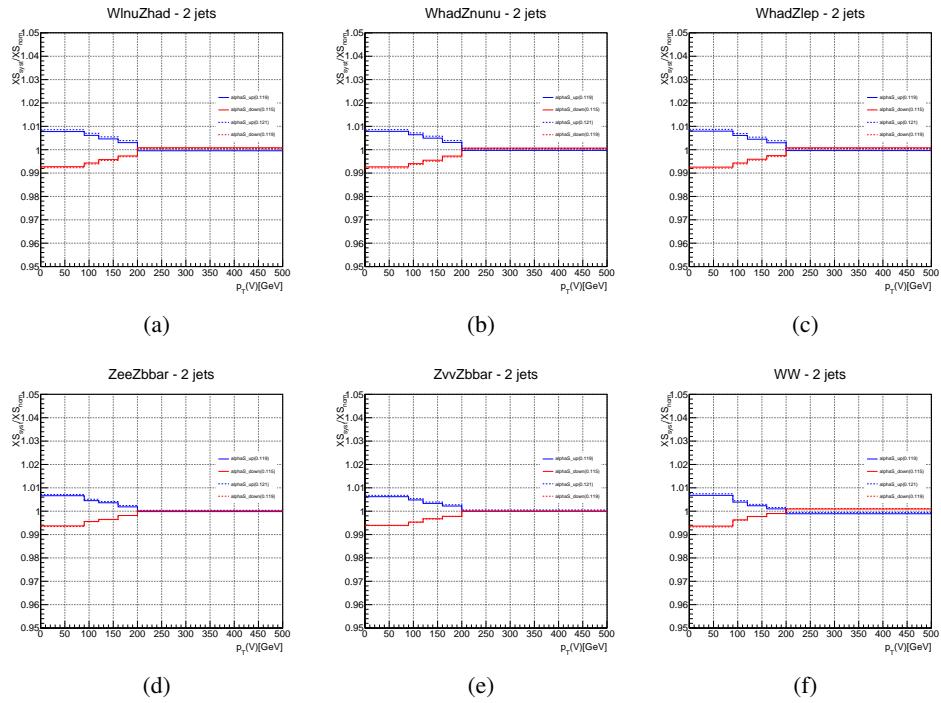


Figure 217: Systematic uncertainties from α_S on the 2-jet exclusive cross section for the six diboson processes, computed from the MSTW PDF set, across the five $p_T(V)$ bins. The solid line corresponds to the variation of the central value $\alpha_S = 0.117$, while the dotted line corresponds to the variation of $\alpha_S = 0.119$.

Not reviewed, for internal circulation only

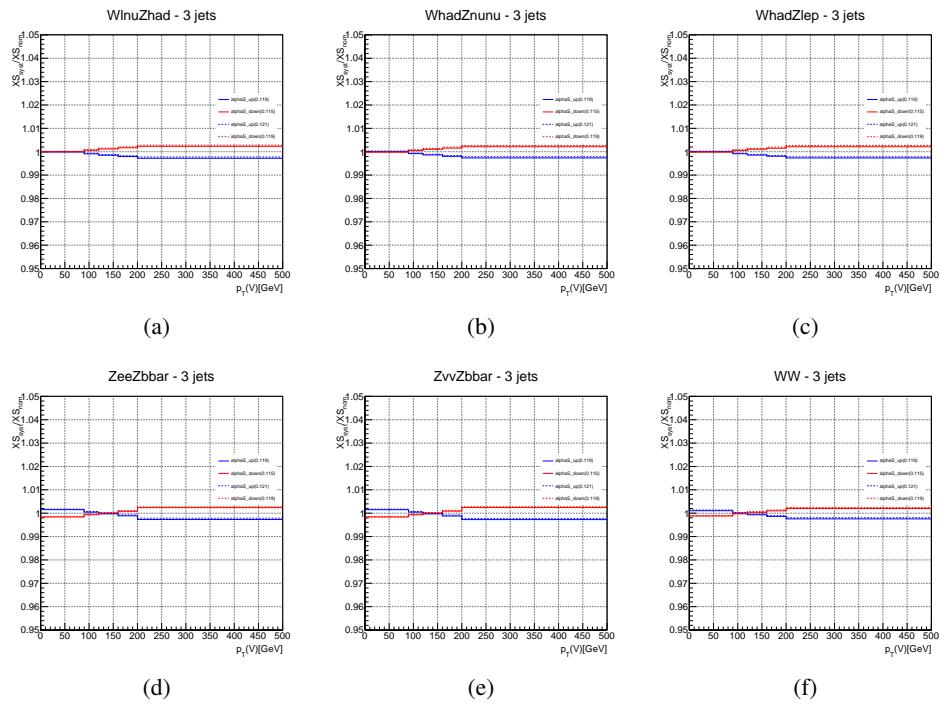


Figure 218: Systematic uncertainties from α_S on the 3-jet inclusive cross section for the six diboson processes, computed from the MSTW PDF set, across the five $p_T(V)$ bins. The solid line corresponds to the variation of the central value $\alpha_S = 0.117$, while the dotted line corresponds to the variation of $\alpha_S = 0.119$.

Not reviewed, for internal circulation only

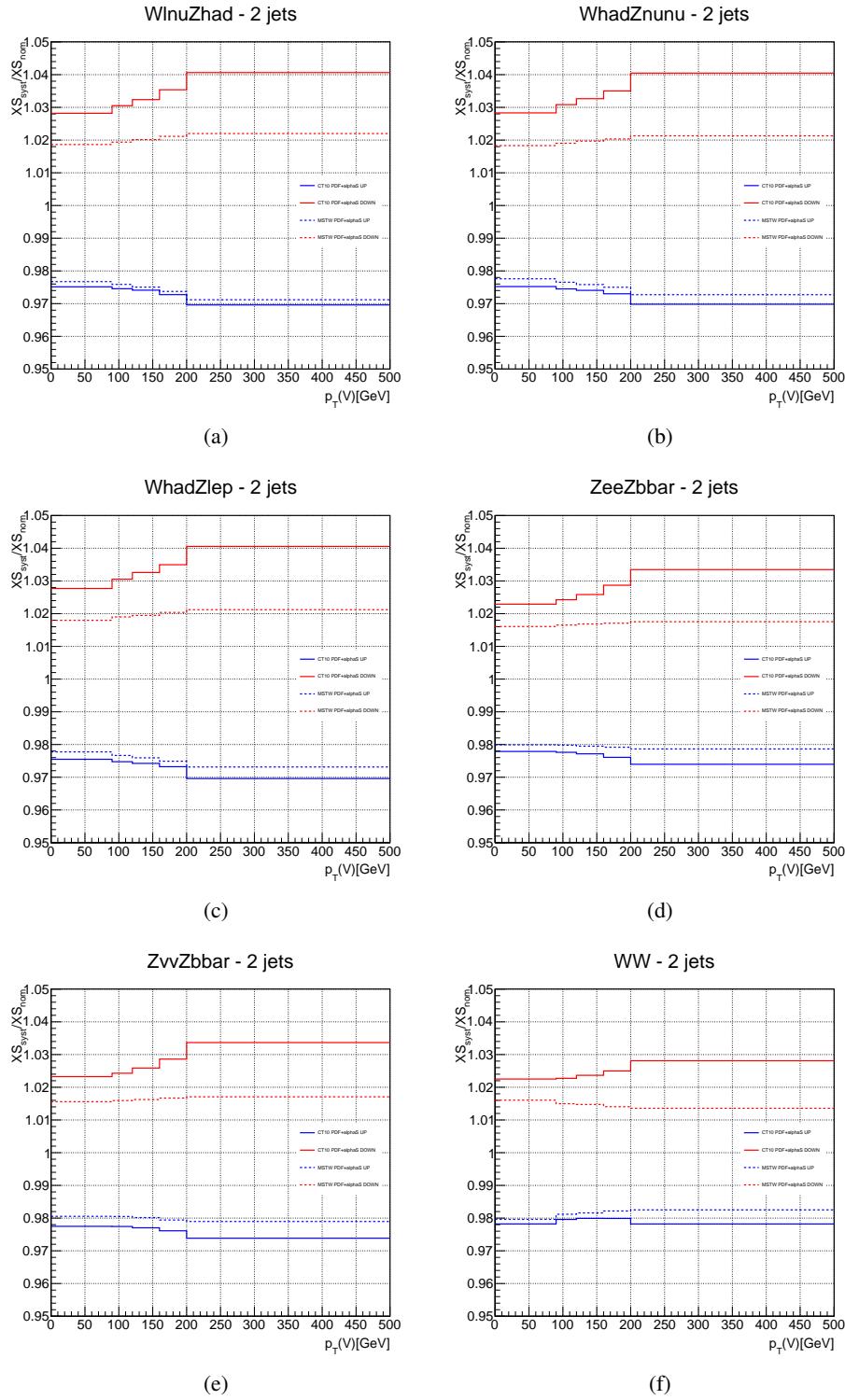


Figure 219: Envelope of the systematic uncertainties from PDF+ α_S on the 2-jet exclusive cross section for the six diboson processes. The solid line corresponds to the variations from the CT10 PDF set, while the dotted line from the MSTW PDF set.

Not reviewed, for internal circulation only

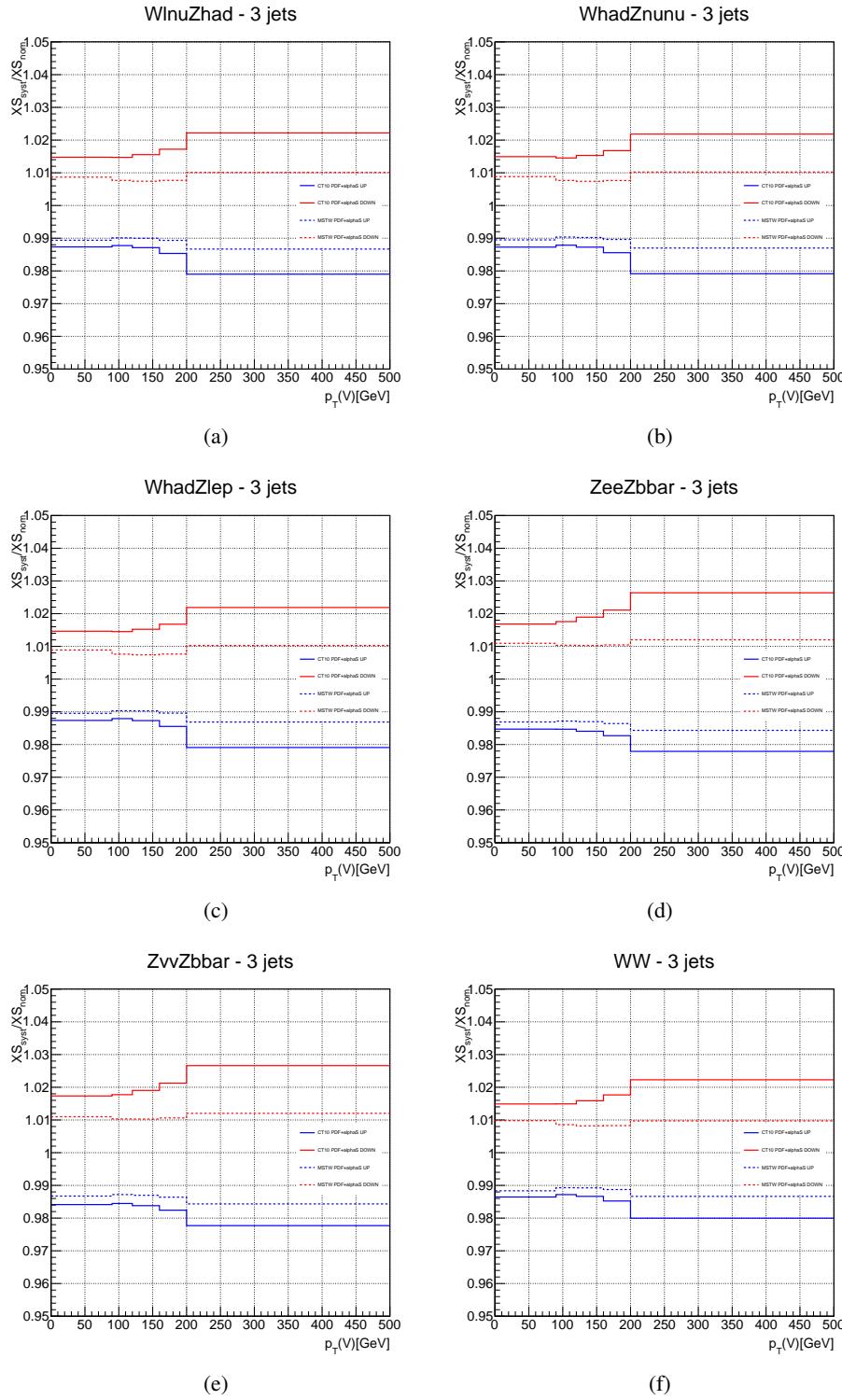


Figure 220: Envelope of the systematic uncertainties from PDF+ α_S on the 3-jet inclusive cross section for the six diboson processes. The solid line corresponds to the variations from the CT10 PDF set, while the dotted line from the MSTW PDF set.

Not reviewed, for internal circulation only

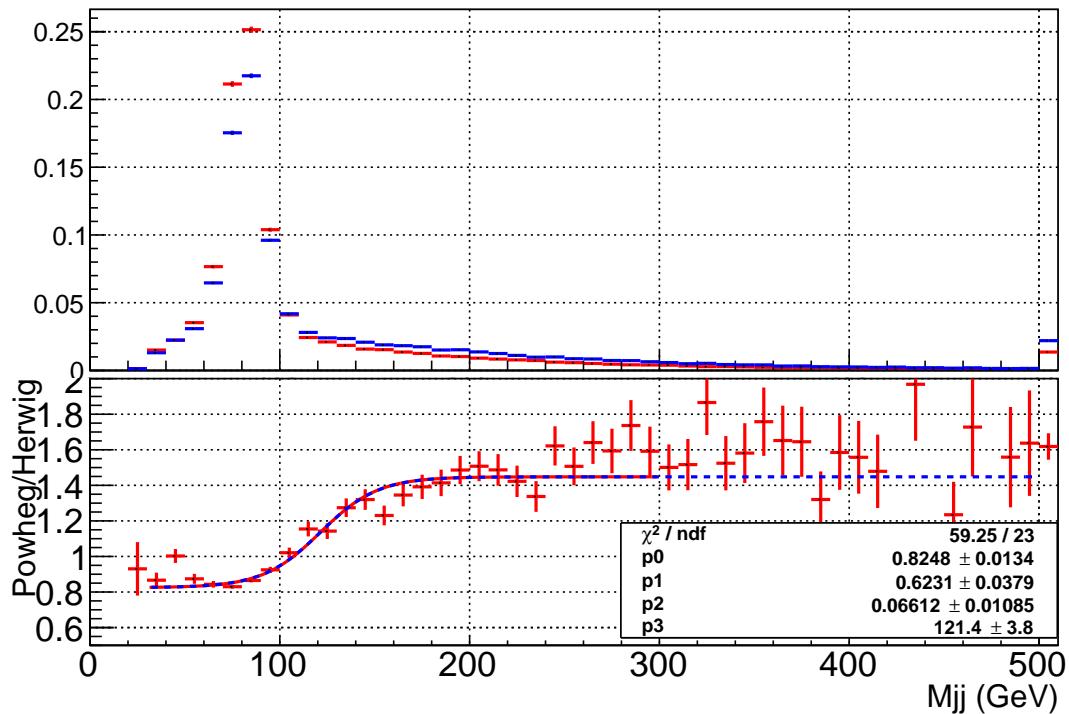


Figure 221: POWHEG+Pythia8 versus Herwig comparison for the WZ diboson processes applying the 0-lepton selection in the 2-tag inclusive (LL+MM+TT) category: the systematic uncertainties from the PS/hadronization model is estimated taking the fit of the ratio of the different MC predictions.

Not reviewed, for internal circulation only

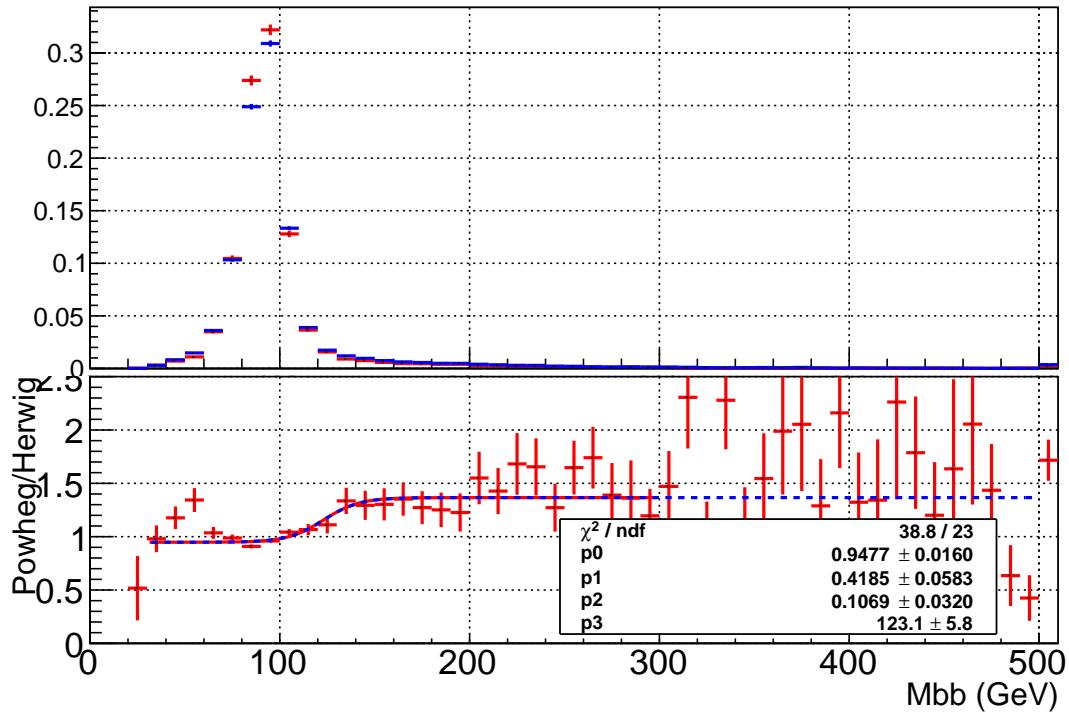


Figure 222: POWHEG+Pythia8 versus Herwig comparison for the ZZ diboson processes applying the 0-lepton selection in the pre-tag category: the systematic uncertainties from the PS/hadronization model is estimated taking the fit of the ratio of the different MC predictions.

Not reviewed, for internal circulation only

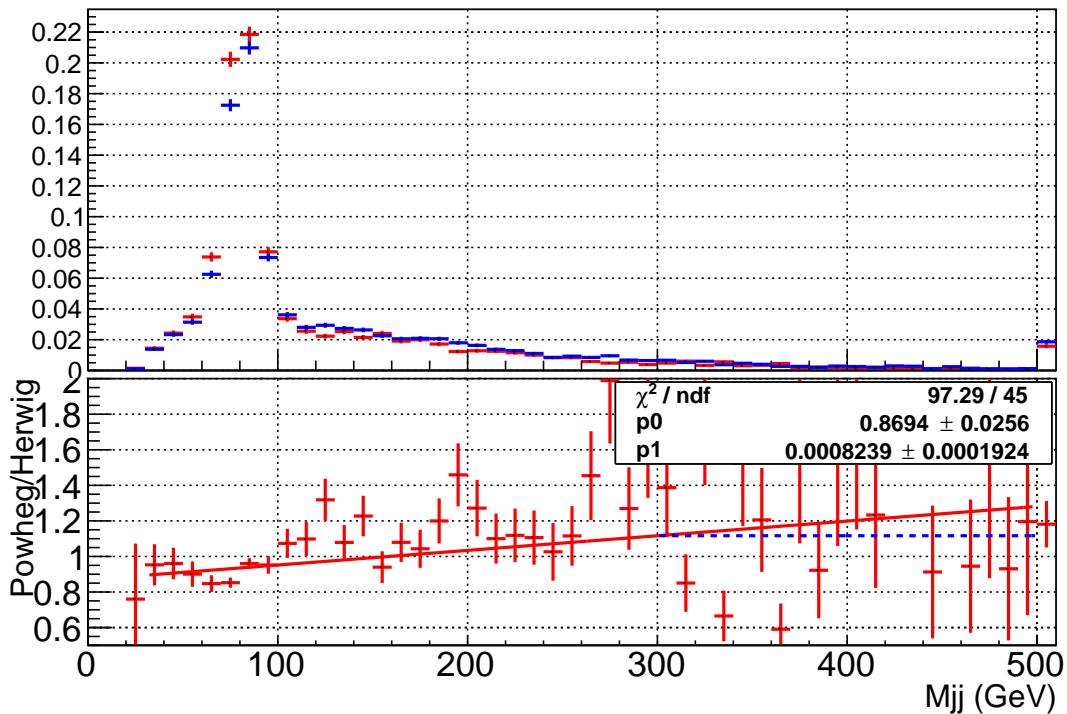


Figure 223: POWHEG+Pythia8 versus Herwig comparison for the WW diboson processes applying the 0-lepton selection in the pre-tag category: the systematic uncertainties from the PS/hadronization model is estimated taking the fit of the ratio of the different MC predictions.

4465 Q Multi-jet background for 0-lepton analysis

4466 The following is a free-standing description of the current rendering of the $ZH \rightarrow v\bar{v}b\bar{b}$ multijet back-
4467 ground estimate, an evaluation of the systematic uncertainties, and recent cross-checks.

4468 The procedure based on the method documented in Section 4.3 of Reference [74] and Section 4.1.1
4469 of Reference [11] contains information pertaining to the previous result. Between EPS and now, no major
4470 changes to this method were introduced.

4471 **Q.1 Introduction: ABCD**

4472 Multijet events with considerable E_T^{miss} (i.e. > 120 GeV) do not occur very often since substantial fluctuations
4473 in calorimeter jet energy measurements are the root cause. However, due to the extremely large
4474 multijet production cross section compared to that of the Higgs, such events are a considerable back-
4475 ground in the $ZH \rightarrow v\bar{v}b\bar{b}$ search. To simulate large- E_T^{miss} multijet events one would need a considerable
4476 amount of MC and the appropriate computing resources. This is not a practical approach, therefore a
4477 data-driven estimate is performed using the ‘ABCD’ method.

4478 Two kinematic variables,

- 4479 1. $\Delta\phi(E_T^{\text{miss}}, p_T^{\text{miss}})$: azimuthal separation between E_T^{miss} and p_T^{miss} (both described in Section 3.2.4)
 - 4480 2. $\min|\Delta\phi(E_T^{\text{miss}}, \text{jet})|$: minimum azimuthal separation between E_T^{miss} and any signal jet,
- 4481 in which the multijet background has a markedly different distribution from the EW backgrounds and
the Higgs signal have been chosen and are show in Figure 224.

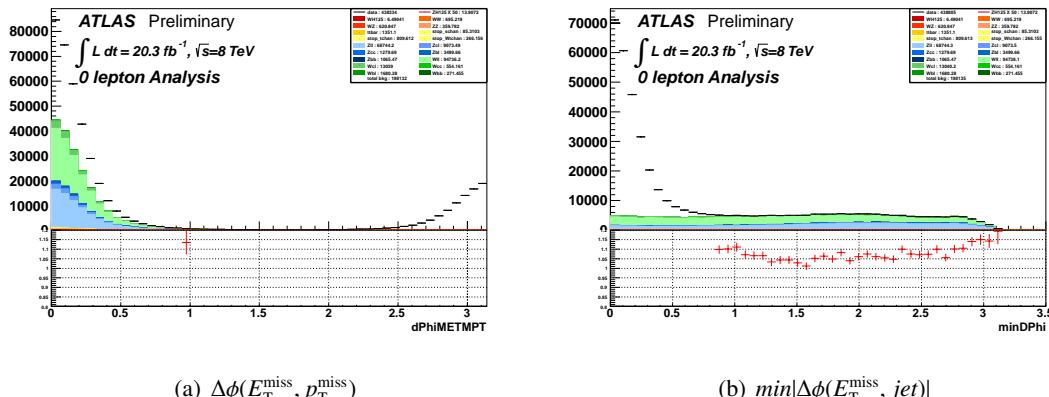


Figure 224: $\Delta\phi(E_T^{\text{miss}}, p_T^{\text{miss}})$ and $\min|\Delta\phi(E_T^{\text{miss}}, \text{jet})|$ distribution

4482
4483 Figure 225 shows the two-dimensional plane defining four regions A, B, C, and D where A/C is
4484 $\Delta\phi(E_T^{\text{miss}}, p_T^{\text{miss}}) > \pi/2$. The prediction for multijet events in the signal region (region A) is given by

$$N_{QCD}(A) = \frac{N(B)}{N(D)} \times N(C), \quad (41)$$

4485 where $N(B)$, $N(C)$ and $N(D)$ represent the data yield minus the contributions from the EW backgrounds
4486 (described in Section 5) in regions B, C and D, respectively, after all event selection cuts (described in
4487 Section 3.4) are applied except $\Delta\phi(E_T^{\text{miss}}, p_T^{\text{miss}})$ and $\min|\Delta\phi(E_T^{\text{miss}}, \text{jet})|$ cuts themselves.

4488 In order to use the ABCD method, these two variables should be at most weakly correlated for
4489 multijet events. This was checked by showing the $\min|\Delta\phi(E_T^{\text{miss}}, \text{jet})|$ shape with $\Delta\phi(E_T^{\text{miss}}, p_T^{\text{miss}})$ on
4490 either side of $\pi/2$ is similar as demonstrated in Figure 226.

Not reviewed, for internal circulation only

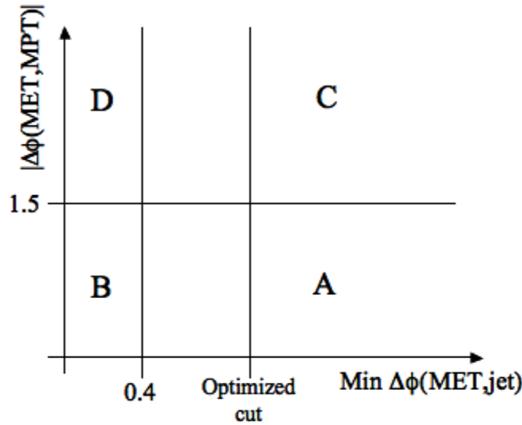


Figure 225: Two-dimensional kinematic plane for estimating QCD multi-jet background in the 0-lepton signal region (region A). $d\phi(E_T^{\text{miss}}, p_T^{\text{miss}}) > \pi/2$ defines region A/C.

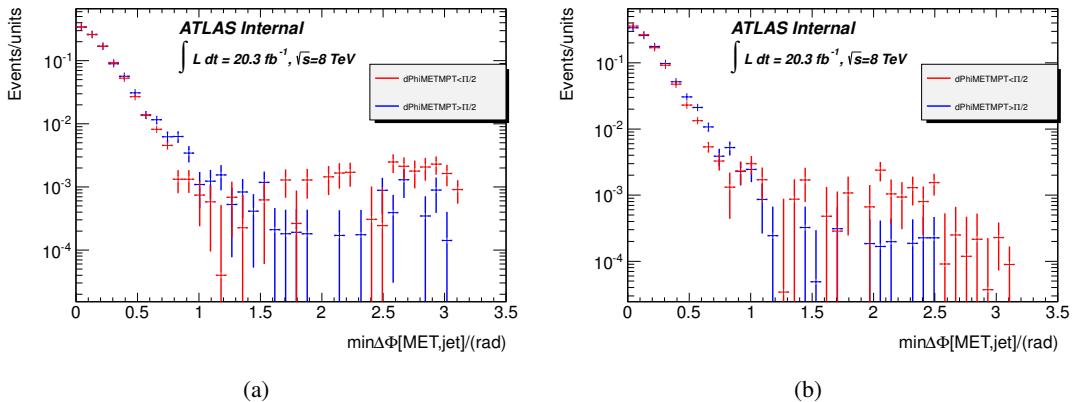


Figure 226: $\min|\Delta\phi(E_T^{\text{miss}}, \text{jet})|$ distribution of multijet background in $\Delta\phi(E_T^{\text{miss}}, p_T^{\text{miss}}) < \pi/2$ in red (region A/B) and in $\Delta\phi(E_T^{\text{miss}}, p_T^{\text{miss}}) > \pi/2$ in blue (region C/D) obtained from the data, after subtracting away contribution from EW processes estimated from simulation. The results shown are before b -tagging, and for events in $90 < E_T^{\text{miss}} < 120$ GeV for two (three) jet events on the left (right).

A/C definition	N(B)	N(D)	N(C)	$N(A)_{pred}$	$N(A)_{obs}$
$0.4 < \min \Delta\phi(E_T^{\text{miss}}, \text{jet}) < 0.9$	267267 ± 586	155094 ± 396	19537.6 ± 147.4	33668.3 ± 278.1	27976.3 ± 346.7
$0.9 < \min \Delta\phi(E_T^{\text{miss}}, \text{jet}) < 1.5$			3659.7 ± 73.3	6306.5 ± 128.2	3987.5 ± 348.2

Table 93: A closure test comparing the predicted number of multijet events from Equation 42 to the observed calculated from data minus MC in different slices of $\min|\Delta\phi(E_T^{\text{miss}}, \text{jet})|$. The results shown are before b -tagging, and for events in $90 < E_T^{\text{miss}} < 120$ GeV.

The population of data events in regions B, C and D are too small after all selection cuts to produce a robust estimate. To increase the data statistics, the b -tagging requirements were lifted from B, C, and D and the ΔR cuts of the dijet mass analysis were also removed from regions B and D. Then the shape obtained in region C is multiplied by the b -tagging rate R_B (R_D) measured in region B (D). The b -tagging rate is defined as the probability that an event passes the two b -tagged jet requirement outlined in Section 3.3.4 after satisfying all other event selection requirements. Equation 41 is then rewritten as

$$N_{QCD}(A) = \frac{N(B)}{N(D)} \times N(C) \times R. \quad (42)$$

where R can be either R_B or R_D .

Q.2 Cross Checks

Several cross checks have been done. Looking closer at Figure 226 one might notice that the red points ($\Delta\phi(E_T^{\text{miss}}, p_T^{\text{miss}}) < \pi/2$ region A/B) above $\min|\Delta\phi(E_T^{\text{miss}}, \text{jet})| = \pi/2$ are systematically much higher than the blue ($\Delta\phi(E_T^{\text{miss}}, p_T^{\text{miss}}) > \pi/2$ region C/D). Recall, the histograms in Figure 226 are obtained from data minus MC and Figure 224 shows that the difference between MC and data is very small in the region $\min|\Delta\phi(E_T^{\text{miss}}, \text{jet})| > \pi/2$ and therefore highly sensitive to the MC prediction. For example, increasing the MC prediction 5% brings N(C) and N(A) into agreement in Figure 226. To show this, and to prove that the number of events in C is representative of the number of events in A (within a factor equal to the ratio of N(B)/N(D)), a closer test comparing the predicted number of multijet events in different $\min|\Delta\phi(E_T^{\text{miss}}, \text{jet})|$ regions

- $0.4 < \min|\Delta\phi(E_T^{\text{miss}}, \text{jet})| < 0.9$,
- $0.9 < \min|\Delta\phi(E_T^{\text{miss}}, \text{jet})| < 1.5$

was performed and shown in Table 93. For $0.4 < \min|\Delta\phi(E_T^{\text{miss}}, \text{jet})| < 0.9$ the predicted number of multijet events is not sensitive to the number of MC events and agrees to a 20 % accuracy with the observed value. Stepping closer to the signal region, $0.9 < \min|\Delta\phi(E_T^{\text{miss}}, \text{jet})| < 1.5$, where the multijet prediction is more sensitive to the MC normalization, the estimated multijet yield is larger than the observed but within the systematics described below. This suggests that the method is sound but the regions used are very sensitive to the predicted EW yield. This has been taken into consideration when the systematic uncertainty described below was chosen.

To further build confidence that the $\min|\Delta\phi(E_T^{\text{miss}}, \text{jet})|$ variable and the $\Delta\phi(E_T^{\text{miss}}, p_T^{\text{miss}})$ are sufficiently de-correlated the PYTHIA8 QCD samples (Pythia8_AU2CT10_jetjet_JZxW, with $x = 2 - 7$) are employed. Figure 227 shows the shape of $\min|\Delta\phi(E_T^{\text{miss}}, \text{jet})|$ is very similar above and below $\phi(E_T^{\text{miss}}, p_T^{\text{miss}}) = \pi/2$.

Another cross check was done to explore the difference in the tagging rate in regions B and D. The tagging rate in region D rather than region B is used to estimate the multijet contamination in region A. Region D is more representative of A since B is enhanced in heavy flavor jets. Figure 228 provides a

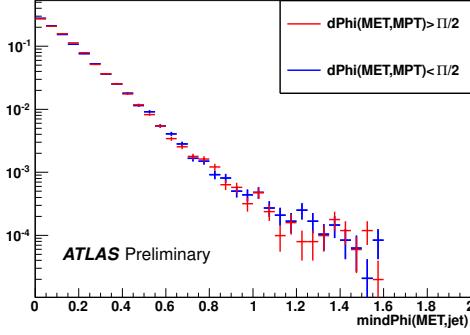


Figure 227: The $\min|\Delta\phi(E_T^{\text{miss}}, \text{jet})|$ variable is shown to have the same shape above and below $\phi(E_T^{\text{miss}}, p_T^{\text{miss}}) = \pi/2$ which supports that the two variables are not correlated. These plots were made using PYTHIA8 QCD samples (Pythia8_AU2CT10_jetjet_JZxW, with $x = 2 - 7$).

$\min \Delta\phi(E_T^{\text{miss}}, \text{jet}) $	0-0.4	0.5-1.0	1.0-1.5
R_B	0.090	0.046	0.018
R_D	0.036	0.022	0.016

Table 94: Event b -tagging rate for different slices of $\min|\Delta\phi(E_T^{\text{miss}}, \text{jet})|$.

visual aid for the following discussion. In region B, both the E_T^{miss} and p_T^{miss} point in a similar azimuthal direction as well as the E_T^{miss} and some jet. This can be a signature of semi-leptonic b -quark decay. While in region D, the E_T^{miss} and p_T^{miss} are pointing in the opposite azimuthal direction, which is more indicative of a calorimeter or an inner-detector mis-measurement. Therefore, with the $\min|\Delta\phi(E_T^{\text{miss}}, \text{jet})|$ increasing, the b -tagging rate will decrease. Table 94 shows the tagging rate in different $\min|\Delta\phi(E_T^{\text{miss}}, \text{jet})|$ ranges. Again, PYTHIA8 QCD samples (Pythia8_AU2CT10_jetjet_JZxW, with $x = 2 - 7$) are used to further validate the above claim. Figure 229 shows the truth label of a jet with the smallest azimuthal separation from the E_T^{miss} . Region B has the largest fraction of b -jets and even though region D is closer to A, it still has a larger b -jet contribution. This also indicates that the multijet background is somehow overestimated when using R_B or R_D .

Please see Reference [11] for previously performed cross-checks.

Q.3 Final Product

As can be seen from Tables 95 and 96, both version of this analysis have very small multijet contamination. Based on the closure test (Table 93) and the b -tagging rate in region D, the multijet events for $E_T^{\text{miss}} > 120$ GeV background is estimated to be well under 2% in most regions as shown in Tables 95 and 96 with respect to the electroweak background. These estimates are inserted into each search categories using the same dijet mass and BDT template shown in Figure 230.

In the fits, a gaussian priors on the multijet normalization is used, with an error of $\pm 100\%$ on its normalization. This systematic uncertainty has been evaluated to cover the different effects described in this. These priors correlate LL, MM, TT categories for the different p_T^V regions (with the exception of the region with $100 < p_T^V < 120$ GeV), while it takes non correlated regions with different number of jets and different number of tagged jets (i.e. 1-tag VS. 2-tag).

Not reviewed, for internal circulation only

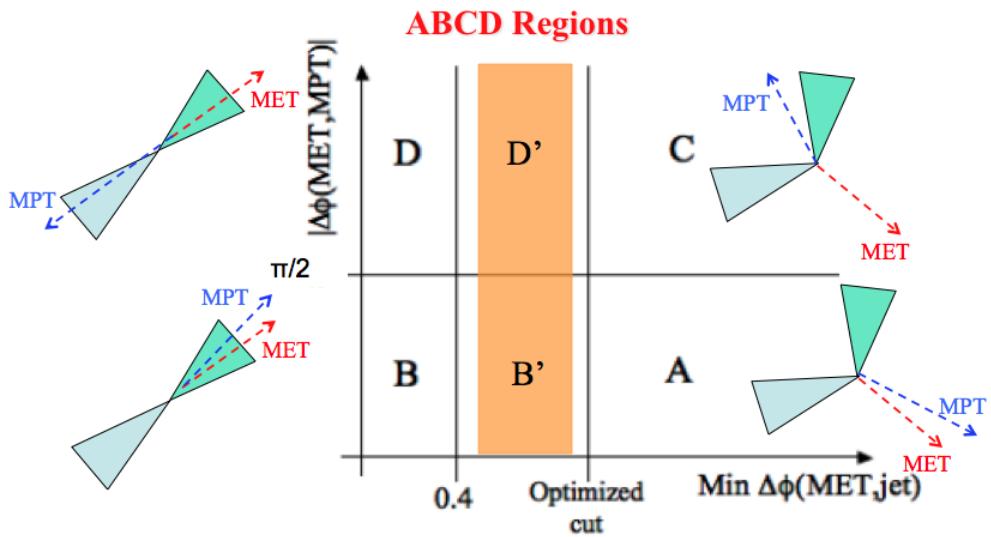


Figure 228: Sketch of jets, E_T^{miss} , and p_T^{miss} in the regions used for the 0-lepton multijet estimate.

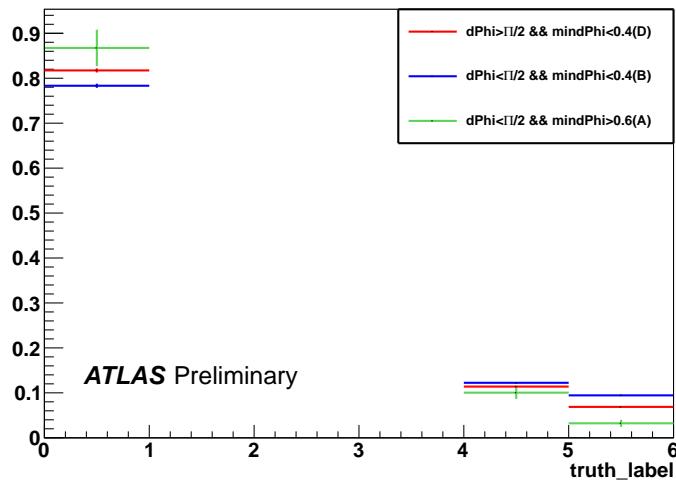


Figure 229: Truth label of the jet closest to the E_T^{miss} in ϕ showing the enhancement of b -jets in region B and that both R_B and R_D will overestimate the tagging rate in region A. This plot was made using Pythia dijet Monte Carlo simulation.

Not reviewed, for internal circulation only

N_{jet}	p_T^Z (GeV)	b -tag Region	MJ Events (with R_D)	EW Background	MJ/EW (%)
2	120-160	LL	12.08	800.16	1.51
		MM	5.77	410.94	1.41
		TT	2.42	284.01	0.85
	160-200	LL	1.48	255.93	0.58
		MM	0.61	118.95	0.52
		TT	0.26	76.95	0.34
	>200	LL	0.98	119.95	0.49
		MM	0.40	81.37	0.49
		TT	0.10	49.21	0.20
3	120-160	LL	2.88	221.29	1.30
		MM	1.56	141.37	1.11
		TT	0.74	100.08	0.74
	160-200	LL	0.71	92.29	0.76
		MM	0.24	49.89	0.47
		TT	0.18	30.40	0.39
	>200	LL	0.37	86.35	0.43
		MM	0.17	35.14	0.48
		TT	0.06	19.25	0.32

Table 95: Result for estimate of multijet events in the signal region of the 0-lepton dijet mass analysis.

N_{jet}	MJ Events (with R_D)	EW Background	MJ/EW (%)
2	15.58	1653.65	0.94
3	3.49	697.88	0.50

Table 96: Result for estimate of multijet events in the signal region of the 0-lepton MVA analysis.

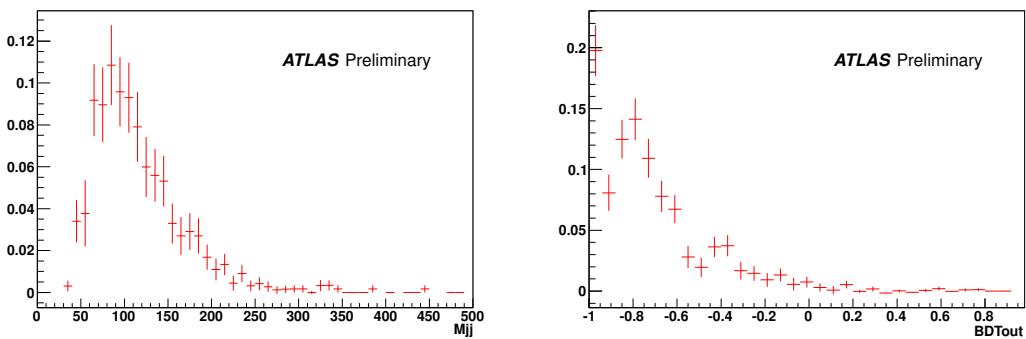


Figure 230: Shape used for the MJ in the 0-lepton analysis for the di-jet mass and BDT on the left and right respectively. For each the same shape is used in all search regions.

4546 R Multijet background for 1-lepton analysis

4547 Multijet events mimicking the $WH \rightarrow \ell v b\bar{b}$ signal topology is a major background of the 1-lepton
 4548 analysis. As with most backgrounds of this type, the efficiency is small but the production rate is so large
 4549 that the background cannot be ignored easily nor can enough MC be produced to simulate the processes.
 4550 For these reasons, the multijet background is estimated directly from data. The following outlines the
 4551 procedure used to estimate this background, an optimization to reduce its contribution, and modeling
 4552 checks performed in order to ascertain the systematic uncertainty.

4553 R.1 Template Overview

4554 Data events are used to estimate the contribution of multijet events which satisfy the 1-lepton selection. A
 4555 multijet model region or template region is defined from which data events are taken and the electroweak
 4556 contribution is subtracted to obtain the multijet template. The multijet model region is defined as Medium
 4557 VH leptons with the modification of $0.05(0.07) < iso_{track} < 0.50$ in the $e(\mu)$ channel, $iso_{calo} < 0.07$ in
 4558 both and the quality of MediumPP [19] in the e channel on top of the *VeryLoose* LH criteria. After overlap
 4559 removal, the iso_{track} range is modified for nominal and systematic evaluations as described below. All
 4560 event level cuts are applied. The following describes the studies used to arrive at the above definition
 4561 which is a modification of the EPS choice. The template is then fit in the signal region to obtain the
 4562 expected multijet yield.

4563 R.2 Multijet Rejection

4564 For EPS [11] the multijet background was reduced with requiring $E_T^{\text{miss}} > 20$ GeV for $p_T^W < 200$ GeV
 4565 and $E_T^{\text{miss}} > 50$ GeV above. Also for $p_T^W < 160$ GeV an $m_T^W > 40$ GeV cut was employed. The signal
 4566 efficiency for the multijet rejection cuts was 65% for $p_T^W < 120$ GeV (using the MVA selection i.e. no
 4567 $\Delta R(bb)$ cuts). An optimization was done using the events in the multijet template region and the signal
 4568 MC. To avoid over-tuning of cuts and to get a realistic estimate of cut efficiencies, a closure test was
 4569 performed. In the signal region, the Monte Carlo predictions for the EW backgrounds are subtracted
 4570 to the data to get another estimate of the multijet templates. The overall S/B is at the per-mill level
 4571 and the multijet yield is much larger than the expected Higgs yield before the application of dedicated
 4572 anti-MJ cuts so this procedure should be relatively safe. As in the signal region multijet is not the
 4573 dominant background, the EW background subtraction can affect significantly the multijet estimation
 4574 through normalization and systematics issues. In conclusion, both multijet templates (from the QCD
 4575 control region and from the signal region) have their own bias, but the use of both of them gave a handle
 4576 on the robustness of the proposed cuts since at the time of this optimization, the modeling of the analysis
 4577 was not stable.

4578 Lepton variables were considered such as properties of jet overlapping the electrons, impact parameters,
 4579 and isolations. A $|d_0 \text{ significance}| < 3$ cut was entertained for a time but was then shown to provide
 4580 no additional rejection after all other cuts are applied. The MV1 output of the jet overlapping an electron
 4581 is interesting but requires a dedicated calibration since MV1 is not calibrated for electrons. The iso_{calo}
 4582 was tightened for the signal region leptons to 0.04 from (0.07) since this rejected between 25 and 35%
 4583 of multijet events with 95% signal efficiency which increased with p_T^W .

4584 Several event level cuts were explored including two-dimensional cuts on m_T^W and E_T^{miss} , STVF E_T^{miss} ,
 4585 and p_T^{miss} , but a cut of $M_{eff} > 180$ GeV for $p_T^W < 120$ GeV with the m_T^W and E_T^{miss} cuts in the same
 4586 region removed was chosen in the end. Figure 231 shows an MVA output for the multijet and signal, left
 4587 and right respectively, for the EPS (optimized) cuts in blue (red). Two different trainings were used but
 4588 one can clearly see that the change in cuts resulted in a large increase in the signal and no considerable
 4589 increase of the multijet component in the sensitive region of the MVA output. This optimization study

4590 called for a $E_{\text{T}}^{\text{miss}}$ cut of 20 GeV for the high p_{T}^W region ($p_{\text{T}}^W > 120$ GeV). Therefore in the dijet analysis
 4591 with $120 < p_{\text{T}}^W < 200$ GeV the $E_{\text{T}}^{\text{miss}}$ cut was reduced to 20 GeV (from 25 GeV [11]). Above p_{T}^W of
 4592 200 GeV a reduction of the $E_{\text{T}}^{\text{miss}}$ cut from 50 GeV decreases the expected dijet mass sensitivity so the
 4593 EPS value was maintained. The success of dropping the m_{T}^W cut for $p_{\text{T}}^W < 120$ GeV prompted a test to
 4594 abandon it in the region $120 < p_{\text{T}}^W < 160$ GeV in the dijet mass analysis which subsequently showed an
 4595 increase in both the signal and background yield by more than 50% and no large increase in the multijet
 4596 component was observed as shown in Figure 232. In total these changes increased the expected statistical
 4597 sensitivity of the 2-jet region in the 1-lepton analysis 5 (8)% in the MVA (dijet) analysis. Note the upper
 4598 bound of m_{T}^W which was present for EPS has been maintained in the dijet mass analysis.

Not reviewed, for internal circulation only

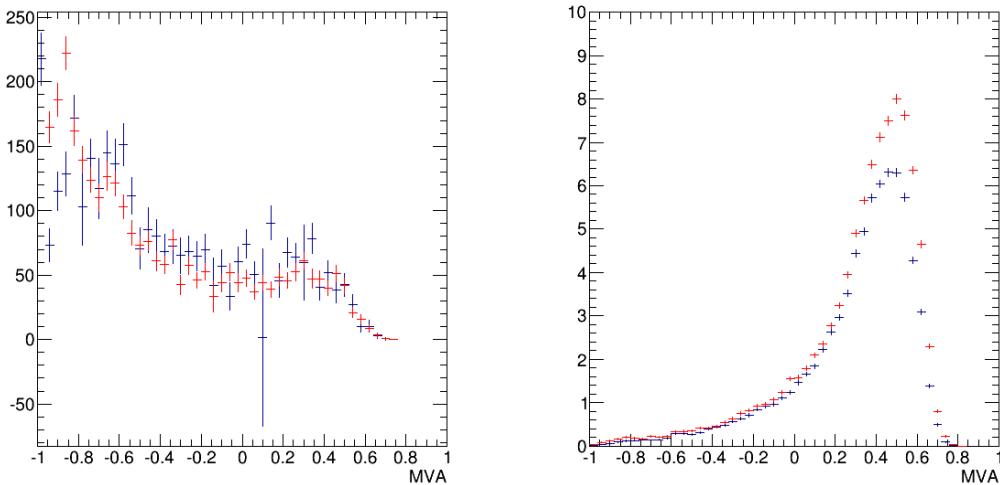


Figure 231: This figure shows an MVA output for the multijet and signal on the left and right respectively for the EPS (optimized) cuts in blue (red) discussed in Section 3.4. Two different trainings were used but one can clearly see that the change in cuts resulted in a large increase in the signal and no considerable increase of the multijet component in the sensitive region of the MVA output. The difference yields a 17% increase in the MVA analysis sensitivity.

4599 R.3 Multijet Template Region

4600 Multijet events are taken from an orthogonal region in data referred to as the multijet template region.
 4601 This region is constructed to be orthogonal to the signal region by selecting leptons with inverted track
 4602 isolation criteria and vetoing any event with multiple leptons (counting both the normal leptons and
 4603 the leptons used to obtain the multijet template described here). The low end of the $\text{iso}_{\text{track}}$ range was
 4604 moved from 0.04 (EPS) to 0.05 (0.07) in the electron (muon) channel in order to reduce the electroweak
 4605 contamination. The upper range was extended to 0.50 to increase statistics. In the muon channel the
 4606 full range is used and statistically half the range is used for the up and down systematics ($0.07 < \text{iso}_{\text{track}} < 0.095$ and $0.095 < \text{iso}_{\text{track}} < 0.50$ respectively) (SysMJJMuTrkIso). In the electron channel
 4607 $0.05 < \text{iso}_{\text{track}} < 0.12$ is used for the nominal template (roughly 1/2 the statistics) and the upper range
 4608 $0.12 < \text{iso}_{\text{track}} < 0.50$ is used for a systematic variation which is symmetrized (SysMJE1TrkIso).
 4609 Regardless of the range used to select the leptons, the full range, $0.05(0.07) < \text{iso}_{\text{track}} < 0.50$ in electron
 4610 (muon) events, is used for the objects in overlap removal. Afterwards, the range is modified for the
 4611 desired selection. As stated above, the iso_{calo} cut was tightened to 0.04 from 0.07 but this was not done
 4612 for the multijet template to increase the available statistics. It has been shown that this change in the range
 4613 also changed the electroweak contamination which has a different effect on the template compared to the
 4614

Not reviewed, for internal circulation only

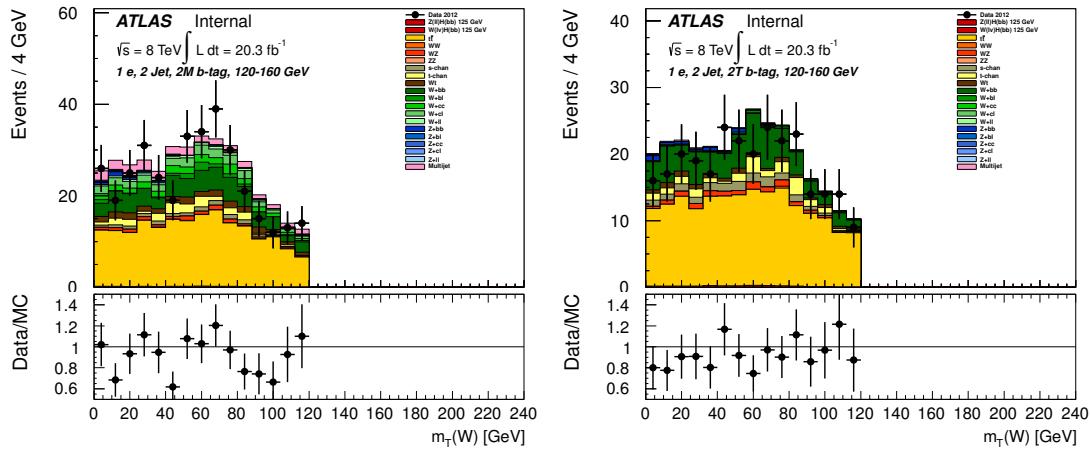


Figure 232: This figure shows the m_T^W distribution in the for $120 < p_T^W < 160$ in the electron channel of the dijet mass analysis after requiring two exclusive medium and tight tags on the left and right respectively. For $m_T^W < 40$ GeV, which was excluded previously [11], the agreement is acceptable and the multijet contribution is not significantly more then above 40 GeV. Removing this cut increases the signal and background in this p_T^W range by 50%.

4615 iso_{track} change in the electron channel only. A reduced upper limit of 0.04, matching the signal region is
 4616 used for a systematic variation in the electron channel with the effect symmetrized (`SysMJE1CaloIso`).
 4617 In terms of object quality, other choices were explored besides using MediumPP in the electron channel.
 4618 VeryTight LH and Tight LH cuts both reduce the available template statistics and while looking very
 4619 similar amongst themselves do differ somewhat from the MediumPP template. The Medium LH cut
 4620 produced a template very similar to the MediumPP template. In light of this information, the choice
 4621 from EPS MediumPP was preserved. An inversion of iso_{calo} was explored for the nominal template and
 4622 for a systematic but was not used since many variables, including m_T^W were adversely affected. The m_T^W
 4623 template seemed to suffer from a very large contamination from electroweak events.

4624 R.4 Multijet Normalization

The above template method does not determine the normalization. A fit to data is performed using the E_T^{miss} distribution. This fit is performed separately for muon and electron events, 2 and 3 jet events, and 1 and 2 b-tag events. The 2 b-tag region is fit inclusively, that is 2L, 2M, and 2T events are all fit with one multijet scale factor. Due to the small contribution of multijet events to the 2T region, this helps stabilize the normalization estimate. Since the multijet normalization is coupled to the electroweak background normalization, a scale factor for the electroweak background is also used. Also, a set of scale factors from the profile likelihood, determined from the ratio of the post-fit yield to the pre-fit yield, are also used to have the electroweak background as close to our best guess as possible. The E_T^{miss} variable was found to be the most stable in terms of template variations. Other variables such as m_T^W and lepton p_T were considered.

4635 The normalization uncertainty (`SysMJMuNorm` and `SysMJE1Norm`) is derived from two sources added
 4636 in quadrature. One is the statistical error of the multijet scale factor. The normalization fit is performed
 4637 inclusively in 2-tag events, but the statistical error is taken from the exclusive fits. That is the normal-
 4638 ization in each 2L, 2M, and 2T events separately. Even though the inclusive fit is used to determine the
 4639 normalization, the statistical error of exclusive fits are used for the systematic to reflect our imperfect
 4640 knowledge of the heavy-flavor contribution to the multijet template. The second, is the difference in the

4641 multijet yield when the EW scale factors are used compared to when they are not used.

4642 R.5 Template Statistics: Using 1 b-tag events for the 2 b-tag regions

4643 The templates have decent statistics but after 2-tags and in the high p_T^W region, the events dry up. It has
 4644 been shown that the kinematics of 1-tag match quite well the kinematic of 2 b-tag events in the muon
 4645 channel (Figures 234–237) and in 2L tag electron events. The 2T tag events are considerably different
 4646 from the 1-tag kinematics in the electron channel. The muon channel multijet is predominantly from
 4647 heavy flavor jet decays, while the electron channel is a mixture of heavy flavor jet decays and light jets
 4648 or photons faking electrons therefore the difference in relationship between 1 and 2 b-tag events based
 4649 on the lepton flavor is not unexpected. A procedure was developed which, given the rank (leading or
 4650 sub-leading) of the un-tagged jet and the MV1c value of the tagged jet, a MV1c value is generated for
 4651 the un-tagged jet promoting this event into the 2-tag region. Said procedure reproduces exactly (by
 4652 construction) the 2D distribution of the MV1c of the two leading jets and is performed separately on
 4653 the muon and electron channel. Afterwards, in the electron + 2-jet events only, the 1-tag events used
 4654 in the 2L, 2M, and 2T tagged template are each kinematically reweighted to match the distribution of the
 4655 ‘real’ 2-tag template. The reweighting is performed sequentially on $\Delta R(bb)$ and p_T^W using the ratio of
 4656 1-tag over 2-tag events. The TH1 smooth function is used five times on the ratio such that the statistical
 4657 fluctuations of the limited 2-tag events are not encapsulated in the reweighting. Figure reffig:mjcorr
 shows the corrections in $\Delta R(bb)$ and p_T^W for LL, MM and TT events.

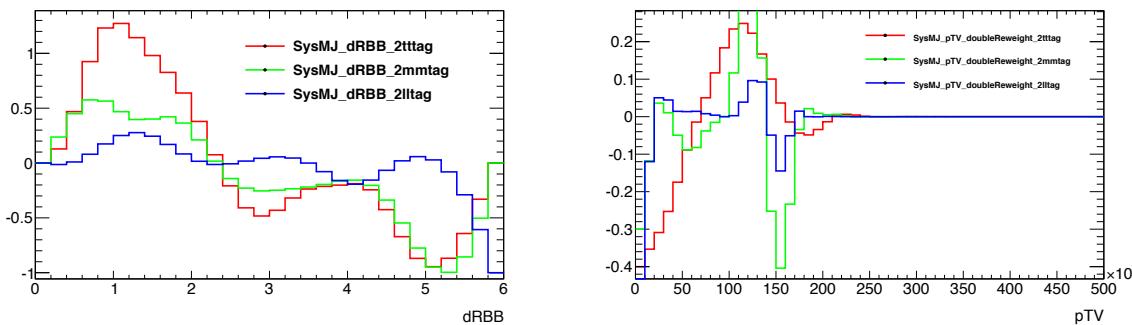


Figure 233: kinematic reweigh functions on $\Delta R(bb)$ and p_T^W used on the 1-tag estimate to match the distribution of the ‘real’ 2-tag template for LL, MM and TT.

4658
 4659 ‘Real’ 2-tag events are not discarded and represent roughly 10% of the events used for the final 2-tag
 4660 multijet templates. The variables used for the reweighting and the dijet invariant mass as well as the BDT
 4661 itself (in the MVA selection) are shown in Figures 238 to 242 for 2L, 2M, and 2T events respectively along
 4662 with several important kinematic variables in Figures 244 to 248 for the same regions. One half of the
 4663 reweight is used as a systematic variation (SysMJDR and SysMJPtV). In the muon channel and in 3-jet
 4664 events, such a reweighting is not applied.

Not reviewed, for internal circulation only

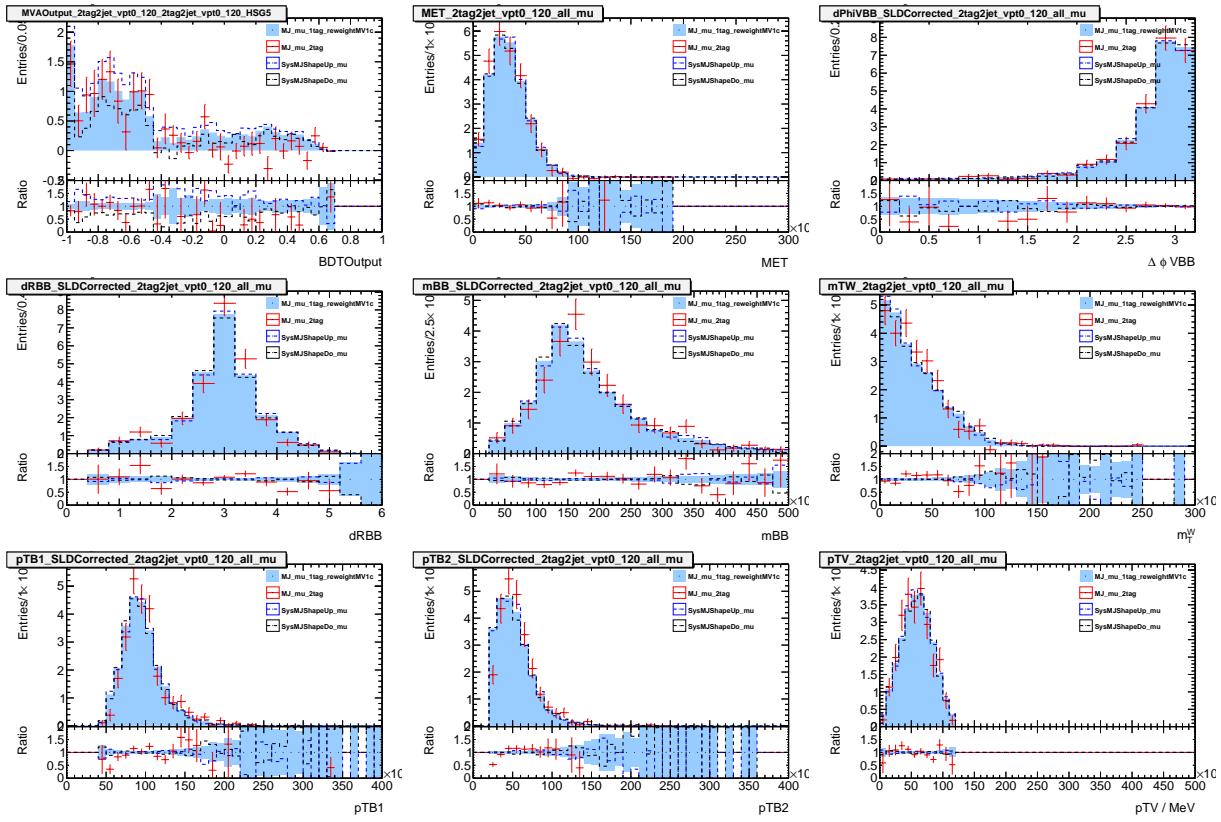


Figure 234: A comparison of 1-tag and 2-tag multijet events in the muon 2-jet channel with $p_T^W < 120$ GeV. The red histogram is 2-tag events, the blue solid histogram is the 1-tag events spoofed into the 2-tag region and the dashed histograms show the effect from the iso_{track} systematics

Not reviewed, for internal circulation only

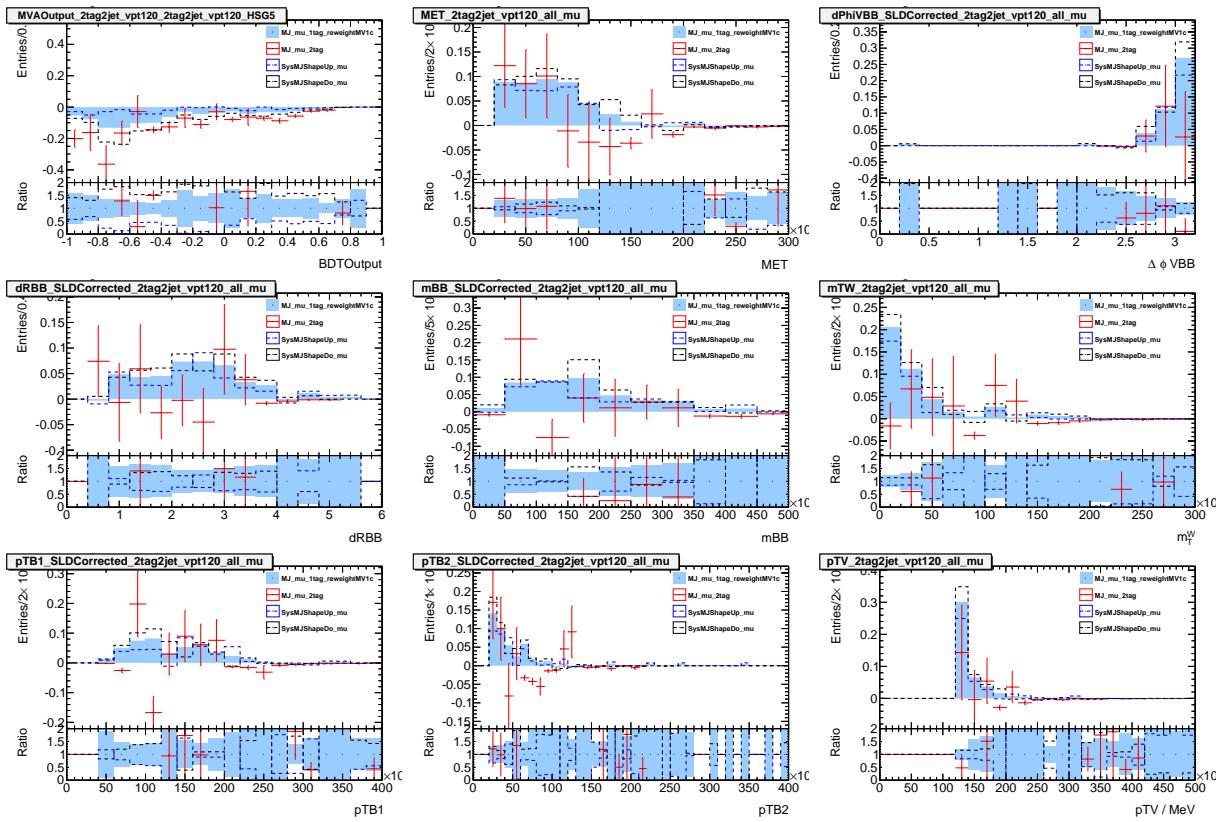


Figure 235: A comparison of 1-tag and 2-tag multijet events in the muon 2-jet channel with $p_T^W > 120$ GeV. The red histogram is 2-tag events, the blue solid histogram is the 1-tag events spoofed into the 2-tag region and the dashed histograms show the effect from the iso_{track} systematics

Not reviewed, for internal circulation only

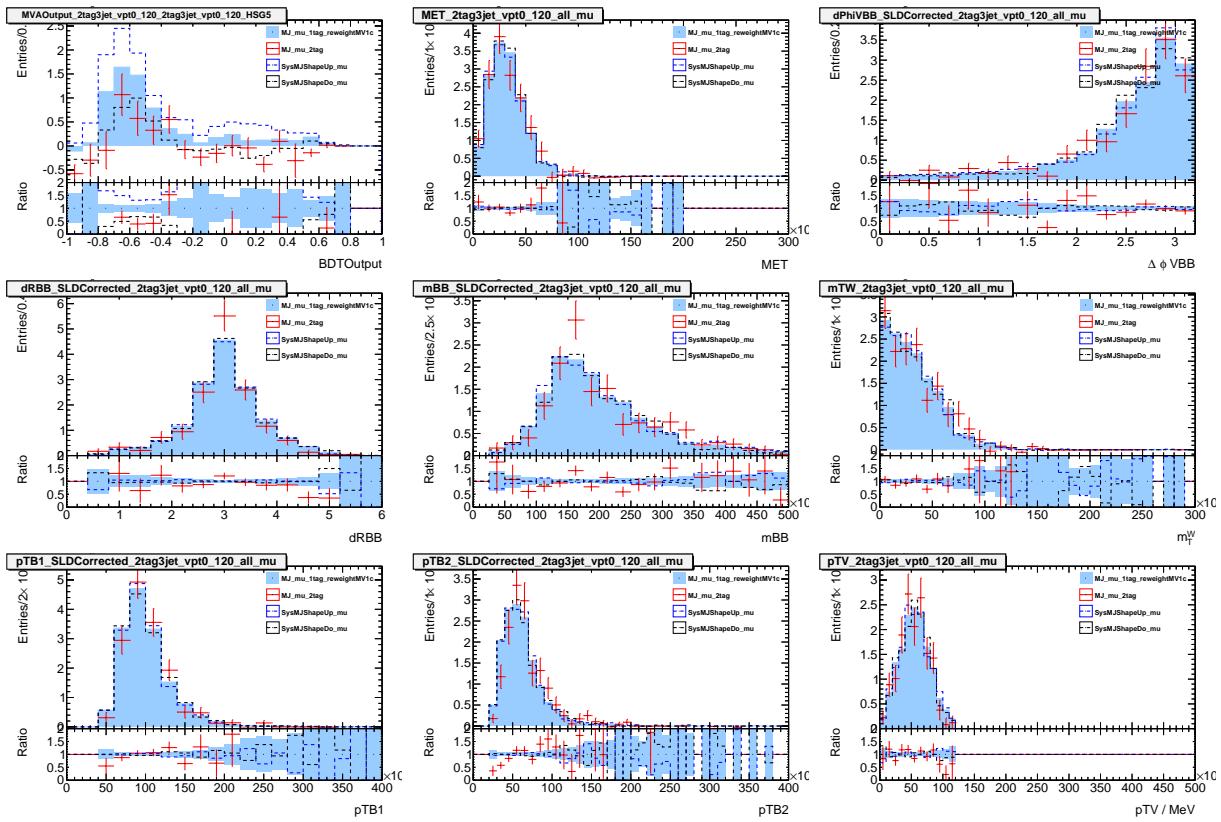


Figure 236: A comparison of 1-tag and 2-tag multijet events in the muon 3-jet channel with $p_T^W < 120$ GeV. The red histogram is 2-tag events, the blue solid histogram is the 1-tag events spoofed into the 2-tag region and the dashed histograms show the effect from the iso_{track} systematics

Not reviewed, for internal circulation only

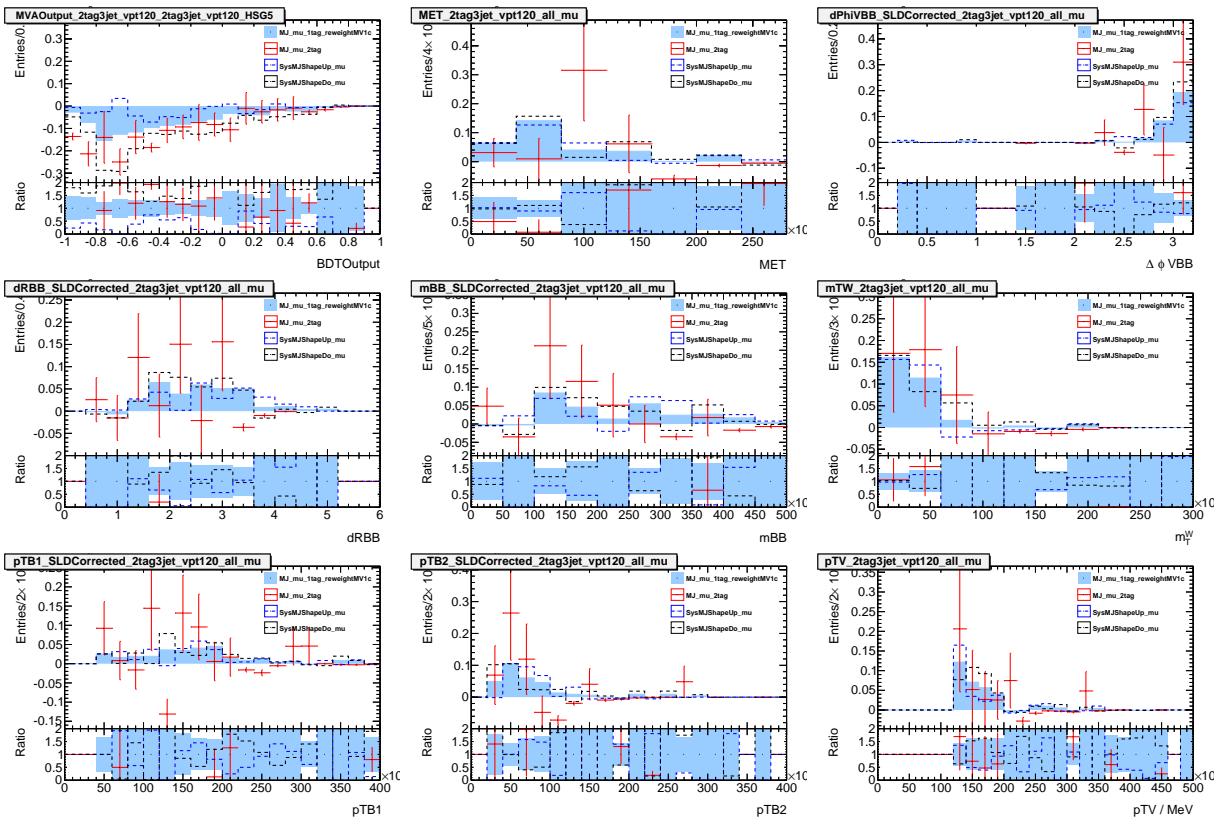


Figure 237: A comparison of 1-tag and 2-tag multijet events in the muon 3-jet channel with $p_T^W > 120$ GeV. The red histogram is 2-tag events, the blue solid histogram is the 1-tag events spoofed into the 2-tag region and the dashed histograms show the effect from the iso_{track} systematics

Not reviewed, for internal circulation only

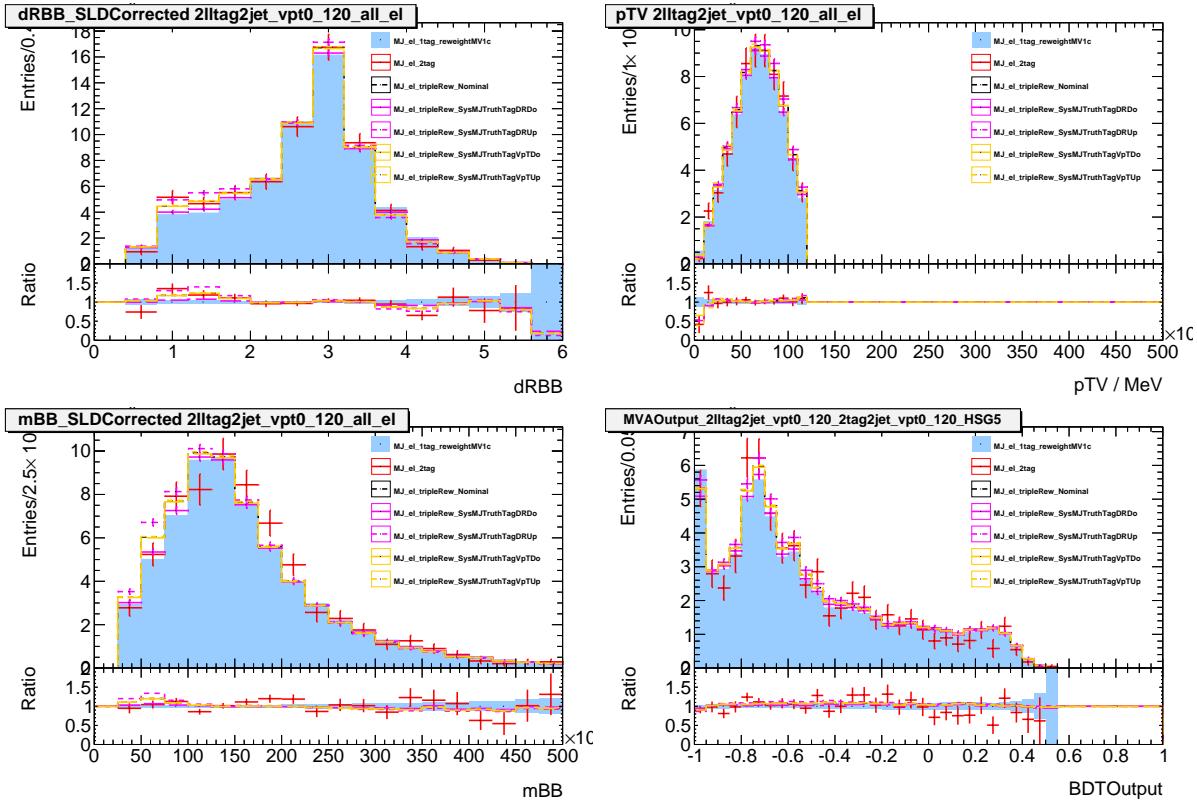


Figure 238: The top two figures show the variables on which the reweighting was derived and the bottom two show the dijet mass and the BDT for 2L tag $p_T^W < 120$ GeV electron events. The red histogram is 2-tag events, the blue solid histogram is the 1-tag events spoofed into the 2-tag region and the black distribution shows the reweighted 1-tag events. The purple and yellow histograms are centered around the black and show the systematic from 1/2 of each reweighting - $\Delta R(bb)$ and p_T^W respectively. The ratio are taken wrt the blue histogram.

Not reviewed, for internal circulation only

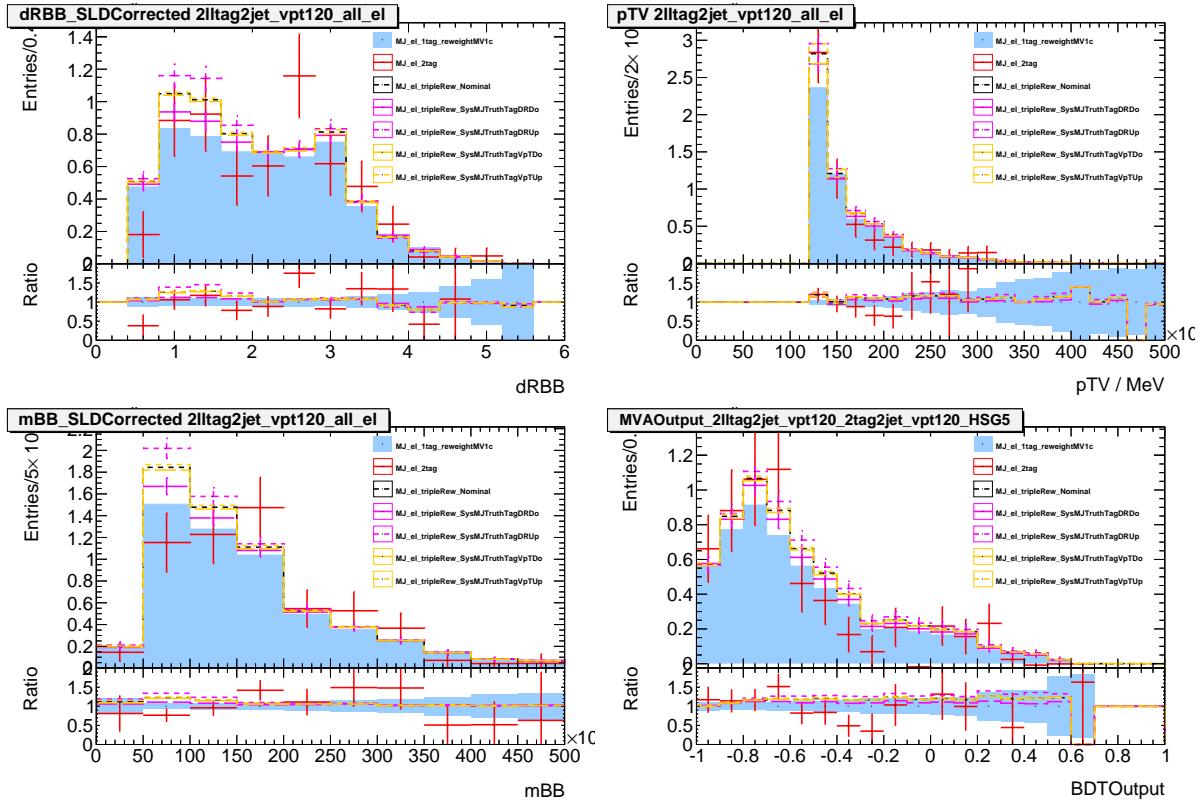


Figure 239: The top two figures show the variables on which the reweighting was derived and the bottom two show the dijet mass and the BDT for 2L tag $p_T^W > 120$ GeV electron events. The red histogram is 2-tag events, the blue solid histogram is the 1-tag events spoofed into the 2-tag region and the black distribution shows the reweighted 1-tag events. The purple and yellow histograms are centered around the black and show the systematic from 1/2 of each reweighting - $\Delta R(bb)$ and p_T^W respectively. The ratio are taken wrt the blue histogram.

Not reviewed, for internal circulation only

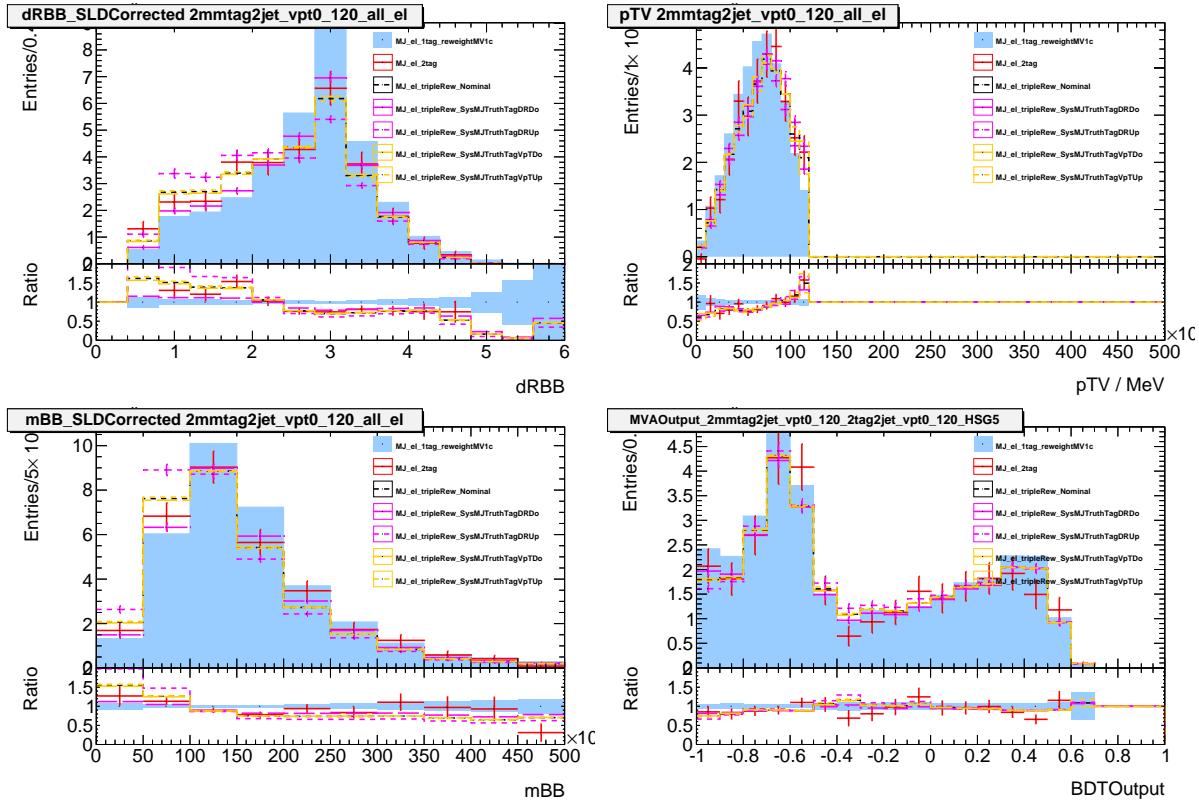


Figure 240: The top two figures show the variables on which the reweighting was derived and the bottom two show the dijet mass and the BDT for 2M tag $p_T^W < 120$ GeV electron events. The red histogram is 2-tag events, the blue solid histogram is the 1-tag events spoofed into the 2-tag region and the black distribution shows the reweighted 1-tag events. The purple and yellow histograms are centered around the black and show the systematic from 1/2 of each reweighting - $\Delta R(bb)$ and p_T^W respectively. The ratio are taken wrt the blue histogram.

Not reviewed, for internal circulation only

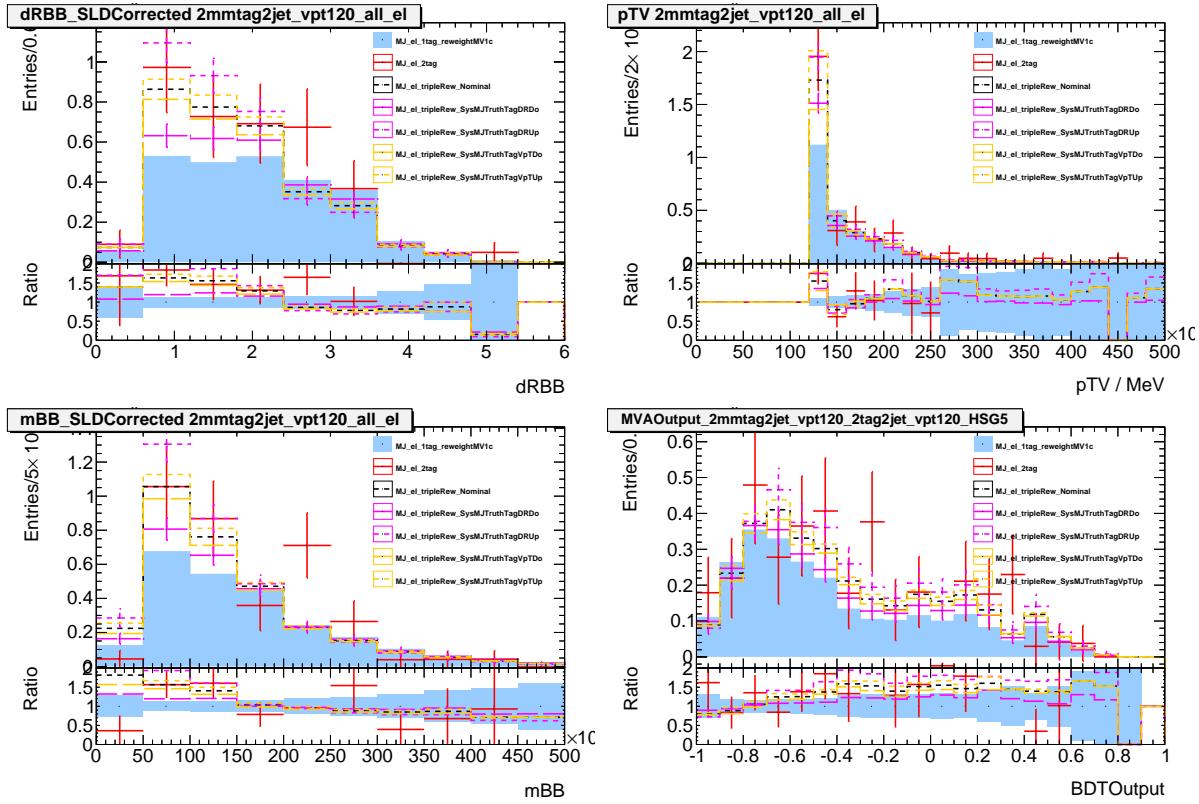


Figure 241: The top two figures show the variables on which the reweighting was derived and the bottom two show the dijet mass and the BDT for 2M tag $p_T^W > 120$ GeV electron events. The red histogram is 2-tag events, the blue solid histogram is the 1-tag events spoofed into the 2-tag region and the black distribution shows the reweighted 1-tag events. The purple and yellow histograms are centered around the black and show the systematic from 1/2 of each reweighting - $\Delta R(bb)$ and p_T^W respectively. The ratio are taken wrt the blue histogram.

Not reviewed, for internal circulation only

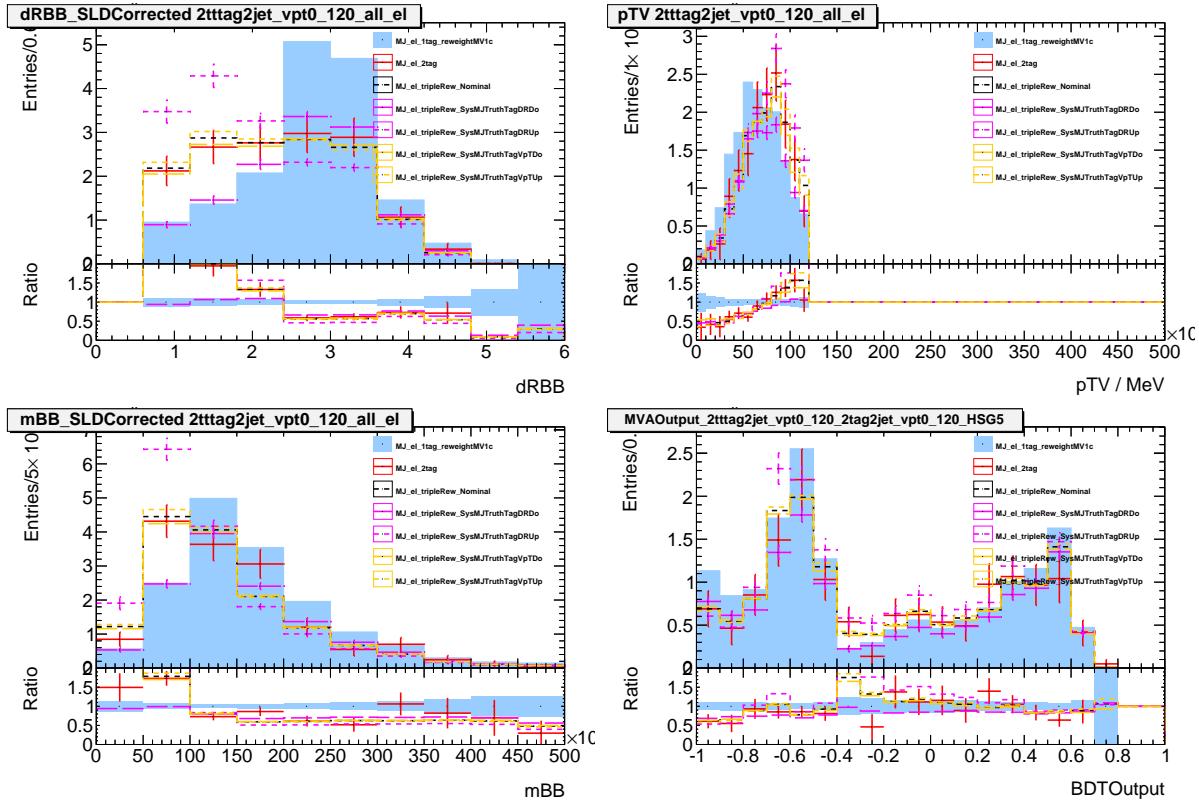


Figure 242: The top two figures show the variables on which the reweighting was derived and the bottom two show the dijet mass and the BDT for 2T tag $p_T^W < 120$ GeV electron events. The red histogram is 2-tag events, the blue solid histogram is the 1-tag events spoofed into the 2-tag region and the black distribution shows the reweighted 1-tag events. The purple and yellow histograms are centered around the black and show the systematic from 1/2 of each reweighting - $\Delta R(bb)$ and p_T^W respectively. The ratio are taken wrt the blue histogram.

Not reviewed, for internal circulation only

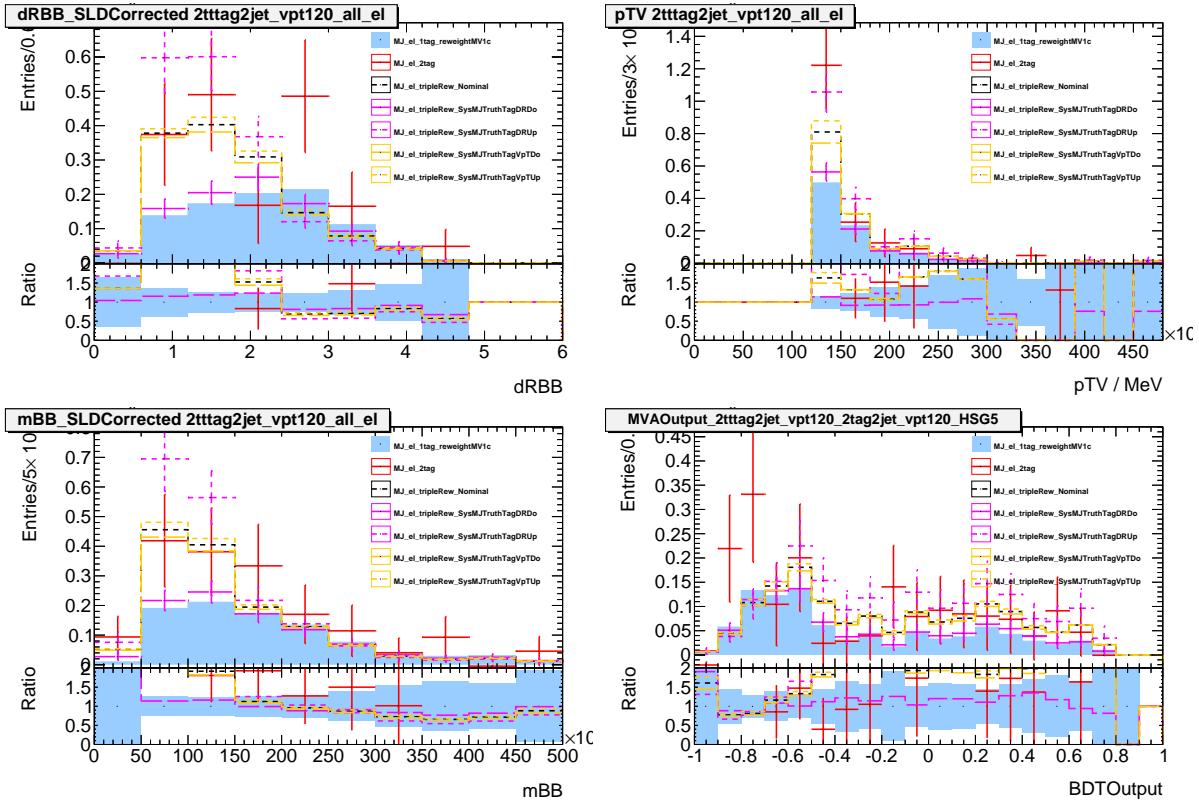


Figure 243: The top two figures show the variables on which the reweighting was derived and the bottom two show the dijet mass and the BDT for 2T tag $p_T^W > 120$ GeV electron events. The red histogram is 2-tag events, the blue solid histogram is the 1-tag events spoofed into the 2-tag region and the black distribution shows the reweighted 1-tag events. The purple and yellow histograms are centered around the black and show the systematic from 1/2 of each reweighting - $\Delta R(bb)$ and p_T^W respectively. The ratio are taken wrt the blue histogram.

Not reviewed, for internal circulation only

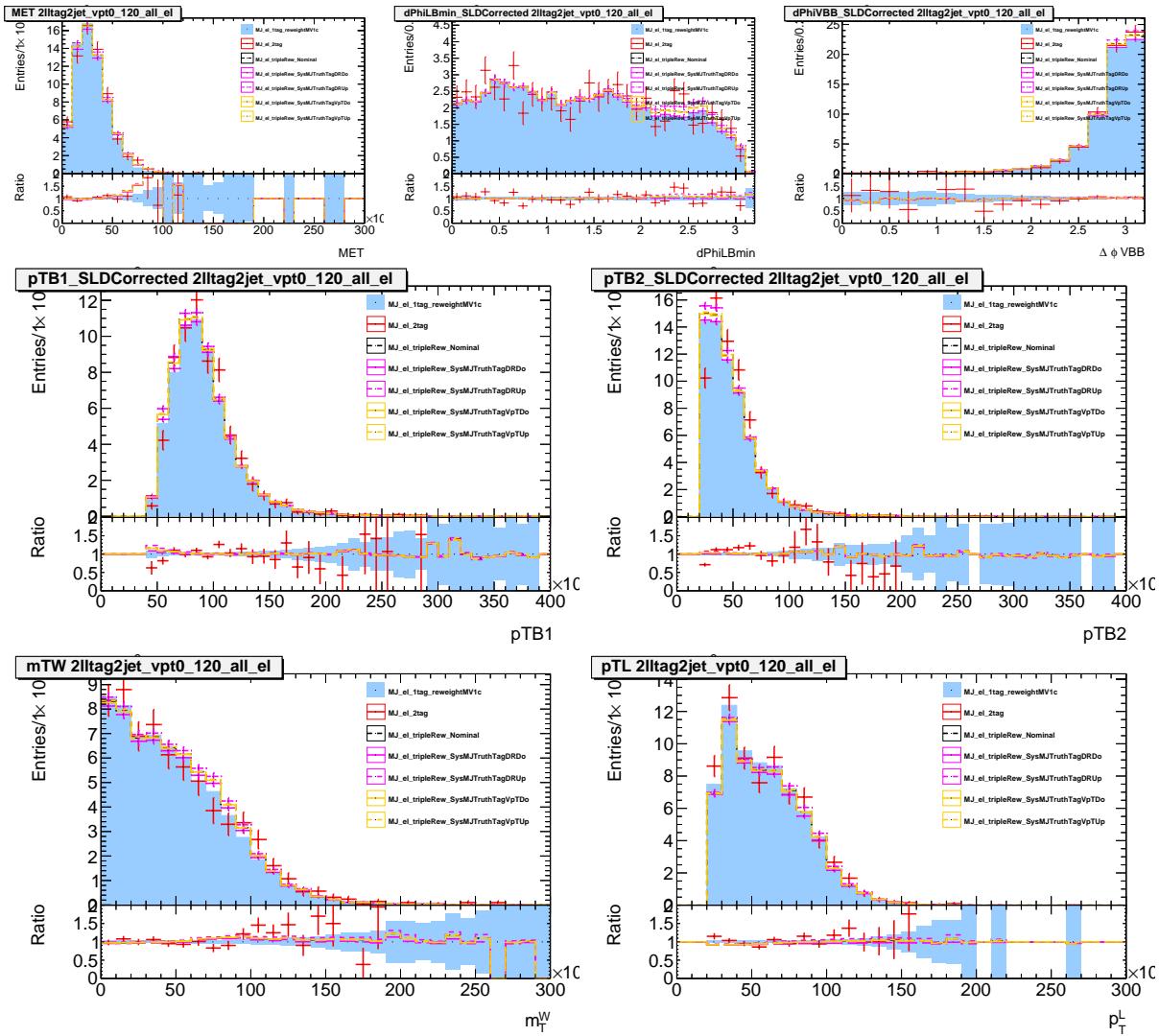


Figure 244: In 2L tag $p_T^W < 120$ GeV electron events, the top three variables are E_T^{miss} , $\Delta\phi(l, b)$, and $\Delta\phi(V, B)$, the middle two show the p_T of the leading two jets and the bottom two are m_T^W and lepton p_T . The red histogram is 2-tag events, the blue solid histogram is the 1-tag events spoofed into the 2-tag region and the black distribution shows the reweighted 1-tag events. The purple and yellow histograms are centered around the black and show the systematic from 1/2 of each reweighting - $\Delta R(bb)$ and p_T^W respectively. The ratio are taken wrt the blue histogram.

Not reviewed, for internal circulation only

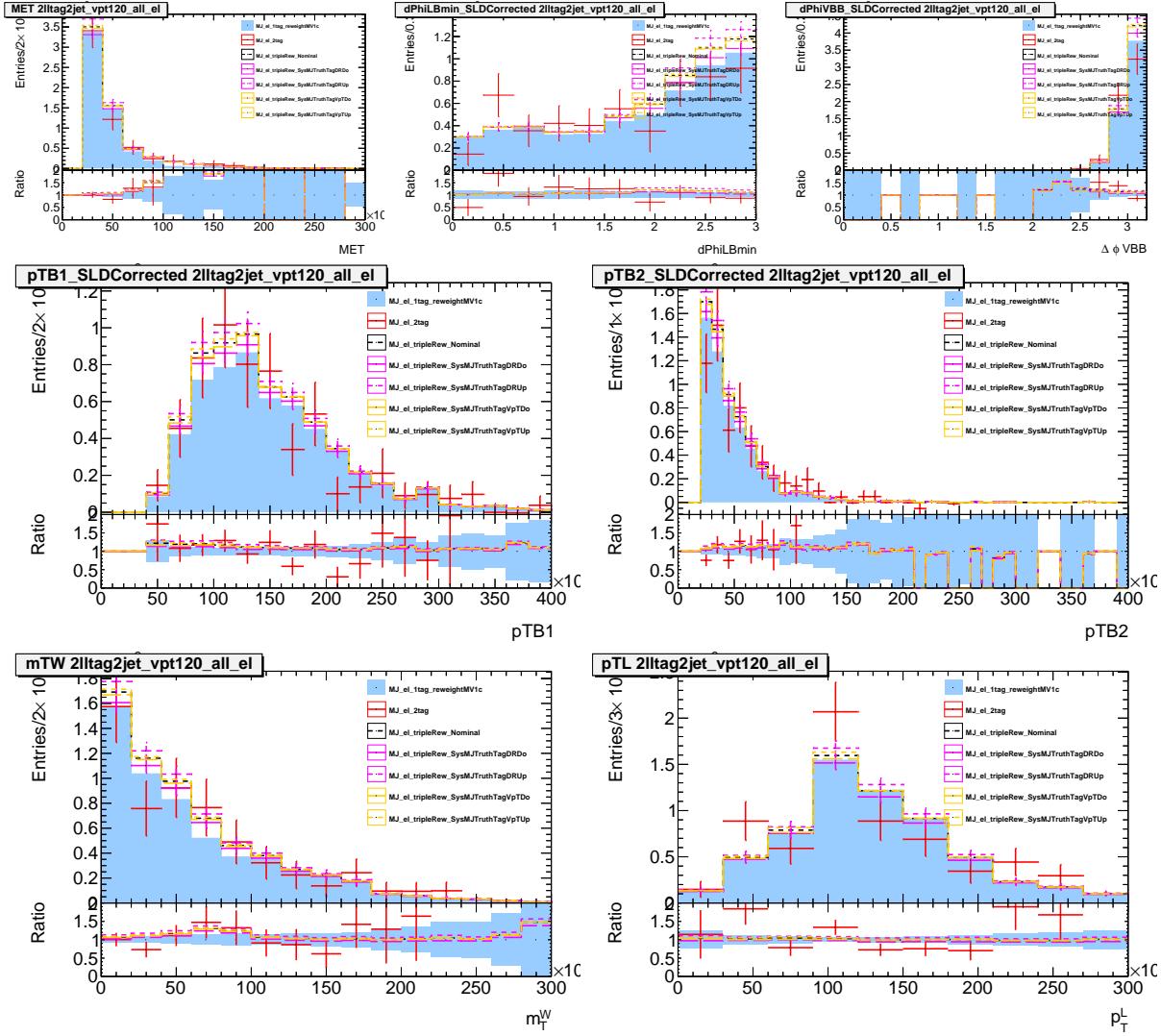


Figure 245: In 2L tag $p_T^W > 120$ GeV electron events, the top three variables are E_T^{miss} , $\Delta\phi(l, b)$, and $\Delta\phi(V, B)$, the middle two show the p_T of the leading two jets and the bottom two are m_T^W and lepton p_T . The red histogram is 2-tag events, the blue solid histogram is the 1-tag events spoofed into the 2-tag region and the black distribution shows the reweighted 1-tag events. The purple and yellow histograms are centered around the black and show the systematic from 1/2 of each reweighting - $\Delta R(bb)$ and p_T^W respectively. The ratio are taken wrt the blue histogram.

Not reviewed, for internal circulation only

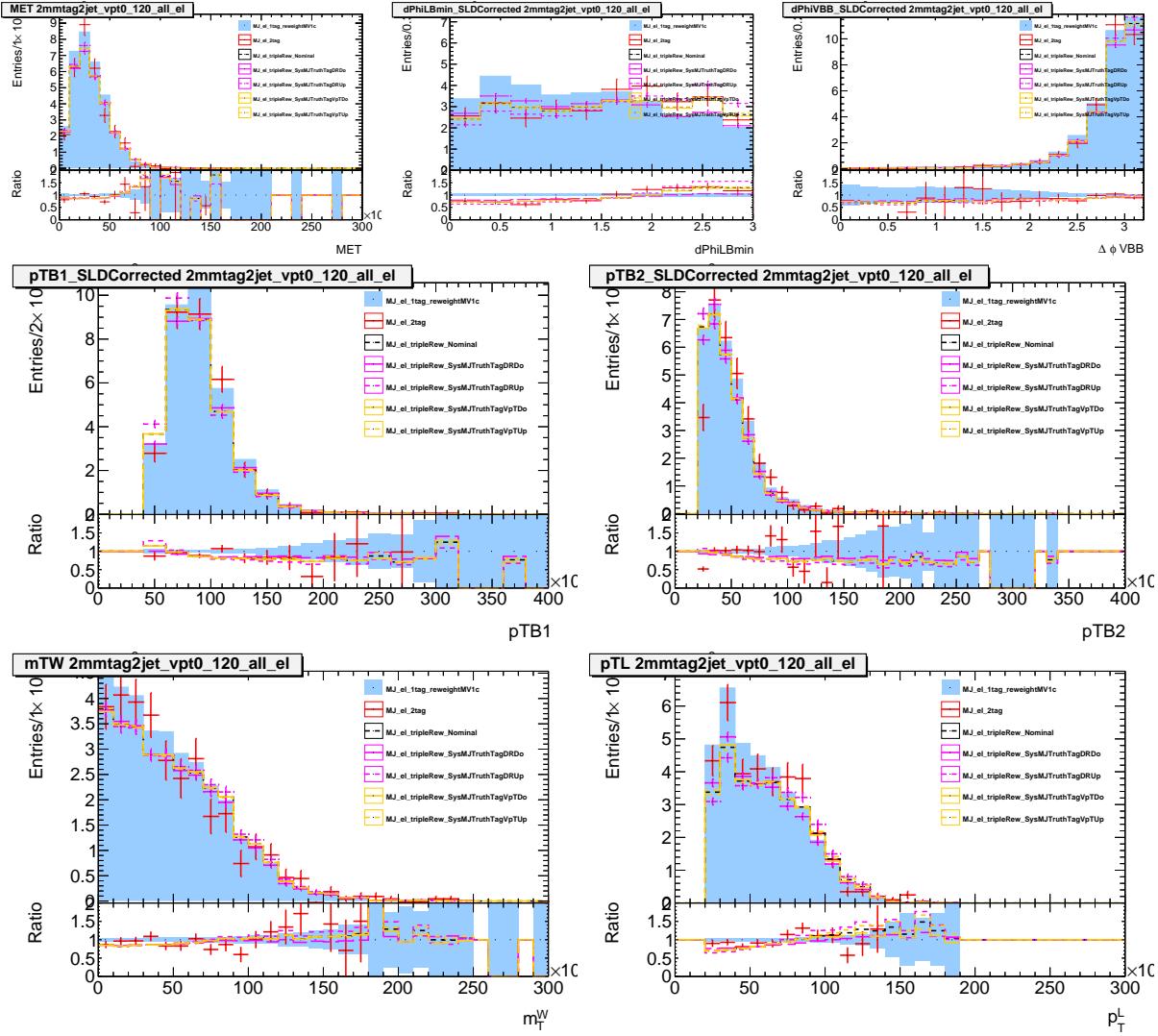


Figure 246: In 2M tag $p_T^W < 120$ GeV electron events, the top three variables are E_T^{miss} , $\Delta\phi(l, b)$, and $\Delta\phi(V, B)$, the middle two show the p_T of the leading two jets and the bottom two are m_T^W and lepton p_T . The red histogram is 2-tag events, the blue solid histogram is the 1-tag events spoofed into the 2-tag region and the black distribution shows the reweighted 1-tag events. The purple and yellow histograms are centered around the black and show the systematic from 1/2 of each reweighting - $\Delta R(bb)$ and p_T^W respectively. The ratio are taken wrt the blue histogram.

Not reviewed, for internal circulation only

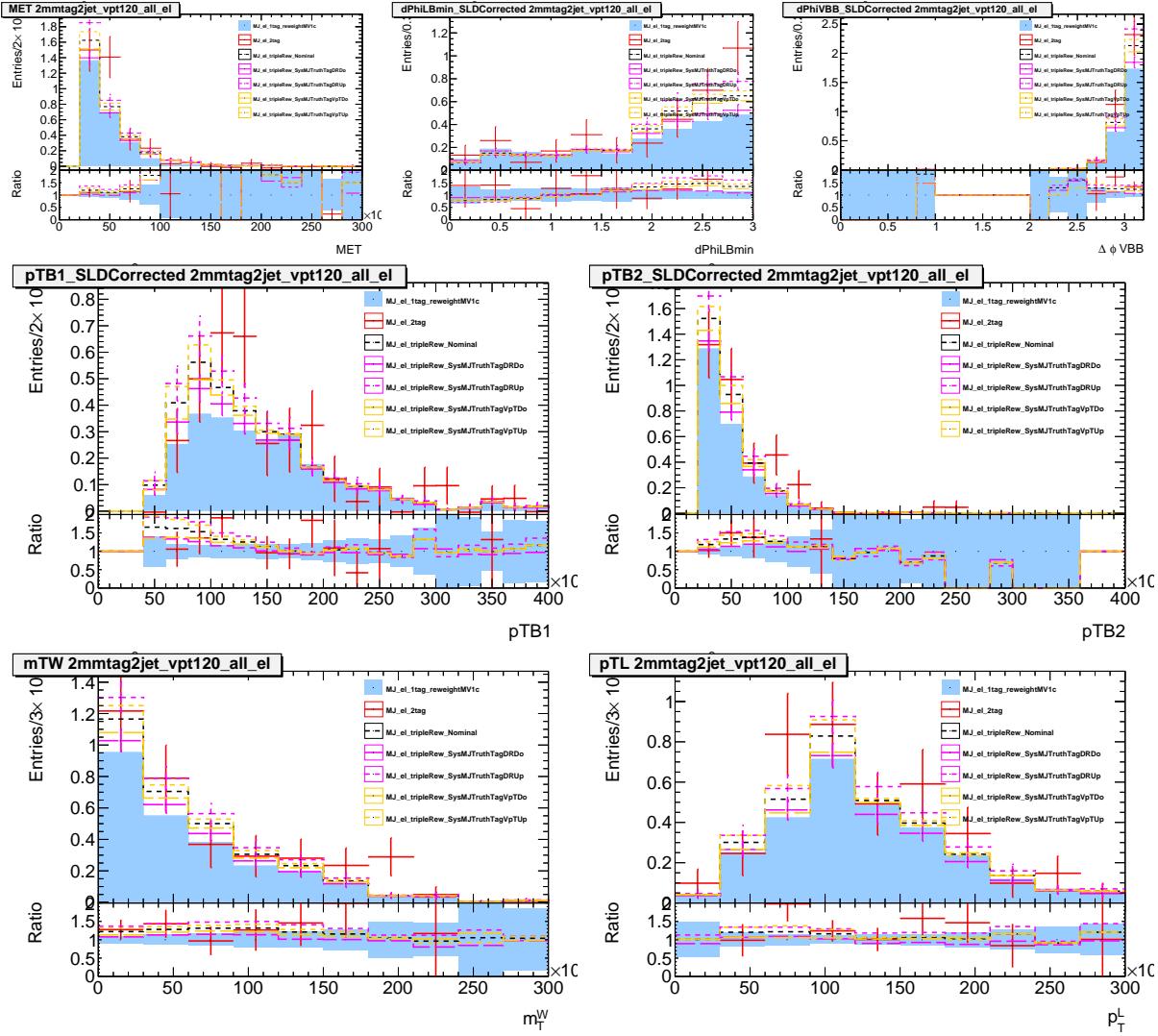


Figure 247: In 2M tag $p_T^W > 120$ GeV electron events, the top three variables are E_T^{miss} , $\Delta\phi(l, b)$, and $\Delta\phi(V, B)$, the middle two show the p_T of the leading two jets and the bottom two are m_T^W and lepton p_T . The red histogram is 2-tag events, the blue solid histogram is the 1-tag events spoofed into the 2-tag region and the black distribution shows the reweighted 1-tag events. The purple and yellow histograms are centered around the black and show the systematic from 1/2 of each reweighting - $\Delta R(bb)$ and p_T^W respectively. The ratio are taken wrt the blue histogram.

Not reviewed, for internal circulation only

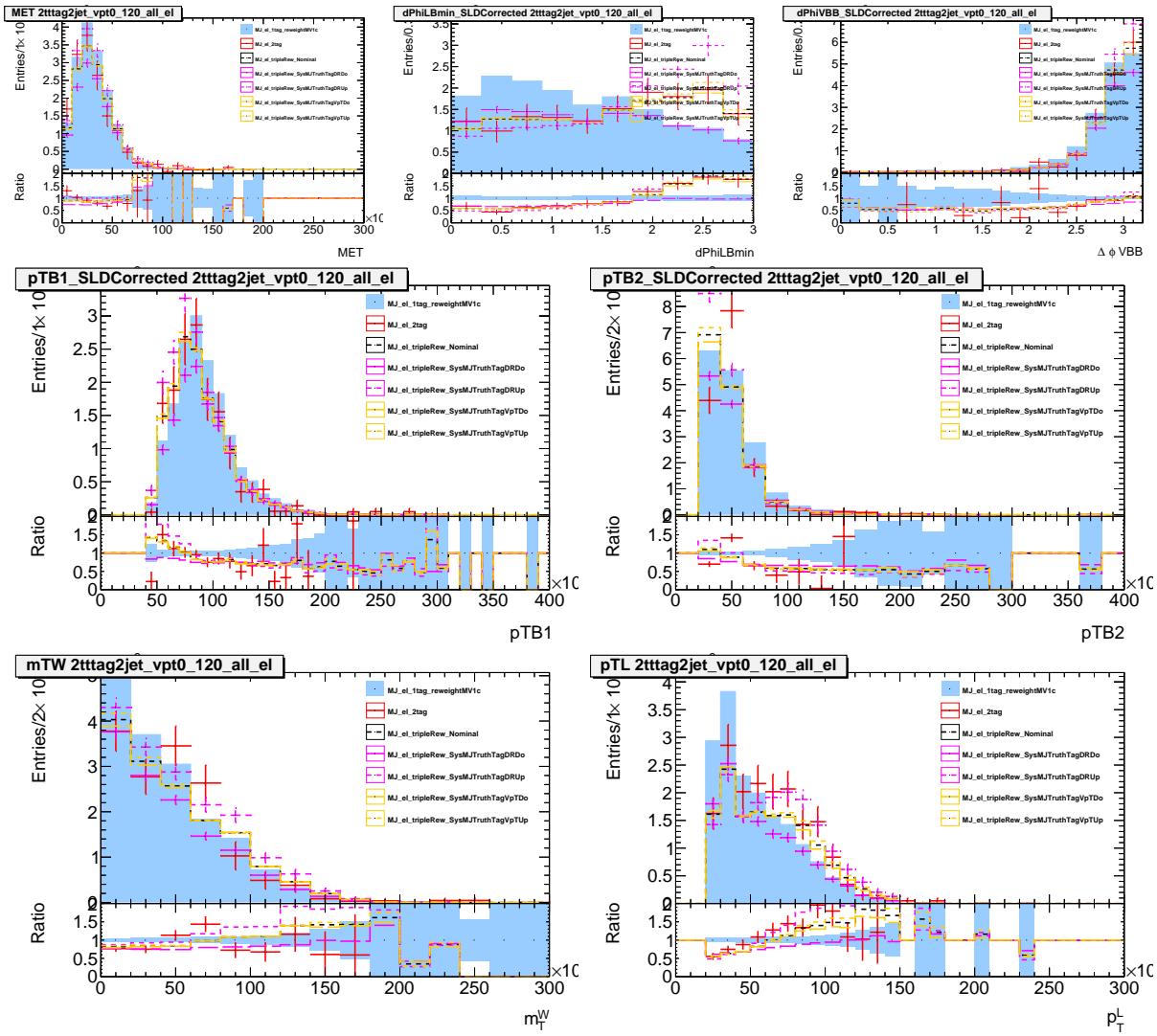


Figure 248: In 2T tag $p_T^W < 120$ GeV electron events, the top three variables are E_T^{miss} , $\Delta\phi(l, b)$, and $\Delta\phi(V, B)$, the middle two show the p_T of the leading two jets and the bottom two are m_T^W and lepton p_T . The red histogram is 2-tag events, the blue solid histogram is the 1-tag events spoofed into the 2-tag region and the black distribution shows the reweighted 1-tag events. The purple and yellow histograms are centered around the black and show the systematic from 1/2 of each reweighting - $\Delta R(bb)$ and p_T^W respectively. The ratio are taken wrt the blue histogram.

Not reviewed, for internal circulation only

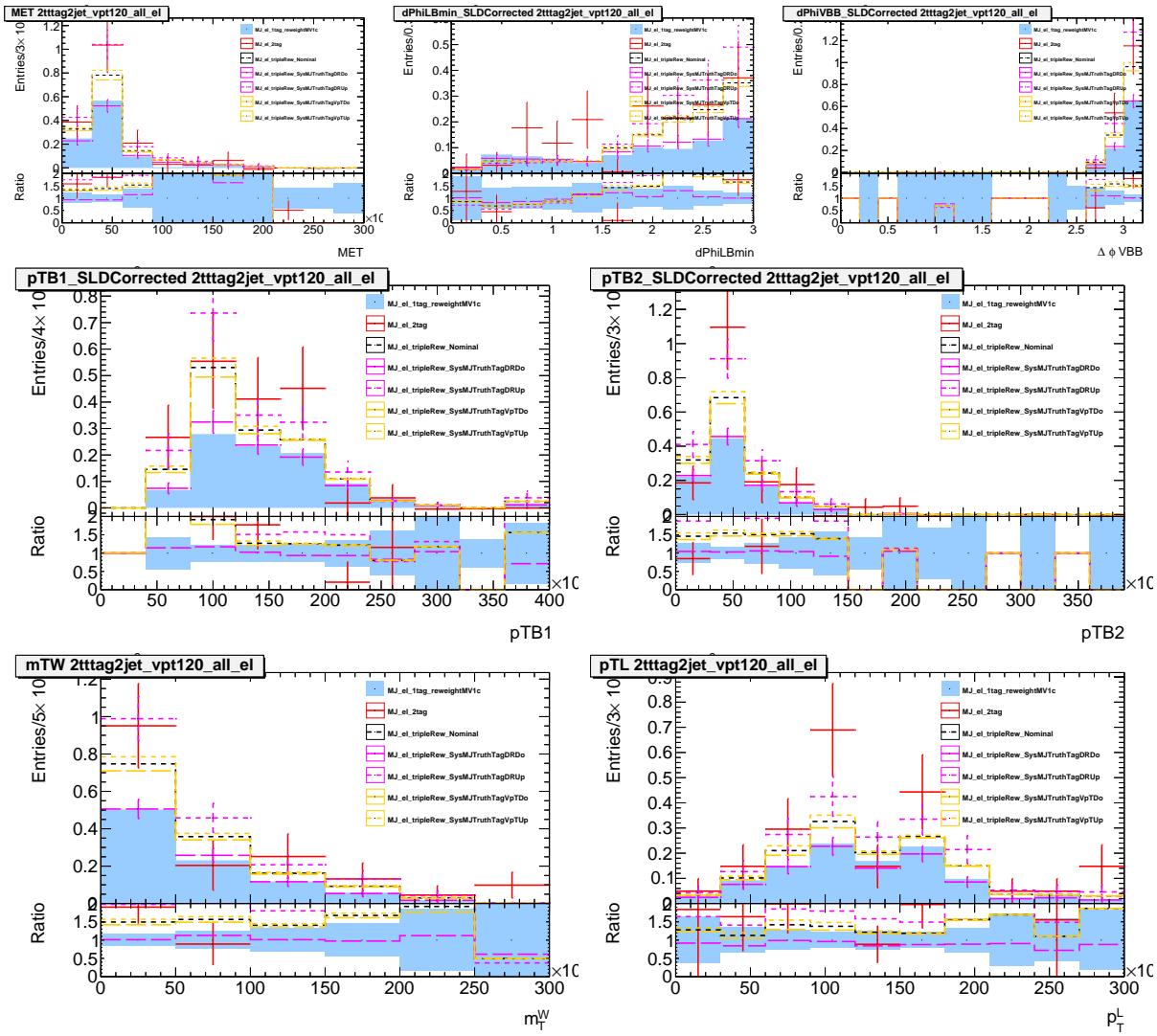


Figure 249: In 2T tag $p_T^W > 120$ GeV electron events, the top three variables are E_T^{miss} , $\Delta\phi(l, b)$, and $\Delta\phi(V, B)$, the middle two show the p_T of the leading two jets and the bottom two are m_T^W and lepton p_T . The red histogram is 2-tag events, the blue solid histogram is the 1-tag events spoofed into the 2-tag region and the black distribution shows the reweighted 1-tag events. The purple and yellow histograms are centered around the black and show the systematic from 1/2 of each reweighting - $\Delta R(bb)$ and p_T^W respectively. The ratio are taken wrt the blue histogram.

Not reviewed, for internal circulation only

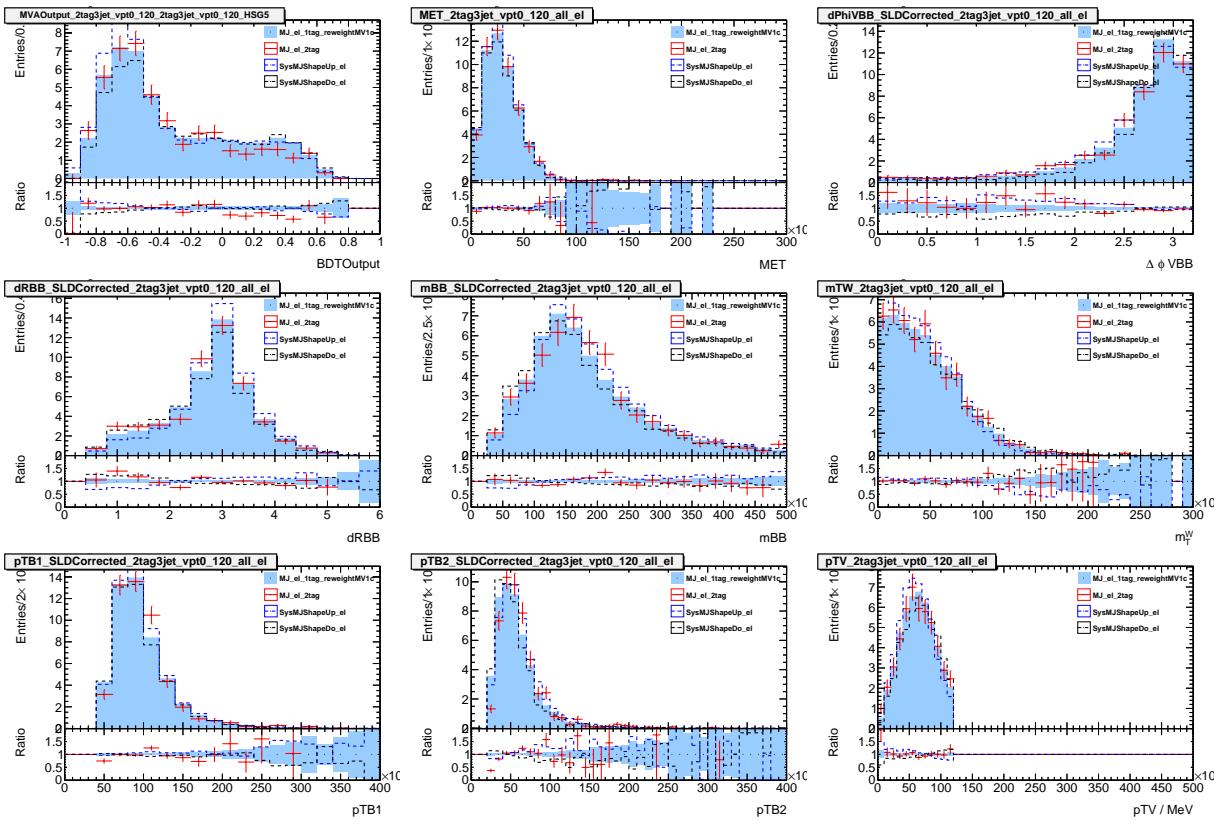


Figure 250: A comparison of 1-tag and 2-tag multijet events in the electron 3-jet channel with $p_{tW} > 120$ GeV. The red histogram is 2-tag events, the blue solid histogram is the 1-tag events spoofed into the 2-tag region and the dashed histograms show the effect from the iso_{track} systematics

Not reviewed, for internal circulation only

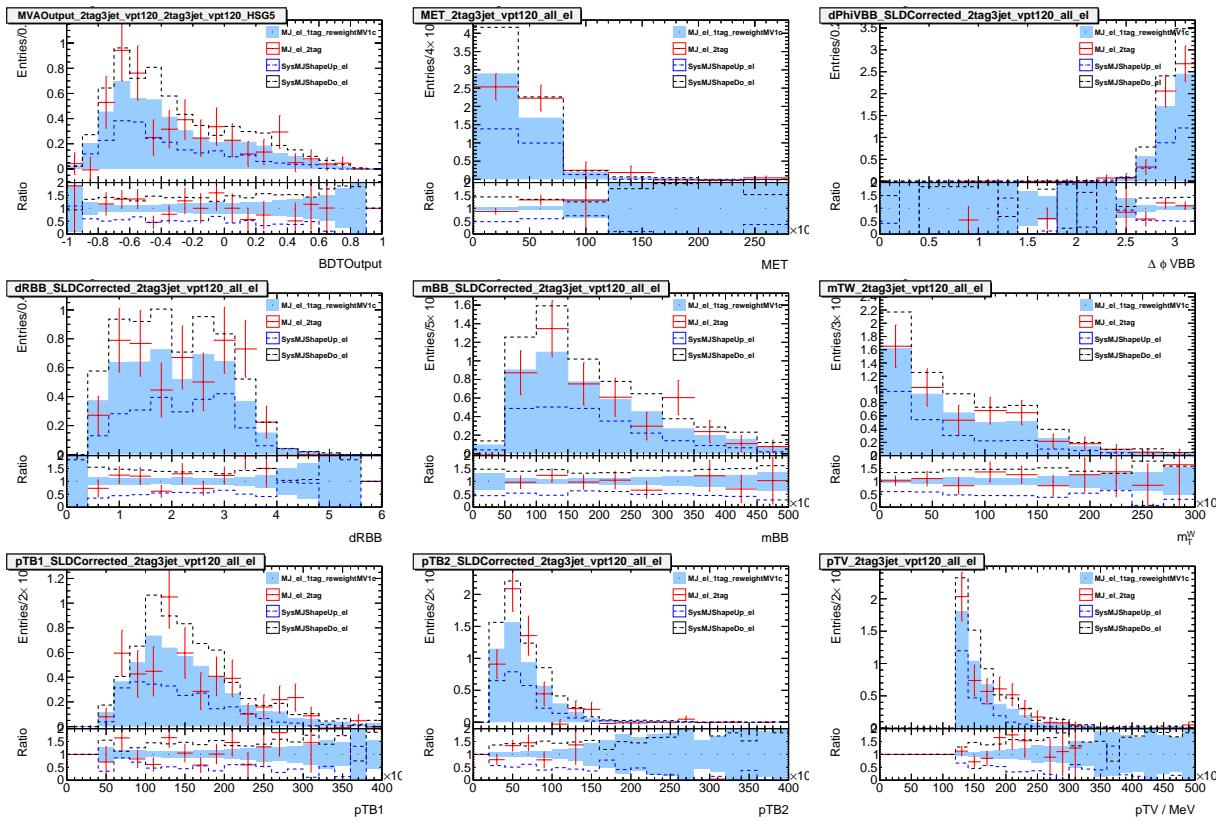


Figure 251: A comparison of 1-tag and 2-tag multijet events in the electron 3-jet channel with $p_{tW} > 120$ GeV. The red histogram is 2-tag events, the blue solid histogram is the 1-tag events spoofed into the 2-tag region and the dashed histograms show the effect from the iso_{track} systematics

4665 S Multi-jet background for 2-lepton analysis

4666 Multijet events in which two jets are mistakenly identified as leptons form a background if the two
 4667 misidentified leptons have an invariant mass compatible with the Z boson mass. Photon conversions also
 4668 contribute in the case of electrons. In addition to fake leptons, true leptons from the semi-leptonic decay
 4669 of heavy flavor hadrons may also contribute.

4670 The multijet background in the electron channel is estimated from data. The shape of the background
 4671 is obtained from a sample dominated by multijet events and then subsequently normalized to the signal
 4672 selection. A data sample dominated by multijet events is obtained by reversing the track isolation cut of
 4673 the two electrons. The remaining analysis selections are applied and the resulting data histograms are
 4674 used as templates to describe the shape of the multijet background in the various distributions.

4675 Although the templates describe the shape of the multijet background, they must be normalized to
 4676 take into account the difference in efficiency between the two electron selections. The normalization is
 4677 estimated by fitting the di-electron invariant mass distribution after applying the nominal selection up
 4678 to the requirement of ≥ 2 jets. The fit is performed over the range $40 < m_{ee} < 150\text{GeV}$ using three
 4679 components:

- 4680 • The multijet template derived from data using an inverted iso_{track} cut ($iso_{track} > 0.1$)
- 4681 • The $Z \rightarrow ee$ background distribution from the Monte Carlo simulation using the nominal electron
 4682 selection.
- 4683 • The sum of the all other background distributions from the Monte Carlo simulation using the
 4684 nominal electron selection.

4685 Only the normalizations of the multijet template and $Z \rightarrow ee$ background are allowed to vary (the other
 4686 backgrounds are fixed). The fit is performed for each 0, 1, and 2-tag samples. For the 2-tag sample
 4687 the m_{ee} sidebands are dominated by $t\bar{t}$ events so the resulting scale factor is very uncertain (since the $t\bar{t}$
 4688 background is not floated but it is known to have a non-unity scale factor in the combined likelihood fit).
 4689 For the 0, 1 and 2 tag samples the resulting multijet scale factor is 2.36 ± 0.02 (stat.), 1.89 ± 0.04 (stat.)
 4690 and 2.22 ± 0.20 (stat.) respectively. The results of the fits are shown in figure 252. Due to the smaller
 4691 backgrounds in the 0 tag, the 0-tag scale factor is used for the 1 and 2-tag samples alike with a 100%
 4692 uncertainty applied (MJ_L0).

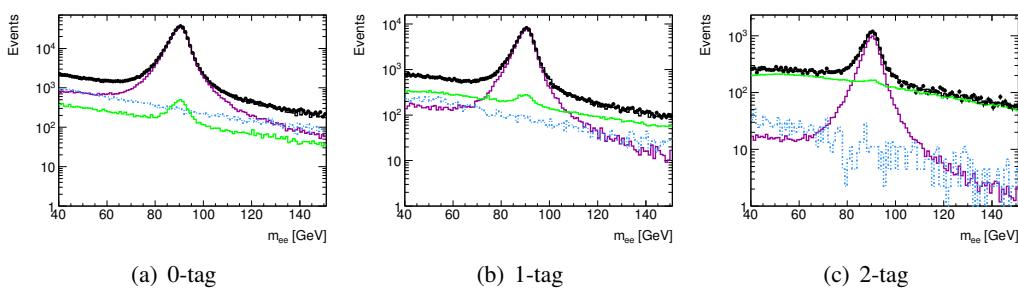


Figure 252: The di-electron invariant mass distribution for (a) 0-tag, (b) 1-tag and (c) 2-tag. The background expectations have been scaled by the results of the fits. The purple distribution is $Z + \text{jets}$, the green is the other non-multijet backgrounds, and the blue histogram is the multijet background.

4693 The statistics of the 2 tag sample are rather poor, so in order to produce a more accurate shape
 4694 in the 2 tag distributions we use a method similar to the truth tagging method used for the Monte Carlo

4695 (Section 3.3.4.1). Each event in the multijet template is used to form the 2 tag template with an additional
 4696 event weight assigned as the fraction of 2 tag events in the multijet sample. Since the binned MV1c values
 4697 of the two jets are used in the analysis, values are randomly assigned, based on the fraction of observed
 4698 events in with each MV1c combination. This is shown in figure 253 where the sum of the MV1c values
 4699 of the two jets is plotted, which (since the MV1c values are binned) displays each combination. The
 4700 plot represents a closure test and displays the large improvement in statistical precision using the truth
 4701 tagging method.

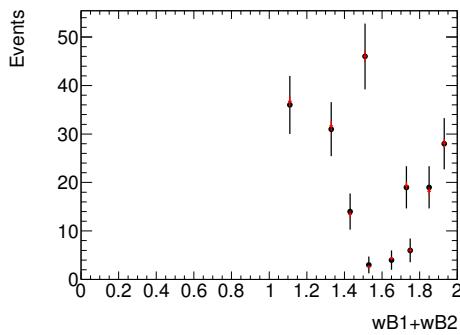


Figure 253: Distribution of the sum of the MV1c values of the two tagged jets in the 2 tag multijet template (black points). Also shown is the distribution of the multijet template using the truth tagging method (red points).

4702 The multijet background in the muon channel was investigated by comparing the data and Monte
 4703 Carlo in the $m_{\mu\mu}$ sidebands and found to be negligible. The 0-tag distribution for the electron and muon
 4704 channel are compared in Figure 254.

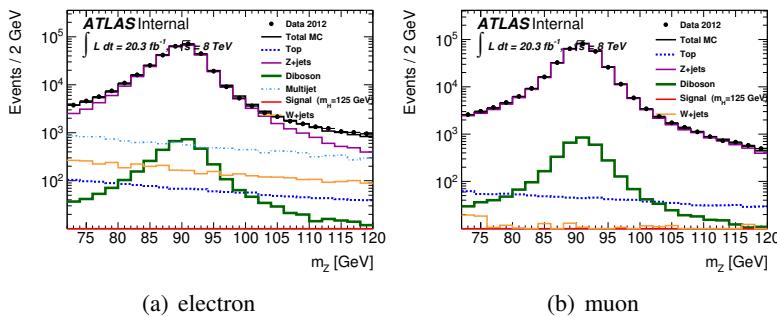


Figure 254: The di-electron (di-muon) invariant mass distribution in a (b) showing the level of multijet contamination. The muon channel shows no evidence for a significant multijet contribution which the electron channel does. The distributions are made with the 2-lepton MVA selection with 2 or more jets requiring 0 b-tags.

4705 T *b*-tagging Related Studies

4706 This appendix discussed the efficiecy maps derived for the truth tagging procedure described in Section 4707 3.3.4.1, the closure test of the truth tagging procedure, and additional scale factors derived to take 4708 into consideration the different intrinsic tagging efficiency in various generators.

4709 **T.1 Custom *b*-tagging Efficiency Maps**

4710 The truth tagging procedure described in Section 3.3.4.1 relies on the knowing the tagging efficiencies 4711 in MC. In preparation for EPS [11], a sample dependence was seen in the MC efficiency [75] so custom 4712 efficiency maps are needed so that a sample-dependent bias is not introduced.

4713 One map for each of the operating points listed in Table 7 (including !Loose) has been derived for 4714 different main backgrounds, $t\bar{t}$, W+jets, and Z+jets, detailed in Section 5. A minimal selection consisting 4715 of the the cleaning cuts described in Section 3.3.1 and at least one jet with $p_T > 15$ GeV and $|\eta| < 2.7$. 4716 The JVF cut and flavor labeling scheme described in Section are both used. When truth tagging is 4717 performed on processes such as single-top and diboson, which is not often, the $t\bar{t}$ derived efficiency map 4718 is used.

4719 The maps are 2-dimensional histograms with dimensions of jet p_T and η . Very fine binning in both 4720 dimensions leaves some bins unpopulated. After extensive studies it was decided to use coarser binning 4721 instead of a smoothing algorithm due to the fewer implicit assumptions. The final bin width in η was 0.2 4722 for *b*-jets in the $t\bar{t}$ sample and 0.3 in all others. In the case of τ efficiency maps an $|\eta|$ symmetrization was 4723 needed in order to compensate for the low statistics. For the jet p_T , and original binning of

$$4724 \quad 0, 10, 15, 17.5, 20, 22.5, 25, 27.5, 30, 35, 40, 45, 50, 55, 60, 65, 70, 75,$$

$$4725 \quad 80, 85, 90, 95, 100, 105, 110, 115, 120, 130, 140, 150, 160, 170, 180, 190,$$

$$4726 \quad 200, 225, 250, 275, 300(325, 350, 400, 450, 500, 550, 600)$$

4727 was chosen such that at low p_T , where the efficiency is steeply falling and many jets are available to 4728 improve the accuracy of the map. However a rebin factor of 2 (3) was necessary for all flavor (τ) maps. 4729 Jets with $p_T > 300$ GeV are gathered into one bin and assigned the efficiency from the penultimate 4730 bin (the one just below 300 GeV). *b*-jet efficiency maps are shown in Figure 255, *c*-jets in Figure 256, 4731 *light-jets* in Figure 257, and *tau-jets* in Figure 258. Table 7 details the operating points including the 4732 corresponding MV1c value.

4733 The tag weight distribution in a given jet p_T and η bin follows a multinomial distribution and using 4734 the total yield such the parameters of such a distribution are obtained. A new set of efficiency maps can 4735 be created by sampling said multinomial distribution. The difference between the result with the varied 4736 efficiency map and the nominal efficiency map can be used to estimate the systematics impact introduced 4737 by the statistical fluctuation of the efficiency maps.

4738 Figure 259 shows the efficiency as a function jet η with the tag weight in the 80% efficiency bin 4739 for both the nominal map and the varied map, between which the difference is less than 1%. Figure 260 4740 shows a comparison of the m_{jj} distribution of $Z+cc$ sample after truth tagging in the the 0-lepton channel with the nominal and varied map. The difference negligible.

Not reviewed, for internal circulation only

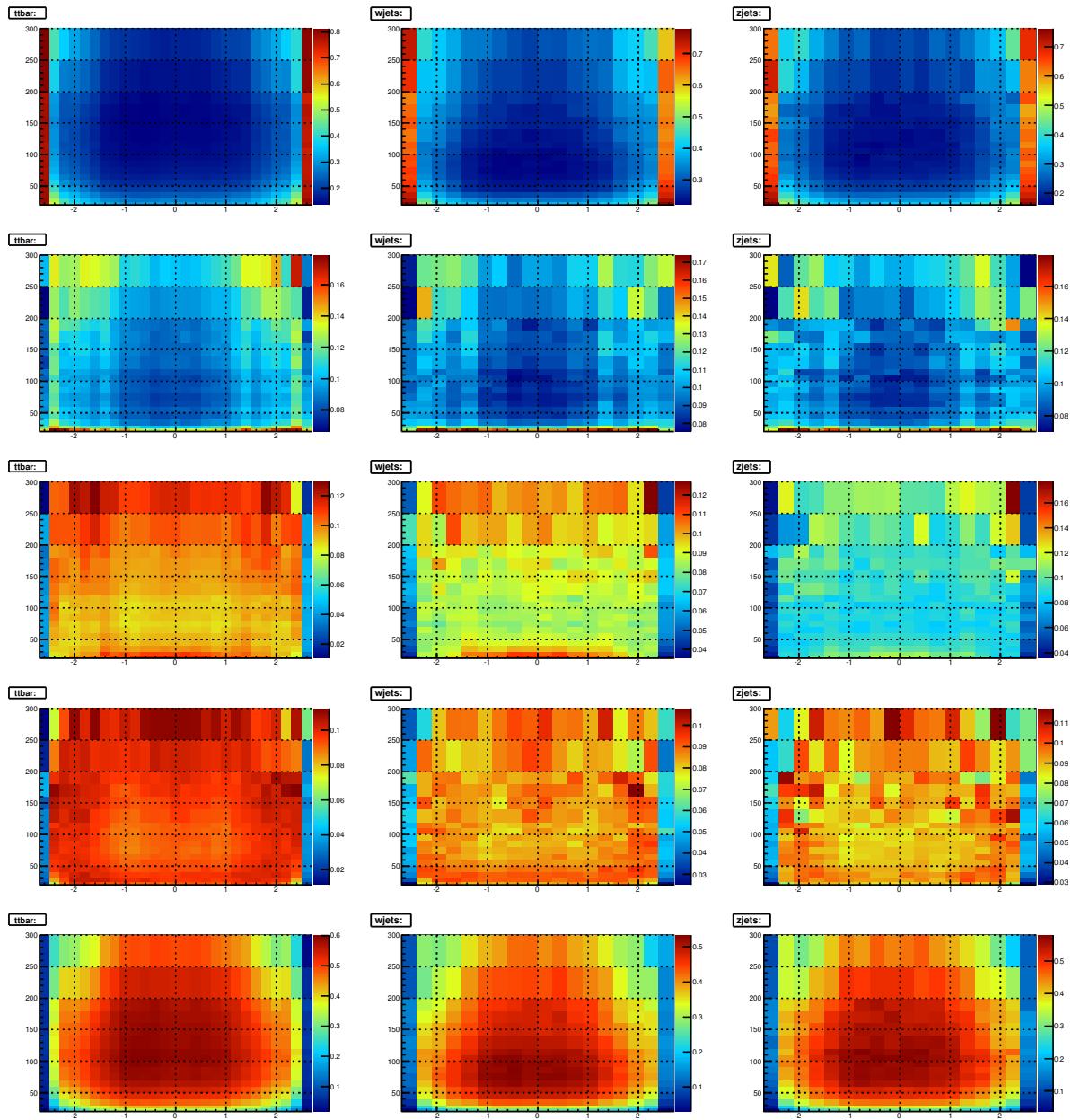


Figure 255: b -jet efficiency maps for $>80\%$ OP $MV1c < 0.4050$ (row 1), 80% OP $0.4050 < MV1c < 0.7028$ (row 2), 70% OP $0.7028 < MV1c < 0.8353$ (row 3), 60% $0.8353 < MV1c < 0.9237$ (row 4), and 50% OP $MV1c > 0.9237$ (row 5) with $t\bar{t}$, Z +jets, and W +jets shown from left to right. Table 7 details the operating points (OP) including the corresponding $MV1c$ value.

Not reviewed, for internal circulation only

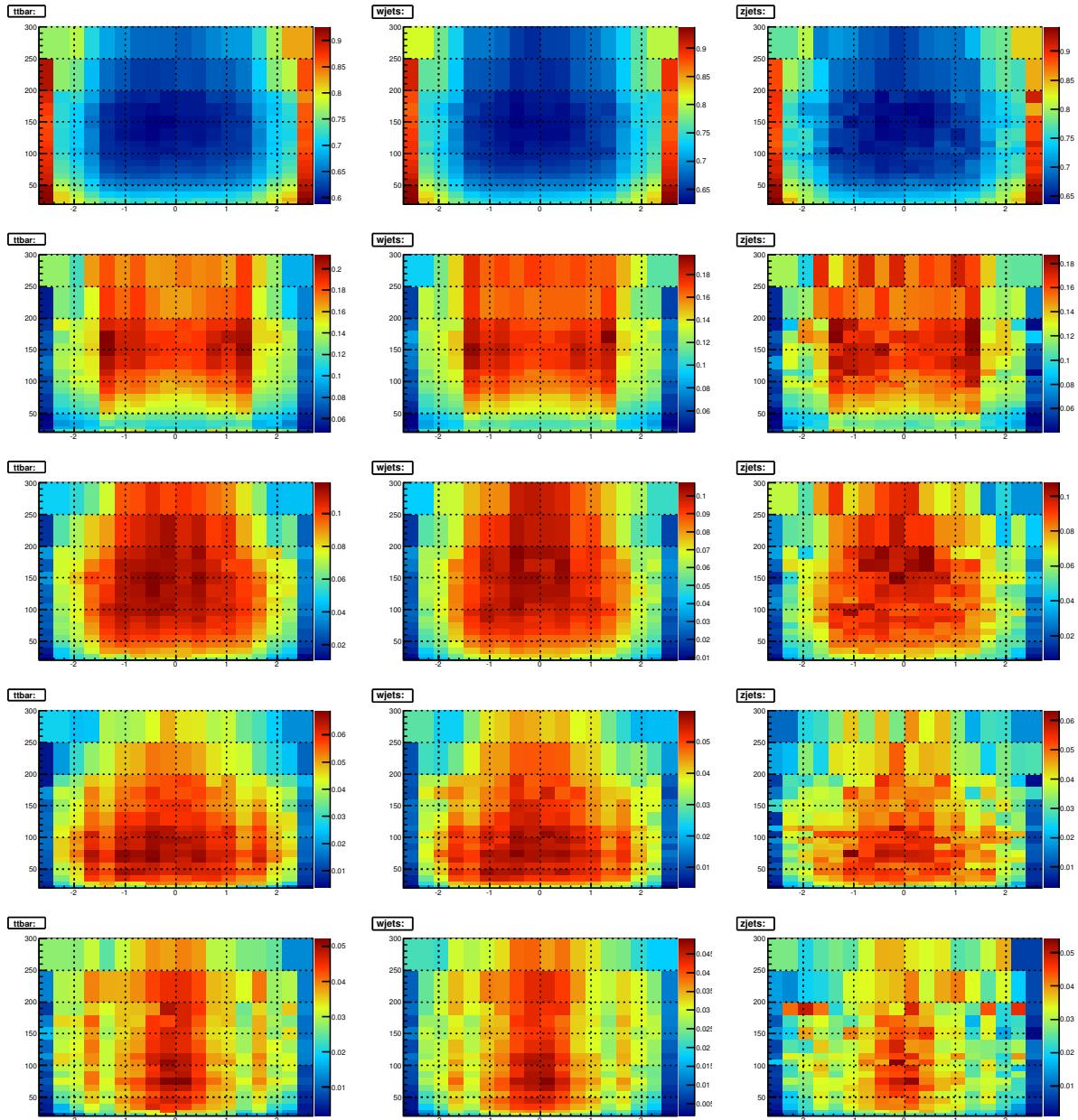


Figure 256: c -jet efficiency maps for $>80\%$ OP $MV1c < 0.4050$ (row 1), 80% OP $0.4050 < MV1c < 0.7028$ (row 2), 70% OP $0.7028 < MV1c < 0.8353$ (row 3), 60% $0.8353 < MV1c < 0.9237$ (row 4), and 50% OP $MV1c > 0.9237$ (row 5) with $t\bar{t}$, Z +jets, and W +jets shown from left to right. Table 7 details the operating points (OP) including the corresponding $MV1c$ value.

Not reviewed, for internal circulation only

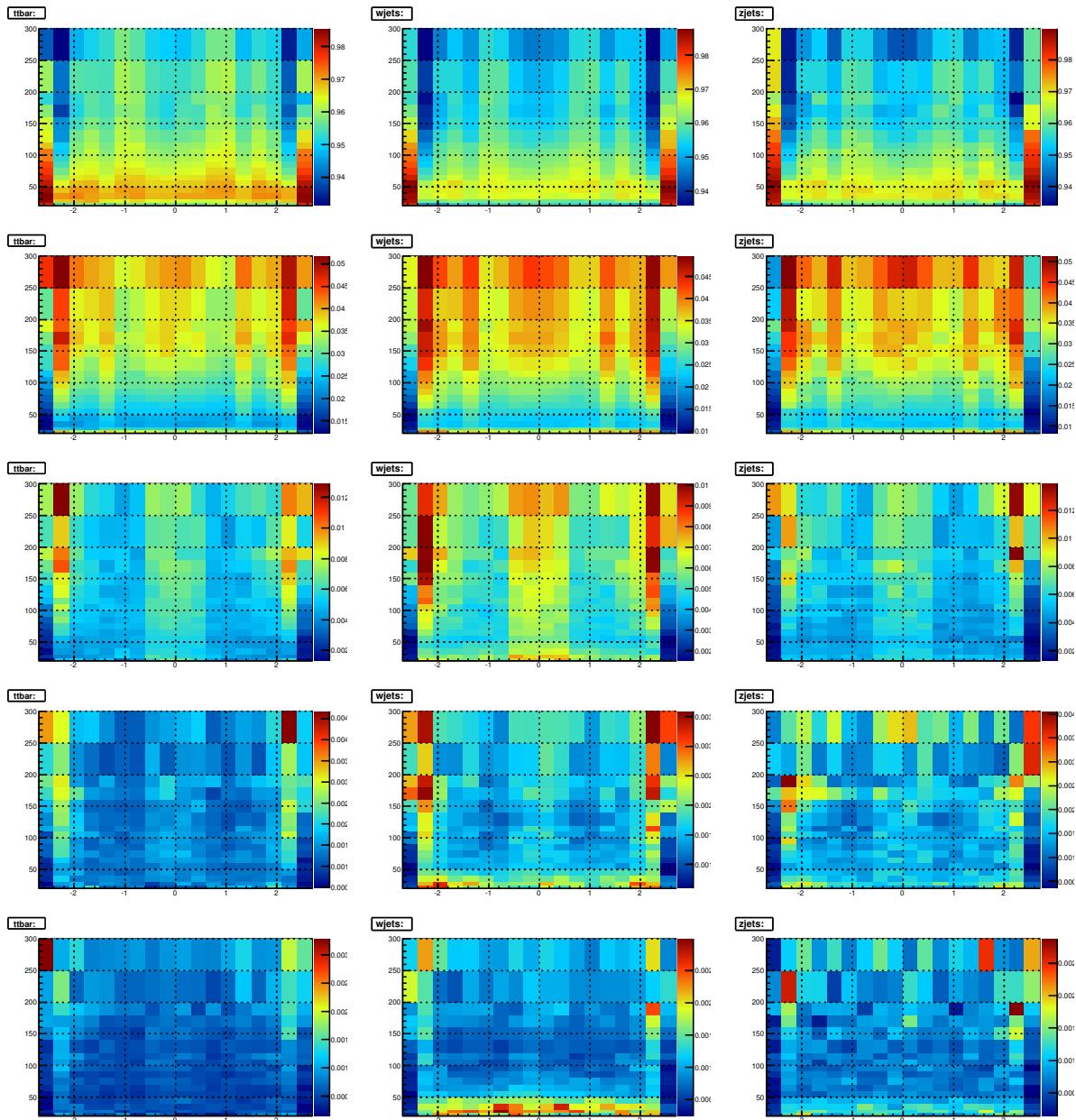


Figure 257: *light-jet* efficiency maps for $>80\%$ OP $MV1c < 0.4050$ (row 1), 80% OP $0.4050 < MV1c < 0.7028$ (row 2), 70% OP $0.7028 < MV1c < 0.8353$ (row 3), 60% $0.8353 < MV1c < 0.9237$ (row 4), and 50% OP $MV1c > 0.9237$ (row 5) with $t\bar{t}$, Z+jets, and W+jets shown from left to right. Table 7 details the operating points (OP) including the corresponding MV1c value.

Not reviewed, for internal circulation only

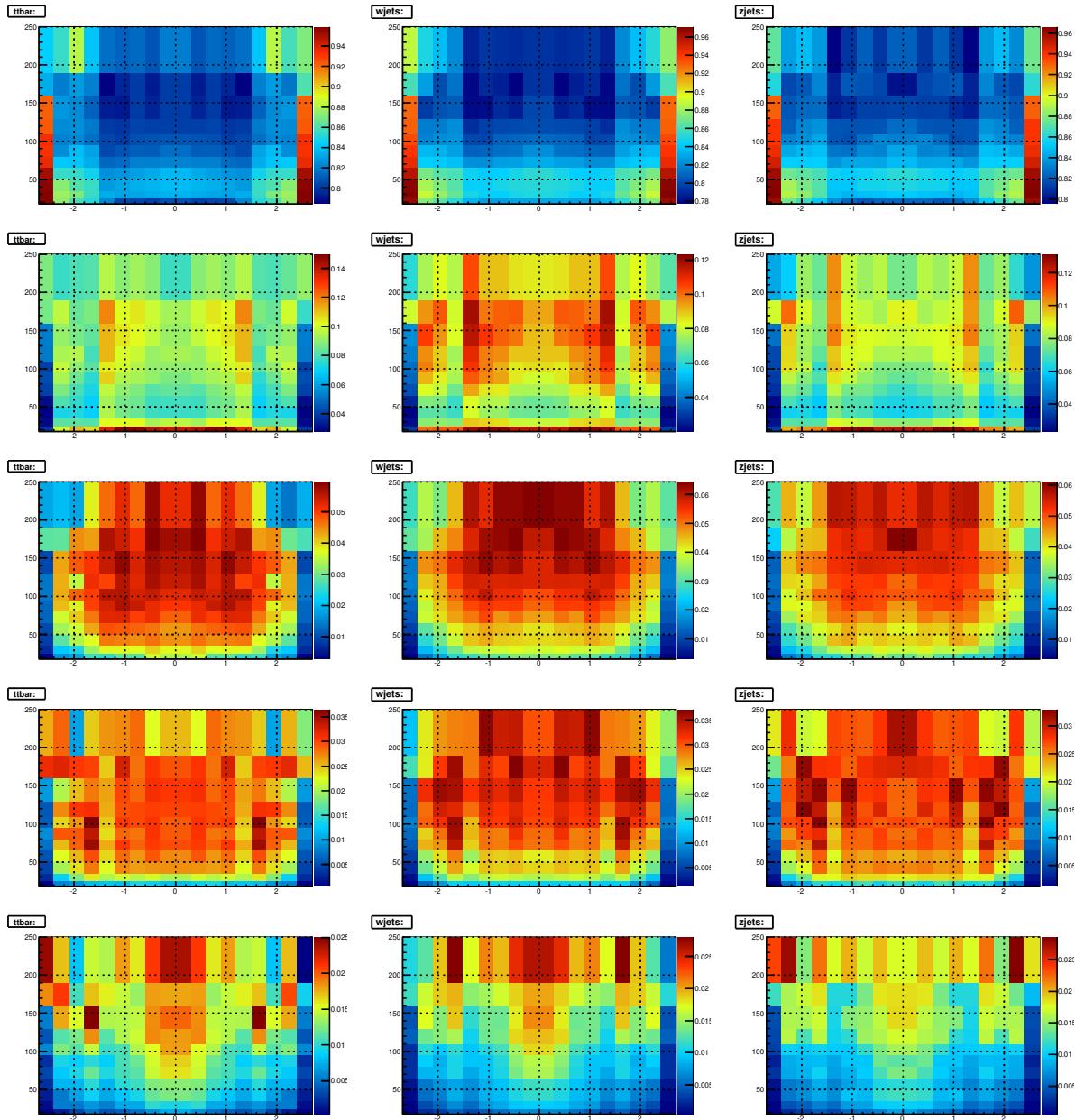


Figure 258: τ -jet efficiency maps for $>80\%$ OP $MV1c < 0.4050$ (row 1), 80% OP $0.4050 < MV1c < 0.7028$ (row 2), 70% OP $0.7028 < MV1c < 0.8353$ (row 3), 60% $0.8353 < MV1c < 0.9237$ (row 4), and 50% OP $MV1c > 0.9237$ (row 5) with $t\bar{t}$, $Z+jets$, and $W+jets$ shown from left to right. Table 7 details the operating points (OP) including the corresponding MV1c value.

Not reviewed, for internal circulation only

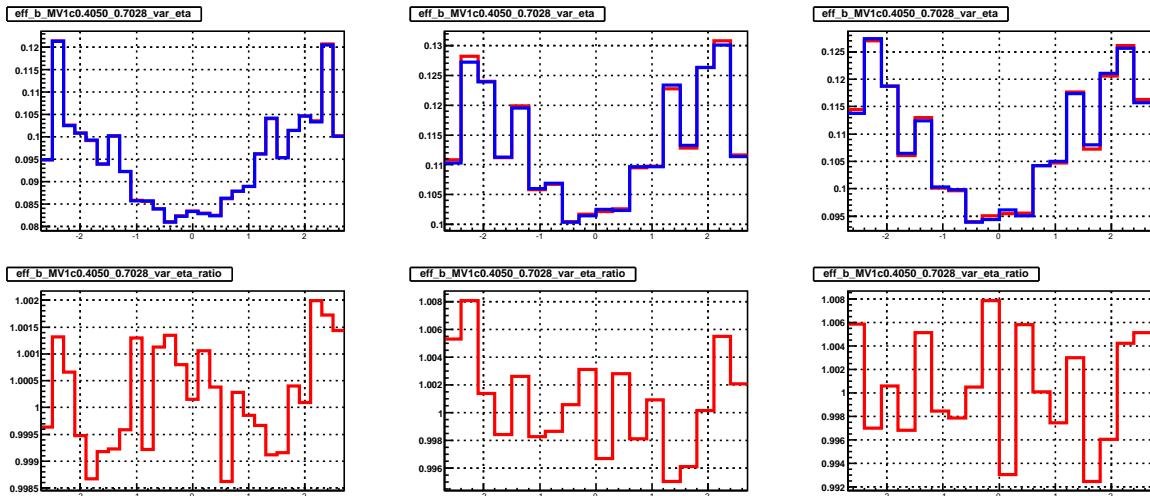


Figure 259: The top plots are the efficiency as function of jet η , while bottom is the ratio between the varied(Red) and the nominal(Blue). The left for $t\bar{t}$, the middle for Z jets, and the right for W jets.

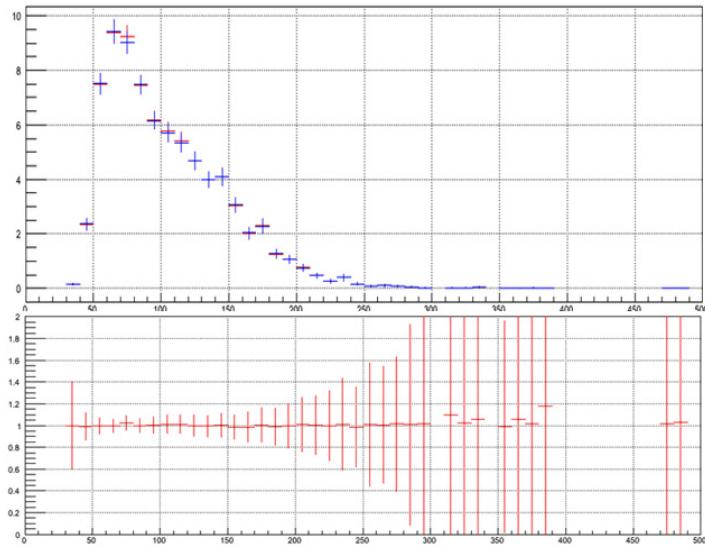


Figure 260: The m_{jj} distribution of Zcc at ll-tag region with truth tagging in the 0-lepton channel. The red is from the varied efficiency map, while the blue is from the nominal efficiency map. The bottom plot is the ratio.

Not reviewed, for internal circulation only

4741 T.2 ***b*-tagging generator dependence scale factor**

4742 As demonstrated in EPS [11], and is widely known, the flavor tagging efficiency is generator dependent
 4743 due to the different parton shower, hadronization models, and hadron branching ratios. The efficiency
 4744 scale factors provided by the flavor tagging group which correct to the efficiency in data, $SF = \epsilon_{data}/\epsilon_{MC}$,
 4745 are with respect to PYTHIA6. An analysis such as this using several generators (PYTHIA6, PYTHIA8 and
 4746 SHERPA), each with a different tagging efficiency, ϵ'_{MC} , must take these differences into consideration. To
 4747 this end, MC-to-MC scale factors, $SF_{MC-to-MC} = \epsilon_{MC}/\epsilon'_{MC}$ have been derived using the following $t\bar{t}$
 4748 samples:

- 4749 • mc12_8TeV.117050.PowhegPythia_P2011C_ttbar.merge.NTUP_SMWZ.e1728_s1581_s1586_r3658_r3549_p1328
- 4750 • mc12_8TeV.18138X.Sherpa_CT10_TTbarX.merge.NTUP_SMWZ.e20_s1581_s1586_r4485_r4540_p1328 (X=0-
 4751 9)
- 4752 • mc12_8TeV.110898.Pythia8_AU2MSTW2008LO_EWttbar.merge.NTUP_TOP.e2512_s1499_s1504_r3658_r3549_p1400

4753 Figures 261 to 265 show the b-tagging efficiency as a function of jet p_T in the 5 MV1c operating
 4754 points for *b* and *c*-jets in $t\bar{t}$ events for the above samples. The ratio to PYTHIA6 is shown and this is the
 4755 value used for the MC-to-MC scale factors for *b* and *c* jets.

4756 Modeling of heavy flavor hadrons is the main difference between the generators. Even though long-
 4757 lived light hadrons i.e. K_s and Λ can differ in a similar way, it has been shown to be a small effect. This,
 4758 plus the fact that the light jet component is relatively small in the most sensitive regions, MC-to-MC
 4759 scale factors have not been applied to light jets.

4760 Half of the correction has been assigned as the systematic uncertainty which is for each generator
 4761 and for *b* and *c* jets separately (BTAGBSherpa, BTAGBPythia8, BTAGCSherpa, BTAGCPythia8).

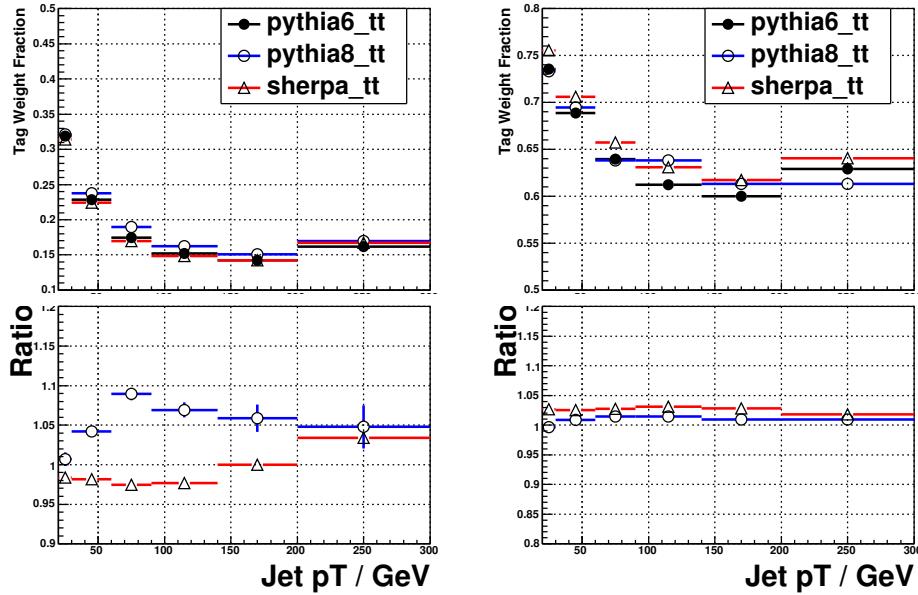


Figure 261: *b*-jet (left) and *c*-jet (right) tagging efficiency for the jets between the 100% OP and 80% OP ($0.0 < MV1c < 0.4050$) in $t\bar{t}$ events produced by PYTHIA6 (Black), PYTHIA8 (Blue) and SHERPA (Red). The ratio is the MC-to-MC scale factor.

Not reviewed, for internal circulation only

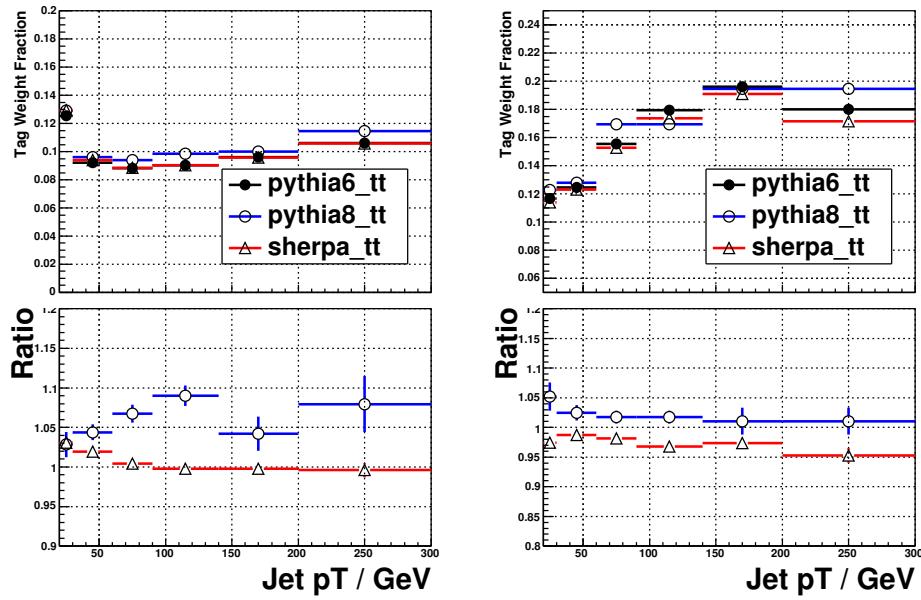


Figure 262: b -jet (left) and c -jet (right) tagging efficiency for the jets between the 80% OP and 70% OP ($0.4050 < \text{MV1c} < 0.7028$) in $t\bar{t}$ events produced by PYTHIA6 (Black), PYTHIA8 (Blue) and SHERPA (Red). The ratio is the MC-to-MC scale factor.

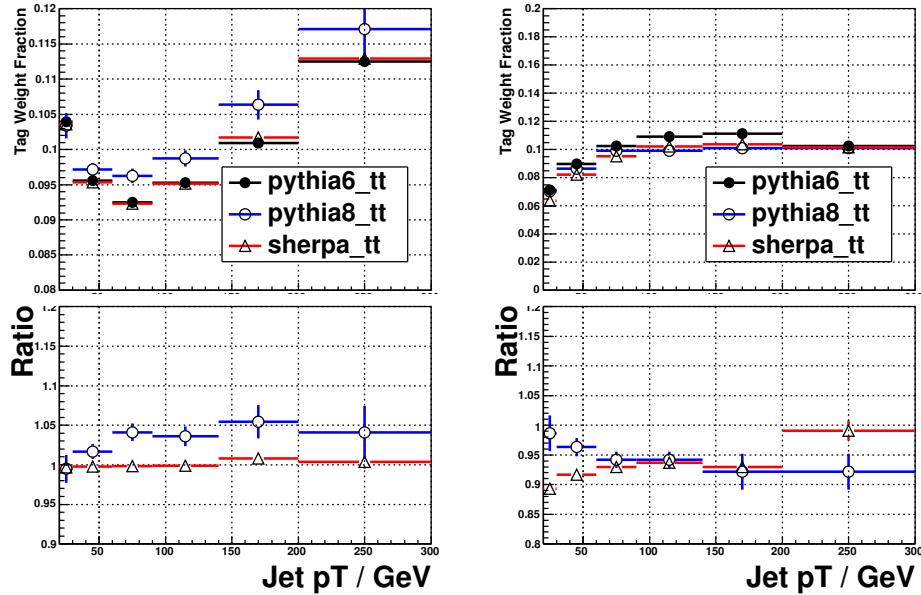


Figure 263: b -jet (left) and c -jet (right) tagging efficiency for the jets between the 70% OP and 60% OP ($0.7028 < \text{MV1c} < 0.8353$) in $t\bar{t}$ events produced by PYTHIA6 (Black), PYTHIA8 (Blue) and SHERPA (Red). The ratio is the MC-to-MC scale factor.

Not reviewed, for internal circulation only

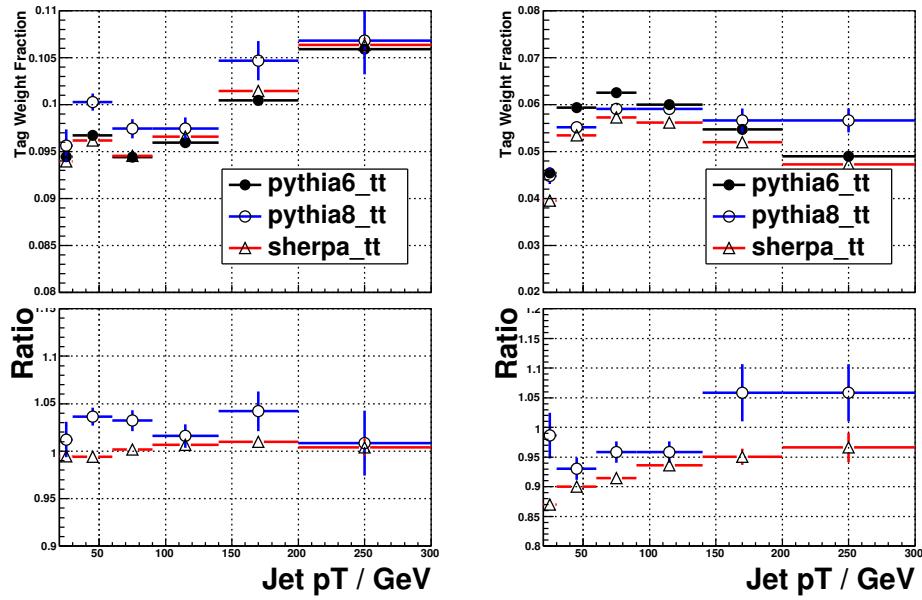


Figure 264: b -jet (left) and c -jet (right) tagging efficiency for the jets between the 60% OP and 50% OP ($0.8353 < \text{MV1c} < 0.9237$) in $t\bar{t}$ events produced by PYTHIA6 (Black), PYTHIA8 (Blue) and SHERPA (Red). The ratio is the MC-to-MC scale factor.

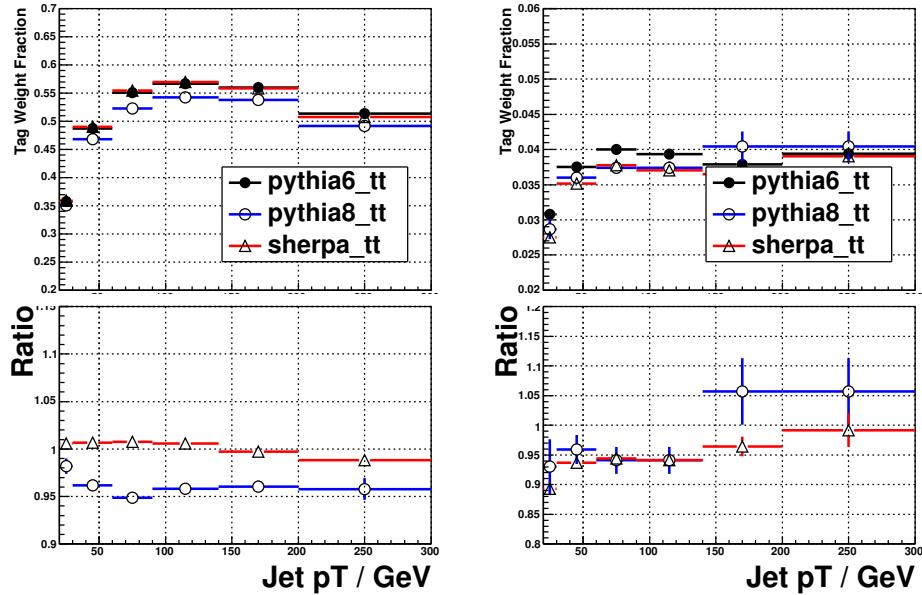


Figure 265: b -jet (left) and c -jet (right) tagging efficiency for the jets above the 50% OP ($0.9237 < \text{MV1c} < 1.0$) in $t\bar{t}$ events produced by PYTHIA6 (Black), PYTHIA8 (Blue) and SHERPA (Red). The ratio is the MC-to-MC scale factor.

4762 T.3 truth b -tagging efficiency maps closure test

4763 In order to gain statistics, truth tagging has been applied to events in which neither of the leading two
 4764 jets is truth matched to a b hadron, as described in Section 3.3.4.1, using the efficiency map as shown
 4765 in Appendix T.1. After applying the truth tagging procedure, the predicted yield and kinematics of each
 4766 sample should be consistent with prediction using the direct tagging procedure (simply cutting on the
 4767 MV1c value itself). The most basic variable which showed a systematic difference in the truth and direct
 4768 tag predictions was $\Delta R(jet_1, jet_2)$ shown in Figures 266-269 for $V+ll$, $V+cl$, $V+cc$, and WW events
 4769 passing the 0-lepton MVA selection with 2 b -tags. Within the available statistics only the $V+cc$ processes
 4770 lack agreement between the two approaches. Tagging efficiency dependence on variables other than
 4771 jet p_T and η are not directly parameterized in the efficiency maps and therefore need to be accounted
 4772 for in another way. Since both $W+cc$ and $Z+cc$ both show consistent behavior in 2 and 3-jet events
 4773 (Figure 270), the four samples have been combined in order to derive a correction (Figure 271) with the
 4774 maximum available statistics. The correction is given by:

$$0.9509 + 0.418 \times \ln(\Delta R) - 0.3697 \times \ln^2(\Delta R) \quad (43)$$

4775 defined only for $\Delta R < 2.7$. After the correction, agreement between the truth tagging and direct tagging
 4776 procedures is restored as demonstrated in Figure 272. Half the correction has been assigned as the
 4777 systematic uncertainty (BTagTruthTagDR).

Not reviewed, for internal circulation only

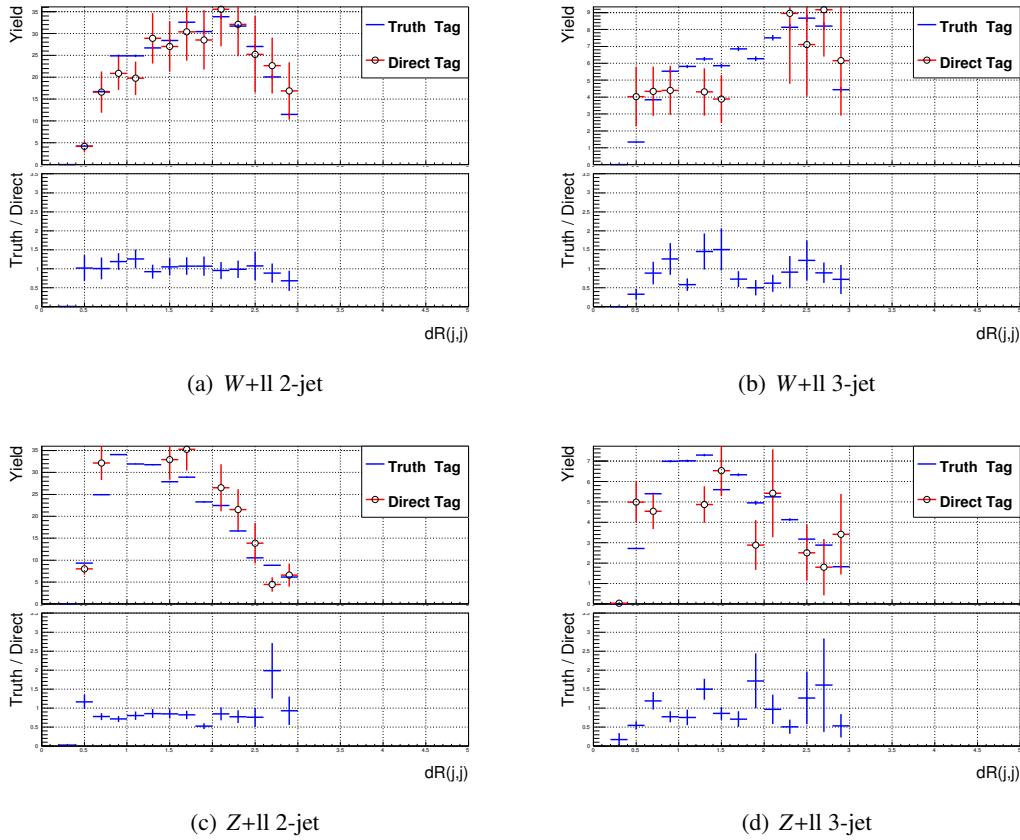


Figure 266: Comparison between truth tagging and direct tagging for $V+ll$ events using the 0-lepton MVA selection and requiring 2 b -tags.

Not reviewed, for internal circulation only

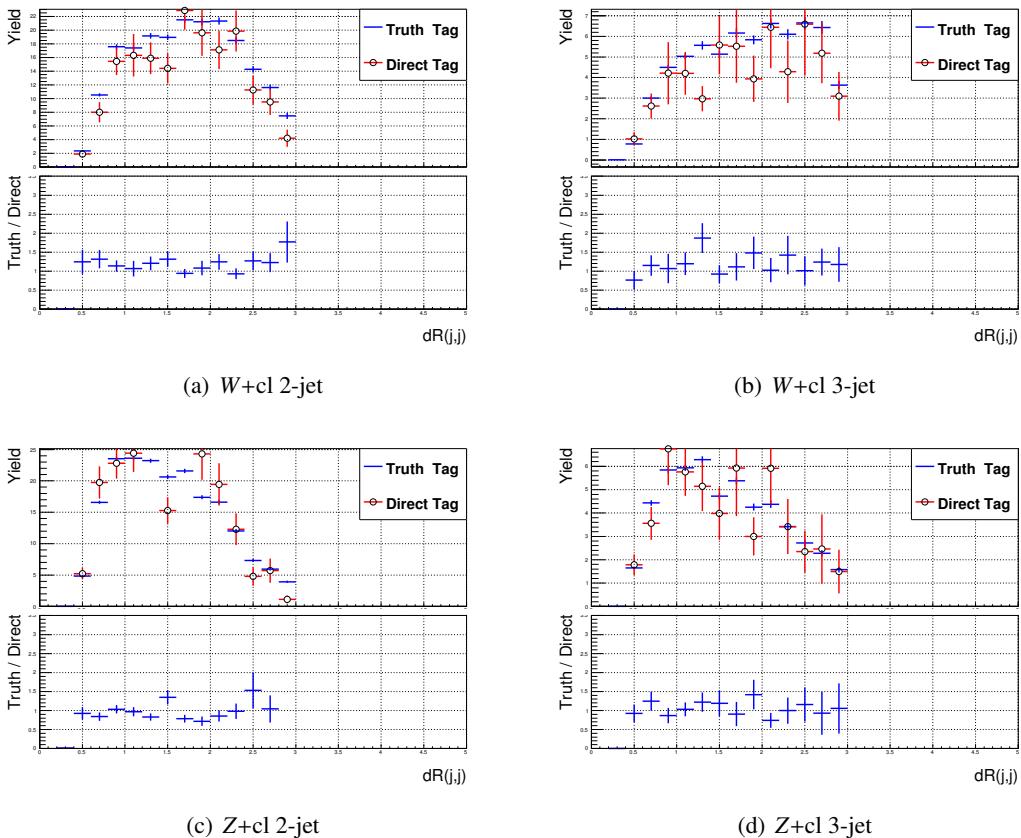


Figure 267: Comparison between truth tagging and direct tagging for $V + \text{cl}$ events using the 0-lepton MVA selection and requiring 2 b -tags.

Not reviewed, for internal circulation only

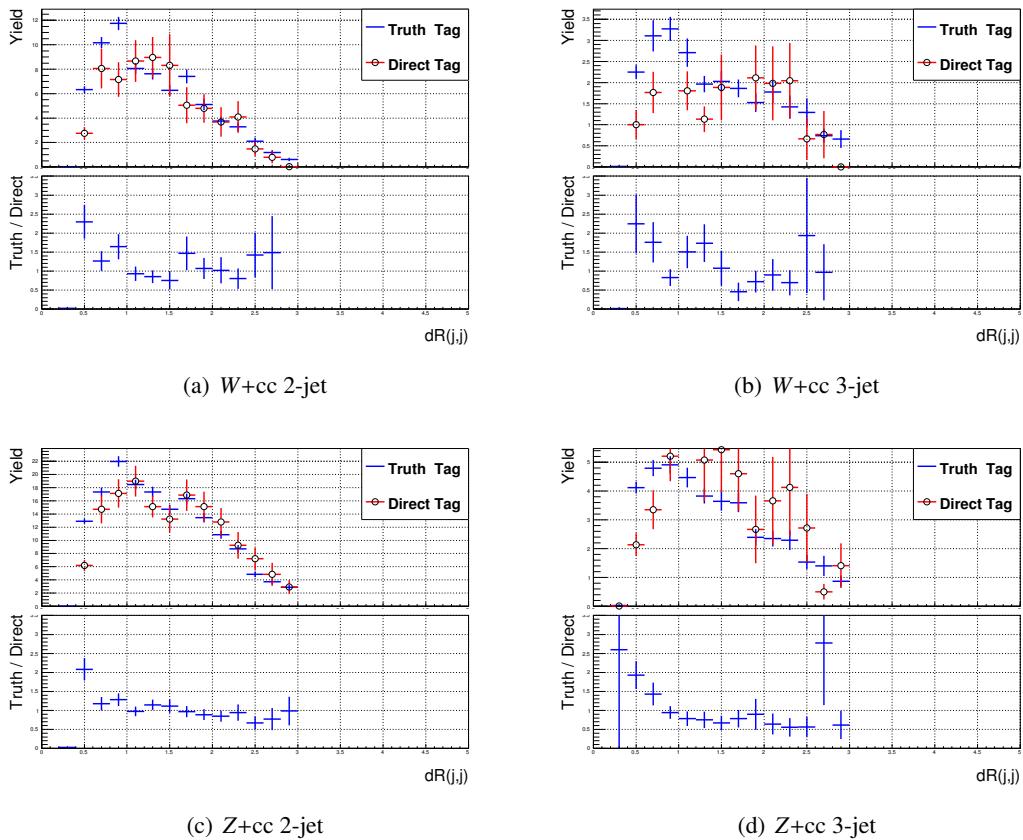


Figure 268: Comparison between truth tagging and direct tagging for $V+cc$ events using the 0-lepton MVA selection and requiring 2 b -tags.

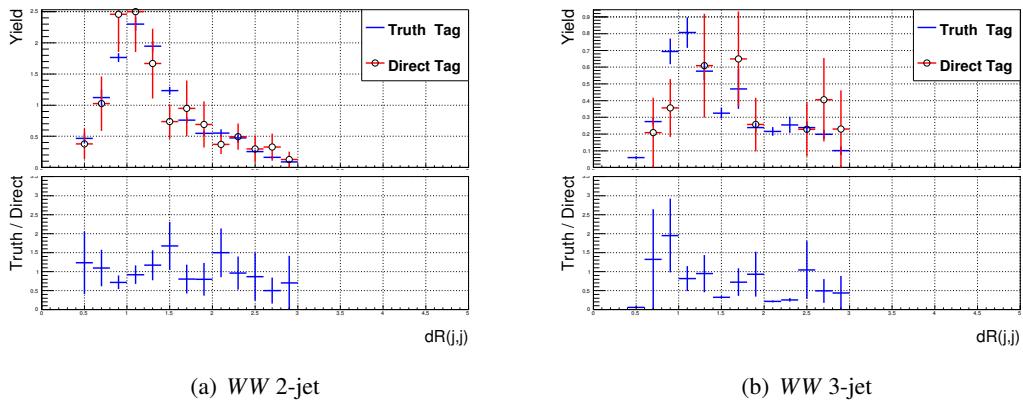


Figure 269: Comparison between truth tagging and direct tagging for WW events using the 0-lepton MVA selection and requiring 2 b -tags.

Not reviewed, for internal circulation only

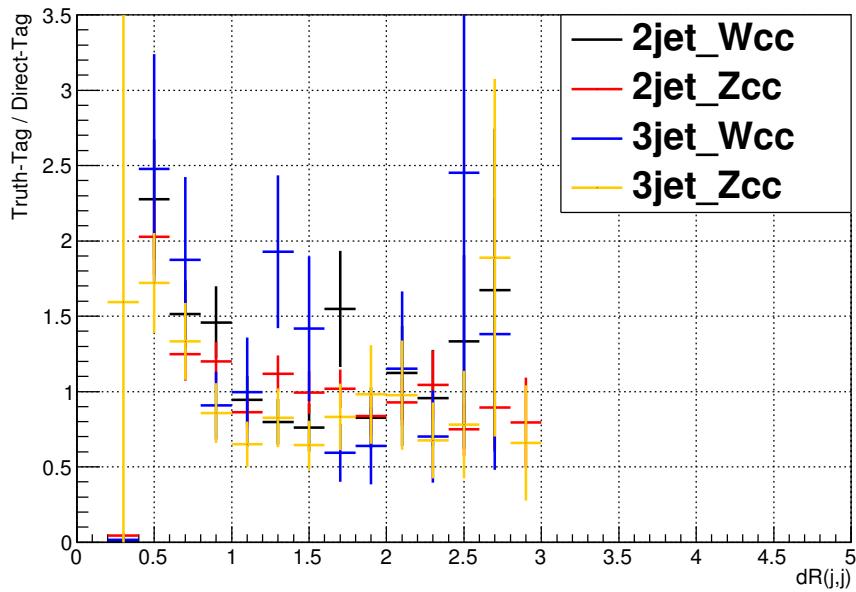


Figure 270: The ratios of truth to direct tagging for $W+cc$ and $Z+cc$ in 2 and 3-jet events using the 0-lepton MVA selection. The four ratios are consistent within the available statistics.

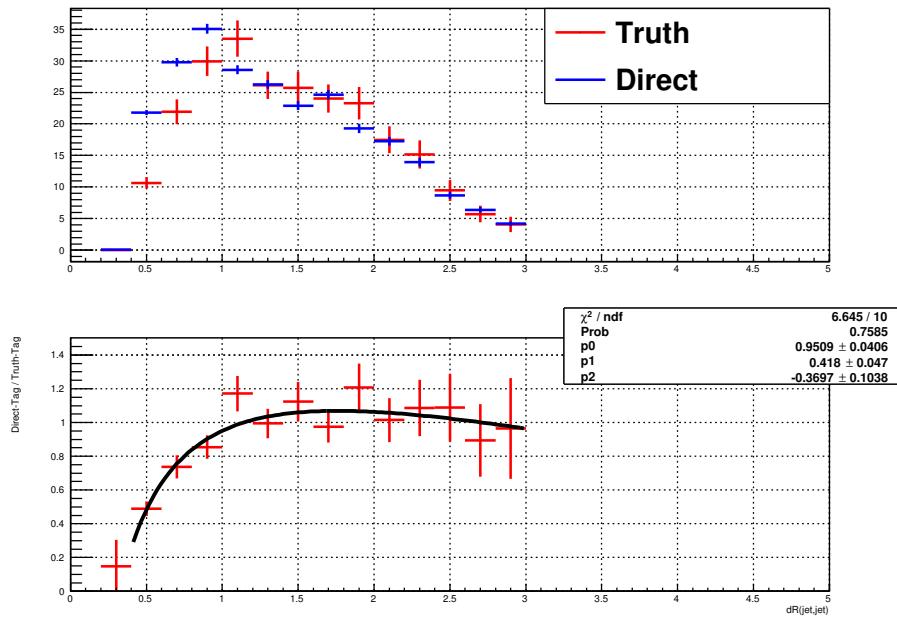


Figure 271: The truth tagging ΔR correction is derived from the ratio truth to directed tagged events using $W+cc$ and $Z+cc$ in 2 and 3-jet events (top). The correction itself is obtained from a fit to the ratio (bottom): $0.9509 + 0.418 \times \ln(\Delta R) - 0.3697 \times \ln^2(\Delta R)$.

Not reviewed, for internal circulation only

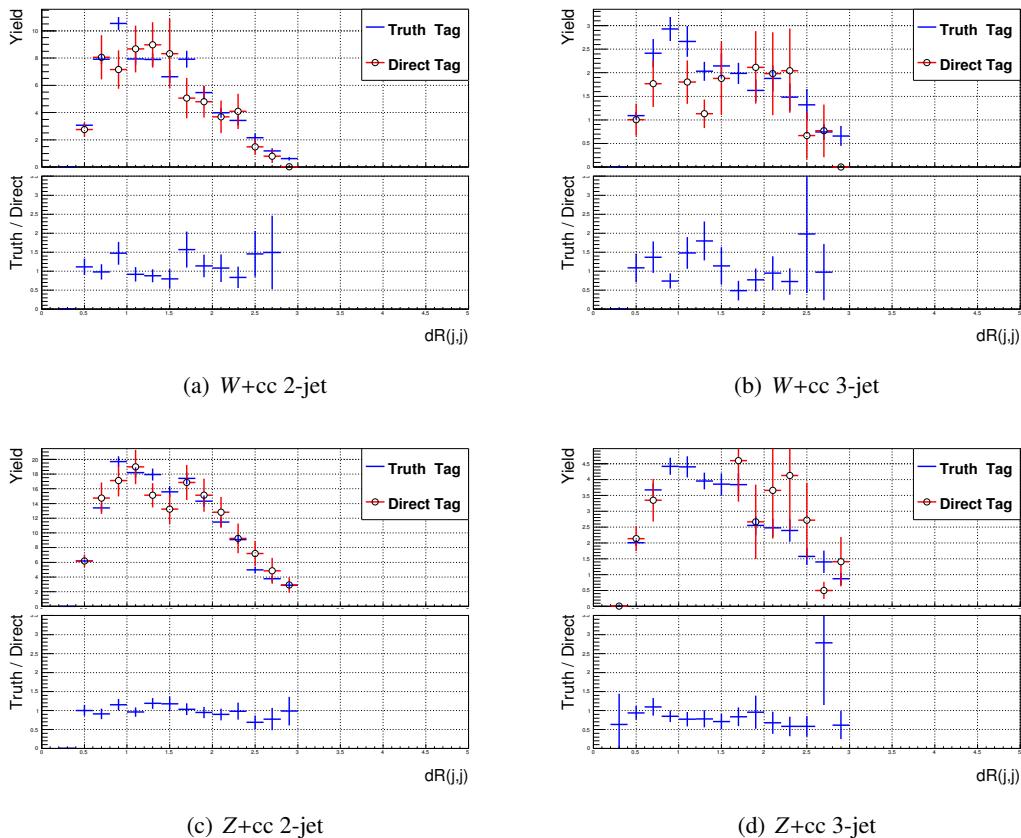


Figure 272: Comparison between truth tagging and direct tagging for after the dR correction for the samples on which the correction is derived.

4778 U Event-level Kinematic Likelihood Fit

4779 Final state radiation and reconstruction effects may decrease the $H \rightarrow b\bar{b}$ resonance resolution significantly while comparably decreasing the probability of observing the decay over the background. One
 4780 powerful technique to improve the resonance resolution and to possibly increase the sensitivity of this
 4781 search is to utilize an event-level Kinematic Likelihood Fit (KF), which exploits the full kinematic potential
 4782 of any event topology within the uncertainty of its reconstructed signatures.

4783 The $ZH \rightarrow \ell\ell b\bar{b}$ analysis has the beneficial feature that the expected signal event topology is fully
 4784 reconstructed and balanced in the transverse plane. At the Monte Carlo truth level, the E_T^{miss} should only
 4785 arise from the inherent transverse momentum of the colliding partons and semi-leptonic b -decays. The
 4786 former determines the resolution to which the transverse energy of any given event can be balanced.
 4787 Therefore, one can adjust the energies of the reconstructed particles in order to force the event into a
 4788 balanced configuration within the event and object resolutions. Effectively, since leptons in general have
 4789 a much better resolution than jets, the jet energies are balanced against the \sim static leptons. This can
 4790 be achieved by maximizing an event-level likelihood built from the expected signal topology without
 4791 considering the Higgs mass.

4792 The other event topologies, such as $WH \rightarrow \ell v b\bar{b}$, are left for future versions of the analysis.

4794 U.1 Likelihood Model

4795 A model has been constructed in which the reconstructed $\ell\ell b\bar{b}$ system is constrained to be balanced in
 4796 the transverse plane. The baseline version of this model is intended for events containing 2 b -tagged
 4797 jets, which can be extended for events with additional jets yielding more contributions from hard final or
 4798 initial state radiation.

4799 The inputs for this model are comprised by 12 fit parameters,

- 4800 • energies of 2 electrons or inverse transverse momenta of 2 muons and the energies of 2 jets,
- 4801 • pseudorapidity and azimuthal angles of the 2 leptons and 2 jets,
- 4802 • transverse momentum of the $\ell\ell b\bar{b}$ system,
- 4803 • reconstructed dilepton mass $m_{\ell\ell}$,

4804 and 3 constraints for the variation of these parameters,

- 4805 • the $m_{\ell\ell}$ is constrained to follow a Breit-Wigner (BW) distribution around a pole mass and width of
 the Z boson,
- 4806 • the $\sum P_{x,y}^{\ell\ell b\bar{b}}$ is constraint to be zero with a width of ~ 9 GeV obtained from ZH Monte Carlo events,
- 4807 • assume parameters to follow Gaussian distributions (except for the jets, for which dedicated asymmetric
 transfer functions are derived).

Given the fit parameters and constraints defined above, the probability density function is defined as

$$\begin{aligned}\mathcal{L} &= \prod_i f(y_i^{obs}, y_i^{pred}) \\ &= G(\Omega_\ell^n; \Omega_\ell^0, \sigma_\Omega) L^j(P_T^n; P_T^0, \eta_j^0) L_{truth}^j(P_T^n; \eta_j^0) \\ &\quad \prod_{i=j} G(\phi_i^n; \phi_i^0, \sigma_\phi) \\ &\quad \prod_{i=x,y} G\left(\sum p_i^n; \sum P_i, \sigma_{\sum p_i}\right) \\ &\quad \mathcal{B}(m_{\ell\ell}^n; M_Z, \Gamma_Z),\end{aligned}$$

where the energy E of electrons or $1/p_T$ of muons are denoted by $\Omega = \{E, 1/p_T\}$ respectively, the L^j corresponds to a p_T and *eta*-dependent jet response likelihood (the ‘transfer functions’ for jets), the G indicates Gaussian terms and \mathcal{B} a Z boson Breit-Wigner function. The likelihood also integrates the p_T^{reco} correction L_{truth}^j (introduced in Sec. X) by adding a prior for the underlying p_T^{true} spectrum of the jets according to what is found after signal event selection cuts in $ZH \rightarrow \ell\ell b\bar{b}$ Monte Carlo events.

Building a test statistics and dropping all constant terms we obtain

$$\begin{aligned}-2 \ln(\mathcal{L}) &= \sum_{i=j} \left(\frac{(\phi_i^n - \phi_i^0)^2}{\sigma_\phi^2} \right) + \frac{(\Omega_\ell^n - \Omega_\ell^0)^2}{\sigma_\Omega^2} - 2 \ln(L^j) - 2 \ln(L_{truth}^j) \\ &\quad + \sum_{i=x,y} \frac{(\sum p_i^n - \sum P_i)^2}{\sigma_{\sum p_i}^2} + 2 \ln((m_{\ell\ell}^2 - M_Z^2)^2 + M_Z^2 \Gamma_Z^2)\end{aligned}$$

where M_Z and Γ_Z are the Z boson mass and width respectively. Finally this statistics is used to minimize and balance the reconstructed $\ell\ell b\bar{b}$ system on an event-by-event basis.

U.2 Resolutions

This method relies on having the resolutions of objects in hand. The standard CP provided resolutions were used for electrons [76] [77] and muons [64] [78]. Jet resolutions were derived from the signal sample in 5 p_T bins ($< 40, 40 - 60, 60 - 80, 80 - 100, > 100$ GeV) separately for η above and below 1.2 and for jets with and without a reconstructed muon. The balance of the system is constrained to 9 GeV from MC studies. The studies were redone after a series of bug-fixes to the underling framework. The updated width is shown in Figure 273 is 11 GeV. The dependence of the choice of system balance constraint on the final width is discussed in the following section.

U.3 Results

A kinematic likelihood fit with the above model has been used to balance the $ZH \rightarrow \ell\ell b\bar{b}$ system in ZH Monte Carlo events for a Higgs mass hypothesis of $m_H = 125$ GeV. As shown in Fig. 274, the fit achieves an improvement of the dijet invariant mass resolution of $\approx 21.64\%$. In parentheses, the sigma over the mean is given. As expected the fit moves the peak closer to the true Higgs mass.

The kinematic fit uses features of the signal event to improve the signal invariant mass reconstruction. In that process, the invariant mass distribution of the backgrounds is expected to change. For this reason it is important to verify that the fit does not increase the background rates in the region of the peak. Results for Z +jets Monte Carlo events have shown that the shape of the m_{bb} distribution changes in such a way that events migrate from ≈ 100 GeV to higher m_{bb} . This leads to an improvement in sensitivity

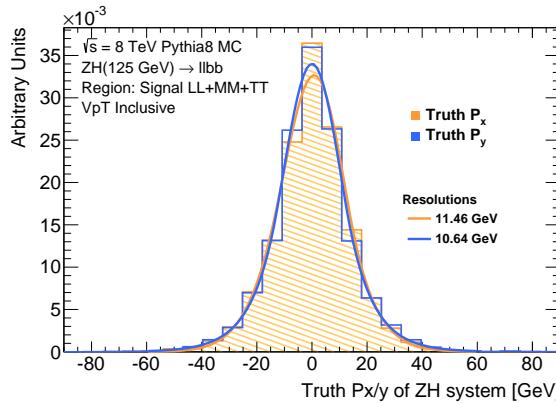


Figure 273: Dijet invariant mass before and after applying a kinematic likelihood fit in ZH $m_H = 125$ GeV signal Monte Carlo events showing a $\sim 22\%$ resolution improvement.

of $\approx 4\%$, when estimating it using S/\sqrt{B} in an m_{bb} window between 80 GeV and 150 GeV. This is smaller than what was expected by looking at the resolution improvement in the signal sample, but still significant. Given that $Z+jets$ is the predominant background for this channel, this is evidence that the kinematic fit improves the performance of the analysis as desired.

The dependence of the resolution improvement is shown in Figure 275. For a balance resolution of 4 GeV the improvement is minimal. A more constrained system results in a resolution degradation. This could be due to the fact that the imbalance can be caused by low p_T objects which are not reconstructed and are not properly recovered in this method. Above 4 GeV the resolution improves plateauing above 12 GeV. The choice of 9 GeV is therefore not completely optimal but the analysis was too mature to make a change. The expected improvement is stable around the chosen operating point.

Not reviewed, for internal circulation only

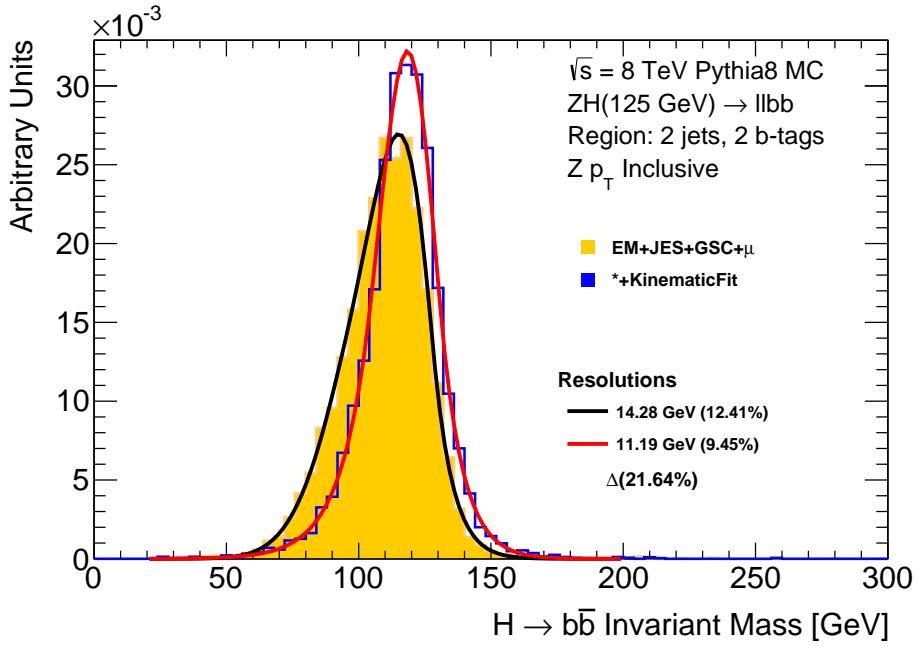


Figure 274: Dijet invariant mass before and after applying a kinematic likelihood fit in ZH $m_H = 125$ GeV signal Monte Carlo events showing a $\sim 19\%$ resolution improvement.

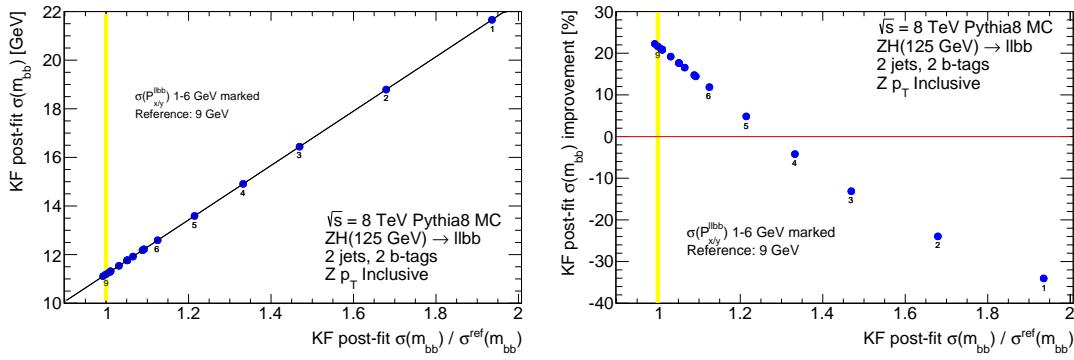


Figure 275: The postfit dijet mass resolution shown as a function of the resolution of the system balance is shown on the left while the right shows the improvement with respect to the prefit resolution. The resolution here is obtained from the width of a Bukin fit.

Not reviewed, for internal circulation only

4845 V Dijet Mass (m_{jj}) Distributions: Zero Lepton

4846 This appendix contains m_{jj} distributions of the dijet mass analysis selection outlined in Section 3.3 for
 4847 the the 0-Lepton analysis. Note: the 3-jet region for $p_T^Z < 120$ GeV is shown in the plots, but it is not
 4848 used in the analysis. In particular, in this region we expect to have a non negligible contribution of multi-
 4849 jet, which is not properly shown in the plot. These plots are done by applying the latest scale factors,
 4850 obtained for the 2 jet region and the 3 jet region separately, by comparing the event yield before and after
 the MVA combined fit. They are summarized in Table 97. Explicitly stated, the theoretical expectation

Sample	2-jets	3-jets
Zl	1.03 ± 0.05	0.98 ± 0.06
Zcl	0.89 ± 0.11	0.99 ± 0.12
Zcc	1.13 ± 0.13	1.12 ± 0.13
Zbl	1.10 ± 0.05	0.95 ± 0.05
Zbc	1.10 ± 0.11	1.09 ± 0.12
Zbb	1.12 ± 0.06	1.13 ± 0.07
Wl	1.00 ± 0.06	0.92 ± 0.06
Wcl	1.14 ± 0.07	1.07 ± 0.07
Wcc	0.75 ± 0.16	0.73 ± 0.16
Wbl	0.63 ± 0.15	0.64 ± 0.15
Wbc	0.81 ± 0.16	0.81 ± 0.16
Wbb	0.82 ± 0.16	0.86 ± 0.17
Wt	1.06 ± 0.09	1.05 ± 0.11
single top t-ch.	1.34 ± 0.27	1.08 ± 0.08
single top s-ch.	1.07 ± 0.11	1.04 ± 0.10
$0 l t\bar{t}$	1.36 ± 0.13	1.12 ± 0.10
$1 l t\bar{t}$	1.16 ± 0.07	1.00 ± 0.03
$2 l t\bar{t}$	1.01 ± 0.04	1.11 ± 0.05
WW	1.01 ± 0.05	1.01 ± 0.05
ZZ	1.03 ± 0.04	1.02 ± 0.05
WZ	1.01 ± 0.04	1.01 ± 0.03
$0 l$ Multijet	0.97 ± 0.78	1.13 ± 0.93
1μ Multijet	0.94 ± 0.13	1.11 ± 0.25
$1 e$ Multijet	0.98 ± 0.07	1.00 ± 0.07
$2 l$ Multijet	0.73 ± 0.47	0.73 ± 0.47

Table 97: Normalization scale factors obtained by comparing the event yield for the different backgrounds before and after the 0+1+2-lepton MVA fit. The normalization scale factors are given for 2-jet events and 3-jet events

4851 for each background is used for the given luminosity. All the plots in this section are done with the
 4852 status-of-art analysis. Figure 276 shows events with one b -tag and two jets.
 4853 Figure 277 shows events with one b -tag and three jets.
 4854 Figure 278 shows events with two exclusive loose b -tags and two jets.
 4855 Figure 279 shows events with two exclusive loose b -tags and three jets.
 4856 Figure 280 shows events with two exclusive medium b -tags and two jets.
 4857 Figure 281 shows events with two exclusive medium b -tags and three jets.
 4858 Figure 282 shows events with two exclusive tight b -tags and two jets.

4860 Figure 283 shows events with two exclusive tight b -tags and three jets.

4861

[Not reviewed, for internal circulation only]

Not reviewed, for internal circulation only

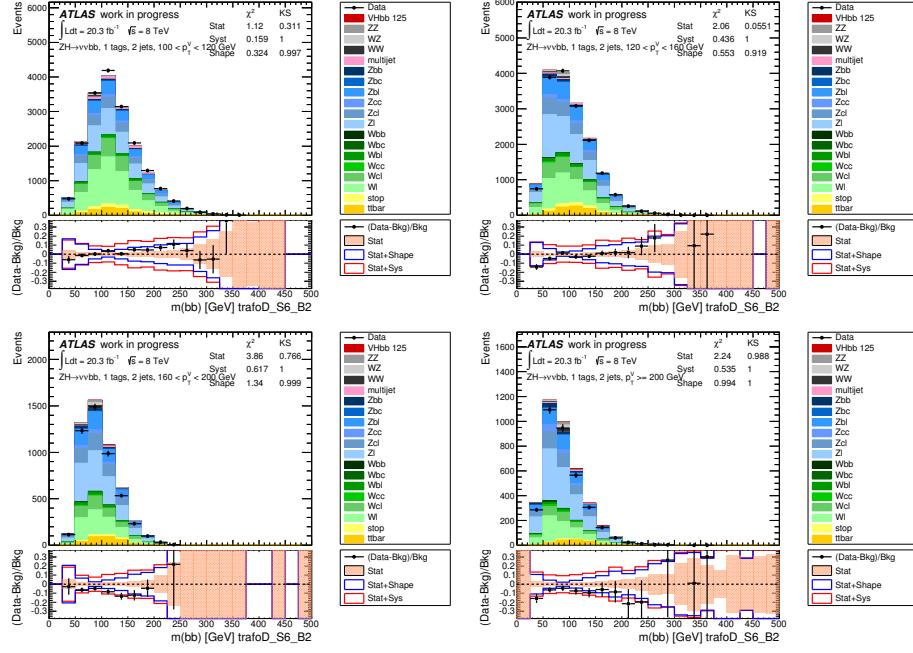


Figure 276: m_{jj} in 0-lepton events in the dijet mass analysis with 1 b -tag and 2 jets. From left to right: Row 1 - $100 < p_T^Z < 120$ GeV and $120 < p_T^Z < 160$ GeV. Row 2 - $160 < p_T^Z < 200$ GeV and $p_T^Z > 200$ GeV. Section 6.1 details the selection criteria.

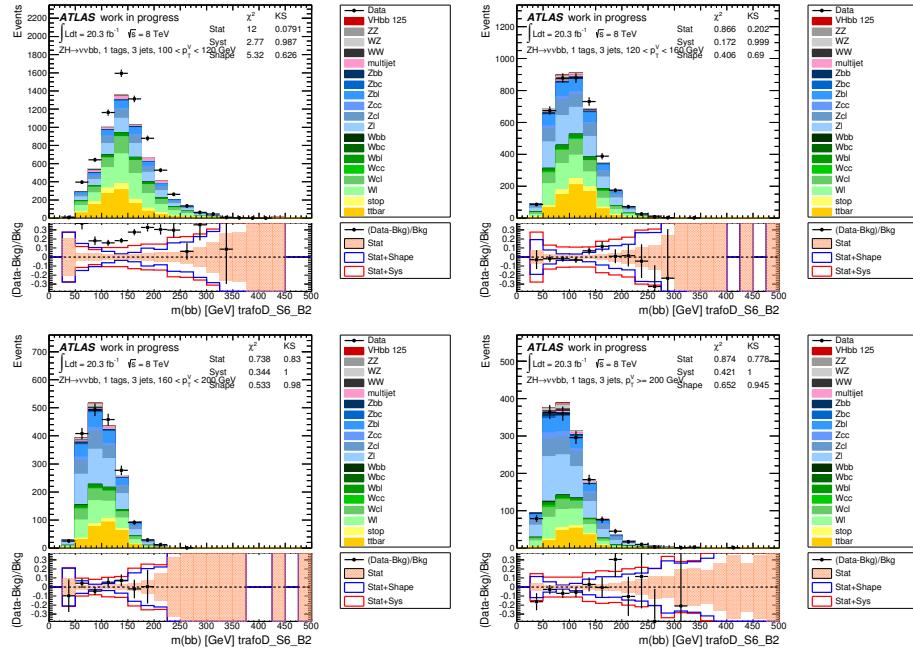


Figure 277: m_{jj} in 0-lepton events in the dijet mass analysis with 1 b -tag and 3 jets. From left to right: Row 1 - $100 < p_T^Z < 120$ GeV and $120 < p_T^Z < 160$ GeV. Row 2 - $160 < p_T^Z < 200$ GeV and $p_T^Z > 200$ GeV. Section 6.1 details the selection criteria.

Not reviewed, for internal circulation only

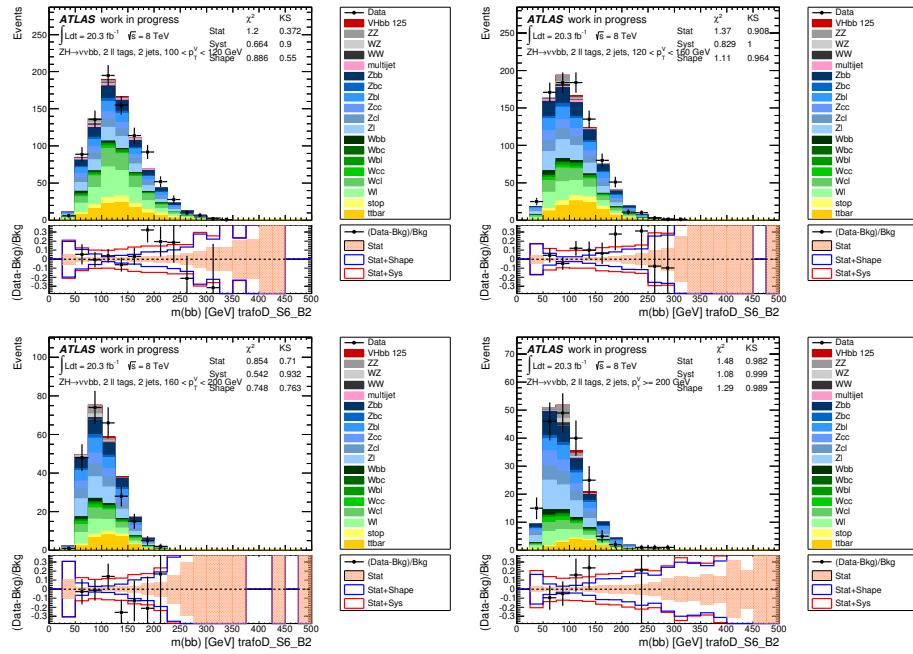


Figure 278: m_{jj} in 0-lepton events in the dijet mass analysis with 2L exclusive b -tags and 2 jets. From left to right: Row 1 - $100 < p_T^Z < 120$ GeV and $120 < p_T^Z < 160$ GeV. Row 2 - $160 < p_T^Z < 200$ GeV and $p_T^Z > 200$ GeV. Section 6.1 details the selection criteria.

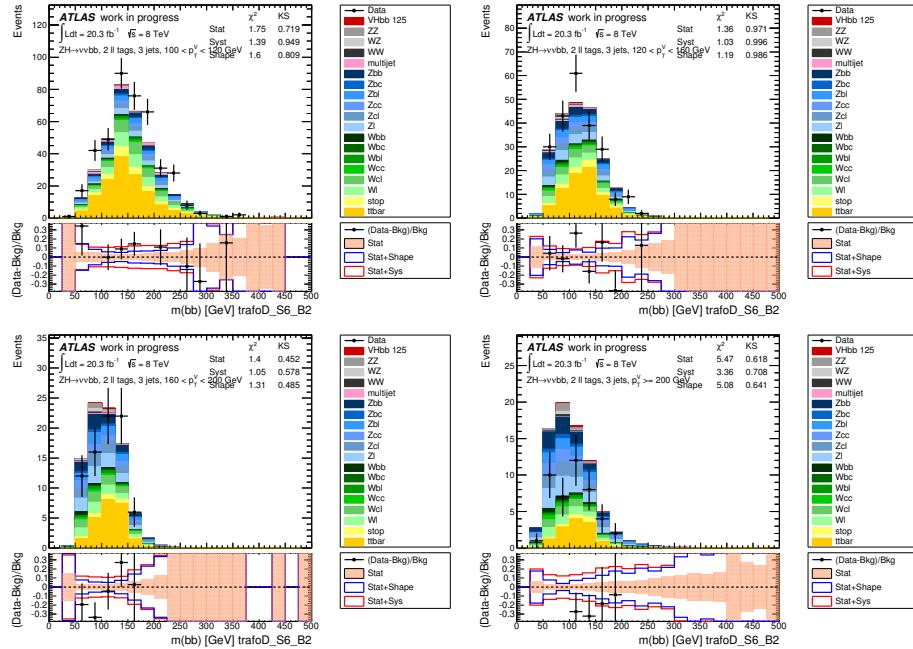


Figure 279: m_{jj} in 0-lepton events in the dijet mass analysis with 2L exclusive b -tags and 3 jets. From left to right: Row 1 - $100 < p_T^Z < 120$ GeV and $120 < p_T^Z < 160$ GeV. Row 2 - $160 < p_T^Z < 200$ GeV and $p_T^Z > 200$ GeV. Section 6.1 details the selection criteria.

Not reviewed, for internal circulation only

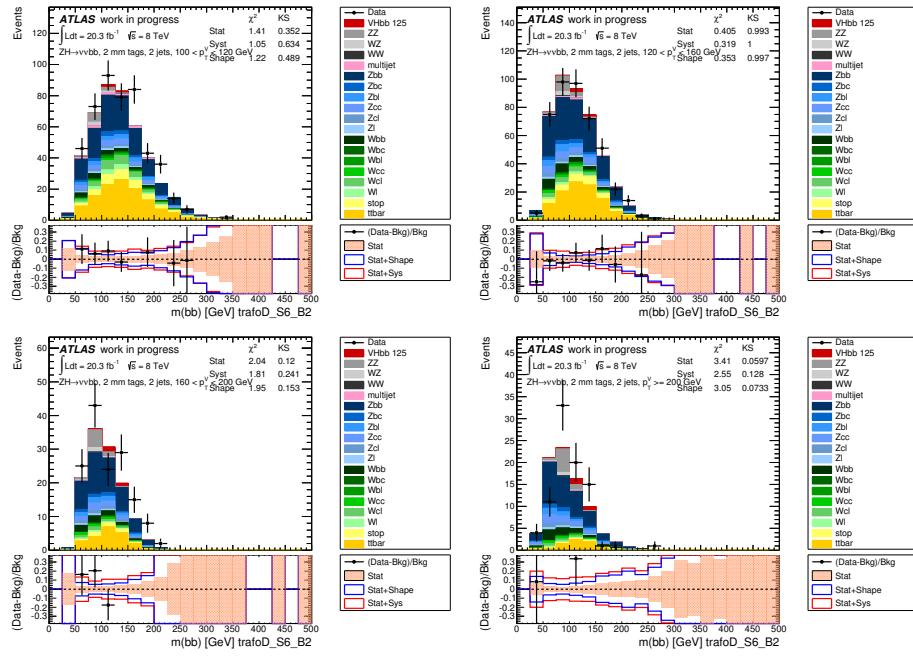


Figure 280: m_{jj} in 0-lepton events in the dijet mass analysis with 2M exclusive b -tags and 2 jets. From left to right: Row 1 - $100 < p_T^Z < 120$ GeV and $120 < p_T^Z < 160$ GeV. Row 2 - $160 < p_T^Z < 200$ GeV and $p_T^Z > 200$ GeV. Section 6.1 details the selection criteria.

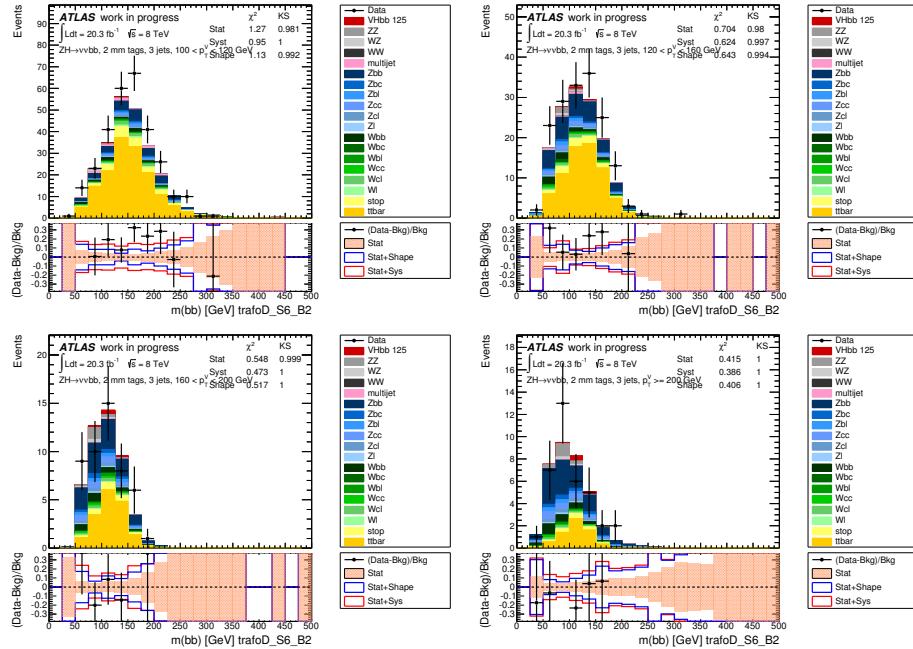


Figure 281: m_{jj} in 0-lepton events in the dijet mass analysis with 2M exclusive b -tags and 3 jets. From left to right: Row 1 - $100 < p_T^Z < 120$ GeV and $120 < p_T^Z < 160$ GeV. Row 2 - $160 < p_T^Z < 200$ GeV and $p_T^Z > 200$ GeV. Section 6.1 details the selection criteria.

Not reviewed, for internal circulation only

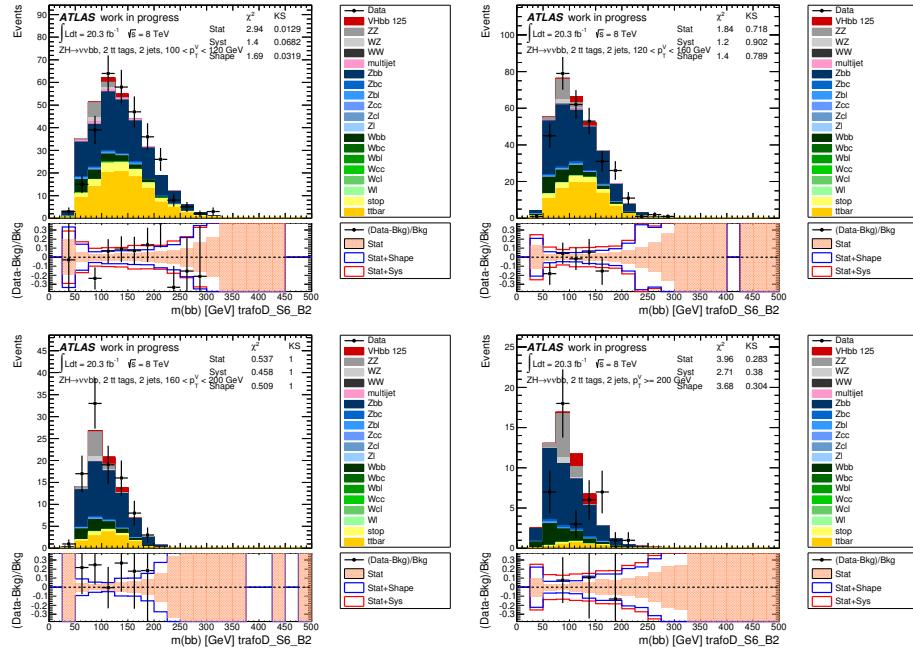


Figure 282: m_{jj} in 0-lepton events in the dijet mass analysis with 2T exclusive b -tags and 2 jets. From left to right: Row 1 - $100 < p_T^Z < 120$ GeV and $120 < p_T^Z < 160$ GeV. Row 2 - $160 < p_T^Z < 200$ GeV and $p_T^Z > 200$ GeV. Section 6.1 details the selection criteria.

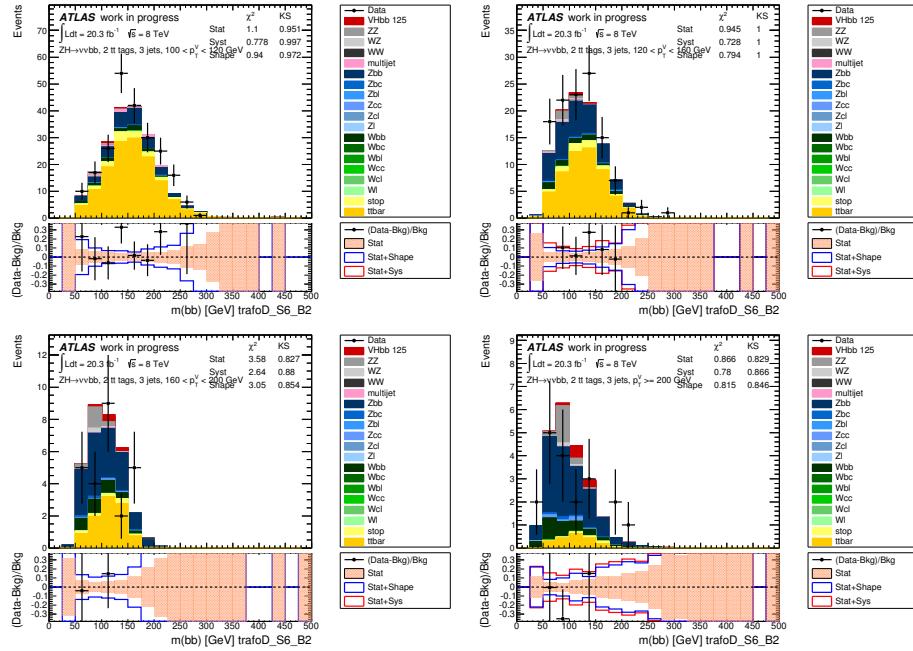


Figure 283: m_{jj} in 0-lepton events in the dijet mass analysis with 2T exclusive b -tags and 3 jets. From left to right: Row 1 - $100 < p_T^Z < 120$ GeV and $120 < p_T^Z < 160$ GeV. Row 2 - $160 < p_T^Z < 200$ GeV and $p_T^Z > 200$ GeV. Section 6.1 details the selection criteria.

4862 **W Dijet Mass (m_{jj}) Distributions: One Lepton**

4863 This appendix contains m_{jj} distributions of the dijet mass analysis selection outlined in Section 3.3 for
4864 the the 1-Lepton analysis. These plots are done by applying the latest scale factors, obtained for the 2 jet
4865 region and the 3 jet region separately, by comparing the event yield before and after the MVA combined
4866 fit. They are summarized in Table 97. Explicitly stated, the theoretical expectation for each background
4867 is used for the given luminosity. All the plots in this section are done with the status-of-art analysis.

4868 Figure 284 shows events with one b -tag and two jets.

4869 Figure 285 shows events with one b -tag and three jets.

4870 Figure 286 shows events with two exclusive loose b -tags and two jets.

4871 Figure 287 shows events with two exclusive loose b -tags and three jets.

4872 Figure 288 shows events with two exclusive medium b -tags and two jets.

4873 Figure 289 shows events with two exclusive medium b -tags and three jets.

4874 Figure 290 shows events with two exclusive tight b -tags and two jets.

4875 Figure 291 shows events with two exclusive tight b -tags and three jets.

4876

Not reviewed, for internal circulation only

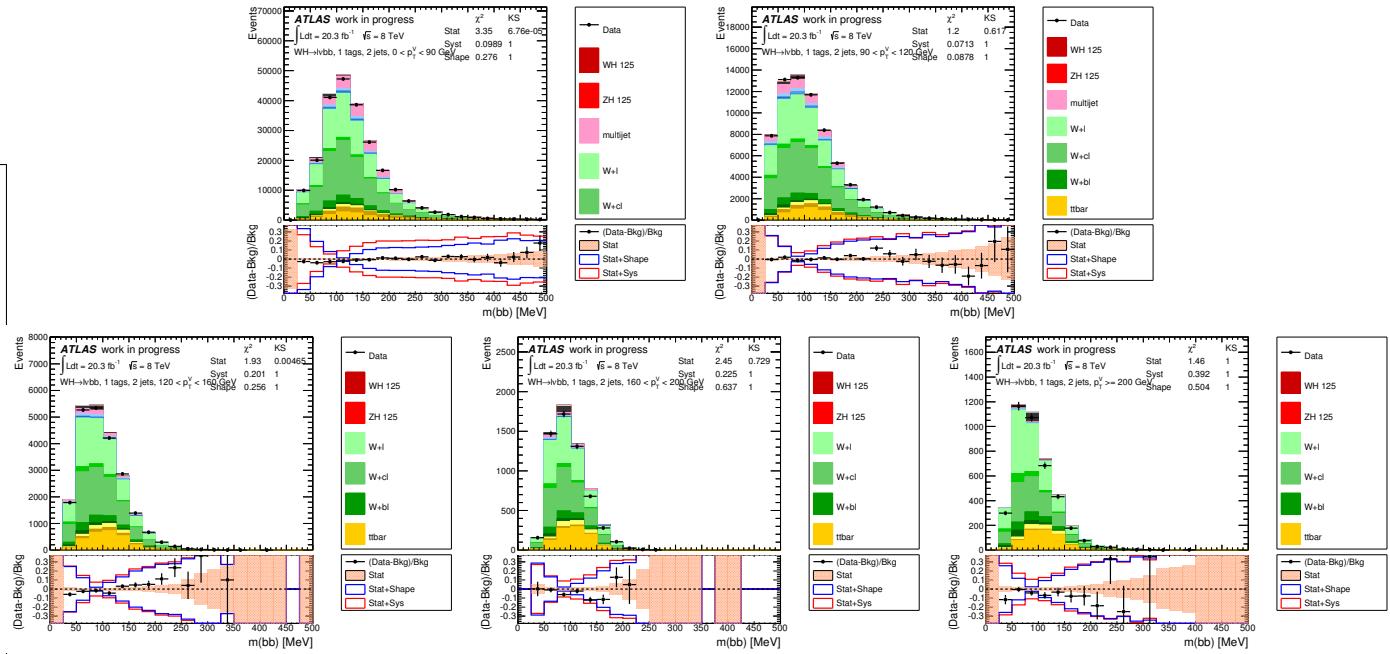


Figure 284: m_{jj} in 1-lepton events in the dijet mass analysis with 1 b -tag and 2 jets. From left to right: Row 1 - inclusive in p_T^W , $p_T^W < 90$ GeV, and $90 < p_T^W < 120$ GeV. Row 2 - $120 < p_T^W < 160$ GeV, $160 < p_T^W < 200$ GeV, and $p_T^W > 200$ GeV. Section 6.1 details the selection criteria.

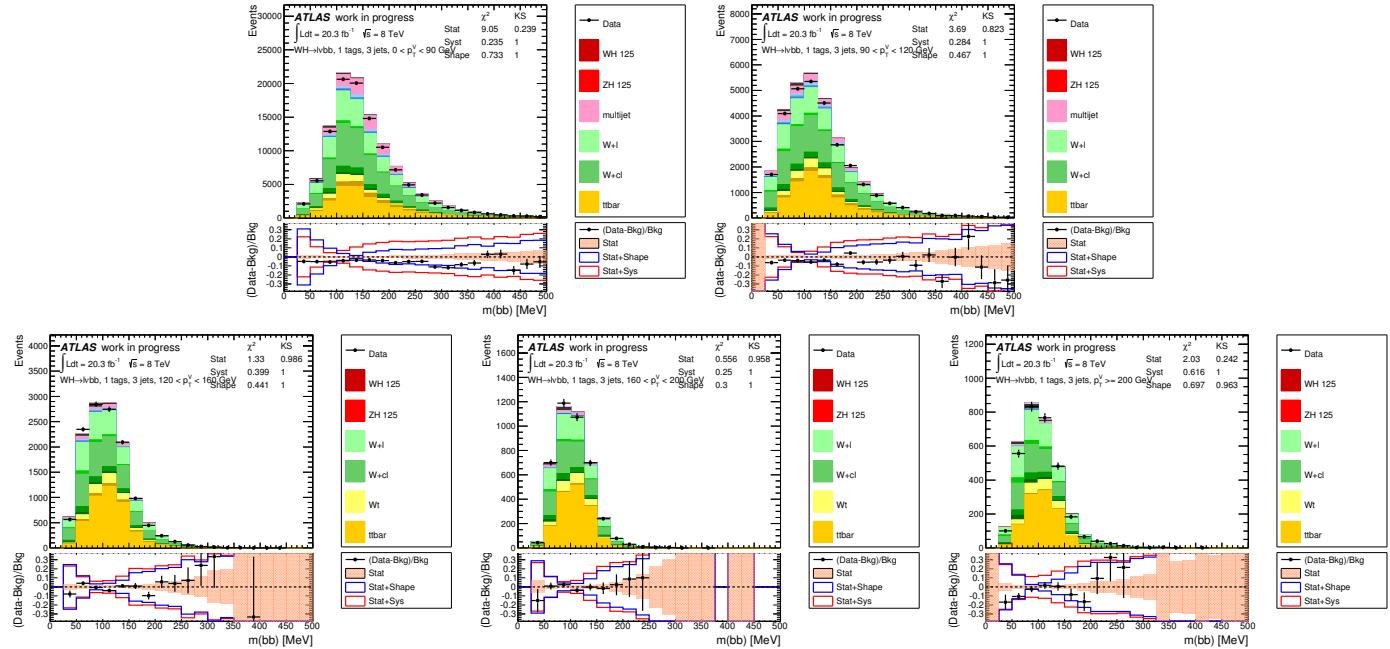


Figure 285: m_{jj} in 1-lepton events in the dijet mass analysis with 1 b -tag and 3 jets. From left to right: Row 1 - inclusive in p_T^W , $p_T^W < 90$ GeV, and $90 < p_T^W < 120$ GeV. Row 2 - $120 < p_T^W < 160$ GeV, $160 < p_T^W < 200$ GeV, and $p_T^W > 200$ GeV. Section 6.1 details the selection criteria.

Not reviewed, for internal circulation only

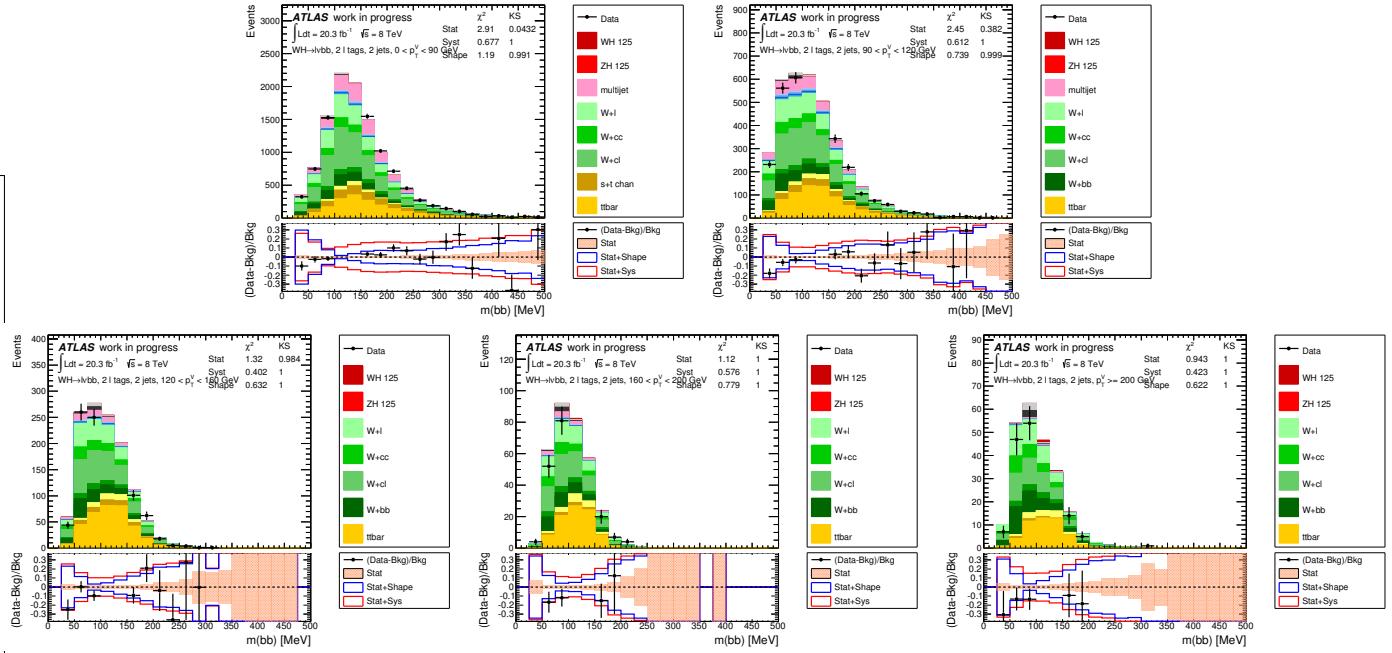


Figure 286: m_{jj} in 1-lepton events in the dijet mass analysis with 2L exclusive b -tags and 2 jets. From left to right: Row 1 - inclusive in p_T^W , $p_T^W < 90$ GeV, and $90 < p_T^W < 120$ GeV. Row 2 - $120 < p_T^W < 160$ GeV, $160 < p_T^W < 200$ GeV, and $p_T^W > 200$ GeV. Section 6.1 details the selection criteria.

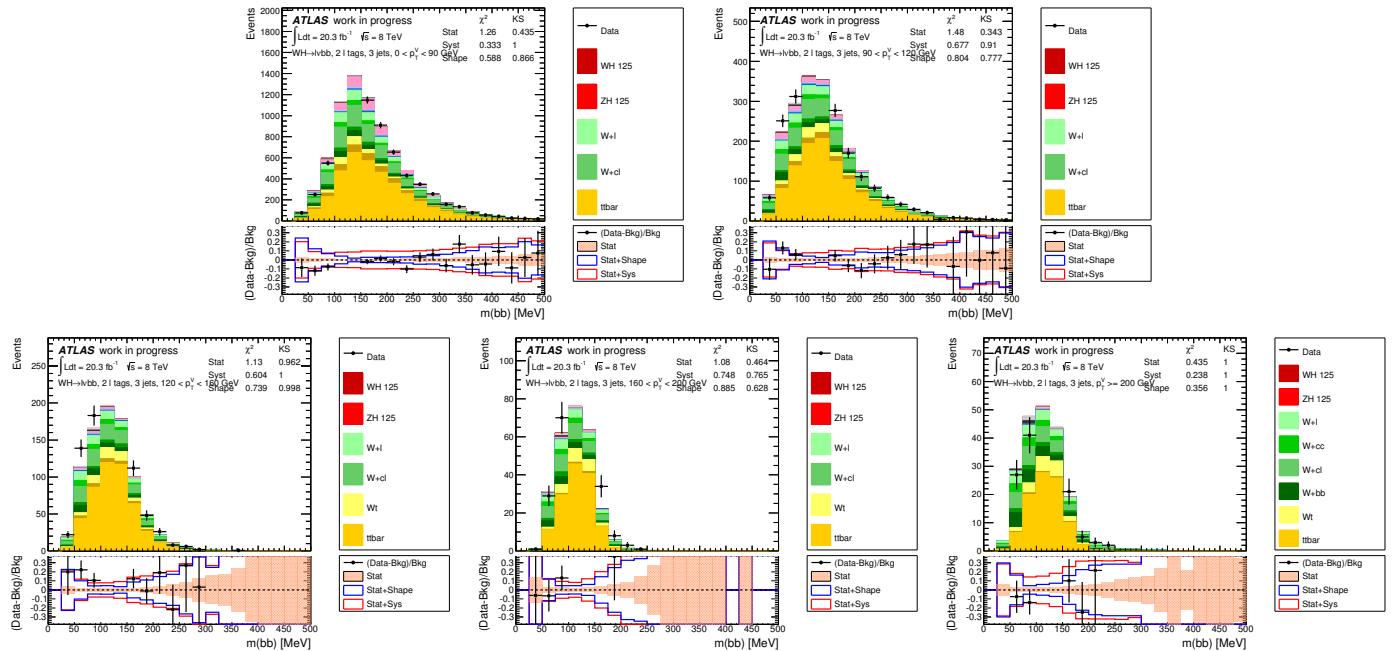


Figure 287: m_{jj} in 1-lepton events in the dijet mass analysis with 2L exclusive b -tags and 3 jets. From left to right: Row 1 - inclusive in p_T^W , $p_T^W < 90$ GeV, and $90 < p_T^W < 120$ GeV. Row 2 - $120 < p_T^W < 160$ GeV, $160 < p_T^W < 200$ GeV, and $p_T^W > 200$ GeV. Section 6.1 details the selection criteria.

Not reviewed, for internal circulation only

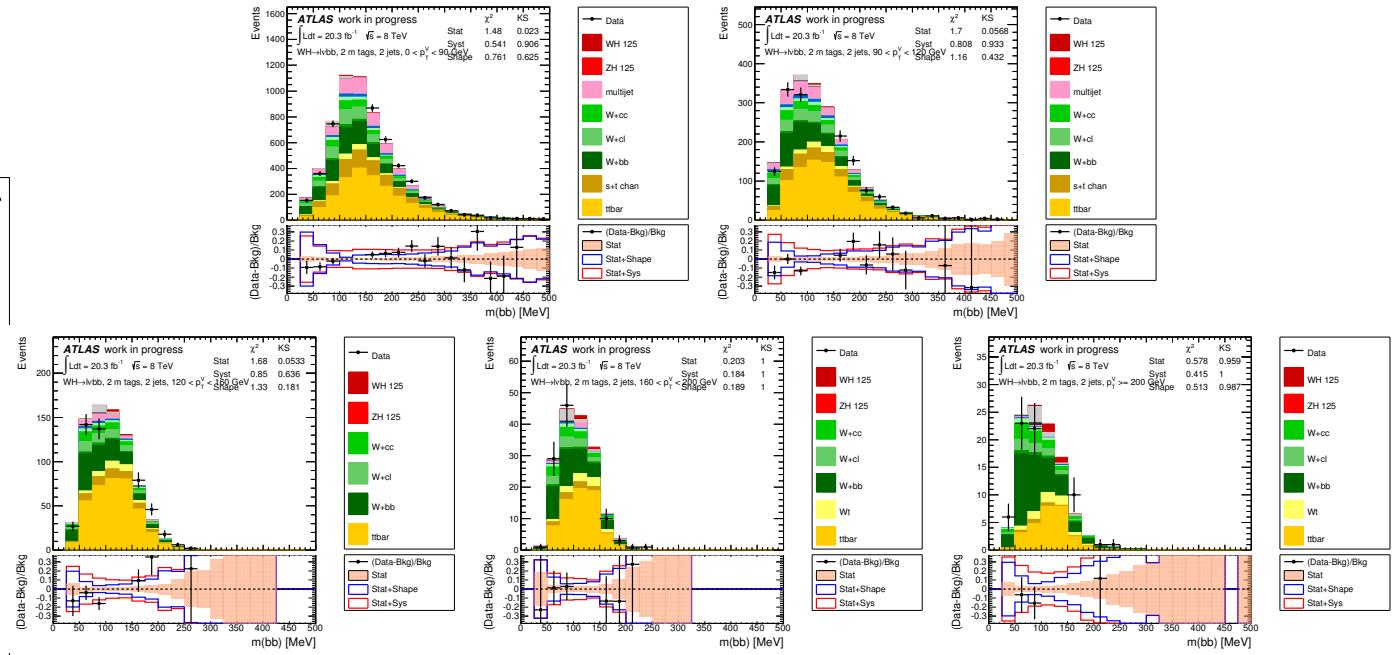


Figure 288: m_{jj} in 1-lepton events in the dijet mass analysis with 2M exclusive b -tags and 2 jets. From left to right: Row 1 - inclusive in p_T^W , $p_T^W < 90$ GeV, and $90 < p_T^W < 120$ GeV. Row 2 - $120 < p_T^W < 160$ GeV, $160 < p_T^W < 200$ GeV, and $p_T^W > 200$ GeV. Section 6.1 details the selection criteria.

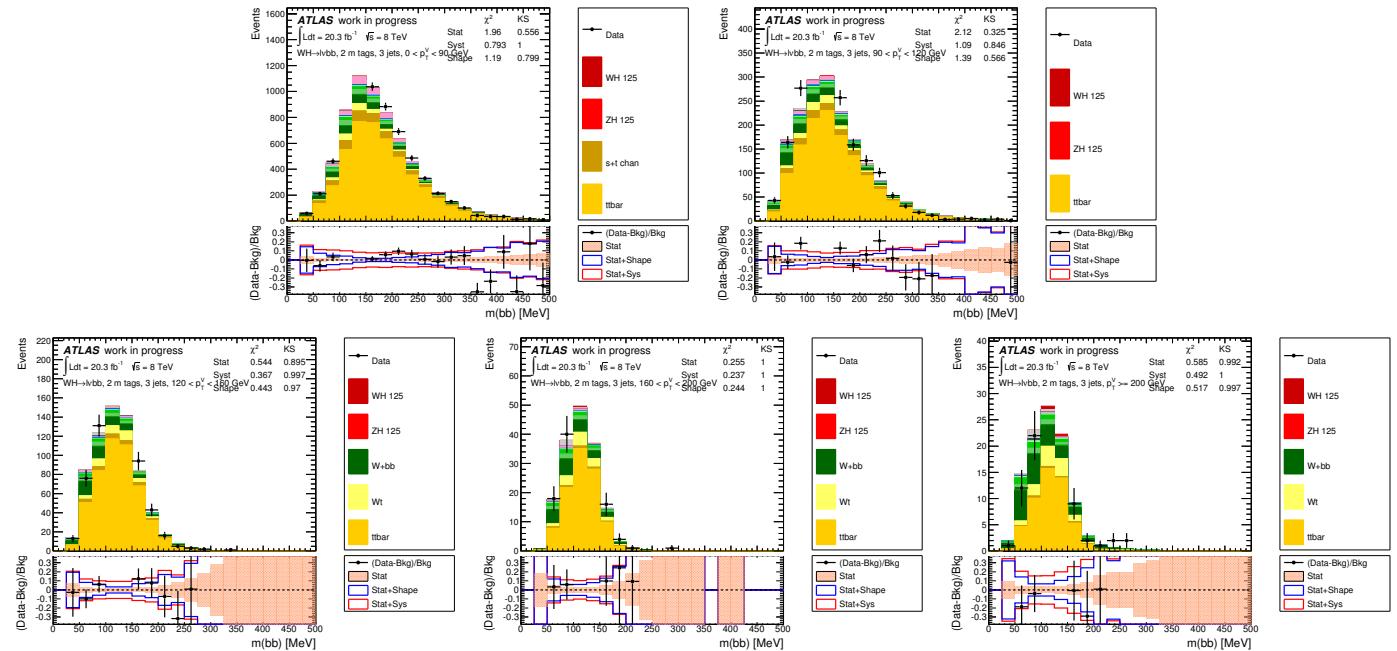


Figure 289: m_{jj} in 1-lepton events in the dijet mass analysis with 2M exclusive b -tags and 3 jets. From left to right: Row 1 - inclusive in p_T^W , $p_T^W < 90$ GeV, and $90 < p_T^W < 120$ GeV. Row 2 - $120 < p_T^W < 160$ GeV, $160 < p_T^W < 200$ GeV, and $p_T^W > 200$ GeV. Section 6.1 details the selection criteria.

Not reviewed, for internal circulation only

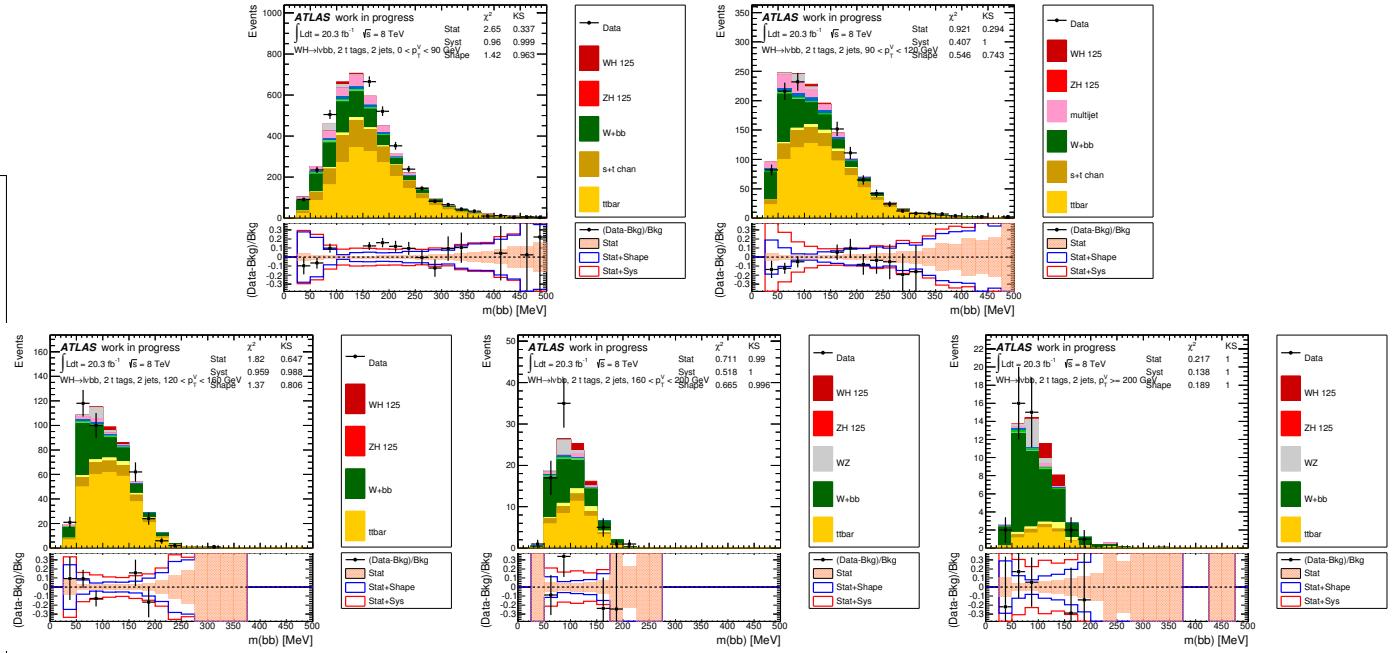


Figure 290: m_{jj} in 1-lepton events in the dijet mass analysis with 2T exclusive b -tags and 2 jets. From left to right: Row 1 - inclusive in p_T^W , $p_T^W < 90$ GeV, and $90 < p_T^W < 120$ GeV. Row 2 - $120 < p_T^W < 160$ GeV, $160 < p_T^W < 200$ GeV, and $p_T^W > 200$ GeV. Section 6.1 details the selection criteria.

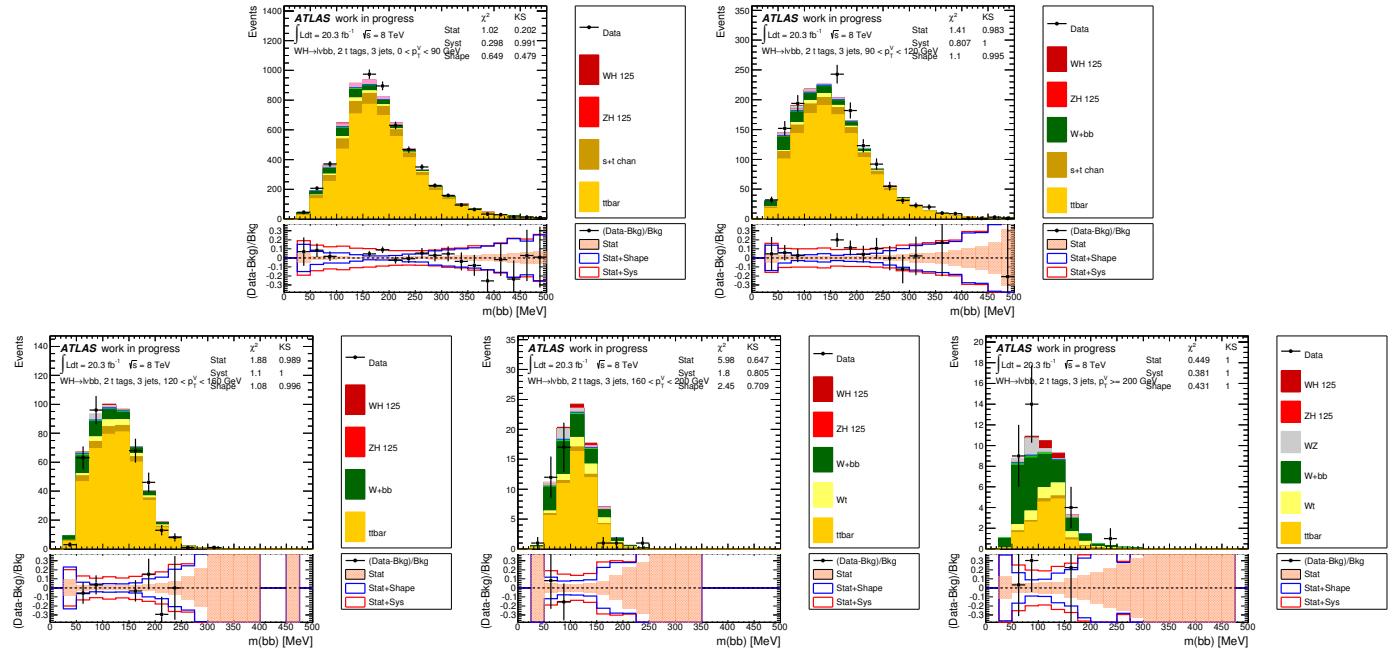


Figure 291: m_{jj} in 1-lepton events in the dijet mass analysis with 2T exclusive b -tags and 3 jets. From left to right: Row 1 - inclusive in p_T^W , $p_T^W < 90$ GeV, and $90 < p_T^W < 120$ GeV. Row 2 - $120 < p_T^W < 160$ GeV, $160 < p_T^W < 200$ GeV, and $p_T^W > 200$ GeV. Section 6.1 details the selection criteria.

4877 X Dijet Mass (m_{jj}) Distributions: Two Lepton

4878 This appendix contains m_{jj} distributions of the dijet mass analysis selection outlined in Section 3.3 for
4879 the the 2-lepton analysis. These plots are done by applying the latest scale factors, obtained for the 2 jet
4880 region and the 3 jet region separately, by comparing the event yield before and after the MVA combined
4881 fit. They are summarized in Table 97. Explicitly stated, the theoretical expectation for each background
4882 is used for the given luminosity. All the plots in this section are done with the status-of-art analysis.

4883 Figure 292 shows events with one b -tag and two jets.

4884 Figure 293 shows events with one b -tag and three jets.

4885 Figure 294 shows events with two exclusive loose b -tags and two jets.

4886 Figure 295 shows events with two exclusive loose b -tags and three jets.

4887 Figure 296 shows events with two exclusive medium b -tags and two jets.

4888 Figure 297 shows events with two exclusive medium b -tags and three jets.

4889 Figure 298 shows events with two exclusive tight b -tags and two jets.

4890 Figure 299 shows events with two exclusive tight b -tags and three jets.

4891

Not reviewed, for internal circulation only

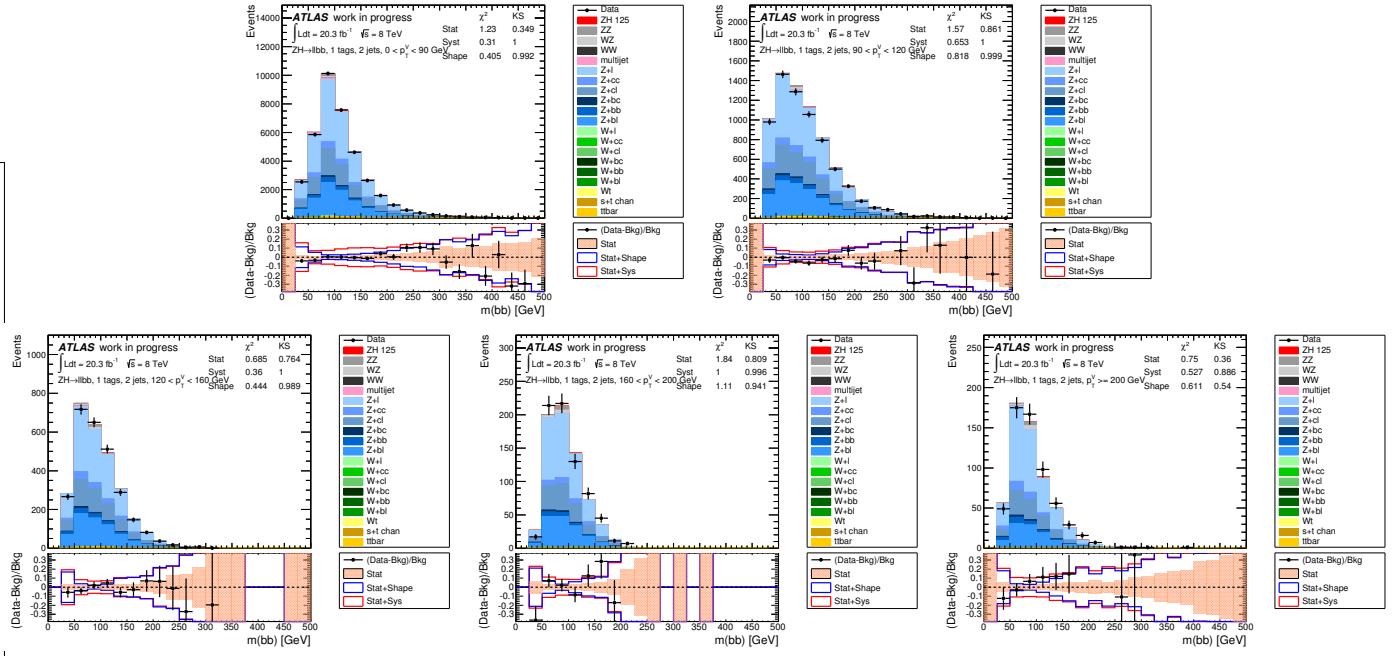


Figure 292: m_{jj} in 2-lepton events in the dijet mass analysis with 1 b -tag and 2 jets. From left to right: Row 1 - $p_T^Z < 90$ GeV, and $90 < p_T^Z < 120$ GeV. Row 2 - $120 < p_T^Z < 160$ GeV, $160 < p_T^Z < 200$ GeV, and $p_T^Z > 200$ GeV. Section 6.1 details the selection criteria.

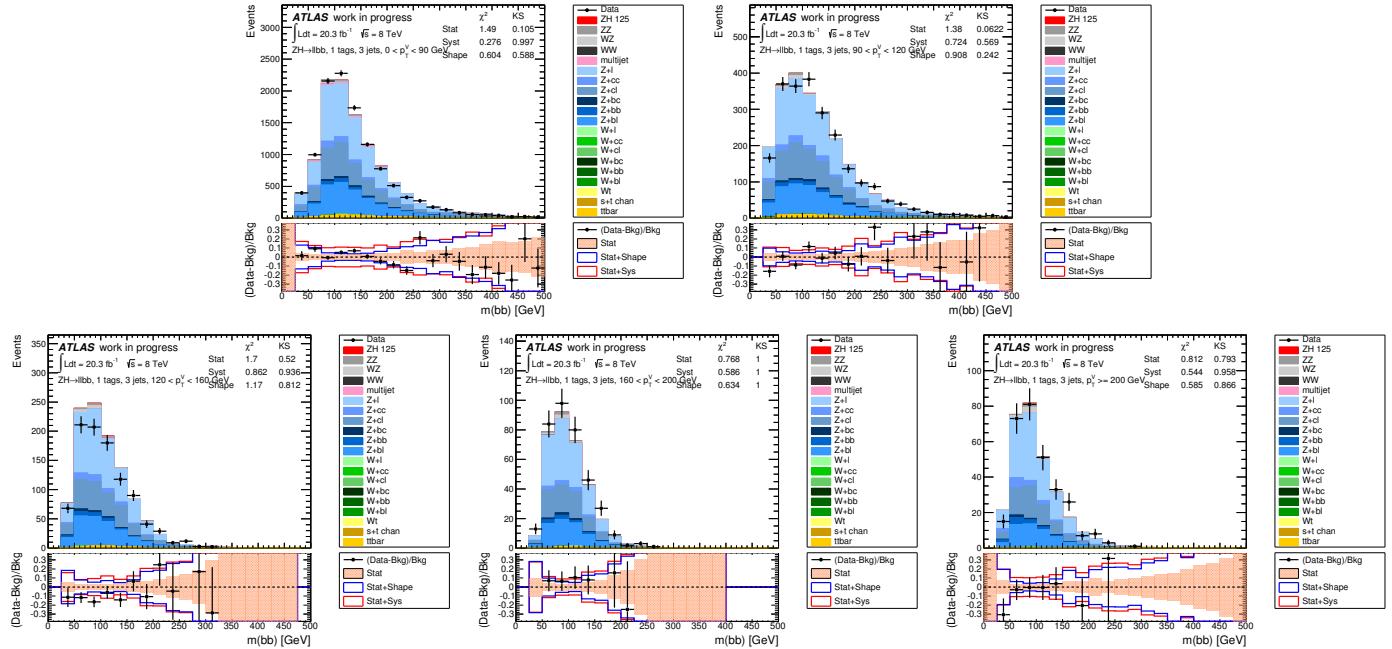


Figure 293: m_{jj} in 2-lepton events in the dijet mass analysis with 1 b -tag and 3 jets. From left to right: Row 1 - $p_T^Z < 90$ GeV, and $90 < p_T^Z < 120$ GeV. Row 2 - $120 < p_T^Z < 160$ GeV, $160 < p_T^Z < 200$ GeV, and $p_T^Z > 200$ GeV. Section 6.1 details the selection criteria.

Not reviewed, for internal circulation only

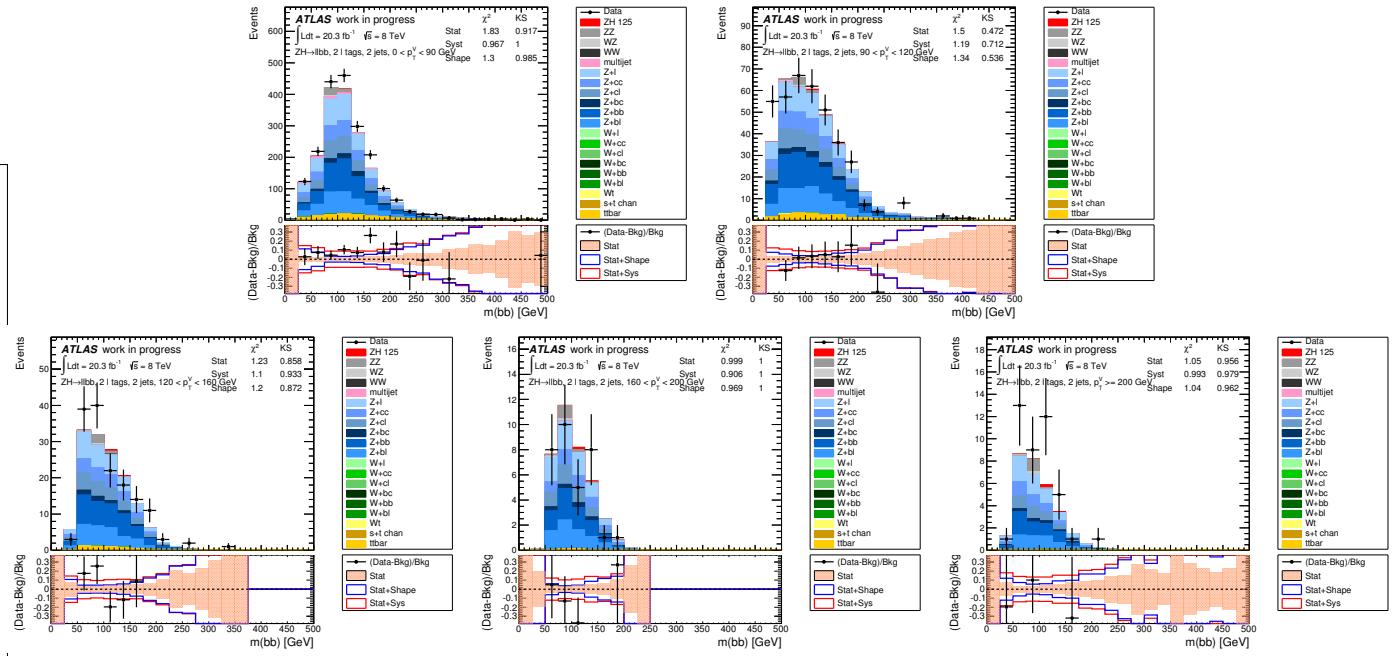


Figure 294: m_{jj} in 2-lepton events in the dijet mass analysis with 2L exclusive b -tags and 2 jets. From left to right: Row 1 - $p_T^Z < 90$ GeV, and $90 < p_T^Z < 120$ GeV. Row 2 - $120 < p_T^Z < 160$ GeV, $160 < p_T^Z < 200$ GeV, and $p_T^Z > 200$ GeV. Section 6.1 details the selection criteria.

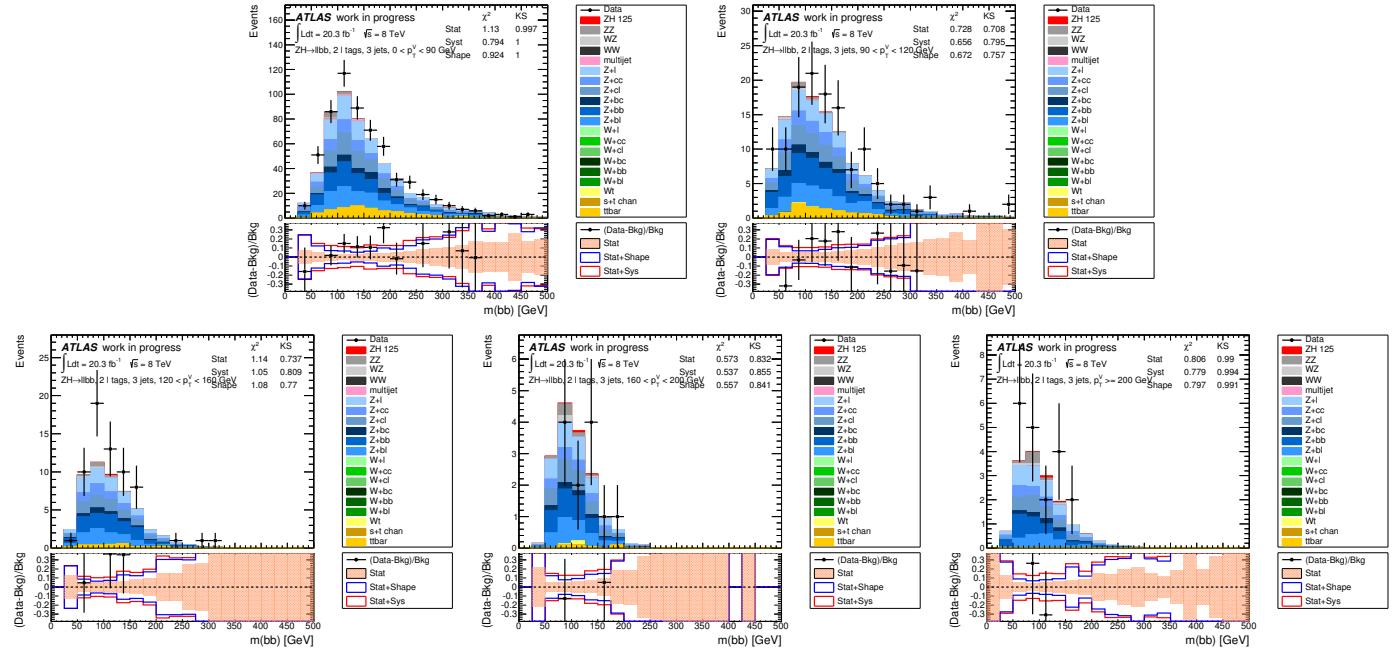


Figure 295: m_{jj} in 2-lepton events in the dijet mass analysis with 2L exclusive b -tags and 3 jets. From left to right: Row 1 - $p_T^Z < 90$ GeV, and $90 < p_T^Z < 120$ GeV. Row 2 - $120 < p_T^Z < 160$ GeV, $160 < p_T^Z < 200$ GeV, and $p_T^Z > 200$ GeV. Section 6.1 details the selection criteria.

Not reviewed, for internal circulation only

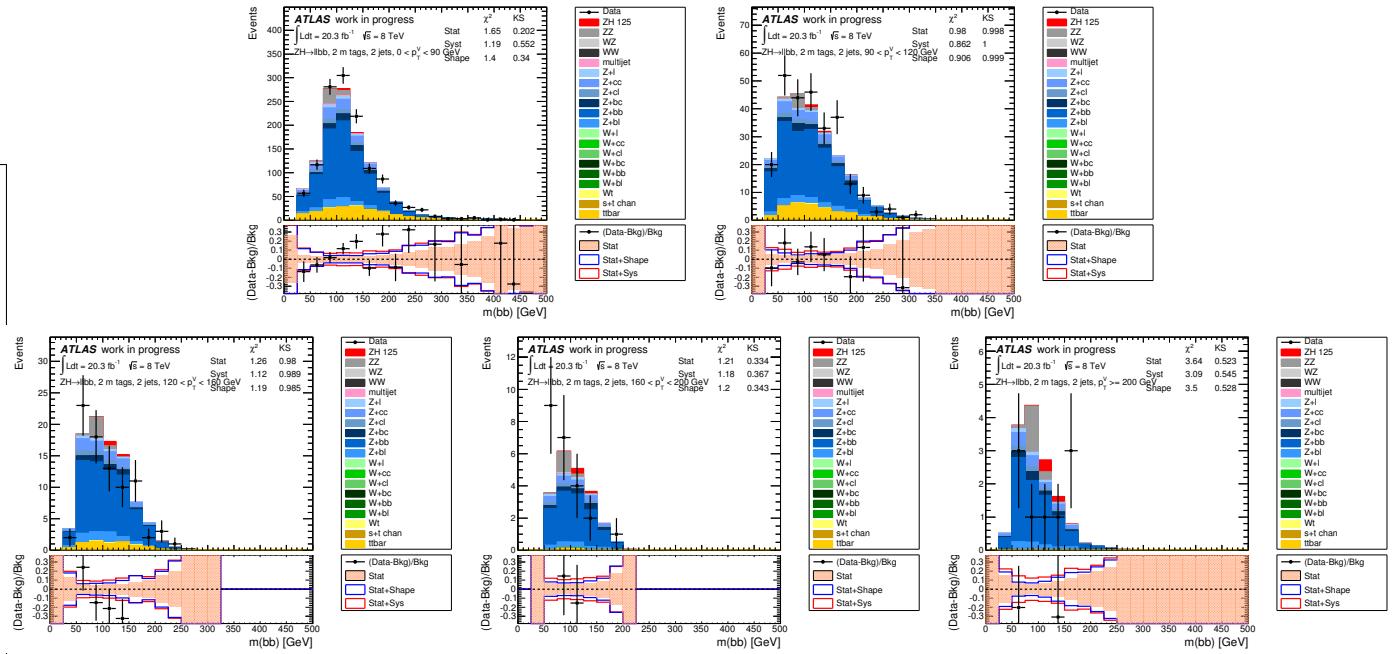


Figure 296: m_{jj} in 2-lepton events in the dijet mass analysis with 2M exclusive b -tags and 2 jets. From left to right: Row 1 - $p_T^Z < 90$ GeV, and $90 < p_T^Z < 120$ GeV. Row 2 - $120 < p_T^Z < 160$ GeV, $160 < p_T^Z < 200$ GeV, and $p_T^Z > 200$ GeV. Section 6.1 details the selection criteria.

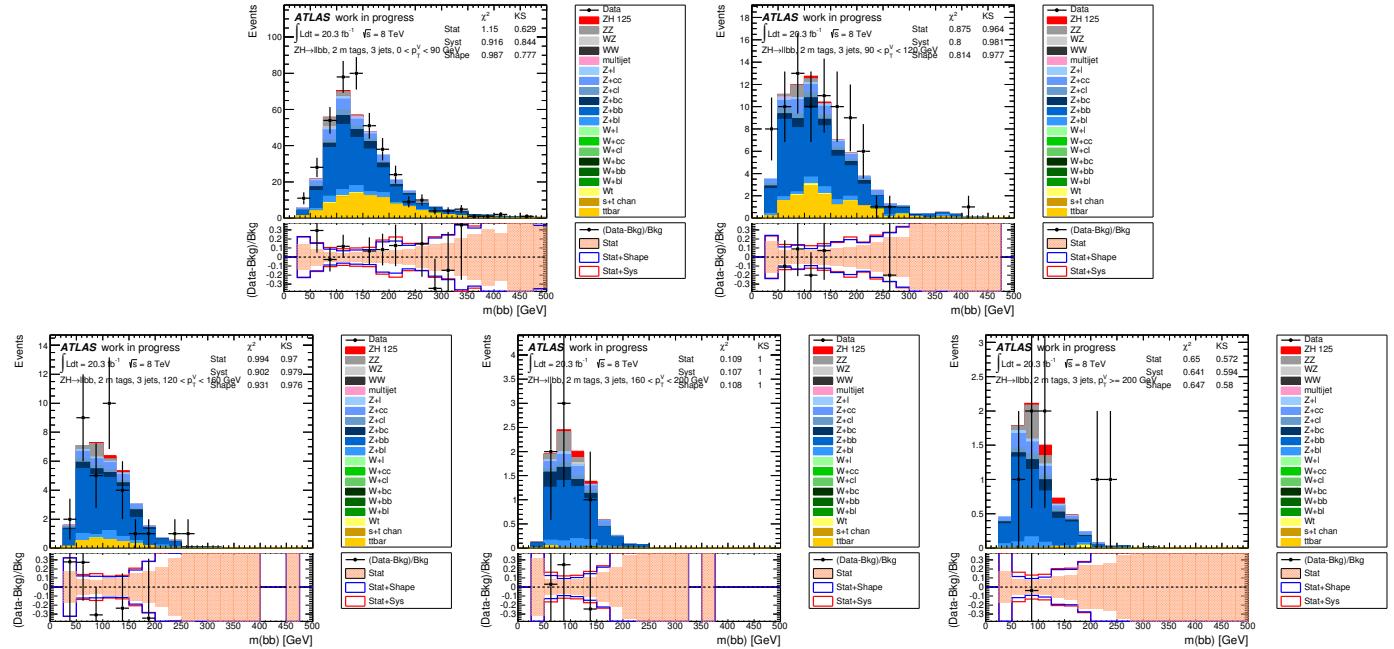


Figure 297: m_{jj} in 2-lepton events in the dijet mass analysis with 2M exclusive b -tags and 3 jets. From left to right: Row 1 - $p_T^Z < 90$ GeV, and $90 < p_T^Z < 120$ GeV. Row 2 - $120 < p_T^Z < 160$ GeV, $160 < p_T^Z < 200$ GeV, and $p_T^Z > 200$ GeV. Section 6.1 details the selection criteria.

Not reviewed, for internal circulation only

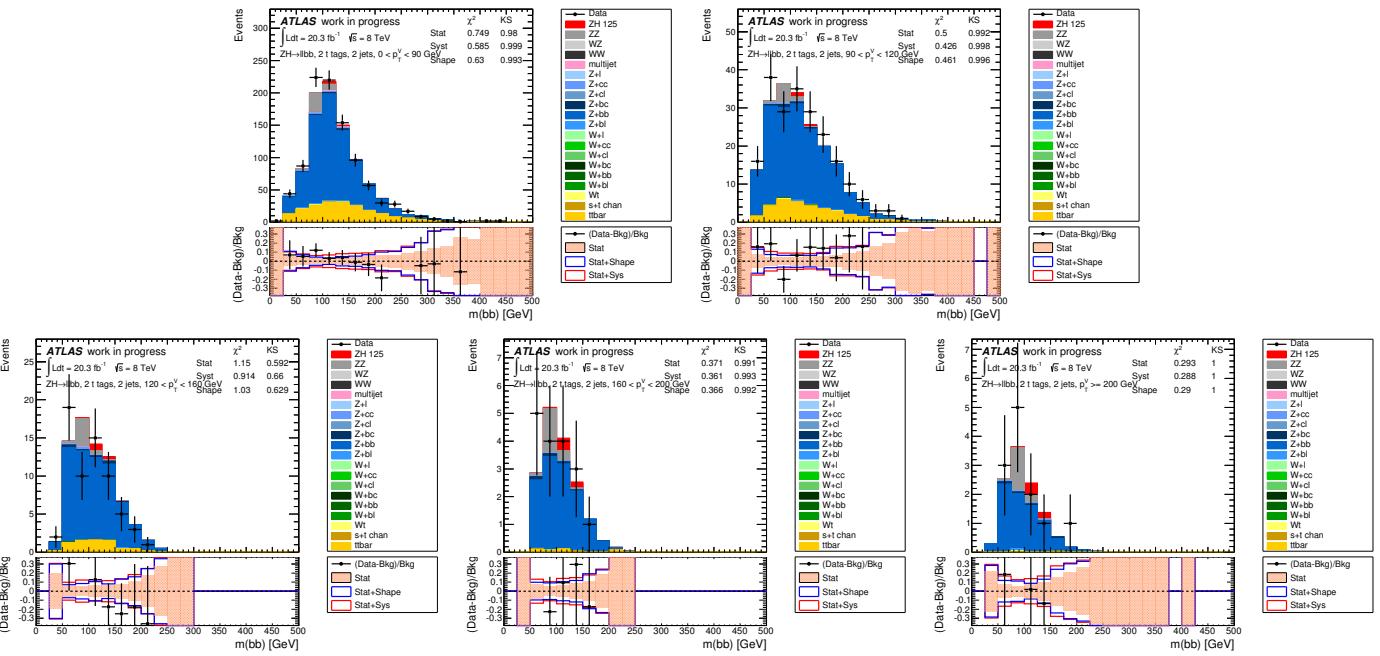


Figure 298: m_{jj} in 2-lepton events in the dijet mass analysis with 2T exclusive b -tags and 2 jets. From left to right: Row 1 - $p_T^Z < 90$ GeV, and $90 < p_T^Z < 120$ GeV. Row 2 - $120 < p_T^Z < 160$ GeV, $160 < p_T^Z < 200$ GeV, and $p_T^Z > 200$ GeV. Section 6.1 details the selection criteria.

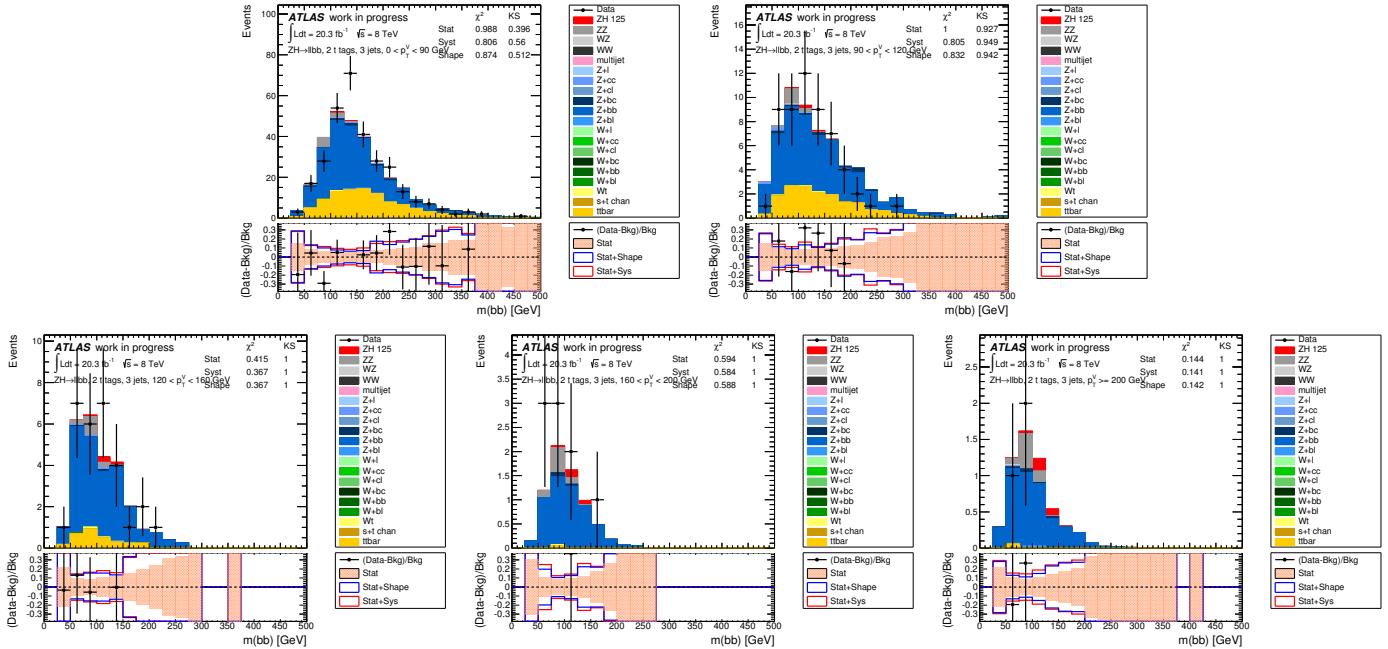


Figure 299: m_{jj} in 2-lepton events in the dijet mass analysis with 2T exclusive b -tags and 3 jets. From left to right: Row 1 - $p_T^Z < 90$ GeV, and $90 < p_T^Z < 120$ GeV. Row 2 - $120 < p_T^Z < 160$ GeV, $160 < p_T^Z < 200$ GeV, and $p_T^Z > 200$ GeV. Section 6.1 details the selection criteria.

4892 Y MVA Input Variable Distributions: Zero Lepton

4893 This appendix contains distributions of the BDT input variables defined in Section 6 in the 0-lepton anal-
4894 ysis. Note the the 0-lepton selection only included events with $p_T^Z > 120$ GeV in the MVA analysis.

4895 These plots are done by applying the latest scale factors, obtained for the 2-jet region and the 3-jet region
4896 separately, by comparing the event yield before and after the MVA combined fit. They are summarized in
4897 Table 97. Explicitly stated, the theoretical expectation for each background is used for the given lumi-
4898 nosity. All the plots in this section are done with the status-of-art analysis.

4899 Figure 300 shows one b -tag two jet events prefit and Figure 301 postfit.

4900 Figure 302 shows two loose b -tag two jet events prefit and Figure 303 postfit.

4901 Figure 304 shows two medium or two tight b -tag two jet events prefit and Figure 305 postfit.

4902 Figure 306 shows one b -tag three jet events prefit and Figure 307 postfit.

4903 Figure 308 shows two loose b -tag three jet events prefit and Figure 309 postfit.

4904 Figure 310 shows two medium or two tight b -tag two jet events prefit and Figure 311 postfit.

4905

Not reviewed, for internal circulation only

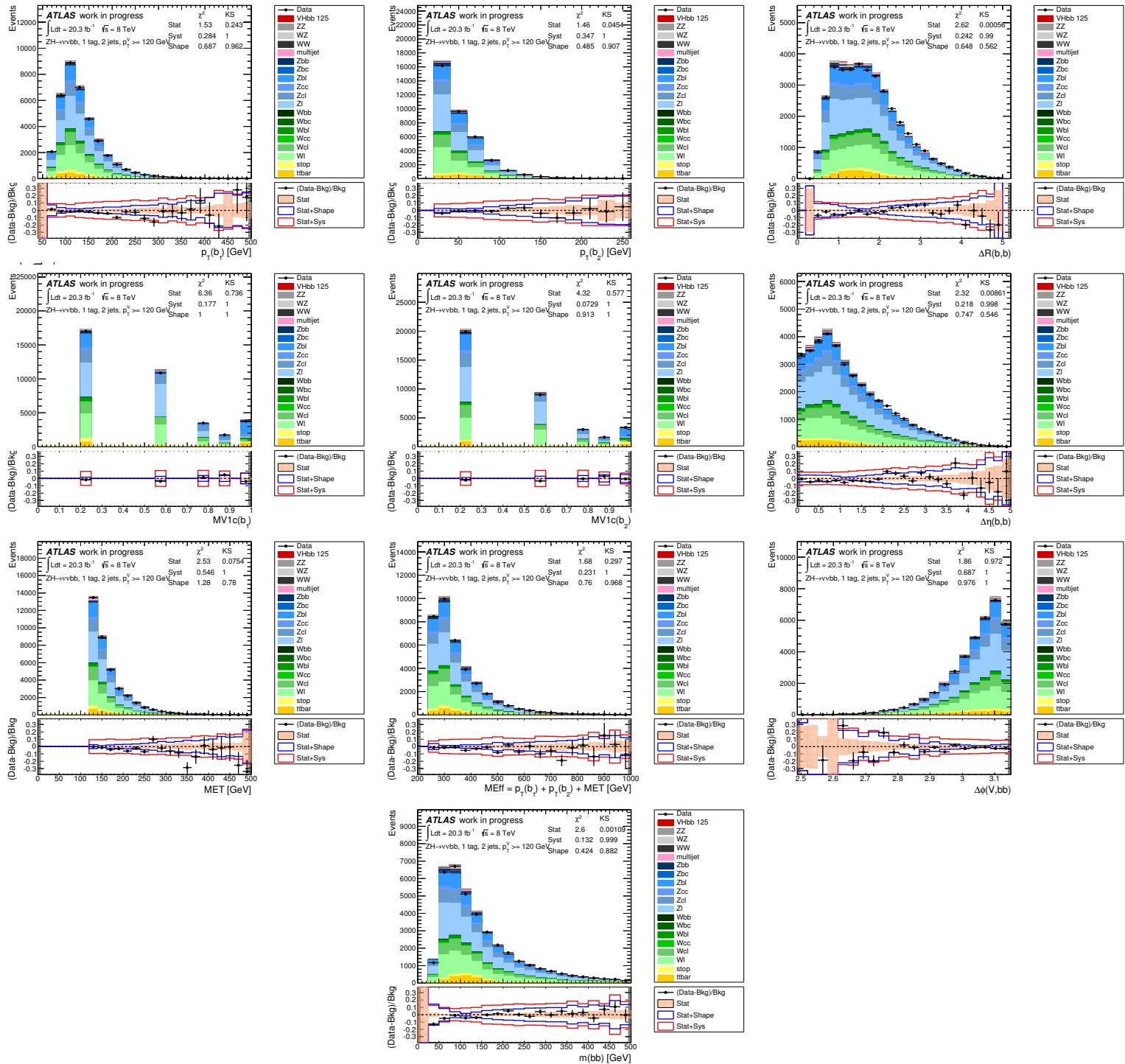


Figure 300: Distributions of MVA training variables used in 0-lepton events ($p_T^Z > 120$ GeV) with 1 b -tag and 2 jets. From left to right: Row 1 - leading then sub-leading jet p_T and ΔR of the same jets. Row 2 - pseudo-continuous MV1c distributions for leading then sub-leading jet and the $\Delta\eta$ of the same jets. Row 3 - E_T^{miss} , H_T , and $\Delta\phi(V,H)$. Row 4 - m_{jj} . Section 6.1 details the definition of each variable.

Not reviewed, for internal circulation only

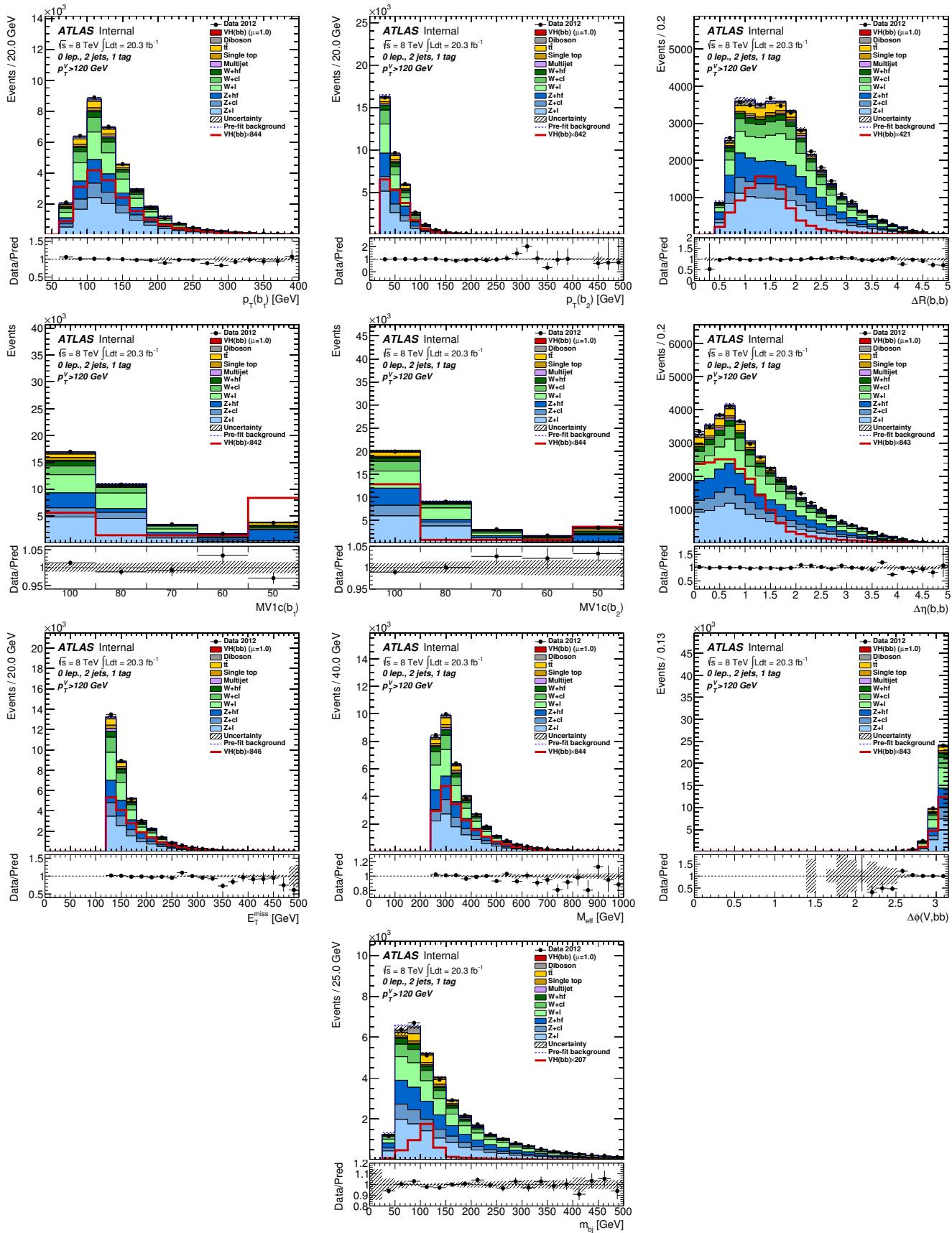


Figure 301: Distributions of MVA training variables used in 0-lepton events ($p_T^Z > 120 \text{ GeV}$) with 1 b -tag and 2 jets after the combined 0+1+2 lepton MVA fit. From left to right: Row 1 - leading then sub-leading jet p_T and ΔR of the same jets. Row 2 - pseudo-continuous MV1c distributions for leading then sub-leading jet and the $\Delta\eta$ of the same jets. Row 3 - E_T^{miss} , H_T , and $\Delta\phi(V,H)$. Row 4 - m_{jj} . Section 6.1 details the definition of each variable.

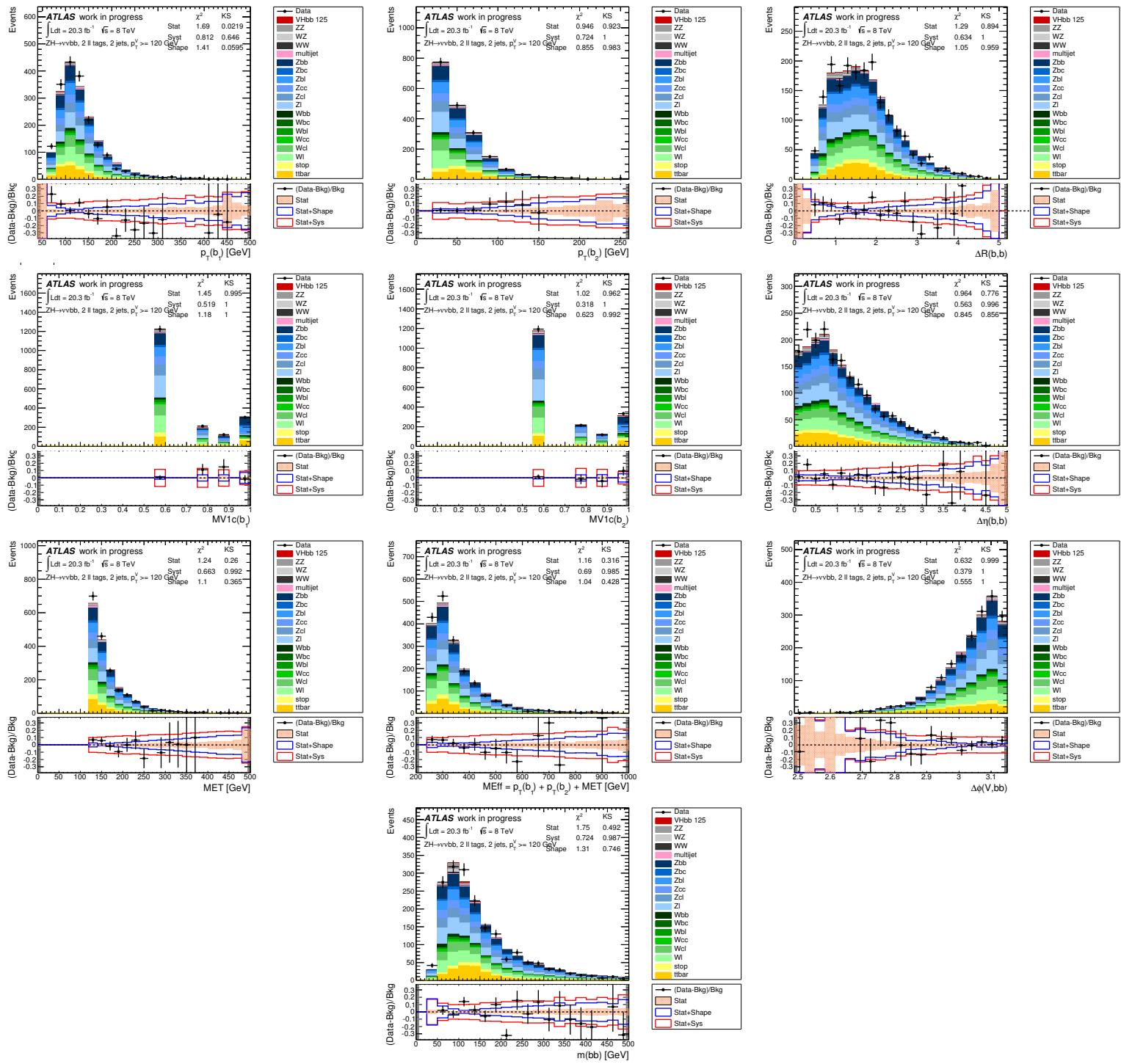


Figure 302: Distributions of MVA training variables used in 0-lepton events ($p_T^Z > 120$ GeV) with 2 loose b -tags and 2 jets. From left to right: Row 1 - leading then sub-leading jet p_T and ΔR of the same jets. Row 2 - pseudo-continuous MV1c distributions for leading then sub-leading jet and the $\Delta\eta$ of the same jets. Row 3 - E_T^{miss} , H_T , and $\Delta\phi(V,H)$. Row 4 - m_{jj} . Section 6.1 details the definition of each variable.

Not reviewed, for internal circulation only

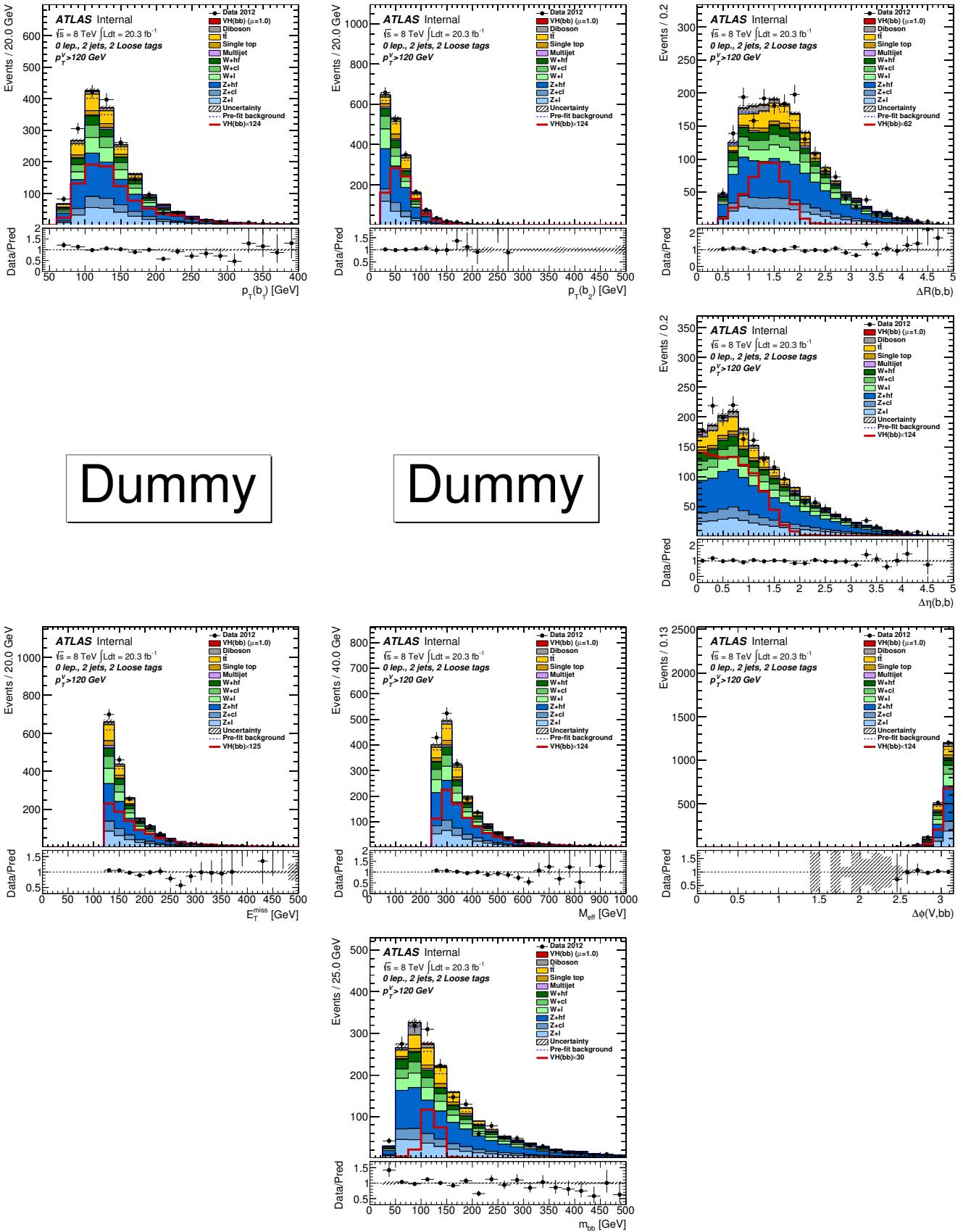


Figure 303: Distributions of MVA training variables used in 0-lepton events ($p_T^Z > 120$ GeV) with 2 loose b -tags and 2 jets after the combined 0+1+2 lepton MVA fit. From left to right: Row 1 - leading then sub-leading jet p_T and ΔR of the same jets. Row 2 - pseudo-continuous MV1c distributions for leading then sub-leading jet and the $\Delta\eta$ of the same jets. Row 3 - E_T^{miss} , H_T , and $\Delta\phi(V, H)$. Row 4 - m_{bb} . Section 6.1 details the definition of each variable.

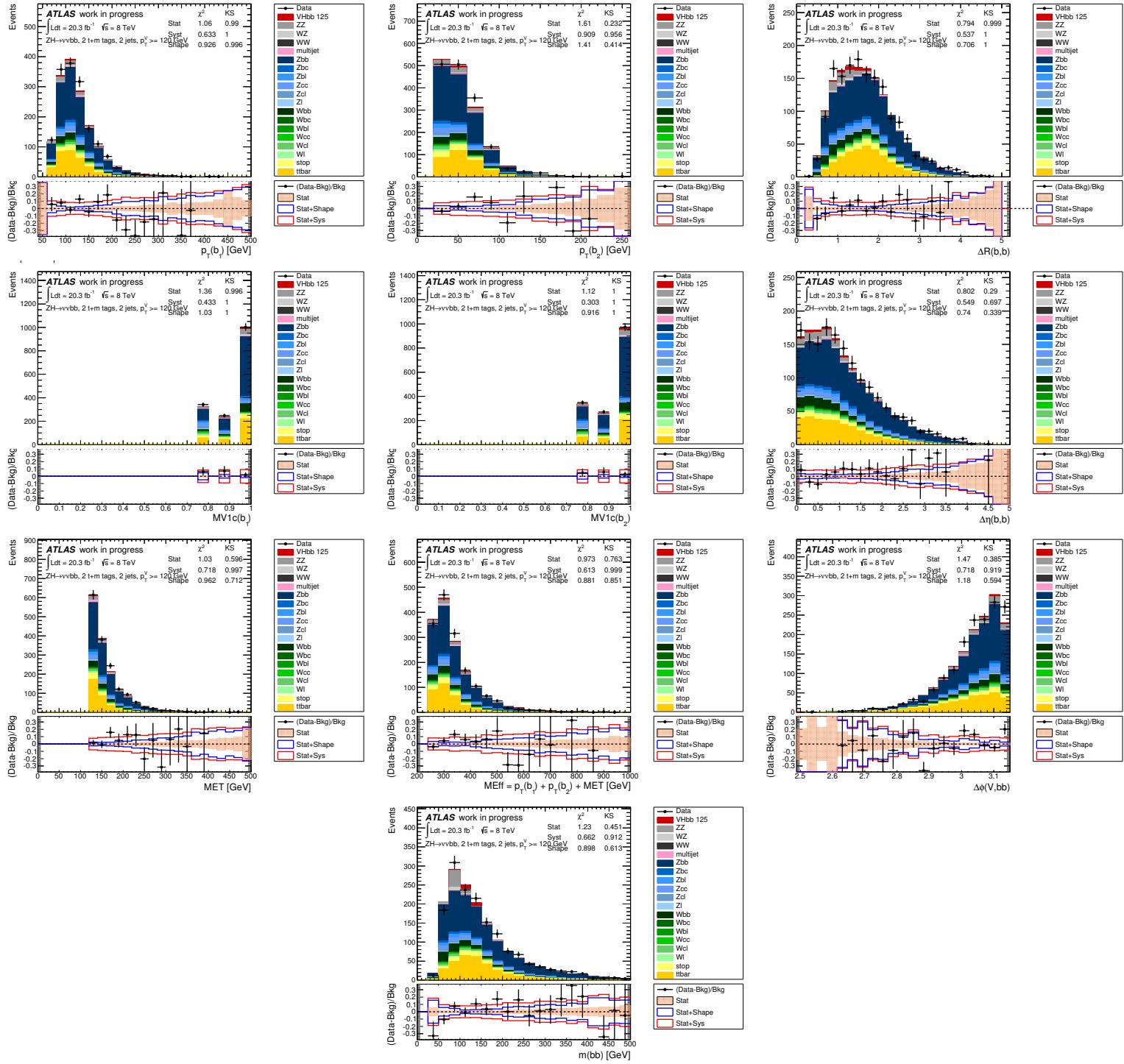


Figure 304: Distributions of MVA training variables used in 0-lepton events ($p_T^Z > 120$ GeV) with 2 MM+TT b -tags and 2 jets. From left to right: Row 1 - leading then sub-leading jet p_T and ΔR of the same jets. Row 2 - pseudo-continuous MV1c distributions for leading then sub-leading jet and the $\Delta\eta$ of the same jets. Row 3 - E_T^{miss} , H_T , and $\Delta\phi(V,H)$. Row 4 - m_{jj} . Section 6.1 details the definition of each variable.

Not reviewed, for internal circulation only

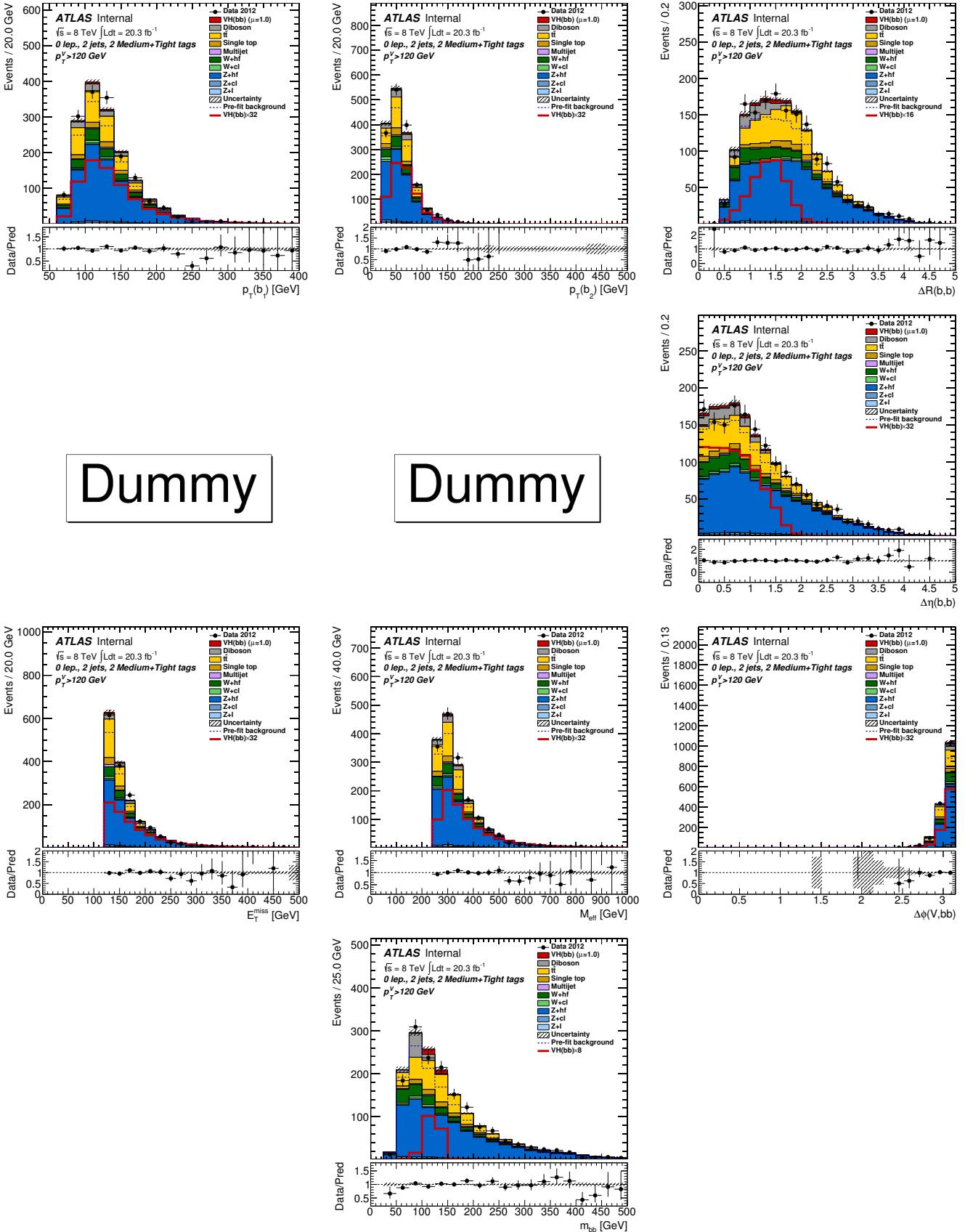


Figure 305: Distributions of MVA training variables used in 0-lepton events ($p_T^Z > 120$ GeV) with 2 MM+TT b -tags and 2 jets after the combined 0+1+2 lepton MVA fit. From left to right: Row 1 - leading then sub-leading jet p_T and ΔR of the same jets. Row 2 - pseudo-continuous MV1c distributions for leading then sub-leading jet and the $\Delta\eta$ of the same jets. Row 3 - E_T^{miss} , H_T , and $\Delta\phi(V, H)$. Row 4 - m_{bb} . Section 6.1 details the definition of each variable.

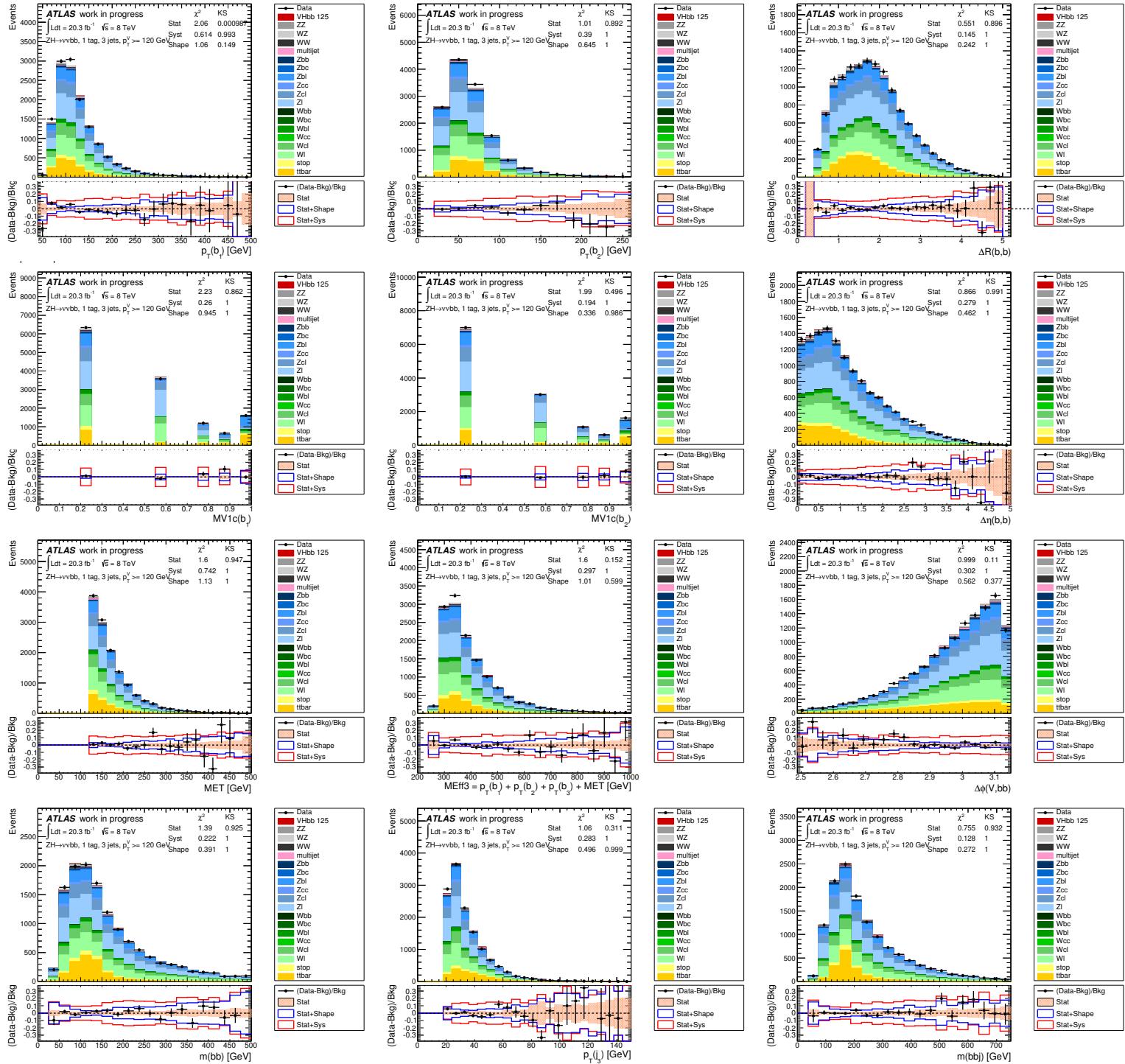


Figure 306: Distributions of MVA training variables used in 0-lepton events ($p_T^Z > 120$ GeV) with 1 b -tag and 3 jets. From left to right: Row 1 - leading then sub-leading jet p_T and ΔR of the same jets. Row 2 - pseudo-continuous MV1c distributions for leading then sub-leading jet and the $\Delta\eta$ of the same jets. Row 3 - E_T^{miss} , H_T , and $\Delta\phi(V, H)$. Row 4 - m_{jj} , the 3rd jet p_T , and the tri-jet mass (m_{bjj}). Section 6.1 details the definition of each variable.

Not reviewed, for internal circulation only

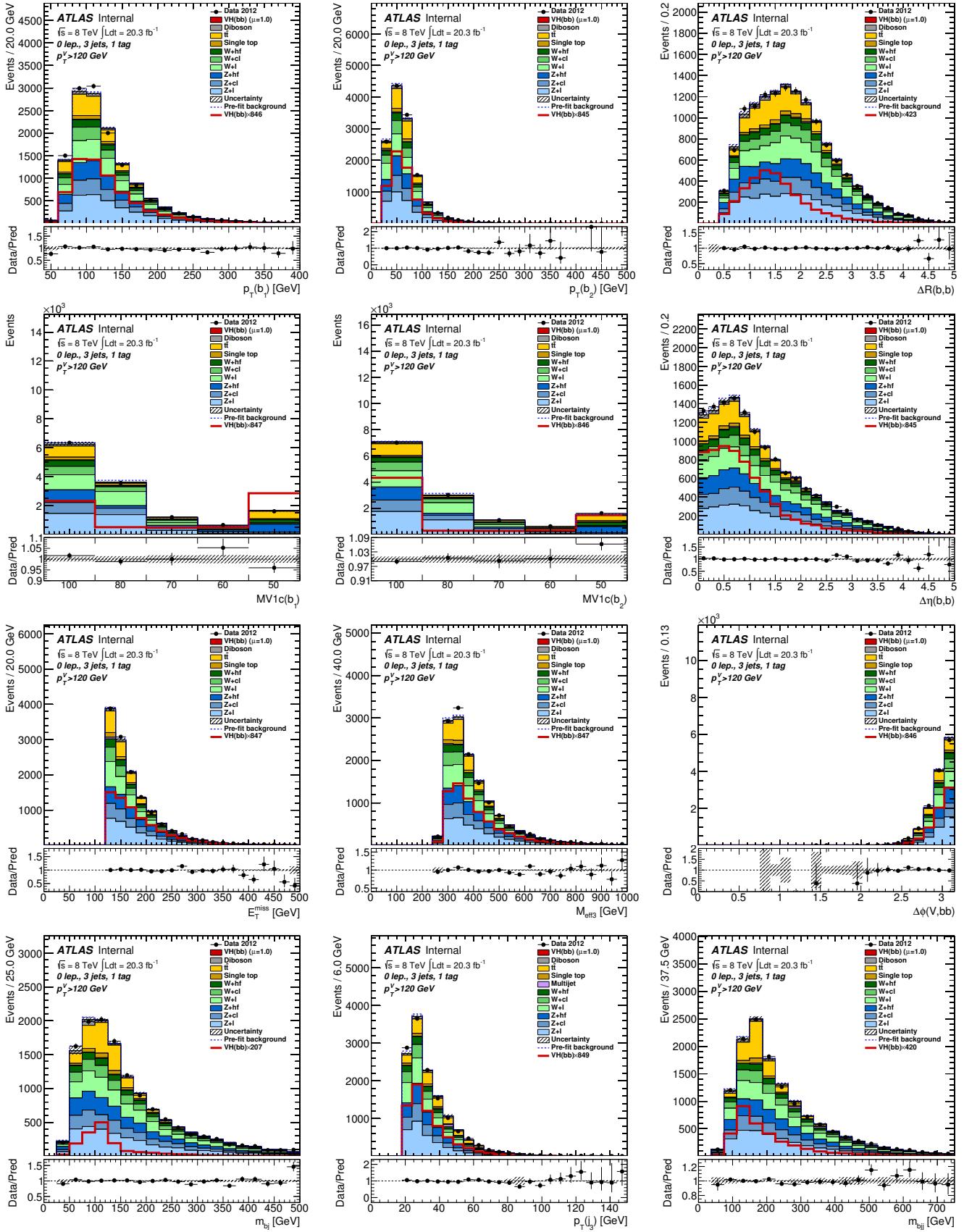


Figure 307: Distributions of MVA training variables used in 0-lepton events ($p_T^Z > 120$ GeV) with 1 b -tag and 3 jets after the combined 0+1+2 lepton MVA fit. From left to right: Row 1 - leading then sub-leading jet p_T and ΔR of the same jets. Row 2 - pseudo-continuous MV1c distributions for leading then sub-leading jet and the $\Delta\eta$ of the same jets. Row 3 - E_T^{miss} , H_T , and $\Delta\phi(V, H)$. Row 4 - m_{jj} , the 3rd jet p_T , and the tri-jet mass (m_{jjj}). Section 6.1 details the definition of each variable.

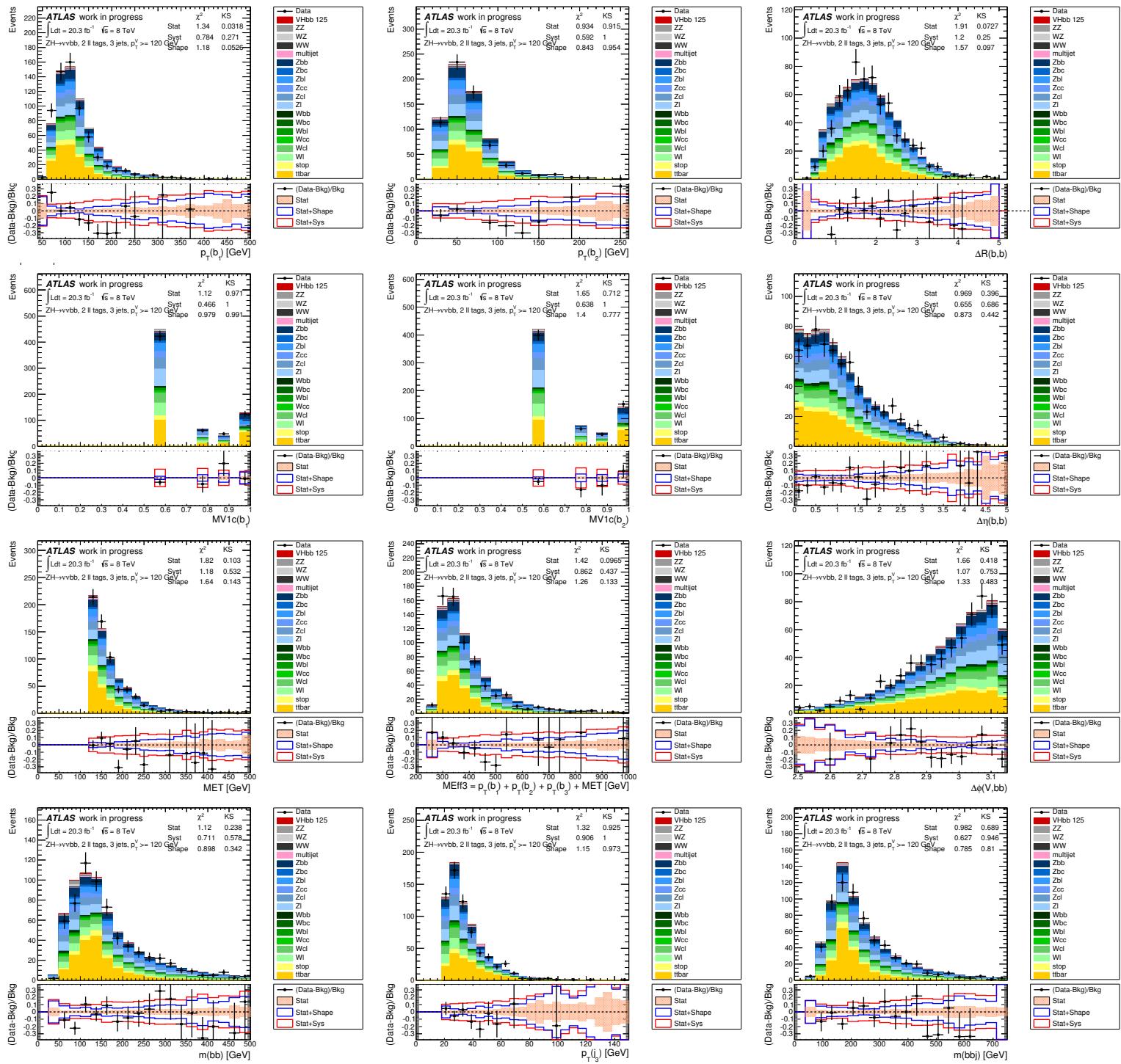


Figure 308: Distributions of MVA training variables used in 0-lepton events ($p_T^Z > 120$ GeV) with 2 loose b -tags and 3 jets. From left to right: Row 1 - leading then sub-leading jet p_T and ΔR of the same jets. Row 2 - pseudo-continuous MV1c distributions for leading then sub-leading jet and the $\Delta\eta$ of the same jets. Row 3 - E_T^{miss} , H_T , and $\Delta\phi(V, H)$. Row 4 - m_{jj} , the 3rd jet p_T , and the tri-jet mass (m_{jjj}). Section 6.1 details the definition of each variable.

Not reviewed, for internal circulation only

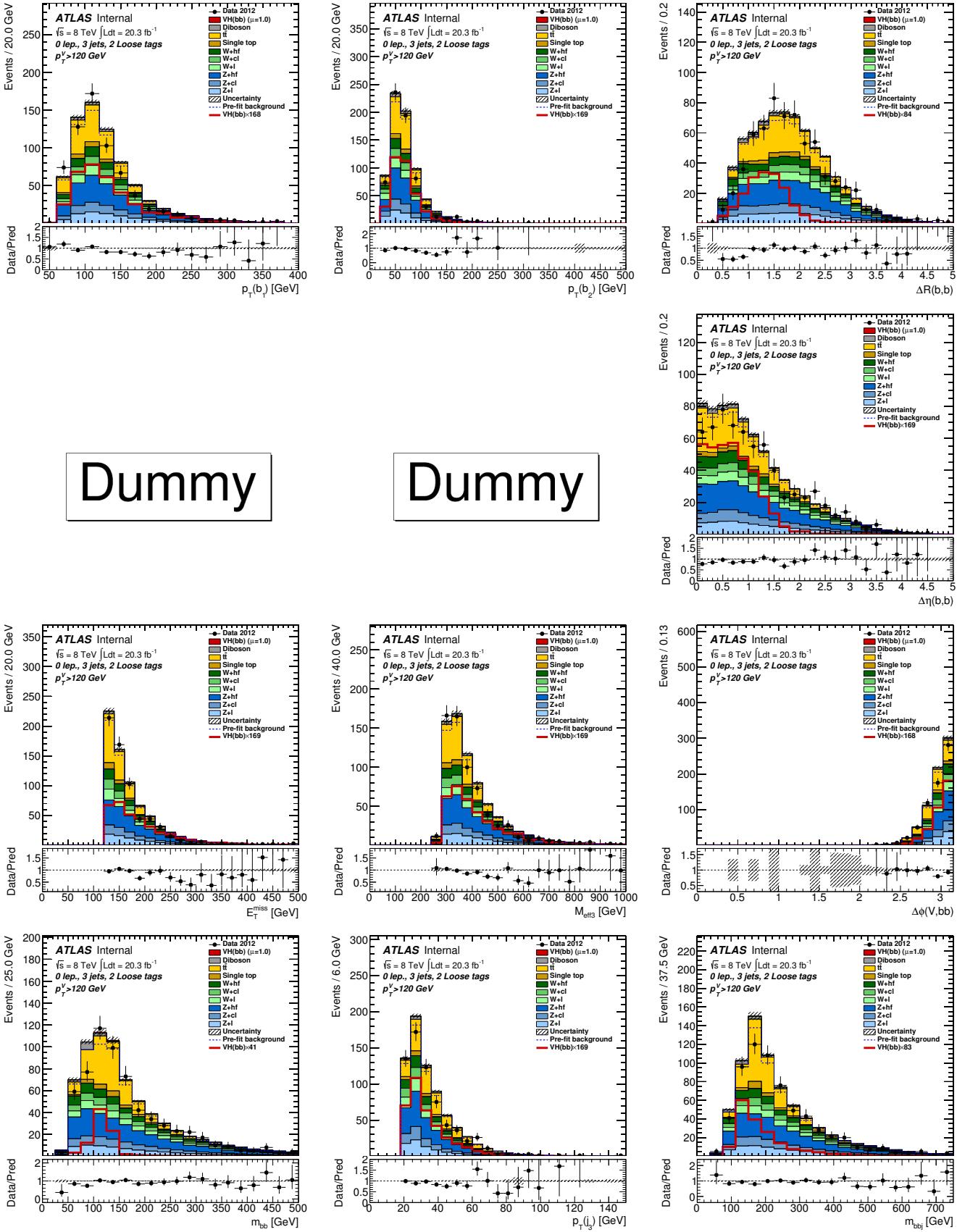


Figure 309: Distributions of MVA training variables used in 0-lepton events ($p_T^Z > 120$ GeV) with 2 loose b -tags and 3 jets after the combined 0+1+2 lepton MVA fit. From left to right: Row 1 - leading then sub-leading jet p_T and ΔR of the same jets. Row 2 - pseudo-continuous MV1c distributions for leading then sub-leading jet and the $\Delta\eta$ of the same jets. Row 3 - E_T^{miss} , H_T , and $\Delta\phi(V, H)$. Row 4 - m_{jj} , the 3rd jet p_T , and the tri-jet mass (m_{bb}). Section 6.1 details the definition of each variable.

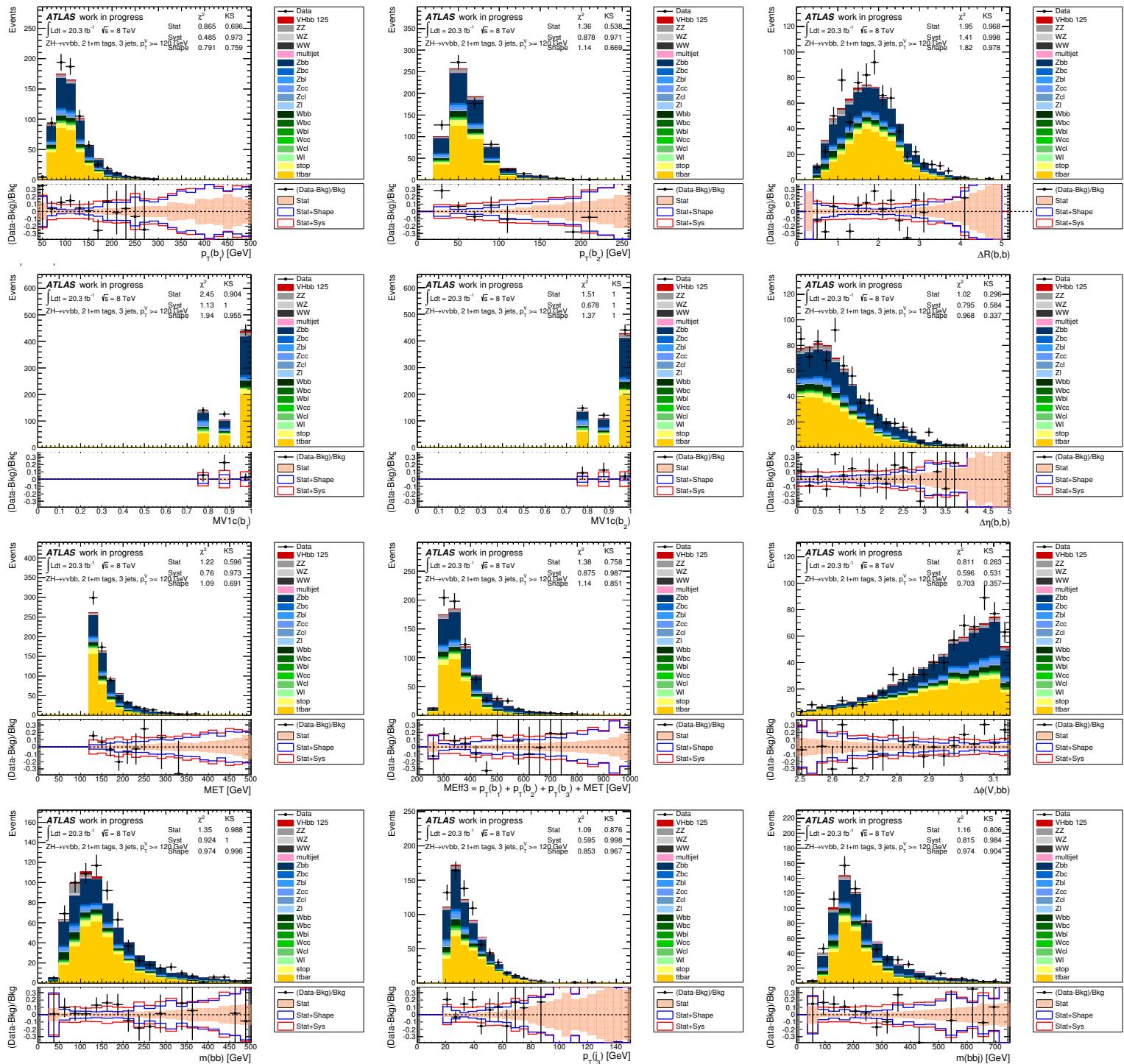


Figure 310: Distributions of MVA training variables used in 0-lepton events ($p_T^Z > 120$ GeV) with 2 MM+TT b -tags and 3 jets. From left to right: Row 1 - leading then sub-leading jet p_T and ΔR of the same jets. Row 2 - pseudo-continuous MV1c distributions for leading then sub-leading jet and the $\Delta\eta$ of the same jets. Row 3 - E_T^{miss} , H_T , and $\Delta\phi(V, H)$. Row 4 - m_{jj} , the 3rd jet p_T , and the tri-jet mass (m_{bjj}). Section 6.1 details the definition of each variable.

Not reviewed, for internal circulation only

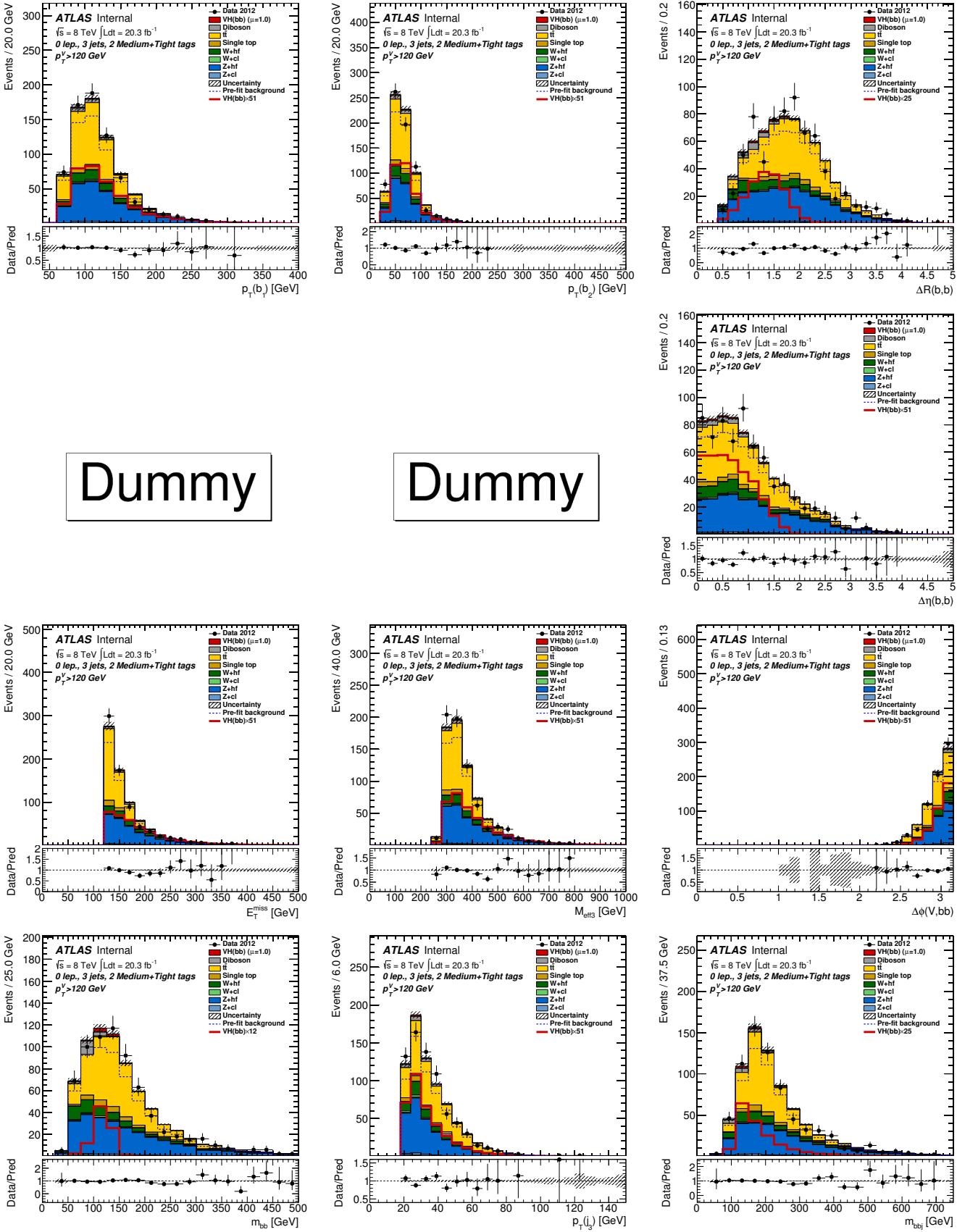


Figure 311: Distributions of MVA training variables used in 0-lepton events ($p_T^Z > 120 \text{ GeV}$) with 2 MM+TT b -tags and 3 jets after the combined 0+1+2 lepton MVA fit. From left to right: Row 1 - leading then sub-leading jet p_T and ΔR of the same jets. Row 2 - pseudo-continuous MV1c distributions for leading then sub-leading jet and the $\Delta\eta$ of the same jets. Row 3 - E_T^{miss} , H_T , and $\Delta\phi(V, H)$. Row 4 - m_{jj} , the 3rd jet p_T , and the tri-jet mass (m_{bbj}). Section 6.1 details the definition of each variable.

4906 Z MVA Input Variable Distributions: One Lepton

4907 This appendix contains distributions of the BDT input variables defined in Section 6 in the 1-lepton anal-
 4908 ysis for low and high p_T^W regions ($p_T^W < 120$ GeV and $p_T^W > 120$ GeV respectively). The electron and
 4909 muon events have been combined. These plots are done by applying the latest scale factors, obtained for
 4910 the 2-jet region and the 3-jet region separately, by comparing the event yield before and after the MVA
 4911 combined fit. They are summarized in Table 97. Explicitly stated, the theoretical expectation for each
 4912 background is used for the given luminosity. All the plots in this section are done with the status-of-art
 4913 analysis.

4914 Figure 312 shows one b -tag two jet events with $p_T^W < 120$ GeV prefit and Figure 313 postfit.
 4915 Figure 314 shows one b -tag two jet events with $p_T^W > 120$ GeV prefit and Figure 315 postfit.
 4916 Figure 316 shows LL b -tag two jet events with $p_T^W < 120$ GeV prefit and Figure 317 postfit.
 4917 Figure 318 shows LL b -tag two jet events with $p_T^W > 120$ GeV prefit and Figure 319 postfit.
 4918 Figure 320 shows MM b -tag two jet events with $p_T^W < 120$ GeV prefit and Figure 321 postfit.
 4919 Figure 322 shows MM b -tag two jet events with $p_T^W > 120$ GeV prefit and Figure 323 postfit.
 4920 Figure 324 shows TT b -tag two jet events with $p_T^W < 120$ GeV prefit and Figure 325 postfit.
 4921 Figure 326 shows TT b -tag two jet events with $p_T^W > 120$ GeV prefit and Figure 327 postfit.
 4922 Figure 328 shows one b -tag three jet events with $p_T^W < 120$ GeV prefit and Figure 329 postfit.
 4923 Figure 330 shows one b -tag three jet events with $p_T^W > 120$ GeV prefit and Figure 331 postfit.
 4924 Figure 332 shows LL b -tag three jet events with $p_T^W < 120$ GeV prefit and Figure 333 postfit.
 4925 Figure 334 shows LL b -tag three jet events with $p_T^W > 120$ GeV prefit and Figure 335 postfit.
 4926 Figure 336 shows MM b -tag three jet events with $p_T^W < 120$ GeV prefit and Figure 337 postfit.
 4927 Figure 338 shows MM b -tag three jet events with $p_T^W > 120$ GeV prefit and Figure 339 postfit.
 4928 Figure 340 shows TT b -tag three jet events with $p_T^W < 120$ GeV prefit and Figure 341 postfit.
 4929 Figure 342 shows TT b -tag three jet events with $p_T^W > 120$ GeV prefit and Figure 343 postfit.
 4930

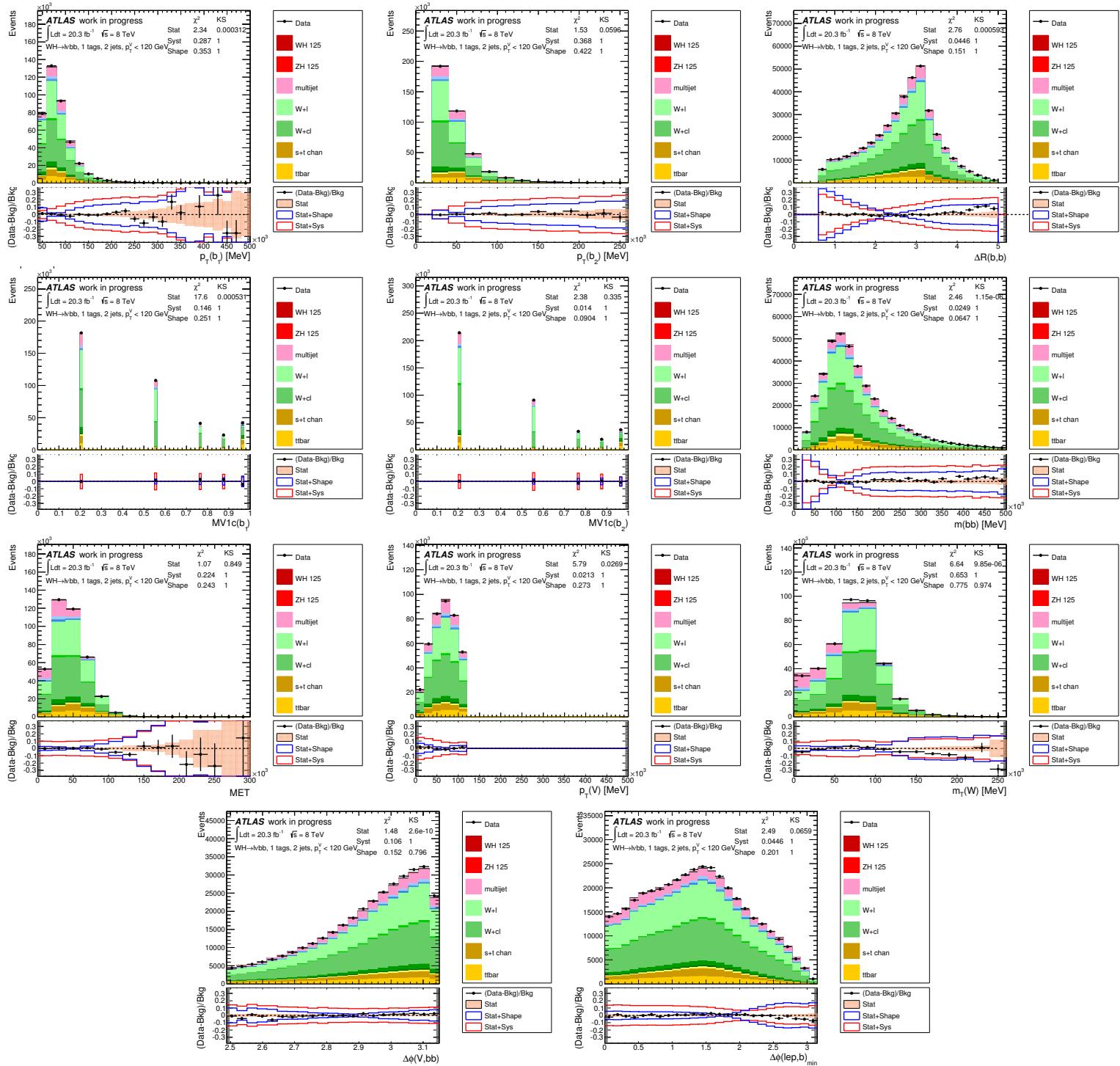


Figure 312: Distributions of MVA training variables used in 1-lepton events for $p_T^W < 120 \text{ GeV}$ with 1 b -tag and 2 jets. From left to right: Row 1 - leading then sub-leading jet p_T and ΔR of the same two jets. Row 2 - pseudo-continuous MV1c distributions for leading then sub-leading jet and the m_{jj} of the same two jets. Row 3 - E_T^{miss} , p_T^W , and m_T^W . Row 4 - $\Delta\phi(V, H)$ and $\min|\Delta\phi(\ell, jet)|$. Section 6.1 details the definition of each variable.

Not reviewed, for internal circulation only

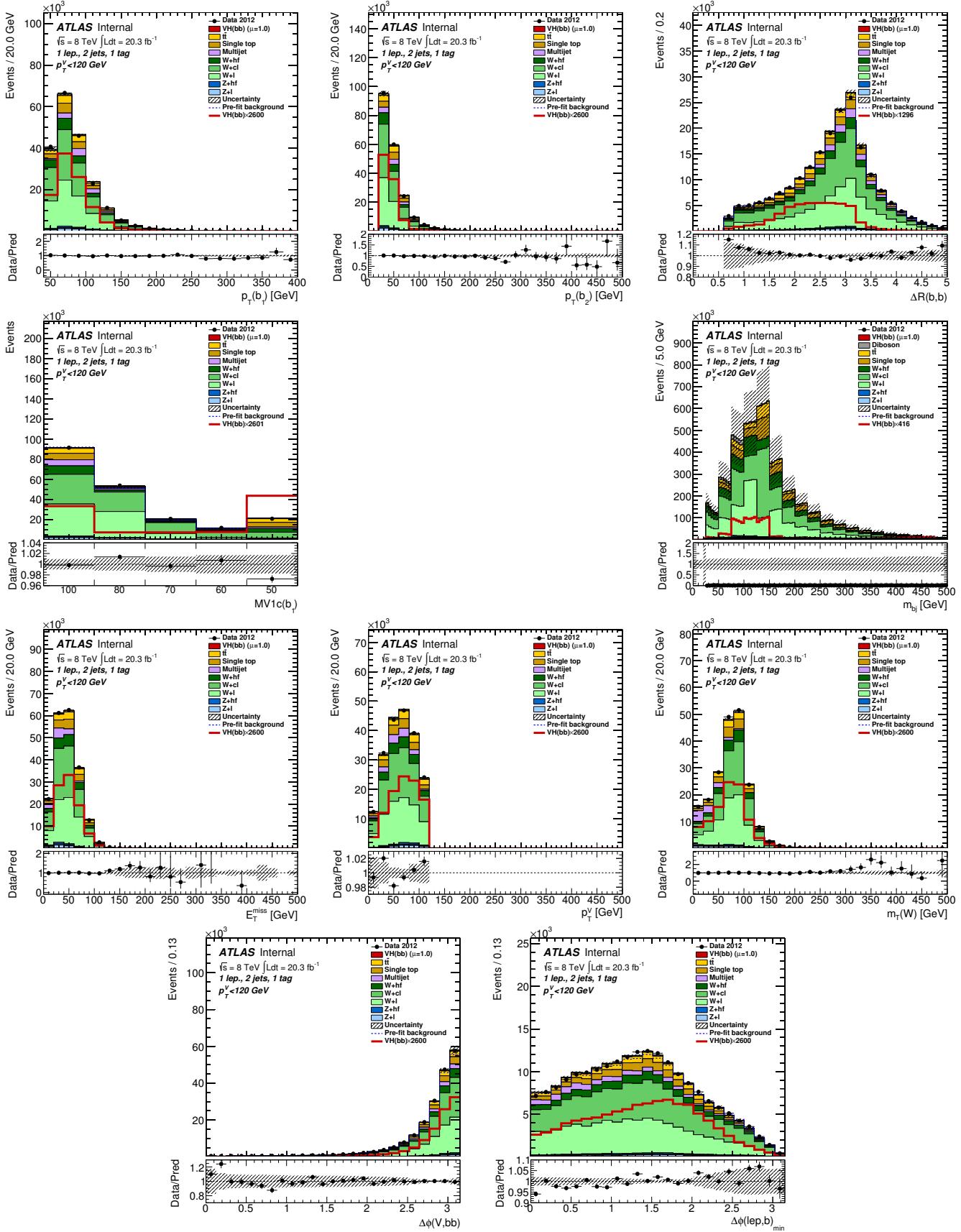


Figure 313: Distributions of MVA training variables used in 1-lepton events for $p_T^W < 120 \text{ GeV}$ with 1 b -tag and 2 jets after the combined 0+1+2 lepton MVA fit. From left to right: Row 1 - leading then sub-leading jet p_T and ΔR of the same two jets. Row 2 - pseudo-continuous MV1c distributions for leading then sub-leading jet and the m_{jj} of the same two jets. Row 3 - E_T^{miss} , p_T^W , and m_T^W . Row 4 - $\Delta\phi(V, H)$ and $\min|\Delta\phi(\ell, \text{jet})|$. Section 6.1 details the definition of each variable.

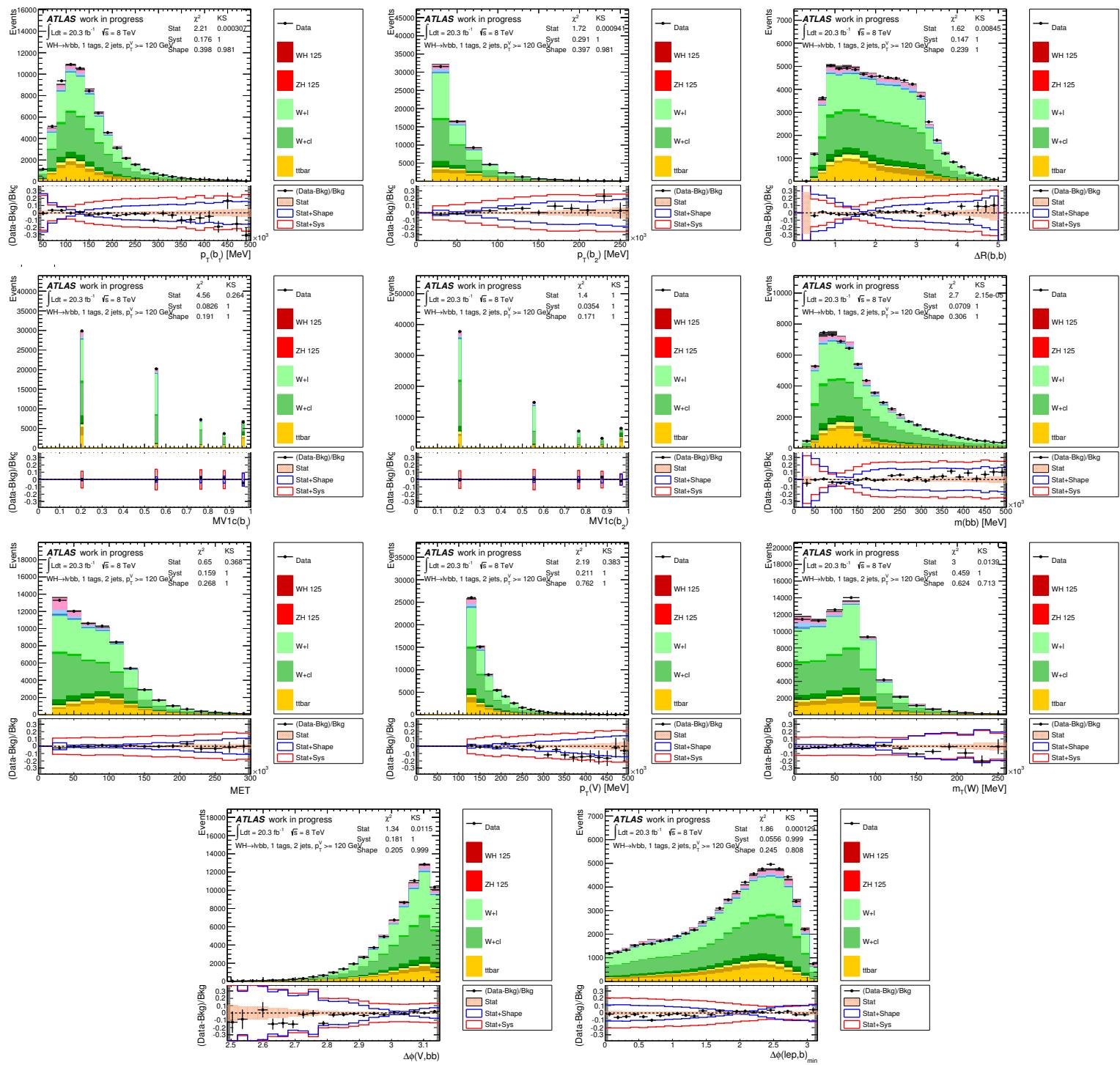


Figure 314: Distributions of MVA training variables used in 1-lepton events for $p_T^W > 120$ GeV with 1 b -tag and 2 jets. From left to right: Row 1 - leading then sub-leading jet p_T and ΔR of the same two jets. Row 2 - pseudo-continuous MV1c distributions for leading then sub-leading jet and the m_{jj} of the same two jets. Row 3 - E_T^{miss} , p_T^W , and m_T^W . Row 4 - $\Delta\phi(V, H)$ and $\min|\Delta\phi(\ell, jet)|$. Section 6.1 details the definition of each variable.

Not reviewed, for internal circulation only

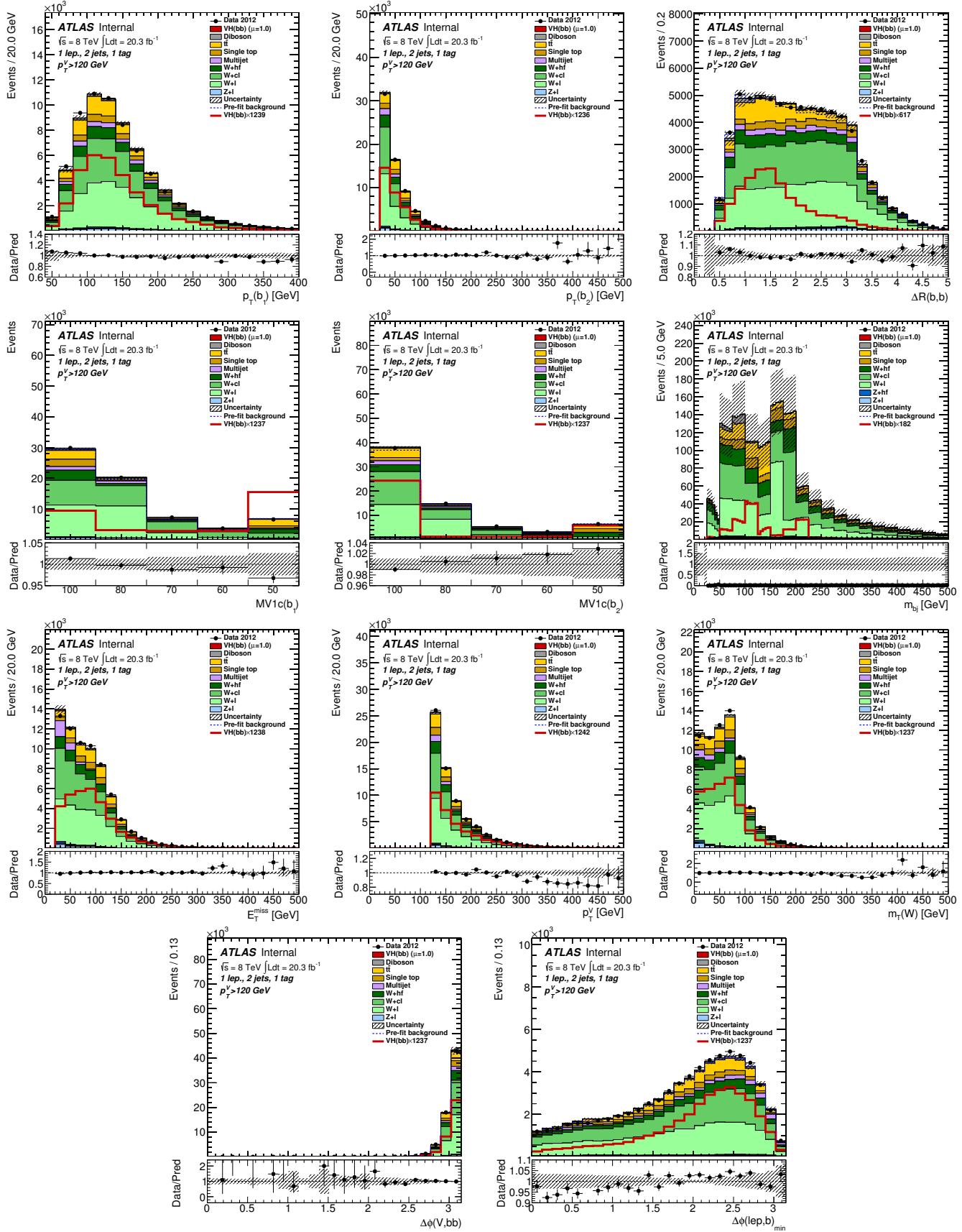


Figure 315: Distributions of MVA training variables used in 1-lepton events for $p_T^W > 120$ GeV with 1 b -tag and 2 jets after the combined 0+1+2 lepton MVA fit. From left to right: Row 1 - leading then sub-leading jet p_T and ΔR of the same two jets. Row 2 - pseudo-continuous MV1c distributions for leading then sub-leading jet and the m_{jj} of the same two jets. Row 3 - E_T^{miss} , p_T^W , and m_T^W . Row 4 - $\Delta\phi(V, H)$ and $\min|\Delta\phi(\ell, \text{jet})|$. Section 6.1 details the definition of each variable.

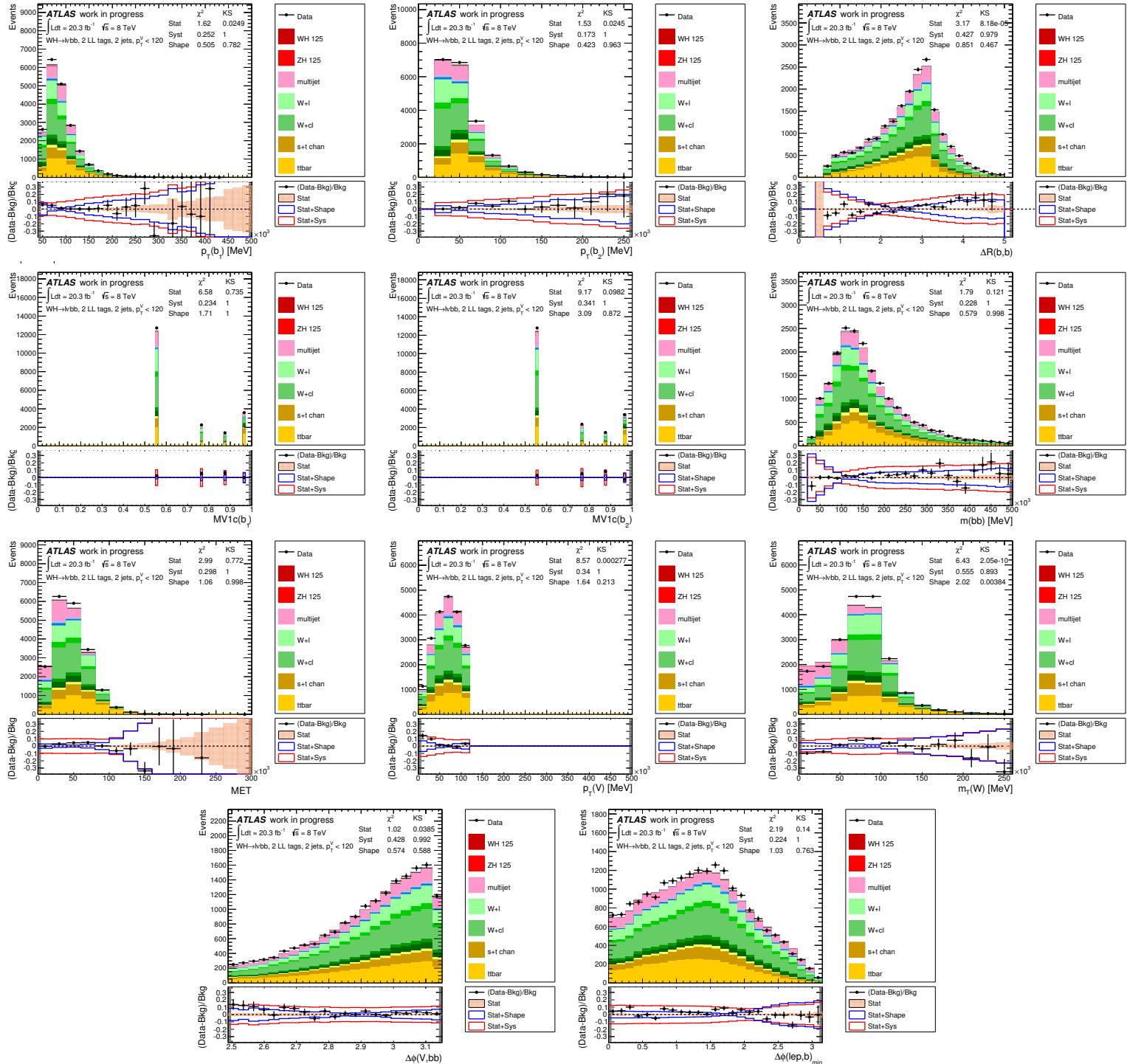


Figure 316: Distributions of MVA training variables used in 1-lepton events for $p_T^W < 120 \text{ GeV}$ with 2 LL b -tags and 2 jets. From left to right: Row 1 - leading then sub-leading jet p_T and ΔR of the same two jets. Row 2 - pseudo-continuous MV1c distributions for leading then sub-leading jet and the m_{jj} of the same two jets. Row 3 - E_T^{miss} , p_T^W , and m_T^W . Row 4 - $\Delta\phi(V, H)$ and $\min|\Delta\phi(\ell, jet)|$. Section 6.1 details the definition of each variable.

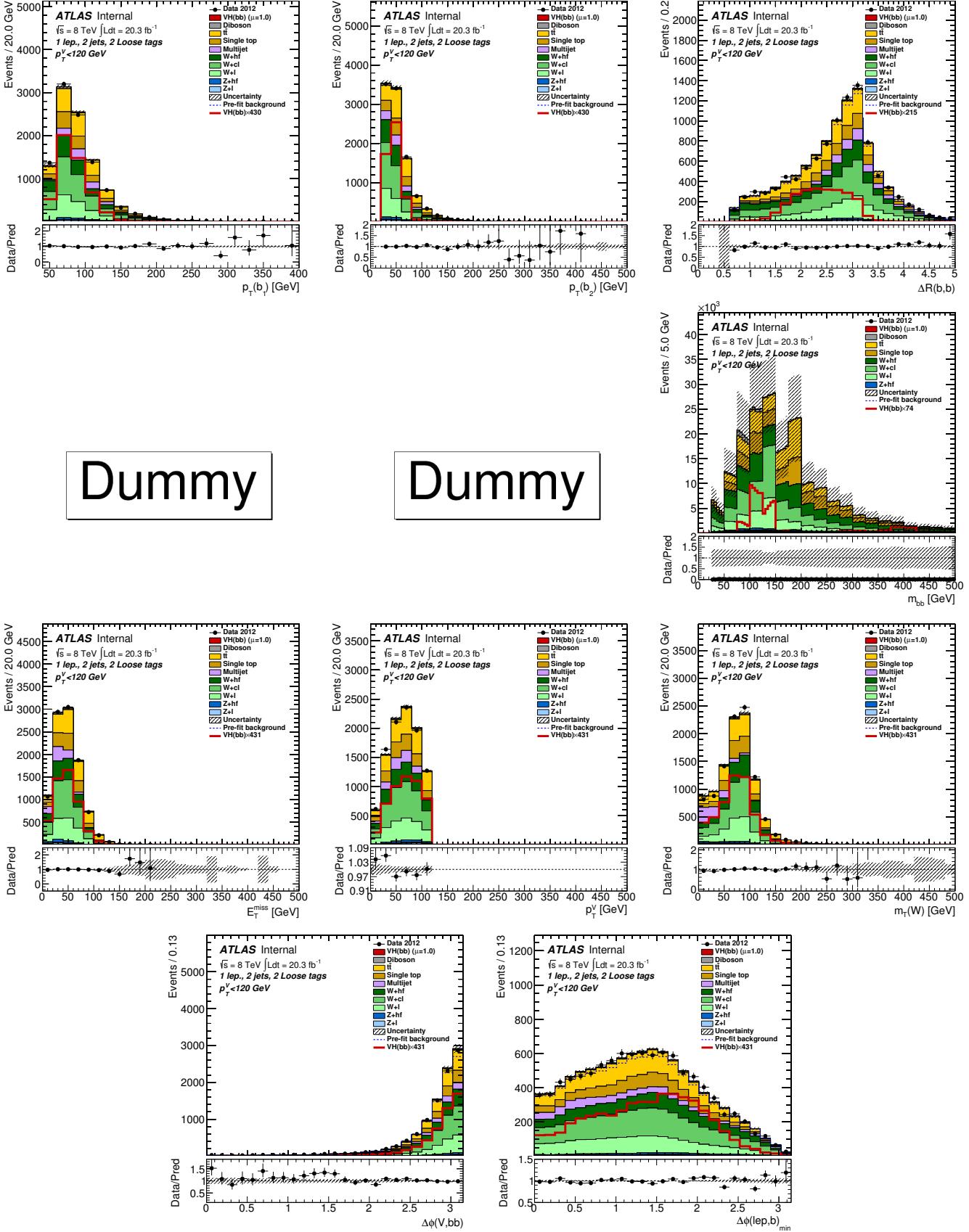


Figure 317: Distributions of MVA training variables used in 1-lepton events for $p_T^W < 120$ GeV with 2 LL b -tags and 2 jets after the combined 0+1+2 lepton MVA fit. From left to right: Row 1 - leading then sub-leading jet p_T and ΔR of the same two jets. Row 2 - pseudo-continuous MV1c distributions for leading then sub-leading jet and the m_{jj} of the same two jets. Row 3 - E_T^{miss} , p_T^W , and m_T^W . Row 4 - $\Delta\phi(V, H)$ and $\min|\Delta\phi(\ell, \text{jet})|$. Section 6.1 details the definition of each variable.

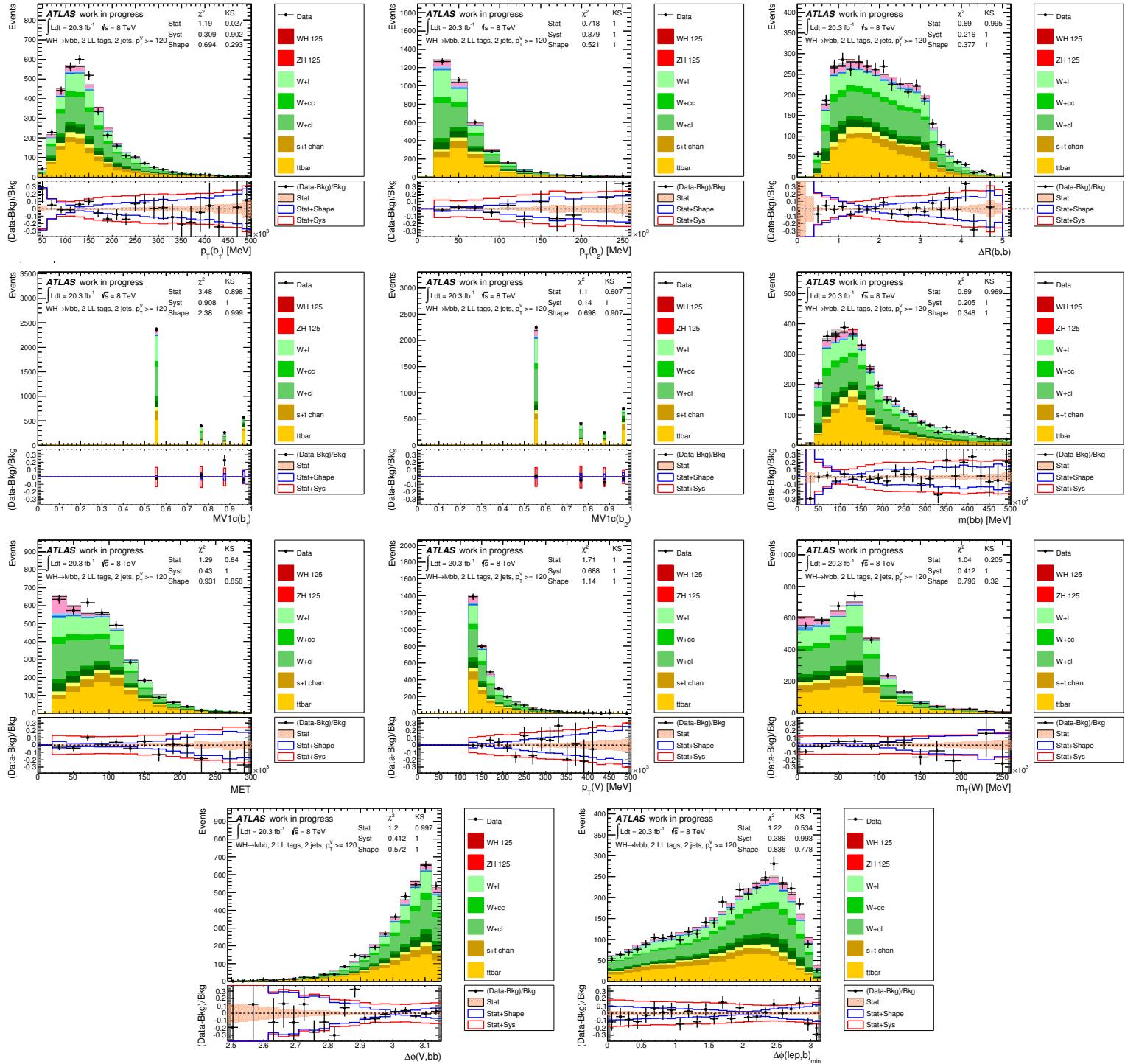
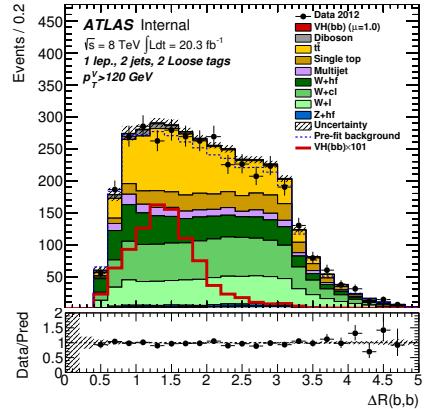
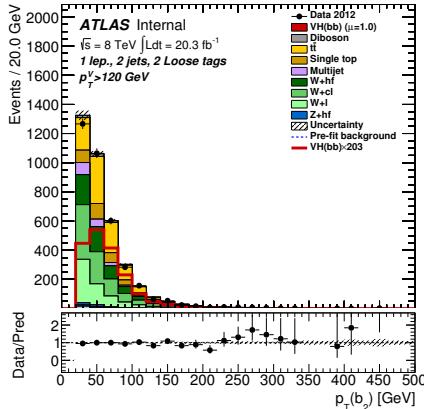
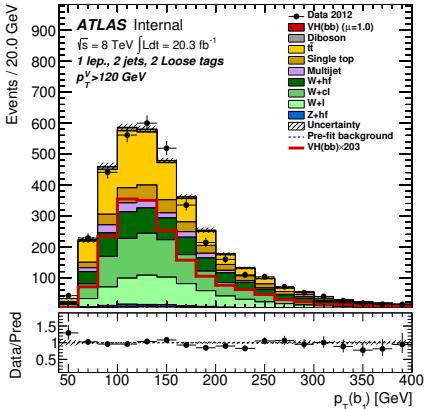


Figure 318: Distributions of MVA training variables used in 1-lepton events for $p_T^W > 120$ GeV with 2 LL b -tags and 2 jets. From left to right: Row 1 - leading then sub-leading jet p_T and ΔR of the same two jets. Row 2 - pseudo-continuous MV1c distributions for leading then sub-leading jet and the m_{jj} of the same two jets. Row 3 - E_T^{miss} , p_T^W , and m_T^W . Row 4 - $\Delta\phi(V, H)$ and $\min|\Delta\phi(\ell, jet)|$. Section 6.1 details the definition of each variable.



Dummy

Dummy

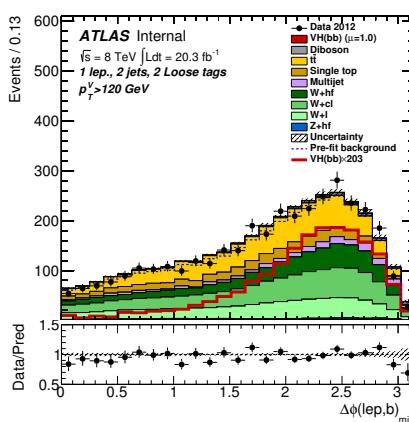
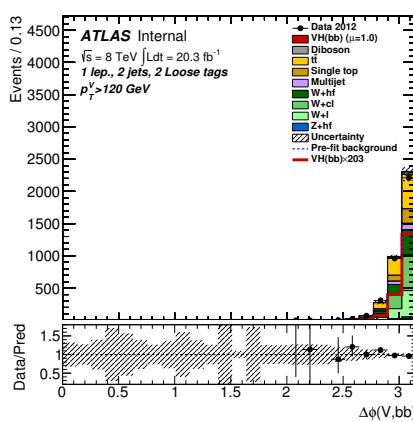
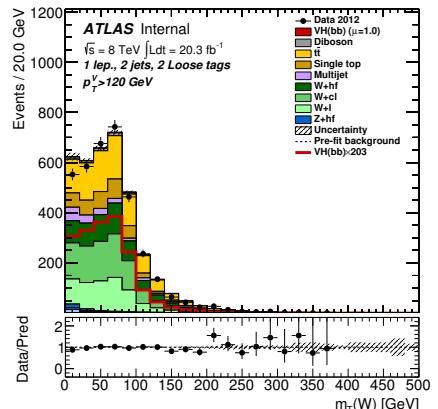
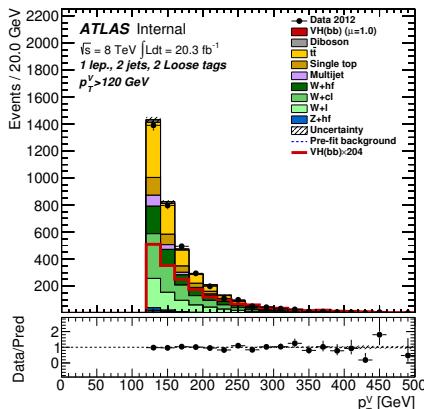
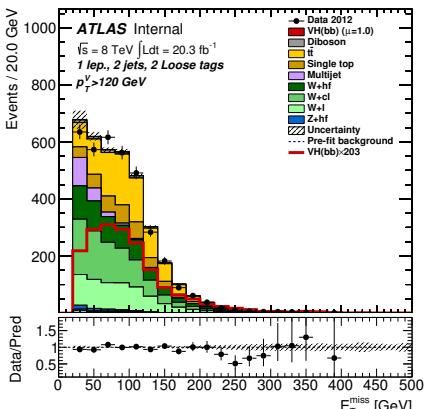
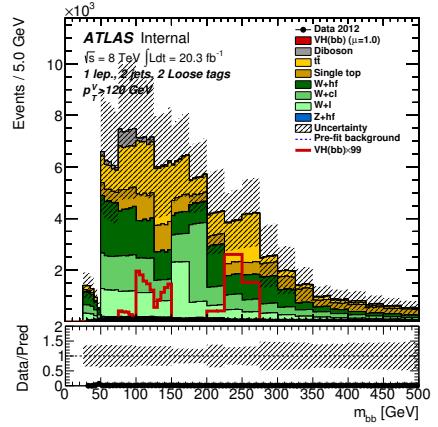


Figure 319: Distributions of MVA training variables used in 1-lepton events for $p_T^W > 120$ GeV with 2 LL b -tags and 2 jets after the combined 0+1+2 lepton MVA fit. From left to right: Row 1 - leading then sub-leading jet p_T and ΔR of the same two jets. Row 2 - pseudo-continuous MV1c distributions for leading then sub-leading jet and the m_{jj} of the same two jets. Row 3 - E_T^{miss} , p_T^W , and m_T^W . Row 4 - $\Delta\phi(V, H)$ and $\min|\Delta\phi(\ell, \text{jet})|$. Section 6.1 details the definition of each variable.

Not reviewed, for internal circulation only

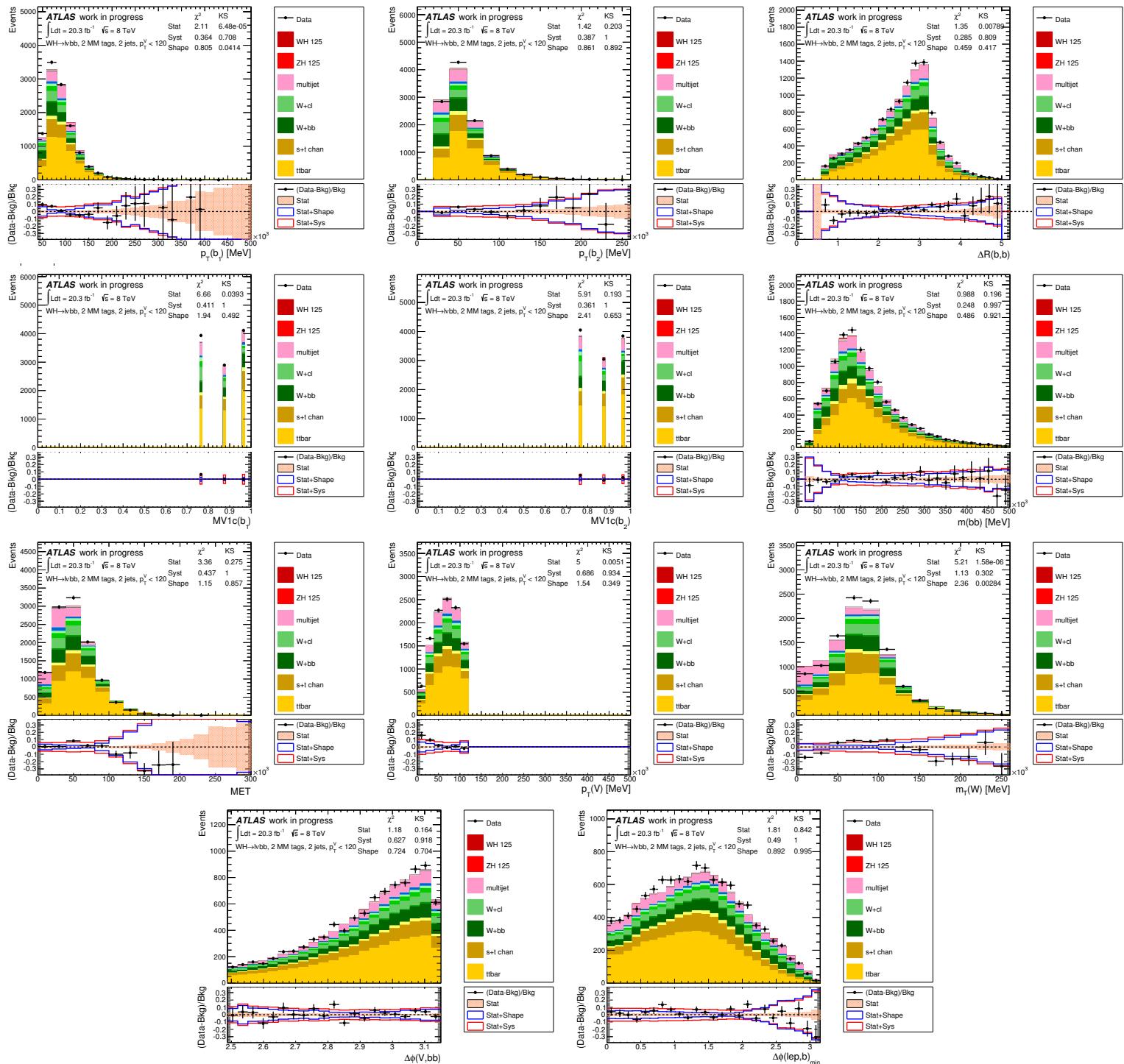


Figure 320: Distributions of MVA training variables used in 1-lepton events for $p_T^W < 120$ GeV with 2 MM b -tags and 2 jets. From left to right: Row 1 - leading then sub-leading jet p_T and ΔR of the same two jets. Row 2 - pseudo-continuous MV1c distributions for leading then sub-leading jet and the m_{jj} of the same two jets. Row 3 - E_T^{miss} , p_T^W , and m_T^W . Row 4 - $\Delta\phi(V, H)$ and $\min|\Delta\phi(\ell, jet)|$. Section 6.1 details the definition of each variable.

Not reviewed, for internal circulation only

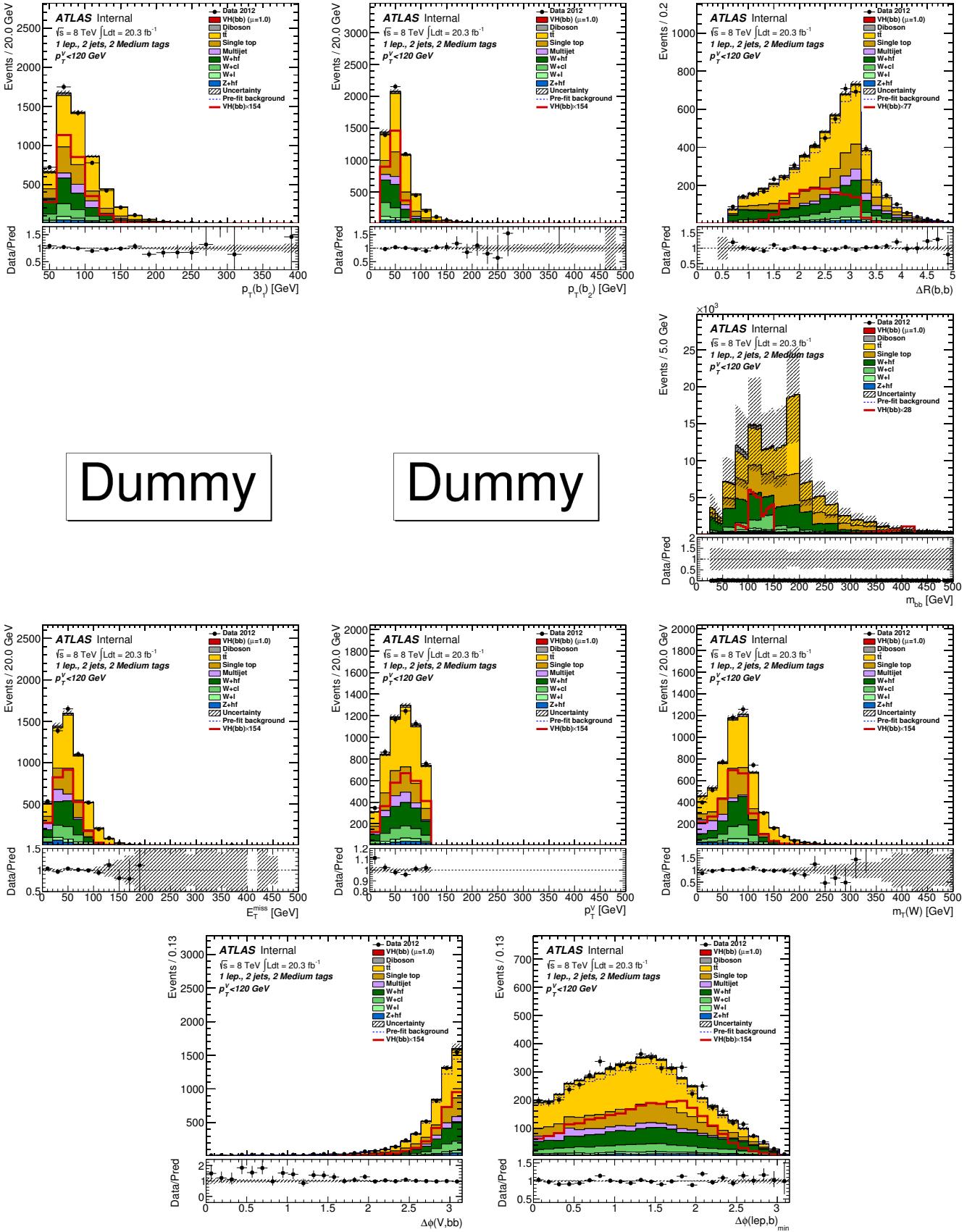


Figure 321: Distributions of MVA training variables used in 1-lepton events for $p_T^W < 120$ GeV with 2 MM b -tags and 2 jets after the combined 0+1+2 lepton MVA fit. From left to right: Row 1 - leading then sub-leading jet p_T and ΔR of the same two jets. Row 2 - pseudo-continuous MV1c distributions for leading then sub-leading jet and the m_{jj} of the same two jets. Row 3 - E_T^{miss} , p_T^W , and m_T^W . Row 4 - $\Delta\phi(V, H)$ and $\min|\Delta\phi(\ell, \text{jet})|$. Section 6.1 details the definition of each variable.

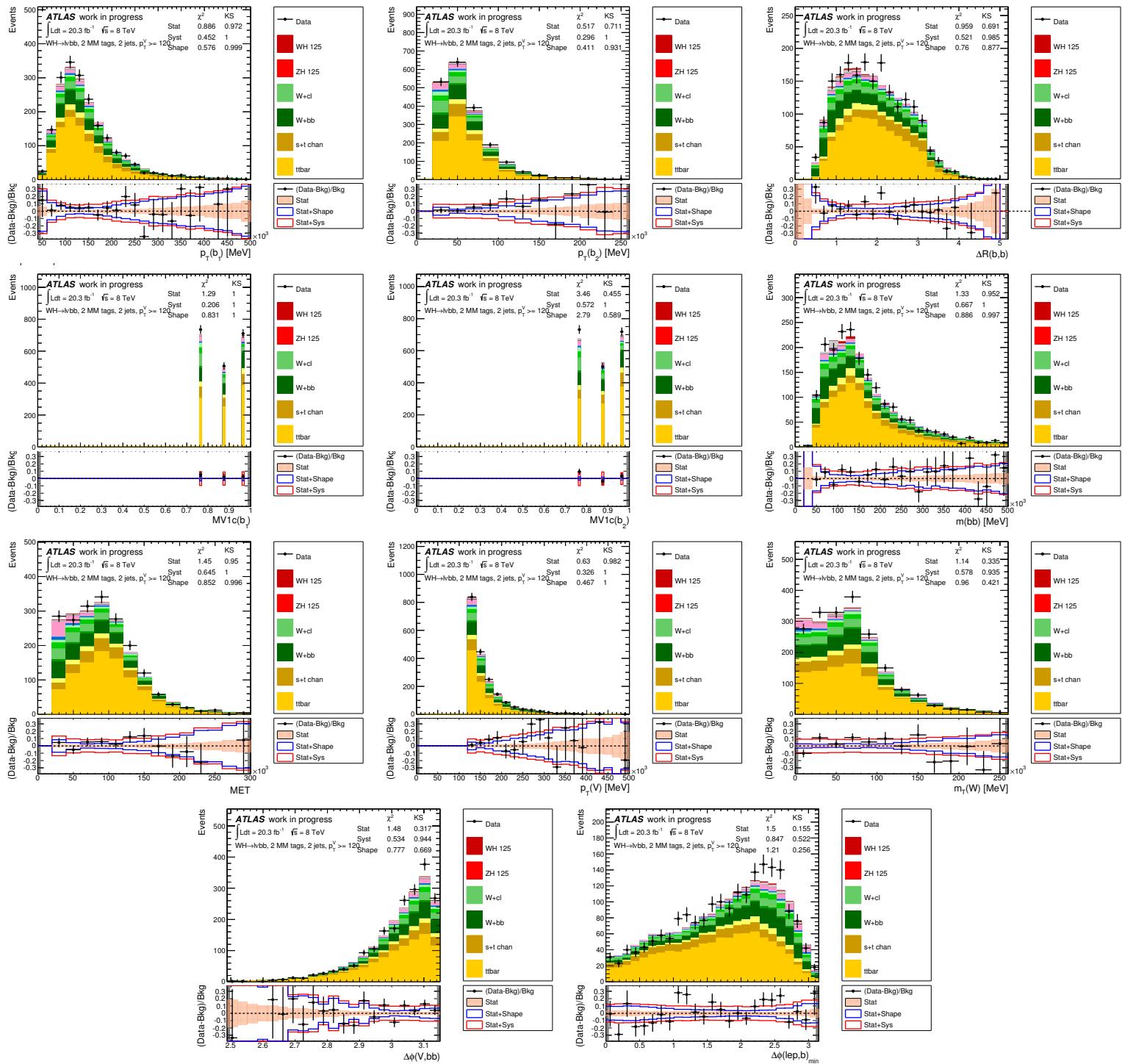


Figure 322: Distributions of MVA training variables used in 1-lepton events for $p_T^W > 120$ GeV with 2 MM b -tags and 2 jets. From left to right: Row 1 - leading then sub-leading jet p_T and ΔR of the same two jets. Row 2 - pseudo-continuous $MV1c$ distributions for leading then sub-leading jet and the m_{jj} of the same two jets. Row 3 - E_T^{miss} , p_T^W , and m_T^W . Row 4 - $\Delta\phi(V, H)$ and $\min|\Delta\phi(\ell, \text{jet})|$. Section 6.1 details the definition of each variable.

Not reviewed, for internal circulation only

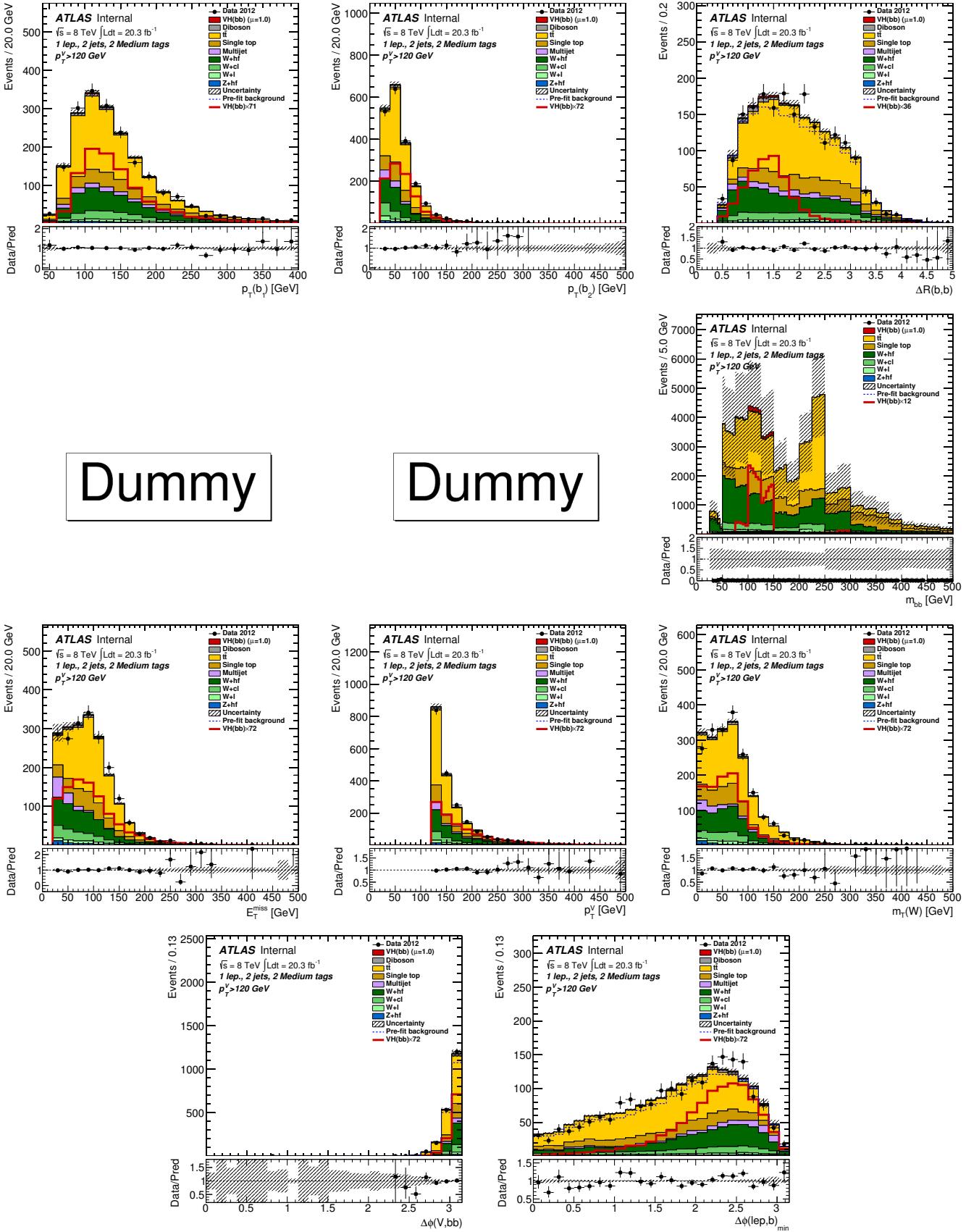


Figure 323: Distributions of MVA training variables used in 1-lepton events for $p_T^W > 120$ GeV with 2 MM b -tags and 2 jets after the combined 0+1+2 lepton MVA fit. From left to right: Row 1 - leading then sub-leading jet p_T and ΔR of the same two jets. Row 2 - pseudo-continuous MV1c distributions for leading then sub-leading jet and the m_{jj} of the same two jets. Row 3 - E_T^{miss} , p_T^W , and m_T^W . Row 4 - $\Delta\phi(V, H)$ and $\min|\Delta\phi(\ell, \text{jet})|$. Section 6.1 details the definition of each variable.

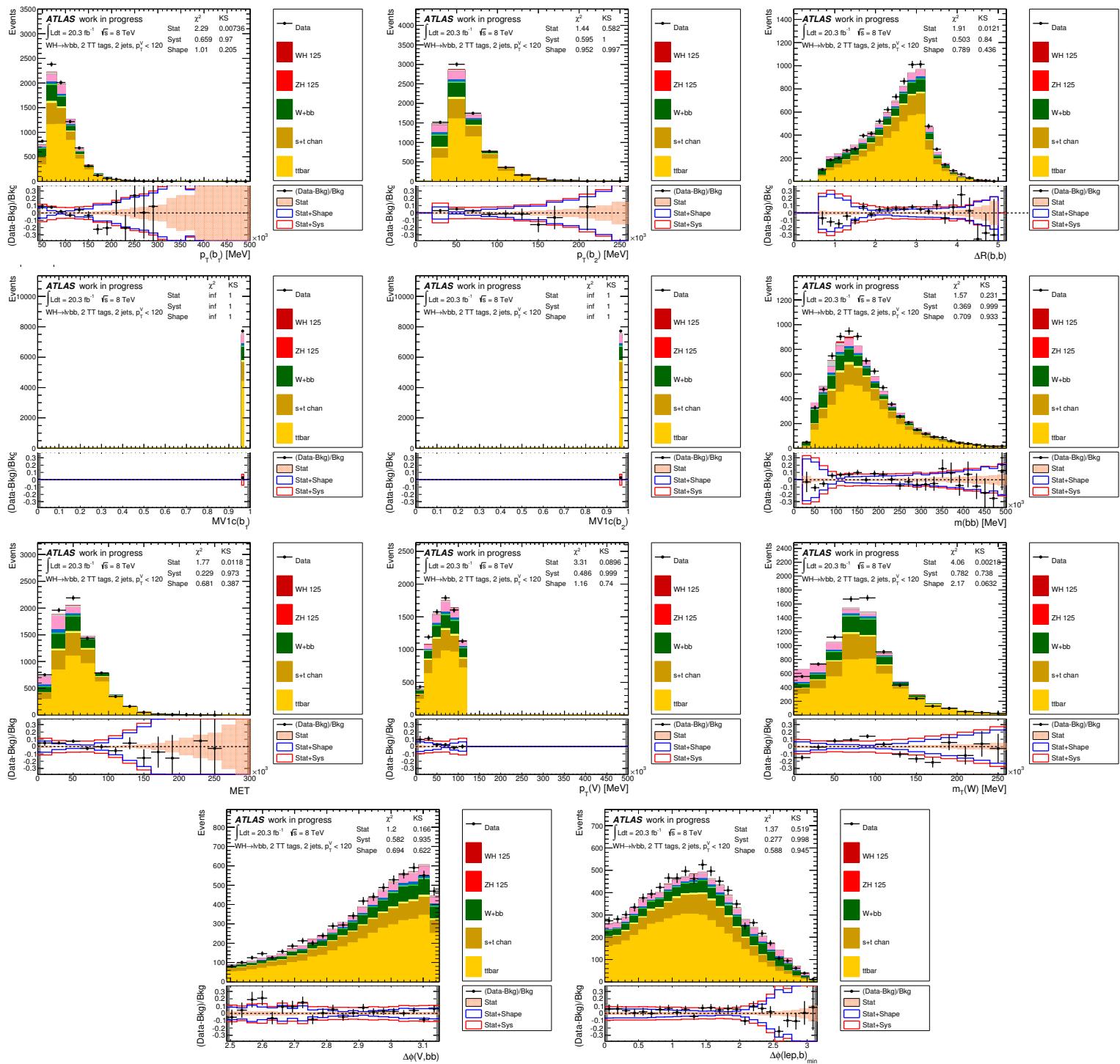


Figure 324: Distributions of MVA training variables used in 1-lepton events for $p_T^W < 120 \text{ GeV}$ with 2 TT b -tags and 2 jets. From left to right: Row 1 - leading then sub-leading jet p_T and ΔR of the same two jets. Row 2 - pseudo-continuous MV1c distributions for leading then sub-leading jet and the m_{jj} of the same two jets. Row 3 - E_T^{miss} , p_T^W , and m_T^W . Row 4 - $\Delta\phi(V, H)$ and $\min|\Delta\phi(\ell, jet)|$. Section 6.1 details the definition of each variable.

Not reviewed, for internal circulation only

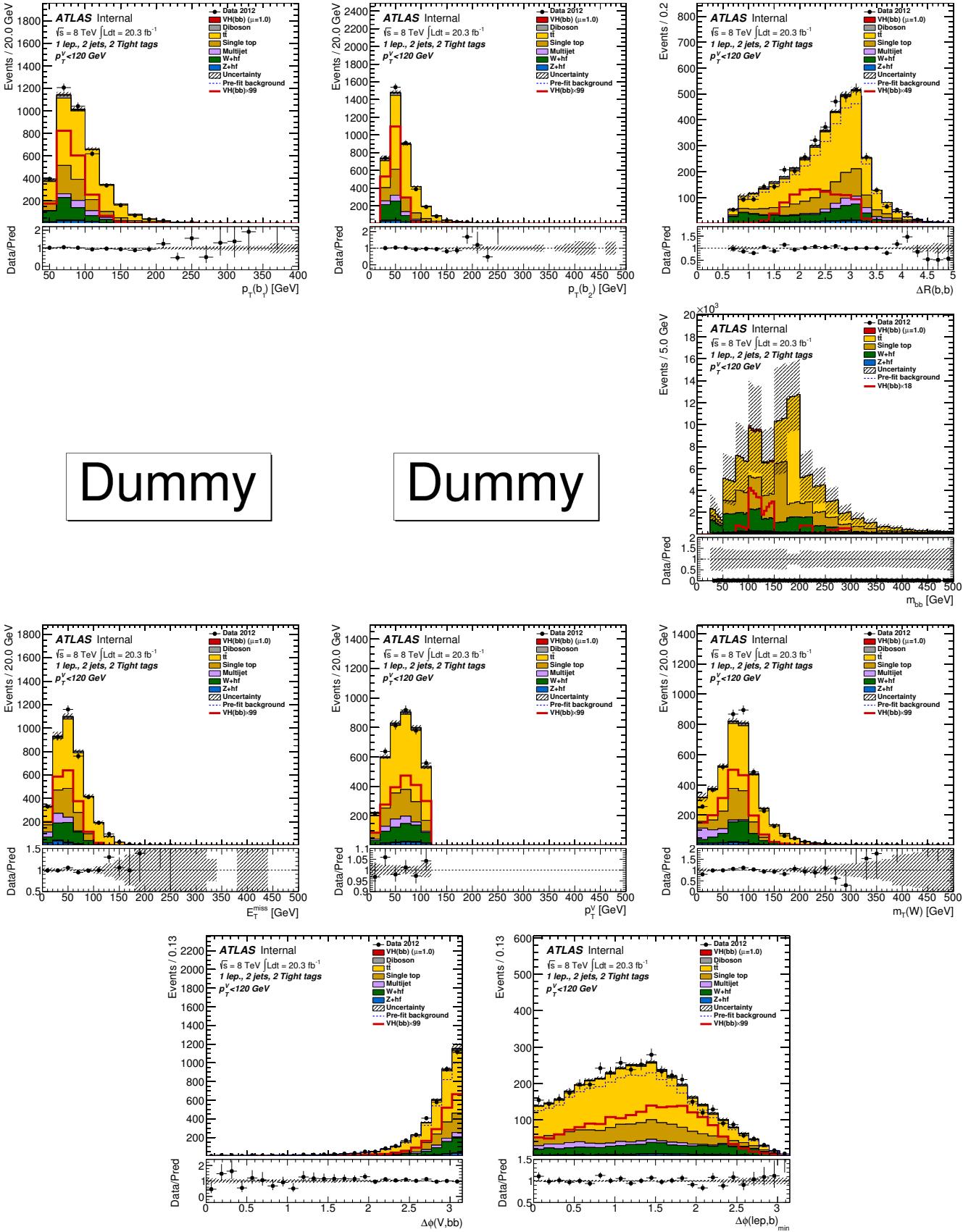


Figure 325: Distributions of MVA training variables used in 1-lepton events for $p_T^W < 120$ GeV with 2 TT b -tags and 2 jets after the combined 0+1+2 lepton MVA fit. From left to right: Row 1 - leading then sub-leading jet p_T and ΔR of the same two jets. Row 2 - pseudo-continuous MV1c distributions for leading then sub-leading jet and the m_{jj} of the same two jets. Row 3 - E_T^{miss} , p_T^W , and m_T^W . Row 4 - $\Delta\phi(V, H)$ and $\min|\Delta\phi(\ell, \text{jet})|$. Section 6.1 details the definition of each variable.

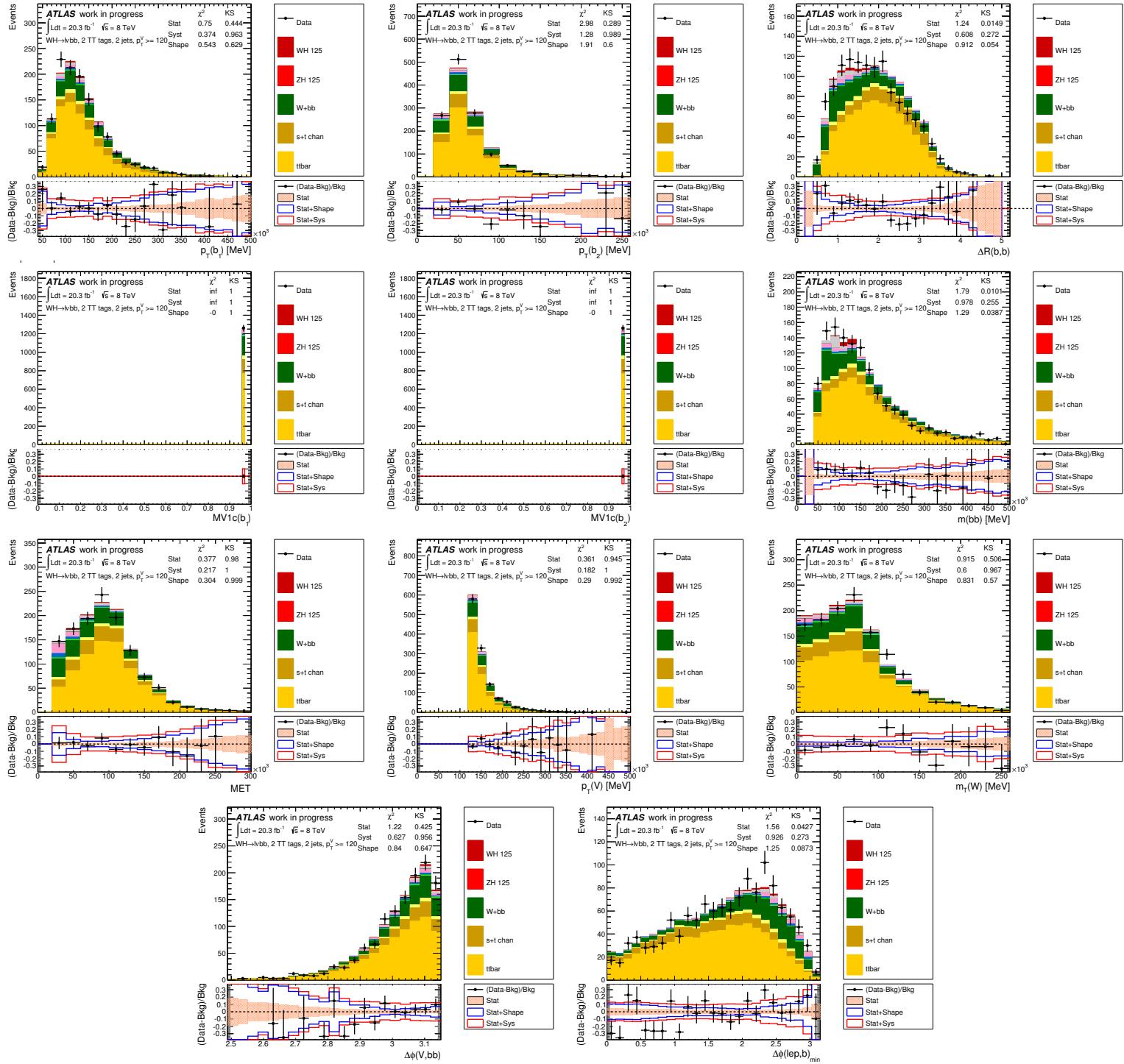


Figure 326: Distributions of MVA training variables used in 1-lepton events for $p_T^W > 120$ GeV with 2 TT b -tags and 2 jets. From left to right: Row 1 - leading then sub-leading jet p_T and ΔR of the same two jets. Row 2 - pseudo-continuous MV1c distributions for leading then sub-leading jet and the m_{jj} of the same two jets. Row 3 - E_T^{miss} , p_T^W , and m_T^W . Row 4 - $\Delta\phi(V, H)$ and $\min|\Delta\phi(\ell, jet)|$. Section 6.1 details the definition of each variable.

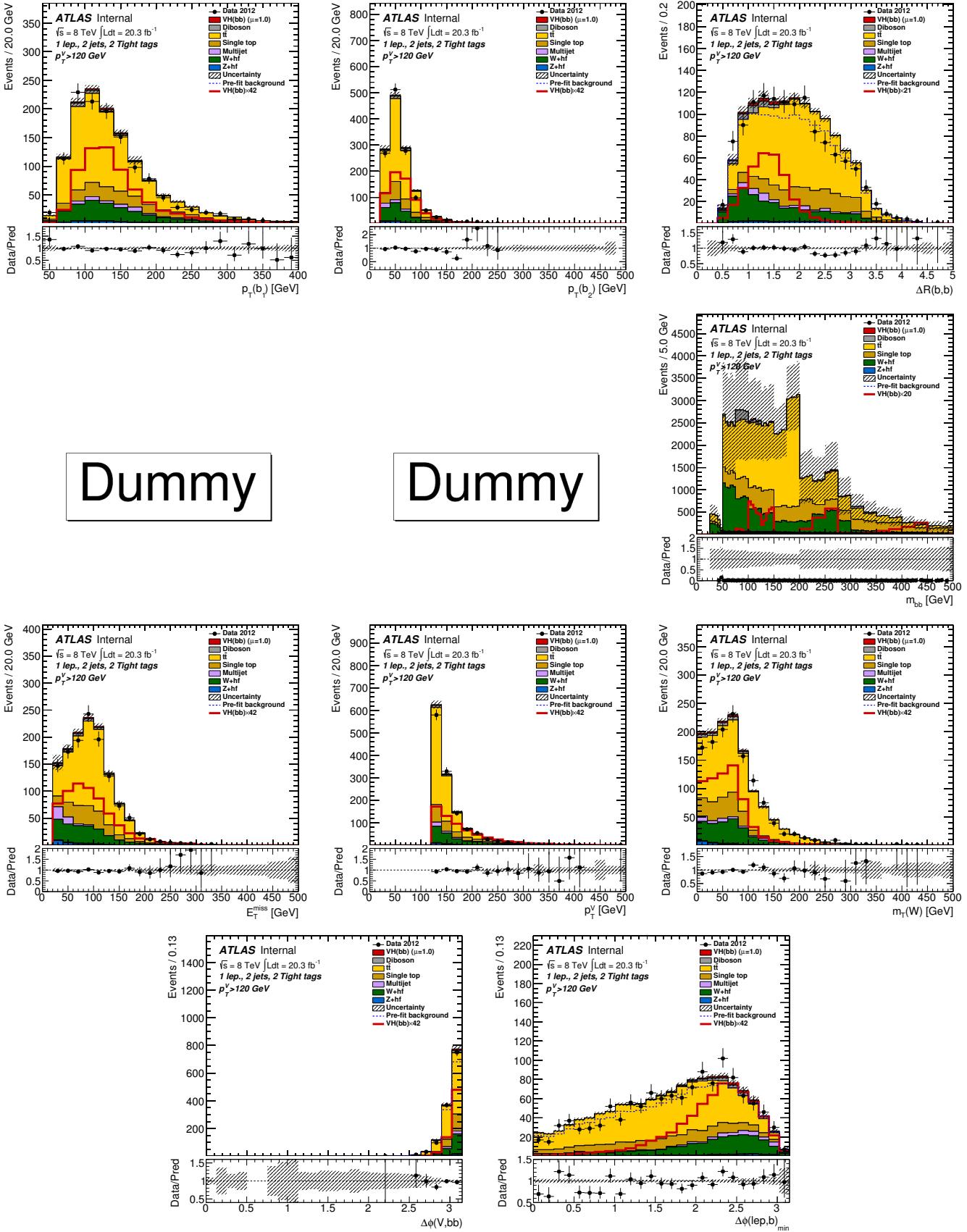


Figure 327: Distributions of MVA training variables used in 1-lepton events for $p_T^W > 120$ GeV with 2 TT b -tags and 2 jets after the combined 0+1+2 lepton MVA fit. From left to right: Row 1 - leading then sub-leading jet p_T and ΔR of the same two jets. Row 2 - pseudo-continuous MV1c distributions for leading then sub-leading jet and the m_{jj} of the same two jets. Row 3 - E_T^{miss} , p_T^W , and m_T^W . Row 4 - $\Delta\phi(V, H)$ and $\min|\Delta\phi(\ell, \text{jet})|$. Section 6.1 details the definition of each variable.

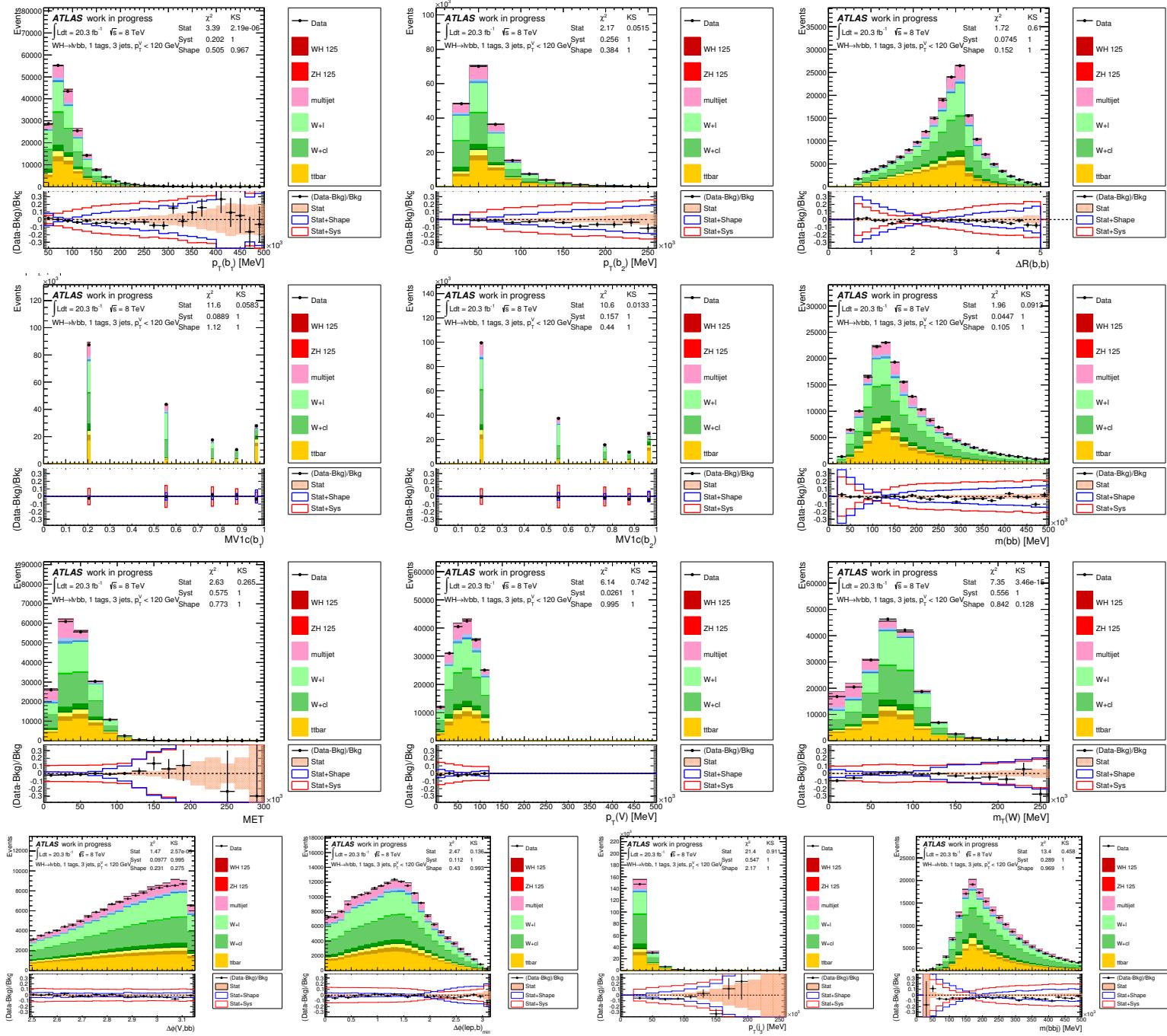


Figure 328: Distributions of MVA training variables used in 1-lepton events for $p_T^W < 120$ GeV with 1 b -tag and 3 jets. From left to right: Row 1 - leading then sub-leading jet p_T and ΔR of the same two jets. Row 2 - pseudo-continuous MV1c distributions for leading then sub-leading jet and the m_{jj} of the same two jets. Row 3 - E_T^{miss} , p_T^W , and m_T^W . Row 4 - $\Delta\phi(V,H)$, $\min|\Delta\phi(\ell, jet)|$, the 3rd jet p_T , and the tri-jet mass (m_{jjj}). Section 6.1 details the definition of each variable.

Not reviewed, for internal circulation only

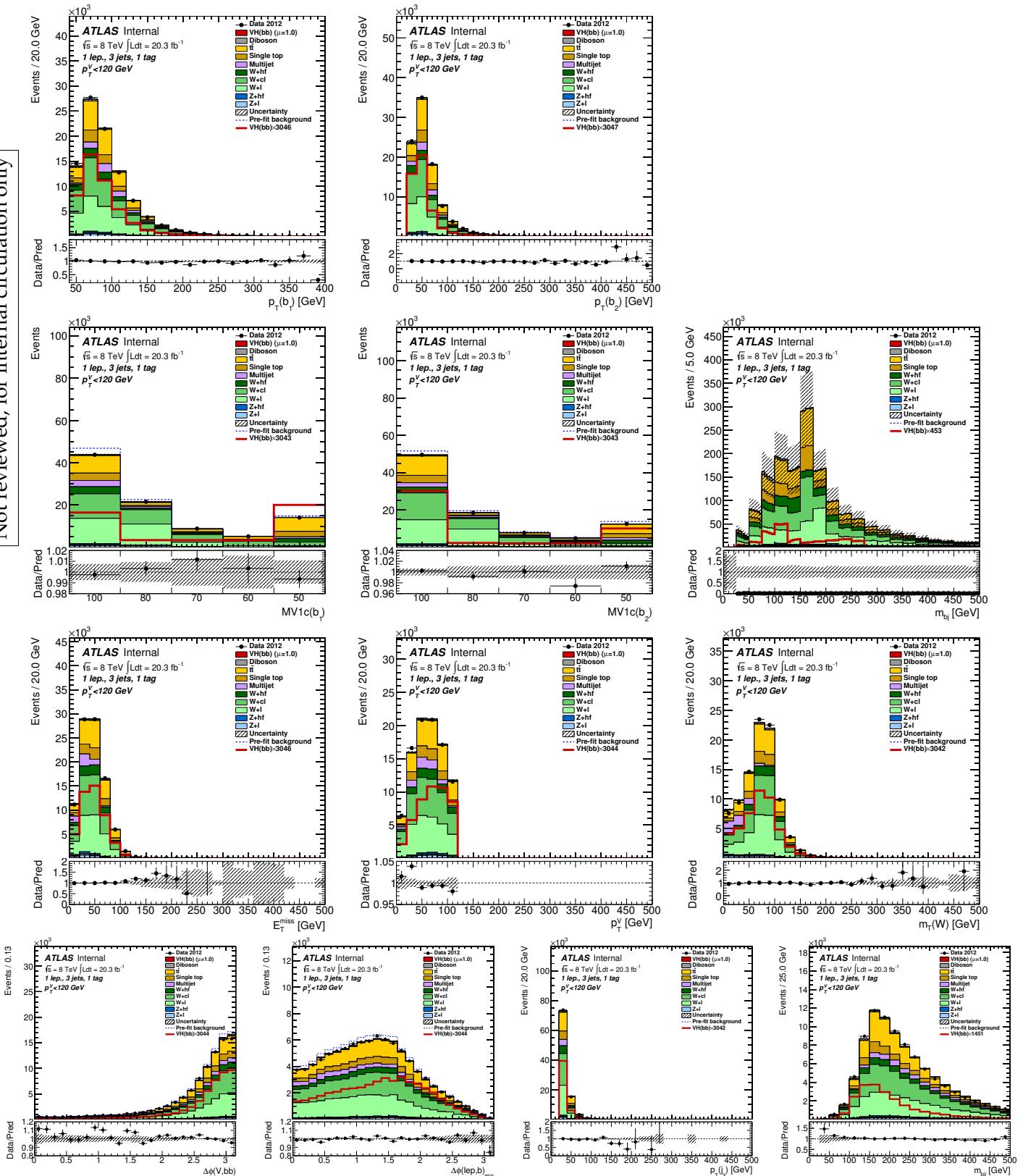


Figure 329: Distributions of MVA training variables used in 1-lepton events for $p_T^W < 120$ GeV with 1 b -tag and 3 jets after the combined $0+1+2$ lepton MVA fit. From left to right: Row 1 - leading then sub-leading jet p_T and ΔR of the same two jets. Row 2 - pseudo-continuous MV1c distributions for leading then sub-leading jet and the m_{jj} of the same two jets. Row 3 - E_T^{miss} , p_T^W , and m_T^W . Row 4 - $\Delta\phi(V, H)$, $\min|\Delta\phi(\ell, \text{jet})|$, the 3rd jet p_T , and the tri-jet mass (m_{jjj}). Section 6.1 details the definition of each variable.

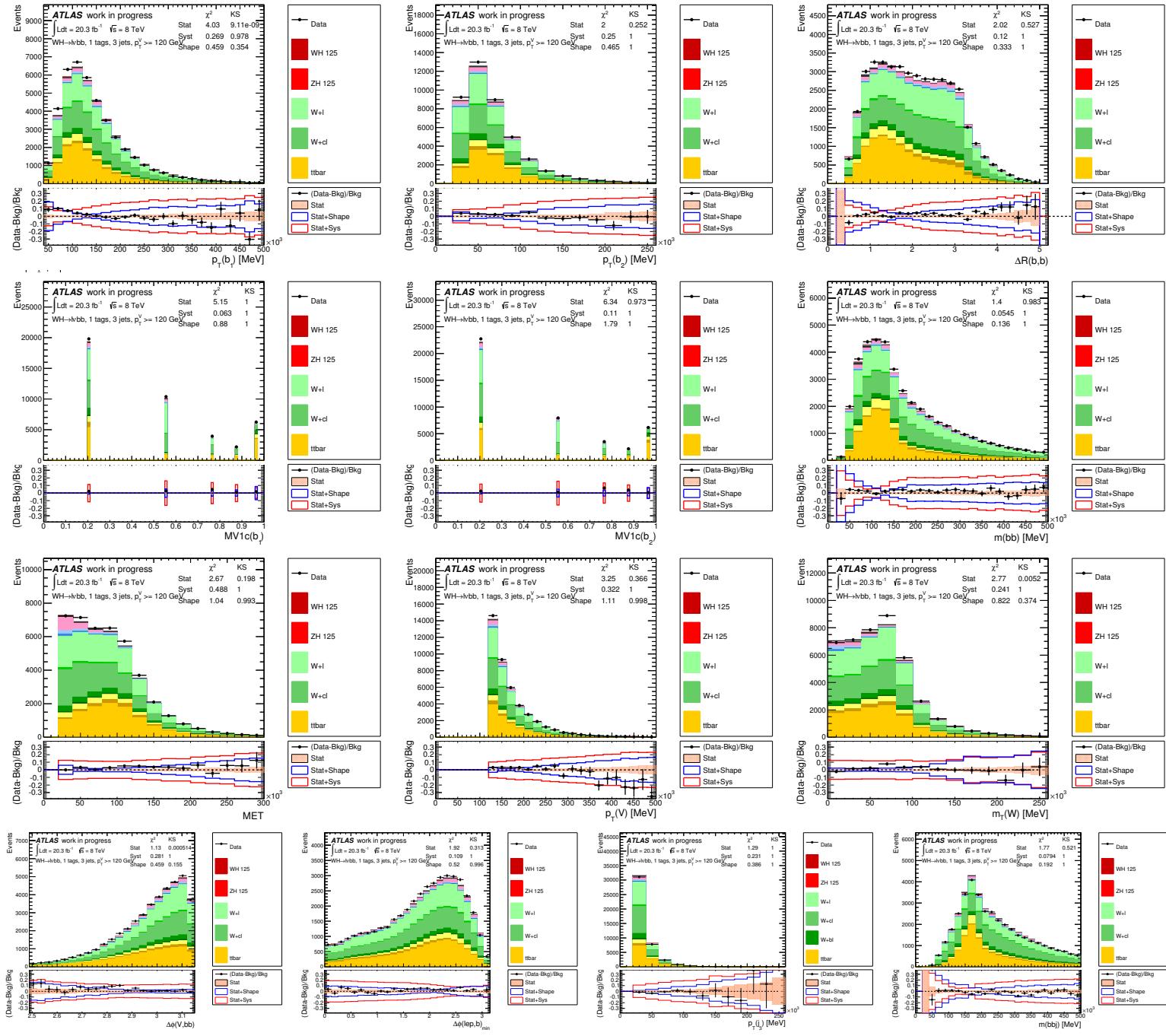


Figure 330: Distributions of MVA training variables used in 1-lepton events for $p_T^W > 120$ GeV with 1 b -tag and 3 jets. From left to right: Row 1 - leading then sub-leading jet p_T and ΔR of the same two jets. Row 2 - pseudo-continuous MV1c distributions for leading then sub-leading jet and the m_{jj} of the same two jets. Row 3 - E_T^{miss} , p_T^W , and m_T^W . Row 4 - $\Delta\phi(V, H)$, $\min|\Delta\phi(\ell, jet)|$, the 3rd jet p_T , and the tri-jet mass (m_{jjj}). Section 6.1 details the definition of each variable.

Not reviewed, for internal circulation only

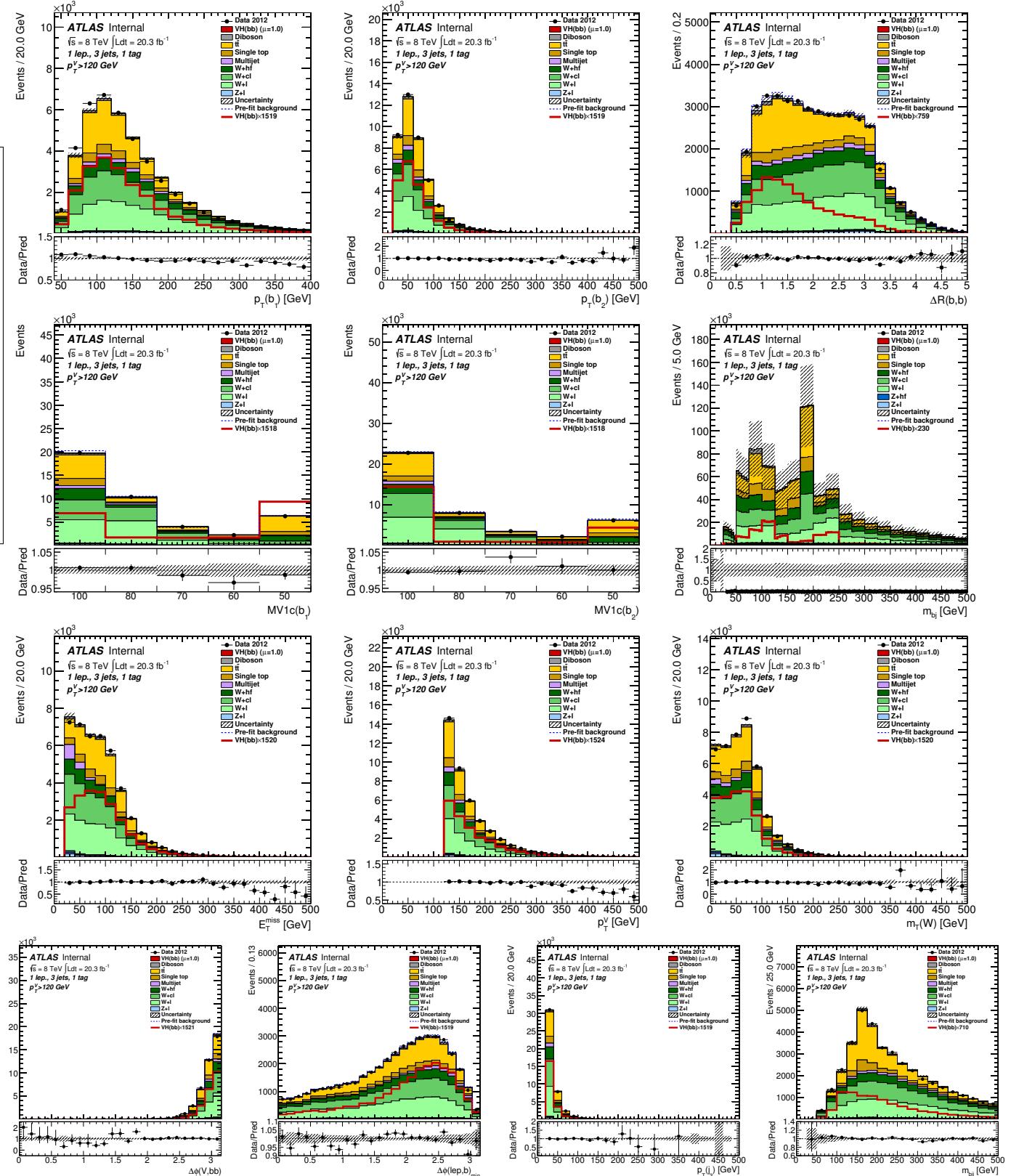


Figure 331: Distributions of MVA training variables used in 1-lepton events for $p_T^W > 120 \text{ GeV}$ with 1 b -tag and 3 jets after the combined $0+1+2$ lepton MVA fit. From left to right: Row 1 - leading then sub-leading jet p_T and ΔR of the same two jets. Row 2 - pseudo-continuous MV1c distributions for leading then sub-leading jet and the m_{jj} of the same two jets. Row 3 - E_T^{miss} , p_T^W , and m_T^W . Row 4 - $\Delta\phi(V,H)$, $\min|\Delta\phi(\ell, jet)|$, the 3rd jet p_T , and the tri-jet mass (m_{jjj}). Section 6.1 details the definition of each variable.

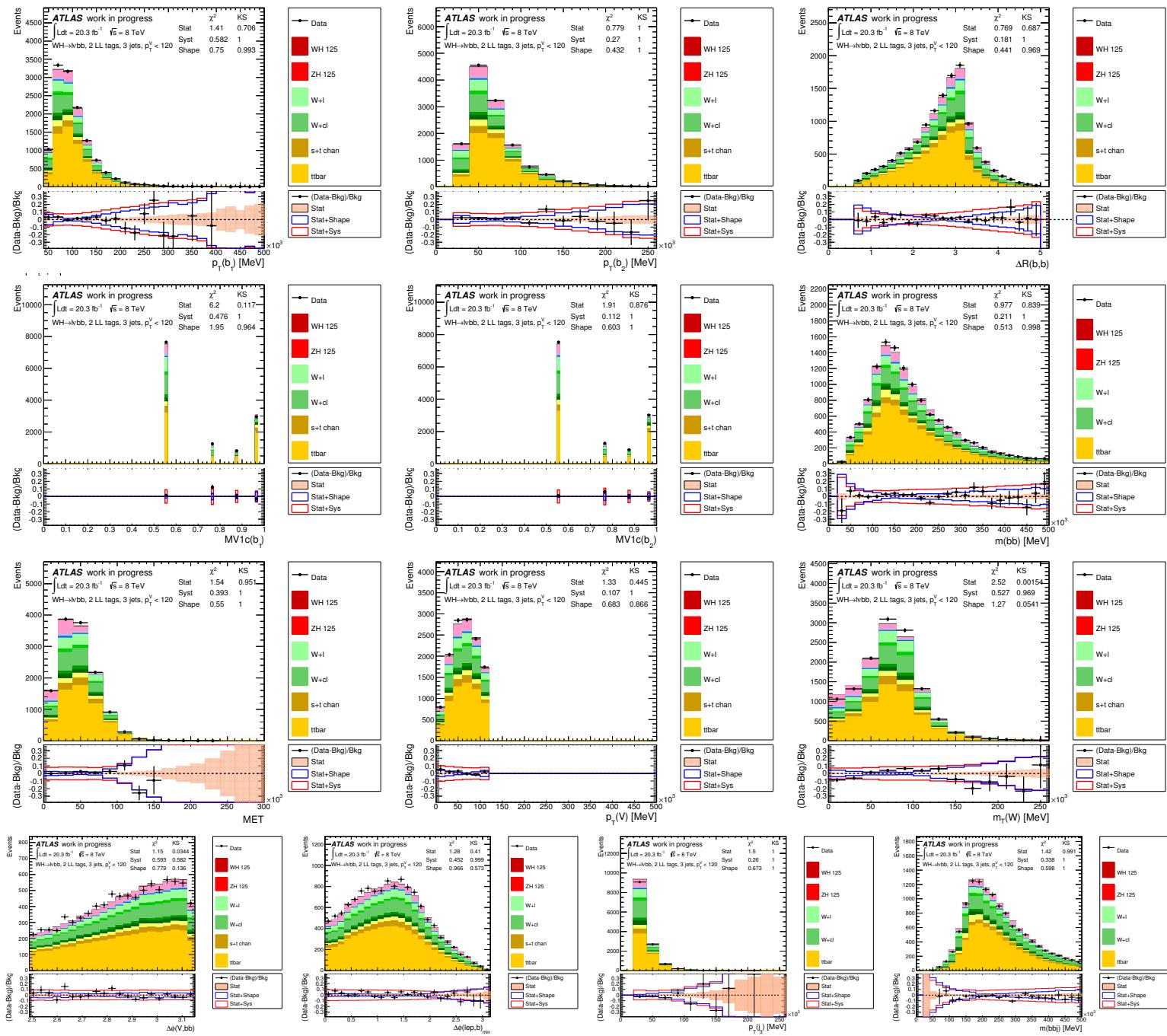


Figure 332: Distributions of MVA training variables used in 1-lepton events for $p_T^W < 120$ GeV with 2 LL b -tags and 3 jets. From left to right: Row 1 - leading then sub-leading jet p_T and ΔR of the same two jets. Row 2 - pseudo-continuous MV1c distributions for leading then sub-leading jet and the m_{jj} of the same two jets. Row 3 - E_T^{miss} , p_T^W , and m_W^W . Row 4 - $\Delta\phi(V, H)$, $\min|\Delta\phi(\ell, \text{jet})|$, the 3rd jet p_T , and the tri-jet mass (m_{jjj}). Section 6.1 details the definition of each variable.

Not reviewed, for internal circulation only

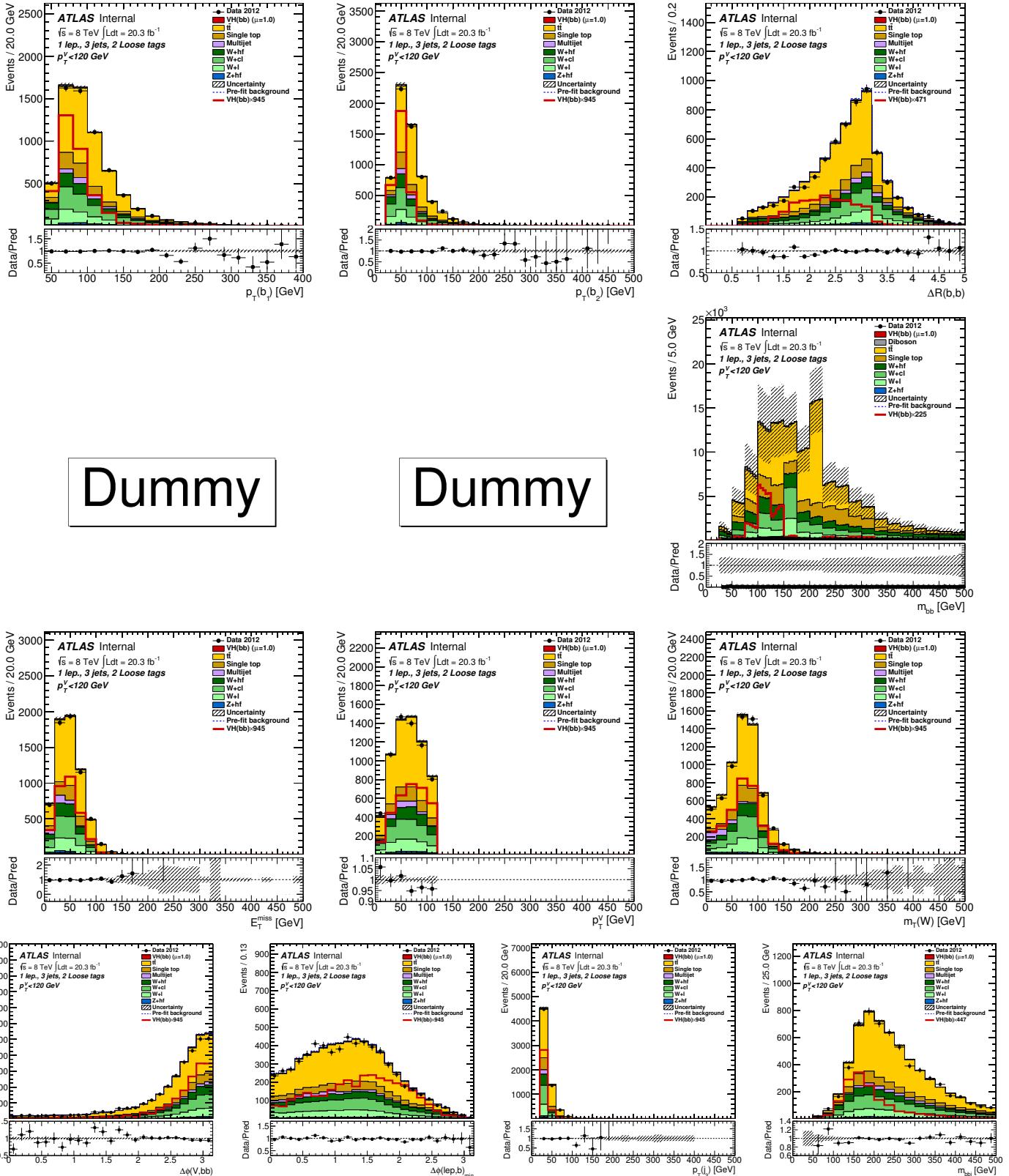


Figure 333: Distributions of MVA training variables used in 1-lepton events for $p_T^W < 120$ GeV with 2 LL b -tags and 3 jets after the combined 0+1+2 lepton MVA fit. From left to right: Row 1 - leading then sub-leading jet p_T and ΔR of the same two jets. Row 2 - pseudo-continuous MV1c distributions for leading then sub-leading jet and the m_{jj} of the same two jets. Row 3 - E_T^{miss} , p_T^W , and m_T^W . Row 4 - $\Delta\phi(V,H)$, $\min|\Delta\phi(\ell, \text{jet})|$, the 3rd jet p_T , and the tri-jet mass (m_{jjj}). Section 6.1 details the definition of each variable.

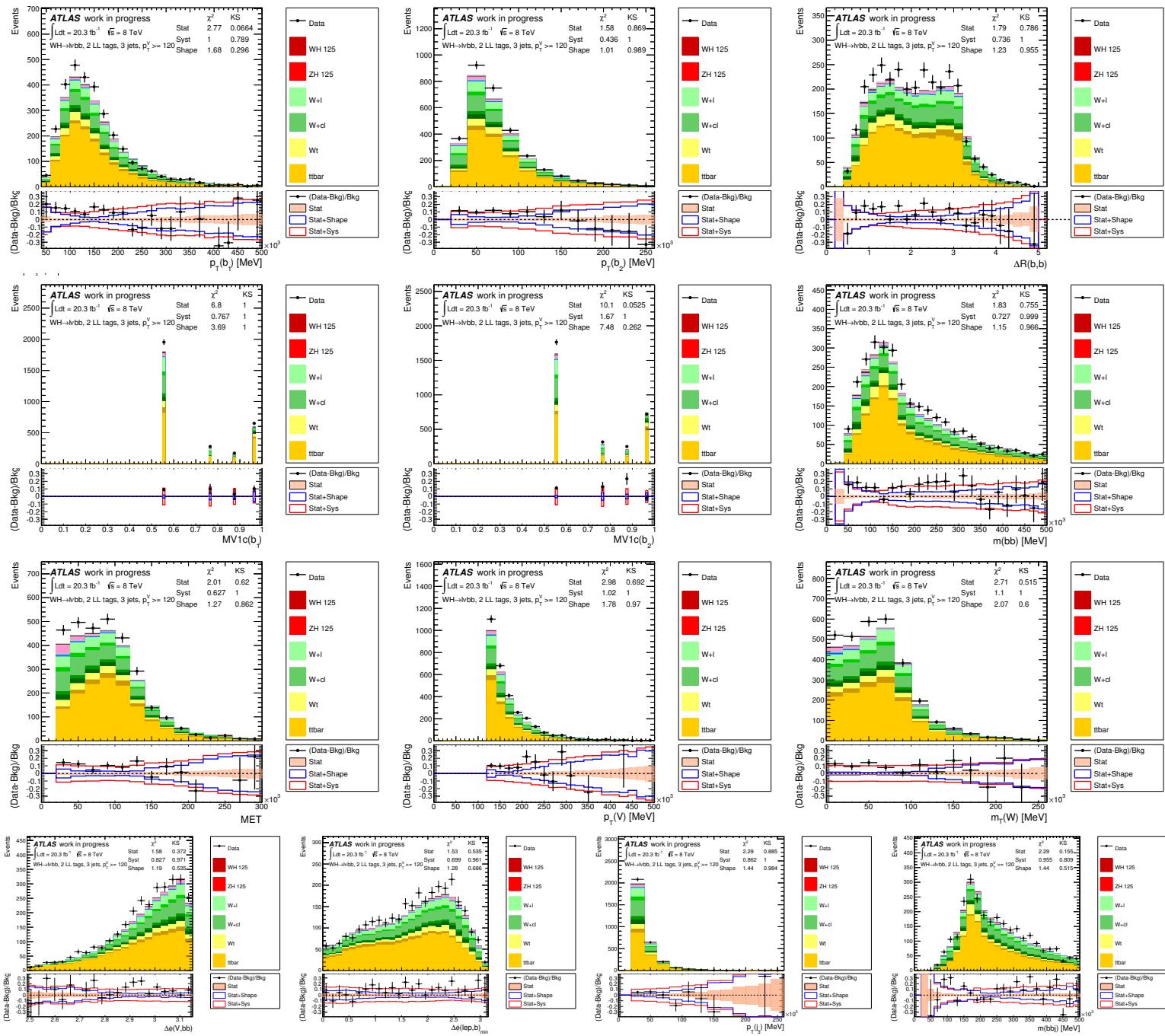


Figure 334: Distributions of MVA training variables used in 1-lepton events for $p_T^W > 120$ GeV with 2 LL b -tags and 3 jets. From left to right: Row 1 - leading then sub-leading jet p_T and ΔR of the same two jets. Row 2 - pseudo-continuous MV1c distributions for leading then sub-leading jet and the m_{jj} of the same two jets. Row 3 - E_T^{miss} , p_T^W , and m_W^W . Row 4 - $\Delta\phi(V, H)$, $\min|\Delta\phi(\ell, jet)|$, the 3rd jet p_T , and the tri-jet mass (m_{bbb}). Section 6.1 details the definition of each variable.

Not reviewed, for internal circulation only

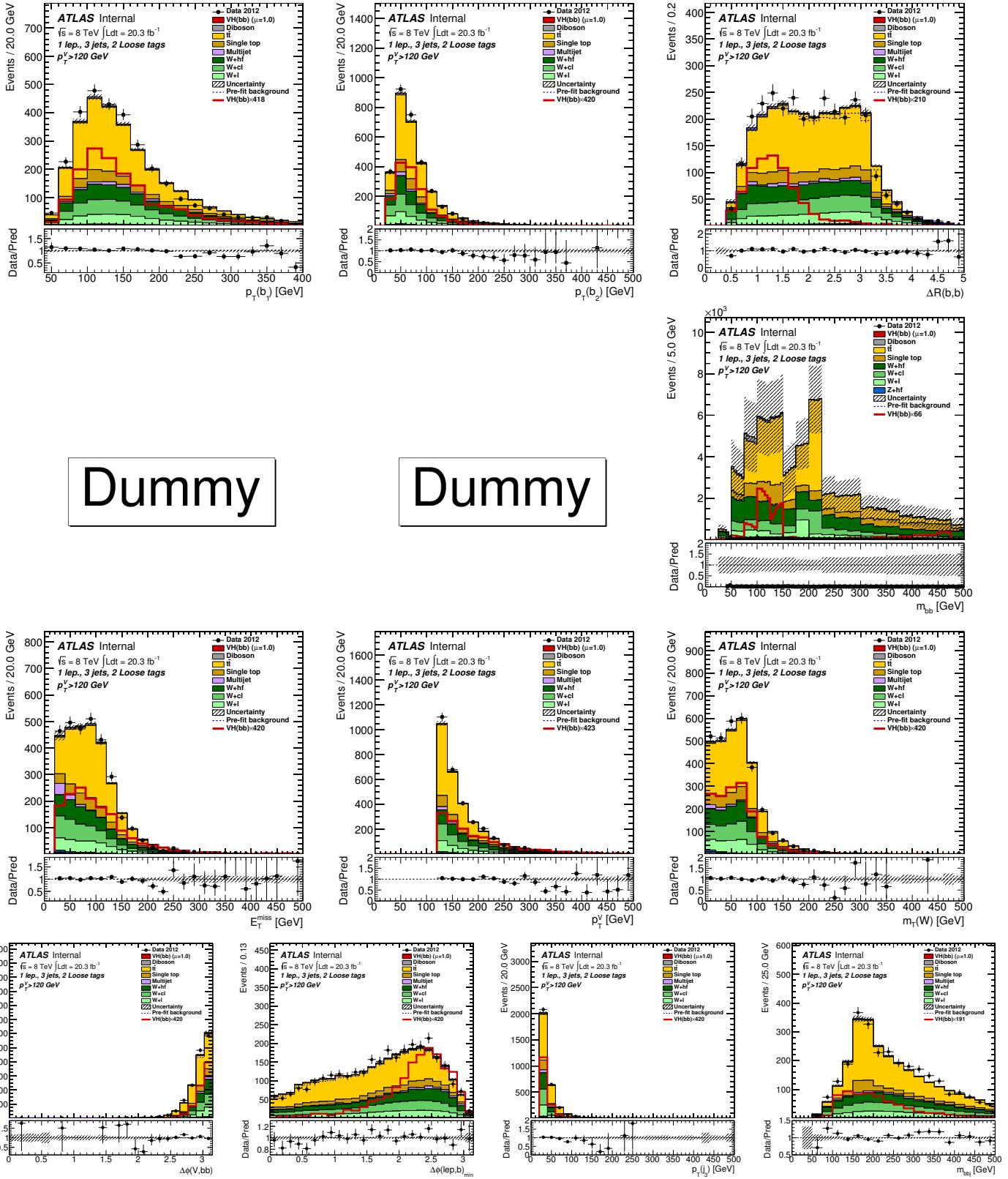


Figure 335: Distributions of MVA training variables used in 1-lepton events for $p_T^W > 120$ GeV with 2 LL b -tags and 3 jets after the combined 0+1+2 lepton MVA fit. From left to right: Row 1 - leading then sub-leading jet p_T and ΔR of the same two jets. Row 2 - pseudo-continuous MV1c distributions for leading then sub-leading jet and the m_{jj} of the same two jets. Row 3 - E_T^{miss} , p_T^W , and m_T^W . Row 4 - $\Delta\phi(V, H)$, $\min|\Delta\phi(\ell, \text{jet})|$, the 3rd jet p_T , and the tri-jet mass (m_{jjj}). Section 6.1 details the definition of each variable.

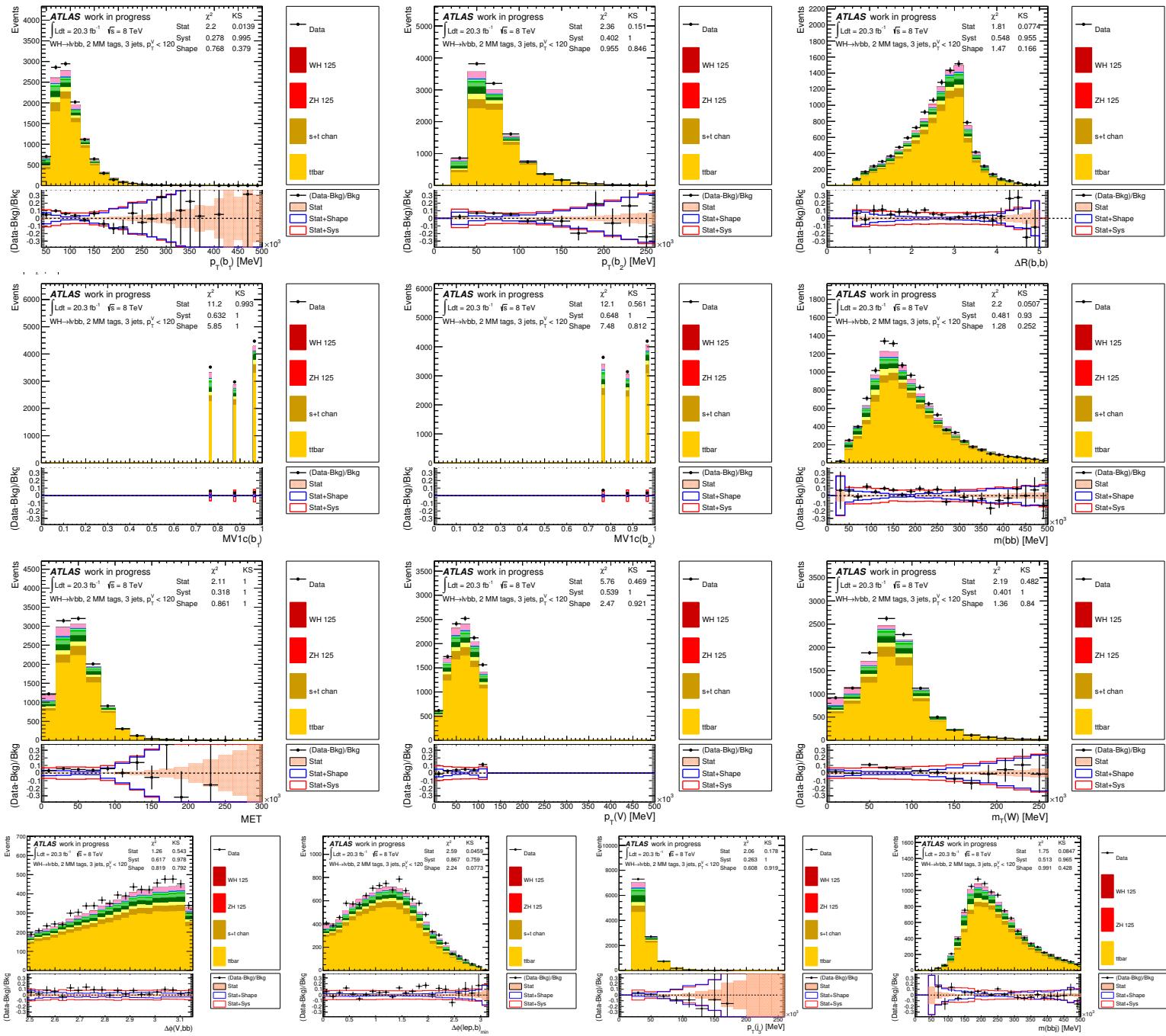


Figure 336: Distributions of MVA training variables used in 1-lepton events for $p_T^W < 120$ GeV with 2 MM b -tags and 3 jets. From left to right: Row 1 - leading then sub-leading jet p_T and ΔR of the same two jets. Row 2 - pseudo-continuous MV1c distributions for leading then sub-leading jet and the m_{jj} of the same two jets. Row 3 - E_T^{miss} , p_T^W , and m_W . Row 4 - $\Delta\phi(V, H)$, $\min|\Delta\phi(\ell, \text{jet})|$, the 3rd jet p_T , and the tri-jet mass (m_{jjj}). Section 6.1 details the definition of each variable.

Not reviewed, for internal circulation only

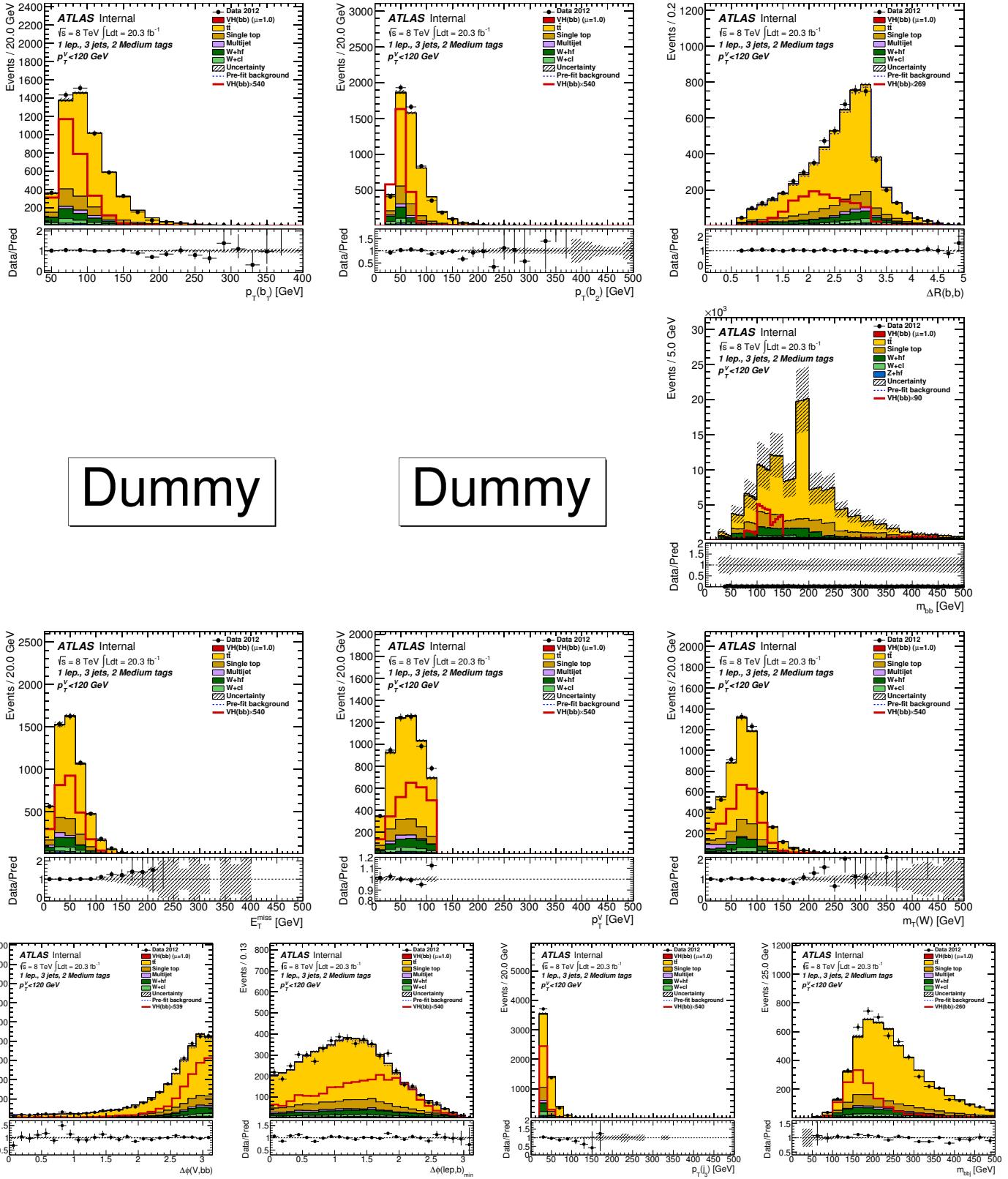


Figure 337: Distributions of MVA training variables used in 1-lepton events for $p_T^W < 120$ GeV with 2 MM b -tags and 3 jets after the combined 0+1+2 lepton MVA fit. From left to right: Row 1 - leading then sub-leading jet p_T and ΔR of the same two jets. Row 2 - pseudo-continuous MV1c distributions for leading then sub-leading jet and the m_{jj} of the same two jets. Row 3 - E_T^{miss} , p_T^W , and m_T^W . Row 4 - $\Delta\phi(V, H)$, $\min|\Delta\phi(\ell, \text{jet})|$, the 3rd jet p_T , and the tri-jet mass (m_{jjj}). Section 6.1 details the definition of each variable.

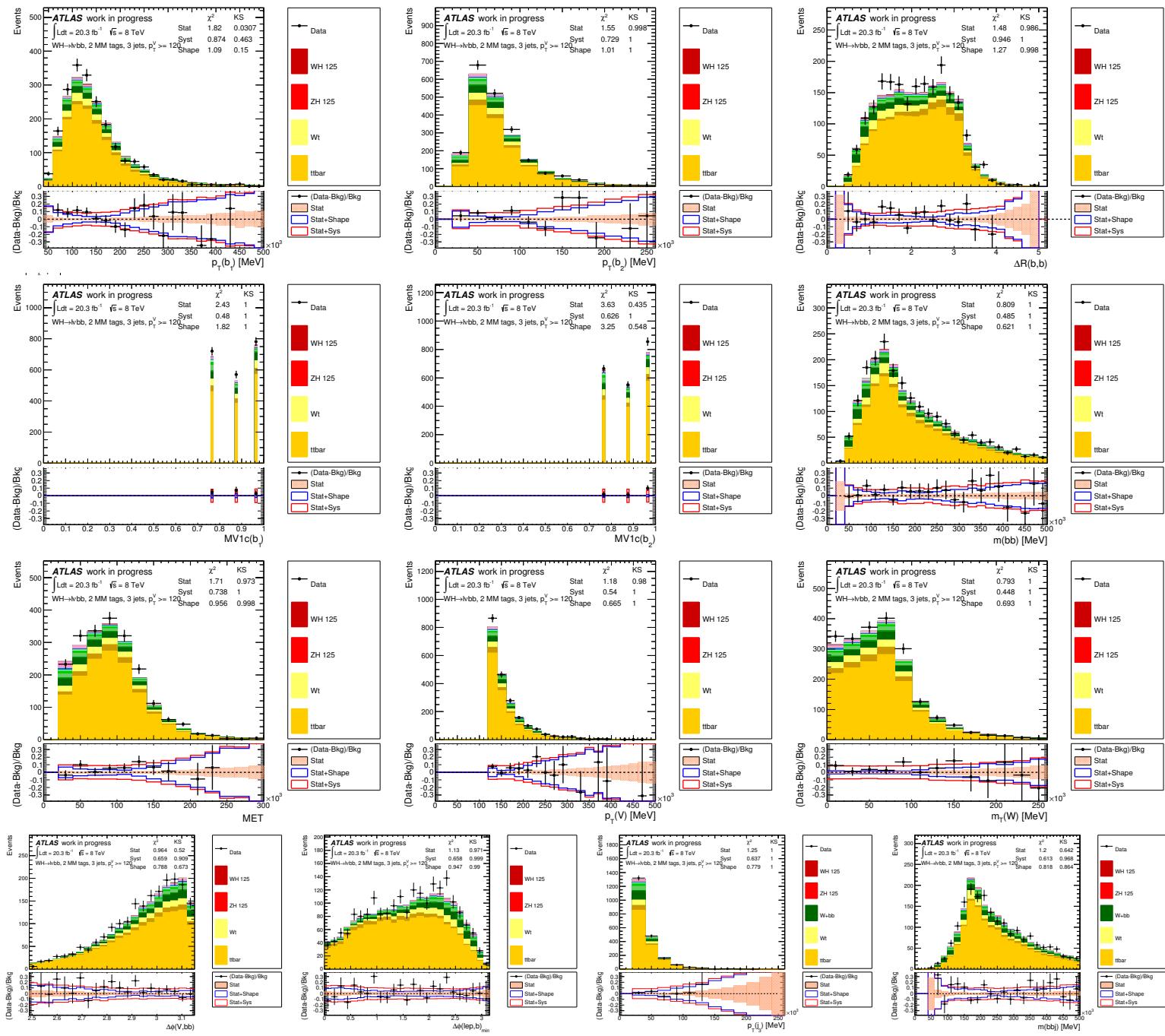


Figure 338: Distributions of MVA training variables used in 1-lepton events for $p_T^W > 120$ GeV with 2 MM b -tags and 3 jets. From left to right: Row 1 - leading then sub-leading jet p_T and ΔR of the same two jets. Row 2 - pseudo-continuous MV1c distributions for leading then sub-leading jet and the m_{jj} of the same two jets. Row 3 - E_T^{miss} , p_T^W , and m_T^W . Row 4 - $\Delta\phi(V, H)$, $\min|\Delta\phi(\ell, \text{jet})|$, the 3rd jet p_T , and the tri-jet mass (m_{jjj}). Section 6.1 details the definition of each variable.

Not reviewed, for internal circulation only

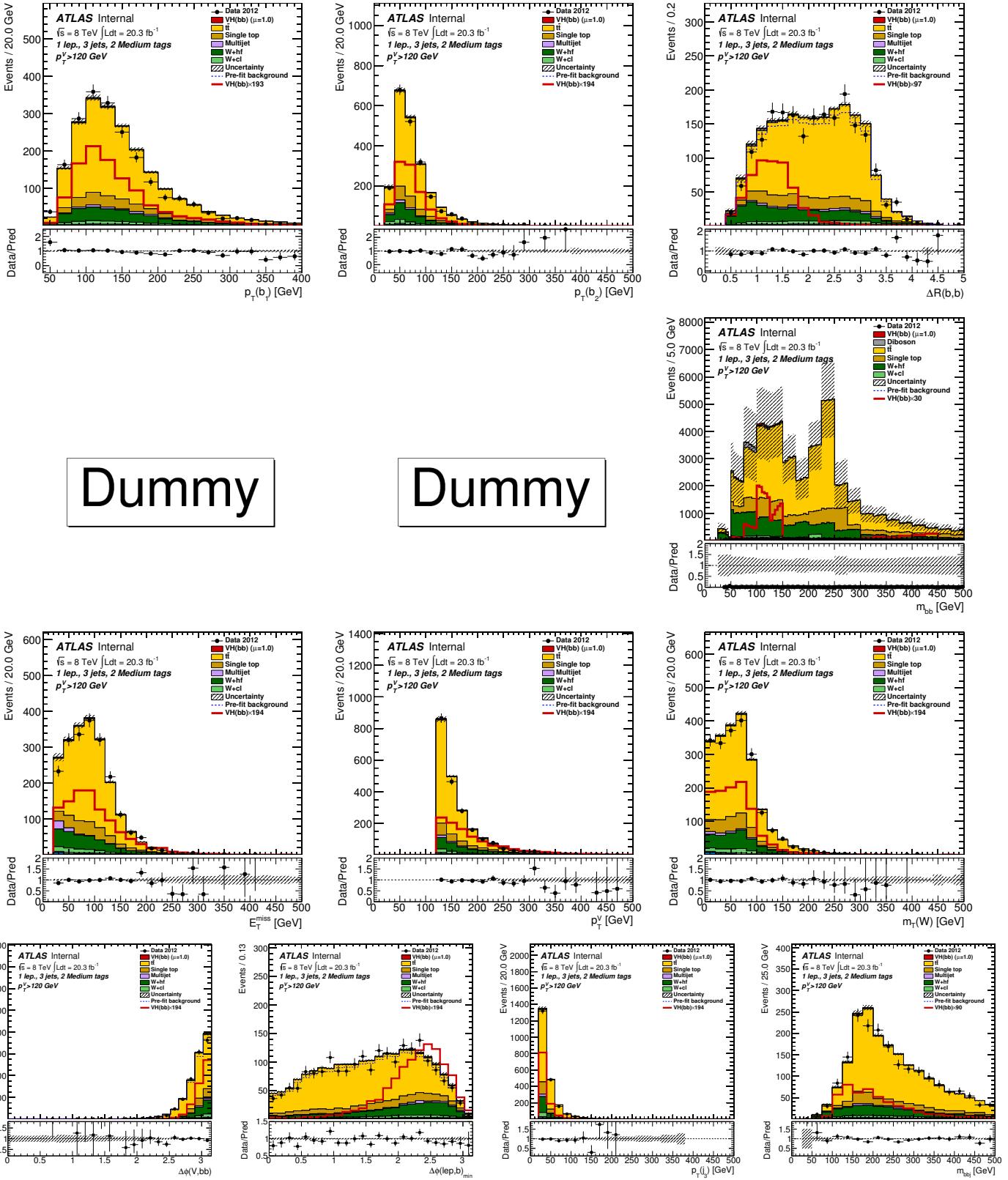


Figure 339: Distributions of MVA training variables used in 1-lepton events for $p_T^W > 120$ GeV with 2 MM b -tags and 3 jets after the combined 0+1+2 lepton mva fit. From left to right: Row 1 - leading then sub-leading jet p_T and ΔR of the same two jets. Row 2 - pseudo-continuous MV1c distributions for leading then sub-leading jet and the m_{jj} of the same two jets. Row 3 - E_T^{miss} , p_T^W , and m_T^W . Row 4 - $\Delta\phi(V,H)$, $\min|\Delta\phi(\ell, \text{jet})|$, the 3rd jet p_T , and the tri-jet mass (m_{jjj}). Section 6.1 details the definition of each variable.

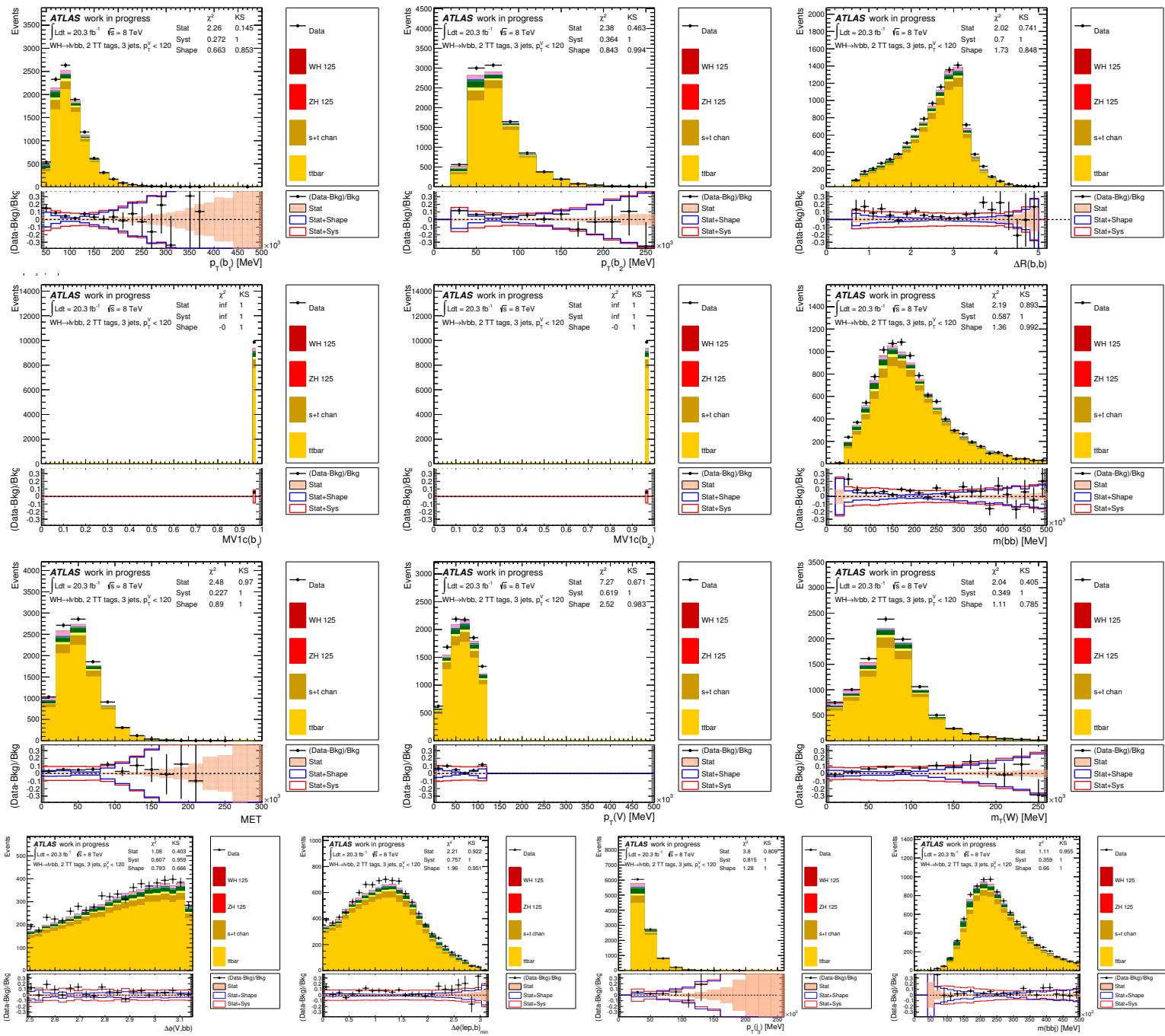


Figure 340: Distributions of MVA training variables used in 1-lepton events for $p_T^W < 120$ GeV with 2 TT b -tags and 3 jets. From left to right: Row 1 - leading then sub-leading jet p_T and ΔR of the same two jets. Row 2 - pseudo-continuous MV1c distributions for leading then sub-leading jet and the m_{jj} of the same two jets. Row 3 - E_T^{miss} , p_T^W , and m_W^W . Row 4 - $\Delta\phi(V, H)$, $\min|\Delta\phi(\ell, \text{jet})|$, the 3rd jet p_T , and the tri-jet mass (m_{bbb}). Section 6.1 details the definition of each variable.

Not reviewed, for internal circulation only

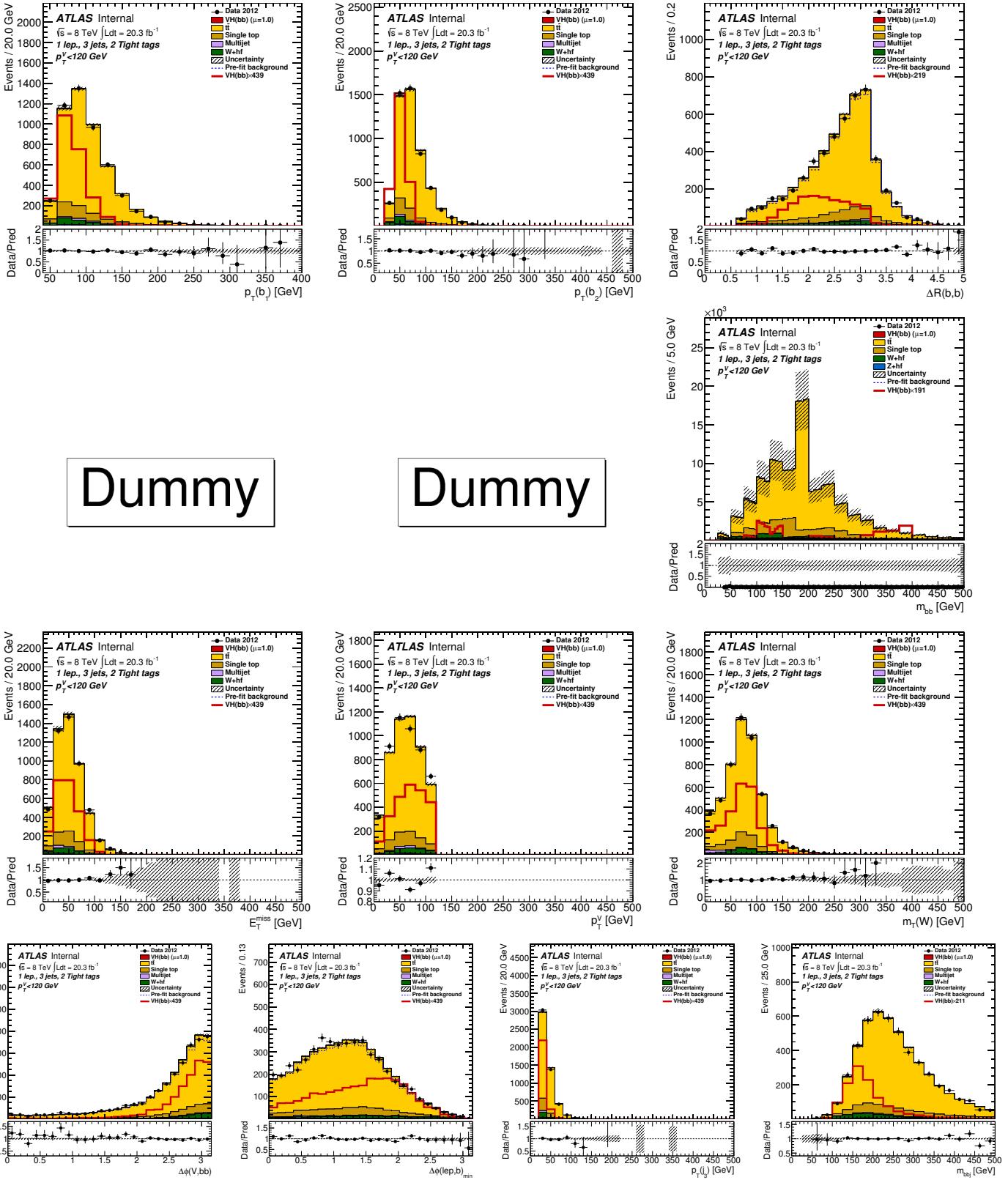


Figure 341: Distributions of MVA training variables used in 1-lepton events for $p_T^W < 120$ GeV with 2 TT b -tags and 3 jets after the combined 0+1+2 lepton MVA fit. From left to right: Row 1 - leading then sub-leading jet p_T and ΔR of the same two jets. Row 2 - pseudo-continuous MV1c distributions for leading then sub-leading jet and the m_{jj} of the same two jets. Row 3 - E_T^{miss} , p_T^W , and m_T^W . Row 4 - $\Delta\phi(V,H)$, $\min|\Delta\phi(\ell, \text{jet})|$, the 3rd jet p_T , and the tri-jet mass (m_{jjj}). Section 6.1 details the definition of each variable.

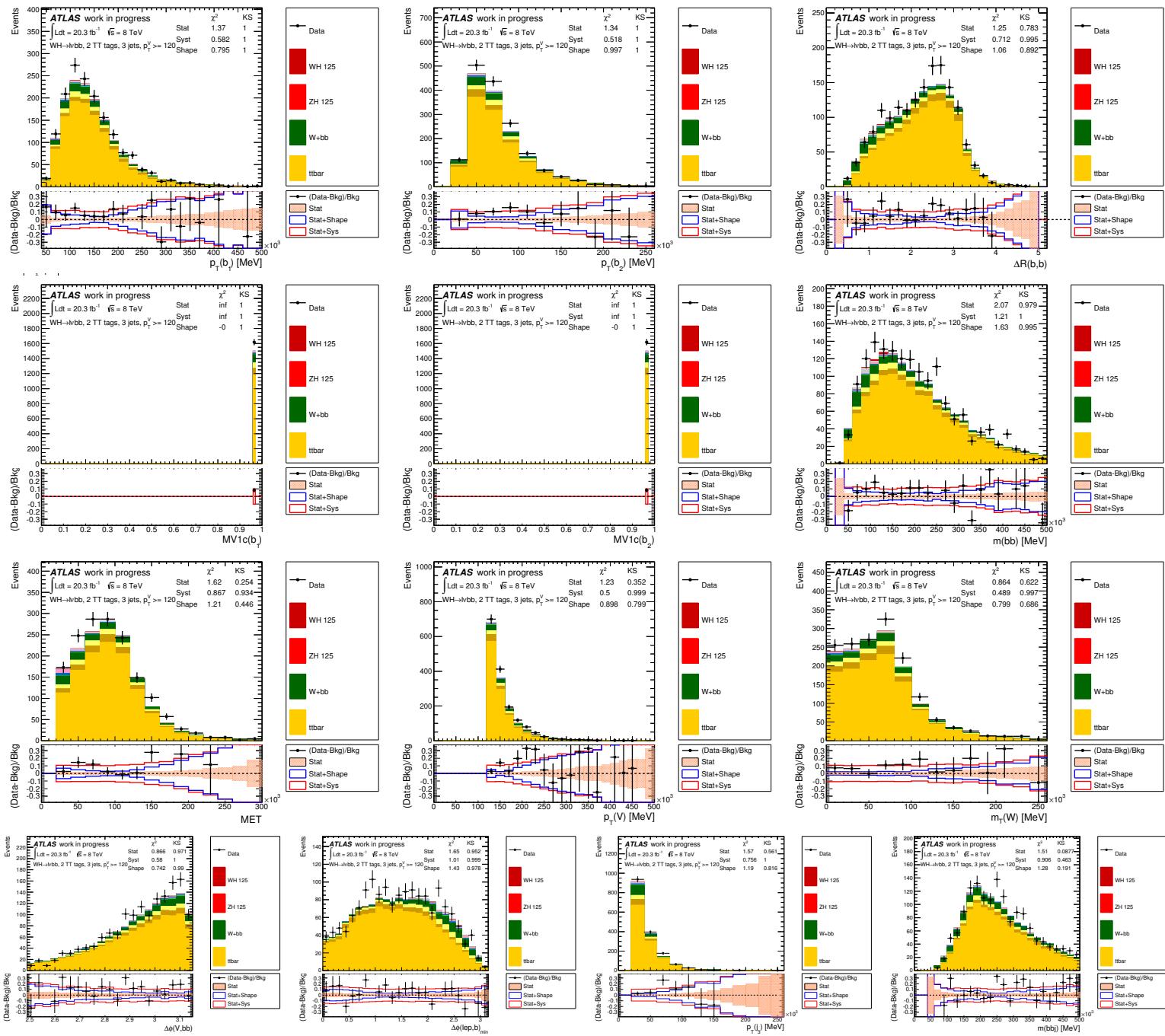


Figure 342: Distributions of MVA training variables used in 1-lepton events for $p_T^W > 120$ GeV with 2 TT b -tags and 3 jets. From left to right: Row 1 - leading then sub-leading jet p_T and ΔR of the same two jets. Row 2 - pseudo-continuous MV1c distributions for leading then sub-leading jet and the m_{jj} of the same two jets. Row 3 - E_T^{miss} , p_T^W , and m_T^W . Row 4 - $\Delta\phi(V, H)$, $\min|\Delta\phi(\ell, \text{jet})|$, the 3rd jet p_T , and the tri-jet mass (m_{bbj}). Section 6.1 details the definition of each variable.

Not reviewed, for internal circulation only

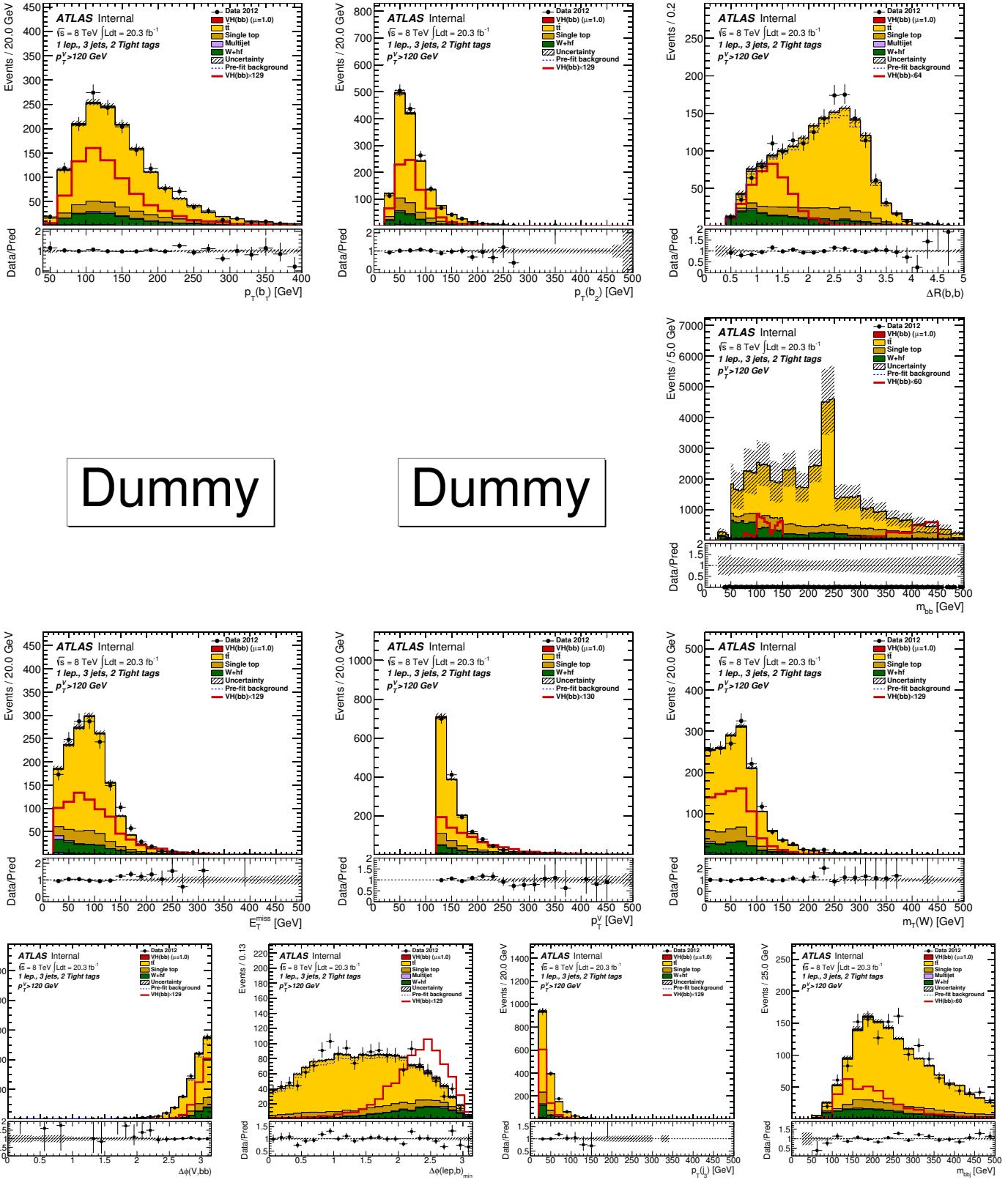


Figure 343: Distributions of MVA training variables used in 1-lepton events for $p_T^W > 120$ GeV with 2 TT b -tags and 3 jets after the combined 0+1+2 lepton MVA fit. From left to right: Row 1 - leading then sub-leading jet p_T and ΔR of the same two jets. Row 2 - pseudo-continuous MV1c distributions for leading then sub-leading jet and the m_{jj} of the same two jets. Row 3 - E_T^{miss} , p_T^W , and m_T^W . Row 4 - $\Delta\phi(V,H)$, $\min|\Delta\phi(\ell, \text{jet})|$, the 3rd jet p_T , and the tri-jet mass (m_{jjj}). Section 6.1 details the definition of each variable.

4931 AA MVA Input Variable Distributions: Two Lepton

4932 This appendix contains distributions of the BDT input variables defined in Section 6 in the 2-lepton anal-
 4933 ysis for low and high p_T^Z regions ($p_T^Z < 120$ GeV and $p_T^Z > 120$ GeV respectively). The electron and
 4934 muon events have been combined. These plots are done by applying the latest scale factors, obtained for
 4935 the 2 jet region and the 3-jet region separately, by comparing the event yield before and after the MVA
 4936 combined fit. They are summarized in Table 97. Explicitly stated, the theoretical expectation for each
 4937 background is used for the given luminosity. All the plots in this section are done with the status-of-art
 4938 analysis.

4939 Figure 344 shows one b -tag two jet events with $p_T^Z < 120$ GeV prefit and Figure 345 postfit.
 4940 Figure 346 shows one b -tag two jet events with $p_T^Z > 120$ GeV prefit and Figure 347 postfit.
 4941 Figure 348 shows LL b -tag two jet events with $p_T^Z < 120$ GeV prefit and Figure 349 postfit.
 4942 Figure 350 shows LL b -tag two jet events with $p_T^Z > 120$ GeV prefit and Figure 351 postfit.
 4943 Figure 352 shows MM+TT b -tag two jet events with $p_T^Z < 120$ GeV prefit and Figure 353 postfit.
 4944 Figure 354 shows MM+TT b -tag two jet events with $p_T^Z > 120$ GeV prefit and Figure 355 postfit.
 4945 Figure 356 shows one b -tag three jet events with $p_T^Z < 120$ GeV prefit and Figure 357 postfit.
 4946 Figure 358 shows one b -tag three jet events with $p_T^Z > 120$ GeV prefit and Figure 359 postfit.
 4947 Figure 360 shows LL b -tag three jet events with $p_T^Z < 120$ GeV prefit and Figure 361 postfit.
 4948 Figure 362 shows LL b -tag three jet events with $p_T^Z > 120$ GeV prefit and Figure 363 postfit.
 4949 Figure 364 shows MMTT b -tag three jet events with $p_T^Z < 120$ GeV prefit and Figure 365 postfit.
 4950 Figure 366 shows MMTT b -tag three jet events with $p_T^Z > 120$ GeV prefit and Figure 367 postfit.

4951

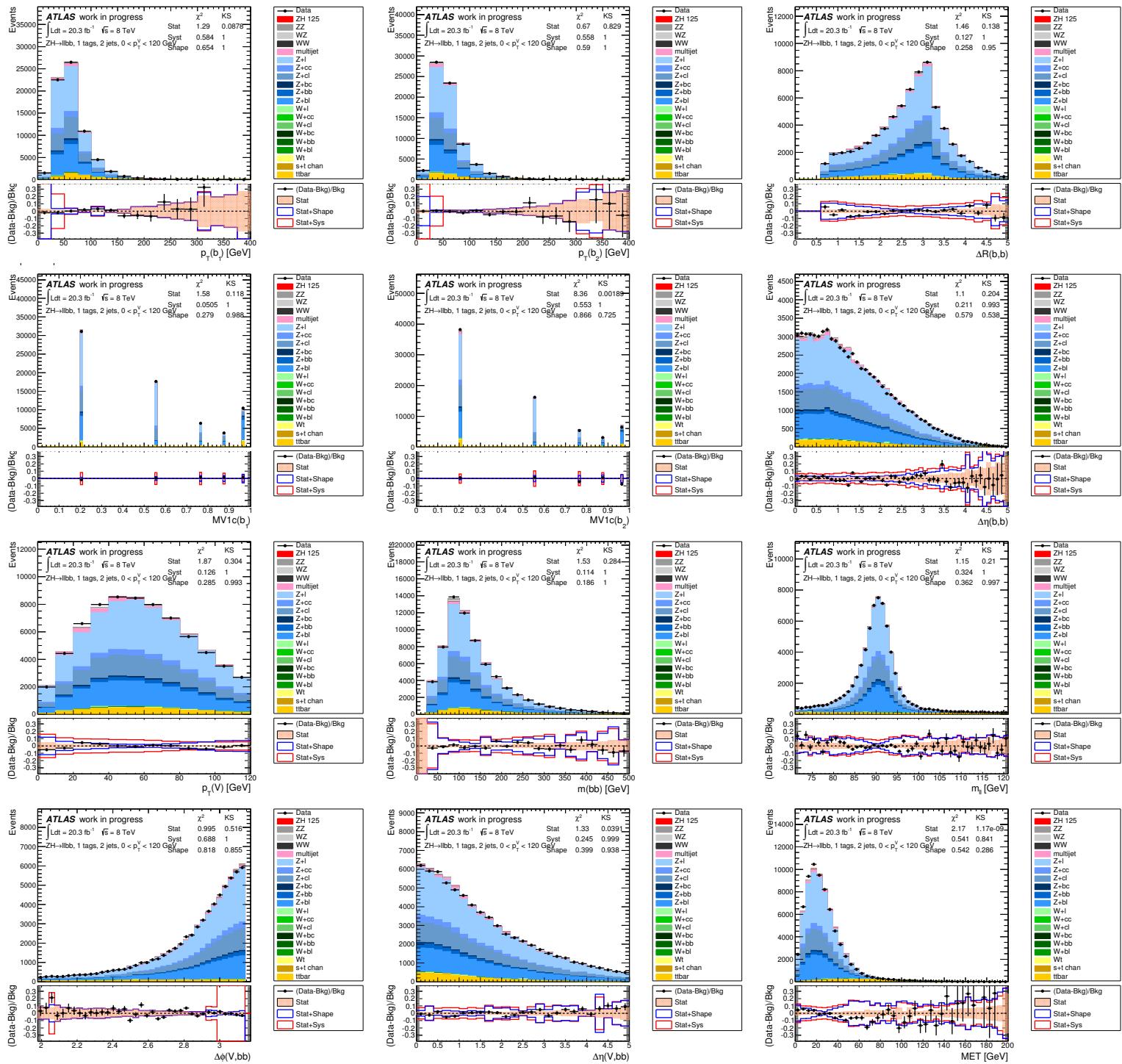


Figure 344: Distributions of MVA training variables used in 2-lepton events for $p_T^Z < 120$ GeV with 1 b -tag and 2-jets. From left to right: Row 1 - leading then sub-leading jet p_T and ΔR of the same two jets. Row 2 - pseudo-continuous MV1c distributions for leading then sub-leading jet and the $\Delta\eta$ of the same two jets. Row 3 - p_T^Z , m_{jj} , and m_{ll} . Row 4 - $\Delta\phi(V, H)$, $\Delta\eta(V, H)$, and E_T^{miss} . Section 6.1 details the definition of each variable.

Not reviewed, for internal circulation only

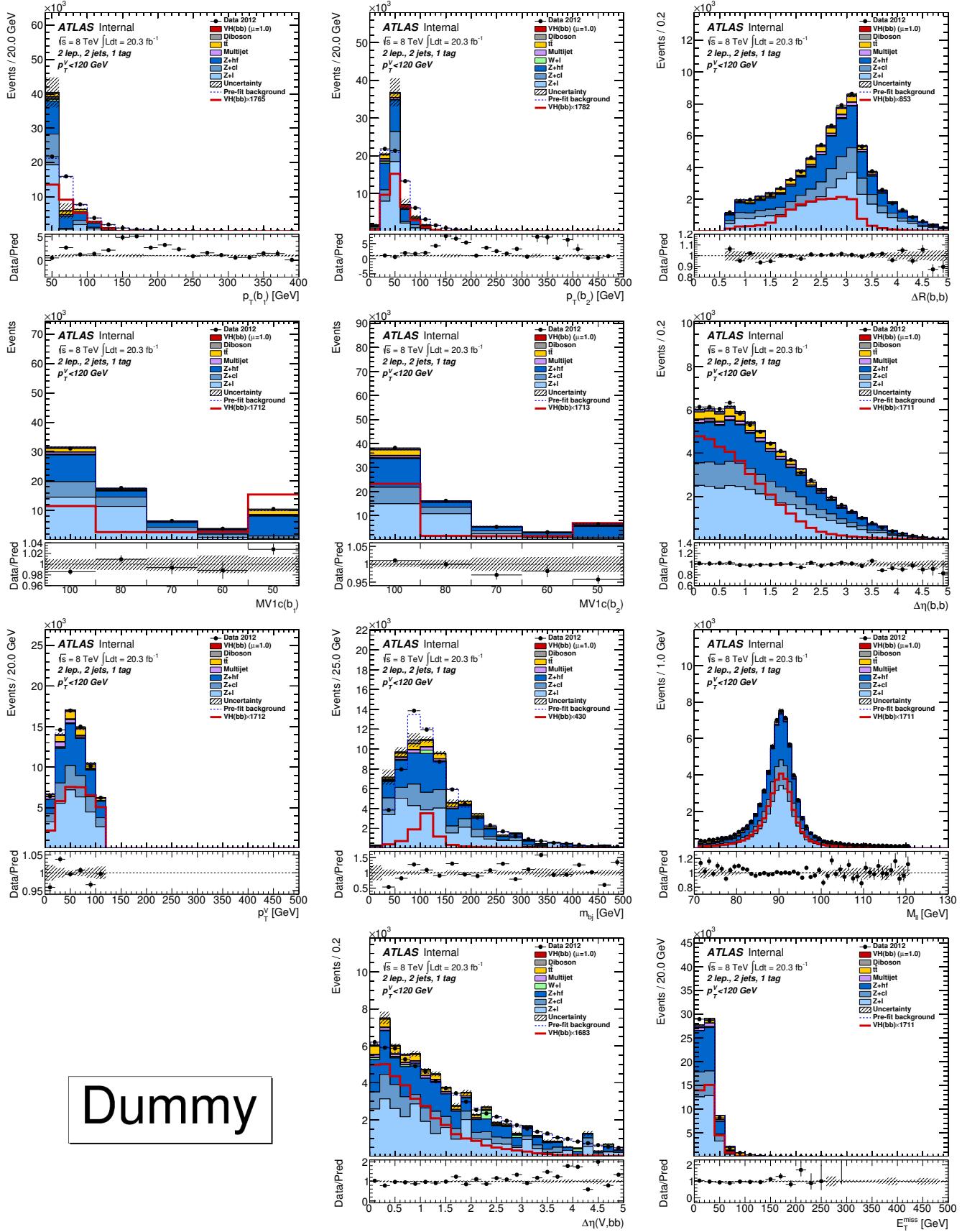


Figure 345: Distributions of MVA training variables used in 2-lepton events for $p_T^Z < 120$ GeV with 1 b -tag and 2-jets after the combined 0+1+2 lepton MVA fit. From left to right: Row 1 - leading then sub-leading jet p_T and ΔR of the same two jets. Row 2 - pseudo-continuous MV1c distributions for leading then sub-leading jet and the $\Delta\eta$ of the same two jets. Row 3 - p_T^Z , m_{jj} , and m_{ll} . Row 4 - $\Delta\phi(V, H)$, $\Delta\eta(V, H)$, and E_T^{miss} . Section 6.1 details the definition of each variable.

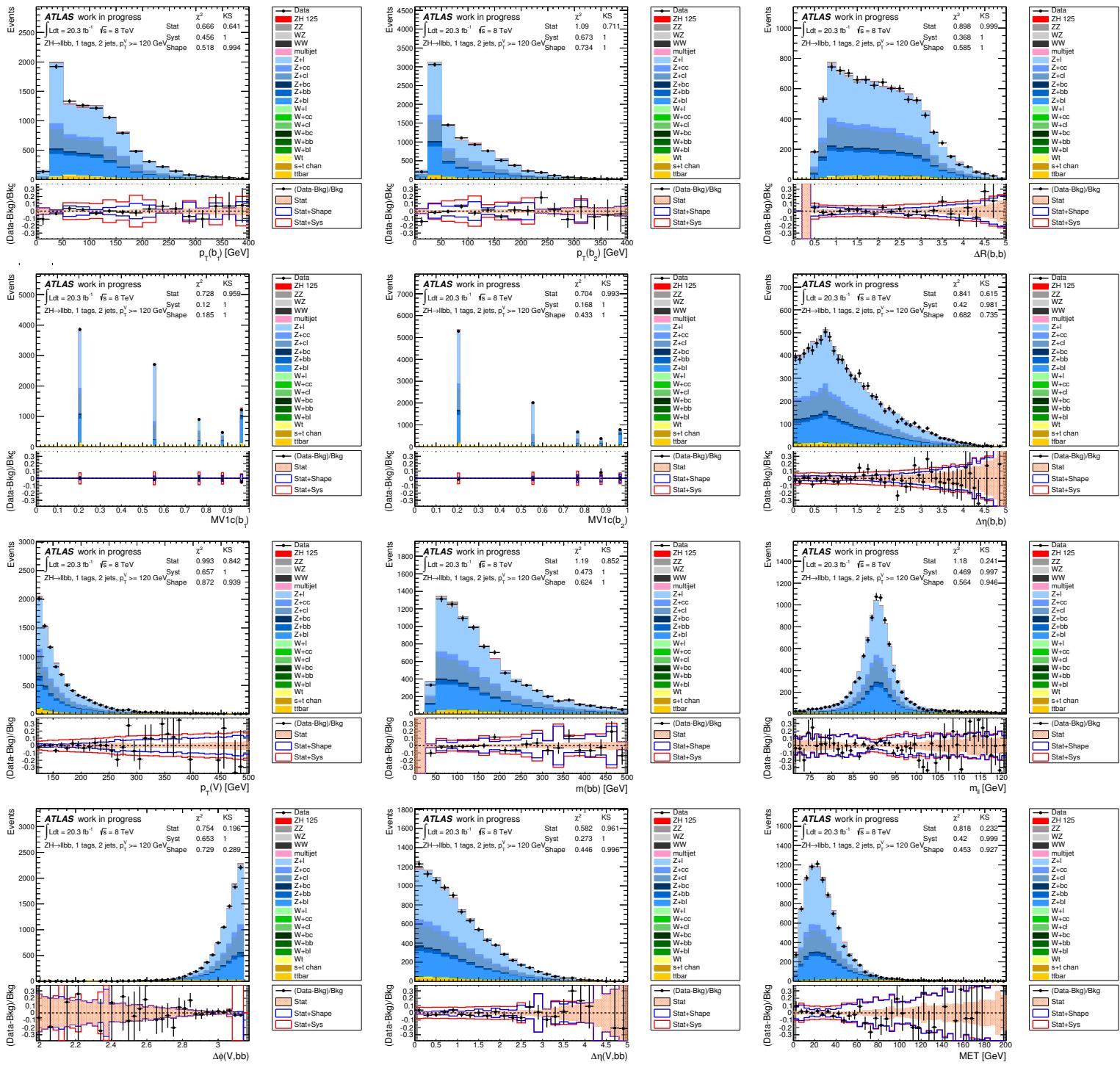


Figure 346: Distributions of MVA training variables used in 2-lepton events for $p_T^Z > 120$ GeV with 1 b -tag and 2-jets. From left to right: Row 1 - leading then sub-leading jet p_T and ΔR of the same two jets. Row 2 - pseudo-continuous MV1c distributions for leading then sub-leading jet and the $\Delta\eta$ of the same two jets. Row 3 - p_T^V , m_{jj} , and m_{ll} . Row 4 - $\Delta\phi(V, H)$, $\Delta\eta(V, H)$, and E_T^{miss} . Section 6.1 details the definition of each variable.

Not reviewed, for internal circulation only

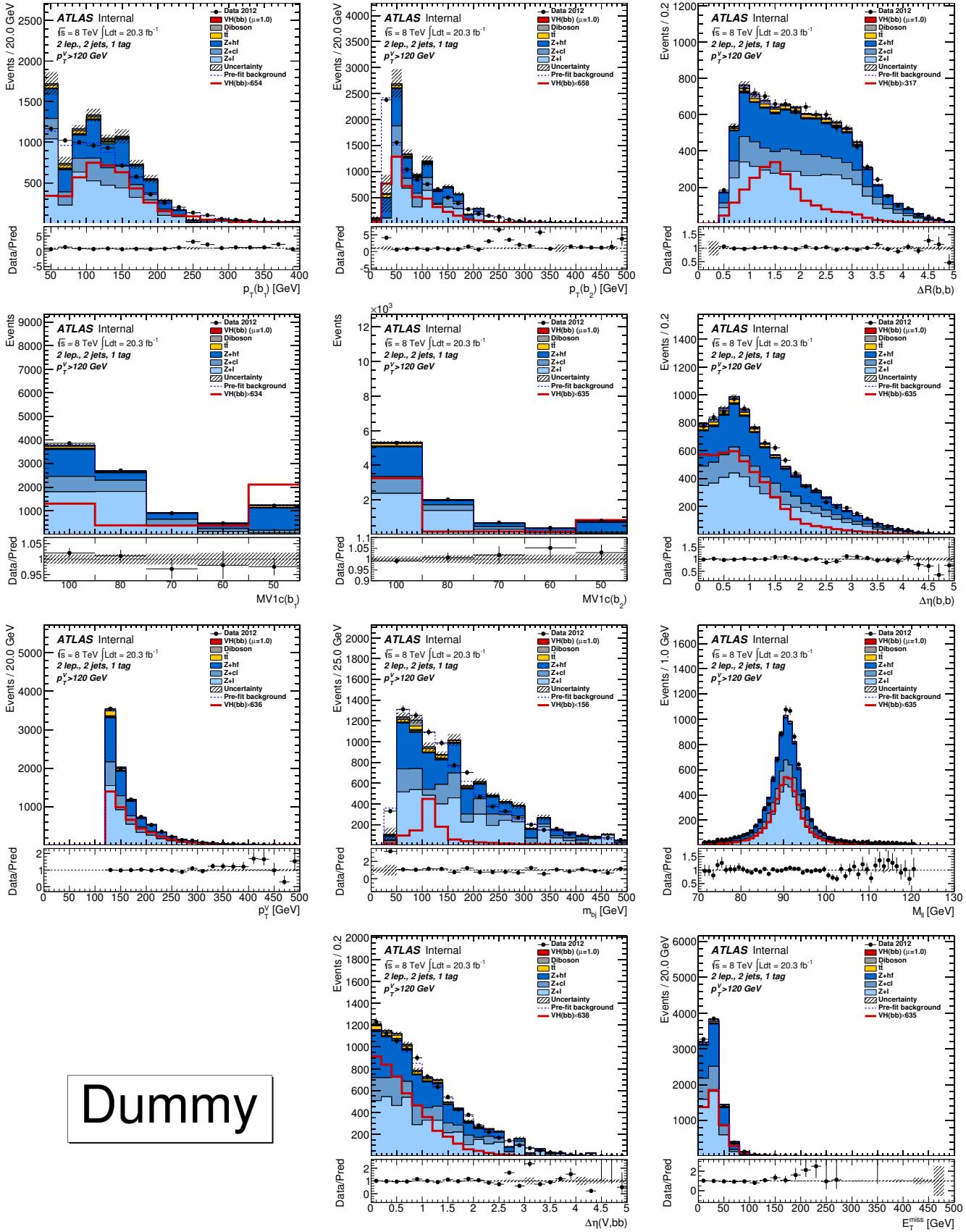


Figure 347: Distributions of MVA training variables used in 2-lepton events for $p_T^Z > 120$ GeV with 1 b -tag and 2-jets after the combined 0+1+2 lepton MVA fit. From left to right: Row 1 - leading then sub-leading jet p_T and ΔR of the same two jets. Row 2 - pseudo-continuous MV1c distributions for leading then sub-leading jet and the $\Delta\eta$ of the same two jets. Row 3 - p_T^Z , m_{jj} , and m_{ll} . Row 4 - $\Delta\phi(V, H)$, $\Delta\eta(V, H)$, and E_T^{miss} . Section 6.1 details the definition of each variable.

Dummy

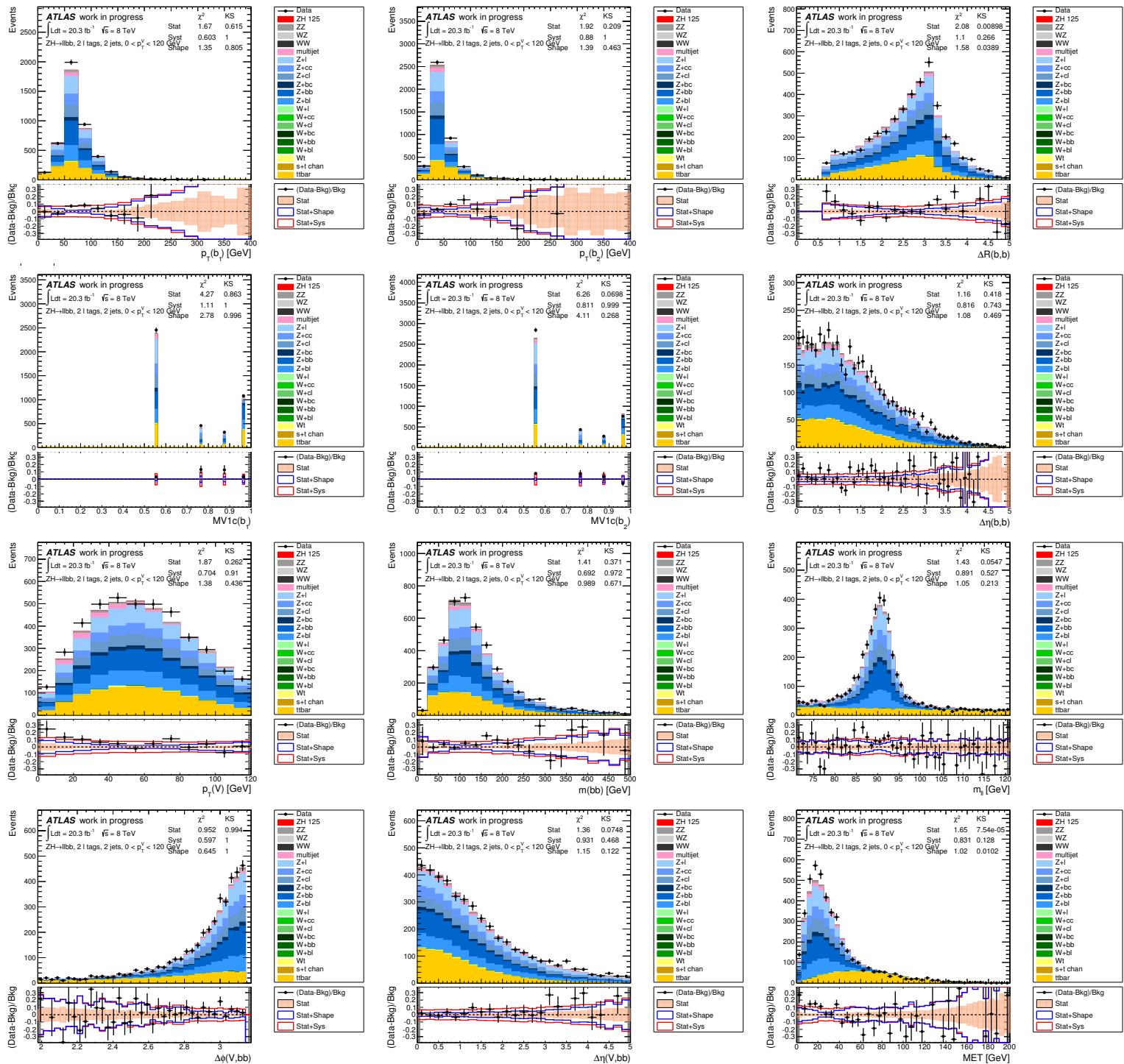


Figure 348: Distributions of MVA training variables used in 2-lepton events for $p_T^Z < 120$ GeV with 2 LL b -tags and 2-jets. From left to right: Row 1 - leading then sub-leading jet p_T and ΔR of the same two jets. Row 2 - pseudo-continuous MV1c distributions for leading then sub-leading jet and the $\Delta\eta$ of the same two jets. Row 3 - p_T^Z , m_{jj} , and m_{ll} . Row 4 - $\Delta\phi(V, H)$, $\Delta\eta(V, H)$, and E_T^{miss} . Section 6.1 details the definition of each variable.

Not reviewed, for internal circulation only

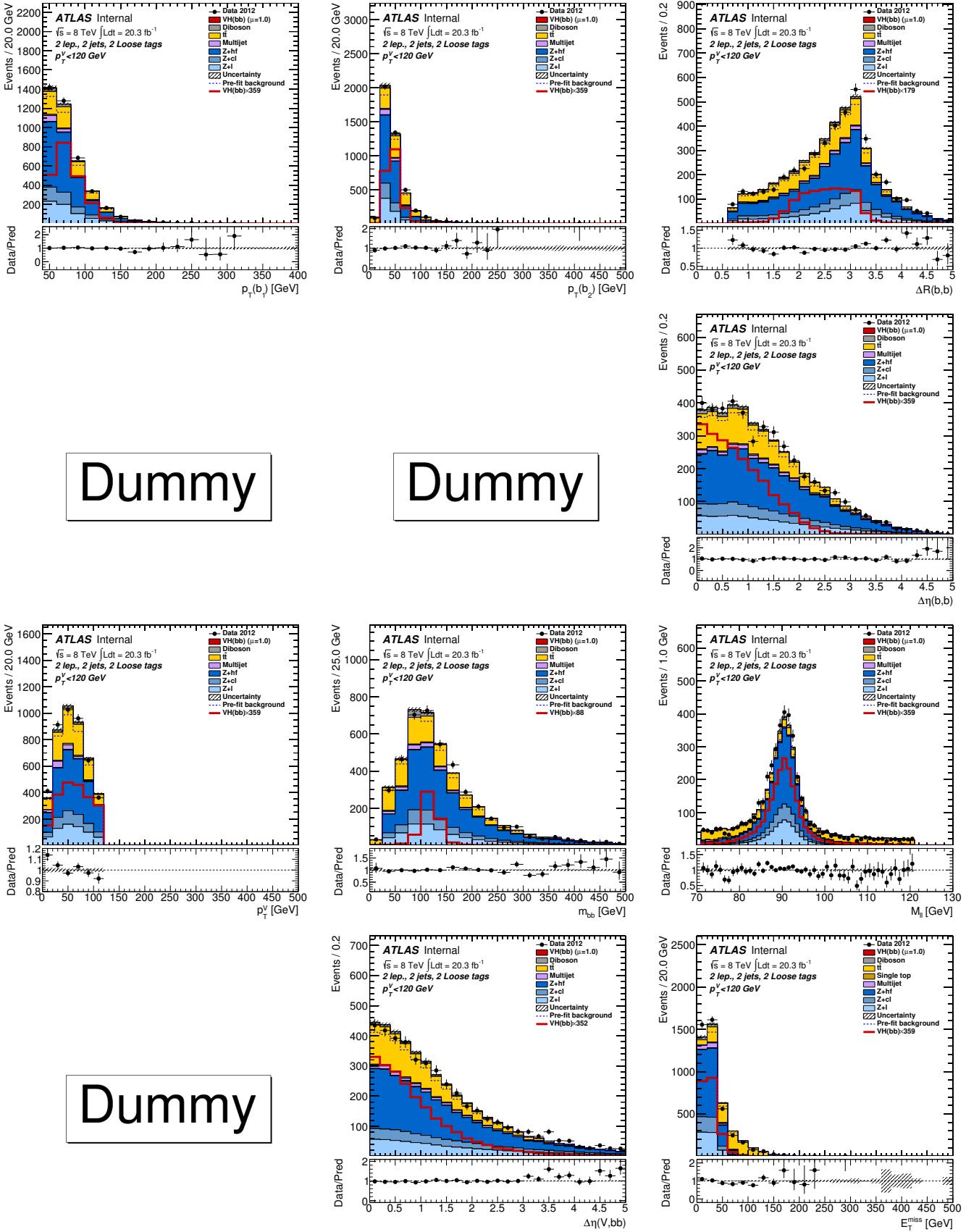


Figure 349: Distributions of MVA training variables used in 2-lepton events for $p_T^Z < 120$ GeV with 2 LL b -tags and 2-jets after the combined 0+1+2 lepton MVA fit. From left to right: Row 1 - leading then sub-leading jet p_T and ΔR of the same two jets. Row 2 - pseudo-continuous MV1c distributions for leading then sub-leading jet and the $\Delta\eta$ of the same two jets. Row 3 - p_T^Z , m_{jj} , and m_{ll} . Row 4 - $\Delta\phi(V, H)$, $\Delta\eta(V, H)$, and E_T^{miss} . Section 6.1 details the definition of each variable.

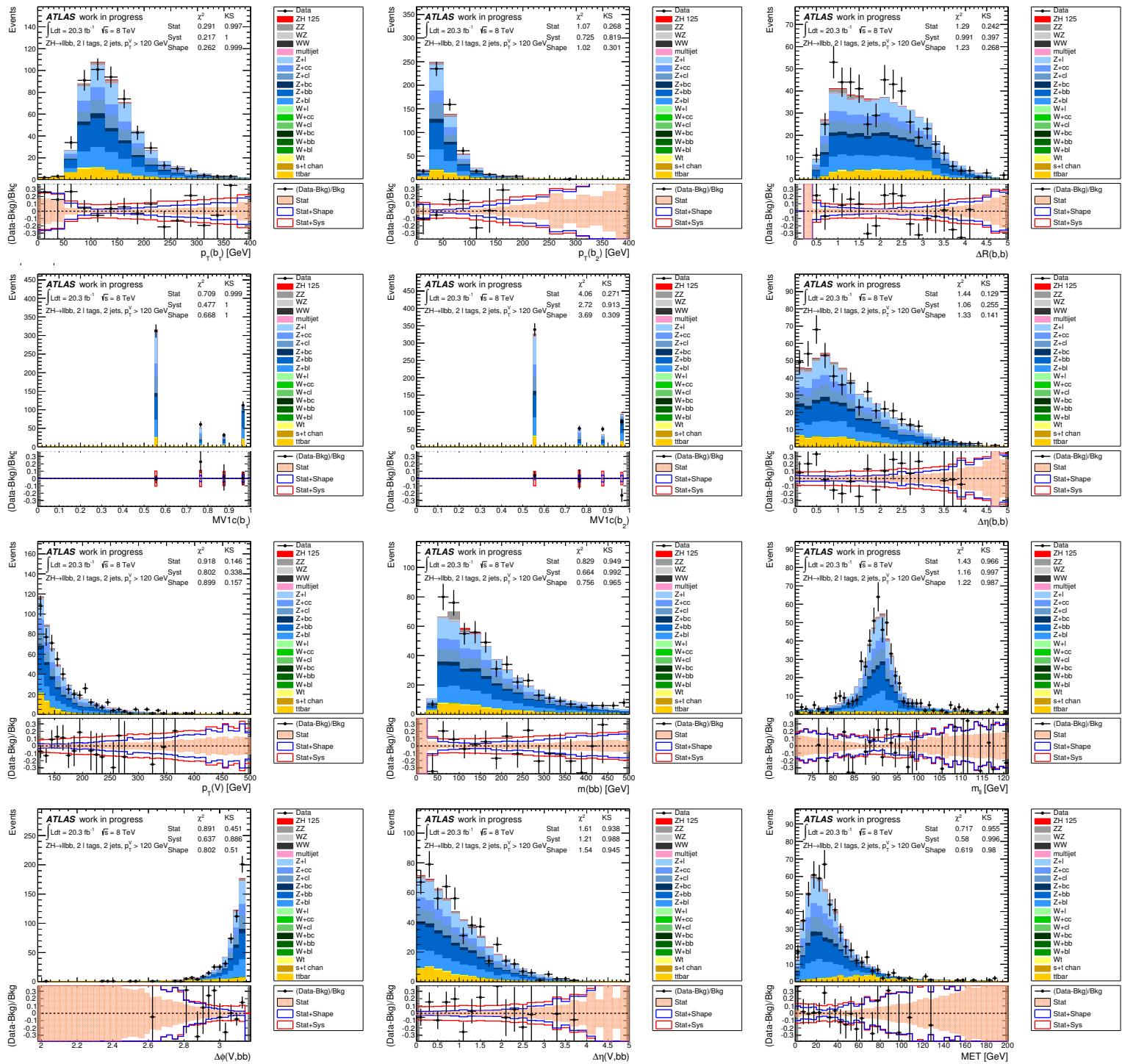
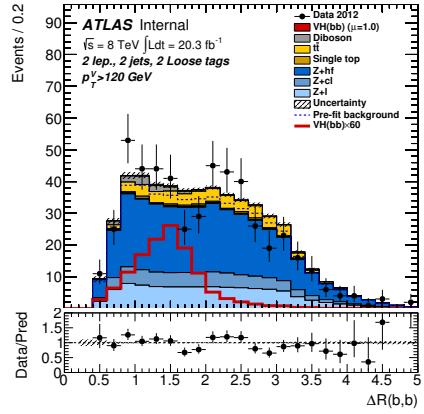
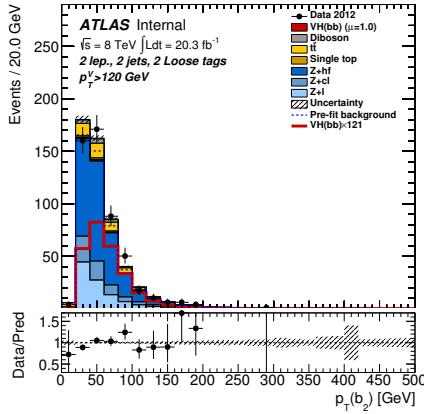
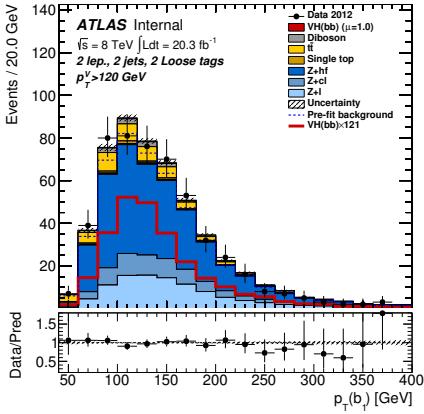
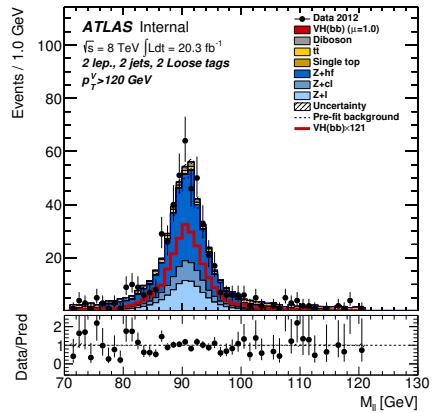
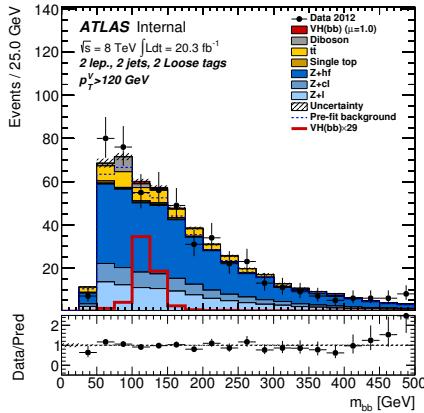
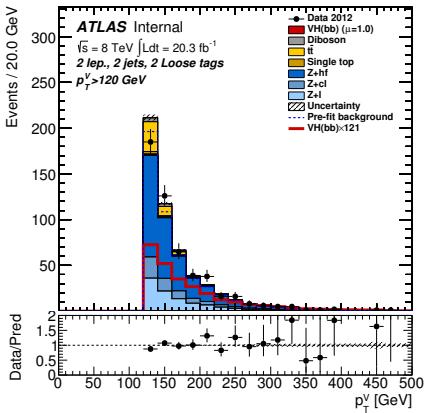


Figure 350: Distributions of MVA training variables used in 2-lepton events for $p_T^Z > 120$ GeV with 2 LL b -tags and 2-jets. From left to right: Row 1 - leading then sub-leading jet p_T and ΔR of the same two jets. Row 2 - pseudo-continuous MV1c distributions for leading then sub-leading jet and the $\Delta\eta$ of the same two jets. Row 3 - p_T^Z , m_{jj} , and m_{ll} . Row 4 - $\Delta\phi(V, H)$, $\Delta\eta(V, H)$, and E_T^{miss} . Section 6.1 details the definition of each variable.



Dummy

Dummy



Dummy

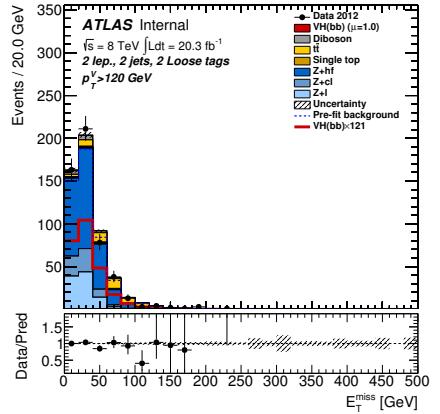
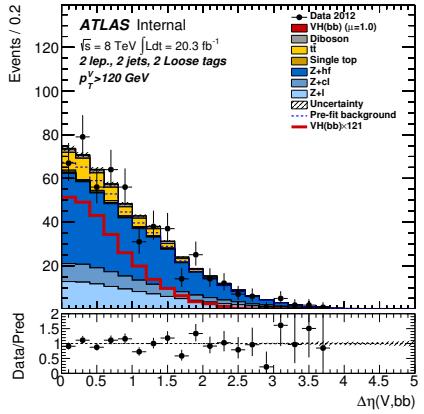


Figure 351: Distributions of MVA training variables used in 2-lepton events for $p_T^Z > 120$ GeV with 2 LL b -tags and 2-jets after the combined 0+1+2 lepton MVA fit. From left to right: Row 1 - leading then sub-leading jet p_T and ΔR of the same two jets. Row 2 - pseudo-continuous MV1c distributions for leading then sub-leading jet and the $\Delta\eta$ of the same two jets. Row 3 - p_T^Z , m_{jj} , and $m_{\ell\ell}$. Row 4 - $\Delta\phi(V, H)$, $\Delta\eta(V, H)$, and E_T^{miss} . Section 6.1 details the definition of each variable.

Not reviewed, for internal circulation only

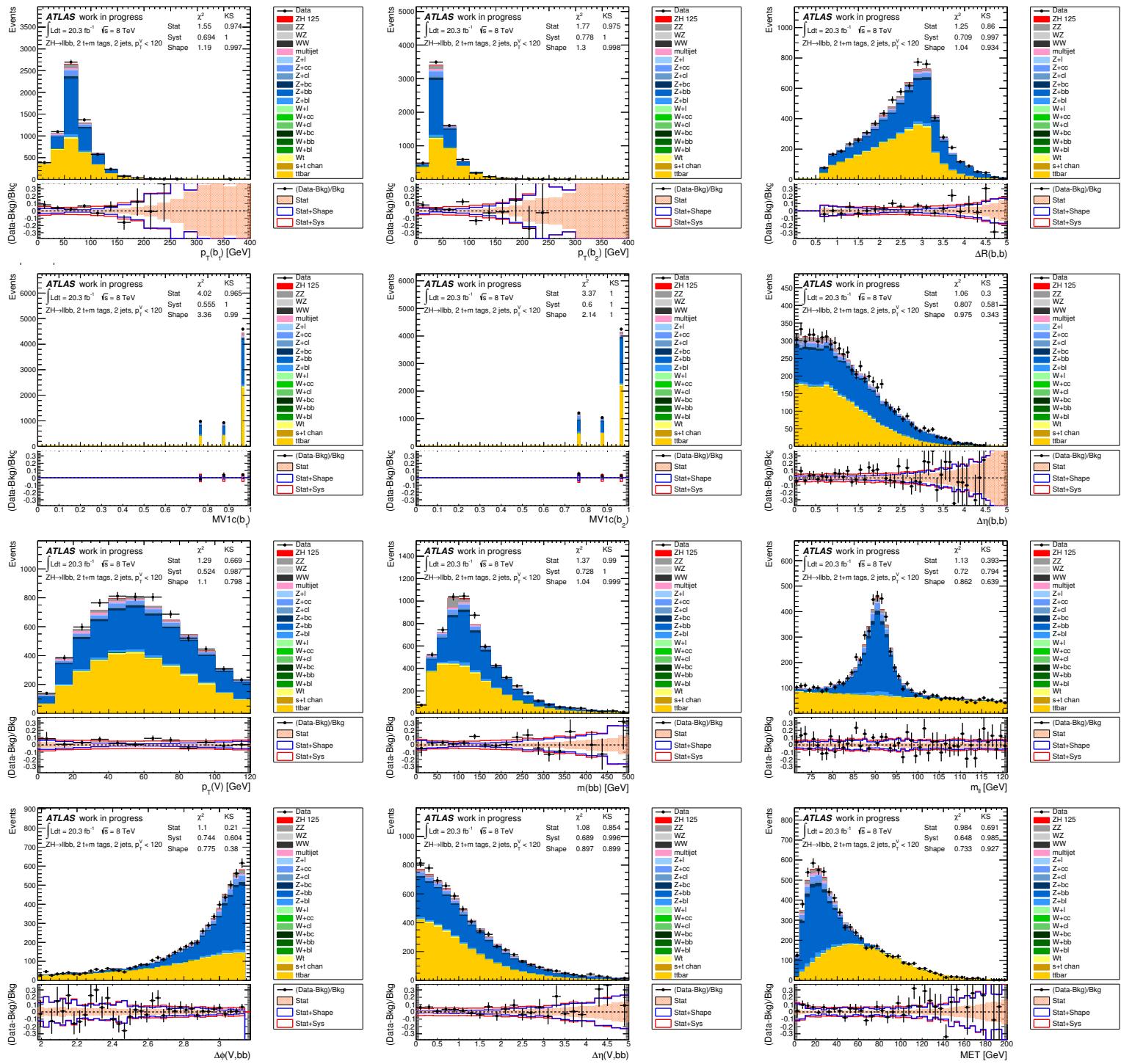


Figure 352: Distributions of MVA training variables used in 2-lepton events for $p_T^Z < 120$ GeV with 2 MM+TT b -tags and 2-jets. From left to right: Row 1 - leading then sub-leading jet p_T and ΔR of the same two jets. Row 2 - pseudo-continuous MV1c distributions for leading then sub-leading jet and the $\Delta\eta$ of the same two jets. Row 3 - p_T^Z , m_{jj} , and $m_{\ell\ell}$. Row 4 - $\Delta\phi(V,H)$, $\Delta\eta(V,H)$, and E_T^{miss} . Section 6.1 details the definition of each variable.

Not reviewed, for internal circulation only

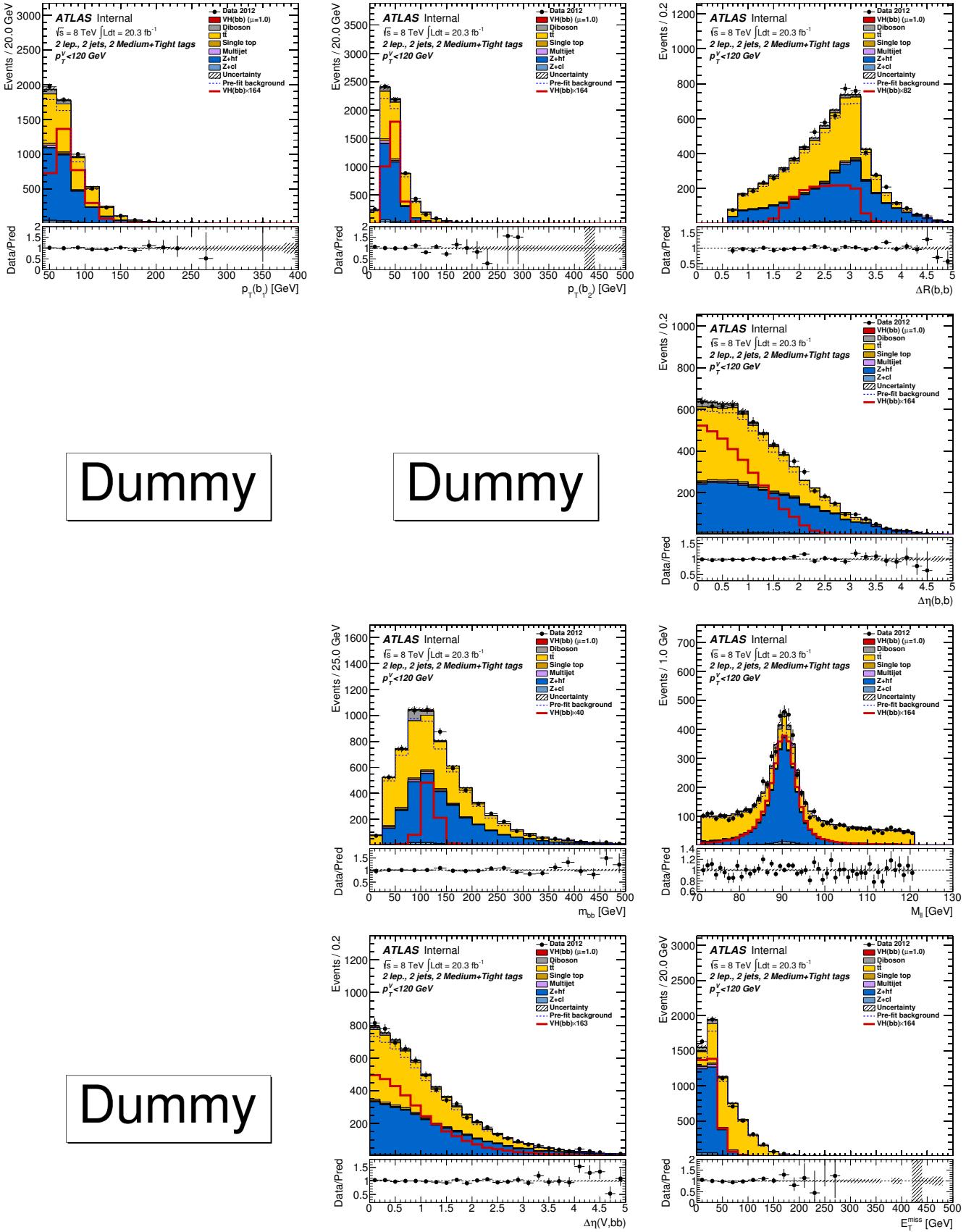


Figure 353: Distributions of MVA training variables used in 2-lepton events for $p_T^Z < 120$ GeV with 2 MM+TT b -tags and 2-jets after the combined 0+1+2 lepton MVA fit. From left to right: Row 1 - leading then sub-leading jet p_T and ΔR of the same two jets. Row 2 - pseudo-continuous MV1c distributions for leading then sub-leading jet and the $\Delta\eta$ of the same two jets. Row 3 - p_T^Z , m_{jj} , and $m_{\ell\ell}$. Row 4 - $\Delta\phi(V, H)$, $\Delta\eta(V, H)$, and E_T^{miss} . Section 6.1 details the definition of each variable.

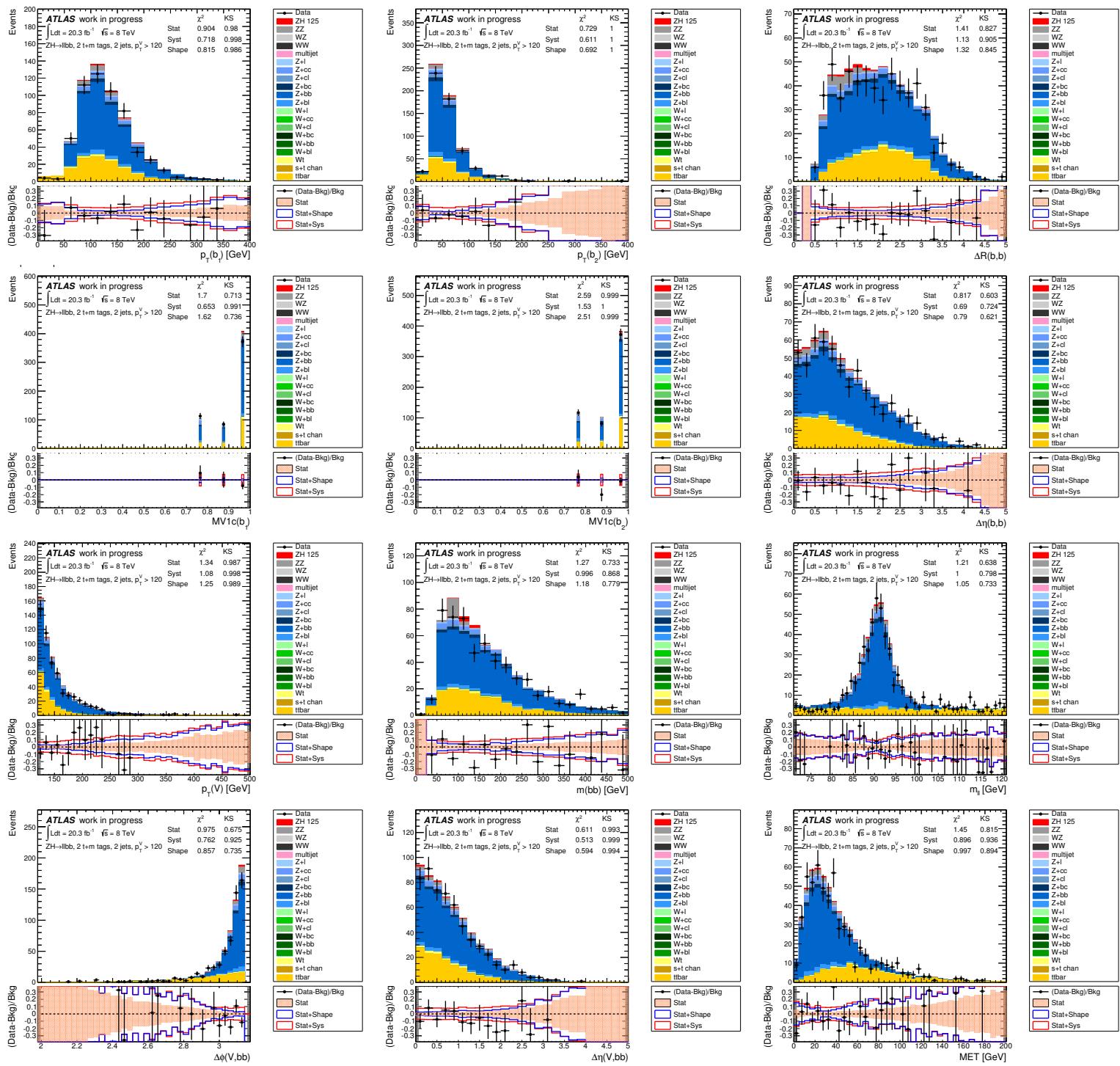


Figure 354: Distributions of MVA training variables used in 2-lepton events for $p_T^Z > 120$ GeV with 2 MM+TT b -tags and 2-jets. From left to right: Row 1 - leading then sub-leading jet p_T and ΔR of the same two jets. Row 2 - pseudo-continuous MV1c distributions for leading then sub-leading jet and the $\Delta\eta$ of the same two jets. Row 3 - p_T^Z , m_{jj} , and m_{ll} . Row 4 - $\Delta\phi(V, H)$, $\Delta\eta(V, H)$, and E_T^{miss} . Section 6.1 details the definition of each variable.

Not reviewed, for internal circulation only

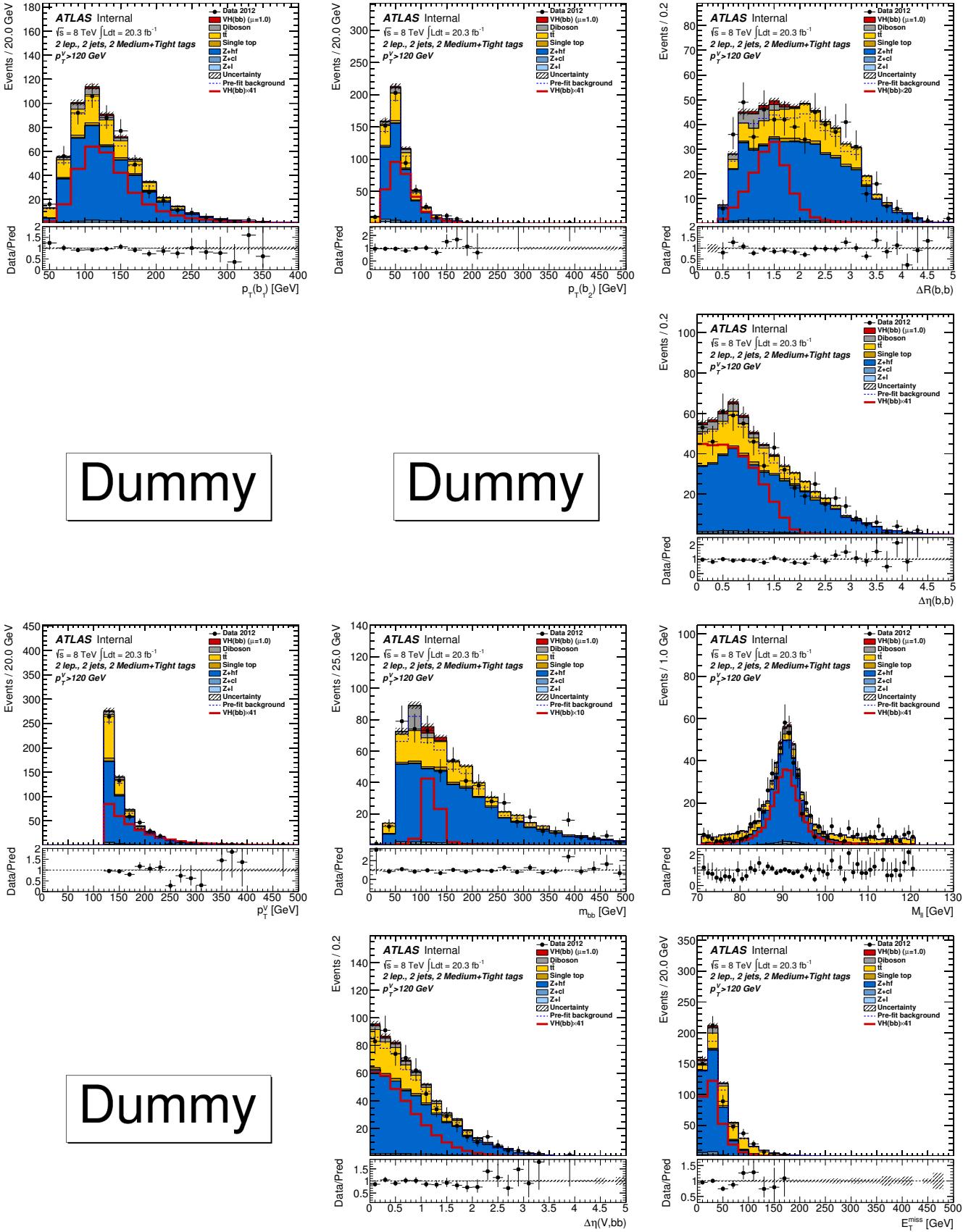


Figure 355: Distributions of MVA training variables used in 2-lepton events for $p_T^Z > 120$ GeV with 2 MM+TT b -tags and 2-jets after the combined 0+1+2 lepton MVA fit. From left to right: Row 1 - leading then sub-leading jet p_T and ΔR of the same two jets. Row 2 - pseudo-continuous MV1c distributions for leading then sub-leading jet and the $\Delta\eta$ of the same two jets. Row 3 - p_T^Z , m_{jj} , and m_{ll} . Row 4 - $\Delta\phi(V, H)$, $\Delta\eta(V, H)$, and E_T^{miss} . Section 6.1 details the definition of each variable.

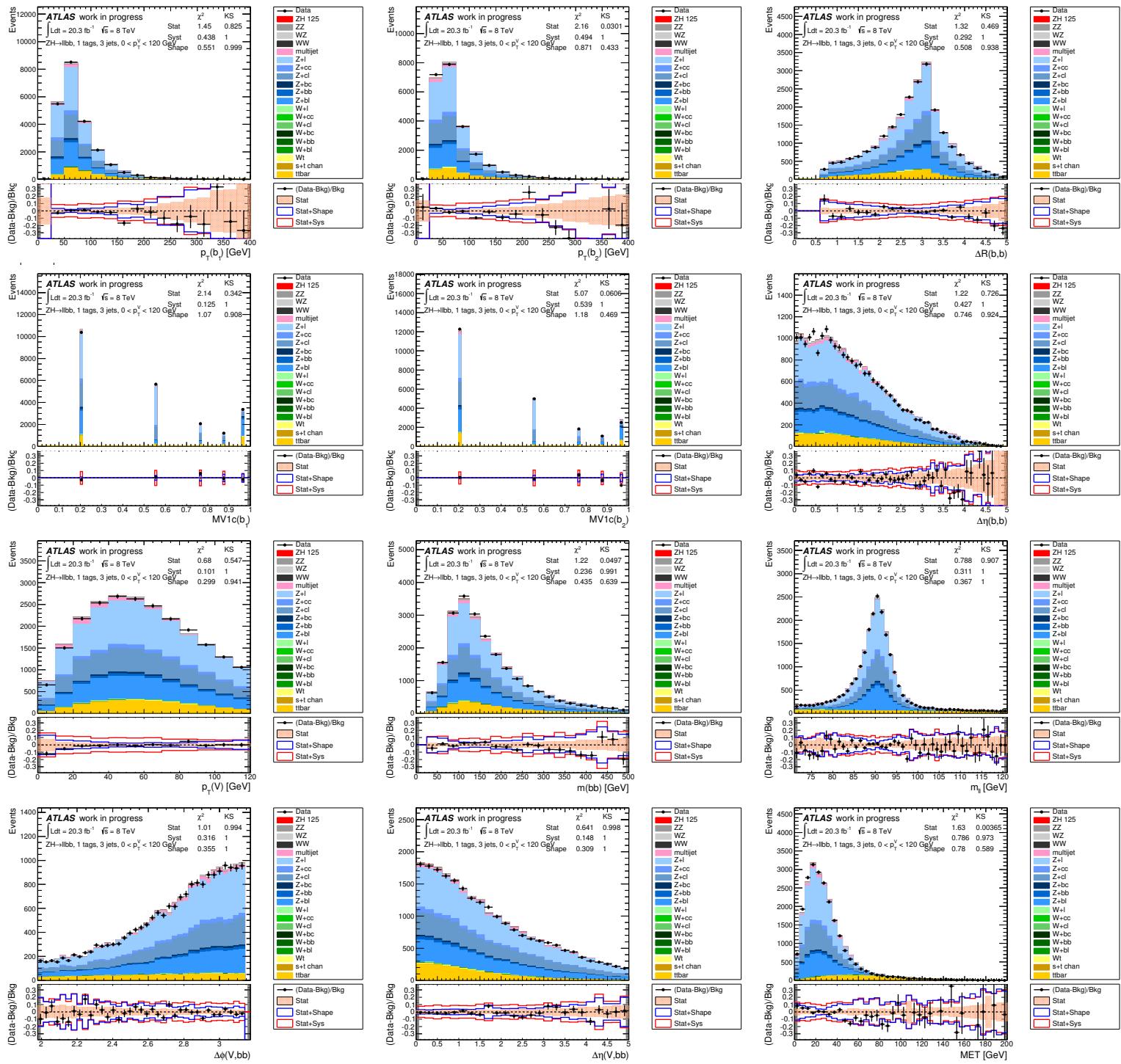


Figure 356: Distributions of MVA training variables used in 2-lepton events for $p_T^Z < 120$ GeV with 1 b -tag and 3 jets. From left to right: Row 1 - leading then sub-leading jet p_T and ΔR of the same two jets. Row 2 - pseudo-continuous MV1c distributions for leading then sub-leading jet and the $\Delta\eta$ of the same two jets. Row 3 - p_T^Z , m_{bb} , and $m_{\ell\ell}$. Row 4 - $\Delta\phi(V, H)$, $\Delta\eta(V, H)$, and E_T^{miss} . Section 6.1 details the definition of each variable.

Not reviewed, for internal circulation only

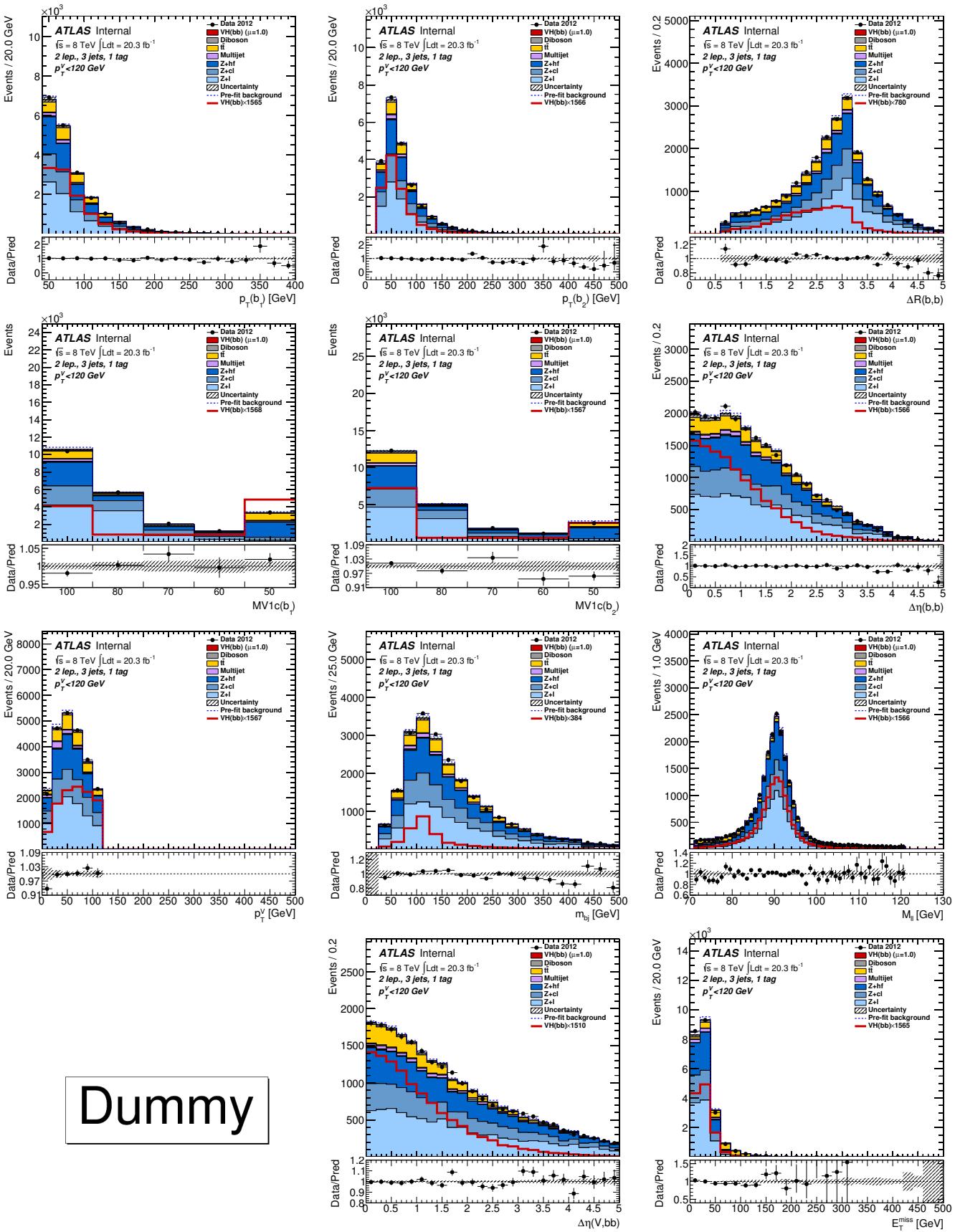


Figure 357: Distributions of MVA training variables used in 2-lepton events for $p_T^Z < 120$ GeV with 1 b -tag and 3-jets after the combined 0+1+2 lepton MVA fit. From left to right: Row 1 - leading then sub-leading jet p_T and ΔR of the same two jets. Row 2 - pseudo-continuous MV1c distributions for leading then sub-leading jet and the $\Delta\eta$ of the same two jets. Row 3 - p_T^Z , m_{jj} , and m_{ll} . Row 4 - $\Delta\phi(V,H)$, $\Delta\eta(V,H)$, and E_T^{miss} . Section 6.1 details the definition of each variable.

Dummy

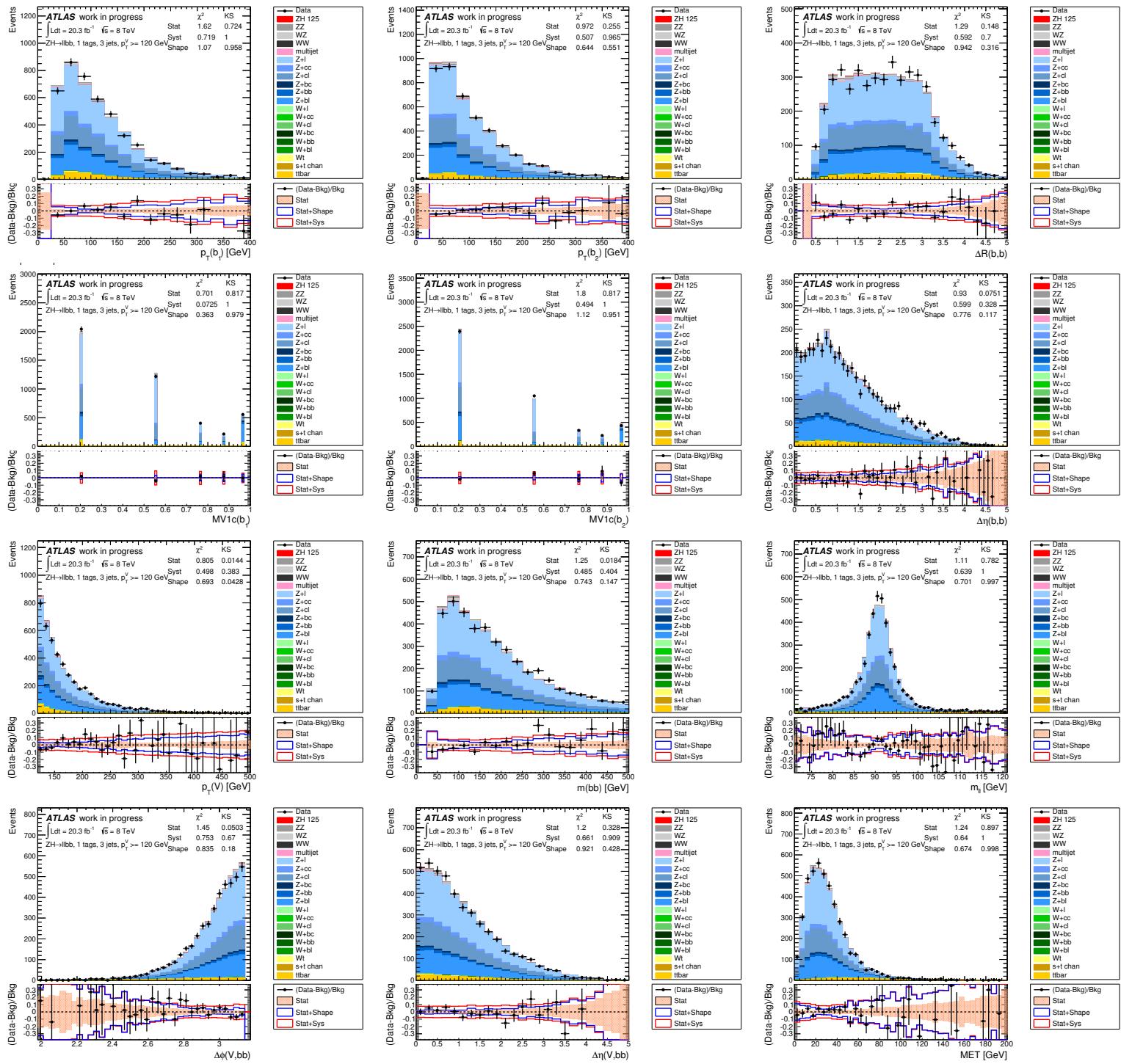


Figure 358: Distributions of MVA training variables used in 2-lepton events for $p_T^Z > 120 \text{ GeV}$ with 1 b -tag and 3 jets. From left to right: Row 1 - leading then sub-leading jet p_T and ΔR of the same two jets. Row 2 - pseudo-continuous MV1c distributions for leading then sub-leading jet and the $\Delta\eta$ of the same two jets. Row 3 - p_T^Z , m_{jj} , and $m_{\ell\ell}$. Row 4 - $\Delta\phi(V, H)$, $\Delta\eta(V, H)$, and E_T^{miss} . Section 6.1 details the definition of each variable.

Not reviewed, for internal circulation only

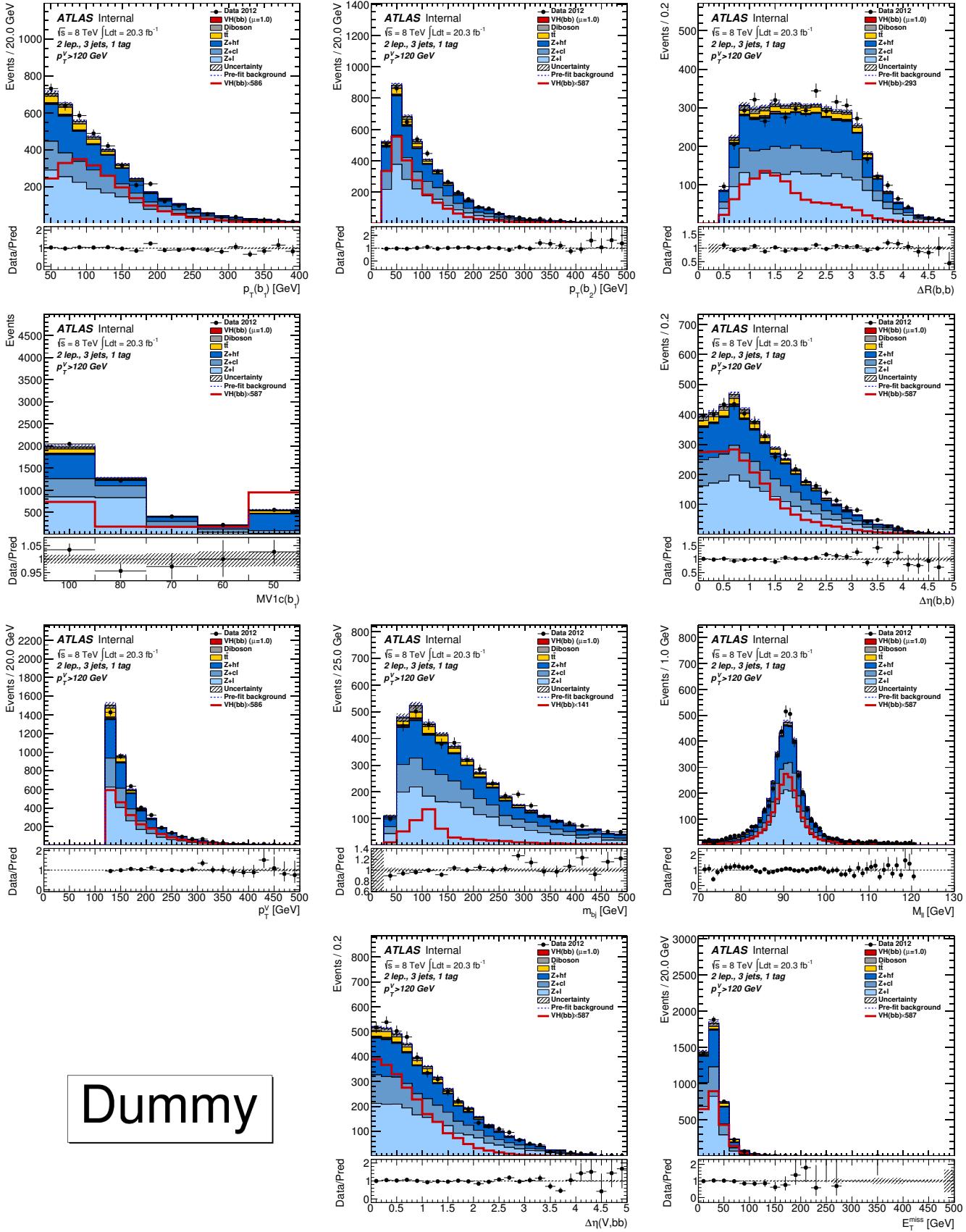


Figure 359: Distributions of MVA training variables used in 2-lepton events for $p_T^Z > 120$ GeV with 1 b -tag and 3-jets after the combined 0+1+2 lepton MVA fit. From left to right: Row 1 - leading then sub-leading jet p_T and ΔR of the same two jets. Row 2 - pseudo-continuous MV1c distributions for leading then sub-leading jet and the $\Delta\eta$ of the same two jets. Row 3 - p_T^Z , m_{jj} , and $m_{\ell\ell}$. Row 4 - $\Delta\phi(V, H)$, $\Delta\eta(V, H)$, and E_T^{miss} . Section 6.1 details the definition of each variable.

Dummy

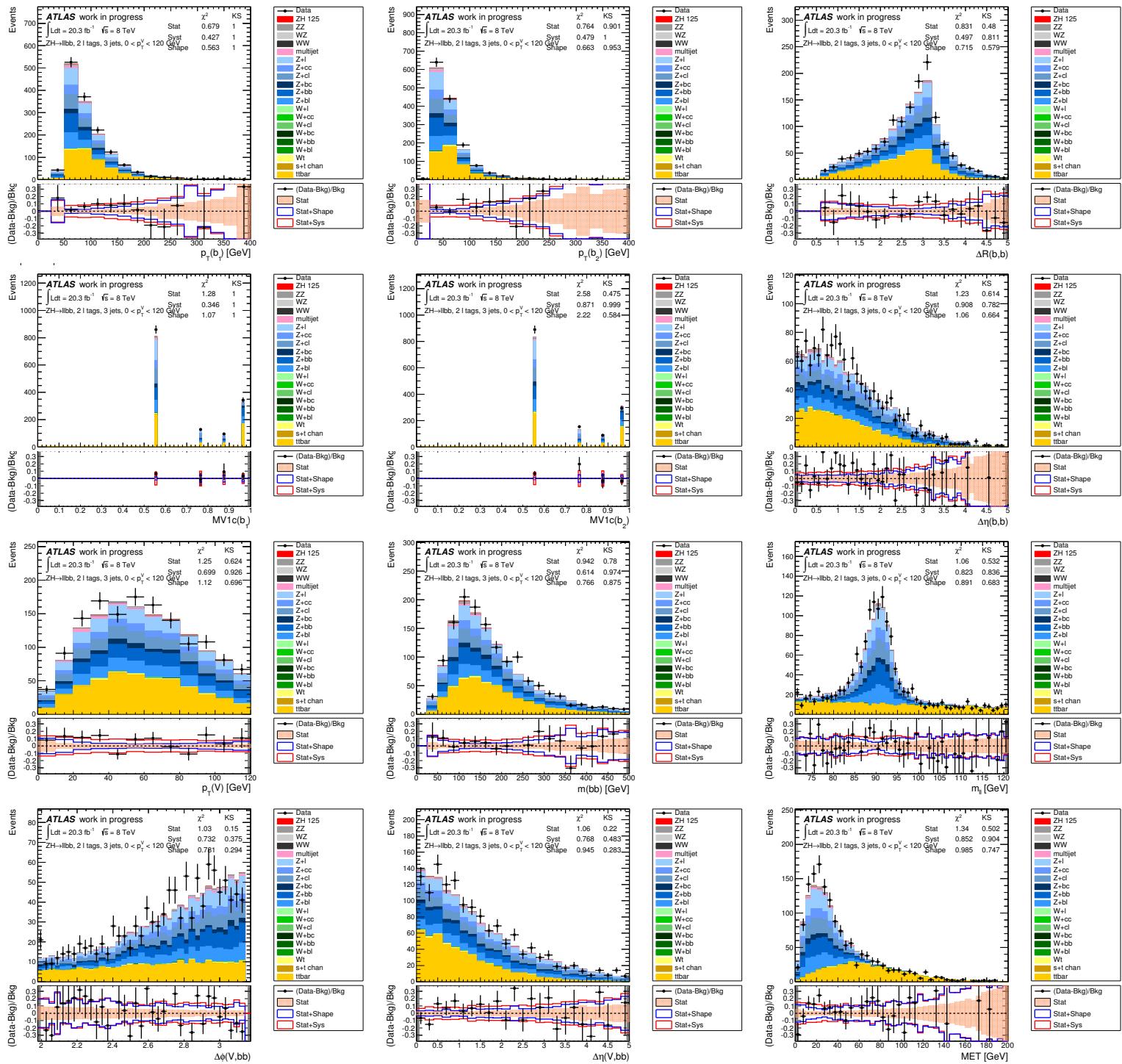


Figure 360: Distributions of MVA training variables used in 2-lepton events for $p_T^Z < 120$ GeV with 2 LL b -tags and 3 jets. From left to right: Row 1 - leading then sub-leading jet p_T and ΔR of the same two jets. Row 2 - pseudo-continuous MV1c distributions for leading then sub-leading jet and the $\Delta\eta$ of the same two jets. Row 3 - p_T^Z , m_{jj} , and m_{ll} . Row 4 - $\Delta\phi(V, H)$, $\Delta\eta(V, H)$, and E_T^{miss} . Section 6.1 details the definition of each variable.

Not reviewed, for internal circulation only

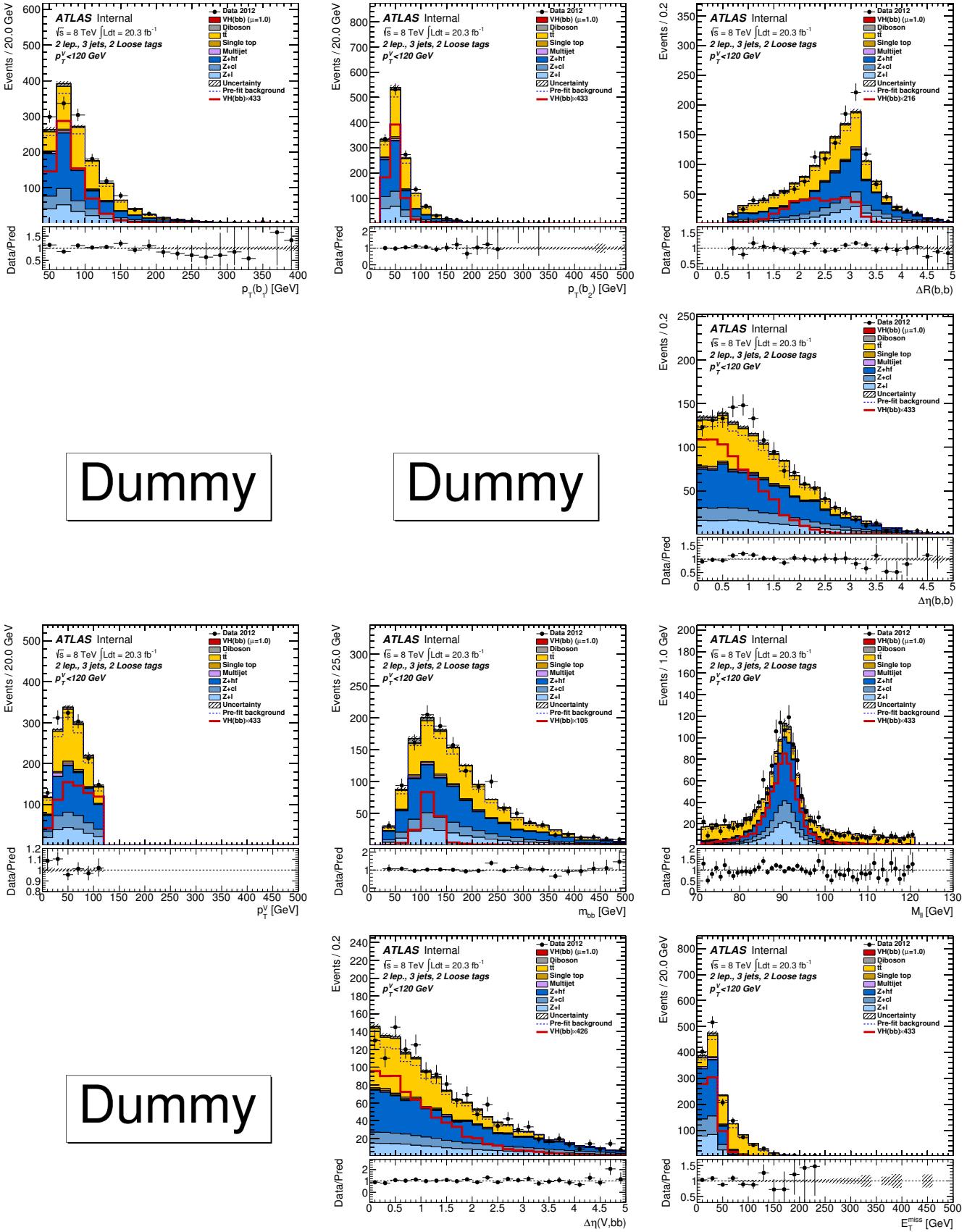


Figure 361: Distributions of MVA training variables used in 2-lepton events for $p_T^Z < 120$ GeV with 2 LL b -tags and 3-jets after the combined 0+1+2 lepton MVA fit. From left to right: Row 1 - leading then sub-leading jet p_T and ΔR of the same two jets. Row 2 - pseudo-continuous MV1c distributions for leading then sub-leading jet and the $\Delta\eta$ of the same two jets. Row 3 - p_T^Z , m_{jj} , and m_{ll} . Row 4 - $\Delta\phi(V, H)$, $\Delta\eta(V, H)$, and E_T^{miss} . Section 6.1 details the definition of each variable.

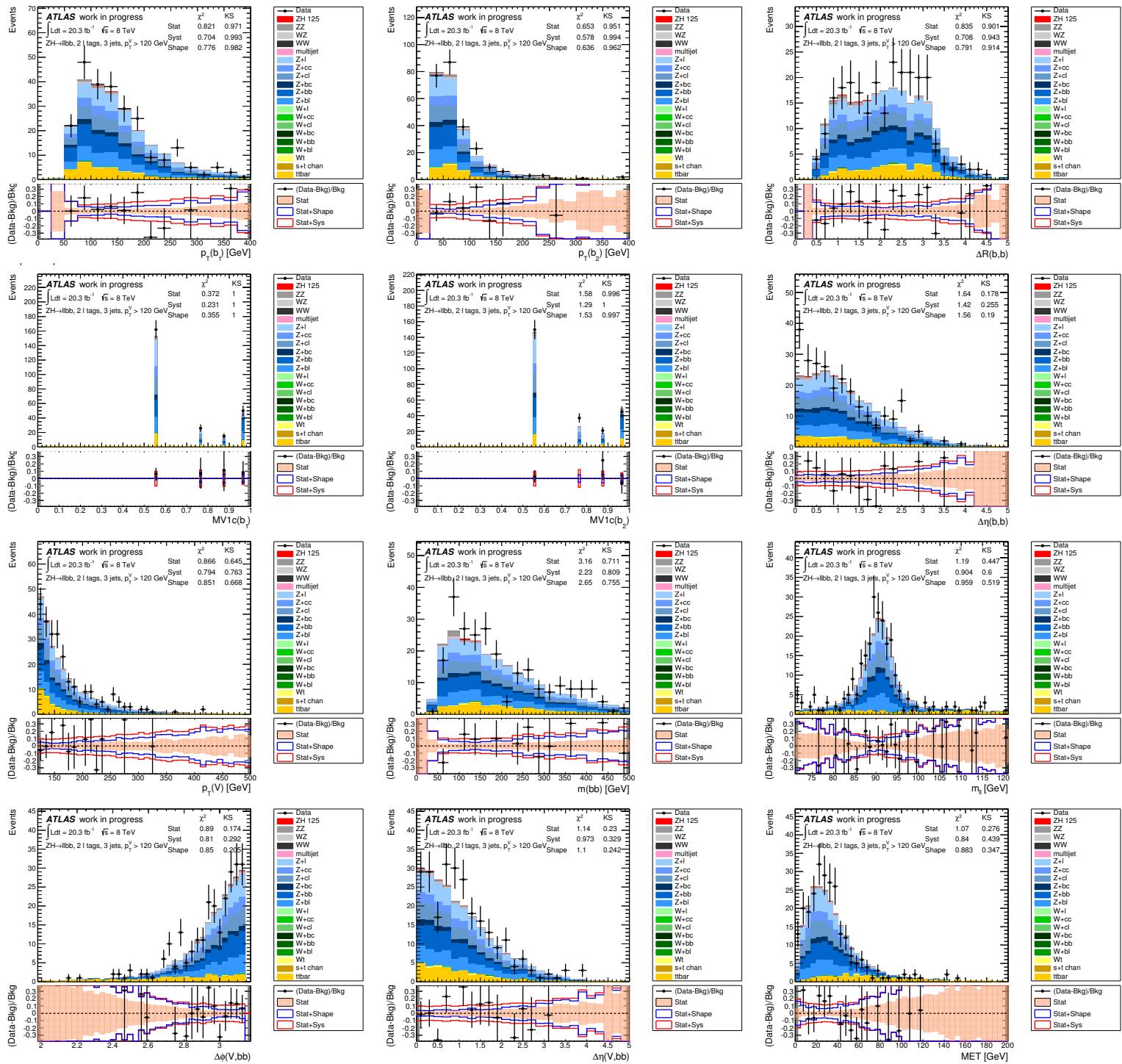


Figure 362: Distributions of MVA training variables used in 2-lepton events for $p_T^Z > 120$ GeV with 2 LL b -tags and 3 jets. From left to right: Row 1 - leading then sub-leading jet p_T and ΔR of the same two jets. Row 2 - pseudo-continuous MV1c distributions for leading then sub-leading jet and the $\Delta\eta$ of the same two jets. Row 3 - p_T^Z , m_{jj} , and m_{ll} . Row 4 - $\Delta\phi(V, H)$, $\Delta\eta(V, H)$, and E_T^{miss} . Section 6.1 details the definition of each variable.

Not reviewed, for internal circulation only

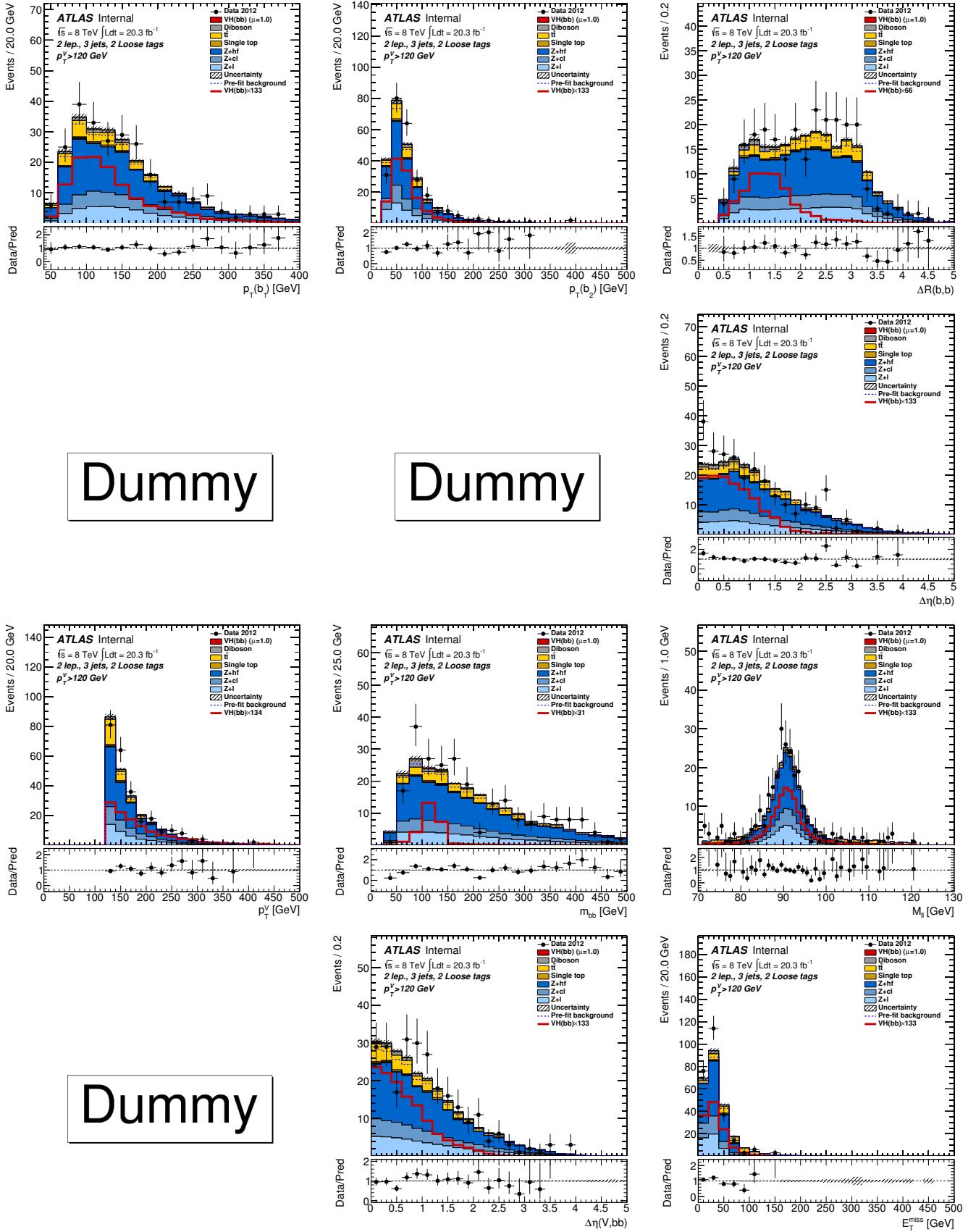


Figure 363: Distributions of MVA training variables used in 2-lepton events for $p_T^Z > 120$ GeV with 2 LL b -tags and 3-jets after the combined 0+1+2 lepton MVA fit. From left to right: Row 1 - leading then sub-leading jet p_T and ΔR of the same two jets. Row 2 - pseudo-continuous MV1c distributions for leading then sub-leading jet and the $\Delta\eta$ of the same two jets. Row 3 - p_T^Z , m_{jj} , and m_{ll} . Row 4 - $\Delta\phi(V, H)$, $\Delta\eta(V, H)$, and E_T^{miss} . Section 6.1 details the definition of each variable.

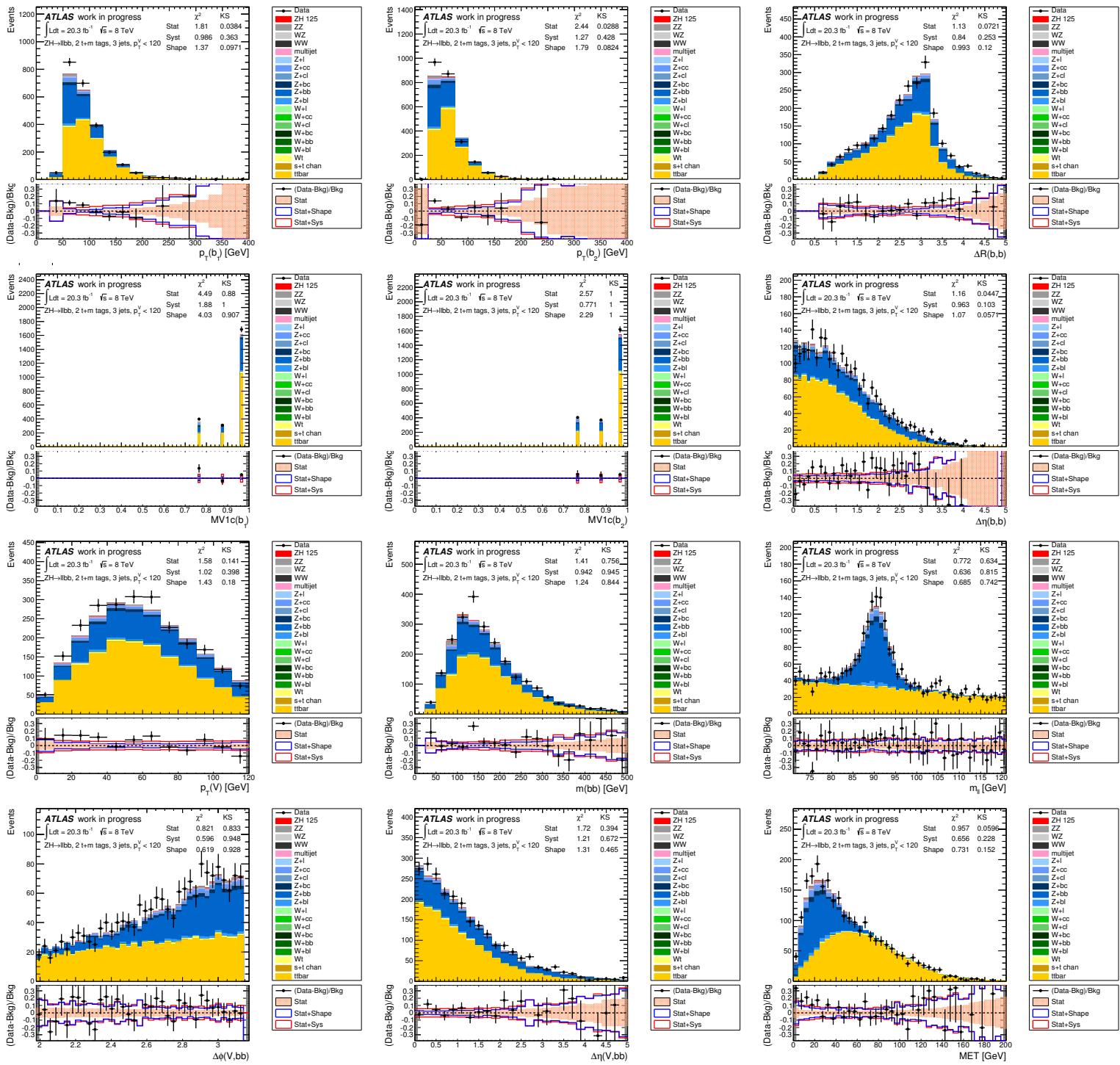


Figure 364: Distributions of MVA training variables used in 2-lepton events for $p_T^Z < 120$ GeV with 2 MM+TT b -tags and 3 jets. From left to right: Row 1 - leading then sub-leading jet p_T and ΔR of the same two jets. Row 2 - pseudo-continuous MV1c distributions for leading then sub-leading jet and the $\Delta\eta$ of the same two jets. Row 3 - p_T^Z , m_{jj} , and m_{ll} . Row 4 - $\Delta\phi(V, H)$, $\Delta\eta(V, H)$, and E_T^{miss} . Section 6.1 details the definition of each variable.

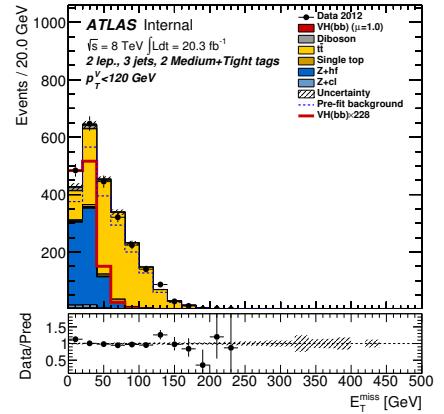
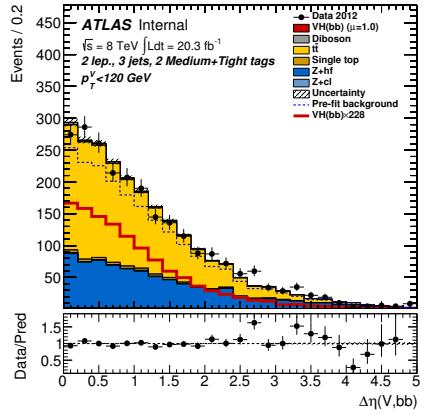
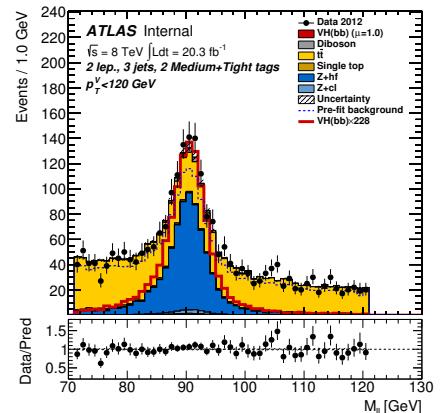
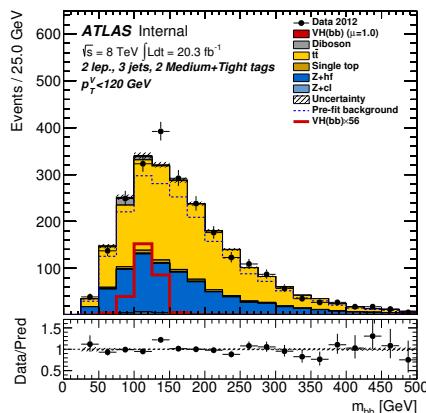
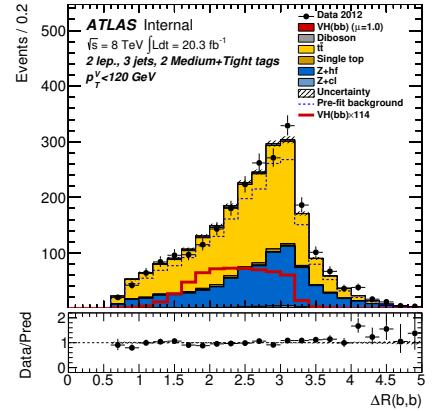
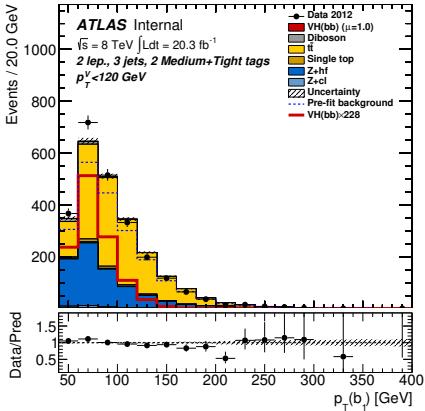


Figure 365: Distributions of MVA training variables used in 2-lepton events for $p_T^Z < 120$ GeV with 2 MM+TT b -tags and 3-jets after the combined 0+1+2 lepton MVA fit. From left to right: Row 1 - leading then sub-leading jet p_T and ΔR of the same two jets. Row 2 - pseudo-continuous MV1c distributions for leading then sub-leading jet and the $\Delta\eta$ of the same two jets. Row 3 - p_T^Z , m_{jj} , and $m_{\ell\ell}$. Row 4 - $\Delta\phi(V, H)$, $\Delta\eta(V, H)$, and E_T^{miss} . Section 6.1 details the definition of each variable.

Not reviewed, for internal circulation only

Dummy

Dummy

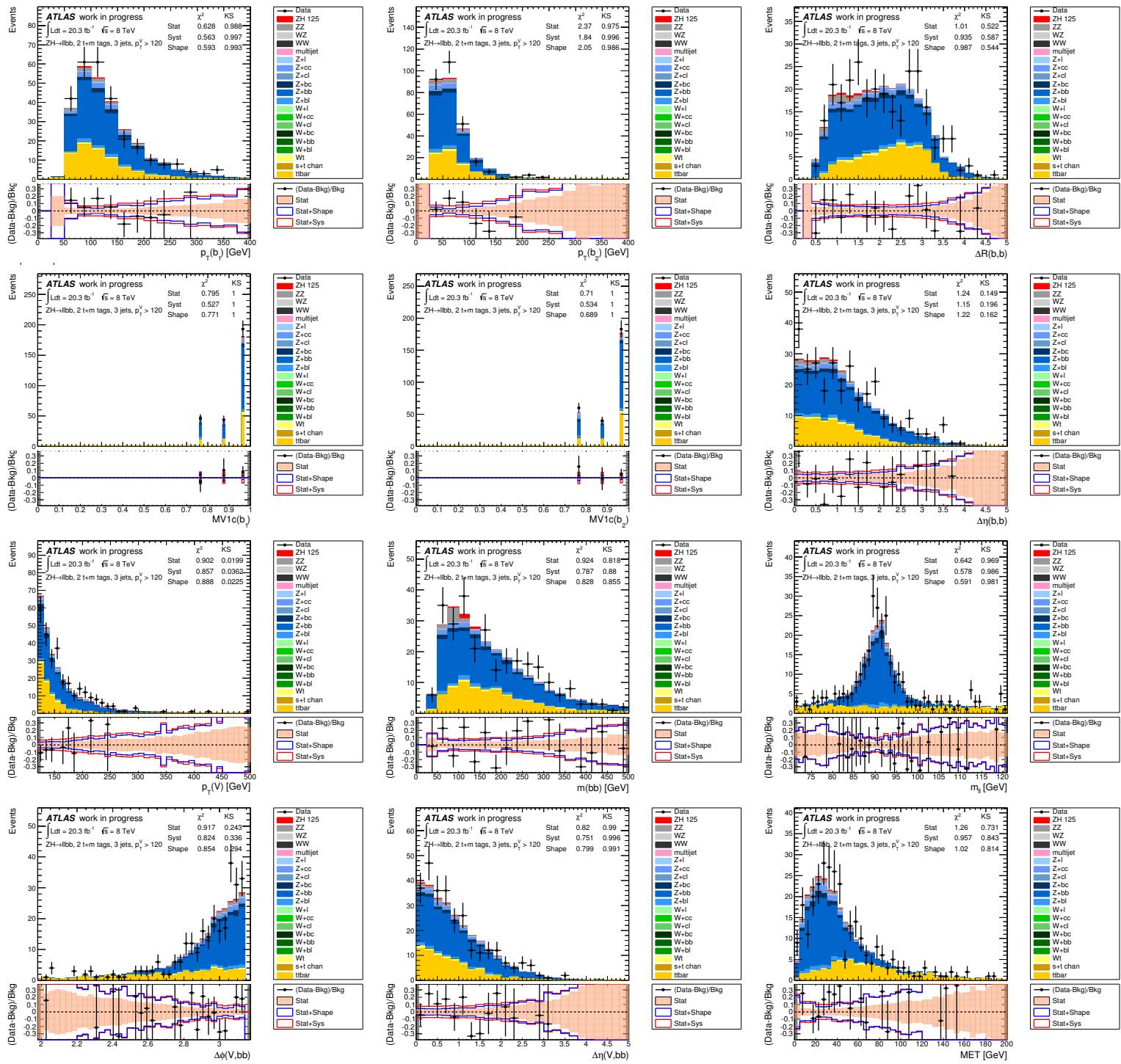


Figure 366: Distributions of MVA training variables used in 2-lepton events for $p_T^Z > 120$ GeV with 2 MM+TT b -tags and 3 jets. From left to right: Row 1 - leading then sub-leading jet p_T and ΔR of the same two jets. Row 2 - pseudo-continuous MV1c distributions for leading then sub-leading jet and the $\Delta\eta$ of the same two jets. Row 3 - p_T^Z , m_{jj} , and m_{ll} . Row 4 - $\Delta\phi(V, H)$, $\Delta\eta(V, H)$, and E_T^{miss} . Section 6.1 details the definition of each variable.

Not reviewed, for internal circulation only

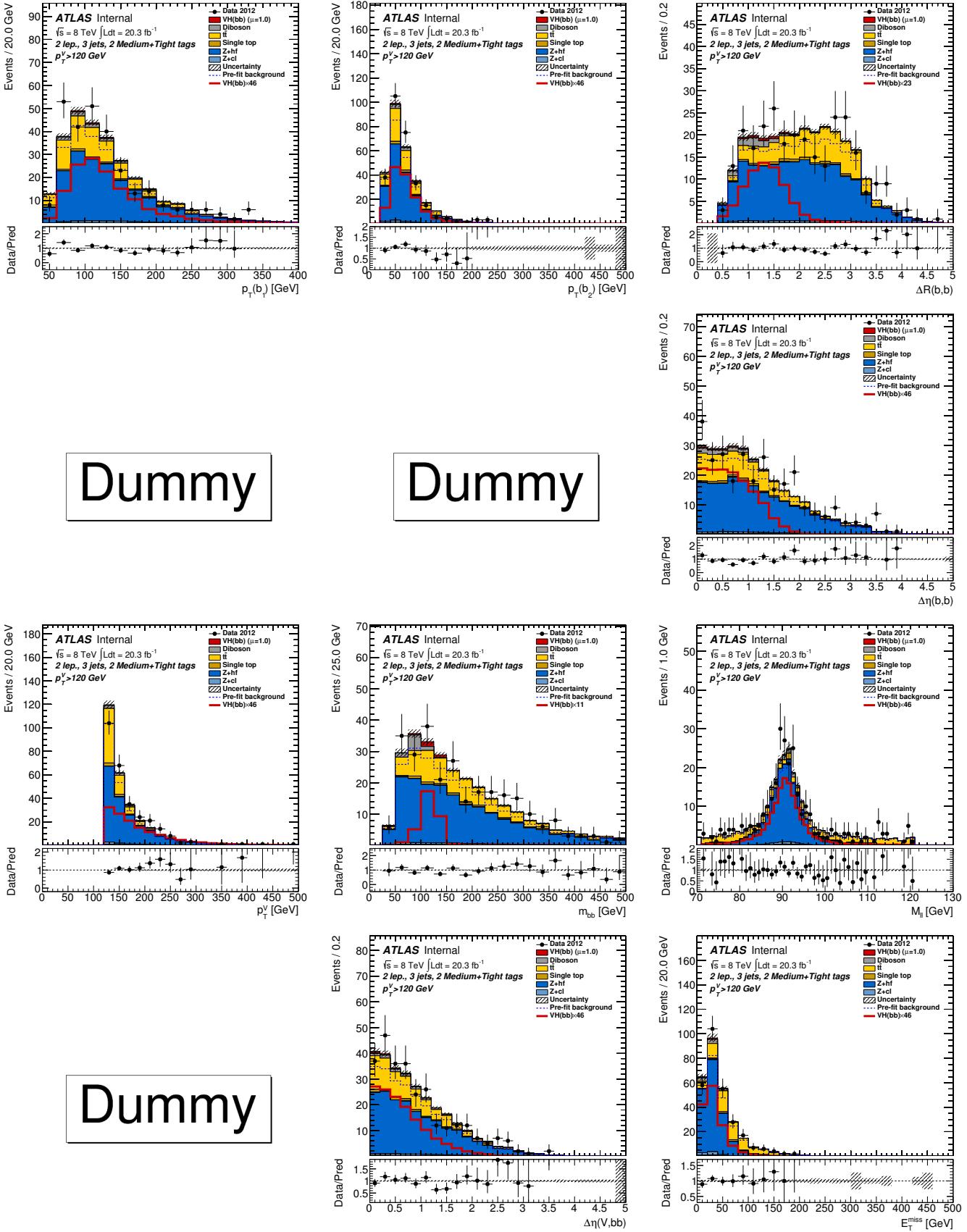


Figure 367: Distributions of MVA training variables used in 2-lepton events for $p_T^Z > 120$ GeV with 2 MM+TT b -tags and 3-jets after the combined 0+1+2 lepton MVA fit. From left to right: Row 1 - leading then sub-leading jet p_T and ΔR of the same two jets. Row 2 - pseudo-continuous MV1c distributions for leading then sub-leading jet and the $\Delta\eta$ of the same two jets. Row 3 - p_T^Z , m_{jj} , and m_{ll} . Row 4 - $\Delta\phi(V, H)$, $\Delta\eta(V, H)$, and E_T^{miss} . Section 6.1 details the definition of each variable.

4952 AB MVA Training Diagnostics

4953 This section contains diagnostic plots for the mva training. The layout is identical in the following pages.
4954 The input variables shown first with the signal in red and background in blue both normalized to the same
4955 integral. This is followed by the background (signal) correlation matrix on the left (right). Finally an
4956 overtraining check is shown with the corresponding KS test values. As noted in Section 6.2.3 the total
4957 statistics are divided into sample A and B for training and evaluation. Only diagnostic plots from sample
4958 A are shown to conserve space. No large differences have been seen between the two sets.
4959 Figures 368 to 369 are for the 0-lepton $m_H = 125$ GeV training.
4960 Figures 370 to 371 are for the 1-lepton $m_H = 125$ GeV training.
4961 Figures 374 to 375 are for the 2-lepton $m_H = 125$ GeV training.
4962

Not reviewed, for internal circulation only

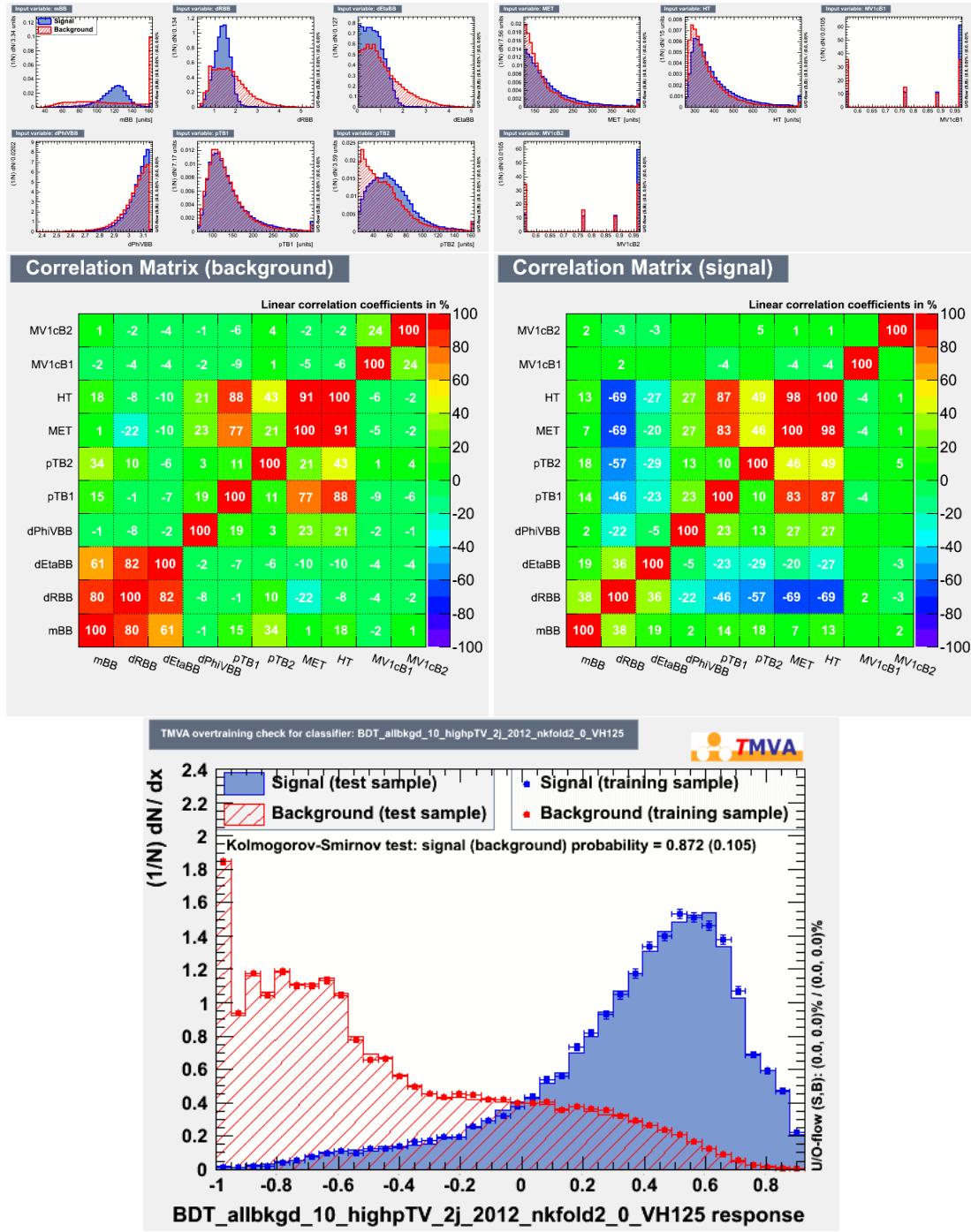


Figure 368: Zero Lepton analysis, 2 jets final state $p_T^V > 120$ GeV. Training variables distributions and correlations for the sum of the backgrounds and for the signal in sample A. The overtraining have been evaluated in the plot on the bottom.

Not reviewed, for internal circulation only

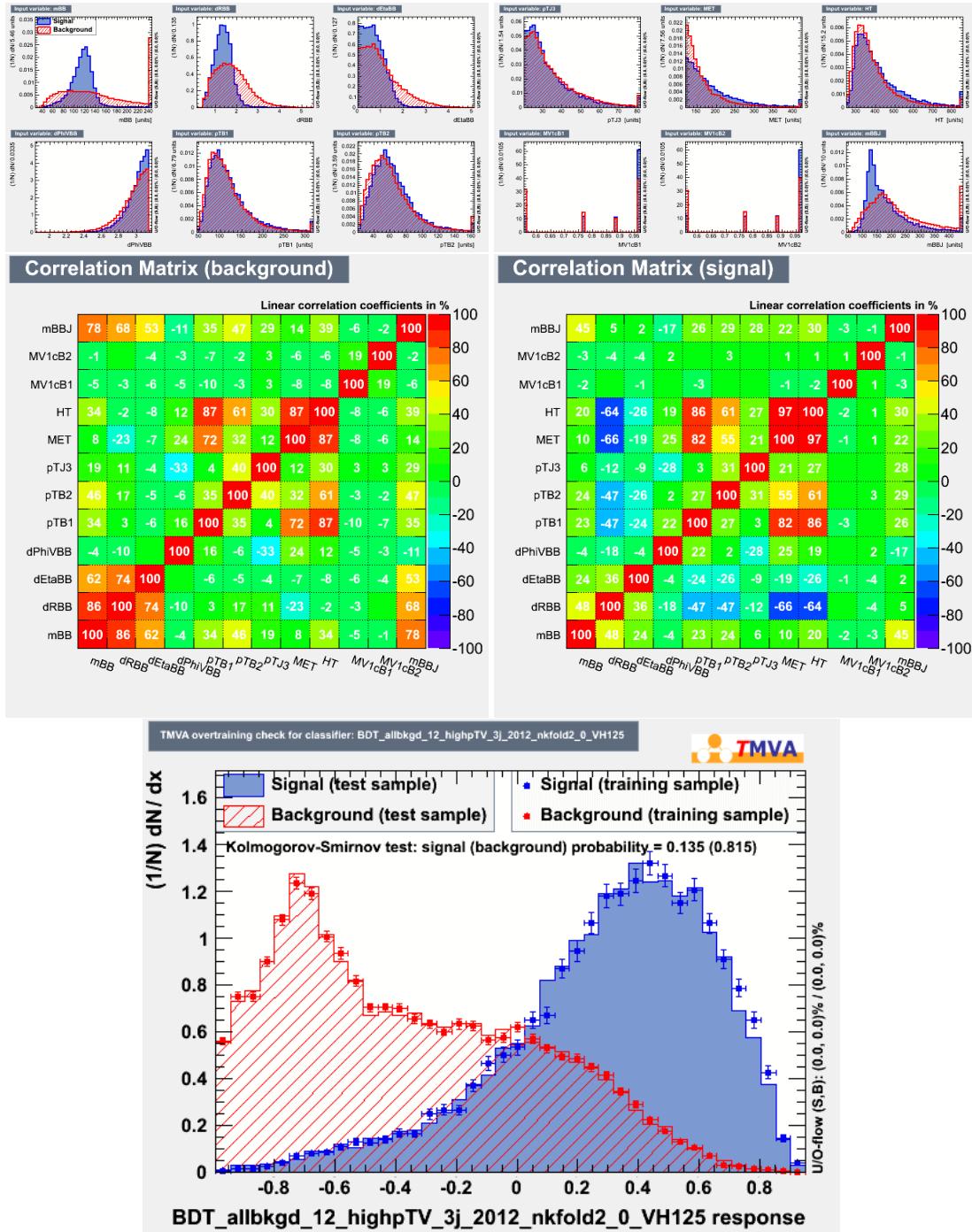


Figure 369: Zero Lepton analysis, 3 jets final state $p_T^V > 120$ GeV. Training variables distributions and correlations for the sum of the backgrounds and for the signal in sample A. The overtraining have been evaluated in the plot on the bottom.

Not reviewed, for internal circulation only

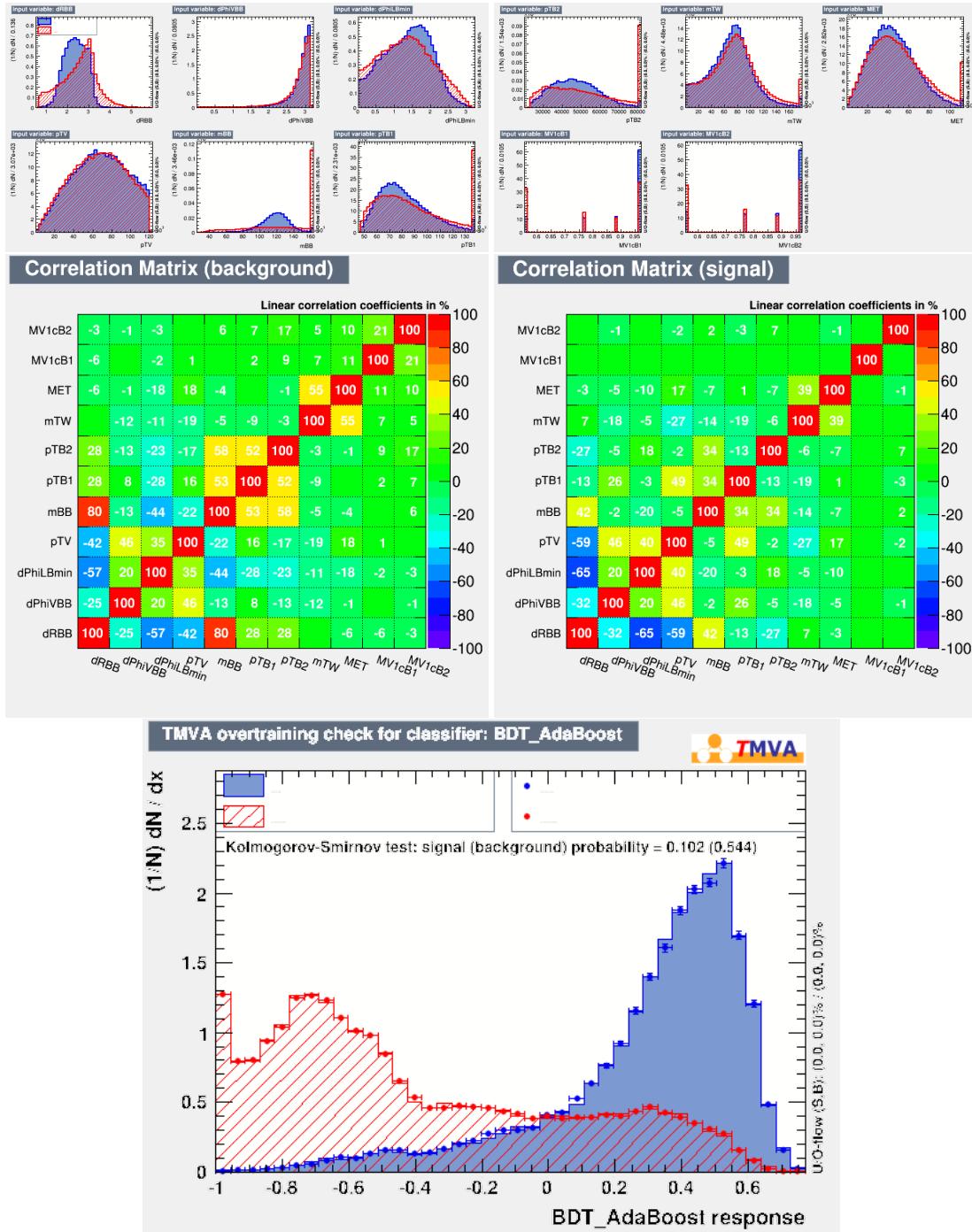


Figure 370: One Lepton analysis, 2 jets final state $p_T^V < 120$ GeV. Training variables distributions and correlations for the sum of the backgrounds and for the signal in sample A. The overtraining have been evaluated in the plot on the bottom.

Not reviewed, for internal circulation only

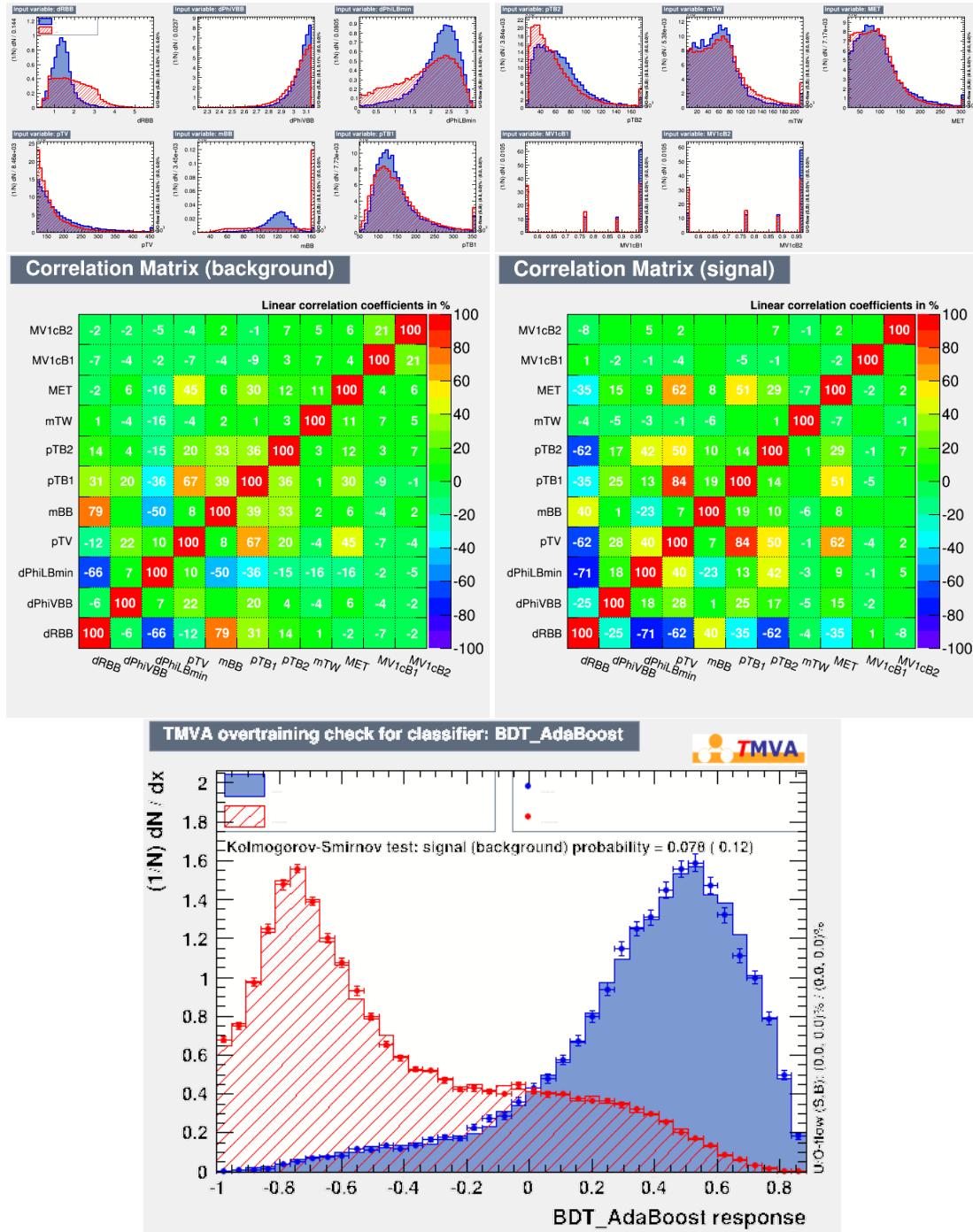


Figure 371: One Lepton analysis, 2 jets final state $p_T^V > 120$ GeV. Training variables distributions and correlations for the sum of the backgrounds and for the signal in sample A. The overtraining have been evaluated in the plot on the bottom.

Not reviewed, for internal circulation only

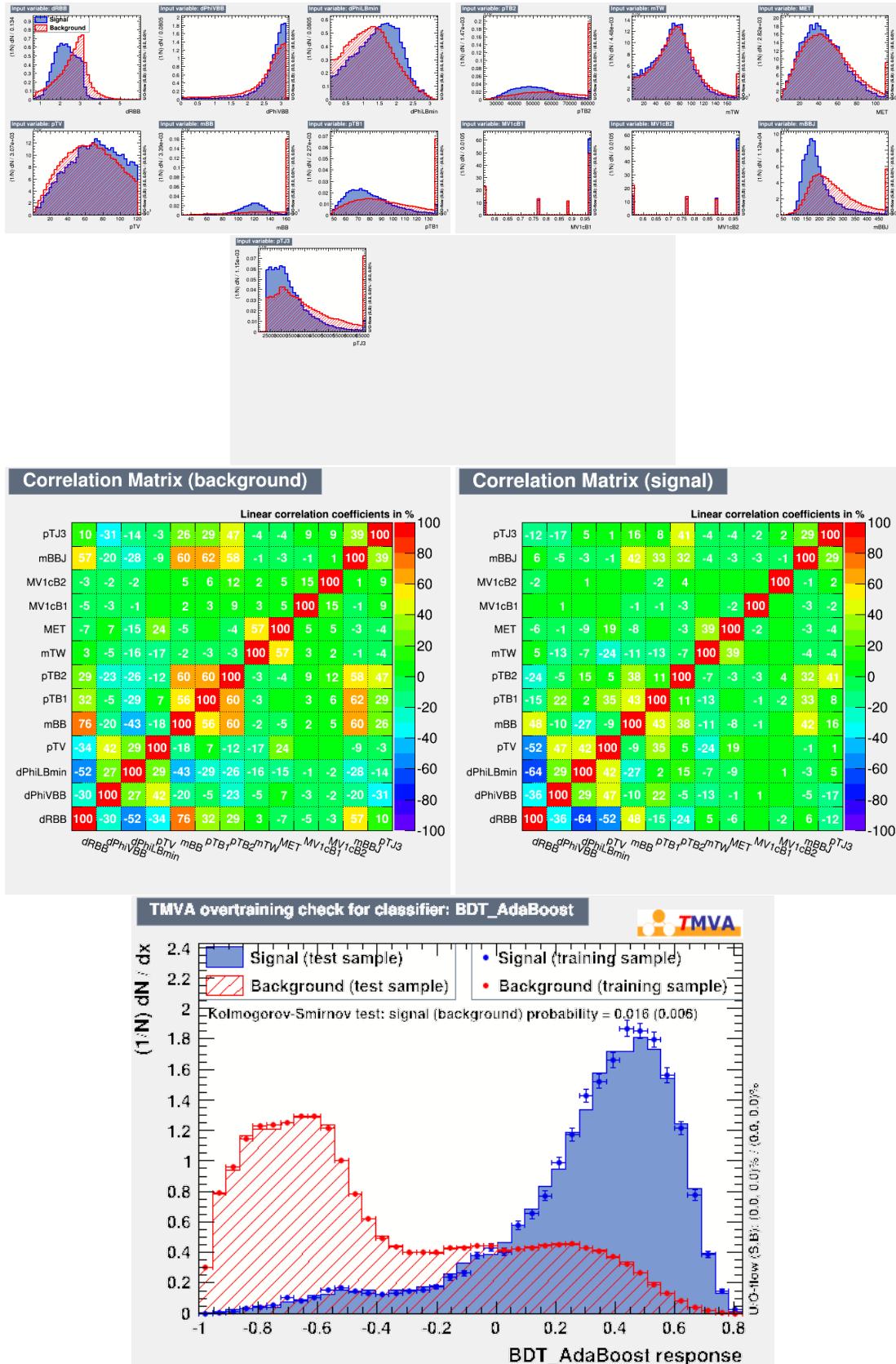


Figure 372: One Lepton analysis, 3 jets final state $p_T^V < 120$ GeV. Training variables distributions and correlations for the sum of the backgrounds and for the signal in sample A. The overtraining have been evaluated in the plot on the bottom.

Not reviewed, for internal circulation only

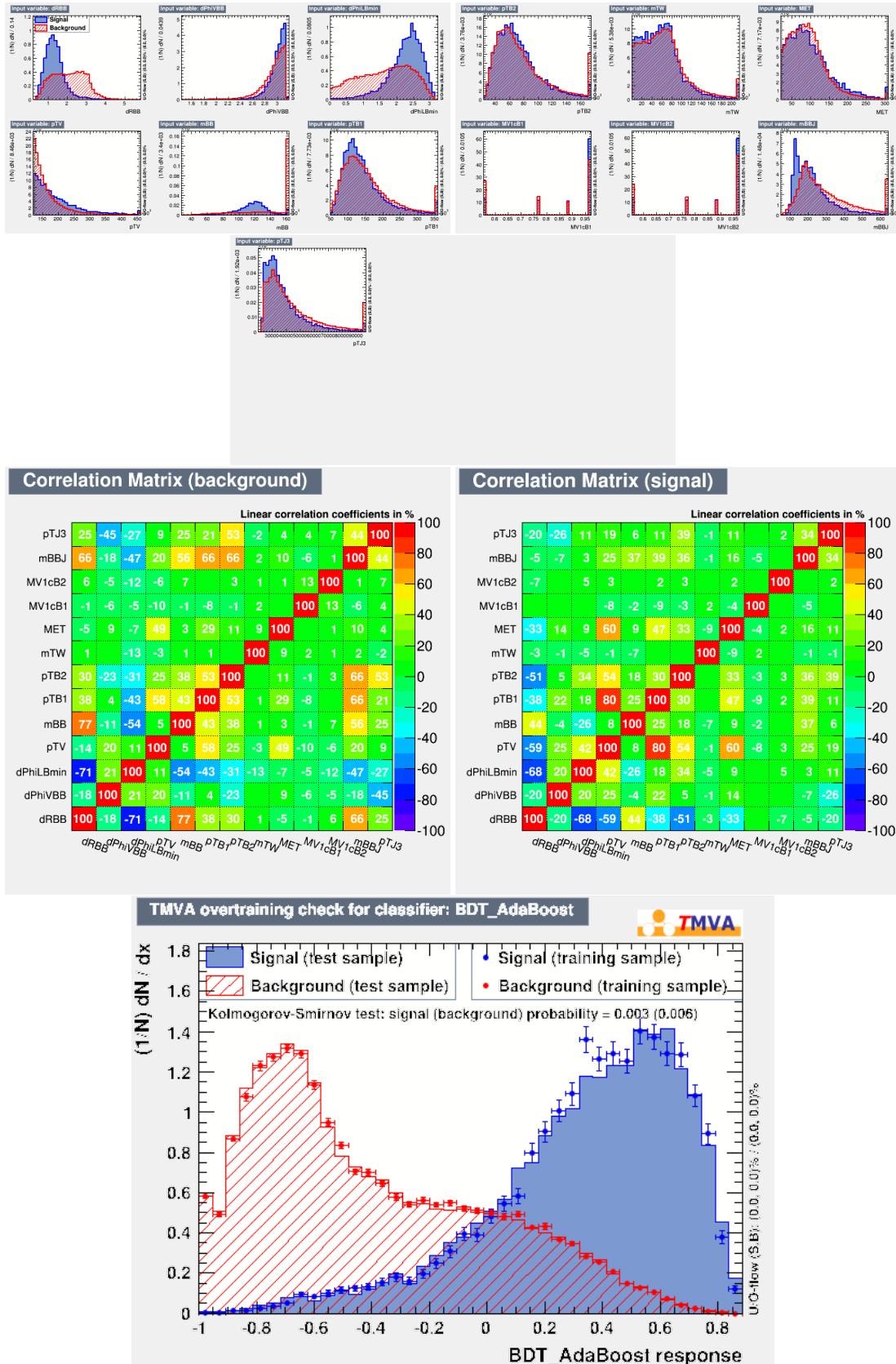


Figure 373: One Lepton analysis, 3 jets final state $p_T^V > 120$ GeV. Training variables distributions and correlations for the sum of the backgrounds and for the signal in sample A. The overtraining have been evaluated in the plot on the bottom.

Not reviewed, for internal circulation only

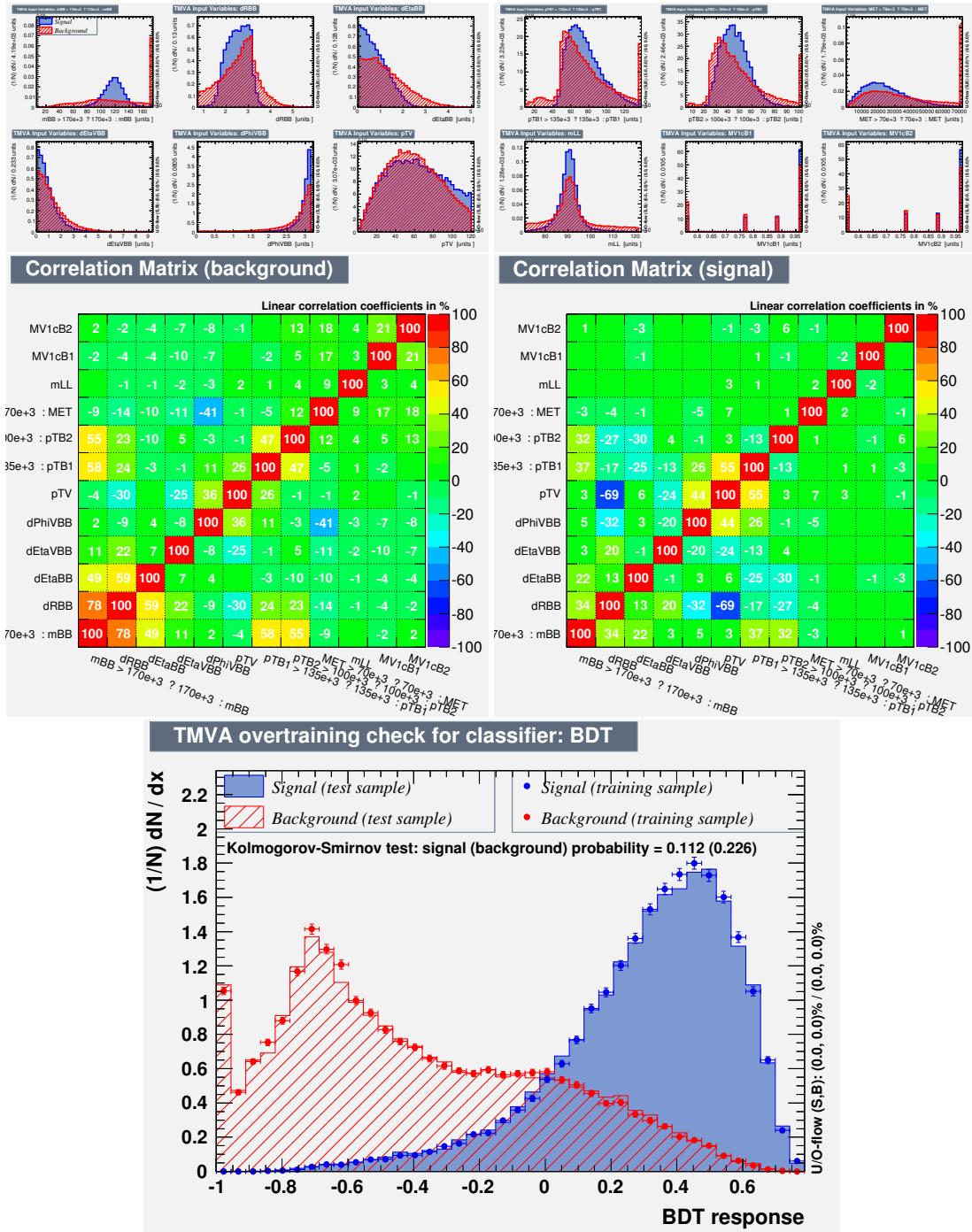


Figure 374: Two Leptons analysis, 2 jets final state $p_T^V < 120$ GeV. Training variables distributions and correlations for the sum of the backgrounds and for the signal in sample A. The overtraining have been evaluated in the plot on the bottom.

Not reviewed, for internal circulation only

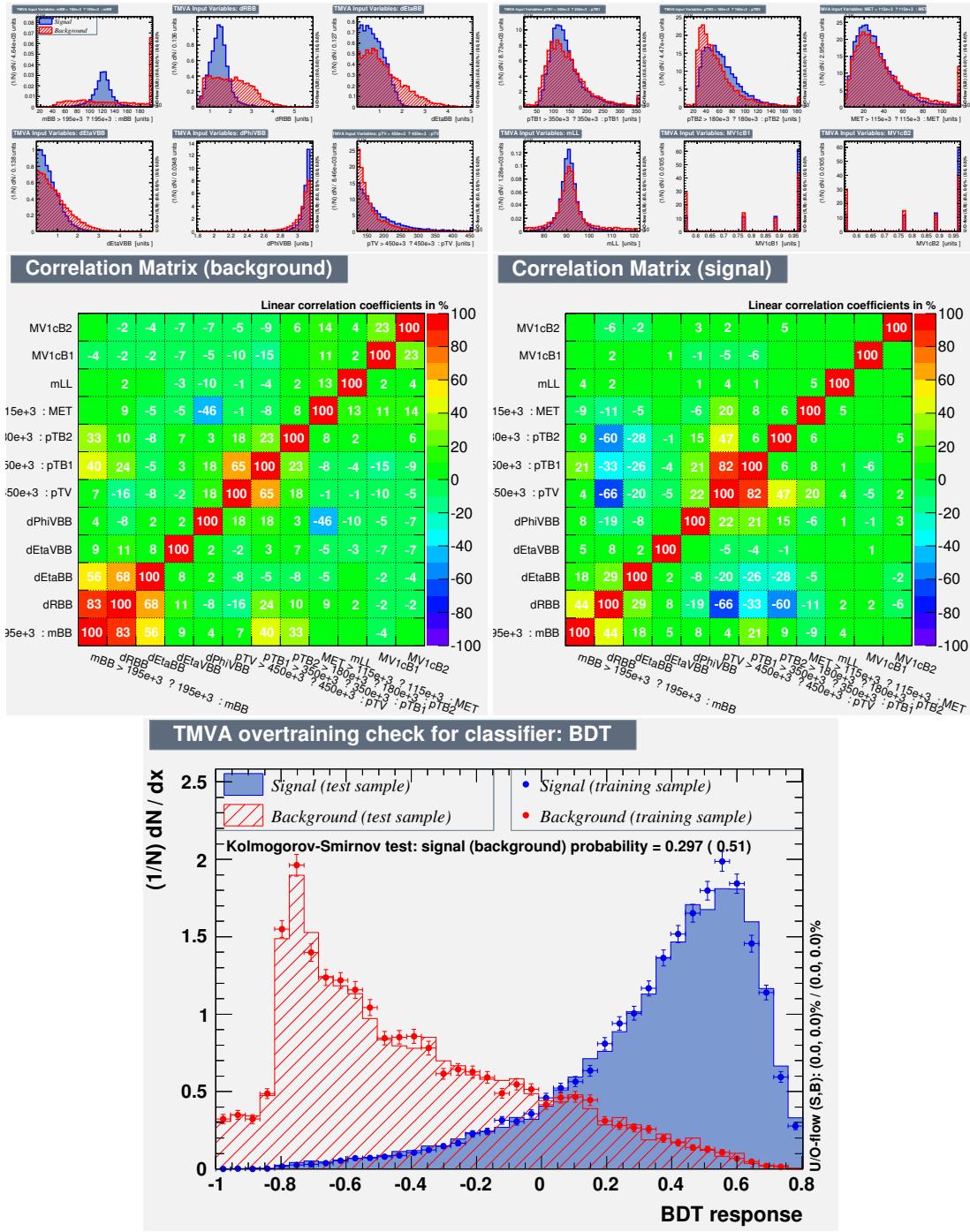


Figure 375: Two Lepton analysis, 2 jets final state $p_T^V > 120$ GeV. Training variables distributions and correlations for the sum of the backgrounds and for the signal in sample A. The overtraining have been evaluated in the plot on the bottom.

Not reviewed, for internal circulation only

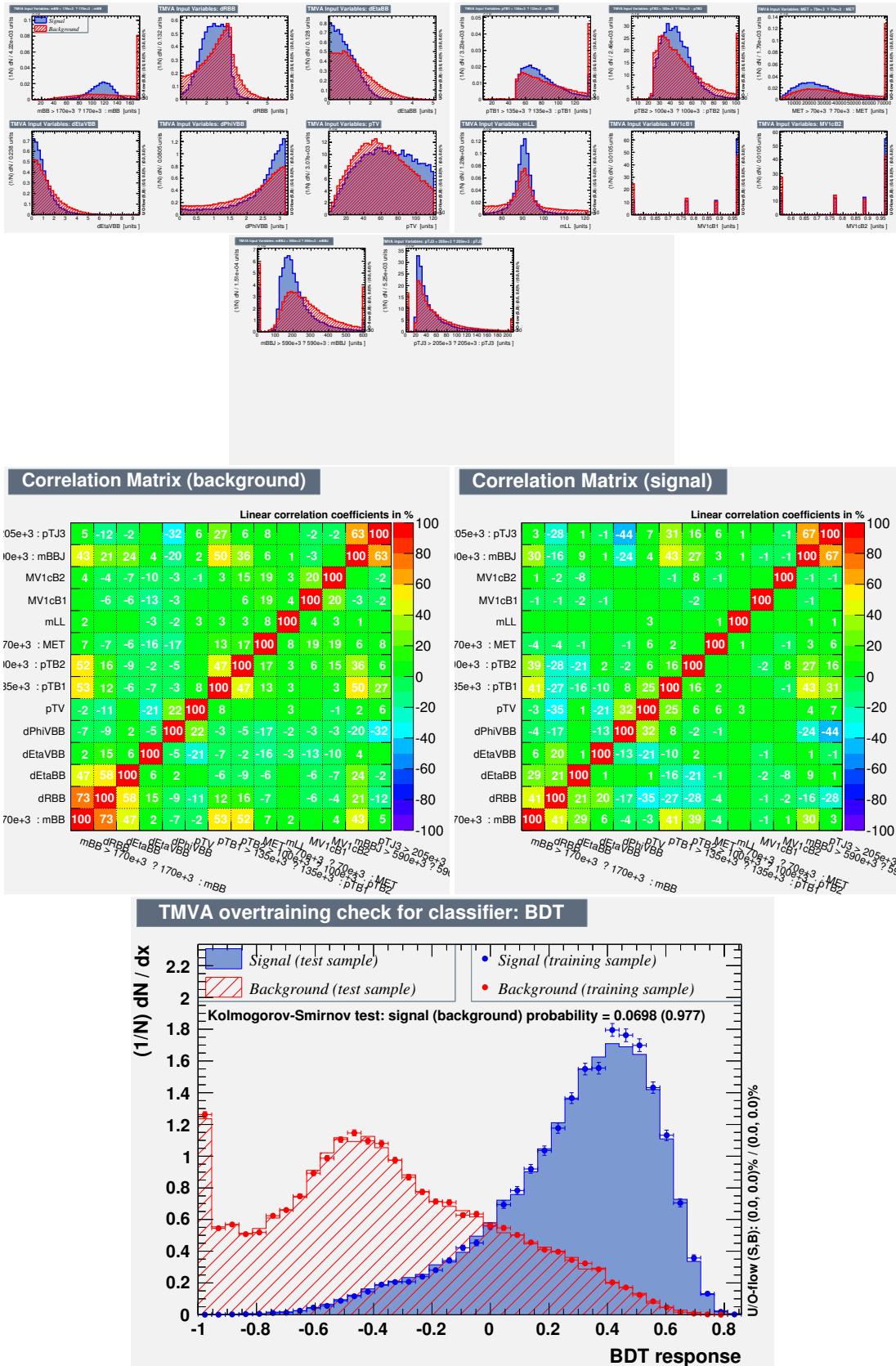


Figure 376: Two Leptons analysis, 3 jets final state $p_T^V < 120$ GeV. Training variables distributions and correlations for the sum of the backgrounds and for the signal in sample A. The overtraining have been evaluated in the plot on the bottom.

Not reviewed, for internal circulation only

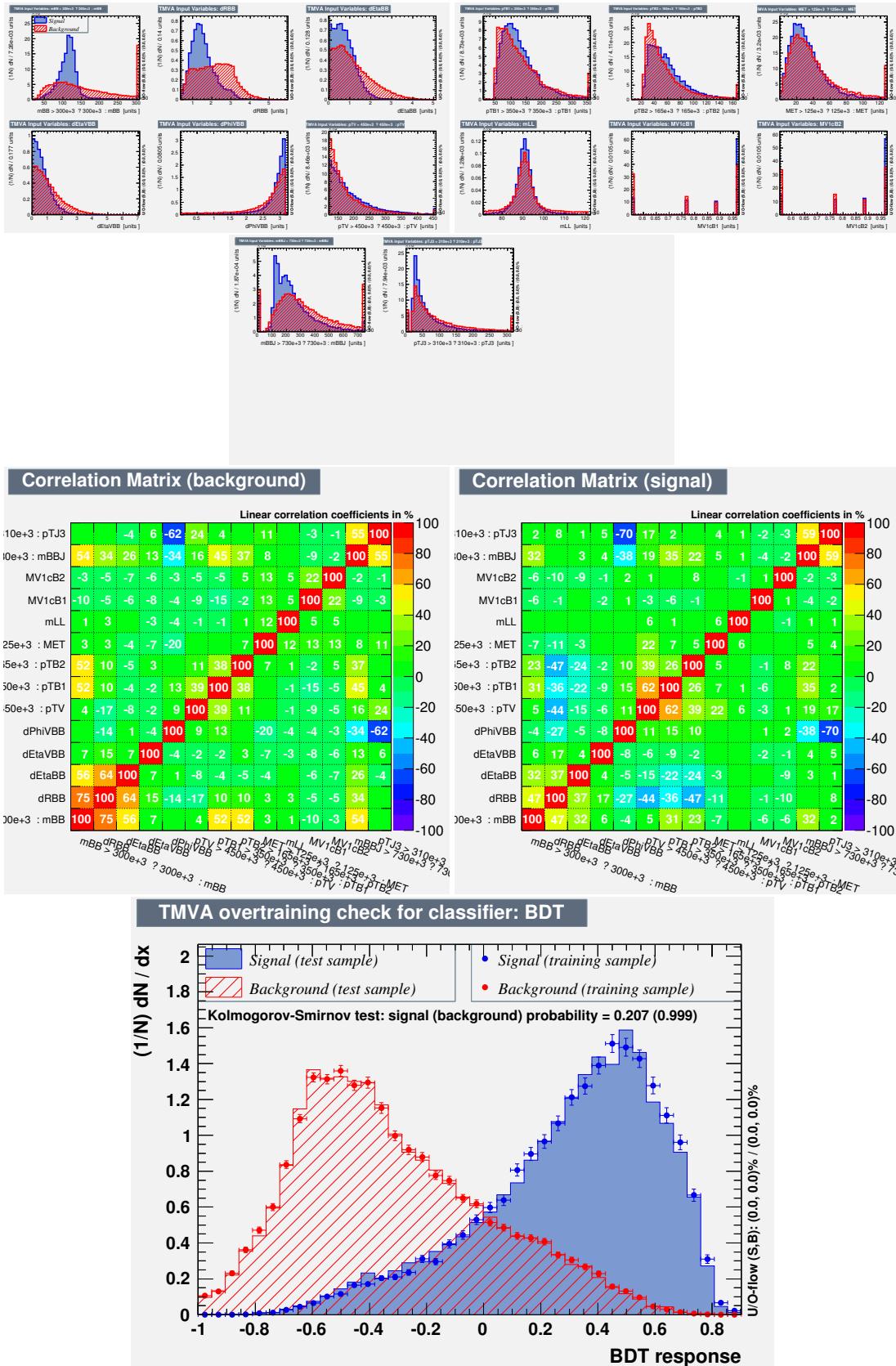


Figure 377: Two Leptons analysis, 3 jets final state $p_T^V > 120$ GeV. Training variables distributions and correlations for the sum of the backgrounds and for the signal in sample A. The overtraining have been evaluated in the plot on the bottom.

4963 AC MVA optimization and the transformation D

4964 As described in Section 8.4, the transformation D have been optimize for the mva analisis, and this
 4965 appendix contains the dexcritption of the these studies. This can be useful as reference for future studies,
 4966 and in to read some of the plots in the note, in case they result to be done with this transformation.

4967 For the mva analysis, a first study defined the working point $(z_s, z_b) = (6, 6)$ as a good starting point for
 4968 additional optimizations. From this working point, the values for z_s and z_b have been redefined for each
 4969 of the the multi-variate analysis region following the formula:

$$4970 z_s = f_{tags} \times f_{jets} \times f_{p_T^V} \times f_{leptons} \times \zeta_s \quad (44)$$

$$4970 z_b = f_{tags} \times f_{jets} \times f_{p_T^V} \times f_{leptons} \times \zeta_b \quad (45)$$

4971 where each term have been optimized in a sequence. By keeping all the other f parameters equal to 1,
 4972 $\zeta_s = \zeta_b = 6$, and fixing the total number of bins, the impact of the fraction of bins in the different tagging
 4973 categories (LL VS. MM+TT for 0 and 2 leptons, LL VS. MM VS. TT for 1 lepton) have been studied
 4974 by changing the parameter f_{tags} . Once the best working point for the parameter f_{tags} was obtained, the
 4975 optimization strategy moved to the fraction of bins in the 2-jet category versus 3-jet category (f_{jets}), then
 4976 to the fraction of bins in the low p_T^V versus the high p_T^V region ($f_{p_T^V}$), and finally to the fraction of bins
 4977 in the 3 lepton categories ($f_{leptons}$). In each step of the sequence, the optimized value of the parameters
 4978 studies in the previous steps have been used. For each step, the expected limit as a function of the
 4979 parameter of interest is shown in Figures 378. Finally, the optimal values for the 2 parameters ζ_s, ζ_b have
 4980 been reevaluated to be $\zeta_s = 6$ and $\zeta_b = 4$. The complete list of parameters can be found in Table 98. This
 4981 output transform reduced the number of bins by almost 60% with a degradation of less than 1% in the
 4982 final significance.

4983 As an example, one of the mva distributions, before and after the transform can be seen in Figure 379
 4984 The mva output distributions are all contained in Appendix AD showing both the original shape with a
 4985 reduced number of bins and the transformed output.

Parameter	Description	N leptons	Tag	N Jets	p_T^V region	value
f_{tags}	fractions in the different tagging regions	0,2	LL	2,3	low and high p_T^V	0.6
			MM+TT			1.4
		1	LL	2	low and high p_T^V	0.2
			MM			0.9
			TT			0.9
f_{jets}	fractions in the different jet categories	0,1,2	LL,MM,TT	2	low and high p_T^V	0.8
				3		1.2
$f_{p_T^V}$	fractions in low and high p_T^V	1,2	LL,MM,TT	2,3	low p_T^V	0.6
					high p_T^V	1.4
$f_{leptons}$	fractions in the different lepton categories	0 1 2	LL,MM,TT	2,3	low and high p_T^V	0.9
						1.2
						0.9
$\zeta_s = 6$	weight for the signal	0,1,2	LL,MM,TT	2,3	low and high p_T^V	6
$\zeta_b = 4$	weight for the background	0,1,2	LL,MM,TT	2,3	low and high p_T^V	4

Table 98: Binning optimization for the cut based analysis

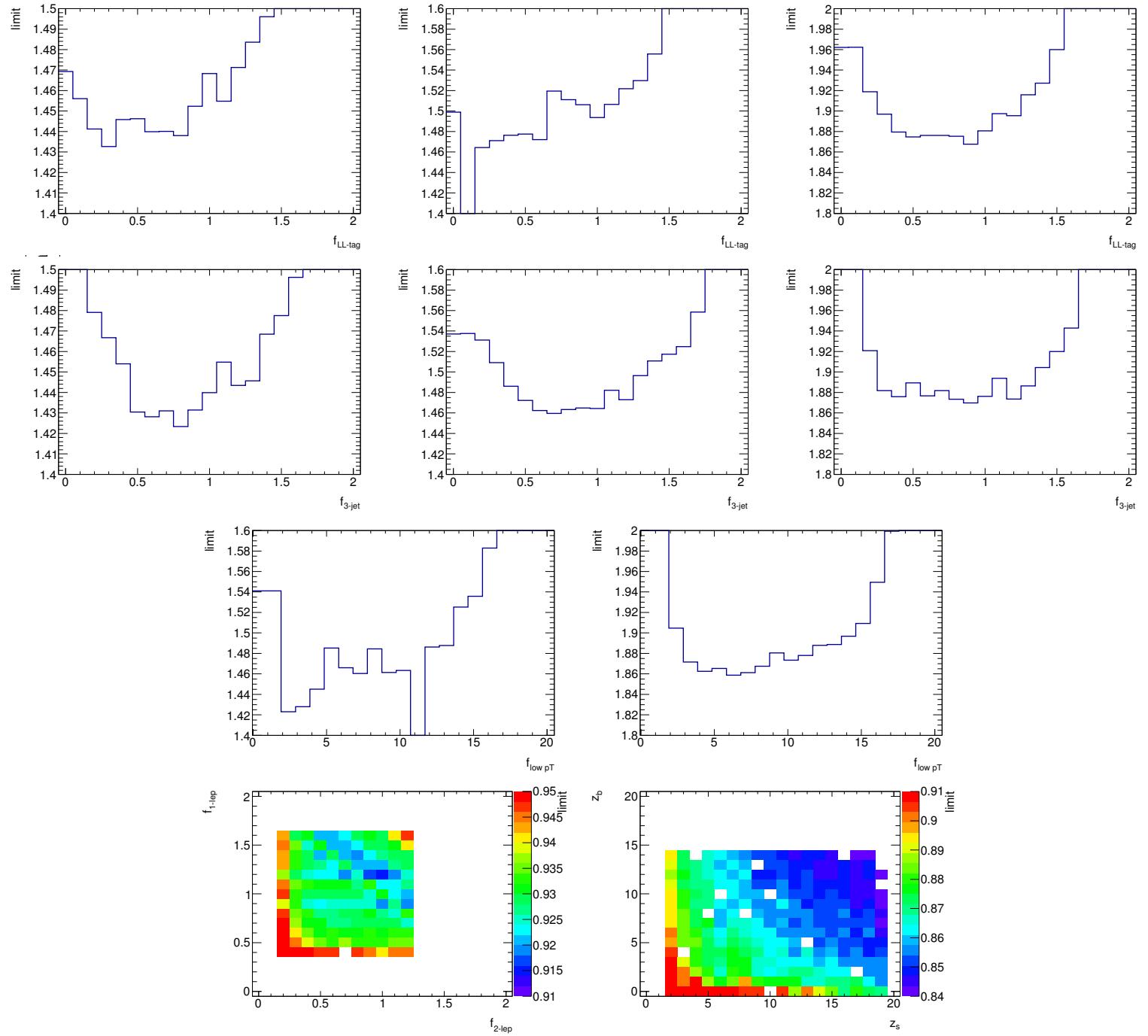


Figure 378: Dependence of the expected limit as a function of the f parameters. From the left to the right:
Row 1 - Expected limit dependence on f_{tags} for 0,1 and 2 leptons. Row 2 - Expected limit dependence on f_{jets} for 0,1 and 2 leptons. Row 3 - Expected limit dependence on $f_{p_T^V}$ for 1 and 2 leptons. Row 4 - 2D Expected limit dependence on the fraction of bins in 1 lepton and 2 leptons, and 2D Expected limit dependence on ζ_s, ζ_b .

Not reviewed, for internal circulation only

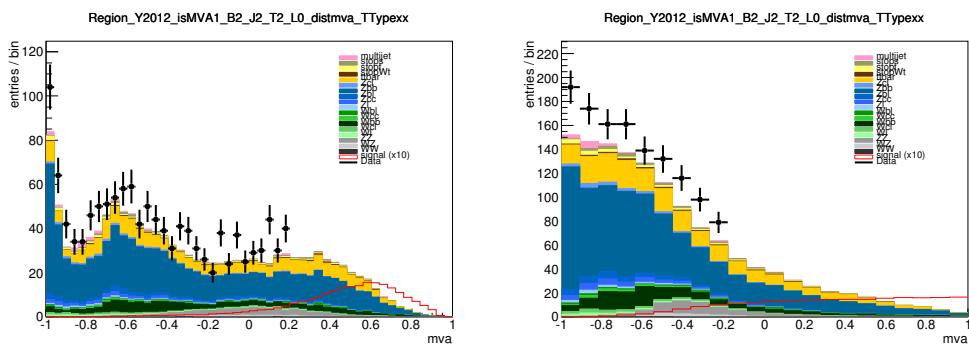


Figure 379: Example of the effect of the binning transform on the MVAoutput for one of the signal regions. Left: before the binning transform; Right: After the binning Transform.

Not reviewed, for internal circulation only

4986 AD MVA Distributions

4987 This appendix contains the MVA distributions for low and high p_T^V regions ($p_T^V < 120$ GeV and $p_T^V >$
 4988 120 GeV respectively) for the $m_H = 125$ GeV training. When leptons are selected, the electron and
 4989 muon events have been combined. The MVA configuration is detailed in Section 6 and the input variable
 4990 distributions are show in Appendix Y, Z, and AA for the 0, 1, and 2 lepton selections respectively. The
 4991 binning strategy discussed in Section 8.4 has not been applied in these plots. Note the the 0-lepton
 4992 selection only included events with $p_T^Z > 120$ GeV in the MVA analysis. These plots are done by
 4993 applying the latest scale factors, obtained for the 2 jet region and the 3 jet region separately, by comparing
 4994 the event yield before and after the MVA combined fit. They are summarized in Table 97. Explicitly stated,
 4995 the theoretical expectation for each background is used for the given luminosity. All the plots in this
 4996 section are done with the status-of-art analysis.
 4997 Zero Lepton BDT distributions are shown in Figures 380, 381 before the transformation discussed in
 4998 Section 8.4. One Lepton low p_T^W ($p_T^W < 120$ GeV) BDT distributions are shown in Figures 382, 383 before
 4999 the transformation discussed in Section 8.4. One Lepton high p_T^W ($p_T^W > 120$ GeV) BDT distributions
 5000 are shown in Figures 384 385 before the transformation discussed in Section 8.4. Two Lepton low
 5001 p_T^Z ($p_T^Z < 120$ GeV) BDT distributions are shown in Figures 386, 387 before the transformation discussed
 5002 in Section 8.4. Two Lepton high p_T^Z ($p_T^Z > 120$ GeV) BDT distributions are shown in Figures 388, 389
 5003 before the transformation discussed in Section 8.4.

Not reviewed, for internal circulation only

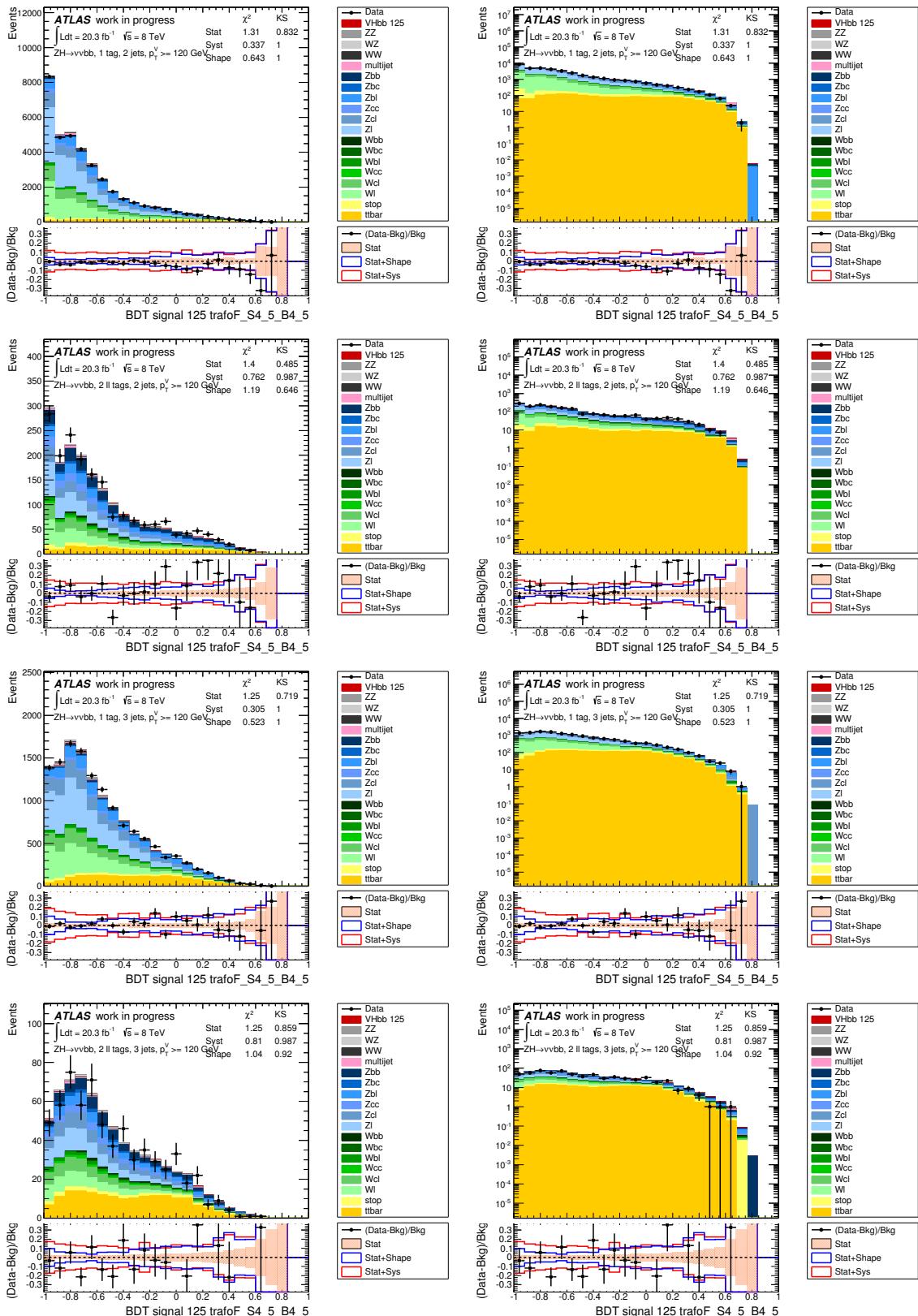


Figure 380: MVA distribution in 0-lepton events ($p_T^Z > 120$ GeV). Each row contains the same plot with the left (right) in linear (log) scale. From top to bottom: Row 1 - 1 b -tag 2 jet events. Row 2 - 2 loose b -tags 2 jet events. Row 3 - 1 b -tag 3 jet events. Row 4 - 2 loose b -tags 3 jet events. Section 6 details the MVA configuration.

Not reviewed, for internal circulation only

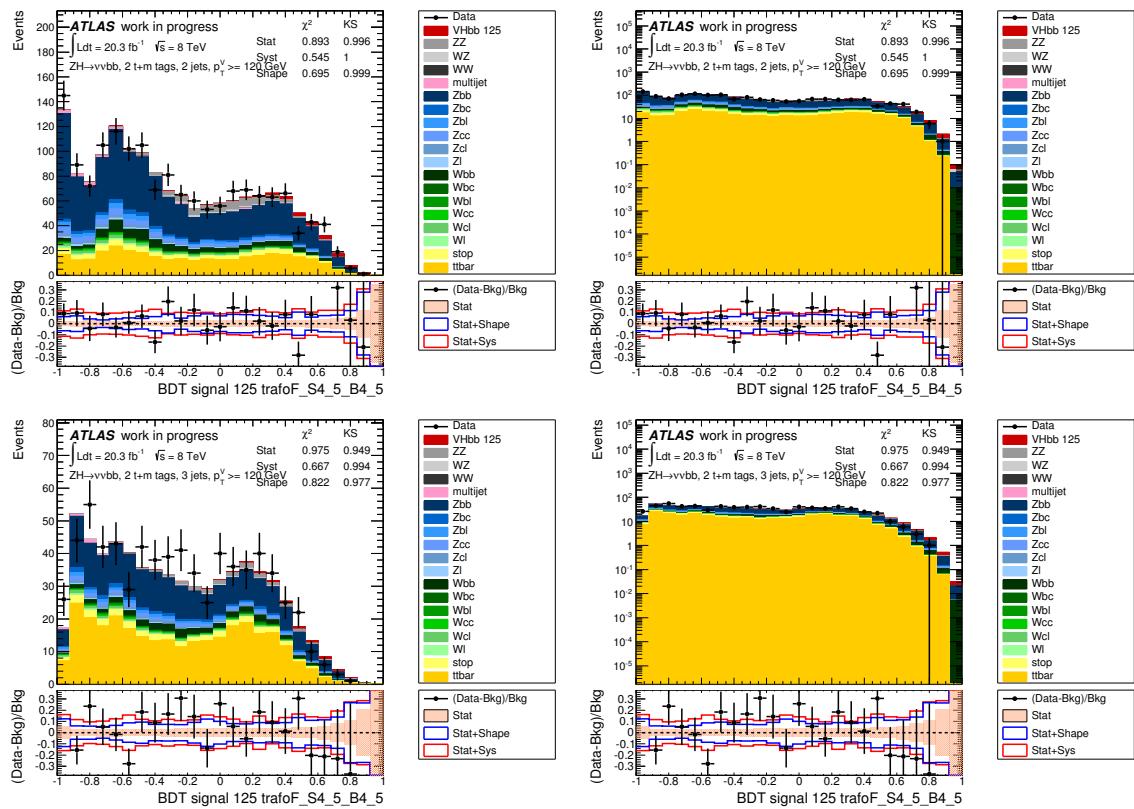


Figure 381: MVA distribution in 0-lepton events ($p_T^Z > 120$ GeV). Each row contains the same plot with the left (right) in linear (log) scale. From top to bottom: Row 1 - 2 MM+TT b-tag 2 jet events. Row 2 - 2 MM+TT b-tag 3 jet events. Section 6 details the MVA configuration.

Not reviewed, for internal circulation only

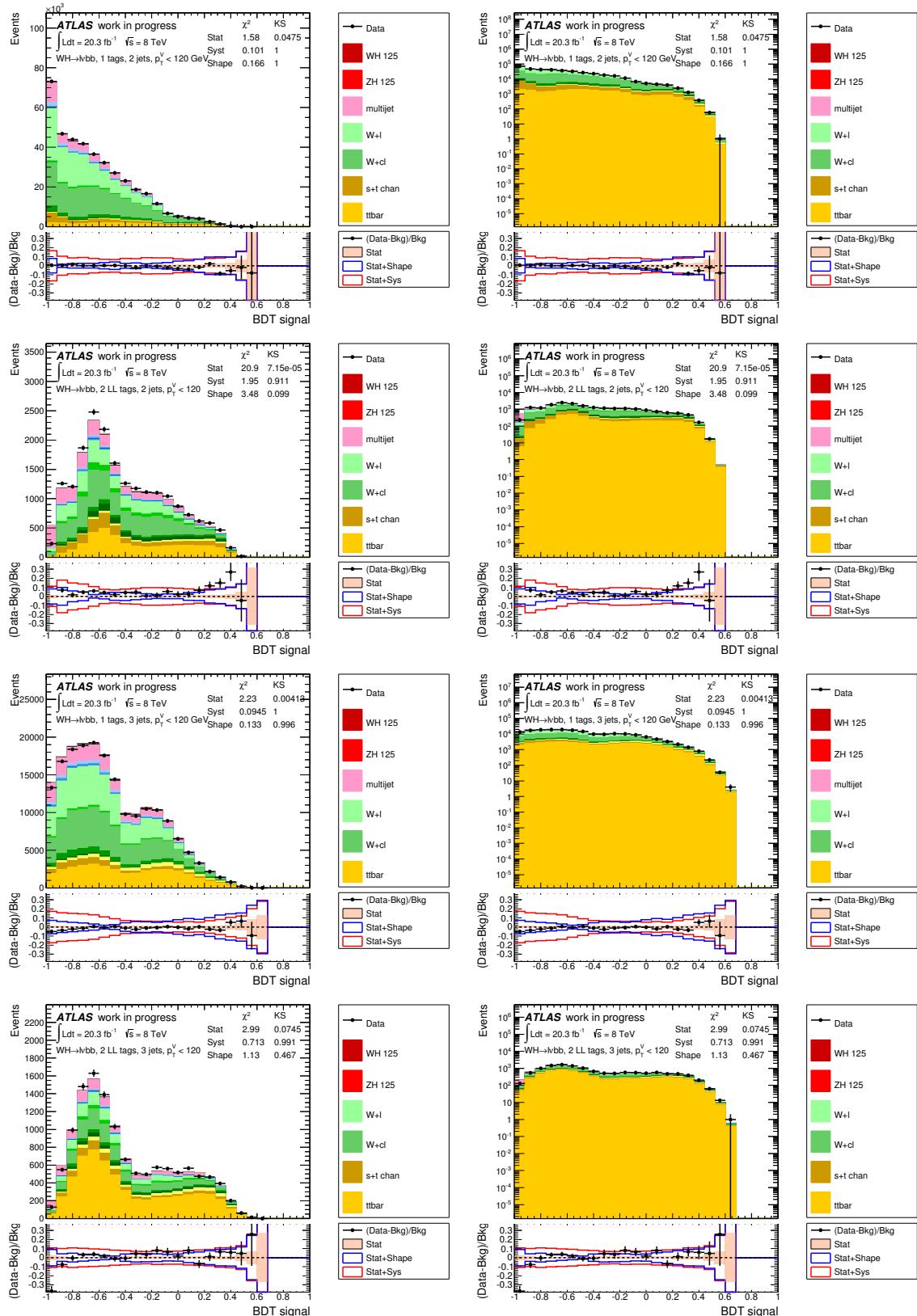


Figure 382: MVA distribution in 1-lepton events with $p_T^W < 120$ GeV. Each row contains the same plot with the left (right) in linear (log) scale. From top to bottom: Row 1 - 1 b -tag 2 jet events. Row 2 - 2 LL b -tags 2 jet events. Row 3 - 1 b -tag 3 jet events. Row 4 - 2 LL b -tags 3 jet events. Section 6 details the MVA configuration.

Not reviewed, for internal circulation only

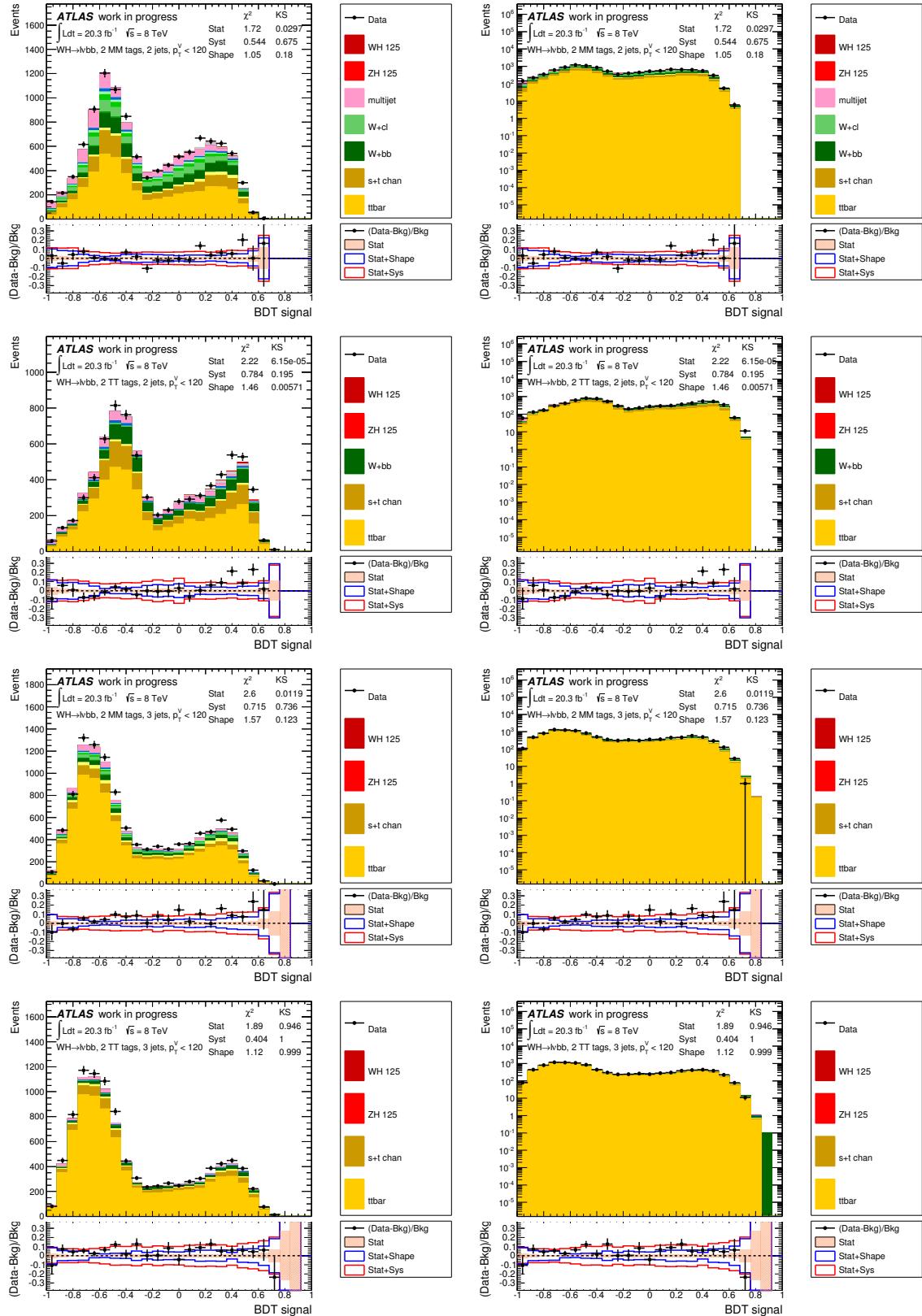


Figure 383: MVA distribution in 1-lepton events with $p_T^W < 120$ GeV. Each row contains the same plot with the left (right) in linear (log) scale. From top to bottom: Row 1 - 2 MM b -tag 2 jet events. Row 2 - 2 TT b -tags 2 jet events. Row 3 - 2 MM b -tag 3 jet events. Row 4 - 2 TT b -tags 3 jet events. Section 6 details the MVA configuration.

Not reviewed, for internal circulation only

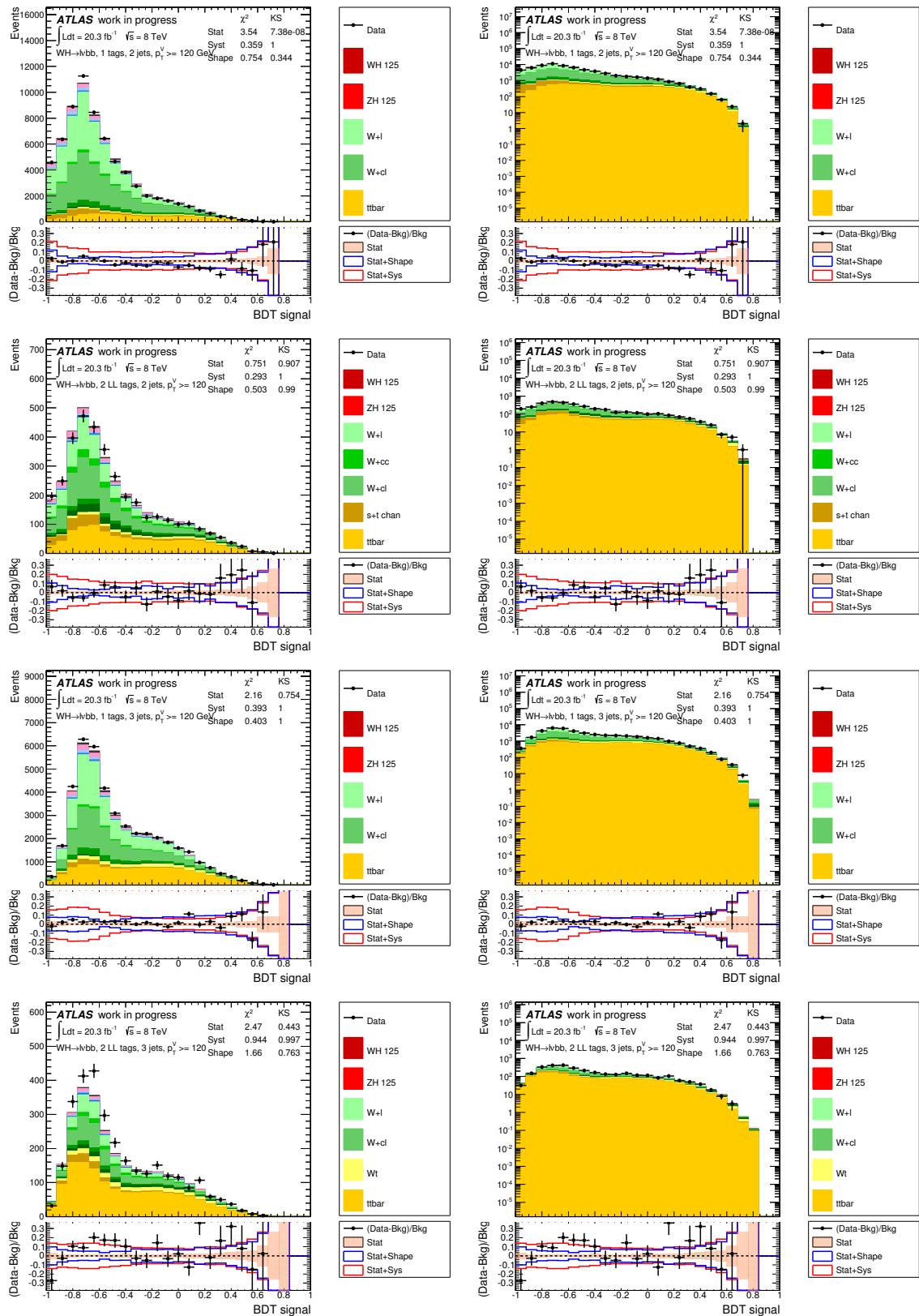


Figure 384: MVA distribution in 1-lepton events with $p_T^W > 120$ GeV. Each row contains the same plot with the left (right) in linear (log) scale. From top to bottom: Row 1 - 1 b -tag 2 jet events. Row 2 - 2 LL b -tags 2 jet events. Row 3 - 1 b -tag 3 jet events. Row 4 - 2 LL b -tags 3 jet events. Section 6 details the MVA configuration.

Not reviewed, for internal circulation only

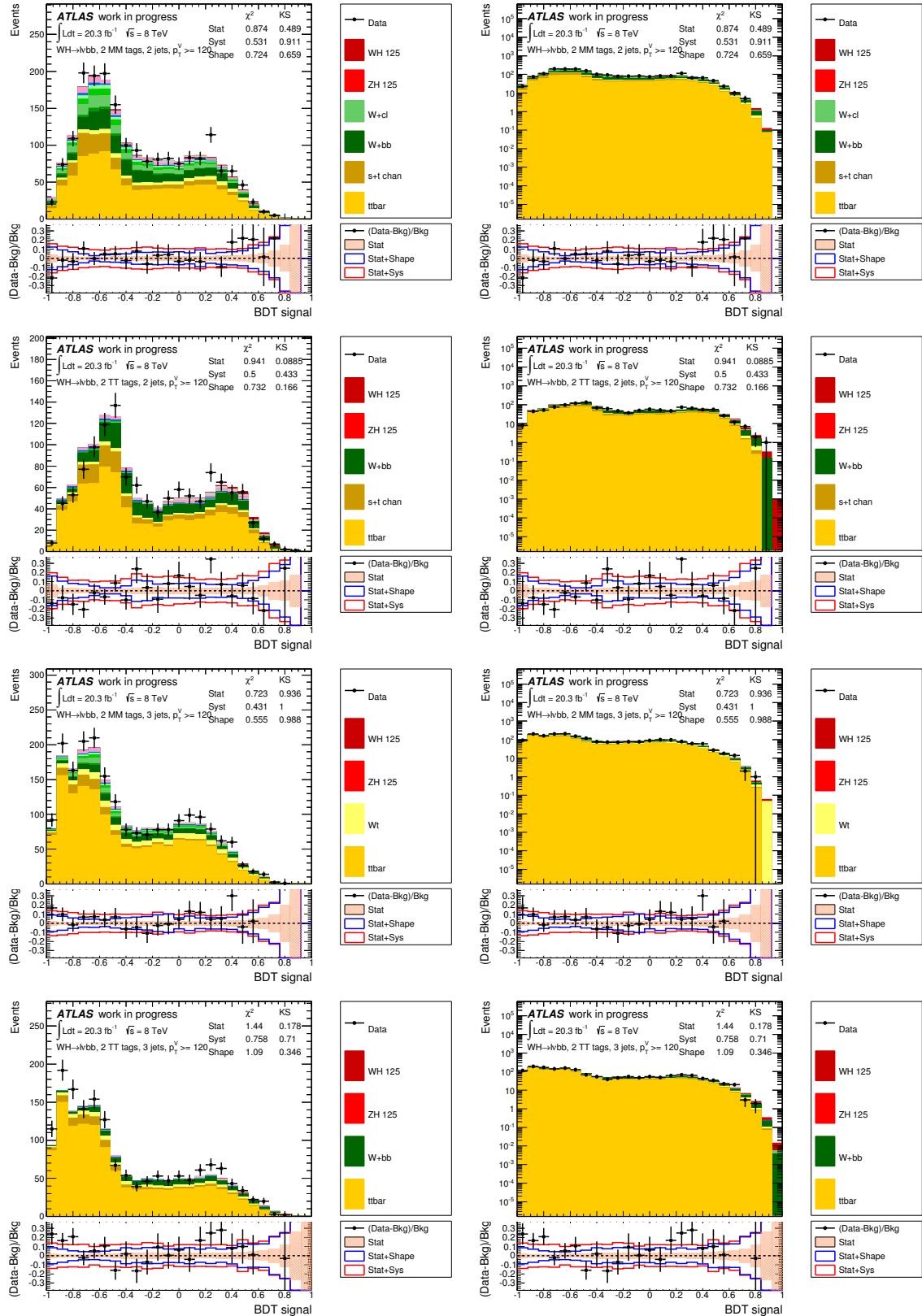


Figure 385: MVA distribution in 1-lepton events with $p_T^W > 120$ GeV. Each row contains the same plot with the left (right) in linear (log) scale. From top to bottom: Row 1 - 2MM b -tag 2 jet events. Row 2 - 2 TT b -tags 2 jet events. Row 3 - 2 MM b -tag 3 jet events. Row 4 - 2 TT b -tags 3 jet events. Section 6 details the MVA configuration.

Not reviewed, for internal circulation only

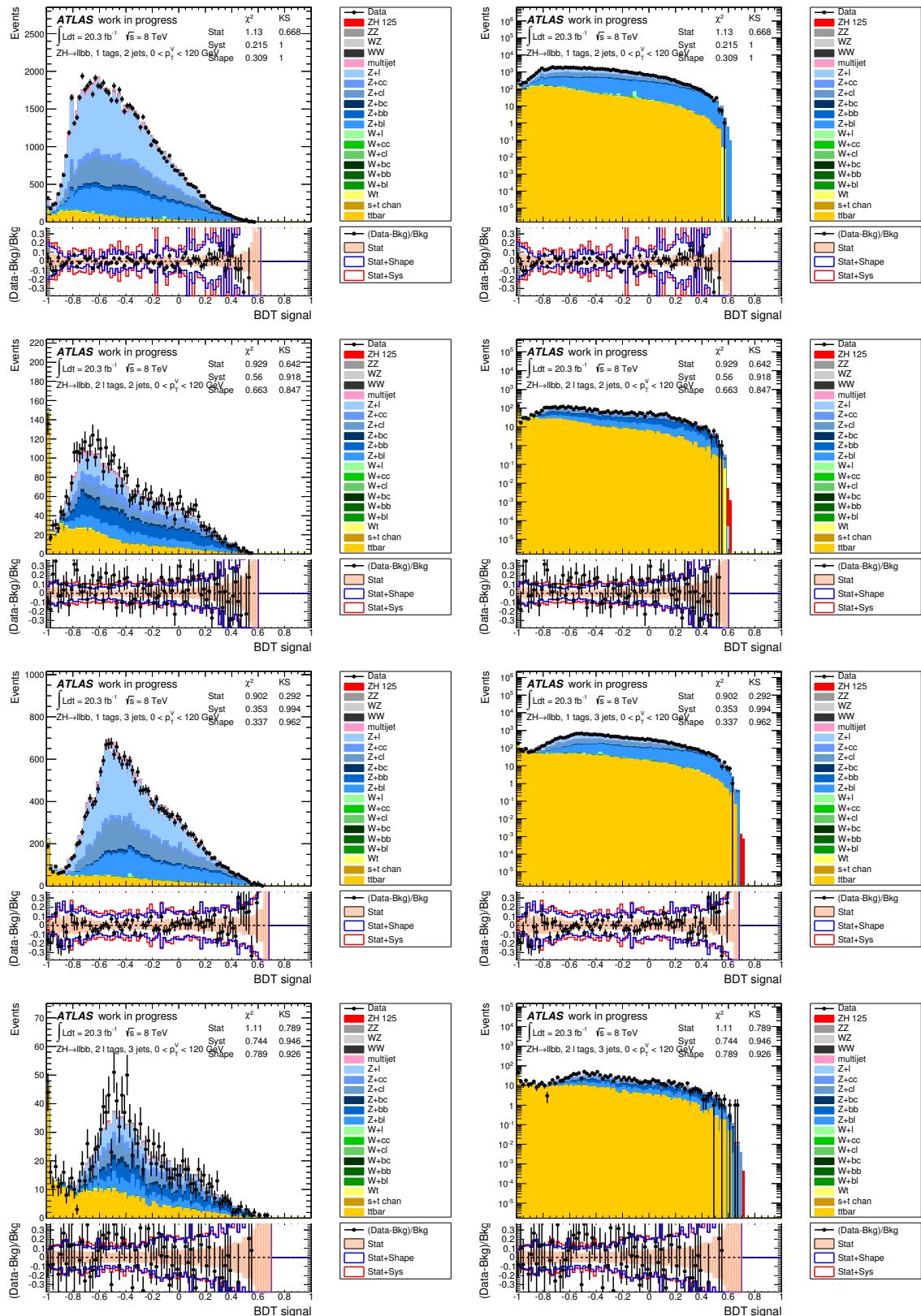


Figure 386: MVA distribution in 2-lepton events with $p_T^W < 120 \text{ GeV}$. Each row contains the same plot with the left (right) in linear (log) scale. From top to bottom: Row 1 - 1 b -tag 2 jet events. Row 2 - 2 LL b -tags 2 jet events. Row 3 - 1 b -tag 3 jet events. Row 4 - 2 LL b -tags 3 jet events. Section 6 details the MVA configuration.

Not reviewed, for internal circulation only

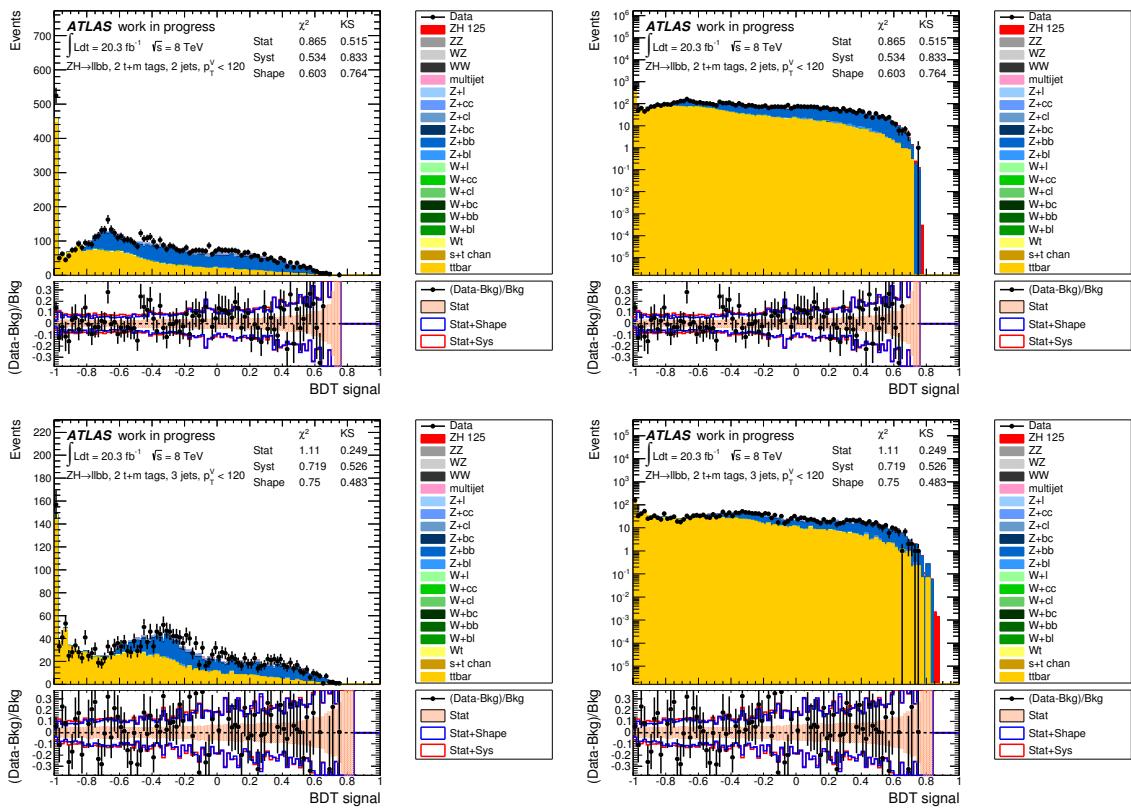


Figure 387: MVA distribution in 2-lepton events with $p_T^W < 120$ GeV. Each row contains the same plot with the left (right) in linear (log) scale. From top to bottom: Row 1 - 2 MM+TT b-tag 2 jet events. Row 2 - 2 MM+TT b-tag 3 jet events. Section 6 details the MVA configuration.

Not reviewed, for internal circulation only

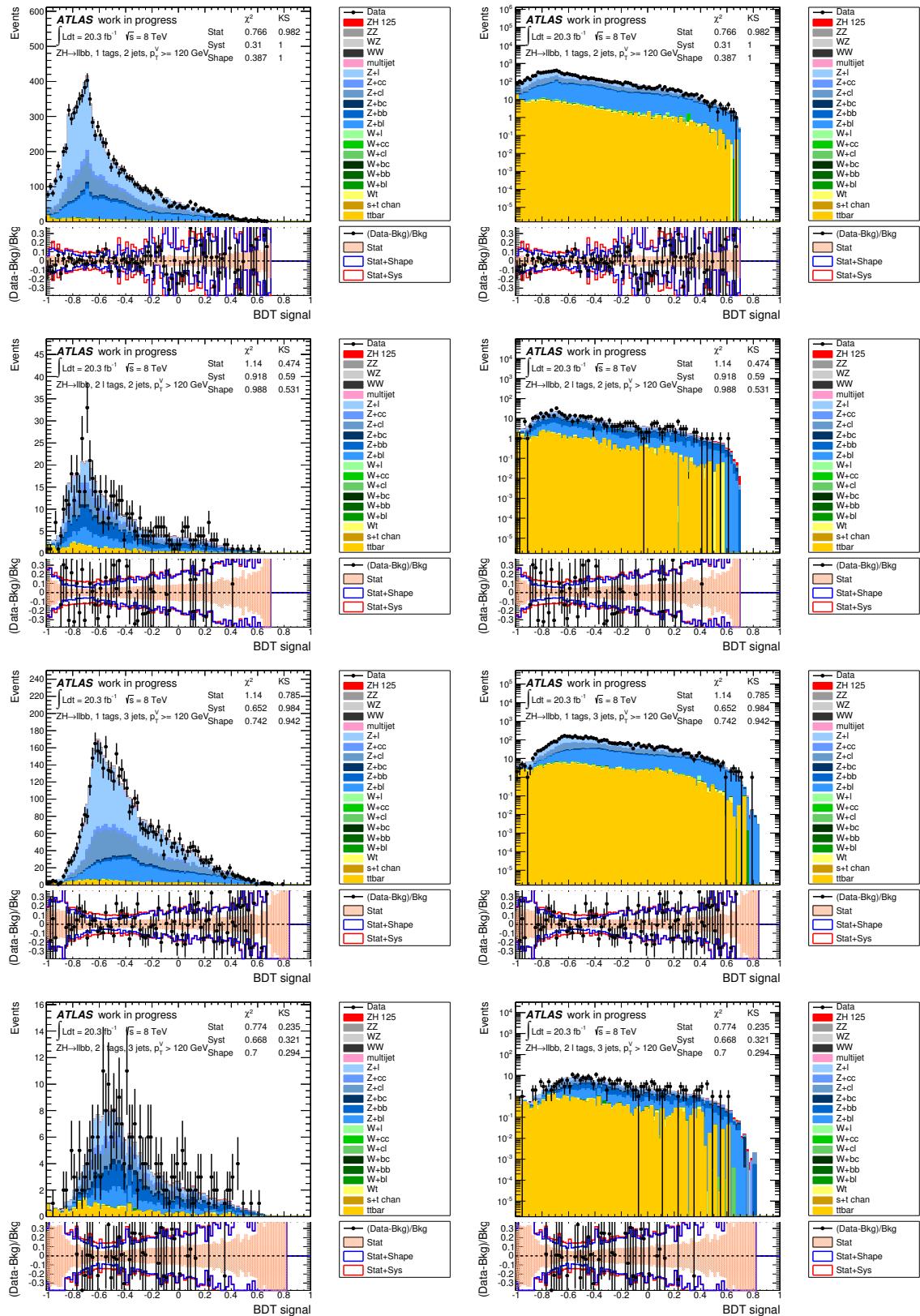


Figure 388: MVA distribution in 2-lepton events with $p_T^W > 120$ GeV. Each row contains the same plot with the left (right) in linear (log) scale. From top to bottom: Row 1 - 1 b -tag 2 jet events. Row 2 - 2 LL b -tags 2 jet events. Row 3 - 1 b -tag 3 jet events. Row 4 - 2 LL b -tags 3 jet events. Section 6 details the MVA configuration.

Not reviewed, for internal circulation only

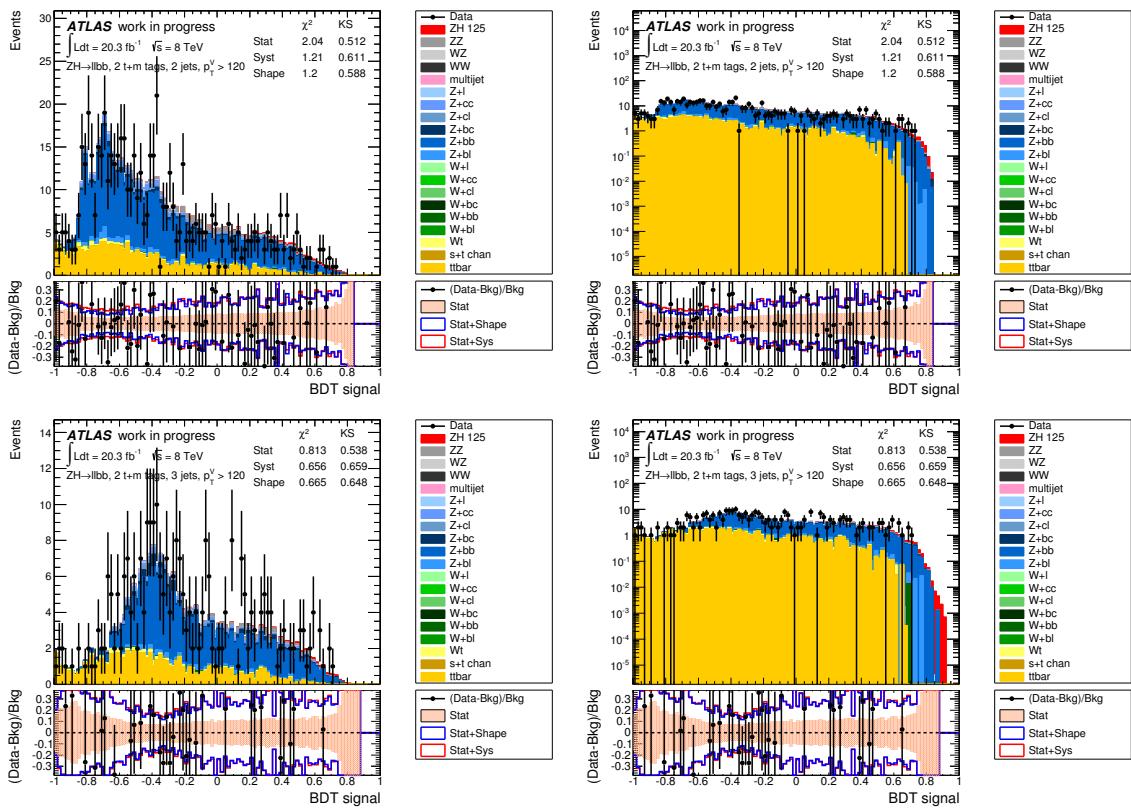


Figure 389: MVA distribution in 2-lepton events with $p_T^W > 120$ GeV. Each row contains the same plot with the left (right) in linear (log) scale. From top to bottom: Row 1 - 2 MM+TT b-tag 2 jet events. Row 2 - 2 MM+TT b-tag 3 jet events. Section 6 details the MVA configuration.

5004 AE Correlations between MVA Variables: Zero Lepton

5005 This appendix contains correlations between input and output variables of the BDT, defined in Section 6
5006 in the 0-lepton analysis. Note that the 0-lepton selection only included events with $p_T^Z > 120$ GeV in the
5007 MVA analysis. These plots are done by applying the latest scale factors, obtained for the 2 jet region and
5008 the 3 jet region separately, by comparing the event yield before and after the MVA combined fit. They are
5009 summarized in Table 97. Explicitly stated, the theoretical expectation for each background is used for
5010 the given luminosity. All the plots in this section are done with the status-of-art analysis.

Not reviewed, for internal circulation only

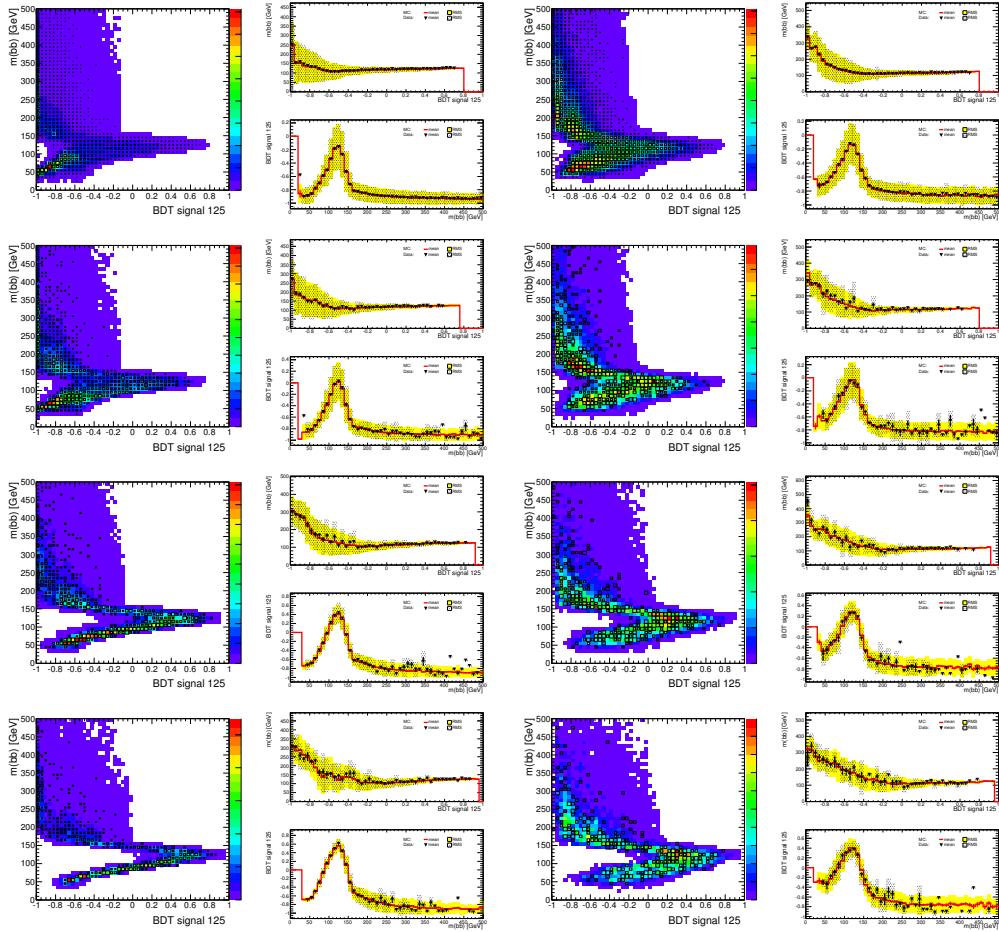


Figure 390: Correlation between BDTinput and output variables used in 0-lepton events ($p_T^Z > 120$ GeV)
Row 1 - Left: 1 tag 2 jets Right: 1 tag 3 jets; Row 2 - Left: 2 LL tag 2 jets Right: 2 LL tag 3 jets; Row
3 - Left: 2 MM tag 2 jets Right: 2 MM tag 3 jets; Row 4 - Left: 2 TT tag 2 jets Right: 2 TT tag 3 jets.
Section 6.1 details the definition of each variable.

Not reviewed, for internal circulation only

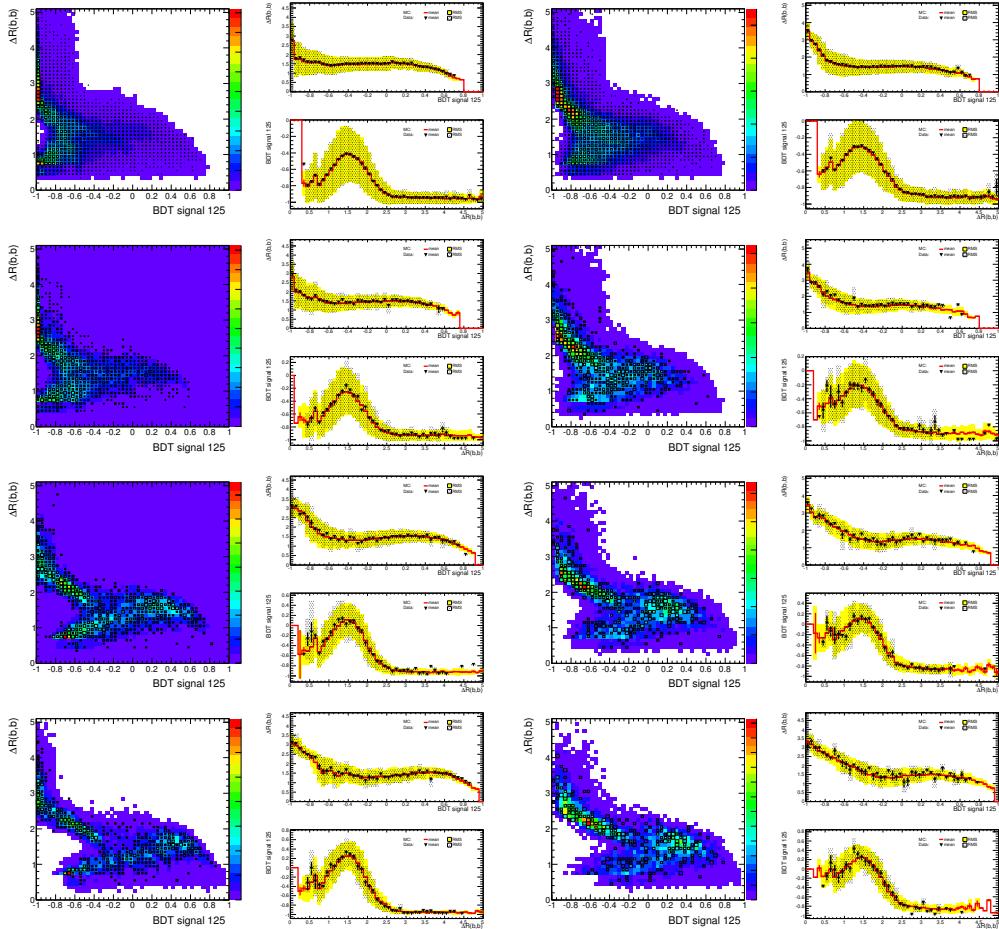


Figure 391: Correlation between BDTinput and output variables used in 0-lepton events ($p_T^Z > 120$ GeV)
Row 1 - Left: 1 tag 2 jets Right: 1 tag 3 jets; Row 2 - Left: 2 LL tag 2 jets Right: 2 LL tag 3 jets; Row
3 - Left: 2 MM tag 2 jets Right: 2 MM tag 3 jets; Row 4 - Left: 2 TT tag 2 jets Right: 2 TT tag 3 jets.
Section 6.1 details the definition of each variable.

Not reviewed, for internal circulation only

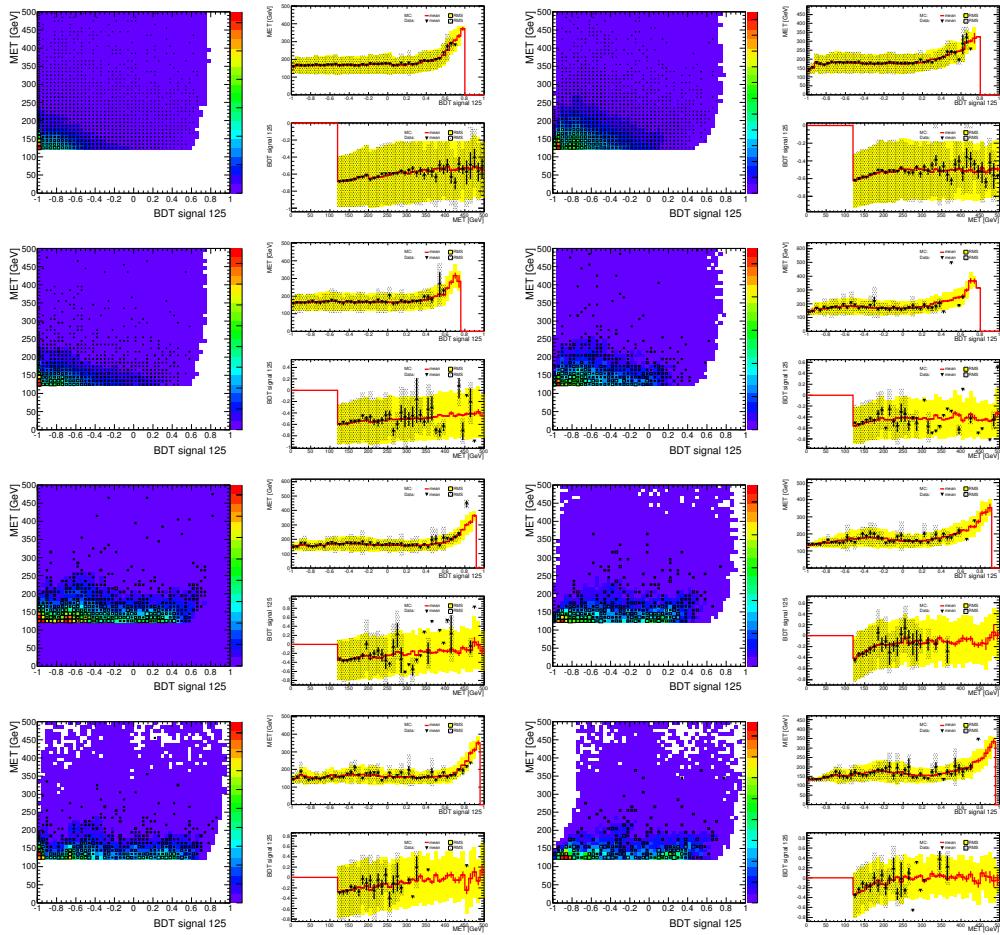


Figure 392: Correlation between `BDTinput` and output variables used in 0-lepton events ($p_T^Z > 120$ GeV)
Row 1 - Left: 1 tag 2 jets Right: 1 tag 3 jets; Row 2 - Left: 2 LL tag 2 jets Right: 2 LL tag 3 jets; Row
3 - Left: 2 MM tag 2 jets Right: 2 MM tag 3 jets; Row 4 - Left: 2 TT tag 2 jets Right: 2 TT tag 3 jets.
Section 6.1 details the definition of each variable.

Not reviewed, for internal circulation only

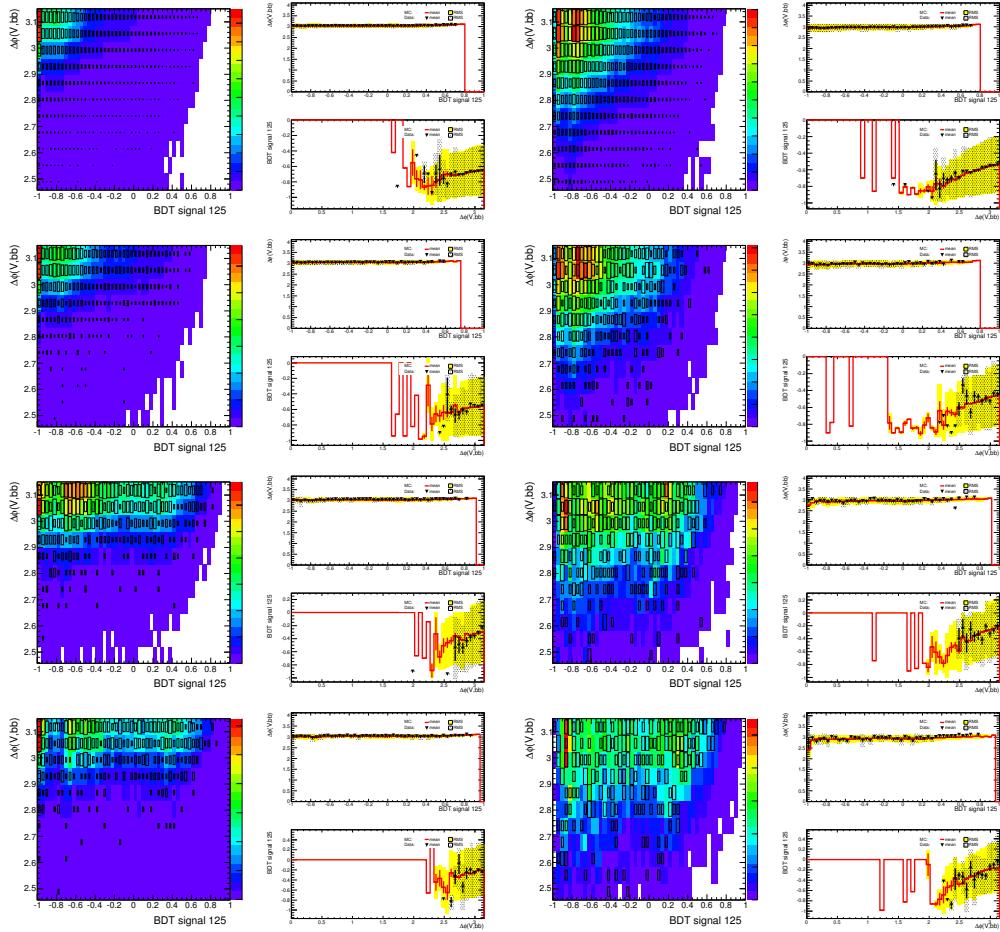


Figure 393: Correlation between BDTinput and output variables used in 0-lepton events ($p_T^Z > 120$ GeV)
Row 1 - Left: 1 tag 2 jets Right: 1 tag 3 jets; Row 2 - Left: 2 LL tag 2 jets Right: 2 LL tag 3 jets; Row 3 - Left: 2 MM tag 2 jets Right: 2 MM tag 3 jets; Row 4 - Left: 2 TT tag 2 jets Right: 2 TT tag 3 jets.
Section 6.1 details the definition of each variable.

Not reviewed, for internal circulation only

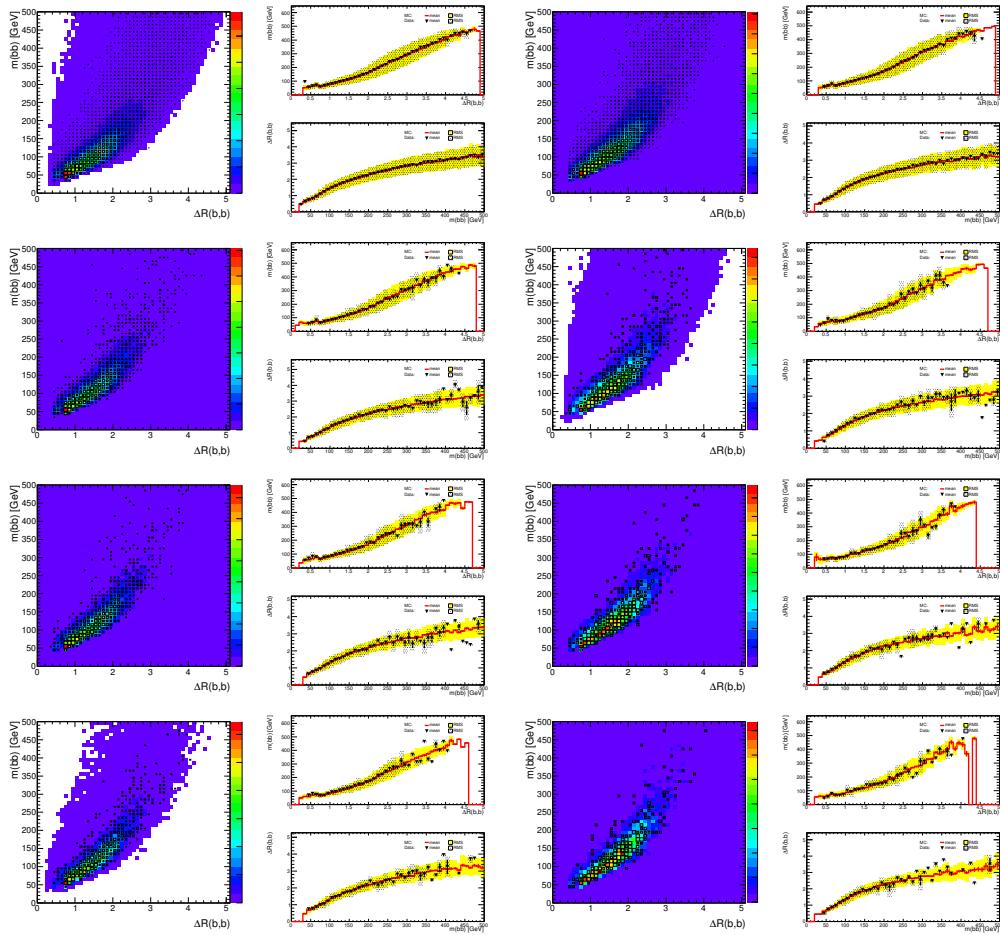


Figure 394: Correlation between BDTinput and output variables used in 0-lepton events ($p_T^Z > 120$ GeV)
Row 1 - Left: 1 tag 2 jets Right: 1 tag 3 jets; Row 2 - Left: 2 LL tag 2 jets Right: 2 LL tag 3 jets; Row
3 - Left: 2 MM tag 2 jets Right: 2 MM tag 3 jets; Row 4 - Left: 2 TT tag 2 jets Right: 2 TT tag 3 jets.
Section 6.1 details the definition of each variable.

Not reviewed, for internal circulation only

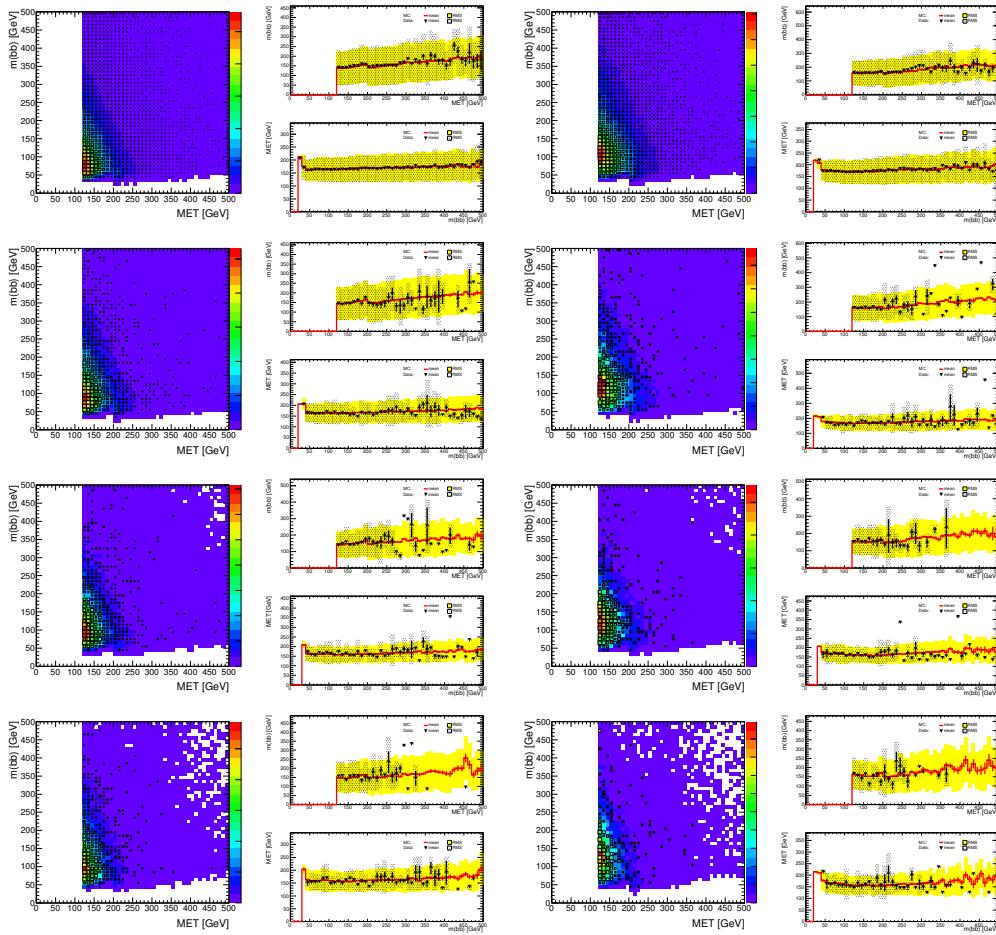


Figure 395: Correlation between BDTinput and output variables used in 0-lepton events ($p_T^Z > 120$ GeV)
Row 1 - Left: 1 tag 2 jets Right: 1 tag 3 jets; Row 2 - Left: 2 LL tag 2 jets Right: 2 LL tag 3 jets; Row
3 - Left: 2 MM tag 2 jets Right: 2 MM tag 3 jets; Row 4 - Left: 2 TT tag 2 jets Right: 2 TT tag 3 jets.
Section 6.1 details the definition of each variable.

Not reviewed, for internal circulation only

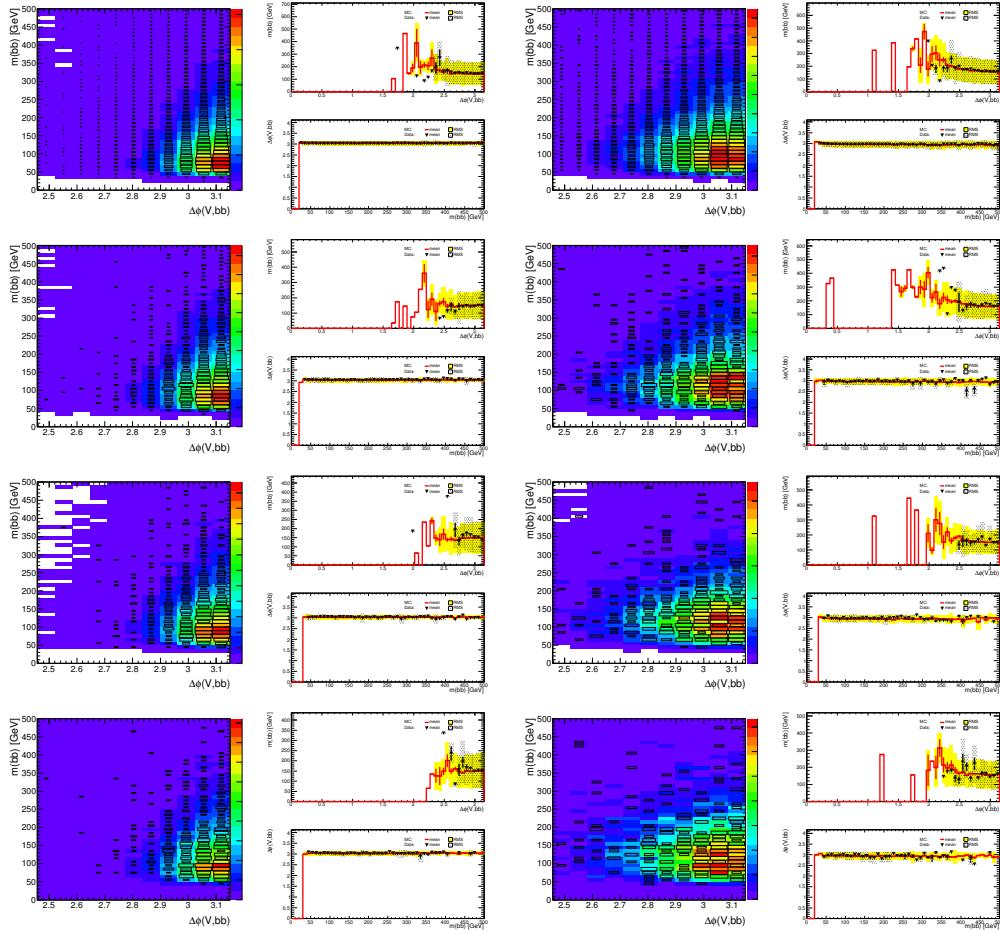


Figure 396: Correlation between BDTinput and output variables used in 0-lepton events ($p_T^Z > 120$ GeV)
Row 1 - Left: 1 tag 2 jets Right: 1 tag 3 jets; Row 2 - Left: 2 LL tag 2 jets Right: 2 LL tag 3 jets; Row 3 - Left: 2 MM tag 2 jets Right: 2 MM tag 3 jets; Row 4 - Left: 2 TT tag 2 jets Right: 2 TT tag 3 jets.
Section 6.1 details the definition of each variable.

Not reviewed, for internal circulation only

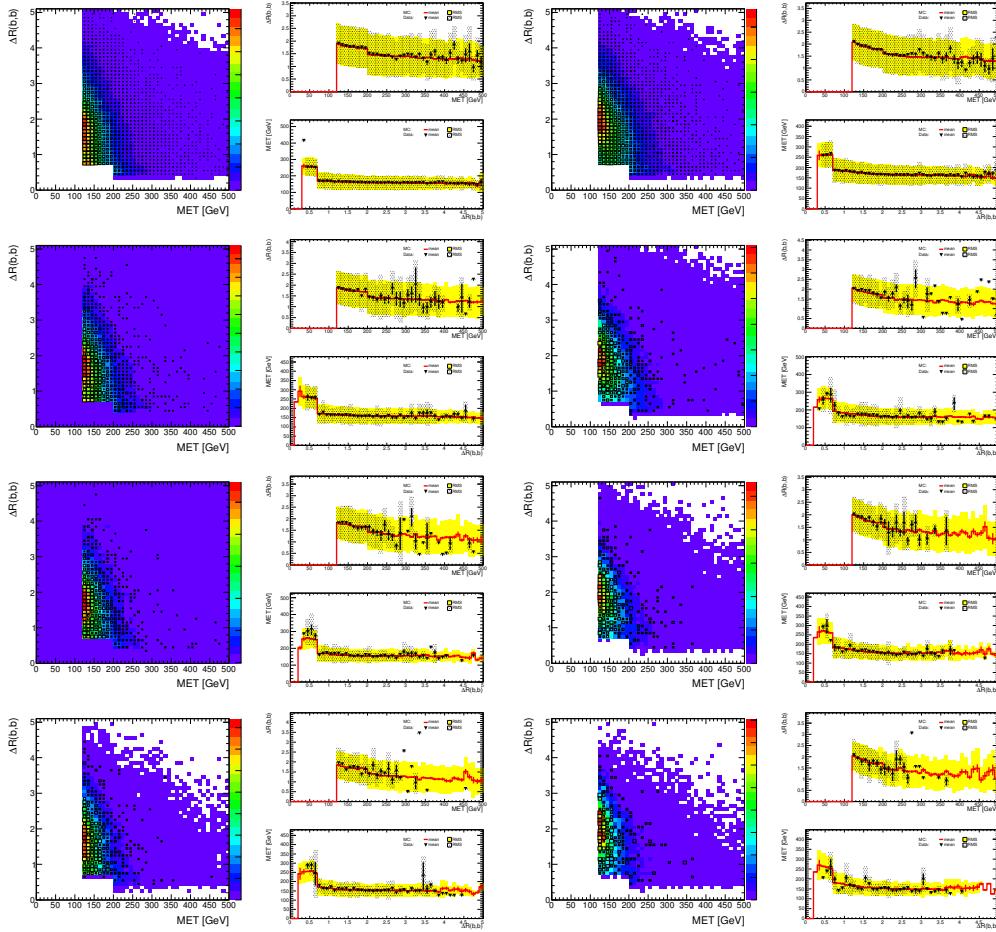


Figure 397: Correlation between BDTinput and output variables used in 0-lepton events ($p_T^Z > 120$ GeV)
Row 1 - Left: 1 tag 2 jets Right: 1 tag 3 jets; Row 2 - Left: 2 LL tag 2 jets Right: 2 LL tag 3 jets; Row
3 - Left: 2 MM tag 2 jets Right: 2 MM tag 3 jets; Row 4 - Left: 2 TT tag 2 jets Right: 2 TT tag 3 jets.
Section 6.1 details the definition of each variable.

Not reviewed, for internal circulation only

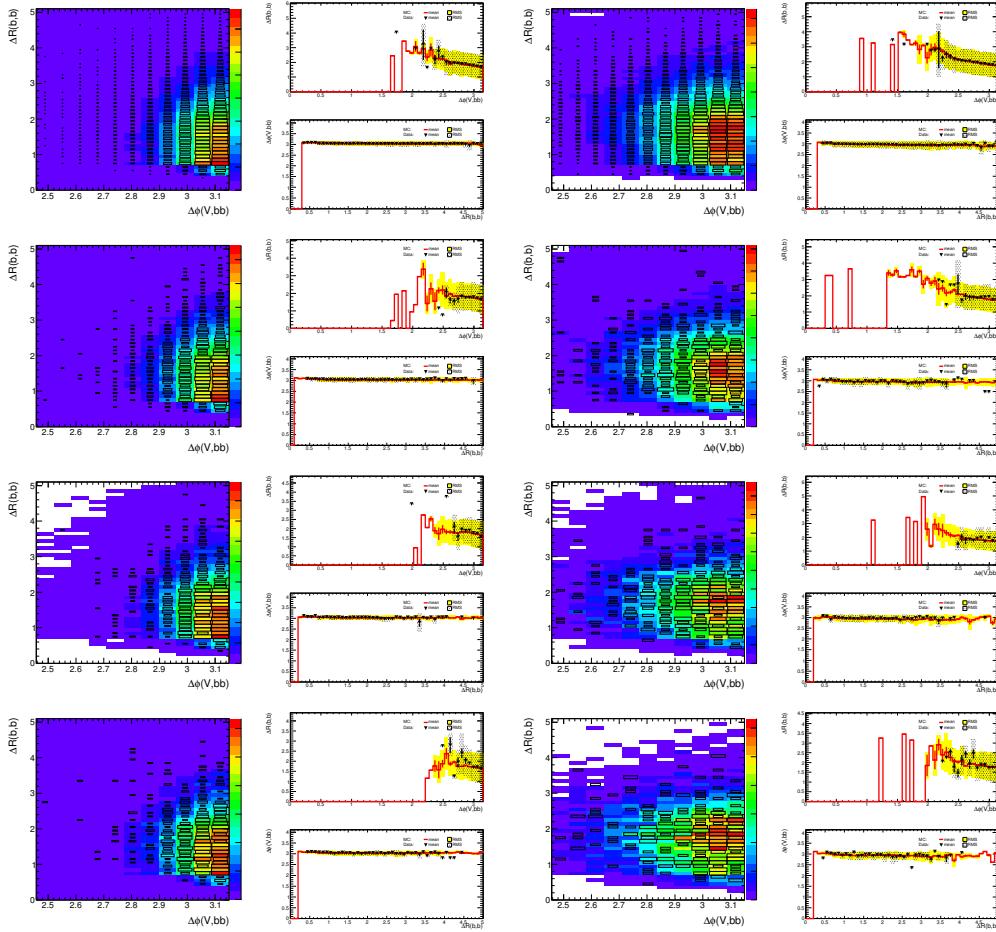


Figure 398: Correlation between BDTinput and output variables used in 0-lepton events ($p_T^Z > 120$ GeV)
Row 1 - Left: 1 tag 2 jets Right: 1 tag 3 jets; Row 2 - Left: 2 LL tag 2 jets Right: 2 LL tag 3 jets; Row 3 - Left: 2 MM tag 2 jets Right: 2 MM tag 3 jets; Row 4 - Left: 2 TT tag 2 jets Right: 2 TT tag 3 jets.
Section 6.1 details the definition of each variable.

Not reviewed, for internal circulation only

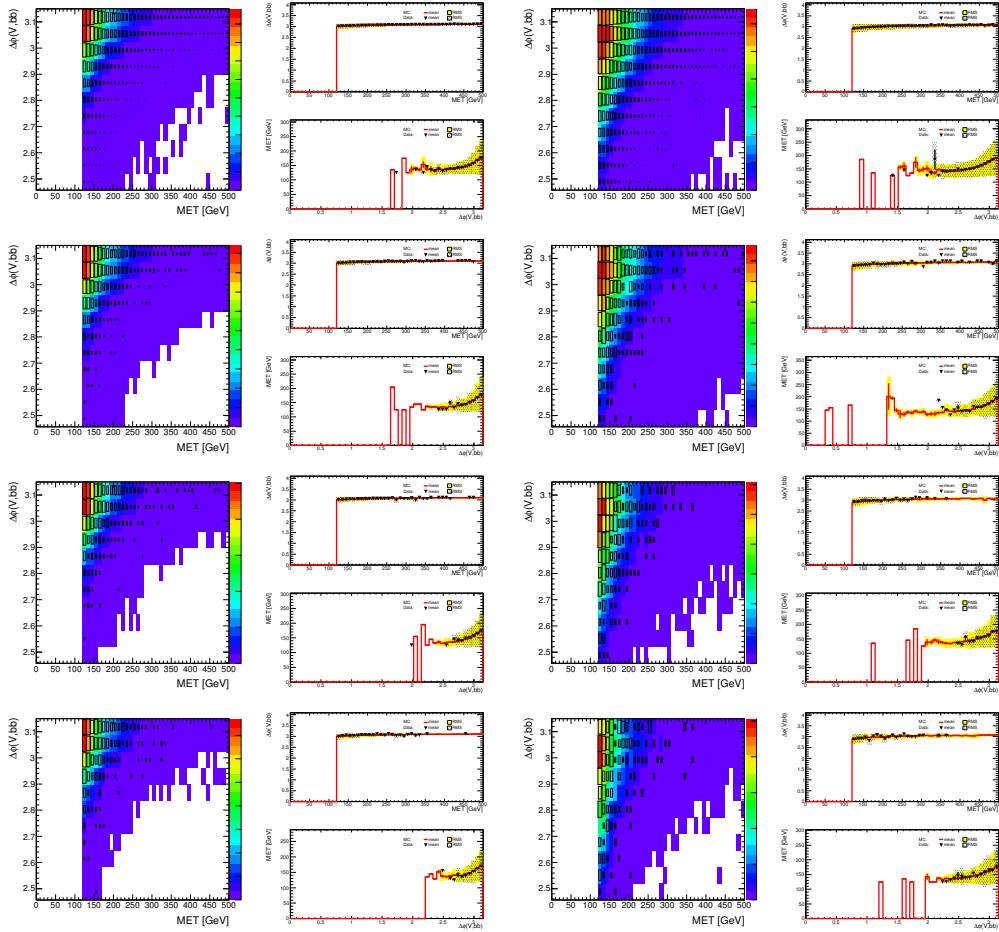


Figure 399: Correlation between BDTinput and output variables used in 0-lepton events ($p_T^Z > 120$ GeV)
Row 1 - Left: 1 tag 2 jets Right: 1 tag 3 jets; Row 2 - Left: 2 LL tag 2 jets Right: 2 LL tag 3 jets; Row
3 - Left: 2 MM tag 2 jets Right: 2 MM tag 3 jets; Row 4 - Left: 2 TT tag 2 jets Right: 2 TT tag 3 jets.
Section 6.1 details the definition of each variable.

5011 AF Correlations between MVA Variables: One Lepton

5012 This appendix contains correlations between input and output variables of the BDT, defined in Section 6
5013 in the 1-lepton analysis. These plots are done by applying the latest scale factors, obtained for the 2 jet
5014 region and the 3 jet region separately, by comparing the event yield before and after the MVA combined
5015 fit. They are summarized in Table 97. Explicitly stated, the theoretical expectation for each background
5016 is used for the given luminosity. All the plots in this section are done with the status-of-art analysis.

Not reviewed, for internal circulation only

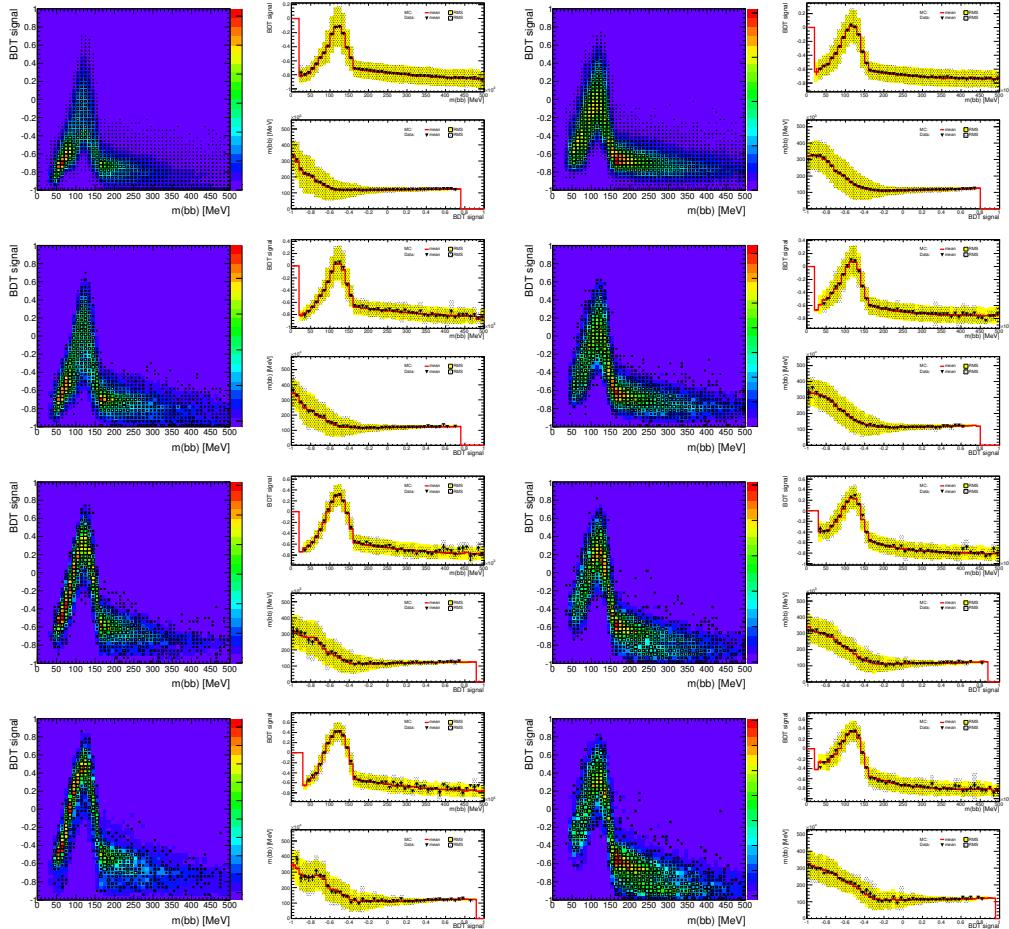


Figure 400: Correlation between BDTinput and output variables used in 0-lepton events ($p_T^W > 120$ GeV)
Row 1 - Left: 1 tag 2 jets Right: 1 tag 3 jets; Row 2 - Left: 2 LL tag 2 jets Right: 2 LL tag 3 jets; Row
3 - Left: 2 MM tag 2 jets Right: 2 MM tag 3 jets; Row 4 - Left: 2 TT tag 2 jets Right: 2 TT tag 3 jets.
Section 6.1 details the definition of each variable.

Not reviewed, for internal circulation only

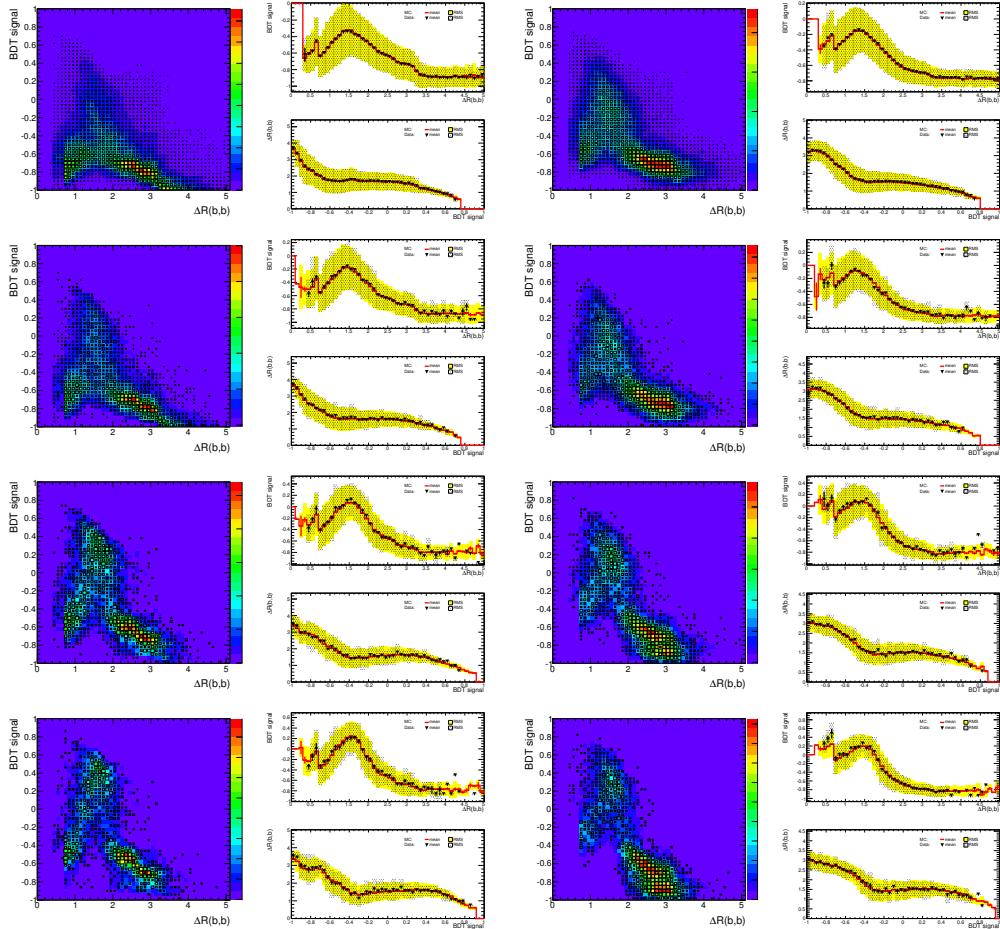


Figure 401: Correlation between $bDTinput$ and output variables used in 0-lepton events ($p_T^W > 120$ GeV)
 Row 1 - Left: 1 tag 2 jets Right: 1 tag 3 jets; Row 2 - Left: 2 LL tag 2 jets Right: 2 LL tag 3 jets; Row
 3 - Left: 2 MM tag 2 jets Right: 2 MM tag 3 jets; Row 4 - Left: 2 TT tag 2 jets Right: 2 TT tag 3 jets.
 Section 6.1 details the definition of each variable.

Not reviewed, for internal circulation only

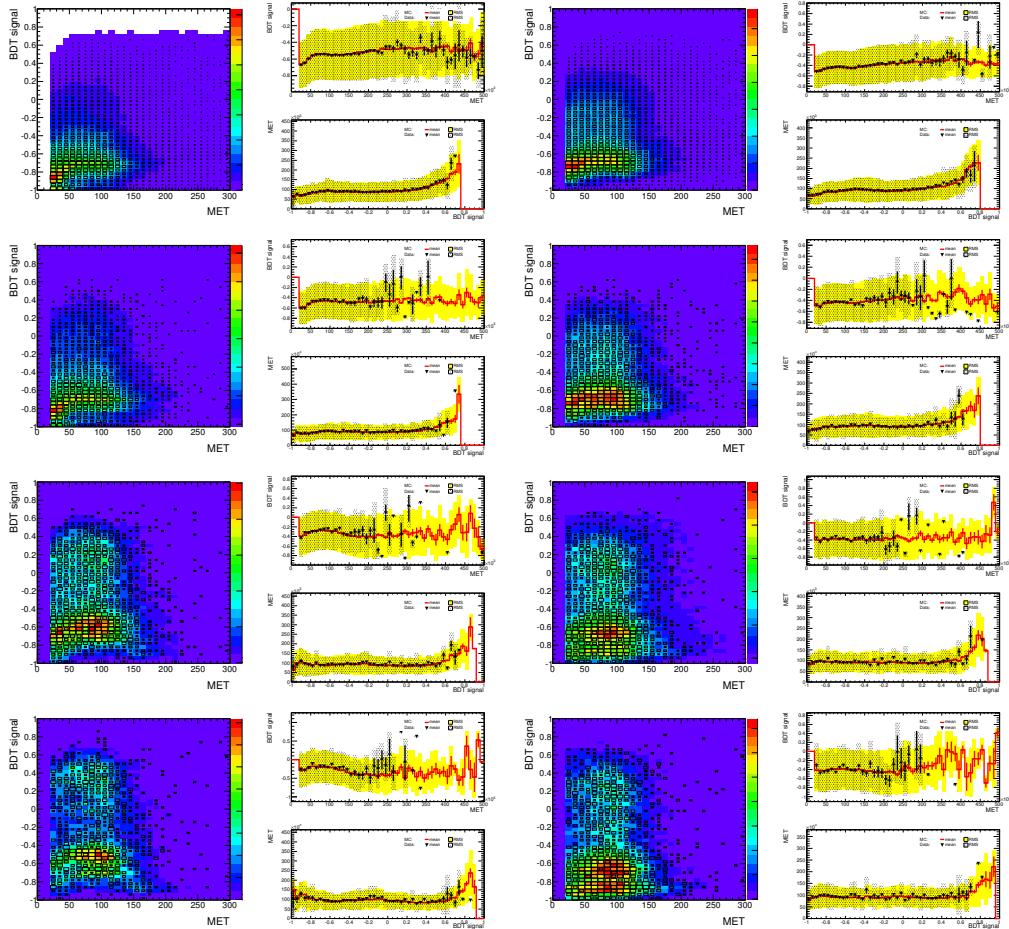


Figure 402: Correlation between BDTinput and output variables used in 0-lepton events ($p_T^W > 120$ GeV)
Row 1 - Left: 1 tag 2 jets Right: 1 tag 3 jets; Row 2 - Left: 2 LL tag 2 jets Right: 2 LL tag 3 jets; Row
3 - Left: 2 MM tag 2 jets Right: 2 MM tag 3 jets; Row 4 - Left: 2 TT tag 2 jets Right: 2 TT tag 3 jets.
Section 6.1 details the definition of each variable.

Not reviewed, for internal circulation only

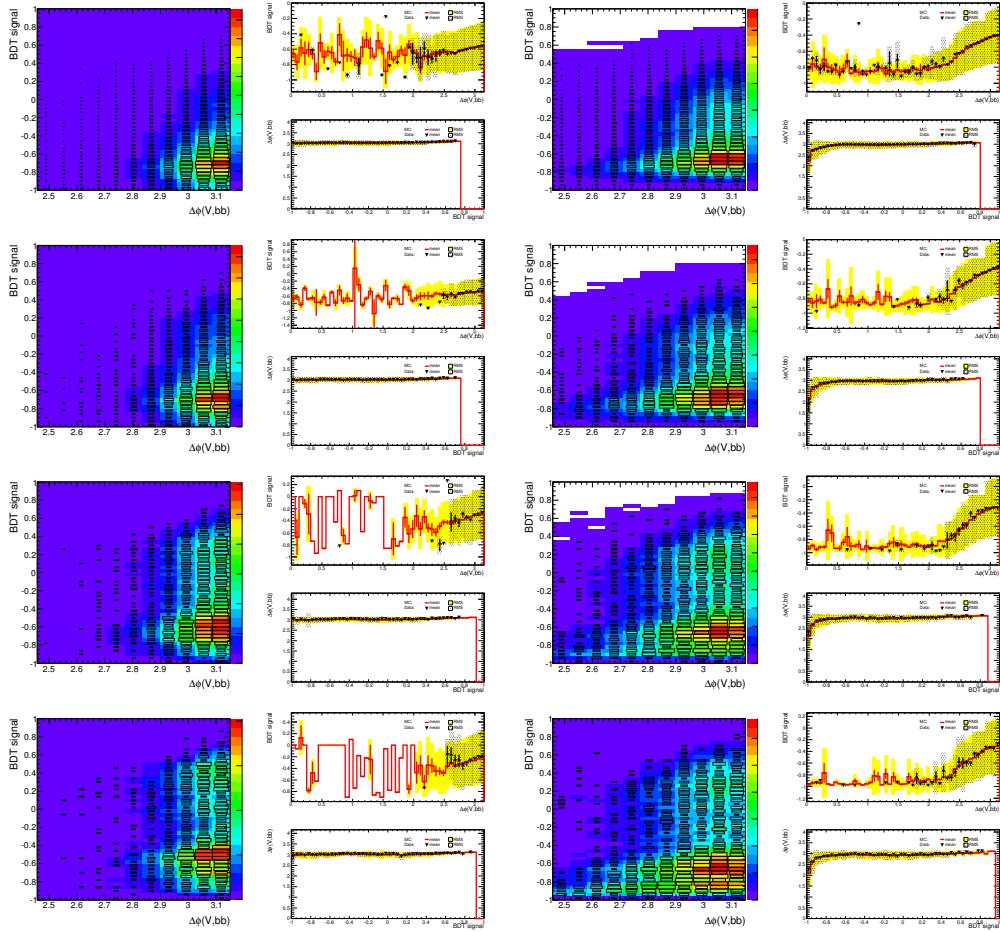


Figure 403: Correlation between BDTinput and output variables used in 0-lepton events ($p_T^W > 120$ GeV)
Row 1 - Left: 1 tag 2 jets Right: 1 tag 3 jets; Row 2 - Left: 2 LL tag 2 jets Right: 2 LL tag 3 jets; Row
3 - Left: 2 MM tag 2 jets Right: 2 MM tag 3 jets; Row 4 - Left: 2 TT tag 2 jets Right: 2 TT tag 3 jets.
Section 6.1 details the definition of each variable.

Not reviewed, for internal circulation only

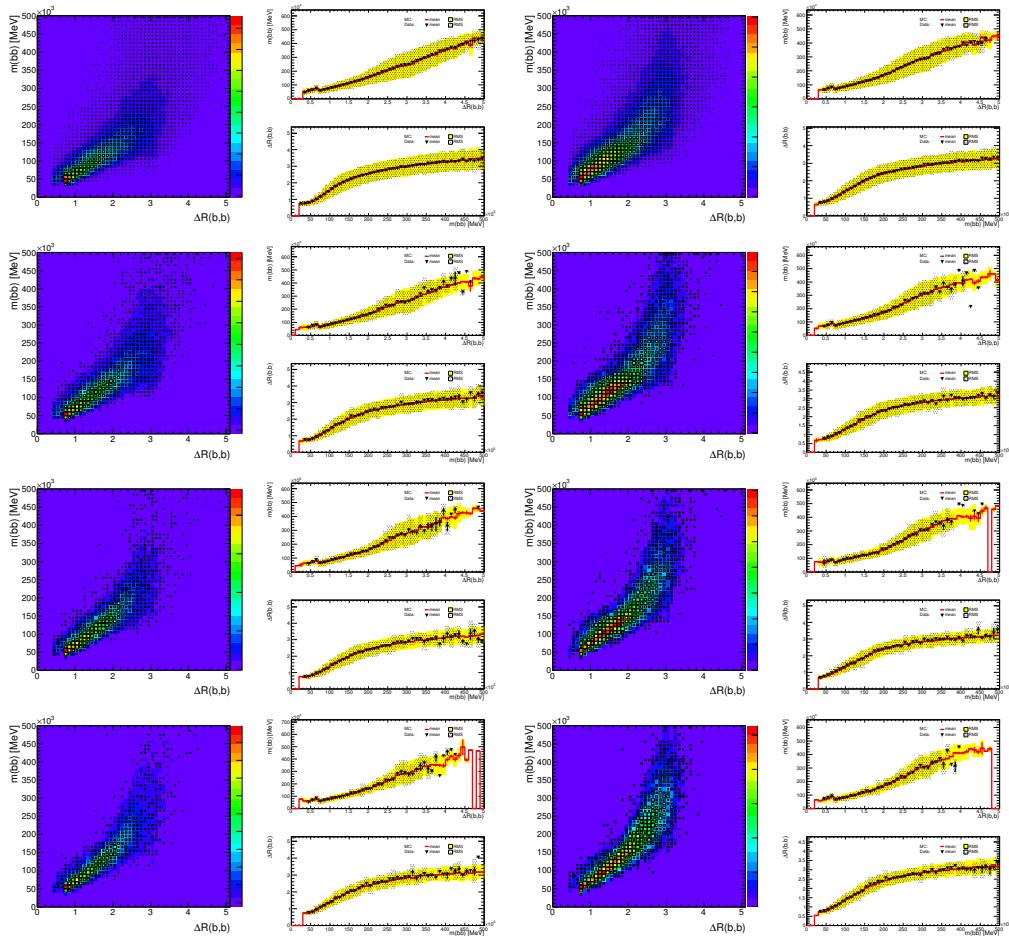


Figure 404: Correlation between bdtinput and output variables used in 0-lepton events ($p_T^W > 120$ GeV)
Row 1 - Left: 1 tag 2 jets Right: 1 tag 3 jets; Row 2 - Left: 2 LL tag 2 jets Right: 2 LL tag 3 jets; Row 3 - Left: 2 MM tag 2 jets Right: 2 MM tag 3 jets; Row 4 - Left: 2 TT tag 2 jets Right: 2 TT tag 3 jets.
Section 6.1 details the definition of each variable.

Not reviewed, for internal circulation only

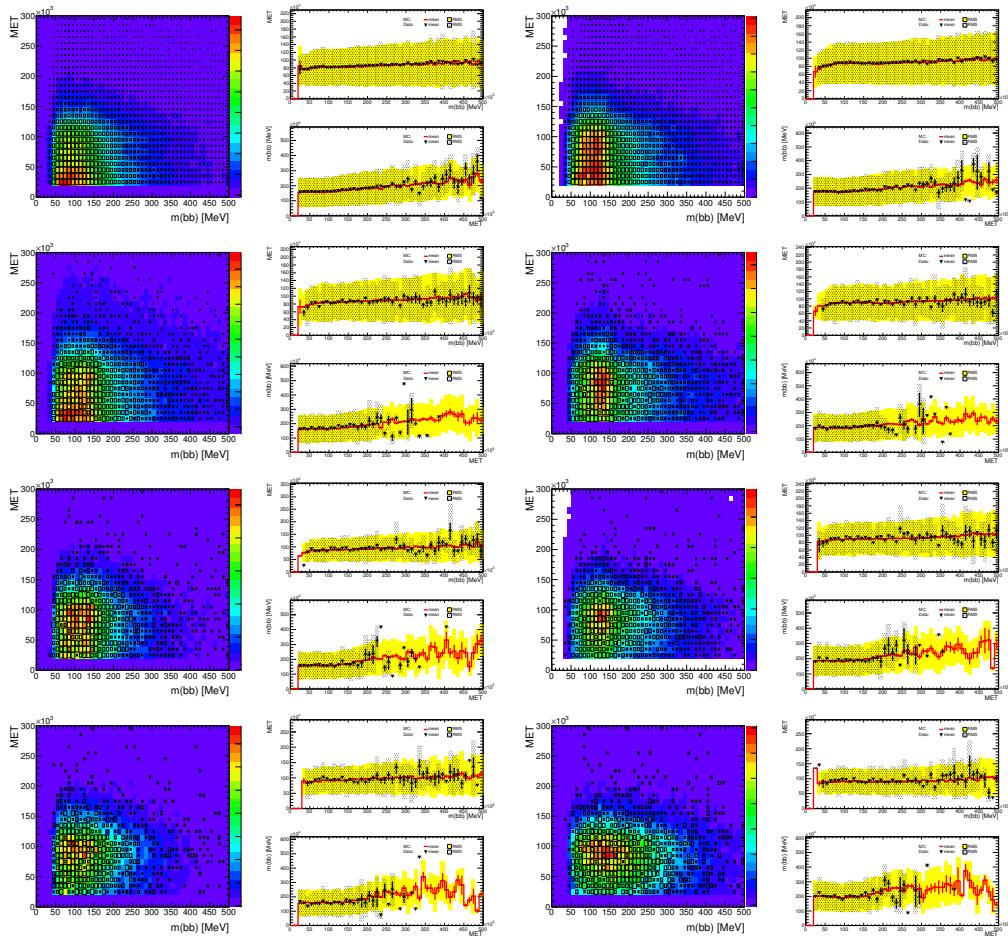


Figure 405: Correlation between bdtinput and output variables used in 0-lepton events ($p_T^W > 120$ GeV)
Row 1 - Left: 1 tag 2 jets Right: 1 tag 3 jets; Row 2 - Left: 2 LL tag 2 jets Right: 2 LL tag 3 jets; Row
3 - Left: 2 MM tag 2 jets Right: 2 MM tag 3 jets; Row 4 - Left: 2 TT tag 2 jets Right: 2 TT tag 3 jets.
Section 6.1 details the definition of each variable.

Not reviewed, for internal circulation only

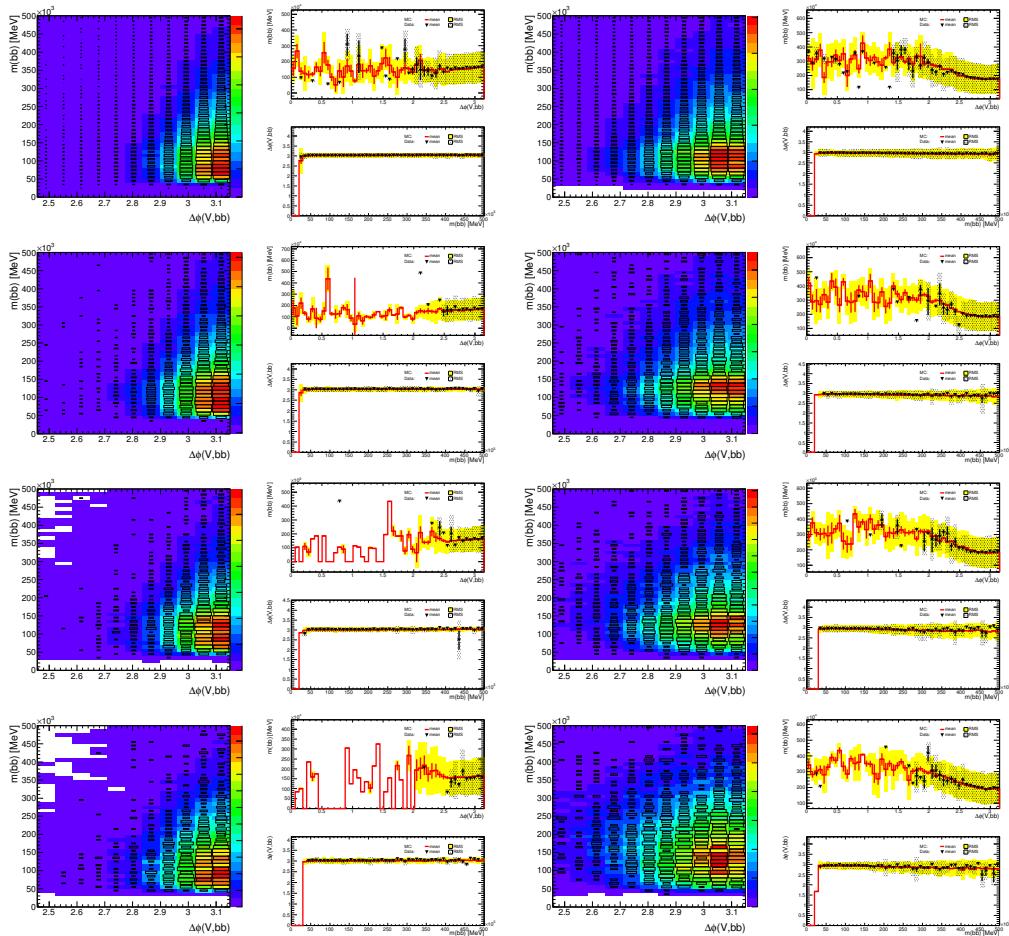


Figure 406: Correlation between bdtinput and output variables used in 0-lepton events ($p_T^W > 120$ GeV)
Row 1 - Left: 1 tag 2 jets Right: 1 tag 3 jets; Row 2 - Left: 2 LL tag 2 jets Right: 2 LL tag 3 jets; Row
3 - Left: 2 MM tag 2 jets Right: 2 MM tag 3 jets; Row 4 - Left: 2 TT tag 2 jets Right: 2 TT tag 3 jets.
Section 6.1 details the definition of each variable.

Not reviewed, for internal circulation only

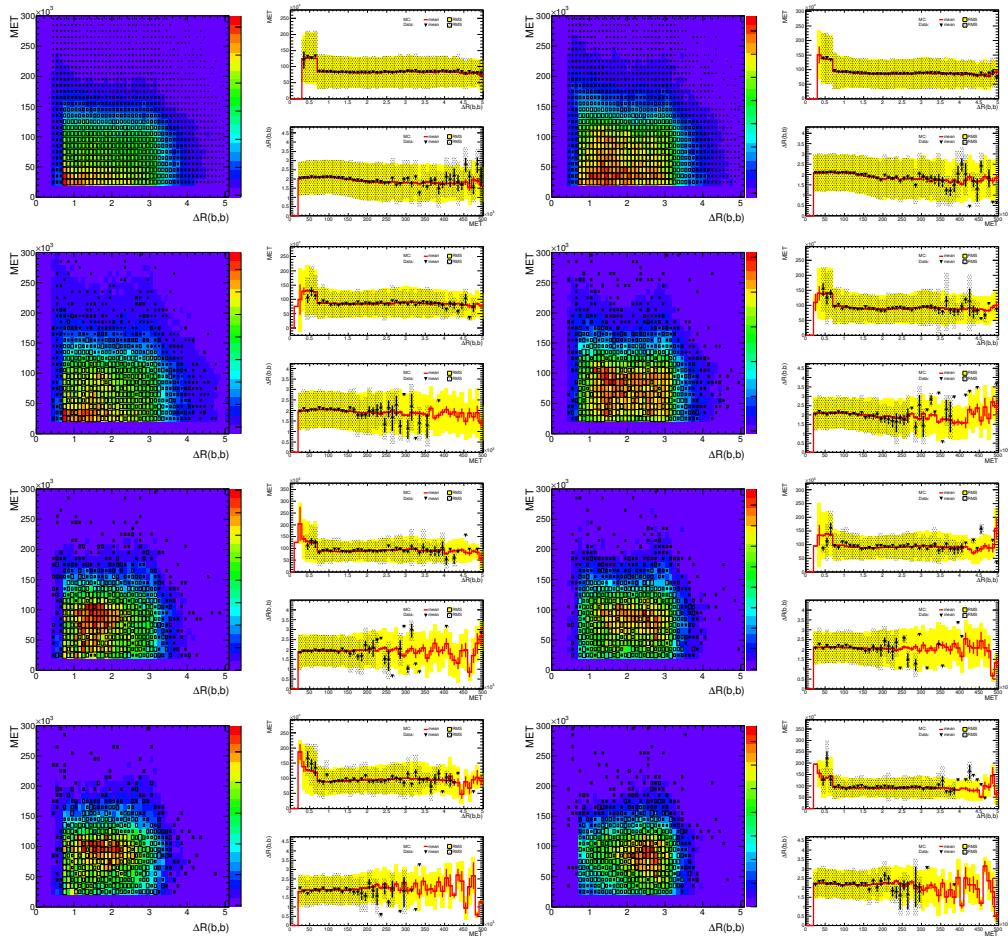


Figure 407: Correlation between bdtinput and output variables used in 0-lepton events ($p_T^W > 120$ GeV)
Row 1 - Left: 1 tag 2 jets Right: 1 tag 3 jets; Row 2 - Left: 2 LL tag 2 jets Right: 2 LL tag 3 jets; Row 3 - Left: 2 MM tag 2 jets Right: 2 MM tag 3 jets; Row 4 - Left: 2 TT tag 2 jets Right: 2 TT tag 3 jets.
Section 6.1 details the definition of each variable.

Not reviewed, for internal circulation only

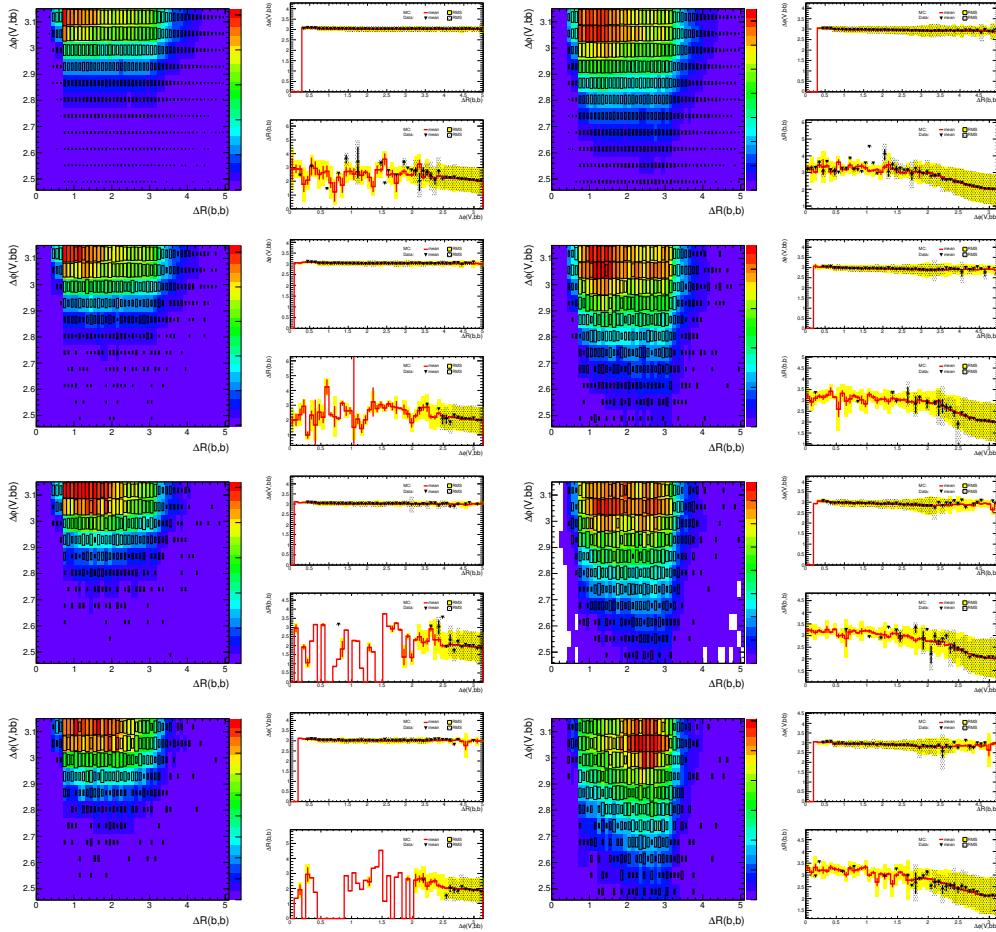


Figure 408: Correlation between bdtinput and output variables used in 0-lepton events ($p_T^W > 120$ GeV)
Row 1 - Left: 1 tag 2 jets Right: 1 tag 3 jets; Row 2 - Left: 2 LL tag 2 jets Right: 2 LL tag 3 jets; Row 3 - Left: 2 MM tag 2 jets Right: 2 MM tag 3 jets; Row 4 - Left: 2 TT tag 2 jets Right: 2 TT tag 3 jets.
Section 6.1 details the definition of each variable.

Not reviewed, for internal circulation only

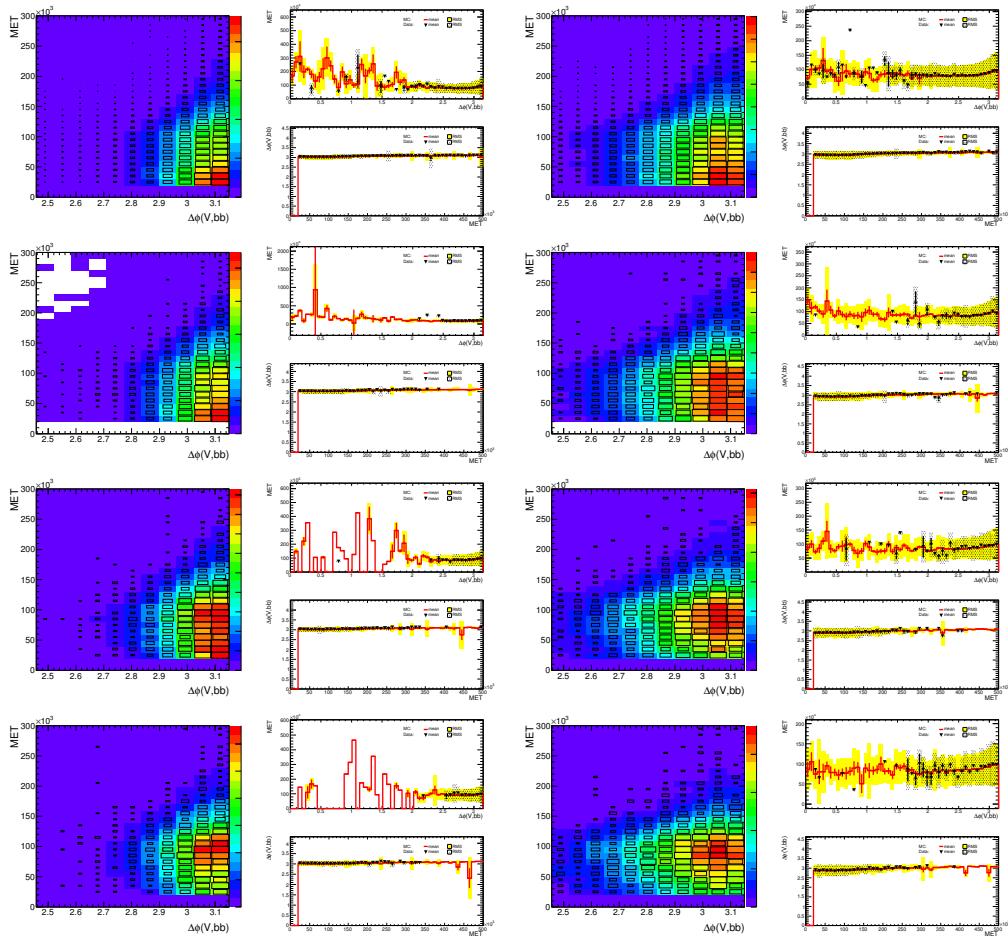


Figure 409: Correlation between bdtinput and output variables used in 0-lepton events ($p_T^W > 120$ GeV)
Row 1 - Left: 1 tag 2 jets Right: 1 tag 3 jets; Row 2 - Left: 2 LL tag 2 jets Right: 2 LL tag 3 jets; Row 3 - Left: 2 MM tag 2 jets Right: 2 MM tag 3 jets; Row 4 - Left: 2 TT tag 2 jets Right: 2 TT tag 3 jets.
Section 6.1 details the definition of each variable.

Not reviewed, for internal circulation only

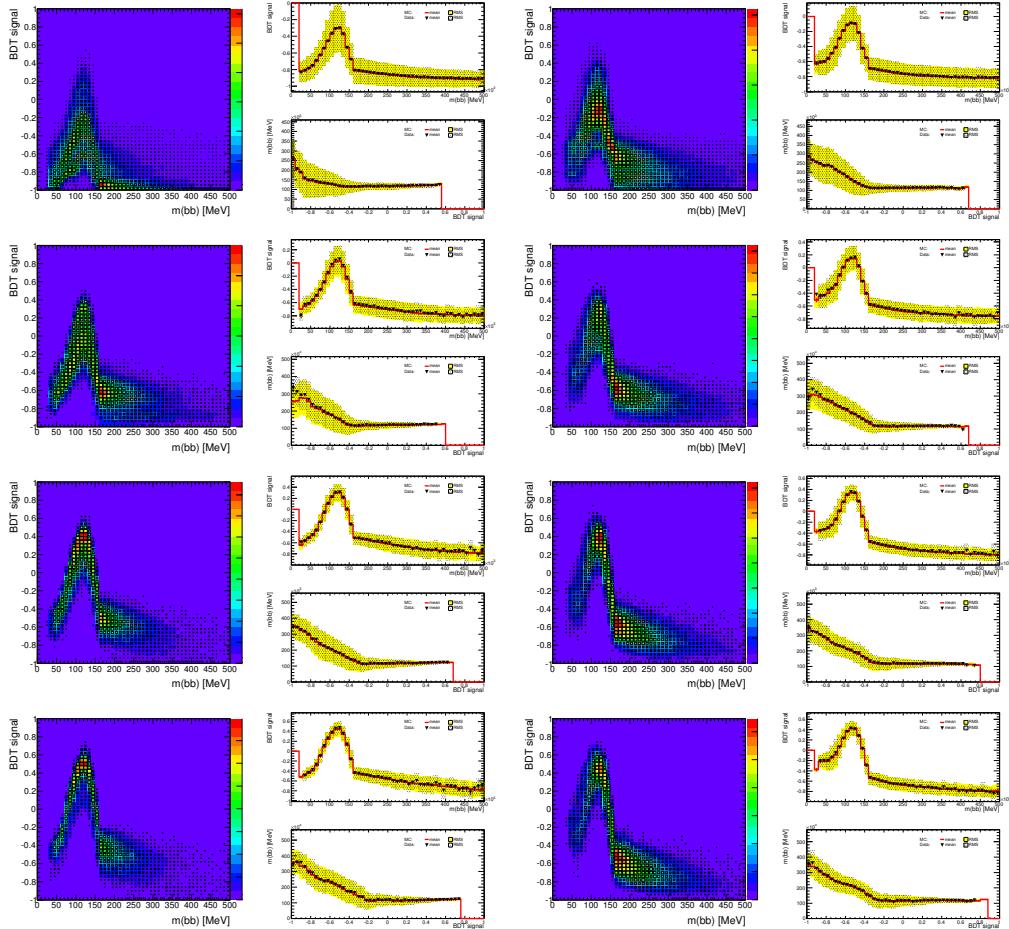


Figure 410: Correlation between BDTinput and output variables used in 0-lepton events ($p_T^W < 120$ GeV)
Row 1 - Left: 1 tag 2 jets Right: 1 tag 3 jets; Row 2 - Left: 2 LL tag 2 jets Right: 2 LL tag 3 jets; Row 3 - Left: 2 MM tag 2 jets Right: 2 MM tag 3 jets; Row 4 - Left: 2 TT tag 2 jets Right: 2 TT tag 3 jets.
Section 6.1 details the definition of each variable.

Not reviewed, for internal circulation only

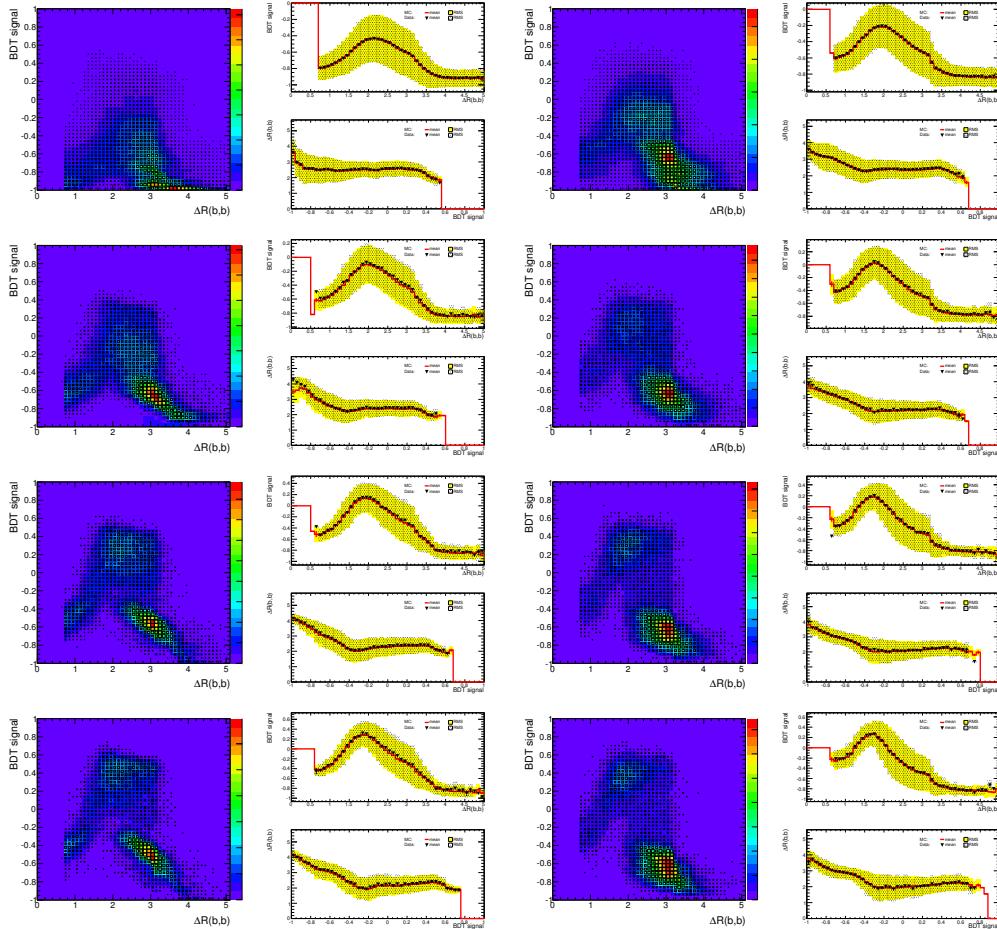


Figure 411: Correlation between BDTinput and output variables used in 0-lepton events ($p_T^W < 120$ GeV)
Row 1 - Left: 1 tag 2 jets Right: 1 tag 3 jets; Row 2 - Left: 2 LL tag 2 jets Right: 2 LL tag 3 jets; Row
3 - Left: 2 MM tag 2 jets Right: 2 MM tag 3 jets; Row 4 - Left: 2 TT tag 2 jets Right: 2 TT tag 3 jets.
Section 6.1 details the definition of each variable.

Not reviewed, for internal circulation only

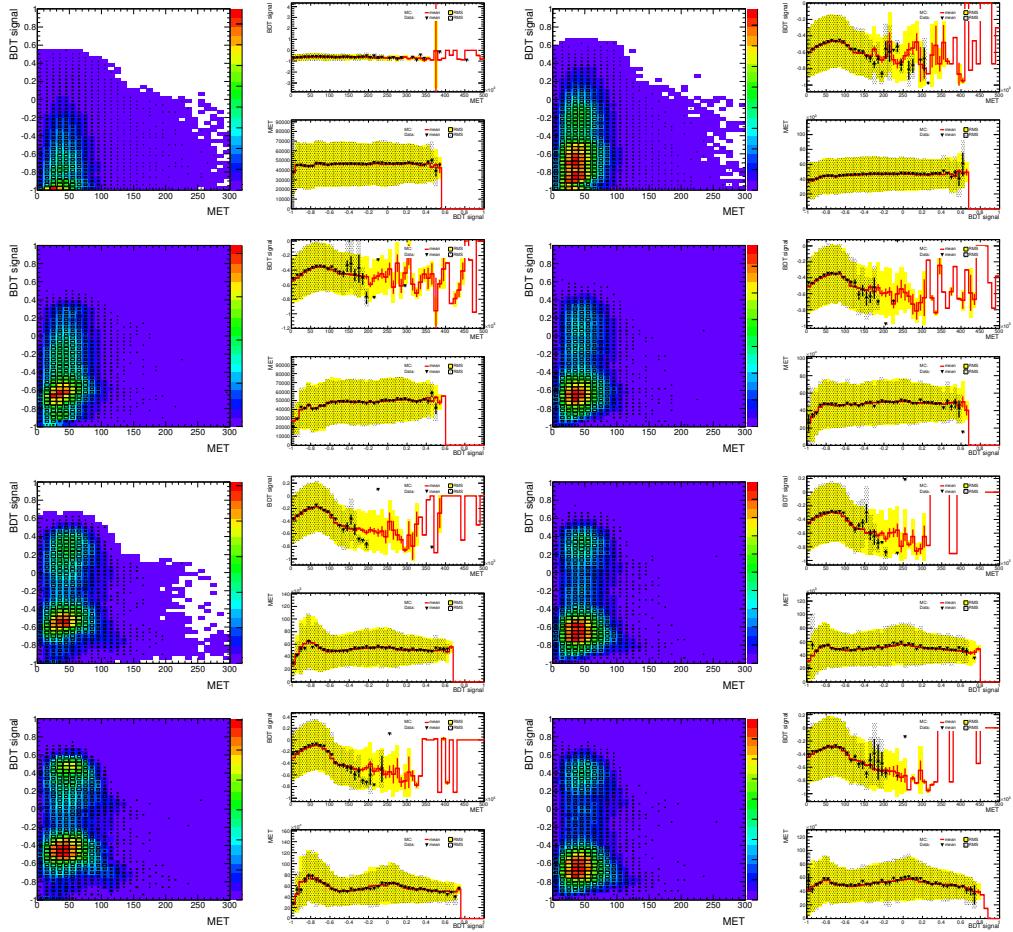


Figure 412: Correlation between BDTinput and output variables used in 0-lepton events ($p_T^W < 120$ GeV)
Row 1 - Left: 1 tag 2 jets Right: 1 tag 3 jets; Row 2 - Left: 2 LL tag 2 jets Right: 2 LL tag 3 jets; Row
3 - Left: 2 MM tag 2 jets Right: 2 MM tag 3 jets; Row 4 - Left: 2 TT tag 2 jets Right: 2 TT tag 3 jets.
Section 6.1 details the definition of each variable.

Not reviewed, for internal circulation only

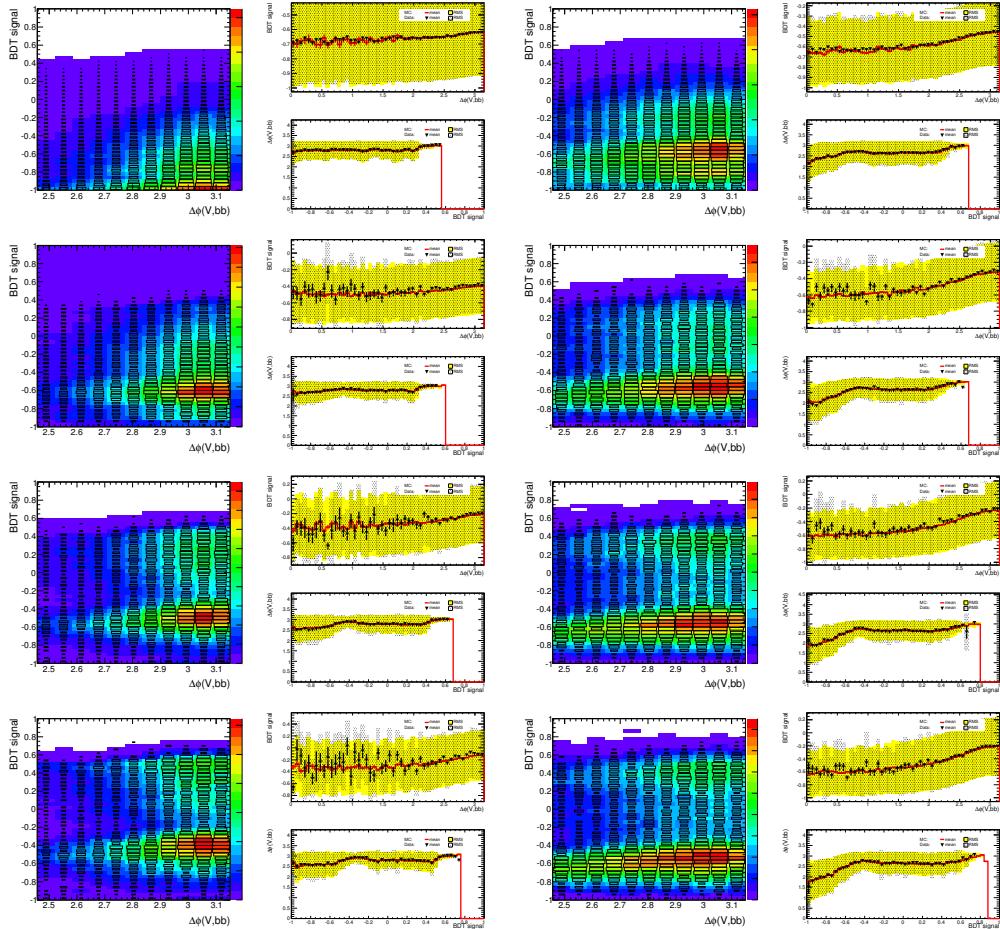


Figure 413: Correlation between BDTinput and output variables used in 0-lepton events ($p_T^W < 120$ GeV)
Row 1 - Left: 1 tag 2 jets Right: 1 tag 3 jets; Row 2 - Left: 2 LL tag 2 jets Right: 2 LL tag 3 jets; Row
3 - Left: 2 MM tag 2 jets Right: 2 MM tag 3 jets; Row 4 - Left: 2 TT tag 2 jets Right: 2 TT tag 3 jets.
Section 6.1 details the definition of each variable.

Not reviewed, for internal circulation only

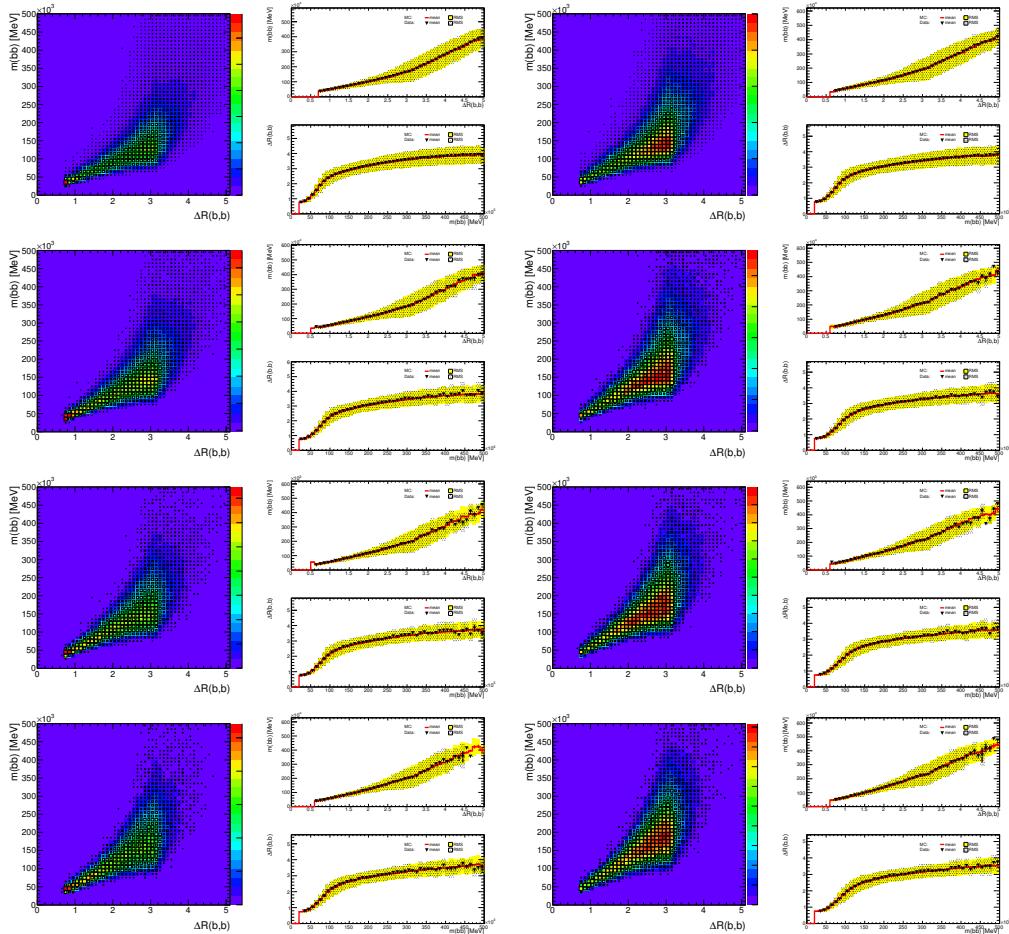


Figure 414: Correlation between bdtinput and output variables used in 0-lepton events ($p_T^W < 120$ GeV)
Row 1 - Left: 1 tag 2 jets Right: 1 tag 3 jets; Row 2 - Left: 2 LL tag 2 jets Right: 2 LL tag 3 jets;
Row 3 - Left: 2 MM tag 2 jets Right: 2 MM tag 3 jets; Row 4 - Left: 2 TT tag 2 jets Right: 2 TT tag 3 jets.
Section 6.1 details the definition of each variable.

Not reviewed, for internal circulation only

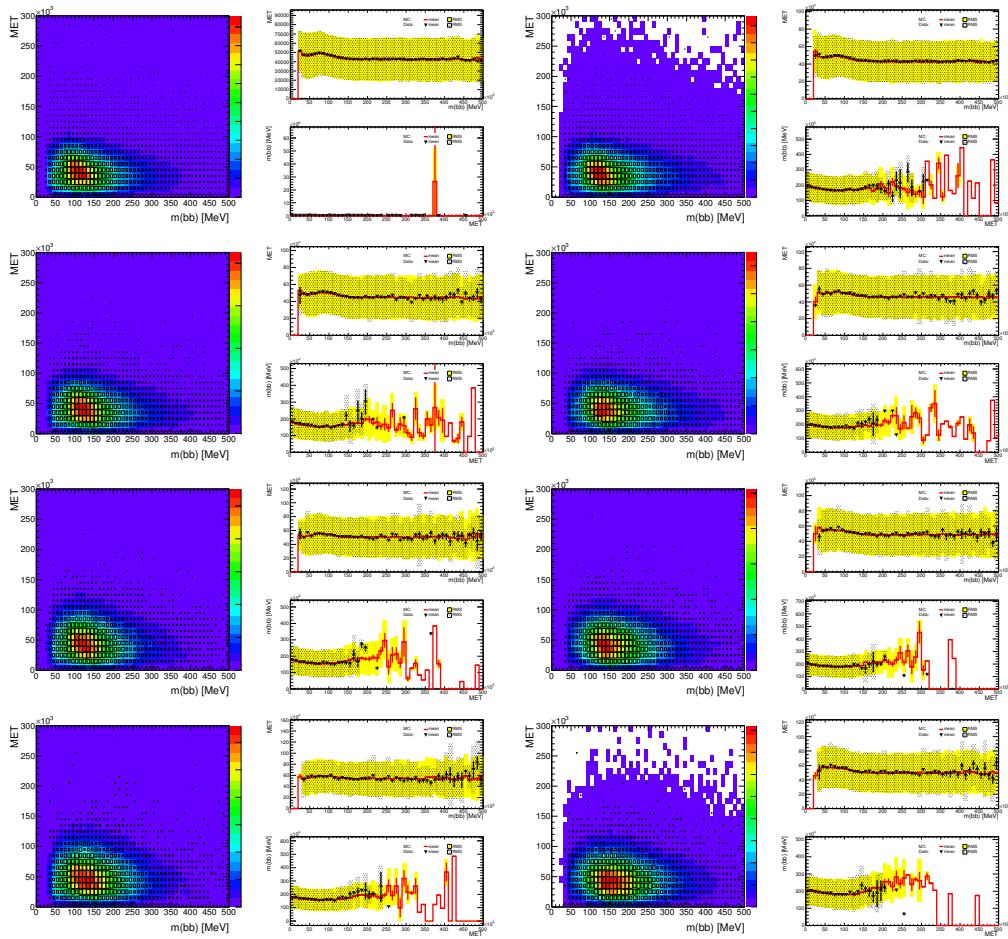


Figure 415: Correlation between bdtinput and output variables used in 0-lepton events ($p_T^W < 120$ GeV)
Row 1 - Left: 1 tag 2 jets Right: 1 tag 3 jets; Row 2 - Left: 2 LL tag 2 jets Right: 2 LL tag 3 jets; Row
3 - Left: 2 MM tag 2 jets Right: 2 MM tag 3 jets; Row 4 - Left: 2 TT tag 2 jets Right: 2 TT tag 3 jets.
Section 6.1 details the definition of each variable.

Not reviewed, for internal circulation only

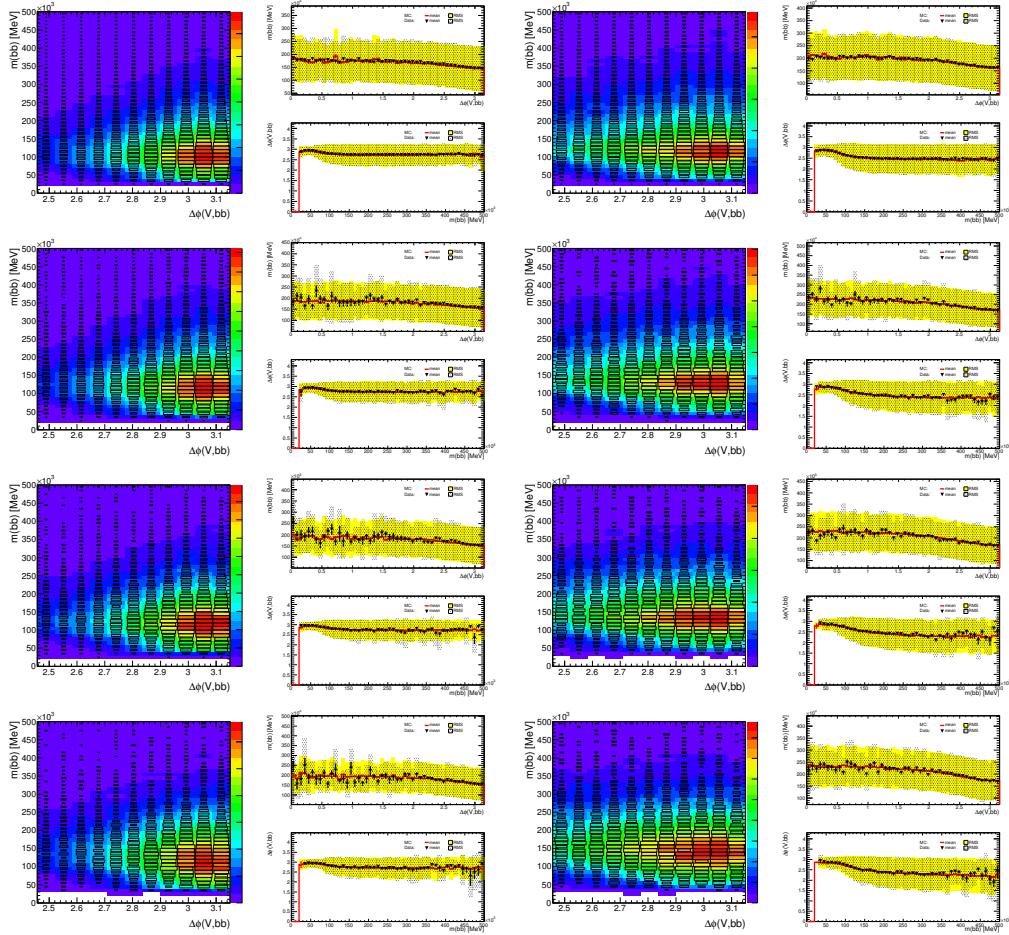


Figure 416: Correlation between bdtinput and output variables used in 0-lepton events ($p_T^W < 120$ GeV)
Row 1 - Left: 1 tag 2 jets Right: 1 tag 3 jets; Row 2 - Left: 2 LL tag 2 jets Right: 2 LL tag 3 jets; Row 3 - Left: 2 MM tag 2 jets Right: 2 MM tag 3 jets; Row 4 - Left: 2 TT tag 2 jets Right: 2 TT tag 3 jets.
Section 6.1 details the definition of each variable.

Not reviewed, for internal circulation only

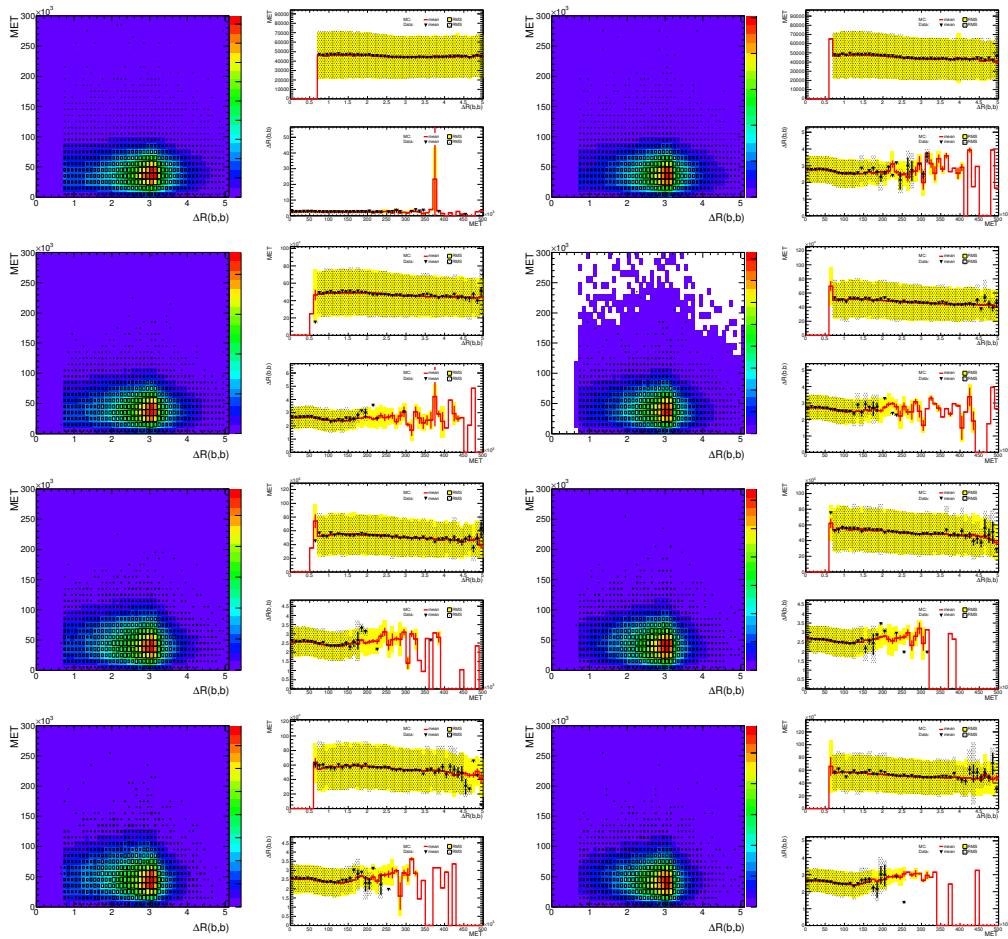


Figure 417: Correlation between bdtinput and output variables used in 0-lepton events ($p_T^W < 120$ GeV)
Row 1 - Left: 1 tag 2 jets Right: 1 tag 3 jets; Row 2 - Left: 2 LL tag 2 jets Right: 2 LL tag 3 jets; Row
3 - Left: 2 MM tag 2 jets Right: 2 MM tag 3 jets; Row 4 - Left: 2 TT tag 2 jets Right: 2 TT tag 3 jets.
Section 6.1 details the definition of each variable.

Not reviewed, for internal circulation only

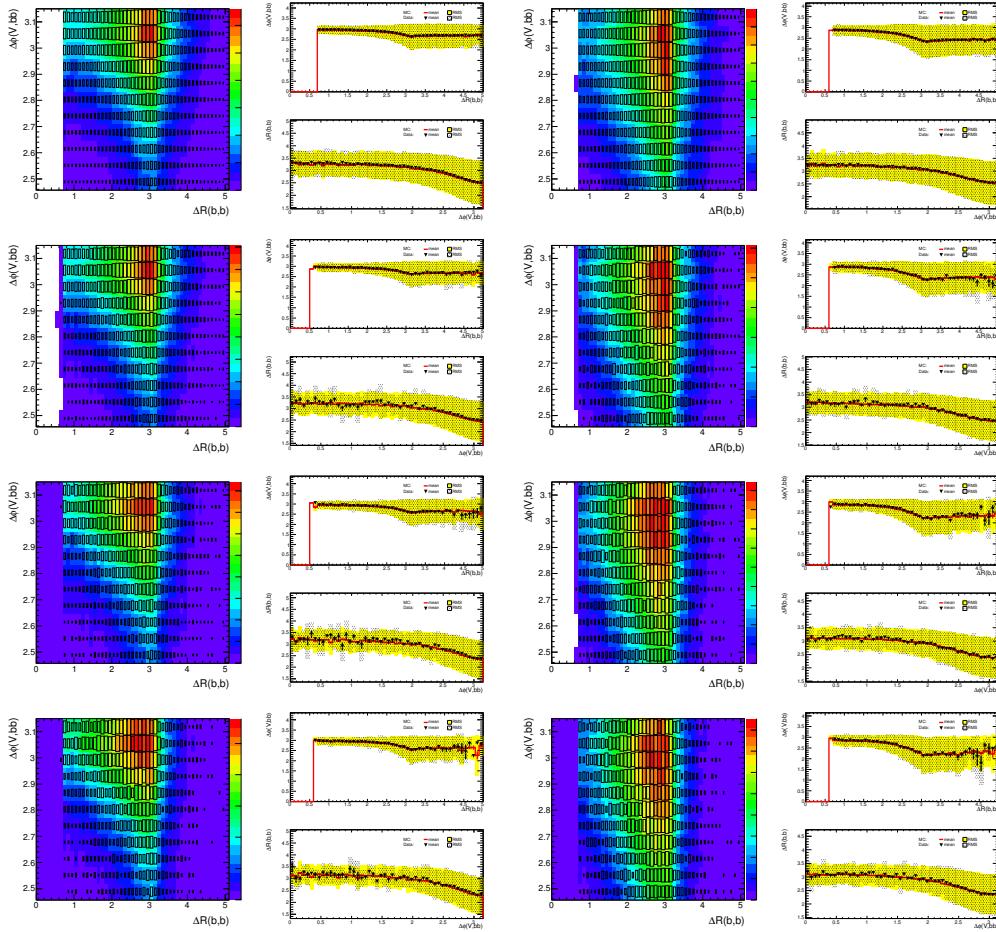


Figure 418: Correlation between $bdtinput$ and output variables used in 0-lepton events ($p_T^W < 120$ GeV)
Row 1 - Left: 1 tag 2 jets Right: 1 tag 3 jets; Row 2 - Left: 2 LL tag 2 jets Right: 2 LL tag 3 jets;
Row 3 - Left: 2 MM tag 2 jets Right: 2 MM tag 3 jets; Row 4 - Left: 2 TT tag 2 jets Right: 2 TT tag 3 jets.
Section 6.1 details the definition of each variable.

Not reviewed, for internal circulation only

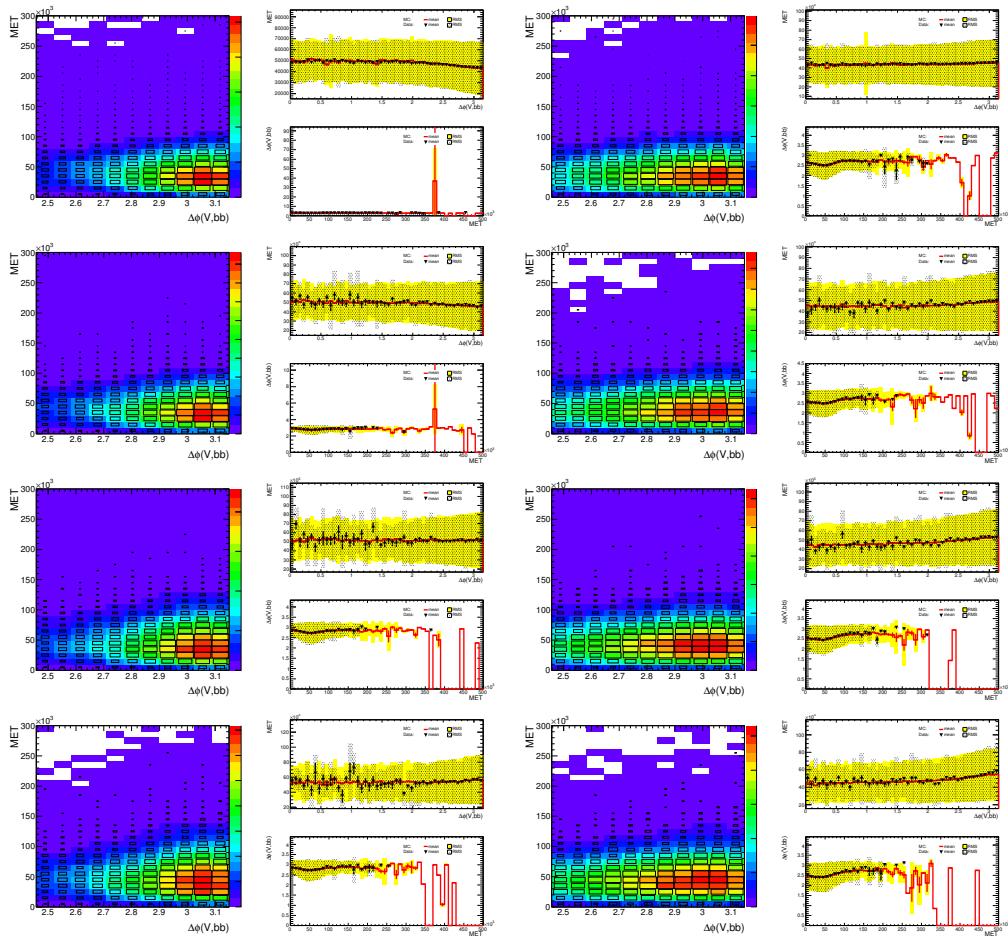


Figure 419: Correlation between bdtinput and output variables used in 0-lepton events ($p_T^W < 120$ GeV)
Row 1 - Left: 1 tag 2 jets Right: 1 tag 3 jets; Row 2 - Left: 2 LL tag 2 jets Right: 2 LL tag 3 jets; Row 3 - Left: 2 MM tag 2 jets Right: 2 MM tag 3 jets; Row 4 - Left: 2 TT tag 2 jets Right: 2 TT tag 3 jets.
Section 6.1 details the definition of each variable.

5017 AG Correlations between MVA Variables: Two Lepton

5018 This appendix contains correlations between input and output variables of the BDT, defined in Section 6
5019 in the 2-lepton analysis. These plots are done by applying the latest scale factors, obtained for the 2 jet
5020 region and the 3 jet region separately, by comparing the event yield before and after the MVA combined
5021 fit. They are summarized in Table 97. Explicitly stated, the theoretical expectation for each background
5022 is used for the given luminosity. All the plots in this section are done with the status-of-art analysis. Part
5023 of the plots in this appendix will be added in a future version of the note.

Not reviewed, for internal circulation only

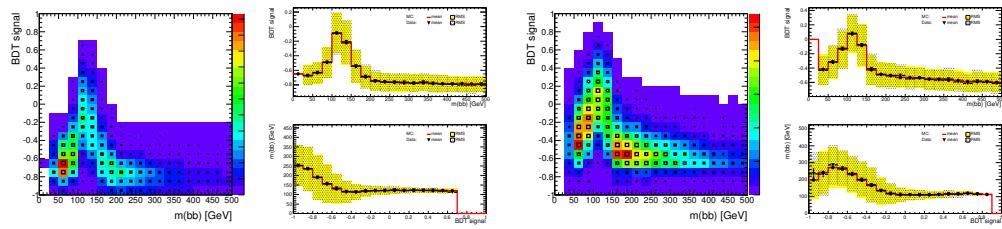


Figure 420: Correlation between mva and mBB variables used in 2-lepton MVA analysis ($p_T^Z > 120$ GeV)
Row 1 - Left: 1 tag 2 jets Right: 1 tag 3 jets; Row 2 - Left: 2 LL tag 2 jets Right: 2 LL tag 3 jets; Row 3 - Left: 2 MM tag 2 jets Right: 2 MM tag 3 jets; Row 4 - Left: 2 TT tag 2 jets Right: 2 TT tag 3 jets.
Section 6.1 details the definition of each variable.

[Not reviewed, for internal circulation only]

Figure 421: Correlation between mva and dRBB variables used in 2-lepton MVAanalysis ($p_T^Z > 120$ GeV)
Row 1 - Left: 1 tag 2 jets Right: 1 tag 3 jets; Row 2 - Left: 2 LL tag 2 jets Right: 2 LL tag 3 jets; Row
3 - Left: 2 MM tag 2 jets Right: 2 MM tag 3 jets; Row 4 - Left: 2 TT tag 2 jets Right: 2 TT tag 3 jets.
Section 6.1 details the definition of each variable.

Not reviewed, for internal circulation only

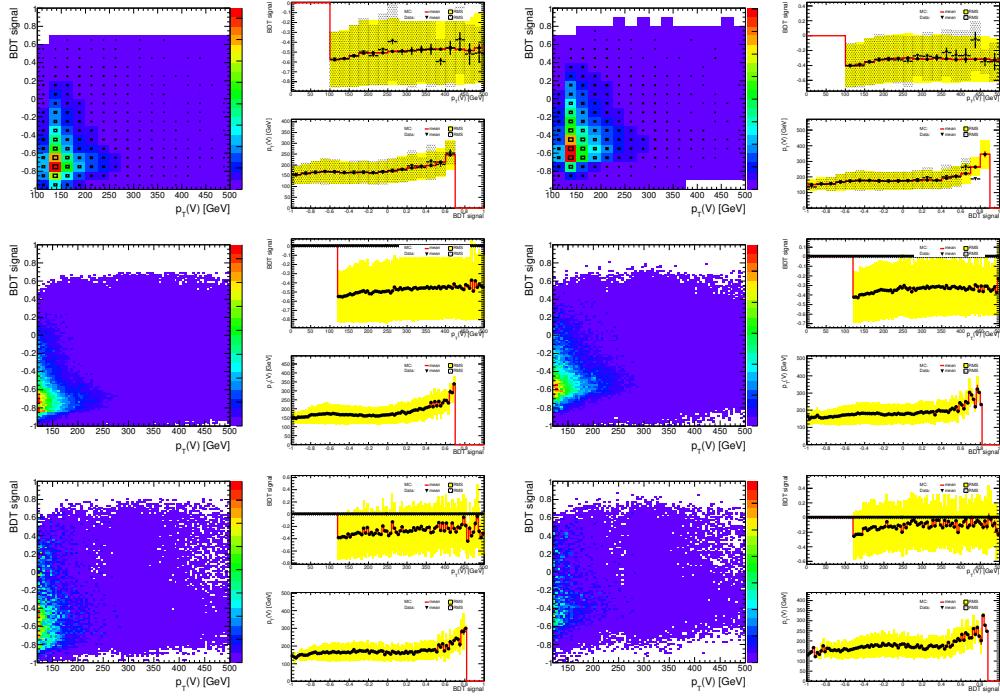


Figure 422: Correlation between mva and pTV variables used in 2-lepton MVAanalysis ($p_T^Z > 120$ GeV)
Row 1 - Left: 1 tag 2 jets Right: 1 tag 3 jets; Row 2 - Left: 2 LL tag 2 jets Right: 2 LL tag 3 jets; Row 3 - Left: 2 MM tag 2 jets Right: 2 MM tag 3 jets; Row 4 - Left: 2 TT tag 2 jets Right: 2 TT tag 3 jets.
Section 6.1 details the definition of each variable.

Not reviewed, for internal circulation only

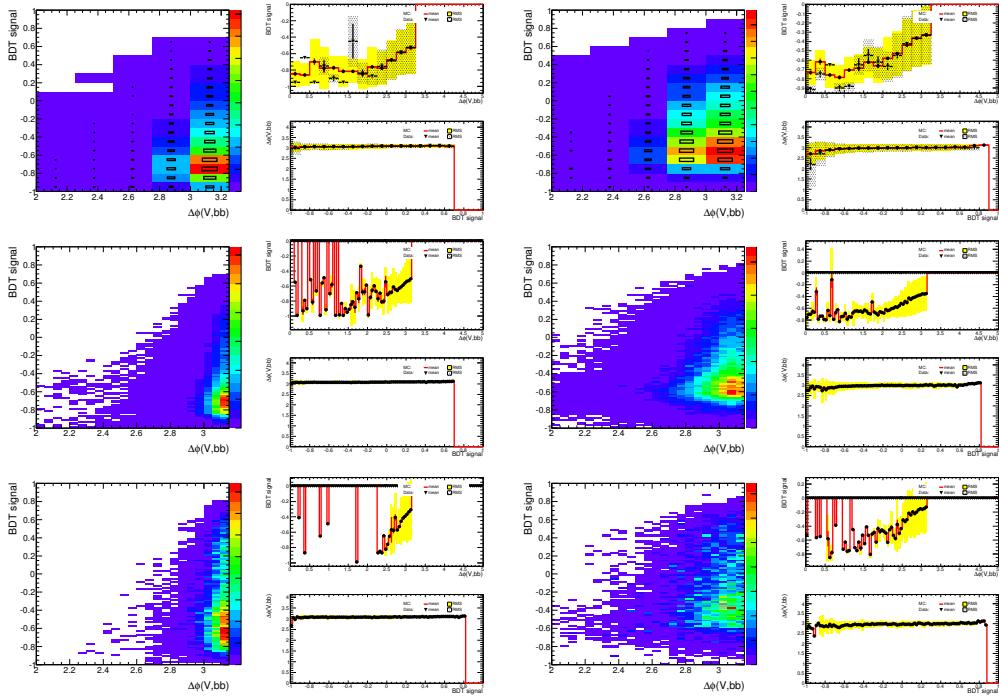


Figure 423: Correlation between mva and dPhiVBB variables used in 2-lepton MVAanalysis ($p_T^Z > 120$ GeV) Row 1 - Left: 1 tag 2 jets Right: 1 tag 3 jets; Row 2 - Left: 2 LL tag 2 jets Right: 2 LL tag 3 jets; Row 3 - Left: 2 MM tag 2 jets Right: 2 MM tag 3 jets; Row 4 - Left: 2 TT tag 2 jets Right: 2 TT tag 3 jets. Section 6.1 details the definition of each variable.

Not reviewed, for internal circulation only

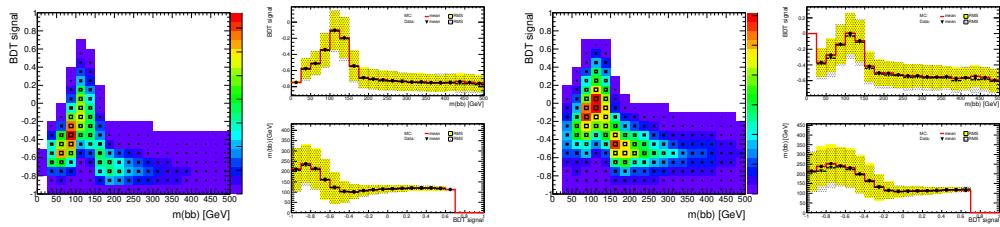


Figure 424: Correlation between mva and mBB variables used in 2-lepton MVAanalysis ($p_T^Z < 120$ GeV)
Row 1 - Left: 1 tag 2 jets Right: 1 tag 3 jets; Row 2 - Left: 2 LL tag 2 jets Right: 2 LL tag 3 jets; Row 3 - Left: 2 MM+TT tag 2 jets Right: 2 MM+TT tag 3 jets; Section 6.1 details the definition of each variable.

[Not reviewed, for internal circulation only]

Figure 425: Correlation between mva and dRBB variables used in 2-lepton MVAanalysis ($p_T^Z < 120$ GeV)
Row 1 - Left: 1 tag 2 jets Right: 1 tag 3 jets; Row 2 - Left: 2 LL tag 2 jets Right: 2 LL tag 3 jets; Row 3 -
Left: 2 MM+TT tag 2 jets Right: 2 MM+TT tag 3 jets; Section 6.1 details the definition of each variable.

Not reviewed, for internal circulation only

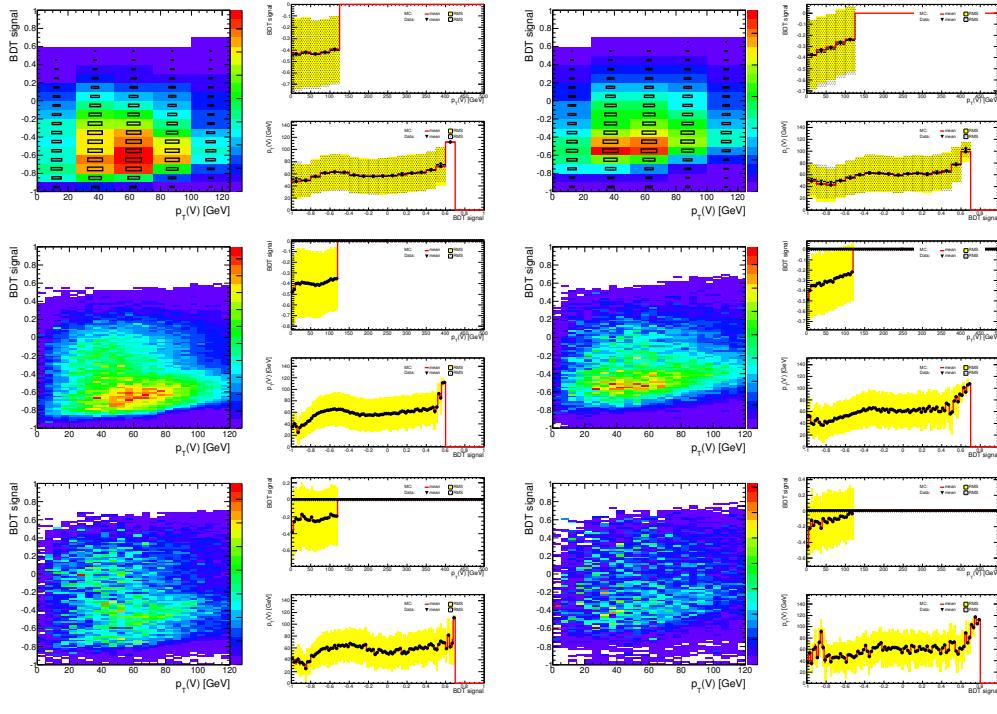


Figure 426: Correlation between mva and pTV variables used in 2-lepton MVAanalysis ($p_T^Z < 120$ GeV) Row 1 - Left: 1 tag 2 jets Right: 1 tag 3 jets; Row 2 - Left: 2 LL tag 2 jets Right: 2 LL tag 3 jets; Row 3 - Left: 2 MM+TT tag 2 jets Right: 2 MM+TT tag 3 jets; Section 6.1 details the definition of each variable.

Not reviewed, for internal circulation only

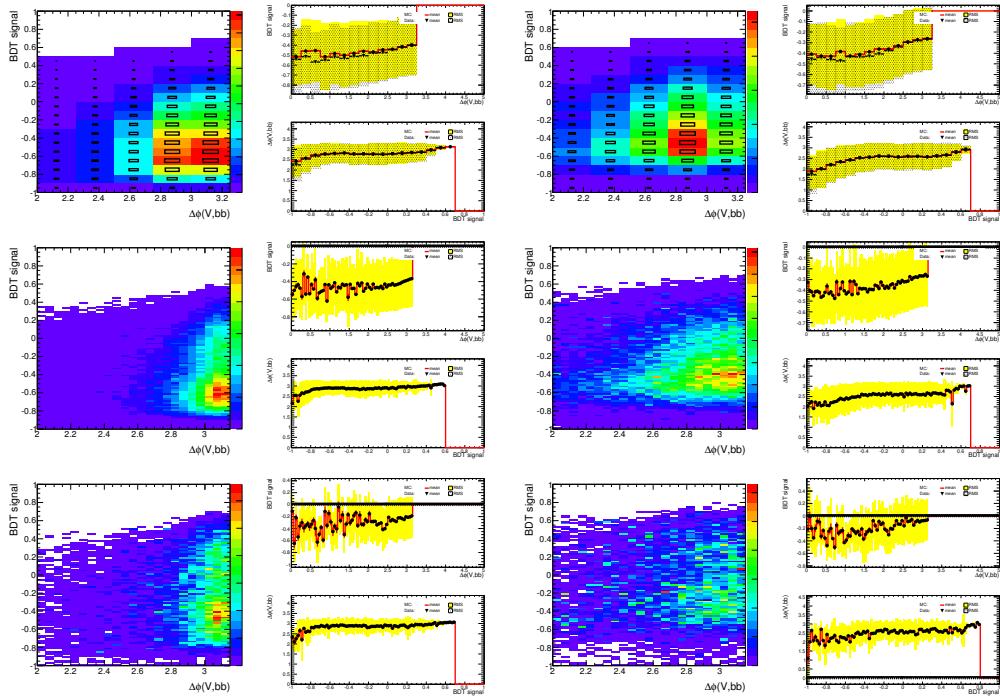


Figure 427: Correlation between mva and dPhiVBB variables used in 2-lepton MVA analysis ($p_T^Z < 120$ GeV) Row 1 - Left: 1 tag 2 jets Right: 1 tag 3 jets; Row 2 - Left: 2 LL tag 2 jets Right: 2 LL tag 3 jets; Row 3 - Left: 2 MM+TT tag 2 jets Right: 2 MM+TT tag 3 jets; Section 6.1 details the definition of each variable.

5024 **AH Pulls for the Individual Channels**

5025 Fits to the nominal Asimov are shown in red and the data pulls in black. Each fit is performed in the
 5026 individual channels alone. The $e - \mu$ control sample is included in the 2-lepton fit.

5027 **AH.1 Dijet Mass Analysis**

5028 **AH.1.1 0-lepton**

The pull plots for 0-lepton are shown in Figure. 428-432.

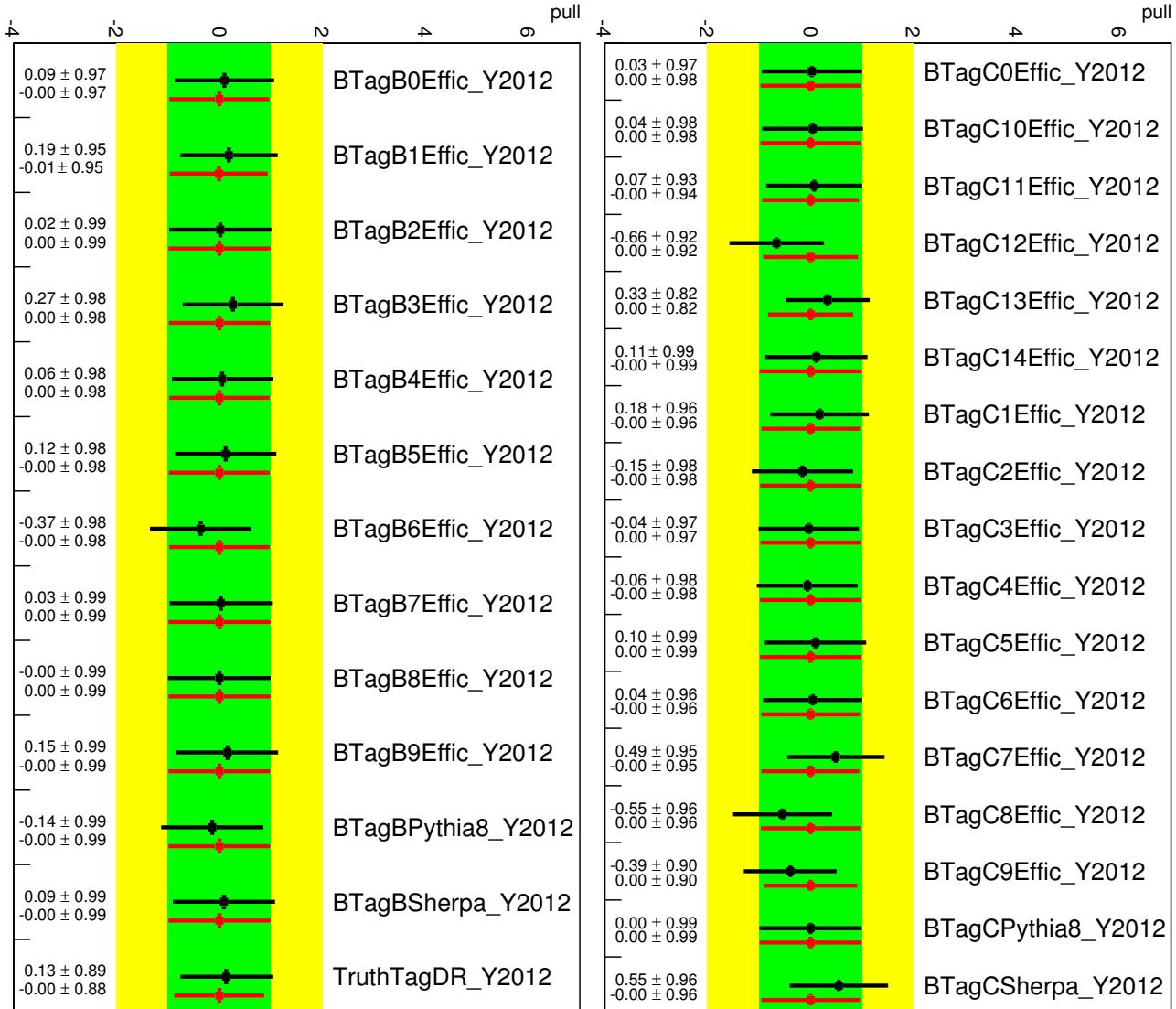


Figure 428: Pull plots for 0-lepton channel: b - and c -jet tagging.

Not reviewed, for internal circulation only

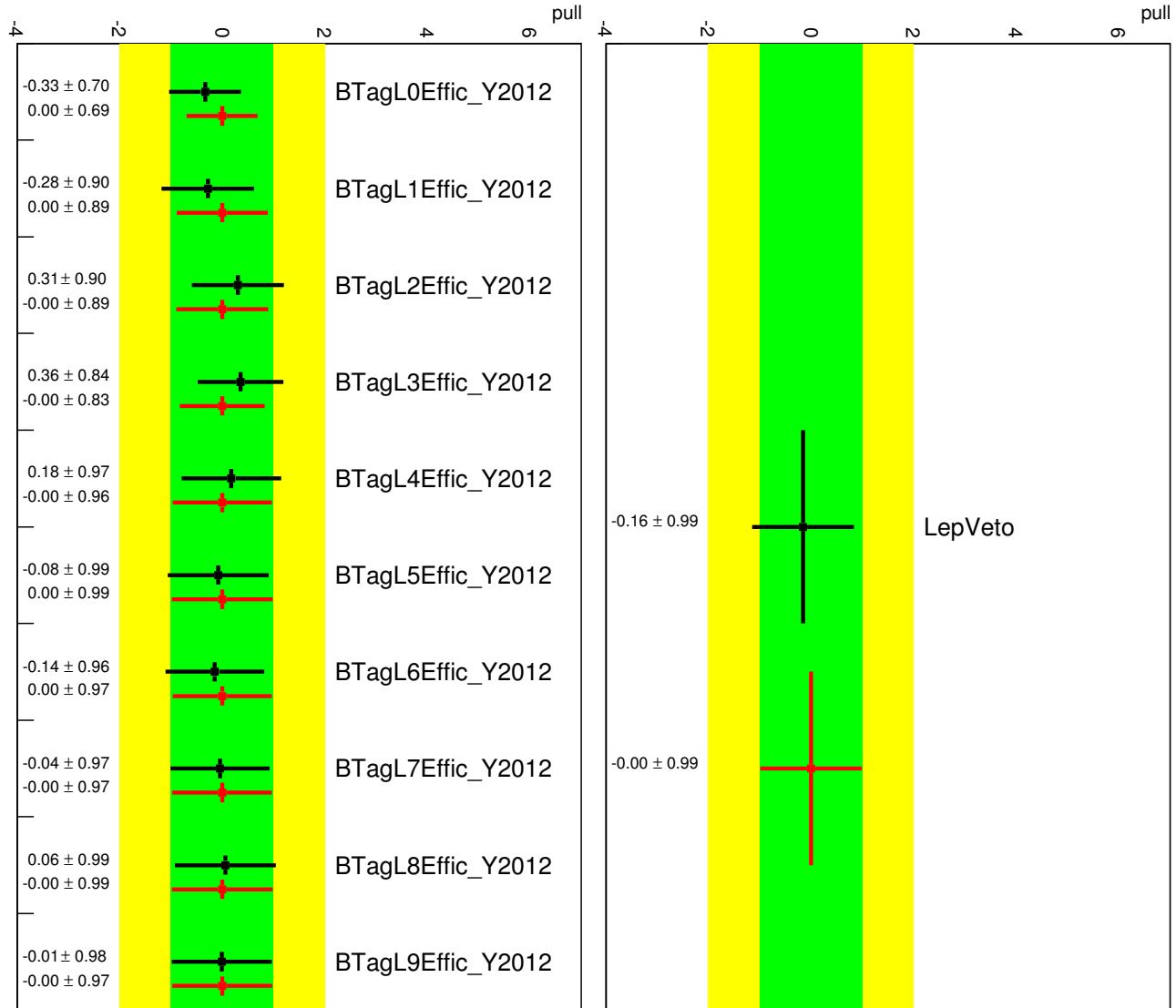


Figure 429: Pull plots for 0-lepton channel: light-jet tagging and leptons.

Not reviewed, for internal circulation only

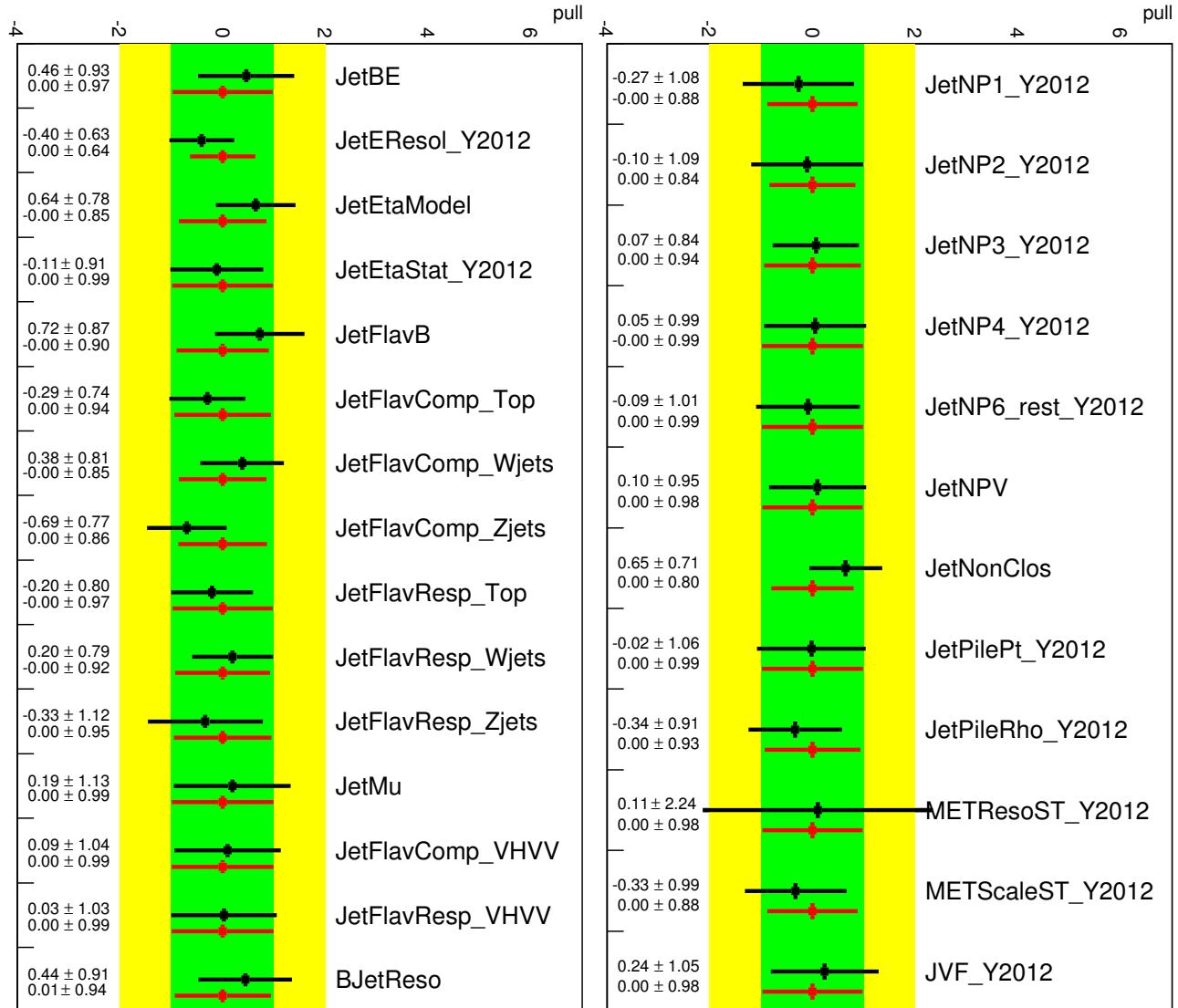


Figure 430: Pull plots for 0-lepton channel: Jet NPs.

Not reviewed, for internal circulation only

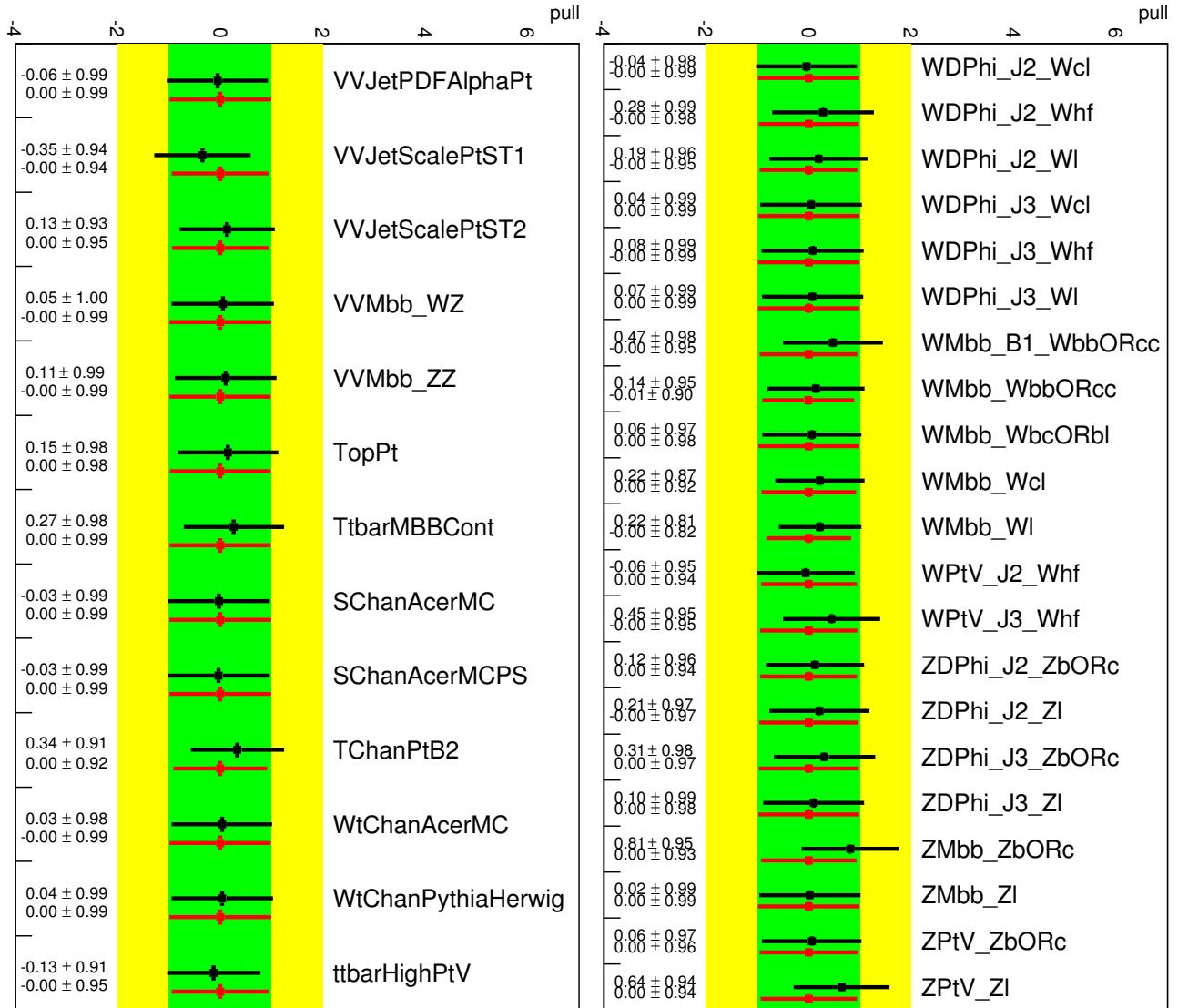


Figure 431: Pull plots for 0-lepton channel: Diboson and Top related uncertainties.

Not reviewed, for internal circulation only

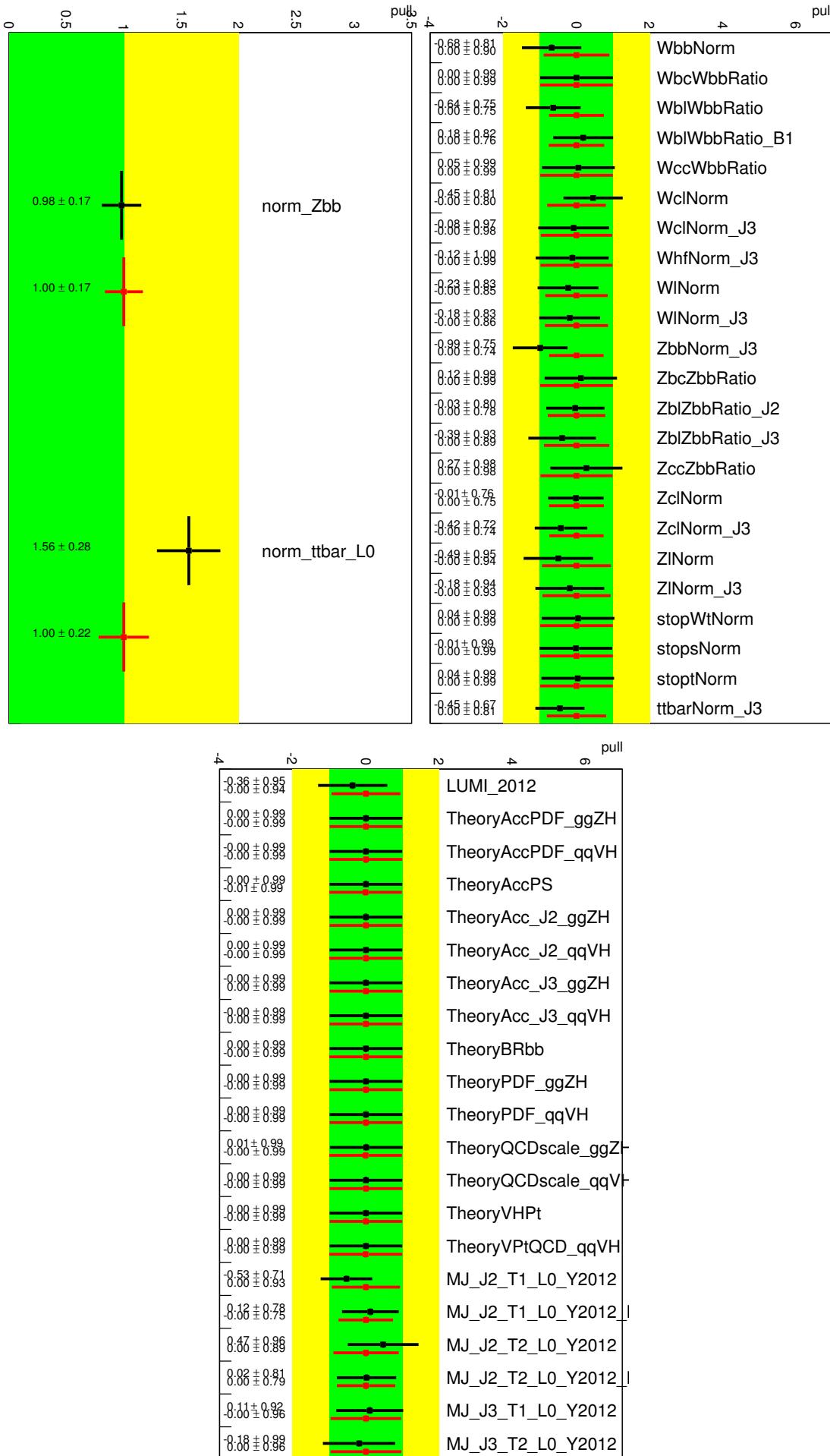


Figure 432: Pull plots for 0-lepton channel: Normalization and residual uncertainties.

5030 **AH.1.2 Pre-fit and Post-Fit for the m_{jj} shape analysis in the 0-lepton fit**

[Not reviewed, for internal circulation only]

Not reviewed, for internal circulation only

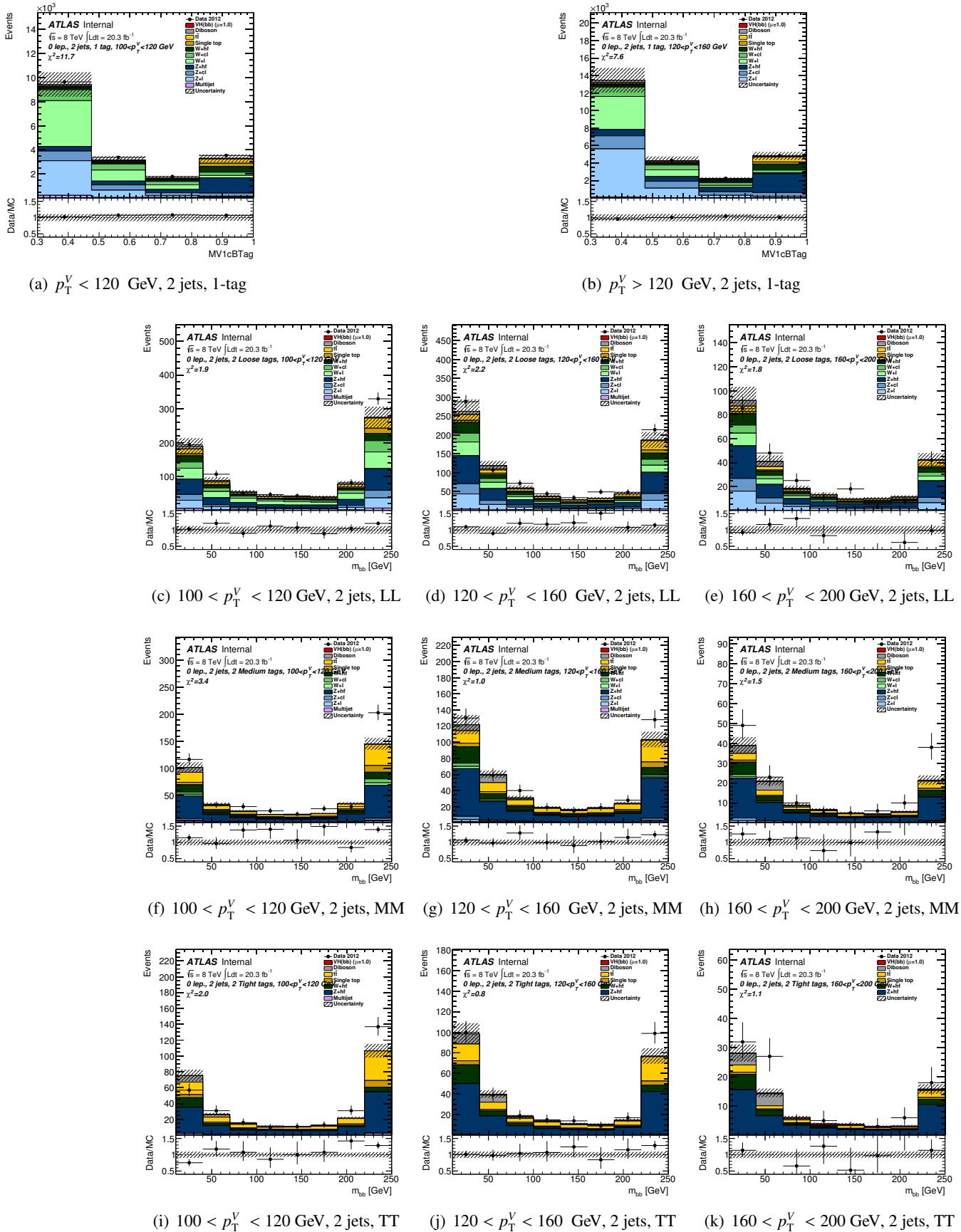


Figure 433: Pre-fit plots for m_{jj} distribution in 0-lepton events in the 1-tag (where mv1c is used in the fit) *LL*, *MM* and *TT* tag categories for the 2-jets events in the 0-lepton fit. Plots are shown for $100 < p_T^V < 120$ GeV, $120 < p_T^V < 160$ GeV and $160 < p_T^V < 200$ GeV.

Not reviewed, for internal circulation only

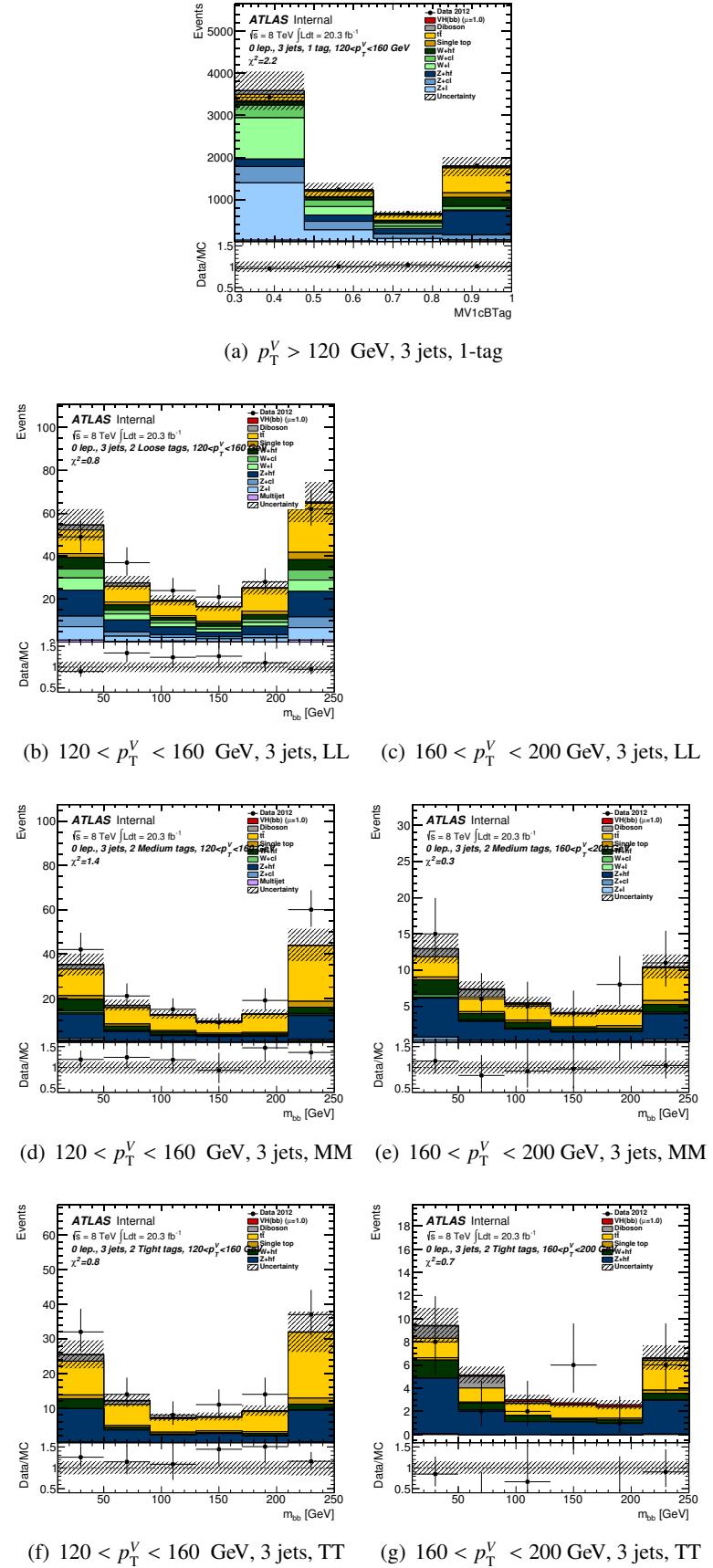


Figure 434: Pre-fit plots for m_{jj} distribution in 0-lepton events in the 1-tag (where mv1c is used in the fit) LL, MM and TT tag categories for the 3-jets events in the 0-lepton fit. Plots are shown for $120 < p_T^V < 160$ GeV and $160 < p_T^V < 200$ GeV.

Not reviewed, for internal circulation only

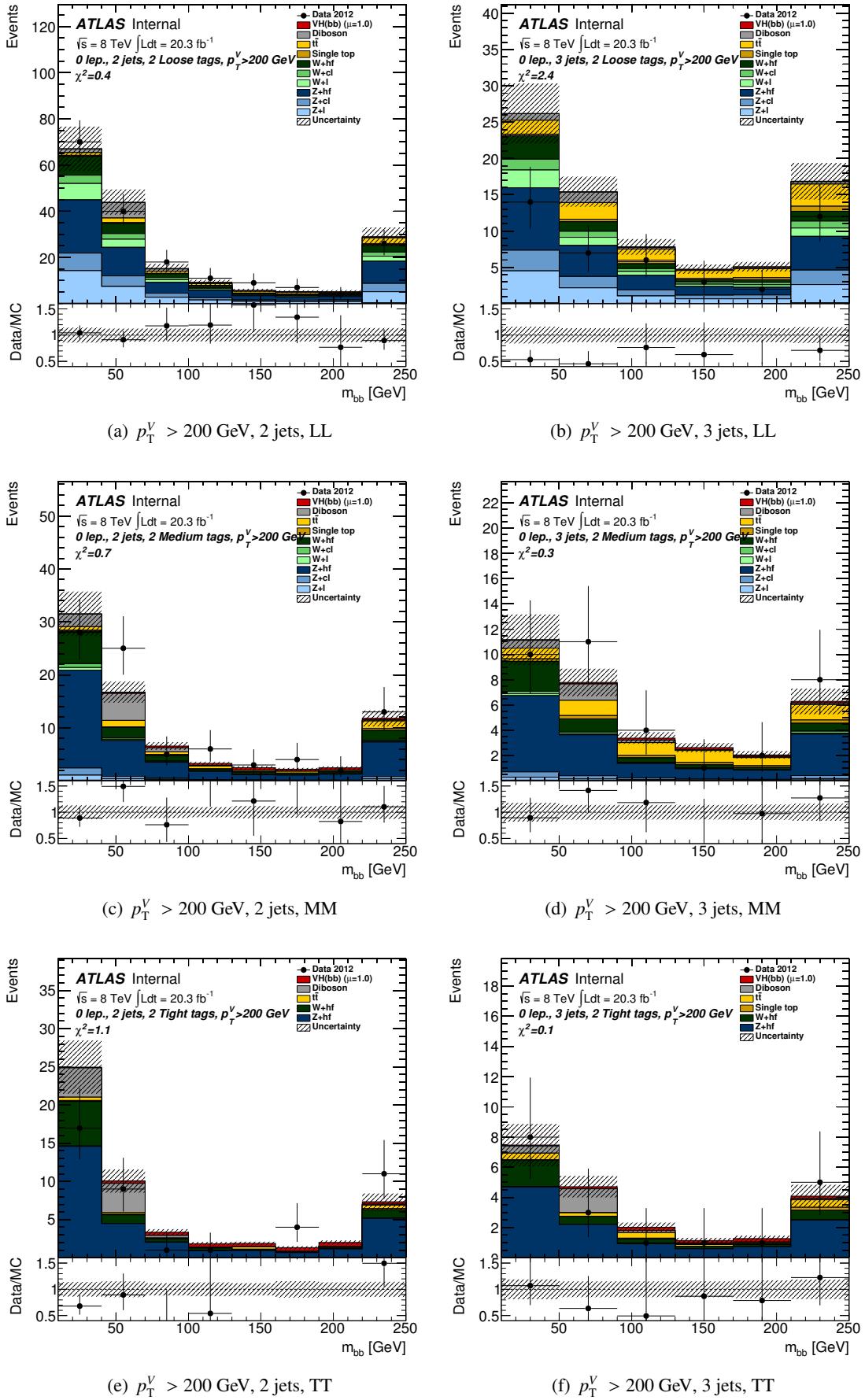


Figure 435: Pre-fit plots for m_{jj} distribution in 0-lepton events in the LL , MM and TT tag categories for the 2-jets and the 3-jets events in the 0-lepton fit. Plots are shown for $p_T^V > 200 \text{ GeV}$.

Not reviewed, for internal circulation only

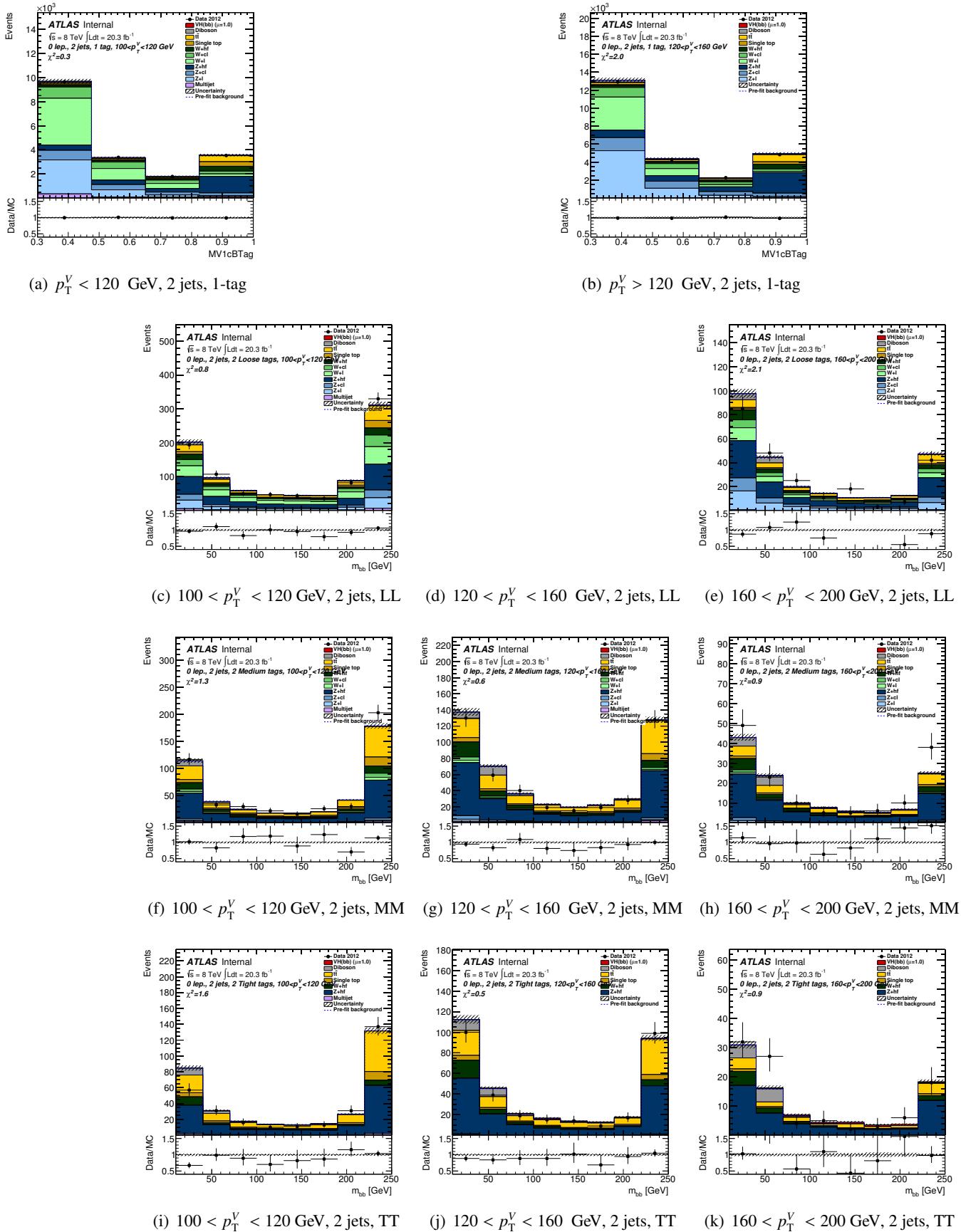


Figure 436: Post-fit plots for m_{jj} distribution in 0-lepton events in the 1-tag (where mv1c is used in the fit) *LL*, *MM* and *TT* tag categories for the 2-jets events in the 0-lepton fit. Plots are shown for $100 < p_T^V < 120$ GeV, $120 < p_T^V < 160$ GeV and $160 < p_T^V < 200$ GeV. The pre-fit background expectation is indicated by the dashed blue line.

Not reviewed, for internal circulation only

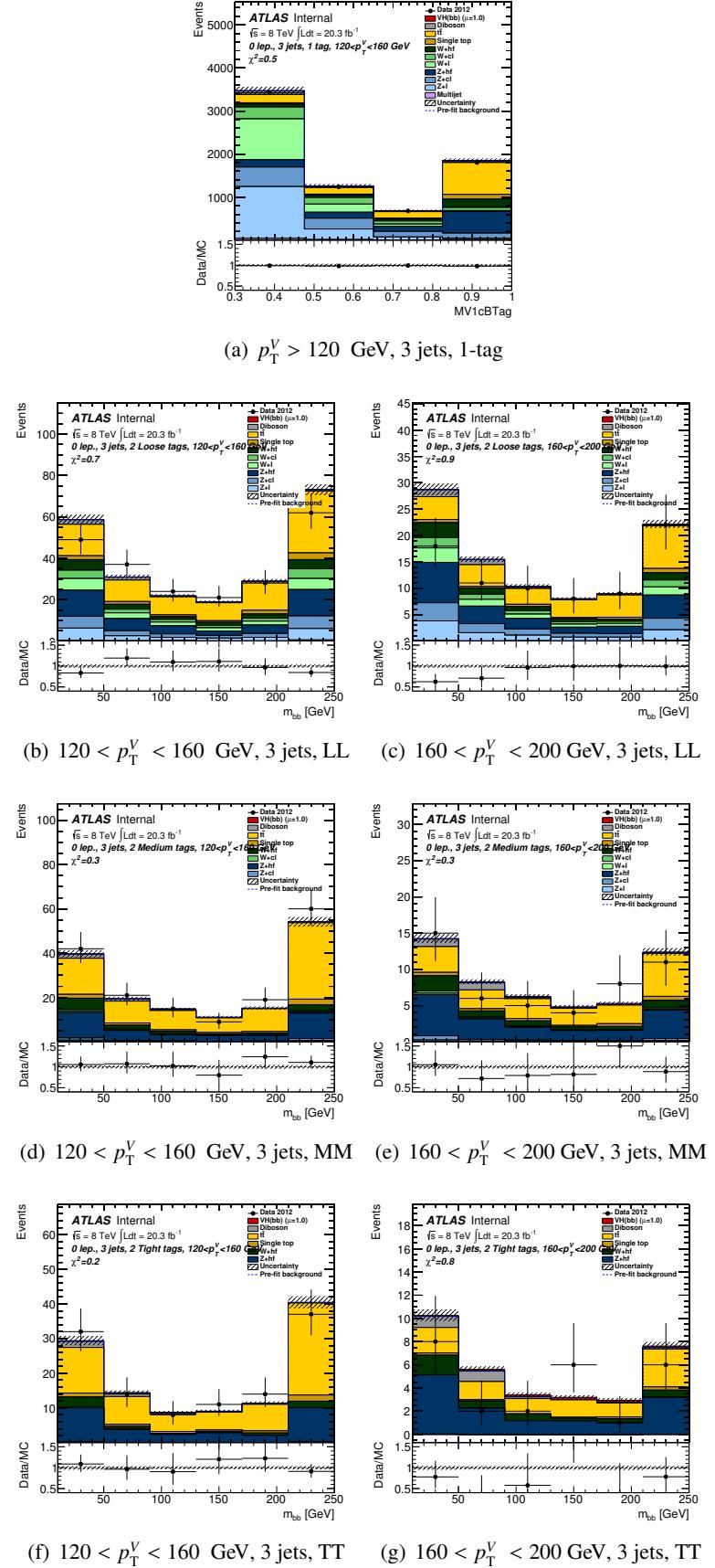


Figure 437: Post-fit plots for m_{jj} distribution in 0-lepton events in the 1-tag (where mv1c is used in the fit) LL, MM and TT tag categories for the 3-jets events in the 0-lepton fit. Plots are shown for $120 < p_T^V < 160$ GeV and $160 < p_T^V < 200$ GeV. The pre-fit background expectation is indicated by the dashed blue line.

Not reviewed, for internal circulation only

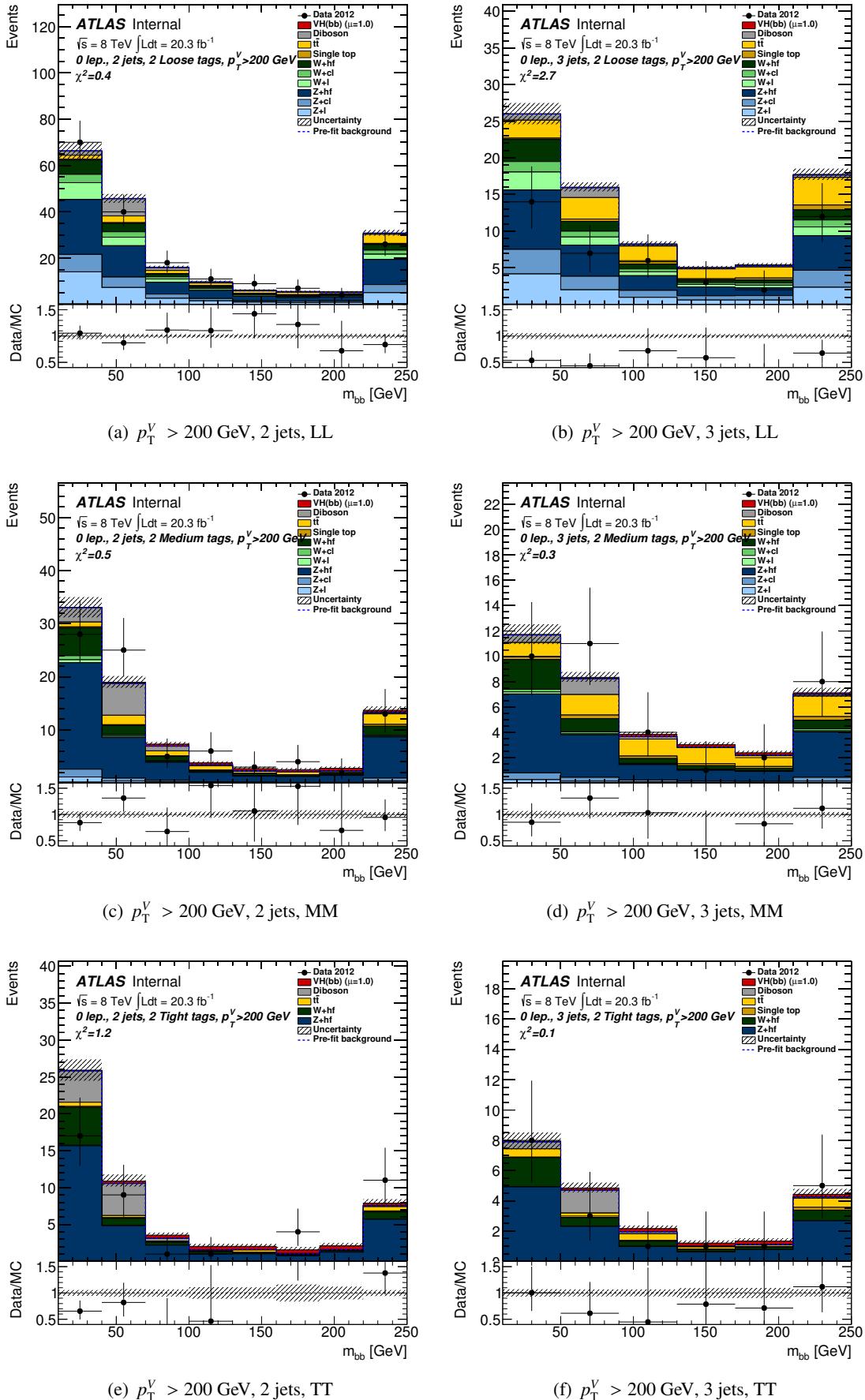


Figure 438: Post-fit plots for m_{jj} distribution in 0-lepton events in the LL , MM and TT tag categories for the 2-jets and the 3-jets events in the 0-lepton fit. Plots are shown for $p_T^V > 200 \text{ GeV}$. The pre-fit background expectation is indicated by the dashed blue line.

5031 **AH.1.3 1-lepton**

The pull plots for 1-lepton are shown in Figure. 439-443.

Not reviewed, for internal circulation only

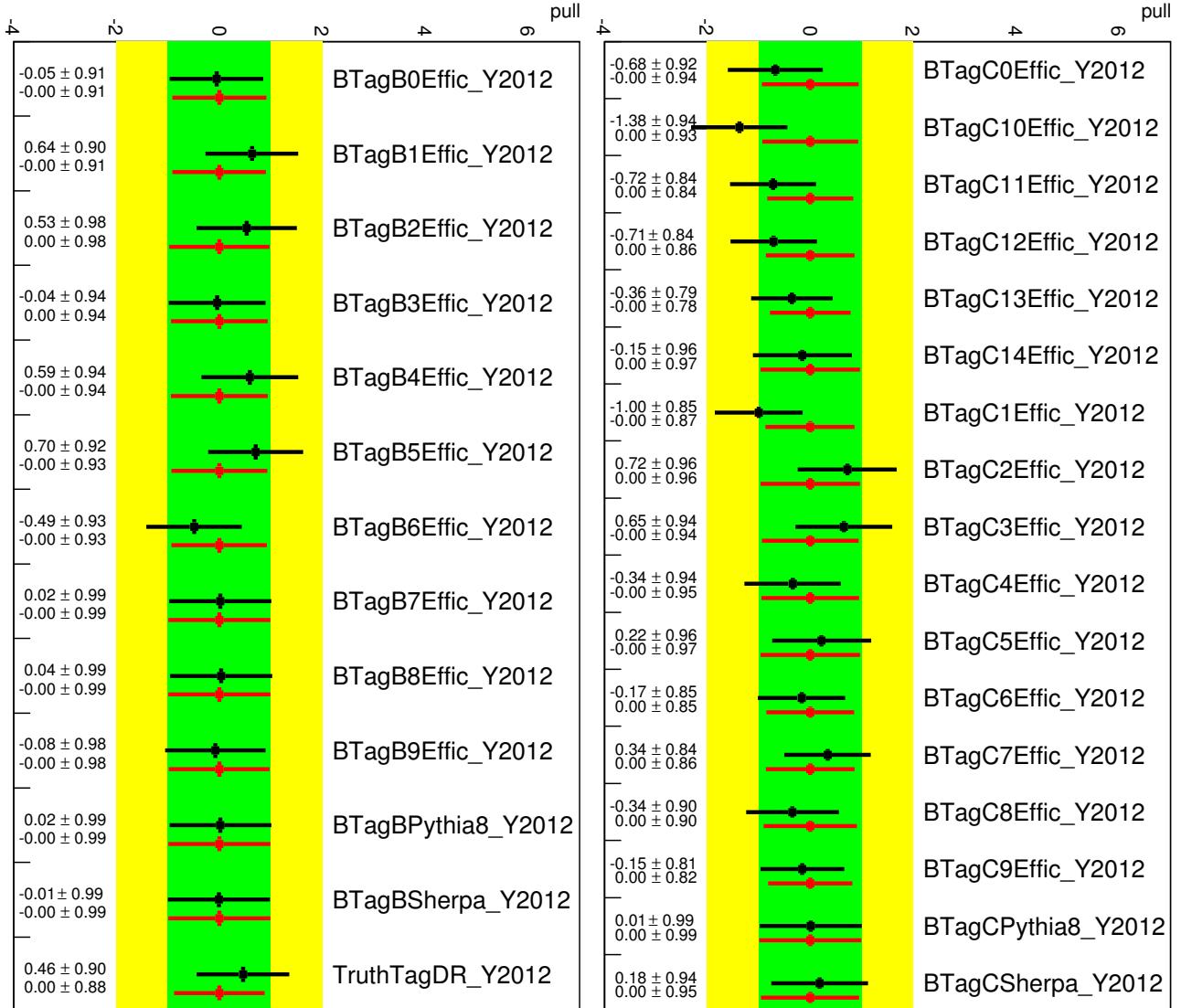


Figure 439: Pull plots for 1-lepton channel: *b*- and *c*-jet tagging.

5032

Not reviewed, for internal circulation only

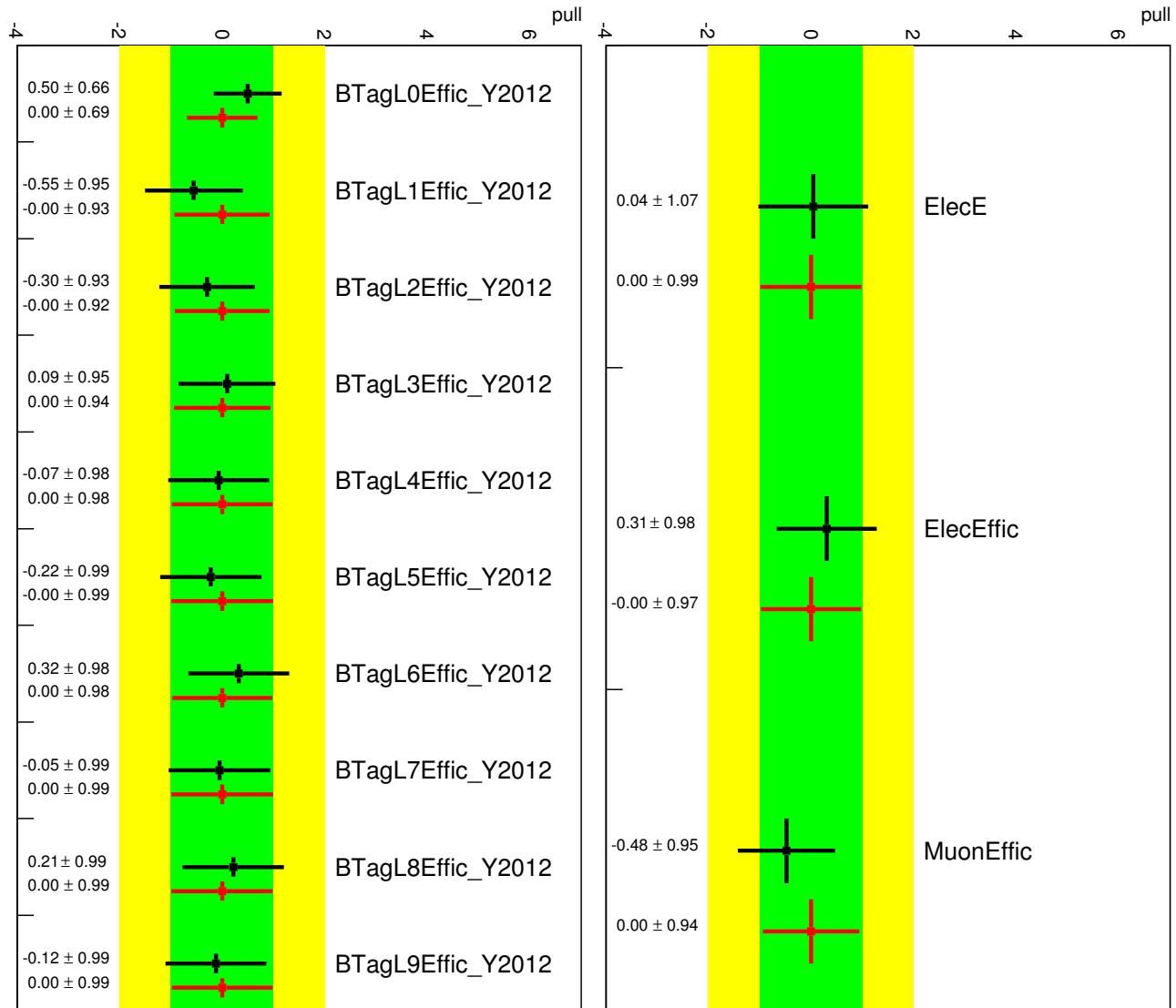


Figure 440: Pull plots for 1-lepton channel: light-jet tagging and leptons.

Not reviewed, for internal circulation only

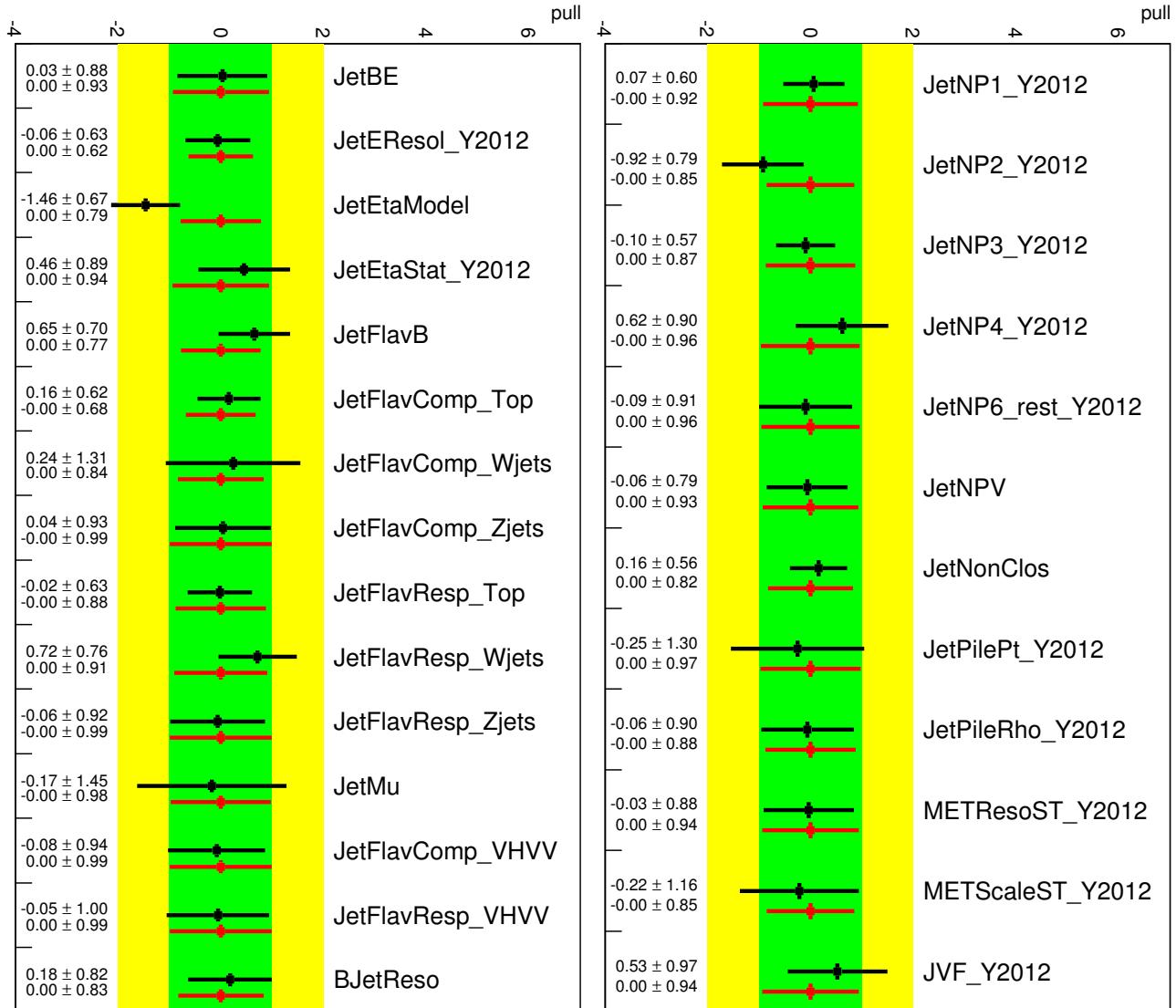


Figure 441: Pull plots for 1-lepton channel: Jet NPs.

Not reviewed, for internal circulation only



Figure 442: Pull plots for 1-lepton channel: Diboson and Top related uncertainties.

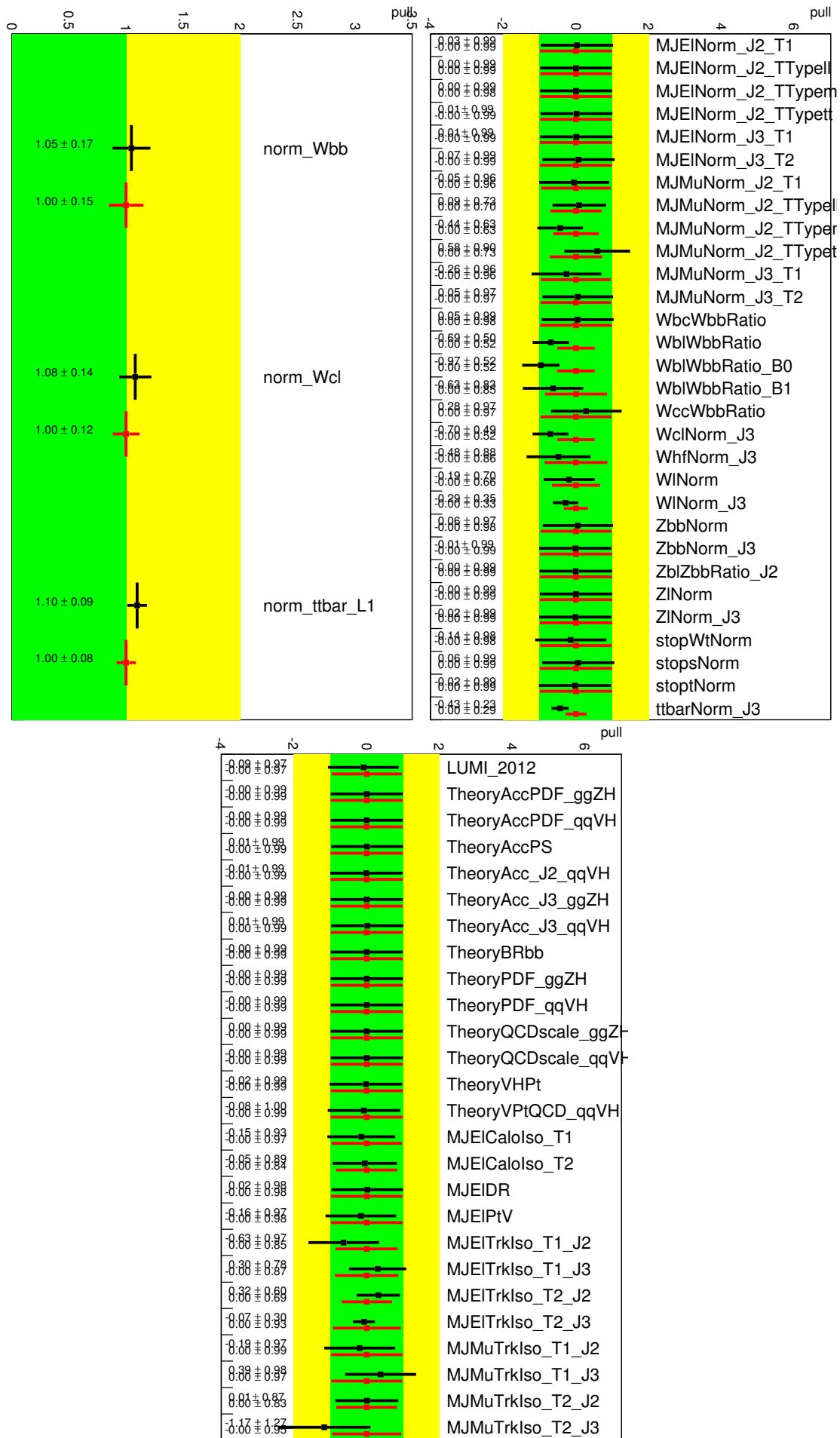


Figure 443: Pull plots for 1-lepton channel: Normalization and residual uncertainties.

5033 **AH.1.4 Pre-fit and Post-Fit for the m_{jj} shape analysis in the 1-lepton fit**

[Not reviewed, for internal circulation only]

final circulation only

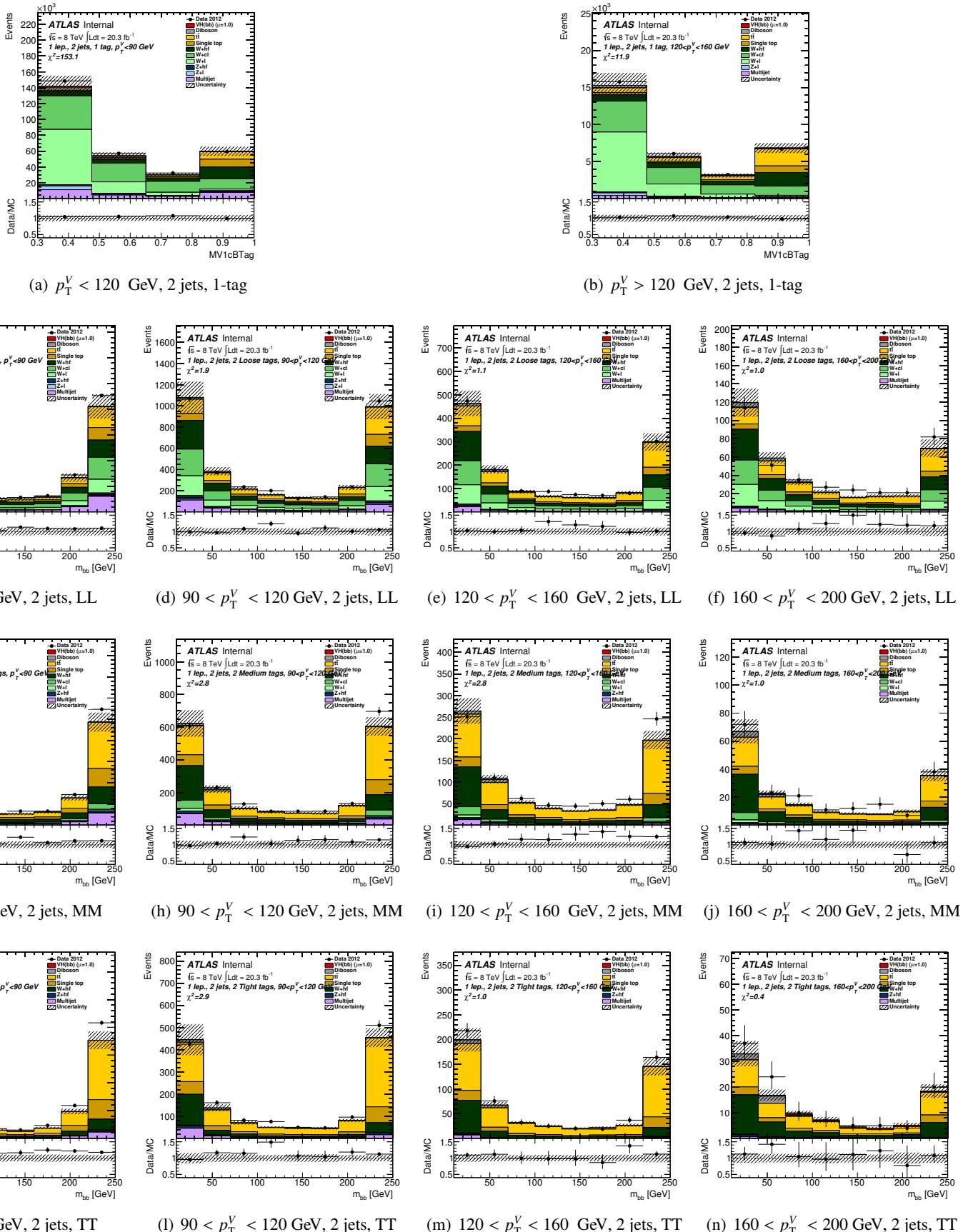


Figure 444: Pre-fit plots for m_{jj} distribution in 1-lepton events in the 1-tag (where mv1c is used in the fit) ***LL***, ***MM*** and ***TT*** tag categories for the 2-jets events in the 1-lepton fit. Plots are shown for $p_T^V < 90$ GeV, $90 < p_T^V < 120$ GeV, $120 < p_T^V < 160$ GeV and $160 < p_T^V < 200$ GeV. The pre-fit background expectation is indicated by the dashed blue line.

internal circulation only

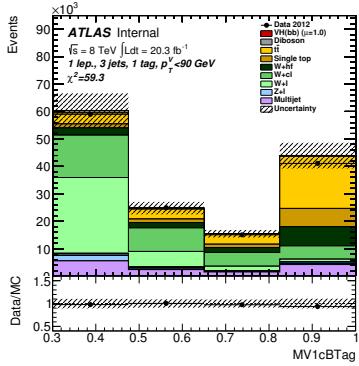
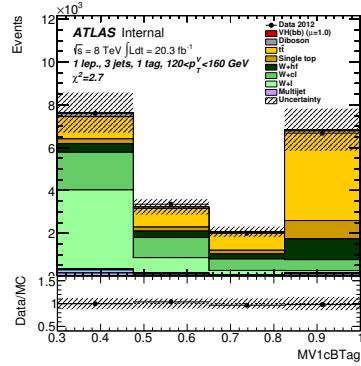
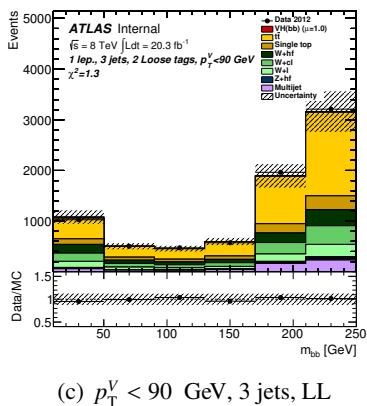
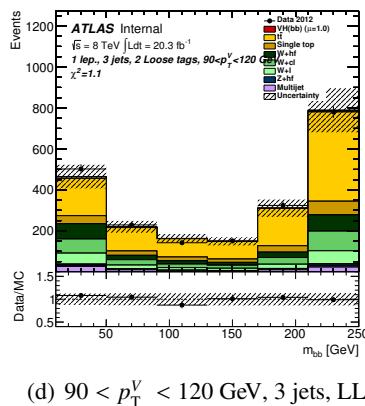
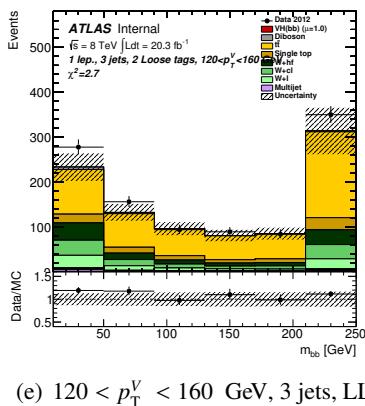
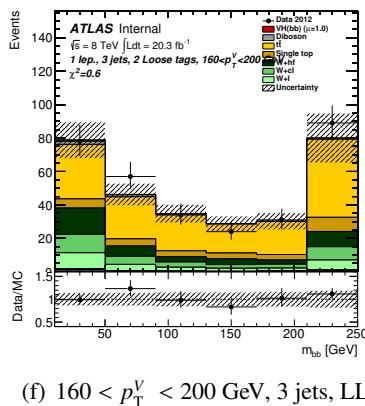
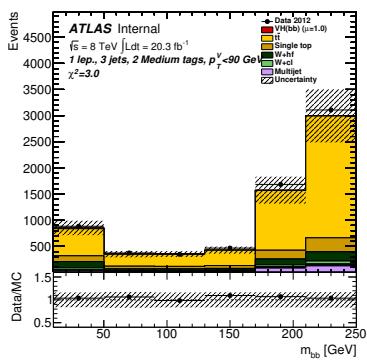
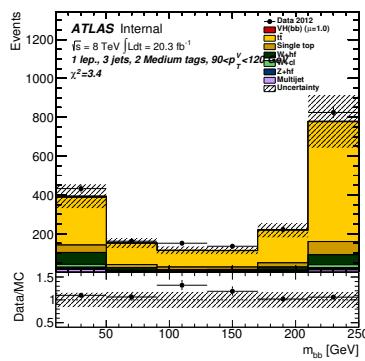
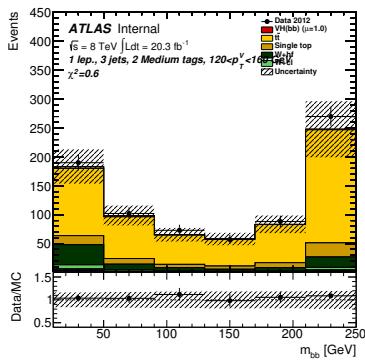
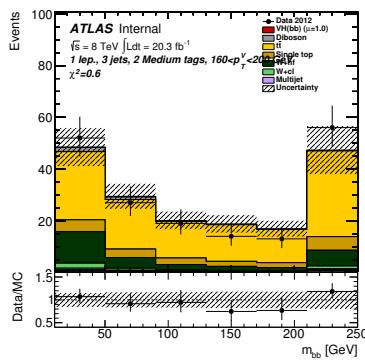
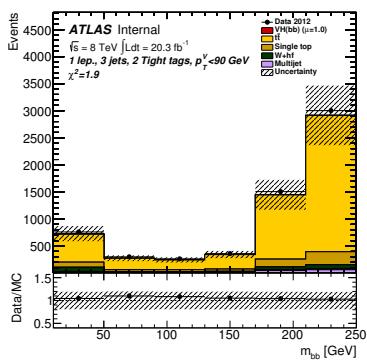
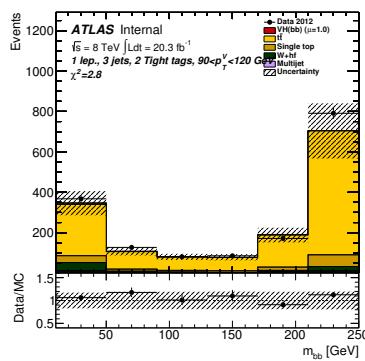
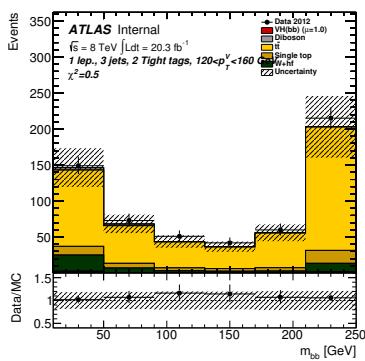
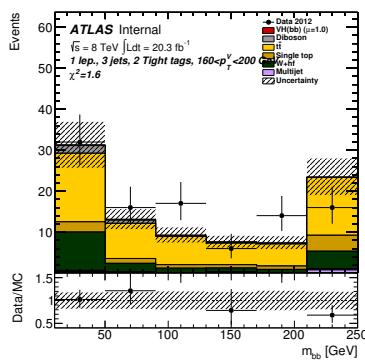
(a) $p_T^V < 120 \text{ GeV}$, 3 jets, 1-tag(b) $p_T^V > 120 \text{ GeV}$, 3 jets, 1-tag(c) $p_T^V < 90 \text{ GeV}$, 3 jets, LL(d) $90 < p_T^V < 120 \text{ GeV}$, 3 jets, LL(e) $120 < p_T^V < 160 \text{ GeV}$, 3 jets, LL(f) $160 < p_T^V < 200 \text{ GeV}$, 3 jets, LL(g) $p_T^V < 90 \text{ GeV}$, 3 jets, MM(h) $90 < p_T^V < 120 \text{ GeV}$, 3 jets, MM(i) $120 < p_T^V < 160 \text{ GeV}$, 3 jets, MM(j) $160 < p_T^V < 200 \text{ GeV}$, 3 jets, MM(k) $p_T^V < 90 \text{ GeV}$, 3 jets, TT(l) $90 < p_T^V < 120 \text{ GeV}$, 3 jets, TT(m) $120 < p_T^V < 160 \text{ GeV}$, 3 jets, TT(n) $160 < p_T^V < 200 \text{ GeV}$, 3 jets, TT

Figure 445: Pre-fit plots for m_{jj} distribution in 1-lepton events in the 1-tag (where mv1c is used in the fit) **LL**, **MM** and **TT** tag categories for the 3-jets events in the 1-lepton fit. Plots are shown for $p_T^V < 90 \text{ GeV}$, $90 < p_T^V < 120 \text{ GeV}$, $120 < p_T^V < 160 \text{ GeV}$ and $160 < p_T^V < 200 \text{ GeV}$. The pre-fit background expectation is indicated by the dashed blue line.

Not reviewed, for internal circulation only

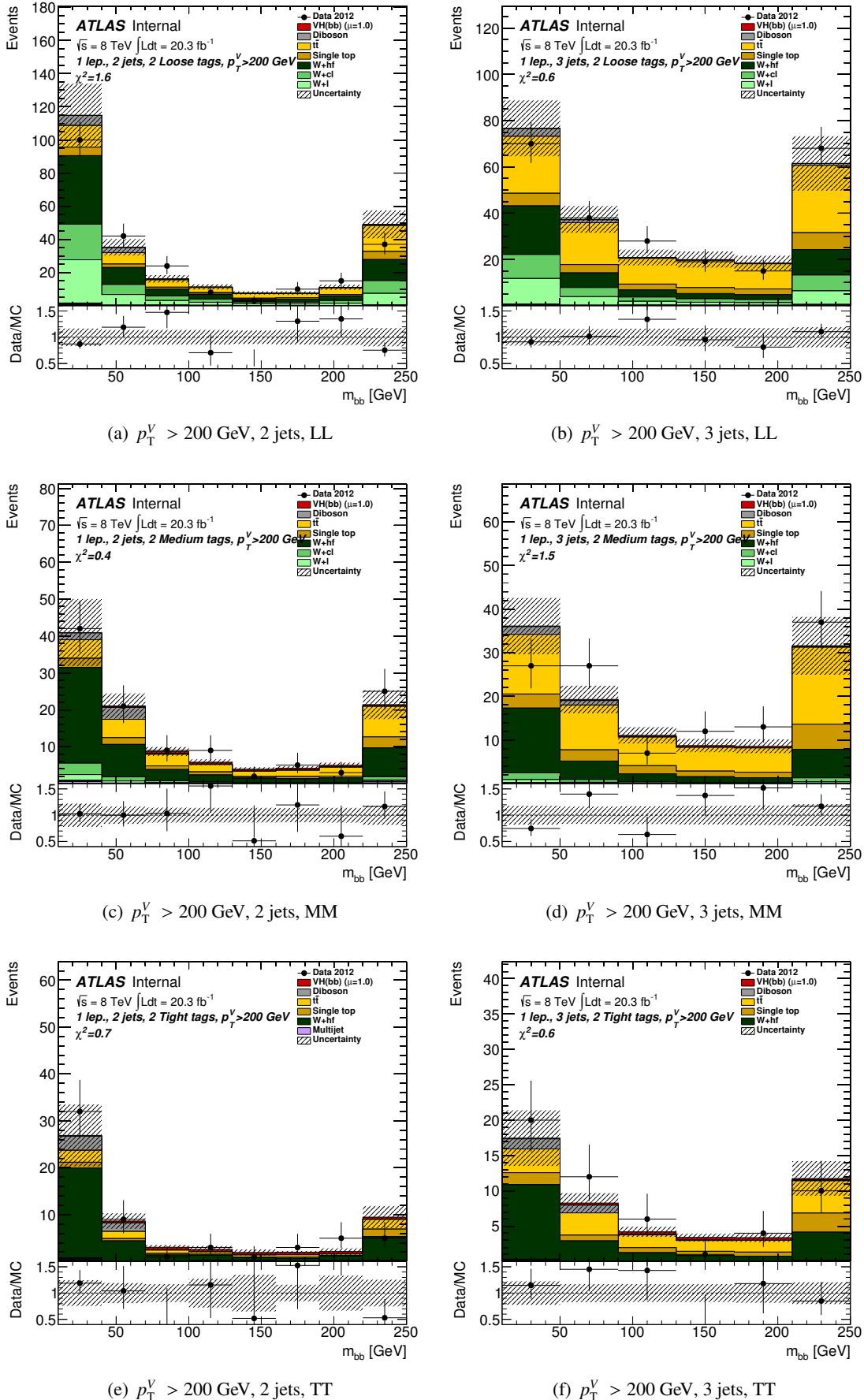


Figure 446: Pre-fit plots for m_{jj} distribution in 1-lepton events in the *LL*, *MM* and *TT* tag categories for the 2-jets and the 3-jets events in the 1-lepton fit. Plots are shown for $p_T^V > 200$ GeV. The pre-fit background expectation is indicated by the dashed blue line.

internal circulation only

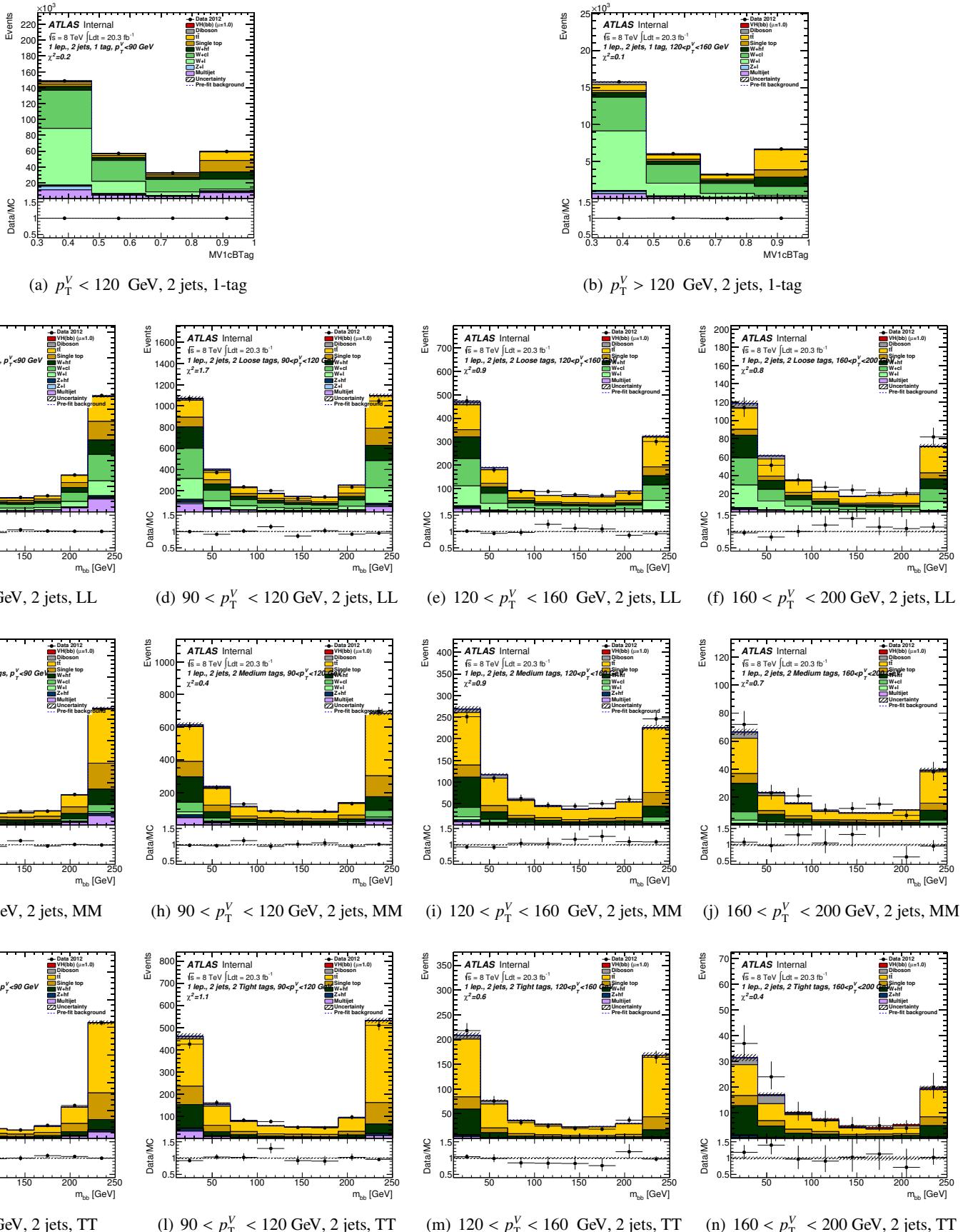


Figure 447: Post-fit plots for m_{jj} distribution in 1-lepton events in the 1-tag (where mv1c is used in the fit) *LL*, *MM* and *TT* tag categories for the 2-jets events in the 1-lepton fit. Plots are shown for $p_T^V < 90$ GeV, $90 < p_T^V < 120$ GeV, $120 < p_T^V < 160$ GeV and $160 < p_T^V < 200$ GeV. The pre-fit background expectation is indicated by the dashed blue line.

internal circulation only

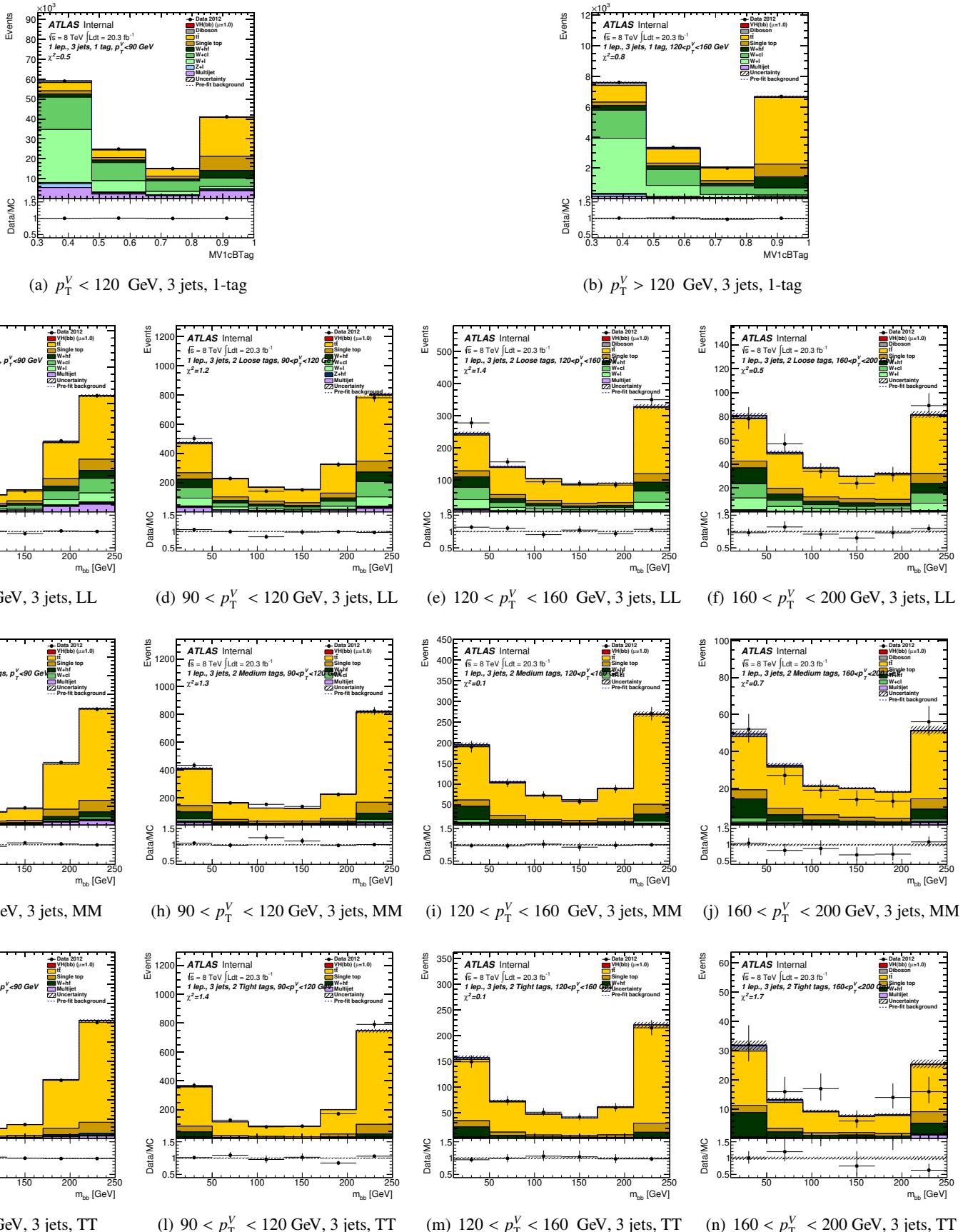


Figure 448: Post-fit plots for m_{jj} distribution in 1-lepton events in the 1-tag (where mv1c is used in the fit) **LL**, **MM** and **TT** tag categories for the 3-jets events in the 1-lepton fit. Plots are shown for $p_T^V < 90$ GeV, $90 < p_T^V < 120$ GeV, $120 < p_T^V < 160$ GeV and $160 < p_T^V < 200$ GeV. The pre-fit background expectation is indicated by the dashed blue line.

Not reviewed, for internal circulation only

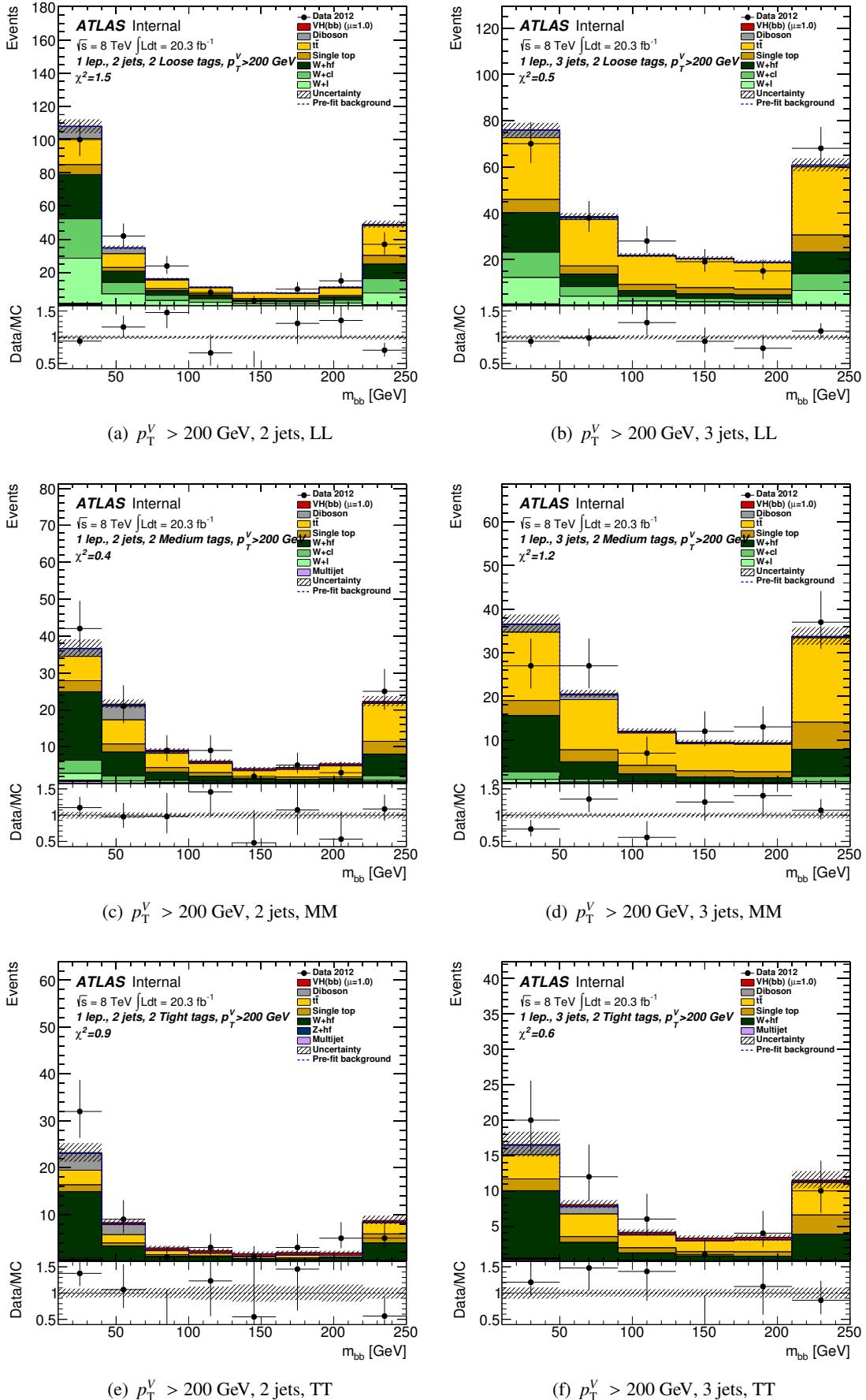


Figure 449: Post-fit plots for m_{jj} distribution in 1-lepton events in the LL , MM and TT tag categories for the 2-jets and the 3-jets events in the 1-lepton fit. Plots are shown for $p_T^V > 200$ GeV. The pre-fit background expectation is indicated by the dashed blue line.

5034 **AH.1.5 2-lepton**

5035 The pull plots for 2-lepton are shown in Figure. 450-454.

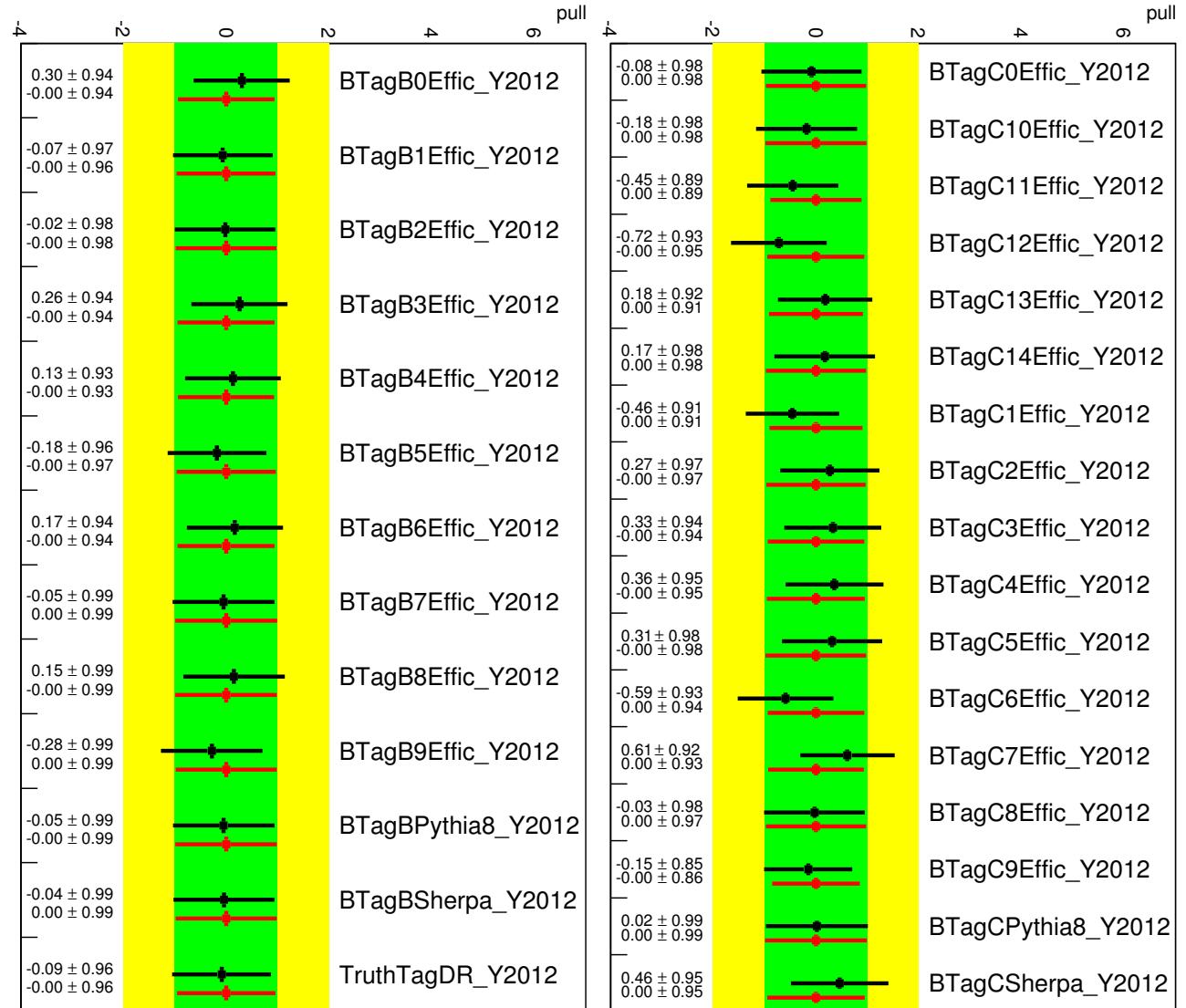


Figure 450: Pull plots for 2-lepton channel: *b*- and *c*-jet tagging.

Not reviewed, for internal circulation only

Not reviewed, for internal circulation only

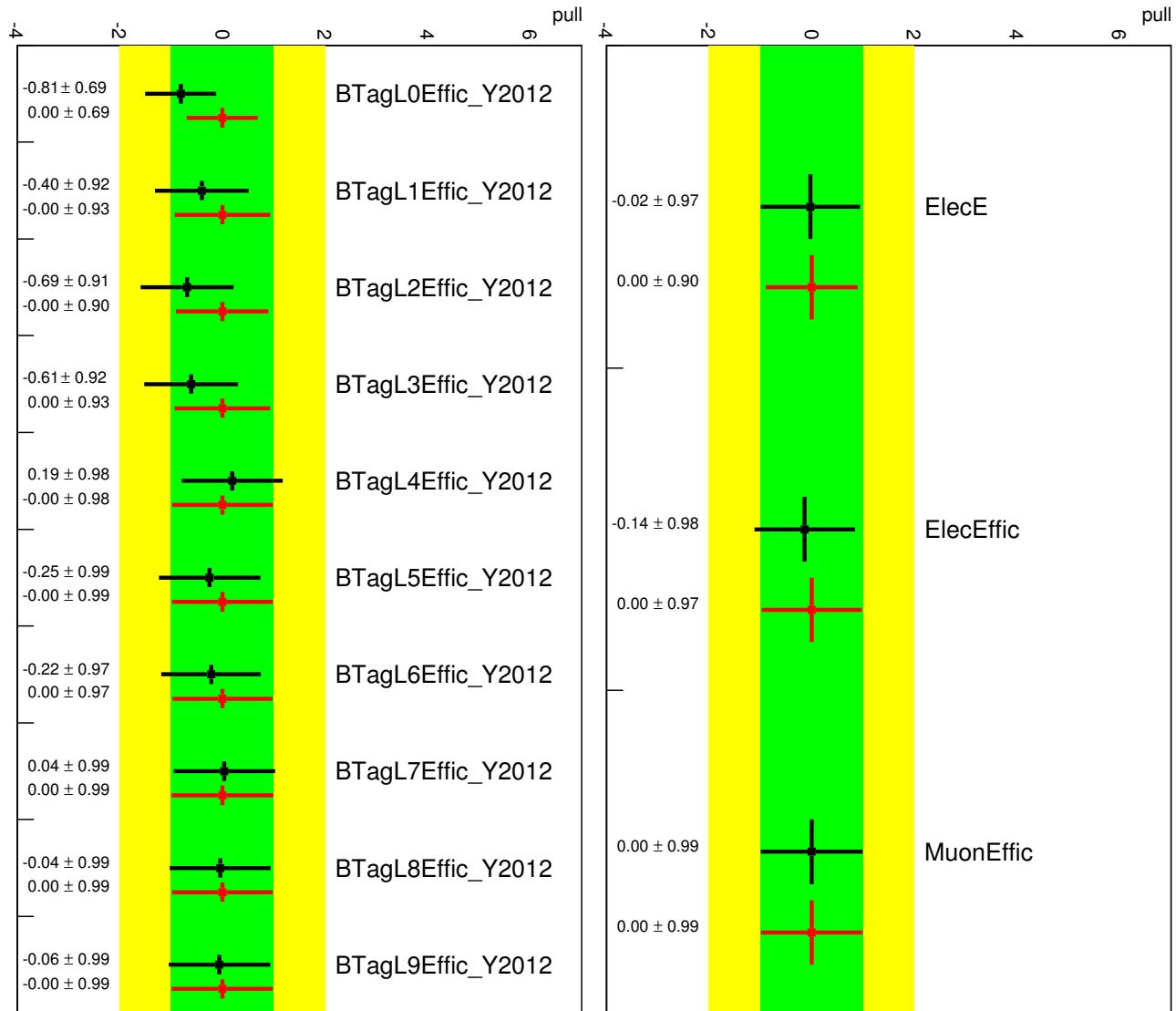


Figure 451: Pull plots for 2-lepton channel: light-jet tagging and leptons.

Not reviewed, for internal circulation only

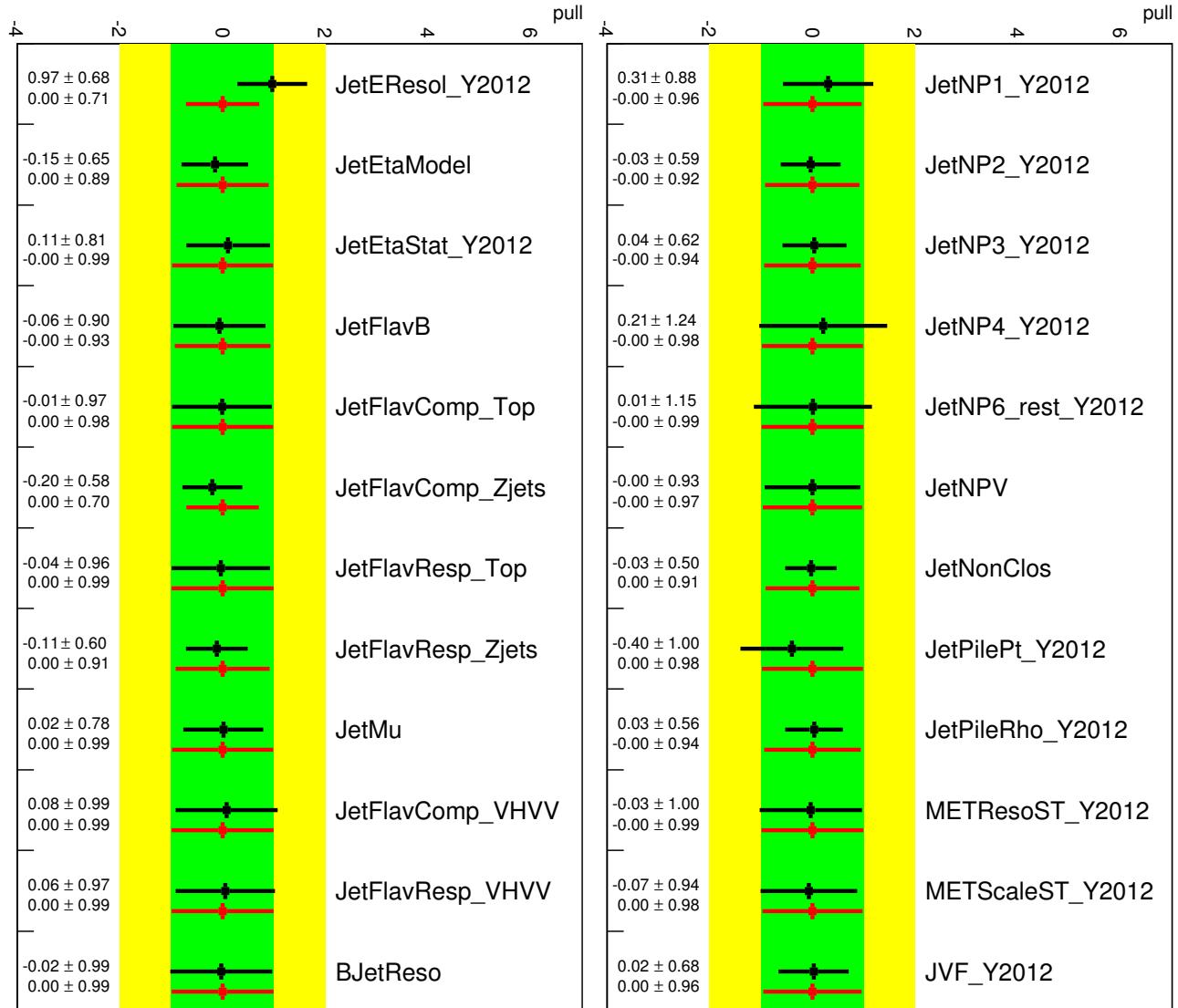


Figure 452: Pull plots for 2-lepton channel: Jet NPs.

Not reviewed, for internal circulation only

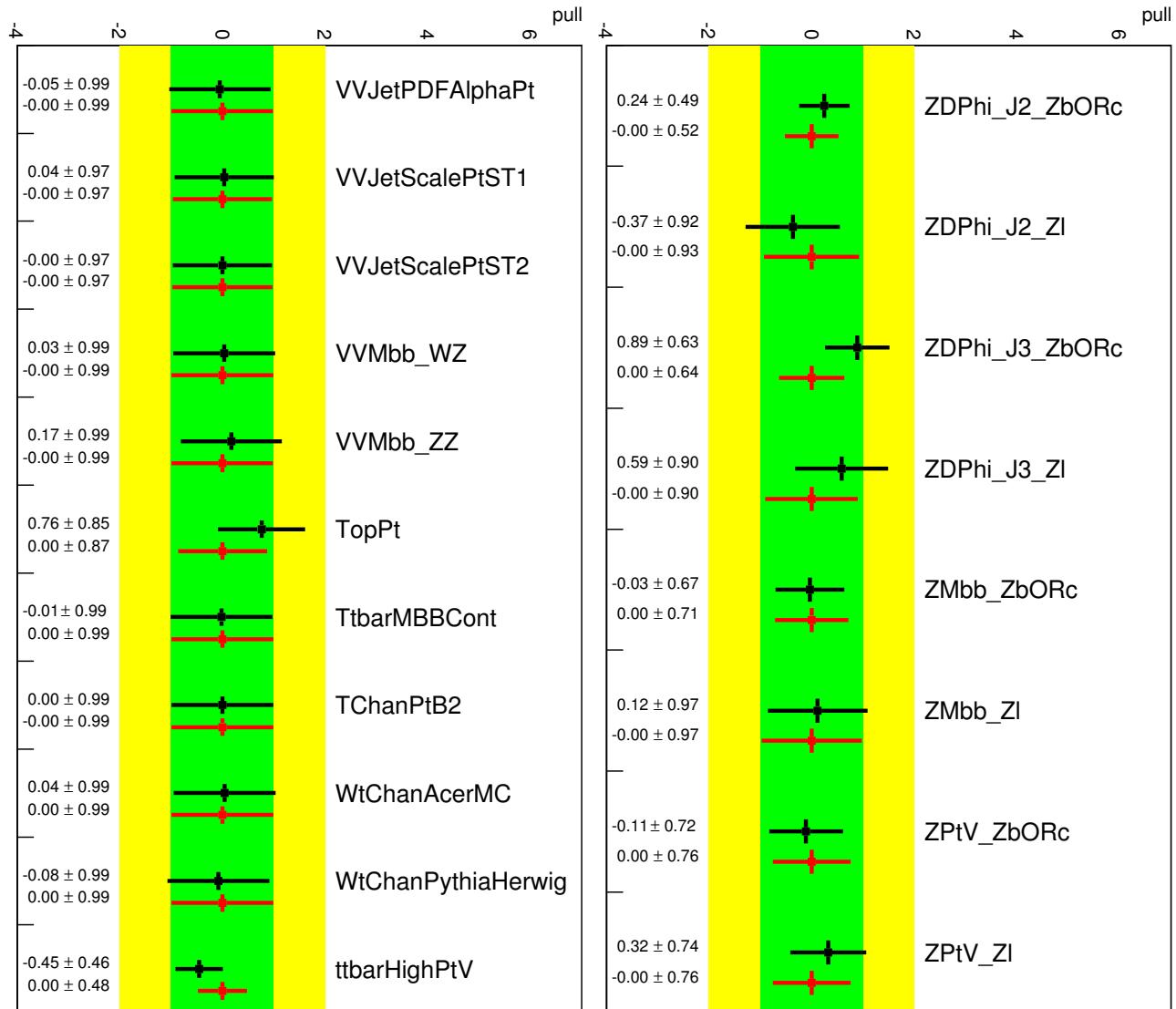


Figure 453: Pull plots for 2-lepton channel: Diboson and Top related uncertainties.

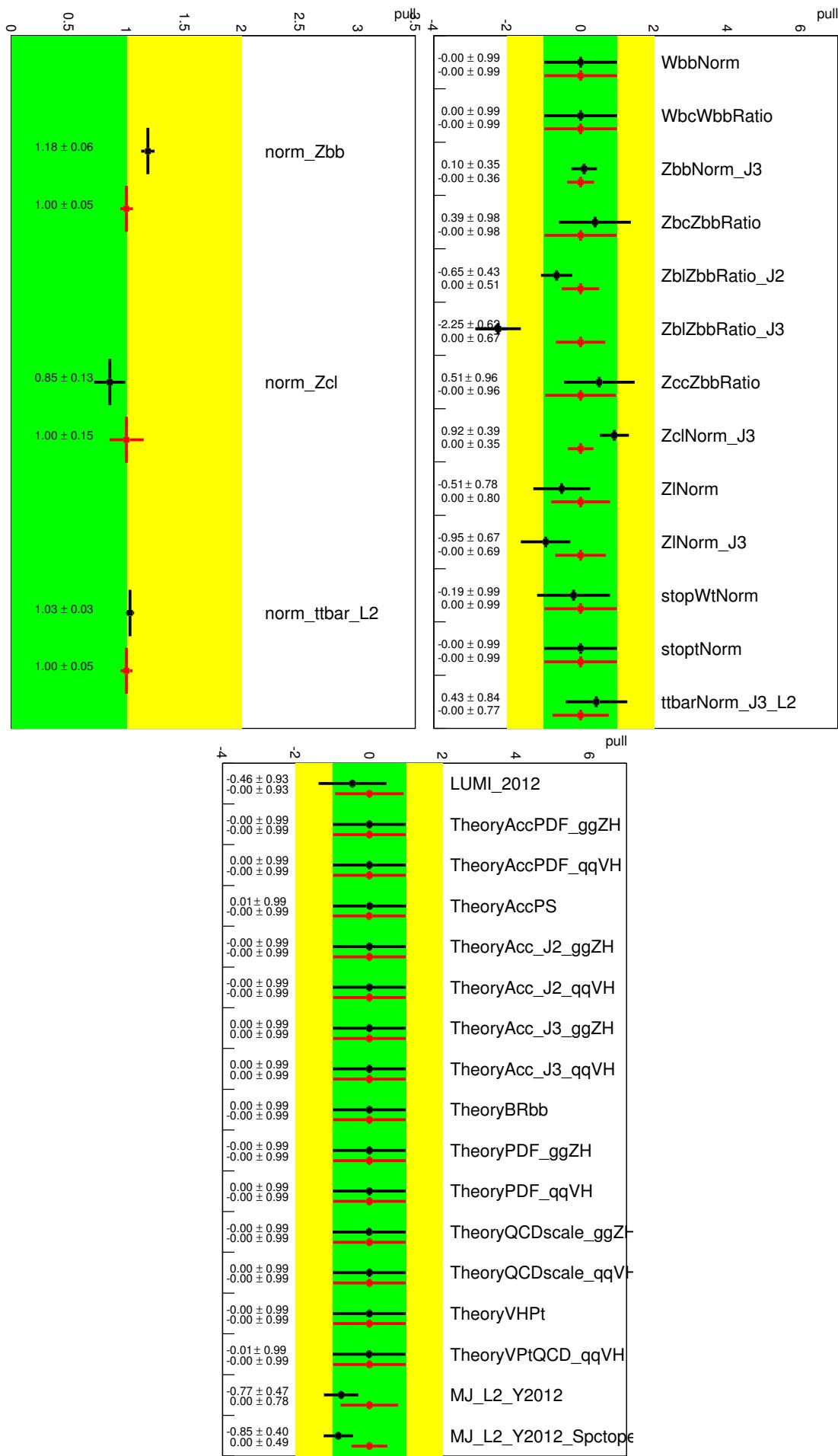


Figure 454: Pull plots for 2-lepton channel: Normalization and residual uncertainties.

Not reviewed, for internal circulation only

5036 **AH.1.6 Pre-fit and Post-Fit for the m_{jj} shape analysis in the 2-lepton fit**

[Not reviewed, for internal circulation only]

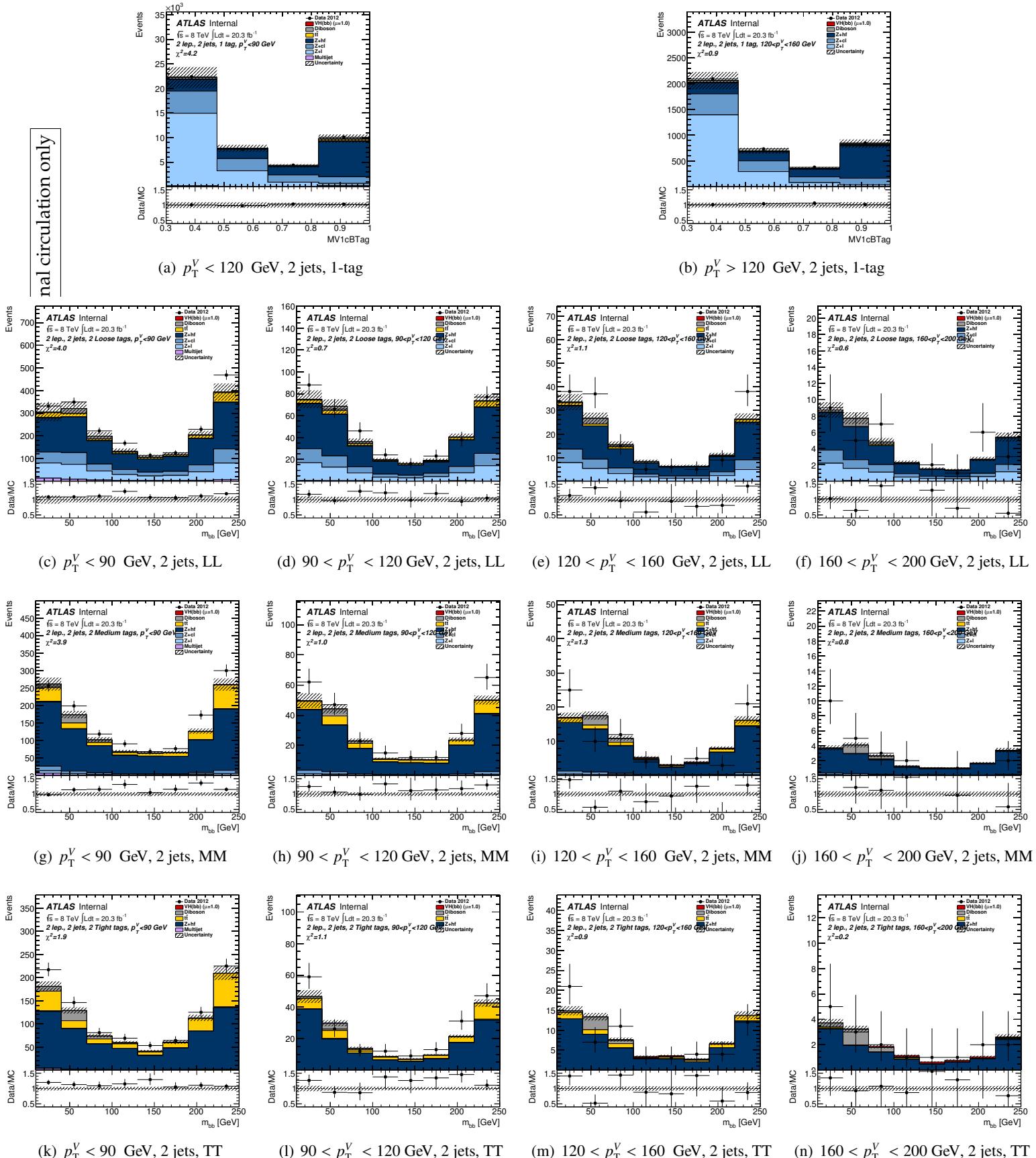


Figure 455: Pre-fit plots for m_{jj} distribution in 2-lepton events in the 1-tag (where mv1c is used in the fit) *LL*, *MM* and *TT* tag categories for the 2-jets events in the 2-lepton fit. Plots are shown for $p_T^V < 90$ GeV, $90 < p_T^V < 120$ GeV, $120 < p_T^V < 160$ GeV and $160 < p_T^V < 200$ GeV. The pre-fit background expectation is indicated by the dashed blue line.

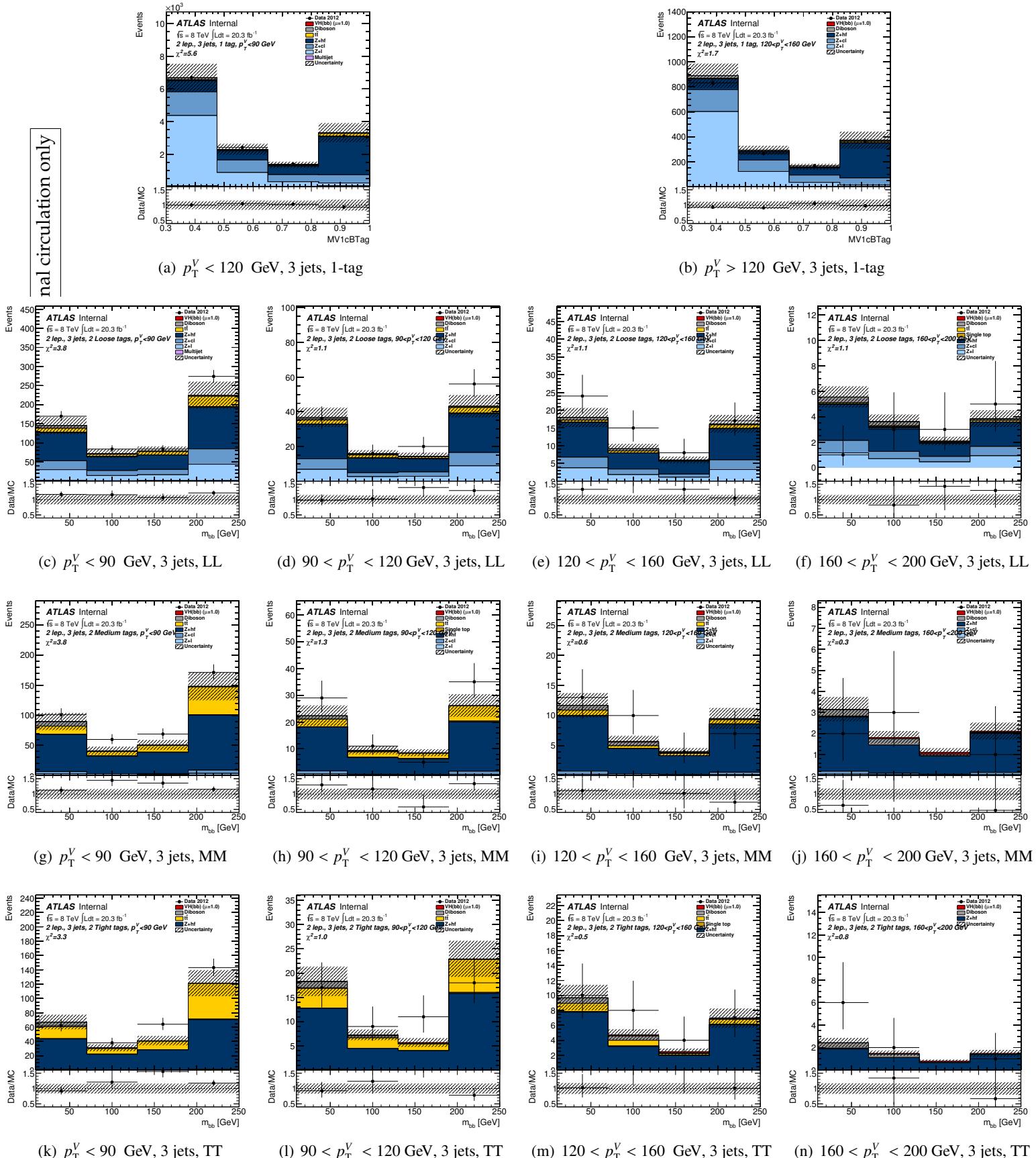


Figure 456: Pre-fit plots for m_{jj} distribution in 2-lepton events in the 1-tag (where mv1c is used in the fit) *LL*, *MM* and *TT* tag categories for the 3-jets events in the 2-lepton fit. Plots are shown for $p_T^V < 90$ GeV, $90 < p_T^V < 120$ GeV, $120 < p_T^V < 160$ GeV and $160 < p_T^V < 200$ GeV. The pre-fit background expectation is indicated by the dashed blue line.

Not reviewed, for internal circulation only

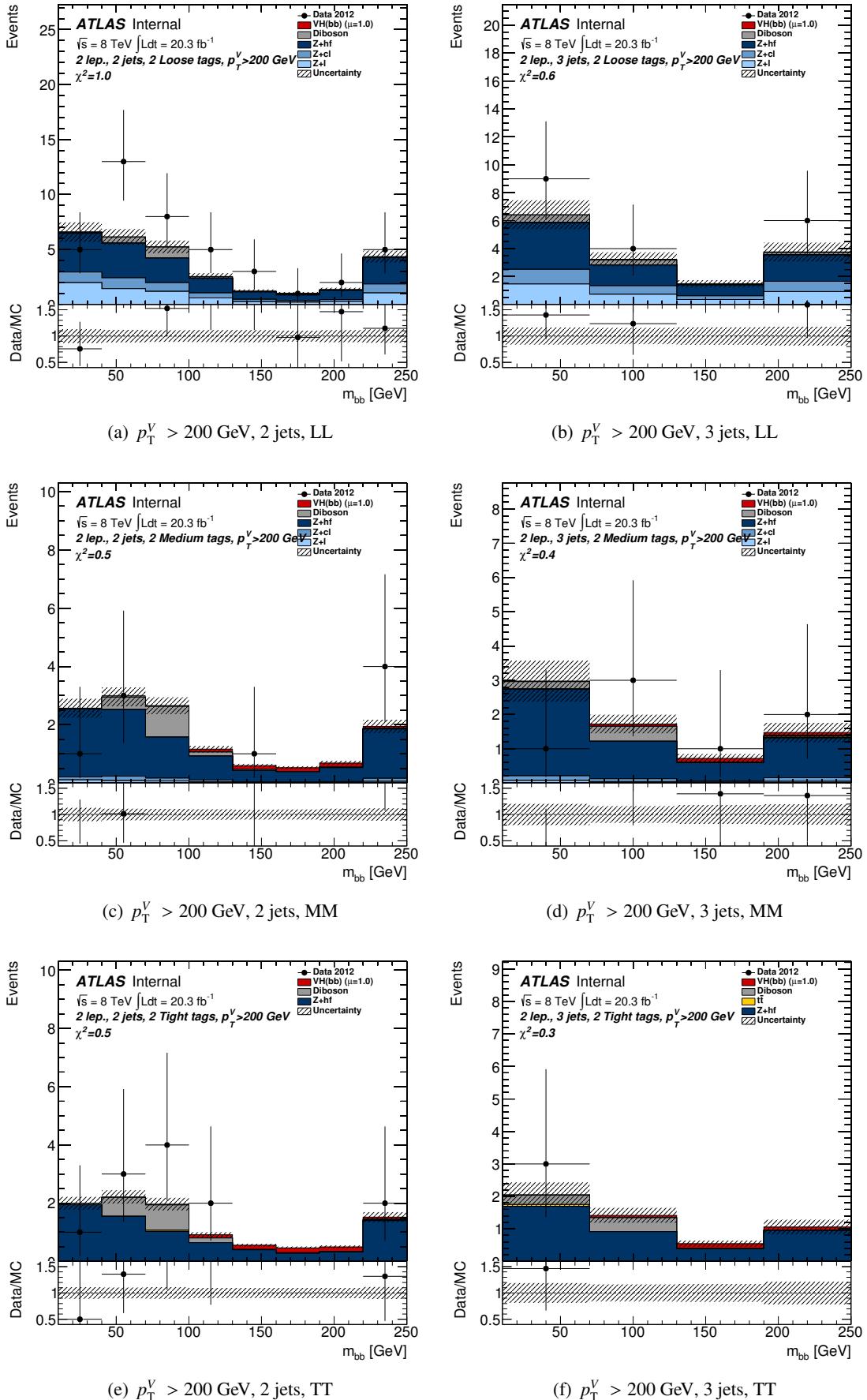


Figure 457: Pre-fit plots for m_{jj} distribution in 2-lepton events in the LL , MM and TT tag categories for the 2-jets and the 3-jets events in the 2-lepton fit. Plots are shown for $p_T^V > 200$ GeV. The pre-fit background expectation is indicated by the dashed blue line.

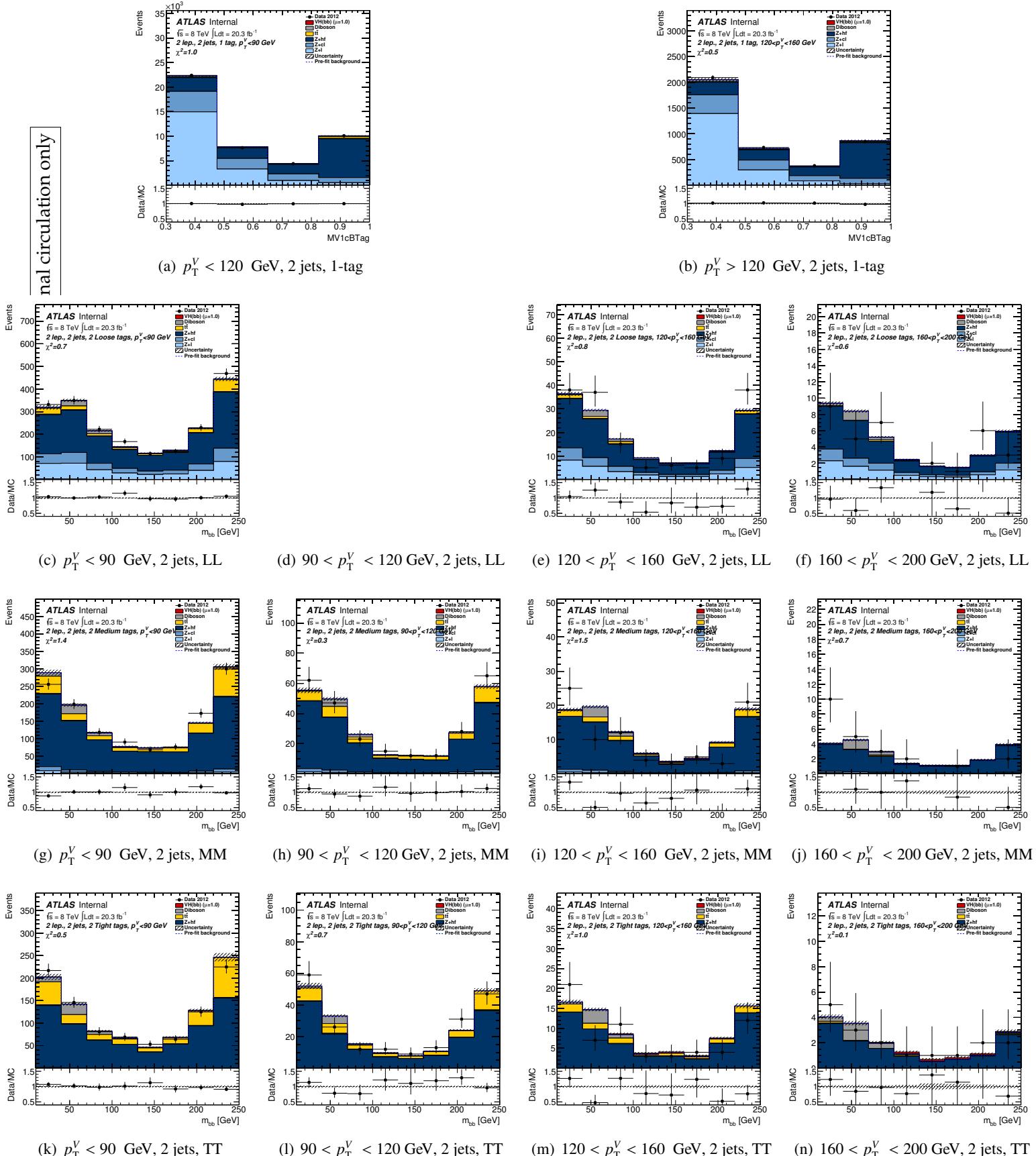


Figure 458: Post-fit plots for m_{jj} distribution in 2-lepton events in the 1-tag (where mv1c is used in the fit) *LL*, *MM* and *TT* tag categories for the 2-jets events in the 2-lepton fit. Plots are shown for $p_T^V < 90$ GeV, $90 < p_T^V < 120$ GeV, $120 < p_T^V < 160$ GeV and $160 < p_T^V < 200$ GeV. The pre-fit background expectation is indicated by the dashed blue line.

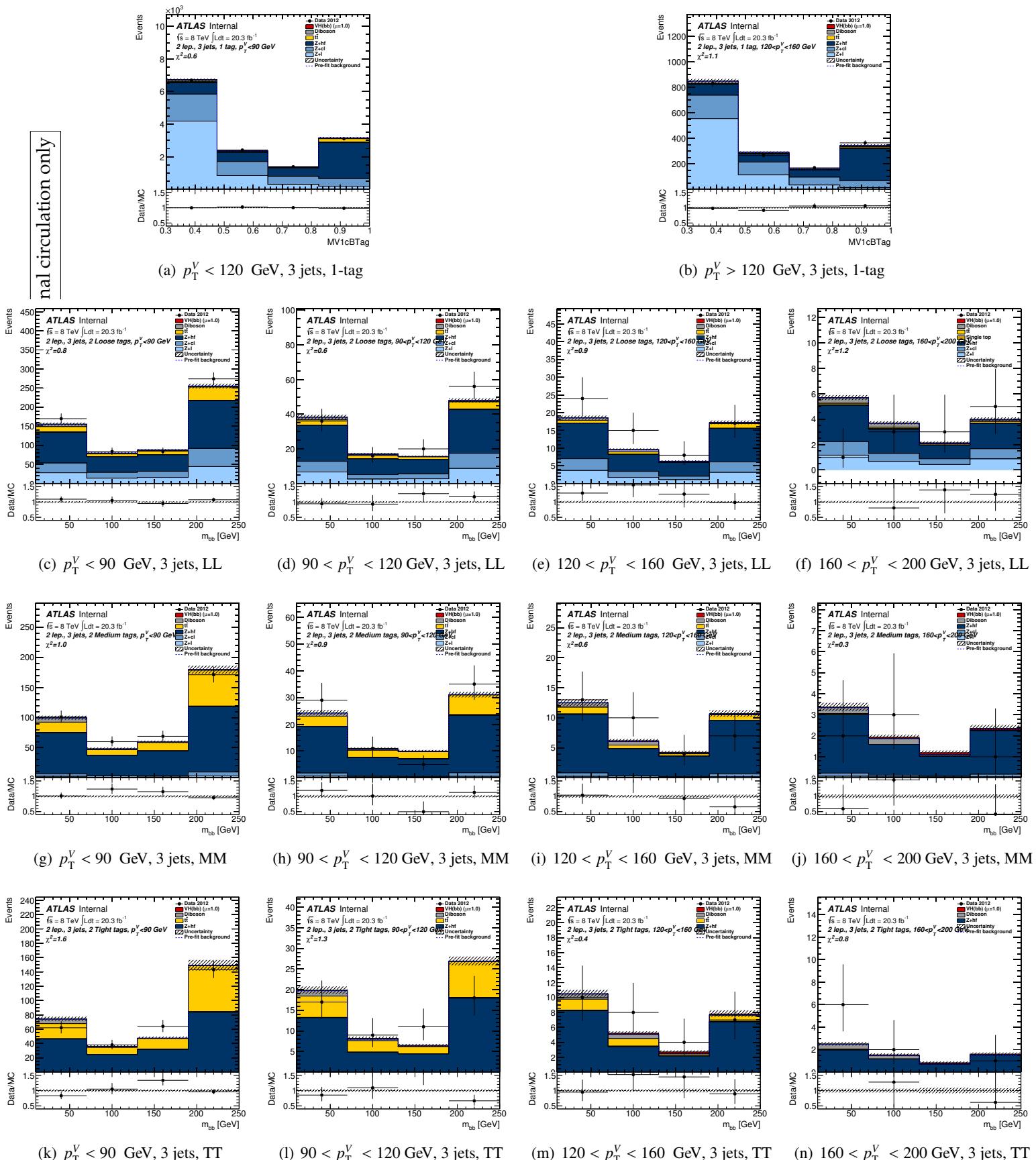


Figure 459: Post-fit plots for m_{jj} distribution in 2-lepton events in the 1-tag (where mv1c is used in the fit) *LL*, *MM* and *TT* tag categories for the 3-jets events in the 2-lepton fit. Plots are shown for $p_T^V < 90$ GeV, $90 < p_T^V < 120$ GeV, $120 < p_T^V < 160$ GeV and $160 < p_T^V < 200$ GeV. The pre-fit background expectation is indicated by the dashed blue line.

Not reviewed, for internal circulation only

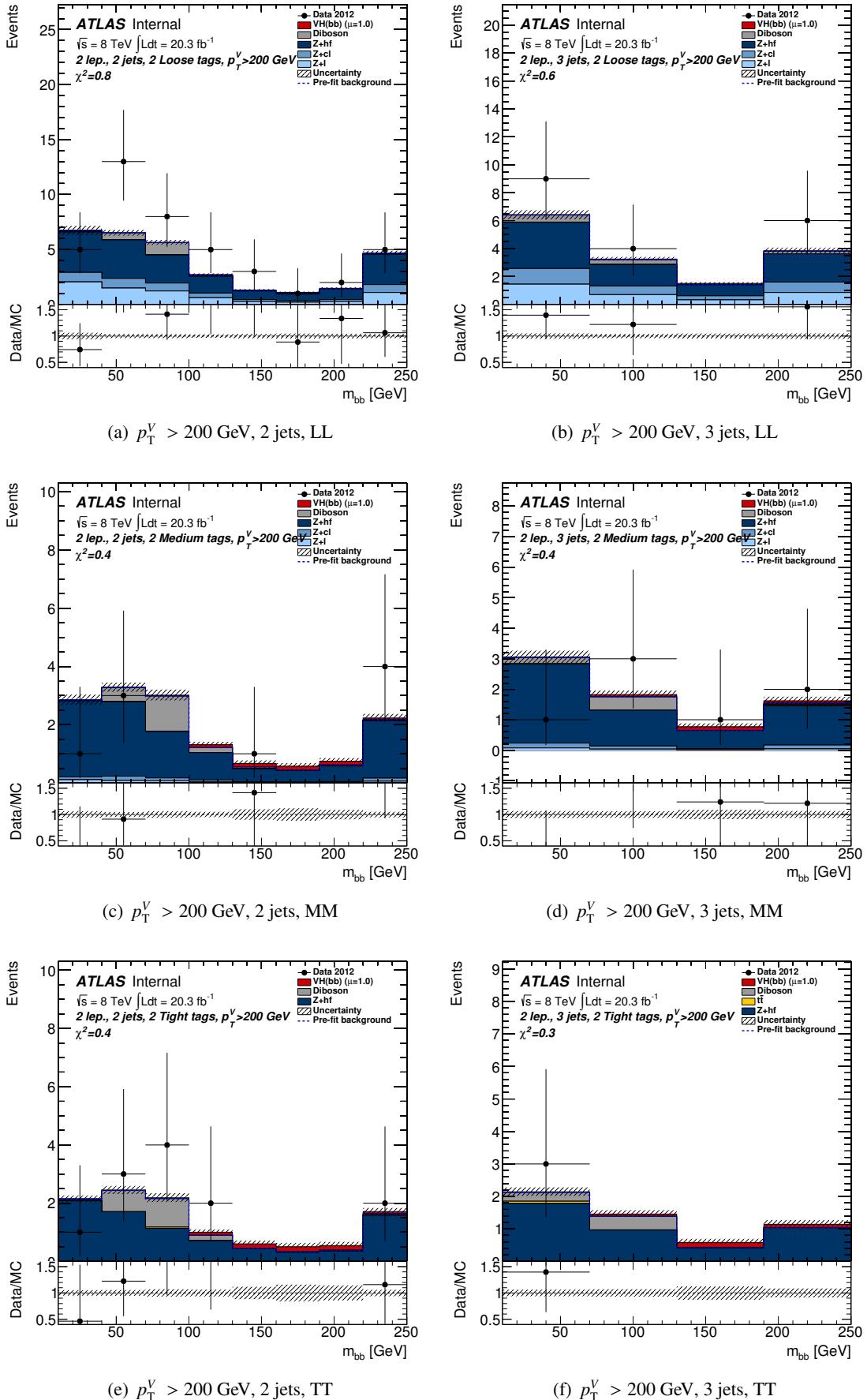


Figure 460: Post-fit plots for m_{jj} distribution in 2-lepton events in the LL , MM and TT tag categories for the 2-jets and the 3-jets events in the 2-lepton fit. Plots are shown for $p_T^V > 200$ GeV. The pre-fit background expectation is indicated by the dashed blue line.

5037 **AH.2 MVA**5038 **AH.2.1 0-lepton pull plots**

The pull plots for 0-lepton are shown in Figure. 461-465.

Not reviewed, for internal circulation only

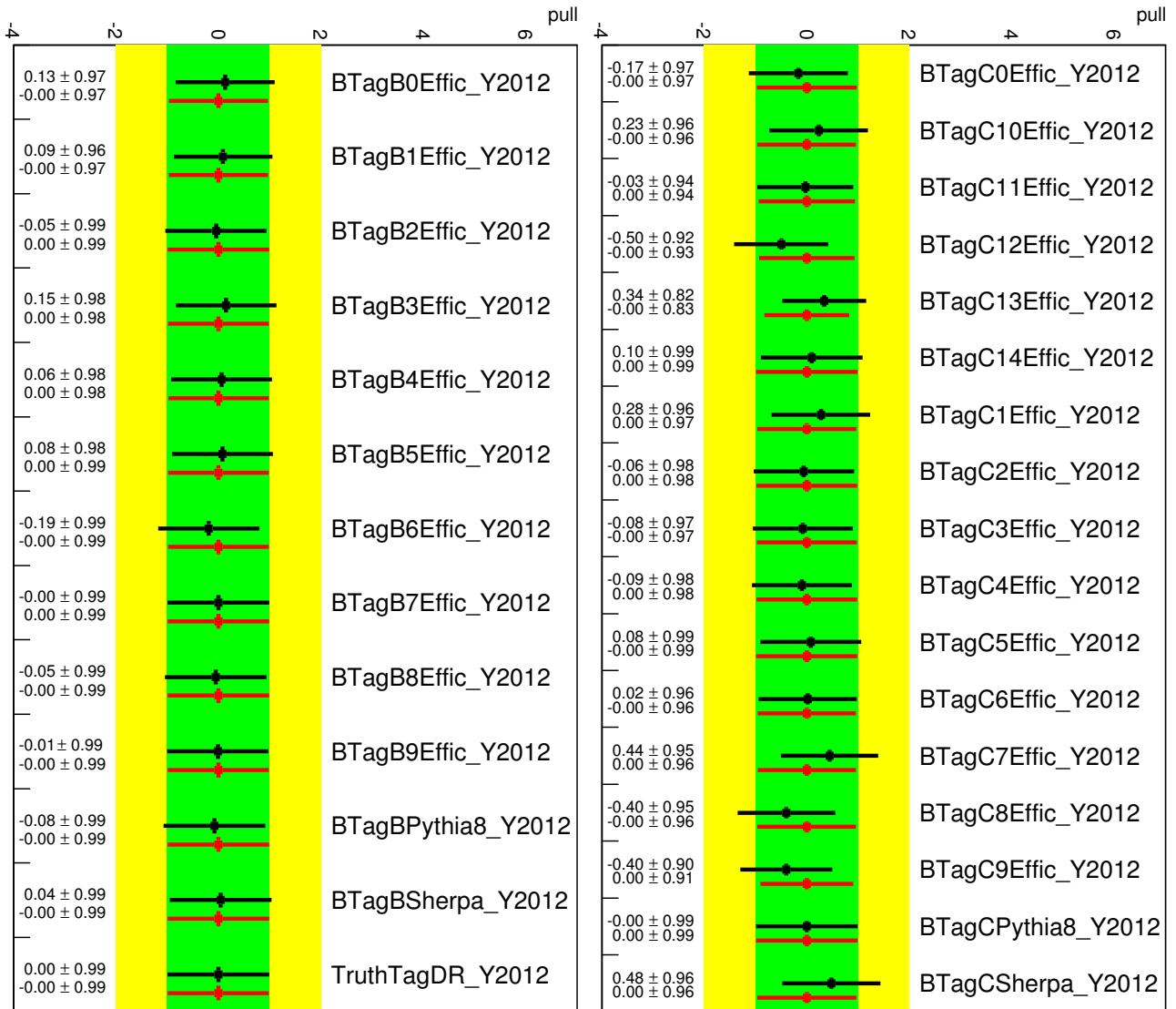


Figure 461: Pull plots for 0-lepton channel: b - and c -jet tagging.

Not reviewed, for internal circulation only

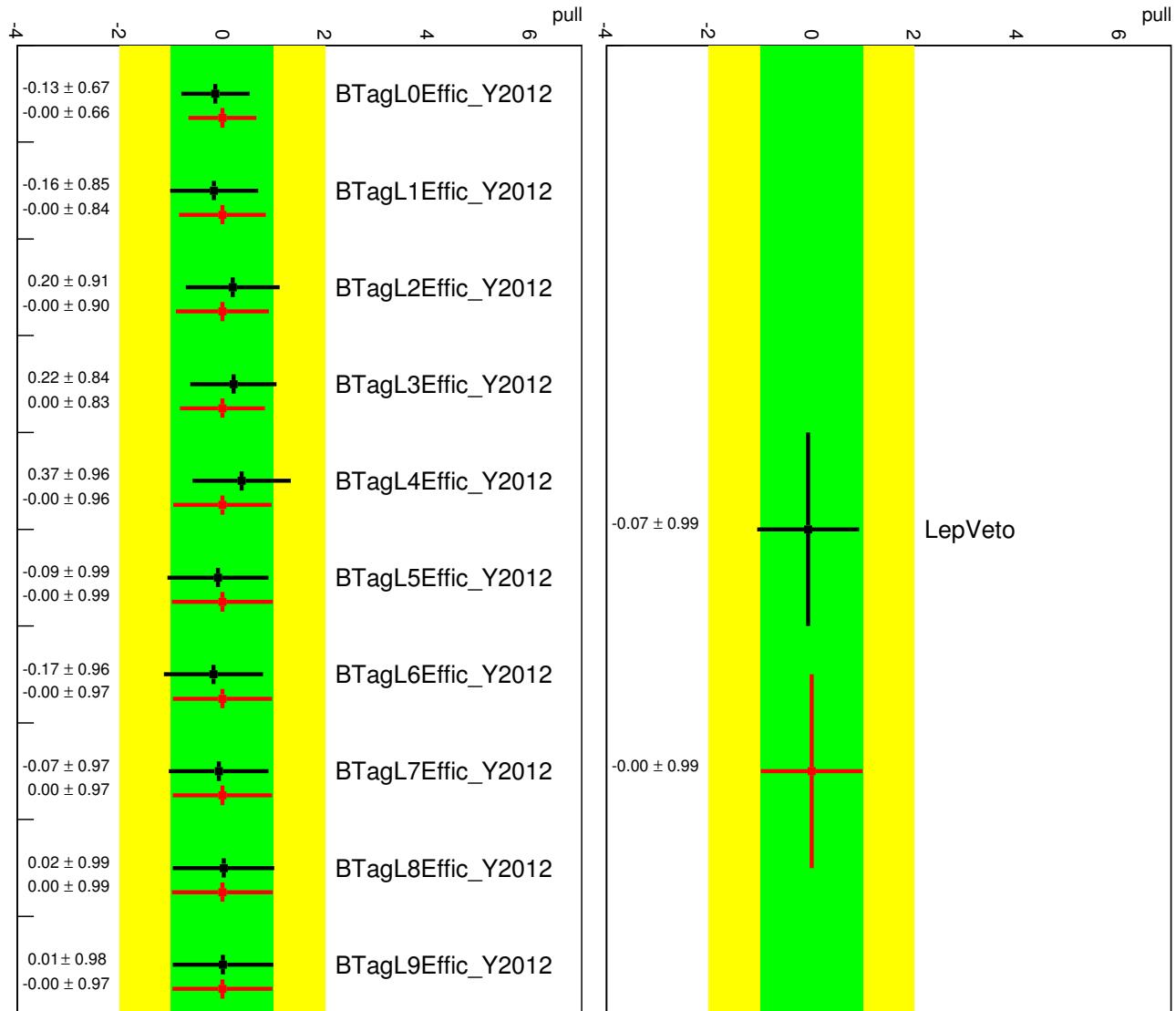


Figure 462: Pull plots for 0-lepton channel: light-jet tagging and leptons.

Not reviewed, for internal circulation only

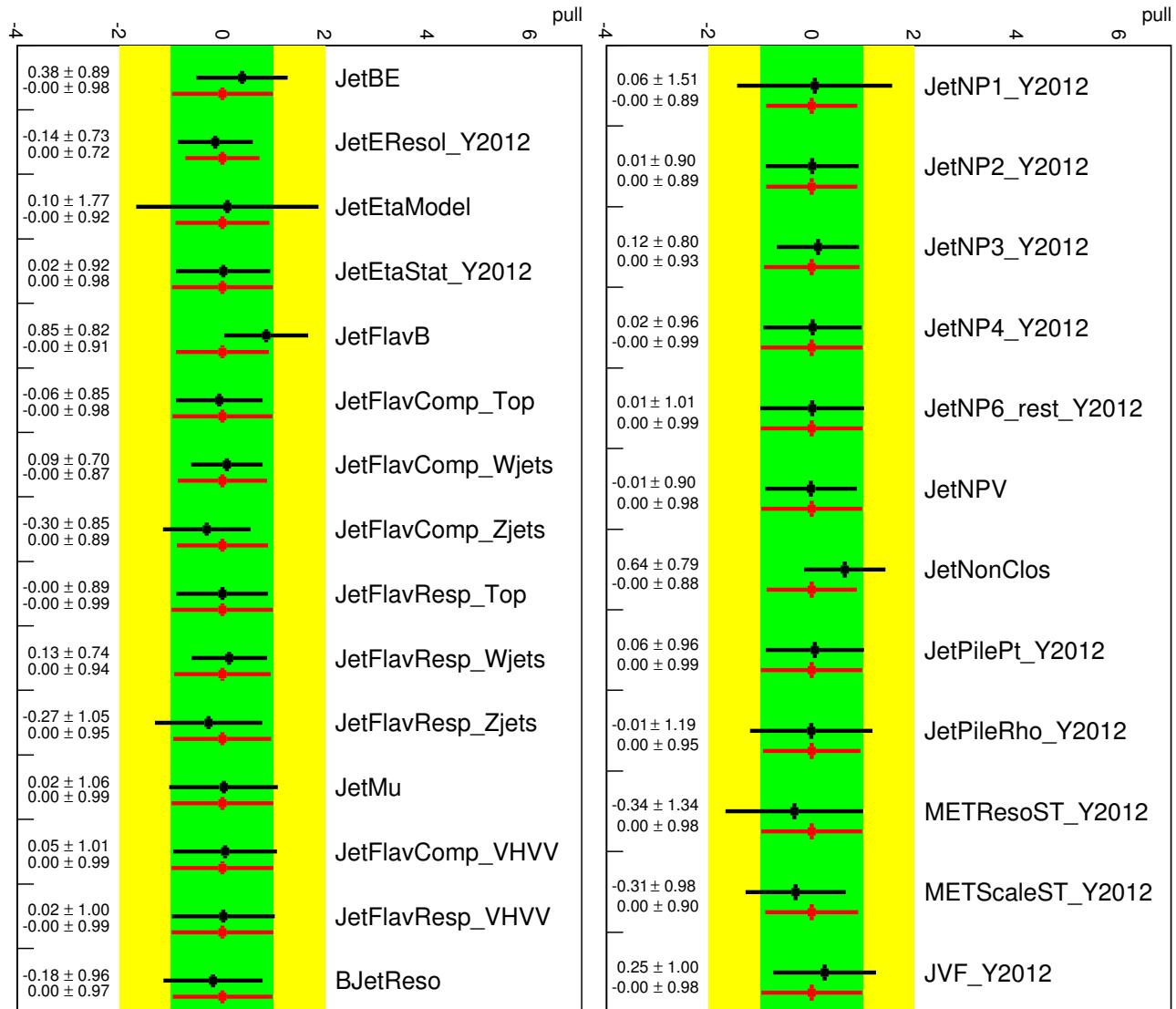


Figure 463: Pull plots for 0-lepton channel: Jet NPs.

Not reviewed, for internal circulation only

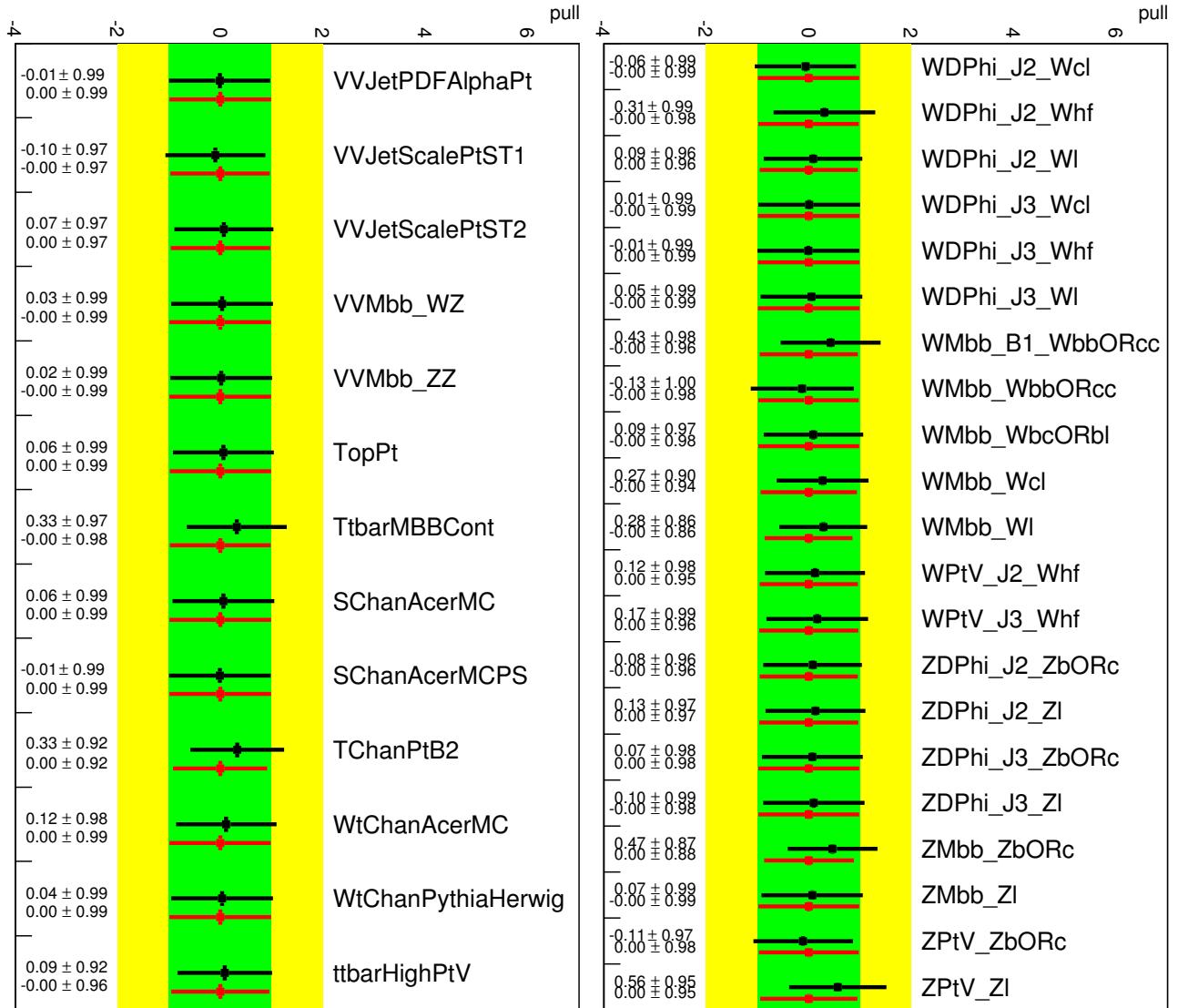


Figure 464: Pull plots for 0-lepton channel: Diboson/Top and W/Z related uncertainties.

Not reviewed, for internal circulation only

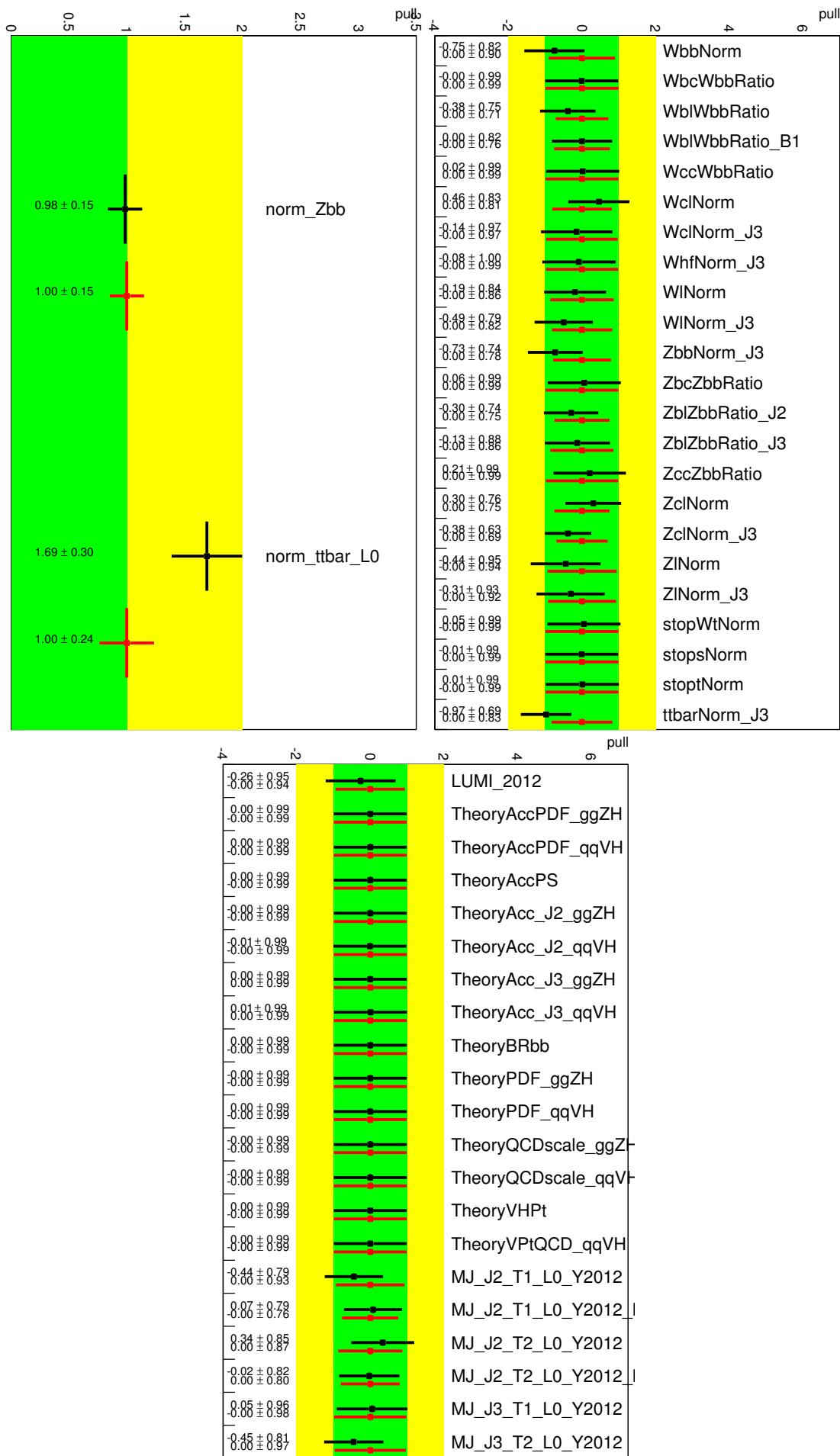


Figure 465: Pull plots for 0-lepton channel: Other model and normalization uncertainties.

5040 **AH.2.2 Pre-fit and Post-Fit for the MVA analysis in the 0-lepton fit**

[Not reviewed, for internal circulation only]

Not reviewed, for internal circulation only

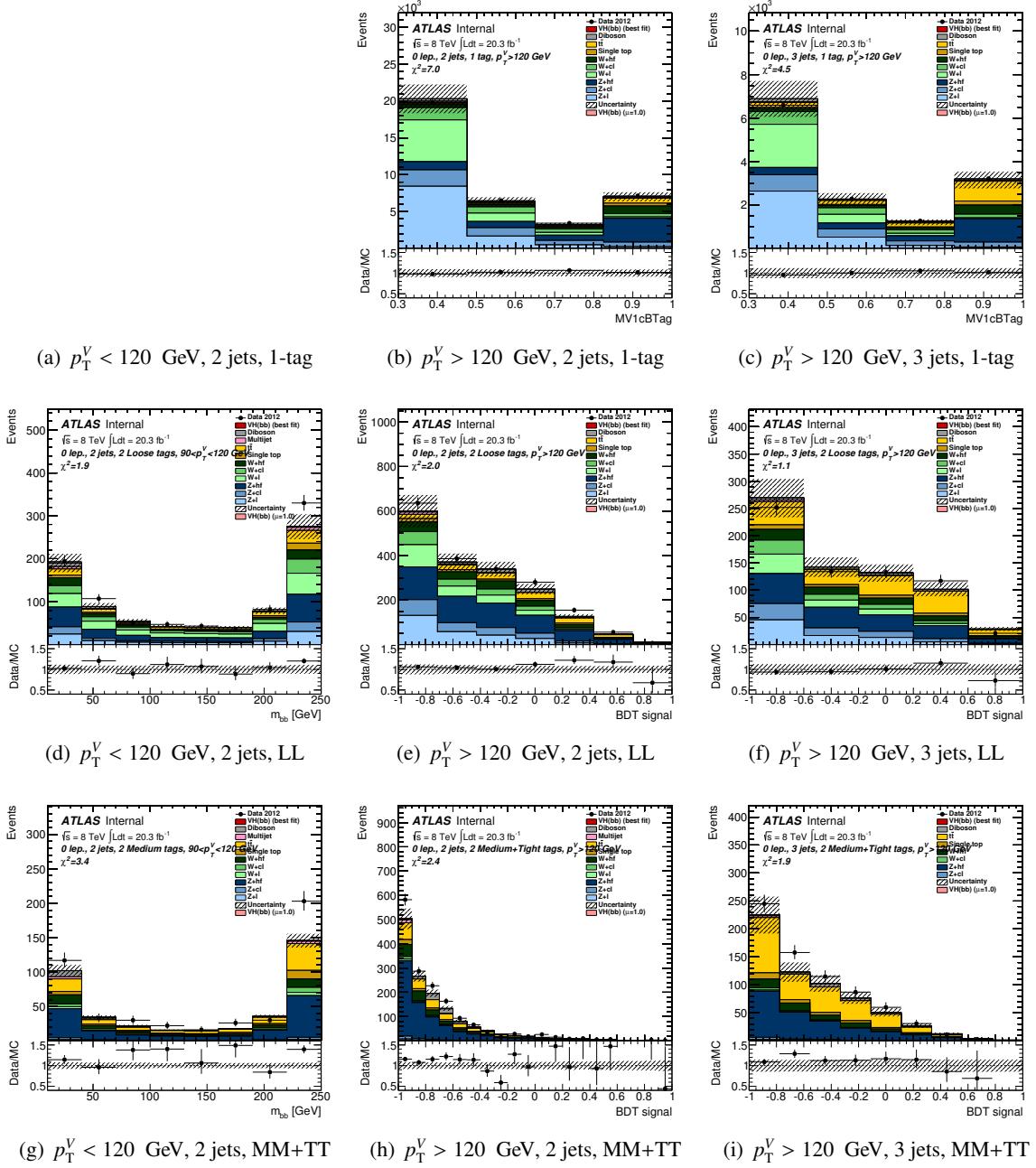


Figure 466: Pre-fit plots for MVA distribution in 0-lepton events with 1 b-tag (MV1c is fit here), LL and MM + TT b-tags in the 0 lepton fit.

Not reviewed, for internal circulation only

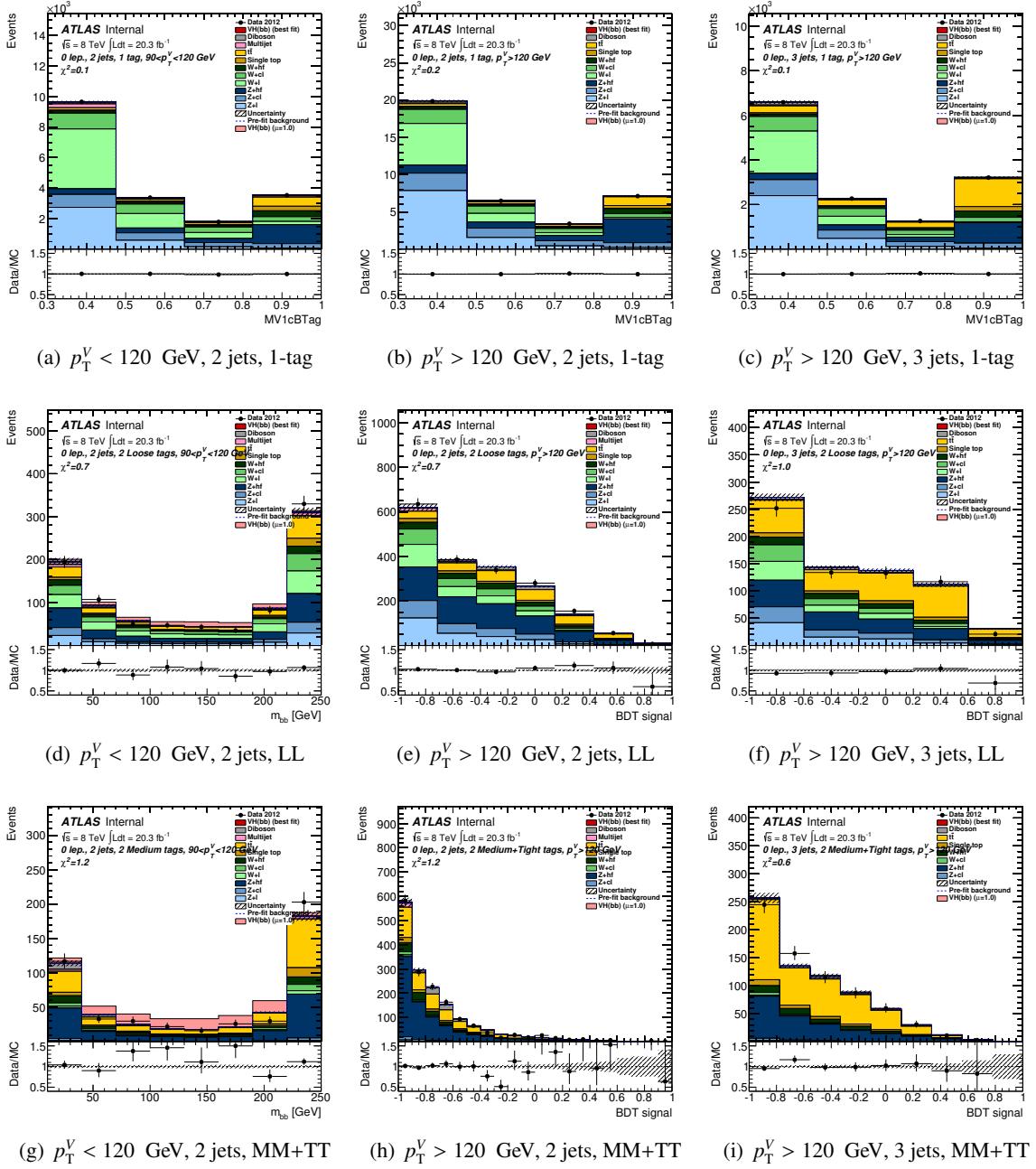


Figure 467: Post-fit plots for MVA distribution in 0-lepton events with 1 b-tag (MV1c is fit here), *LL* and *MM + TT* b-tags in the 0 lepton fit. The pre-fit background expectation is indicated by the dashed blue line.

5041 **AH.2.3 1-lepton pull plots**

5042 The pull plots for 1-lepton are shown in Figure. 468-472.

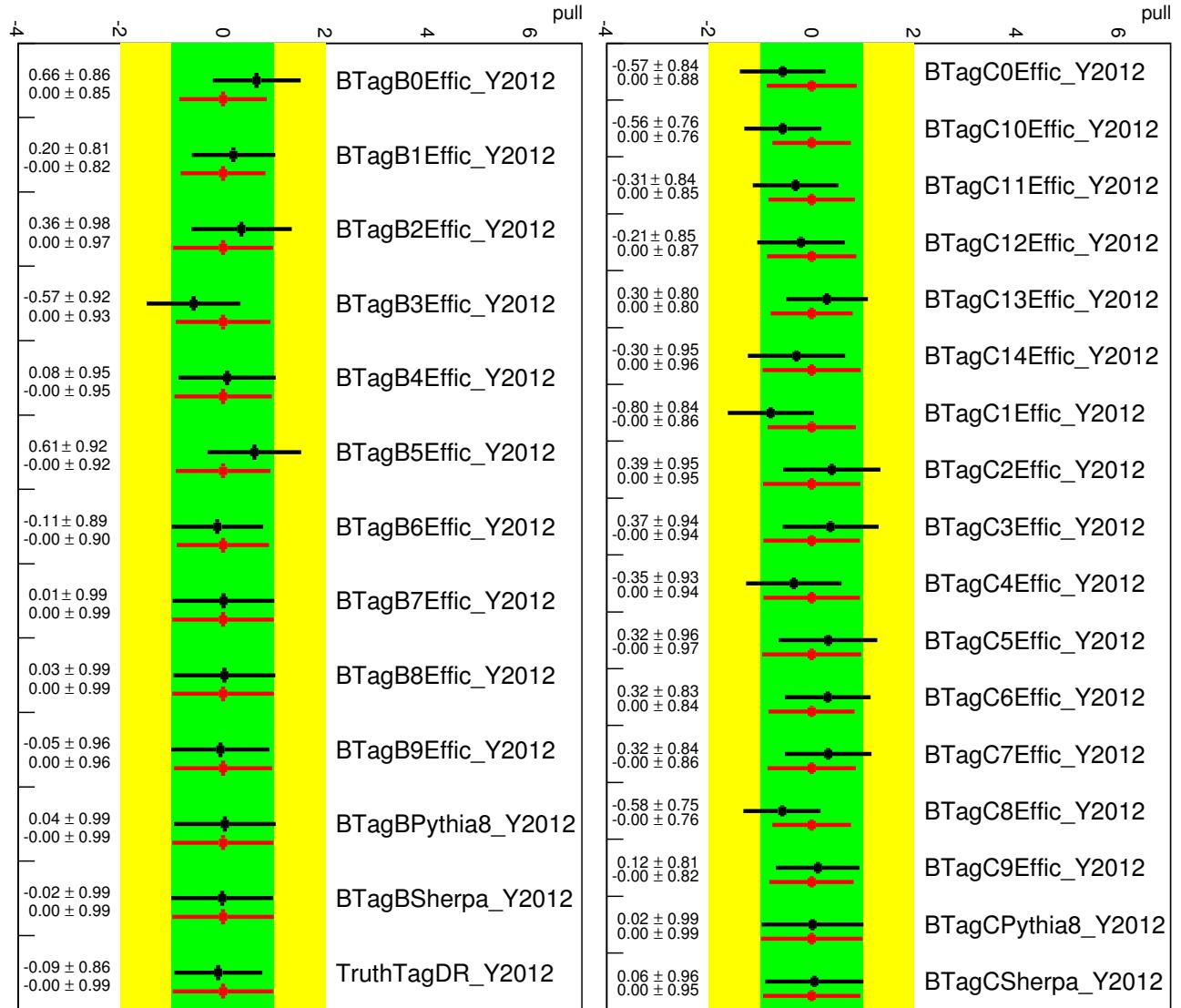


Figure 468: Pull plots for 1-lepton channel: *b*- and *c*-jet tagging.

Not reviewed, for internal circulation only

Not reviewed, for internal circulation only

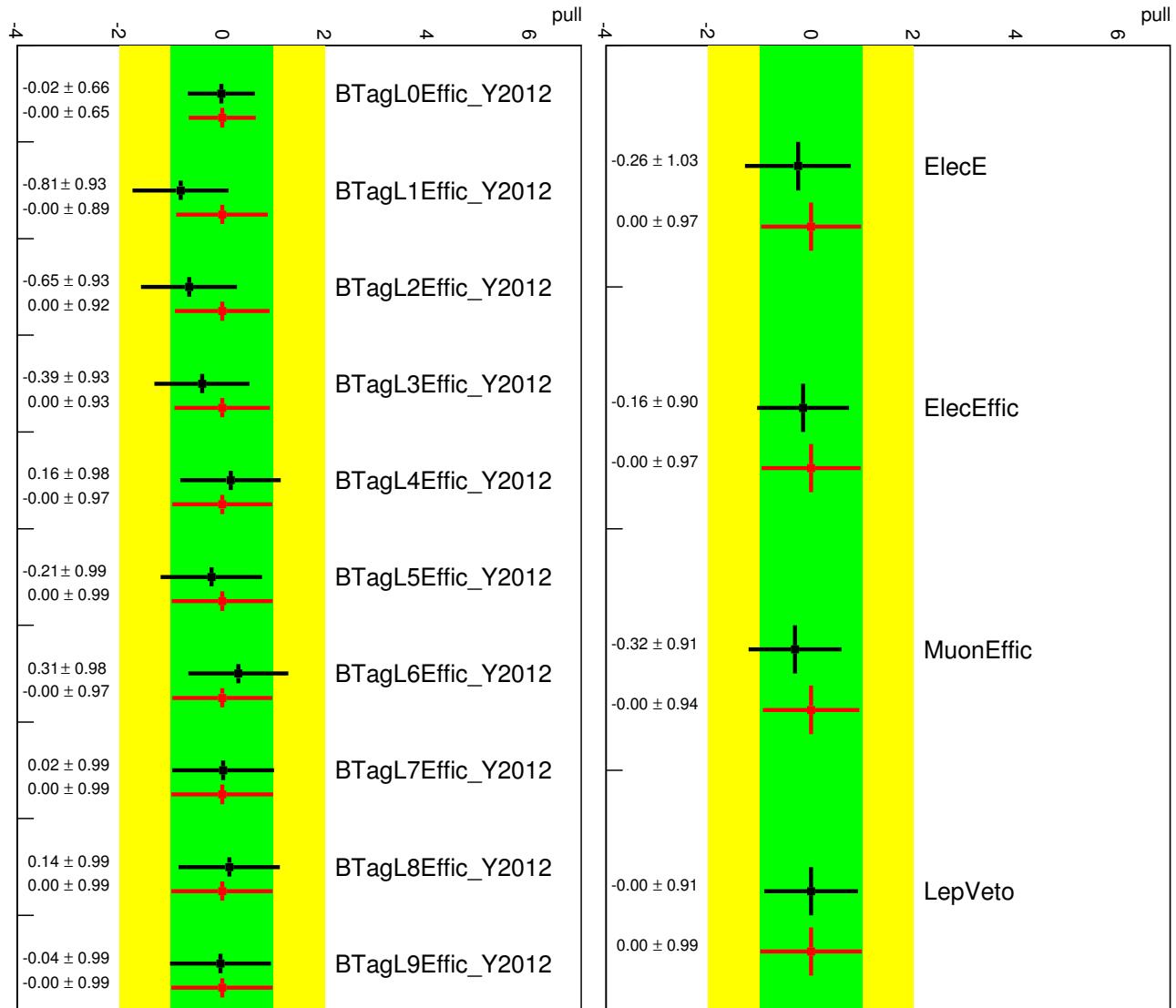


Figure 469: Pull plots for 1-lepton channel: light-jet tagging and leptons.

Not reviewed, for internal circulation only

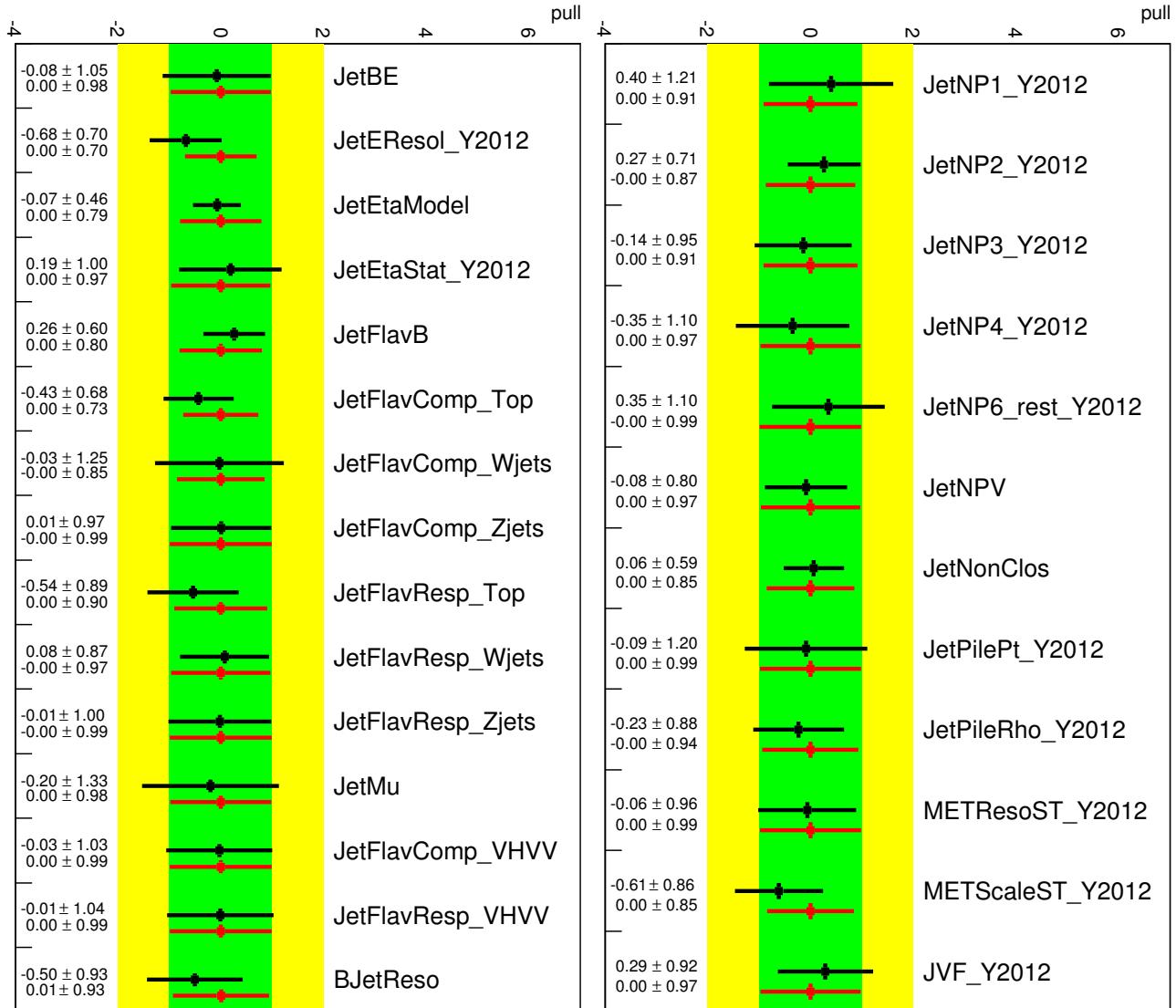


Figure 470: Pull plots for 1-lepton channel: Jet NPs.

Not reviewed, for internal circulation only

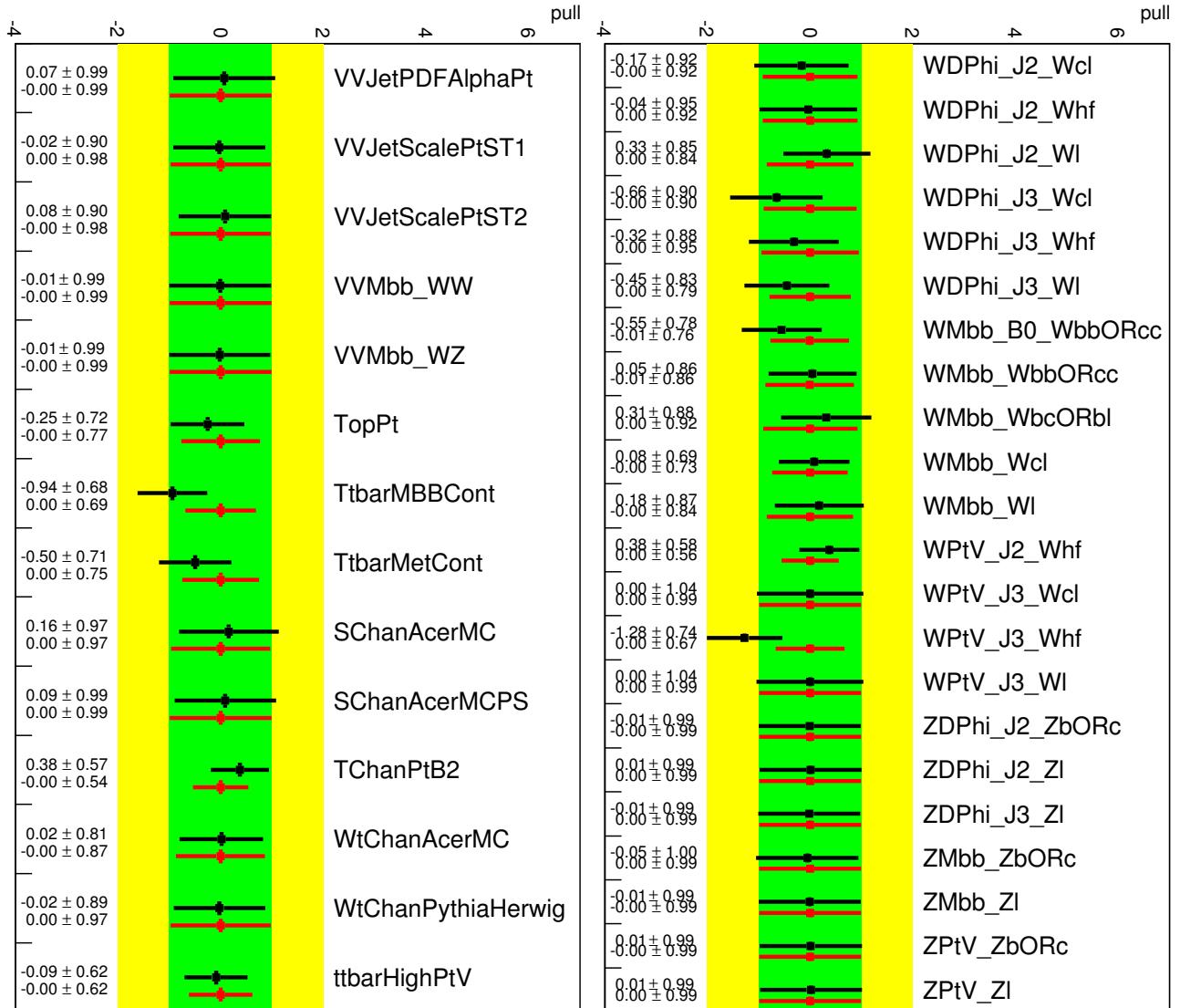


Figure 471: Pull plots for 1-lepton channel: Diboson/Top and W/Z related uncertainties.

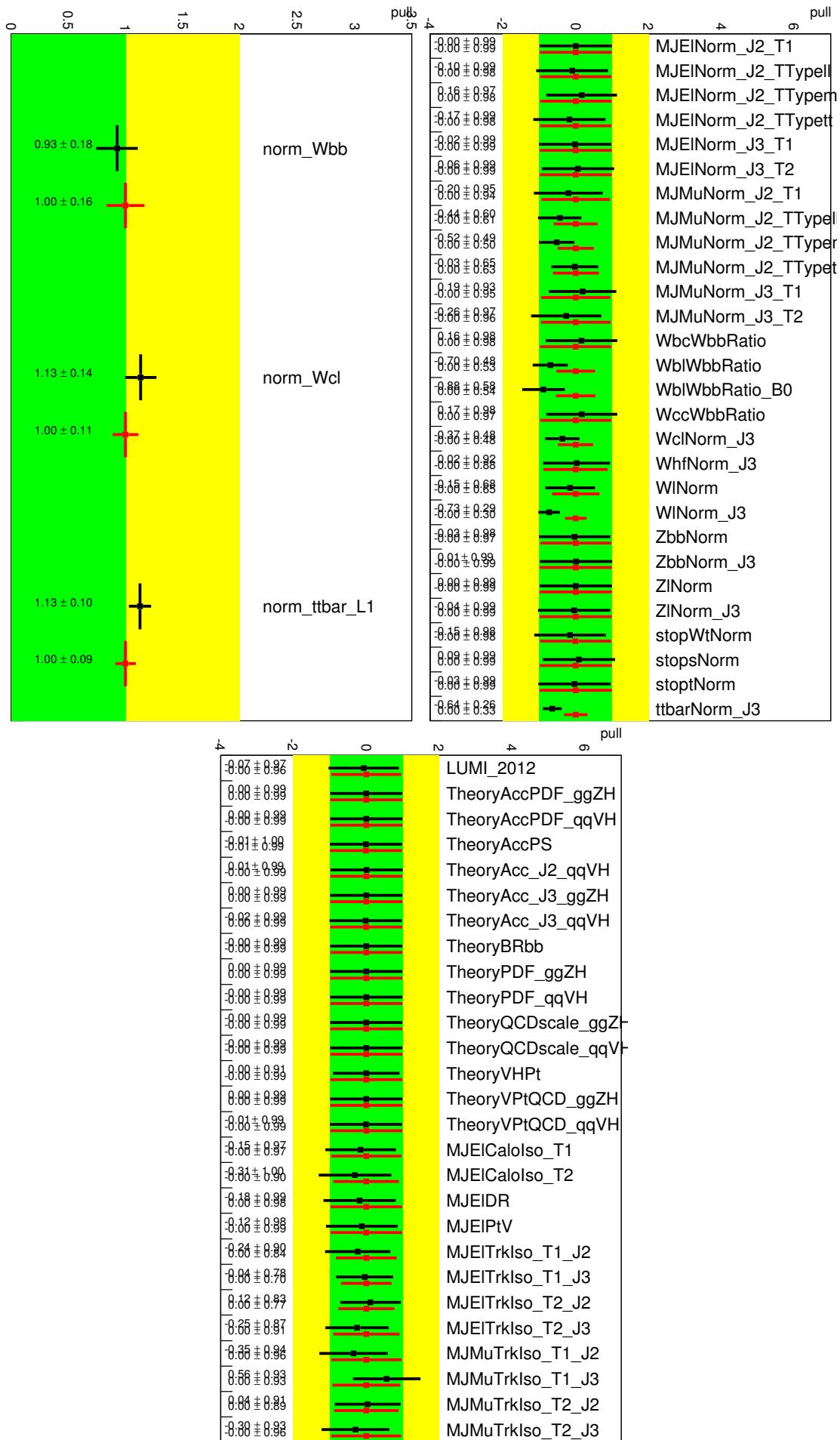


Figure 472: Pull plots for 1-lepton channel: Other model and normalization uncertainties.

Not reviewed, for internal circulation only

5043 AH.2.4 Pre-fit and Post-Fit for the MVA analysis in the 1-lepton fit

5044 For the moment, the prefit plots are in the section.

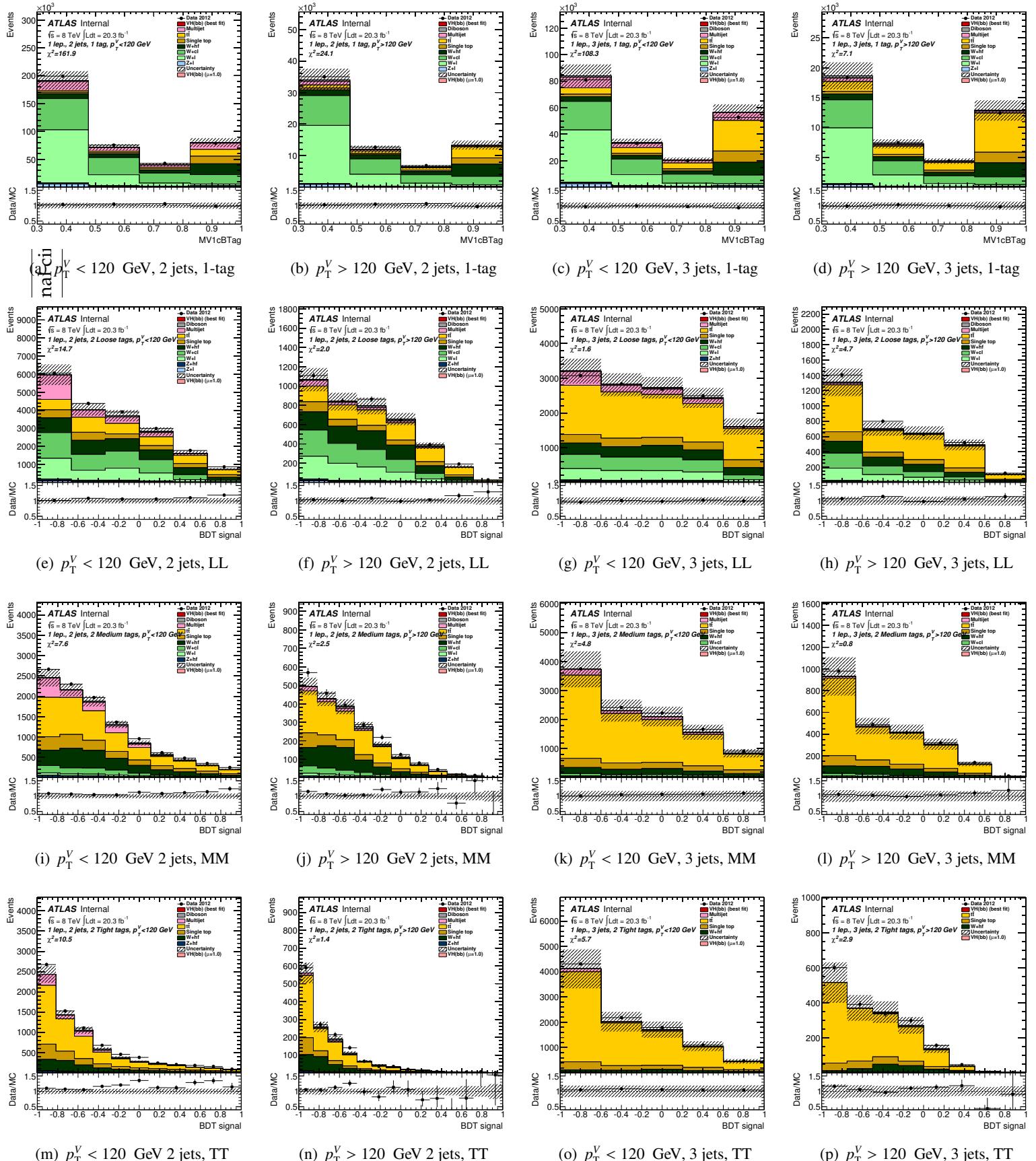


Figure 473: Pre-fit plots for MVA distribution in 1-lepton 2-jet and 3-jets, $p_T^V < 120$ GeV (left) and $p_T^V > 120$ GeV (right) events with 1 b-tag (MV1c is fit here), LL, MM and TT b-tags in the 1 lepton fit.

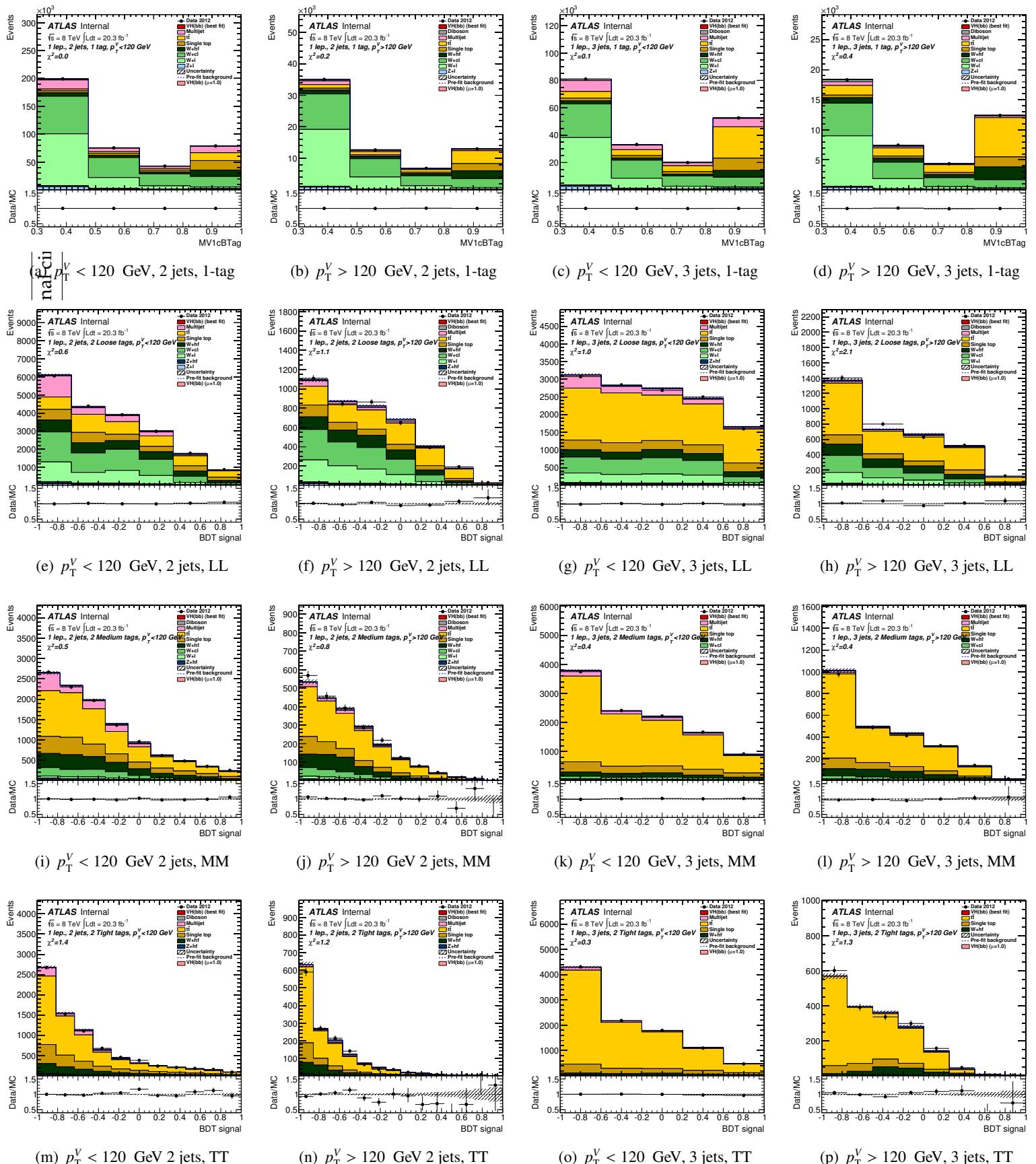


Figure 474: Post-fit plots for MVA distribution in 1-lepton 2-jet and 3-jets, $p_T^V < 120$ GeV (left) and $p_T^V > 120$ GeV (right) events with 1 b-tag (MV1c is fit here), LL, MM and TT b-tags in the 1 lepton fit.

5045 **AH.2.5 2-lepton pull plots**

5046 The pull plots for 2-lepton are shown in Figure. 475-479.

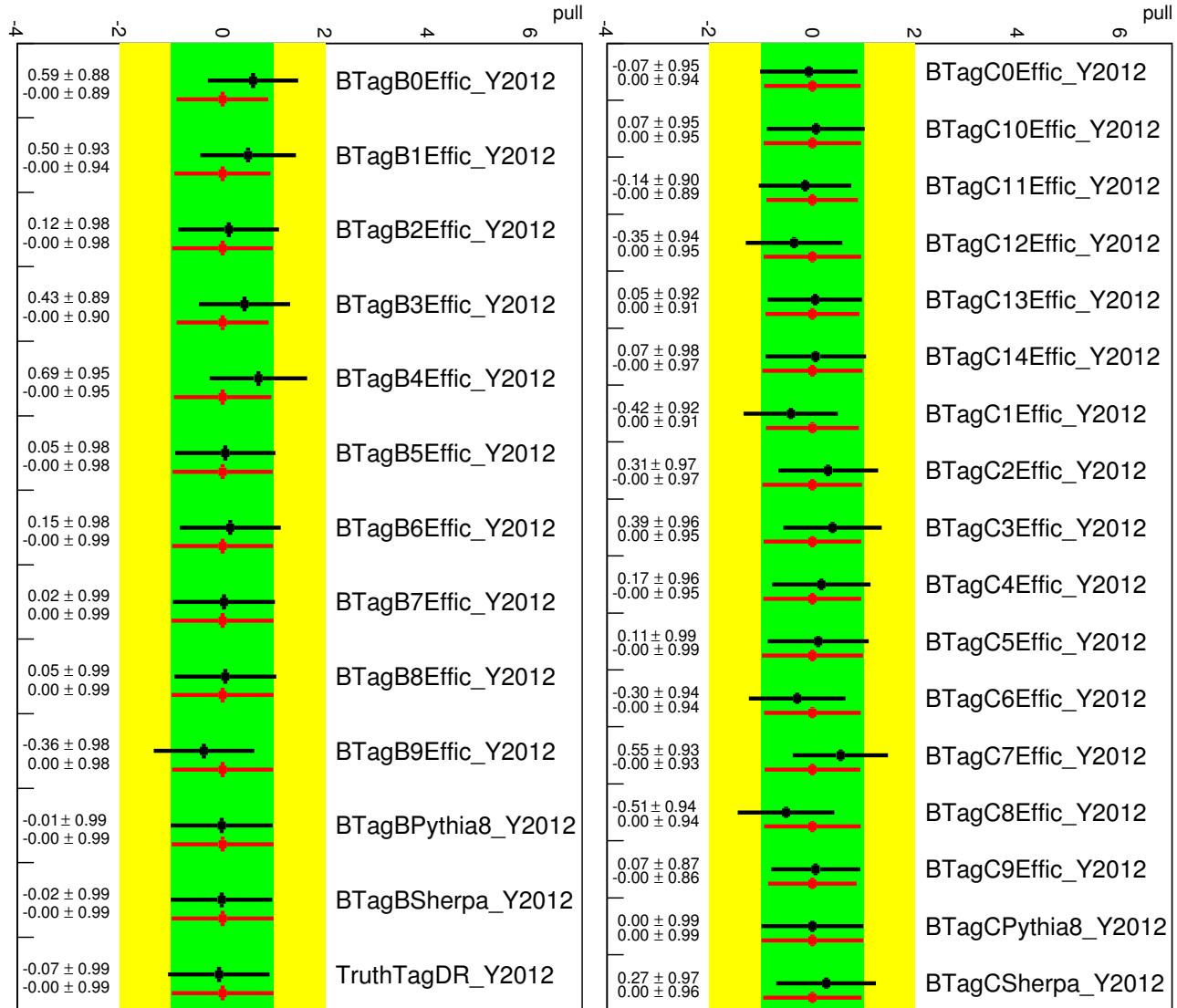


Figure 475: Pull plots for 2-lepton channel: *b*- and *c*-jet tagging.

Not reviewed, for internal circulation only

Not reviewed, for internal circulation only

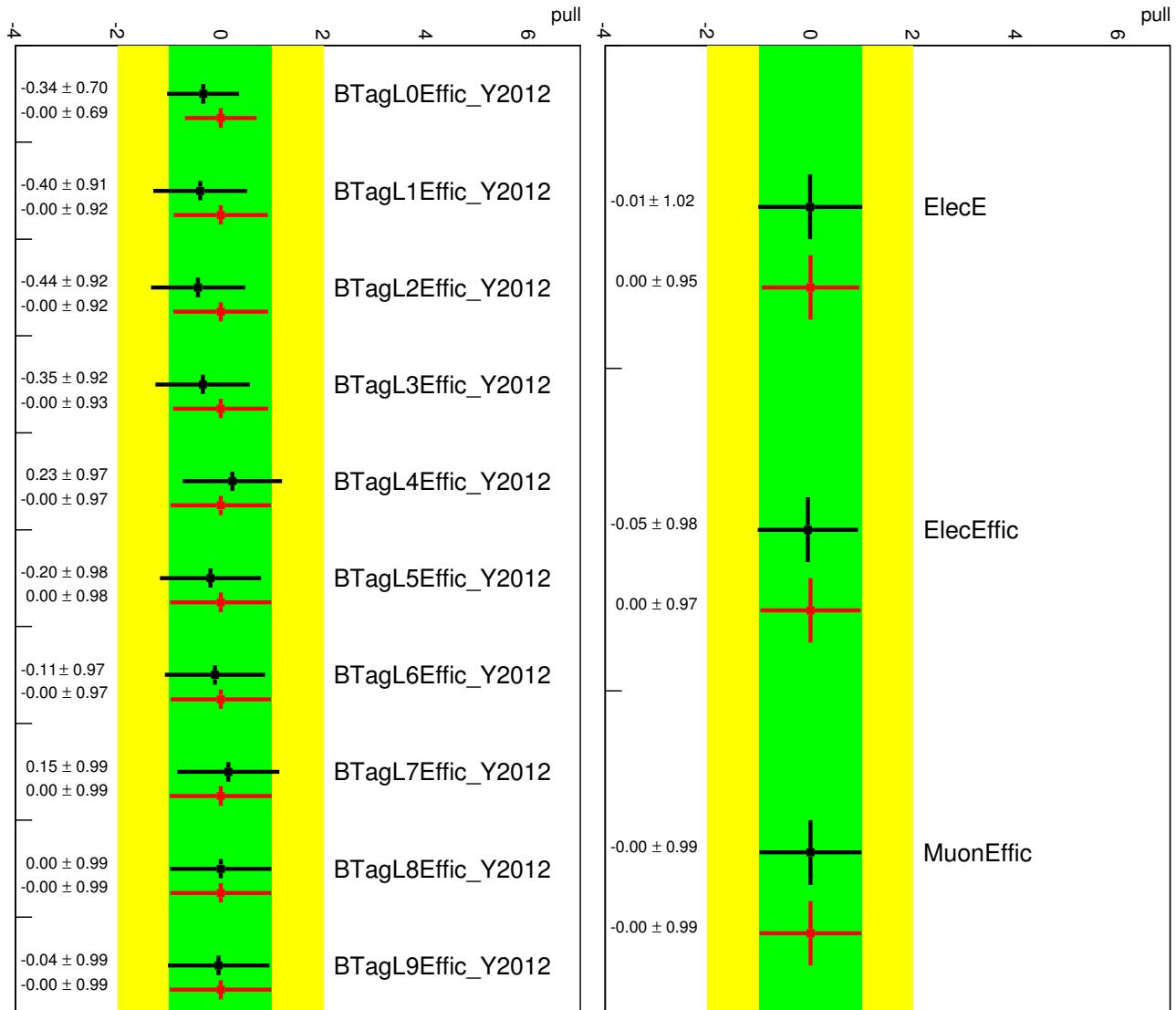


Figure 476: Pull plots for 2-lepton channel: light-jet tagging and leptons.

Not reviewed, for internal circulation only

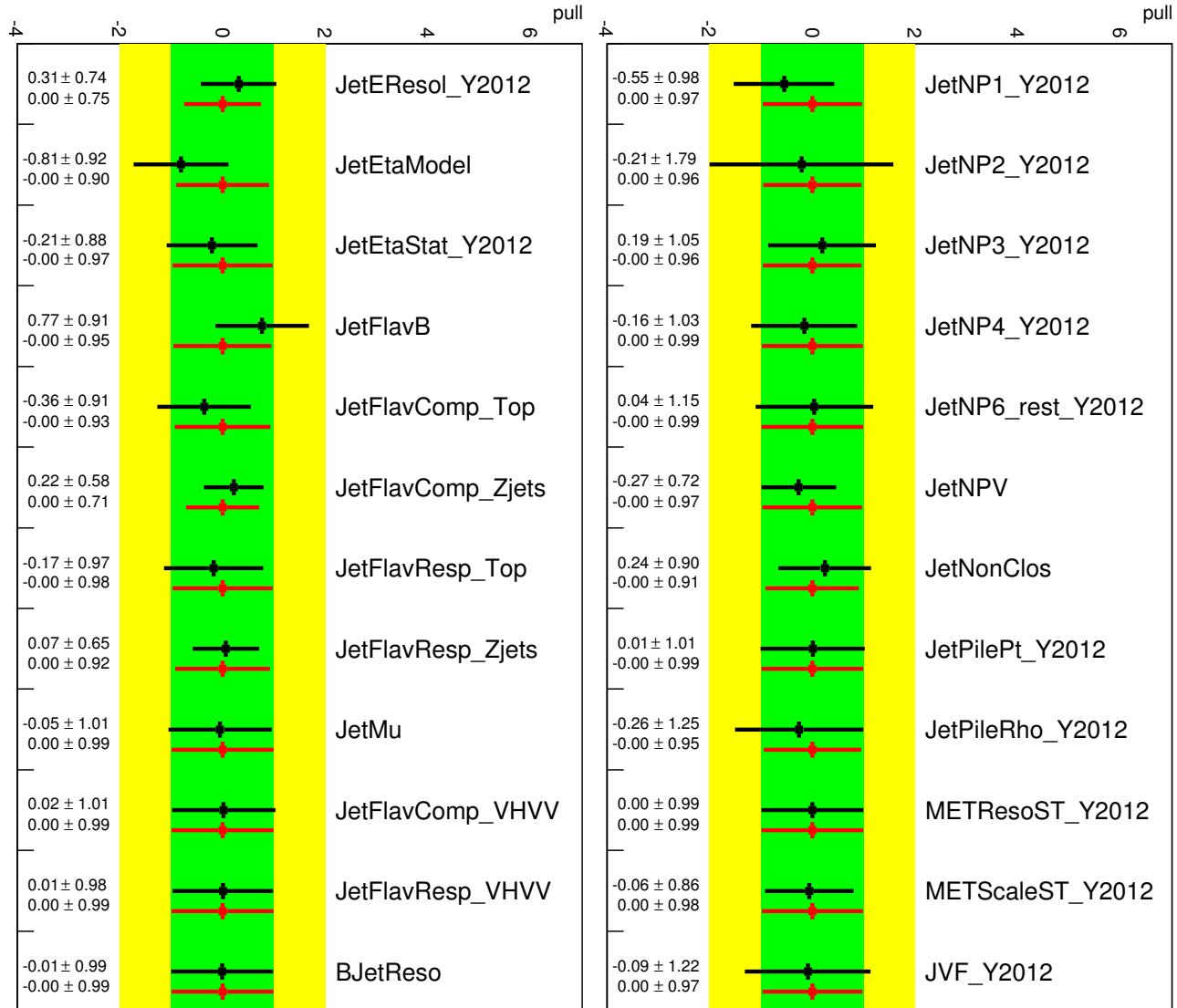


Figure 477: Pull plots for 2-lepton channel: Jet NPs.

Not reviewed, for internal circulation only

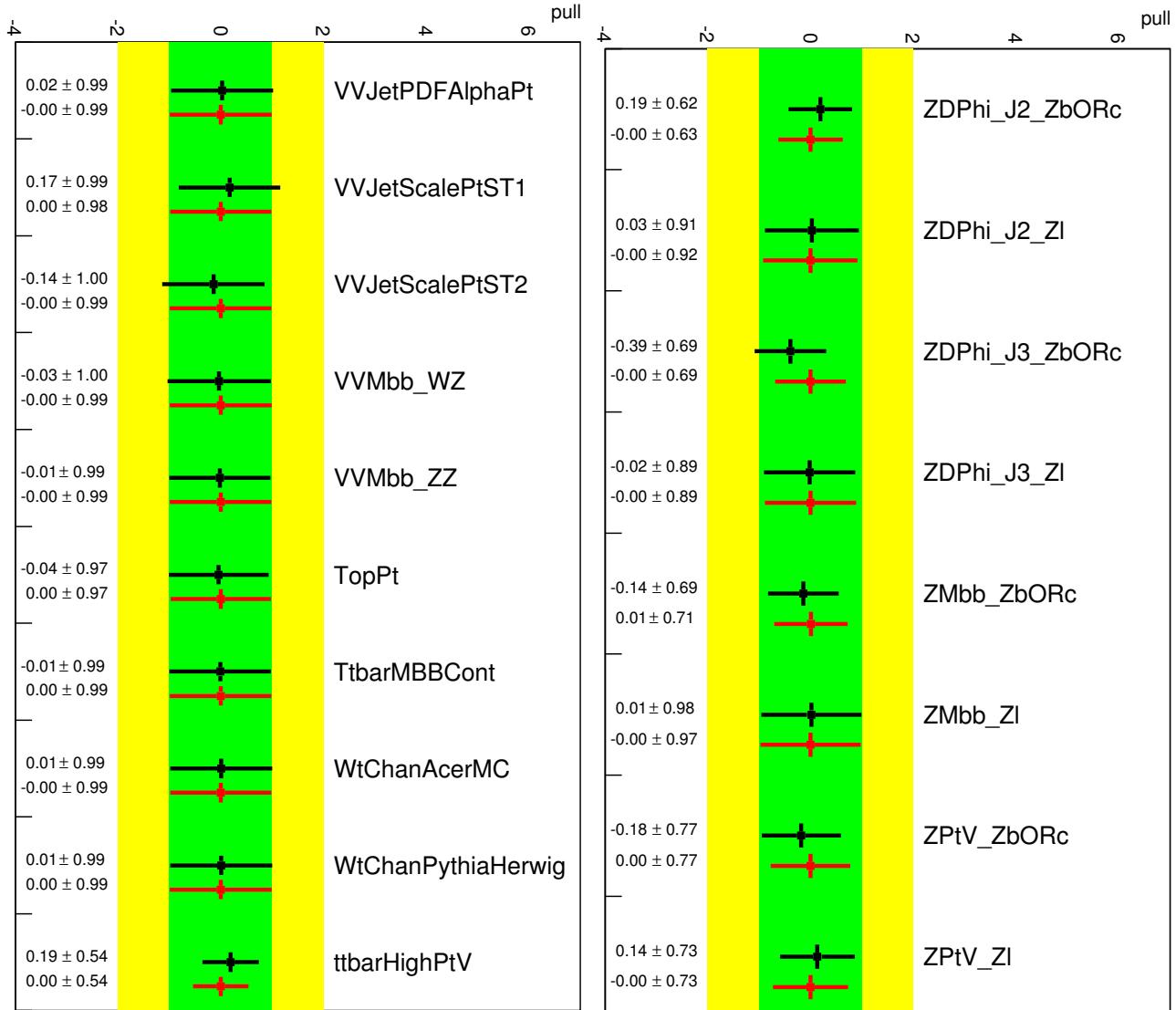


Figure 478: Pull plots for 2-lepton channel: Diboson/Top and W/Z related uncertainties.

Not reviewed, for internal circulation only

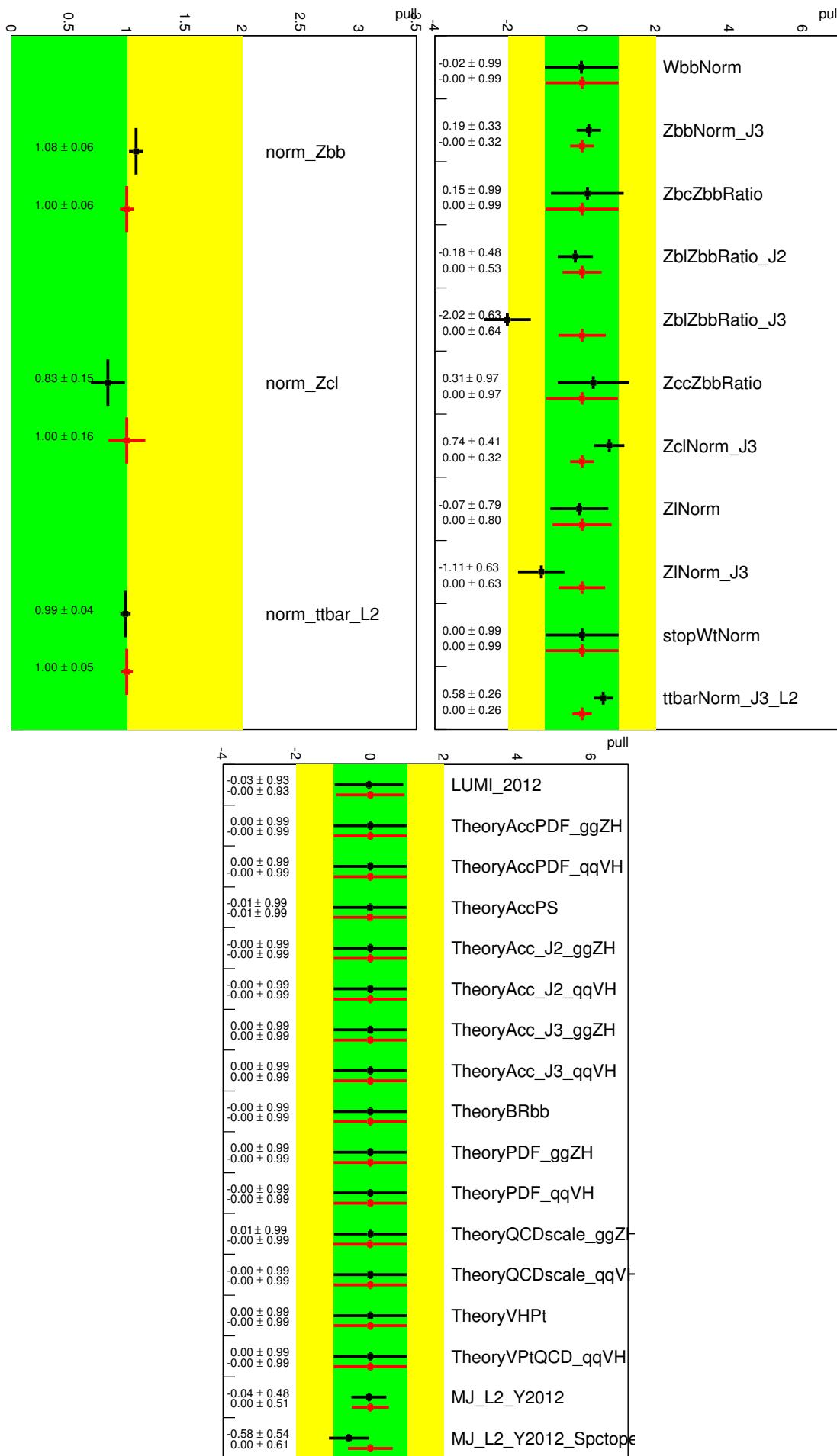


Figure 479: Pull plots for 2-lepton channel: Other model and normalization uncertainties.

5047 **AH.2.6 Pre-fit and Post-Fit for the MVA analysis in the 2-lepton fit**

[Not reviewed, for internal circulation only]

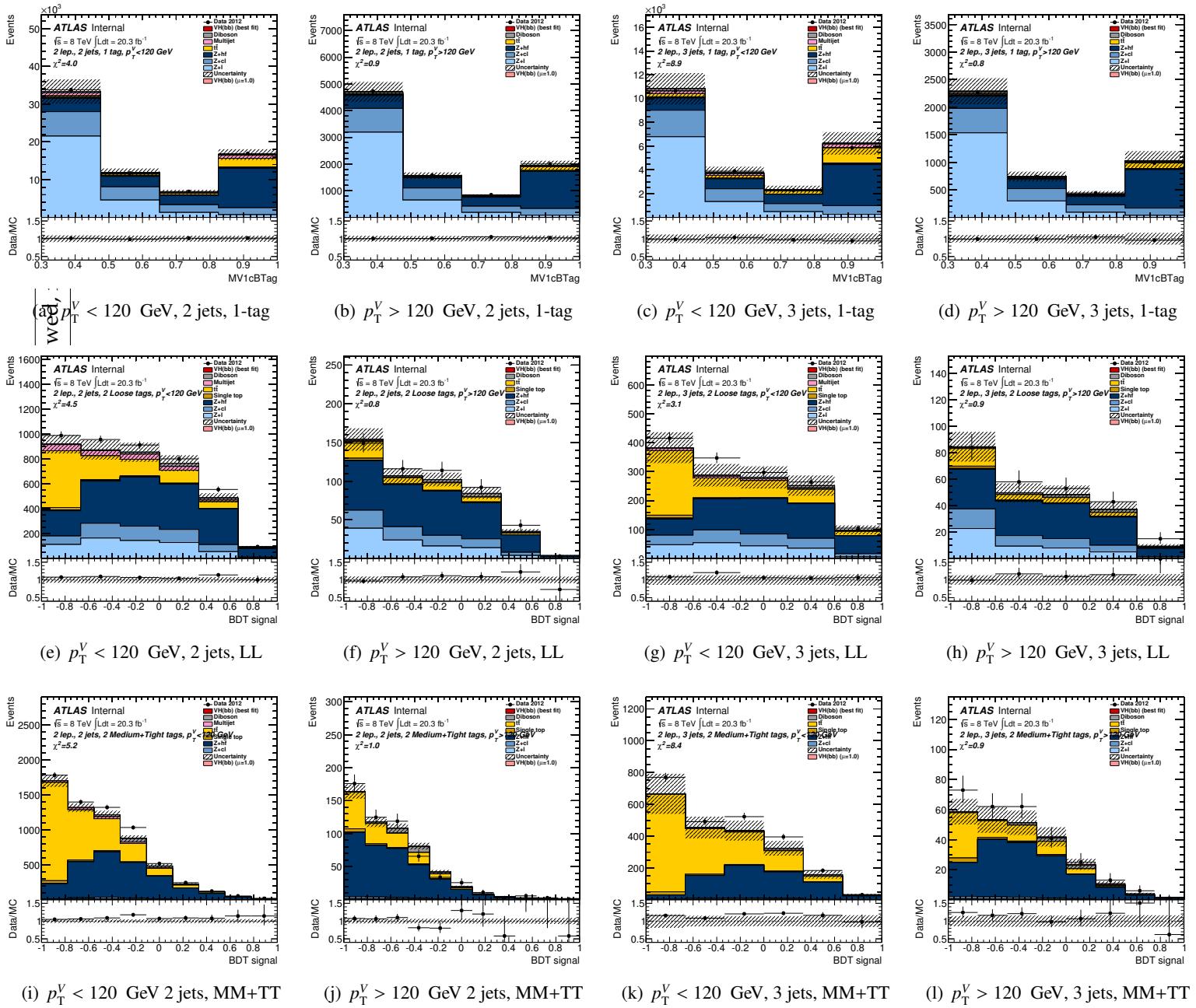


Figure 480: Pre-fit plots for MVA distribution in 2-lepton 2-jet and 3-jets, $p_T^V < 120 \text{ GeV}$ (left) and $p_T^V > 120 \text{ GeV}$ (right) events with 1 b-tag (MV1c is fit here), LL and MM + TT b-tags in the 2 lepton fit.

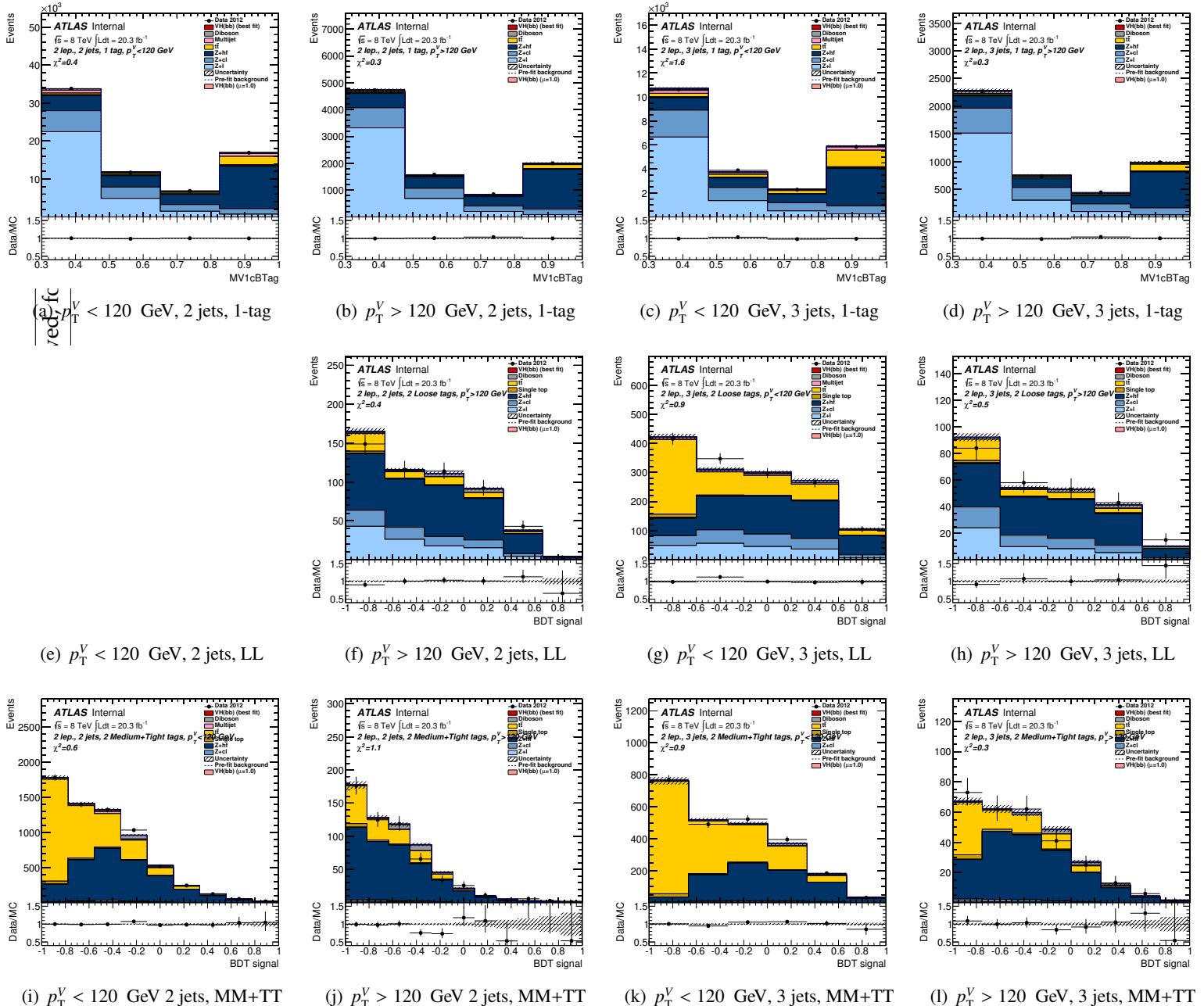


Figure 481: Post-fit plots for MVA distribution in 2-lepton 2-jet and 3-jets , $p_T^V < 120 \text{ GeV}$ (left) and $p_T^V > 120 \text{ GeV}$ (right) events with 1 b-tag (MV1c is fit here), *LL* and *MM + TT* b-tags in the 2 lepton fit. The pre-fit background expectation is indicated by the dashed blue line.

5048 **AH.3 Dijet Mass versus MVA**

5049 ?? The following shows a comparison of the dijet mass pulls (red) to the MVA pulls (black) in each
 5050 channel.

5051 **AH.3.1 0-lepton pull plots**

The pull plot comparison for 0-lepton are shown in Figure. 482-486.

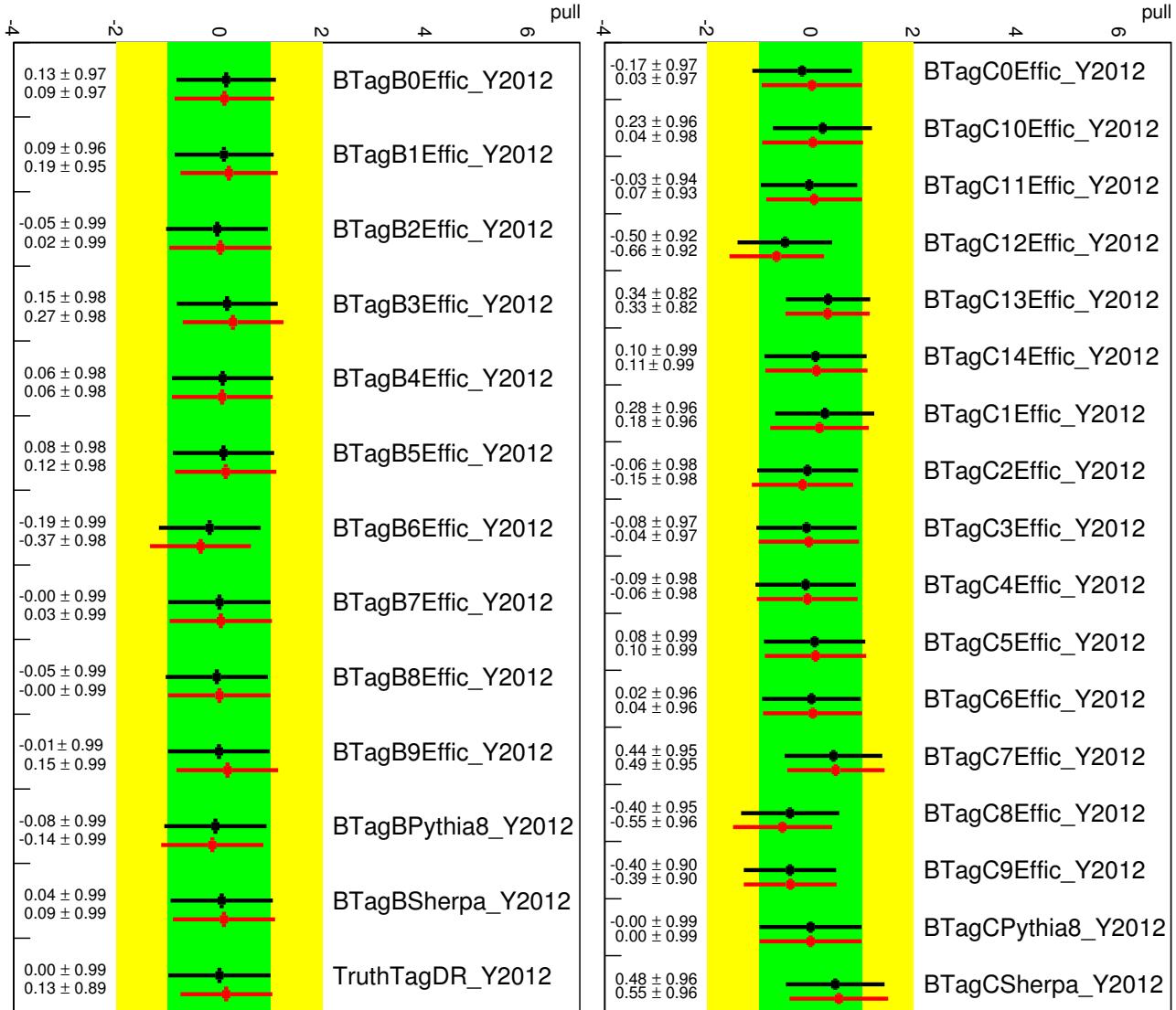


Figure 482: Pull plots for 0-lepton channel: *b*- and *c*-jet tagging.

Not reviewed, for internal circulation only

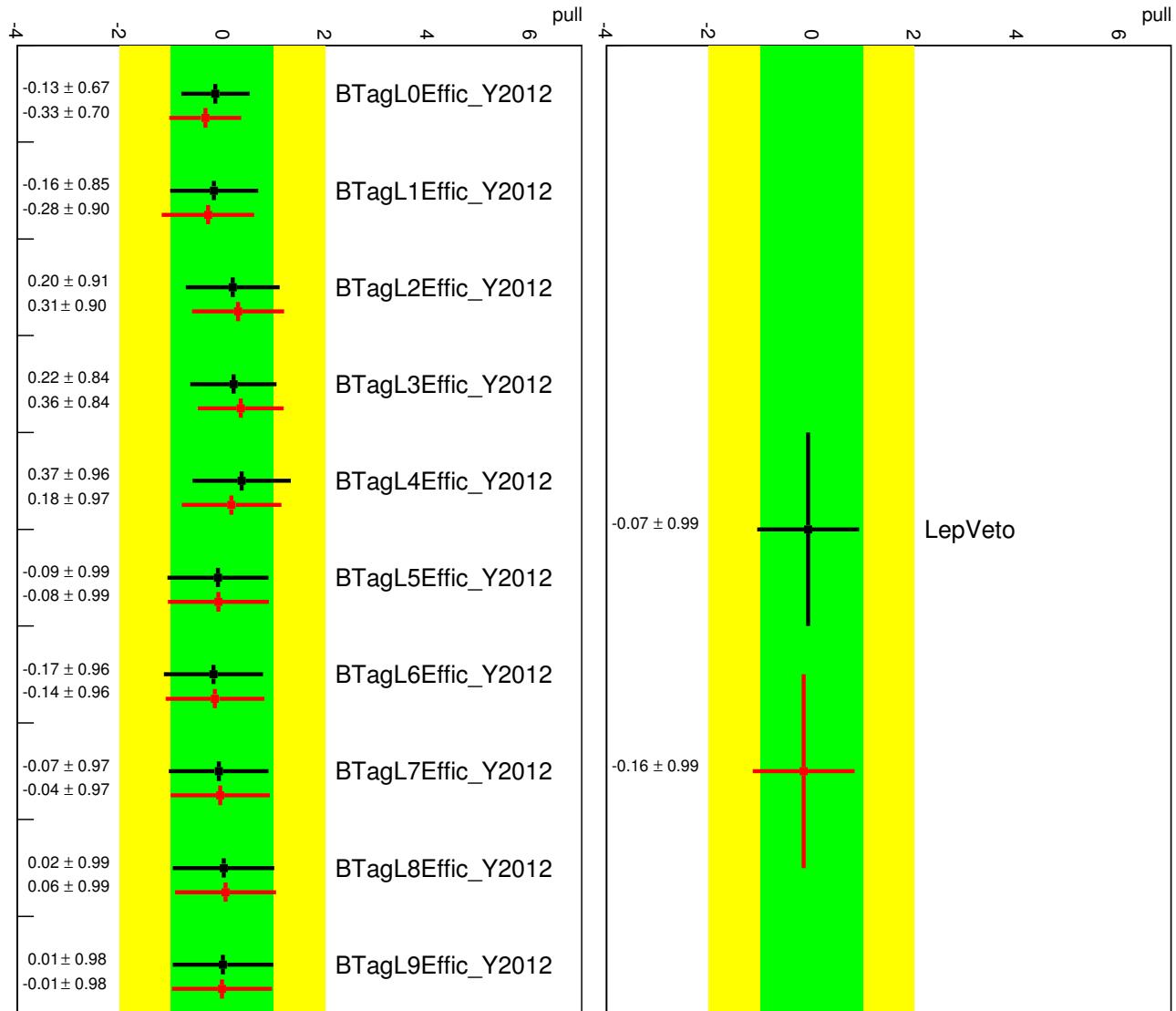


Figure 483: Pull plots for 0-lepton channel: light-jet tagging and leptons.

Not reviewed, for internal circulation only

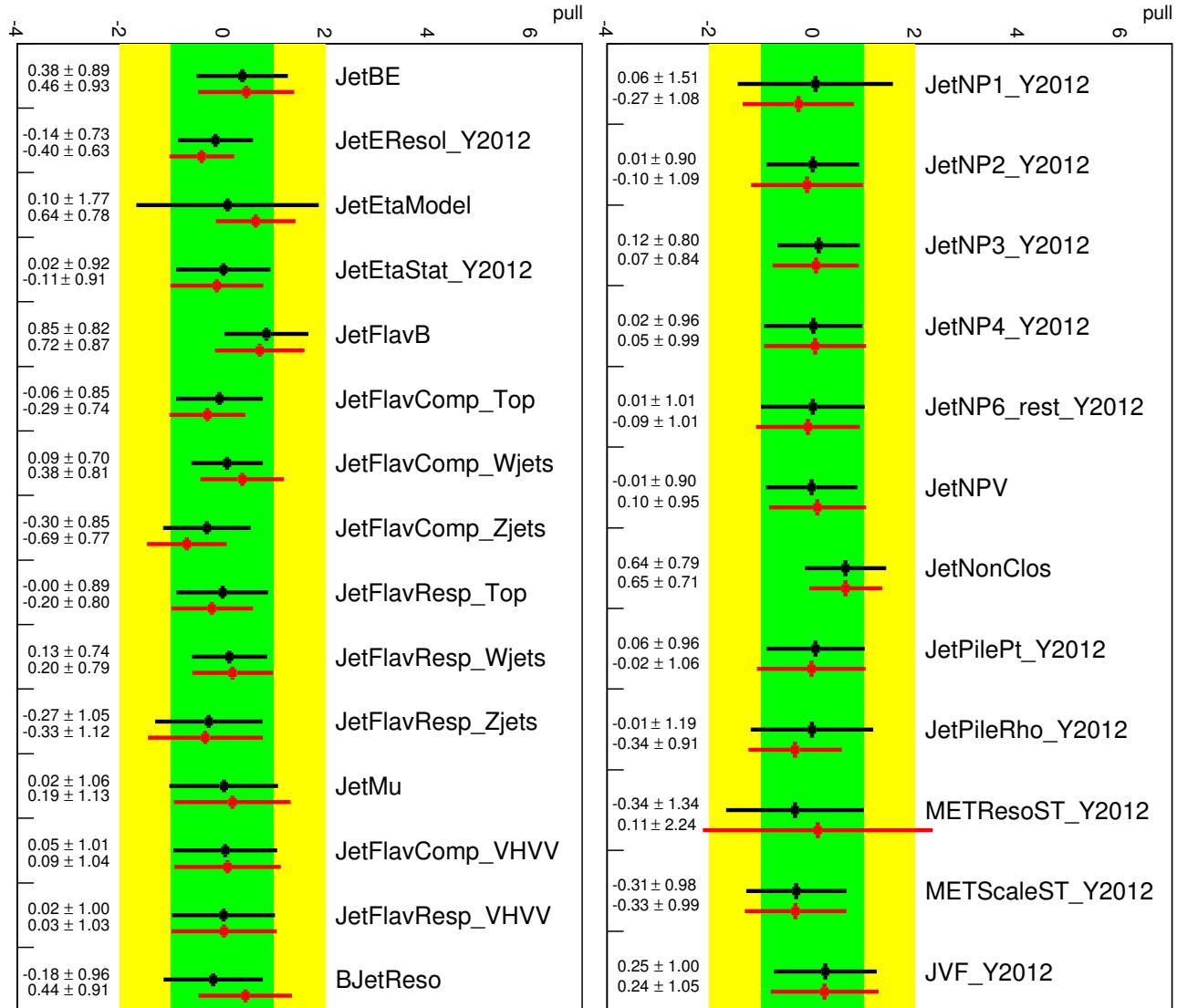


Figure 484: Pull plots for 0-lepton channel: Jet NPs.

Not reviewed, for internal circulation only

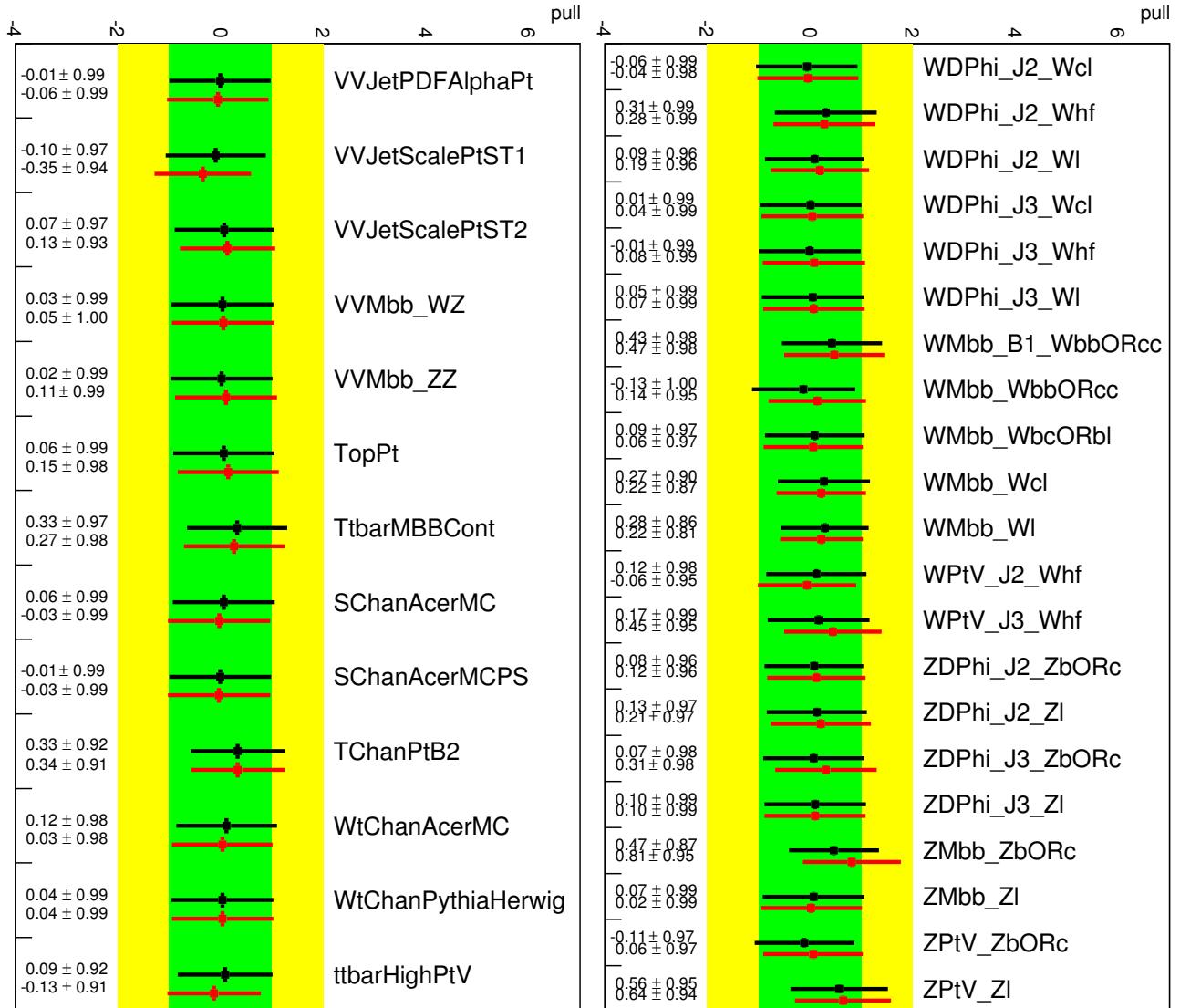


Figure 485: Pull plots for 0-lepton channel: Diboson/Top and W/Z related uncertainties.

Not reviewed, for internal circulation only

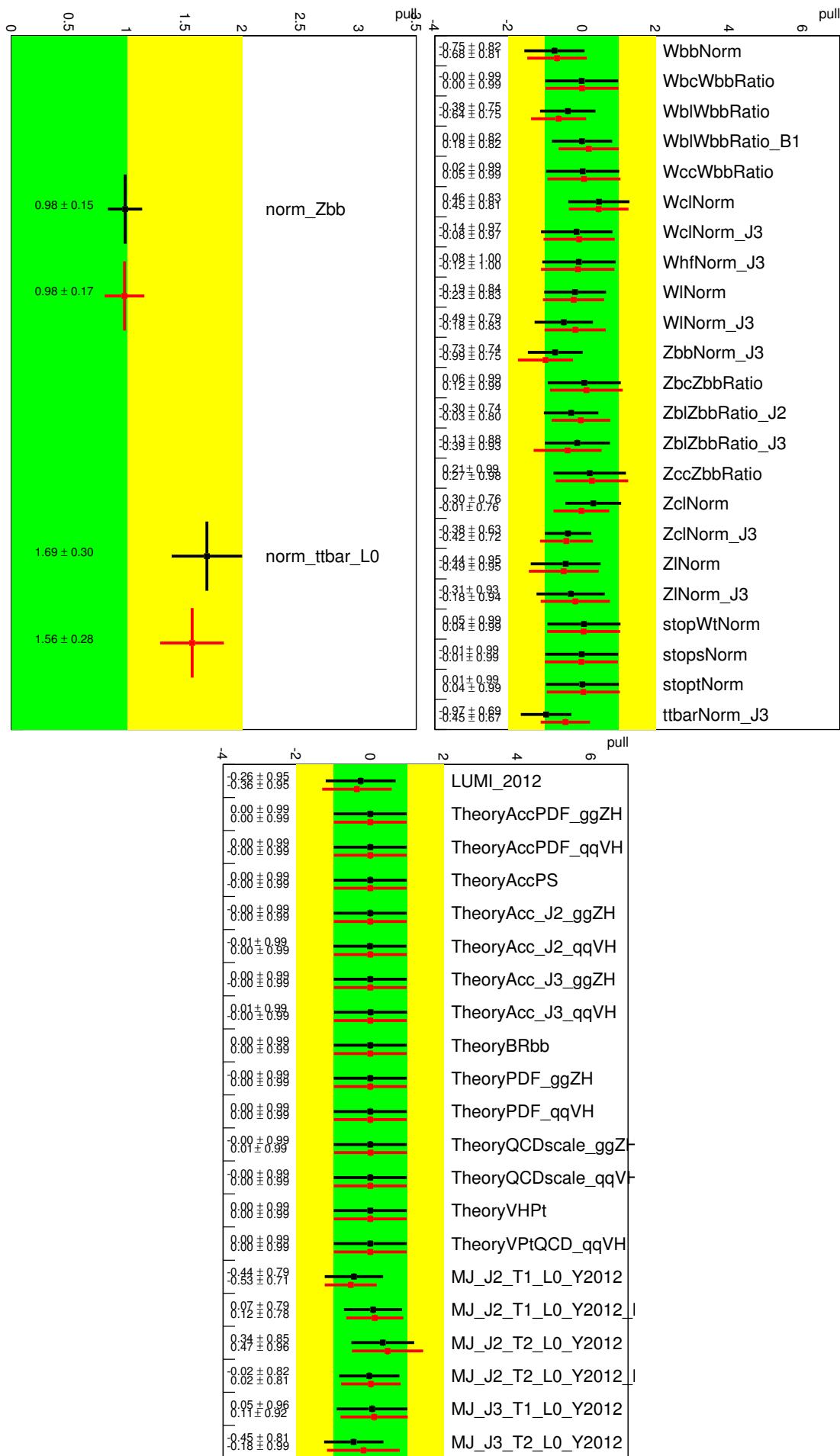


Figure 486: Pull plots for 0-lepton channel: Other model and normalization uncertainties.

5053 **AH.3.2 1-lepton pull plots**

5054 The pull plots for 1-lepton are shown in Figure. 487-491.

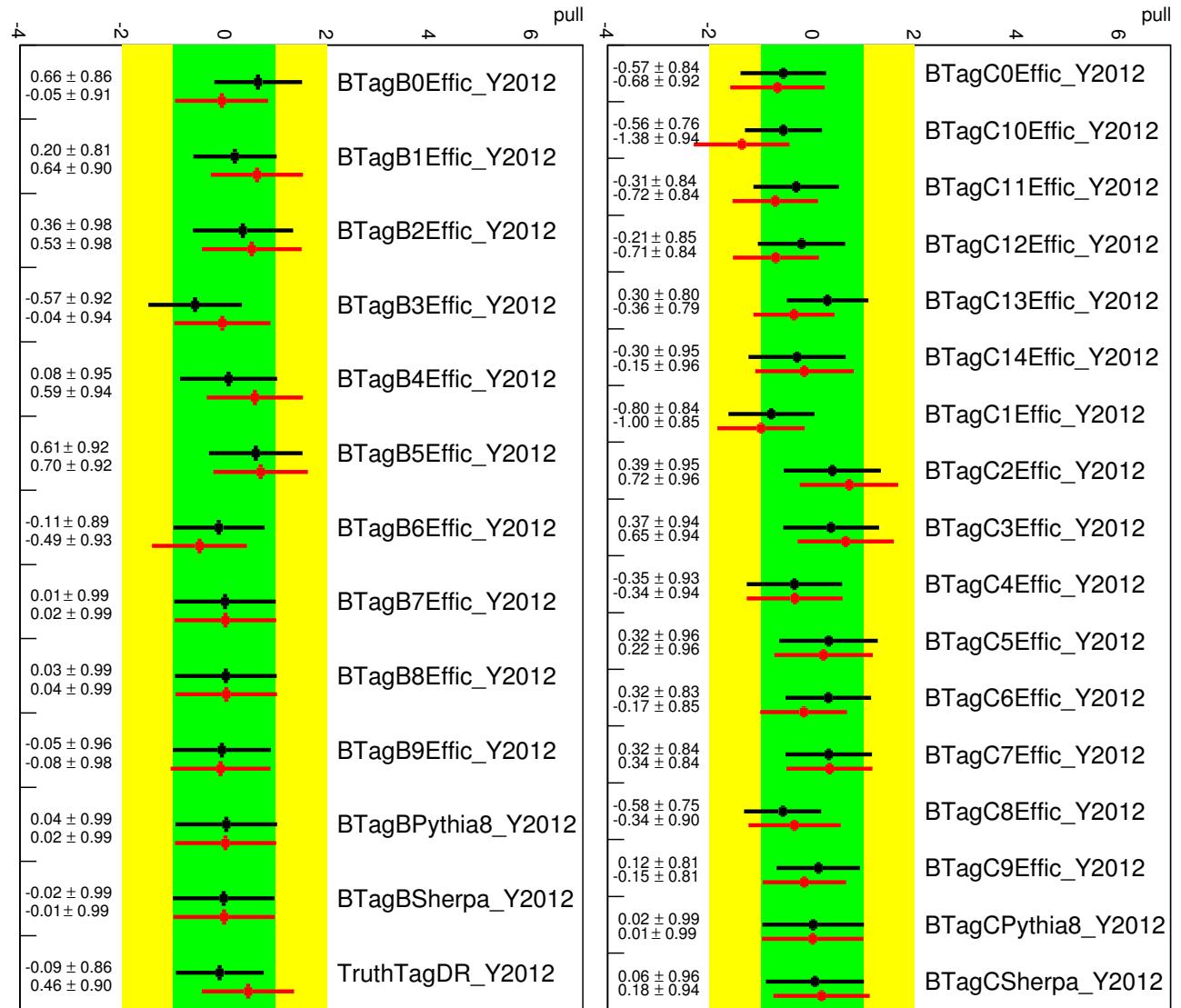


Figure 487: Pull plots for 1-lepton channel: *b*- and *c*-jet tagging.

Not reviewed, for internal circulation only

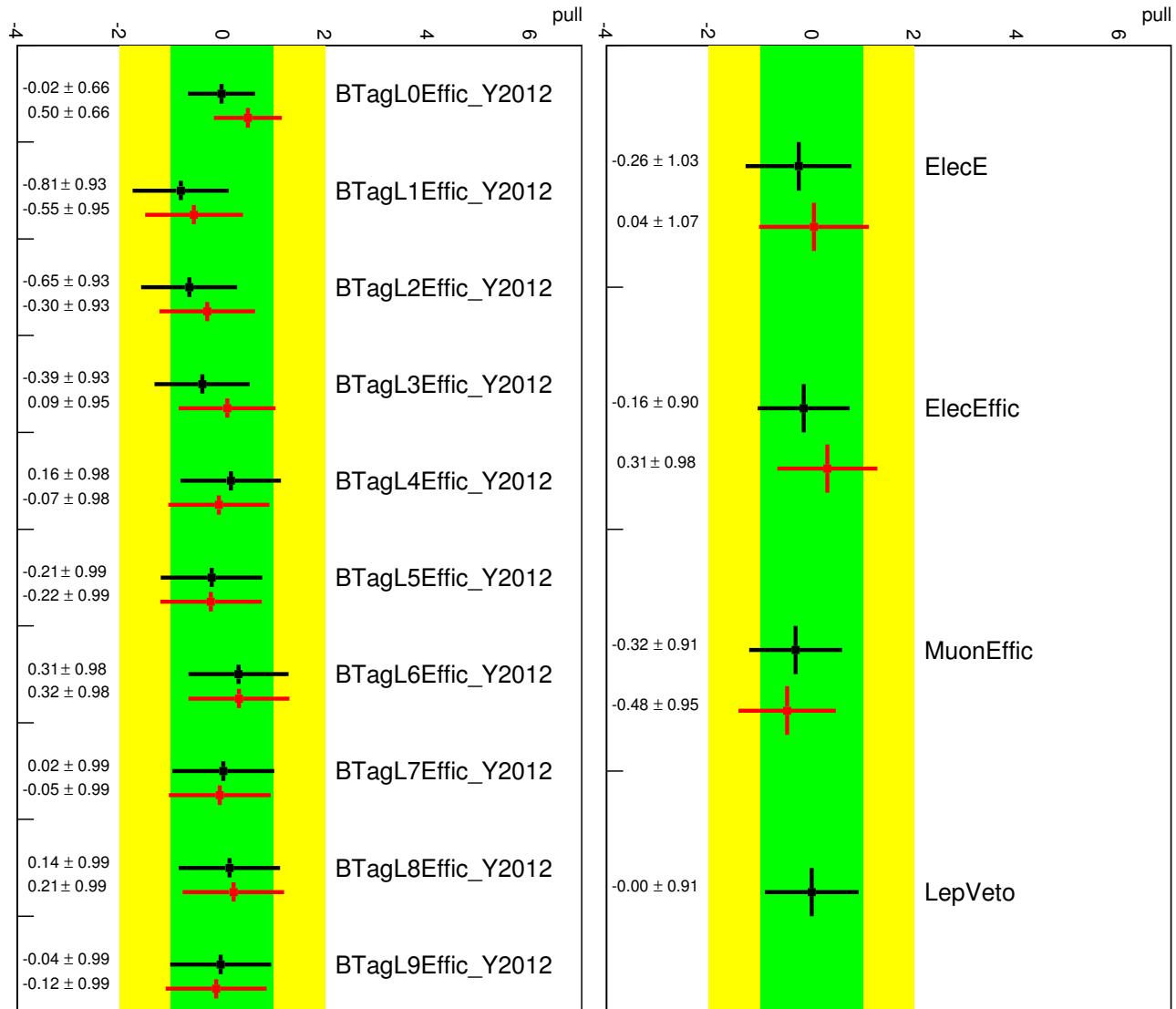


Figure 488: Pull plots for 1-lepton channel: light-jet tagging and leptons.

Not reviewed, for internal circulation only

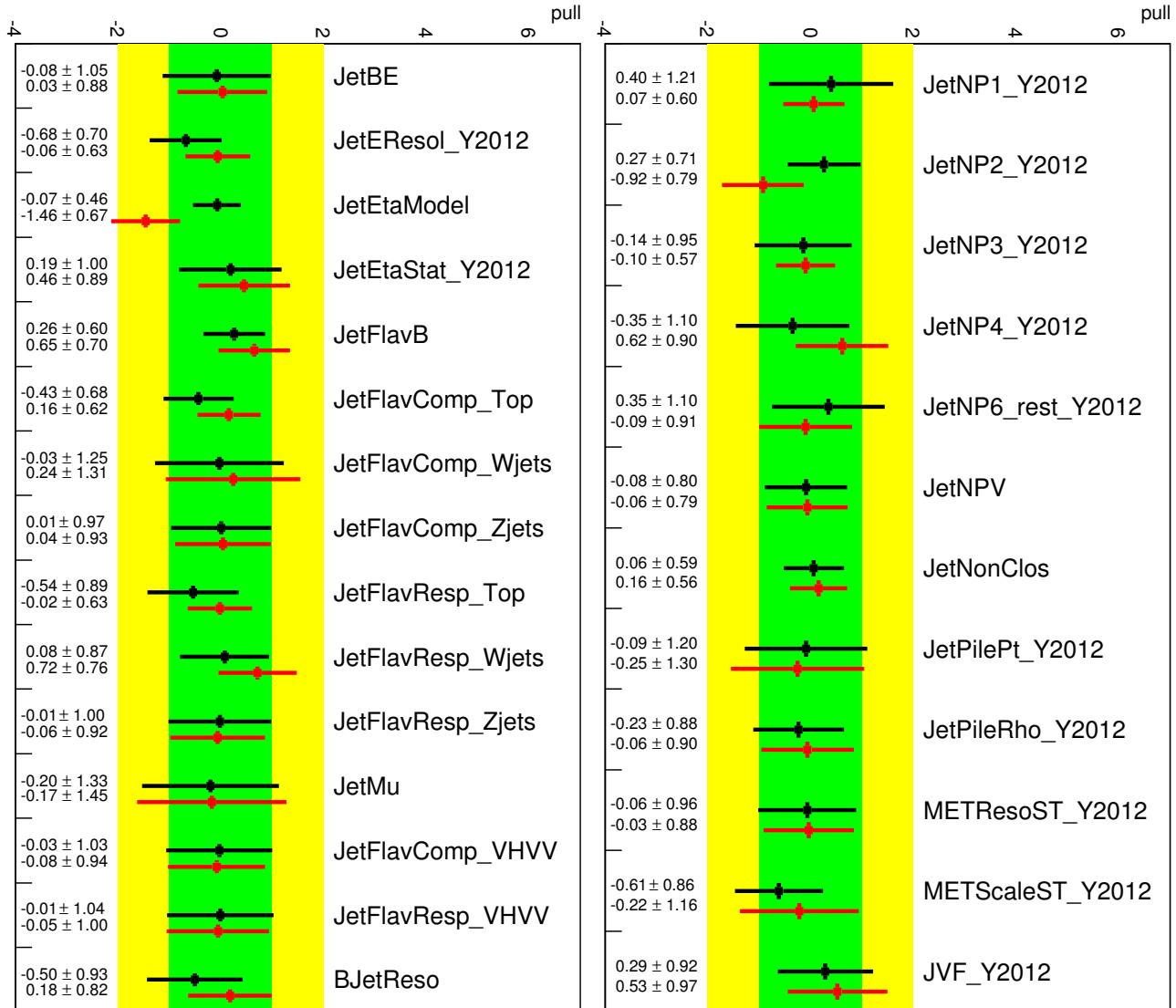


Figure 489: Pull plots for 1-lepton channel: Jet NPs.

Not reviewed, for internal circulation only

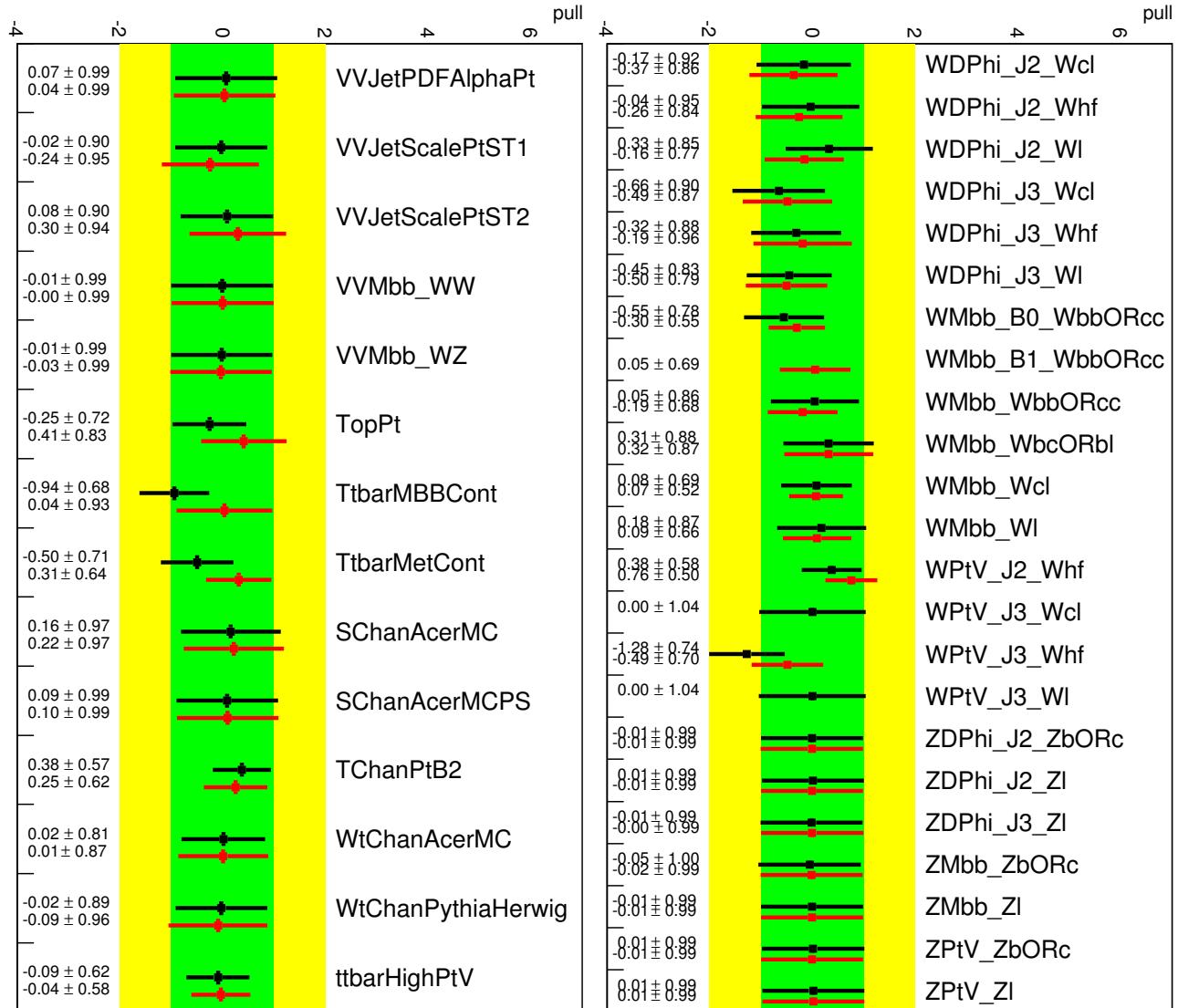


Figure 490: Pull plots for 1-lepton channel: Diboson/Top and W/Z related uncertainties.

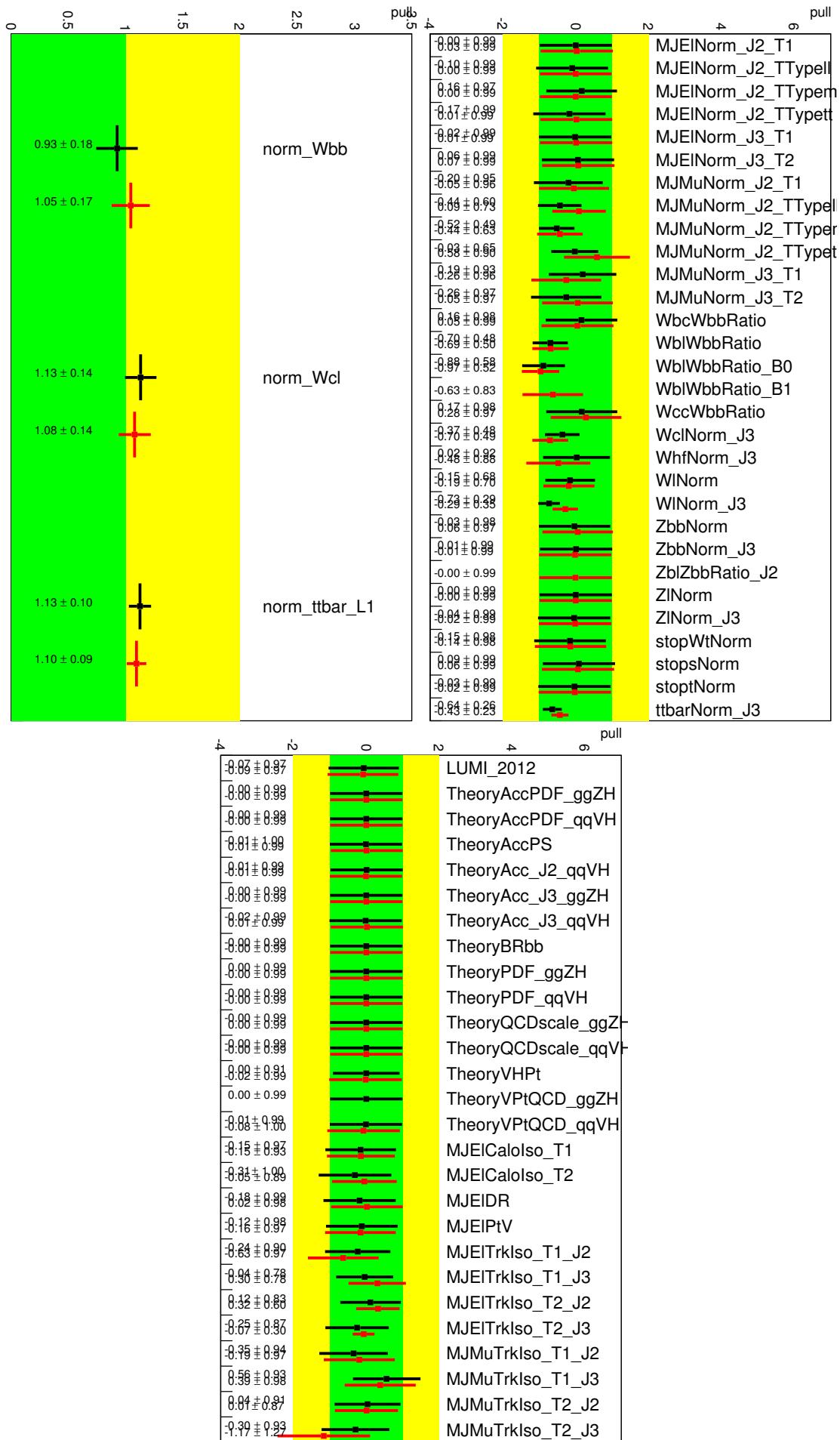


Figure 491: Pull plots for 1-lepton channel: Other model and normalization uncertainties.

Not reviewed, for internal circulation only

5055 **AH.3.3 2-lepton pull plots**

5056 The pull plots for 2-lepton are shown in Figure. 492-496.

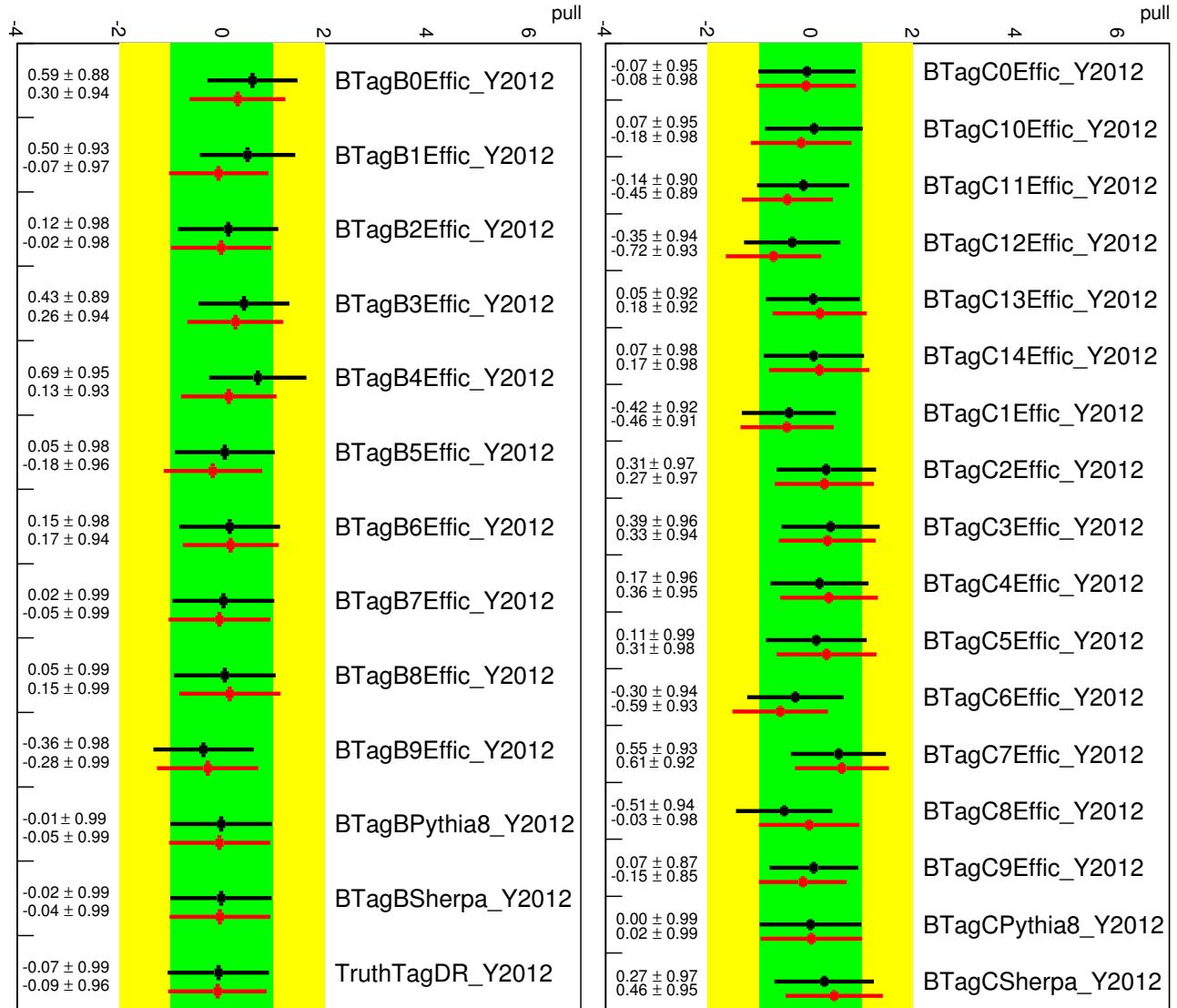


Figure 492: Pull plots for 2-lepton channel: *b*- and *c*-jet tagging.

Not reviewed, for internal circulation only

Not reviewed, for internal circulation only

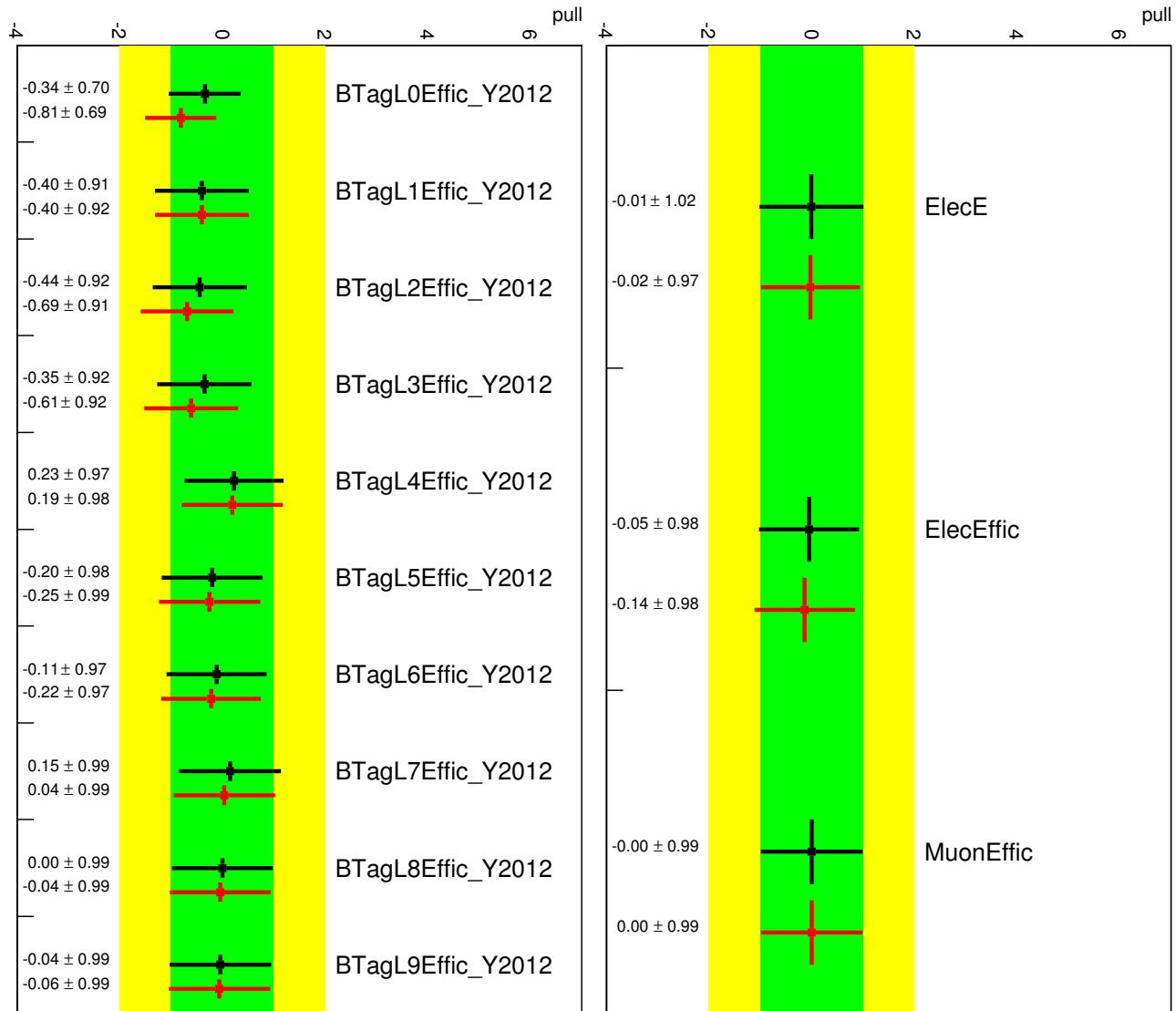


Figure 493: Pull plots for 2-lepton channel: light-jet tagging and leptons.

Not reviewed, for internal circulation only

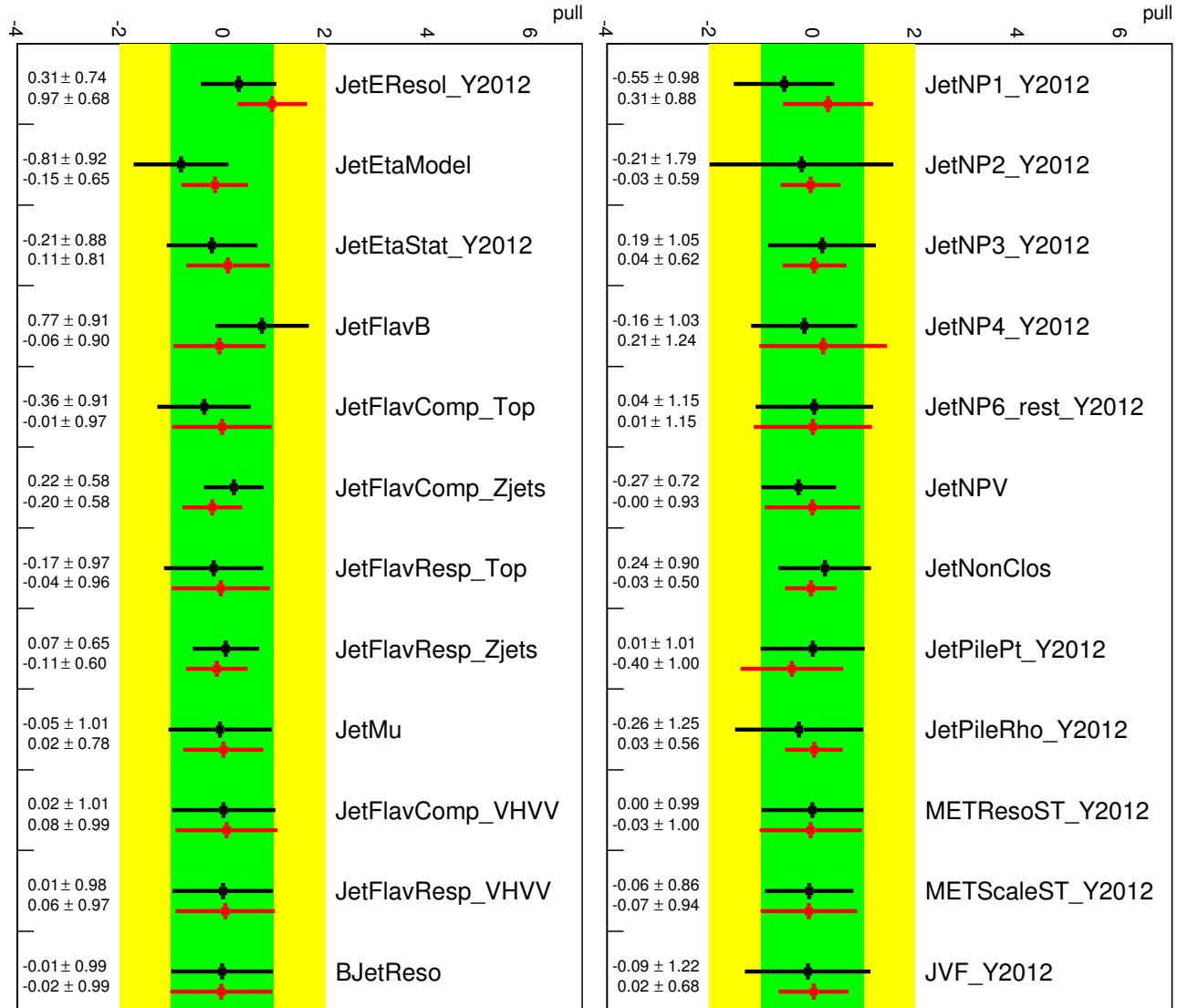


Figure 494: Pull plots for 2-lepton channel: Jet NPs.

Not reviewed, for internal circulation only

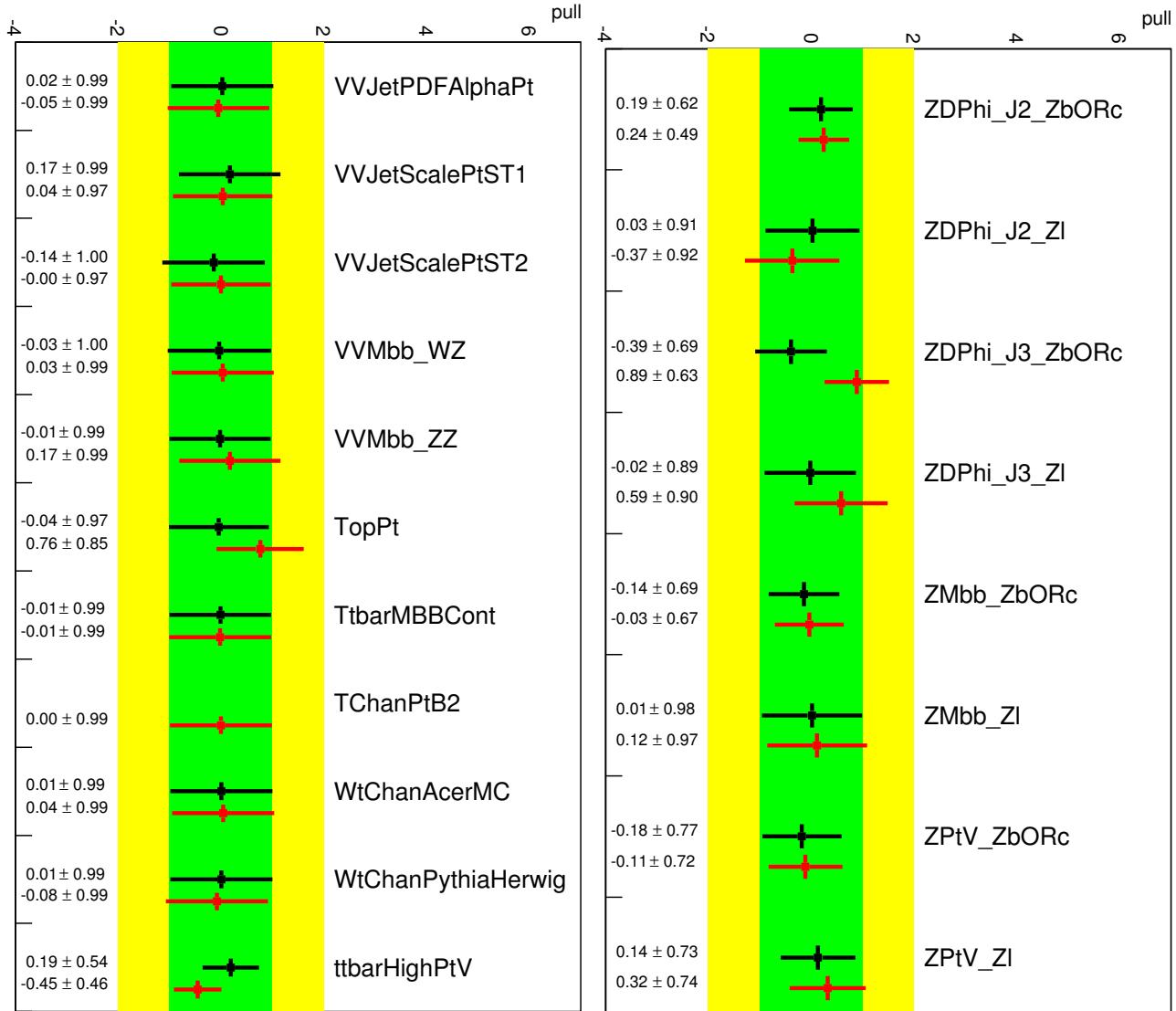


Figure 495: Pull plots for 2-lepton channel: Diboson/Top and W/Z related uncertainties.

Not reviewed, for internal circulation only

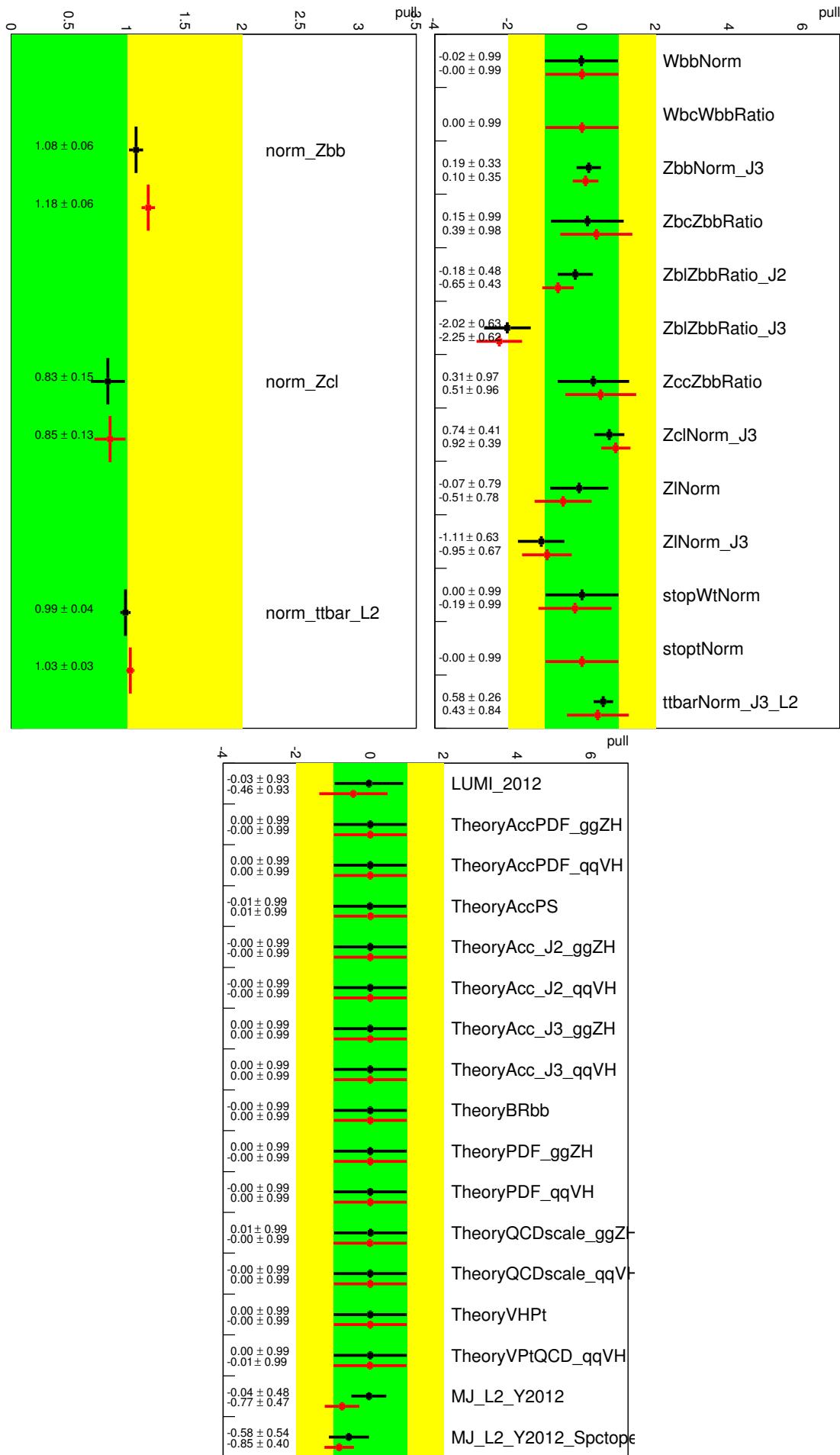


Figure 496: Pull plots for 2-lepton channel: Other model and normalization uncertainties.

5057 AI Postfit p_T^V Spectrums

5058 The following contains the postfit p_T^V spectrums for the dijet mass analysis [AI.1](#) and the [MVA](#) analy-
 5059 sis [AI.2](#) where the error is the full post-unconditional-fit error including the constraints on all nuisance
 5060 parameters from the respective fits.

5061 AI.1 Dijet Mass p_T^V

5062 The p_T^V binning reflects the bins used in the profile likelihood in the 2-tag distributions. For the 1-tag the
 5063 bins shown are $p_T^V < 90$ GeV, $90 < p_T^V < 120$ GeV, and $p_T^V > 120$ GeV while in the profile likelihood
 5064 $p_T^V < 120$ GeV and $p_T^V > 120$ GeV are used (with the MV1c distribution).

5065 Figure [497](#) shows the p_T^V distribution in 0-lepton 1 and 2-tag inclusive regions for 2 and 3-jets and
 5066 Figure [498](#) shows the 3 2-tag regions. Figure [499](#) and [500](#) show the same for 1-lepton and Figure [501](#)
 5067 and [502](#) shows the 2-lepton channel.

5068 AI.2 MVA p_T^V

5069 The p_T^V binning reflects the bins used in the profile likelihood.

5070 Figure [503](#) shows the p_T^V distribution in 0-lepton 1 and 2-tag inclusive regions for 2 and 3-jets and
 5071 Figure [504](#) shows the 3 2-tag regions. Figure [505](#) and [506](#) show the same for 1-lepton and Figure [507](#)
 5072 and [508](#) shows the 2-lepton channel.

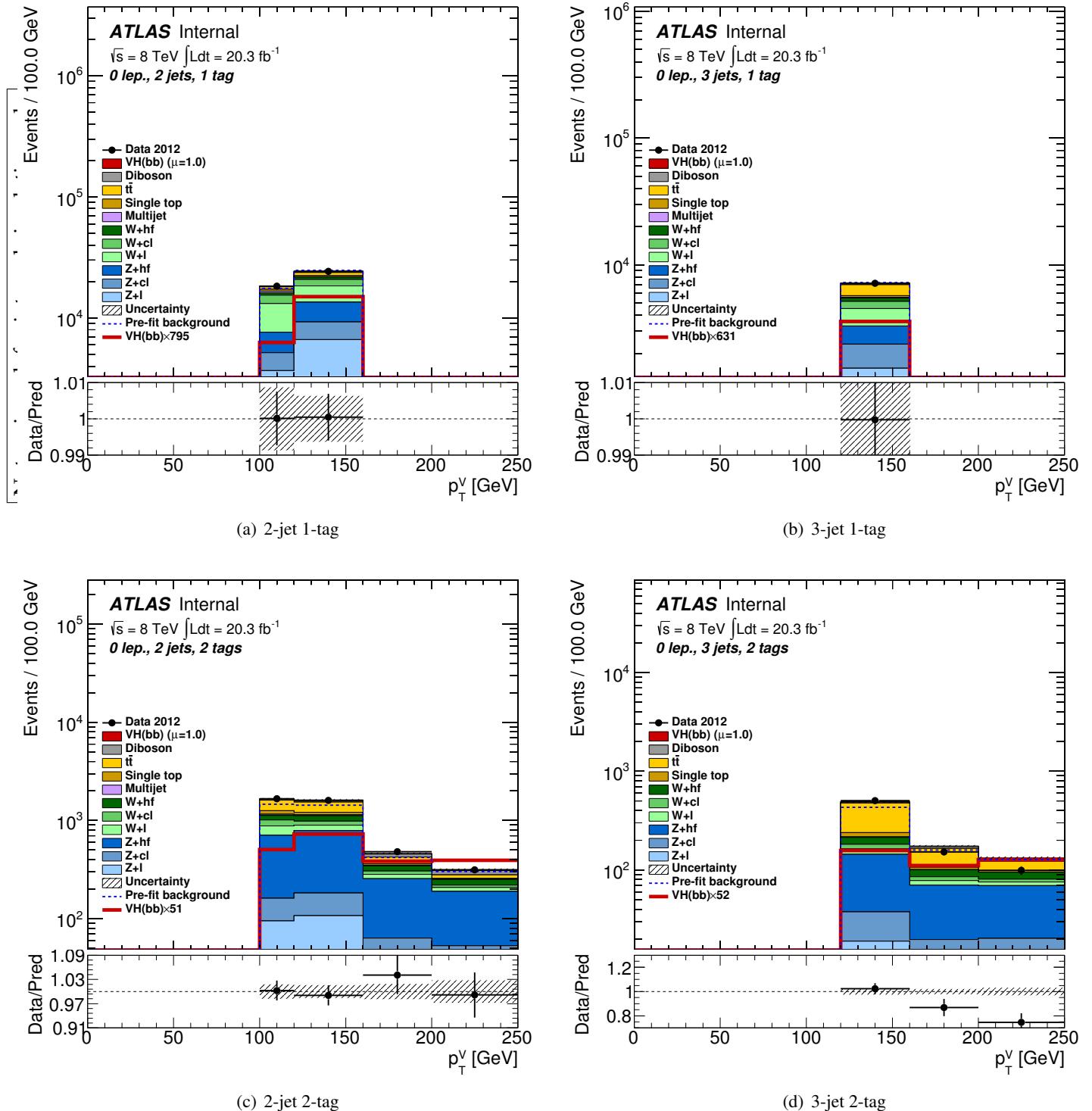


Figure 497: p_T^V distribution in the 0-lepton dijet mass analysis using the postfit NPs for the corresponding $0+1+2$ lepton unconditional fit. The 2 and 3-jet regions are shown in the 1-tag and inclusive 2-tag regions. In the 1-tag plot, the bin from 120 – 160 GeV contains events with $p_T^V > 120$ GeV.

Not reviewed, for internal circulation only

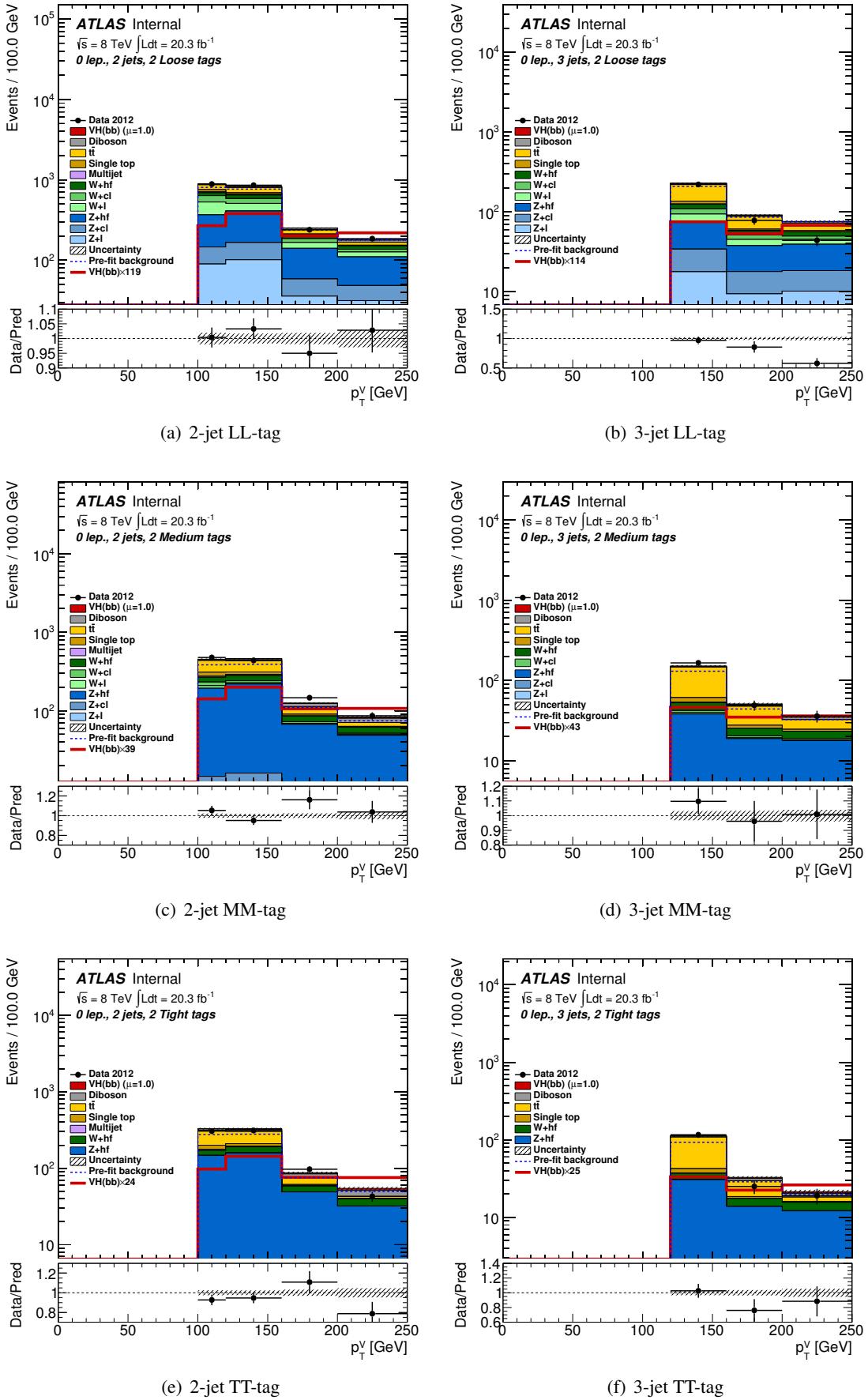


Figure 498: p_T^V distribution in the 0-lepton dijet mass analysis using the postfit NPs for the corresponding 0+1+2 lepton unconditional fit. The 2 and 3-jet regions are shown in the three 2-tag regions.

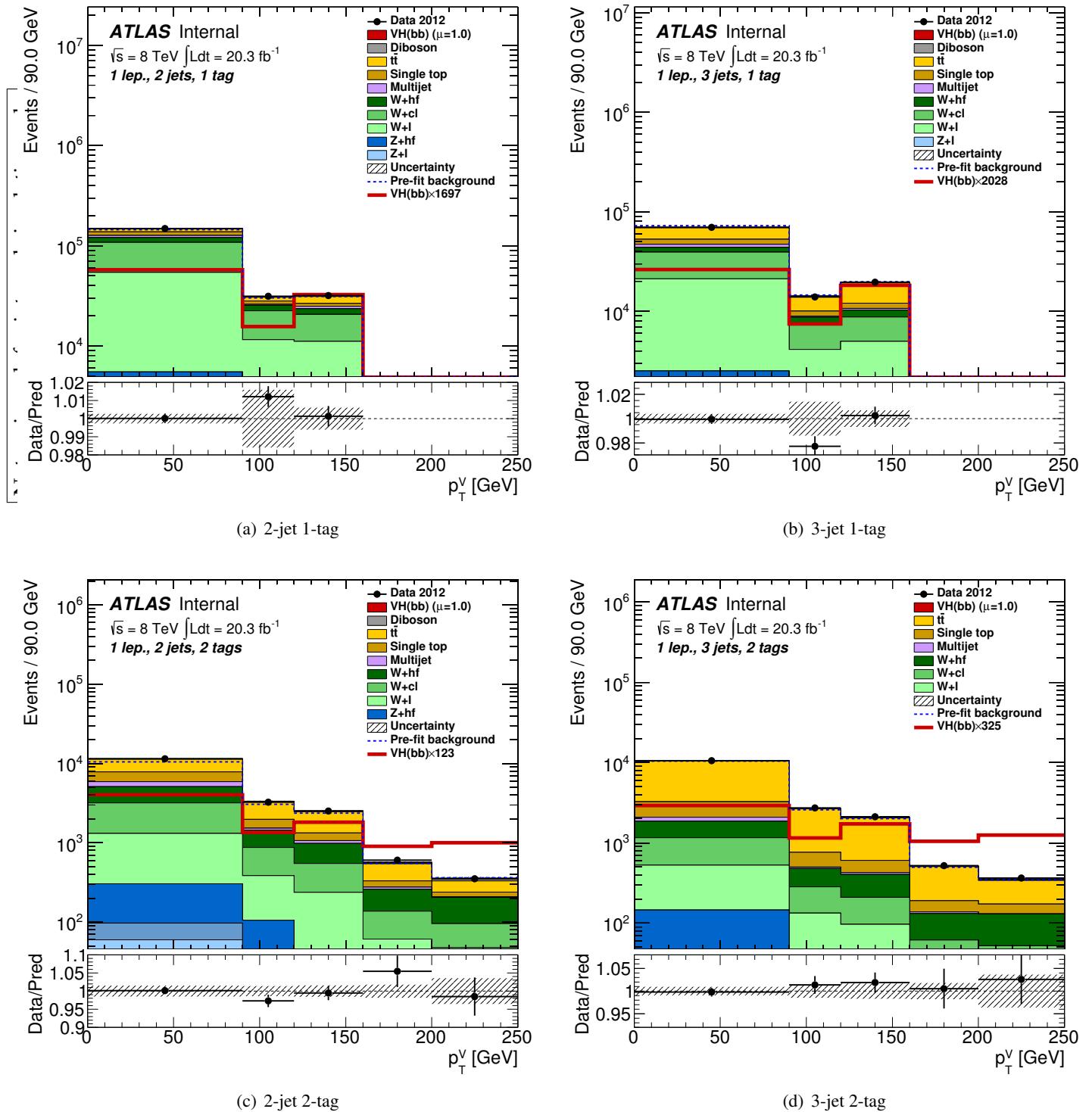


Figure 499: p_T^V distribution in the 1-lepton dijet mass analysis using the postfit NPs for the corresponding $0+1+2$ lepton unconditional fit. The 2 and 3-jet regions are shown in the 1-tag and inclusive 2-tag regions. In the 1-tag plot, the bin from $120 - 160$ GeV contains events with $p_T^V > 120$ GeV.

Not reviewed, for internal circulation only

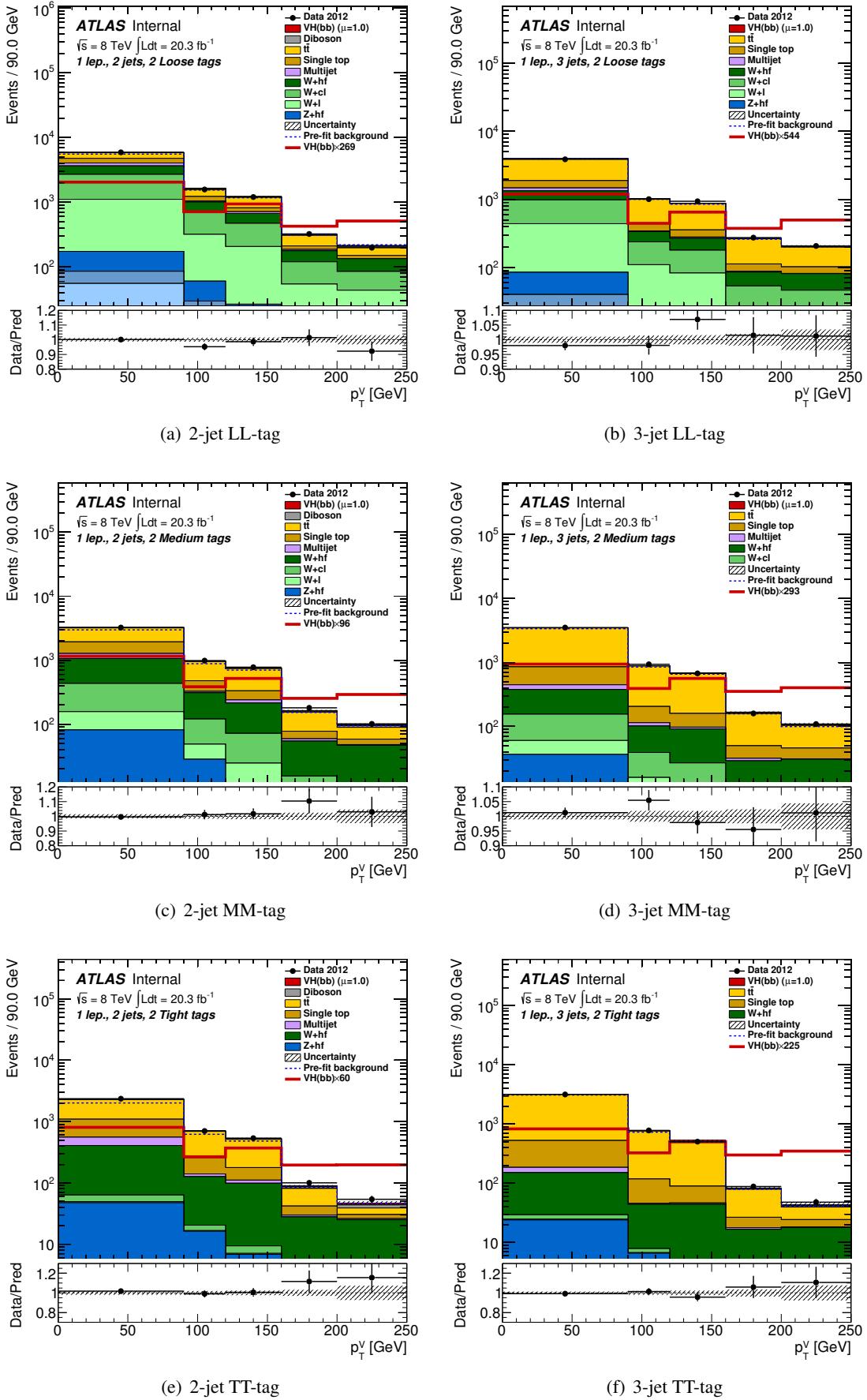


Figure 500: p_T^V distribution in the 1-lepton dijet mass analysis using the postfit NPs for the corresponding 0+1+2 lepton unconditional fit. The 2 and 3-jet regions are shown in the three 2-tag regions.

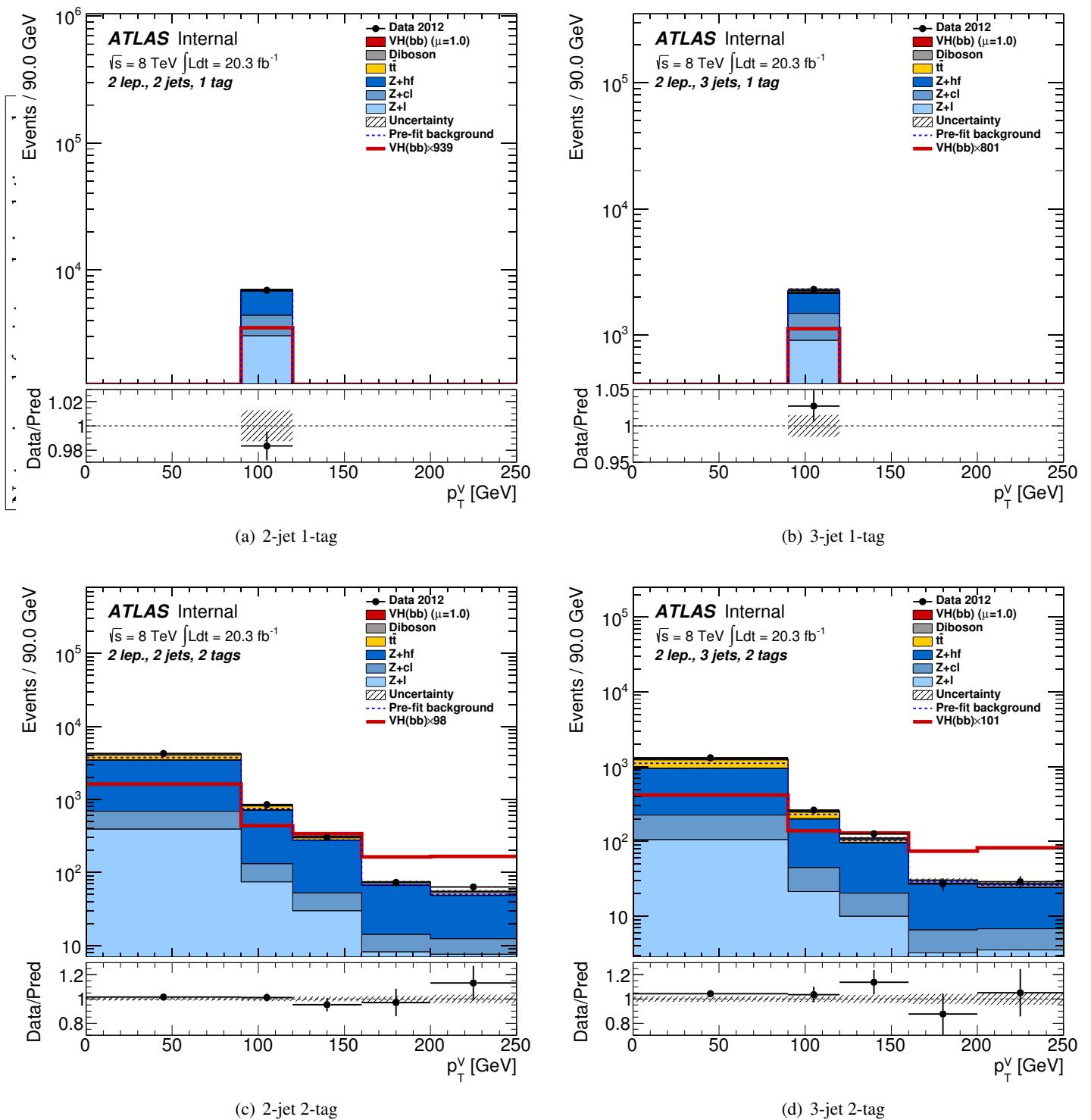


Figure 501: p_T^V distribution in the 2-lepton dijet mass analysis using the postfit NPs for the corresponding $0+1+2$ lepton unconditional fit. The 2 and 3-jet regions are shown in the 1-tag and inclusive 2-tag regions. In the 1-tag plot, the bin from $120 - 160$ GeV contains events with $p_T^V > 120$ GeV.

Not reviewed, for internal circulation only

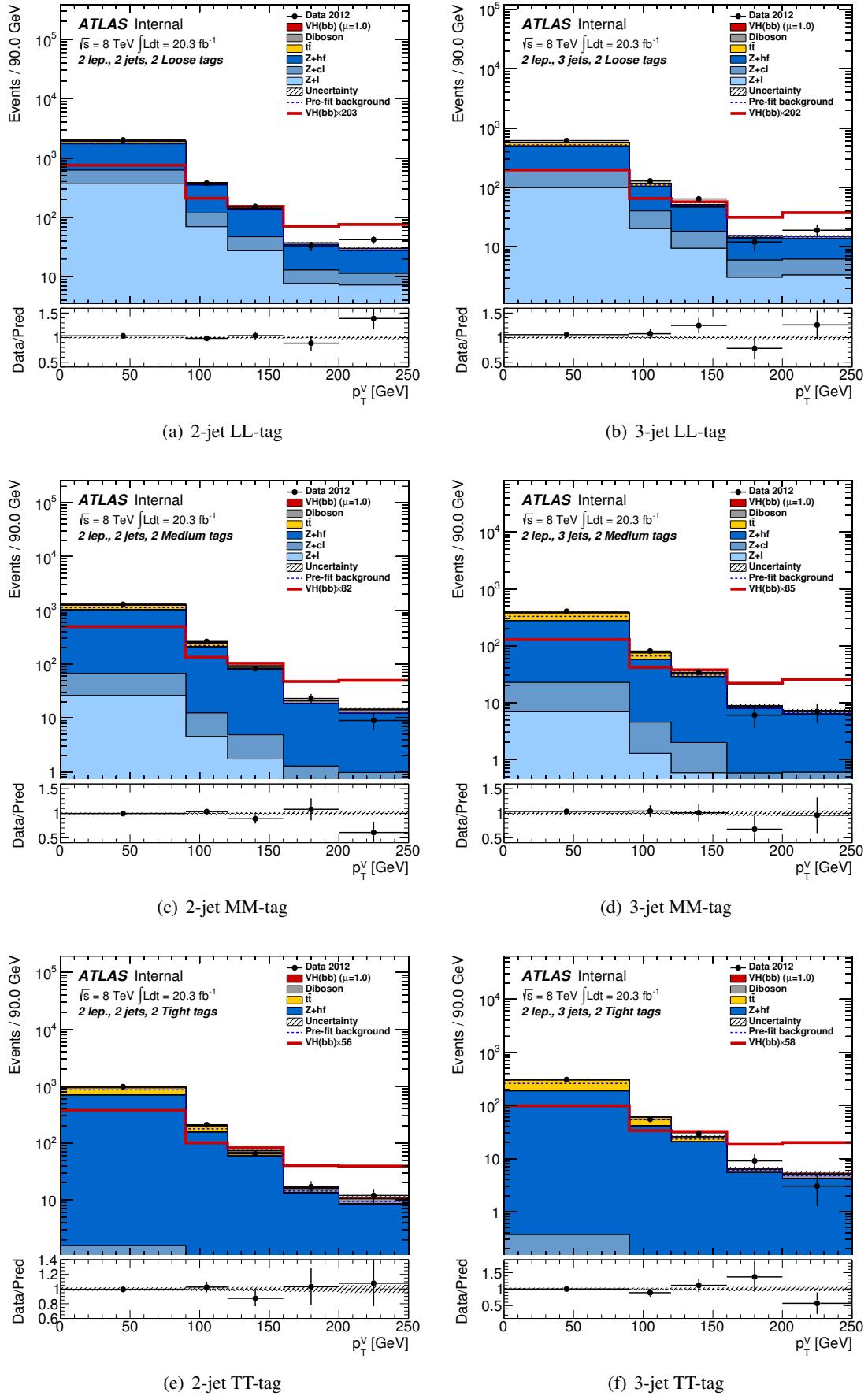


Figure 502: p_T^V distribution in the 2-lepton dijet mass analysis using the postfit NPs for the corresponding 0+1+2 lepton unconditional fit. The 2 and 3-jet regions are shown in the three 2-tag regions.

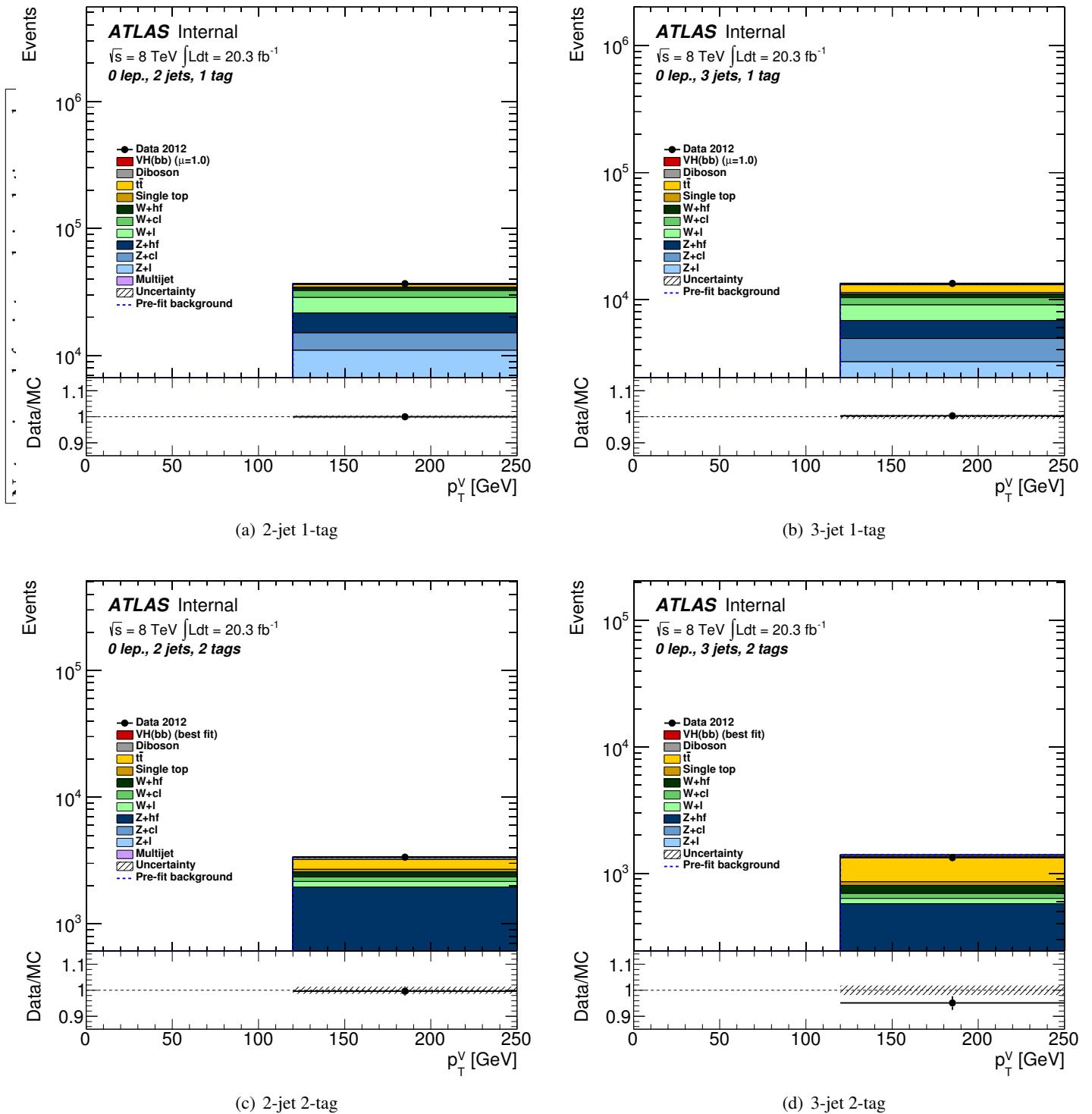


Figure 503: p_T^V distribution in the 0-lepton MVA analysis using the postfit NPs for the corresponding $0+1+2$ lepton unconditional fit. The 2 and 3-jet regions are shown in the 1-tag and inclusive 2-tag regions. In the 1-tag plot, the bin from 120 – 160 GeV contains events with $p_T^V > 120$ GeV.

Not reviewed, for internal circulation only

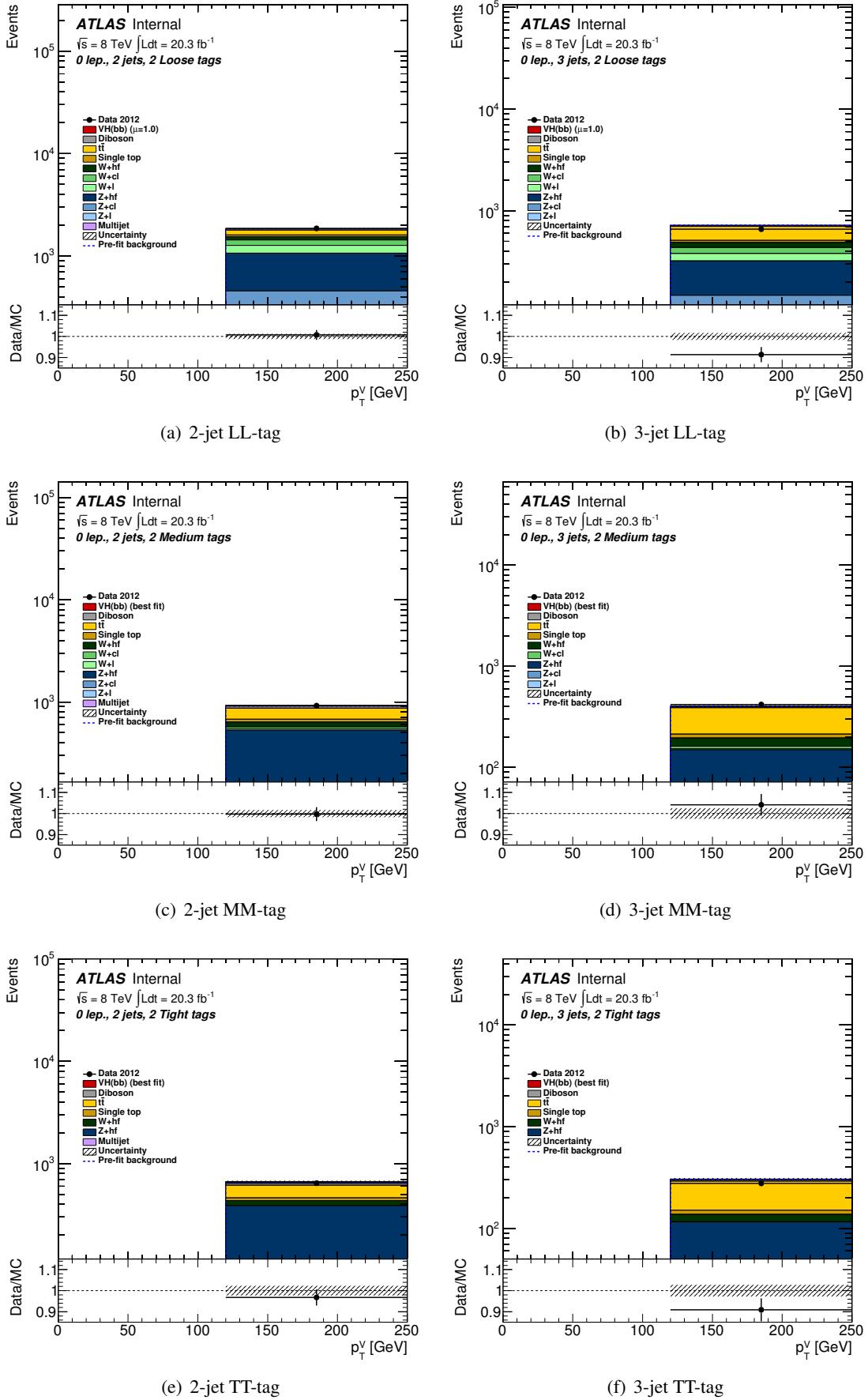


Figure 504: p_T^V distribution in the 0-lepton MVA analysis using the postfit NPs for the corresponding 0+1+2 lepton unconditional fit. The 2 and 3-jet regions are shown in the three 2-tag regions.

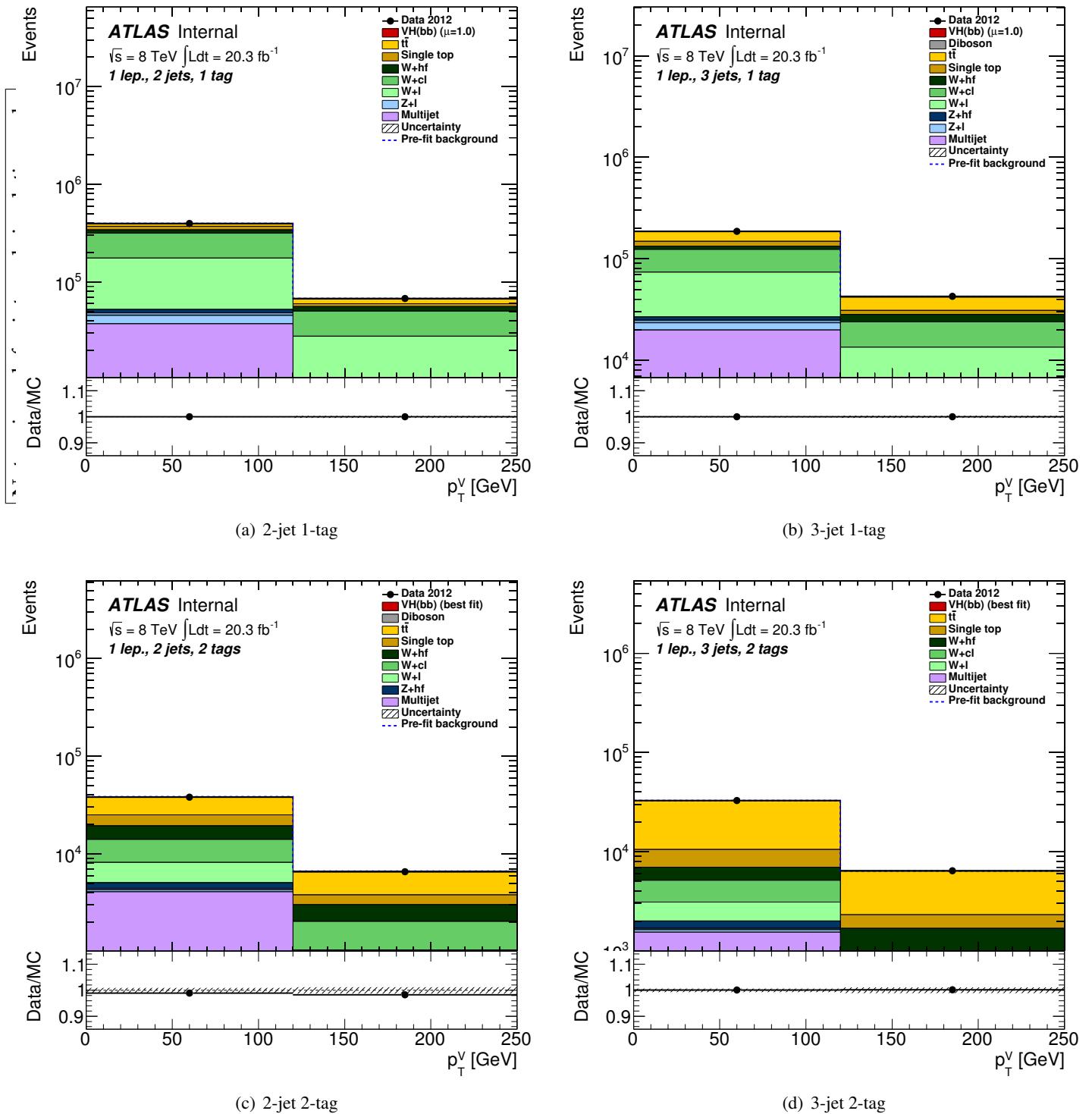


Figure 505: p_T^V distribution in the 1-lepton MVA analysis using the postfit NPs for the corresponding $0+1+2$ lepton unconditional fit. The 2 and 3-jet regions are shown in the 1-tag and inclusive 2-tag regions. In the 1-tag plot, the bin from $120 - 160$ GeV contains events with $p_T^V > 120$ GeV.

Not reviewed, for internal circulation only

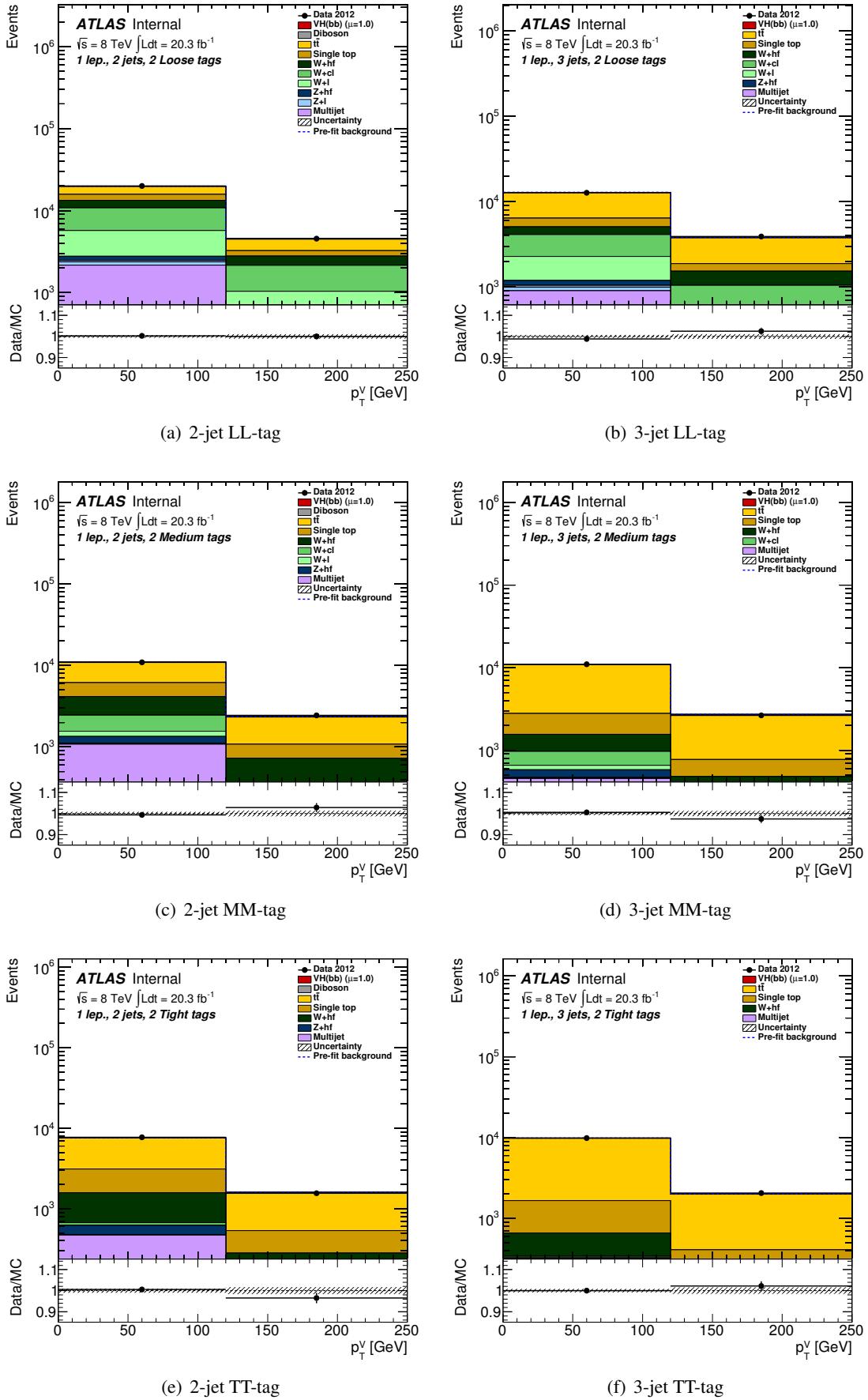


Figure 506: p_T^V distribution in the 1-lepton MVA analysis using the postfit NPs for the corresponding 0+1+2 lepton unconditional fit. The 2 and 3-jet regions are shown in the three 2-tag regions.

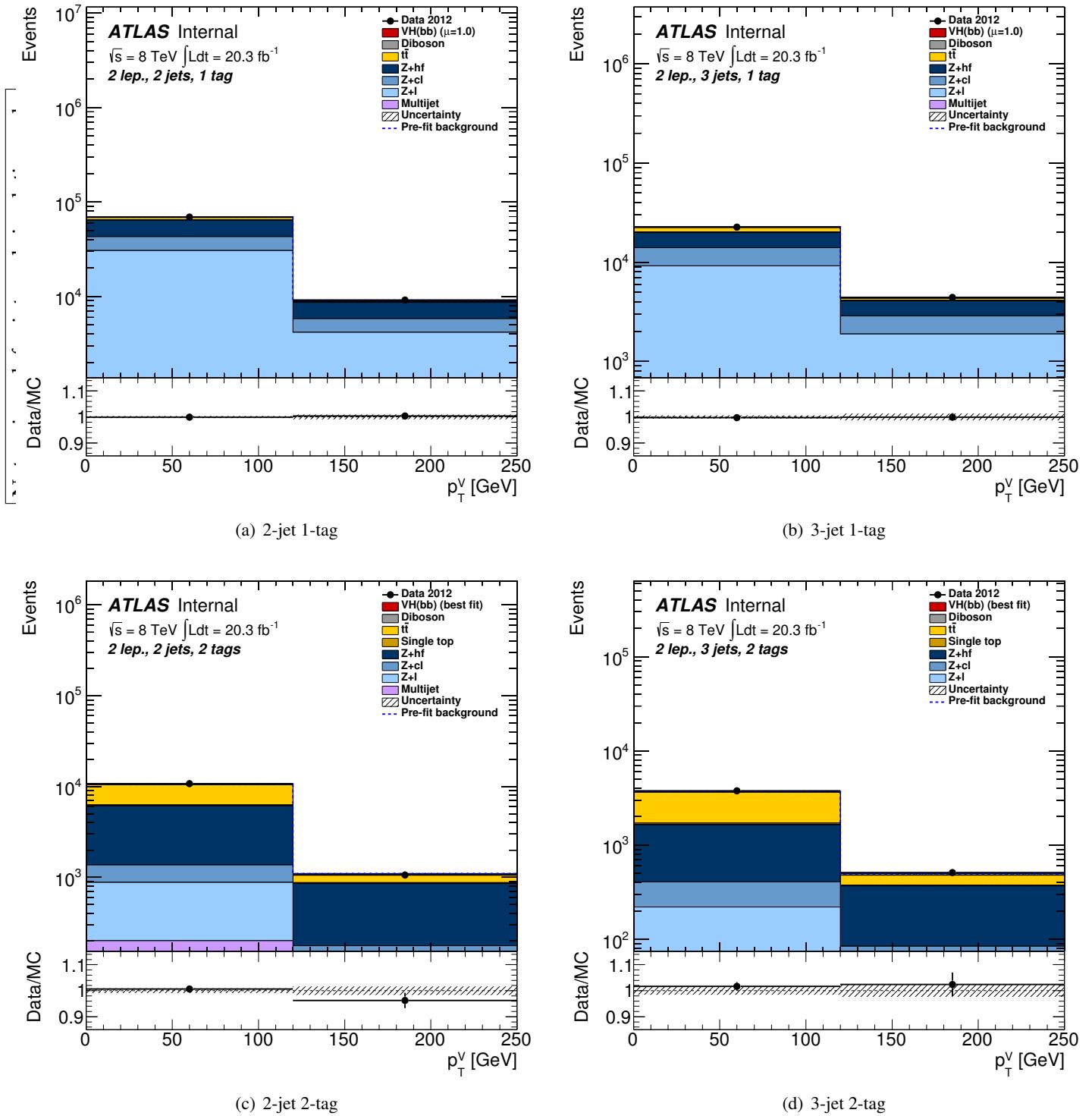


Figure 507: p_T^V distribution in the 2-lepton MVA analysis using the postfit NPs for the corresponding $0+1+2$ lepton unconditional fit. The 2 and 3-jet regions are shown in the 1-tag and inclusive 2-tag regions. In the 1-tag plot, the bin from 120 – 160 GeV contains events with $p_T^V > 120$ GeV.

Not reviewed, for internal circulation only

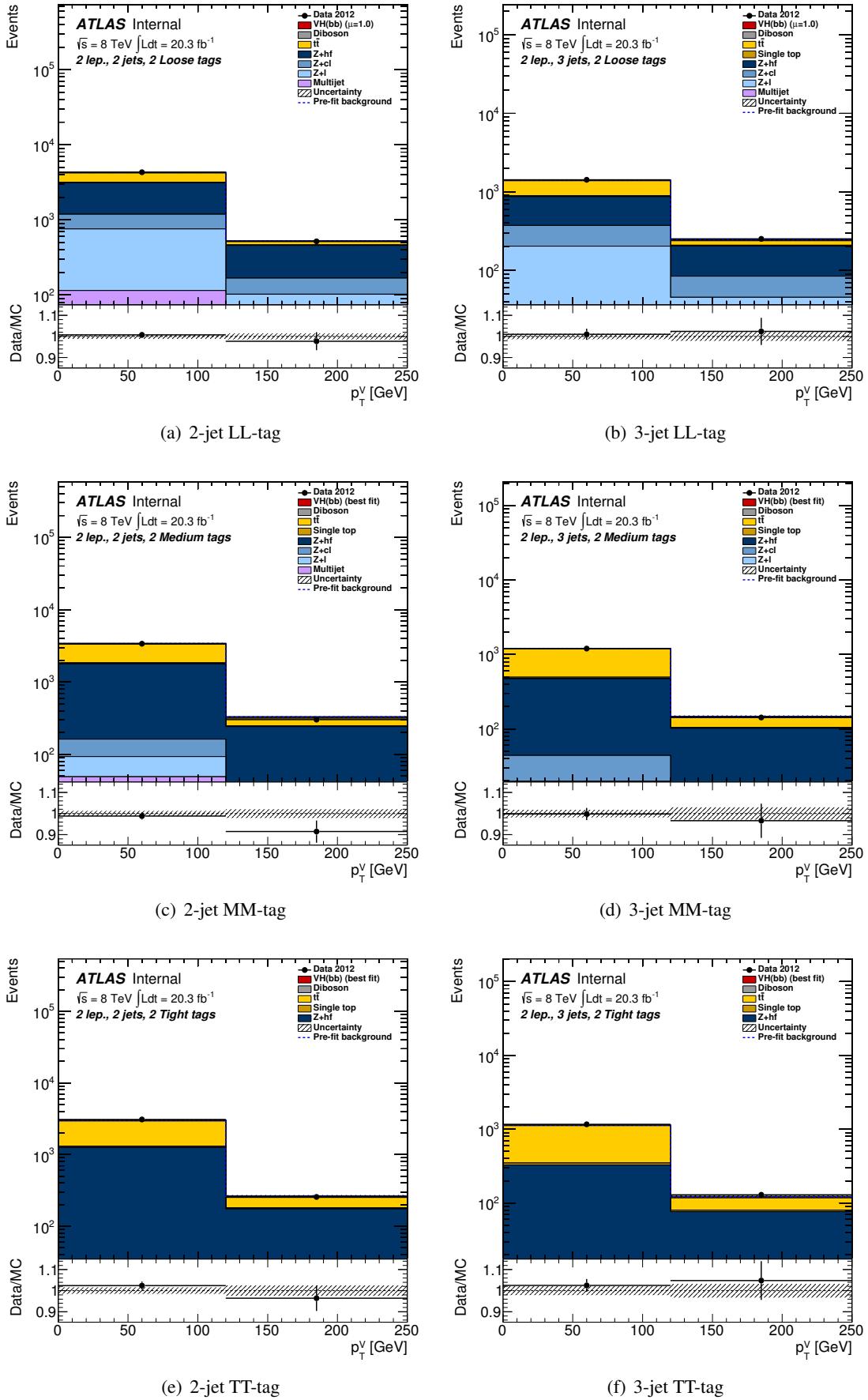


Figure 508: p_T^V distribution in the 2-lepton MVA analysis using the postfit NPs for the corresponding 0+1+2 lepton unconditional fit. The 2 and 3-jet regions are shown in the three 2-tag regions.

5073 **AJ Yield Tables**

5074 **AJ.1 Dijet Mass Analysis: Prefit**

[Not reviewed, for internal circulation only]

Not reviewed, for internal circulation only

Sample	$100 < p_T^V < 120 \text{ GeV}$	$p_T^V > 120 \text{ GeV}$
VH	7.9	19.3
VV	233.5	547.1
$t\bar{t}$	596.6	968.7
s-top	443.2	421.3
$W+l$	5290.0	4880.9
$W+c\ell$	1975.9	2212.7
$W+hf$	883.2	1334.8
$Z+l$	3709.6	7026.1
$Z+c\ell$	1741.4	3105.1
$Z+hf$	2236.6	3942.1
MJ	410.6	244.4
Total	17528.5 ± 1477.1	24702.6 ± 2001.1
Data	18343.0 ± 135.4	24289.0 ± 155.8
<hr/>		
VH	–	5.8
VV	–	167.1
$t\bar{t}$	–	985.9
s-top	–	184.1
$W+l$	–	1251.5
$W+c\ell$	–	617.0
$W+hf$	–	398.5
$Z+l$	–	1722.5
$Z+c\ell$	–	823.6
$Z+hf$	–	1019.4
MJ	–	71.7
Total	–	7247.1 ± 772.8
Data	–	7148.0 ± 84.5

Table 99: Table of prefit yields for 0-lepton 2 and 3-jet 1-tag events in the dijet mass selection. The uncertainties are from the full prefit nuisance parameters (NPs) except the floating normalizations under the assumption that each NP is independent (uncorrelated).

Not reviewed, for internal circulation only

Sample	100 < p_T^V < 120 GeV			120 < p_T^V < 160 GeV			160 < p_T^V < 200 GeV			$p_T^V > 200$ GeV		
	VH	2.2	3.1	1.6	1.8	2L-tag 2-jet						
VV		16.8	23.0	10.5	10.2							
$t\bar{t}$		78.2	77.6	19.8	9.6							
s-top		34.4	26.4	5.6	1.9							
W+l		159.0	97.1	25.5	16.1							
W+cl		93.9	66.2	17.6	10.0							
W+hf		64.4	74.6	22.4	19.0							
Z+l		89.1	102.6	36.8	33.1							
Z+cl		63.8	73.6	26.4	20.4							
Z+hf		187.7	214.3	70.6	57.5							
MJ		18.9	11.4	1.4	0.9							
Total		808.4 ± 77.6	769.8 ± 74.9	238.2 ± 25.3	180.6 ± 21.2							
Data		887.0 ± 29.8	856.0 ± 29.3	239.0 ± 15.5	185.0 ± 13.6							
3-jet												
VH	–	0.7	0.5	0.6	0.6							
VV	–	5.0	2.9	3.1	3.1							
$t\bar{t}$	–	65.1	21.4	11.3	11.3							
s-top	–	10.0	2.6	2.0	2.0							
W+l	–	18.9	7.3	5.9	5.9							
W+cl	–	14.8	6.0	4.3	4.3							
W+hf	–	17.5	7.3	7.3	7.3							
Z+l	–	19.4	10.3	11.4	11.4							
Z+cl	–	15.7	8.1	8.2	8.2							
Z+hf	–	39.2	19.6	21.8	21.8							
MJ	–	2.7	0.6	0.3	0.3							
Total	–	209.0 ± 24.9	86.5 ± 10.4	76.2 ± 10.2	76.2 ± 10.2							
Data	–	221.0 ± 14.9	78.0 ± 8.8	44.0 ± 6.6	44.0 ± 6.6							

Table 100: Table of profit yields for 0-lepton 2 and 3-jet 2L-tag events in the dijet mass selection. The uncertainties are from the full profit nuisance parameters (NPs) except the floating normalizations under the assumption that each NP is independent (uncorrelated).

Not reviewed, for internal circulation only

Sample	100 < p_T^V < 120 GeV			120 < p_T^V < 160 GeV			160 < p_T^V < 200 GeV			$p_T^V > 200$ GeV		
	2M-tag			2-jet								
VH	3.5			5.0			2.6			2.7		
VV	13.9			20.7			9.5			8.6		
$t\bar{t}$	90.1			81.6			15.5			5.3		
s-top	27.2			20.7			3.8			1.0		
W+1	13.2			7.2			1.7			1.0		
W+cl	20.9			11.7			2.8			1.5		
W+hf	39.1			48.6			14.7			12.4		
Z+1	5.2			5.8			2.0			1.8		
Z+cl	9.9			10.8			3.5			2.8		
Z+hf	155.9			177.7			55.3			39.4		
MJ	9.0			5.4			0.6			0.4		
Total	387.9 ± 25.7			395.2 ± 29.0			112.2 ± 9.9			77.0 ± 8.0		
Data	477.0 ± 21.8			438.0 ± 20.9			146.0 ± 12.1			86.0 ± 9.3		
3-jet												
VH	–			1.0			0.8			0.8		
VV	–			3.6			2.5			2.3		
$t\bar{t}$	–			64.8			15.2			5.9		
s-top	–			7.2			2.1			1.2		
W+1	–			1.2			0.5			0.4		
W+cl	–			2.6			0.9			0.6		
W+hf	–			12.7			5.4			4.8		
Z+1	–			1.1			0.6			0.6		
Z+cl	–			2.3			1.2			1.2		
Z+hf	–			33.4			15.7			15.3		
MJ	–			1.4			0.2			0.2		
Total	–			131.4 ± 18.6			45.0 ± 6.5			33.3 ± 4.8		
Data	–			166.0 ± 12.9			49.0 ± 7.0			36.0 ± 6.0		

Table 101: Table of profit yields for 0-lepton 2 and 3-jet 2M-tag events in the dijet mass selection. The uncertainties are from the full profit nuisance parameters (NPs) except the floating normalizations under the assumption that each NP is independent (uncorrelated).

Not reviewed, for internal circulation only

Sample	100 < p_T^V < 120 GeV			120 < p_T^V < 160 GeV			2T-tag 2-jet			$p_T^V > 200$ GeV																																																																																									
	VH	4.0		VV	5.8		$t\bar{t}$	19.1	9.0	s-top	65.9	9.2	W+1	13.5	2.3	W+cl	0.2	0.0	W+hf	0.9	0.5	Z+1	26.2	35.8	Z+cl	0.1	0.1	Z+hf	0.3	0.4	MJ	129.2	141.3	Total	6.5	2.4	Data	279.9 ± 18.4	284.9 ± 22.9	Total	306.0 ± 17.5	312.0 ± 17.7	Data	-	-																																																						
VH	-	1.3		VH	1.3		VH	3.1	2.4	VH	0.9	1.0	VV	-	-	VV	-	-	VV	-	-	$t\bar{t}$	-	-	$t\bar{t}$	-	-	s-top	-	-	$t\bar{t}$	-	-	W+1	-	-	$t\bar{t}$	-	-	W+cl	-	-	$t\bar{t}$	-	-	W+hf	-	-	$t\bar{t}$	-	-	Z+1	-	-	$t\bar{t}$	-	-	Z+cl	-	-	$t\bar{t}$	-	-	Z+hf	-	-	$t\bar{t}$	-	-	MJ	-	-	$t\bar{t}$	-	-	Total	-	-	$t\bar{t}$	-	-	Data	-	-	$t\bar{t}$	-	-												
VH	4.0			VH	5.8		VH	3.1	2.4	VH	0.9	1.0	VV	12.4		VV	19.1	9.0	VV	81.4	65.9	$t\bar{t}$	8.3		$t\bar{t}$	13.5	2.3	s-top	18.8		$t\bar{t}$	0.2	0.0	W+1	0.2		$t\bar{t}$	0.1	0.0	W+cl	0.9		$t\bar{t}$	0.5	0.2	W+hf	26.2		$t\bar{t}$	35.8	10.9	Z+1	0.1		$t\bar{t}$	0.1	0.0	Z+cl	0.3		$t\bar{t}$	0.4	0.1	Z+hf	129.2		$t\bar{t}$	141.3	43.7	MJ	6.5		$t\bar{t}$	2.4	0.3	Total	279.9 ± 18.4		$t\bar{t}$	284.9 ± 22.9	78.7 ± 6.6	Data	306.0 ± 17.5		$t\bar{t}$	312.0 ± 17.7	97.0 ± 9.8	Total	306.0 ± 17.5		$t\bar{t}$	312.0 ± 17.7	97.0 ± 9.8	Data	-		$t\bar{t}$	-	0.1
VH	4.0			VH	5.8		VH	3.1	2.4	VH	0.9	1.0	VV	12.4		VV	19.1	9.0	VV	81.4	65.9	$t\bar{t}$	8.3		$t\bar{t}$	13.5	2.3	s-top	18.8		$t\bar{t}$	0.2	0.0	W+1	0.2		$t\bar{t}$	0.1	0.0	W+cl	0.9		$t\bar{t}$	0.5	0.2	W+hf	26.2		$t\bar{t}$	35.8	10.9	Z+1	0.1		$t\bar{t}$	0.1	0.0	Z+cl	0.3		$t\bar{t}$	0.4	0.1	Z+hf	129.2		$t\bar{t}$	141.3	43.7	MJ	6.5		$t\bar{t}$	2.4	0.3	Total	279.9 ± 18.4		$t\bar{t}$	284.9 ± 22.9	78.7 ± 6.6	Data	306.0 ± 17.5		$t\bar{t}$	312.0 ± 17.7	97.0 ± 9.8	Total	306.0 ± 17.5		$t\bar{t}$	312.0 ± 17.7	97.0 ± 9.8	Data	-		$t\bar{t}$	-	0.1
VH	4.0			VH	5.8		VH	3.1	2.4	VH	0.9	1.0	VV	12.4		VV	19.1	9.0	VV	81.4	65.9	$t\bar{t}$	8.3		$t\bar{t}$	13.5	2.3	s-top	18.8		$t\bar{t}$	0.2	0.0	W+1	0.2		$t\bar{t}$	0.1	0.0	W+cl	0.9		$t\bar{t}$	0.5	0.2	W+hf	26.2		$t\bar{t}$	35.8	10.9	Z+1	0.1		$t\bar{t}$	0.1	0.0	Z+cl	0.3		$t\bar{t}$	0.4	0.1	Z+hf	129.2		$t\bar{t}$	141.3	43.7	MJ	6.5		$t\bar{t}$	2.4	0.3	Total	279.9 ± 18.4		$t\bar{t}$	284.9 ± 22.9	78.7 ± 6.6	Data	306.0 ± 17.5		$t\bar{t}$	312.0 ± 17.7	97.0 ± 9.8	Total	306.0 ± 17.5		$t\bar{t}$	312.0 ± 17.7	97.0 ± 9.8	Data	-		$t\bar{t}$	-	0.1

Table 102: Table of profit yields for 0-lepton 2 and 3-jet 2T-tag events in the dijet mass selection. The uncertainties are from the full profit nuisance parameters (NPs) except the floating normalizations under the assumption that each NP is independent (uncorrelated).

Not reviewed, for internal circulation only

Sample	$p_T^V < 120 \text{ GeV}$		$p_T^V > 120 \text{ GeV}$
	1-tag	2-jet	
VH	34.4		19.6
VV	1672.9		649.9
$t\bar{t}$	7827.7		3919.5
s-top	8418.6		1543.2
$W+1$	48093.7		10421.4
$W+cl$	49714.6		8865.1
$W+hf$	16338.4		3920.3
Z+1	2926.8		455.4
Z+cl	1193.3		151.2
Z+hf	1448.9		181.2
MJ_e	–		853.8
MJ_μ	6607.5		55.5
Total	144276.7 ± 11471.9	-31035.9 ± 2745.0	–
Data	148390.0 ± 385.2	31777.0 ± 178.3	–
3-jet			
VH	12.9		9.1
VV	894.2		356.4
$t\bar{t}$	15652.4		6917.2
s-top	5534.8		1433.0
$W+1$	19163.8		4672.3
$W+cl$	18399.8		3749.5
$W+hf$	7240.0		1915.7
Z+1	1324.9		188.8
Z+cl	588.2		79.0
Z+hf	690.4		88.5
MJ_e	–		381.9
MJ_μ	3241.0		25.3
Total	72742.3 ± 6431.3	-19816.6 ± 2153.0	–
Data	69956.0 ± 264.5	19649.0 ± 140.2	–

Table 103: Table of prefit yields for 1-lepton 2 and 3-jet 1-tag events in the dijet mass selection. The uncertainties are from the full prefit nuisance parameters (NPs) except the floating normalizations under the assumption that each NP is independent (uncorrelated).

Not reviewed, for internal circulation only

Sample	$p_T^V < 90 \text{ GeV}$	$90 < p_T^V < 120 \text{ GeV}$	$120 < p_T^V < 160 \text{ GeV}$	2L-tag		$p_T^V > 200 \text{ GeV}$
				2-jet	3-jet	
VH						
VV	7.4	2.6	3.4	1.6	1.8	
$t\bar{t}$	68.9	22.1	22.1	8.2	9.1	
s-top	871.7	334.4	324.6	83.5	45.6	
W+l	573.7	138.6	95.1	22.9	14.3	
W+cI	908.4	253.7	176.4	49.2	41.3	
W+hf	1404.2	364.7	236.0	59.8	38.0	
Z+l	1077.6	316.6	243.2	71.0	68.0	
Z+cI	55.6	20.4	9.3	1.5	0.6	
Z+hf	35.0	11.9	5.3	0.9	0.4	
MJ _e	81.9	28.7	11.9	2.1	0.9	
MJ _{μ}	–	–	45.5	10.2	2.0	
Total	5541.4 ± 512.9	1547.8 ± 139.3	1177.8 ± 109.4	311.7 ± 33.4	222.1 ± 32.7	
Data	5891.0 ± 76.8	1570.0 ± 39.6	1208.0 ± 34.8	323.0 ± 18.0	198.0 ± 14.1	
3-jet						
VH						
VV	2.1	0.8	1.2	0.6	0.9	
$t\bar{t}$	31.3	9.7	10.3	4.5	4.9	
s-top	1938.2	537.2	477.0	141.7	92.9	
W+l	389.8	94.2	75.9	24.5	20.8	
W+cI	358.0	88.7	68.4	21.9	21.7	
W+hf	534.9	126.5	91.4	27.6	22.3	
Z+l	480.9	113.3	100.3	35.3	39.4	
Z+cI	24.5	6.8	3.4	0.7	0.4	
Z+hf	17.9	4.6	2.3	0.5	0.3	
MJ _e	41.9	9.7	6.3	1.0	0.6	
MJ _{μ}	–	–	11.9	2.5	0.8	
Total	138.3	10.8	1.2	–	–	
Data	3882.0 ± 62.3	1004.0 ± 31.7	938.0 ± 30.6	273.0 ± 16.5	207.0 ± 14.4	

Table 104: Table of profit yields for 1-lepton 2 and 3-jet 2L-tag events in the dijet mass selection. The uncertainties are from the full profit nuisance parameters (NPs) except the floating normalizations under the assumption that each NP is independent (uncorrelated).

Not reviewed, for internal circulation only

Sample	$p_T^V < 90 \text{ GeV}$	$90 < p_T^V < 120 \text{ GeV}$	$120 < p_T^V < 160 \text{ GeV}$	2M-tag		$160 < p_T^V < 200 \text{ GeV}$	$p_T^V > 200 \text{ GeV}$
				2-jet	3-jet		
VH	11.6	3.9	5.2	2.5	2.9		
VV	44.2	14.0	14.7	5.8	5.0		
$t\bar{t}$	1073.5	403.0	348.3	64.1	25.3		
s-top	521.8	123.3	79.9	16.7	9.4		
W+l	66.4	18.7	12.1	3.2	2.6		
W+c1	243.1	63.6	40.6	9.6	5.7		
W+hf	702.0	213.3	167.6	47.3	44.8		
Z+l	4.3	1.5	0.7	0.1	0.0		
Z+c1	7.3	2.4	1.1	0.1	0.0		
Z+hf	63.5	21.4	8.7	1.3	0.6		
MJ _e	–	–	26.8	4.9	1.2		
MJ _{μ}	242.4	19.1	1.4	–	–		
Total	2980.2 ± 251.0	884.3 ± 66.1	707.1 ± 59.3	155.5 ± 15.9	97.5 ± 16.5		
Data	3230.0 ± 56.8	984.0 ± 31.4	776.0 ± 27.9	180.0 ± 13.4	101.0 ± 10.0		
Sample	$p_T^V < 90 \text{ GeV}$	$90 < p_T^V < 120 \text{ GeV}$	$120 < p_T^V < 160 \text{ GeV}$	3-jet		$160 < p_T^V < 200 \text{ GeV}$	$p_T^V > 200 \text{ GeV}$
				3-jet	3-jet		
VH	3.2	1.3	1.9	1.2	1.3		
VV	14.5	4.9	5.7	2.7	2.8		
$t\bar{t}$	2484.8	642.3	487.0	104.5	51.3		
s-top	371.0	83.4	61.9	17.1	14.1		
W+l	24.1	6.1	4.7	1.4	1.3		
W+c1	88.8	21.0	15.6	4.2	3.1		
W+hf	290.3	73.4	68.9	24.2	26.1		
Z+l	1.6	0.5	0.3	0.1	0.0		
Z+c1	3.0	0.8	0.3	0.1	0.0		
Z+hf	30.0	8.0	4.7	1.0	0.4		
MJ _e	–	–	5.8	2.1	0.4		
MJ _{μ}	70.5	6.6	–	0.6	–		
Total	3381.9 ± 564.1	848.4 ± 143.3	656.9 ± 115.1	159.1 ± 25.8	100.8 ± 17.2		
Data	3519.0 ± 59.3	936.0 ± 30.6	674.0 ± 26.0	160.0 ± 12.6	109.0 ± 10.4		

Table 105: Table of prefit yields for 1-lepton 2 and 3-jet 2M-tag events in the dijet mass selection. The uncertainties are from the full prefit nuisance parameters (NPs) except the floating normalizations under the assumption that each NP is independent (uncorrelated).

Not reviewed, for internal circulation only

Sample	$p_T^V < 90 \text{ GeV}$	$90 < p_T^V < 120 \text{ GeV}$	$120 < p_T^V < 160 \text{ GeV}$	2T-tag		
				2-jet	$160 < p_T^V < 200 \text{ GeV}$	$p_T^V > 200 \text{ GeV}$
VH	13.1	4.4	6.0	3.2	3.2	3.2
VV	34.6	11.6	12.6	5.0	4.2	4.2
$t\bar{t}$	1019.8	367.2	284.8	34.6	7.2	7.2
s-top	424.2	94.2	59.1	10.5	3.9	3.9
W+1	2.0	0.4	0.3	0.1	0.1	0.1
W+c1	12.6	3.2	2.0	0.5	0.3	0.3
W+hf	372.1	119.0	104.7	30.5	29.2	29.2
Z+1	0.1	0.0	0.0	0.0	0.0	0.0
Z+c1	0.4	0.1	0.0	0.0	–	–
Z+hf	42.6	15.1	5.8	1.3	0.4	0.4
MJ _e	–	–	11.6	2.4	1.2	1.2
MJ _{μ}	99.1	9.3	–	–	–	–
Total	2020.4 ± 183.8	624.4 ± 50.2	486.9 ± 45.3	88.1 ± 10.7	49.8 ± 10.3	49.8 ± 10.3
Data	2364.0 ± 48.6	700.0 ± 26.5	535.0 ± 23.1	100.0 ± 10.0	54.0 ± 7.3	54.0 ± 7.3
3-jet						
VH	3.6	1.4	2.2	1.3	1.5	1.5
VV	9.2	3.4	5.2	2.6	2.4	2.4
$t\bar{t}$	2551.9	607.8	397.0	49.7	14.7	14.7
s-top	309.2	64.8	43.9	8.7	6.3	6.3
W+1	0.7	0.2	0.1	0.0	0.0	0.0
W+c1	4.2	1.0	0.9	0.2	0.1	0.1
W+hf	153.1	41.6	41.9	16.2	17.6	17.6
Z+1	0.0	0.0	0.0	0.0	0.0	0.0
Z+c1	0.1	0.0	0.0	0.0	0.0	0.0
Z+hf	22.2	6.1	3.5	0.7	0.3	0.3
MJ _e	–	–	2.3	0.7	0.3	0.3
MJ _{μ}	35.5	1.9	–	0.3	–	–
Total	3089.7 ± 587.0	728.3 ± 138.1	497.0 ± 97.2	80.5 ± 14.5	43.2 ± 7.8	43.2 ± 7.8
Data	3161.0 ± 56.2	779.0 ± 27.9	505.0 ± 22.5	88.0 ± 9.4	48.0 ± 6.9	48.0 ± 6.9

Table 106: Table of profit yields for 1-lepton 2 and 3-jet 2T-tag events in the dijet mass selection. The uncertainties are from the full profit nuisance parameters (NPs) except the floating normalizations under the assumption that each NP is independent (uncorrelated).

Not reviewed, for internal circulation only

Sample	$p_T^V < 120 \text{ GeV}$	1-tag 2-jet	$p_T^V > 120 \text{ GeV}$
VH	16.3		4.5
VV	614.4		83.7
$t\bar{t}$	493.0		23.5
s-top	53.6	3.8	
$W+l$	69.8	1.1	
$W+cl$	37.5	2.9	
$W+hf$	20.3	2.2	
$Z+l$	19153.6	1796.9	
$Z+cl$	9818.8	854.4	
$Z+hf$	13260.2	1172.5	
MJ	606.5	4.7	
Total	44144.1 ± 3561.5	3950.2 ± 284.9	
Data	44551.0 ± 211.1	4052.0 ± 63.7	
		3-jet	
VH	5.7	2.1	
VV	252.0	47.2	
$t\bar{t}$	279.2	14.8	
s-top	19.0	1.9	
$W+l$	7.7	0.9	
$W+cl$	11.6	1.4	
$W+hf$	9.4	0.9	
$Z+l$	5602.5	769.0	
$Z+cl$	3157.5	381.5	
$Z+hf$	4107.3	491.8	
MJ	172.3	2.4	
Total	13624.1 ± 1771.5	1713.8 ± 192.3	
Data	13595.0 ± 116.6	1631.0 ± 40.4	

Table 107: Table of prefit yields for 2-lepton 2 and 3-jet 1-tag events in the dijet mass selection. The uncertainties are from the full prefit nuisance parameters (NPs) except the floating normalizations under the assumption that each NP is independent (uncorrelated).

Not reviewed, for internal circulation only

Sample	$p_T^V < 90 \text{ GeV}$	$90 < p_T^V < 120 \text{ GeV}$	$120 < p_T^V < 160 \text{ GeV}$	2-jet	2L-tag	$160 < p_T^V < 200 \text{ GeV}$	$p_T^V > 200 \text{ GeV}$
VH	3.6	1.0	0.7	0.3	0.3	0.3	0.4
VV	46.2	7.8	4.7	1.8	1.8	1.7	1.7
$t\bar{t}$	117.5	18.6	4.4	0.3	0.3	0.0	0.0
s-top	4.8	0.9	0.5	0.0	0.0	0.1	0.1
W+1	0.6	0.1	0.0	0.0	0.0	0.0	0.0
W+cJ	0.9	0.2	0.0	0.0	0.0	0.0	0.0
W+hf	2.4	0.4	0.1	0.0	0.0	0.0	0.0
Z+1	352.1	67.3	27.6	7.6	7.6	7.0	7.0
Z+cJ	280.4	54.0	20.9	5.8	5.8	4.5	4.5
Z+hf	926.5	195.9	75.1	18.7	18.7	14.7	14.7
MJ	45.9	2.4	0.4	0.1	0.1	—	—
Total	1780.8 ± 165.9	348.6 ± 29.3	134.4 ± 12.1	34.6 ± 3.5	34.6 ± 3.5	28.5 ± 3.3	28.5 ± 3.3
Data	2009.0 ± 44.8	378.0 ± 19.4	153.0 ± 12.4	33.0 ± 5.7	33.0 ± 5.7	42.0 ± 6.5	42.0 ± 6.5
			3-jet				
VH	0.9	0.3	0.3	0.2	0.2	0.2	0.2
VV	12.4	2.9	1.7	0.9	0.9	1.1	1.1
$t\bar{t}$	52.0	8.2	2.2	0.3	0.3	—	—
s-top	1.8	0.5	0.1	0.2	0.2	—	—
W+1	0.2	0.0	0.0	0.0	0.0	0.0	0.0
W+cJ	0.4	0.0	0.0	0.0	0.0	0.0	0.0
W+hf	0.3	0.0	0.0	0.0	0.0	0.0	0.0
Z+1	100.0	20.9	9.9	3.2	3.2	3.5	3.5
Z+cJ	90.1	18.5	8.2	2.7	2.7	2.6	2.6
Z+hf	257.1	58.5	26.8	7.7	7.7	7.5	7.5
MJ	6.0	0.1	0.1	—	—	—	—
Total	521.3 ± 79.4	110.1 ± 15.8	49.3 ± 7.3	15.1 ± 2.3	15.1 ± 2.3	14.9 ± 2.4	14.9 ± 2.4
Data	612.0 ± 24.7	128.0 ± 11.3	64.0 ± 8.0	12.0 ± 3.5	12.0 ± 3.5	19.0 ± 4.4	19.0 ± 4.4

Table 108: Table of profit yields for 2-lepton 2 and 3-jet 2L-tag events in the dijet mass selection. The uncertainties are from the full profit nuisance parameters (NPs) except the floating normalizations under the assumption that each NP is independent (uncorrelated).

Not reviewed, for internal circulation only

Sample	$p_T^V < 90 \text{ GeV}$	$90 < p_T^V < 120 \text{ GeV}$	$120 < p_T^V < 160 \text{ GeV}$	2M^{tag} 2-jet	$160 < p_T^V < 200 \text{ GeV}$	$p_T^V > 200 \text{ GeV}$
VH	5.8	1.6	1.2	0.6	0.6	0.6
VV	46.2	7.6	4.5	1.8	1.8	1.7
$t\bar{t}$	179.9	31.2	6.7	0.3	0.3	0.0
s-top	5.7	1.5	0.4	0.0	0.0	–
W+1	0.0	0.0	0.0	0.0	0.0	0.0
W+c1	0.2	0.0	0.0	0.0	0.0	0.0
W+hf	0.7	0.1	0.0	–	0.0	0.0
Z+1	23.3	4.1	1.6	0.4	0.4	0.4
Z+c1	46.4	8.6	3.3	0.9	0.9	0.6
Z+hf	803.1	168.6	64.4	15.0	15.0	9.8
MJ	16.3	0.4	0.1	–	–	–
Total	1127.6 ± 63.0	223.7 ± 14.1	82.4 ± 5.5	19.0 ± 1.5	13.1 ± 1.4	9.0 ± 3.0
Data	1284.0 ± 35.8	264.0 ± 16.2	83.0 ± 9.1	23.0 ± 4.8		
			3-jet			
VH	1.4	0.5	0.4	0.3	0.3	0.3
VV	9.7	1.8	1.5	0.7	0.7	0.7
$t\bar{t}$	77.4	12.4	2.5	0.1	0.1	0.0
s-top	2.5	0.7	0.1	–	0.0	0.0
W+1	0.0	0.0	0.0	0.0	0.0	0.0
W+c1	0.1	0.0	0.0	0.0	0.0	0.0
W+hf	0.2	0.0	0.0	0.0	0.0	0.0
Z+1	6.4	1.2	0.6	0.2	0.2	0.2
Z+c1	13.2	3.0	1.3	0.4	0.4	0.4
Z+hf	216.2	46.7	24.5	6.7	5.3	5.3
MJ	2.9	0.1	–	–	–	–
Total	330.0 ± 51.8	66.5 ± 10.6	30.9 ± 5.3	8.2 ± 1.5	6.9 ± 1.3	6.9 ± 1.3
Data	401.0 ± 20.0	80.0 ± 8.9	34.0 ± 5.8	6.0 ± 2.4	7.0 ± 2.6	7.0 ± 2.6

Table 109: Table of prefit yields for 2-lepton 2 and 3-jet 2M-tag events in the dijet mass selection. The uncertainties are from the full prefit nuisance parameters (NPs) except the floating normalizations under the assumption that each NP is independent (uncorrelated).

Not reviewed, for internal circulation only

Sample	2T-tag						$p_T^V > 200 \text{ GeV}$
	$p_T^V < 90 \text{ GeV}$	$90 < p_T^V < 120 \text{ GeV}$	$120 < p_T^V < 160 \text{ GeV}$	$160 < p_T^V < 200 \text{ GeV}$	2-jet		
VH	6.6	1.8	1.5	0.7	0.7	0.7	
VV	42.1	6.9	4.7	2.1	1.8		
$t\bar{t}$	196.6	32.3	7.1	0.3	–		
s-top	4.7	1.3	0.2	0.1	0.1		
$W+1$	0.0	–	–	–	–		
$W+\text{hf}$	0.7	0.3	0.0	0.0	–		
Z+1	0.4	0.1	0.0	0.0	0.0		
Z+c1	1.4	0.2	0.1	0.0	0.0		
Z+hf	606.2	136.3	52.6	11.8	7.5		
MJ	10.4	0.2	0.1	–	–		
Total	869.0 ± 44.0	179.4 ± 9.7	66.3 ± 4.5	15.1 ± 1.1	10.1 ± 1.0		
Data	980.0 ± 31.3	209.0 ± 14.5	65.0 ± 8.1	17.0 ± 4.1	12.0 ± 3.5		
3-jet	2T-tag						$p_T^V > 200 \text{ GeV}$
	$p_T^V < 90 \text{ GeV}$	$90 < p_T^V < 120 \text{ GeV}$	$120 < p_T^V < 160 \text{ GeV}$	$160 < p_T^V < 200 \text{ GeV}$	2-jet		
	VH	1.6	0.6	0.5	0.3	0.3	
	VV	7.9	2.0	1.4	0.8	0.7	
	$t\bar{t}$	85.6	14.4	2.7	0.0	0.0	
	s-top	1.9	0.3	0.3	0.0	–	
	$W+1$	0.0	–	–	–	–	
	$W+\text{hf}$	0.1	–	0.0	0.0	–	
Z+1	0.1	0.0	0.0	0.0	0.0	0.0	
Z+c1	0.3	0.1	0.1	0.0	0.0	0.0	
Z+hf	161.8	36.8	18.9	5.0	3.9		
MJ	1.8	0.1	–	–	–		
Total	261.1 ± 38.6	54.2 ± 8.6	23.9 ± 4.1	6.2 ± 1.1	5.1 ± 0.9		
Data	307.0 ± 17.5	55.0 ± 7.4	29.0 ± 5.4	9.0 ± 3.0	3.0 ± 1.7		

Table 110: Table of profit yields for 2-lepton 2 and 3-jet 2T-tag events in the dijet mass selection. The uncertainties are from the full profit nuisance parameters (NPs) except the floating normalizations under the assumption that each NP is independent (uncorrelated).

5075 **A.J.2 Dijet Mass Analysis: Postfit**

[Not reviewed, for internal circulation only]

Not reviewed, for internal circulation only

Sample	100 < p_T^V < 120 GeV		1-tag
	2-jet		p_T^V > 120 GeV
VH	9.7		23.2
VV	232.6		545.0
$t\bar{t}$	838.1		1367.7
s-top	571.5		465.5
W+l	5566.7		4849.0
W+cl	2203.4		2432.9
W+hf	750.6		958.5
Z+l	3677.7		6643.1
Z+cl	1488.4		2652.7
Z+hf	2458.8		4250.9
MJ	515.7		135.0
Total	18313.2 ± 155.0		24323.5 ± 151.3
Data	18343.0 ± 135.4		24289.0 ± 155.8
$\frac{\text{Sim}-\text{Data}}{\sigma}$	-0.14		0.16
3-jet			
VH	–		6.9
VV	–		166.5
$t\bar{t}$	–		1256.6
s-top	–		183.7
W+l	–		1221.0
W+cl	–		629.5
W+hf	–		315.6
Z+l	–		1527.7
Z+cl	–		839.9
Z+hf	–		922.3
MJ	–		76.1
Total	–		7145.7 ± 72.5
Data	–		7148.0 ± 84.5
$\frac{\text{Sim}-\text{Data}}{\sigma}$	–		-0.02

Table 111: Table of post unconditional fit yields for 0-lepton 2 and 3-jet 1-tag events in the dijet mass selection. The uncertainties are the full postfit errors including all nuisance parameters with priors, floating normalizations, and the correlations deduced from the data. The difference in the data and the postfit simulation is compared to σ which is obtained from the sum in simulation as the sum in quadrature of the postfit and Poissonian error.

Not reviewed, for internal circulation only

Sample	2L-tag				$p_T^V > 200 \text{ GeV}$
	$100 < p_T^V < 120 \text{ GeV}$	$120 < p_T^V < 160 \text{ GeV}$	2-jet	$160 < p_T^V < 200 \text{ GeV}$	
VH	2.7	3.9	2.1	2.1	2.2
VV	17.5	24.1	11.3	11.3	10.8
$t\bar{t}$	112.3	112.8	27.3	27.3	13.3
s-top	43.0	28.7	5.8	5.8	1.9
$W+1$	161.8	97.9	25.7	25.7	16.4
$W+c1$	105.8	74.8	19.6	19.6	10.8
$W+hf$	56.6	62.2	17.9	17.9	13.9
Z+l	89.5	101.2	35.7	35.7	31.4
Z+c1	56.5	64.9	22.8	22.8	17.1
Z+hf	220.4	244.4	81.9	81.9	61.4
MJ	18.2	14.5	1.7	1.7	1.1
Total	884.3 ± 17.3	829.4 ± 14.1	252.0 ± 4.8	252.0 ± 4.8	180.4 ± 5.3
Data	887.0 ± 29.8	856.0 ± 29.3	239.0 ± 15.5	239.0 ± 15.5	185.0 ± 13.6
Sim-Data	-	-	0.78	0.78	-0.32
σ	-	-	-	-	-
3-jet					
VH	-	0.8	0.6	0.6	0.7
VV	-	5.0	2.9	2.9	3.0
$t\bar{t}$	-	86.7	27.1	27.1	14.0
s-top	-	10.1	2.6	2.6	1.9
$W+1$	-	18.8	7.3	7.3	5.9
$W+c1$	-	15.6	6.2	6.2	4.4
$W+hf$	-	14.6	6.4	6.4	6.4
Z+l	-	17.8	9.4	9.4	10.2
Z+c1	-	16.4	8.5	8.5	8.2
Z+hf	-	40.9	19.8	19.8	20.9
MJ	-	1.5	0.4	0.4	0.2
Total	-	228.2 ± 5.2	91.2 ± 2.0	91.2 ± 2.0	75.9 ± 2.2
Data	-	221.0 ± 14.9	78.0 ± 8.8	78.0 ± 8.8	44.0 ± 6.6
Sim-Data	-	0.45	1.35	1.35	3.55
σ	-	-	-	-	-

Table 112: Table of post unconditional fit yields for 0-lepton 2 and 3-jet 2L-tag events in the dijet mass selection. The uncertainties are the full postfit errors including all nuisance parameters with priors, floating normalizations, and the correlations deduced from the data. The difference in the data and the postfit simulation is compared to σ which is obtained from the sum in quadrature of the postfit and Poissonian error.

Not reviewed, for internal circulation only

Sample	2M-tag				$p_T^V > 200 \text{ GeV}$
	$100 < p_T^V < 120 \text{ GeV}$	$120 < p_T^V < 160 \text{ GeV}$	$160 < p_T^V < 200 \text{ GeV}$	2-jet	
VH	4.4	6.3	3.3	3.3	3.3
VV	14.7	22.1	10.2	10.2	9.6
$t\bar{t}$	126.0	120.8	22.6	22.6	7.6
s-top	32.6	23.4	4.5	4.5	1.0
$W+1$	14.6	7.6	1.9	1.9	1.0
$W+c1$	24.0	13.6	3.3	3.3	1.8
$W+hf$	35.8	41.4	12.7	12.7	10.0
$Z+1$	5.6	6.2	2.1	2.1	1.8
$Z+c1$	9.0	9.8	3.1	3.1	2.6
$Z+hf$	178.5	203.3	61.9	61.9	44.2
MJ	8.7	6.9	0.7	0.7	0.5
Total	454.0 ± 9.4	461.4 ± 8.9	126.3 ± 2.9	126.3 ± 2.9	83.4 ± 2.9
Data	477.0 ± 21.8	438.0 ± 20.9	146.0 ± 12.1	146.0 ± 12.1	86.0 ± 9.3
Sim-Data	-0.99	1.01	-1.7	-1.7	-0.27
<hr/>					
Sample	3-jet				$p_T^V > 200 \text{ GeV}$
	$100 < p_T^V < 120 \text{ GeV}$	$120 < p_T^V < 160 \text{ GeV}$	$160 < p_T^V < 200 \text{ GeV}$	3-jet	
VH	-	1.3	1.0	1.0	1.0
VV	-	3.5	2.5	2.5	2.3
$t\bar{t}$	-	85.4	19.9	19.9	8.0
s-top	-	7.4	2.3	2.3	1.2
$W+1$	-	1.4	0.6	0.6	0.4
$W+c1$	-	2.6	1.0	1.0	0.7
$W+hf$	-	10.8	5.0	5.0	4.4
$Z+1$	-	1.2	0.5	0.5	0.6
$Z+c1$	-	2.3	1.3	1.3	1.3
$Z+hf$	-	34.7	17.1	17.1	16.0
MJ	-	0.8	0.1	0.1	0.1
Total	-	151.5 ± 4.8	51.1 ± 1.7	51.1 ± 1.7	35.9 ± 1.4
Data	-	166.0 ± 12.9	49.0 ± 7.0	49.0 ± 7.0	36.0 ± 6.0
Sim-Data	-	-1.1	0.29	-1.1	-0.02
σ	-	-	-	-	-

Table 113: Table of post unconditional fit yields for 0-lepton 2 and 3-jet 2M-tag events in the dijet mass selection. The uncertainties are the full postfit errors including all nuisance parameters with priors, floating normalizations, and the correlations deduced from the data. The difference in the data and the postfit simulation is compared to σ which is obtained from the sum in quadrature of the postfit and Poissonian error.

Not reviewed, for internal circulation only

Sample	2T-tag				$p_T^V > 200 \text{ GeV}$
	$100 < p_T^V < 120 \text{ GeV}$	$120 < p_T^V < 160 \text{ GeV}$	$160 < p_T^V < 200 \text{ GeV}$	2-jet	
VH	4.9	7.2	3.8	3.8	3.8
VV	12.7	20.3	9.6	9.6	8.9
$t\bar{t}$	113.5	94.1	13.5	13.5	2.2
s-top	22.8	15.3	2.4	2.4	0.5
$W+1$	0.2	0.1	0.0	0.0	0.0
$W+c1$	1.0	0.5	0.2	0.2	0.1
$W+hf$	22.6	32.3	9.3	9.3	7.7
Z+l	0.1	0.1	0.0	0.0	0.0
Z+c1	0.3	0.3	0.1	0.1	0.1
Z+hf	146.4	157.6	48.9	48.9	32.0
MJ	6.2	3.0	0.3	0.3	0.1
Total	330.7 ± 8.4	330.8 ± 7.8	88.2 ± 2.7	88.2 ± 2.7	55.3 ± 2.6
Data	306.0 ± 17.5	312.0 ± 17.7	97.0 ± 9.8	97.0 ± 9.8	43.0 ± 6.6
Sim-Data	1.23	0.95	-0.9	-0.9	1.57
<hr/>					
Sample	3-jet				$p_T^V > 200 \text{ GeV}$
	$100 < p_T^V < 120 \text{ GeV}$	$120 < p_T^V < 160 \text{ GeV}$	$160 < p_T^V < 200 \text{ GeV}$	3-jet	
VH	–	1.6	1.1	1.1	1.3
VV	–	3.1	2.2	2.2	2.3
$t\bar{t}$	–	66.1	11.2	11.2	2.2
s-top	–	5.2	0.9	0.9	0.3
$W+1$	–	0.0	0.0	0.0	0.0
$W+c1$	–	0.1	0.0	0.0	0.0
$W+hf$	–	6.2	3.6	3.6	3.5
Z+l	–	0.0	0.0	0.0	0.0
Z+c1	–	0.1	0.0	0.0	0.0
Z+hf	–	30.6	13.8	13.8	12.1
MJ	–	0.4	0.1	0.1	0.0
Total	–	113.4 ± 3.9	33.0 ± 1.2	33.0 ± 1.2	21.7 ± 1.2
Data	–	116.0 ± 10.8	25.0 ± 5.0	25.0 ± 5.0	19.0 ± 4.4
Sim-Data	–	-0.23	1.36	1.36	0.57
σ	–	–	–	–	–

Table 114: Table of post unconditional fit yields for 0-lepton 2 and 3-jet 2T-tag events in the dijet mass selection. The uncertainties are the full postfit errors including all nuisance parameters with priors, floating normalizations, and the correlations deduced from the data. The difference in the data and the postfit simulation is compared to σ which is obtained from the sum in quadrature of the postfit and Poissonian error.

Not reviewed, for internal circulation only

Sample	$p_T^V < 120 \text{ GeV}$		$p_T^V > 120 \text{ GeV}$
	1-tag 2-jet	$p_T^V > 120 \text{ GeV}$	
VH	41.5	23.5	
VV	1666.6	669.6	
$t\bar{t}$	9014.6	4514.2	
s-top	10802.1	1659.4	
W+1	48673.8	10354.5	
W+cl	53859.1	9548.8	
W+hf	12275.1	2866.1	
Z+1	2899.8	419.6	
Z+cl	1033.0	130.9	
Z+hf	1560.4	195.1	
MJ _e	–	1301.9	
MJ _{μ}	6551.2	55.5	
Total	148377.2 ± 392.5	31739.2 ± 191.1	
Data	148390.0 ± 385.2	31777.0 ± 178.3	
$\frac{\text{Sim}-\text{Data}}{\sigma}$	-0.02	-0.14	
3-jet			
VH	15.9	11.0	
VV	890.8	341.8	
$t\bar{t}$	16167.0	7185.0	
s-top	5761.7	1394.2	
W+1	18606.7	4658.9	
W+cl	18072.1	3797.1	
W+hf	4699.6	1515.7	
Z+1	1280.1	188.1	
Z+cl	509.2	68.4	
Z+hf	743.5	95.3	
MJ _e	–	349.2	
MJ _{μ}	3231.2	25.3	
Total	69977.9 ± 272.1	19630.1 ± 132.1	
Data	69956.0 ± 264.5	19649.0 ± 140.2	
$\frac{\text{Sim}-\text{Data}}{\sigma}$	0.06	-0.1	

Table 115: Table of post unconditional fit yields for 1-lepton 2 and 3-jet 1-tag events in the dijet mass selection. The uncertainties are the full postfit errors including all nuisance parameters with priors, floating normalizations, and the correlations deduced from the data. The difference in the data and the postfit simulation is compared to σ which is obtained from the sum in simulation as the sum in quadrature of the postfit and Poissonian error.

Not reviewed, for internal circulation only

Sample	$p_T^V < 90 \text{ GeV}$	$90 < p_T^V < 120 \text{ GeV}$	$120 < p_T^V < 160 \text{ GeV}$	2-jet	2L-tag	$160 < p_T^V < 200 \text{ GeV}$	$p_T^V > 200 \text{ GeV}$
<hr/>							
VH	9.3	3.3	4.3	1.9	1.9	1.9	2.3
VV	68.6	22.0	22.1	8.6	8.6	10.1	10.1
$t\bar{t}$	1031.6	396.6	377.5	97.1	97.1	52.0	52.0
s-top	743.7	175.0	106.8	24.2	24.2	15.1	15.1
$W+1$	937.1	259.6	179.7	50.0	50.0	41.8	41.8
$W+c1$	1586.3	407.4	264.7	65.5	65.5	41.3	41.3
$W+hf$	943.0	276.8	198.0	57.6	57.6	48.9	48.9
Z+1	55.5	19.4	9.2	1.5	1.5	0.6	0.6
Z+c1	30.3	10.3	4.6	0.8	0.8	0.3	0.3
Z+hf	88.2	31.0	12.8	2.2	2.2	0.9	0.9
MJ_e	–	–	40.9	8.5	8.5	1.7	1.7
MJ_μ	389.0	46.9	5.1	–	–	–	–
Total	5882.5 ± 66.5	1648.2 ± 21.4	1225.6 ± 18.5	318.9 ± 5.8	318.9 ± 5.8	215.1 ± 6.8	215.1 ± 6.8
Data	5891.0 ± 76.8	1570.0 ± 39.6	1208.0 ± 34.8	323.0 ± 18.0	323.0 ± 18.0	198.0 ± 14.1	198.0 ± 14.1
$\frac{\text{Sim}-\text{Data}}{\sigma}$	-0.08	1.71	0.44	-0.22	-0.22	1.06	1.06
<hr/>							
<hr/>							
VH	2.7	1.0	1.5	0.8	0.8	1.1	1.1
VV	31.2	9.6	10.3	4.5	4.5	4.7	4.7
$t\bar{t}$	2035.4	567.5	510.3	151.2	151.2	96.7	96.7
s-top	419.5	100.8	76.2	24.8	24.8	20.5	20.5
$W+1$	353.4	88.4	70.3	22.4	22.4	22.1	22.1
$W+c1$	544.5	127.5	96.3	28.6	28.6	22.6	22.6
$W+hf$	351.8	97.5	87.1	32.0	32.0	34.8	34.8
Z+1	24.4	6.8	3.4	0.7	0.7	0.4	0.4
Z+c1	15.5	4.0	2.0	0.4	0.4	0.2	0.2
Z+hf	45.1	10.4	6.7	1.1	1.1	0.7	0.7
MJ_e	–	–	12.4	2.5	2.5	0.8	0.8
MJ_μ	135.7	10.6	1.2	–	–	–	–
Total	3959.3 ± 41.4	1024.0 ± 14.7	877.7 ± 14.1	269.1 ± 5.4	269.1 ± 5.4	204.6 ± 7.1	204.6 ± 7.1
Data	3882.0 ± 62.3	1004.0 ± 31.7	938.0 ± 30.6	273.0 ± 16.5	273.0 ± 16.5	207.0 ± 14.4	207.0 ± 14.4
$\frac{\text{Sim}-\text{Data}}{\sigma}$	1.03	0.57	-1.84	-0.23	-0.23	-0.15	-0.15

Table 116: Table of post unconditional fit yields for 1-lepton 2 and 3-jet 2L-tag events in the dijet mass selection. The uncertainties are the full postfit errors including all nuisance parameters with priors, floating normalizations, and the correlations deduced from the data. The difference in the data and the postfit simulation is compared to σ which is obtained from the sum in simulation as the sum in quadrature of the postfit and Poissonian error.

Not reviewed, for internal circulation only

Sample	2M-tag				$p_T^V > 200 \text{ GeV}$	
	$p_T^V < 90 \text{ GeV}$	$90 < p_T^V < 120 \text{ GeV}$	$120 < p_T^V < 160 \text{ GeV}$	$160 < p_T^V < 200 \text{ GeV}$	$p_T^V > 200 \text{ GeV}$	
2-jet						
VH	14.6	4.9	6.6	3.2	3.7	
VV	45.1	14.7	15.8	5.9	5.6	
$t\bar{t}$	1243.3	475.0	409.3	76.8	31.0	
s-top	666.6	152.6	92.4	18.7	10.6	
$W+1$	74.9	20.4	13.3	3.5	2.9	
$W+c1$	275.4	71.8	47.4	10.3	6.6	
$W+hf$	628.2	189.7	142.6	39.2	36.6	
Z+1	4.3	1.5	0.7	0.1	0.0	
Z+c1	6.3	2.1	0.9	0.1	0.0	
Z+hf	71.0	24.7	9.7	1.4	0.6	
MJ_e	–	–	24.5	4.5	1.2	
MJ_μ	213.6	16.2	1.2	–	–	
Total	$\bar{3}243.5 \pm 48.7$	$\bar{9}73.6 \pm 15.9$	$\bar{7}64.4 \pm 14.6$	$\bar{1}63.7 \pm 4.0$	$\bar{9}8.7 \pm 4.5$	
Data	3230.0 ± 56.8	984.0 ± 31.4	776.0 ± 27.9	180.0 ± 13.4	101.0 ± 10.0	
$\frac{\text{Sim}-\text{Data}}{\sigma}$	0.18	-0.3	-0.37	-1.22	-0.21	
3-jet						
VH	4.0	1.6	2.4	1.5	1.7	
VV	14.5	4.9	5.7	2.4	2.9	
$t\bar{t}$	2606.0	676.5	521.1	113.9	57.5	
s-top	405.1	90.6	61.8	18.2	14.8	
$W+1$	24.0	6.1	4.7	1.4	1.3	
$W+c1$	95.3	23.3	16.5	4.6	3.5	
$W+hf$	222.7	62.3	64.8	21.7	25.4	
Z+1	1.6	0.5	0.3	0.1	0.0	
Z+c1	2.6	0.7	0.3	0.1	0.0	
Z+hf	32.3	8.6	5.1	1.1	0.5	
MJ_e	–	–	6.1	2.2	0.4	
MJ_μ	69.2	12.8	–	0.6	–	
Total	$\bar{3}477.2 \pm 36.7$	$\bar{8}87.9 \pm 16.2$	$\bar{6}88.7 \pm 12.9$	$\bar{1}67.8 \pm 3.9$	$\bar{1}08.0 \pm 4.8$	
Data	3519.0 ± 59.3	936.0 ± 30.6	674.0 ± 26.0	160.0 ± 12.6	109.0 ± 10.4	
$\frac{\text{Sim}-\text{Data}}{\sigma}$	-0.6	-1.42	0.5	0.58	-0.08	

Table 1117: Table of post unconditional fit yields for 1-lepton 2 and 3-jet 2M-tag events in the dijet mass selection. The uncertainties are the full postfit errors including all nuisance parameters with priors, floating normalizations, and the correlations deduced from the data. The difference in the data and the postfit simulation is compared to σ which is obtained from the sum in simulation as the sum in quadrature of the postfit and Poissonian error.

Not reviewed, for internal circulation only

Sample	$p_T^V < 90 \text{ GeV}$	$90 < p_T^V < 120 \text{ GeV}$	$120 < p_T^V < 160 \text{ GeV}$	2T-tag		$p_T^V > 200 \text{ GeV}$
				2-jet	3-jet	
VH	16.2	5.4	7.5	3.9	3.9	3.9
VV	35.3	11.9	13.5	5.3	4.7	4.7
$t\bar{t}$	1184.0	434.4	334.6	39.4	8.5	8.5
s-top	536.8	117.1	67.6	12.0	4.3	4.3
$W+1$	2.0	0.4	0.3	0.1	0.1	0.1
$W+c1$	14.0	3.7	2.3	0.5	0.3	0.3
$W+hf$	343.5	105.4	88.9	25.7	24.1	24.1
Z+1	0.1	0.0	0.0	0.0	0.0	0.0
Z+c1	0.3	0.1	0.0	0.0	–	–
Z+hf	47.0	16.1	6.7	1.5	0.4	0.4
MJ_e	–	–	12.1	1.9	1.1	1.1
MJ_μ	147.9	13.5	–	–	–	–
Total	2327.2 ± 46.5	708.1 ± 14.3	533.5 ± 12.8	90.3 ± 2.9	47.5 ± 3.4	47.5 ± 3.4
Data	2364.0 ± 48.6	700.0 ± 26.5	535.0 ± 23.1	100.0 ± 10.0	54.0 ± 7.3	54.0 ± 7.3
$\frac{\text{Sim}-\text{Data}}{\sigma}$	-0.55	0.27	-0.06	-0.97	-0.85	-0.85
2-jet	3-jet					
VH	4.5	1.8	2.7	1.6	1.9	1.9
VV	9.2	3.4	5.2	2.5	2.3	2.3
$t\bar{t}$	2648.6	646.2	431.2	52.7	15.2	15.2
s-top	341.0	71.9	42.6	8.8	6.2	6.2
$W+1$	0.7	0.2	0.1	0.0	0.0	0.0
$W+c1$	4.6	1.1	0.9	0.2	0.1	0.1
$W+hf$	121.7	36.1	39.2	15.6	17.4	17.4
Z+1	0.0	0.0	0.0	0.0	0.0	0.0
Z+c1	0.1	0.0	0.0	0.0	0.0	0.0
Z+hf	23.9	6.6	3.7	0.8	0.4	0.4
MJ_e	–	–	2.4	0.8	0.3	0.3
MJ_μ	34.8	1.9	–	0.3	–	–
Total	3189.1 ± 41.0	769.1 ± 14.7	528.2 ± 12.3	83.4 ± 3.0	43.8 ± 3.3	43.8 ± 3.3
Data	3161.0 ± 56.2	779.0 ± 27.9	505.0 ± 22.5	88.0 ± 9.4	48.0 ± 6.9	48.0 ± 6.9
$\frac{\text{Sim}-\text{Data}}{\sigma}$	0.4	-0.31	0.89	-0.48	-0.57	-0.57

Table 118: Table of post unconditional fit yields for 1-lepton 2 and 3-jet 2T-tag events in the dijet mass selection. The uncertainties are the full postfit errors including all nuisance parameters with priors, floating normalizations, and the correlations deduced from the data. The difference in the data and the postfit simulation is compared to σ which is obtained from the sum in simulation as the sum in quadrature of the postfit and Poissonian error.

Not reviewed, for internal circulation only

Sample	1-tag		
	$p_T^V < 120 \text{ GeV}$	2-jet	$p_T^V > 120 \text{ GeV}$
VH	20.0		5.5
VV	612.0		89.3
$t\bar{t}$	583.8		27.0
s-top	53.4	3.8	
$W+l$	69.6	1.1	
$W+cl$	40.9	3.2	
$W+hf$	17.9	1.9	
$Z+l$	19491.9		1806.2
$Z+cl$	8855.1		759.8
$Z+hf$	14773.7		1313.3
MJ	113.9	0.9	
Total	44632.3 \pm 207.3		4012.0 \pm 55.9
Data	44551.0 \pm 211.1		4052.0 \pm 63.7
$\frac{\text{Sim}-\text{Data}}{\sigma}$	0.27	-0.47	
3-jet			
VH	6.9		2.6
VV	248.6		45.9
$t\bar{t}$	346.3		18.1
s-top	18.9		1.9
$W+l$	7.6		0.9
$W+cl$	12.7		1.5
$W+hf$	8.3		0.8
$Z+l$	5434.3		712.6
$Z+cl$	3526.6		402.8
$Z+hf$	3988.2		457.8
MJ	32.4		0.4
Total	13630.9 \pm 111.9		1645.4 \pm 30.7
Data	13595.0 \pm 116.6		1631.0 \pm 40.4
$\frac{\text{Sim}-\text{Data}}{\sigma}$	0.22	0.28	

Table 119: Table of post unconditional fit yields for 2-lepton 2 and 3-jet 1-tag events in the dijet mass selection. The uncertainties are the full postfit errors including all nuisance parameters with priors, floating normalizations, and the correlations deduced from the data. The difference in the data and the postfit simulation is compared to σ which is obtained from the sum in simulation as the sum in quadrature of the postfit and Poissonian error.

Not reviewed, for internal circulation only

Sample	$p_T^V < 90 \text{ GeV}$	$90 < p_T^V < 120 \text{ GeV}$	$120 < p_T^V < 160 \text{ GeV}$	$160 < p_T^V < 200 \text{ GeV}$	$p_T^V > 200 \text{ GeV}$
2L-tag					
VH	4.6	1.3	0.9	0.4	0.5
VV	49.0	8.4	5.0	1.9	1.9
$t\bar{t}$	142.3	22.0	5.4	0.3	0.1
s-top	4.8	0.9	0.5	0.0	0.1
$W+1$	0.6	0.1	0.0	0.0	0.0
$W+c1$	1.0	0.2	0.1	0.0	0.0
$W+h1$	2.1	0.4	0.1	0.0	0.0
Z+1	365.5	69.3	28.0	7.7	7.2
Z+c1	256.5	49.1	19.0	5.2	4.1
Z+h1	1105.2	232.0	88.4	21.6	16.4
MJ	8.6	0.4	0.4	0.1	—
Total	1940.1 ± 29.1	384.2 ± 7.0	147.6 ± 2.7	37.3 ± 0.8	30.3 ± 1.1
Data	2009.0 ± 44.8	378.0 ± 19.4	153.0 ± 12.4	33.0 ± 5.7	42.0 ± 6.5
$\frac{\text{Sim}-\text{Data}}{\sigma}$	-1.3	0.3	-0.43	0.7	-2.08
2-jet					
VH	1.2	0.4	0.3	0.2	0.2
VV	12.3	3.0	1.8	0.9	1.1
$t\bar{t}$	65.4	10.8	2.8	0.4	—
s-top	1.8	0.5	0.1	0.2	—
$W+1$	0.2	0.0	0.0	0.0	0.0
$W+c1$	0.5	0.0	0.0	0.0	0.0
$W+h1$	0.3	0.0	0.0	0.0	0.0
Z+1	99.0	20.1	9.4	3.1	3.3
Z+c1	104.4	20.1	8.9	2.9	2.8
Z+h1	291.0	63.4	28.0	7.8	7.6
MJ	1.1	0.1	0.0	—	—
Total	577.2 ± 11.0	118.5 ± 2.6	51.4 ± 1.4	15.4 ± 0.5	15.1 ± 0.6
Data	612.0 ± 24.7	128.0 ± 11.3	64.0 ± 8.0	12.0 ± 3.5	19.0 ± 4.4
$\frac{\text{Sim}-\text{Data}}{\sigma}$	-1.32	-0.84	-1.72	0.87	-0.98

Table 120: Table of post unconditional fit yields for 2-lepton 2 and 3-jet 2L-tag events in the dijet mass selection. The uncertainties are the full postfit errors including all nuisance parameters with priors, floating normalizations, and the correlations deduced from the data. The difference in the data and the postfit simulation is compared to σ which is obtained from the sum in quadrature of the postfit and Poissonian error.

Not reviewed, for internal circulation only

Sample	$p_T^V < 90 \text{ GeV}$	2M-tag				$p_T^V > 200 \text{ GeV}$
		$90 < p_T^V < 120 \text{ GeV}$	$120 < p_T^V < 160 \text{ GeV}$	$160 < p_T^V < 200 \text{ GeV}$	$p_T^V > 200 \text{ GeV}$	
2-jet						
VH	7.4	2.0	1.5	0.7	0.7	0.7
VV	48.2	8.0	4.8	1.9	1.9	1.9
$t\bar{t}$	215.5	36.7	8.3	0.3	0.0	0.0
s-top	5.7	1.5	0.4	0.0	–	–
$W+1$	0.0	0.0	0.0	0.0	0.0	0.0
$W+c1$	0.2	0.0	0.0	0.0	0.0	0.0
$W+hf$	0.6	0.1	0.0	–	0.0	0.0
Z+1	26.0	4.5	1.7	0.5	0.4	0.4
Z+c1	41.7	7.9	3.1	0.8	0.6	0.6
Z+hf	942.6	194.6	73.7	17.2	11.2	11.2
MJ	3.1	0.1	0.1	–	–	–
Total	1290.9 ± 22.9	255.5 ± 5.5	93.7 ± 2.2	21.4 ± 0.7	14.9 ± 0.7	14.9 ± 0.7
Data	1284.0 ± 35.8	264.0 ± 16.2	83.0 ± 9.1	23.0 ± 4.8	9.0 ± 3.0	9.0 ± 3.0
$\frac{\text{Sim}-\text{Data}}{\sigma}$	0.16	-0.5	1.08	-0.35	1.5	1.5
3-jet						
VH	1.8	0.6	0.5	0.3	0.4	0.4
VV	9.4	1.9	1.5	0.7	0.7	0.7
$t\bar{t}$	98.6	16.1	2.9	0.1	0.0	0.0
s-top	2.5	0.7	0.1	–	0.0	0.0
$W+1$	0.0	0.0	0.0	0.0	0.0	0.0
$W+c1$	0.1	0.0	0.0	0.0	0.0	0.0
$W+hf$	0.2	0.0	0.0	0.0	0.0	0.0
Z+1	6.9	1.3	0.6	0.2	0.2	0.2
Z+c1	15.7	3.2	1.4	0.4	0.4	0.4
Z+hf	250.7	52.5	26.6	7.3	5.6	5.6
MJ	0.5	0.1	–	–	–	–
Total	386.3 ± 11.4	76.5 ± 2.5	33.6 ± 1.5	8.9 ± 0.5	7.4 ± 0.4	7.4 ± 0.4
Data	401.0 ± 20.0	80.0 ± 8.9	34.0 ± 5.8	6.0 ± 2.4	7.0 ± 2.6	7.0 ± 2.6
$\frac{\text{Sim}-\text{Data}}{\sigma}$	-0.65	-0.38	-0.06	0.97	0.13	0.13

Table 121: Table of post unconditional fit yields for 2-lepton 2 and 3-jet 2M-tag events in the dijet mass selection. The uncertainties are the full postfit errors including all nuisance parameters with priors, floating normalizations, and the correlations deduced from the data. The difference in the data and the postfit simulation is compared to σ which is obtained from the sum in quadrature of the postfit and Poissonian error.

Not reviewed, for internal circulation only

Sample	$p_T^V < 90 \text{ GeV}$	$90 < p_T^V < 120 \text{ GeV}$	$120 < p_T^V < 160 \text{ GeV}$	2T-tag 2-jet		$p_T^V > 200 \text{ GeV}$
				$160 < p_T^V < 200 \text{ GeV}$	$p_T^V > 200 \text{ GeV}$	
VH	8.2	2.2	1.8	0.9	0.9	0.9
VV	43.7	7.2	4.9	2.2	2.0	2.0
$t\bar{t}$	232.4	38.0	8.6	0.4	–	–
s-top	4.7	1.3	0.2	0.1	0.1	0.1
$W+1$	0.0	–	–	–	–	–
$W+hf$	0.6	0.3	0.0	0.0	–	–
$Z+1$	0.4	0.1	0.0	0.0	0.0	0.0
$Z+c1$	1.2	0.2	0.1	0.0	0.0	0.0
$Z+hf$	693.5	154.5	59.1	13.0	8.4	8.4
MJ	1.9	0.0	0.0	–	–	–
Total	986.7 ± 22.2	203.8 ± 5.1	74.7 ± 2.1	16.7 ± 0.7	11.3 ± 0.6	11.3 ± 0.6
Data	980.0 ± 31.3	209.0 ± 14.5	65.0 ± 8.1	17.0 ± 4.1	12.0 ± 3.5	12.0 ± 3.5
$\frac{\text{Sim}-\text{Data}}{\sigma}$	0.17	-0.34	1.1	-0.08	-0.21	
3-jet						
VH	2.0	0.7	0.7	0.4	0.4	0.4
VV	7.9	1.9	1.4	0.8	0.8	0.7
$t\bar{t}$	108.6	18.1	3.3	0.0	0.1	0.1
s-top	1.9	0.3	0.2	0.0	–	–
$W+1$	0.0	–	–	–	–	–
$W+hf$	0.1	–	0.0	0.0	–	–
$Z+1$	0.1	0.0	0.0	0.0	0.0	0.0
$Z+c1$	0.2	0.1	0.1	0.0	0.0	0.0
$Z+hf$	186.8	40.7	20.5	5.4	4.2	4.2
MJ	0.3	0.1	–	–	–	–
Total	308.0 ± 12.0	62.0 ± 2.4	26.2 ± 1.2	6.6 ± 0.4	5.4 ± 0.4	5.4 ± 0.4
Data	307.0 ± 17.5	55.0 ± 7.4	29.0 ± 5.4	9.0 ± 3.0	3.0 ± 1.7	3.0 ± 1.7
$\frac{\text{Sim}-\text{Data}}{\sigma}$	0.05	0.85	-0.53	-0.91	1.02	

Table 122: Table of post unconditional fit yields for 2-lepton 2 and 3-jet 2T-tag events in the dijet mass selection. The uncertainties are the full postfit errors including all nuisance parameters with priors, floating normalizations, and the correlations deduced from the data. The difference in the data and the postfit simulation is compared to σ which is obtained from the sum in quadrature of the postfit and Poissonian error.

5076 **A.J.3 Dijet Mass Analysis: Postfit over Prefit**

[Not reviewed, for internal circulation only]

Not reviewed, for internal circulation only

Sample	$100 < p_T^V < 120 \text{ GeV}$	1-tag 2-jet	$p_T^V > 120 \text{ GeV}$
VH	1.22	1.2	
VV	1.0	1.0	
$t\bar{t}$	1.4	1.41	
s-top	1.29	1.1	
W+l	1.05	0.99	
W+cl	1.12	1.1	
W+hf	0.85	0.72	
Z+l	0.99	0.95	
Z+cl	0.85	0.85	
Z+hf	1.1	1.08	
MJ	1.26	0.55	
Total	1.04	0.98	
3-jet			
VH	–	1.2	
VV	–	1.0	
$t\bar{t}$	–	1.27	
s-top	–	1.0	
W+l	–	0.98	
W+cl	–	1.02	
W+hf	–	0.79	
Z+l	–	0.89	
Z+cl	–	1.02	
Z+hf	–	0.9	
MJ	–	1.06	
Total	–	0.99	

Table 123: Table of post unconditional fit over prefit yields for 0-lepton 2 and 3-jet 1-tag events in the dijet mass selection.

Not reviewed, for internal circulation only

Sample	2L-tag 2-jet			$p_T^V > 200 \text{ GeV}$	
	$100 < p_T^V < 120 \text{ GeV}$	$120 < p_T^V < 160 \text{ GeV}$	$160 < p_T^V < 200 \text{ GeV}$	$160 < p_T^V < 200 \text{ GeV}$	$p_T^V > 200 \text{ GeV}$
VH	1.26	1.26	1.26	1.26	1.25
VV	1.04	1.05	1.08	1.08	1.06
$t\bar{t}$	1.44	1.45	1.38	1.38	1.39
s-top	1.25	1.09	1.05	1.05	0.99
W+1	1.02	1.01	1.01	1.01	1.02
W+cl	1.13	1.13	1.11	1.11	1.07
W+hf	0.88	0.83	0.8	0.8	0.73
Z+1	1.0	0.99	0.97	0.97	0.95
Z+cl	0.89	0.88	0.86	0.86	0.84
Z+hf	1.17	1.14	1.16	1.16	1.07
MJ	0.97	1.27	1.27	1.27	1.27
Total	1.09	1.08	1.06	1.06	1.0
3-jet					
VH	–	1.24	1.24	1.24	1.26
VV	–	0.98	1.01	1.01	0.96
$t\bar{t}$	–	1.33	1.27	1.27	1.24
s-top	–	1.02	1.01	1.01	0.98
W+1	–	1.0	1.01	1.01	1.0
W+cl	–	1.05	1.03	1.03	1.02
W+hf	–	0.84	0.87	0.87	0.88
Z+1	–	0.91	0.92	0.92	0.89
Z+cl	–	1.04	1.05	1.05	1.0
Z+hf	–	1.04	1.01	1.01	0.96
MJ	–	0.56	0.56	0.56	0.56
Total	–	1.09	1.05	1.05	1.0

Table 124: Table of post unconditional fit over prefit yields for 0-lepton 2 and 3-jet 2L-tag events in the dijet mass selection.

Not reviewed, for internal circulation only

Sample	2M-tag				
	100 < p_T^V < 120 GeV	120 < p_T^V < 160 GeV	2-jet	160 < p_T^V < 200 GeV	p_T^V > 200 GeV
VH	1.25	1.25	1.25	1.25	1.26
VV	1.05	1.07	1.07	1.07	1.12
$t\bar{t}$	1.4	1.48	1.46	1.46	1.43
s-top	1.2	1.13	1.17	1.17	1.04
W+1	1.11	1.06	1.1	1.1	1.03
W+cl	1.15	1.16	1.17	1.17	1.19
W+hf	0.92	0.85	0.86	0.86	0.8
Z+1	1.08	1.06	1.04	1.04	1.0
Z+cl	0.91	0.91	0.88	0.88	0.91
Z+hf	1.15	1.14	1.12	1.12	1.12
MJ	0.97	1.27	1.27	1.27	1.27
Total	1.17	1.17	1.13	1.13	1.08
3-jet					
VH	–	1.25	1.25	1.25	1.24
VV	–	0.97	1.0	1.0	0.98
$t\bar{t}$	–	1.32	1.31	1.31	1.35
s-top	–	1.02	1.07	1.07	1.03
W+1	–	1.11	1.11	1.11	1.09
W+cl	–	0.99	1.03	1.03	1.08
W+hf	–	0.85	0.92	0.92	0.91
Z+1	–	1.11	0.97	0.97	0.96
Z+cl	–	1.04	1.09	1.09	1.07
Z+hf	–	1.04	1.09	1.09	1.05
MJ	–	0.56	0.56	0.56	0.56
Total	–	1.15	1.14	1.14	1.08

Table 125: Table of post unconditional fit over prefit yields for 0-lepton 2 and 3-jet 2M-tag events in the dijet mass selection.

Not reviewed, for internal circulation only

Sample	2T-tag 2-jet				$p_T^V > 200 \text{ GeV}$	
	$100 < p_T^V < 120 \text{ GeV}$	$120 < p_T^V < 160 \text{ GeV}$	$160 < p_T^V < 200 \text{ GeV}$	$p_T^V > 200 \text{ GeV}$		
VH	1.23	1.24	1.23	1.24		
VV	1.03	1.06	1.07	1.07		
$t\bar{t}$	1.39	1.43	1.47	1.34		
s-top	1.21	1.13	1.05	1.12		
W+1	1.0	1.0	1.0	1.0		
W+cl	1.17	1.09	1.12	1.09		
W+hf	0.86	0.9	0.86	0.82		
Z+1	1.0	1.0	1.0	1.0		
Z+cl	0.87	0.87	0.87	0.87		
Z+hf	1.13	1.12	1.12	1.07		
MJ	0.97	1.27	1.27	1.27		
Total	1.18	1.16	1.12	1.05		
3-jet						
VH	–	1.23	1.25	1.23		
VV	–	0.99	0.91	0.96		
$t\bar{t}$	–	1.37	1.31	1.24		
s-top	–	1.05	1.1	0.95		
W+1	–	1.0	1.0	1.0		
W+cl	–	1.09	1.09	1.09		
W+hf	–	0.94	0.97	0.99		
Z+1	–	1.0	1.0	1.0		
Z+cl	–	0.87	0.7	0.87		
Z+hf	–	1.06	1.07	1.05		
MJ	–	0.56	0.56	0.56		
Total	–	1.2	1.12	1.05		

Table 126: Table of post unconditional fit over prefit yields for 0-lepton 2 and 3-jet 2T-tag events in the jet mass selection.

Not reviewed, for internal circulation only

Sample	$p_T^V < 120 \text{ GeV}$		$p_T^V > 120 \text{ GeV}$
	1-tag	2-jet	
VH	1.21		1.2
VV	1.0		1.03
$t\bar{t}$	1.15		1.15
s-top	1.28		1.08
$W+1$	1.01		0.99
$W+cl$	1.08		1.08
$W+hf$	0.75		0.73
$Z+1$	0.99		0.92
$Z+cl$	0.87		0.87
$Z+hf$	1.08		1.08
MJ_e	–		1.52
MJ_μ	0.99		1.0
Total	1.03		1.02
3 jet			
VH	1.23		1.22
VV	1.0		0.96
$t\bar{t}$	1.03		1.04
s-top	1.04		0.97
$W+1$	0.97		1.0
$W+cl$	0.98		1.01
$W+hf$	0.65		0.79
$Z+1$	0.97		1.0
$Z+cl$	0.87		0.87
$Z+hf$	1.08		1.08
MJ_e	–		0.91
MJ_μ	1.0		1.0
Total	0.96		0.99

Table 127: Table of post unconditional fit over prefit yields for 1-lepton 2 and 3-jet 1-tag events in the dijet mass selection.

Not reviewed, for internal circulation only

Sample	2L-tag			2L-tag		
	$p_T^V < 90 \text{ GeV}$	$90 < p_T^V < 120 \text{ GeV}$	$120 < p_T^V < 160 \text{ GeV}$	$160 < p_T^V < 200 \text{ GeV}$	$200 < p_T^V < 240 \text{ GeV}$	$p_T^V > 240 \text{ GeV}$
2-jet						
VH	1.26	1.27	1.27	1.25	1.28	
VV	1.0	1.0	1.0	1.04	1.12	
$t\bar{t}$	1.18	1.19	1.16	1.16	1.14	
s-top	1.3	1.26	1.12	1.06	1.05	
$W+l$	1.03	1.02	1.02	1.02	1.01	
$W+c\ell$	1.13	1.12	1.12	1.1	1.09	
$W+hf$	0.88	0.87	0.81	0.81	0.72	
$Z+l$	1.0	0.95	1.0	1.0	1.0	
$Z+c\ell$	0.87	0.87	0.87	0.87	0.87	
$Z+hf$	1.08	1.08	1.08	1.08	1.08	
MJ_e	–	–	0.9	0.84	0.85	
MJ_μ	0.85	0.87	1.0	1.0	–	
Total	1.06	1.06	1.04	1.02	–	0.97
3-jet						
VH	1.26	1.29	1.27	1.34	1.22	
VV	1.0	1.0	1.0	1.0	0.95	
$t\bar{t}$	1.05	1.06	1.07	1.07	1.04	
s-top	1.08	1.07	1.0	1.01	0.98	
$W+l$	0.99	1.0	1.03	1.02	1.01	
$W+c\ell$	1.02	1.01	1.05	1.04	1.01	
$W+hf$	0.73	0.86	0.87	0.91	0.88	
$Z+l$	1.0	1.0	1.0	1.0	1.0	
$Z+c\ell$	0.87	0.87	0.87	0.87	0.87	
$Z+hf$	1.08	1.08	1.08	1.08	1.08	
MJ_e	–	–	1.04	1.0	1.0	
MJ_μ	0.98	0.98	1.0	–	–	
Total	1.0	1.02	1.03	1.03	1.0	

Table 128: Table of post unconditional fit over prefit yields for 1-lepton 2 and 3-jet 2L-tag events in the dijet mass selection.

Not reviewed, for internal circulation only

Sample	$p_T^V < 90 \text{ GeV}$	$90 < p_T^V < 120 \text{ GeV}$	$120 < p_T^V < 160 \text{ GeV}$	2M-tag	
				2-jet	$160 < p_T^V < 200 \text{ GeV}$
2-jet					
VH	1.26	1.26	1.25	1.26	1.27
VV	1.02	1.05	1.07	1.02	1.13
$t\bar{t}$	1.16	1.18	1.18	1.2	1.22
s-top	1.28	1.24	1.16	1.12	1.12
$W+1$	1.13	1.09	1.1	1.1	1.09
$W+c1$	1.13	1.13	1.17	1.08	1.18
$W+hf$	0.89	0.89	0.85	0.83	0.82
$Z+1$	1.0	1.0	1.0	1.0	1.0
$Z+c1$	0.87	0.87	0.87	0.87	0.87
$Z+hf$	1.12	1.15	1.11	1.05	1.08
MJ_e	–	–	0.91	0.91	0.97
MJ_μ	0.88	0.85	0.88	–	–
Total	1.09	1.1	1.08	1.05	1.01
3-jet					
VH	1.25	1.26	1.24	1.24	1.26
VV	1.0	1.0	1.0	0.92	1.04
$t\bar{t}$	1.05	1.05	1.07	1.09	1.12
s-top	1.09	1.09	1.0	1.07	1.05
$W+1$	1.0	1.0	1.0	1.0	1.05
$W+c1$	1.07	1.11	1.06	1.1	1.13
$W+hf$	0.77	0.85	0.94	0.9	0.97
$Z+1$	1.0	1.0	1.0	1.0	1.0
$Z+c1$	0.87	0.87	0.87	0.87	0.87
$Z+hf$	1.08	1.08	1.08	1.08	1.08
MJ_e	–	–	1.05	1.08	1.09
MJ_μ	0.98	1.94	–	1.0	–
Total	1.03	1.05	1.05	1.05	1.07

Table 129: Table of post unconditional fit over prefit yields for 1-lepton 2 and 3-jet 2M-tag events in the dijet mass selection.

Not reviewed, for internal circulation only

Sample	2T-tag			2T-tag		
	$p_T^V < 90 \text{ GeV}$	$90 < p_T^V < 120 \text{ GeV}$	$120 < p_T^V < 160 \text{ GeV}$	$160 < p_T^V < 200 \text{ GeV}$	$200 < p_T^V < 240 \text{ GeV}$	$p_T^V > 240 \text{ GeV}$
VH	1.24	1.23	1.24	1.24	1.24	1.23
VV	1.02	1.03	1.07	1.06	1.12	1.12
$t\bar{t}$	1.16	1.18	1.17	1.14	1.18	1.18
s-top	1.27	1.24	1.14	1.14	1.1	1.1
$W+1$	1.0	1.0	1.0	1.0	1.0	1.0
$W+c1$	1.11	1.16	1.17	1.02	0.95	0.95
$W+hf$	0.92	0.89	0.85	0.84	0.82	0.82
$Z+1$	1.0	1.0	1.0	1.0	1.0	1.0
$Z+c1$	0.87	0.87	0.89	0.87	–	–
$Z+hf$	1.1	1.07	1.17	1.12	1.0	1.0
MJ_e	–	–	1.05	0.79	0.95	0.95
MJ_μ	1.49	1.44	–	–	–	–
Total	1.15	1.13	1.1	1.03	–	0.95
3 jet						
VH	1.24	1.26	1.25	1.22	1.23	1.23
VV	1.0	1.0	1.0	0.95	0.95	0.95
$t\bar{t}$	1.04	1.06	1.09	1.06	1.04	1.04
s-top	1.1	1.11	0.97	1.01	0.98	0.98
$W+1$	1.0	1.0	1.0	1.0	1.0	1.0
$W+c1$	1.09	1.09	1.09	1.09	1.09	1.09
$W+hf$	0.8	0.87	0.94	0.96	0.99	0.99
$Z+1$	1.0	1.0	1.0	1.0	1.0	1.0
$Z+c1$	0.87	0.87	0.87	0.87	0.87	0.87
$Z+hf$	1.08	1.08	1.08	1.08	1.32	1.32
MJ_e	–	–	1.04	1.1	1.07	1.07
MJ_μ	0.98	1.01	–	0.98	–	–
Total	1.03	1.06	1.06	1.04	1.01	1.01

Table 130: Table of post unconditional fit over prefit yields for 1-lepton 2 and 3-jet 2T-tag events in the dijet mass selection.

Not reviewed, for internal circulation only

Sample	$p_T^V < 120 \text{ GeV}$	1-tag 2-jet	$p_T^V > 120 \text{ GeV}$
VH	1.22		1.21
VV	1.0		1.07
$t\bar{t}$	1.18		1.15
s-top	1.0		1.0
W+1	1.0		1.0
W+cl	1.09		1.09
W+hf	0.88		0.88
Z+1	1.02		1.01
Z+cl	0.9		0.89
Z+hf	1.11		1.12
MJ	0.19		0.19
Total	-	1.01	1.02
3 jet			
VH	1.22		1.22
VV	0.99		0.97
$t\bar{t}$	1.24		1.22
s-top	1.0		1.0
W+1	1.0		1.0
W+cl	1.09		1.09
W+hf	0.88		0.88
Z+1	0.97		0.93
Z+cl	1.12		1.06
Z+hf	0.97		0.93
MJ	0.19		0.19
Total	-	1.0	0.96

Table 131: Table of post unconditional fit over prefit yields for 2-lepton 2 and 3-jet 1-tag events in the dijet mass selection.

Not reviewed, for internal circulation only

Sample	2L-tag 2-jet						$p_T^V > 200 \text{ GeV}$
	$p_T^V < 90 \text{ GeV}$	$90 < p_T^V < 120 \text{ GeV}$	$120 < p_T^V < 160 \text{ GeV}$	$160 < p_T^V < 200 \text{ GeV}$	$p_T^V > 200 \text{ GeV}$		
VH	1.28	1.28	1.26	1.26	1.26	1.26	1.26
VV	1.06	1.07	1.06	1.06	1.09	1.08	1.08
$t\bar{t}$	1.21	1.18	1.24	1.24	1.2	1.15	1.15
s-top	1.0	1.0	1.0	1.0	1.0	1.0	1.06
W+1	1.0	1.0	1.0	1.0	1.0	1.0	1.0
W+c1	1.09	1.09	1.09	1.09	1.09	1.09	1.09
W+hf	0.88	0.88	0.88	0.88	0.83	0.88	0.88
Z+1	1.04	1.03	1.03	1.03	1.01	1.01	1.03
Z+c1	0.91	0.91	0.91	0.91	0.9	0.91	0.91
Z+hf	1.19	1.18	1.18	1.18	1.16	1.16	1.12
MJ	0.19	0.19	0.19	0.19	1.0	1.0	—
Total	1.09	1.1	1.1	1.1	1.08	1.08	1.06
3-jet							
VH	1.28	1.27	1.27	1.25	1.25	1.25	1.25
VV	0.99	1.02	1.02	1.06	1.06	0.99	0.99
$t\bar{t}$	1.26	1.32	1.3	1.21	1.21	—	—
s-top	1.0	1.0	1.0	1.04	1.04	—	—
W+1	1.0	1.0	1.0	1.0	1.0	1.0	1.0
W+c1	1.09	1.09	1.09	1.09	1.09	1.09	1.09
W+hf	0.88	0.88	0.88	0.88	0.88	0.88	0.88
Z+1	0.99	0.96	0.95	0.95	0.95	0.96	0.96
Z+c1	1.16	1.09	1.08	1.07	1.07	1.06	1.06
Z+hf	1.13	1.08	1.04	1.02	1.02	1.02	1.02
MJ	0.19	1.0	0.19	—	—	—	—
Total	1.11	1.08	1.04	1.02	1.02	1.01	1.01

Table 132: Table of post unconditional fit over prefit yields for 2-lepton 2 and 3-jet 2L-tag events in the dijet mass selection.

Not reviewed, for internal circulation only

Sample	2M-tag						$p_T^V > 200 \text{ GeV}$
	$p_T^V < 90 \text{ GeV}$	$90 < p_T^V < 120 \text{ GeV}$	$120 < p_T^V < 160 \text{ GeV}$	$160 < p_T^V < 200 \text{ GeV}$	2-jet		
VH	1.28	1.27	1.26	1.24			1.26
VV	1.04	1.05	1.07	1.07			1.12
$t\bar{t}$	1.2	1.18	1.23	1.14			1.15
s-top	1.0	0.97	0.97	1.0			–
$W+1$	1.0	1.0	1.0	1.0			1.0
$W+c\ell$	1.09	1.09	1.09	1.09			1.09
$W+h\ell$	0.88	0.88	0.85	–			0.88
$Z+1$	1.12	1.11	1.09	1.08			1.07
$Z+c\ell$	0.9	0.92	0.94	0.93			0.97
$Z+h\ell$	1.17	1.15	1.14	1.14			1.14
MJ	0.19	0.19	1.0	–			–
Total	1.14	1.14	1.14	1.13			1.14
3-jet							
VH	1.27	1.28	1.25	1.26			1.29
VV	0.97	1.03	0.98	0.97			1.02
$t\bar{t}$	1.27	1.3	1.18	1.22			1.39
s-top	1.0	1.03	1.0	–			1.01
$W+1$	1.0	1.0	1.0	1.0			1.0
$W+c\ell$	1.09	1.09	1.09	1.09			1.09
$W+h\ell$	0.88	0.88	0.88	0.87			0.88
$Z+1$	1.07	1.03	1.03	1.02			1.03
$Z+c\ell$	1.19	1.09	1.12	1.11			1.16
$Z+h\ell$	1.16	1.12	1.09	1.1			1.06
MJ	0.19	1.0	–	–			–
Total	1.17	1.15	1.09	1.09			1.07

Table 133: Table of post unconditional fit over prefit yields for 2-lepton 2 and 3-jet 2M-tag events in the dijet mass selection.

Not reviewed, for internal circulation only

Sample	$p_T^V < 90 \text{ GeV}$	$90 < p_T^V < 120 \text{ GeV}$	$120 < p_T^V < 160 \text{ GeV}$	2T-tag		$160 < p_T^V < 200 \text{ GeV}$	$p_T^V > 200 \text{ GeV}$
				2-jet	2-jet		
2-jet							
VH	1.25	1.24	1.24	1.24	1.22	1.22	1.24
VV	1.04	1.03	1.05	1.05	1.06	1.06	1.09
$t\bar{t}$	1.18	1.18	1.22	1.24	—	—	—
s-top	1.0	0.98	1.13	1.28	1.07	1.07	—
$W+1$	1.0	—	—	—	—	—	—
$W+hf$	0.88	0.89	0.88	0.88	0.88	0.88	—
$Z+1$	1.0	1.0	1.0	1.0	1.0	1.0	1.0
$Z+c1$	0.87	0.87	0.91	0.91	0.87	0.87	0.87
$Z+hf$	1.14	1.13	1.12	1.12	1.11	1.11	1.11
MJ	0.19	0.19	0.19	0.19	—	—	—
Total	1.14	1.14	1.14	1.13	1.11	1.11	1.11
3-jet							
VH	1.26	1.26	1.25	1.25	1.23	1.23	1.24
VV	1.0	0.99	1.0	1.0	0.96	0.96	0.98
$t\bar{t}$	1.27	1.26	1.26	1.26	1.15	1.15	1.25
s-top	1.0	1.0	0.95	0.95	1.0	1.0	—
$W+1$	1.0	—	—	—	—	—	—
$W+hf$	0.88	—	0.88	0.88	0.88	0.88	—
$Z+1$	1.0	1.0	1.0	1.0	1.0	1.0	1.0
$Z+c1$	0.87	0.87	0.87	0.87	0.87	0.87	0.87
$Z+hf$	1.15	1.11	1.08	1.08	1.07	1.07	1.06
MJ	0.19	1.0	—	—	—	—	—
Total	1.18	1.14	1.14	1.1	1.06	1.06	1.06

Table 134: Table of post unconditional fit over prefit yields for 2-lepton 2 and 3-jet 2T-tag events in the dijet mass selection.

5077 **A.J.4 MVA Analysis: Prefit**

[Not reviewed, for internal circulation only]

Not reviewed, for internal circulation only

Sample	1-tag		2L-tag		2M-tag		2M+2T-tag		2T-tag	
	$100 < p_T^V < 120 \text{ GeV}$	$p_T^V > 120 \text{ GeV}$	$100 < p_T^V < 120 \text{ GeV}$	$p_T^V > 120 \text{ GeV}$	$100 < p_T^V < 120 \text{ GeV}$	$p_T^V > 120 \text{ GeV}$	$p_T^V > 120 \text{ GeV}$	$p_T^V > 120 \text{ GeV}$	$100 < p_T^V < 120 \text{ GeV}$	$100 < p_T^V < 120 \text{ GeV}$
VH	7.9	22.8	2.2	6.9	3.5	23.4	4.0	—	—	—
VV	233.5	631.8	16.8	47.8	13.9	78.2	12.4	—	—	—
$t\bar{t}$	596.6	1163.6	78.2	133.2	90.1	236.1	81.4	—	—	—
s-top	443.2	666.6	34.4	51.5	27.2	58.9	18.8	—	—	—
W+l	5290.0	7371.0	159.0	210.5	13.2	14.7	0.2	—	—	—
W+cl	1975.9	3408.2	93.9	144.2	20.9	24.3	0.9	—	—	—
W+hf	883.2	1967.2	64.4	159.4	39.1	162.1	26.2	—	—	—
Z+l	3709.6	10805.1	89.1	266.4	5.2	14.8	0.1	—	—	—
Z+cl	1741.4	4571.6	63.8	180.9	9.9	26.1	0.3	—	—	—
Z+hf	2236.6	5909.2	187.7	525.5	155.9	752.4	129.2	—	—	—
Total	17528.5 ± 1477.1	36860.0 ± 3070.9	808.4 ± 77.6	1742.6 ± 179.7	387.9 ± 25.7	1405.1 ± 113.7	279.9 ± 18.4	—	—	—
Data	18343.0 ± 135.4	36903.0 ± 192.1	887.0 ± 29.8	1860.0 ± 43.1	477.0 ± 21.8	1592.0 ± 39.9	306.0 ± 17.5	—	—	—
DRAFT										
3-jet										
VH	—	8.1	—	2.0	—	6.6	—	—	—	—
VV	—	261.1	—	15.8	—	19.1	—	—	—	—
$t\bar{t}$	—	1497.2	—	157.2	—	263.9	—	—	—	—
s-top	—	329.4	—	25.1	—	30.2	—	—	—	—
W+l	—	2536.7	—	63.8	—	4.2	—	—	—	—
W+cl	—	1206.5	—	50.6	—	8.4	—	—	—	—
W+hf	—	757.6	—	56.4	—	55.2	—	—	—	—
Z+l	—	3347.7	—	80.8	—	4.3	—	—	—	—
Z+cl	—	1571.8	—	62.1	—	9.1	—	—	—	—
Z+hf	—	1913.7	—	156.1	—	220.0	—	—	—	—
Total	—	13496.9 ± 1443.4	—	673.4 ± 83.2	—	624.4 ± 90.2	—	—	—	—
Data	—	13344.0 ± 115.5	—	657.0 ± 25.6	—	710.0 ± 26.6	—	—	—	—

Table 135: Table of prefit yields for 0-lepton 2 and 3-jet events in the MVA selection. The uncertainties are from the full prefit nuisance parameters (NPs) except the floating normalizations under the assumption that each NP is independent (uncorrelated).

[Not reviewed, for internal circulation only]

August 6, 2014 – 13:00

Sample	1-tag		2L-tag		2M-tag		2T-tag	
	$p_T^V < 120 \text{ GeV}$	$p_T^V > 120 \text{ GeV}$	$p_T^V < 120 \text{ GeV}$	$p_T^V > 120 \text{ GeV}$	$p_T^V > 120 \text{ GeV}$	$p_T^V < 120 \text{ GeV}$	$p_T^V > 120 \text{ GeV}$	$p_T^V > 120 \text{ GeV}$
DRAFT								
VH	39.0	28.1	10.8	9.3	16.8	14.3	18.8	16.4
VV	1936.2	928.9	103.1	61.5	64.0	35.2	50.0	28.3
$t\bar{t}$	10082.5	5917.1	1640.0	885.1	2054.7	902.5	1951.4	736.3
s-top	11353.0	3486.1	925.3	350.9	790.4	265.7	605.9	187.5
W+1	65430.3	23658.0	1565.9	682.0	111.6	43.7	3.1	0.9
W+cl	65725.4	19678.5	2347.4	862.9	400.6	134.7	19.7	6.1
W+hf	21723.1	7979.0	1784.8	828.2	1132.7	508.4	583.7	293.1
Z+1	3821.8	1221.2	98.0	37.2	7.3	2.8	0.1	0.0
Z+cl	1533.5	380.0	60.1	19.9	11.5	3.5	0.6	0.2
Z+hf	1910.2	436.9	147.7	40.9	110.1	28.0	76.0	19.7
MJ _e	–	2323.8	–	148.9	–	74.9	–	34.8
MJ _{μ}	10855.8	164.1	851.4	16.0	435.5	4.8	181.4	1.3
Total	194410.9 ± 15096.9	66201.7 ± 5762.1	9534.4 ± 858.7	3942.8 ± 397.9	5135.2 ± 415.6	2018.5 ± 183.1	3490.5 ± 301.2	1324.6 ± 130.5
Data	198544.0 ± 445.6	67603.0 ± 260.0	9941.0 ± 99.7	4072.0 ± 63.8	5499.0 ± 74.2	2199.0 ± 46.9	3923.0 ± 62.6	1405.0 ± 37.5
3-jet								
VH	15.2	14.0	3.2	3.8	4.8	5.8	5.4	6.5
VV	1089.8	676.5	49.6	39.4	22.5	17.9	14.0	13.8
$t\bar{t}$	19008.4	10937.5	3092.4	1569.1	3946.9	1601.0	3979.1	1323.9
s-top	7089.9	2967.9	607.4	320.4	550.6	249.4	443.2	178.4
W+1	27260.9	11958.2	635.1	334.4	41.9	19.9	1.1	0.4
W+cl	25303.4	9640.6	909.8	430.2	148.9	63.5	6.8	2.8
W+hf	10053.0	4613.7	795.5	445.4	461.4	263.4	229.2	143.9
Z+1	1811.2	594.8	43.1	18.0	2.8	1.4	0.0	0.0
Z+cl	787.1	219.7	30.9	11.2	5.1	1.8	0.2	0.1
Z+hf	942.1	250.3	70.8	23.8	49.3	17.3	37.1	12.8
MJ _e	–	1285.8	–	58.7	–	30.0	–	12.5
MJ _{μ}	5096.6	91.1	255.8	4.9	128.2	3.2	63.4	0.8
Total	98457.5 ± 8520.4	43250.1 ± 4406.9	6493.5 ± 774.5	3259.0 ± 436.1	5362.5 ± 885.8	2274.6 ± 386.4	4779.5 ± 900.8	1696.0 ± 324.9
Data	93359.0 ± 305.5	42557.0 ± 206.3	6336.0 ± 79.6	3472.0 ± 58.9	5551.0 ± 74.5	2356.0 ± 48.5	4977.0 ± 70.5	1838.0 ± 42.9

Table 136: Table of prefit yields for 1-lepton 2 and 3-jet events in the MVA selection. The uncertainties are from the full prefit nuisance parameters (NPs) except the floating normalizations under the assumption that each NP is independent (uncorrelated).

Not reviewed, for internal circulation only

Sample	1-tag		2L-tag		2M+2T-tag	
	$p_T^V < 120 \text{ GeV}$	$p_T^V > 120 \text{ GeV}$	$p_T^V < 120 \text{ GeV}$	$p_T^V > 120 \text{ GeV}$	$p_T^V < 120 \text{ GeV}$	$p_T^V > 120 \text{ GeV}$
VH	20.4	7.4	5.5	2.0	18.6	7.0
VV	793.0	134.5	67.7	11.8	122.5	21.2
$t\bar{t}$	3570.7	221.9	947.4	47.2	3026.1	135.5
s-top	383.3	43.9	40.0	5.3	89.5	11.2
W+1	244.1	11.4	3.7	0.4	0.3	0.0
W+cl	146.7	15.5	5.1	0.5	0.9	0.1
W+hf	107.9	15.7	9.0	0.8	5.9	0.7
Z+1	28159.8	4107.0	612.2	97.4	39.5	5.5
Z+cl	13802.3	1832.7	472.8	70.2	78.0	10.5
Z+hf	19252.5	2590.5	1658.4	247.8	2519.2	360.9
Total	68583.4 ± 5529.1	9020.6 ± 624.0	3997.4 ± 326.7	486.2 ± 42.7	6008.0 ± 276.2	554.2 ± 36.5
Data	69313.0 ± 263.3	9150.0 ± 95.7	4313.0 ± 65.7	517.0 ± 22.7	6501.0 ± 80.6	570.0 ± 23.9
2-jet						
VH	7.4	3.9	1.5	0.9	4.9	2.8
VV	345.4	97.5	21.3	6.5	26.2	8.1
$t\bar{t}$	2025.4	172.7	412.2	25.2	1273.2	65.0
s-top	143.5	21.5	16.4	2.9	38.2	6.3
W+1	75.6	7.1	1.3	0.2	0.1	0.0
W+cl	50.3	7.9	2.0	0.3	0.4	0.0
W+hf	47.6	7.7	3.7	0.9	0.9	0.5
Z+1	8854.2	1963.5	187.3	45.5	11.5	2.5
Z+cl	4709.3	929.9	162.9	36.0	24.1	5.3
Z+hf	6126.9	1252.9	466.6	110.3	672.6	153.6
Total	23159.7 ± 2754.3	4488.1 ± 470.4	1300.6 ± 167.8	229.3 ± 31.7	2069.0 ± 305.1	244.7 ± 36.4
Data	22662.0 ± 150.5	4436.0 ± 66.6	1428.0 ± 37.8	253.0 ± 15.9	2394.0 ± 48.9	283.0 ± 16.8
3-jet						

Table 137: Table of prefit yields for 2-lepton 2 and 3-jet events in the MVA selection. The uncertainties are from the full prefit nuisance parameters (NPs) except the floating normalizations under the assumption that each NP is independent (uncorrelated).

5078 **A.J.5 MVA Analysis: Postfit**

[Not reviewed, for internal circulation only]

Sample	1-tag			2L-tag			2M-tag			2M+2T-tag			2T-tag		
	$100 < p_T^V < 120 \text{ GeV}$	$p_T^V > 120 \text{ GeV}$	$100 < p_T^V < 120 \text{ GeV}$	$p_T^V > 120 \text{ GeV}$	$100 < p_T^V < 120 \text{ GeV}$	$p_T^V > 120 \text{ GeV}$	$100 < p_T^V < 120 \text{ GeV}$	$p_T^V > 120 \text{ GeV}$	$100 < p_T^V < 120 \text{ GeV}$	$p_T^V > 120 \text{ GeV}$	$100 < p_T^V < 120 \text{ GeV}$	$p_T^V > 120 \text{ GeV}$	$100 < p_T^V < 120 \text{ GeV}$	$p_T^V > 120 \text{ GeV}$	
2-jet															
VH	5.2	14.2	1.6	4.8	2.4	15.9	2.7								
VV	234.7	635.1	17.5	48.5	14.7	80.7	13.3								
$t\bar{t}$	840.1	1523.8	114.3	183.1	129.4	331.8	116.1								
s-top	530.7	704.4	40.4	55.7	32.6	66.4	22.8								
W+1	5471.9	7102.6	159.2	205.7	14.4	15.5	0.2								
W+cl	2232.6	3705.8	106.3	159.3	23.4	27.0	1.1								
W+hf	761.9	1522.0	54.4	123.8	33.6	127.6	21.8								
Z+1	3891.6	10749.2	95.5	271.5	6.1	16.6	0.1								
Z+cl	1594.8	3993.2	59.4	161.9	9.4	24.0	0.3								
Z+hf	2549.1	6505.9	225.1	607.0	186.4	876.4	150.5								
Total	-	18336.0 ± 150.3	36886.2 ± 199.2	886.3 ± 16.9	1841.1 ± 24.7	458.5 ± 9.8	1598.9 ± 28.2	333.2 ± 8.9							
Data	18343.0 ± 135.4	36903.0 ± 192.1	887.0 ± 29.8	1860.0 ± 43.1	477.0 ± 21.8	1592.0 ± 39.9	306.0 ± 17.5								
<u>Sim-Data</u>	-0.03	-0.06	-0.02	-0.38	-0.79	0.14	1.34								
σ															
3-jet															
VH	-	5.1	-	1.4	-	4.5	-								
VV	-	262.5	-	16.6	-	20.3	-								
$t\bar{t}$	-	1671.8	-	186.0	-	314.8	-								
s-top	-	318.2	-	24.6	-	30.4	-								
W+1	-	2276.4	-	59.2	-	4.3	-								
W+cl	-	1243.1	-	53.0	-	8.9	-								
W+hf	-	754.1	-	59.8	-	61.7	-								
Z+1	-	3194.7	-	78.9	-	4.5	-								
Z+cl	-	1623.7	-	64.7	-	9.8	-								
Z+hf	-	1888.9	-	173.3	-	258.6	-								
Total	-	13314.9 ± 104.7	-	718.4 ± 11.8	-	718.7 ± 17.3	-								
Data	-	13344.0 ± 115.5	-	657.0 ± 25.6	-	710.0 ± 26.6	-								
<u>Sim-Data</u>	-	-0.19	-	2.1	-	0.27	-								
σ															

Table 138: Table of post unconditional fit yields for 0-lepton 2 and 3-jet events in the mva selection. The uncertainties are the full postfit errors including all nuisance parameters with priors, floating normalizations, and the correlations deduced from the data. The difference in the data and the postfit simulation is compared to σ which is obtained from the sum in quadrature of the postfit and Poissonian error.

Sample	$p_T^V < 120 \text{ GeV}$	1-tag		2L-tag		2M-tag		2T-tag	
		$p_T^V > 120 \text{ GeV}$	$p_T^V < 120 \text{ GeV}$	$p_T^V > 120 \text{ GeV}$	$p_T^V < 120 \text{ GeV}$	$p_T^V > 120 \text{ GeV}$	$p_T^V < 120 \text{ GeV}$	$p_T^V > 120 \text{ GeV}$	$p_T^V > 120 \text{ GeV}$
2-jet									
VH	24.8	17.8	7.5	6.6	11.5	9.9	12.7	11.2	
VV	1946.4	926.7	103.6	61.8	64.3	36.3	52.4	29.5	
$t\bar{t}$	11380.7	6641.1	1953.9	1051.3	2426.1	1075.6	2289.5	890.2	
s-top	13676.7	3730.6	1152.4	397.7	974.7	306.8	739.0	218.8	
W+l	65967.2	23702.1	1603.0	697.2	124.3	47.9	3.1	0.9	
W+cl	71927.7	21652.1	2627.7	966.4	464.5	152.9	23.1	6.5	
W+hf	16025.4	6111.7	1470.1	647.6	953.9	401.6	505.8	226.6	
Z+l	3942.9	1222.9	100.9	37.4	7.4	2.8	0.1	0.0	
Z+cl	1345.1	333.4	52.7	17.5	10.1	3.1	0.5	0.2	
Z+hf	2076.4	474.9	160.6	44.5	125.8	30.4	85.1	23.5	
MJ _e	–	2618.2	–	161.7	–	89.4	–	39.7	
MJ _{μ}	10227.0	164.1	720.6	16.0	329.4	4.8	177.5	1.3	
Total	198540.4 ± 506.7	67595.5 ± 287.5	9953.0 ± 90.8	4105.5 ± 49.7	5492.0 ± 65.5	2161.4 ± 33.0	3888.9 ± 55.1	1448.4 ± 26.5	
Data	198544.0 ± 445.6	67603.0 ± 260.0	9941.0 ± 99.7	4072.0 ± 63.8	5499.0 ± 74.2	2199.0 ± 46.9	3923.0 ± 62.6	1405.0 ± 37.5	
Sim-Data	-0.01	-0.02	0.09	0.41	-0.07	-0.66	-0.41	0.93	
3-jet									
VH	10.0	9.1	2.2	2.6	3.3	4.0	3.7	4.5	
VV	1095.6	688.9	49.9	39.6	22.6	18.0	14.1	14.4	
$t\bar{t}$	18656.6	10491.7	3239.6	1622.0	4119.0	1672.1	4181.1	1388.4	
s-top	7385.5	2815.3	664.0	318.4	619.0	261.3	502.5	187.7	
W+l	24977.3	11321.2	588.4	321.8	42.2	20.0	1.1	0.4	
W+cl	25898.1	10077.8	951.9	454.2	164.1	71.8	7.7	3.2	
W+hf	6532.1	4743.5	576.3	490.2	352.7	297.0	186.6	167.8	
Z+l	1776.7	572.0	43.3	18.1	2.8	1.4	0.0	0.0	
Z+cl	690.4	192.7	27.1	9.8	4.5	1.6	0.2	0.1	
Z+hf	1024.0	272.0	77.0	25.9	53.5	18.8	40.4	14.0	
MJ _e	–	1290.2	–	68.6	–	35.9	–	14.7	
MJ _{μ}	5302.7	91.1	227.1	4.9	117.0	3.2	57.4	0.8	
Total	93349.0 ± 316.8	42565.6 ± 200.9	6446.6 ± 57.1	3376.1 ± 42.6	5500.8 ± 49.9	2405.0 ± 33.0	4994.7 ± 55.2	1796.1 ± 29.6	
Data	93359.0 ± 305.5	42557.0 ± 206.3	6336.0 ± 79.6	3472.0 ± 58.9	5551.0 ± 74.5	2356.0 ± 48.5	4977.0 ± 70.5	1838.0 ± 42.9	
Sim-Data	-0.02	0.03	1.12	-1.33	-0.56	0.83	0.2	-0.81	

Table 139: Table of post unconditional fit yields for 1-lepton 2 and 3-jet events in the MVA selection. The uncertainties are the full postfit errors including all nuisance parameters with priors, floating normalizations, and the correlations deduced from the data. The difference in the data and the postfit simulation is compared to σ which is obtained from the sum in quadrature of the postfit and Poissonian error.

Not reviewed, for internal circulation only

Not reviewed, for internal circulation only

Sample	1-tag		2L-tag		2M+2T-tag	
	$p_T^V < 120 \text{ GeV}$	$p_T^V > 120 \text{ GeV}$	$p_T^V < 120 \text{ GeV}$	$p_T^V > 120 \text{ GeV}$	$p_T^V < 120 \text{ GeV}$	$p_T^V > 120 \text{ GeV}$
2-jet						
VH	13.2	4.7	3.9	1.4	12.8	4.7
VV	797.1	135.2	72.5	12.2	129.4	21.8
$t\bar{t}$	3485.8	212.5	1022.9	49.3	3179.7	136.5
s-top	385.3	44.1	40.2	5.8	96.0	11.9
W+1	245.4	11.5	3.7	0.4	0.3	0.0
W+c1	166.4	17.6	5.8	0.6	1.0	0.1
W+hf	89.9	13.1	7.5	0.7	4.9	0.6
Z+1	29408.5	4179.7	648.0	101.0	41.0	6.2
Z+c1	12126.7	1621.8	420.9	63.5	70.6	9.7
Z+hf	21091.0	2853.5	1916.2	287.7	2858.1	414.0
Total	69362.0 ± 279.6	9123.3 ± 85.8	4271.3 ± 49.5	524.6 ± 7.9	6473.1 ± 75.9	606.7 ± 12.7
Data	69313.0 ± 263.3	9150.0 ± 95.7	4313.0 ± 65.7	517.0 ± 22.7	6501.0 ± 80.6	570.0 ± 23.9
Sim-Data	0.13	-0.21	-0.51	0.31	-0.25	1.33
σ						
3-jet						
VH	4.7	2.4	1.1	0.6	3.4	1.9
VV	347.2	99.6	22.2	6.9	28.8	8.7
$t\bar{t}$	2171.3	181.6	485.6	29.0	1475.6	74.3
s-top	144.3	21.6	18.0	3.0	40.7	6.5
W+1	76.0	7.1	1.4	0.2	0.1	0.0
W+c1	57.0	8.9	2.3	0.4	0.4	0.1
W+hf	39.7	6.4	3.1	0.8	0.8	0.4
Z+1	8872.0	1913.0	190.0	45.5	11.6	2.7
Z+c1	4645.9	948.8	163.6	37.5	25.0	5.7
Z+hf	5792.0	1223.2	497.2	120.8	765.9	180.0
Total	22721.7 ± 149.9	4430.1 ± 55.9	1403.0 ± 19.6	245.2 ± 5.2	2364.8 ± 42.5	280.9 ± 8.4
Data	22662.0 ± 150.5	4436.0 ± 66.6	1428.0 ± 37.8	253.0 ± 15.9	2394.0 ± 48.9	283.0 ± 16.8
Sim-Data	0.28	-0.07	-0.59	-0.47	-0.45	-0.11
σ						

Table 140: Table of post unconditional fit yields for 2-lepton 2 and 3-jet events in the mva selection. The uncertainties are the full postfit errors including all nuisance parameters with priors, floating normalizations, and the correlations deduced from the data. The difference in the data and the postfit simulation is compared to σ which is obtained from the sum in quadrature of the postfit and Poissonian error.

5079 **A.J.6 MVA Analysis: Postfit over Preft**

[Not reviewed, for internal circulation only]

Not reviewed, for internal circulation only

Sample	1-tag			2L-tag			2M-tag			2M+2T-tag			2T-tag		
	$100 < p_T^V < 120 \text{ GeV}$	$p_T^V > 120 \text{ GeV}$	$100 < p_T^V < 120 \text{ GeV}$	$p_T^V > 120 \text{ GeV}$	$100 < p_T^V < 120 \text{ GeV}$	$p_T^V > 120 \text{ GeV}$	$100 < p_T^V < 120 \text{ GeV}$	$p_T^V > 120 \text{ GeV}$	$100 < p_T^V < 120 \text{ GeV}$	$p_T^V > 120 \text{ GeV}$	$100 < p_T^V < 120 \text{ GeV}$	$p_T^V > 120 \text{ GeV}$	$100 < p_T^V < 120 \text{ GeV}$	$p_T^V > 120 \text{ GeV}$	
2-jet															
VH	0.65	0.62	0.71	0.69	0.69	0.68	0.68	0.68	0.69	0.69	0.68	0.68	0.68	0.68	
VV	1.01	1.01	1.04	1.01	1.01	1.06	1.03	1.03	1.01	1.01	1.03	1.03	1.07	1.07	
$t\bar{t}$	1.41	1.31	1.46	1.37	1.37	1.44	1.41	1.41	1.37	1.37	1.44	1.44	1.43	1.43	
s-top	1.2	1.06	1.17	1.08	1.08	1.2	1.13	1.13	1.17	1.17	1.13	1.13	1.21	1.21	
W+l	1.03	0.96	1.0	0.98	0.98	1.09	1.06	1.06	1.09	1.09	1.06	1.06	1.01	1.01	
W+cl	1.13	1.09	1.13	1.13	1.13	1.1	1.12	1.12	1.12	1.12	1.11	1.11	1.33	1.33	
W+hf	0.86	0.77	0.85	0.78	0.78	0.86	0.79	0.79	0.78	0.78	0.79	0.79	0.83	0.83	
Z+l	1.05	0.99	1.07	1.02	1.02	1.18	1.12	1.12	1.07	1.07	1.18	1.18	1.01	1.01	
Z+cl	0.92	0.87	0.93	0.9	0.9	0.95	0.92	0.92	0.93	0.93	0.95	0.95	0.88	0.88	
Z+hf	1.14	1.1	1.2	1.16	1.16	1.2	1.16	1.16	1.17	1.17	1.16	1.16	1.17	1.17	
Total	1.05	1.0	1.1	1.06	1.06	1.18	1.14	1.14	1.17	1.17	1.14	1.14	1.19	1.19	
3-jet															
VH	–	0.63	–	0.69	–	–	0.68	–	–	0.68	–	–	–	–	
VV	–	1.01	–	–	1.05	–	–	1.06	–	–	1.06	–	–	–	
$t\bar{t}$	–	1.12	–	–	1.18	–	–	1.19	–	–	1.19	–	–	–	
s-top	–	0.97	–	0.98	–	–	1.01	–	–	1.01	–	–	–	–	
W+l	–	0.9	–	0.93	–	–	1.03	–	–	1.03	–	–	–	–	
W+cl	–	1.03	–	1.05	–	–	1.06	–	–	1.06	–	–	–	–	
W+hf	–	1.0	–	1.06	–	–	1.12	–	–	1.12	–	–	–	–	
Z+l	–	0.95	–	0.98	–	–	1.04	–	–	1.04	–	–	–	–	
Z+cl	–	1.03	–	1.04	–	–	1.07	–	–	1.07	–	–	–	–	
Z+hf	–	0.99	–	1.11	–	–	1.18	–	–	1.18	–	–	–	–	
Total	–	0.99	–	1.07	–	–	1.15	–	–	1.15	–	–	–	–	

Table 141: Table of post unconditional fit over prefit yields for 0-lepton 2 and 3-jet events in the mva selection.

Not reviewed, for internal circulation only

Sample	1-tag			2L-tag			2M-tag			2T-tag		
	$p_T^V < 120 \text{ GeV}$	$p_T^V > 120 \text{ GeV}$	$p_T^V < 120 \text{ GeV}$	$p_T^V > 120 \text{ GeV}$	$p_T^V < 120 \text{ GeV}$	$p_T^V > 120 \text{ GeV}$	$p_T^V < 120 \text{ GeV}$	$p_T^V > 120 \text{ GeV}$	$p_T^V < 120 \text{ GeV}$	$p_T^V > 120 \text{ GeV}$	$p_T^V < 120 \text{ GeV}$	$p_T^V > 120 \text{ GeV}$
2-jet												
VH	0.64	0.63	0.7	0.71	0.69	0.68	0.69	0.68	0.69	0.68	0.69	0.69
VV	1.01	1.0	1.01	1.0	1.03	1.04	1.03	1.05	1.03	1.05	1.04	1.04
$t\bar{t}$	1.13	1.12	1.19	1.19	1.18	1.17	1.19	1.17	1.19	1.17	1.21	1.21
s-top	1.2	1.07	1.25	1.13	1.23	1.15	1.23	1.22	1.23	1.22	1.17	1.17
$W+1$	1.01	1.0	1.02	1.02	1.01	1.01	1.01	1.01	1.01	1.01	1.01	1.01
$W+cl$	1.09	1.1	1.12	1.12	1.16	1.14	1.16	1.17	1.14	1.17	1.06	1.06
$W+hf$	0.74	0.77	0.82	0.78	0.84	0.79	0.84	0.87	0.79	0.87	0.77	0.77
Z+1	1.03	1.0	1.03	1.01	1.01	1.01	1.01	1.01	1.01	1.01	1.01	1.01
Z+cl	0.88	0.88	0.88	0.88	0.88	0.88	0.88	0.88	0.88	0.88	0.88	0.88
Z+hf	1.09	1.09	1.09	1.09	1.14	1.09	1.14	1.12	1.09	1.12	1.2	1.2
MJ _e	–	–	–	–	–	–	–	–	–	–	–	–
MJ _{μ}	0.94	1.0	0.85	1.0	0.76	1.0	0.76	1.0	0.98	1.0	1.14	1.14
Total	1.02	1.02	1.02	1.04	1.04	1.04	1.07	1.07	1.11	1.11	1.02	1.02
3 jet												
VH	0.66	0.65	0.69	0.7	0.69	0.68	0.69	0.68	0.69	0.68	0.69	0.69
VV	1.01	1.02	1.01	1.01	1.01	1.01	1.01	1.01	1.01	1.01	1.01	1.05
$t\bar{t}$	0.98	0.96	1.05	1.03	1.04	1.04	1.04	1.05	1.04	1.05	1.05	1.05
s-top	1.04	0.95	1.09	0.99	1.12	1.05	1.12	1.13	1.05	1.13	1.05	1.05
$W+1$	0.92	0.95	0.93	0.96	1.01	1.01	1.01	1.01	1.01	1.01	1.01	1.01
$W+cl$	1.02	1.05	1.05	1.06	1.1	1.1	1.1	1.13	1.13	1.13	1.13	1.13
$W+hf$	0.65	1.03	0.72	1.1	0.76	1.13	0.76	0.81	1.13	1.13	1.17	1.17
Z+1	0.98	0.96	1.01	1.01	1.01	1.01	1.01	1.01	1.01	1.01	1.01	1.01
Z+cl	0.88	0.88	0.88	0.88	0.88	0.88	0.88	0.88	0.88	0.88	0.88	0.88
Z+hf	1.09	1.09	1.09	1.09	1.09	1.09	1.09	1.09	1.09	1.09	1.09	1.09
MJ _e	–	1.0	–	1.17	–	1.2	–	–	–	–	–	–
MJ _{μ}	1.04	1.0	0.89	1.0	0.91	1.0	0.91	1.0	0.91	1.0	1.03	1.03
Total	0.95	0.98	0.99	1.04	1.03	1.06	1.03	1.05	1.05	1.05	1.06	1.06

Table 142: Table of post unconditional fit over prefit yields for 1-lepton 2 and 3-jet events in the MVA selection.

Not reviewed, for internal circulation only

Sample	$p_T^V < 120 \text{ GeV}$	1-tag		2L-tag		2M+2T-tag	
		$p_T^V > 120 \text{ GeV}$	$p_T^V < 120 \text{ GeV}$	$p_T^V > 120 \text{ GeV}$	$p_T^V < 120 \text{ GeV}$	$p_T^V < 120 \text{ GeV}$	$p_T^V > 120 \text{ GeV}$
2-jet							
VH	0.65	0.63	0.71	0.69	0.69	0.67	0.67
VV	1.01	1.01	1.07	1.04	1.06	1.03	1.03
$t\bar{t}$	0.98	0.96	1.08	1.04	1.05	1.01	1.01
s-top	1.01	1.01	1.01	1.1	1.07	1.06	1.06
W+l	1.01	1.01	1.01	1.01	1.01	1.01	1.01
W+c1	1.13	1.13	1.13	1.13	1.13	1.13	1.13
W+hf	0.83	0.83	0.83	0.83	0.83	0.76	0.76
Z+l	1.04	1.02	1.06	1.04	1.04	1.13	1.13
Z+c1	0.88	0.88	0.89	0.9	0.91	0.92	0.92
Z+hf	1.1	1.1	1.16	1.16	1.13	1.15	1.15
Total	1.01	1.01	1.07	1.08	1.08	1.09	1.09
3 jet							
VH	0.64	0.63	0.71	0.7	0.69	0.69	0.69
VV	1.01	1.02	1.04	1.05	1.1	1.07	1.07
$t\bar{t}$	1.07	1.05	1.18	1.15	1.16	1.14	1.14
s-top	1.01	1.01	1.1	1.02	1.07	1.04	1.04
W+l	1.01	1.01	1.01	1.01	1.01	1.01	1.01
W+c1	1.13	1.13	1.13	1.13	1.13	1.13	1.13
W+hf	0.83	0.83	0.83	0.83	0.83	0.83	0.83
Z+l	1.0	0.97	1.01	1.0	1.01	1.09	1.09
Z+c1	0.99	1.02	1.0	1.04	1.03	1.09	1.09
Z+hf	0.95	0.98	1.07	1.1	1.14	1.17	1.17
Total	0.98	0.99	1.08	1.07	1.14	1.15	1.15

Table 143: Table of post unconditional fit over prefit yields for 2-lepton 2 and 3-jet events in the mva selection.

Not reviewed, for internal circulation only

5080 AK Combining 7 TeV and 8 TeV results

5081 This section describe the combination of the 7 TeV data and 8 TeV data to get the final results. For the 7
 5082 TeV data, we use the public results discussed in detail in [11] The 7 TeV dataset has not been re-analyzed
 5083 following the new strategy described in the note, because some of the needed improvements in the
 5084 understanding of the object performance (i.e. the pseudo-continuous b-tagging or the global sequential
 5085 calibration) are not completely available/validated for 7 TeV data. The decision is to combine the new
 5086 8 TeV data, with the 7 TeV results described in [11]. To decide which correlation to keep across the 2
 5087 years, one should consider that among the two years:

- 5088 • the jet calibration is different;
- 5089 • the lepton identification algorithm is different
- 5090 • the MET soft term is calculated in a slightly different way
- 5091 • the b-tagging algorithm is different

5092 so the decision is to keep all the systematic uncertainties on the reconstructed object as non correlated.

5093 The extended phase space of the new 8 TeV analysis requested a more mature understanding of
 5094 the background modeling, resulting in corrections and systematic uncertainties which are consistent but
 5095 different from the ones used in the 7 TeV data. For this reason, it is hard to assume correlations across
 5096 years for the nuisance parameters on the modeling of the backgrounds.

5097 Given the conditions discussed above, the 2 analyses are treated as non correlated. In this section,
 5098 we report the preliminary studies on the combination of the new 8 TeV analysis, with the 7 TeV results
 5099 reported in [11]. The structure is the following:

- 5100 • Consistency of the 2 results and expected final μ
- 5101 • Checks on the pulls and correlations
- 5102 • Post fit plots for 7 TeV distribution

5103 The 7 TeV result is shown in Figure 509, 8 TeV in Figure 510, and the combination in Figure 511.

5104 AK.1 Consistency of the results

5105 The measured μ for the 7 TeV analysis in [11] is -2.1 ± 1.4 . Let's assume that in the new 8 TeV analysis
 5106 result we get a different μ , what would be the compatibility of the 2 results? In combining the 2 years,
 5107 what is the expected final μ ?

5108 To answer these 2 questions, we generated Asimov datasets with different assumption on μ_{8TeV} , we
 5109 combined these Asimov with the 7 TeV results, and we studied the compatibility of the two years results,
 5110 and the final combined μ , as a function of μ_{8TeV} . The results are shown on Figure 512.

5111 The consistency between the 2 years has been evaluated by studying the $\Delta \ln(L)$ when different
 5112 nuisance parameters for the signal strength are used for each year, and when the 2 years have a common
 5113 nuisance parameters for the signal strength. The probability is bigger than 4% if the 8 TeV result has a
 5114 signal strength smaller than 1.6.

5115 The combination of the two years follows the naive expectation coming from the weighted average
 5116 of the two years, with a shift of more or less -0.3 if compared with the 8 TeV fit alone. Note that the final
 5117 error on μ is of the order of 0.4, meaning a shift due to the 2011 data smaller than 1 standard deviation.

Not reviewed

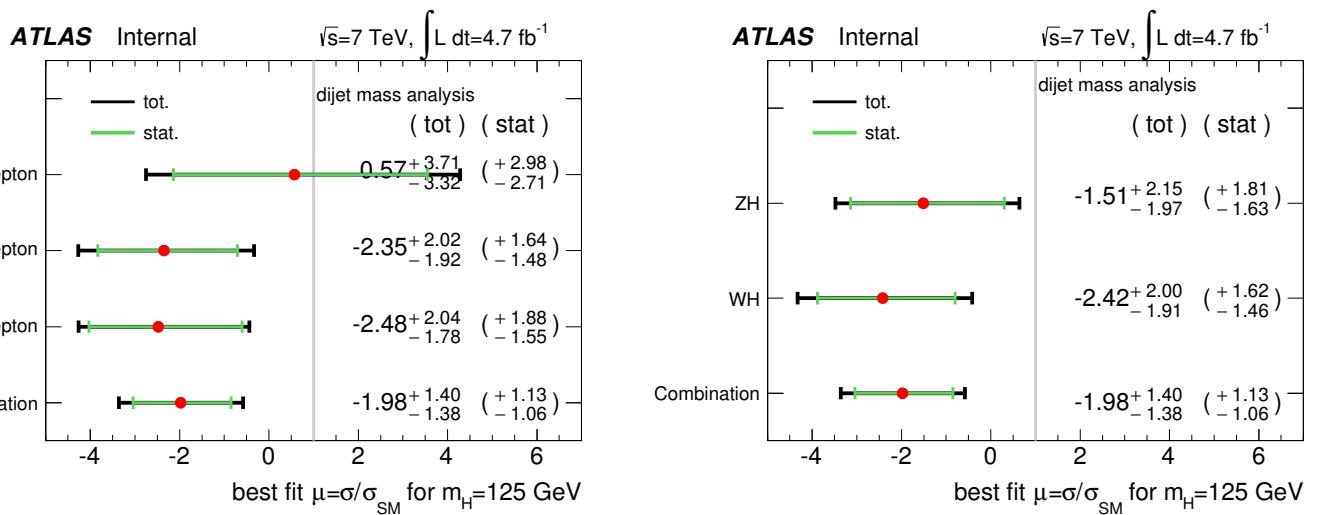


Figure 509: The fitted values of the Higgs-boson signal strength parameter μ for dijet mass 7 TeV result. Both plot have been created in the context on the full 0+1+2 lepton fit. The left plot was made fitting a signal strength in each lepton selection while the right was made fitting a signal strength for WH and ZH separately.

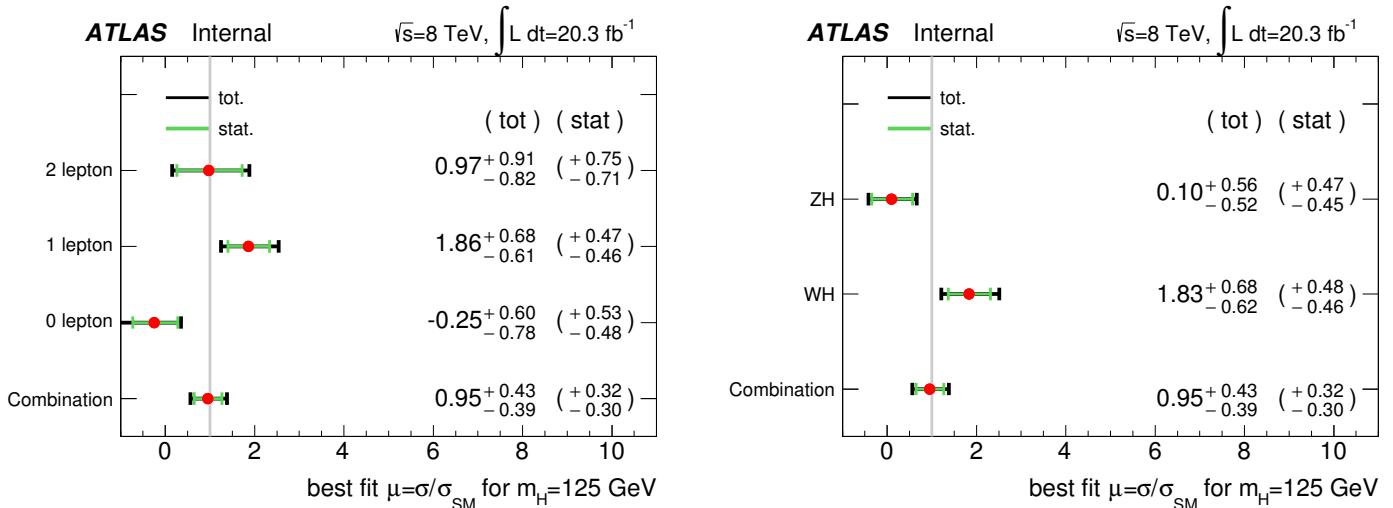


Figure 510: The fitted values of the Higgs-boson signal strength parameter μ for MVA 8 TeV result. Both plot have been created in the context on the full 0+1+2 lepton fit. The left plot was made fitting a signal strength in each lepton selection while the right was made fitting a signal strength for WH and ZH separately.

Not revi

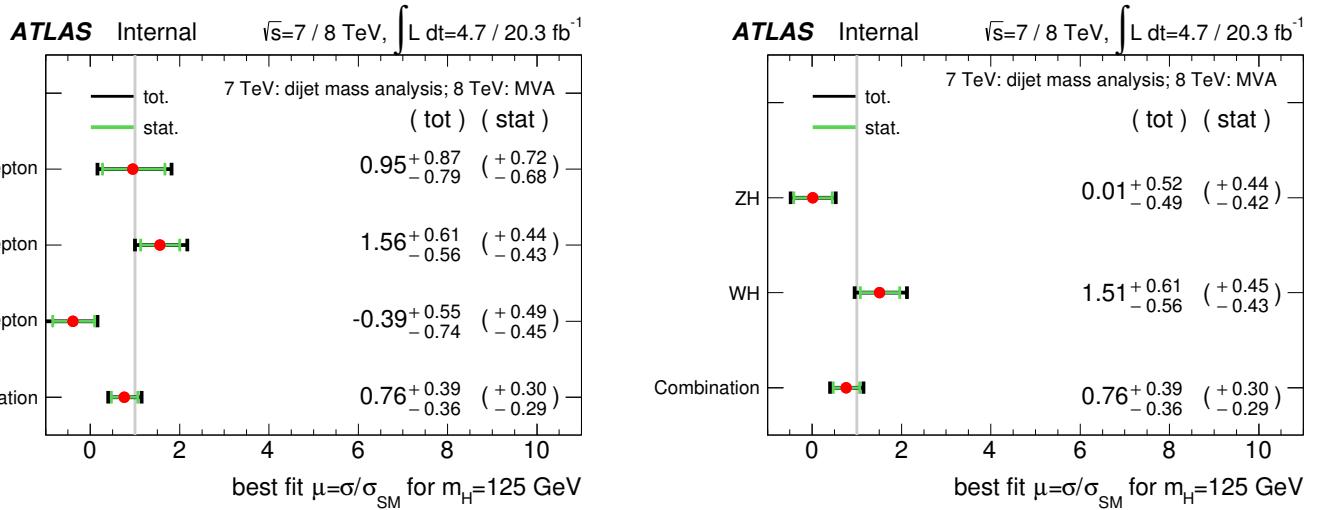


Figure 511: The fitted values of the Higgs-boson signal strength parameter μ for the combination of the 7 TeV dijet mass and MVA 8 TeV result. Both plots have been created in the context of the full 0+1+2 lepton fit. The left plot was made fitting a signal strength in each lepton selection while the right was made fitting a signal strength for WH and ZH separately.

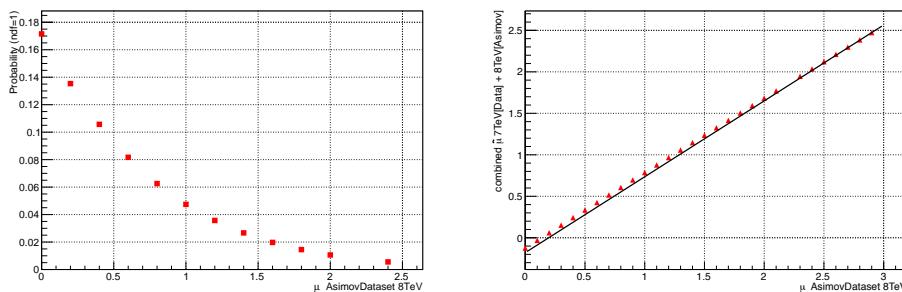


Figure 512: Left: Compatibility of the fit results in the 2 years, as a function of the injected signal in the Asimov dataset for the 8 TeV MVA analysis. Right: Final extracted μ as a function of the injected signal in the Asimov dataset for the 8 TeV MVA analysis. In red: fit result. In black: the expectation from the naive calculation.

AK.2 Pulls on the combination

Since we are fitting the two years as completely independent measurements, we expect that the pulls for the different NP in the combination follow identically their behavior in the individual fit. This is shown in Figures 513–515. In these plots, we used the 2011 data, and the 2012 Asimov dataset, coherently with the rest of the studies in this section. As can be seen, the combined fit shows pulls and constrains which are coherent with the individual 7 TeV and 8 TeV fit (with minimal negligible deviations). NOTE: the plots on this section need to be updated.

Figure 516 shows the correlation induced by the fit between the 2011 and the 2012 NP. Correlation smaller than 0.3% are induced between NP of two years.

AK.3 Post-fit 2011 distributions

This part of the appendix contains the post-fit plots for the 7 TeV analysis from the new combined fit.

Not reviewed, for internal circulation only

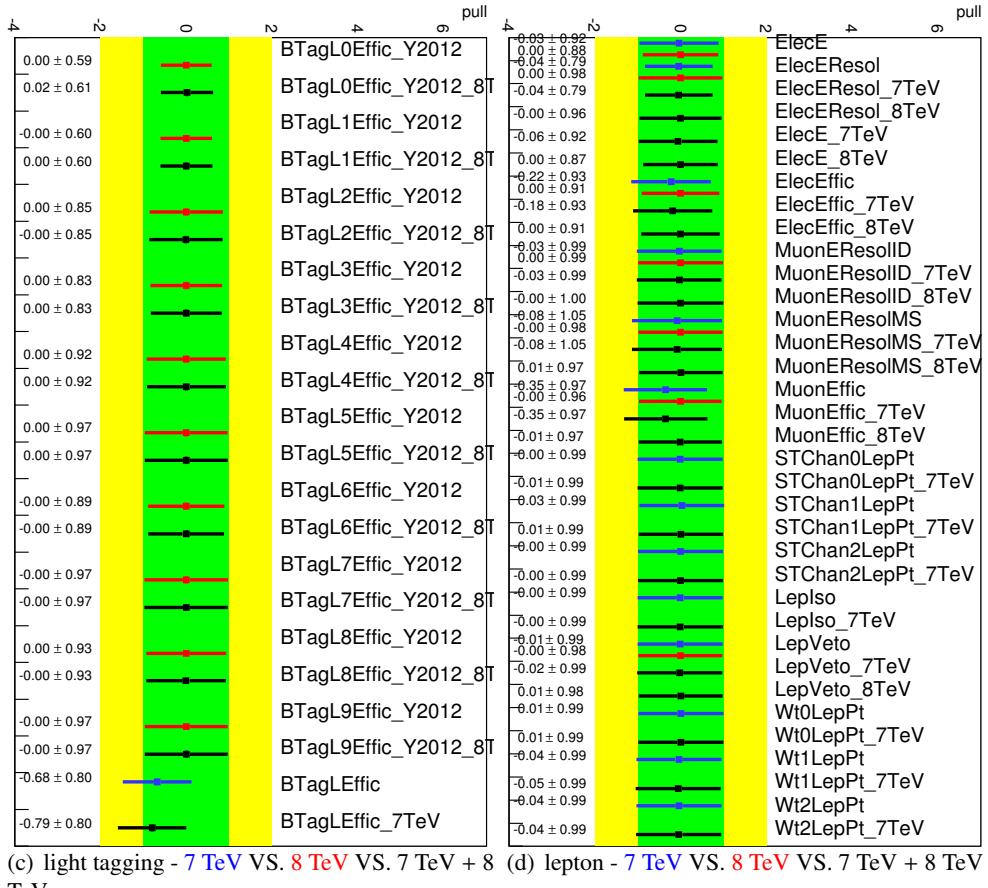
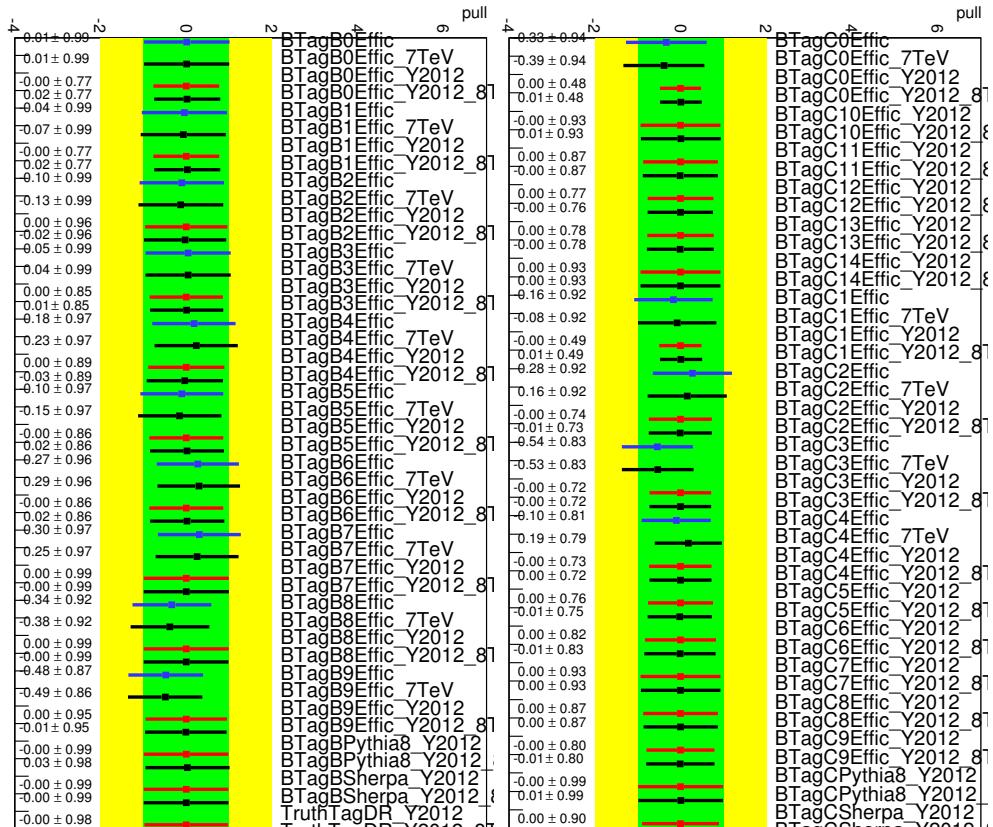


Figure 513: Pull plots for *b*, *c*, light tagging and lepton systematics in the 0+1+2 lepton MVA fit. Comparison of the 7 TeV, 8 TeV and the combined fit.

Not reviewed, for internal circulation only

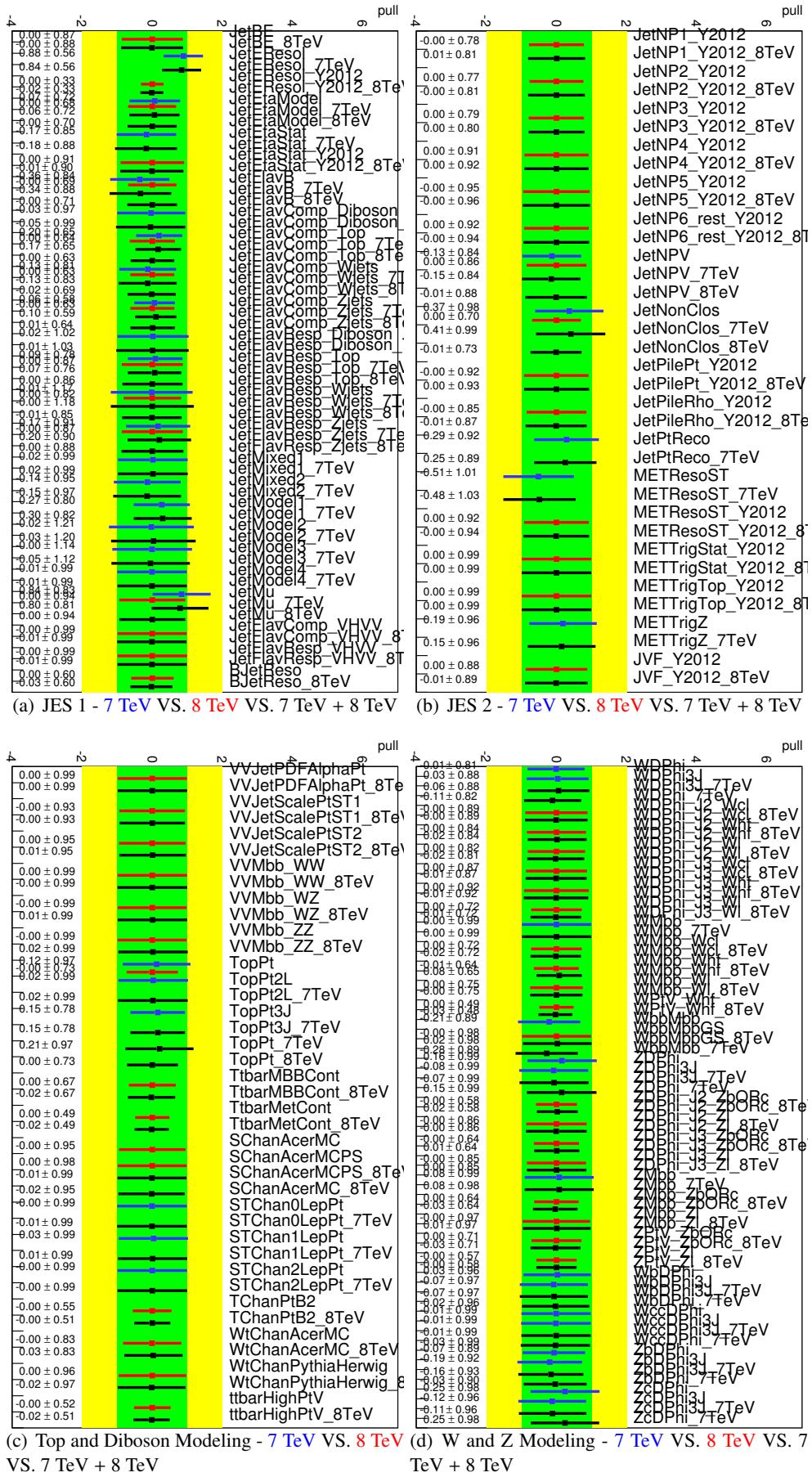
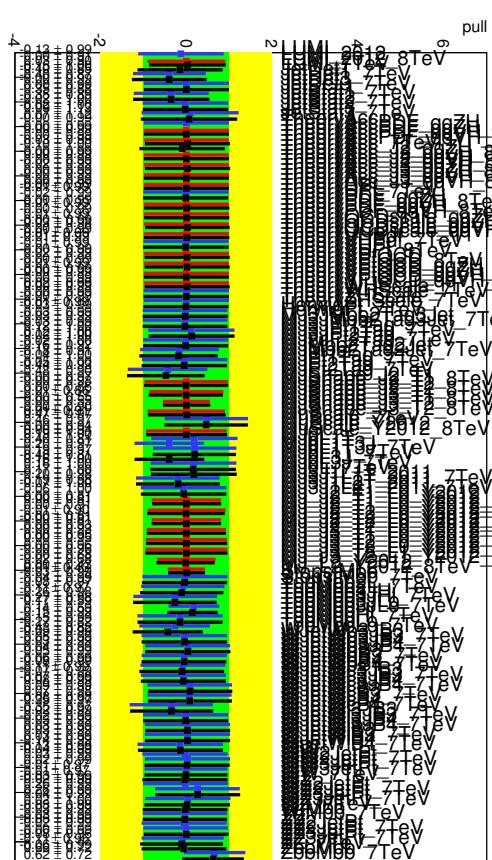
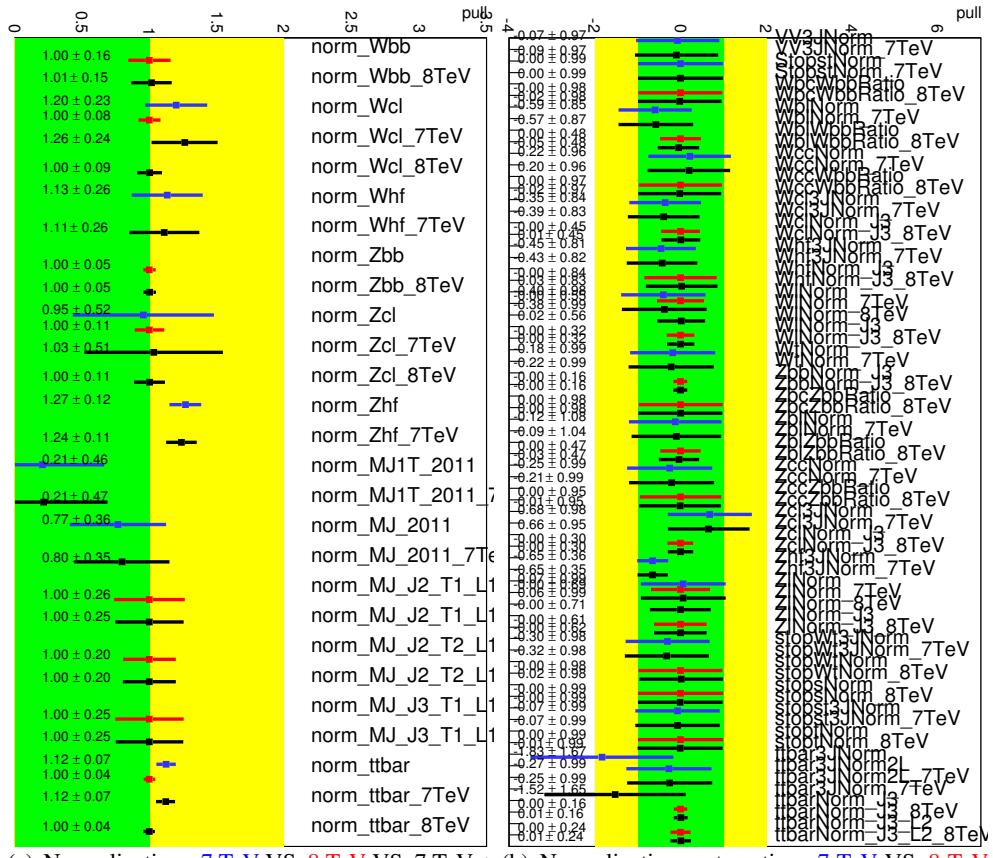


Figure 514: Pull plots for JES systematics, diboson/top and W/Z systematics in the 0+1+2 lepton MVA fit. Comparison of the 7 TeV, 8 TeV and the combined fit.

Not reviewed, for internal circulation only



(c) Remaining NP - 7 TeV VS. 8 TeV VS. 7 TeV + 8 TeV

Figure 515: Pull plots for normalization NPs and remaining NPs in the 0+1+2 lepton MVA fit. Comparison of the 7 TeV, 8 TeV and the combined fit.

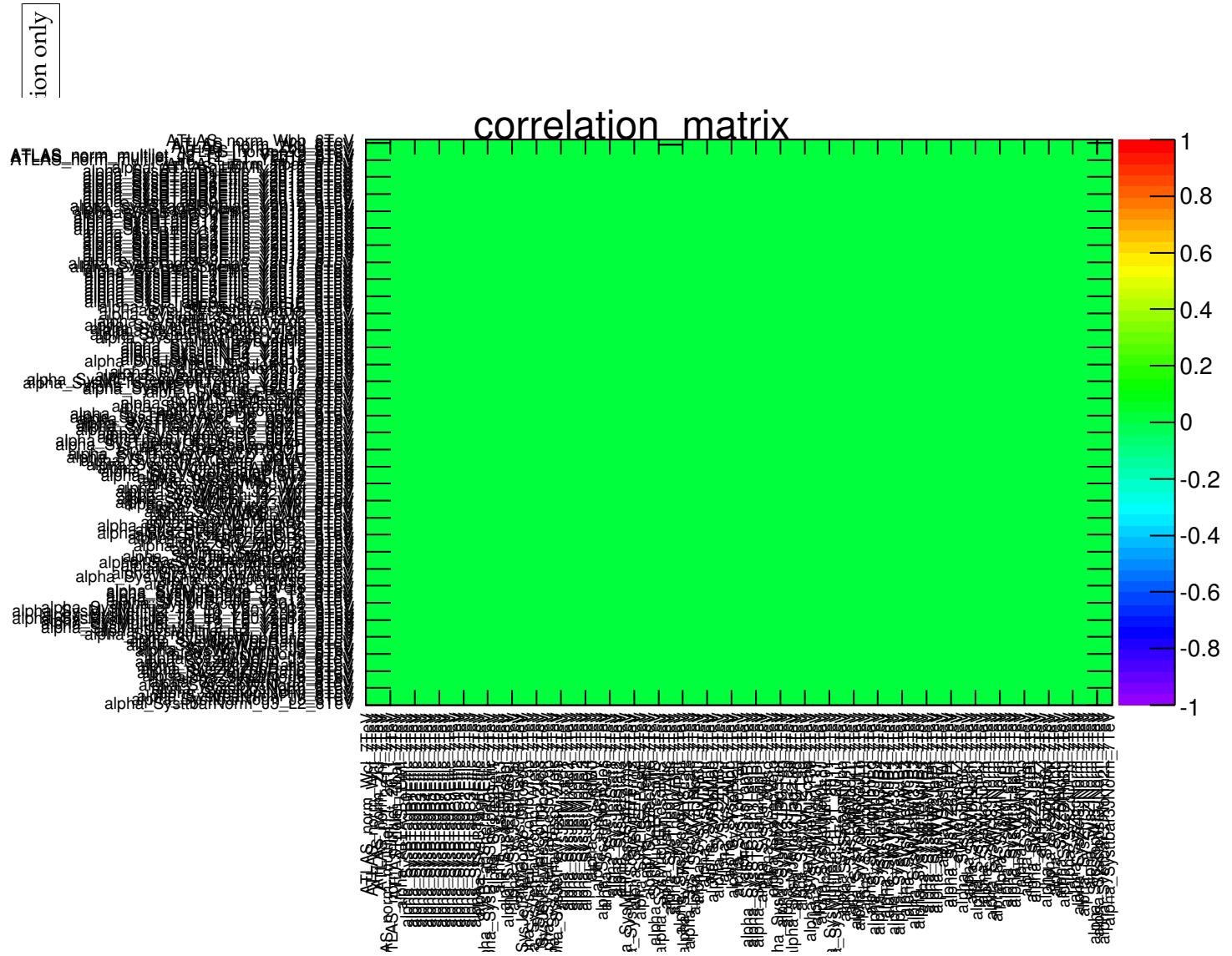


Figure 516: The correlation between 7 TeV NP and 8 TeV NP, induced by the fit. The maximum correlation induced by the fit is of the order of 0.3%.

Not reviewed, for internal circulation only

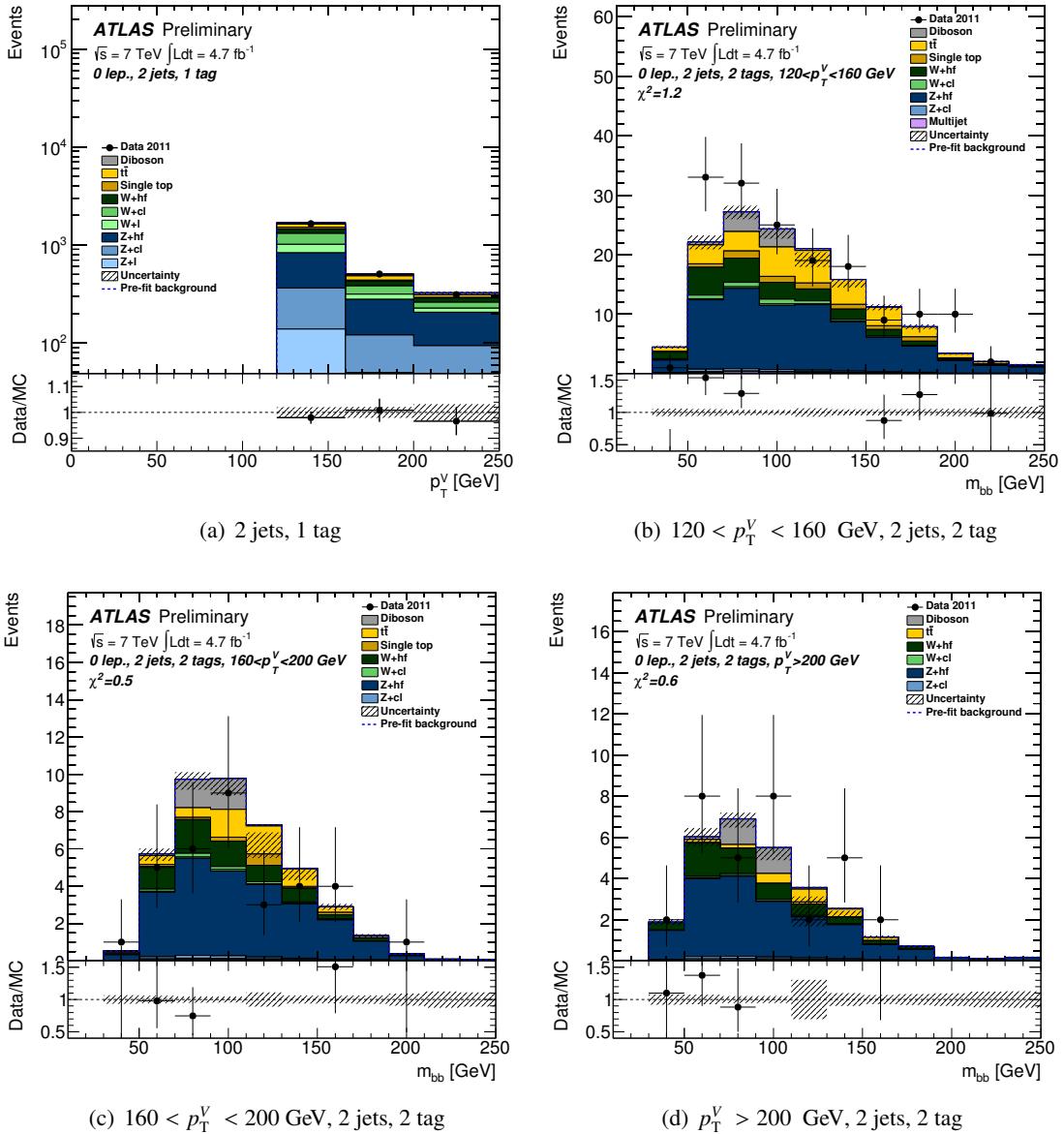


Figure 517: Post-fit plots for m_{jj} distribution in 0-lepton events in the 1-tag (where p_T^V is used in the fit) and 2-tag categories for the 2-jets events. Plots are shown for $120 < p_T^V < 160$ GeV and $160 < p_T^V < 200$ GeV and $p_T^V > 200$ GeV. The pre-fit background expectation is indicated by the dashed blue line.

Not reviewed, for internal circulation only

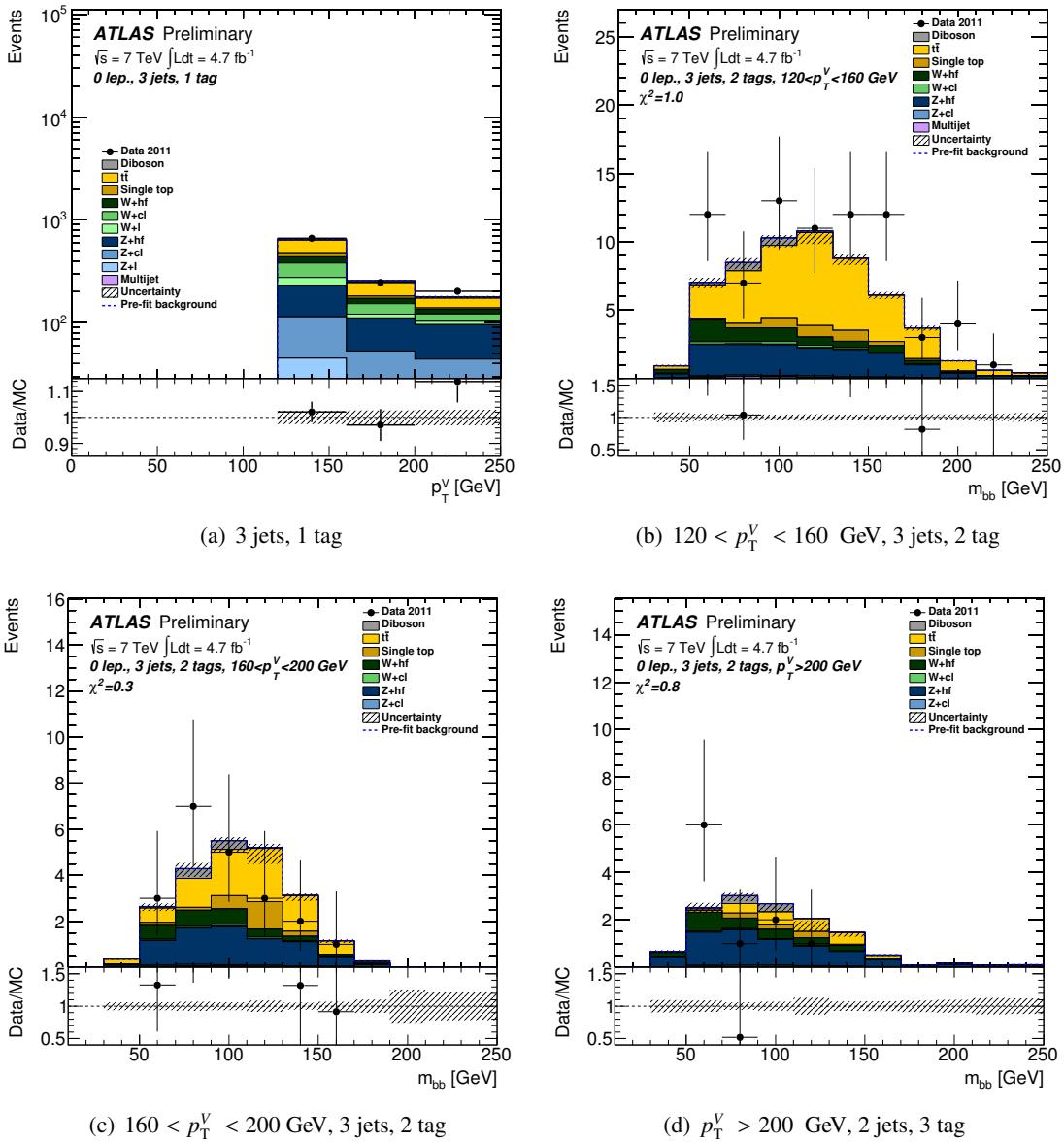


Figure 518: Post-fit plots for m_{jj} distribution in 0-lepton events in the 1-tag (where p_T^V is used in the fit) and 2-tag categories for the 3-jets events. Plots are shown for $p_T^V < 90$ GeV, $90 < p_T^V < 120$ GeV, $120 < p_T^V < 160$ GeV and $160 < p_T^V < 200$ GeV and $p_T^V > 200$ GeV. The pre-fit background expectation is indicated by the dashed blue line.

Not reviewed, for internal circulation only

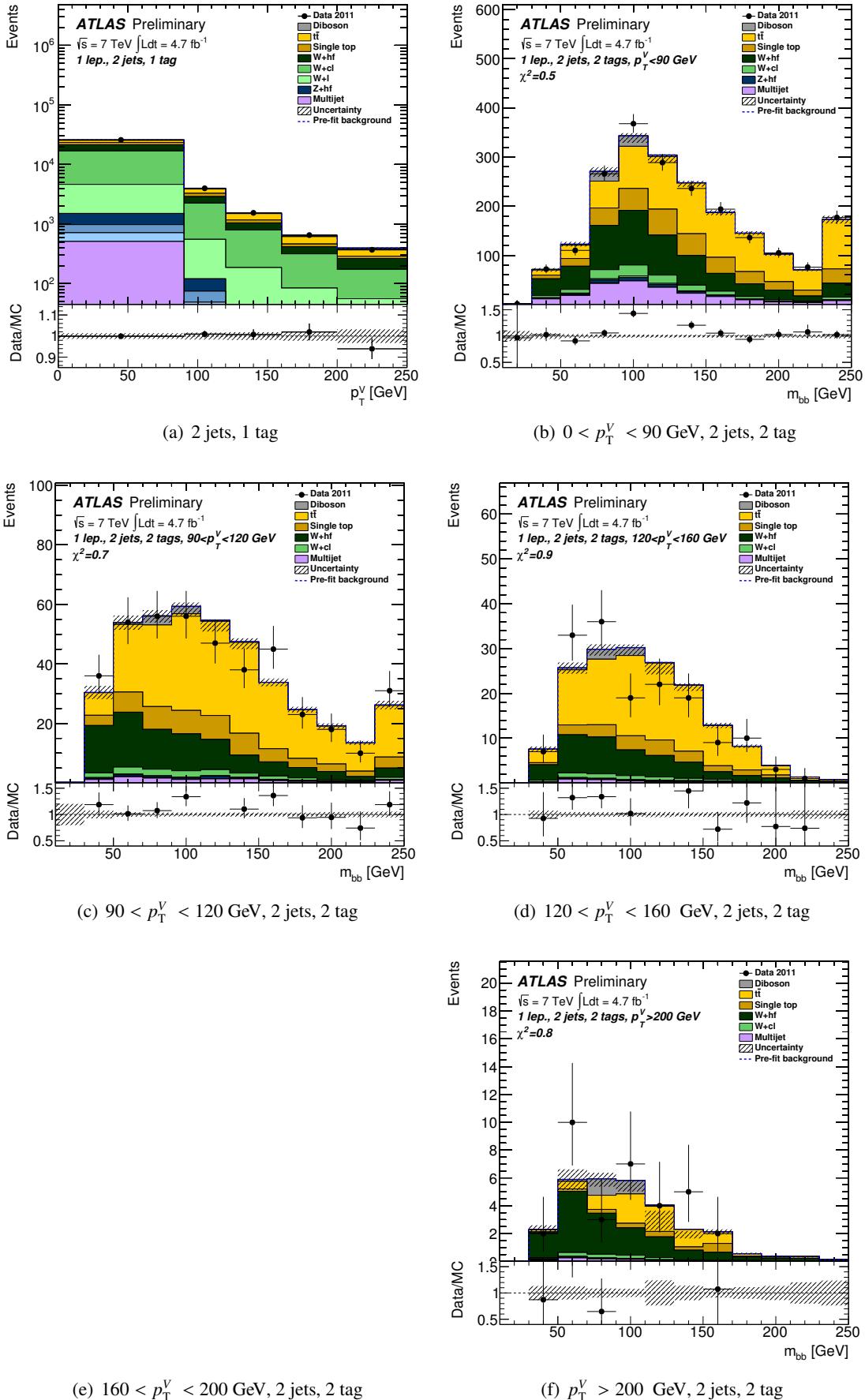


Figure 519: Post-fit plots for m_{jj} distribution in 1-lepton events in the 1-tag (where p_T^V is used in the fit) and 2-tag categories for the 2-jets events. Plots are shown for $p_T^V < 90$ GeV, $90 < p_T^V < 120$ GeV, $120 < p_T^V < 160$ GeV and $160 < p_T^V < 200$ GeV and $p_T^V > 200$ GeV. The pre-fit background expectation is indicated by the dashed blue line.

Not reviewed, for internal circulation only

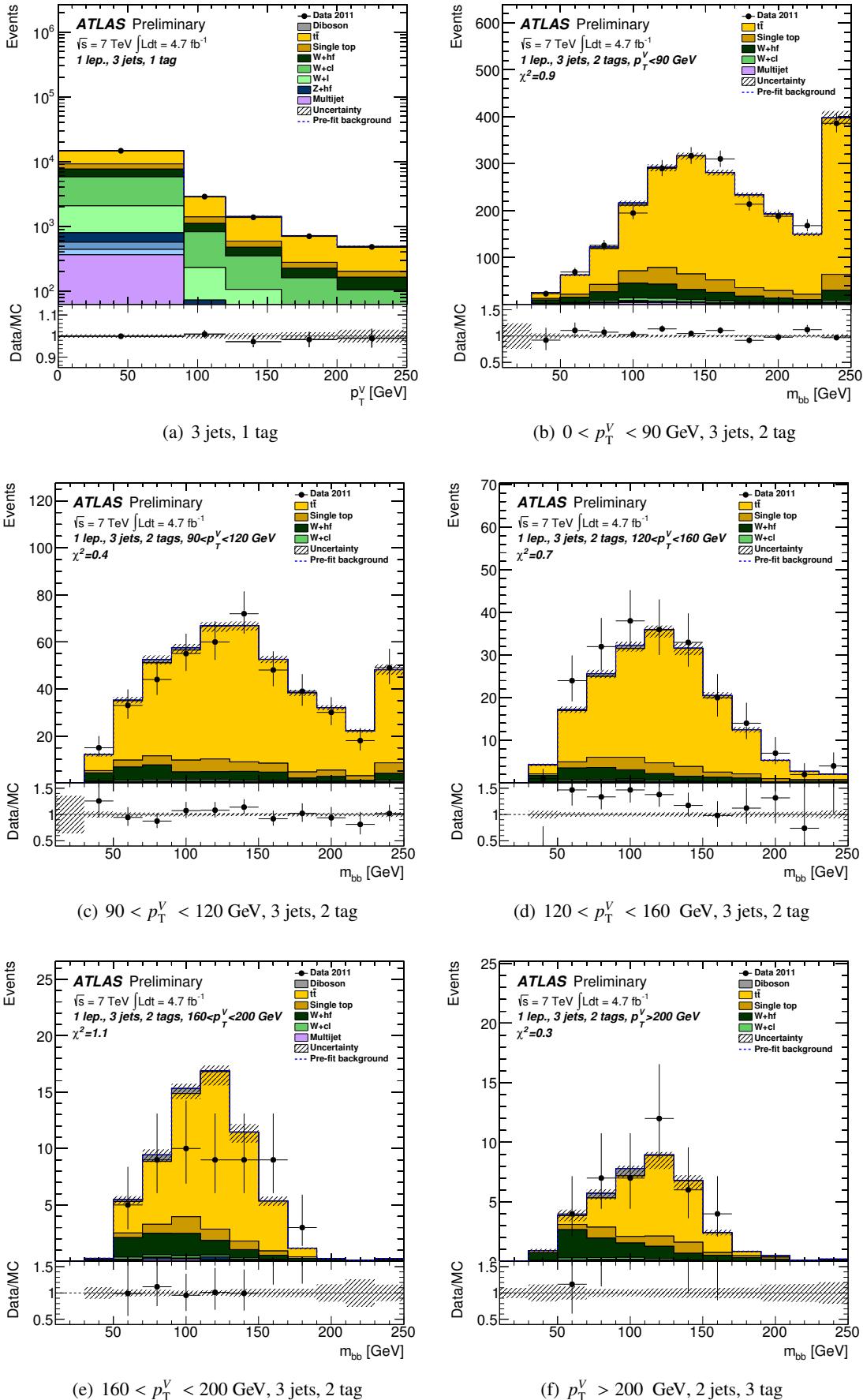


Figure 520: Post-fit plots for m_{jj} distribution in 1-lepton events in the 1-tag (where p_T^V is used in the fit) and 2-tag categories for the 3-jets events. Plots are shown for $p_T^V < 90 \text{ GeV}$, $90 < p_T^V < 120 \text{ GeV}$, $120 < p_T^V < 160 \text{ GeV}$ and $160 < p_T^V < 200 \text{ GeV}$ and $p_T^V > 200 \text{ GeV}$. The pre-fit background expectation is indicated by the dashed blue line.

Not reviewed, for internal circulation only

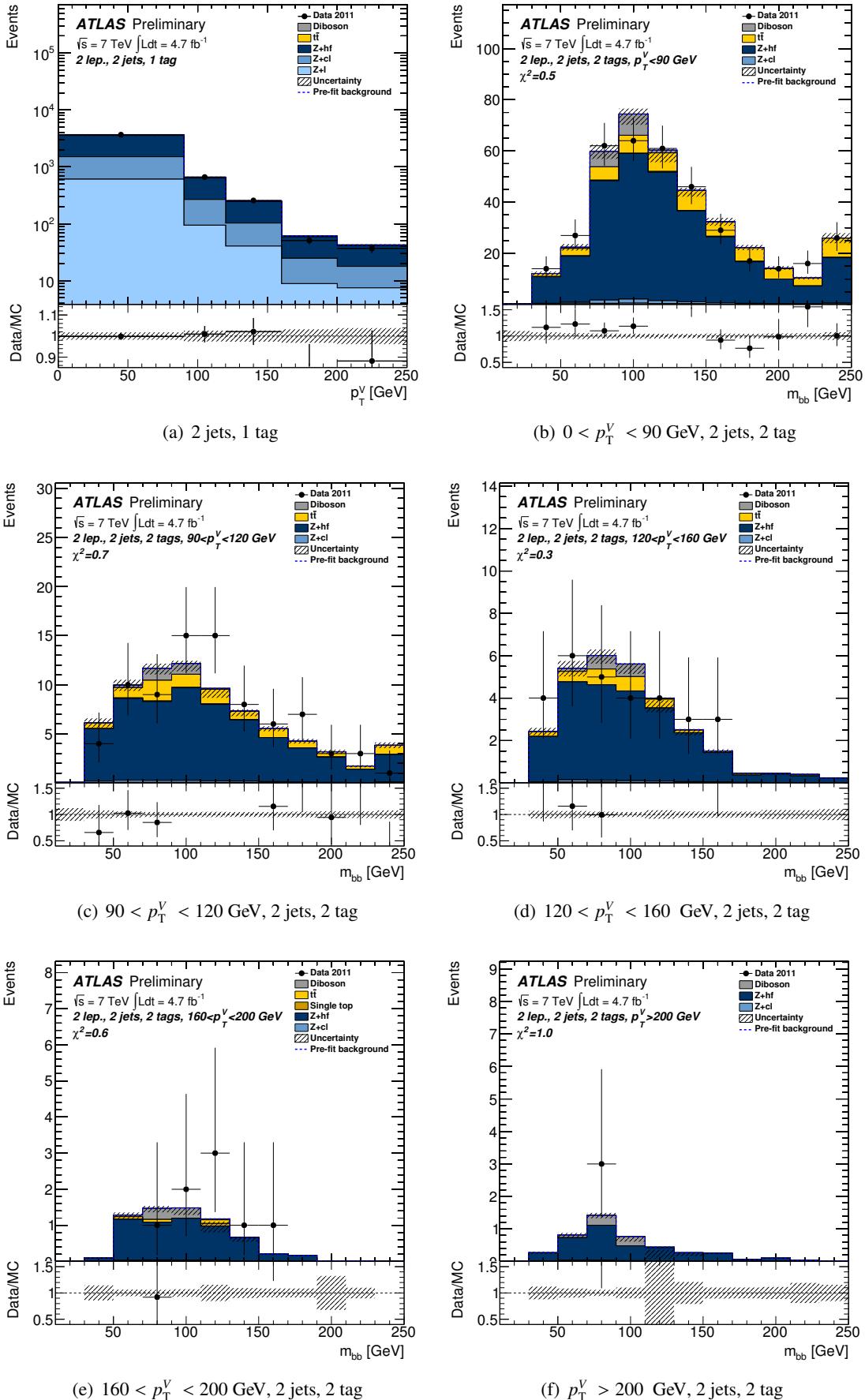


Figure 521: Post-fit plots for m_{jj} distribution in 2-lepton events in the 1-tag (where p_T^V is used in the fit) and 2-tag categories for the 2-jets events. Plots are shown for $p_T^V < 90 \text{ GeV}$, $90 < p_T^V < 120 \text{ GeV}$, $120 < p_T^V < 160 \text{ GeV}$ and $160 < p_T^V < 200 \text{ GeV}$ and $p_T^V > 200 \text{ GeV}$. The pre-fit background expectation is indicated by the dashed blue line.

Not reviewed, for internal circulation only

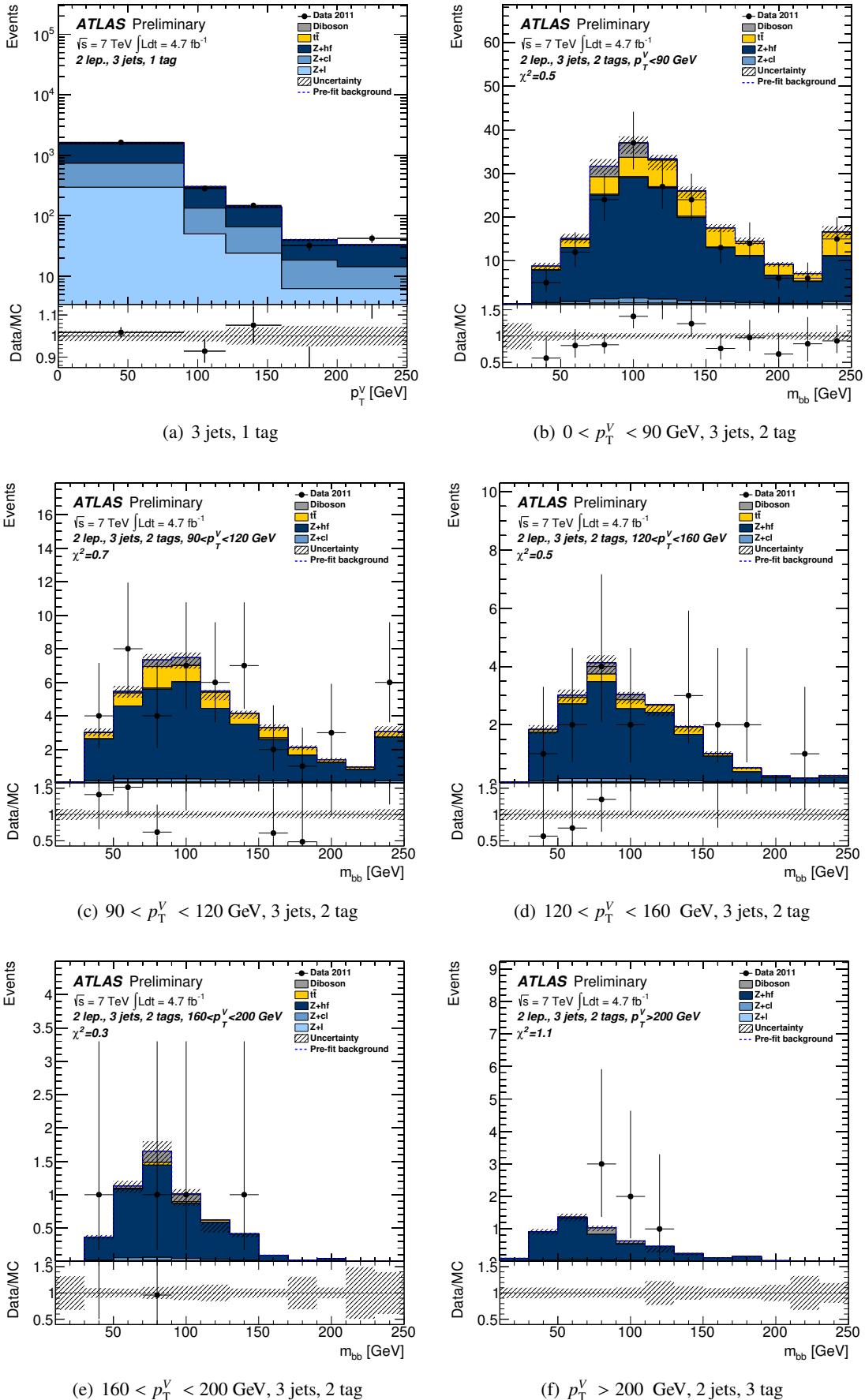


Figure 522: Post-fit plots for m_{jj} distribution in 2-lepton events in the 1-tag (where p_T^V is used in the fit) and 2-tag categories for the 3-jets events. Plots are shown for $p_T^V < 90$ GeV, $90 < p_T^V < 120$ GeV, $120 < p_T^V < 160$ GeV and $160 < p_T^V < 200$ GeV and $p_T^V > 200$ GeV. The pre-fit background expectation is indicated by the dashed blue line.

5129 **AL Studies for the diboson VZ fit**

5130 This section contains the checks and the studies done for the diboson:

- 5131 • Ranking plots;
- 5132 • Pulls, comparing the Higgs analysis and the diboson analysis, an comparing the different lepton
5133 channels;
- 5134 • Correlation among highly correlated variables;
- 5135 • Correlation between diboson and Higgs signal.

5136 Since the diboson fit is now unblindend, all the results on this section will show the results of the un-
5137 blinded results. For the time being, particular attention is given to the MVA analysis, but in the future this
5138 appendix will contain the studies on the fit for both the m_{bb} shape analysis and the MVA shape analysis.

5139 **AL.1 Ranking plots for MVA diboson analysis**

5140 Figures 523 and 524 show the ranking plots on data. In general, the ranking plot show similarities with
5141 the Higgs fit described in the bulk of the note.

Not reviewed, for internal circulation only

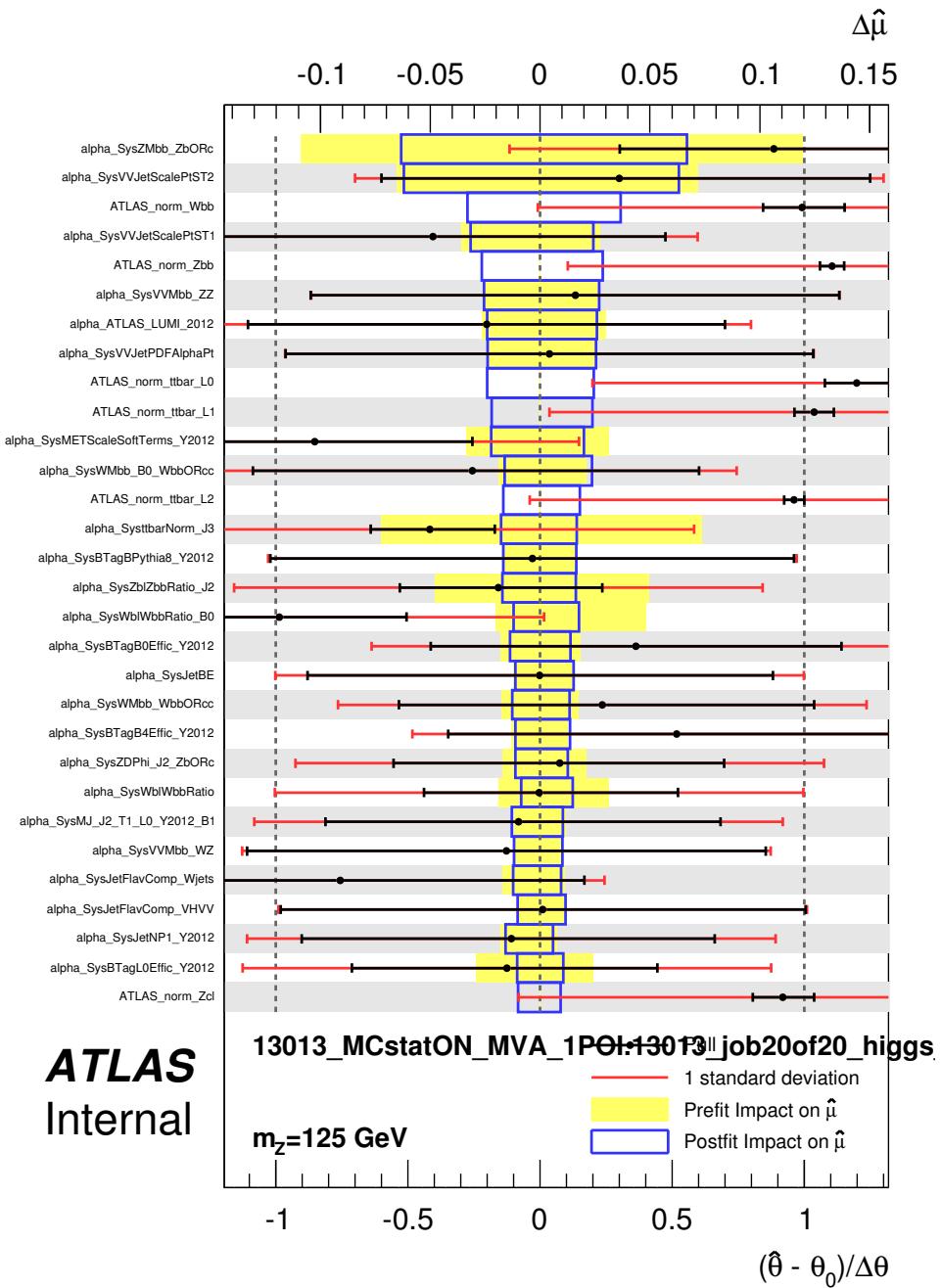


Figure 523: Ranking of systematic uncertainties in the MVA analysis for the combined fit.

Not reviewed, for internal circulation only

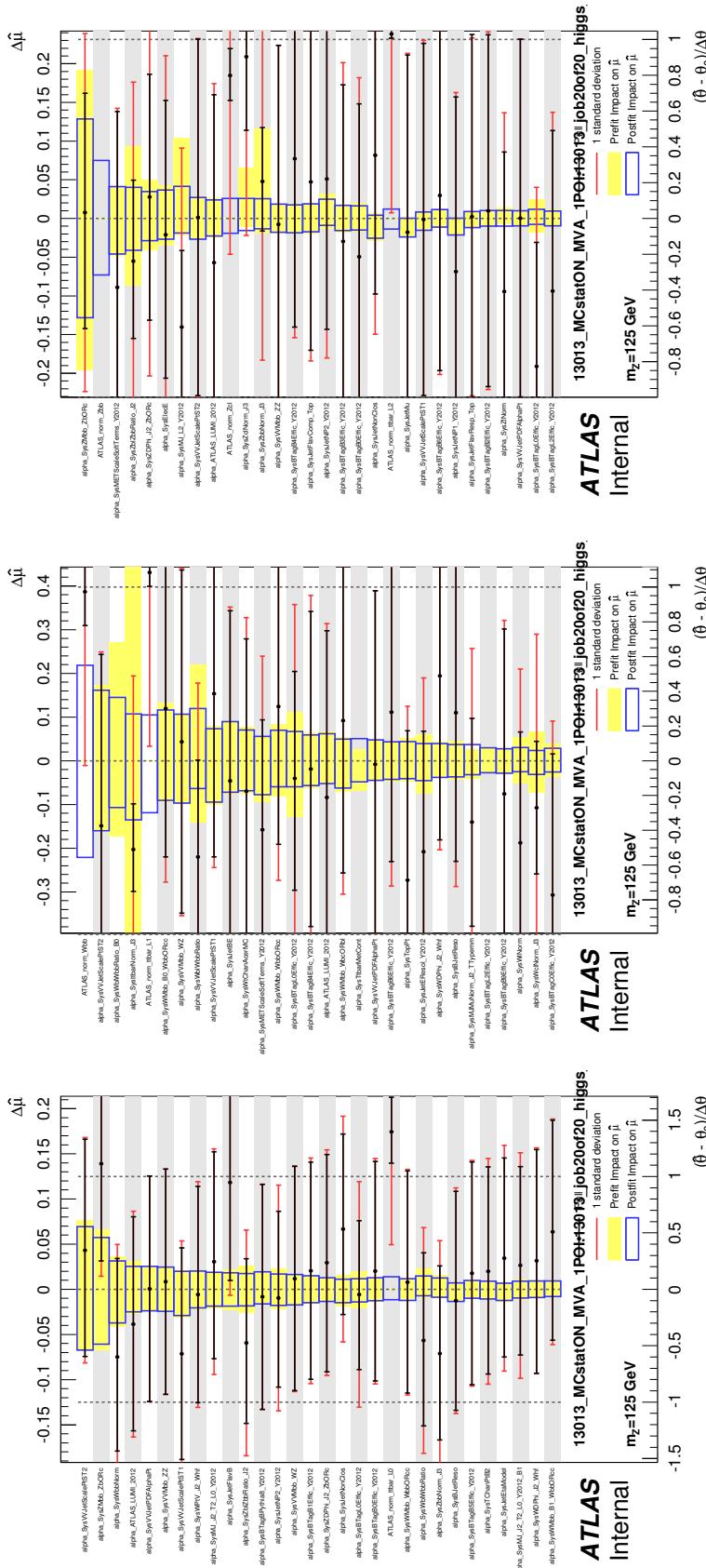


Figure 524: Ranking of systematic uncertainties in the MVA analysis for the 0-lepton, 1 lepton and 2-leptons channels.

5142 AL.2 Pulls for MVA diboson analysis

5143 The pull plots for combined fit for the diboson MVA analysis are shown in Figures 525-530. Each plot
5144 compares the result from a fit to either the observed data in the diboson fit (black) and in the Higgs fit
5145 (red) on the left, and the result of the fit for each individual lepton channel on the right. Note that the BDT
5146 functions obtained for the diboson and for the Higgs are different.

5147 AL.3 Correlation Plots for the MVA diboson fit

5148 Figure 531 shows the largest correlations in the full MVA diboson analysis. This plot is produced by
5149 selecting all NP, which have a correlation larger than 20% with any another NP. Note that the parameter
5150 of interest, μ has been included by default not because it has particularly large correlations.

5151 AL.4 Ranking plots for m_{jj} shape diboson analysis

5152 Figures 532 and 533 show the ranking plots on data. In general, the ranking plot show similarities with
5153 the Higgs fit described in the bulk of the note.

Not reviewed, for internal circulation only

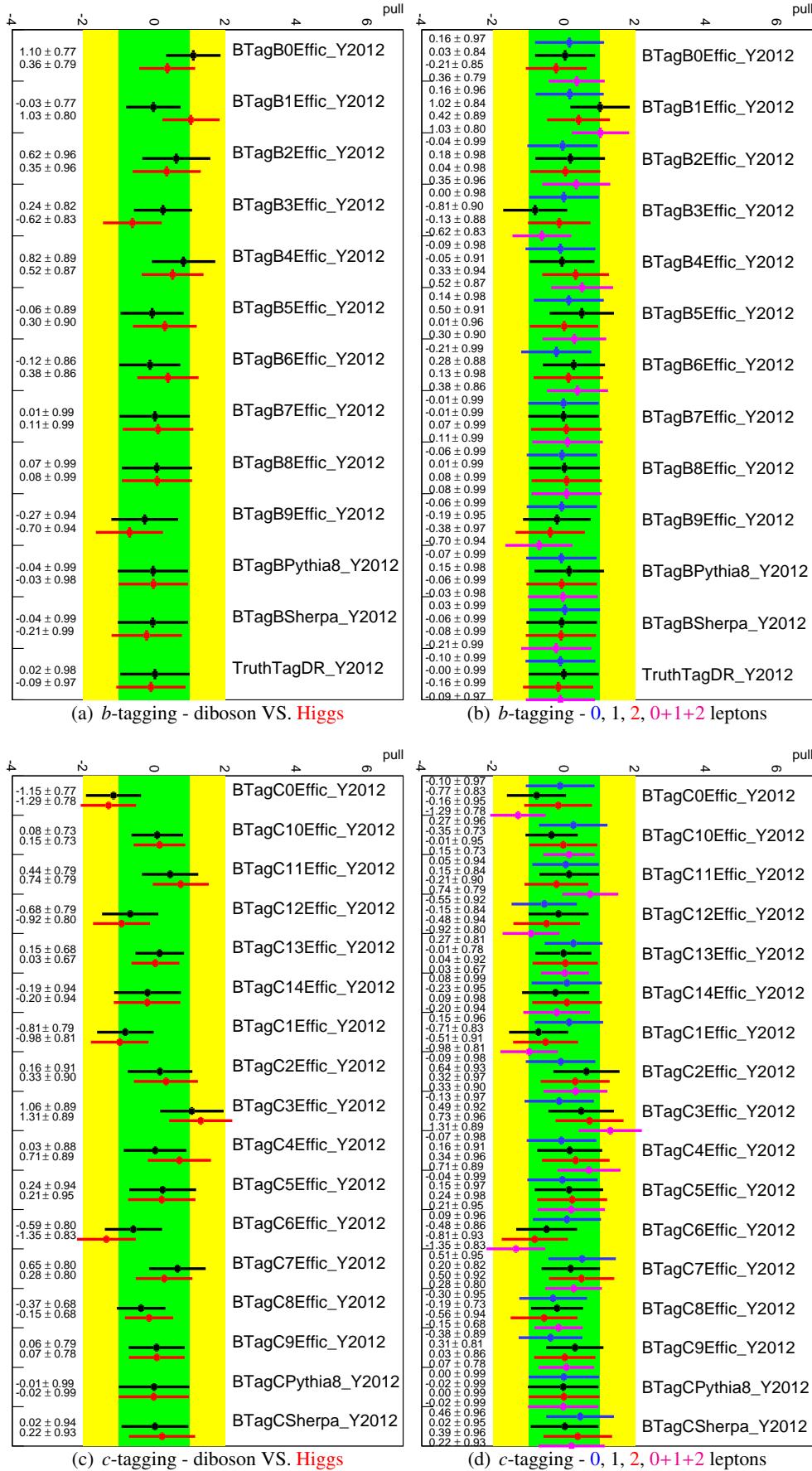


Figure 525: Pull plots for b and c tagging in the 0+1+2 lepton MVA diboson fit. The diboson fit in black is compared to the Higgs fit in red. Note that different BDT functions are used for the 2 fits. The fits to 0 lepton (blue), 1 lepton (black) and 2 leptons (red) data and the combined diboson fit to data (magenta) is shown on the right.

Not reviewed, for internal circulation only

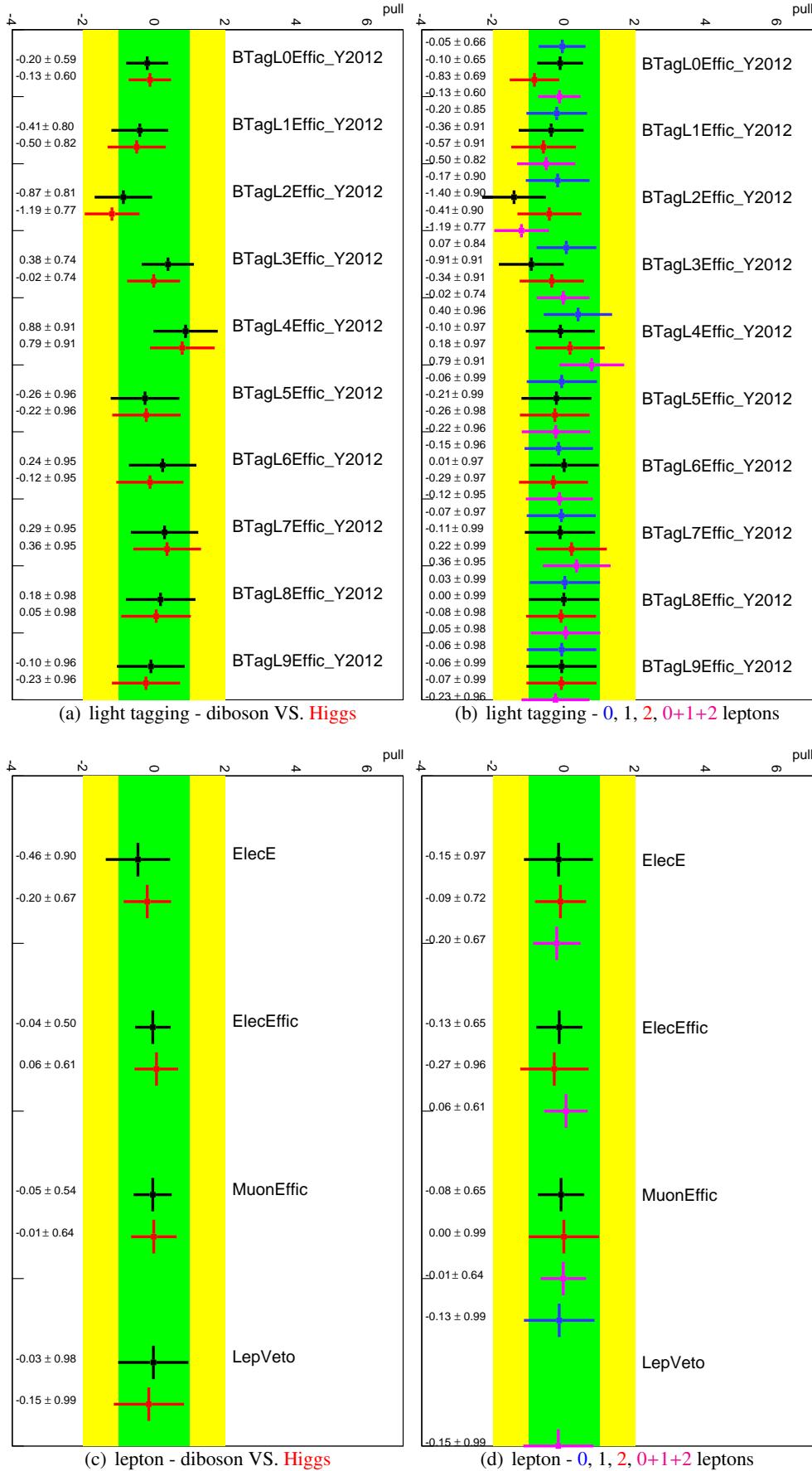


Figure 526: Pull plots for light-jet tagging and lepton related systematics in the 0+1+2 lepton MVA diboson fit. The diboson fit in black is compared to the Higgs fit in red. Note that different BDT functions are used for the 2 fits. The fits to 0 lepton (blue), 1 lepton (black) and 2 leptons (red) data and the combined diboson fit to data (magenta) is shown on the right.

Not reviewed, for internal circulation only

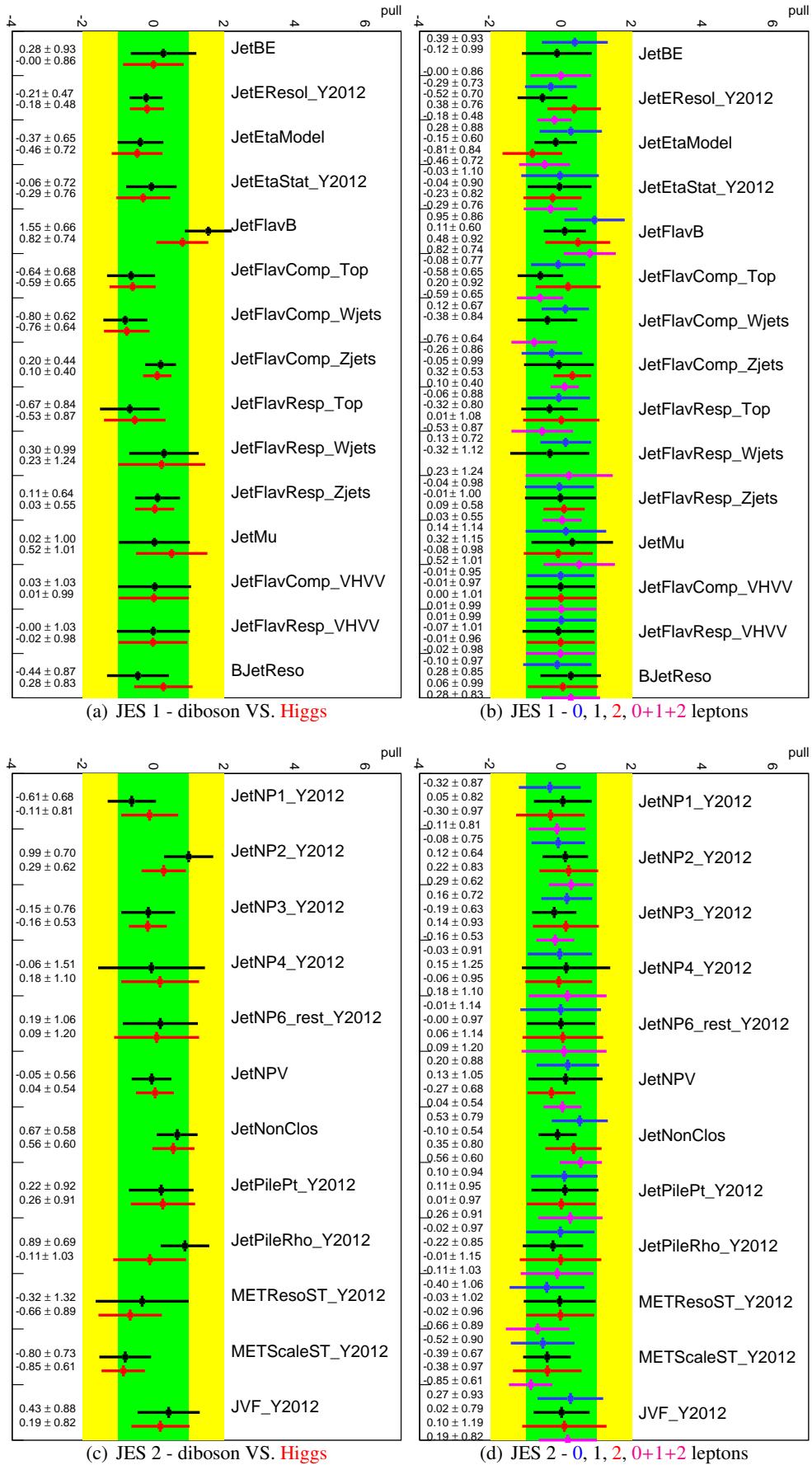


Figure 527: Pull plots for JES systematics in the 0+1+2 lepton MVA diboson fit. The diboson fit in black is compared to the Higgs fit in red. Note that different BDT functions are used for the 2 fits. The fits to 0 lepton (blue), 1 lepton (black) and 2 leptons (red) data and the combined diboson fit to data (magenta) is shown on the right.

Not reviewed, for internal circulation only

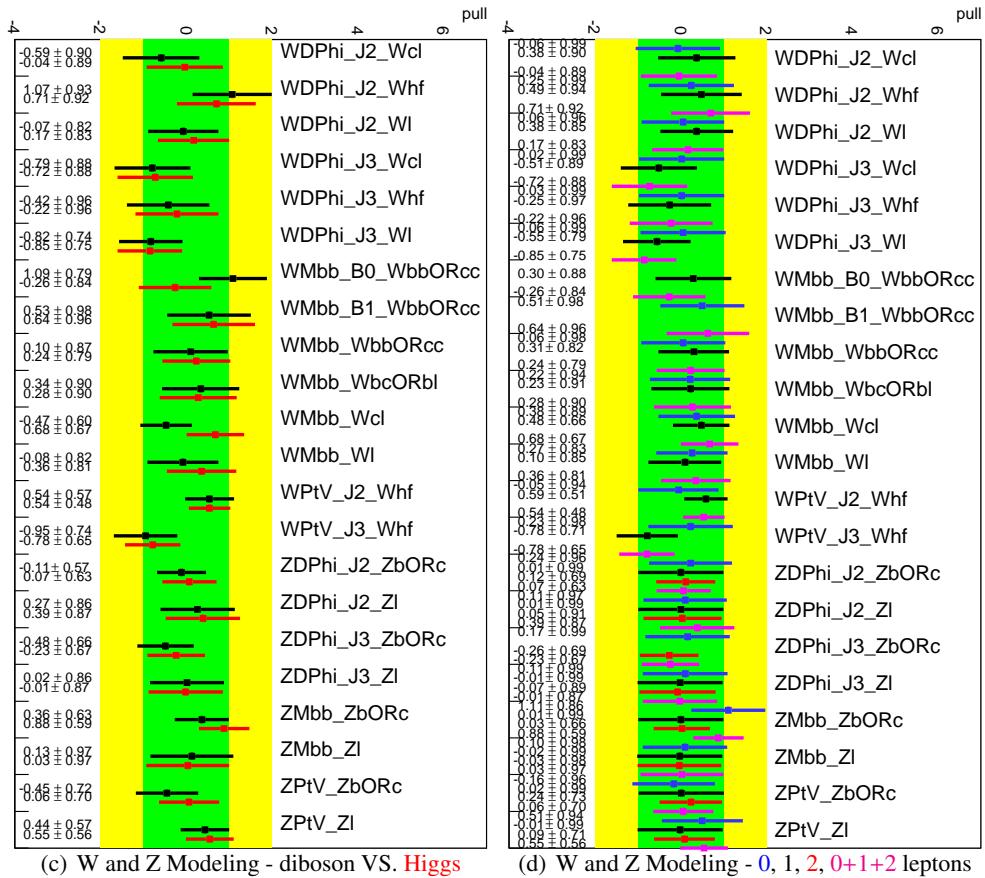
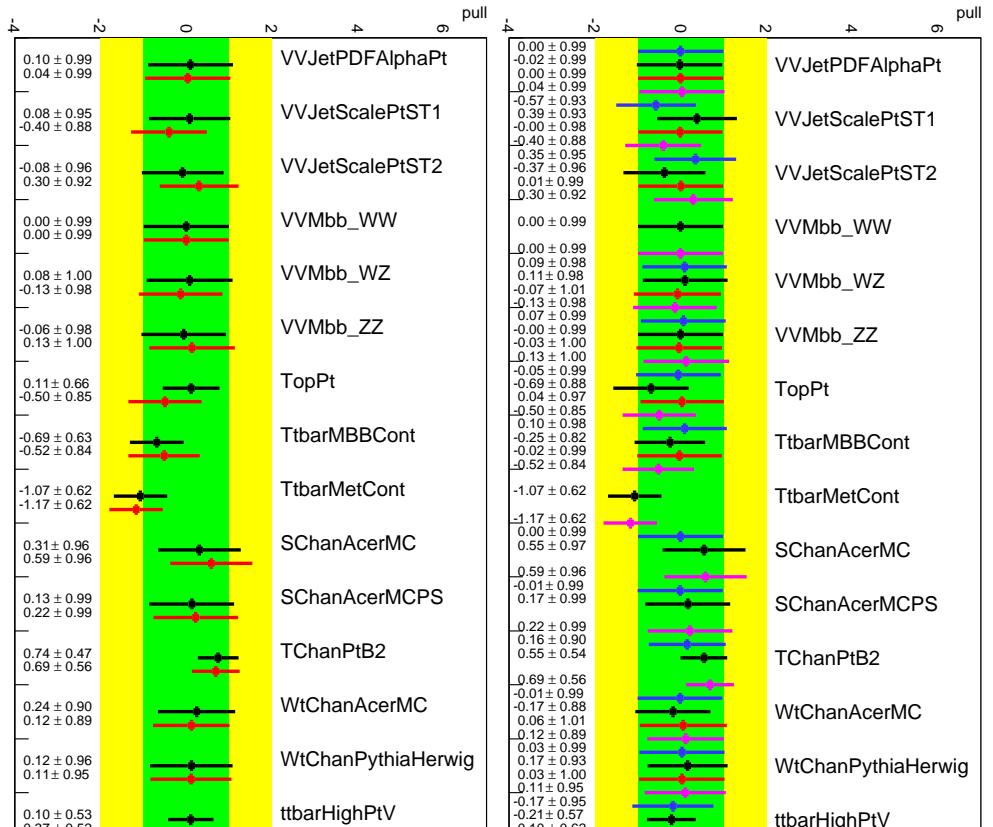


Figure 528: Pull plots for diboson/top and W/Z systematics in the 0+1+2 lepton mva diboson fit. The diboson fit in black is compared to the Higgs fit in red. Note that different BDT functions are used for the 2 fits. The fits to 0 lepton (blue), 1 lepton (black) and 2 leptons (red) data and the combined diboson fit to data (magenta) is shown on the right.

Not reviewed, for internal circulation only

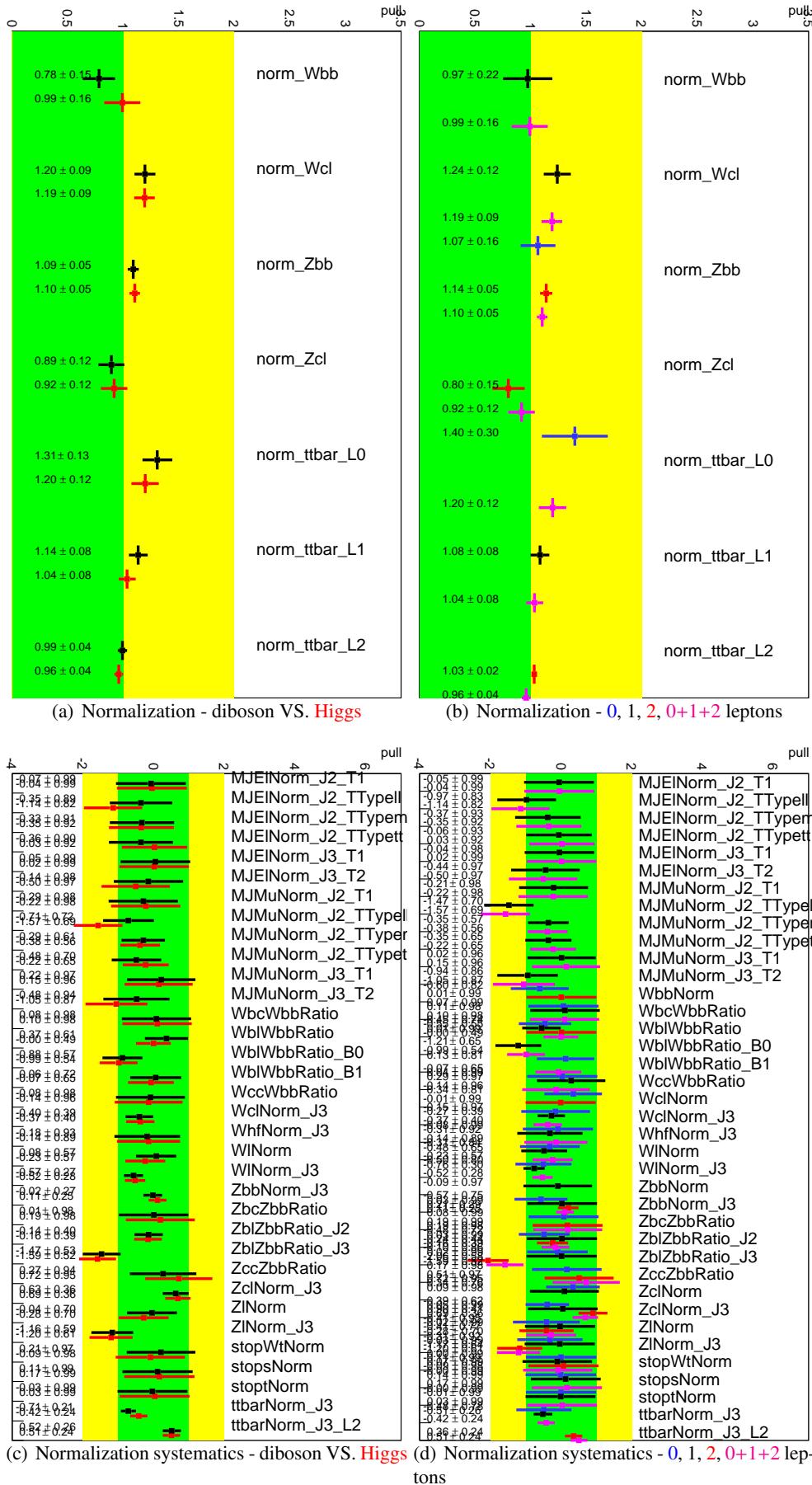


Figure 529: Pull plots for normalization in the 0+1+2 lepton MVA diboson fit. The diboson fit in black is compared to the Higgs fit in red. Note that different BDT functions are used for the 2 fits. The fits to 0 lepton (blue), 1 lepton (black) and 2 leptons (red) data and the combined diboson fit to data (magenta) is shown on the right.

Not reviewed, for internal circulation only

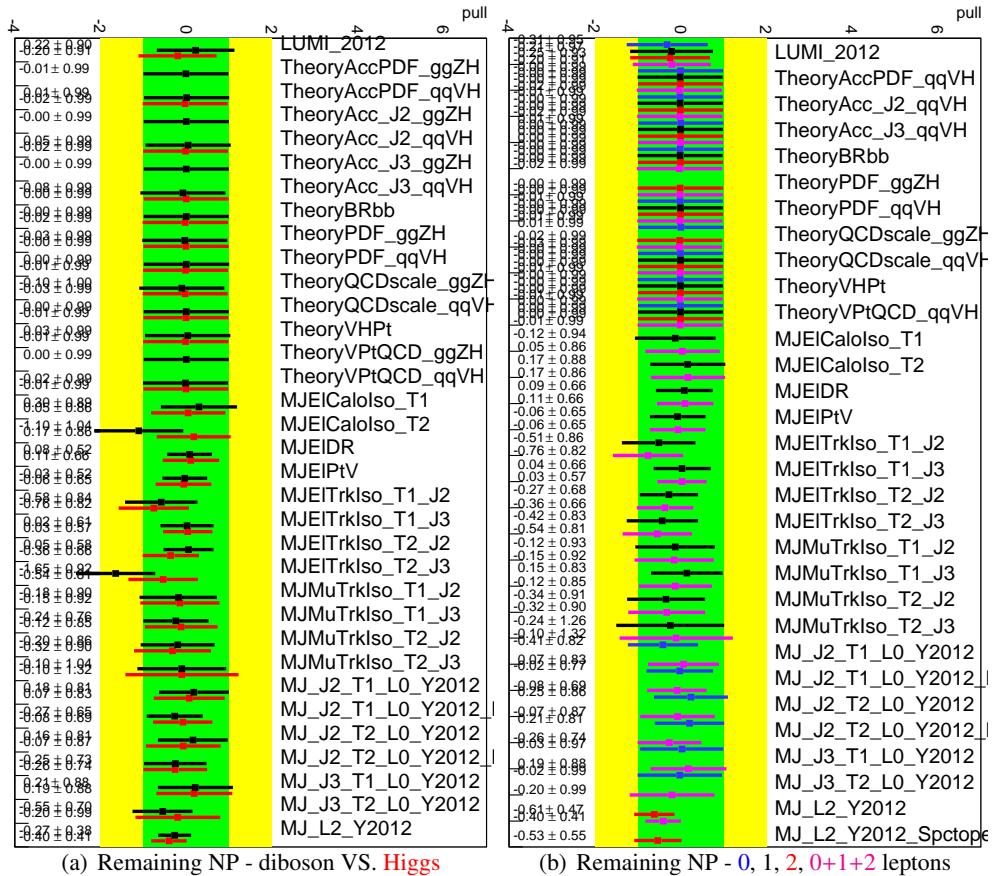


Figure 530: Pull plots for remaining systematics in the 0+1+2 lepton MVA diboson fit. The diboson fit in black is compared to the Higgs fit in red. Note that different BDT functions are used for the 2 fits. The fits to 0 lepton (blue), 1 lepton (black) and 2 leptons (red) data and the combined diboson fit to data (magenta) is shown on the right.

July

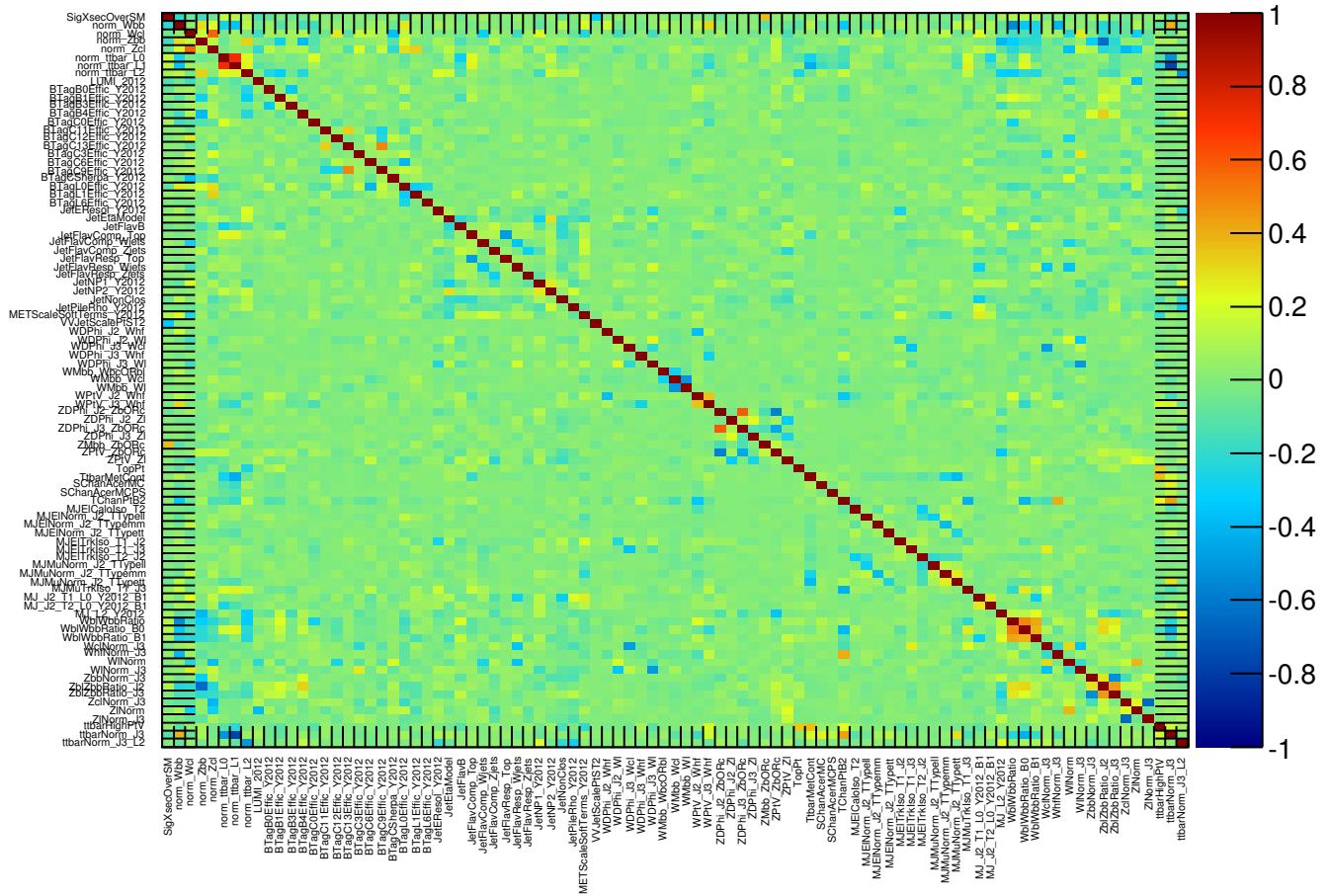


Figure 531: The correlation of all NP with a correlation larger than 20% in the 0+1+2 lepton MVA diboson fit. Note that the parameter of interest, μ has been included by default not because it has particularly large correlations.

Not reviewed, for internal circulation only

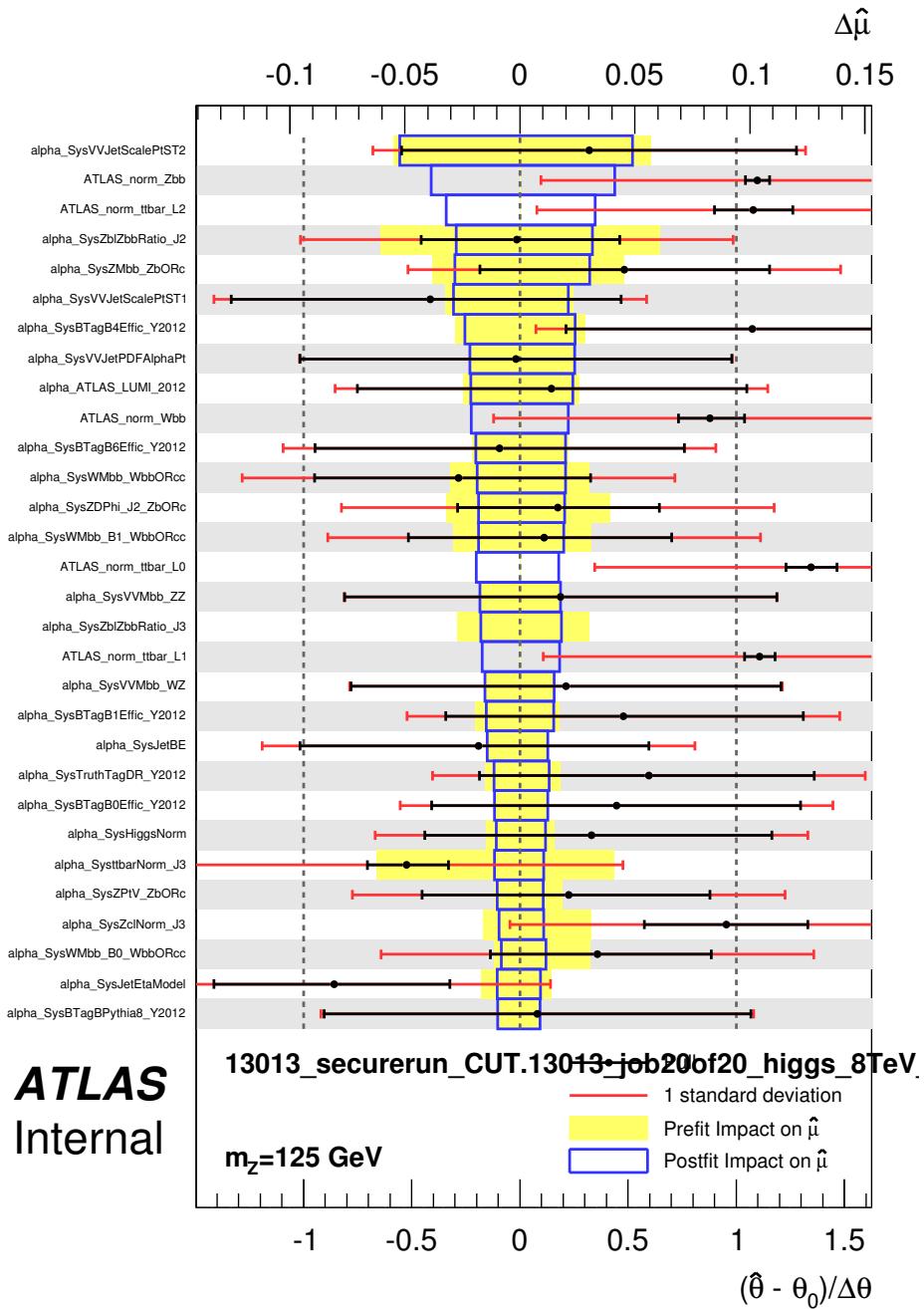


Figure 532: Ranking of systematic uncertainties in the m_{jj} shape analysis for the combined fit.

Not reviewed, for internal circulation only

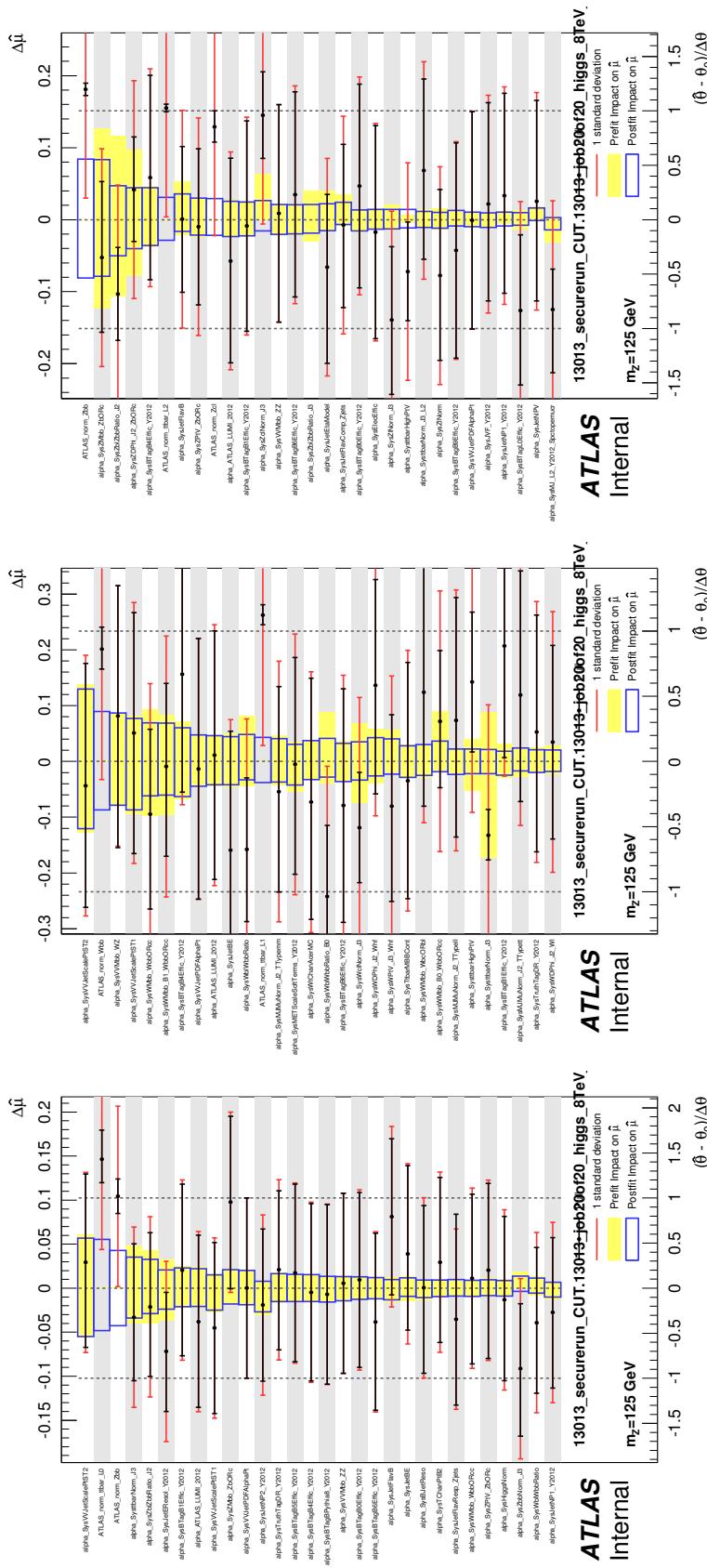


Figure 533: Ranking of systematic uncertainties in the m_{ij} shape analysis for the 0-lepton, 1 lepton and 2-leptons channels.

5154 AL.5 Pulls for m_{jj} shape diboson analysis

5155 The pull plots for combined fit for the diboson m_{jj} shape analysis are shown in Figures 534-539. Each
5156 plot compares the result from a fit to either the observed data in the diboson fit (black) and in the Higgs
5157 fit (red) on the left, and the result of the fit for each individual lepton channel on the right. Note that as
5158 a result of the re-binning strategy, the histograms used in the diboson fit and the Higgs fit have different
5159 binning.

5160 AL.6 Correlation Plots for the m_{jj} diboson fit

5161 Figure 540 shows the largest correlations in the full m_{jj} shape diboson analysis. This plot is produced by
5162 selecting all NP, which have a correlation larger than 20% with any other NP. Note that the parameter
5163 of interest, μ has been included by default not because it has particularly large correlations.

Not reviewed, for internal circulation only

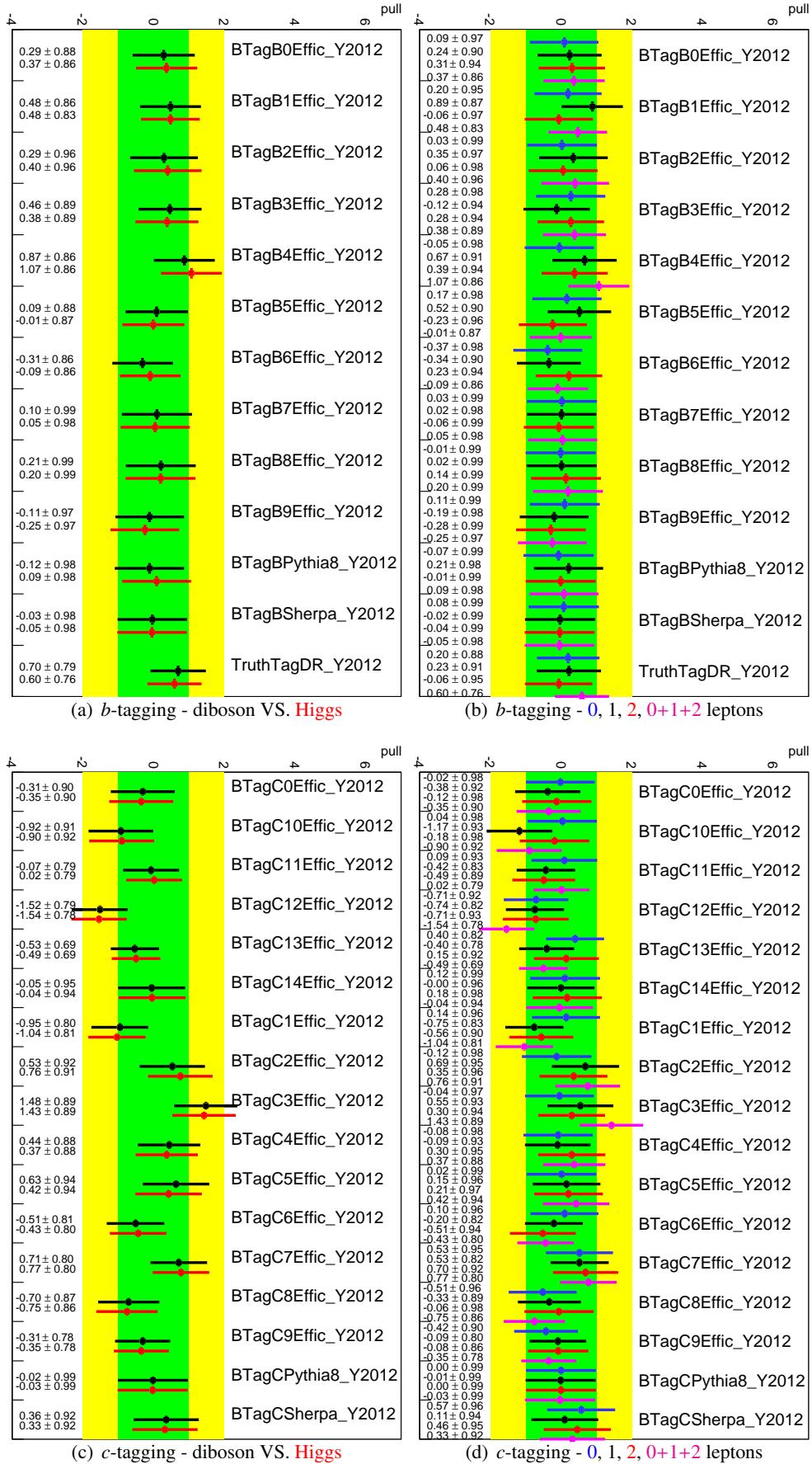


Figure 534: Pull plots for b and c tagging in the $0+1+2$ lepton m_{jj} diboson fit. The diboson fit in black is compared to the Higgs fit in red. Note that different binnings are used for the 2 fits. The fits to 0 lepton (blue), 1 lepton (black) and 2 leptons (red) data and the combined diboson fit to data (magenta) is shown on the right.

Not reviewed, for internal circulation only

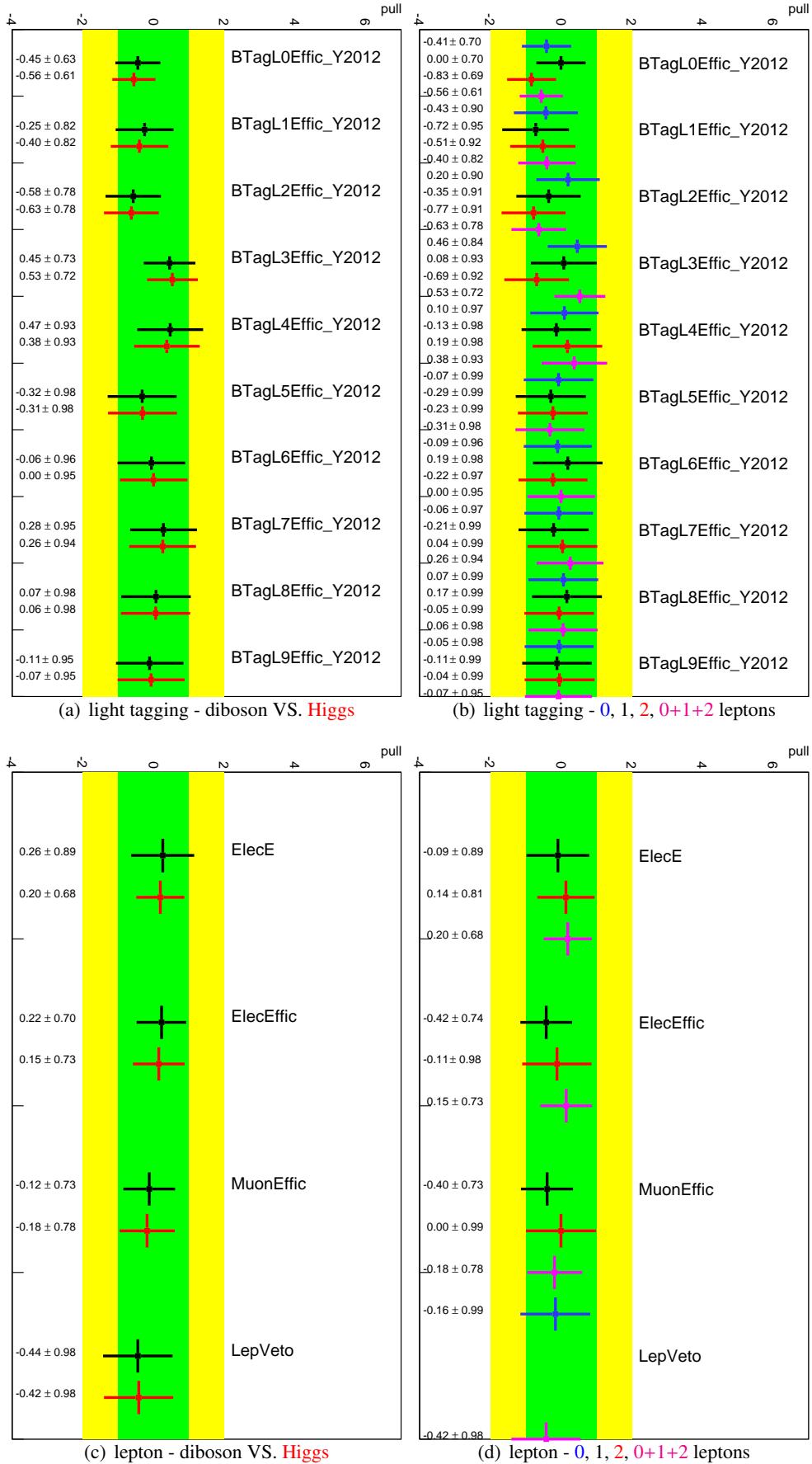


Figure 535: Pull plots for light-jet tagging and lepton related systematics in the $0+1+2$ lepton m_{jj} shape diboson fit. The diboson fit in black is compared to the Higgs fit in red. Note that different binnings are used for the 2 fits. The fits to 0 lepton (blue), 1 lepton (black) and 2 leptons (red) data and the combined diboson fit to data (magenta) is shown on the right.

Not reviewed, for internal circulation only

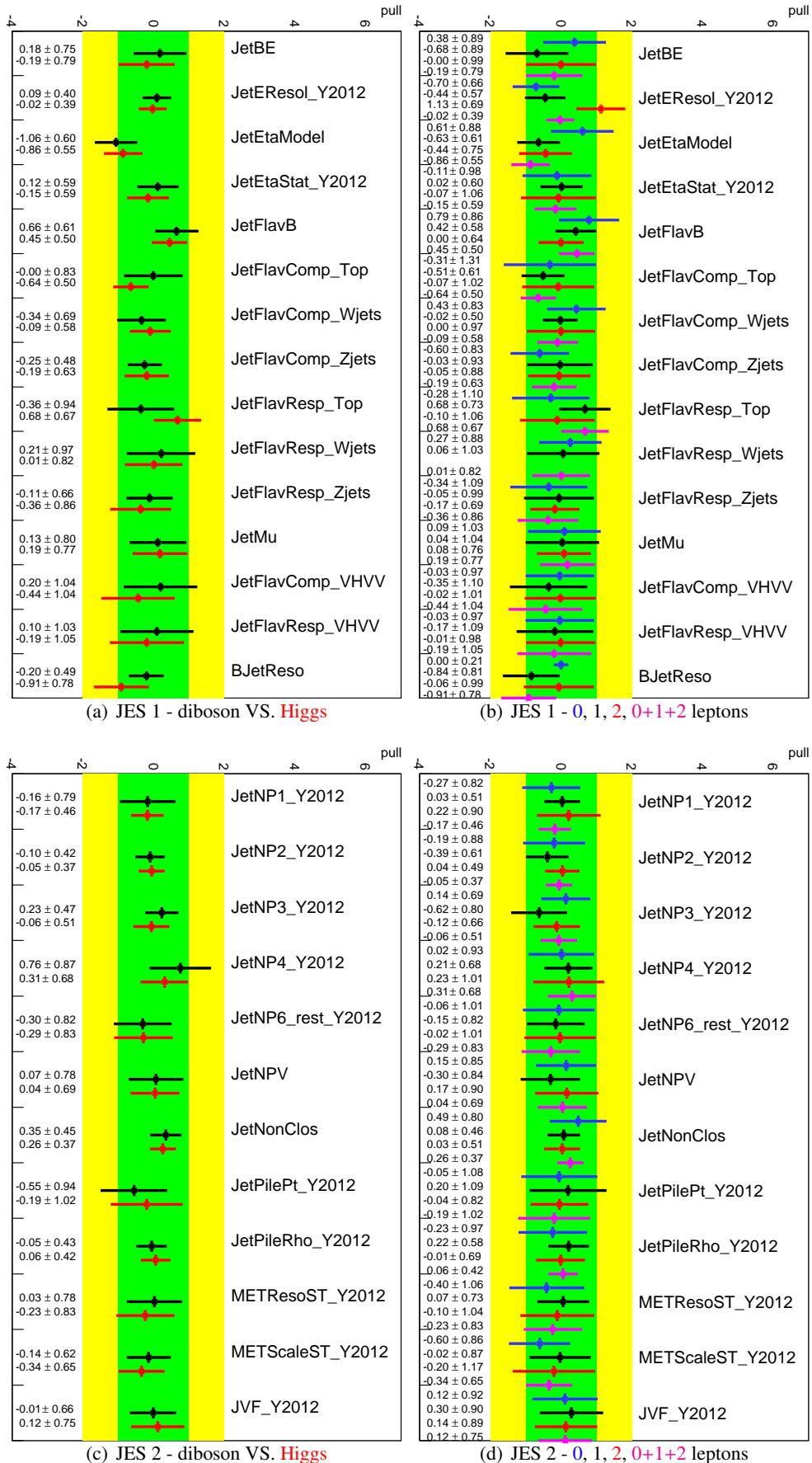


Figure 536: Pull plots for JES systematics in the 0+1+2 lepton m_{jj} shape diboson fit. The diboson fit in black is compared to the Higgs fit in red. Note that different binnings are used for the 2 fits. The fits to 0 lepton (blue), 1 lepton (black) and 2 leptons (red) data and the combined diboson fit to data (magenta) is shown on the right.

Not reviewed, for internal circulation only

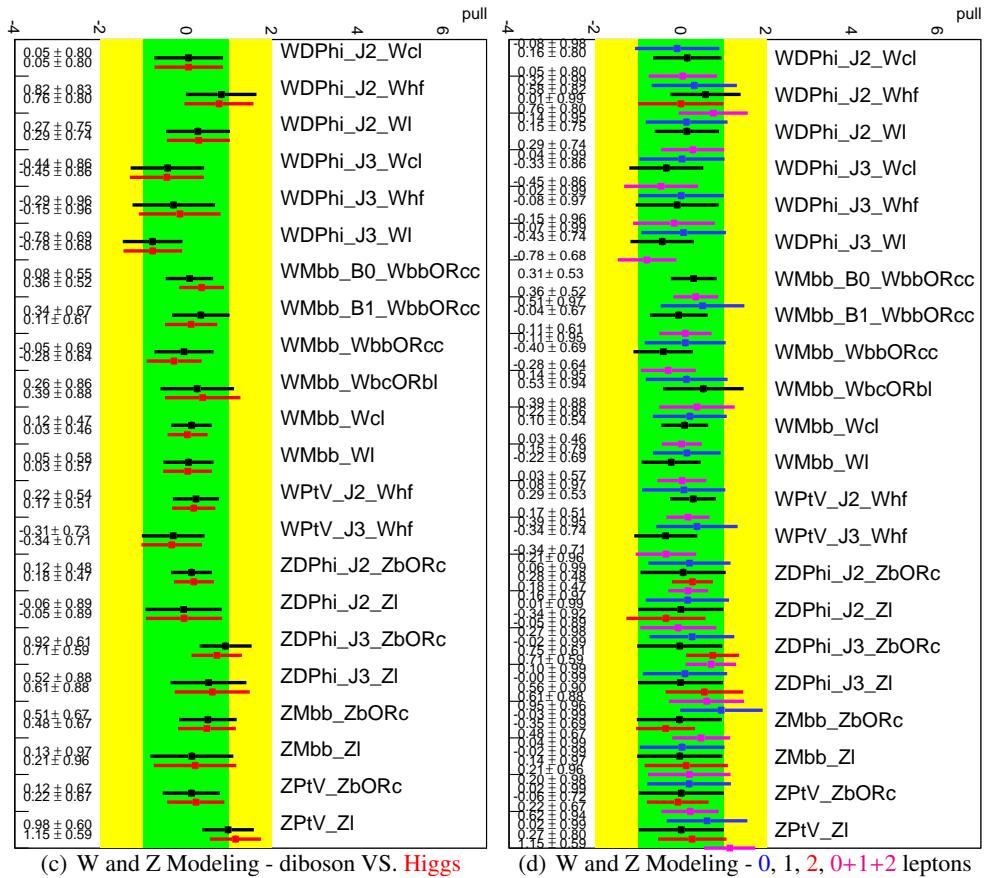
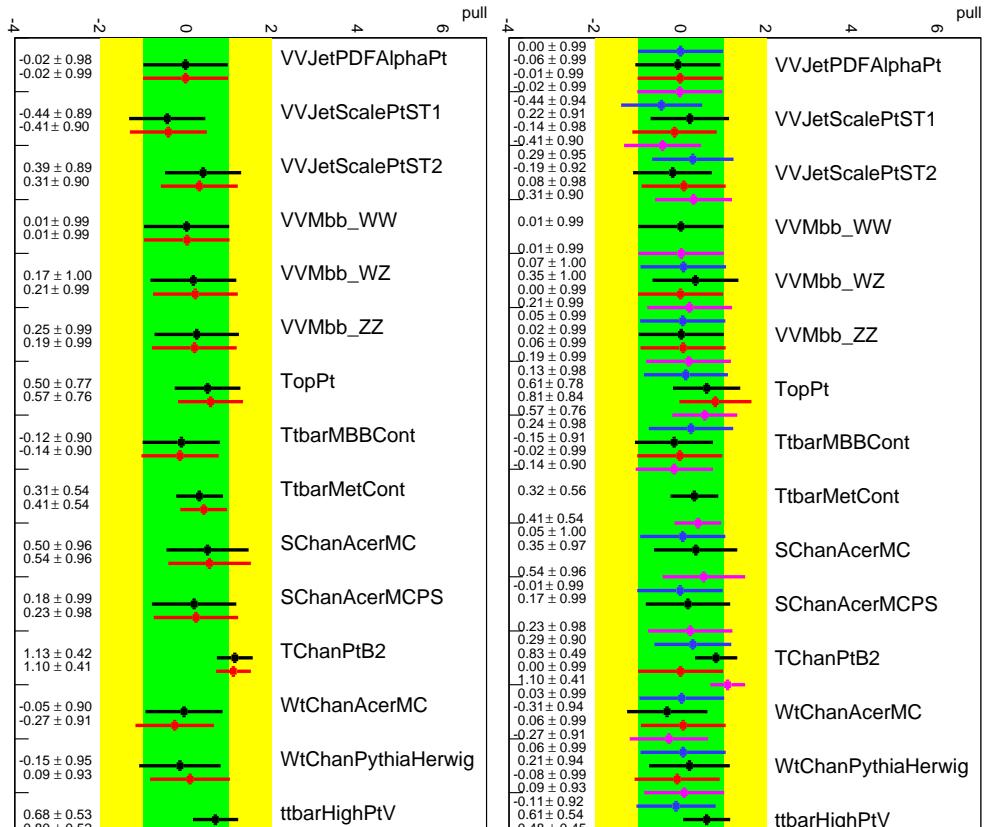


Figure 537: Pull plots for diboson/top and W/Z systematics in the 0+1+2 lepton m_{jj} shape diboson fit. The diboson fit in black is compared to the Higgs fit in red. Note that different binnings are used for the 2 fits. The fits to 0 lepton (blue), 1 lepton (black) and 2 leptons (red) data and the combined diboson fit to data (magenta) is shown on the right.

Not reviewed, for internal circulation only

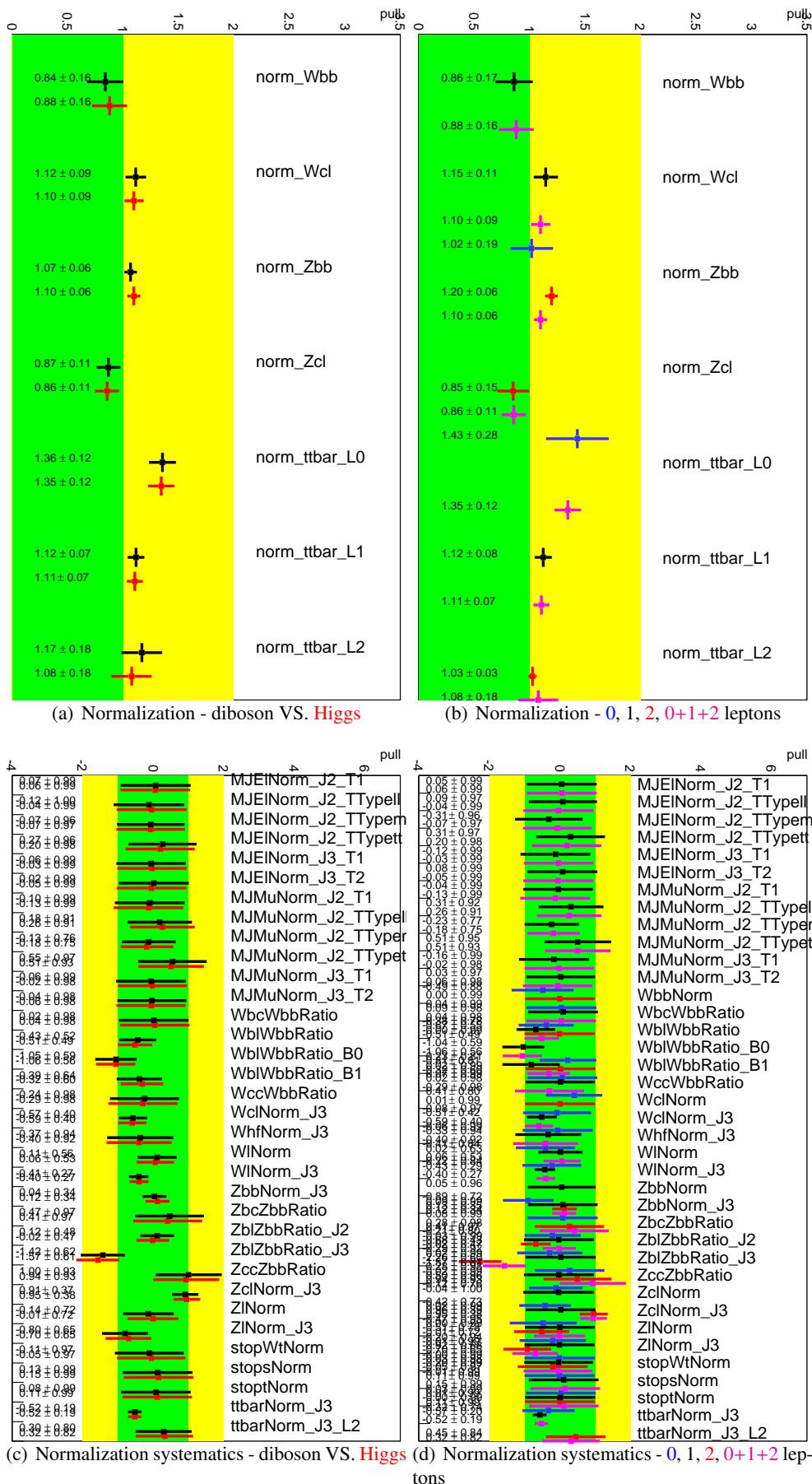


Figure 538: Pull plots for normalization in the 0+1+2 lepton m_{jj} shape diboson fit. The diboson fit in black is compared to the Higgs fit in red. Note that different binnings are used for the 2 fits. The fits to 0 lepton (blue), 1 lepton (black) and 2 leptons (red) data and the combined diboson fit to data (magenta) is shown on the right.

Not reviewed, for internal circulation only

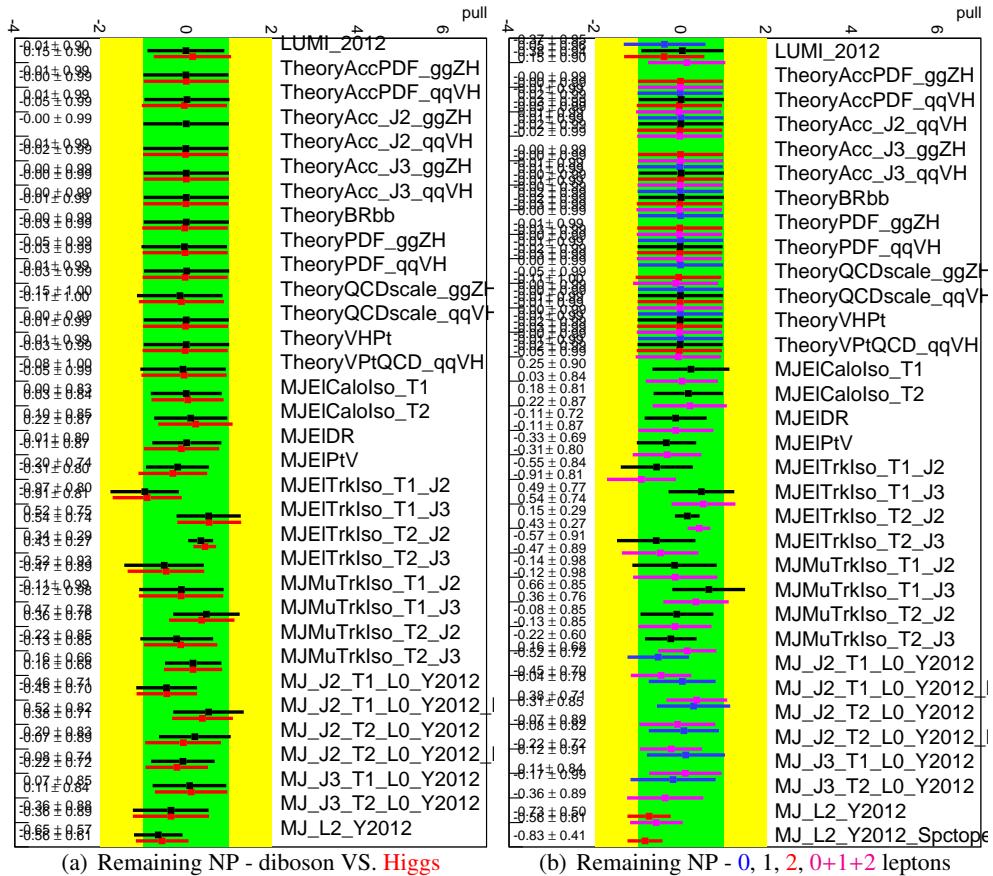


Figure 539: Pull plots for remaining systematics in the $0+1+2$ lepton m_{jj} shape diboson fit. The diboson fit in black is compared to the Higgs fit in red. Note that different binnings are used for the 2 fits. The fits to 0 lepton (blue), 1 lepton (black) and 2 leptons (red) data and the combined diboson fit to data (magenta) is shown on the right.

in only

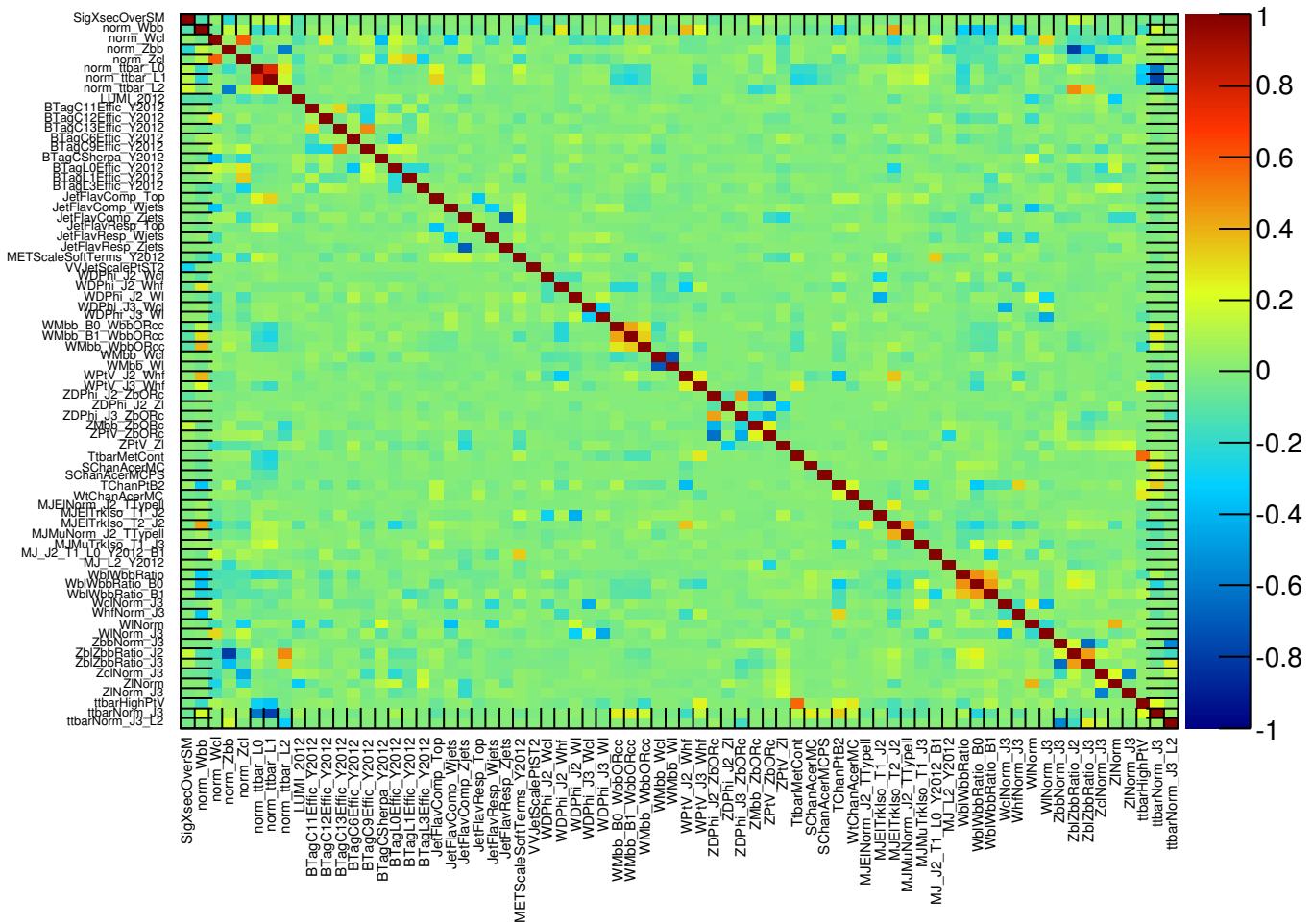


Figure 540: The correlation of all NP with a correlation larger than 20% in the 0+1+2 lepton m_{jj} shape diboson fit. Note that the parameter of interest, μ has been included by default not because it has particularly large correlations.

5164 AL.7 Correlation between diboson and Higgs signal strength

5165 To check the correlation between the Higgs and the diboson strength , we generate one workspace from
5166 the Higgs MVA distributions, in which both the Higgs and the diboson have floating normalization: μ_H
5167 and μ_{VZ} , and we perform fits on the Asimov dataset. The result, for each lepton channel, and for the
5168 combination 0+1+2 leptons is shown in Figure 542. In general the correlation is small.

Not reviewed, for internal circulation only

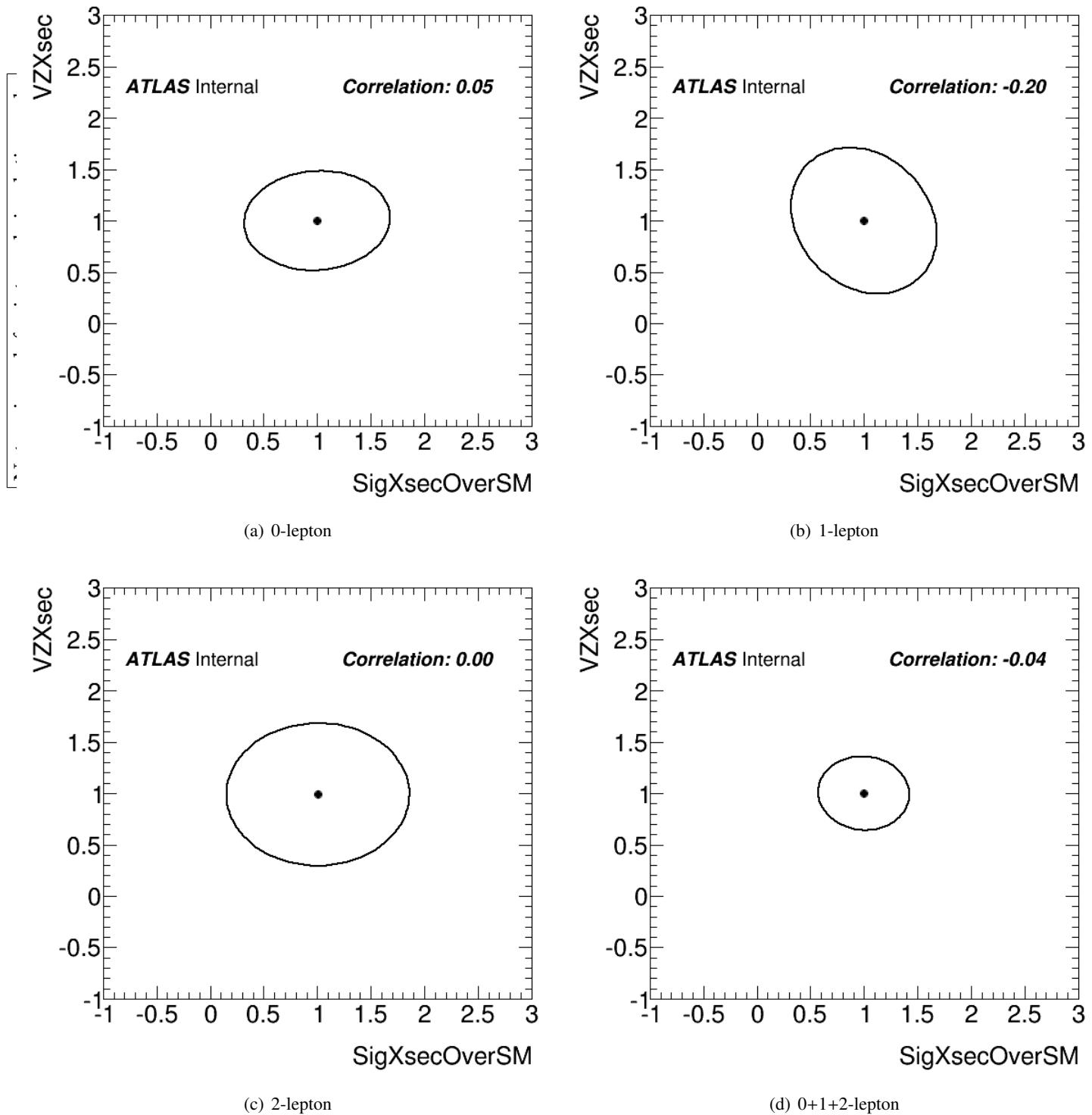


Figure 541: The correlation of Higgs and diboson VZ signal strength in the MVA fit for 0, 1, 2 and 0+1+2 lepton channels.

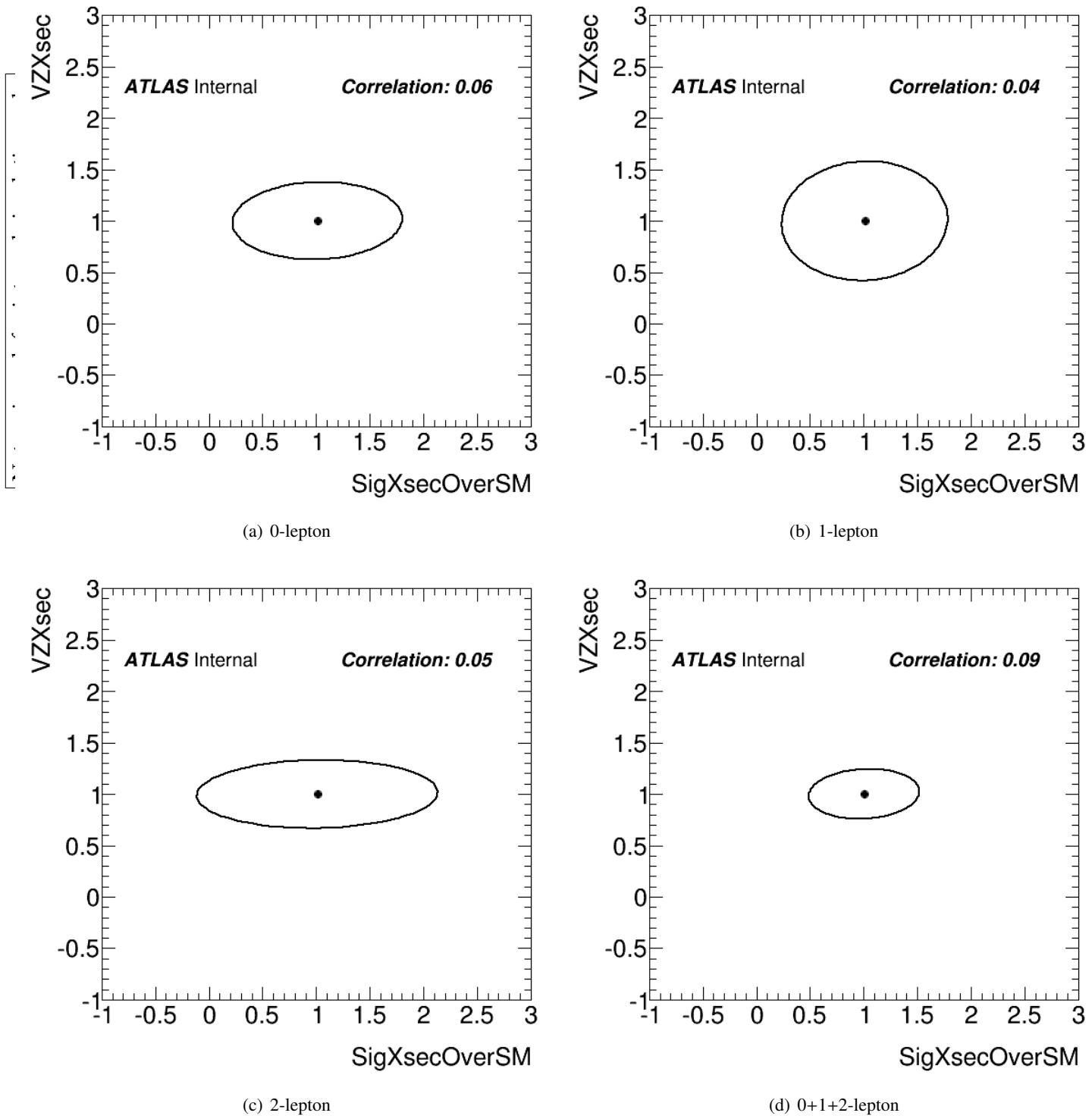


Figure 542: The correlation of Higgs and diboson VZ signal strength in the m_{jj} shape fit for 0, 1, 2 and 0+1+2 lepton channels.

5169 AL.8 Diboson MVA post fit plots

5170 In the following sections post-fit plots corresponding to fits to the data for the MVA analysis are presented.
5171 In all cases the MC expectations have been adapted to the pulls from the data in the combined 0+1+2
5172 lepton fit. As a comparison, the total nominal background prediction is indicated by the dashed blue
5173 curve. Only statistical uncertainties are indicated.

5174 In Figures 543, 544 and 545 shown the post-fit distribution for the variables used in the MVA shape
5175 analysis for the 0, 1 and 2-lepton channel respectively in the various 2-tag categories in different p_T^V bins.

Not reviewed, for internal circulation only

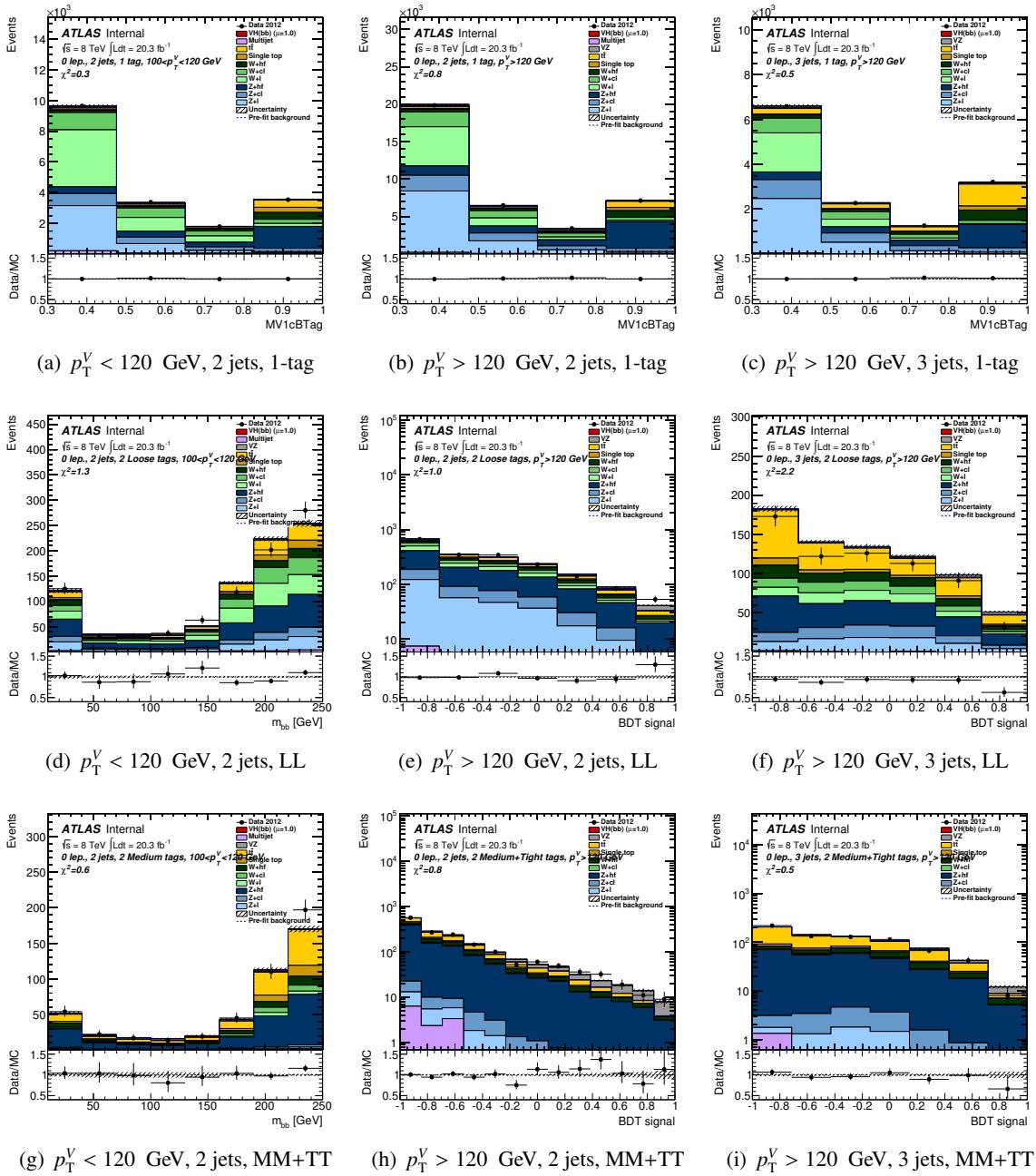


Figure 543: Post-fit plots for MVA distribution in 0-lepton events with 1 b-tag (MV1c is fit here), LL and $MM + TT$ b-tags in the 0+1+2 lepton fit. The pre-fit background expectation is indicated by the dashed blue line. Only statistical uncertainties are indicated.

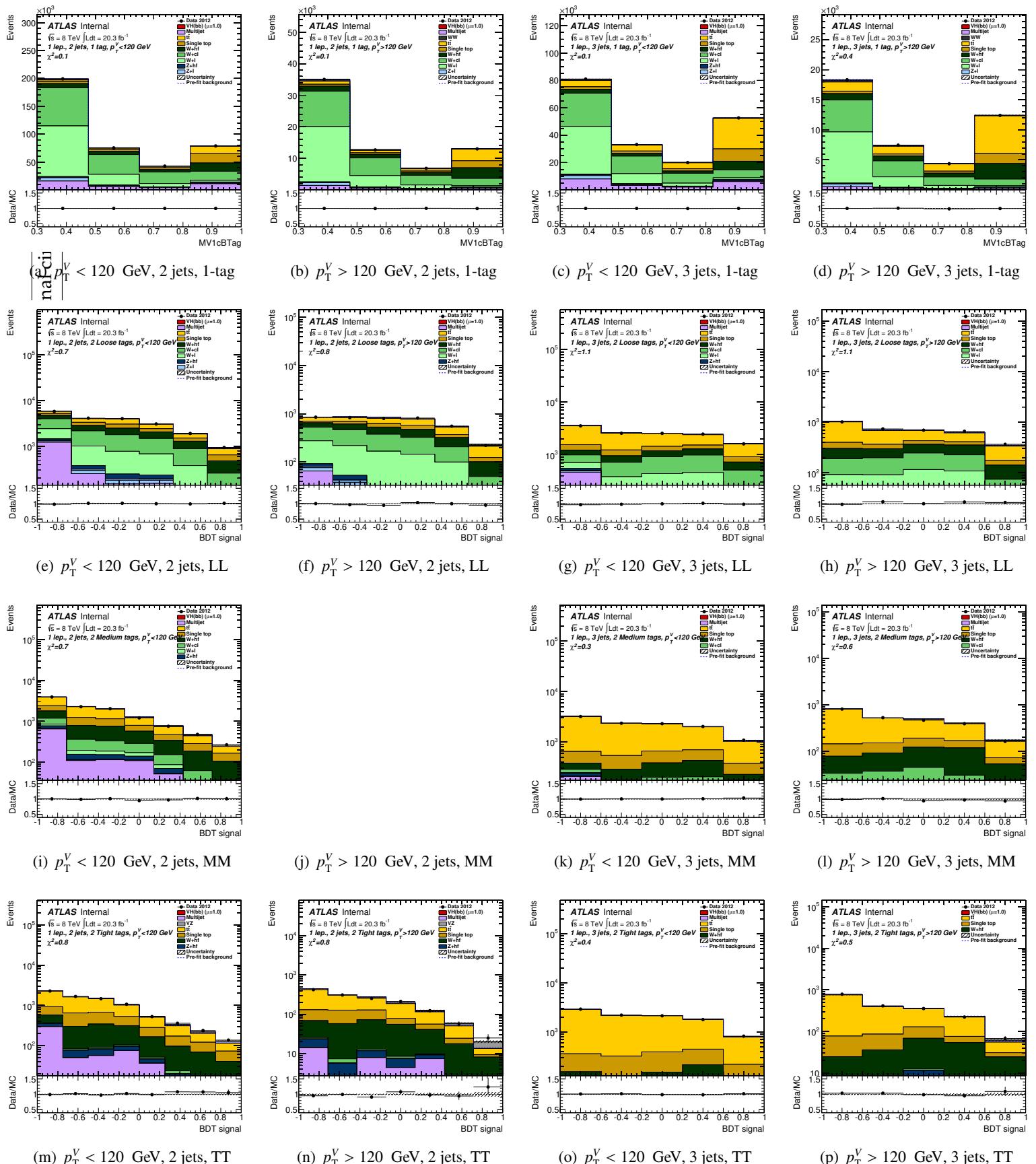


Figure 544: Post-fit plots for mva distribution in 1-lepton 2-jet and 3-jets, $p_T^V < 120$ GeV and $p_T^V > 120$ GeV events with 1 b-tag (MV1c is fit here), LL, MM and TT b-tags in the 0+1+2 lepton fit. The pre-fit background expectation is indicated by the dashed blue line. Only statistical uncertainties are indicated.

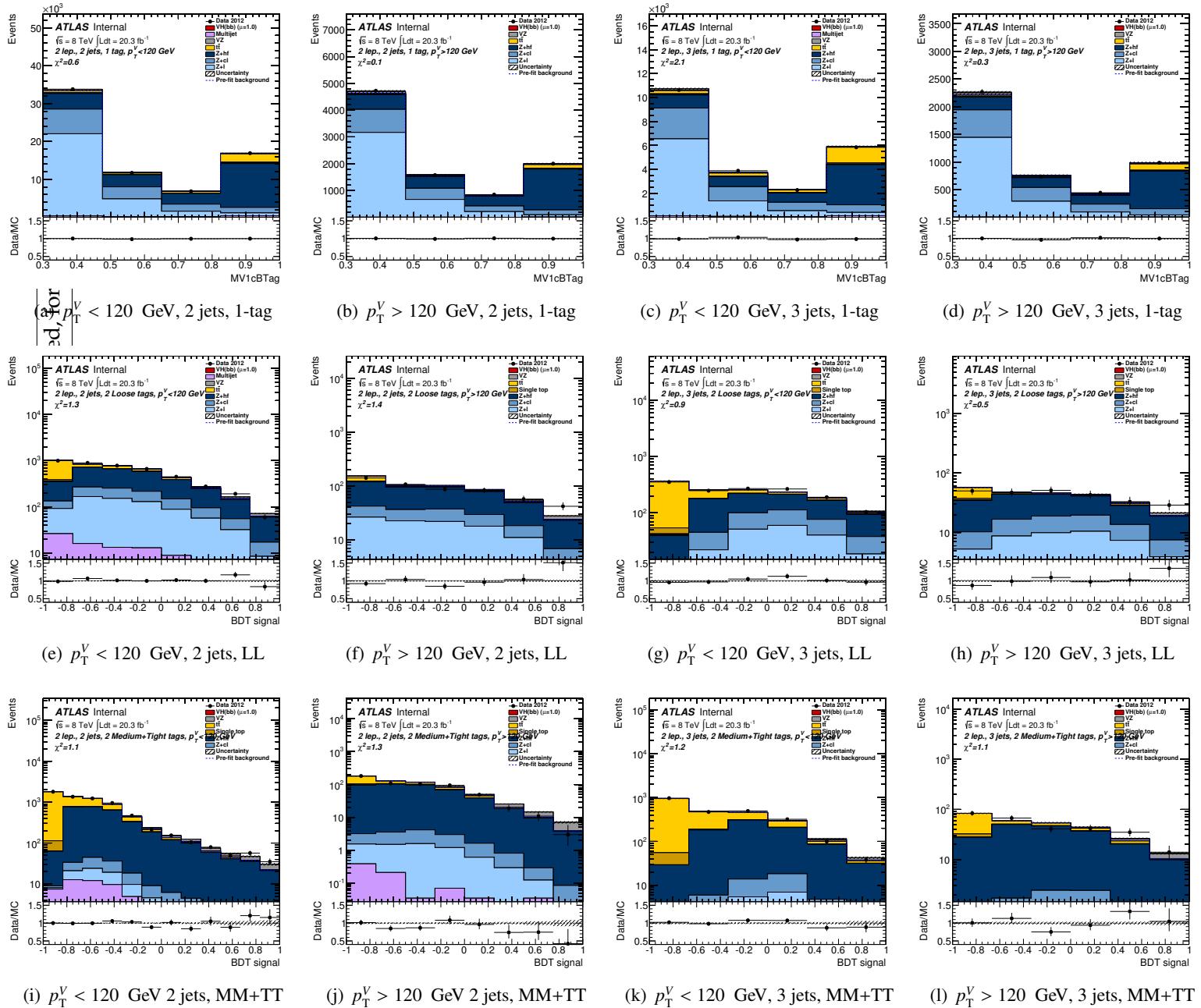


Figure 545: Post-fit plots for MVA distribution in 2-lepton 2-jet and 3-jets , $p_T^V < 120$ GeV (left) and $p_T^V > 120$ GeV (right) events with 1 b-tag (MV1c is fit here), LL and MM + TT b-tags in the 0+1+2 lepton fit. The pre-fit background expectation is indicated by the dashed blue line. Only statistical uncertainties are indicated.

AL.9 Diboson dijet Mass Analysis Post Fit Plots

In the following sections post-fit plots corresponding to unconditionnal μ fits to the data for the dijet mass analysis for the diboson search are presented. In all cases the MC expectations have been adapted to the pulls from the data in the combined 0+1+2 lepton fit. As a comparison, the total nominal background prediction is indicated by the dashed blue curve.

In Figures 546 - 548, 549 - 551, 552 - 74 post-fit plots for the m_{bb} shape analysis are shown for the 0, 1 and 2-lepton channel respectively in the various 1-tag and 2-tag categories in different p_T^V bins.

Not reviewed, for internal circulation only

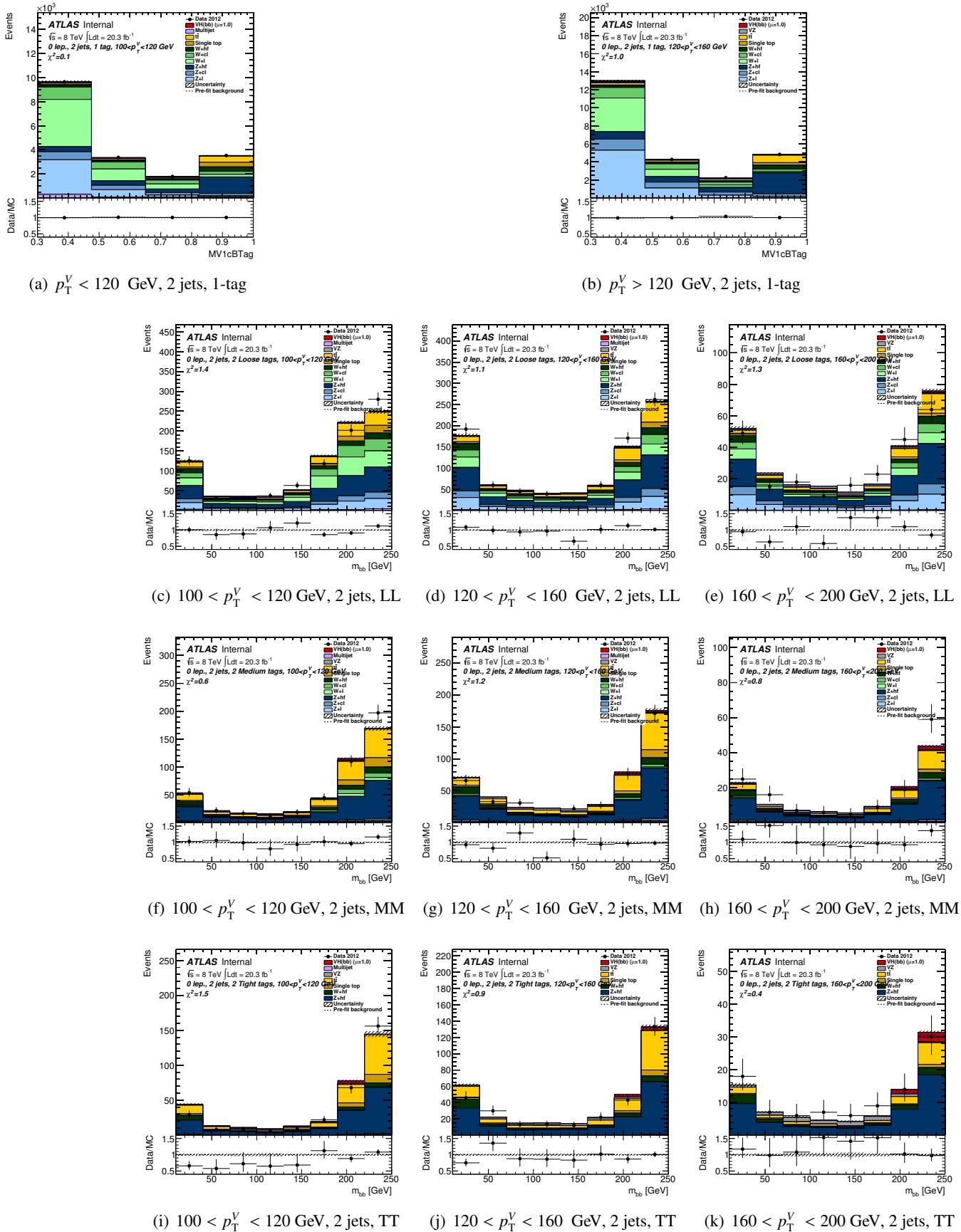


Figure 546: Post diboson fit plots for m_{jj} distribution in 0-lepton events in the 1-tag (where mv1c is used in the fit) LL , MM and TT tag categories for the 2-jets events. Plots are shown for $100 < p_T^V < 120$ GeV, $120 < p_T^V < 160$ GeV and $160 < p_T^V < 200$ GeV. The pre-fit background expectation is indicated by the dashed blue line.

Not reviewed, for internal circulation only

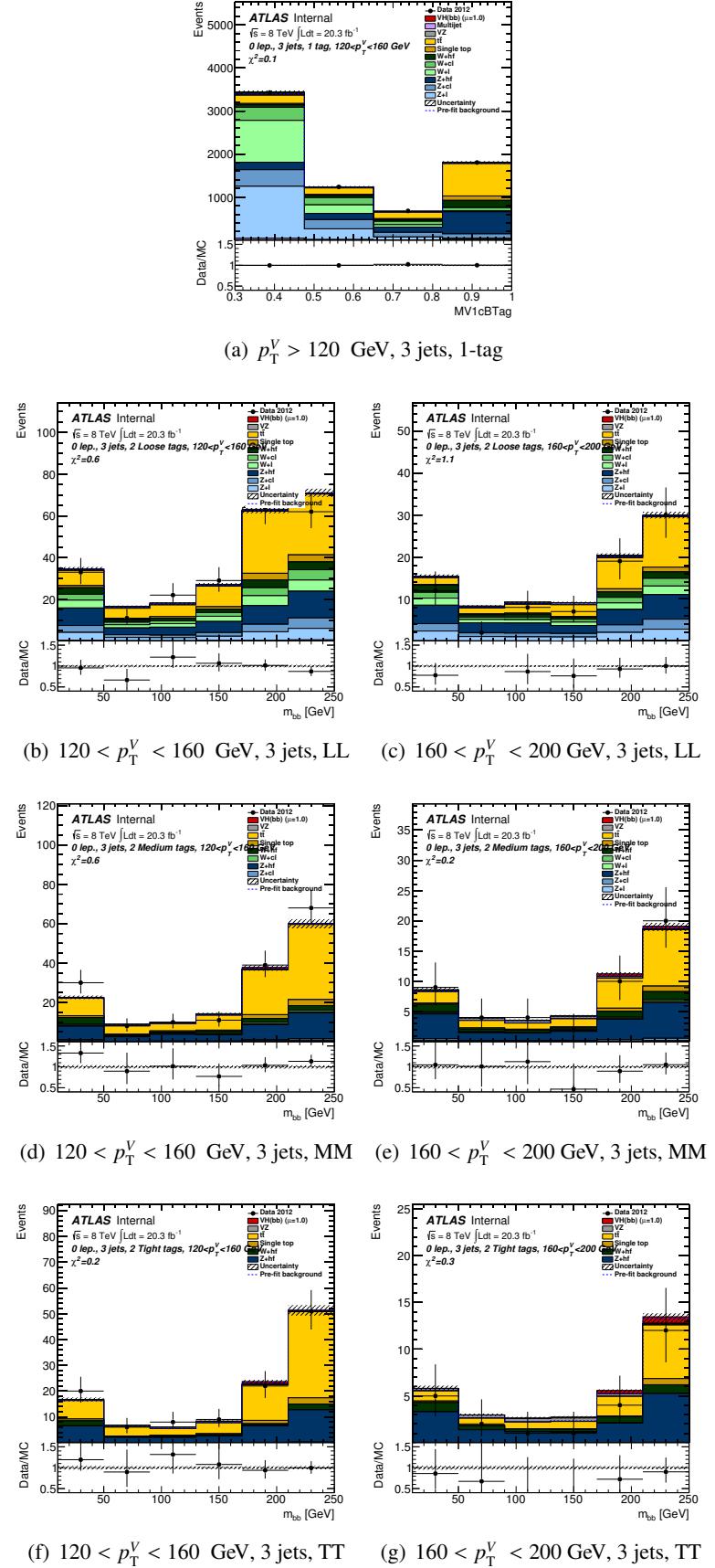


Figure 547: Post diboson fit plots for m_{jj} distribution in 0-lepton events in the 1-tag (where mv1c is used in the fit) LL , MM and TT tag categories for the 3-jets events. Plots are shown for $120 < p_T^V < 160$ GeV and $160 < p_T^V < 200$ GeV. The pre-fit background expectation is indicated by the dashed blue line.

Not reviewed, for internal circulation only

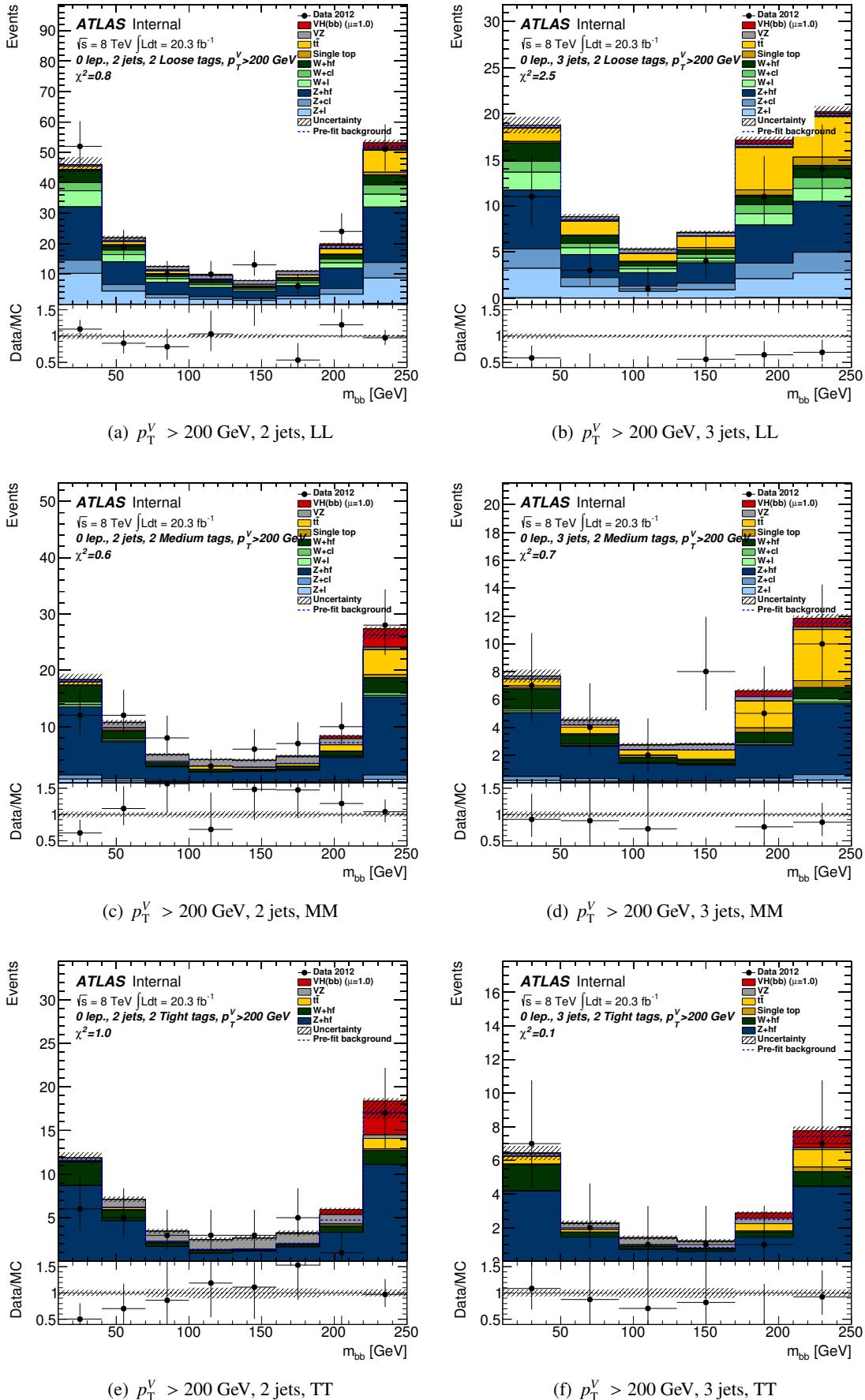


Figure 548: Post diboson fit plots for m_{jj} distribution in 0-lepton events in the *LL*, *MM* and *TT* tag categories for the 2-jets and the 3-jets events. Plots are shown for $p_T^V > 200$ GeV. The pre-fit background expectation is indicated by the dashed blue line.

internal circulation only

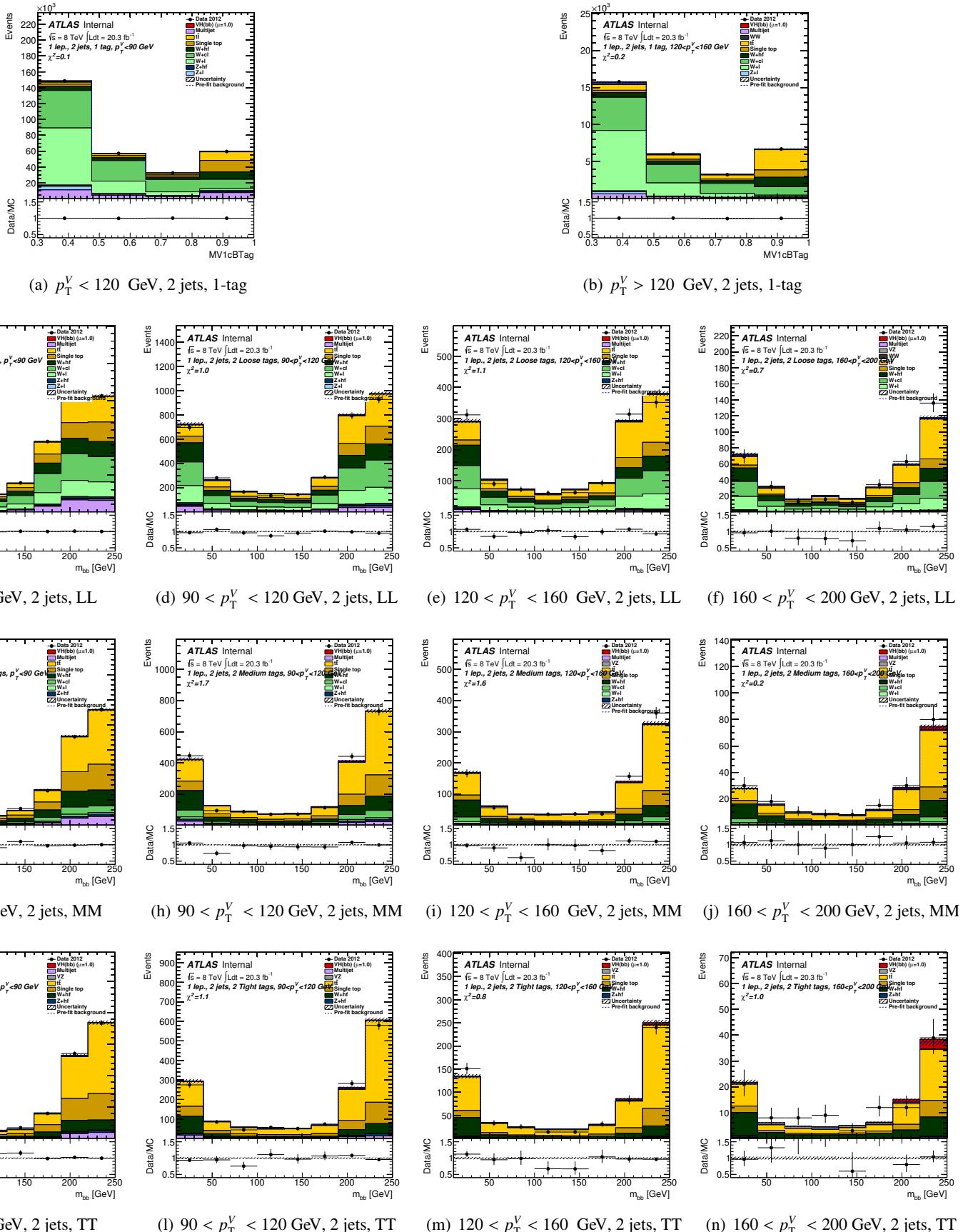


Figure 549: Post diboson fit plots for m_{jj} distribution in 1-lepton events in the 1-tag (where mv1c is used in the fit) LL , MM and TT tag categories for the 2-jets events. Plots are shown for $p_T^V < 90$ GeV, $90 < p_T^V < 120$ GeV, $120 < p_T^V < 160$ GeV and $160 < p_T^V < 200$ GeV. The pre-fit background expectation is indicated by the dashed blue line.

internal circulation only

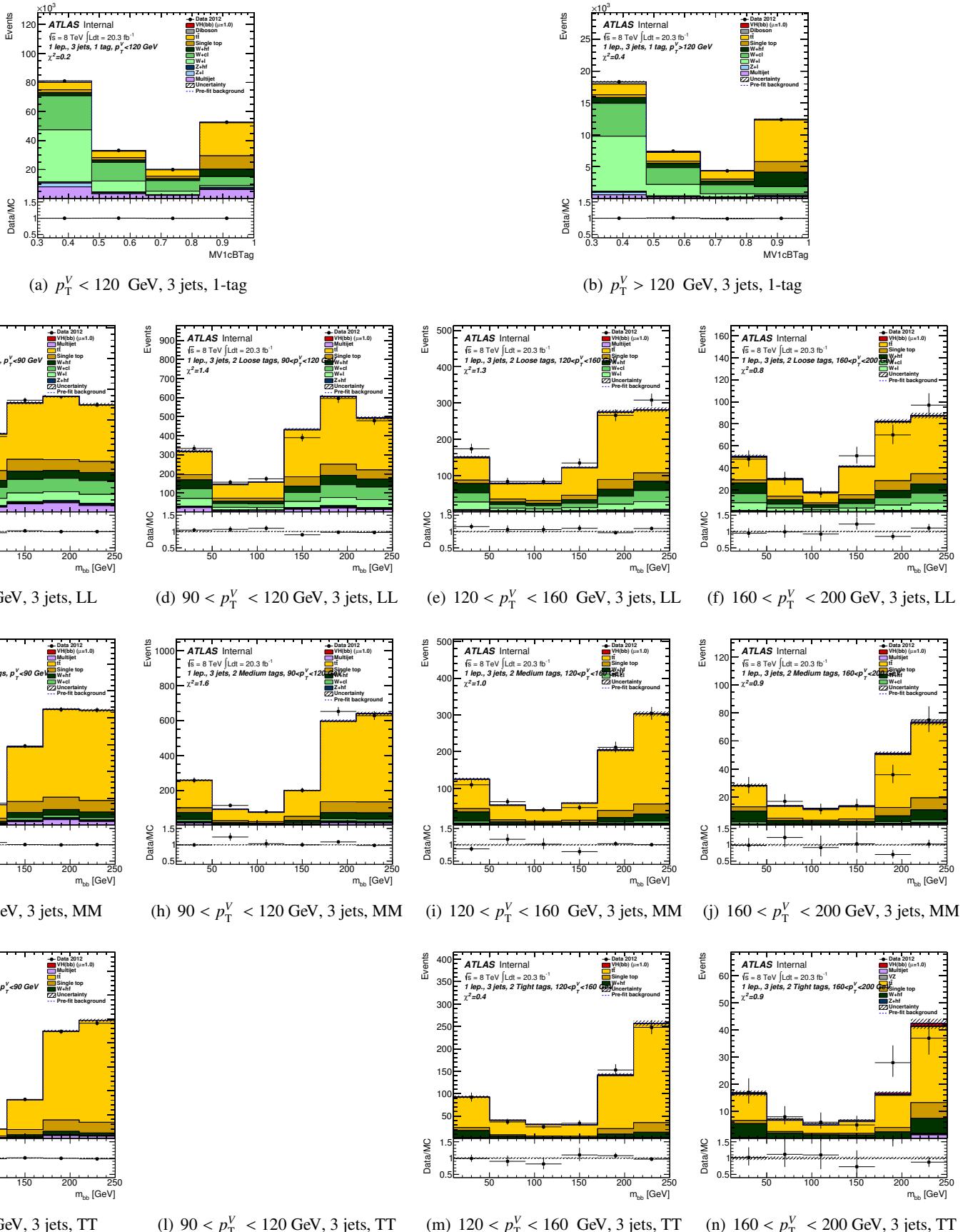


Figure 550: Post diboson fit plots for m_{jj} distribution in 1-lepton events in the 1-tag (where mv1c is used in the fit) LL , MM and TT tag categories for the 3-jets events. Plots are shown for $p_T^V < 90$ GeV, $90 < p_T^V < 120$ GeV, $120 < p_T^V < 160$ GeV and $160 < p_T^V < 200$ GeV. The pre-fit background expectation is indicated by the dashed blue line.

Not reviewed, for internal circulation only

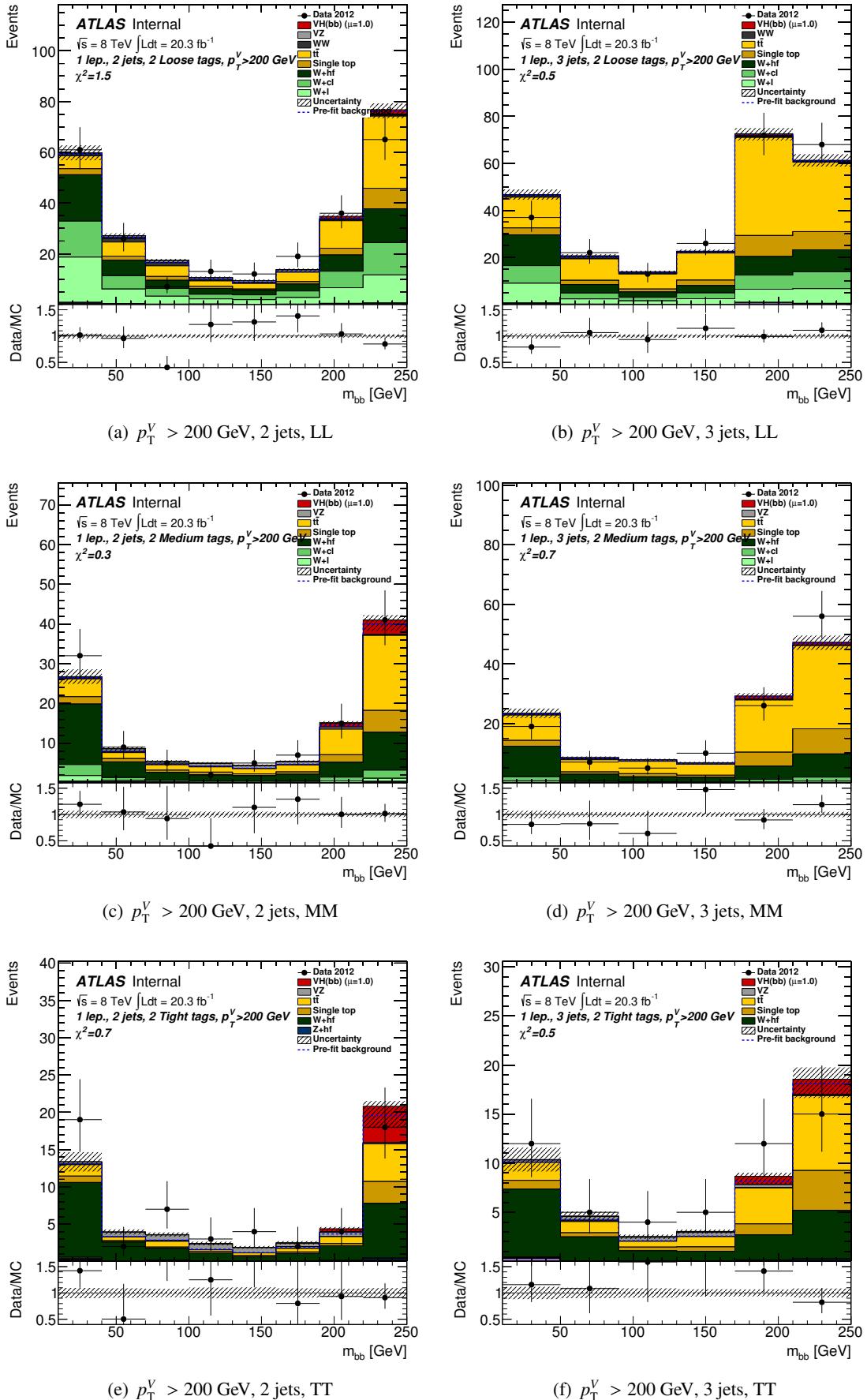


Figure 551: Post diboson fit plots for m_{jj} distribution in 1-lepton events in the *LL*, *MM* and *TT* tag categories for the 2-jets and the 3-jets events. Plots are shown for $p_T^V > 200 \text{ GeV}$. The pre-fit background expectation is indicated by the dashed blue line.

internal circulation only

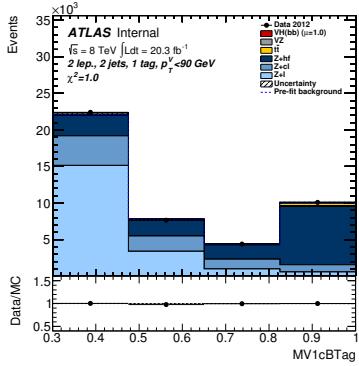
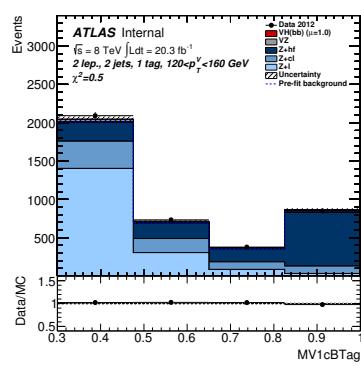
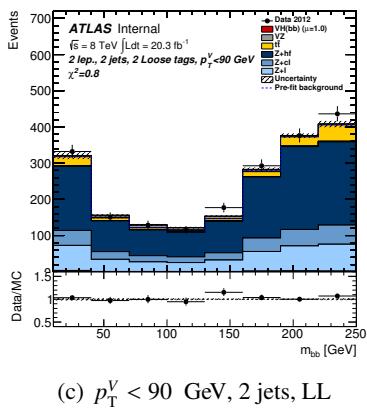
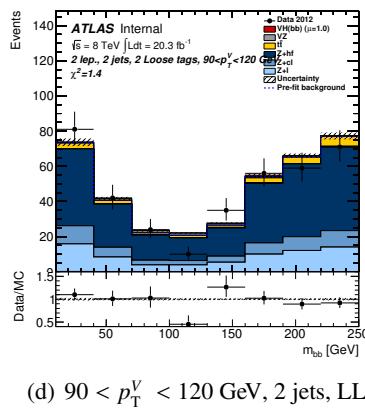
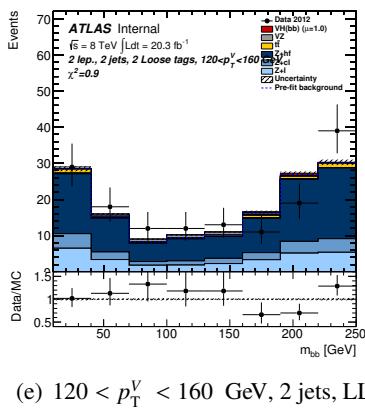
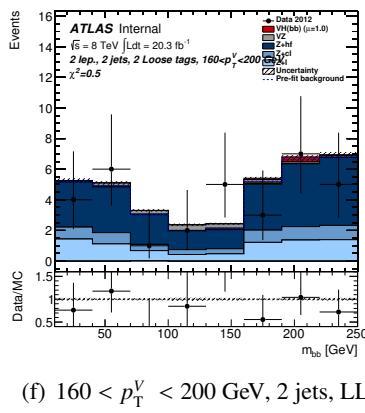
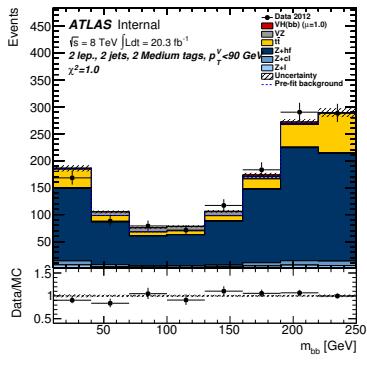
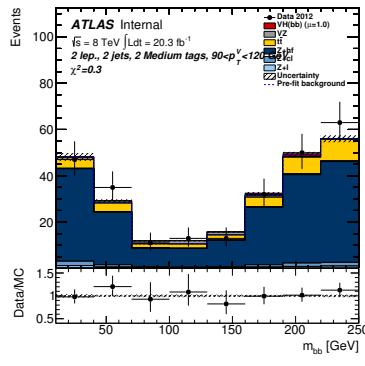
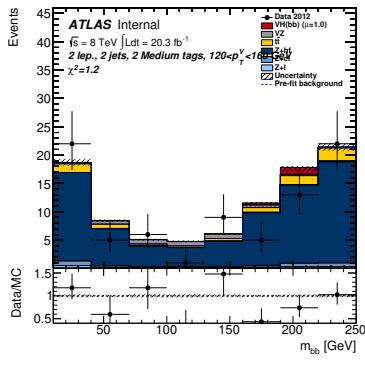
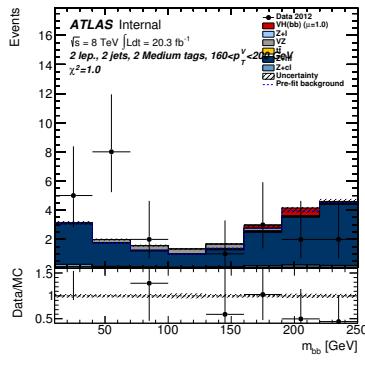
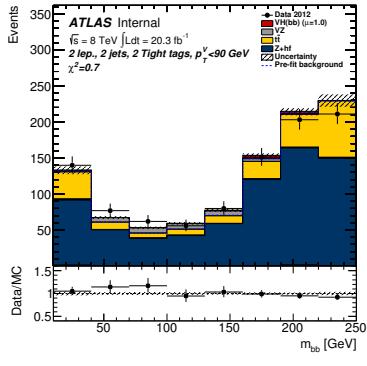
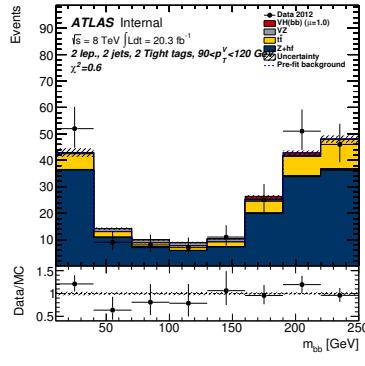
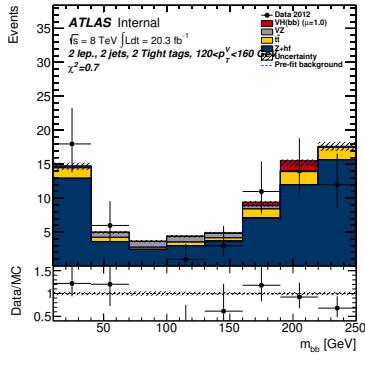
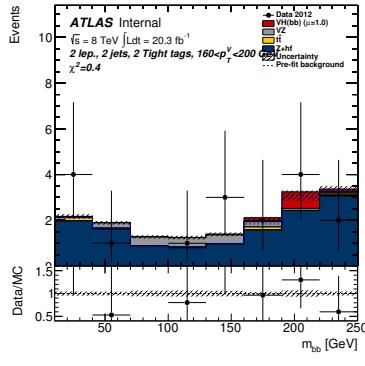
(a) $p_T^V < 120$ GeV, 2 jets, 1-tag(b) $p_T^V > 120$ GeV, 2 jets, 1-tag(c) $p_T^V < 90$ GeV, 2 jets, LL(d) $90 < p_T^V < 120$ GeV, 2 jets, LL(e) $120 < p_T^V < 160$ GeV, 2 jets, LL(f) $160 < p_T^V < 200$ GeV, 2 jets, LL(g) $p_T^V < 90$ GeV, 2 jets, MM(h) $90 < p_T^V < 120$ GeV, 2 jets, MM(i) $120 < p_T^V < 160$ GeV, 2 jets, MM(j) $160 < p_T^V < 200$ GeV, 2 jets, MM(k) $p_T^V < 90$ GeV, 2 jets, TT(l) $90 < p_T^V < 120$ GeV, 2 jets, TT(m) $120 < p_T^V < 160$ GeV, 2 jets, TT(n) $160 < p_T^V < 200$ GeV, 2 jets, TT

Figure 552: Post diboson fit plots for m_{jj} distribution in 2-lepton events in the 1-tag (where mv1c is used in the fit) *LL*, *MM* and *TT* tag categories for the 2-jets events. Plots are shown for $p_T^V < 90$ GeV, $90 < p_T^V < 120$ GeV, $120 < p_T^V < 160$ GeV and $160 < p_T^V < 200$ GeV. The pre-fit background expectation is indicated by the dashed blue line.

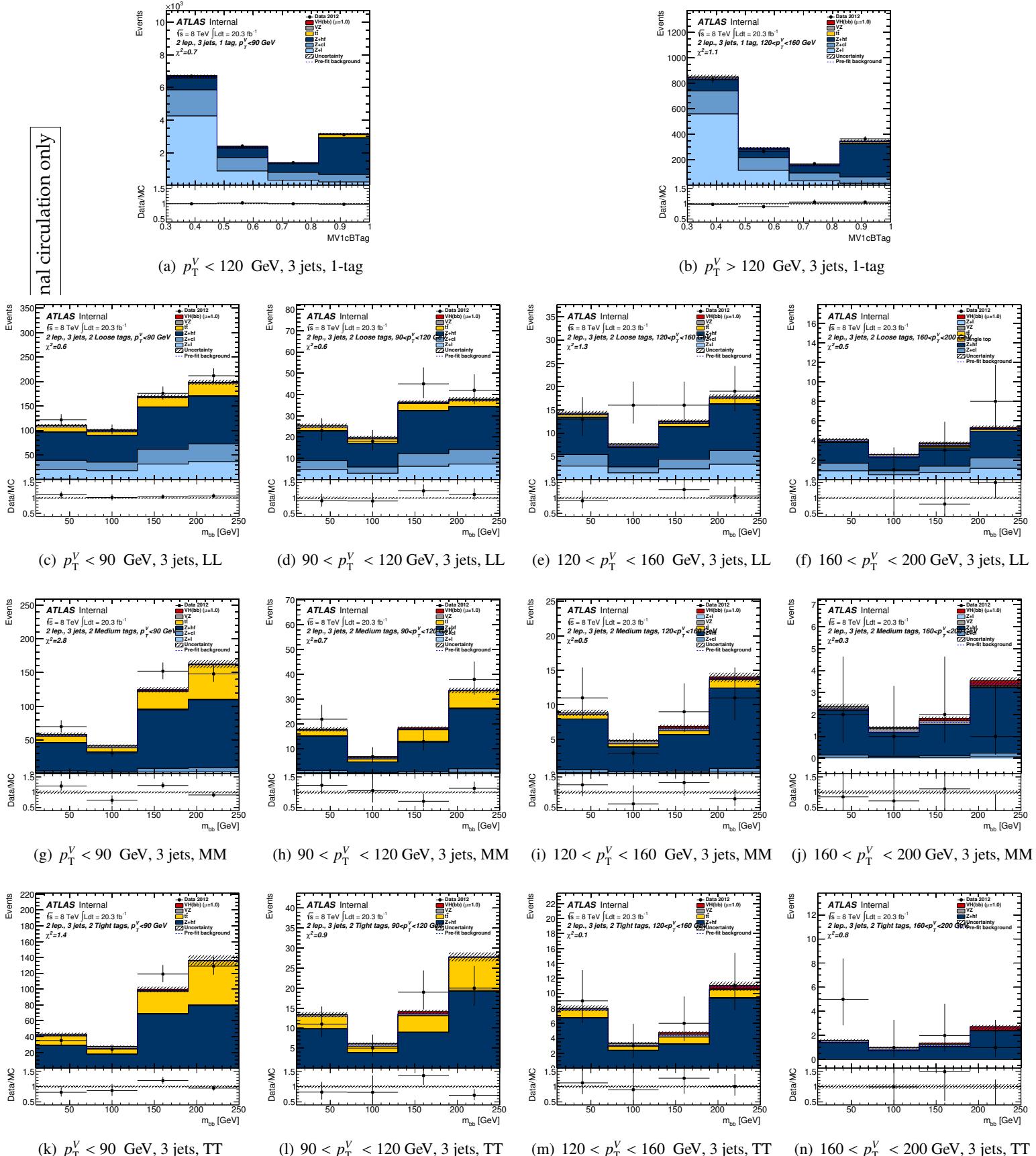


Figure 553: Post diboson fit plots for m_{jj} distribution in 2-lepton events in the 1-tag (where mv1c is used in the fit) LL , MM and TT tag categories for the 3-jets events. Plots are shown for $p_T^V < 90$ GeV, $90 < p_T^V < 120$ GeV, $120 < p_T^V < 160$ GeV and $160 < p_T^V < 200$ GeV. The pre-fit background expectation is indicated by the dashed blue line.

Not reviewed, for internal circulation only

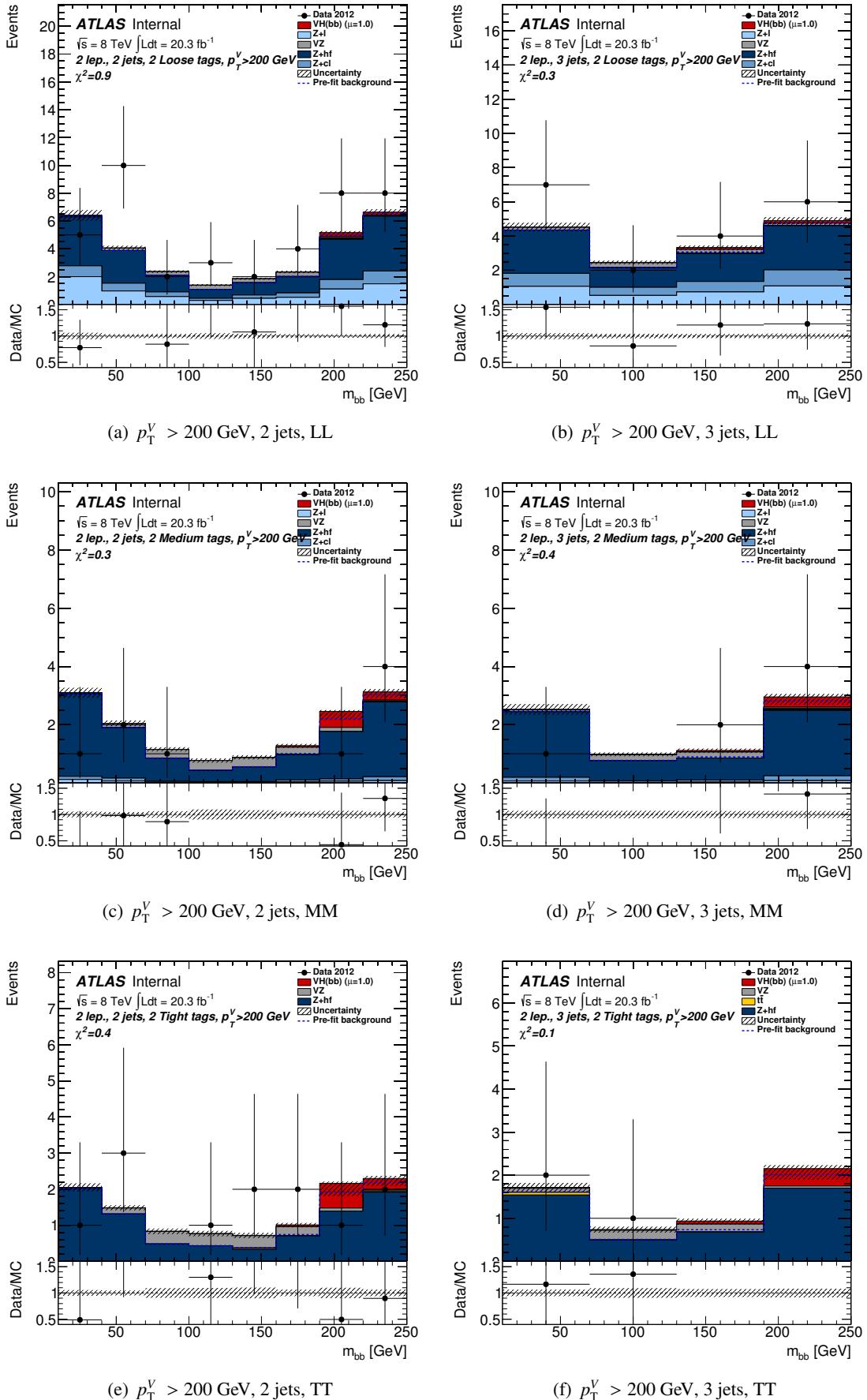


Figure 554: Post diboson fit plots for m_{jj} distribution in 2-lepton events in the LL , MM and TT tag categories for the 2-jets and the 3-jets events. Plots are shown for $p_T^V > 200$ GeV. The pre-fit background expectation is indicated by the dashed blue line.

5183 AM Impact of the BCH cleaning on the VH analysis

5184 AM.1 BCH cleaning for dummies

5185 During data taking, some tile modules were either temporarily or permanently masked. One of them, off
 5186 in the full dataset, was masked in the MC production. A correction based on adjacent live modules was
 5187 developed but it sometimes fails to properly estimate the lost energy. Jets in the masked modules (core
 5188 region) tend to be undercorrected, while jets in adjacent modules (edge region) are overcorrected. The
 5189 `BCHCleaningTool` [?] was developed to reject events with badly corrected jets, by picking random run
 5190 and lumiblock numbers to emulate the data taking conditions of the full dataset.

5191 The tool can run in two modes:

- 5192 • *tight*: purely geometrical rejection of events with a jet in the core or edge regions;
- 5193 • *medium*: rejection of events with jets in the core region, or jets in the edge region depending on
 5194 their `emfrac` and `BCH_CORR_CELL` values.

5195 AM.2 Samples used

5196 Nominal signal samples for the 0 and 1 lepton analyses were used:

- 5197 • $ZH \rightarrow vvbb$:

5198 `mc12_8TeV.161849.Pythia8_AU2CTEQ6L1_ZH125_nunubb.merge.NTUP_SMWZ.e1812_a188_a171_r3549_p1328_tid01219822_00`

- 5199 • $WH \rightarrow \ell vbb$:

5200 `mc12_8TeV.161805.Pythia8_AU2CTEQ6L1_WH125_lnubb.merge.NTUP_SMWZ.e1812_a188_a171_r3549_p1328_tid01219824_00`

5201 For data comparison the full `JetTauEtMiss` stream was processed.

5202 Special signal samples were also produced, with all four problematic modules masked (worst data
 5203 taking conditions). The $ZH \rightarrow vvbb$ sample was used in the following comparisons:

5204 `mc12_8TeV.161849.Pythia8_AU2CTEQ6L1_ZH125_nunubb.merge.NTUP_SMWZ.e1812_a188_a249_r4540_p1328/`

5205 AM.3 Impact on selection yield

5206 In the 0-lepton analysis several triggers are used, with the following luminosities:

- 5207 • `EF_xe80T_tclcw_loose` (1.91 fb^{-1} in periods A–B5)
- 5208 • `EF_xe80_tclcw` (2.12 fb^{-1} in periods A–B5)
- 5209 • `EF_xe80_tclcw_loose` (18.1 fb^{-1} in periods B6–End)

5210 The impact on the yield after applying the full 0-lepton selection is shown in Table 144 for both signal
 5211 MC and `JetTauEtMiss` stream, and it is very similar between data and MC. As expected the impact is
 5212 smaller for the first two triggers, used during early data taking when fewer modules were problematic.
 5213 For the remainder of this Appendix, only the `EF_xe80_tclcw_loose` trigger (representing 90% of the total
 5214 luminosity) will be used.

5215 The BCH cleaning acceptance loss is high for the tight selection (7–9%) and was deemed unacceptable
 5216 for the analysis. In the following, medium cleaning is the only considered option.

5217 The impact after the full 1-lepton selection on the $WH \rightarrow \ell vbb$ sample is reported in Table 145. It is
 5218 very similar to the 0-lepton analysis.

	EF_xe80T_tclcw_loose		EF_xe80_tclcw		EF_xe80_tclcw_loose		Data
	Medium	Tight	Medium	Tight	Medium	Tight	Medium
Full selection	1.3%	4.0%	1.3%	4.1%	2.3%	7.4%	2.5%
Exactly 2 jets	1.3%	4.0%	1.3%	4.1%	2.1%	6.9%	2.3%
Exactly 3 jets	1.4%	4.0%	1.5%	4.4%	3.3%	9.7%	3.1%
Btagging TT	1.5%	4.3%	1.3%	4.3%	2.3%	7.7%	2.2%
Btagging MM	1.2%	4.2%	1.4%	4.3%	2.2%	7.0%	2.8%
Btagging LL	1.3%	3.1%	1.3%	3.6%	2.5%	7.5%	2.3%

Table 144: Impact of BCH cleaning on yield after the full 0-lepton selection in data (last column) and for the signal sample for all triggers. For MC both the medium and tight BCH cleaning are given.

	Medium
Full selection (2+3 jets)	2.7%
Exactly 2jets	2.4%
Exactly 3jets	3.7%

Table 145: Impact of BCH cleaning on signal yield after the full 1-lepton selection.

	All quarks	All gluons
Full selection	0.2%	-0.2%
Exactly 2 jets	0.1%	-0.2%
Exactly 3 jets	0.6%	-0.1%
Btagging TT	0.3%	-0.2%
Btagging MM	0.3%	-0.2%
Btagging LL	0.1%	-0.1%

Table 146: Impact of BCH cleaning systematic uncertainty on yield after the full 0-lepton selection for the signal sample. The percentages shown correspond to the difference between applying the nominal BCH cleaning and the all-quark or all-gluon BCH mode.

The `BCHCleaningTool` provides a systematic uncertainty associated to the quark/gluon content of jets. Variations when assuming an all-quark (`isUp= 1`) or all-gluon (`isUp= -1`) content are reported in Table 146 and show a negligible effect.

For the 0-lepton analysis, the BCH effect was also measured when not applying the $\Delta\phi_{min}(E_T^{\text{miss}}, \text{jet})$ requirement, as this would enrich the sample in multijet-like events in a region used as a template for the multijet estimate. The impact was very similar to the full analysis, with a slightly more pronounced effect in data in the low $\Delta\phi_{min}(E_T^{\text{miss}}, \text{jet})$ region. More details can be found in Ref. [?].

Finally the 0-lepton analysis was also run on the special sample with four masked modules. Results were found in complete agreement with the default sample.

AM.4 Impact on distribution shapes

The leading jet p_T , m_{bb} , E_T^{miss} , $\phi(E_T^{\text{miss}})$, $\Delta\phi_{min}(E_T^{\text{miss}}, \text{jet})$ and $\Delta R(jj)$ distributions for events in the 0-lepton analysis that pass and fail BCH medium cleaning are shown in Fig. 555 for the signal sample and in Fig. 556 for the `JetTauEtMiss` stream. More distributions are available in Ref. [?], also split in E_T^{miss} bins as in the analysis. Within the limited statistics of events failing the BCH cleaning, one can conclude that there is no particular impact on the kinematic distributions. The $\phi(E_T^{\text{miss}})$ distributions

5234 do look different for pass and fail, as expected since the problematic modules are located at $\phi > 0$,
5235 generating E_T^{miss} in the opposite direction.

5236 The most important distribution in the end is the m_{bb} invariant mass. In data they look identical for
5237 pass and fail. In signal MC there may be a small shift observed, but even if it is indeed the case this
5238 would only affect a tiny fraction of the signal (2.5%) and the analysis would be insensitive to it.

5239 **AM.5 Impact on b -tagging**

5240 **AM.6 Conclusion**

5241 Given the very limited impact the BCH cleaning has on all kinematic variables, both in signal MC and
5242 in data, it was decided to not apply this procedure in order to avoid losing 2.5% signal efficiency

Not reviewed, for internal circulation only

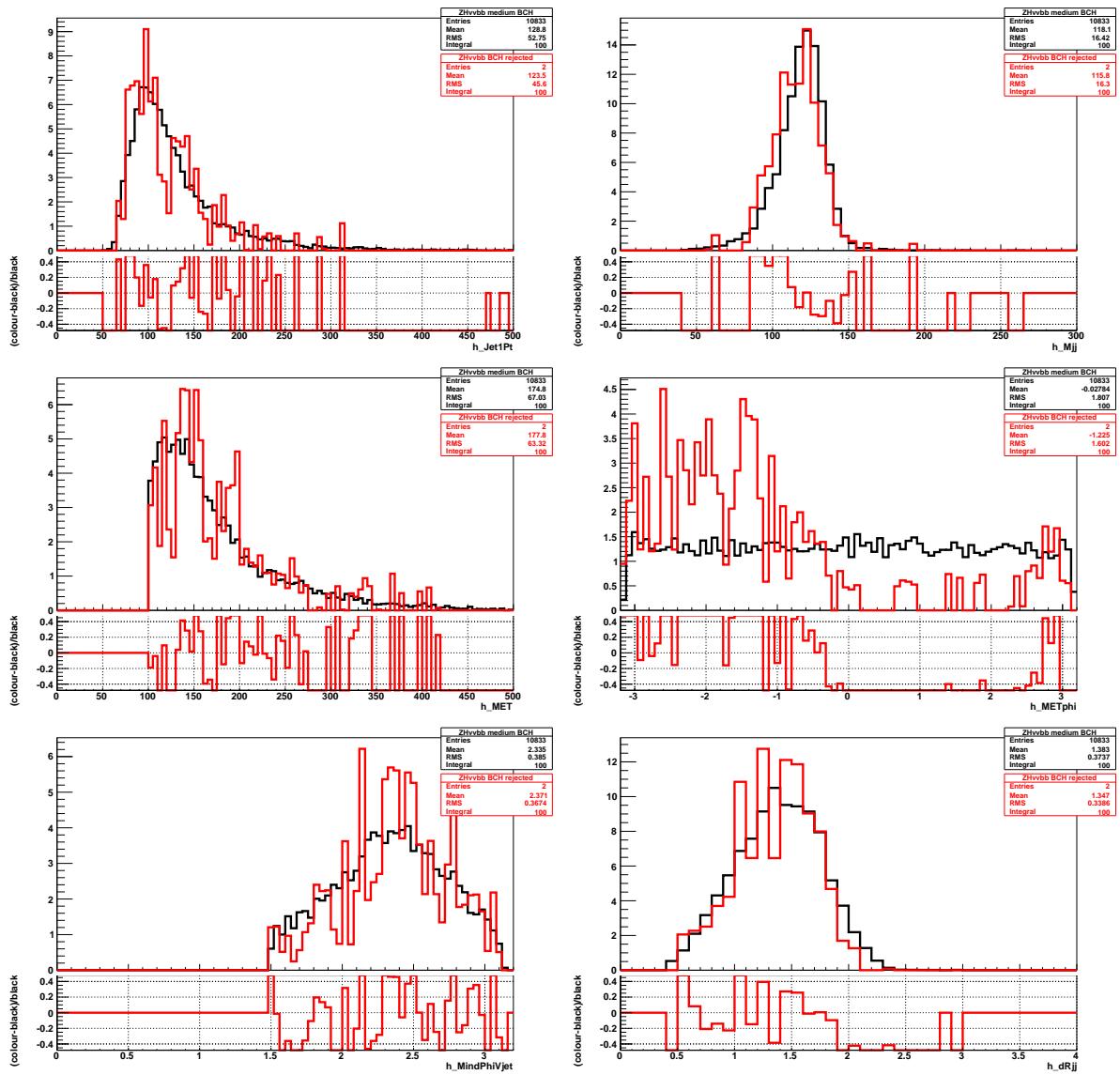


Figure 555: Leading jet p_T , m_{bb} , E_T^{miss} , $\phi(E_T^{\text{miss}})$, $\Delta\phi_{\min}(E_T^{\text{miss}}, \text{jet})$ and $\Delta R(jj)$ in the 0-lepton signal sample for events passing (black) and failing (red) BCH cleaning.

Not reviewed, for internal circulation only

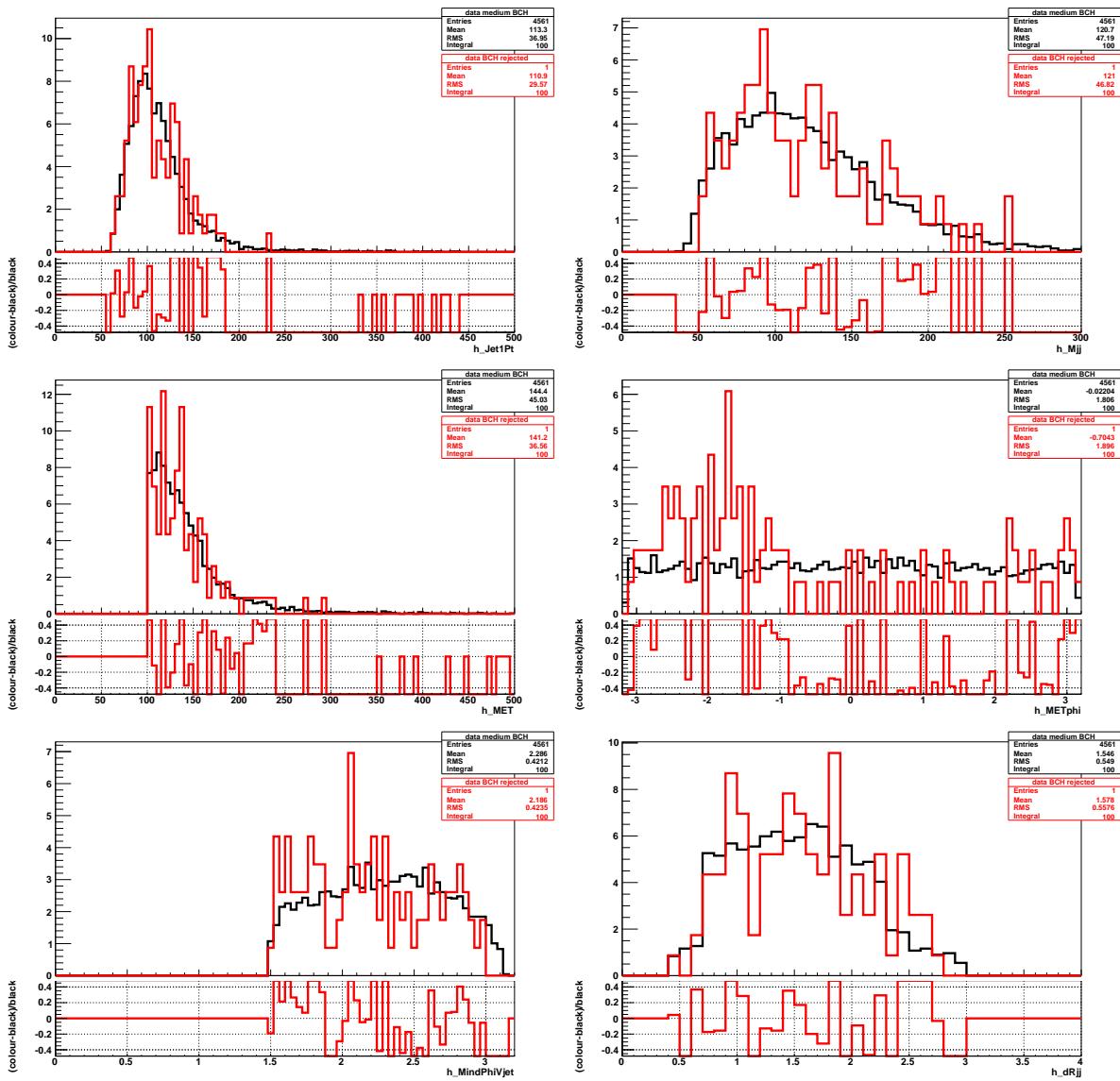


Figure 556: Leading jet p_T , m_{bb} , E_T^{miss} , $\phi(E_T^{\text{miss}})$, $\Delta\phi_{\min}(E_T^{\text{miss}}, \text{jet})$ and $\Delta R(jj)$ in the 0-lepton JetTauEtMiss sample for events passing (black) and failing (red) BCH cleaning.

Not reviewed, for internal circulation only

5243 AN Changes in different versions of this note

5244 AN.1 v0.1

5245 The object and event selections were included as well as a description of the MVA.

5246 AN.2 v0.2

5247 Changes included with respect to the previous version:

- 5248 • small typographical errors and beautification
- 5249 • replaced b-tagging cut table with a figure
- 5250 • missing upper m_T^W cut in 1 lepton dijet mass analysis fixed
- 5251 • major typo: iso_{calo} was tightened from EPS not iso_{track}
- 5252 • added track selection for jet variables
- 5253 • quantification of improvements from tightening iso_{calo} and 1-lepton event level cut changes
- 5254 • more information about continuous tagging/calibration used
- 5255 • p_T -reco correction plot
- 5256 • appendices for plots of MVA input variables, MVA output and dijet mass, for low MET (90-120 GeV) bin in 0-lepton, 0-lepton delayed steam, 1 lepton in MET triggered events, GSC calibration, muon in jet overlap, package list and table with all pkgs

5259 AN.3 v0.3

5260 Changes included with respect to the previous version:

- 5261 • small typographical errors and beautification
- 5262 • included missing plots (still have a few outstanding)
- 5263 • expanded modeling sections with specific references to EPS note and list of planned studies for MC specific systematics
- 5264 • remove d0 significance cut in muon channel
- 5265 • remove d0 cut in electron channel
- 5266 • expanded MVA section including optimization studies plot and an appendix with training diagnostic plots
- 5267 • 0-lepton multijet appendix
- 5268 • MVA training plots appendix
- 5269 • Switch H_T variable name to M_{eff} as it is a more accurate name.

Not reviewed, for internal circulation only

5272 **AN.4 v0.4**

5273 Changes included with respect to the previous version:

- 5274 • small typographical errors and beautification
- 5275 • including an update for most of the modeling systematics for the background
- 5276 • Brief W+jets systematic description and $t\bar{t}$ description
- 5277 • expand the MVA section to include some of the 2 dimensional checks
- 5278 • added experimental systematics section
- 5279 • added first description of the statistical model
- 5280 • added first draft of pulls, etc from the fit
- 5281 • added new appendixes which will contain a complete description of the studies done to determine the modeling systematics
- 5282
- 5283 • update of the cut based histograms, including systematic bands. Multi variate input and output plots will come in the next version of the note.
- 5284
- 5285 • Added 2-lepton MJ estimate

5286 **AN.5 v0.5**

5287 Changes included with respect to the previous version:

- 5288 • small typographical errors and beautification
- 5289 • improved fit model section including links from tables of systematics back to sections describing the source
- 5290
- 5291 • HAWK MC NLO EW correction summary from EPS note
- 5292 • Signal and background modeling sections were all revisited and revamped including summary tables
- 5293
- 5294 • kinematic fit mentioned in selection section
- 5295 • Added appendices: kinematic fit, $W+hf$, $t\bar{t}$ modeling
- 5296 • output transformation section has been expanded and moved into the statistical model section
- 5297 • up-to-date description of re-binning procedure (moved to stat model section)
- 5298 • update and additional post fit plots and fit diagnostic plots for the combined and individual fits
- 5299 • ordered log(S/B) plots
- 5300 • list of missing sections and appendices
- 5301 • list of outstanding ed board requests

Not reviewed, for internal circulation only

5302 **AN.6 v0.6**

- 5303 • add new NP pruning cuts since EPS(Section 8.5)
- 5304 • replace p_T^V plots with MV1c for MVA 1tag as this is what is used in the fit (Figures ??-??)

5305 **AN.7 v0.7**

- 5306 • Add closure test for truth tagging and dR correction
- 5307 • Add b-tagging generator dependent scale factors
- 5308 • Complete dedicated appendixes to describe the studies for the background modeling
- 5309 • Reorganization of the plots in the stat model, to make the reading easier, showing for each fit the
5310 list of distribution used in the fit - NOTE, some of the plots could come from different fits, and
5311 they need to be updated again with the next set of fit results
- 5312 • Add the unfolded post fit b-tagging scale factors
- 5313 • Update the description of the binning transformation for the MVA, adding a dedicated section to
5314 show the optimization of the previously used algorithm
- 5315 • Add a first preliminary version of the expected exclusion and local p_0 for both the MVA and the m_{bb}
5316 shape analysis
- 5317 • Add a first placeholder which will contain the description of the studies of important systematics
5318 or nuisance parameters.
- 5319 • Update of the description of the MET trigger appendix
- 5320 • Add Variations of MVA training including removing m_{bb} from input variables (example for 0
5321 lepton)

5322 **AN.8 What we had foreseen from version v0.6 to version v0.7**

- 5323 • deeper description of the studies done to estimate the modeling systematic, in the dedicated ap-
5324 pendixes **Done**
- 5325 • Full set of plots to check the correlations between the variables entering in the multivariate analysis
5326 **Some examples are given, but still looking for a convenient way to include them**
- 5327 • Update the plots for the pulls and fit results **Done for MVA, but they need to be updated**
- 5328 • Update the multivariate input and output plots **Done apart the 1 lepton channel, but they need to**
5329 **be updated**
- 5330 • Appendix for the diboson fit **For the next version**
- 5331 • Expand 1-lepton MJ section/appendix as more studies are completed **For the next version**
- 5332 • MV1c in the dijet mass analysis 1-tag region in all fit diagnostics and results **Done, but the fits**
5333 **need to be updated**

- 5334 • signal systematic: show comparison for variables other than pTV and add comparisons to Powheg
 5335 MINLO (Maria)[Reply at the end of Section 4.2.2 with additional parton shower differences being](#)
 5336 [checked.](#)
- 5337 • Wbb comparisons for MVA variables. Does assigned systematics cover all differences? Include
 5338 MVA input variable comparisons to the appendix. (Maria)[Appendix L.3](#)

Not reviewed, for internal circulation only

5339 AN.9 v0.8.1

- 5340 • Updates of alla the plots for the MVA analysis
- 5341 • Appendix for the BCH
- 5342 • Appendix for the MultiJet in 1-lepton
- 5343 • Some more text on the result section.
- 5344 • Implementation of most of the comments from the EdBoard of v7. For some of them some follow-up is ongoing.
- 5346 • Add all the unfolded post fit b-tagging scale factors
- 5347 • Update of the smoothing procedure
- 5348 • Up-to-date input variable plots. The 1-lepton needs still an update.
- 5349 • Appendix on the combination with the 7 TeV.

5350 AN.10 v0.9.1

- 5351 • Skematic for 1-lepton selection in iso_{track} versus iso_{calo} plane.
- 5352 • Full set of plots to check the correlations between the variables entering in the multivariate analysis
- 5353 • Keep update the plots for the pulls and fit results
- 5354 • Keep update the multivariate input and output plots
- 5355 • Appendix for the diboson fit
- 5356 • Expand 1-lepton MJ section/appendix as more studies are completed

5357 AN.11 v1.0.1

- 5358 • up-to-date input variable plots.
- 5359 • Update of the smoothing procedure
- 5360 • Fit understanding, including the discussion of the pulls- This is still a work in progress
- 5361 • BCH cleaning studies
- 5362 • unblinded results
- 5363 • diboson analysis description including MVA training

Not reviewed, for internal circulation only

5364 **AN.12 v1.1.1**

- 5365 • post-fit MVA input variables
- 5366 • MVA vs dijet mass pull comparisons
- 5367 • correlation of m_{jj} and MVA analysis
- 5368 • Higgs approved result

5369 **AN.13 v1.2.1**

- 5370 • 8TeV limit and p0 plot were an old version - updated
- 5371 • added tables for p0 and limit as a function of mass
- 5372 • The main body of this note describes the fit model and the fit results excluding events with 1 reconstructed electron and $p_T^W < 120$ GeV. This exactly corresponds to the results presented in the paper entering circulation. The Appendices however have not been completely updated: While the post-fit MVA input variable distribution using the fit result of the 0, 1, and 2-lepton channels together and the pre/post fit tables have been updated, the results of the individual channels has not. Nevertheless in Figures 43-48 and Figures 50-55 the combined fit pulls are compared to the individual channel pulls. Therefore the only missing piece of information from the individual fits is the post-fit plots themselves. The reason for not including the 1-electron channel for $p_T^W < 120$ GeV is summarized in Section 8.1.

5381 **AN.14 Outstanding Specific Ed Board Requests**

- 5382 • None

5383 **AO Missing**

5384 The following is a list of items/sections which are missing or known to be out of date in the main body
 5385 of the text

- 5386 • None
- 5387 The following items are missing from appendices
- 5388 • individual lepton fits in appendices only

5389 AP Package List

The list in table 147 show the version of the common packages used.

atlasoff/DataQuality/GoodRunsLists/tags/GoodRunsLists-00-01-03
atlasoff/PhysicsAnalysis/AnalysisCommon/PATCore/tags/PATCore-00-00-12
atlasoff/PhysicsAnalysis/TileID/TileTripReader/tags/TileTripReader-00-00-15
atlasoff/PhysicsAnalysis/AnalysisCommon/PileupReweighting/tags/PileupReweighting-00-02-11
atlasoff/Reconstruction/egamma/egammaEvent/tags/egammaEvent-03-06-41
atlasoff/Reconstruction/egamma/egammaAnalysis/egammaAnalysisUtils/tags/egammaAnalysisUtils-00-04-46
atlasoff/PhysicsAnalysis/ElectronPhotonID/ElectronEfficiencyCorrection/tags/ElectronEfficiencyCorrection-00-00-34
atlasoff/PhysicsAnalysis/ElectronPhotonID/ElectronPhotonSelectorTools/tags/ElectronPhotonSelectorTools-00-00-55
atlasoff/PhysicsAnalysis/MuonID/MuonIDAAnalysis/MuonMomentumCorrections/tags/MuonMomentumCorrections-00-08-07
atlasoff/PhysicsAnalysis/MuonID/MuonIDAAnalysis/MuonEfficiencyCorrections/tags/MuonEfficiencyCorrections-02-01-17
atlasoff/PhysicsAnalysis/MuonID/MuonIDAAnalysis/MuonIsolationCorrection/tags/MuonIsolationCorrection-01-01
atlasoff/Trigger/TrigAnalysis/TrigMuonEfficiency/tags/TrigMuonEfficiency-00-02-42
atlasoff/Reconstruction/Jet/JetUncertainties/tags/JetUncertainties-00-08-07
atlasoff/Reconstruction/Jet/JetResolution/tags/JetResolution-02-00-02
atlasoff/Reconstruction/Jet/ApplyJetCalibration/tags/ApplyJetCalibration-00-03-18
atlasoff/Reconstruction/Jet/JetAnalysisTools/ApplyJetResolutionSmearing/tags/ApplyJetResolutionSmearing-00-01-02
atlasoff/Reconstruction/Jet/JetAnalysisTools/JVFUncertaintyTool/tags/JVFUncertaintyTool-00-00-04
atlasoff/PhysicsAnalysis/JetMissingEtID/JetSelectorTools/tags/JetSelectorTools-00-00-23
atlasoff/Reconstruction/MissingETUtility/tags/MissingETUtility-01-02-06
atlasoff/PhysicsAnalysis/JetTagging/JetTagPerformanceCalibration/CalibrationDataInterface/CalibrationDataInterface-00-03-06
atlasphys/Physics/Higgs/HSG5/Limits/InputPreparation/TrigMETEfficiency/tags/TrigMETEfficiency-00-00-10

Table 147: Complete list of packages used in the analysis

5390

5391 For the continuous b-tagging calibration the root file used is

5392 **Summer2013_continuous_MV1c.root**

5393 which comes from the file of the same name in

5394 `atlasperf/CombPerf/FlavorTag/JetTagPerformanceCalibration/Continuous/trunk/CDIfiles`

5395 from revision 296440 after the custom efficiency maps discussed in Appendix CITE have been added.Likelihood-

5396 based multijet rejection tool described in Appendix C can be obtained from this TWiki

5397 <https://twiki.cern.ch/twiki/bin/viewauth/AtlasProtected/LikelihoodForLowMETZHvvbb>

5398 Add SVN area.